Advances in Mechanical Engineering

Numerical Simulation of Fluid Flow and Heat Transfer Processes

Guest Editors: Bo Yu, Tomoaki Kunugi, Toshio Tagawa, Shuyu Sun, Moran Wang, and Yi Wang

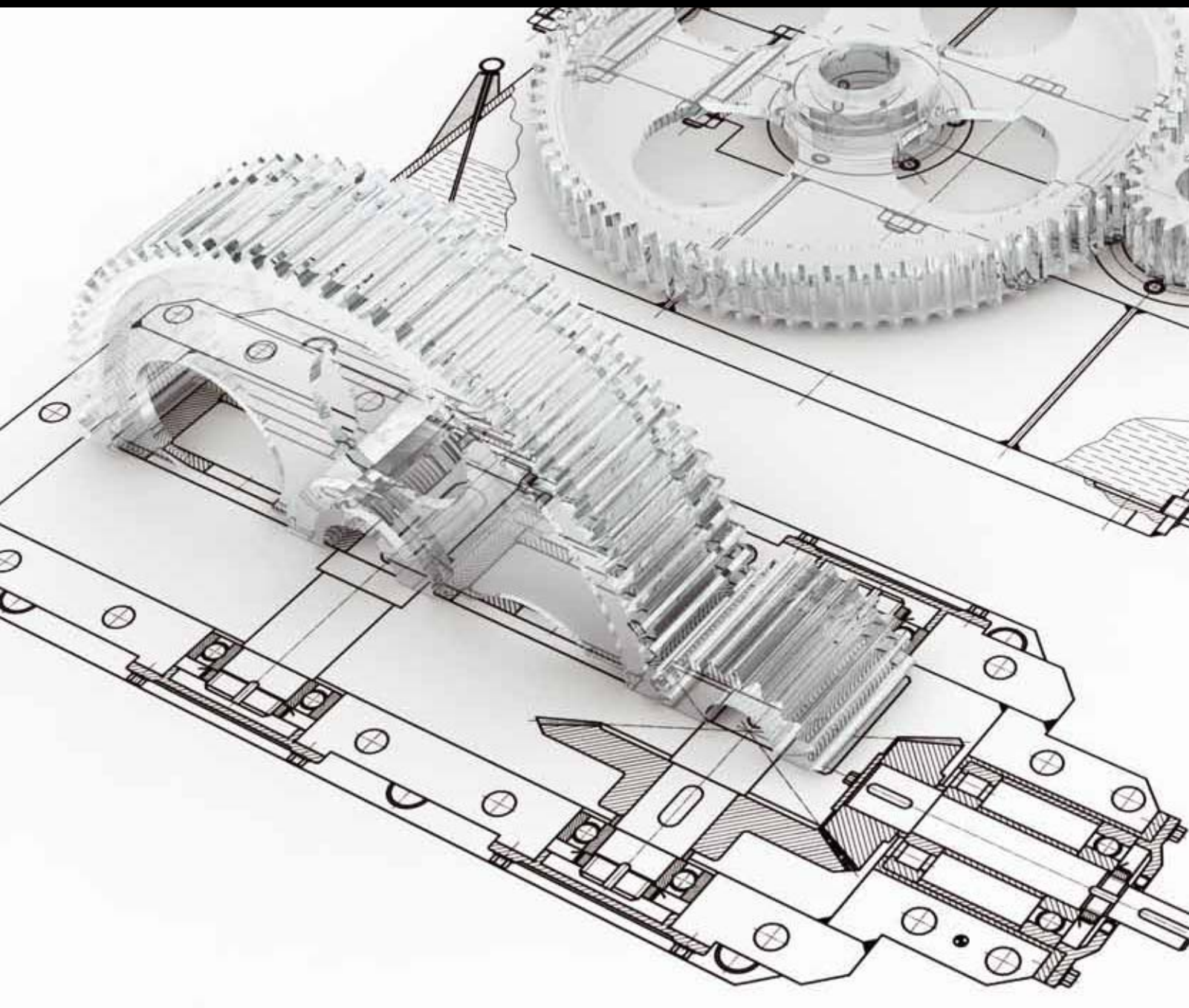

Numerical Simulation of Fluid Flow and Heat Transfer Processes

Advances in Mechanical Engineering

Numerical Simulation of Fluid Flow and Heat Transfer Processes

Guest Editors: Bo Yu, Tomoaki Kunugi, Toshio Tagawa, Shuyu Sun, Moran Wang, and Yi Wang

Editorial Board

Contents

Contents

Hindawi Publishing Corporation
Advances in Mechanical Engineering
Volume 2013, Article ID 497950, 3 pages
http://dx.doi.org/10.1155/2013/497950

Editorial

Numerical Simulation of Fluid Flow and Heat Transfer Processes

Bo Yu,[1] Tomoaki Kunugi,[2] Toshio Tagawa,[3] Shuyu Sun,[4] Moran Wang,[5] and Yi Wang[1,4]

[1] *National Engineering Laboratory for Pipeline Safety, Beijing Key Laboratory of Urban Oil and Gas Distribution Technology, China University of Petroleum, Beijing 102249, China*
[2] *Department of Nuclear Engineering, Kyoto University, C3-d2S06, Kyoto Daigaku-Katsura, Nishikyo-Ku, Kyoto 615-8540, Japan*
[3] *Department of Aerospace Engineering, Tokyo Metropolitan University, 6-6 Asahigaoka, Hino, Tokyo 191-0065, Japan*
[4] *Computational Transport Phenomena Laboratory, Division of Physical Science and Engineering, King Abdullah University of Science and Technology, Thuwal 23955-6900, Saudi Arabia*
[5] *Department of Engineering Mechanics and CNMM, Tsinghua University, Beijing 100084, China*

Correspondence should be addressed to Bo Yu; yubobox@vip.163.com

Received 27 June 2013; Accepted 27 June 2013

Fluid flow and heat transfer processes are ubiquitous in nature and engineering. They exist in many aspects of industrial operations and daily life. Numerical simulations of these processes have been important methods for fundamental and applicable researches. This special issue focuses on the latest achievements in the two aspects. We received 63 active submissions from the United States of America, Canada, Mexico, France, Italy, Norway, Saudi Arabia, Turkey, China, Japan, Pakistan, Republic of Korea, and so forth and finally accepted 35 research articles to publish them in the special issue after peer reviews. The topics cover the researches having solid theoretical fundaments including turbulent fluid flow and heat/mass transfer and the researches having strong backgrounds of applications.

In the field of turbulent fluid flow, 10 articles have been published. The following articles make efforts on direct numerical simulation (DNS), the Reynolds averaged Navier-Stokes (RANS) model, and large eddy simulation (LES) of turbulence. The article "*DNS study of the turbulent Taylor-vortex flow on a ribbed inner cylinder*" by T. Tsukahara et al. shows the investigation of turbulent Taylor-vortex flows over regularly spaced square ribs mounted on a rotating inner cylinder surface. The authors find that Taylor vortices remaining over roughened cylinder surfaces can lead to less pressure drag and an enhanced backflow in the recirculation zone. The article "*Turbulence modulation by small bubbles in the vertical upward channel flow*" by M. Pang et al. presents the mechanisms of the liquid turbulence modulation induced by the addition of small bubbles. Intensified turbulence near the wall and slightly weakened turbulence in the channel region are discovered. In the article entitled "*A modified k-ε model for computation of flows with large streamline curvature*" by J.-L. Yin et al., the authors propose an improved RANS model for system rotation and streamline curvature effects and provide an effective way for turbulence modeling. In the article entitled "*Large eddy simulation of inertial particle preferential dispersion in a turbulent flow over a backward-facing step*" by B. Wang et al., LES of a turbulent flow with inertial particle dispersion over a backward-facing step is performed. The research conclusions are useful for further understanding the two-phase turbulence physics and establishing accurate engineering prediction models of particle dispersion. In the article "*Comparisons of LES and RANS computations with PIV experiments on a cylindrical cavity flow*" by W.-T. Su et al., RANS and LES methods are compared. The results show that LES is more suitable for predicting the complex flow characteristics inside complicated three-dimensional (3D) geometries. In the article "*Experimental validation of volume of fluid method for a sluice gate flow*" by A. A. Oner et al., two-dimensional (2D) open channel flow under a vertical sluice gate can be successfully analyzed by the volume of fluid (VOF) method-based modeling after the experimental validation. The following four articles focus on aerodynamics or drag reduction. "*Aerodynamic performance prediction of straight-bladed vertical axis wind turbine based on CFD*" by L. X. Zhang et al. demonstrates that the leading edge separation

vortex and its movement on the airfoil surface have a significant impact on the aerodynamic performance because blades experience mild and deep stalls at low tip speed ratio. The article "*Vortex-induced vibrations of a square cylinder with damped free-end conditions*" by S. Manzoor et al. summarizes the vortex-induced vibrations of a square cylinder in a wind tunnel and suggests proper revision of the wake model used for analytical lift force predictions. In the article "*The polymer effect on nonlinear processes in decaying homogeneous isotropic turbulence*" by W. H. Cai et al., the authors study the behaviors of nonlinearities affected by polymer additives in decaying homogenous isotropic turbulence. They find that polymer has a negative effect on enstrophy and strain production, that is, depression of nonlinearity. In the article "*Wavelet analysis on turbulent structure in drag-reducing channel flow based on direct numerical simulation*" by X. Wu et al., wavelet transformation is applied to decompose velocity fluctuation time series into ten different frequency components including approximate components and detailed components. Features of turbulent multiscale structures are shown intuitively by continuous wavelet transform, verifying that turbulent structures become much more regular in drag-reducing flow.

In the field of heat/mass transfer, 9 articles have been published. The articles "*Numerical analysis of flow around a moving object by an immersed boundary method with the level set method*" by A. Iijima et al. and "*Comparison study on linear interpolation and cubic B-spline interpolation proper orthogonal decomposition methods*" by X. Wang et al. are investigations of numerical methods for fluid flow and heat transfer. The former develops a new immersed boundary method with advantages of accuracy, flexibility, and rapidness combined with the level set method. The latter concludes that the proper orthogonal decomposition method with cubic B-spline interpolation is more accurate than that with linear interpolation. In the article entitled "*Numerical model on frost height of round plate fin used for outdoor heat exchanger of mobile electric heat pumps*" by M.-Y. Lee, the numerical model for prediction of the frost growth of the round plate fin is established. The prediction on the frost height with time is improved by using the frost thermal conductivity reflecting the void fraction and density of ice crystal with frost growth. In the article entitled "*Understanding of thermal conductance of thin gas layers*" by X. Shan and M. Wang, the authors study heat conductions in a thin gas layer at micro- and nanoscales between two straight walls by atomistic modeling. They indicate that two dominating factors to the thermal conductivity reduction of thin gas layers are the temperature jump on wall surfaces and the properties changing significantly by the confined space. In the article "*Modeling and numerical simulation of the grinding temperature field with nanoparticle jet of MQL*" by C. H. Li et al., the heat transfer model of surface grinding temperature field with nanoparticle jet flow of MQL and the proportionality coefficient model of energy input workpiece is established. It is found that MQL grinding conditions with additive nanoparticles demonstrate great impact on the weakening of temperature effect on the grinding zone. In the article "*An analytical approximation for continuous flow microwave heating of liquids*" by G. Cuccurullo et al., a numerical and analytical model is developed to simulate temperature profiles in continuous laminar pipe flow during microwave heating. The simplified analytical model can lead to an easy way to predict the heat transfer through the pipe. In the article "*On full-tensor permeabilities of porous media from numerical solutions of the Navier-Stokes equation*" by Y. Wang et al., a new method combining Navier-Stokes equation and Darcy's law is proposed to compute full-tensor permeability of porous media instead of simplified tensor in tradition. It is found that anisotropy becomes pronounced especially when convection is dominant. The followed two articles contribute on numerical studies of mixed convection heat transfer. The article "*Numerical study on the mixed convection heat transfer between a sphere particle and high pressure water in pseudocritical zone*" by L. Wei et al. makes efforts on mixed convection heat transfer between supercritical water and particles in supercritical water fluidized bed reactor, which is a new but rare focused topic recently. The results show that buoyancy force has a remarkable effect on flow and heat transfer processes, and variation of specific heat and conductivity plays a main role in determination of heat transfer coefficient. Article "*Numerical simulation of mixed convection in a rotating cylindrical cavity: influence of Prandtl number*" by G. Urquiza et al. describes the influence of the Prandtl number on flow in critical state on a cavity containing a cooling fluid, and the heat transfer in the inferior wall increases as the Prandtl number increases and aspect ratio decreases.

Additional 16 articles with strong backgrounds of applications in industry or daily life are also published. Five articles devote efforts to petroleum industry. In the article "*Numerical study on the effect of wax deposition on the restart process of a waxy crude oil pipeline*" by Q. Miao, the restart process of a wax crude oil pipeline is investigated numerically by a new model for wax deposition. The temperature drop during the shutdown process and the transient inlet pressure are presented, and the effect of the wax deposition on the safety of the restart process is clarified. In the article "*Analyses on heating energy saving of two hot waxy-crude oil pipelines laid parallel in one ditch*" by C. Sun and B. Yu, a new technology laying two oil pipelines in one ditch employed by the petroleum companies of China is numerically presented. It is found that two hot crude oil pipelines laid parallel in one ditch can dramatically save heating energy when compared with two pipelines laid, respectively, in two separate ditches. In the article "*Numerical simulation of gas-liquid-solid three-phase flow in deep wells*" by J. Xie et al., a new model for gas-liquid-solid annulus flow in the deep wells is established considering the effect of the cuttings on the pressure drop. It is found that temperature and pressure are greatly affected by well depth, drilling mud density, and gas kick while the effect of the cuttings on the total pressure drop is small. In the article "*Pressure change in tee branch pipe in oscillatory flow*" by D. Sakamoto et al., the authors propose a simulation method to predict the pressure changes in a pneumatic branch pipe under oscillatory flow. The results contribute to the understanding of unsteady flow of branch pipes in pneumatic systems. In the article "*Optimal model of operation parameters*

of gathering pipeline network with triple-line process" by Y. Liang et al., a mathematic model for the optimal operation of the gathering pipeline network is proposed and applied to the optimal operation analysis in North China Oilfield. Operation cost can be reduced by 2076 RMB/d, which demonstrates that this method contributes to the production cost reduction of old oilfields in their high water-cut stage. The article "*Effective resistance of gas flow in microchannels*" by X.-D. Shan and M.R. Wang studies fluid flow in microscale instead of macroscale for the previous five articles. They turn a complicated micromechanical problem into simple available formulae for designs and optimization of microengineering. Four articles discuss fluid flow in affiliations such as pump, tank, engine, and sprinkler. In the article "*Numerical simulation of the transient process of power failure in a mixed pump*" by X. Ma et al., the authors use a hydraulic-force coupling method to simulate the transient process of power failure condition. They conclude that the rotational speed decreases much faster than the flow rate in power failure accidents. In the article "*Analysis on shift of nature modes of liquid sloshing in a 3D tank subjected to oblique horizontal ground motions with damping devices*" by C.-H. Wu et al., the study of sloshing fluid in tanks with internal structures is extended from 2D to 3D. In the article "*Numerical simulation of PAHs formation and effect of operating conditions in di-diesel engines based on a comprehensive chemical mechanism*" by B.-J. Zhong and J. Xi, numerical simulations of polycyclic aromatic hydrocarbon (PAH) formation in a Chaochai 6102 bzl direct injection diesel engine are performed. PAHs first increase and then decrease with the increase in diesel crank angle. The diesel engine operating conditions have a significant effect on PAH formation. In the article "*Study on the fluidic component of the complete fluidic sprinkler*" by H. Li et al., the offset jet with control stream is analyzed in the simplified model. The yaw angle and the attachment angle of the offset jet flow increase with the pressure increase and vary little when the pressure is more than 0.5 MPa. Six articles are applicable researches relating artificial fish, solar energy, wood preservation, food package, champagne glasses and light. The article "*Evaluation of artificial caudal fin for fish robot with two joints by using three-dimensional fluid-structure simulation*" by Y. Takada et al. confirms that a good caudal fin for fish robot with two active joints is a rigid fin with a flexible material on the root by using the 3D fluid-structure interaction analysis. The article "*Performance analysis and application of three different computational methods for solar heating system with seasonal water tank heat storage*" by D. Sun et al. compares three different computational methods for a solar heating system with seasonal water tank heat storage. In the article "*Mathematical modeling of the high temperature treatment of birch in a prototype furnace*" by D. Kocaefe et al., a reliable and predictive model is developed to simulate numerically the high-temperature heat treatment process of wood preservation. In the article "*Numerical simulation on the food package temperature in refrigerated display cabinet influenced by indoor environment*" by Z. Chang et al., the food package temperature is investigated by numerical simulation under different conditions to study the relation between the food package temperature and ambient environment. A numerical modeling of bubble-driven flow patterns in a glass of champagne has been carried out by F. Beaumont et al. in the article "*Temperature dependence of ascending bubble-driven flow patterns found in champagne glasses as determined through numerical modeling.*" The velocities of the liquid phase significantly vary with the champagne temperature. In the article "*Numerical study of thermal behavior in alternating current light-emitting diodes*" by F.S. Hwu and H.-L. Hsieh, thermal characteristics of an alternating current light-emitting diode chip based on a 3D unsteady numerical simulation are discussed. Results show that the AC LED has a better performance under a higher frequency than under a lower frequency.

Bo Yu
Tomoaki Kunugi
Toshio Tagawa
Shuyu Sun
Moran Wang
Yi Wang

Hindawi Publishing Corporation
Advances in Mechanical Engineering
Volume 2013, Article ID 137086, 11 pages
http://dx.doi.org/10.1155/2013/137086

Research Article

On Full-Tensor Permeabilities of Porous Media from Numerical Solutions of the Navier-Stokes Equation

Yi Wang,[1,2] Shuyu Sun,[2] and Bo Yu[1]

[1] *National Engineering Laboratory for Pipeline Safety, Beijing Key Laboratory of Urban Oil and Gas Distribution Technology, China University of Petroleum, Beijing 102249, China*
[2] *Computational Transport Phenomena Laboratory, Division of Physical Science and Engineering, King Abdullah University of Science and Technology, Thuwal 23955-6900, Saudi Arabia*

Correspondence should be addressed to Shuyu Sun; shuyu.sun@kaust.edu.sa

Received 25 January 2013; Revised 28 May 2013; Accepted 3 June 2013

Academic Editor: Toshio Tagawa

A numerical method is proposed to compute full-tensor permeability of porous media without artificial simplification. Navier-Stokes (N-S) equation and Darcy's law are combined to design these numerical experiments. This method can successfully detect the permeability values in principle directions of the porous media and the anisotropic degrees. It is found that the same configuration of porous media may possess isotropic features at lower Reynolds numbers while manifesting anisotropic features at higher Reynolds numbers due to the nonlinearity from convection. Anisotropy becomes pronounced especially when convection is dominant.

1. Introduction

Permeability is a key parameter of porous media because it relates with many parameters, such as the infiltration, dielectric strength and thermophysics. It may strongly affect the design and production process of fibrous reinforcements, cement paste and so forth and related scientific researches. The permeability may vary over several orders of magnitude, and it plays an important role in petroleum migration and reservoir performance [1]. Therefore, the accurate measurement of permeability is always a hot topic in both industrial and academic fields. Many of these researches adopt experimental approaches, such as free-space methods, open-ended coaxial probe techniques, cavity resonators, transmission-line techniques, and gas-dynamic methods [2, 3].

Jensen and Heriot-Watt [4] proposed a statistical model for small-scale permeability using minipermeameter and core plug measurements. They suggested the minipermeameter measurement as a better choice. Wang et al. [5] discussed two experimental methods to determine the absolute values of in-plane permeability. They concluded that both the radial flow measurement method and the unidirectional flow measurement method were recommended to obtain reliable permeability data. Ferland et al. [6] proposed a concurrent method to estimate permeability at low cost. However, the experimental procedures can introduce uncertainty significantly on the estimated permeability. They suggested some special treatments to increase the reliability of experimental data. Some other researchers [7–10] also realized that permeability is difficult to measure although its definition is simple. Many factors, such as flow rate, pressure, fluid properties, handling process by human factors, edge effect, wall effect, single-equipment reproducibility, and between-equipment repeatability, could strongly influence the results of measurements. Therefore, the ability to obtain consistent permeability data depends on skilled and experienced experimental design, reproducible preparation of specimens, operation of equipment, and evaluation of measured raw data. This is the reason many published data observed by different persons often have significant differences for the same material. Weitzenböck et al. [11] pointed out that numerous practical problems caused three-dimensional (3D) permeability measurements to be very difficult. Then, they proposed an approach to measure the permeability

by a two-dimensional (2D) radial flow method, which allows the experimental axes not to align with the principal direction of permeability [12, 13].

Some researchers made efforts on measuring transport properties (including permeability) by numerical simulation. Keehm et al. obtained good results in estimating permeability and electric conductivity of complicated pore geometries using Lattice-Boltzmann method (LBM) [14]. Kameda et al. applied LBM to estimate 3D permeability through 2D images of small fragments of rocks. They obtained a valid permeability-porosity trend by using a significant number of such small fragments in statistical sense [15]. Saenger et al. estimated permeability through LBM flow simulation and compared mechanical and transport properties for the same digital rocks [16].

Since all physical parameters can be easily and exactly controlled in numerical simulations, the shortcomings of laboratory experiments mentioned previously can be avoided. In particular, numerical methods have the advantage of separately studying different physical processes coexisting in nature, which are uneasily separated in laboratory. It is easier to form standardization of measurement methods and obtain unchangeable results. It will be a very efficient and economical way for measuring properties of porous media combining with the digital rock physics [17, 18]. In the present paper, we studied how to establish this digital laboratory method for measuring permeability of porous media through directly solving the N-S equation, other than reconstructing it by LBM method. To the best knowledge of the authors, all studies of permeability prediction have been concerned only with diagonal permeability tensor actually. Full tensor of permeability has not been studied extensively since it has more general meanings for practical applications. Thus, we expand our research object from the simple diagonal permeability tensor to more general full permeability tensor. We select gravity in periodic domain as the driven force, instead of pressure widely used in previous studies [1–18]. This can avoid the edge effect encountered in experimental measurements. As a first trial, we assume incompressible single-phase flow to pass through the porous media in rectangular geometry, but the methodology can be extended to more complex applications, for example two-phase flow using diffuse interface models, which will be pursued in our future researches. The basic principles and proposed methods in this study will be presented next.

2. Principles and Methods

2.1. General Principles. The basic law that is used by experimental and numerical studies for measuring permeability is the Darcy's law:

$$\mathbf{u}_D = -\frac{\mathbf{k}}{\mu}\left(\nabla p - \rho \mathbf{g}\right), \tag{1}$$

where $\mathbf{u}_D$ is Darcy velocity (m/s), $\mathbf{k}$ is the permeability tensor (m^2), $\mathbf{g}$ is the gravitational acceleration (m/s^2), ∇p is the pressure gradient (Pa/m), ρ is the density of fluid (kg/m^3), and μ is the dynamic viscosity of fluid (Pa · s).

The N-S equation (2) and the continuity equation (3) that describe fluid flow in the continuum sense are as follows (Δ is the Laplace operator):

$$\frac{\partial \mathbf{u}}{\partial t} + (\mathbf{u}\cdot\nabla)\,\mathbf{u} = -\frac{1}{\rho}\nabla p + \frac{\mu}{\rho}\Delta \mathbf{u} + \mathbf{g}, \tag{2}$$

$$\nabla \cdot \mathbf{u} = 0. \tag{3}$$

Conventional methods for measuring permeability neglect gravity and drive the fluid flow by pressure because it is easier to control, especially for laboratory experiments. Here, we select to use the full expressions of (1)~(3) to determine the permeability. Periodic boundary condition is adopted so that boundary pressure needs not to be considered. It is pretty easier for numerical implementation and more sensible in nature because subsurface formation is in fact a periodic system or statistically periodic one. The general procedure is stated below.

Step 1. Solve (2) and (3) for incompressible single-phase flow in porous media and obtain several velocity fields as samples.

Step 2. Obtain volumetric velocity of the whole domain according to the samples obtained in Step 1.

Step 3. Solve permeability for the whole domain by directly setting the volumetric velocity as the Darcy velocity in (1).

The detailed numerical methods used in these three steps will be introduced in the next section.

2.2. Numerical Methods. As stated previously, we only consider simple 2D rectangular cases in the present study. The incompressible single-phase flow in porous media is modeled as the flow passing through a square barrier in a square domain with periodic boundary conditions. The numerical model is shown in Figure 1(a). L is the domain side length while a is the side length of the barrier. Γ_P means periodic boundary.

On this kind of domain, the vectors and tensors in (1)~(3) have the following forms:

$$\mathbf{u} = \begin{bmatrix} u_x \\ u_y \end{bmatrix}, \qquad \mathbf{g} = \begin{bmatrix} g_x \\ g_y \end{bmatrix},$$

$$\mathbf{k} = \begin{bmatrix} k_{xx} & k_{xy} \\ k_{yx} & k_{yy} \end{bmatrix}, \qquad \nabla p = \begin{bmatrix} \dfrac{\partial p}{\partial x} \\ \dfrac{\partial p}{\partial y} \end{bmatrix}. \tag{4}$$

Here $g_x = g\cos\theta$, $g_y = g\sin\theta$, $g = 9.807\ m/s^2$, k_{xx}, and k_{yy} are the diagonal components of the permeability tensor while k_{xy} and k_{yx} are the off-diagonal components of the permeability tensor. These four variables are all independent of each other. Three typical directions of gravity are chosen to calculate the full-tensor permeability. They are represented by $\theta = 3\pi/2, \pi$, and $\pi/4$, respectively, and named "Sample a," and "Sample b," and "Sample c" as shown in Figure 1(b).

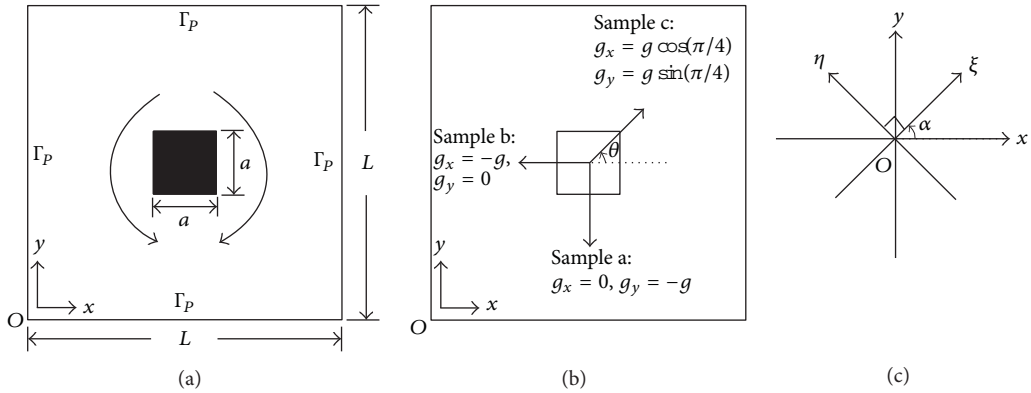

Figure 1: Calculation methodology: (a) numerical model; (b) sampling; and (c) coordinate rotation.

The numerical algorithm for solving (2)~(3) in "Step 1" is projection method with fully explicit spatial discretization (but solve pressure implicitly) using second-order finite difference central type scheme. Cyclic tridiagonal matrix algorithm (CTDMA) is applied to accelerate the convergence of pressure iteration. The mesh size is set as 80×80. Flow is considered to reach the steady state as the temporal truncation $|\partial \mathbf{u}/\partial t|$ averaged over the whole domain is lower than 10^{-6} m/s^2.

The volumetric velocity in "Step 2" is defined as follows:

$$\mathbf{U} = \frac{1}{V_d}\int_{V_d} \mathbf{u} dV_d, \tag{5}$$

where $\mathbf{U} = \begin{bmatrix} U_x \\ U_y \end{bmatrix}$ is the volumetric velocity with the components U_x and U_y in the x and y directions. V_d is the volume of the whole domain. Equation (5) has a discrete expression in this study:

$$U_x = \frac{(\sum u_x)}{N_x}, \qquad U_y = \frac{(\sum u_y)}{N_y}, \tag{6}$$

where N_x and N_y are the total number of u_x and u_y on grid cells, respectively. The values of u_x and u_y can be determined by solving the N-S equation so that U_x and U_y can be determined.

The volumetric velocity in (5) is actually the Darcy velocity in (1); that is, $\mathbf{u}_D = \mathbf{U}$. In the Darcy scale averaged in the whole domain, pressure gradient should be zero because of the periodic boundary condition; that is, $\nabla p = 0$. Thus, (1) can be rewritten as

$$\mathbf{U} = \frac{\mathbf{k}}{\mu}\rho \mathbf{g}. \tag{7}$$

For Sample a ($(g_y)_a = -g$), (7) becomes

$$(U_x)_a = \frac{k_{xy}}{\mu}\rho(g_y)_a, \tag{8a}$$

$$(U_y)_a = \frac{k_{yy}}{\mu}\rho(g_y)_a. \tag{8b}$$

For Sample b ($(g_x)_b = -g$), (7) becomes

$$(U_x)_b = \frac{k_{xx}}{\mu}\rho(g_x)_b, \tag{9a}$$

$$(U_y)_b = \frac{k_{yx}}{\mu}\rho(g_x)_b. \tag{9b}$$

For Sample c ($(g_x)_c = g\cos(\pi/4)$, $(g_y)_c = g\sin(\pi/4)$), (7) becomes

$$(U_x)_c = \frac{k_{xx}}{\mu}\rho(g_x)_c + \frac{k_{xy}}{\mu}\rho(g_y)_c, \tag{10a}$$

$$(U_y)_c = \frac{k_{yx}}{\mu}\rho(g_x)_c + \frac{k_{yy}}{\mu}\rho(g_y)_c. \tag{10b}$$

Theoretically, (8a), (8b), (9a), and (9b) are adequate to determine the four components of the full-tensor permeability. However, $(U_x)_a$ and $(U_y)_b$ are always very close to zeros since they are orthogonal to the bulk flow directions and large numerical errors may exist. Thus, k_{xy} and k_{yx} determined by (8a) and (9b) are always very close to zeros. This apparently violates the fact that k_{xy} and k_{yx} may be far from zeros for some cases. The application of (8a) and (9b) actually makes the full-tensor permeability decay to a diagonal permeability so that they should be canceled. To predict the off-diagonal components accurately, (10a) and (10b) are utilized since the bulk flow in Sample c has equivalent projections in the x and y directions so that $(U_x)_c$ and $(U_y)_c$ are both accurate. Therefore, the final equations to determine the four components of the permeability tensor should be the four equations (8b), (9a), (10a), and (10b), which are used in "Step 3." The procedure is calculating k_{xx} by (9a) and k_{yy} by (8b) and substituting them to (10a) and (10b) to obtain k_{xy} and k_{yx}, respectively.

In practice, it is of interest to detect the maximum permeability, the minimum permeability, principle direction, and anisotropy so that essential features of reservoir, which are independent of coordinate systems and samplings, can be described. Therefore, the original permeability tensor can be transformed by rotating the original xOy coordinate

Table 1: Characteristic parameters.

Case	V (m/s)	R_h (m)	Re	Da	$\mathrm{ReDa}^{1/2}$
Case 1	1.16×10^{-6}	2.50×10^{-8}	2.90×10^{-8}	6.25×10^{-4}	7.25×10^{-10}
Case 2	6.62×10^{-7}	5.00×10^{-8}	3.31×10^{-8}	2.50×10^{-3}	1.66×10^{-9}
Case 3	3.96×10^{-7}	7.50×10^{-8}	2.97×10^{-8}	5.63×10^{-3}	2.23×10^{-9}
Case 4	2.32×10^{-7}	1.00×10^{-7}	2.32×10^{-8}	1.00×10^{-2}	2.32×10^{-9}
Case 5	1.28×10^{-7}	1.25×10^{-7}	1.60×10^{-8}	1.56×10^{-2}	2.00×10^{-9}
Case 6	6.24×10^{-8}	1.50×10^{-7}	9.36×10^{-9}	2.25×10^{-2}	1.40×10^{-9}
Case 7	2.51×10^{-8}	1.75×10^{-7}	4.39×10^{-9}	3.06×10^{-2}	7.69×10^{-10}
Case 8	7.12×10^{-9}	2.00×10^{-7}	1.42×10^{-9}	4.00×10^{-2}	2.85×10^{-10}
Case 9	8.58×10^{-10}	2.25×10^{-7}	1.93×10^{-10}	5.06×10^{-2}	4.34×10^{-11}

to a new $\xi O\eta$ coordinate according to tensors' characteristics [19]. The angle between the $\xi O\eta$ coordinate system and the xOy coordinate system is represented by the angle α (Figure 1(c)). Therefore, a series of transformed permeability tensors $\mathbf{k}_{\mathrm{trans}} = \begin{bmatrix} k_{\xi\xi} & k_{\xi\eta} \\ k_{\eta\xi} & k_{\eta\eta} \end{bmatrix}$ can be obtained by continuously rotating the $\xi O\eta$ coordinate system, that is, continuously changing the value of angle α. Once $k_{\xi\eta} \approx 0$, $k_{\eta\xi} \approx 0$ is achieved at a certain angle α_p; it represents the case that fluid flows no longer in any tangential directions but only in the two normal directions ξ and η so that maximum and minimum components of permeability among all transformed permeability tensors can be examined ($k_{\max} = \max(k_{\xi\xi}, k_{\eta\eta})$, $k_{\min} = \min(k_{\xi\xi}, k_{\eta\eta})$). In this case, α_p represents the principle direction. To examine the principle direction precisely, $\alpha = 0$~360° with interval 1° is adopted. Another important parameter is the anisotropy of the permeability in the porous media. Here, we define the ratio A_k to determine the anisotropic degree of permeability: $A_k = k_{\max}/k_{\min}$. The tensor transformation formula [19] is shown as follows:

$$k_{\xi\xi} = k_{xx}\cos\alpha\cos\alpha + k_{yy}\cos\beta\cos\beta + k_{xy}\cos\alpha\cos\beta + k_{yx}\cos\beta\cos\alpha, \tag{11}$$

$$k_{\eta\eta} = k_{xx}\cos\gamma\cos\gamma + k_{yy}\cos\alpha\cos\alpha + k_{xy}\cos\gamma\cos\alpha + k_{yx}\cos\alpha\cos\gamma, \tag{12}$$

$$k_{\xi\eta} = k_{xx}\cos\alpha\cos\gamma + k_{yy}\cos\beta\cos\alpha + k_{xy}\cos\alpha\cos\alpha + k_{yx}\cos\beta\cos\gamma, \tag{13}$$

$$k_{\eta\xi} = k_{xx}\cos\gamma\cos\alpha + k_{yy}\cos\alpha\cos\beta + k_{xy}\cos\gamma\cos\beta + k_{yx}\cos\alpha\cos\alpha, \tag{14}$$

where $\beta = \pi/2 - \alpha$, $\gamma = \pi/2 + \alpha$.

3. Results and Discussion

Two important factors are discussed here: porosity and Reynolds number. To study them separately, two groups of numerical cases are designed. One is changing porosity by changing the size of barrier but keeping constant length of domain. The other one is changing the length of domain but keeping constant porosity. These two factors are discussed in the following two sections. Fluid passing through the porous media is water with density $\rho = 1000\,\mathrm{kg/m^3}$ and dynamic viscosity $\mu = 0.001\,\mathrm{Pa \cdot s}$.

3.1. Discussion on Porosity. The domain size is set as $L = 10^{-6}$ m. The size of barrier is set as $a = (1/10)L \sim (9/10)L$ with interval $(1/10)L$ so that 9 cases named Case 1~Case 9 are generated. According to the size of the computational domain and spatial element sizes on the fixed mesh, time step is set as its maximum value available: $\Delta t = 10^{-11}$ s.

The flow simulation results by directly solving the Navier-Stokes equation are shown in Figure 2. The contours represent the magnitudes of velocity (i.e., the characteristic speed to be defined later), while the vectors represent the directions of velocity. It can be seen that the flow fields are well represented in the 9 cases. The square barriers are clearly identified by the vectors. We define characteristic speed as $V = \sqrt{U_x^2 + U_y^2}$, characteristic length as the hydraulic radius $R_h = a^2/(4a) = a/4$, Reynolds number as $\mathrm{Re} = \rho V R_h/\mu$, and Darcy number as $\mathrm{Da} = (R_h/L)^2$. The characteristic parameters are listed in Table 1 (results for Samples a, b, and c are the same so that the data in Table 1 are any of them). The very low Reynolds number (order of magnitude 10^{-10}~10^{-8}) indicates that the flows are very slow laminar flows. It can be seen that the dimensionless number $\mathrm{ReDa}^{1/2}$ has the order of magnitude 10^{-11}~10^{-9}, which satisfies the suggested restriction of Darcy's law $\mathrm{ReDa}^{1/2} \ll 1$ by Bear and Cheng [20].

Porosity is defined as the ratio of void space volume to the total volume as follows:

$$\phi = 1 - \frac{a^2}{L^2}. \tag{15}$$

Thus, the 9 cases relate to 9 different values of porosity. Full permeability tensors obtained from flow simulation results of the 9 cases are listed in Table 2. It can be seen that the diagonal components of the permeability tensor all decrease with decreasing porosity. Their values show that the studied porous media fall within the ranges of oil rocks ($10^{-11}\,\mathrm{m^2}$~$10^{-14}\,\mathrm{m^2}$), sandstone ($10^{-14}\,\mathrm{m^2}$~$10^{-16}\,\mathrm{m^2}$), and good limestone ($10^{-16}\,\mathrm{m^2}$~$10^{-18}\,\mathrm{m^2}$) [20]. The diagonal

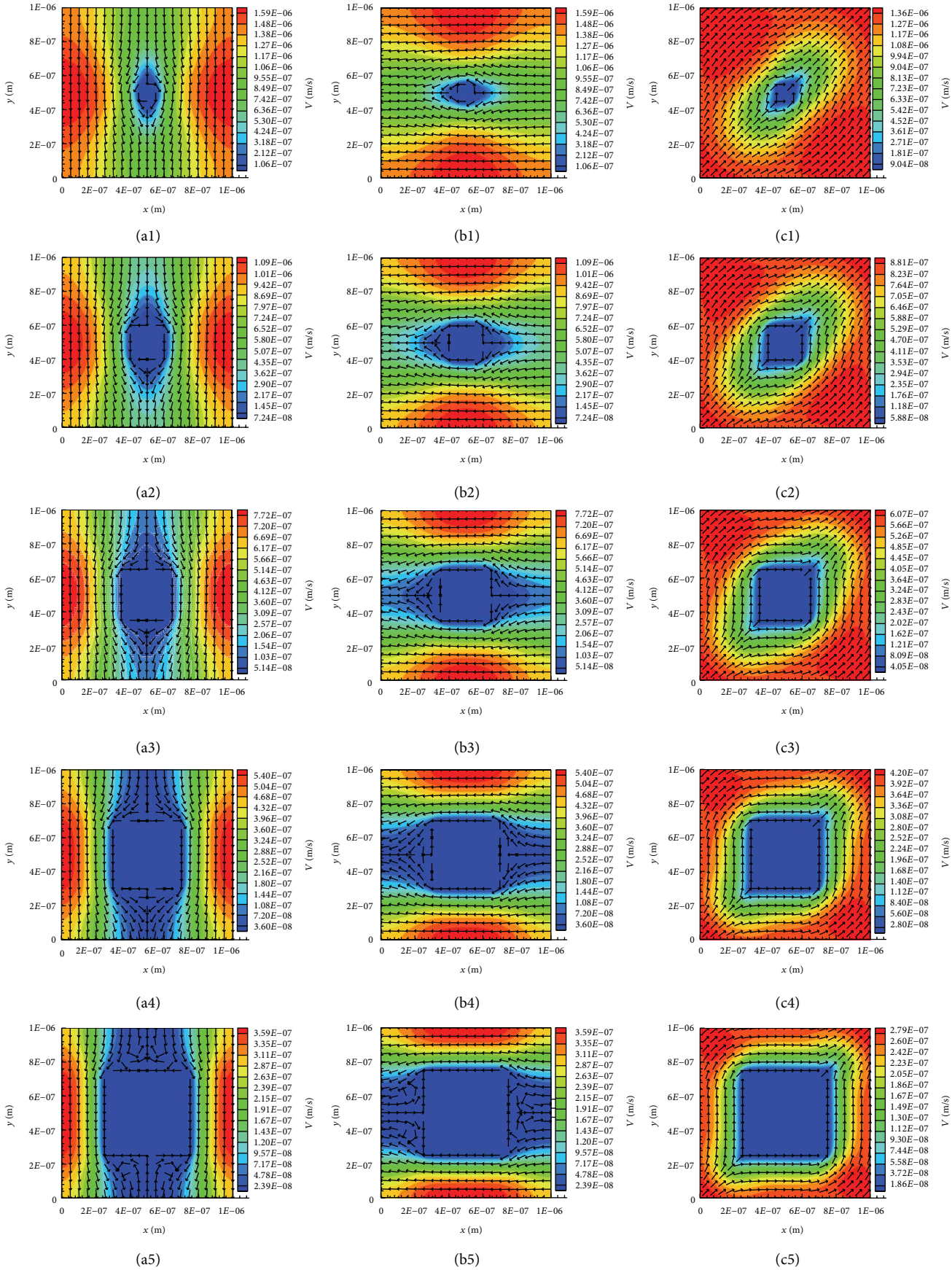

(a)

Figure 2: Continued.

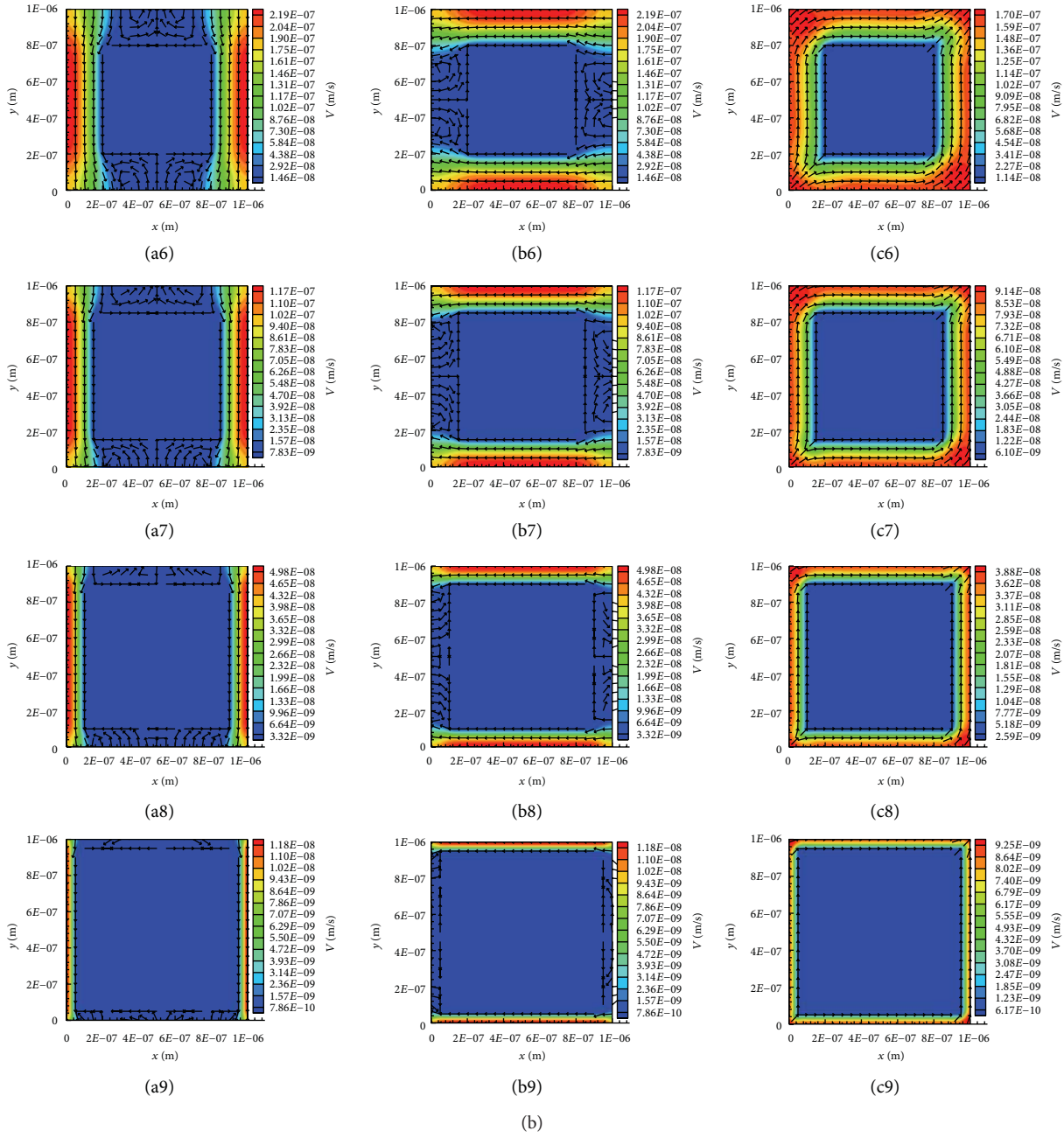

FIGURE 2: Flow fields for different porosities from Navier-Stokes simulation: columns a, b, and c represent Sample a, Sample b, and Sample c; numbers 1~9 represent Case 1~Case 9; the contour shows total speed while the vector shows directions of total velocity.

components of transformed permeability tensor are shown in Figure 3 for the 9 porosities; there always exist $k_{\xi\xi} = k_{\eta\eta}$ and $k_{\xi\xi} = k_{xx}$, $k_{\eta\eta} = k_{yy}$. These mean that the two diagonal components of the full permeability tensor are the same and are always equal to each other along with the rotating coordinate. This indicates that the permeable properties are all the same for any direction so that principle direction does not exist. Therefore, the full-tensor permeabilities are always diagonal tensors with equivalent components for the 9 porosities. The off-diagonal components, which are 3~6 orders of magnitudes lower than the diagonal components (Table 2), should be considered as numerical errors. In this case, the off-diagonal components should be considered as zeros. Revealed from the mathematical meaning, physical meaning is that the porous media in the 9 cases are all isotropic. Corresponding characteristic parameters are listed in Table 3.

3.2. Discussion on Reynolds Number. Besides the porosity, Reynolds number is also a key factor which may strongly affect velocity fields so that the results of permeability may be affected. Thus, it is important to check whether

Table 2: Full-tensor permeabilities at different porosities.

Case	ϕ	k_{xx} (m^2)	k_{yy} (m^2)	k_{xy} (m^2)	k_{yx} (m^2)
Case 1	0.99	1.1808×10^{-13}	1.1808×10^{-13}	-5.6848×10^{-16}	-5.6363×10^{-16}
Case 2	0.96	6.7481×10^{-14}	6.7481×10^{-14}	-3.1129×10^{-17}	-2.8981×10^{-17}
Case 3	0.91	4.0362×10^{-14}	4.0362×10^{-14}	-6.2013×10^{-19}	2.6772×10^{-19}
Case 4	0.84	2.3702×10^{-14}	2.3702×10^{-14}	-2.7576×10^{-19}	3.5447×10^{-20}
Case 5	0.75	1.3026×10^{-14}	1.3026×10^{-14}	-8.3818×10^{-20}	1.6370×10^{-20}
Case 6	0.64	6.3596×10^{-15}	6.3596×10^{-15}	7.1193×10^{-21}	-2.1080×10^{-20}
Case 7	0.51	2.5614×10^{-15}	2.5614×10^{-15}	5.8343×10^{-21}	-3.6183×10^{-20}
Case 8	0.36	7.2643×10^{-16}	7.2643×10^{-16}	1.0640×10^{-21}	-1.0052×10^{-20}
Case 9	0.19	8.7493×10^{-17}	8.7493×10^{-17}	6.4756×10^{-23}	-1.9648×10^{-22}

Table 3: Characteristic permeabilities and anisotropies at different porosities.

Case	ϕ	k_{max} (m^2)	k_{min} (m^2)	A_k ($= k_{max}/k_{min}$)
Case 1	0.99	1.1808×10^{-13}	1.1808×10^{-13}	1.0000
Case 2	0.96	6.7481×10^{-14}	6.7481×10^{-14}	1.0000
Case 3	0.91	4.0362×10^{-14}	4.0362×10^{-14}	1.0000
Case 4	0.84	2.3702×10^{-14}	2.3702×10^{-14}	1.0000
Case 5	0.75	1.3026×10^{-14}	1.3026×10^{-14}	1.0000
Case 6	0.64	6.3596×10^{-15}	6.3596×10^{-15}	1.0000
Case 7	0.51	2.5614×10^{-15}	2.5614×10^{-15}	1.0000
Case 8	0.36	7.2643×10^{-16}	7.2643×10^{-16}	1.0000
Case 9	0.19	8.7493×10^{-17}	8.7493×10^{-17}	1.0000

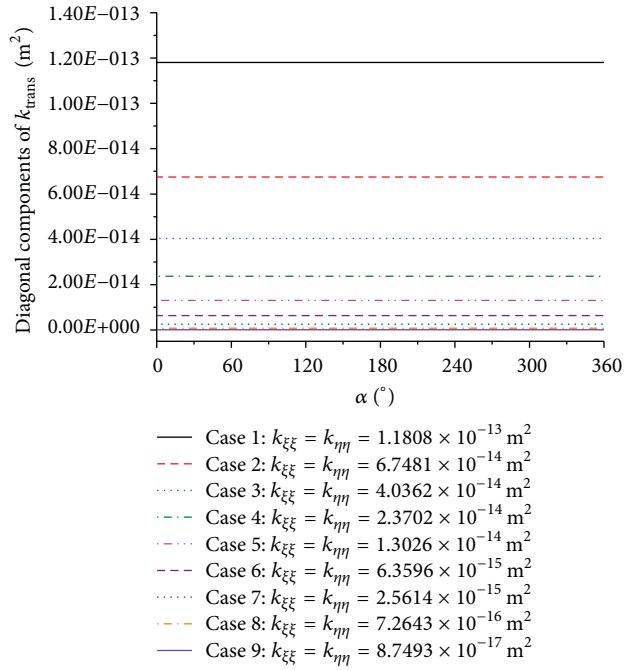

Figure 3: Diagonal components of transformed permeability tensor at different porosities.

the Reynolds number, actually controlled by the domain size, may change the conclusions in Section 3.1. Therefore, the domain size is gradually scaled up from $L = 10^{-6}$ m by keeping porosity at 0.64 (Case 6 in Tables 2 and 3). The results are shown in Table 4.

From 10^{-6} m to 10^{-4} m, the diagonal components of the full-tensor permeability just increase two orders of magnitudes once the domain size increases one order of magnitude. The off-diagonal components should still be considered as numerical errors and set to be zeros as stated previously. These three cases are quite similar, and their difference is only the magnitude. It can be verified by the flow fields in Figures 4(a1), 4(b1), 4(c1)~Figures 4(a3), 4(b3), 4(c3), Figures 5(a)~5(c), and Table 5 that the domain size scaling up from 10^{-6} m to 10^{-4} m just leads the velocity to increase proportionally. They are all isotropic. However, the situation is different when the domain size increases up to 10^{-3} m (see line 5 in Table 4). The off-diagonal components are no longer several orders of magnitudes smaller than the diagonal components so that the full-tensor permeability is no longer diagonal. Figures 4(a4)~4(c4) show that the fluid tends to depart the solid walls and the vortex expands. Figure 5(d) shows that the components of the transformed permeability tensor are no longer constant. Maximum and minimum values of the diagonal components (k_{max}, k_{min}) can always be obtained at the same time once the off-diagonal components become zeros. Their values (Table 5) show that the porous media at the domain length of 10^{-3} m enter the range of clean stand (10^{-9} m^2~10^{-12} m^2) which is a better aquifer than the previous ones [20]. Correspondingly, four angles (α_{I}, α_{II}, α_{III}, and α_{IV}) can be obtained, which are shown in Table 6. Surprisingly from Table 5, the porous media start to show anisotropic property ($A_k = 1.9241$) when the domain length reaches 10^{-3} m.

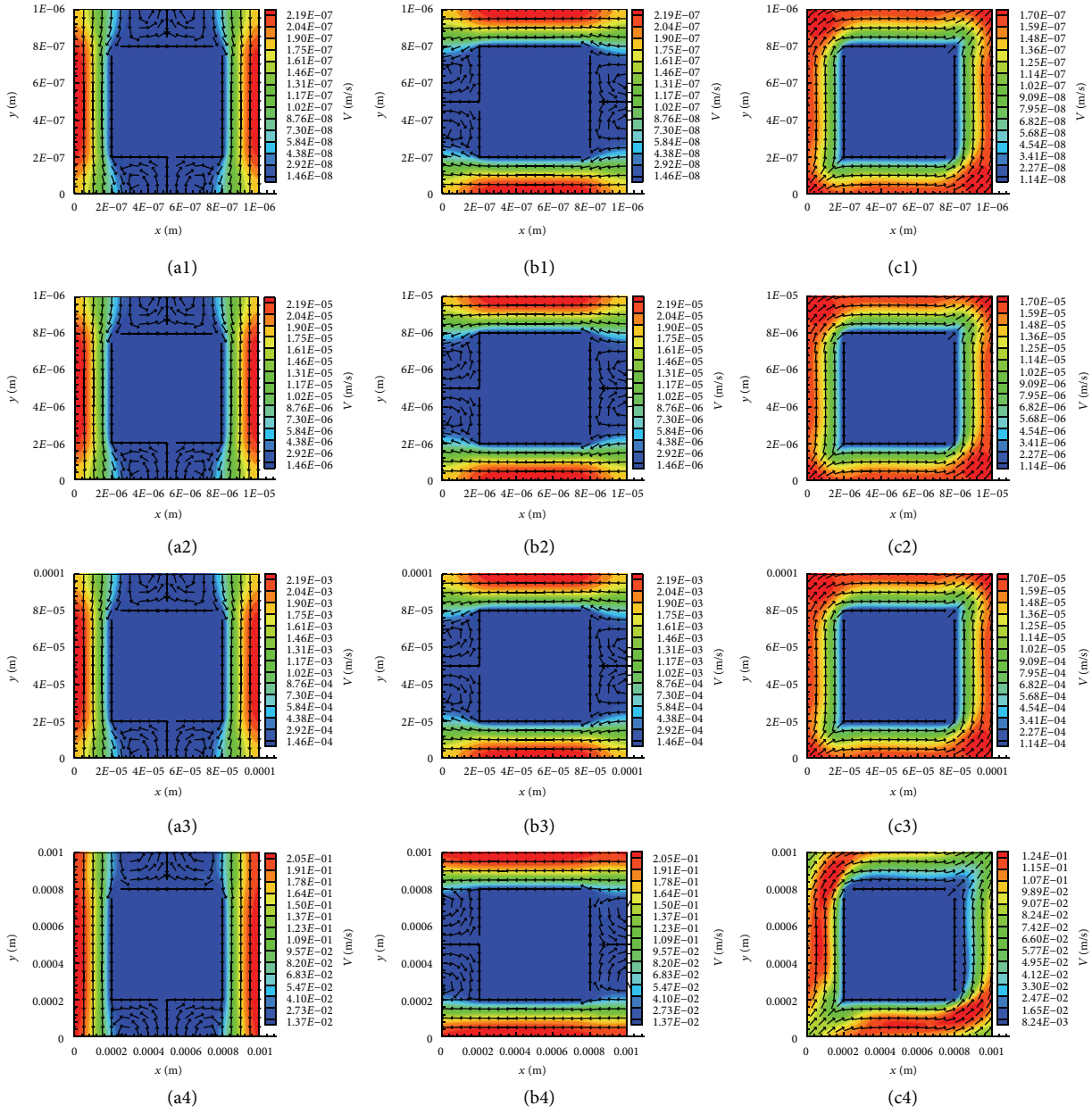

FIGURE 4: Flow fields for different Reynolds numbers from Navier-Stokes simulation: columns a, b, and c represent Sample a, Sample b, and Sample c; numbers 1~4 represent domain size $L = 10^{-6}$ m, 10^{-5} m, 10^{-4} m, and 10^{-3} m, respectively; the contours show total speed while the vectors show directions of total velocity.

It can be summarized from Table 6 that α_p is always equal to angle α_{II} or α_{IV} when $k_{\max}$ equals $k_{\xi\xi}$. These two angles are on the same line across the second and the fourth quadrants in the original xOy coordinate (see Figure 1(c)). This line is the direction where permeability achieves maximum value, that is, the easiest direction where fluid can pass through, so that this is the principle direction. Accordingly, the direction fluid receives the most resistance (i.e., the direction for $k_{\min}$) is the line represented by angles α_{I} and α_{III}, so that this line is the direction orthogonal to the principle direction.

When the length of domain is greater than or equal to 10^{-2} m, the flow simulation is divergent. This is probably because the mesh size 80×80 is not dense enough for larger domain. Larger domains with finer grid, which are very time consuming, will be studied in the future.

To discuss the previous phenomenon that different Reynolds numbers may generate essentially different permeability tensors, or in other words predict different types of porous media for the same configuration, four characteristic parameters are shown in Table 7. R_u and R_v are defined as

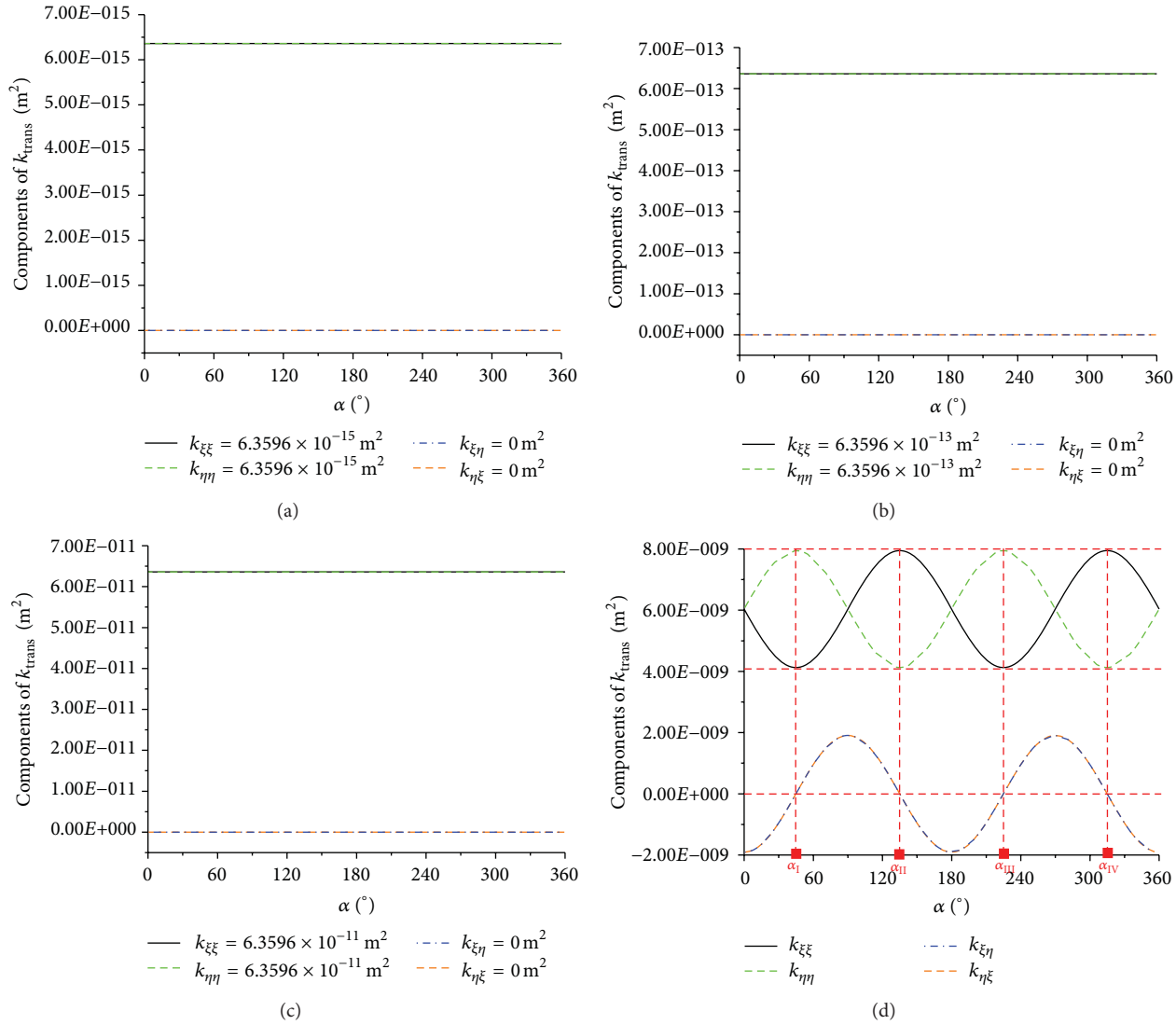

FIGURE 5: Components of transformed permeability tensor at different Reynolds numbers: (a) $L = 10^{-6}$ m, (b) $L = 10^{-5}$ m, (c) $L = 10^{-4}$ m, and (d) $L = 10^{-3}$ m.

TABLE 4: Full-tensor permeabilities at different Reynolds numbers.

L (m)	k_{xx} (m^2)	k_{yy} (m^2)	k_{xy} (m^2)	k_{yx} (m^2)
10^{-6}	6.3596×10^{-15}	6.3596×10^{-15}	7.1193×10^{-21}	-2.1080×10^{-20}
10^{-5}	6.3596×10^{-13}	6.3596×10^{-13}	7.5167×10^{-19}	-2.1064×10^{-18}
10^{-4}	6.3596×10^{-11}	6.3596×10^{-11}	-7.4280×10^{-17}	-3.6338×10^{-16}
10^{-3}	6.0366×10^{-9}	6.0366×10^{-9}	-1.9077×10^{-9}	-1.9077×10^{-9}
$\geq 10^{-2}$	Divergence	Divergence	Divergence	Divergence

TABLE 5: Characteristic permeabilities and anisotropies at different Reynolds numbers.

L (m)	ϕ	k_{max} (m^2)	k_{min} (m^2)	A_k ($= k_{max}/k_{min}$)
10^{-6}	0.64	6.3596×10^{-15}	6.3596×10^{-15}	1.0000
10^{-5}	0.64	6.3596×10^{-13}	6.3596×10^{-13}	1.0000
10^{-4}	0.64	6.3596×10^{-11}	6.3596×10^{-11}	1.0000
10^{-3}	0.64	7.9443×10^{-9}	4.1289×10^{-9}	1.9241

Table 6: Angles at zero off-diagonal components of transformed permeability for $L = 10^{-3}$ m.

L (m)	α_{I}	α_{II}	α_{III}	α_{IV}	α_p
10^{-3}	45°	135°	225°	315°	135°, 315°
Summary	$k_{\max} = k_{\eta\eta}$ $k_{\min} = k_{\xi\xi}$	$k_{\max} = k_{\xi\xi}$ $k_{\min} = k_{\eta\eta}$	$k_{\max} = k_{\eta\eta}$ $k_{\min} = k_{\xi\xi}$	$k_{\max} = k_{\xi\xi}$ $k_{\min} = k_{\eta\eta}$	$\alpha_p = \alpha_{\mathrm{II}}$ or α_{IV}

Table 7: Characteristic parameters at different Reynolds numbers.

L (m)	Re	$\mathrm{ReDa}^{1/2}$	R_u	R_v
10^{-6}	9.36×10^{-9}	1.40×10^{-9}	2.79×10^{-9}	2.79×10^{-9}
10^{-5}	9.36×10^{-6}	1.40×10^{-6}	2.79×10^{-6}	2.79×10^{-6}
10^{-4}	9.36×10^{-3}	1.40×10^{-3}	2.79×10^{-3}	2.79×10^{-3}
10^{-3}	8.88	1.33	1.35	1.35

the ratios of the mean convection effect to the mean diffusion effect in the momentum equation (2):

$$R_u = \frac{\overline{u\left(\partial u/\partial x\right) + v\left(\partial u/\partial y\right)}}{\left(\mu/\rho\right)\left(\partial^2 u/\partial x^2 + \partial^2 u/\partial y^2\right)},$$
$$R_v = \frac{\overline{u\left(\partial v/\partial x\right) + v\left(\partial v/\partial y\right)}}{\left(\mu/\rho\right)\left(\partial^2 v/\partial x^2 + \partial^2 v/\partial y^2\right)}, \tag{16}$$

where the superscript "—" represents the average value over the whole domain. It is clear in Table 7 that the fluid flows are actually diffusion dominated for the domain lengths smaller than 10^{-3} m since R_u and R_v are all much smaller than 1. However, R_u and R_v are greater than 1 at the domain length of 10^{-3} m. This means that the flow is dominated by the convection effect of fluid. It is well known from their intentions that the diffusion effect tends to transport variables to all directions uniformly while the convection effect tends to transport variables along specific directions. Therefore, the existence of convection dominant flow may be the main reason for the anisotropy. It is worth to point out that Table 7 also verifies the conclusion made by Bear and Cheng [20] that Darcy's law is usually valid as long as Reynolds number is lower than 1 (occurred at the domain lengths 10^{-6} m ~ 10^{-4} m where $\mathrm{Re} = 9.36 \times 10^{-9} \sim 9.36 \times 10^{-3}$) but sometimes as high as 10 (occurred at the domain length 10^{-3} m where Re = 8.88 and the suggested restriction $\mathrm{ReDa}^{1/2} \ll 1$ is violated).

4. Conclusion

A numerical method is proposed to compute the permeability in the form of full tensor. The flow simulation results show that flow fields can be well represented by solving the Navier-Stokes equation directly. Original and transformed permeability tensors are obtained so that maximum and minimum components of permeability with principle directions and anisotropies are detected successfully. With this information, the directions of largest and smallest resistances for fluid flow in porous media can be inferred easily.

Through the analyses on the porosity effect and the Reynolds number effect, it is found that porous media with the same porosity and the same configuration can manifest different levels of anisotropy at different Reynolds numbers. At the Reynolds numbers that diffusion dominates flow, isotropy is a good description. At the Reynolds number that convection dominates flow, anisotropy occurs. Thus, it is important to pay attention to Reynolds numbers for porous media applications. This is especially important for applications with large Darcy velocities, such as flow and transport in packed columns and in fractured geological media.

5. Future Issues to Be Addressed

The previous discussions show that the proposed method in the present study is an easy way to determine full-tensor permeability numerically and related characteristics. However, many issues still need to be addressed in future works. Only two of them are briefly listed below as an example.

(1) Method for solving the Navier-Stokes equation in porous media should be improved to accelerate the computation. Current speed is not acceptable for engineering applications. Multigrid method needs to be developed for the flow around solids so that the iteration of pressure can be largely accelerated. High-resolution time integration scheme is expected to largely reduce the number of time steps needed. Since only steady-state results are needed for obtaining the full-tensor permeability, a method directly solving the steady-state Navier-Stokes equation is also expected so that a large amount of time integrations can be avoided.

(2) Shape, number, position, and so forth of inner barriers should be intensively studied to know the application and limitation of this method and to improve precision. Denser meshes are also expected to study what will happen for larger Reynolds numbers.

Acknowledgments

The work presented in this paper has been supported in part by the project entitled "Simulation of Subsurface Geochemical Transport and Carbon Sequestration," funded by the GRP-AEA Program at KAUST. The work has also been supported in part by National Science Foundation of China (no. 51206186, no. 51174206) and Science Foundation of China, University of Petroleum, Beijing (no. 2462012KYJJ0403, no. 2462012KYJJ0404).

References

[1] C. L. Dinwiddie, F. J. Molz III, and J. W. Castle, "A new small drill hole minipermeameter probe for in situ permeability measurement: fluid mechanics and geometrical factors," *Water Resources Research*, vol. 39, no. 7, 2003.

[2] B. J. Wolfson and S. M. Wentworth, "Complex permeability and permeability measurement using a rectangular waveguide," *Microwave and Optical Technology Letters*, vol. 27, no. 3, pp. 180–182, 2000.

[3] A. N. Ivanov, S. N. Kozlova, and A. V. Pechenov, "Permeability measurement," *Measurement Techniques*, vol. 43, no. 12, pp. 1086–1088, 2000.

[4] J. L. Jensen and U. Heriot-Watt, "A model for small-scale permeability measurement with applications to reservoir characterization," in *Proceedings of the SPE/DOE 7th Symposium on Enhanced Oil Recovery*, pp. 891–900, April 1990.

[5] T. J. Wang, C. H. Wu, and L. J. Lee, "In-plane permeability measurement and analysis in liquid composite molding," *Polymer Composites*, vol. 15, no. 4, pp. 278–288, 1994.

[6] P. Ferland, D. Guittard, and F. Trochu, "Concurrent methods for permeability measurement in resin transfer molding," *Polymer Composites*, vol. 17, no. 1, pp. 149–158, 1996.

[7] R. Gauvin, F. Trochu, Y. Lemenn, and L. Diallo, "Permeability measurement and flow simulation through fiber reinforcement," *Polymer Composites*, vol. 17, no. 1, pp. 34–42, 1996.

[8] Y. Luo, I. Verpoest, K. Hoes, M. Vanheule, H. Sol, and A. Cardon, "Permeability measurement of textile reinforcements with several test fluids," *Composites A*, vol. 32, no. 10, pp. 1497–1504, 2001.

[9] T. F. Fwa, S. A. Tan, C. T. Chuai Y, and K. Guwe, "Expedient permeability measurement for porous pavement surface," *The International Journal of Pavement Engineering*, vol. 2, pp. 259–270, 2001.

[10] R. Arbter, J. M. Beraud, C. Binetruy et al., "Experimental determination of the permeability of textiles: a benchmark exercise," *Composites A*, vol. 42, no. 9, pp. 1157–1168, 2011.

[11] J. R. Weitzenböck, R. A. Shenoi, and P. A. Wilson, "Measurement of principal permeability with the channel flow experiment," *Polymer Composites*, vol. 20, no. 2, pp. 321–335, 1999.

[12] J. R. Weitzenböck, R. A. Shenoi, and P. A. Wilson, "Radial flow permeability measurement. Part A: theory," *Composites A*, vol. 30, no. 6, pp. 781–796, 1999.

[13] J. R. Weitzenböck, R. A. Shenoi, and P. A. Wilson, "Radial flow permeability measurement. Part B: application," *Composites A*, vol. 30, no. 6, pp. 797–813, 1999.

[14] Y. Keehm, T. Mukerji, and A. Nur, "Computational rock physics at the pore scale: transport properties and diagenesis in realistic pore geometries," *Leading Edge*, vol. 20, no. 2, pp. 180–183, 2001.

[15] A. Kameda, J. Dvorkin, Y. Keehm, A. Nur, and W. Bosl, "Permeability-porosity transforms from small sandstone fragments," *Geophysics*, vol. 71, no. 1, pp. N11–N19, 2006.

[16] E. H. Saenger, F. Enzmann, Y. Keehm, and H. Steeb, "Digital rock physics: effect of fluid viscosity on effective elastic properties," *Journal of Applied Geophysics*, vol. 74, no. 4, pp. 236–241, 2011.

[17] B. Quintal, M. Frehner, C. Madonna, N. Tisato, M. Kuteynikova, and E. H. Saenger, "Integrated numerical and laboratory rock physics applied to seismic characterization of reservoir rocks," *Leading Edge*, vol. 30, no. 12, pp. 1360–1367, 2011.

[18] Y. Keehm, T. Mukerji, and A. Nur, "Computational rock physics at the pore scale: transport properties and diagenesis in realistic pore geometries," *Leading Edge*, vol. 20, no. 2, pp. 180–183, 2001.

[19] R. L. Bishop and S. I. Goldberg, *Tensor Analysis on Manifolds*, Dover Publications, 1968.

[20] J. Bear and A. H. D. Cheng, *Modeling Groundwater Flow and Contaminant Transport*, vol. 23 of *Theory and Applications of Transport in Porous Media*, Springer Science+Business Media B.V., 2010.

Hindawi Publishing Corporation
Advances in Mechanical Engineering
Volume 2013, Article ID 627124, 24 pages
http://dx.doi.org/10.1155/2013/627124

Research Article

Analysis on Shift of Nature Modes of Liquid Sloshing in a 3D Tank Subjected to Oblique Horizontal Ground Motions with Damping Devices

Chih-Hua Wu,[1] Odd Magnus Faltinsen,[2] and Bang-Fuh Chen[3]

[1] *Institute of High Performance Computing, A*STAR, 1 Fusionopolis Way, No. 16-16 Connexis, Singapore 138632*
[2] *Centre for Ships and Ocean Structures & Department of Marine Technology, NTNU, 7491 Trondheim, Norway*
[3] *Asia-Pacific Ocean Research Center (APORC), National Sun Yat-sen University, Kaohsiung 802, Taiwan*

Correspondence should be addressed to Bang-Fuh Chen; chenbf@faculty.nsysu.edu.tw

Received 25 January 2013; Accepted 27 March 2013

Academic Editor: Yi Wang

The extended study of Wu et al. (2012) of sloshing fluid in tanks with internal structures from 2D to 3D is presented in the paper. The phenomenon of liquid sloshing in a 3D tank with various damping devices is solved by the time-independent finite difference method combined with the ghost (fictitious) cell approach. Two types of damping devices, a tank bottom-mounted baffle and a vertically surface-piercing plate, are considered in the study. In this work, the experimental measurement of liquid sloshing in a 3D tank with the baffle is carried out to further validate the present simulation. The comparison of the results between the experimental measurement and the present computation shows good accuracy. The effect of the vertically tank bottom-mounted baffle or the vertically surface-piercing plate on various sloshing waves for the tank under horizontal oblique excitation is discussed and investigated. The phenomena of the shift of the nature frequency of the tank with damping devices due to various oblique horizontal excitations under different sloshing waves are presented in detail. The sloshing wave type is varied due to the influence of the baffle or the plate, and the coexistence of two types of sloshing waves is found for the tank under larger excitation frequencies.

1. Introduction

Liquid sloshing is the most prominent phenomenon of liquid motion in either stationary or moving tanks subjected to forced external perturbations. The study of sloshing phenomenon in tanks is related to a wide range of applications such as in ships, rockets, satellites, trucks, and even stationary-petroleum containers. Resonant free-surface flows in tanks in aircrafts, missiles, and rockets have been the focus of extensive research. The amplitude of the sloshing, in general, depends on amplitude and frequency of the tank motion, liquid-fill depth, liquid properties, and tank geometry. These parameters have significant effects on the dynamic stability and performance of moving vehicles carrying containers. One of the passive devices to reduce the influence of sloshing impact on structures or suppress the strength of liquid sloshing is inserted in internal obstacles in containers, such as baffles, plates, rings, and wire screens. The tanks mounted with sloshing-damping devices are called Tuned Liquid Damper (TLD).

Tuned Liquid Dampers (TLDs) are economical and effective dynamic vibration absorbers. The main function of a passive damping device is to absorb portion of the input energy associated with external dynamic excitation acting on the structure. Examples for external excitations are wind and earthquakes. By doing so, the passive damping device minimizes or eliminates the possibility of structural damages. TLDs were used to stabilize marine vessels against rocking and rolling motions [1, 2] in offshore platforms [3, 4] and in tall structures [5–9]. Often the TLD is used as a water storage tank preventing the use of a higher-viscosity liquid. Several approaches have been implemented to increase the energy dissipated by the sloshing fluid, including roughness elements [10], surface contaminants [11], wave breaking in shallow water TLDs [12], and nets or screens [7, 13–15]. Akyildiz and Ünal [16, 17] investigated the pressure variations

in both baffled and unbaffled rectangular tank numerically and experimentally. They observed that the effects of the vertical baffle are most pronounced in shallow water, and consequently the pressure response is reduced by using the baffles. Liquid viscosity cannot be neglected when flow-damping devices are mounted with a tank with fluid and energy is dissipated by viscous action. Celebi and Akyildiz [18] revealed that flow over a vertical baffle produces a shear layer and energy is dissipated by viscous effect of the fluid. They concluded that, in an increased fill depth, the rolling amplitude and frequency of the tank with or without baffle configurations directly affect the degrees of nonlinearity of the sloshing phenomena. As a result, a phase shift in forces and moments occurred. Armenio and La Rocca [19] adopted the finite difference method to solve the 2-D RANS equations and validated the numerical results with their experimental measurement.

The control of the sloshing behavior with baffles is also a subject of interest in the recent years, because of the complexity and highly nonlinear nature of the problem. Cho and Lee [20] reported a parametric investigation on the two-dimensional nonlinear liquid sloshing in baffled tanks under horizontal forced excitation by using fully nonlinear potential flow theory. In their study, the liquid motion and dynamic pressure variation in the vicinity of the baffle tip are more significant than those below the baffle tip. Cho et al. [21] did a further study on the resonance characteristics of liquid sloshing in a 2D baffled tank under surge motion by the linearized potential flow theory. The various positions, baffle heights, and number of baffles were considered in their work and the fundamental resonant frequency, and the peak elevation of sloshing decreases with these parameters. However, the viscous effect on liquid sloshing could not be resolved based on potential theory. Younes et al. [22] experimentally explored the hydrodynamic damping due to vertical baffle arrangements in a rectangular tank with sloshing fluid. The arrangement of upper-mounted and lower-mounted vertical baffles of different heights and numbers were considered in their experiment. They found that the twin-sided upper mounted baffles and center-holed lower mounted baffle arrangement yield a maximum damping ratio on sloshing. More recently, Akyildiz [23] investigated the effect of the vertical baffle height on liquid sloshing in a rolling 2D rectangular tank, and the nonlinear liquid sloshing was solved by the volume of fluid (VOF) technique. He solved the complete Navier-Stokes equations in primitive variables by using of finite difference approximations with the moving coordinate system. He concluded that the blockage effect of the baffle on the liquid convection is predominant to the tip vortex when the baffle height increases. Wu et al. [24] carried out that the fictitious cell approach associated with a coordinate transformation technique was successfully adopted to solve for the sloshing liquid in 2D tanks with baffles. The numerical scheme was validated by their experiment work. The effects of the number of the baffles on the sloshing amplitude were studied. In the study of two baffles, the largest wave damping might occur when the distance between two baffles is 0.2 L. In addition, the influence of baffle height on the shift of the first natural mode of the baffled tank (ω_1) under different water depths is carried out by spectral analyses of sloshing elevation. Several empirical formulas are derived by curve fitting, and they can be used to predict the shift of the fundamental mode of the liquid sloshing in tanks with baffles.

However, the 3D numerical simulation of viscous liquid sloshing in a tank with internal structures is still very limited in the literature. Liu and Lin [25] investigated liquid sloshing in a baffled tank with large-eddy simulation (LES). In their study, the vertical baffle is a more effective tool in reducing the sloshing amplitude. Jung et al. [26] utilized commercial software, ANSYS Fluent, to solve liquid sloshing in a 3D tank with baffles under only lateral excitation. The behavior of tip vortex, free surface elevation depending on the baffle height, and the pressure exerted on the tank wall were discussed in detail.

In the present study, we straightforwardly extend the numerical model of Wu et al. [24] from 2D to 3D to explore sloshing dynamics in tanks with two damping devices, a tank bottom-mounted baffle, and a surface-piercing flat plate. The excitation of a three-dimensional tank (Figure 1) with different dimensionless excitation amplitudes; with multiple degrees of freedom for the excitation direction; with excitation frequencies near and far from the first natural frequency; with arbitrary water depths are considered in this work. In the three-dimensional model, the time-independent finite difference method [24] is utilized to incorporate the 3D Navier-Stokes equations and the fully nonlinear kinematic and dynamic free surface boundary conditions for incompressible fluid in a rectangular tank with a square base. The time varying moving boundary is mapped onto a time-independent domain through proper transformation functions, and a special finite difference approximation is made in order to overcome the difficulty of maintaining the accuracy of the finite difference expression for the second derivative when the difference mesh is stretched near the boundary. The treatment of flow field around flow damping devices is carried out by a fictitious cell approach which is similar to the ghost cell approach [27]. The second order upwind scheme is also used to deal with the convective terms. The main focus of this paper is to discuss the effect of a vertically tank bottom-mounted baffle and a surface-piercing flat plate on the nature modes of various sloshing waves for a tank subjected to oblique horizontal excitation. Not only is the numerical simulation studied in this work, the experiment setup for a tank with a baffle is also investigated to further validate the accuracy of the developed numerical scheme.

Section 2 introduces the equations of motion which are written in a moving frame of reference attached to the accelerating tank. The fully nonlinear free surface boundary conditions are listed in this section. Besides, the fictitious cell approach is implemented to deal with the interfaces of fluid and structure (baffle, tank bottom, and tank walls). The comprehensive benchmark tests of the present numerical scheme are demonstrated in Section 3. The detailed influences of the flow damping devices on various sloshing waves are also dissected in this section. Section 4 summarizes the key conclusions.

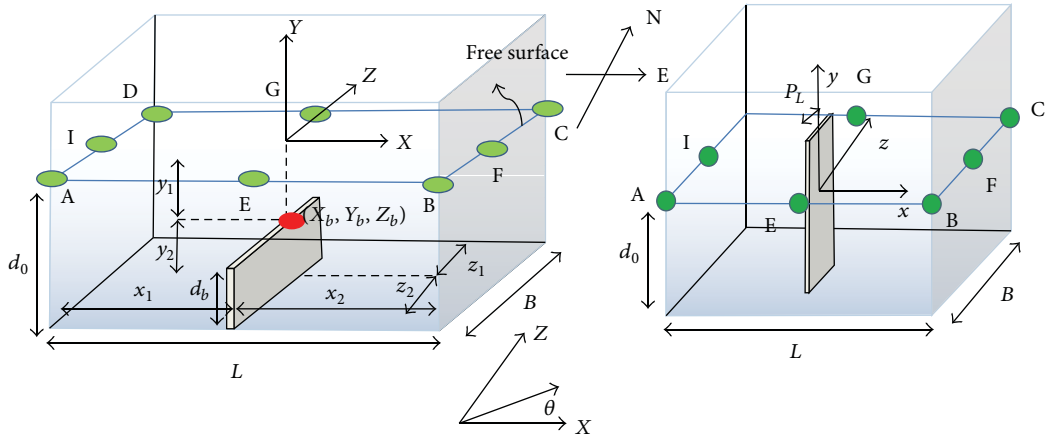

FIGURE 1: Definition sketches of the tank and the coordinate system. (a) A vertically tank bottom-mounted baffle; (b) a vertically surface-piercing flat plate.

2. Mathematical Formulation

In this work, the sloshing phenomenon in a rigid 3D tank with partially filled liquid is analyzed, and two flow damping devices, a vertically tank bottom-mounted baffle, and a surface-piercing flat plate are considered. As illustrated in Figure 1, the breadth of the tank is L, the tank's width is B, and d_0 is the still liquid depth. d_b is the baffle height, and P_L is the width of the plate. The gas flow including the possibility of gas pockets is neglected. The horizontal oblique excitation angle θ is measured between the excitation direction and x-coordinate. The laminar flow is assumed, and the Navier-Stokes equations in a tank-fixed coordinate system can be expressed as

$$\begin{aligned}
&\frac{\partial u}{\partial t} + u\frac{\partial u}{\partial x} + v\frac{\partial u}{\partial y} + w\frac{\partial u}{\partial z} \\
&\quad = -\frac{1}{\rho}\frac{\partial p}{\partial x} - \ddot{x}_C + \upsilon\left(\frac{\partial^2 u}{\partial x^2} + \frac{\partial^2 u}{\partial y^2} + \frac{\partial^2 u}{\partial z^2}\right), \\
&\frac{\partial v}{\partial t} + u\frac{\partial v}{\partial x} + v\frac{\partial v}{\partial y} + w\frac{\partial v}{\partial z} \\
&\quad = -g - \frac{1}{\rho}\frac{\partial p}{\partial y} + \upsilon\left(\frac{\partial^2 v}{\partial x^2} + \frac{\partial^2 v}{\partial y^2} + \frac{\partial^2 v}{\partial z^2}\right), \\
&\frac{\partial w}{\partial t} + u\frac{\partial w}{\partial x} + v\frac{\partial w}{\partial y} + w\frac{\partial w}{\partial z} \\
&\quad = -\frac{1}{\rho}\frac{\partial p}{\partial z} - \ddot{z}_C + \upsilon\left(\frac{\partial^2 w}{\partial x^2} + \frac{\partial^2 w}{\partial y^2} + \frac{\partial^2 w}{\partial z^2}\right),
\end{aligned} \tag{1}$$

where u, v, and w are the relative velocity components in x, y, and z directions, $\ddot{x}_C$ and $\ddot{z}_C$ are the relative acceleration components of the tank in x and z directions, p is the pressure, ρ is the liquid density, υ is kinematic viscosity of the liquid, and g is the components of the acceleration due to gravity.

The continuity equation for incompressible flow is

$$\frac{\partial u}{\partial x} + \frac{\partial v}{\partial y} + \frac{\partial w}{\partial z} = 0. \tag{2}$$

Taking partial derivatives of (1) with respect to x, y, and z, respectively, and summing the results, one can obtain the following equation to solve for the pressure:

$$\begin{aligned}
\frac{\partial^2 p}{\partial x^2} + \frac{\partial^2 p}{\partial y^2} + \frac{\partial^2 p}{\partial z^2} = &-\rho\frac{\partial}{\partial x}\left(u\frac{\partial u}{\partial x} + v\frac{\partial u}{\partial y} + w\frac{\partial u}{\partial z}\right) \\
&-\rho\frac{\partial}{\partial y}\left(u\frac{\partial v}{\partial x} + v\frac{\partial v}{\partial y} + w\frac{\partial v}{\partial z}\right) \\
&-\rho\frac{\partial}{\partial z}\left(u\frac{\partial w}{\partial x} + v\frac{\partial w}{\partial y} + w\frac{\partial w}{\partial z}\right).
\end{aligned} \tag{3}$$

2.1. Boundary Conditions. We assume that the surface tension effect is neglected. The kinematic condition states that the liquid particles at free surface remain on the free surface and can be expressed as

$$\frac{\partial \eta}{\partial t} + u\frac{\partial \eta}{\partial x} + w\frac{\partial \eta}{\partial z} = v, \tag{4}$$

where $\eta = h(x, z, t) - d_0$ is the elevation of free surface measured from the initial liquid depth. The dynamic condition requires that the normal stress is equal to the atmospheric pressure, and the two tangential stresses are zero

along the free surface boundary. The dimensionless dynamic conditions can, then, be derived and expressed as follows:

$$P_F = \frac{y}{\mathrm{Fr}^2} + 2\left[u_x\eta_x^2 + w_z\eta_z^2 + v_y + (u_z + w_x)\eta_x\eta_z - (u_y + v_x)\eta_x - (v_z + w_y)\eta_z\right] \times \left(\mathrm{Re}\left(\eta_x^2 + \eta_z^2 + 1\right)\right)^{-1}, \tag{5}$$

$$u_y = -v_x + \frac{2(u_x - v_y)\eta_x + (u_z + w_x)\eta_z + (v_z + w_y)\eta_x\eta_z}{1 - \eta_x^2}, \tag{6}$$

$$w_y = -v_z + \frac{2(w_z - v_y)\eta_z + (u_z + w_x)\eta_x + (v_z + u_y)\eta_x\eta_z}{1 - \eta_z^2}, \tag{7}$$

where Fr is the Froude number and Re is the Reynolds number that are defined as

$$\mathrm{Fr} = \frac{u_m}{\sqrt{gd_0}}, \qquad \mathrm{Re} = \frac{u_m d_0}{\upsilon}, \tag{8}$$

where $u_m = \omega a_0$ (ω is the angular velocity, and a_0 is the excitation displacement of the tank) is the maximum velocity of the tank, η_x denotes a partial derivative of η with respect to x, and the others have same meanings. In the present study, (5) is used to determine the hydrodynamic pressure at the free surface, while (6) and (7) are used to extrapolate the horizontal velocity (u, w) at the free surface from the flow domain.

2.2. The Coordinate Transformation and Computational Algorithm. As well known, the way of accurately predicting free surface elevation in 3D tanks with external forcing is still a big challenge due to time dependence of free surface, especially when flow damping devices are involved and coupled with the sloshing flow. In the present study, we extend the numerical scheme of [24] from 2D to 3D by using simple mapping functions to remove the time dependence of the free surface of the liquid domain. The time-varying liquid surface can be mapped onto a cube by the proper coordinate transformations. The convenience of coordinate transformation is to map a wavy and time-dependent liquid domain onto a time-independent unit cubic domain. As listed in Figure 1, the distance from the tank west wall to the baffle (plate) center is X_b and from the south wall to the baffle (plate) center is Z_b, and the baffle height is Y_b. We divide the liquid domain into eight parts based on the location and the height of the baffle or plate. The mapping functions of coordinate transformation of eight parts can be expressed as

$$x_1^* = \frac{x_1}{X_b}, \qquad x_2^* = \frac{x_2}{L - X_b},$$
$$y_1^* = 1 - \frac{y_1 + d_0 - Y_b}{h(x, z, t) - Y_b}, \qquad y_2^* = -\frac{y_2}{Y_b}, \tag{9}$$
$$z_1^* = \frac{z_1}{Z_b}, \qquad z_2^* = \frac{z_2}{B - Z_b}.$$

Through the mapping functions in (9), one can transform the west wall to $x_1^* = 0$, the baffle (plate) center to $x_1^* = 1$ and $x_2^* = 0$, the east wall to $x_2^* = 1$, the free surface to $y_1^* = 0$, the baffle tip to $y_1^* = 1$ and $y_2^* = 0$, the tank bottom to $y_2^* = 1$, the south wall $z_1^* = 0$ to the baffle center to $z_1^* = 1$ and $z_2^* = 0$, and the north wall to $z_2^* = 1$. In this way, the computational domain is invariant (eight unit squares), and the more advantage of the transformations is to deal with the tank with internal structures of various positions and scales and to avoid the internal structure surrounded by the irregular meshes. Furthermore, combining with the stretching technique [28], the stretching grids can be arranged around the structure boundaries with the sharp corners. The thickness of the baffle or plate is set only at 1% of the tank's length and is, therefore, negligible compared with the length of the tank.

In this three-dimensional analysis, the liquid flow is solved in a unit cubic mesh in the transformed flow domain. All computations use the dimensionless equations in the X-Y-Z coordinate system. All the numerical results presented in this work are in the dimensionless form [28], and the dimensionless equations can be referred to [24, 29] that are omitted in the text. Central difference approximations are used for the space derivatives, except at the boundary where the fictitious cell approach [24, 27] is employed. A staggered grid system is used in the analysis. That is, the pressure P is defined at the centre of a finite difference grid cell (of dimensions (ΔX, ΔY, and ΔZ)), whereas the velocity components U, V, and W are calculated $0.5\Delta X$, $0.5\Delta Y$, and $0.5\Delta Z$ behind, above, or backward of the cell centre. The Crank-Nicholson second order finite difference scheme and the Gauss-Seidel point successive overrelaxation iterative procedure are used to calculate the velocity and pressure, respectively. The detailed numerical scheme is similar to that reported [24, 28, 29] and is omitted here.

3. Results and Discussion

3.1. Experiment Investigation. It is difficult to be solved by theoretical and numerical studies that the complex and intricate phenomenon of the nonlinearity behavior of resonant sloshing waves occur. The experimental investigation of sloshing with damping devices is very limited and mostly focuses on lateral excitation (only surge motion). In reality, as the tank is excited by accelerations due to an earthquake or waves, the excitation directions of the tank are varied with time. In view of this, an experiment was conceived and attempted to carry out the preliminary investigation on the

Figure 2: Photograph of the experiment setup of a baffled tank.

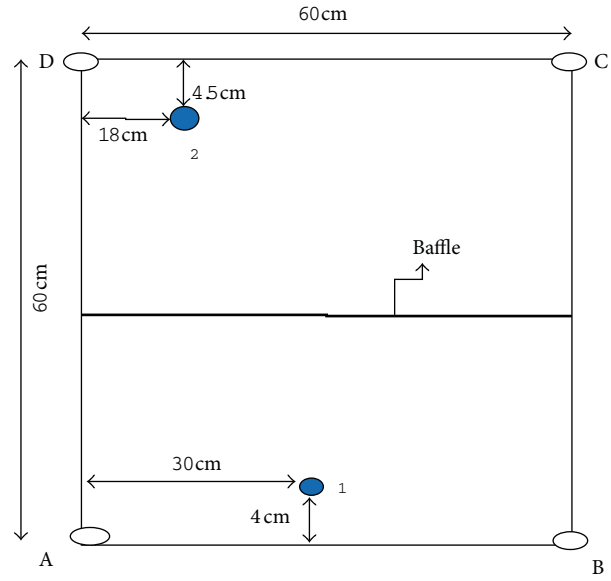

Figure 3: Positions of the wave probes from the top view of the baffled tank. Measurements in cm.

effect of damping devices on sloshing in tanks subjected to various horizontal excitation angles and to further validate the accuracy of the present numerical work.

The photograph of the experiment setup is shown in Figure 2. The excitation direction of shaking table is designed to be altered by an aluminum alloy rotational table. The material of the baffled tank is acryl with 20 mm thickness to prevent the tank deformation from the hydrostatic pressure and hydrodynamic impact of the liquid, and that of the baffle is fibreglass that can avoid the occurrence of baffle deformation due to hydrodynamic forces. The maximum moving distance (r) of the shaking table is ±30 mm, and the highest revolution of the motor is 2000 r.p.m. The frequency level depends on the limitation of the maximum velocity implemented by the AC motor and the motor reducer. In this experiment work, the maximum velocity ($V_m = \omega r$) of the shaking table is about 30 mm/s which indicates that if the excitation displacement (r) becomes large, the corresponding excitation frequency has to be reduced. The measurement of wave elevation is carried out by wave probes, and the locations of wave probes, P_1 and P_2, are depicted in Figure 3. The comparison of wave history at P_1 between the experimental measurement and the present numerical scheme for a baffled tank subjected to an oblique excitation of 15° is illustrated in Figure 4, and a good agreement is demonstrated.

3.2. Effect of a Vertically Tank Bottom-Mounted Baffle on Shift of Nature Modes of Sloshing Waves. In this section, the effect of a vertically tank bottom-mounted baffle parallel to the tank breadth (B) on shift of the nature modes of a tank with liquid is discussed. The natural modes ($\omega_{i,j}$) of 3-D tank can be expressed as

$$\lambda_{i,j} = \pi\sqrt{i^2 + r^2 j^2},$$
$$\omega_{i,j}^2 = g\lambda_{i,j}\tanh\left(\lambda_{i,j}d_0\right), \tag{10}$$

where i, j are the natural mode's components of x- and z-axes, respectively. Wu et al. [24] analyzed the influence of baffle height on the shift of natural modes in 2D tanks with sloshing fluid and concluded that the shift of the lowest natural mode $\omega_{1,0}$ of the tank apparently increases with the growth of baffle height. For the present design of 3D baffled tank, the effect of baffle height on the shift of the lowest natural mode is similar to that in the 2D baffled tank. In other words, the baffle has no influence on the nature mode system in the z-direction. As a 3D baffled tank is subjected to oblique horizontal excitation, the coupled effect of nature modes of sloshing waves will be triggered. Wu and Chen [28, 29] reported that the types of sloshing waves in a 3D tank under various excitation angles and frequencies are the single-directional wave, square-like wave, swirling wave, and irregular wave, and these waves can be triggered by the specific excited frequencies of $0.9\omega_1$, $1.5\omega_1$, $1.0\omega_1$, and $2\omega_1$, respectively. In the following subsections, the effect of the baffle of a fixed height $d_b = 0.5d_0$ on the shift of natural modes of different types of sloshing waves for a 3D tank under oblique excitation is discussed in detail.

3.2.1. Effect of Baffle on Single-Directional Waves ($0.9\omega_1$). For an unbaffled tank under coupled surge-sway motion with an excitation frequency of $0.9\omega_1$, single-directional waves appear at an excitation angle of 5°, and diagonal waves occur at $\theta = 45°$ [28]. The wave histories of points A (H_A) and B (H_B), sloshing wave patterns, and the distribution of absolute peaks of the single-directional waves affected by the baffle for a tank with $d_b/d_0 = 0.5$ are depicted in Figure 5. The inserted plots are the results of the unbaffled tank. For the single-directional waves shown in Figure 5(a), the beating phenomena of H_A and H_B are unobvious, and a nearly steady state of sloshing elevation is shown after $T = 150$. The spectral analysis of H_A depicted in Figure 10(a) shows that only one peak appears when $\theta = 5°$, and this peak ($0.9\omega_1$) is the excitation frequency of the baffled tank. Besides, a smaller peak of $0.927\omega_1$ exists just next to the peak of $0.9\omega_1$, and therefore, it is not presented clearly in Figure 10(a). The smaller peak of $0.927\omega_1$ is close to the first natural mode ($\omega_{b1} = 0.925\omega_1$) by 2D analysis of the baffled tank with $d_b/d_0 = 0.5$ [24]. The wave elevations at points A and B,

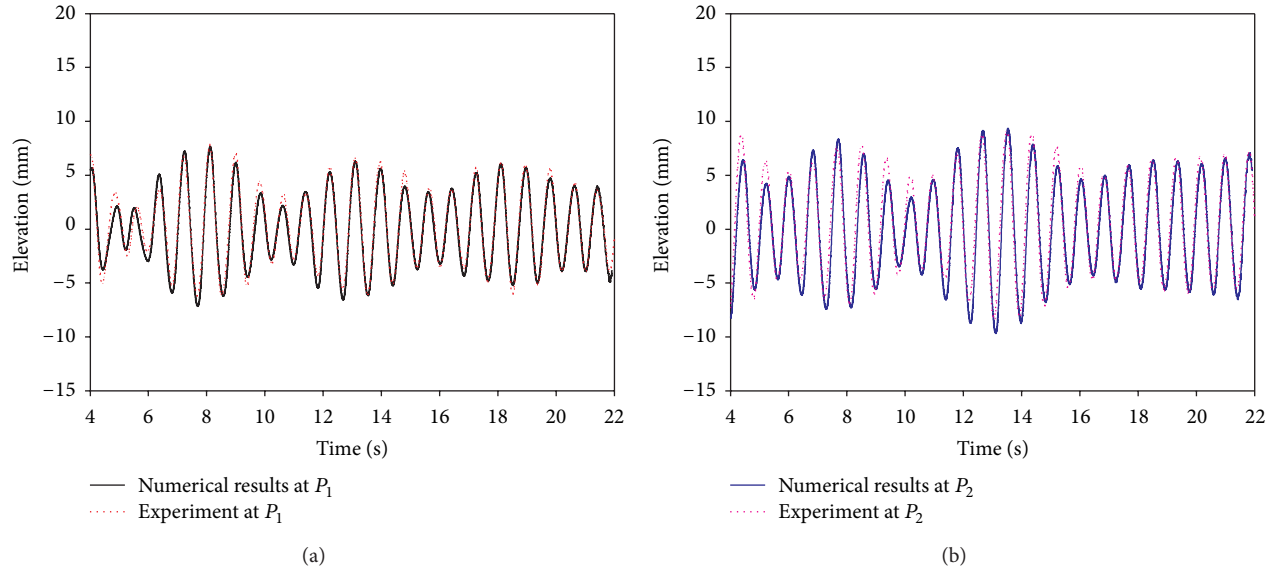

FIGURE 4: The comparison between the results of experimental measurement and those of numerical simulation in a baffled tank; $d_0/L = 0.5$, $a_0/d_0 = 0.005$, $d_b/d_0 = 0.5$, and $\theta = 15^\circ$.

therefore, are dominated by these two frequencies in the first beating, and the nearly steady state of sloshing elevation presented after $T = 150$ indicates that only the external excitation frequency remains to influence the sloshing fluid in the baffled tank. Furthermore, the results of the wave pattern (Figure 5(c)) and the distribution of absolute peaks (Figure 5(e)) of single-directional waves demonstrate the wave type turns into the swirling waves due to the influence of the baffle. Additionally, the dominant sloshing amplitude is still in the longitudinal direction due to $\theta = 5^\circ$.

For the results of diagonal waves affected by the baffle, the sloshing elevation of points A (H_A) and B (H_B) shown in Figure 5(b) presents a beating phenomenon with different periods. Nevertheless, H_B should be very small compared to H_A for diagonal waves [28]. This indicates that the wave type of sloshing waves is varied due to the influence of the baffle. The further evidence of switching the wave type of diagonal waves is demonstrated in Figures 5(d) and 5(f). The wave pattern (Figure 5(d)) and the distribution of peaks (Figure 5(f)) are different from those of the diagonal waves (the inserted plots), whereas they seem to correlate with the swirling waves. From the observation of the snapshots of the free surface (not presented here), the clockwise swirling waves appear after $T = 10$, and the shift direction of the swirling waves occurs as well. Besides, the period of the counter-clockwise swirling waves is very short compared to that of the clockwise swirling waves. That is, the dominant direction of the swirling waves is clockwise. The reason of this phenomenon can be explained by the effect of the baffle. Imagine that when the wave sloshes from the corner A to corner C, the diagonal flow in the vicinity of the baffle mounted on the tank bottom would transgress the baffle or be conducted along the baffle in a direction from south to north. On the other hand, the liquid particles surrounding the baffle would be directed in a north-to-south direction when the wave sloshes back. The tendency of clockwise rotation of the flow caused by the baffle gradually influences the diagonal waves and then turns the waves into the swirling waves.

The sloshing amplitudes of points A and B depicted in Figure 5(b) show several beating waves contributed by three modes, $0.9\omega_1$, $0.927\omega_1$, and $1.0\omega_1$, according to the spectral analysis of H_A illustrated in Figure 10(a). Furthermore, the modes of H_A presented in Figure 10(a) are varied with the alteration of the excitation angle of the baffled tank. In other words, the mode, $1.0\omega_1$, appears when the oblique excitation direction changes from 5° to 45°. As discussed earlier, the influence of the baffle height on the reduction of the first resonant mode for this kind of baffled tank is predominantly in the x-direction. When the oblique excitation angle is small ($\theta = 5^\circ$), the wave principally sloshes in the x-direction, and as a result, the shift of $\omega_{1,0}$ is of significance. Based on the observation mentioned above, the modes of $0.927\omega_{1,0}$ and $1.0\omega_{0,1}$ can be correlated to the first resonant mode in the longitudinal (x) and the transversal (z) directions of the baffled tank, respectively.

3.2.2. Effect of Baffle on Swirling Wave ($1.0\omega_1$). For a 3D tank without baffles under a resonant excited frequency = $1.0\omega_1$ and an oblique horizontal excitation direction $\theta = 5^\circ$, the swirling wave can be generated. As a tank bottom-mounted baffle is involved, the beating phenomenon of the swirling waves in a baffled tank is presented in Figure 6(a), and the elevations of points A and B increase with the sloshing periods that indicate that the tank is under a near-resonant excitation. According to the result of spectral analysis of H_A shown in Figure 10(b), two peaks, $0.927\omega_1$ and $1.0\omega_1$, occur, and the dominant one is the external excitation frequency, which is equal to the first natural mode in the z-direction. The growth of the sloshing elevation is, therefore, mainly influenced by the dominant resonant mode ($1.0\omega_1$). As

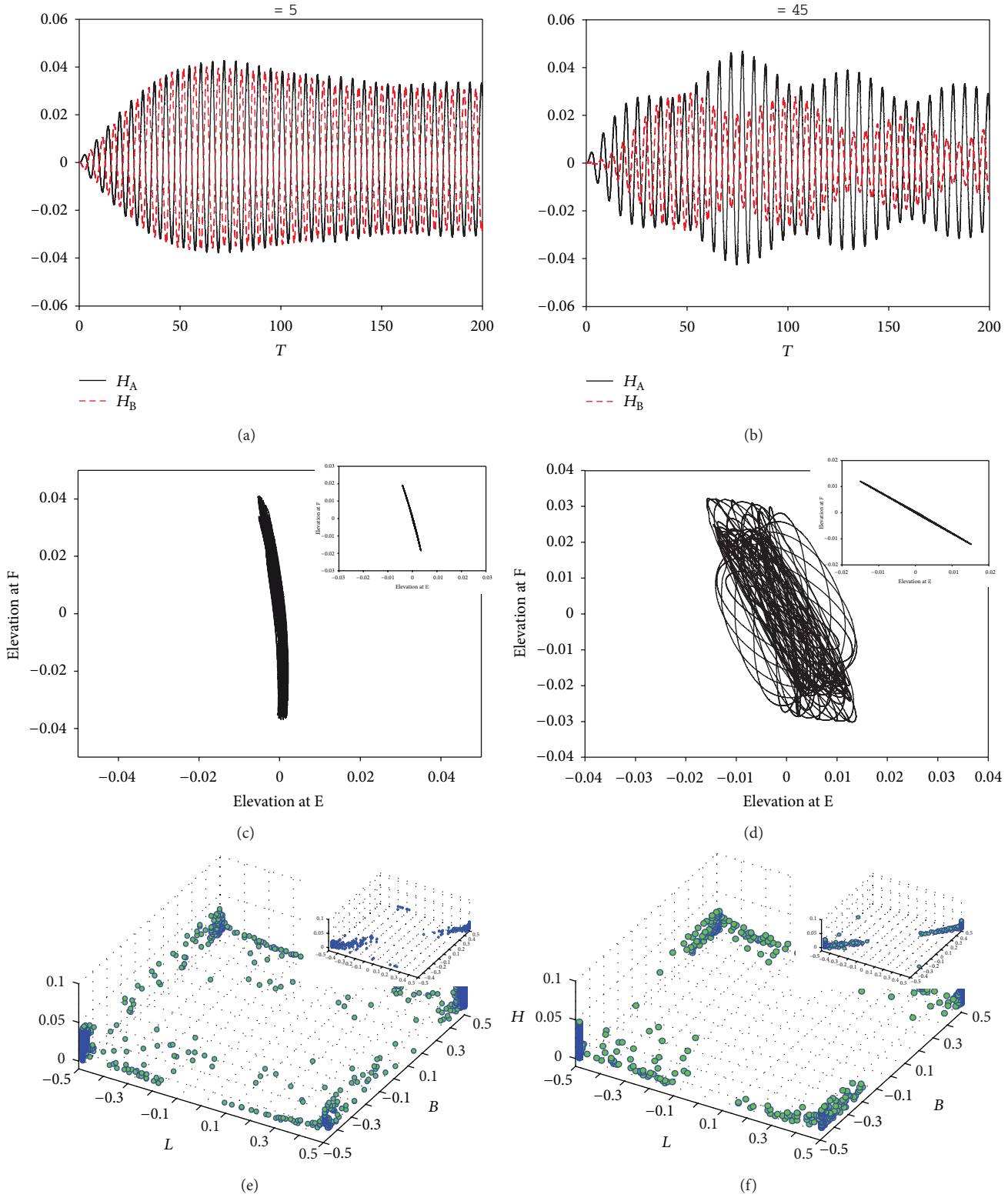

FIGURE 5: The effect of the baffle on the single-directional waves. The wave histories of points A and B, (a) $\theta = 5^{\circ}$; (b) $\theta = 45^{\circ}$; the wave pattern, (c) $\theta = 5^{\circ}$; (d) $\theta = 45^{\circ}$; the distribution of absolute peaks: the locations of the max peaks of the instantaneous free surface, (e) $\theta = 5^{\circ}$; (f) $\theta = 45^{\circ}$; $d_0/L = 0.5$, $d_b/d_0 = 0.5$, $a_0/L = 0.001$, and $\omega_x = \omega_z = 0.9\omega_1$. The inserts are the results of the unbaffled tank. Dimensionless elevation $H = \eta/d_0$ and dimensionless time $T = t/\sqrt{gd_0}$.

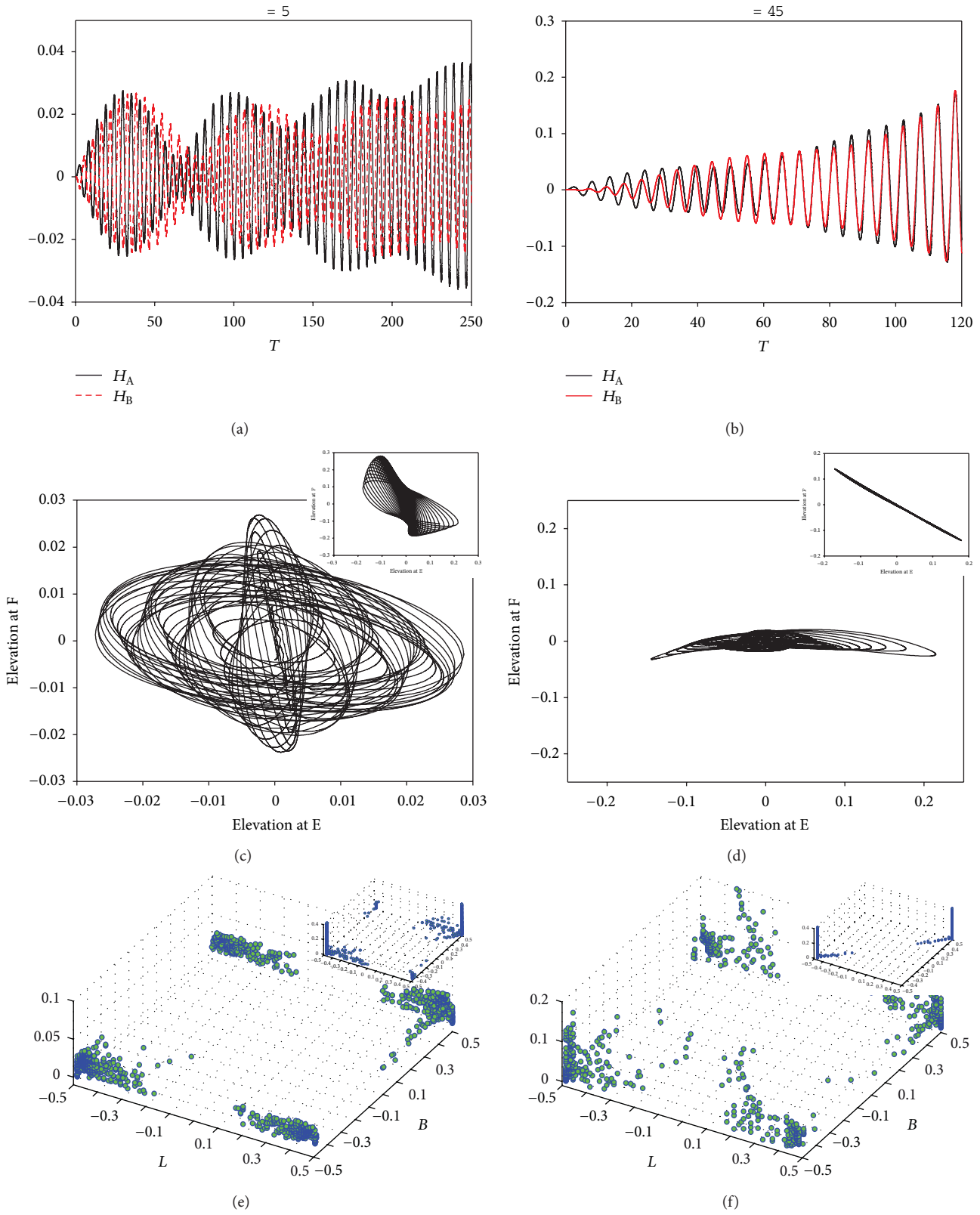

FIGURE 6: The effect of the baffle on the swirling waves. The wave histories of points A and B, (a) $\theta = 5^{\circ}$; (b) $\theta = 45^{\circ}$; the wave pattern, (c) $\theta = 5^{\circ}$; (d) $\theta = 45^{\circ}$; the distribution of peaks (e) $\theta = 5^{\circ}$; (f) $\theta = 45^{\circ}$; $d_0/L = 0.5$, $d_b/d_0 = 0.5$, $a_0/L = 0.001$, and $\omega_x = \omega_z = 1.0\omega_1$. The inserts are the results of the unbaffled tank.

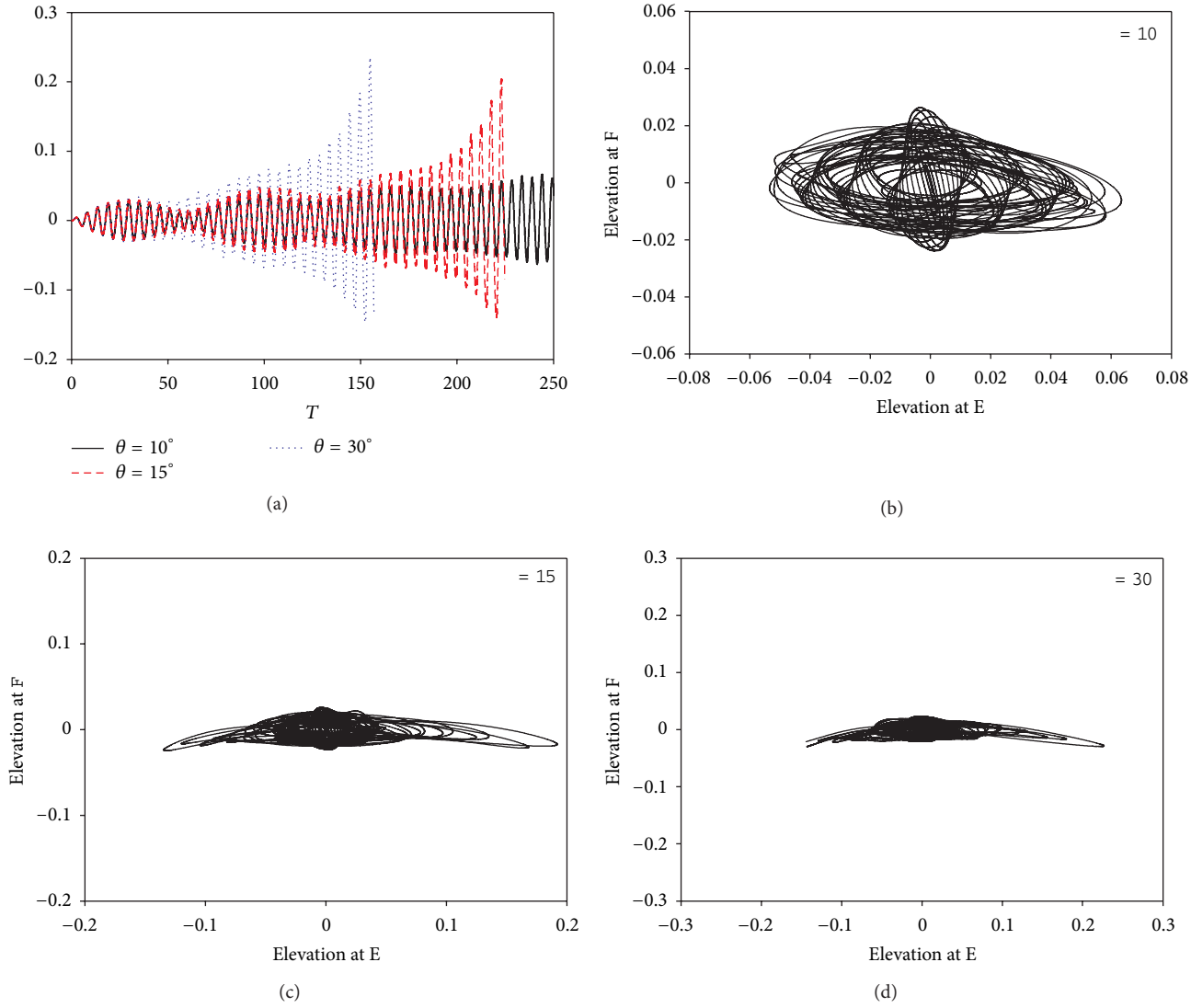

FIGURE 7: The effect of the baffle on the swirling waves under different excitation angles. (a) wave histories of point A; (b) wave pattern, $\theta = 10^{\circ}$; (c) wave pattern, $\theta = 15^{\circ}$; (d) wave pattern, $\theta = 30^{\circ}$; $d_0/L = 0.5$, $d_b/d_0 = 0.5$, $a_0/L = 0.001$, and $\omega_x = \omega_z = 1.0\omega_1$.

demonstrated in Figure 6(c), H_E is obviously larger than H_F, and as a result, an elliptic wave pattern is presented. Besides, the characteristics of the swirling waves are illustrated in Figures 6(c) and 6(e) and are different from those of unbaffled tank (the inserted plots).

When $\theta = 45^{\circ}$, a resonant sloshing elevation is shown in Figure 6(b) that goes beyond the limitation of the present numerical scheme after $T = 120$. In addition, a major peak of $1.0\omega_1$ is presented in the spectral analysis of H_A depicted in Figure 10(b) when $\theta = 45^{\circ}$. The sloshing elevation, consequently, behaves as a resonant phenomenon induced by the resonant mode of $1.0\omega_1$. Moreover, the swirling waves are difficultly generated for an unbaffled tank under a resonant diagonal excitation (see the inserts of Figures 6(d) and 6(f)), whereas it is visibly found for the baffled tank, which is demonstrated in Figure 6(f). The wave pattern depicted in Figure 6(d) shows that H_E is bigger than H_F indicating that the prevailing sloshing amplitude is in the transversal (z) direction.

From the design point of view, the best way in reducing the sloshing amplitude for a tank under a resonant diagonal excitation is to mount a diagonally bottom-mounted baffle from point B to point D. On the other hand, the baffle mounted parallel to the tank width can effectively dampen the sloshing amplitude when the oblique excitation angle is small. As a baffled tank is excited at $1.0\omega_1$ under $\theta = 10^{\circ}$, 15°, and 30°, the results of wave histories at point A depicted in Figure 7(a) demonstrate that the smaller the excitation angle, the larger the damping effect caused by the baffle. Additionally, the wave patterns of $\theta = 10^{\circ}, 15^{\circ}$, and 30° relative to the swirling waves are illustrated in Figures 7(b), 7(c), and 7(d), respectively. The sloshing elevation in the z-direction becomes more dominant with the increase of the oblique excitation angle of the baffled tank. Moreover, the

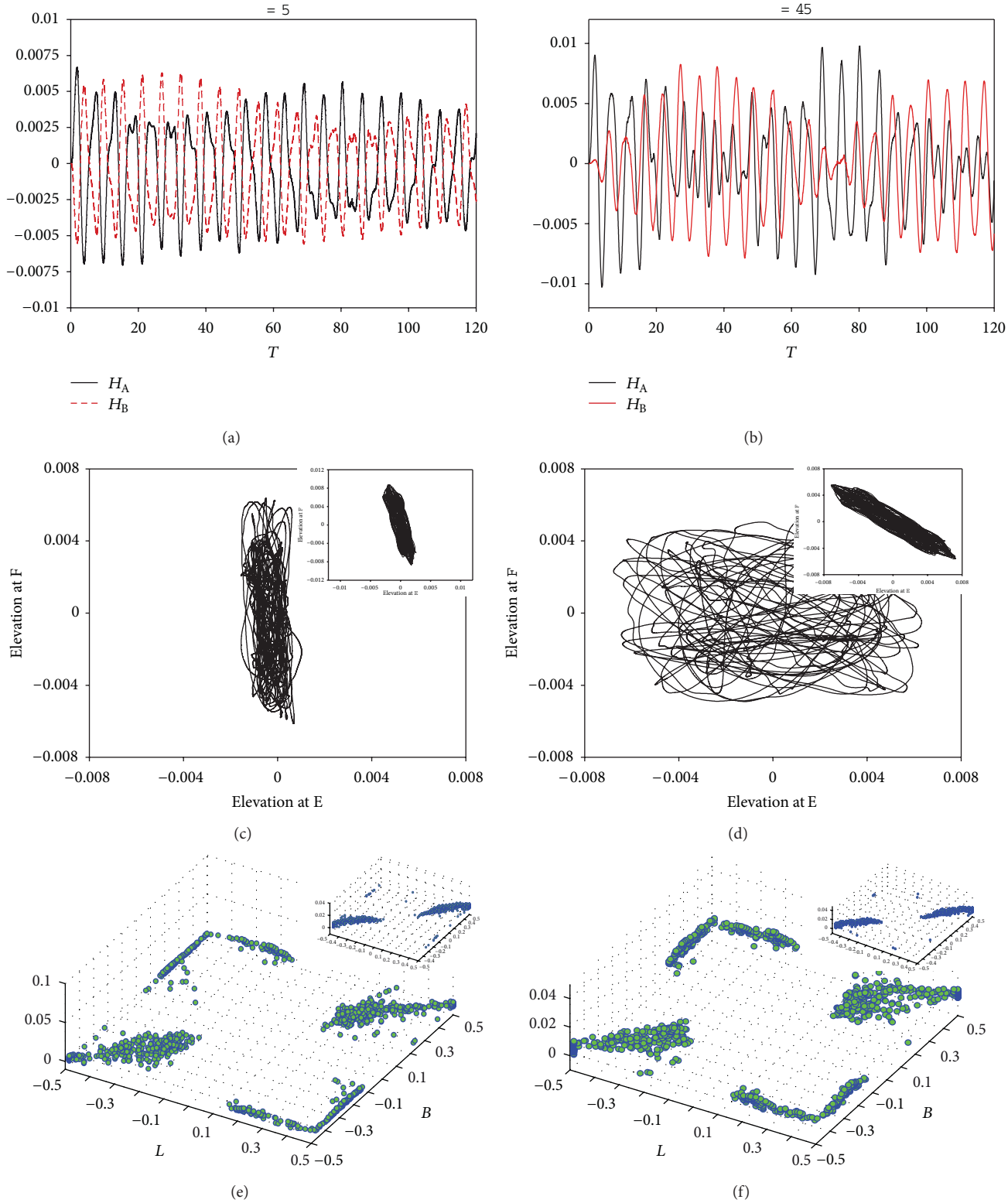

FIGURE 8: The effect of the baffle on the square-like waves. The wave histories of points A and B, (a) $\theta = 5^{\circ}$; (b) $\theta = 45^{\circ}$; the wave pattern, (c) $\theta = 5^{\circ}$; (d) $\theta = 45^{\circ}$; the distribution of peaks (e) $\theta = 5^{\circ}$; (f) $\theta = 45^{\circ}$; $d_0/L = 0.5$, $d_b/d_0 = 0.5$, $a_0/L = 0.001$, and $\omega_x = \omega_z = 1.5\omega_1$. The inserts are the results of the unbaffled tank.

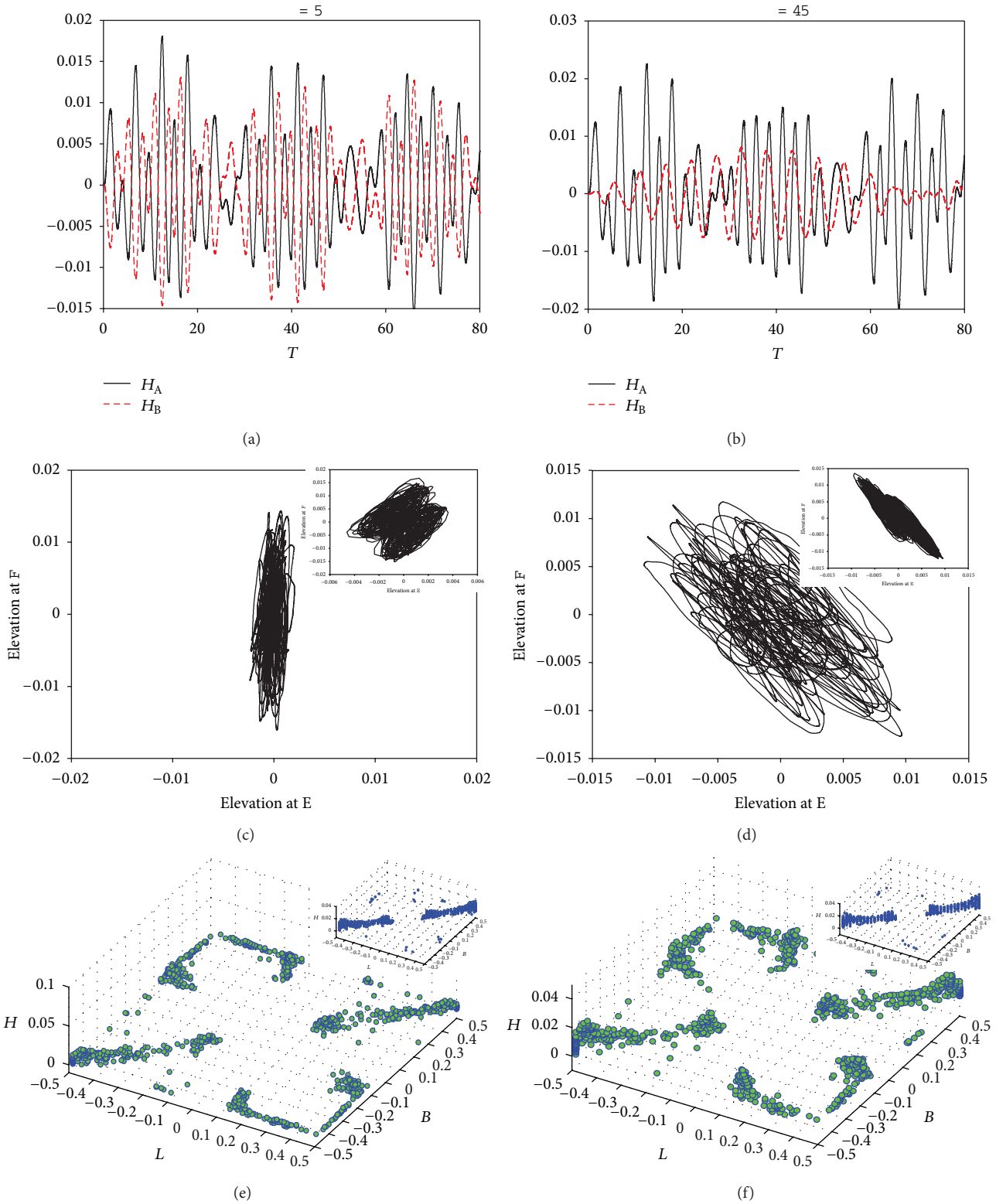

FIGURE 9: The effect of the baffle on the irregular waves. The wave histories of points A and B, (a) $\theta = 5^{\circ}$; (b) $\theta = 45^{\circ}$; the wave pattern, (c) $\theta = 5^{\circ}$; (d) $\theta = 45^{\circ}$; the distribution of peaks (e) $\theta = 5^{\circ}$; (f) $\theta = 45^{\circ}$; $d_0/L = 0.5$, $d_b/d_0 = 0.5$, $a_0/L = 0.001$, and $\omega_x = \omega_z = 2.0\omega_1$. The inserts are the results of the unbaffled tank.

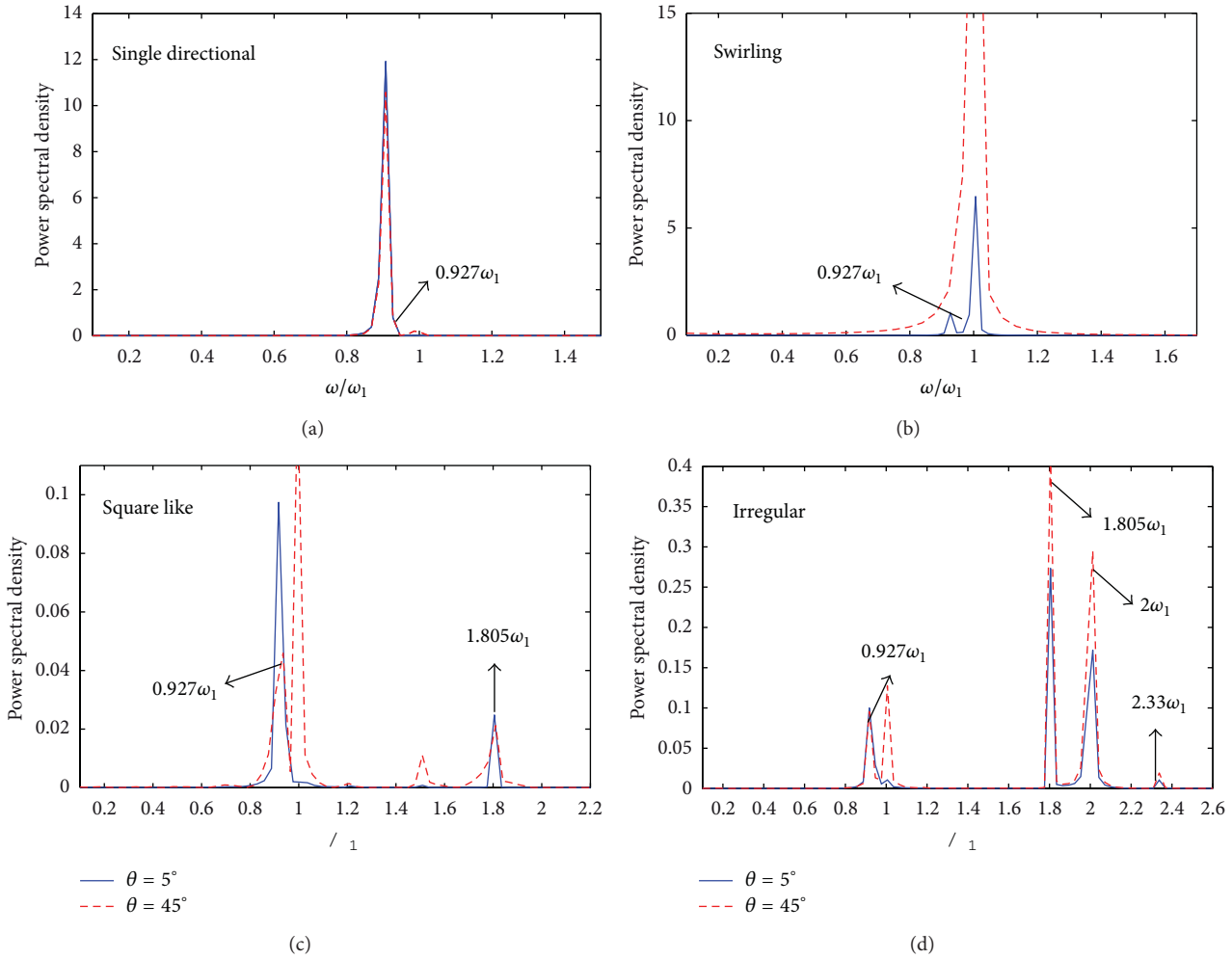

FIGURE 10: The power spectral analysis of the wave elevation at point A for a baffled tank under various excitation angles. The excitation frequency of the tank (a) $0.9\omega_1$, single-directional waves; (b) $1.0\omega_1$, swirling wave; (c) $1.5\omega_1$, square-like wave; (d) $2.0\omega_1$, irregular wave; $d_0/L = 0.5$, $d_b/d_0 = 0.5$, and $a_0/L = 0.001$.

resonant sloshing phenomenon still occurs at $\theta = 15^\circ$ and 30° and is beyond the limitation of the present numerical model.

3.2.3. Effect of Baffle on Square-Like Wave ($1.5\omega_1$). The results of the influence of the baffle on the square-like waves under various excitation angles are delineated in Figure 8. When $\theta = 5^\circ$, Figures 8(a), 8(c), and 8(e) show, respectively, the significant effect of the baffle on the sloshing elevation, wave pattern, and the peaks' distribution of the square-like waves compared to those of unbaffled tank. According to the spectral analysis of H_A shown in Figure 10(c), the elevations of points A and B are dominated by two major modes; one is $0.927\omega_1$, and another other is $1.805\omega_1$. The influence of excitation frequency ($1.5\omega_1$) on sloshing elevation, however, becomes insignificant. The dominant sloshing elevation of unbaffled tank is in the x-direction (inserted plot of Figure 8(c)), and it becomes more dominant due to the effect of the baffle. Besides, it is found that the square-like waves and the swirling waves appear together in the simulation. Although two kinds of sloshing waves coexist, the wave type is still dominated by the square-like waves for this case.

As the oblique excitation angle increases to 45°, the elevation of point A shown in Figure 8(b) becomes irregular. The reason is, by comparing with that of $\theta = 5^\circ$, two more peaks ($1.0\omega_1$ and $1.5\omega_1$) appear in the spectral analysis of H_A depicted in Figure 10(c). Additionally, the spectral density of the mode of $0.927\omega_1$ decreases when θ is switched to 45°. This implies that the influence of the mode of $0.927\omega_1$ on the sloshing amplitude reduces as well. Furthermore, the result of H_B presents a beating-like wave. From the spectral analysis of H_B (not shown here), the beat wave is contributed by two modes, $0.927\omega_1$ and $1.0\omega_1$. The variation of oblique excitation of the baffled tank, therefore, induces the interchange between the modes of sloshing waves. Furthermore, the coexistence of the square-like waves and the swirling waves is demonstrated in Figures 8(d) and 8(f), and the swirling waves of $\theta = 45^\circ$ present more predominantly than that of $\theta = 5^\circ$. The

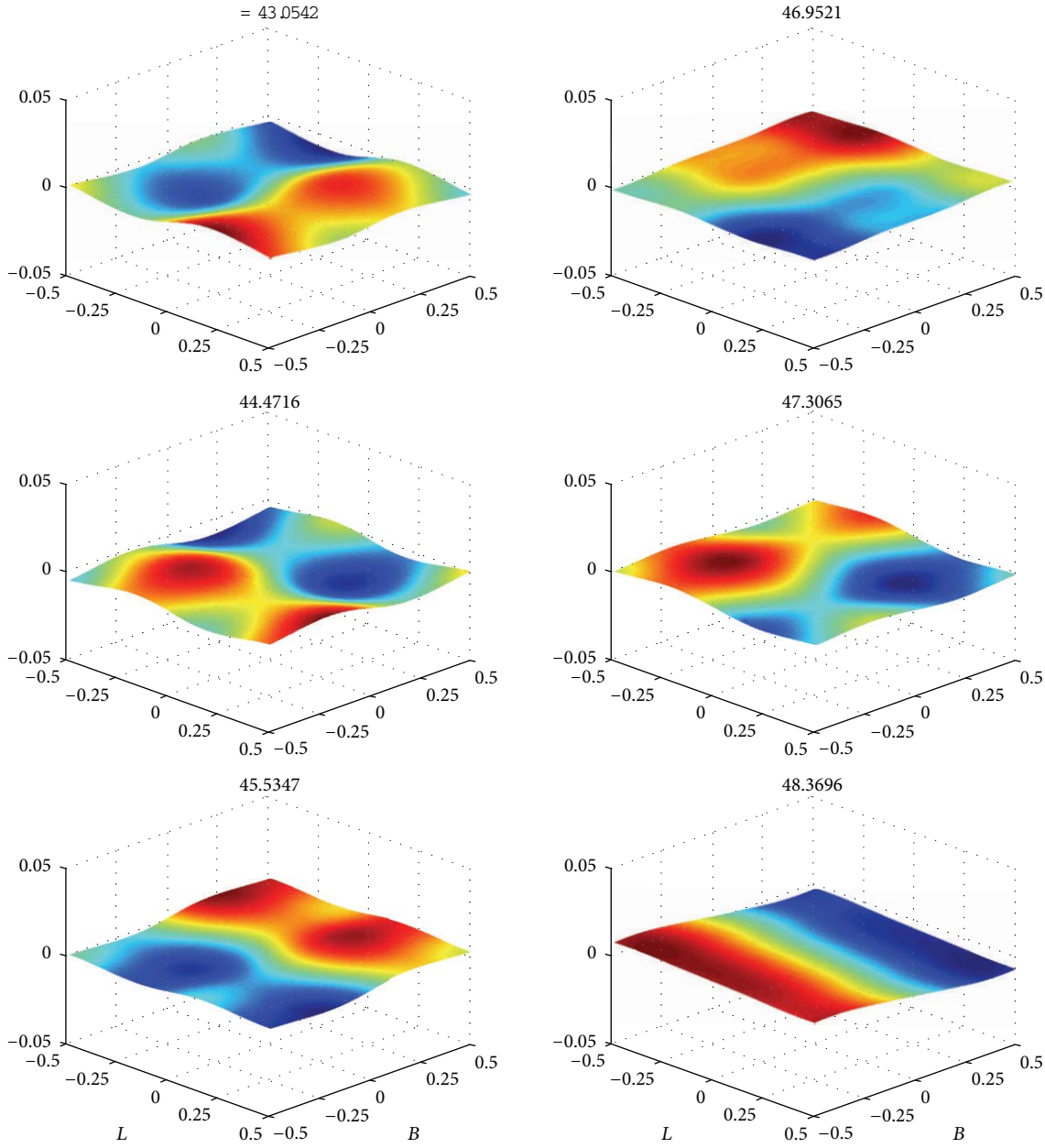

FIGURE 11: The snapshots of the free surface of a baffled tank; $d_0/L = 0.5$, $d_b/d_0 = 0.5$, $a_0/L = 0.001$, $\theta = 45^\circ$, and $\omega_x = \omega_z = 1.5\omega_1$. Dimensionless elevation $H = \eta/d_0$ and dimensionless time $T = t/\sqrt{gd_0}$.

reason might be correlated to the tendency of triggering the circulatory flow when $\theta = 45^\circ$ is easier than that when $\theta = 5^\circ$ due to the effects of the baffle.

3.2.4. Effect of Baffle on Irregular Wave ($2.0\omega_1$). As illustrated in Figure 9, the effect of the baffle on the irregular waves is similar to that on the square-like waves. The shift of the modes due to the variation of excitation angle is demonstrated as well by the result of spectral analysis of H_A illustrated in Figure 10(d). Besides, H_B depicted in Figure 9(b) also presents a beating phenomenon that is induced by $0.927\omega_1$ and $1.0\omega_1$ according to the spectral analysis (not presented here). The irregular waves coexist with the swirling waves, as shown in Figures 9(e) and 9(f). For the snapshots of the free surface, the swirling wave occurring at $\theta = 5^\circ$ is not as obvious as that at $\theta = 45^\circ$ that is similar to the phenomenon found in the results of the square-like waves affected by the baffle. The snapshots of the square-like waves and irregular waves that coexist with the swirling waves are illustrated in Figures 11 and 12, respectively.

3.3. Effect of a Surface-Piercing Flat Plate on Sloshing Waves. In this section, we will explore the effect of a surface-piercing

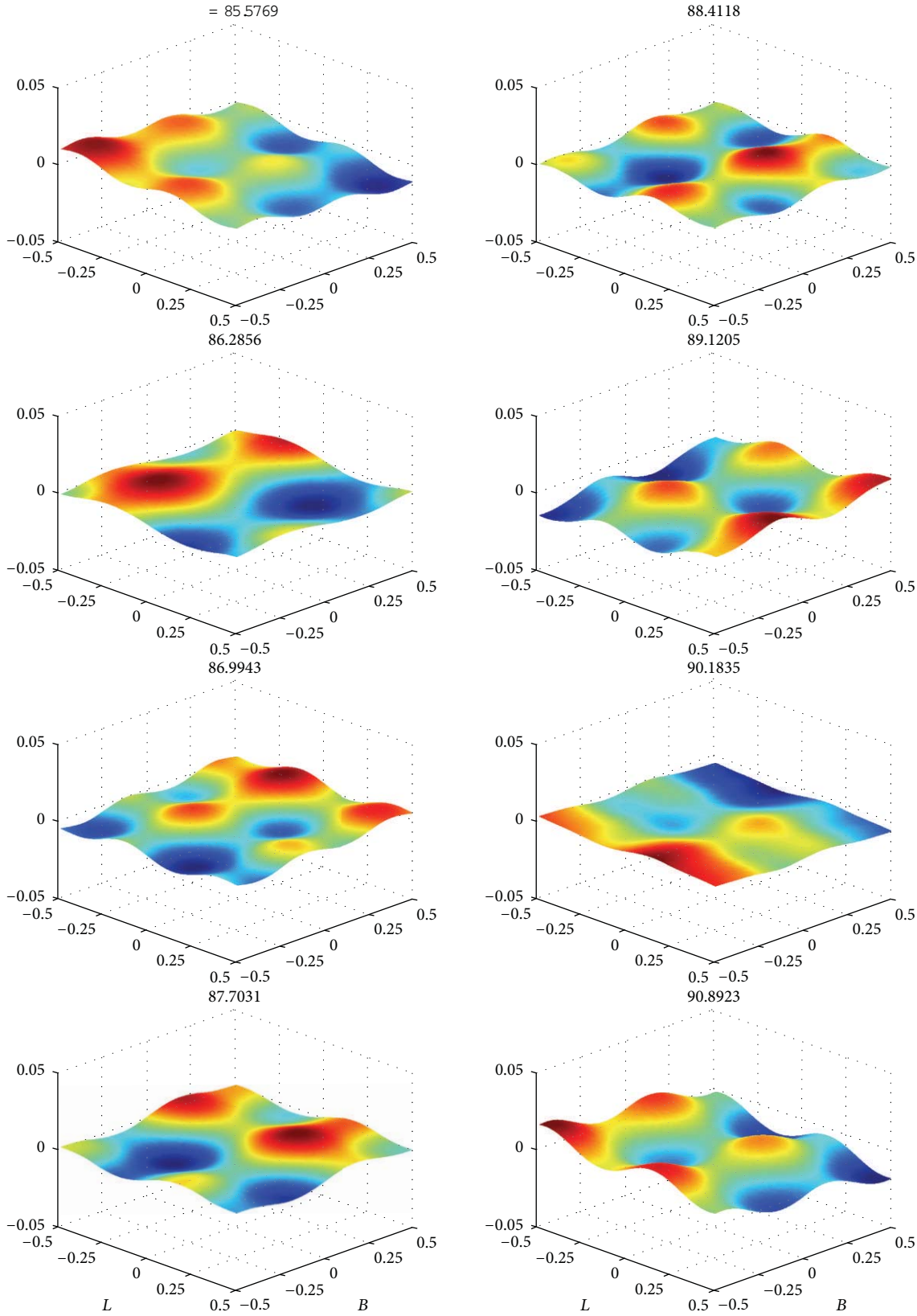

Figure 12: The snapshots of the free surface of a baffled tank; $d_0/L = 0.5$, $d_b/d_0 = 0.5$, $a_0/L = 0.001$, $\theta = 45^\circ$, and $\omega_x = \omega_z = 2.0\omega_1$. Dimensionless elevation $H = \eta/d_0$ and dimensionless time $T = t/\sqrt{gd_0}$.

flat plate in a 3D tank on various sloshing waves. As depicted in Figure 1(b), P_L is the length of the plate and is set to $0.4B$ for all the simulations in this work. The influence of the surface-piercing plate on sloshing dynamics in tanks is definitely different from that of the tank bottom-mounted baffle due to its direct blockage of the free surface. The free surface flow caused by the surface-piercing plate might become more complicated. The shift of the lowest nature mode of the tank with liquid affected by the surface-piercing plate is discussed here as well.

3.3.1. Effect of a Surface-Piercing Flat Plate on Single-Directional Waves ($0.9\omega_1$). The wave histories of points A and B for the single-directional waves affected by the plate are illustrated in Figure 13(a), and the beating phenomena of H_A and H_B are unclear, and the sloshing elevation seems to reach a nearly steady state after $T = 100$. The spectral analysis of H_A depicted in Figure 18(a) shows that two peaks appear when $\theta = 5^\circ$, and the primary peak is $0.91\omega_1$, which is close to the excitation frequency of the tank, and the secondary one ($1.79\omega_1$) is almost twice as big as the dominant frequency. Besides, the peak of $0.91\omega_1$ might be in connection with the first natural mode in the x axis due to the effect of the plate. The wave histories of points A and B depicted in Figure 13(a), therefore, behave as a resonant-like response when $\theta = 5^\circ$. Furthermore, the results of the wave pattern (Figure 13(c)) and the distribution of peaks (Figure 13(e)) demonstrate that the waves predominantly slosh in the x-direction. Moreover, the effect of the surface-piercing plate on the free surface is illustrated in the inserted plot of Figure 13(e). It is apparently seen that two sinks appear close to the corner of the plate on the free surface. These two sinks are 3D vortices induced by free surface flow passing the plate. The vortex sinks are the source of the disturbance on the free surface, which will result in generating more and more complicated free surface wave profiles.

When $\theta = 45^\circ$, the elevations of points A and B depicted in Figure 13(b) show several beating waves attributed to three modes, $0.91\omega_1$, $0.98\omega_1$, and $1.79\omega_1$ based on the spectral analysis of H_A illustrated in Figure 18(a). Furthermore, as depicted in Figure 18(a), the near-resonant mode of $0.98\omega_1$ appears when the excitation angle switches from 5° to 45°, and therefore, the sloshing elevation increases with time due to the influence of the near-resonant mode ($0.98\omega_1$). In addition, the original diagonal wave type is turned into swirling wave type due to the influence of the plate. The phenomenon of 3D sink vortices on the free surface near the plate's corners is presented in the inserted plot of Figure 13(e) as well, and detailed time history of snapshots of free surface are depicted in Figure 19. Note that the near-resonant mode of $0.98\omega_1$ should be the first natural mode of the plated tank in the z-direction. However, it is not equal to $1.0\omega_1$ which is the first natural mode in the z-direction of the baffled tank as we discussed in Section 3.2.1. The free surface disturbance induced by the plate might be the reason to shift the lowest nature mode in the z-direction of the plated tank.

3.3.2. Effect of a Surface-Piercing Flat Plate on Swirling Waves ($1.0\omega_1$). For a plated tank under a resonant excitation and $\theta = 5^\circ$, the beating phenomenon of the swirling waves is presented in Figure 14(a), and the elevations of points A and B increase with time. According to the spectral analysis of H_A shown in Figure 18(b), the dominant peak is the external excitation frequency ($1.0\omega_1$), which is equal to the first resonant mode in the z-direction, and the secondary peak ($0.91\omega_1$) can be correlated with the first natural mode in the x-direction. The growth of the sloshing elevation is, therefore, mainly induced by the dominant resonant mode ($1.0\omega_1$), especially in the transversal (z) direction. An elliptic wave pattern depicted in Figure 14(c) is, therefore, presented due to H_E which is larger than H_F. Moreover, the clockwise swirling waves appear constantly, and the phenomenon of switch direction of swirling waves disappears. In other words, unlike the effect of the tank bottom-mounted baffle, the surface-piercing plate not only shifts the natural mode system of the tank, but alters the characteristic of the swirling waves. The absolute peaks of clockwise swirling waves, as depicted in Figure 14(e), mostly distribute along the tank walls that indicate that the free surface flow is circling the plate. Accordingly, the phenomenon of vortex sinks and free surface disturbance caused by the plate is unapparent (see inserted plot of Figure 14(e)), and the shift of the first natural mode in the z-direction is unaffected.

When $\theta = 45^\circ$, a resonant sloshing amplitude is shown in Figure 14(b), and the result goes beyond the limitation of the present numerical scheme after $T = 110$. The sloshing elevation, consequently, behaves as a resonant phenomenon induced by the resonant mode ($1.0\omega_1$) based on the spectral analysis of H_A depicted in Figure 18(b) when $\theta = 45^\circ$. Moreover, the feature of the swirling waves is manifestly presented in Figures 14(d) and 14(f), and the invariant clockwise swirling waves occur as well for a plated tank under a diagonal resonant excitation. Besides, the dominant sloshing elevation is in the transversal direction due to the effect of the resonant mode ($1.0\omega_1$), and the phenomenon of vortex sinks near the plate's corners is, therefore, unobvious.

The damping effect caused by the vertical plate under various excitation angles is similar to that of the vertical baffle discussed in Section 3.2. The wave histories at point A depicted in Figure 15(a) for a tank with an excitation frequency of $1.0\omega_1$ under $\theta = 10^\circ$, 15°, and 30° also demonstrate that the smaller the excitation angle, the larger the damping effect caused by the plate. Additionally, the wave patterns of $\theta = 10^\circ, 15^\circ$, and 30° are illustrated in Figures 15(b), 15(c), and 15(d), respectively, and the sloshing elevation in the z-direction becomes more dominant with the increase of the excitation angle.

3.3.3. Effect of a Surface-Piercing Flat Plate on Square-Like Waves ($1.5\omega_1$). The effect of the vertical plate on the square-like waves under various excitation angles is delineated in Figure 16. As shown in Figures 16(a) and 16(b), the wave elevations of points A and B present a resonant phenomenon with a higher sloshing frequency. This behaviour of the sloshing waves is similar to a liquid tank which is just excited

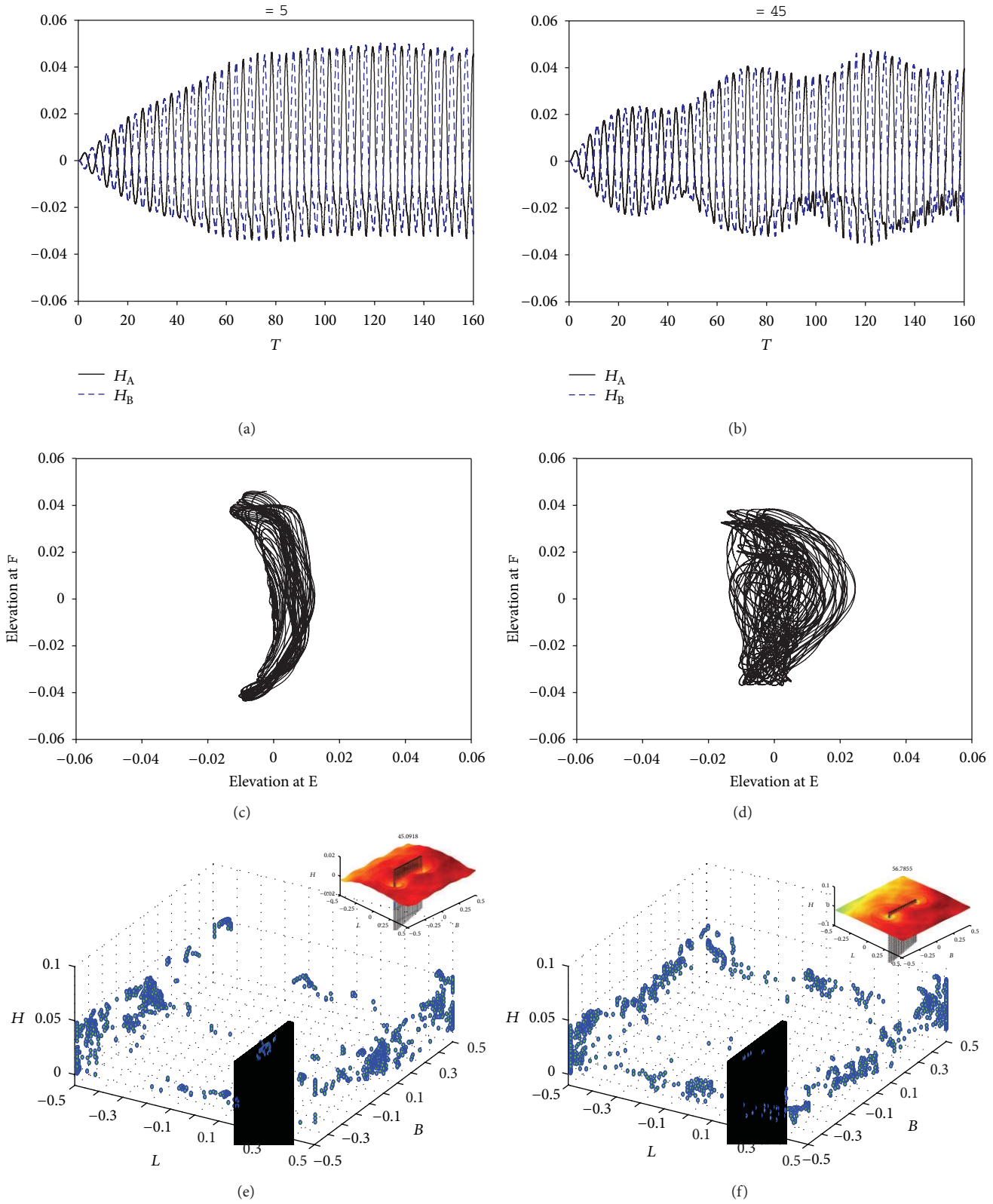

FIGURE 13: The effect of the plate on the single-directional waves. The wave histories of points A and B, (a) $\theta = 5^{\circ}$; (b) $\theta = 45^{\circ}$; the wave pattern, (c) $\theta = 5^{\circ}$; (d) $\theta = 45^{\circ}$; the distribution of peaks (e) $\theta = 5^{\circ}$; (f) $\theta = 45^{\circ}$; $d_0/L = 0.5$, $P_L/B = 0.4$, $a_0/L = 0.001$, and $\omega_x = \omega_z = 0.9\omega_1$. The inserts are the instantaneous free surface. Dimensionless elevation $H = \eta/d_0$ and dimensionless time $T = t/\sqrt{gd_0}$.

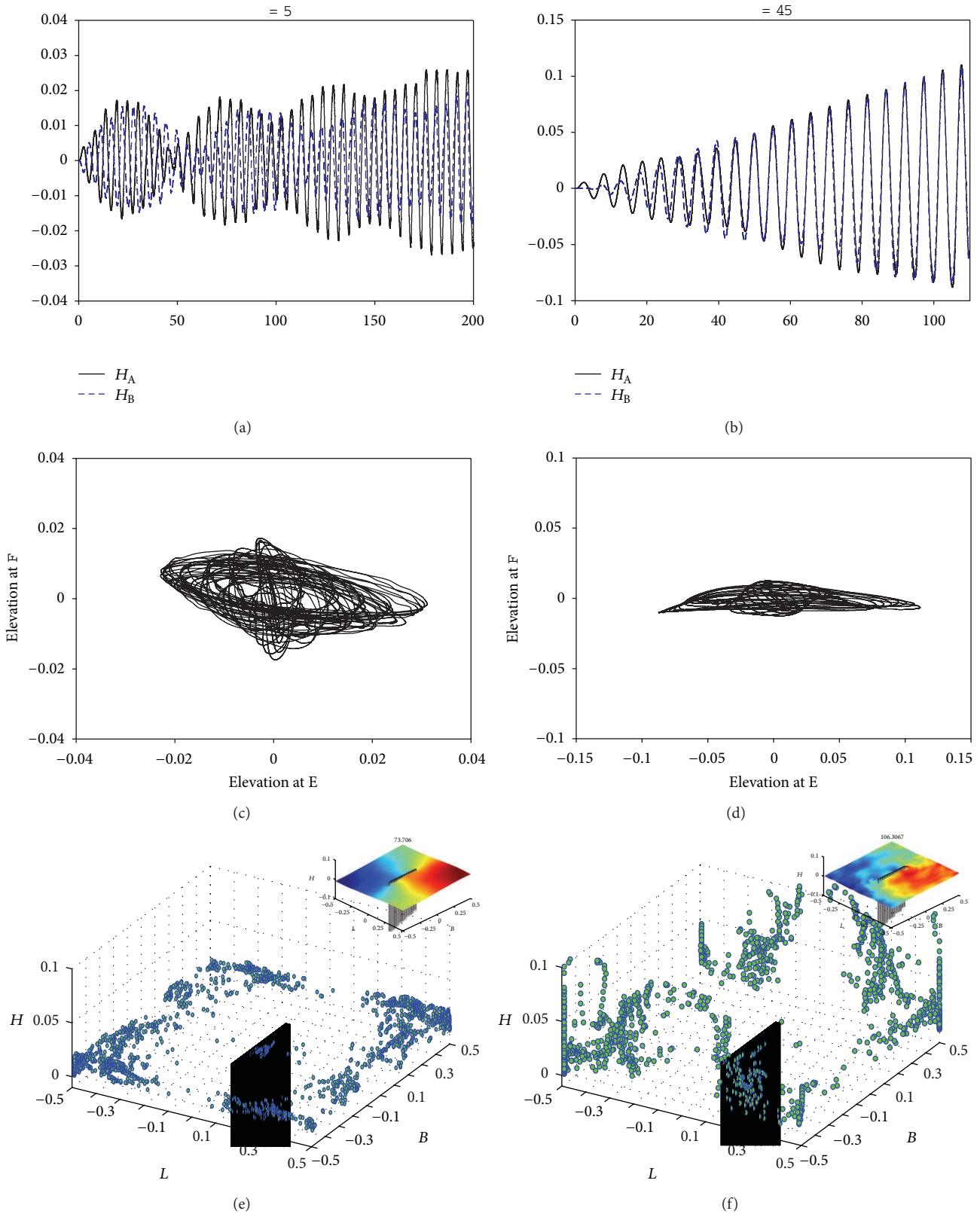

FIGURE 14: The effect of the plate on the swirling waves. The wave histories of points A and B, (a) $\theta = 5^\circ$; (b) $\theta = 45^\circ$; the wave pattern, (c) $\theta = 5^\circ$; (d) $\theta = 45^\circ$; the distribution of peaks (e) $\theta = 5^\circ$; (f) $\theta = 45^\circ$; $d_0/L = 0.5$, $P_L/B = 0.4$, $a_0/L = 0.001$, and $\omega_x = \omega_z = 1.0\omega_1$.

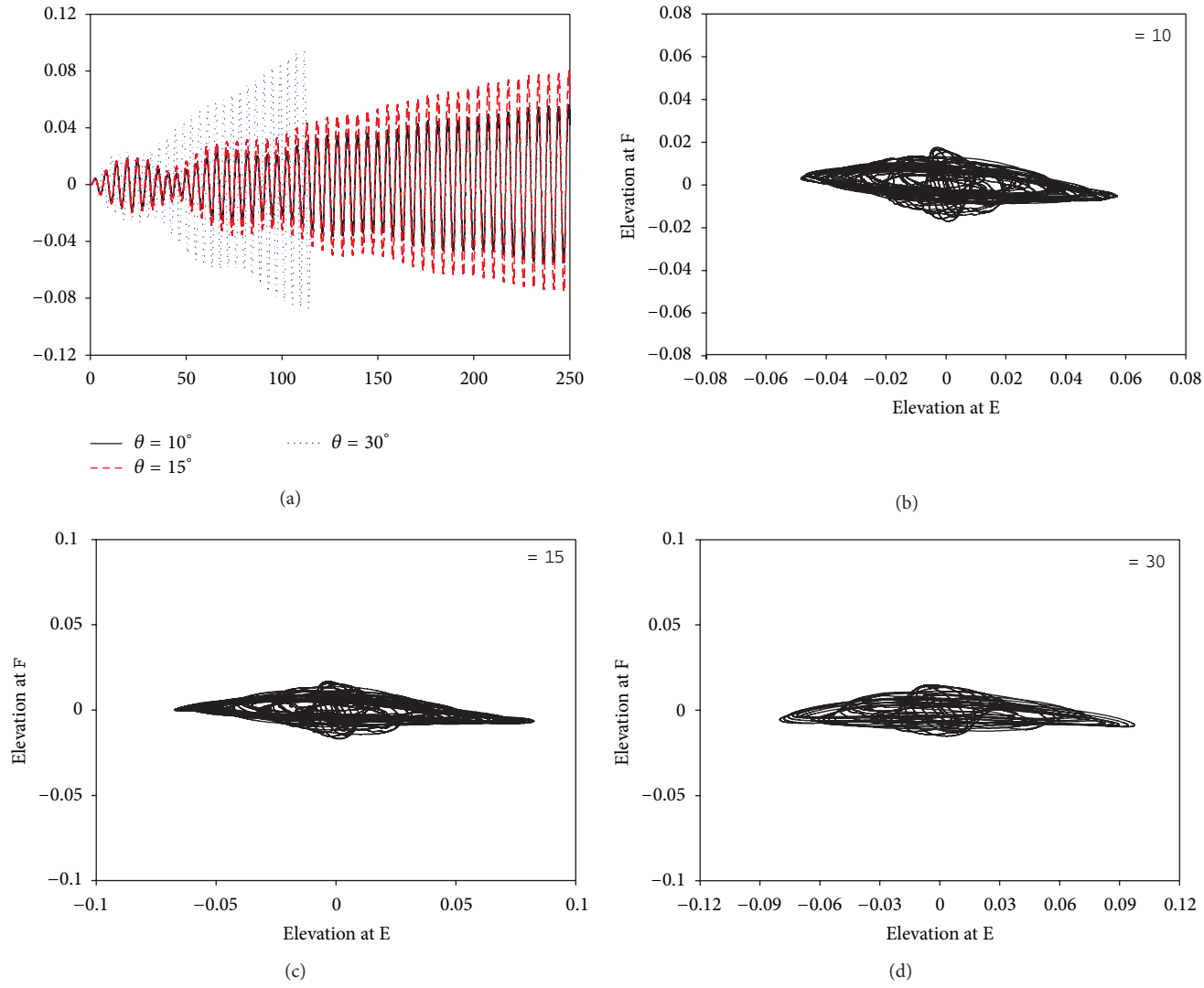

FIGURE 15: The effect of the plate on the swirling waves under different excitation angles. (a) Wave history of point A; (b) wave pattern, $\theta = 10^{\circ}$; (c) wave pattern, $\theta = 15^{\circ}$; (d) wave pattern, $\theta = 30^{\circ}$; $d_0/L = 0.5$, $P_L/B = 0.4$, $a_0/L = 0.001$, and $\omega_x = \omega_z = 1.0\omega_1$.

at a frequency of a higher resonant mode, that is, $i = 2$ or $i = 3$. In addition, the third natural mode ($\omega_{3,0}$) of a tank without the plate is $1.73\omega_1$, and according to the spectral analysis shown in Figure 18(c), the peak of $1.5\omega_1$ appears that it might be correlated with the shift of the third natural mode of the sloshing waves. Moreover, the secondary peak in the figure is $3.0\omega_1$ and is twice as large as the primary one. The wave pattern depicted in Figures 16(c) and 16(d) is not like that of the square-like waves. Furthermore, the distribution of peaks illustrated in Figures 16(e) and 16(f) demonstrates that the peaks not only concentrate on four corners of the tank but scatter in the vicinity of the plate. The corresponding free surface snapshots are illustrated in Figure 20.

3.3.4. Effect of a Surface-Piercing Flat Plate on Irregular Waves ($2.0\omega_1$). As the excitation frequency of the tank becomes $2.0\omega_1$, the irregular waves appear [28]. Figure 17 illustrates the wave histories of points A and B, the wave patterns, and the distribution of peaks for a plated tank under different oblique horizontal excitation. The figure presents all the characteristics of the irregular waves. This indicates that the irregular waves seem to be independent of the influence of the vertical plate. In addition, several peaks appearing in the spectral analysis of H_A (Figure 18(d)) demonstrate that the wave sloshes irregularly in the tank, and the numbers of the peaks are more than those of baffled tank. The disturbance of the surface-piercing plate on the surface waves is the factor to trigger several sloshing modes. The phenomenon of mode shift of irregular waves is found when $\theta = 5^{\circ}$ switches to $\theta = 45^{\circ}$.

4. Conclusion

The extended study of proposed numerical scheme [24] is implemented to investigate sloshing dynamics in tanks with two damping devices, tank bottom-mounted baffle, and

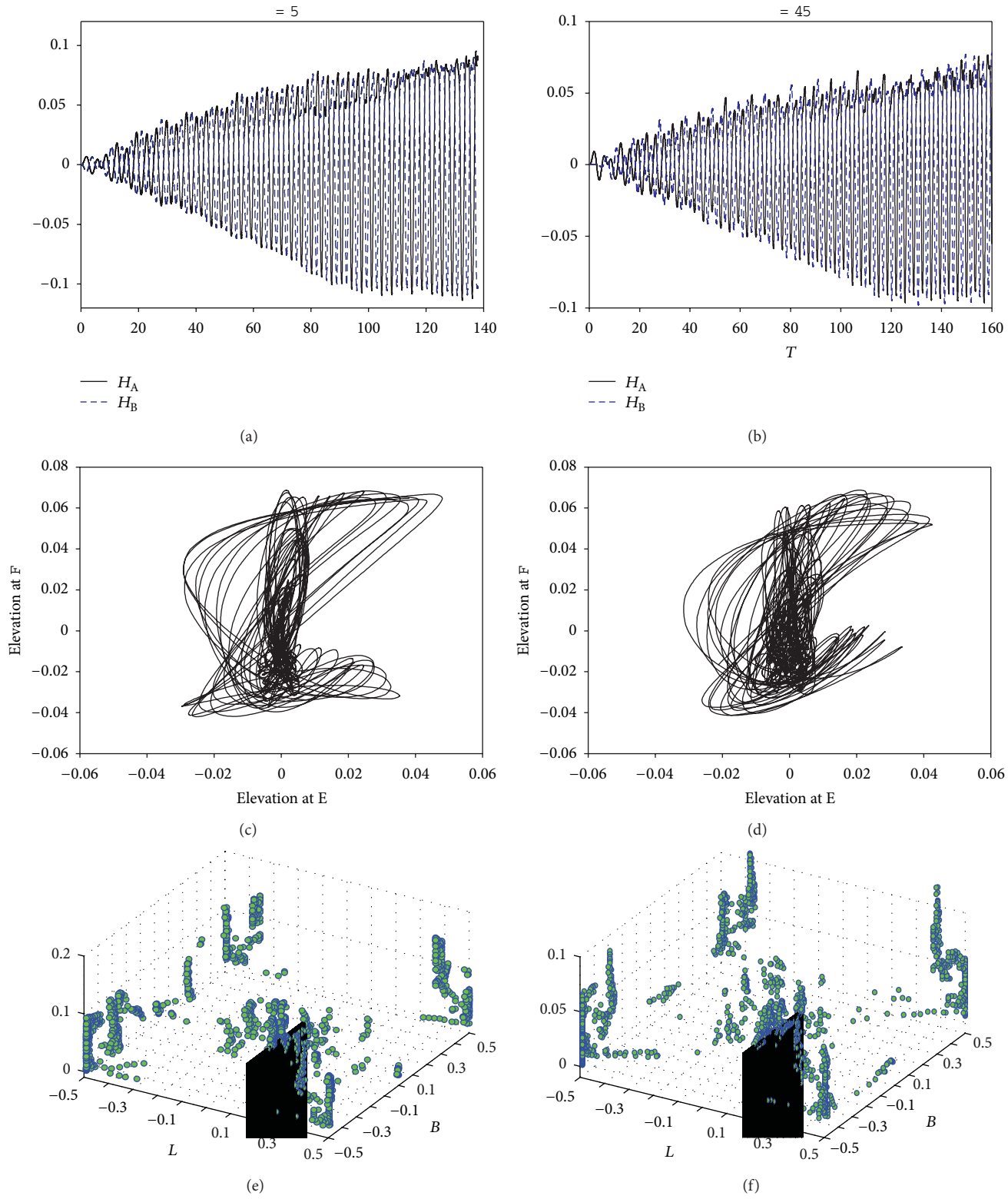

FIGURE 16: The effect of the plate on the square-like waves. The wave histories of points A and B, (a) $\theta = 5^o$; (b) $\theta = 45^o$; the wave pattern, (c) $\theta = 5^o$; (d) $\theta = 45^o$; the distribution of peaks (e) $\theta = 5^o$; (f) $\theta = 45^o$; $d_0/L = 0.5$, $P_L/B = 0.4$, $a_0/L = 0.001$, and $\omega_x = \omega_z = 1.5\omega_1$.

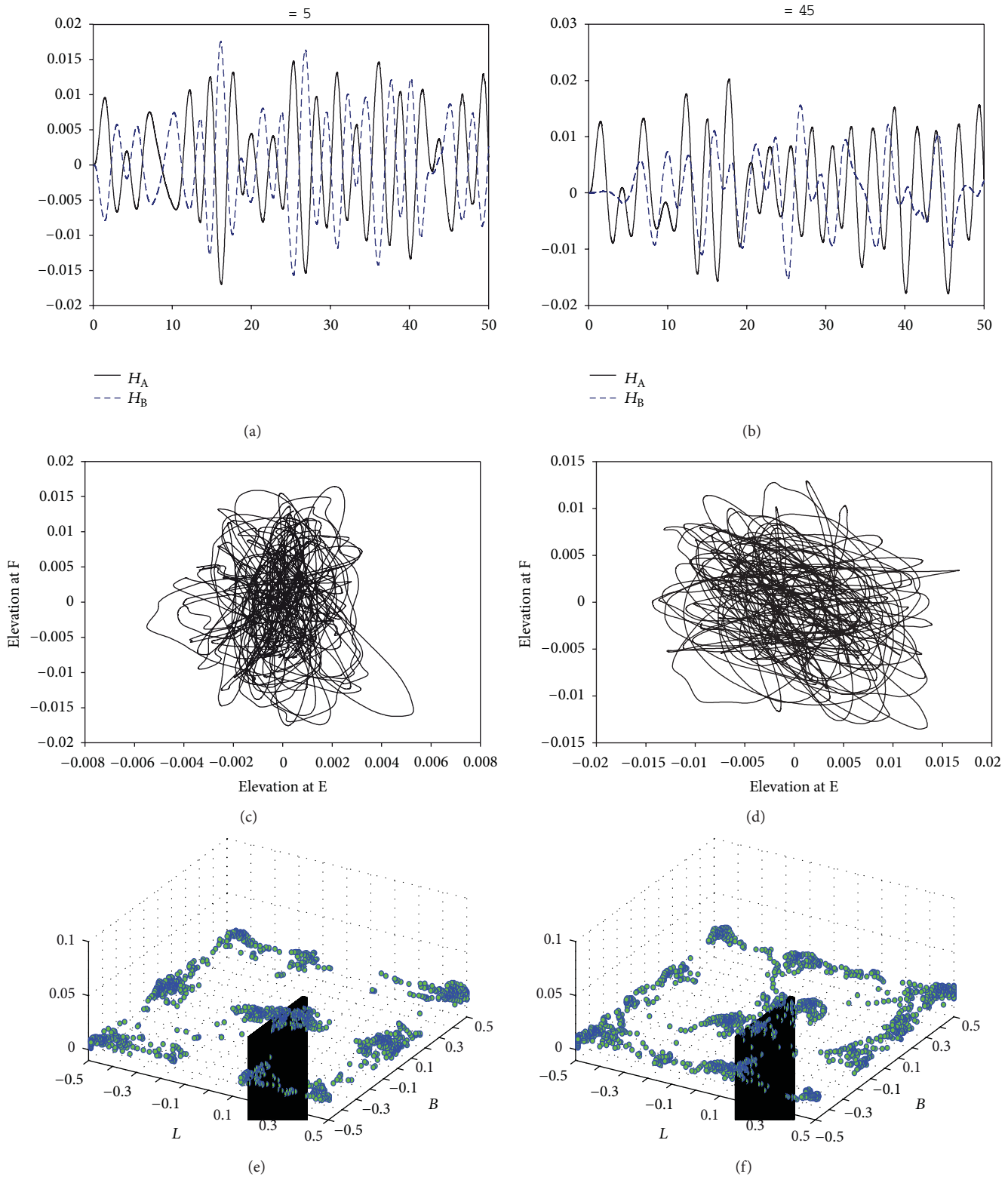

FIGURE 17: The effect of the plate on the irregular waves. The wave histories of points A and B, (a) $\theta = 5^{\circ}$; (b) $\theta = 45^{\circ}$; the wave pattern, (c) $\theta = 5^{\circ}$; (d) $\theta = 45^{\circ}$; the distribution of peaks (e) $\theta = 5^{\circ}$; (f) $\theta = 45^{\circ}$; $d_0/L = 0.5$, $P_L/B = 0.4$, $a_0/L = 0.001$, and $\omega_x = \omega_z = 2.0\omega_1$.

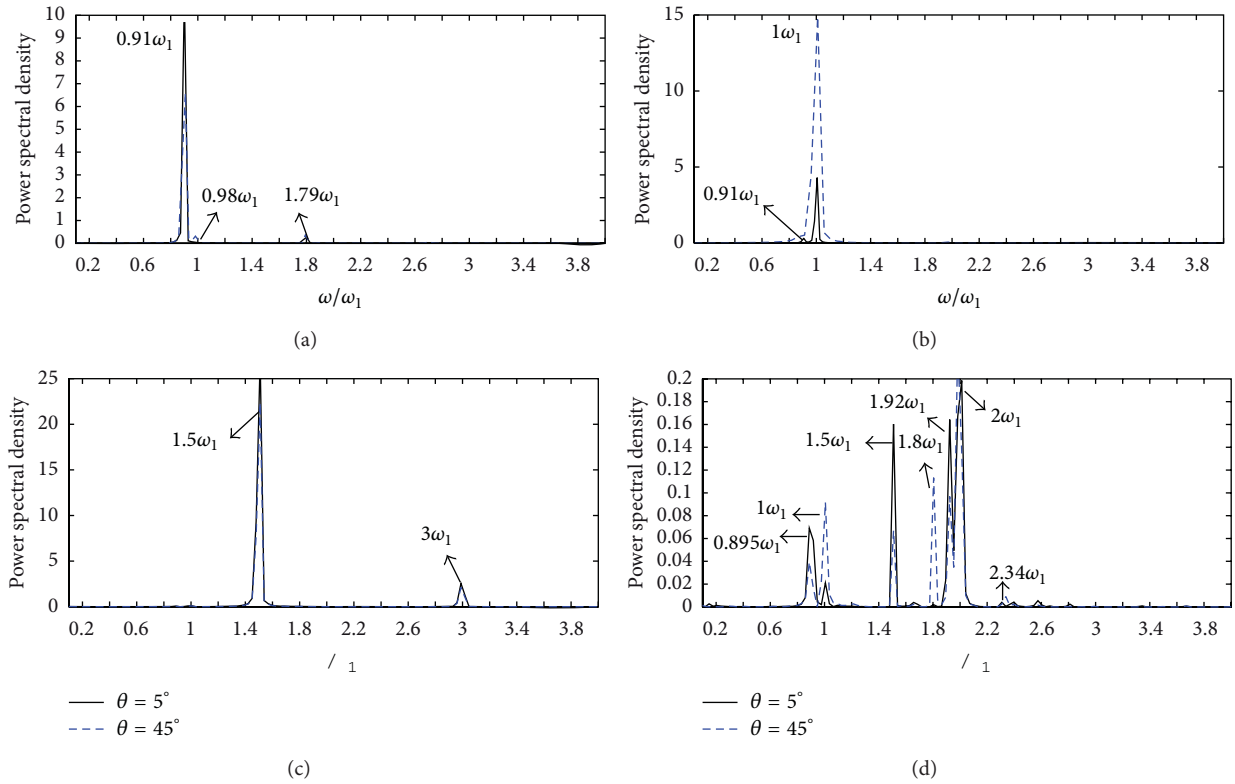

FIGURE 18: The power spectral analysis of the wave elevation at point A for a tank with a vertical plate under various excitation angles. The excitation frequency of the tank (a) $0.9\omega_1$; (b) $1.0\omega_1$; (c) $1.5\omega_1$; (d) $2.0\omega_1$; $d_0/L = 0.5$, $P_L/B = 0.4$, and $a_0/L = 0.001$.

surface-piercing flat plate. The 3D tank with damping devices is subjected to different oblique horizontal excitation under various excitation frequencies. The treatment of flow field around flow damping devices is carried out by a fictitious cell approach. The effects of a vertically tank bottom-mounted baffle and a surface-piercing flat plate on the nature modes of various sloshing waves for a tank subjected to oblique horizontal excitation are examined and discussed. Not only is the numerical simulation studied in this work, the experiment setup for a tank with a baffle is also investigated to further validate the accuracy of the developed numerical scheme. The following key conclusions are made.

(1) The present numerical results are in good agreement with the experimental measurement for a 3D tank with a vertically tank bottom-mounted baffle.

(2) The single-directional waves turn into swirling waves due to the effect of the tank bottom-mounted baffle for the baffled tank under oblique horizontal excitation. The generation of clockwise flow due to the baffle is the main reason to shift the wave type from single-directional to swirling.

(3) The influence of dominant resonant modes on single-directional waves in the baffled tank varies with different oblique excitation angles.

(4) The swirling waves are difficultly generated for an unbaffled tank under a resonant diagonal excitation whereas it is obviously found in the baffled tank due to the effect of the baffle.

(5) As the baffled tank excited at the lowest natural mode, $1.0\omega_1$, the smaller the excitation angle, the larger the sloshing damping effect caused by the baffle. The sloshing elevation in the z-direction becomes more dominant with the increase of the oblique excitation angle of the baffled tank.

(6) Both the square-like waves and the irregular waves can be found to coexist with the swirling waves when the excitation frequency of the baffled tank is $1.5\omega_1$ and $2.0\omega_1$, respectively. Besides, swirling waves of $\theta = 45^\circ$ present more predominantly than that of $\theta = 5^\circ$ because the tendency of triggering the circulatory flow when $\theta = 45^\circ$ is easier than when $\theta = 5^\circ$.

(7) The effect of a surface-piercing plate on the wave surface is significant. The vortex sinks near the corners of the plate are the source of free surface disturbance, which will result in more complicated free surface flow. The disturbance on the free surface caused by the plate might shift the natural mode system of the tank with fluid.

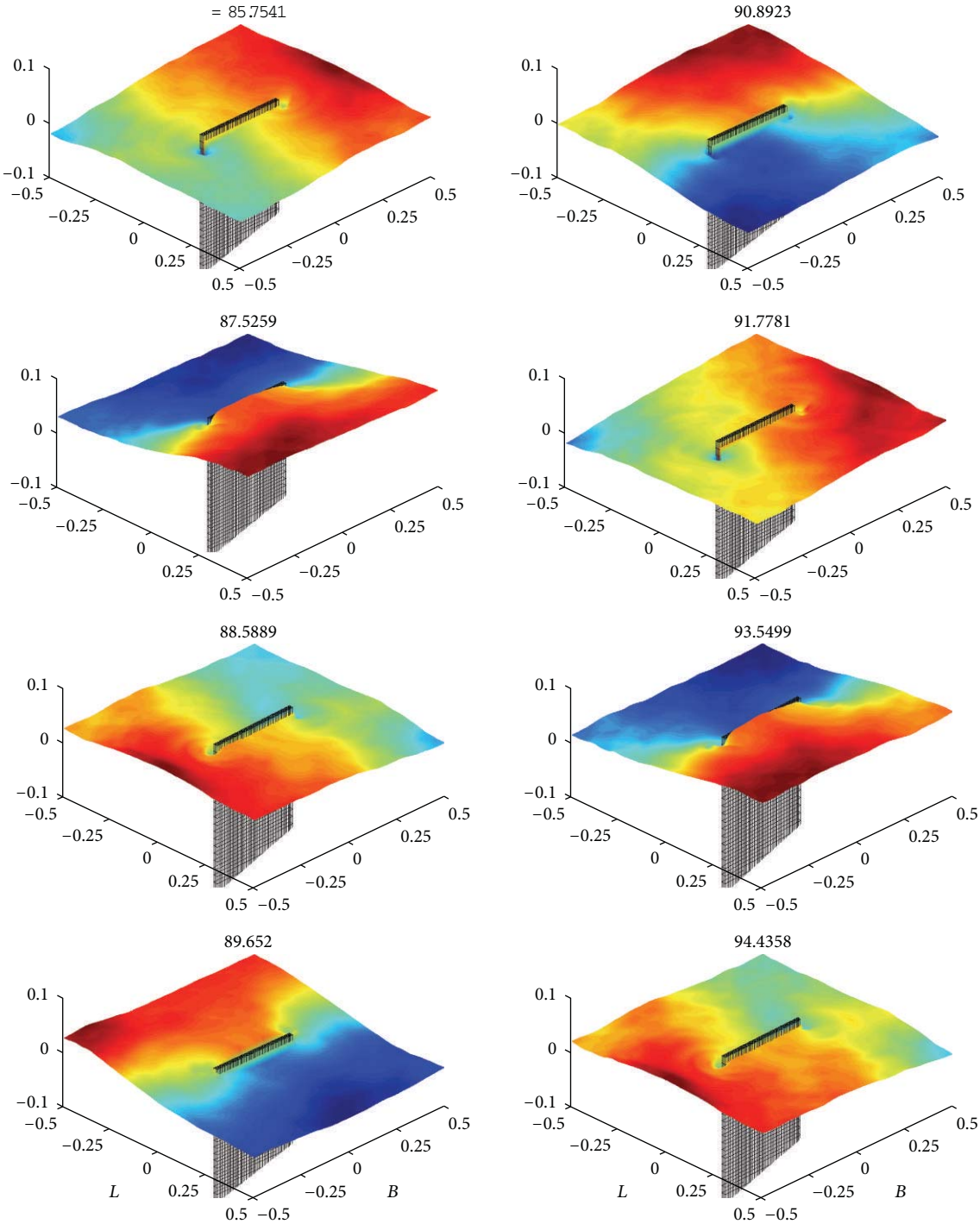

FIGURE 19: The snapshots of the free surface of a tank with a vertical plate; $d_0/L = 0.5$, $P_L/B = 0.4$, $a_0/L = 0.001$, $\theta = 45^\circ$, and $\omega_x = \omega_z = 0.9\omega_1$. Dimensionless elevation $H = \eta/d_0$ and dimensionless time $T = t/\sqrt{gd_0}$.

(8) Unlike the effect of the tank bottom-mounted baffle, the surface-piercing plate not only shifts the natural mode system of the tank, but alters the characteristic of swirling waves. The clockwise swirling waves constantly appear in the plated tank, and the switch direction of swirling waves disappears.

(9) For the effect of the plate on irregular waves, several peaks appearing in the spectral analysis of H_A demonstrate that the wave sloshes irregularly in the tank, and the numbers of the peaks are more than those of baffled tank. The disturbance of the surface-piercing plate on the surface waves is the factor to trigger several sloshing modes. The phenomenon of

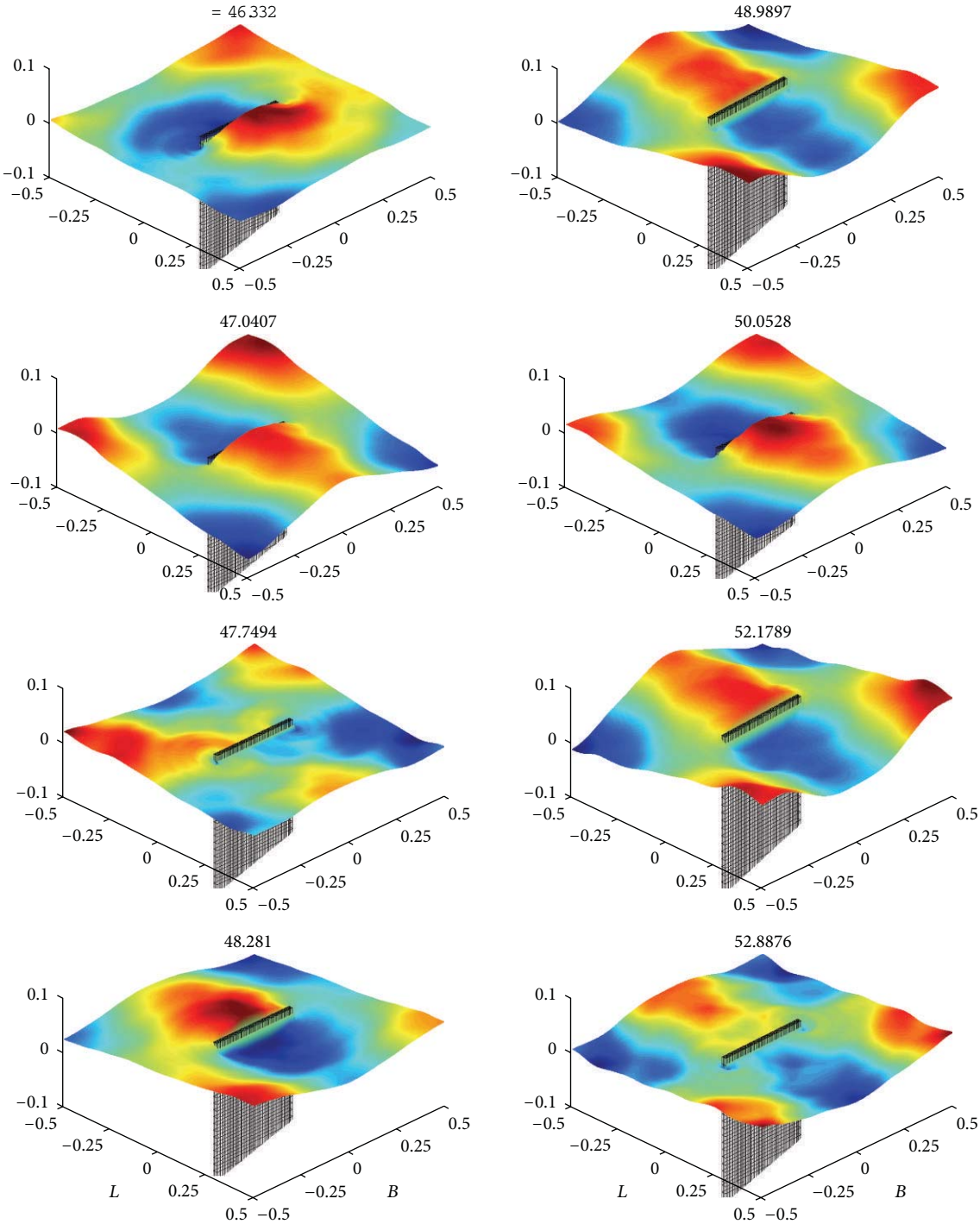

FIGURE 20: The snapshots of the free surface of a tank with a vertical plate. $d_0/L = 0.5$, $P_L/B = 0.4$, $a_0/L = 0.001$, $\theta = 45^\circ$, $\omega_x = \omega_z = 1.5\omega_1$. Dimensionless elevation $H = \eta/d_0$ and dimensionless time $T = t/\sqrt{gd_0}$.

mode shift of irregular waves is found when $\theta = 5^\circ$ switches to $\theta = 45^\circ$.

Acknowledgment

The study is partially supported by National Science Council in Taiwan under Grant NSC101-2221-E-110-019.

References

[1] S. Watanabe, "Methods of vibration reduction," in *Proceedings of the Japan Naval Architects Society Symposium*, pp. 156–189, 1969.

[2] Y. Matsuuara, K. Matsumoto, M. Mizuuki, K. Arima, H. Jouuchi, and S. Hayashi, "On a mean to reduce excited vibration with the sloshing in a tank," *Journal of the Society of Naval Architects of Japan*, vol. 160, pp. 424–432, 1986.

[3] J. K. Vandiver and S. Mitome, "Effect of liquid storage tanks on the dynamic response of offshore platforms," *Applied Ocean Research*, vol. 1, no. 2, pp. 67–74, 1978.

[4] S. C. Lee and D. V. Reddy, "Frequency tuning of offshore platforms by liquid sloshing," *Applied Ocean Research*, vol. 4, no. 4, pp. 226–231, 1982.

[5] A. Kareem and W.-J. Sun, "Stochastic response of structures with fluid-containing appendages," *Journal of Sound and Vibration*, vol. 119, no. 3, pp. 389–408, 1987.

[6] Y. Tamura, K. Fujii, T. Sato, T. Wakahara, and M. Kosugi, "Wind-induced vibration of tall towers and practical applications of tuned sloshing damper," in *Proceedings of the Workshop on Serviceability of Buildings*, pp. 228–241, Ontario, Canada, May 1988.

[7] T. Noji, H. Yoshida, E. Tatsumi, H. Kosaka, and H. Hagiuda, "Study on vibration control damper utilizing sloshing of water," *Journal of Wind Engineering*, vol. 37, pp. 557–566, 1988.

[8] K. Fujii, Y. Tamura, T. Sato, and T. Wakahara, "Wind-induced vibration of tower and practical applications of tuned sloshing damper," *Journal of Wind Engineering and Industrial Aerodynamics*, vol. 33, no. 1-2, pp. 263–272, 1990.

[9] T. Wakahara, "Wind-induced response of TLD-structure coupled system considering non-linearity of liquid motion," *Shimizu Technical Research Bulletin*, vol. 12, pp. 41–52, 1993.

[10] Y. Fujino, B. M. Pacheco, P. Chaiseri, and L. M. Sun, "Parametric studies on tuned liquid damper (TLD) using circular containers by free-oscillation experiments," *Japan Society of Civil Engineers*, vol. 5, pp. 381–391, 1988.

[11] Y. Tamura, K. Fujii, T. Ohtsuki, T. Wakahara, and R. Kohsaka, "Effectiveness of tuned liquid dampers under wind excitation," *Engineering Structures*, vol. 17, no. 9, pp. 609–621, 1995.

[12] L. M. Sun, Y. Fujino, B. M. Pacheco, and P. Chaiseri, "Modelling of tuned liquid damper (TLD)," *Journal of Wind Engineering and Industrial Aerodynamics*, vol. 41–44, no. 1–3, pp. 1883–1894, 1992.

[13] F. Welt, *A parametric study of nutation dampers [M.A.Sc. thesis]*, University of British Columbia, British Columbia, Canada, 1983.

[14] P. Warnitchai and T. Pinkaew, "Modelling of liquid sloshing in rectangular tanks with flow-dampening devices," *Engineering Structures*, vol. 20, no. 7, pp. 593–600, 1998.

[15] S. Kaneko and M. Ishikawa, "Modeling of tuned liquid damper with submerged nets," *ASME Journal of Pressure Vessel Technology*, vol. 121, no. 3, pp. 334–343, 1999.

[16] H. Akyildiz and E. Ünal, "Experimental investigation of pressure distribution on a rectangular tank due to the liquid sloshing," *Ocean Engineering*, vol. 32, no. 11-12, pp. 1503–1516, 2005.

[17] H. Akyildiz and N. E. Ünal, "Sloshing in a three-dimensional rectangular tank: numerical simulation and experimental validation," *Ocean Engineering*, vol. 33, no. 16, pp. 2135–2149, 2006.

[18] M. S. Celebi and H. Akyildiz, "Nonlinear modeling of liquid sloshing in a moving rectangular tank," *Ocean Engineering*, vol. 29, no. 12, pp. 1527–1553, 2002.

[19] V. Armenio and M. La Rocca, "On the analysis of sloshing of water in rectangular containers: numerical study and experimental validation," *Ocean Engineering*, vol. 23, no. 8, pp. 705–739, 1996.

[20] J. R. Cho and H. W. Lee, "Numerical study on liquid sloshing in baffled tank by nonlinear finite element method," *Computer Methods in Applied Mechanics and Engineering*, vol. 193, no. 23–26, pp. 2581–2598, 2004.

[21] J. R. Cho, H. W. Lee, and S. Y. Ha, "Finite element analysis of resonant sloshing response in 2-D baffled tank," *Journal of Sound and Vibration*, vol. 228, no. 4-5, pp. 829–845, 2005.

[22] M. F. Younes, Y. K. Younes, M. El-Madah, I. M. Ibrahim, and E. H. El-Dannanh, "An experimental investigation of hydrodynamic damping due to vertical baffle arrangements in a rectangular tank," *Proceedings of the Institution of Mechanical Engineers M*, vol. 221, no. 3, pp. 115–123, 2007.

[23] H. Akyildiz, "A numerical study of the effects of the vertical baffle on liquid sloshing in two-dimensional rectangular tank," *Journal of Sound and Vibration*, vol. 331, no. 1, pp. 41–52, 2012.

[24] C. H. Wu, O. M. Faltinsen, and B. F. Chen, "Numerical study of sloshing liquid in tanks with baffles by time-independent finite difference and fictitious cell method," *Computers and Fluids*, vol. 63, pp. 9–26, 2012.

[25] D. Liu and P. Lin, "Three-dimensional liquid sloshing in a tank with baffles," *Ocean Engineering*, vol. 36, no. 2, pp. 202–212, 2009.

[26] J. H. Jung, H. S. Yoon, C. Y. Lee, and S. C. Shin, "Effect of the vertical baffle height on the liquid sloshing in a three-dimensional rectangular tank," *Ocean Engineering*, vol. 44, pp. 79–89, 2012.

[27] P. A. Berthelsen and O. M. Faltinsen, "A local directional ghost cell approach for incompressible viscous flow problems with irregular boundaries," *Journal of Computational Physics*, vol. 227, no. 9, pp. 4354–4397, 2008.

[28] C. Wu and B. Chen, "Sloshing waves and resonance modes of fluid in a 3D tank by a time-independent finite difference method," *Ocean Engineering*, vol. 36, no. 6-7, pp. 500–510, 2009.

[29] B. Chen and C. Wu, "Effects of excitation angle and coupled heave-surge-sway motion on fluid sloshing in a three-dimensional tank," *Journal of Marine Science and Technology*, vol. 16, no. 1, pp. 22–50, 2011.

Hindawi Publishing Corporation
Advances in Mechanical Engineering
Volume 2013, Article ID 567159, 19 pages
http://dx.doi.org/10.1155/2013/567159

Research Article

Numerical Simulation of PAHs Formation and Effect of Operating Conditions in DI-Diesel Engines Based on a Comprehensive Chemical Mechanism

Bei-Jing Zhong and Jun Xi

School of Aerospace, Tsinghua University, Beijing 100084, China

Correspondence should be addressed to Bei-Jing Zhong; zhongbj@tsinghua.edu.cn

Received 22 November 2012; Revised 25 April 2013; Accepted 13 May 2013

Academic Editor: Moran Wang

Three-dimensional numerical simulations of polycyclic aromatic hydrocarbon (PAH) formation in a Chaochai 6102bzl direct injection diesel engine are performed. *n*-Heptane is chosen as the fuel. A detailed mechanism, which includes 108 species and 572 elementary reactions that describe *n*-heptane oxidation and PAH formation, is proposed. A reduced kinetic mechanism, with only 86 reactions and 57 species, is developed and incorporated into computational fluid dynamics (CFD) software for the numerical simulations. Results show that PAHs, which were mostly deposited at the bottom of the diesel combustion chamber wall, first increased and then decreased with the increase in diesel crank angle. Furthermore, the diesel engine operating conditions (intake vortex intensity, intake air pressure, fuel injection advance angle, diesel load, and engine speed) had a significant effect on PAH formation.

1. Introduction

The diesel engine is widely used in various kinds of power devices and has gradually become one of the main power sources in different types of vehicles because of its low oil consumption, high thermal efficiency, good compatibility, and energy savings, as well as low HC and CO emissions [1]. However, the diesel engine can emit a large number of soot particles during operation [2–5]. Research indicates that diesel engines may need 0.2–0.5% fuel oil to convert soot particles into extra fine particles (~0.1 μm diameter) [6] emitted from the exhaust pipe. These particles consist of hydrocarbons (including aromatic hydrocarbon materials) adsorbed on carbon black. Therefore, controlling soot emission is a key issue in the development of diesel engines. To improve engine soot emission and engine performance, understanding the soot structure and formation mechanism of diesel engines is necessary.

In general, nucleation and growth are two necessary processes considered in the modelling and simulation of soot formation. Nucleation considers the dehydrogenation of hydrocarbons and recombination of small molecules, which result in the formation of polycyclic aromatic hydrocarbons (PAHs) as the soot core. Growth should consider a series of processes, including the transition of PAHs to small particles and soot particle change by the collision, condensation, absorption, and chemical reactions of gaseous compositions on the surface of the particles [7].

The numerical simulation of turbulent diffusion combustion in direct injection (DI) diesel engines is highly complicated because of the strong nonlinear interaction between turbulent flow and complex chemical reactions. Some researchers [8, 9] directly used the EBU model in three-dimensional simulations to describe diesel engine combustion. Cordiner et al. [10] used a mixed 1D-3D numerical procedure, together with the Shell and characteristic-time combustion models, to analyse combustion and exhaust emission in a dual-fuel diesel/natural gas engine. In the procedure, the 1D code provides the pressure boundary conditions as input information for the 3D simulations. Chen et al. [11] and Lim et al. [12] performed three-dimensional simulations of diesel engine combustion and emission using the eddy-dissipation-conception (EDC) model with simplified reaction mechanisms. Hu et al. [13] developed a mixed-mode combustion

model, which takes advantage of the mixing details provided by large-eddy simulation, to cover the major regimes pertaining to diesel engine combustion. The model uses kinetically controlled, quasisteady homogeneous, quasisteady flamelet, and partially premixed combustion modes. The combustion models used for the simulation of turbulent diffusion flames also include the probability-density-function (PDF) transport equation model and laminar flamelet model [14, 15]. Given detailed chemical kinetics, the first two models require substantial calculation because the transport equations for all species have to be solved. Unlike the first two models, the laminar flamelet model, derived separately by Peters [16] and Kuznetsov [17], treats the mixture fraction as an independent variable. This model uses the scalar dissipation rate for the mixing process and views the turbulent flame as an ensemble of thin, laminar, local one-dimensional flamelet structures embedded within the turbulent flow field [18, 19]. The model is used to solve the local nonequilibrium chemical process caused by aerodynamic strain and can decouple chemistry and turbulent flow in considering the detailed reaction mechanism and molecular transport process. This decoupling considerably reduces the need for additional calculations.

This study aims to perform numerical simulations of the actual operating process of DI diesel engines (Chaochai 6102bzl engine) and formation of PAHs, including benzene (A_1), naphthalene (A_2), phenanthrene (A_3), and pyrene (A_4), using the FLUENT CFD software. To this end, a simplified mechanism that is based on a detailed mechanism is proposed. The effect of diesel operating conditions on PAH formation is also analysed. Commercial diesel does not have a chemical formula and its components are complex, making calculations difficult. A single component of alternative fuels is therefore needed. Cetane number (CN) is a measure of fuel ignition quality. It determines the length of the ignition delay period and has a significant effect on soot formation and the combustion process [20]. Thus, the CN of alternative fuels must first be considered. The CN of commercial diesel is about 50 and that of *n*-heptane—an ideal, widely used alternative fuel [21–23]—is about 56. In the calculations, *n*-heptane is used as the simulated fuel, and the unsteady-state laminar flamelet concept based on the *n*-heptane combustion reaction mechanism is adopted as the turbulent flame model of the diesel engine.

2. Governing Equations

The process occurring in an engine cylinder is a turbulent reaction flow that is dominated by physical conservation laws, including mass, momentum, energy, and species conservations. Therefore, the governing equations describing combustion in cylinder are mass continuity, momentum conservation, energy conservation, species conservation, and the ideal gas equation of state.

2.1. Mass Continuity. The species conservation equation was written as

$$\frac{\partial \rho_m}{\partial t} + \vec{\nabla} \cdot \left(\rho_m \vec{u}\right) = \vec{\nabla} \cdot \left[\rho D \cdot \vec{\nabla}\left(\frac{\rho_m}{\rho}\right)\right] + \dot{\rho}_m^{c} + \dot{\rho}^{s} + \dot{\rho}\,\delta_{ml}, \tag{1}$$

where ρ_m is the mass density of species, m; kg/m^3; ρ is the density of mixtures, kg/m^3; $\vec{u}$ is the velocity of fluid, m/s; D is the diffusion coefficient, m^2/s; δ is the Dirac delta symbol; $\dot{\rho}_m^{c}$ is the source term caused in reaction; $\dot{\rho}^{s}$ is the source term caused in spray.

After adding all species, the equation of continuity for the mixture is obtained:

$$\frac{\partial \rho}{\partial l} + \vec{\nabla}\left(\rho \cdot \vec{u}\right) = \dot{\rho}^{s}. \tag{2}$$

2.2. Momentum Conservation. The momentum conservation equation is written as

$$\frac{\partial\left(\rho \cdot \vec{u}\right)}{\partial t} + \vec{\nabla} \cdot \left(\rho \vec{u} \cdot \vec{u}\right) = -\vec{\nabla} p + \vec{\nabla} \cdot \vec{\sigma} - \vec{\nabla}\left[\frac{2}{3}\rho k\right] + \vec{F}^{s} + \rho \vec{g}, \tag{3}$$

where p is the static pressure, Pa; k is the turbulent kinetic energy, kJ/m^3; g is the gravitational body force; σ is the surface tension, m; $\vec{F}^{s}$ is the momentum increment per unit volume caused in spray, kg/(m^{2}s).

For Cartesian coordinate system, the x-, y-, z-direction momentum conservation equation are given as follows:

x-direction:

$$\begin{aligned}
&\frac{\partial(\rho u)}{\partial t} + \frac{\partial(\rho u u)}{\partial x} + \frac{\partial(\rho u v)}{\partial y} + \frac{\partial(\rho u w)}{\partial z} \\
&\quad = -\frac{\partial p}{\partial x} - \frac{2}{3}A_0\frac{\partial(\rho k)}{\partial x} + \frac{\partial}{\partial x}\left[2\mu\frac{\partial u}{\partial x}\right] \\
&\qquad + \frac{\partial}{\partial y}\left[\mu\left(\frac{\partial v}{\partial x} + \frac{\partial u}{\partial y}\right)\right] \\
&\qquad + \frac{\partial}{\partial z}\left\|\mu\left(\frac{\partial w}{\partial x} + \frac{\partial u}{\partial z}\right)\right\| \\
&\qquad + \frac{\partial}{\partial x}\left[\lambda\left(\frac{\partial u}{\partial x} + \frac{\partial v}{\partial y} + \frac{\partial w}{\partial z}\right)\right] + \rho g_x,
\end{aligned} \tag{4a}$$

y-direction:

$$\begin{aligned}
&\frac{\partial(\rho v)}{\partial t} + \frac{\partial(\rho v u)}{\partial x} + \frac{\partial(\rho v v)}{\partial y} + \frac{\partial(\rho v w)}{\partial z} \\
&\quad = -\frac{\partial p}{\partial y} - \frac{2}{3}A_0\frac{\partial(\rho k)}{\partial y} \\
&\qquad + \frac{\partial}{\partial y}\left[2\eta\frac{\partial u}{\partial y}\right] + \frac{\partial}{\partial x}\left[\eta\left(\frac{\partial v}{\partial x} + \frac{\partial u}{\partial y}\right)\right] \\
&\qquad + \frac{\partial}{\partial z}\left\|\eta\left(\frac{\partial v}{\partial z} + \frac{\partial w}{\partial y}\right)\right\| \\
&\qquad + \frac{\partial}{\partial y}\left[\eta\left(\frac{\partial u}{\partial x} + \frac{\partial v}{\partial y} + \frac{\partial w}{\partial z}\right)\right] + \rho g_y,
\end{aligned} \tag{4b}$$

z-direction:

$$\begin{aligned}&\frac{\partial(\rho w)}{\partial t}+\frac{\partial(\rho w u)}{\partial x}+\frac{\partial(\rho w v)}{\partial y}+\frac{\partial(\rho w w)}{\partial z}\\&\quad=-\frac{\partial p}{\partial z}-\frac{2}{3}A_0\frac{\partial(\rho k)}{\partial z}\\&\qquad+\frac{\partial}{\partial x}\left[2\mu\frac{\partial w}{\partial z}\right]+\frac{\partial}{\partial x}\left[\mu\left(\frac{\partial w}{\partial x}+\frac{\partial u}{\partial y}\right)\right]\\&\qquad+\frac{\partial}{\partial y}\left\|\mu\left(\frac{\partial v}{\partial z}+\frac{\partial w}{\partial y}\right)\right\|\\&\qquad+\frac{\partial}{\partial z}\left[\lambda\left(\frac{\partial u}{\partial x}+\frac{\partial v}{\partial y}+\frac{\partial w}{\partial z}\right)\right]+\rho g_z.\end{aligned}\tag{4c}$$

2.3. Energy Conservation. The energy conservation equation is written as

$$\begin{aligned}\frac{\partial(\rho I)}{\partial t}+\vec{\nabla}(\rho I\vec{u})&=-p\vec{\nabla}\vec{u}+(1-A_0)\rho\vec{\nabla}u\\&\quad-\vec{\nabla}\cdot J+A_0\rho\varepsilon+\dot{Q}^{c}+\dot{Q}^{s},\end{aligned}\tag{5}$$

where I is the specific internal energy, kJ/kg; J is the vector of heat flux, kJ, equals the sum of heat conduction and thermal diffusion, and is given by

$$J=-\lambda\vec{\nabla}T-\rho D\sum_m h_m\vec{\nabla}\left(\frac{\rho_m}{\rho}\right),\tag{6}$$

where λ is the heat conductivity; T is the gas temperature, K; h_m is the m species enthalpy; $\dot{Q}^{c}$ is the heat of combustion; $\dot{Q}^{s}$ is the thermal source term caused in spray.

2.4. The Ideal Gas Equation of State. One has

$$P=R_0T\sum_m\left(\frac{\rho_m}{W_m}\right),\tag{7}$$

$$I(T)=\sum_m\left(\frac{\rho_m}{\rho}\right)I_m(T),\tag{8}$$

$$c_p(T)=\sum_m\left(\frac{\rho_m}{\rho}\right)c_{pm}(T),\tag{9}$$

$$h_m(T)=I_m(T)+\frac{R_0T}{W_m},\tag{10}$$

where R_0 is the universal gas constant, kJ/(kg·K); W_m is the molecular weight of m species; $I_m(T)$ is the specific internal energy of m species; c_{pm} is the constant-pressure specific heat of m species, J/(kg·K).

3. Models and Boundary Conditions

3.1. Turbulence Model. Numerous models can describe turbulent flow; these include the single equation model, double equation model (the standard k-ε, RNG k-ε, and realisable k-ε models), Reynolds stress model, and large eddy simulation. Given the geometric curvature of combustor configuration and high-speed piston movement, the in-cylinder fluid flow is complex and involves eddy and secondary flow; hence, the k-ε realisable turbulence model proposed by Shih et al. [24] is selected for the present study. The realisable k-ε model is a relatively recent development and differs from the standard k-ε model. The kinetic energy and transport equations of the former have the same form as the standard and renormalisation group models, but the dissipation rate equations are different. The produced items of dissipation rate do not contain the produced items of turbulent kinetic energy. The realisable k-ε model is adopted for fluid flow, including boundary eddy flow, strong adverse pressure gravity, separate flow, and secondary flow [25, 26].

The modelled transport equations for k and ε in the realisable k-ε model are as follows:

$$\begin{aligned}\frac{D(\rho k)}{Dt}&=\frac{\partial}{\partial x_j}\left[\left(\mu+\frac{\mu_t}{\sigma_k}\right)\frac{\partial k}{\partial x_j}\right]+G_k+G_b-\rho\varepsilon-Y_M+S_k,\\\frac{D(\rho\varepsilon)}{Dt}&=\frac{\partial}{\partial x_j}\left[\left(\mu+\frac{\mu_t}{\sigma_\varepsilon}\right)\frac{\partial\varepsilon}{\partial x_j}\right]+\rho C_1S\varepsilon\\&\quad-\rho C_2\frac{\varepsilon^2}{k+\sqrt{\nu\varepsilon}}+C_{1\varepsilon}\frac{\varepsilon}{k}C_{3\varepsilon}G_b+S_\varepsilon,\end{aligned}\tag{11}$$

where

$$C_1=\max\left[0.43,\frac{\eta}{\eta+5}\right],\quad\eta=S\frac{k}{\varepsilon},\quad S=\sqrt{2S_{ij}S_{ij}}.\tag{12}$$

In these equations, G_k represents the generation of turbulent kinetic energy by mean velocity gradients; G_b is the generation of turbulent kinetic energy by buoyancy; Y_M denotes the contribution of the fluctuating dilatation in compressible turbulence to the overall dissipation rate; C_1, C_2, $C_{1\varepsilon}$, and $C_{3\varepsilon}$ are constants; σ_k and σ_ε represent the turbulent Prandtl numbers for k and ε, respectively; and S_k and S_ε are user-defined source terms.

3.2. Turbulence-Chemistry Interaction Model. In diesel engines, fuel is sprayed into the cylinder. The fuel evaporates, mixes with the surrounding gases, and then autoignites as compression raises temperature and pressure. The diesel engine nonsteady-state laminar flamelet model that is based on the works of Pitsch et al. [27] and Barths et al. [28] can describe the chemistry in a single one-dimensional laminar flamelet and model ignition, as well as the formation of the product, intermediate, and pollutant species. It is chosen in this study to predict the combustion process in the diesel engine with compression ignition [25]. Computationally expensive chemical kinetics is reduced to a one-dimensional model, which is significantly faster than the laminar-finite-rate, EDC, or PDF transport models, and calculates kinetics in two or three dimensions. The simulation results confirm good accuracy.

In a laminar diffusion flame, the species mass fraction and temperature along the x-axis can be mapped from the physical space to the mixture fraction space. Thus, they can be uniquely described by two parameters: mixture fraction f, defined in (7), and strain rate (or equivalently, scalar dissipation χ, defined in (8)). The chemistry is therefore reduced and completely described by quantities f and χ. Finally, a set of simplified laminar flamelet equations can be obtained in the mixture fraction space, including N species mass fraction equations:

$$\rho\frac{\partial Y_i}{\partial t} = \frac{1}{2}\rho\chi\frac{\partial^2 Y_i}{\partial f^2} + S_i, \tag{13}$$

and a temperature equation:

$$\begin{aligned}\rho\frac{\partial T}{\partial t} &= \frac{1}{2}\rho\chi\frac{\partial^2 T}{\partial f^2} - \frac{1}{c_p}\sum_i H_i S_i \\ &\quad + \frac{1}{2c_p}\rho\chi\left[\frac{\partial c_p}{\partial f} + \sum_i c_{p,i}\frac{\partial Y_i}{\partial f}\right]\frac{\partial T}{\partial f}.\end{aligned} \tag{14}$$

In (13) and (14), Y_i, T, ρ, and f are the ith species mass fraction, temperature, density, and mixture fraction, respectively; $c_{p,i}$ and c_p are the ith species specific heat and mixture-averaged specific heat, respectively; S_i denotes the ith species reaction rate; and H_i represents the specific enthalpy of the ith species.

The mixture fraction can be written in terms of the atomic mass fraction as [29]

$$f = \frac{Z_i - Z_{i,\mathrm{ox}}}{Z_{i,\mathrm{fuel}} - Z_{i,\mathrm{ox}}}, \tag{15}$$

where Z_i is the elemental mass fraction for element i; the subscript ox is the value at the oxidiser stream inlet; and the subscript fuel denotes the value at the fuel stream inlet. If the diffusion coefficients for all the species are equal, then (15) is identical for all the elements and the mixture fraction definition is unique. The mixture fraction is therefore the elemental mass fraction that originates from the fuel stream.

Scalar dissipation χ varies along the axis of a flamelet and must be modeled across the flamelet. An χ expression for variable density is used [30]:

$$\chi(f) = \frac{a_s}{4\pi}\frac{3\left(\sqrt{\rho_\infty/\rho}+1\right)^2}{2\sqrt{\rho_\infty/\rho}+1}\exp\left(-2\left[\mathrm{erfc}^{-1}(2f)\right]^2\right), \tag{16}$$

where ρ_∞ is the density of the oxidizer stream. For a counterflow diffusion flamelet, flamelet train rate α_s can be related to the scalar dissipation at f_{st}:

$$\chi_{\mathrm{st}} = \frac{a_s\exp\left(-2\left[\mathrm{erfc}^{-1}(2f_{\mathrm{st}})\right]^2\right)}{\pi}, \tag{17}$$

where χ_{st} is the scalar dissipation at the stoichiometric ratio; a_s is the characteristic strain rate; f_{st} denotes the stoichiometric mixture fraction; and erfc^{-1} is the inverse complementary error function.

In an adiabatic turbulent diffusion flame system, the species mass fraction and temperature in the laminar flamelets are completely parameterized by f and χ_{st}, and the time-averaged characteristic scalars can be determined from the PDF of f and χ_{st} as

$$\overline{\phi} = \iint \phi(f,\chi_{\mathrm{st}})\,p(f,\chi_{\mathrm{st}})\,df d\chi_{\mathrm{st}}, \tag{18}$$

where ϕ represents the species mass fraction and temperature and $p(f,\chi_{\mathrm{st}})$ denotes a joint probability density function. For nonadiabatic laminar flamelets, considering the computational cost, heat transfer to the system is assumed to have a negligible effect on flamelet species mass fractions. So the flamelet profiles are convoluted with the assumed-shape PDFs as in (18).

The flamelet species and energy equations ((13) and (14)) are simultaneously solved with the flow. To account for the temperature rise during compression, the flamelet energy equation (14) contains an additional term on the right-hand side:

$$\dot{q} = \frac{1}{c_p}\frac{\partial p}{\partial t}, \tag{19}$$

where c_p is the specific heat and p is the volume-averaged pressure in the cylinder. This rise in flamelet temperature caused by compression eventually ignites the flamelet.

The flamelet equations are advanced for a fractional step using properties from the flow, which is then advanced for the same fractional time step using properties from the flamelet. The initial flamelet condition at the beginning of the diesel simulation is a mixed-but-unburned distribution. For the flamelet fractional time step, the volume-averaged scalar dissipation and pressure, as well as the fuel and oxidiser temperatures, are passed from the flow solver to the flamelet solver. After the flamelet equations are advanced for the fractional time step, a PDF table is converted into a nonadiabatic steady flamelet table. Using the properties in this table, the CFD flow field is then advanced for the same fractional time step.

3.3. Kinetic Model. Turbulent combustion in an engine cylinder is highly complex. Hence, three-dimensional turbulent combustion simulation with a detailed reaction mechanism is difficult to complete using current computer resources. Detailed reaction mechanisms should be reduced. For this purpose, we first propose a detailed chemical mechanism describing n-heptane as a surrogate fuel for kerosene, oxidation, and PAH formation. It is then simplified to obtain the reduced-detail mechanism that can be coupled with CFD.

The detailed n-heptane reaction mechanism that describes PAH formation and oxidation consists of 108 species and 572 elementary reactions [31]. The mechanism was taken from Wang and Frenklach [32] (R31–R572, refer to [31]) and Curran et al. [33] (R1–R30, refer to [31]). As the first aromatic ring (benzene) is formed, the growth of larger aromatic species essentially follows the H-abstraction-C_2H_2-addition (HACA) mechanism. The HACA mechanism and aromatic combination, which describe the details of the growth of

Table 1: Skeleton reaction mechanism obtained by sensitivity analysis.

Number	Reactions	A	b	E
	Key reactions for *n*-heptane decomposition			
SR1	$C_5H_8 + O_2 = C_2H_2 + C_3H_5 + HO_2$	$3.00E + 12$	0.0	0.0
SR2	$C_7H_{16} = CH_3 + 2C_2H_4 + C_2H_5$	$1.00E + 18$	0.0	85325.1
SR3	$C_7H_{16} + H = H_2 + 3C_2H_4 + CH_3$	$1.32E + 06$	2.5	6763.9
SR4	$C_7H_{16} + H = H_2 + C_5H_{10} + C_2H_5$	$1.30E + 06$	2.4	4469.4
SR5	$C_7H_{16} + OH = H_2O + C_5H_{10} + C_2H_5$	$5.46E + 06$	2.0	−1314.5
SR6	$C_7H_{16} + OH = H_2O + 3C_2H_4 + CH_3$	$2.18E + 07$	1.8	979.9
	Reactions for decomposition and oxidation of small molecules			
SR7	$H + O_2 = O + OH$	$8.30E + 13$	0.0	14413.0
SR8	$OH + H_2 = H + H_2O$	$2.56E + 08$	1.5	3430.0
SR9	$OH + OH = O + H_2O$	$3.57E + 04$	2.4	−2110.0
SR10	$H + OH + M = H_2O + M$	$2.20E + 22$	−2.0	0.0
SR11	$H + O_2 + H_2O = HO_2 + H_2O$	$9.38E + 18$	−0.8	0.0
SR12	$H + O_2 + N_2 = HO_2 + N_2$	$3.75E + 20$	−1.7	0.0
SR13	$HO_2 + O = OH + O_2$	$2.00E + 13$	0.0	0.0
SR14	$HO_2 + OH = O_2 + H_2O$	$2.90E + 13$	0.0	−500.0
SR15	$CO + O + M = CO_2 + M$	$6.02E + 14$	0.0	3000.0
SR16	$CO + OH = CO_2 + H$	$4.76E + 07$	1.2	70.0
SR17	$C + O_2 = CO + O$	$5.80E + 13$	0.0	576.0
SR18	$CH + H = C + H_2$	$1.10E + 14$	0.0	0.0
SR19	$CH + H_2 = CH_2 + H$	$1.11E + 08$	1.8	1670.0
SR20	$CH + H_2O = CH_2O + H$	$5.71E + 12$	0.0	−755.0
SR21	$CH + CO_2 = HCO + CO$	$3.40E + 12$	0.0	690.0
SR22	$HCO + M = CO + H + M$	$1.87E + 17$	−1.0	17000.0
SR23	$CH_2 + O_2 = CO_2 + H + H$	$1.32E + 13$	0.0	1500.0
SR24	$CH_2^* + N_2 = CH_2 + N_2$	$1.50E + 13$	0.0	600.0
SR25	$CH_2^* + H_2 = CH_3 + H$	$7.00E + 13$	0.0	0.0
SR26	$CH_2^* + H_2O = CH_2 + H_2O$	$3.00E + 13$	0.0	0.0
SR27	$CH_2^* + CO_2 = CH_2O + CO$	$1.40E + 13$	0.0	0.0
SR28	$CH_2O + OH = HCO + H_2O$	$3.43E + 09$	1.2	−447.0
SR29	$CH_3 + H(+M) = CH_4(+M)$	$1.27E + 16$	−0.6	383.0
SR30	$CH_3 + O = CH_2O + H$	$8.43E + 13$	0.0	0.0
SR31	$CH_3 + HO_2 = CH_3O + OH$	$2.00E + 13$	0.0	0.0
SR32	$CH_3 + CH_3(+M) = C_2H_6(+M)$	$2.12E + 16$	−1.0	620.0
SR33	$CH_3 + CH_3 = H + C_2H_5$	$4.99E + 12$	0.1	10600.0
SR34	$CH_4 + H = CH_3 + H_2$	$6.60E + 08$	1.6	10840.0
SR35	$HCCO + H = CH_2^* + CO$	$1.00E + 14$	0.0	0.0
SR36	$C_2H_2 + H(+M) = C_2H_3(+M)$	$5.60E + 12$	0.0	2400.0
SR37	$C_2H_2 + O = HCCO + H$	$1.02E + 07$	2.0	1900.0
SR38	$C_2H_2 + O = CH_2 + CO$	$1.02E + 07$	2.0	1900.0
SR39	$C_2H_3 + H = C_2H_2 + H_2$	$4.00E + 13$	0.0	0.0
SR40	$C_2H_3 + O_2 = C_2H_3O + O$	$3.64E + 11$	0.3	101.0
SR41	$C_2H_4 + H(+M) = C_2H_5(+M)$	$1.08E + 12$	0.5	1820.0
SR42	$C_2H_4 + H = C_2H_3 + H_2$	$1.42E + 06$	2.5	12240.0
SR43	$C_2H_4 + OH = C_2H_3 + H_2O$	$3.60E + 06$	2.0	2500.0
SR44	$C_2H_4 + CH_3 = C_2H_3 + CH_4$	$2.27E + 05$	2.0	9200.0
SR45	$C_2H_6 + CH_3 = C_2H_5 + CH_4$	$6.14E + 06$	1.7	10450.0
SR46	$C_2H_2 + CH = C_3H_2 + H$	$3.00E + 13$	0.0	0.0
SR47	$C_2H_2 + CH_2 = C_3H_3 + H$	$2.50E + 13$	0.0	6620.0
SR48	$C_2H_2 + C_2H_3 = C_4H_4 + H$	$2.00E + 18$	−1.7	10600.0

Table 1: Continued.

Number	Reactions	A	b	E
	Reactions for decomposition and oxidation of small molecules			
SR49	$C_2H_2 + C_2H_3 = n\text{-}C_4H_5$	$9.30E+38$	−8.8	12000.0
SR50	$C_2H_3 + C_2H_3 = n\text{-}C_4H_5 + H$	$2.40E+20$	−2.0	15361.0
SR51	$C_3H_2 + OH = HCO + C_2H_2$	$6.80E+13$	0.0	0.0
SR52	$C_3H_3 + OH = C_3H_2 + H_2O$	$2.00E+13$	0.0	0.0
SR53	$C_3H_3 + OH = C_2H_3 + HCO$	$4.00E+13$	0.0	0.0
	Reactions for formation and oxidation of PAHs			
SR54	$C_3H_3 + C_3H_3 \rightarrow A_1$	$6.00E+12$	0.0	0.0
SR55	$n\text{-}C_4H_5 + C_2H_2 = A_1 + H$	$5.60E+16$	−1.3	5400.0
SR56	$c\text{-}C_6H_4 + H = A_1^-$	$2.40E+60$	−13.7	29500.0
SR57	$C_6H_8 + OH = n\text{-}C_6H_7 + H_2O$	$6.20E+06$	2.0	3430.0
SR58	$A_1 + H = A_1^- + H_2$	$2.50E+14$	0.0	16000.0
SR59	$A_1 + OH = A_1^- + H_2O$	$1.60E+08$	1.4	1450.0
SR60	$A_1^- + H(+M) = A_1(+M)$	$1.20E+14$	0.0	0.0
SR61	$A_1 + C_2H = A_1C_2H + H$	$5.00E+13$	0.0	0.0
SR62	$A_1 + C_2H_3 = A_1C_2H_3 + H$	$7.90E+11$	0.0	6400.0
SR63	$A_1C_2H^* + C_2H_2 = A_2^{-1}$	$2.20E+62$	−14.6	33100.0
SR64	$A_2 + H = A_2^{-1} + H_2$	$2.50E+14$	0.0	16000.0
SR65	$A_2 + H = A_2^{-2} + H_2$	$2.50E+14$	0.0	16000.0
SR66	$A_2 + OH = A_2^{-1} + H_2O$	$1.60E+08$	1.4	1450.0
SR67	$A_3 + H = A_3^{-1} + H_2$	$2.50E+14$	0.0	16000.0
SR68	$A_3 + H = A_3^{-4} + H_2$	$2.50E+14$	0.0	16000.0
SR69	$A_1^- + C_4H_4 = A_2 + H$	$3.30E+33$	−5.7	25500.0
SR70	$A_2^{-1} + C_4H_4 = A_3 + H$	$3.30E+33$	−5.7	25500.0
SR71	$A_1C_2H^* + A_1 = A_3 + H$	$1.10E+23$	−2.9	15890.0
SR72	$A_3^{-4} + C_2H_2 = A_4 + H$	$6.60E+24$	−3.4	17800.0
SR73	$A_4 + H = A_4^- + H_2$	$2.50E+14$	0.0	16000.0
SR74	$A_1 + A_1^- = P_2 + H$	$1.10E+23$	−2.9	15890.0
SR75	$P_2 + H = P_2^- + H_2$	$2.50E+14$	0.0	16000.0
SR76	$P_2^- + C_2H_2 = A_3 + H$	$4.60E+06$	2.0	7300.0
SR77	$A_1 + O = C_6H_5O + H$	$2.20E+13$	0.0	4530.0
SR78	$A_1 + OH = C_6H_5OH + H$	$1.30E+13$	0.0	10600.0
SR79	$A_1^- + O_2 = C_6H_5O + O$	$2.10E+12$	0.0	7470.0
SR80	$A_3 + OH \rightarrow A_2C_2HB + CH_2CO + H$	$6.50E+12$	0.0	10600.0
SR81	$A_4 + OH \rightarrow A_3^{-4} + CH_2CO$	$1.30E+13$	0.0	10600.0
SR82	$A_2 + O \rightarrow CH_2CO + A_1C_2H$	$2.20E+13$	0.0	4530.0
SR83	$A_3 + O \rightarrow A_2C_2HA + CH_2CO$	$1.10E+13$	0.0	4530.0
SR84	$A_4 + O \rightarrow A_3^{-4} + HCCO$	$2.20E+13$	0.0	4530.0
SR85	$A_2^{-1} + O_2 \rightarrow A_1C_2H + HCO + CO$	$2.10E+12$	0.0	7470.0
SR86	$A_4^- + O_2 \rightarrow A_3^{-4} + CO + CO$	$2.10E+12$	0.0	7470.0

A_1: benzene; A_2: naphthalene; A_3: phenanthrene; A_4: pyrene; P_2: biphenyl.

aromatic hydrocarbons, can be found in [15]. The next stage is to integrate reaction kinetics in the multidimensional CFD solver. The detailed mechanism is simplified prior to multidimensional CFD modelling. Net reaction rate analysis and sensitivity analysis are conducted to simplify the detailed mechanism. The simplified mechanism includes 57 components and 86 elementary reactions (see Table 1), and can be coupled with the CFD multidimensional model. A comparison of the simplified and detailed mechanisms shows very close calculation results, with a 15% relative error for intermediate profiles. These results confirm that the authenticity of the prediction of flame structure and PAH (A_1, A_2, A_3, and A_4) formation generated by the mechanism simplification procedure is indistinguishable from that yielded by the detailed mechanism over the specified fixed range of conditions. The details of the simplification of this mechanism and its testing can be found in [34].

3.4. Spray Model. FLUENT provides different spray models for droplet collision and breakup, as well as a dynamically

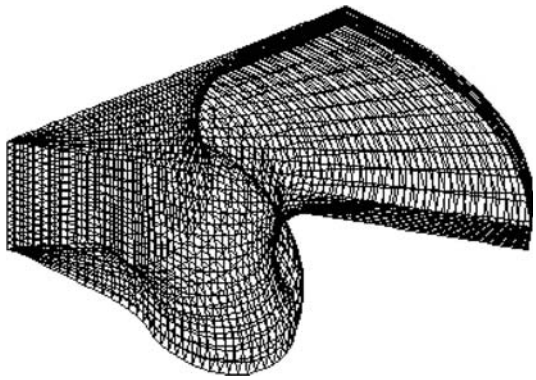

Figure 1: One-sixth of calculation grids at the location of 10°CA BTDC.

varying drag coefficient that accounts for variations in droplet shape. These models are the droplet collision model, applicable to low-Weber-number collisions, and droplet breakup models; the latter include the Taylor analogy breakup (TAB) model, applicable to low-Weber-number injections and low-speed sprays into a standard atmosphere, and the wave model that is applicable to Weber numbers greater than 100 and popular in high-speed fuel injection applications [14]. The dynamic drag model provided by FLUENT is adopted for the accurate determination of droplet drag coefficients, which are crucial for accurate spray modelling in this work. It is compatible with the TAB and wave models for droplet breakup. When the collision model is switched on, the collisions reset the distortion and distortion velocities of the colliding droplets. When sprayed into the combustion chamber through the nozzle, the droplets may merge or break up.

3.5. Initial and Boundary Conditions. Even as the precise geometric shapes of a physical model are an important precondition to accurate simulation, creating a computational module strictly in accordance with actual conditions is very difficult because the overall structure of the diesel engine is highly complex. Therefore, the treatment of the structures requires simplification. In this study, the approaches to simplification are as follows. (1) The intake and exhaust strokes are disregarded, with initial and boundary conditions obtained through experiments. (2) The calculation is completed only for one-sixth of the full geometry because the diesel cylinder that is adopted is a fuel injection nozzle with six uniform jet holes. Figure 1 shows the geometric model and calculation grid of the DI diesel engine at a 10° crack angle (CA) before top dead centre.

The parameters of the geometric model and initial boundary conditions are shown in Table 2. The calculations, including those for the compression, combustion, and expansion strokes, are completed using the FLUENT CFD software solver.

4. Results and Discussion

4.1. Reliability Analysis of the Models. Comprehensively verifying the models is very difficult because limited test results

Table 2: Dimensional and operational conditions for diesel modeled.

Cylinder diameter (mm)	102	Crank shaft speed (rpm)	2800
Piston stroke (mm)	118	Surrogate fuel molecular formula	C_7H_{16}
Compression ratio	17.5	Oil specific consumption (g/kw·h)	244.7
Injector type	Orifice	Initial oil temperature (K)	320
Injector number	6	Spray span angle (°)	12.5
Injector diameter (mm)	0.22	Pressure (MPa)	70
Spray angle of advance (°CA)	−10	Chamber shape	ω
Initial ε (m^2/s^3)	1.0	Initial k (m^2/s^2)	0.01

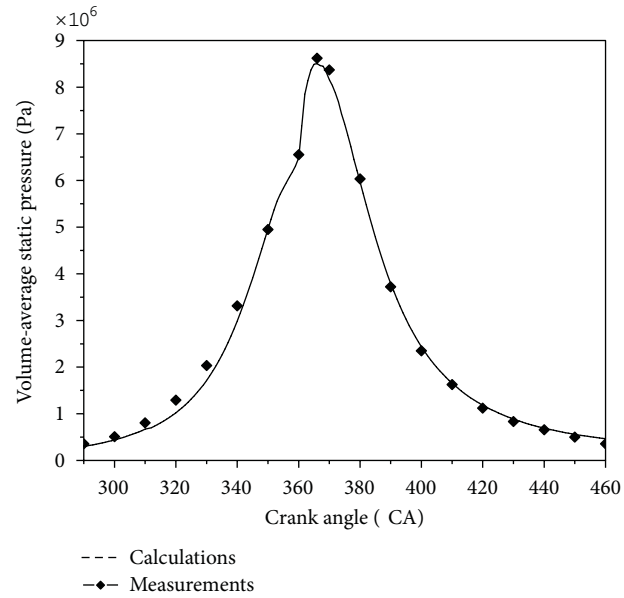

Figure 2: The variation of volume-average pressure in engine cylinder with crank angles.

are available for comparison. Usually, pressure and temperature are the standards of simulation. The examined comparisons of the detailed mechanism were completed in the laminar flames [31, 35]. The results show that the mechanism can describe flame characteristics. As shown in [34], the simplified mechanism that is based on the detailed mechanism can also reproduce the major features of the detailed mechanism. Figure 2 shows the variations in average pressure in the cylinder with CA; these variations were determined by numerical simulation and testing. The figure shows that the computed pressure rise and maximum pressure, as well as their corresponding crank positions are essentially consistent with experimental data [36]. The maximum pressure in the cylinder (about 8.5 MPa) occurred at 4°CA after top dead centre. The maximum pressure showed an error of 1.16% only in comparison with the experimental results for 8.6 MPa. The comparison of the pressure curves shows that the numerical simulation of the DI diesel engine reflects actual conditions.

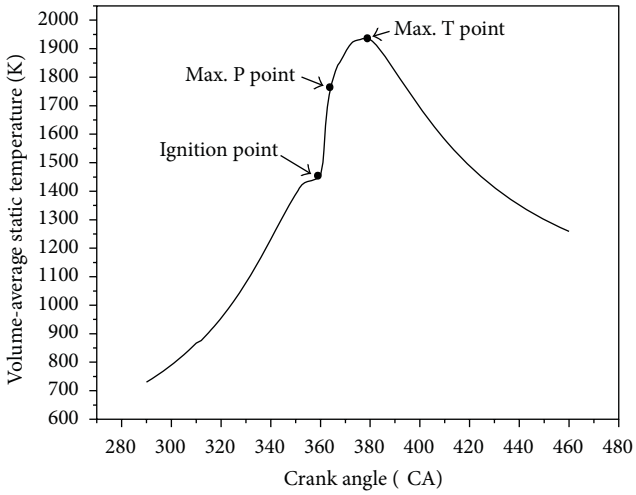

Figure 3: The variation of the simulated average temperature in cylinder with crank angle.

Figure 3 shows the computed volume-average temperature in the cylinder against variations in CAs. The figure shows three special points, which correspond to the ignition of the fuel at 360°CA, maximum pressure at 364°CA, and maximum temperature at 379°CA. The average temperature in the engine cylinder was about 1400 K at the ignition point (i.e., 360°CA). Below this temperature, the engine flamed out, which is generally consistent with the conclusion of Liu et al. [37]. Kinetic analysis shows that the following important reactions occurred at the ignition point:

$$C_7H_{16} = CH_3 + 2C_2H_4 + C_2H_5 \quad \text{(SR2)}$$

$$C_7H_{16} + H = H_2 + 2C_2H_4 + CH_3 \quad \text{(SR3)}$$

$$H + O_2 = O + OH \quad \text{(SR7)}$$

$$OH + H_2 = H + H_2O \quad \text{(SR8)}$$

$$CH_2O + OH = HCO + H_2O \quad \text{(SR49)}$$

$$CH_3 + H + M = CH_4 + M \quad \text{(SR50)}$$

$$CH_3 + O = CH_2O + H \quad \text{(SR51)}$$

$$C_3H_3 + C_3H_3 \longrightarrow A_1 \quad \text{(SR54)}$$

$$A_1 + OH = A_{1^-} + H_2O \quad \text{(SR59)}$$

$$A_2 + H = A_{2\text{-}1} + H \quad \text{(SR64)}$$

$$A_3 + H = A_{3\text{-}4} + H_2 \quad \text{(SR68)}$$

$$A_{1^-} + C_4H_4 = A_2 + H \quad \text{(SR69)}$$

$$A_{2\text{-}1} + C_4H_4 = A_3 + H \quad \text{(SR70)}$$

$$A_{3\text{-}4} + C_2H_2 = A_4 + H \quad \text{(SR72)}$$

$$A_4 + OH \longrightarrow A_{3\text{-}4} + CH_2CO \quad \text{(SR81)}$$

It is found that H, O, and OH imposed important effects on ignition, and H_2 and C_2H_4 were produced from the decomposition of C_7H_{16}. On the one hand, the small hydrocarbon gases can be conducive to burning. On the other hand, they can increase CH_3 and C_3H_3, after which C_3H_3 can be converted to A_1. This conversion may, in turn, generate A_2, A_3, and A_4.

As the fuel is burned, the considerable heat produced by combustion caused the gas pressure and temperature in the cylinder to sharply rise until the average temperature reached a maximum value of 1935 K at 379°CA, where fuel injection was terminated and combustion was completed. Similarly, the kinetic analysis shows that in addition to reactions (SR2), (SR3), (SR8), (SR54), (SR59), (SR64), (SR68), (SR69), (SR70), (SR72), and (SR81) (see Table 1), other important reactions occurred at the maximum temperature (i.e., 379°CA):

$$OH + OH = O + H_2O \quad \text{(SR9)}$$

$$H + O_2 + H_2O = HO_2 + H_2O \quad \text{(SR11)}$$

$$HO_2 + OH = O_2 + H_2O \quad \text{(SR14)}$$

$$C + O_2 = CO + O \quad \text{(SR17)}$$

$$CH_3 + CH_3 + M = C_2H_6 + M \quad \text{(SR29)}$$

$$C_2H_2 + H + M = C_2H_3 + M \quad \text{(SR33)}$$

At this point, adequate H, OH, and O were produced but less C_3H_3 was generated. Figure 4 shows the corresponding spatial temperature distributions at 360°, 364°, and 379°CA.

4.2. Spatial Distributions of Temperature and Species Concentrations. Figure 5 shows the spatial distributions of temperature and concentrations of the major species (C_7H_{16}, O_2, CO_2, and H_2O) and PAHs (A_1, A_2, A_3, and A_4) at 360°, 364°, and 379°CA. The figure illustrates that the eddy formed in the combustion chamber caused the high-temperature region to propagate through the bottom of the chamber. When the crank moved to 364°CA, a local high-temperature region at 2643 K was formed at the bottom centre of the chamber. Conversely, when the crank moved forward to 379°CA, a high-temperature flame fully propagated through the bottom of the chamber. At the starting point of combustion (360°CA), the fuel (i.e., C_7H_{16}) aggregated at the jet flow centre, thereby producing severely insufficient and excess oxygen inside and outside the fuel jet, respectively. When the C_7H_{16} was consumed, only a little fuel remained near the wall at the bottom of the chamber at 364°CA because of the low combustion rate near this wall. This low combustion rate resulted in a lower wall temperature and lower O_2 concentration. In the subsequent combustion (up to 379°CA), the remaining fuel continued to combust until it was completely consumed, the O_2 concentration at the bottom of the chamber continued to decrease, and the CO_2 and H_2O concentrations gradually rose, thereby forming a high-temperature region with maximum temperature and severe oxygen deficiency. Nevertheless, the oxygen concentration remained high in the unburned region.

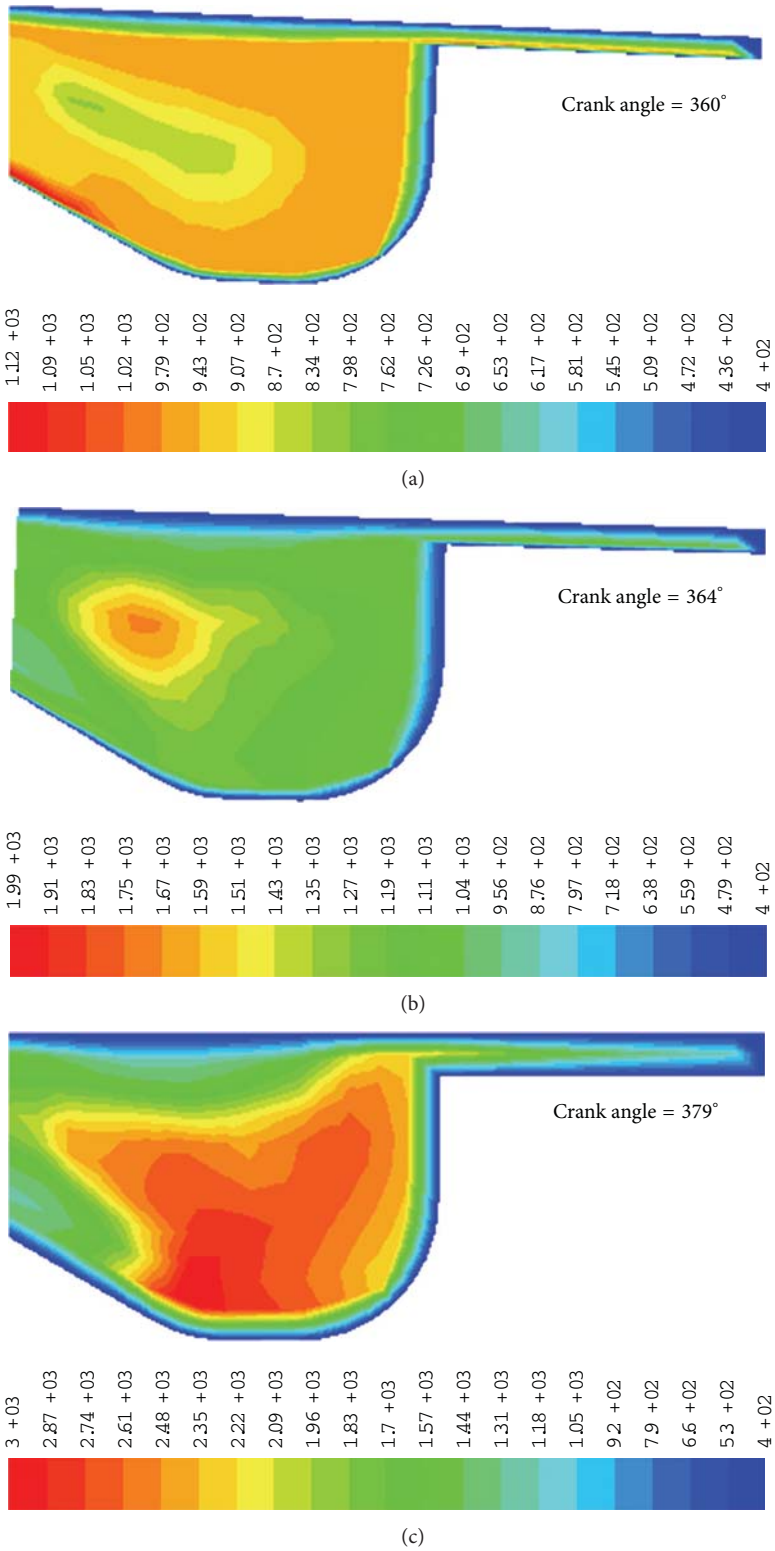

Figure 4: Temperature spatial distributions in three crank angles (i.e., corresponding to ignition, maximum average pressure, and maximum average temperature).

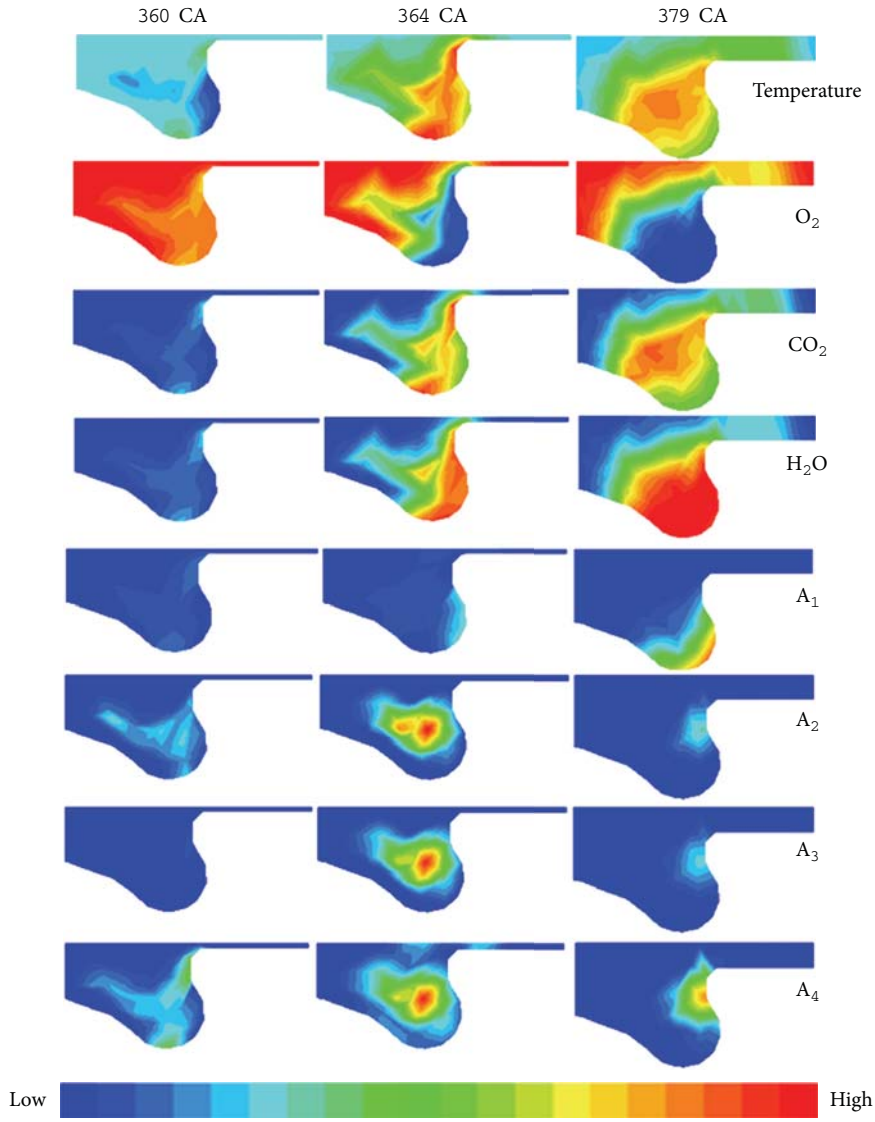

FIGURE 5: Spatial distribution of the temperature and the mass fractions of C_7H_{16}, O_2, CO_2, H_2O, A_1, A_2, A_3, and A_4 at three different positions of the crank angle (temperature: 1077–2643 K; C_7H_{16} mass fraction: 0–0.1184195, O_2 mass fraction: $7.139123e^{-05}$–0.233; CO_2 mass fraction: 0–0.1285799; H_2O mass fraction: 0–0.1123324; A_1 mass fraction: 0–0.02788063; A_2 mass fraction: 0–$3.926658e^{-09}$; A_3 mass fraction: 0–$1.383634e^{-11}$; A_4 mass fraction: 0–$1.92e^{-9}$).

As shown in Figure 5, large quantities of A_1, A_2, A_3, and A_4 started forming near the wall of the combustion chamber bottom at the ignition point (1750 K), which corresponds to 360°CA. The species continued to form at 379°CA (i.e., the point at which the largest average temperature occurred). At 360°CA, the temperature further improved after ignition, but the fuel remained in the stage of diffusion combustion. It was poorly mixed with air, resulting in pyrolysis and incomplete fuel combustion. At 364°CA (i.e., the point at which the maximum average pressure occurred), the mixing of fuel with air continued to proceed poorly because the diffusion flame had only begun to propagate through the bottom of the chamber. Thus, the fuel jet achieved easy pyrolysis near the wall at the bottom of the combustion chamber, forming A_1, A_2, A_3, and A_4. Moving the crank to 379°CA caused large quantities of PAHs to continue forming near the wall at the bottom of the chamber until they were nearly completely oxidised at the high-temperature region because of adequate O_2 concentration.

Figure 6 shows the spatial distributions of the concentrations of some intermediate species (H, C_3H_3, A_{3-4}), C_4H_4, and C_2H_2) at 360°, 364°, and 379°CA. The figure indicates that H, C_2H_2, and C_3H_3 formed primarily at the high-temperature region because of the combustion and decomposition of fuel, which resulted in more A_1 production through the reaction $C_3H_3 + C_3H_3 \rightarrow A_1$.

4.3. Species Concentration Profiles. Figures 7 and 8 show the variation curves of the concentrations of the major species (C_7H_{16}, O_2, CO_2, and H_2O) and PAHs (A_1, A_2, A_3, and A_4) as

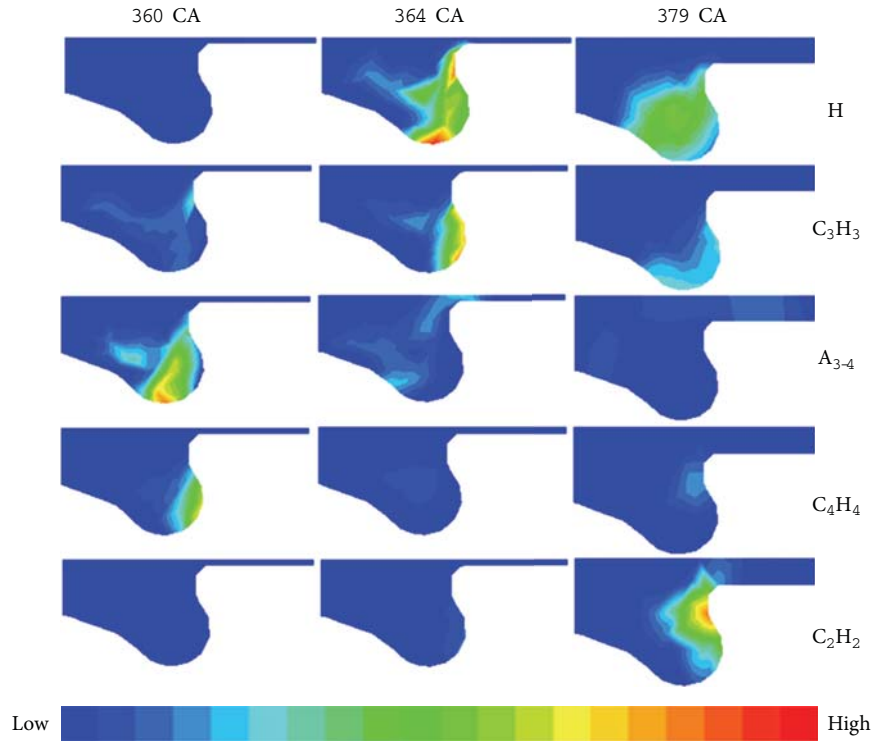

FIGURE 6: The spatial concentration distributions of the intermediate species (H, C_3H_3, A_{3-4}, C_4H_4, and C_2H_2) at positions of 360°, 364°, and 379°CA (A_{3-4}) mass fraction: 0–$4.366237e^{-13}$; C_4H_4 mass fraction: 0–$8.300977e^{-08}$; C_3H_3 mass fraction: 0–0.0003500804; C_2H_2 mass fraction: 0–0.02670222; H mass fraction: 0–$3.321838e^{-05}$.

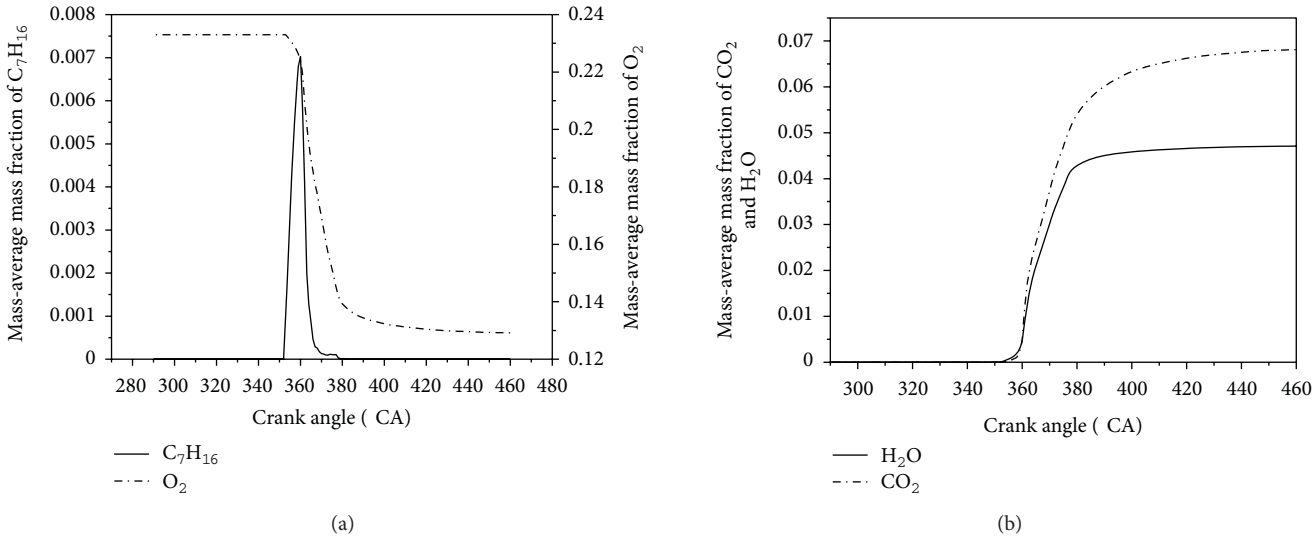

FIGURE 7: The variation of the C_7H_{16}, O_2, CO_2, and H_2O concentrations with crank angle.

a function of the CA corresponding to the conditions shown in Table 2. Figure 7 illustrates that the C_7H_{16} concentration first increased with fuel injection during the delay period prior to ignition. C_7H_{16} was then quickly consumed until it reached its maximum at 360°CA (the C_7H_{16} ignition point). The C_7H_{16} injected during the delay (360°–364°CA) and slow burning (364°–379°CA) periods continued to combust during the spray process and was quickly and almost fully consumed when the injection process was terminated (379°CA). O_2 gradually decreased as combustion progressed, whereas CO_2 and H_2O gradually increased until they reached a fixed value at the end of the fuel combustion process.

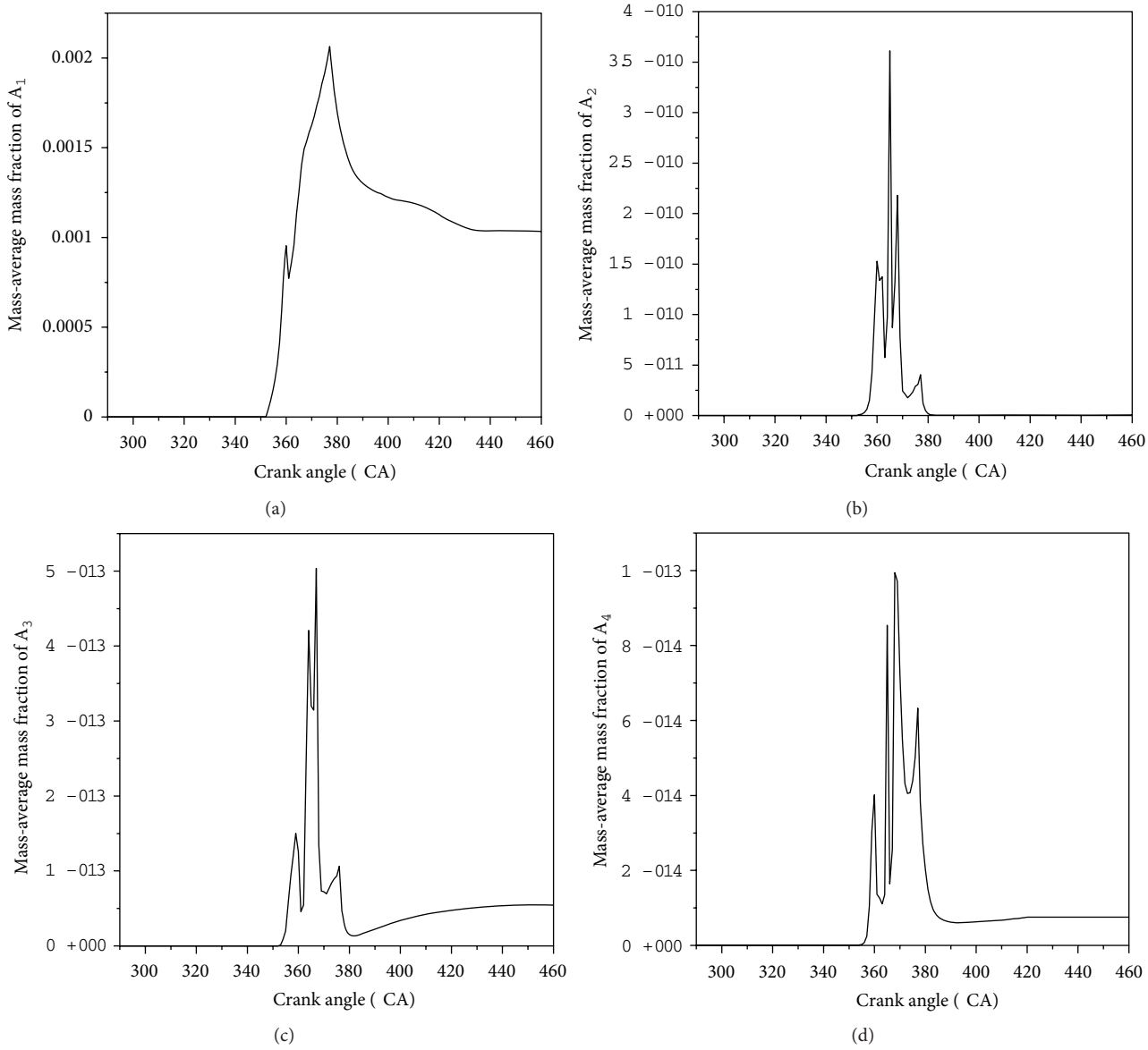

Figure 8: The variation of the PAHs concentrations with crank angle.

As shown in Figure 8, the PAH concentrations first increased and then decreased with CA. During the delay period (~360°CA), A_1, A_2, A_3, and A_4 started to form because of C_7H_{16} pyrolysis before fuel ignition. These species gradually increased in the range 360–364°CA until they reached their maximum at 364°CA. This behaviour implies that the pollutants formed in a dominant manner, corresponding to the stages of diffusion flames in the diesel engine. The fuel injected in the combustion chamber underwent pyrolysis under severe oxygen deficiency before the ignition and diffusion combustion of the formed rich mixture at the jet centre in the initial stage of combustion after ignition. The pyrolysis generated a number of A_1, A_2, A_3, and A_4 species. The kinetic analysis shows that the important reactions for PAH formation occurred at (SR54), (SR69), (SR70), and (SR72). After moving the crank to 364°CA, strong turbulent flow and fuel vapour in the cylinder accelerated the mixing of fuel with air and considerably improved combustion, thereby generating less A_1, A_2, A_3, and A_4. At the same time, large quantities of previously formed A_1, A_2, A_3, and A_4 were oxidised at high temperature by reactions (SR59), (SR64), (SR68), and (SR81). Thus, the A_1, A_2, A_3, and A_4 concentrations were quickly reduced beyond 364°CA because of their dominant oxidation. Beyond 379°CA, fuel injection was terminated, and combustion gradually ceased. Therefore, the pressure and temperature in the cylinder of the diesel engine quickly decreased, and PAH concentrations gradually reached constant levels.

4.4. Effect of Operating Conditions on PAHs

4.4.1. Effect of Intake Vortex Intensity. Vortex intensity is one of the important performance parameters that affect fuel combustion and emissions, especially particle emissions, in

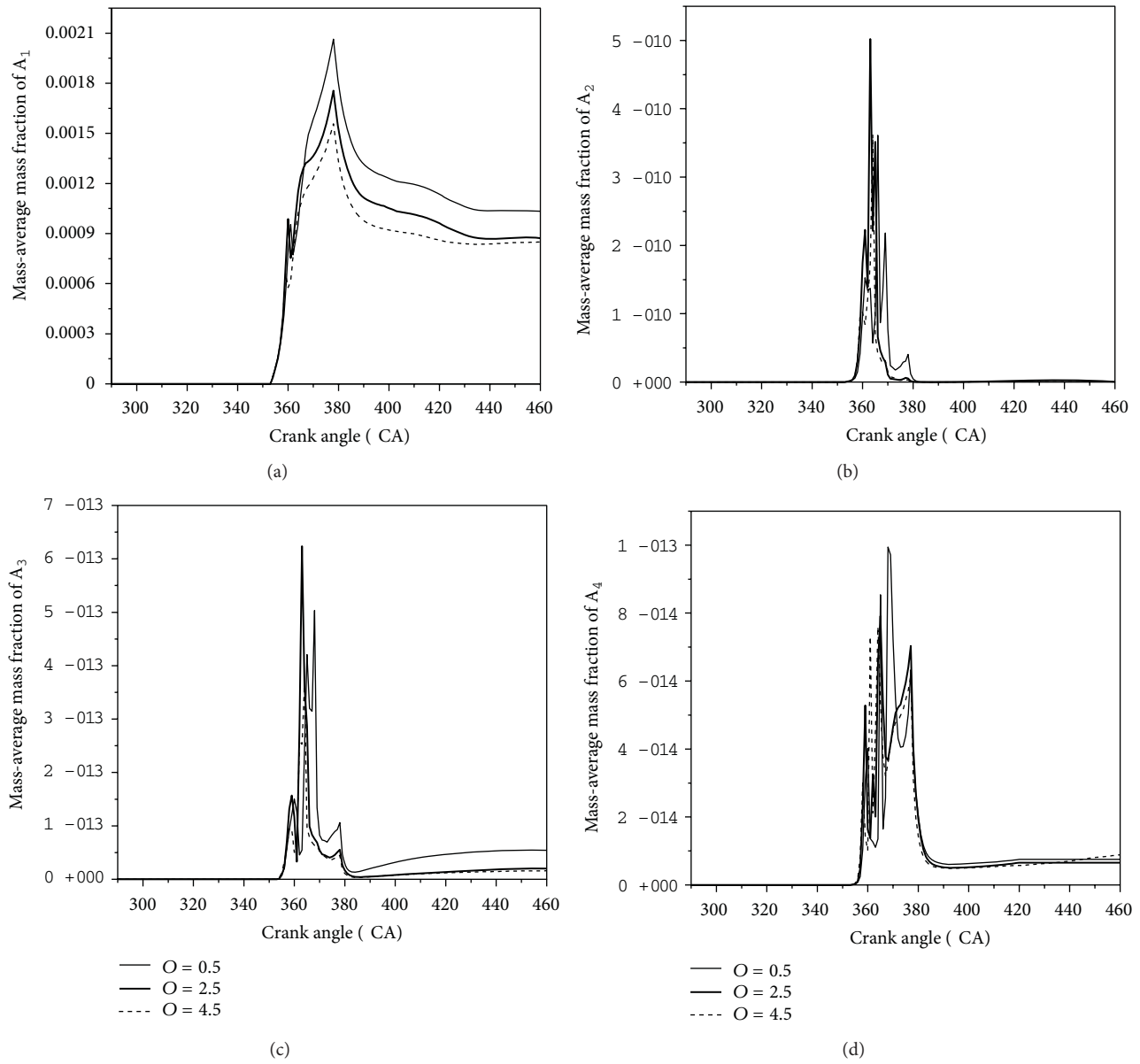

Figure 9: The effect of the intake vortex intensity on PAHs formation.

diesel engines. Eddy motion promotes mixing of fuel and air, improves the formation of combustible mixtures, and enhances combustion efficiency. To study the effect of intake vortex intensity (defined as the ratio of the intake swirl speed to the engine speed) on combustion and emission, we simulated the diesel engine combustion process and PAH formation under different vortex intensities (0.5, 2.5, and 4.5), with the other parameters maintained at relatively constant levels.

Figure 9 shows the mean-averaged mass fractions of A_1, A_2, A_3, and A_4 as a function of CA under vortex intensities of 0.5, 2.5, and 4.5. We can see from the figure that A_1 gradually decreased, whereas A_2, A_3, and A_4 only slightly changed with increasing intake vortex intensity. The sharp points of A_2, A_3, and A_4 were $5e^{-10}$, $6e^{-13}$, and $1e^{-13}$, respectively. Increasing the intake vortex intensity is advantageous to increasing airflow velocity and turbulence intensity in the engine combustion chamber, accelerating mixture formation, expanding the high-temperature region, and controlling combustion in the cylinder. The end results are improved combustion conditions and reduced combustion time, increased combustion efficiency, and reduced PAH formation, as confirmed by the simulation results.

4.4.2. Effect of Intake Air Pressure. Figure 10 shows the mean-averaged mass fractions of A_1, A_2, A_3, and A_4 as a function of CA under intake air pressures of 3.5, 4, and 4.5 MPa. The figure illustrates that A_1 gradually decreased, whereas A_2, A_3, and A_4 only minimally changed with increasing intake air pressure. The variations in PAHs showed a similar trend (Figure 9).

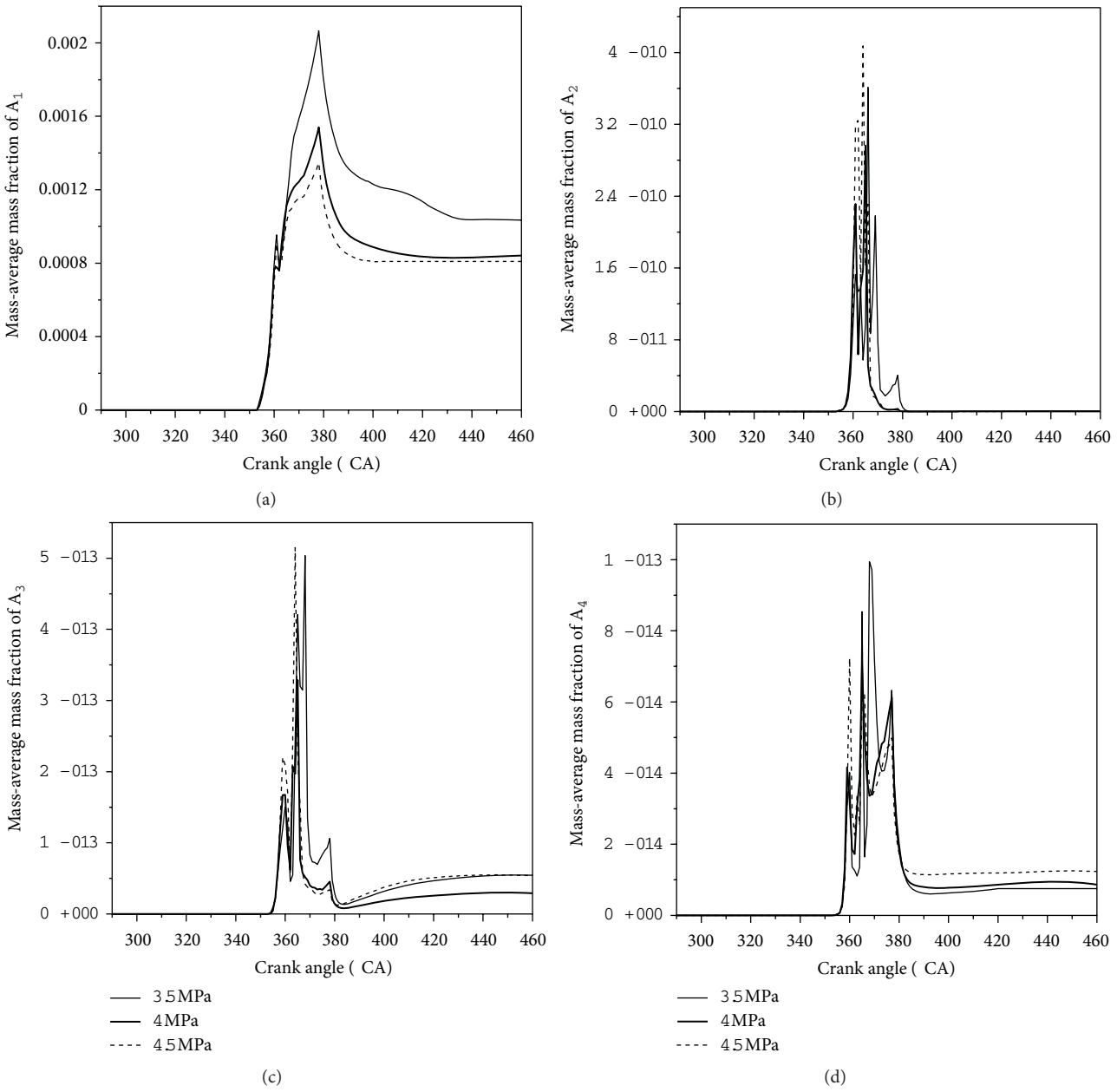

Figure 10: The effect of the intake air pressure on PAHs formation.

The intake air pressure was higher, and the gas density and oxygen concentration of the engine cylinder were greater. These conditions enabled complete diesel engine combustion under greater excess air coefficients, resulting in more complete fuel combustion and less PAH formation. Increasing the amount of air in the cylinder may reduce PAH production and simultaneously promote the oxidation of previously formed PAHs. Hence, PAH concentrations decreased with increasing intake air pressure.

4.4.3. Effect of Diesel Fuel Injection Advance Angle. Fuel injection advance angle is defined as the time at which fuel is injected into the cylinder and then to the piston only as the experience point of the crank angle. It is an important parameter that affects diesel fuel combustion. Previous studies have shown that the fuel injection advance angle in DI diesel engines has a more significant effect on fuel economy, power, and emission performance than do other parameters. Large or small, injection advance angles have a direct effect on diesel engine power output and fuel consumption, resulting in crude diesel engine and unstable running conditions.

Figure 11 shows the mean-averaged mass fractions of A_1, A_2, A_3, and A_4 as a function of CAs under fuel injection advance angles of 6°, 8°, and 10°CA, with the other parameters kept constant. The figure illustrates that A_1 gradually decreased, whereas A_2, A_3, and A_4 did not change much with increasing fuel injection advance angle.

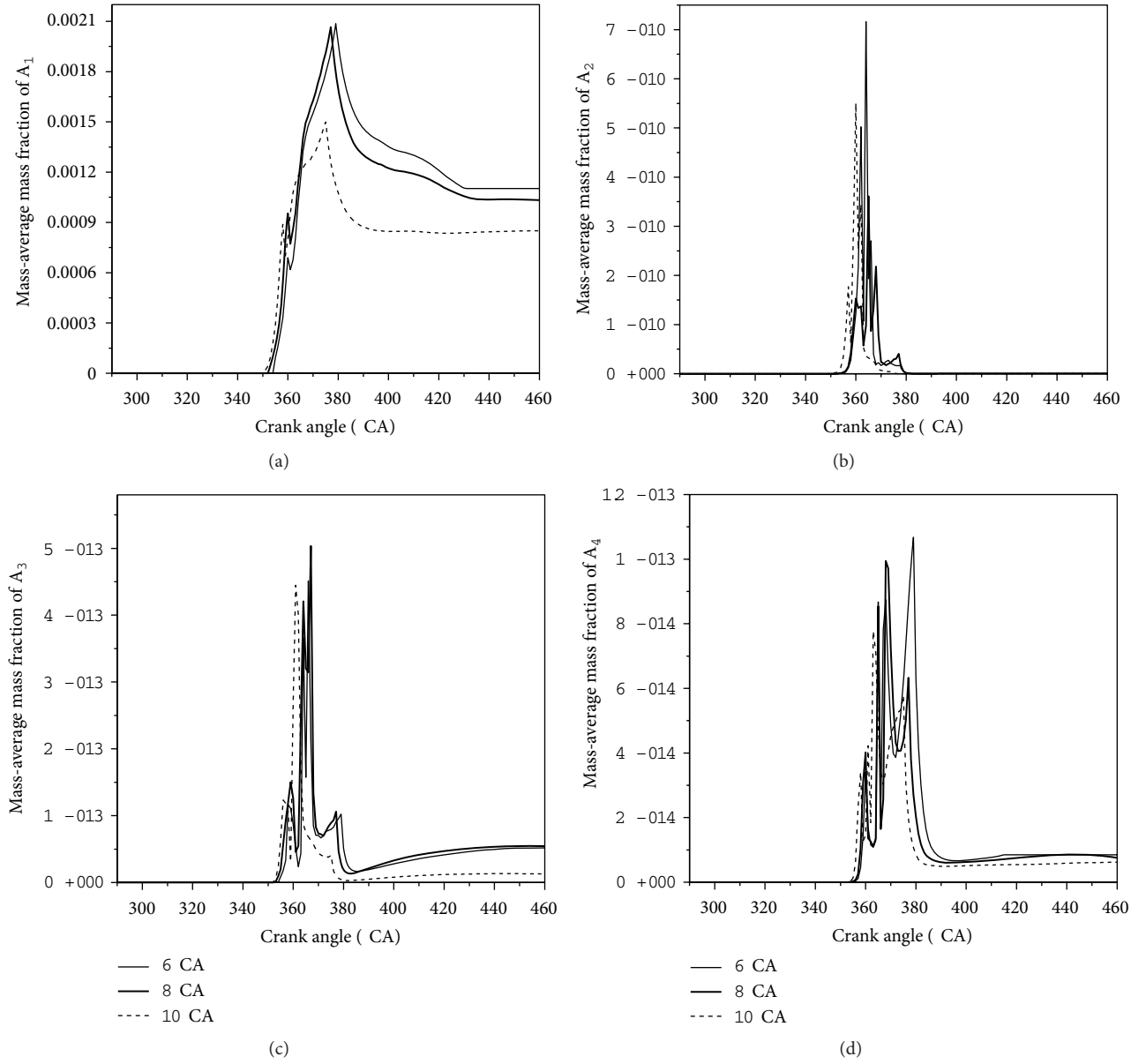

Figure 11: The effect of the diesel fuel injection advance angle on PAHs formation.

Increasing the fuel injection advance angle decreased the pressure and temperature when the fuel was injected into the cylinder. Thus, the delay period of ignition was extended. Fuel can mix well with air at a level before the top dead centre (TDC), and then the mixture promptly ignites and burns at the nearby TDC. Therefore, appropriate increments in injection advance angle can improve fuel quality and air mixture. Consequently, combustion efficiency is enhanced. However, immoderate increments in fuel injection advance angle increase the amount of fuel injected into the cylinder before ignition. When the fuel is ignited, the cylinder pressure rapidly rises, resulting in crude diesel. At an excessively small fuel injection advance angle, a fuel mixture begins to form and burn at a level beyond the TDC, where the cylinder pressure and temperature are low, resulting in reduced fuel efficiency.

4.4.4. Effect of Diesel Load. Diesel load regulation is controlled with the quantity of diesel fuel injection. The fuel injected into the cylinder increases with rising diesel load. Accordingly, the heat released by combustion is greater and the engine produces more peak torque. We completed a numerical simulation of different fuel deliveries per cycle per cylinder, keeping the same other parameters constant, to study the effect of diesel load on PAH formation and oxidation in the DI diesel engine.

Figure 12 presents the mean-averaged mass fractions of A_1, A_2, A_3, and A_4 as a function of CA under fuel delivery

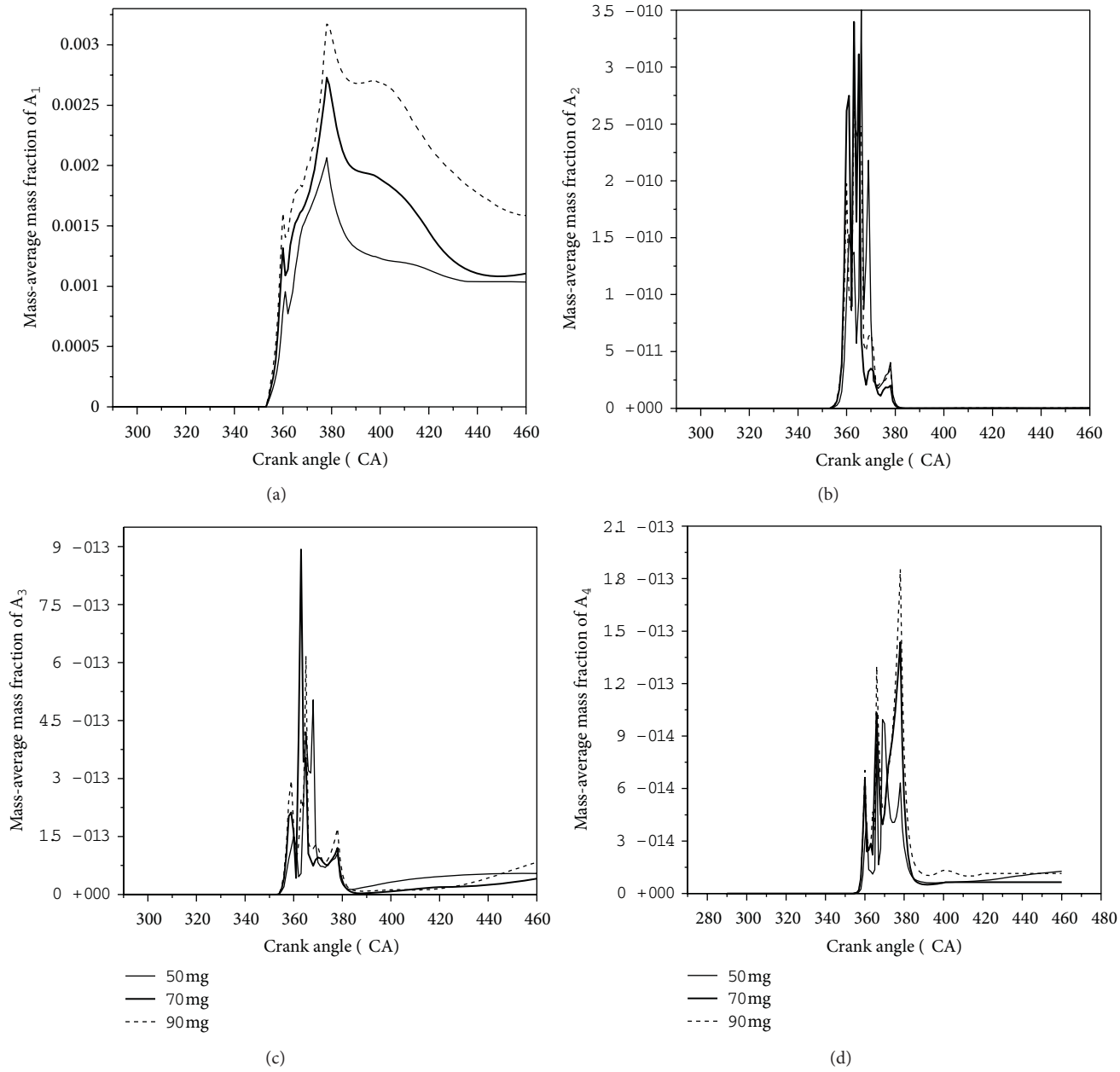

Figure 12: The effect of the fuel delivery per cycle per cylinder (load) on PAHs formation.

per cycle per cylinder levels of 50, 70, and 90 mg. The figure shows that A_1 gradually increased, whereas A_2, A_3, and A_4 only slightly changed with increasing fuel delivery per cycle per cylinder.

The different engine loads correspond to different fuel-to-air equivalence ratios. Hence, the effect of engine load on harmful gases in the exhaust is essentially attributed to the equivalence ratio. The fuel and air mixture deteriorated with increasing equivalence ratio, leading to the increased formation of PAHs. During heavy load conditions, the equivalence ratio and temperature are high, and the excess concentrated fuel/air mixture produced in the combustion chamber causes fuel pyrolysis and incomplete combustion. By contrast, during light load conditions, the diesel engine operates with substantial excess air. Thus, combustion is more complete and fewer PAHs are formed.

4.4.5. Effect of Engine Speed. The effect of diesel engine speed on diesel engine combustion and PAH formation was also investigated under fixed parameters. Figure 13 shows the mean-averaged mass fractions of A_1, A_2, A_3, and A_4 as a function of CA under engine speeds of 1800, 2300, and 2800 rpm. As shown in the figure, A_1 gradually increased, whereas A_2, A_3, and A_4 only minimally changed with increasing engine speed.

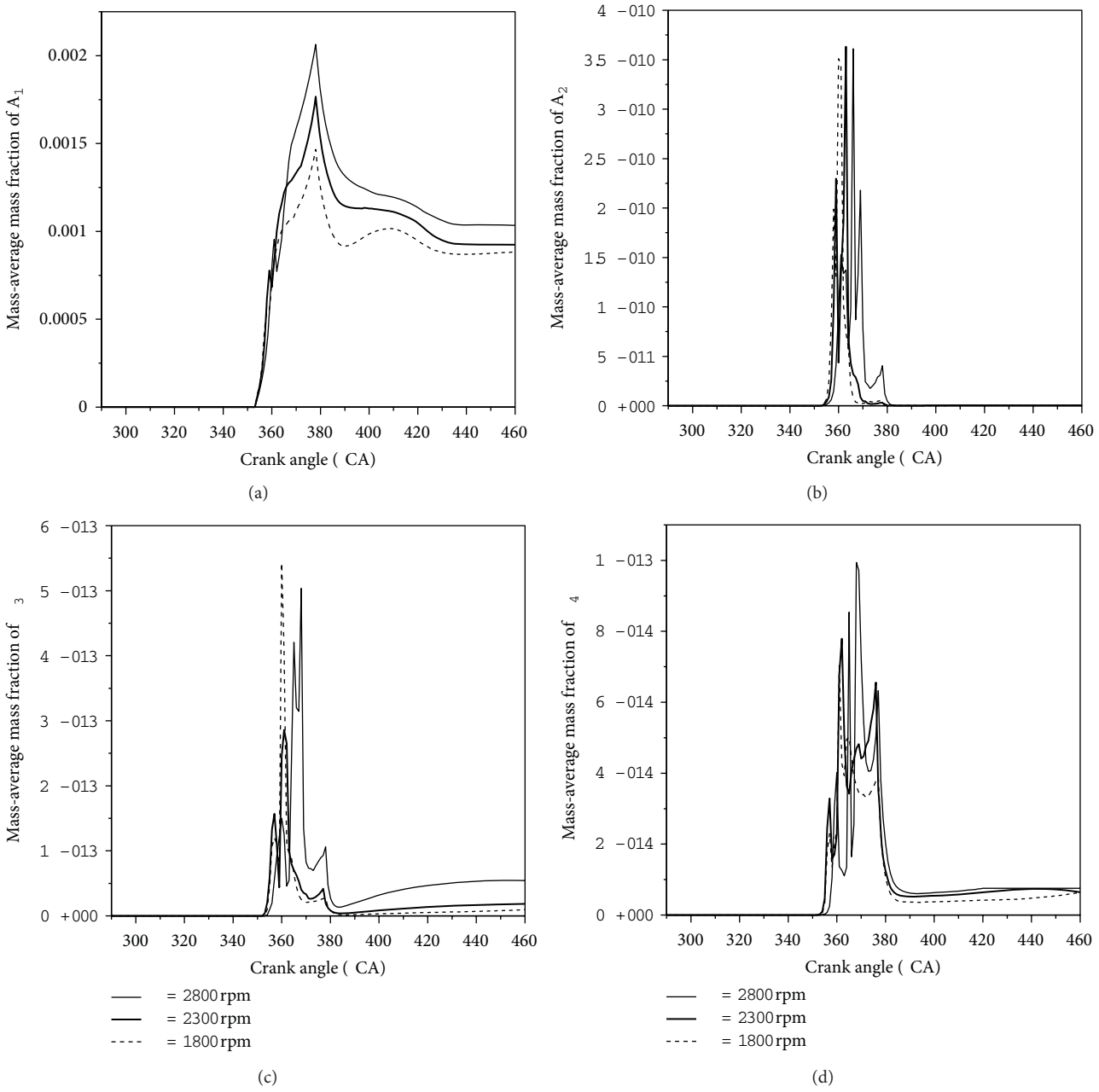

Figure 13: The effect of the engine speed on PAHs formation.

When the engine speed increased, more fuel was injected into the engine chamber over a short period, which was insufficient for fuel evaporation and fuel-air mixing. In turn, these resulted in incomplete combustion and the formation of large quantities of PAHs.

5. Conclusion

Three-dimensional numerical simulations of an *n*-heptane-fuelled Chaochai 6102bzl DI diesel engine were performed. The simulations were carried out under actual working conditions and PAH formation (A_1, A_2, A_3, and A_4). A combustion model, along with laminar flamelet, nonsteady-state, turbulent flow, and spray models, was used in the numerical simulation. The comparison of the simulation and experimental results for the delay period and variation trends of the cylinder pressure indicates that the models established in this study can accurately describe the actual working conditions of an in-cylinder diesel engine. The numerical results show that during the delay period, large quantities of PAHs were formed because of the high-temperature pyrolysis of fuel at the front of the fuel jet. PAHs were formed near the wall at the bottom of the combustion chamber during the ignition stage and were then completely oxidised at a temperature higher than 2000 K. The simulated results

for the diesel engine operating conditions indicate that increasing the intake vortex intensity and intake air pressure promotes complete fuel combustion and reduces PAH formation. Appropriate increases in fuel injection advance angles can also reduce PAH generation. The effect of engine load on the combustion process is essentially attributed to the equivalence ratio. The load increase caused a rise in equivalence ratio, creating a rich fuel mixture and resulting in elevated PAH production. Finally, increasing engine speed shortened the time consumed in fuel and air mixing, resulting in combustion deterioration and the formation of large quantities of PAHs.

Acknowledgments

The authors gratefully acknowledge the financial support of the China National Science Fund (Grant no. 51036004) and the National High Technology Research and Development Program of China (Grant no. 2009AA05Z219).

References

[1] S. Daido, Y. Kodama, T. Inohara, N. Ohyama, and T. Sugiyama, "Analysis of soot accumulation inside diesel engines," *JSAE Review*, vol. 21, no. 3, pp. 303–308, 2000.

[2] A. D. H. Clague, J. B. Donnet, T. K. Wang, and J. C. M. Peng, "A comparison of diesel engine soot with carbon black," *Carbon*, vol. 37, no. 10, pp. 1553–1565, 1999.

[3] L. M. Pickett and D. L. Siebers, "Soot in diesel fuel jets: effects of ambient temperature, ambient density, and injection pressure," *Combustion and Flame*, vol. 138, no. 1-2, pp. 114–135, 2004.

[4] Z. John, M. J. Wen, S. H. Thomson, S. N. Park, and M. F. Rogak, "Study of soot growth in a plug flow reactor using a moving sectional model," *Proceedings of the Combustion Institute*, vol. 30, no. 1, pp. 1477–1484, 2005.

[5] Y. Xin and P. G. Jay, "Two-dimensional soot distributions in buoyant turbulent fires," *Proceedings of the Combustion Institute*, vol. 30, no. 1, pp. 719–726, 2005.

[6] J. B. Heywood, *Internal Combustion Engine Fundamentals*, McGraw-Hill International, 1988.

[7] J. Xi and B. J. Zhong, "Soot in diesel combustion systems," *Chemical Engineering and Technology*, vol. 29, no. 6, pp. 665–673, 2006.

[8] Y. Han, W. Park, and K. Min, "Soot and temperature distribution in a diesel diffusion flame: 3-D CFD simulation and measurement with laser diagnostics," *International Journal of Automotive Technology*, vol. 12, no. 1, pp. 21–28, 2011.

[9] Z. Zheng and M. Yao, "Mechanism of oxygen concentration effects on combustion process and emissions of diesel engine," *Energy and Fuels*, vol. 23, no. 12, pp. 5835–5845, 2009.

[10] S. Cordiner, M. Gambino, S. Iannaccone, V. Rocco, and R. Scarcelli, "Numerical and experimental analysis of combustion and exhaust emissions in a dual-fuel diesel/natural gas engine," *Energy and Fuels*, vol. 22, no. 3, pp. 1418–1424, 2008.

[11] W. Chen, S. Shuai, and J. Wang, "Effect of the cetane number on the combustion and emissions of diesel engines by chemical kinetics modeling," *Energy and Fuels*, vol. 24, no. 2, pp. 856–862, 2010.

[12] J. Lim, Y. Kim, S. Lee, J. Chung, W. Kang, and K. Min, "3-D Simulation of the combustion process for di-methyl ether-fueled diesel engine," *Journal of Mechanical Science and Technology*, vol. 24, no. 12, pp. 2597–2604, 2010.

[13] B. Hu, C. J. Rutland, and T. A. Shethaji, "A mixed-mode combustion model for large-eddy simulation of diesel engines," *Combustion Science and Technology*, vol. 182, no. 9, pp. 1279–1320, 2010.

[14] I. Dhuchakallaya and A. P. Watkins, "Application of spray combustion simulation in DI diesel engine," *Applied Energy*, vol. 87, no. 4, pp. 1427–1432, 2010.

[15] M. Frenklach and H. Wang, "Detailed mechanism and modeling of soot particle formation," *Springer Series in Chemical Physics*, no. 59, pp. 165–192, 1994.

[16] N. Peters, "Local quenching due to flame stretch and non-premixed turbulent combustion," in *Western States Section of the Combustion Institute*, Spring Meeting, Irvine, CA, 1980, Paper WSS 80-4.

[17] V. R. Kuznetsov, "Influence of turbulence on the formation of high nonequilibrium concentrations of atoms and free radicals in diffusion flames," *Fluid Dynamics*, vol. 17, no. 6, pp. 815–820, 1982.

[18] N. Peters, "Laminar diffusion flamelet models in non-premixed turbulent combustion," *Progress in Energy and Combustion Science*, vol. 10, no. 3, pp. 319–339, 1984.

[19] N. Peters, "Laminar Flamelet Concepts in Turbulent Combustion," in *Proceedings of the 21st Symposium (Int'l.) on Combustion*, pp. 1231–1250, The Combustion Institute, 1986.

[20] H. Pitsch, H. Barths, and N. Peters, "Three-D in ensional modeling of NO_x and soot formation in DI-diesel engines using detailed chemistry based on the interactive flamelet approach," *SAE Transactions*, vol. 105, no. 4, pp. 2010–2024, 1996.

[21] H. Pitsch, Y. P. Wan, and N. Peters, "Numerical investigation of soot formation and oxidation under diesel engine conditions," *SAE Transactions*, vol. 104, no. 3, pp. 938–949, 1995.

[22] F. Tao and J. Chomiak, "Numerical investigation of reaction zone structure and flame liftoff of DI diesel sprays with complex chemistry," *SAE Transactions*, vol. 111, no. 3, pp. 1836–1854, 2002.

[23] Z. J. Peng, H. Zhao, and N. Ladommatos, *Effects of Air/Fuel ratios and EGR Rates on HCCI Combustion of n-heptane, a Diesel Type Fuel*, SAE Paper, 2003.

[24] T. H. Shih, W. W. Liou, A. Shabbir, Z. Yang, and J. Zhu, "New k-ε eddy-viscosity model for high reynolds number turbulent flows—model development and validation," *Computers and Fluids*, vol. 24, no. 3, pp. 227–238, 1995.

[25] FLUENT User's Guide, FLUENT Inc., 2006.

[26] K. Van Maele and B. Merci, "Application of two buoyancy-modified k-ε turbulence models to different types of buoyant plumes," *Fire Safety Journal*, vol. 41, no. 2, pp. 122–138, 2006.

[27] H. Pitsch, H. Barths, and N. Peters, "Three-dimensional modeling of NO_x and soot formation in DI-diesel engines using detailed chemistry based on the interactive flamelet approach," SAE Paper 962057, 1996.

[28] H. Barths, C. Antoni, and N. Peters, "Three-dimensional simulation of pollutant formation in a DI-diesel engine using multiple interactive flamelets," SAE Paper, 1998.

[29] Y. R. Sivathanu and G. M. Faeth, "Generalized state relationships for scalar properties in nonpremixed hydrocarbon/air flames," *Combustion and Flame*, vol. 82, no. 2, pp. 211–230, 1990.

[30] J. S. Kim and F. A. Williams, "Extinction of diffusion flames with non-unity lewis number," *Journal of Engineering Mathematics*, vol. 31, no. 2-3, pp. 101–118, 1997.

[31] B. J. Zhong, D. S. Dang, and Y. N. Song, "3-D simulation of soot formation in a direct-injection diesel engine based on a comprehensive chemical mechanism and method of moments," *Combustion Theory and Modeling*, vol. 16, no. 1, pp. 143–171, 2012.

[32] H. Wang and M. Frenklach, "A detailed kinetic modeling study of aromatics formation in laminar premixed acetylene and ethylene flames," *Combustion and Flame*, vol. 110, no. 1-2, pp. 173–221, 1997.

[33] H. J. Curran, P. Gaffuri, W. J. Pitz, and C. K. Westbrook, "A comprehensive modeling study of n-heptane oxidation," *Combustion and Flame*, vol. 114, no. 1-2, pp. 149–177, 1998.

[34] J. Xi and B. J. Zhong, "Reduced kinetic mechanism of n-heptane oxidation in modeling polycyclic aromatic hydrocarbon formation in diesel combustion," *Chemical Engineering and Technology*, vol. 29, no. 12, pp. 1461–1468, 2006.

[35] Y. Zhang and B. Zhong, "Benzene formation mechanism in n-heptane/air partially premixed counterflow flame," *Journal of Tsinghua University*, vol. 48, no. 5, pp. 904–908, 2008.

[36] T. C. Zhang, C. L. Song, Y. Q. Pei, S. R. Dong, G. D. Wei, and T. Z. Yang, "Experimental and CFD study on exhaust particulate from diesel engine with common rail injection system," *Journal of Combustion Science and Technology*, vol. 13, no. 2, pp. 136–140, 2007 (Chinese).

[37] Y. Liu, Y. Zhang, J. Qin, and N. Peters, "Simulation and experiment for three-dimensional combustion temperation field in direct-injection diesel engine," *Chinese Journal of Mechanical Engineering*, vol. 43, no. 2, pp. 196–201, 2007 (Chinese).

Hindawi Publishing Corporation
Advances in Mechanical Engineering
Volume 2013, Article ID 156430, 10 pages
http://dx.doi.org/10.1155/2013/156430

Research Article

Temperature Dependence of Ascending Bubble-Driven Flow Patterns Found in Champagne Glasses as Determined through Numerical Modeling

Fabien Beaumont,[1] Catalin Popa,[1] Gérard Liger-Belair,[2] and Guillaume Polidori[1]

[1] *Laboratoire de Thermomécanique, GRESPI-EA 4301, Université de Reims, 51687 Reims Cedex 2, France*
[2] *Equipe Effervescence, Champagne et Applications, Groupe de Spectrométrie Moléculaire et Atmosphérique UMR CNRS 7331, Université de Reims, 51687 Reims Cedex 2, France*

Correspondence should be addressed to Fabien Beaumont; fabien.beaumont@univ-reims.fr

Received 25 January 2013; Accepted 11 April 2013

Academic Editor: Bo Yu

A numerical modeling of bubble-driven flow patterns in a glass of champagne has been carried out for three champagne temperatures, by using the finite-volume method by CFD (computational fluid dynamics). In order to define source terms for flow regime and to reproduce accurately the bubble nucleation process responsible for champagne effervescence, specific subroutines for the gaseous phase have been added to the main numerical model. These subroutines allow the modeling of bubbles behavior based on semiempirical formulas relating to bubble diameter, mass transfer, velocity, and drag force. Both ascending bubble dynamics and bubble-driven flow patterns dynamics were examined, respectively, 60 s, 180 s, and 300 s after pouring champagne into the glass. Details and development of the various steps of modeling are presented in this paper, showing that the bubble-driven flow patterns velocities of the liquid phase significantly vary with the champagne temperature.

1. Introduction

Ascending bubbles are indeed very common in our everyday life. They play a crucial role in many natural as well as industrial processes (in physics, chemical and mechanical engineering, oceanography, food science, and even medicine) [1–6]. Nevertheless, their behavior is often surprising and, in many cases, still not fully understood. In the science of champagne, much interest has been devoted to bubble dynamics in the past decade. A large piece of experimental works has focused on what could be called the bubble trilogy, namely, the bubble nucleation, the bubble rise, and the bubble collapse, as they reach the champagne surface (for a global review see [7] and references therein).

Since the end of the 17th century, champagne has been a worldwide renowned French sparkling wine. From a strictly physicochemical point of view, champagne wines are multicomponent hydroalcoholic systems, with a density close to unity, a surface tension $\gamma \approx 50\,\mathrm{mN\,m^{-1}}$ (indeed highly ethanol dependent), and a viscosity about 50% larger than that of pure water (also mainly due to the presence of 12,5% v/v ethanol) [7]. Champagne wines are also supersaturated with CO_2-dissolved gas molecules formed together with ethanol during the second fermentation process (called *prise de mousse*, and promoted by adding yeasts and a certain amount of sugar inside bottles filled with a base wine and sealed with a cap). It is worth noting that a standard 75-centiliters champagne bottle typically holds about 9 grams of dissolved CO_2, which correspond to a volume close to 5 liters of gaseous CO_2 under standard conditions for temperature and pressure. No wonder champagne and sparkling wine tasting mainly differs from still noneffervescent wine tasting due to their large amount of dissolved carbon dioxide.

When a bottle is uncorked, and champagne is poured into a glass, there are indeed two pathways for progressive CO_2 and volatile organic compounds (VOCs) losses. CO_2 and VOCs escape (i) into the form of heterogeneously nucleated bubbles, the so-called *effervescence* process and (ii) by "invisible" diffusion through the champagne/air interface [8–10]. Glass shape, and especially its open aperture, is therefore also

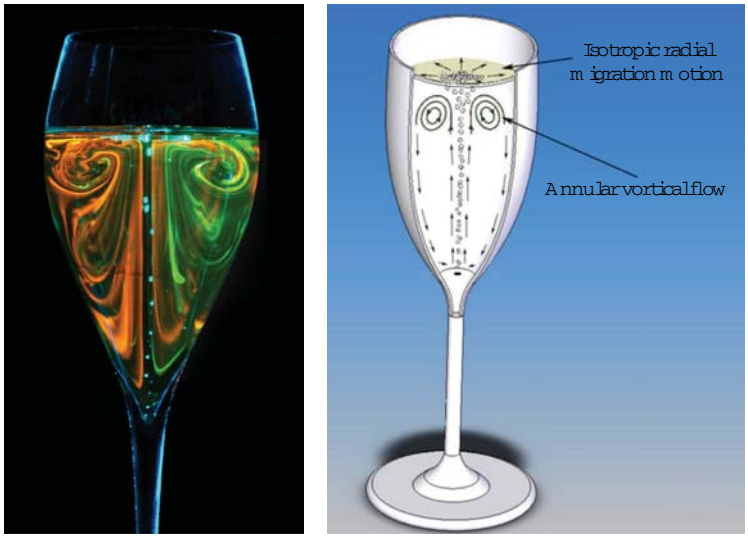

(a) (b)

Figure 1: Flow visualization evidenced through laser tomography technique (a); and 3D scheme of flow patterns found in a glass (b).

suspected to play an important role as concerns the kinetics of CO_2 and flavor release during champagne tasting. From the taster's point of view, the perception of wine flavors was indeed found to be influenced by glass shape [11, 12]. From the consumer point of view, the role of effervescence is indeed essential in champagne, sparkling wines, beers, and to a great extent, in any other carbonated beverage [13–15]. Without bubbles, champagne would be unrecognizable as such, beers and sodas would be flat. However, the role of effervescence is suspected to go far beyond the solely aesthetical point of view. Effervescence and dissolved CO_2 impact champagne and sparkling wine tasting in terms of (i) visual perception, by the presence of dancing bubbles in the glass, (ii) taste and mouthfeel, by the fizzy and chemosensory excitation of nociceptors in the oral cavity (via the conversion of dissolved CO_2 to carbonic acid) [16–18], and (iii) aromatic perception, as bubbles release their content in gaseous CO_2 and VOCs above the champagne surface. Furthermore, ascending bubbles were strongly suspected to play an indirect role on the release of gaseous CO_2 and VOCs above the champagne surface. Actually, it is worth noting that, at the bubble scale, the lower part of a rising bubble is a low-pressure area which literally attracts the fluid molecules around. A rising bubble is thus able to drain by viscous effect some fluid along its path toward the free surface. The huge number of bubbles released from the several nucleation sites found in a typical champagne glass (of order of several hundreds of bubbles released per second during the first minutes of champagne tasting) was therefore suspected to set the whole liquid bulk in motion. In turn, the release of gaseous CO_2 by diffusion through the free air/champagne interface, as well as the release of the numerous VOCs found in the liquid phase (which both strongly depend on the mixing flow conditions of the liquid medium), should be logically enhanced in case of ascending bubble-driven flow patterns. For all the aforementioned reasons, a very strong coupling was therefore strongly suspected in champagne and sparkling wines tasting, between dissolved CO_2, the presence of rising bubbles, glass shape, CO_2 discharge, and VOCs release [19].

Recently, the simultaneous quantification of CO_2 and ethanol in the headspace of a champagne glass was monitored, in real tasting conditions, all along the first 15 minutes following pouring, depending on whether the glass shows effervescence or not. Both CO_2 and ethanol were found to be enhanced by the presence of ascending bubbles, thus confirming the close link between rising bubbles and the release of gaseous CO_2 and volatile organic compounds [7]. Only quite recently, laser tomography techniques combined with fluorescent continuous dyes or solid discrete tracers were used to evidence ascending bubble-driven flow patterns found in champagne glasses [20–22]. Flow patterns found in champagne glasses were characterized by a vortex ring showing axisymmetry with regard to the ascending bubble column [23–25], as illustrated in Figure 1. Very recently also, numerical modeling was used in order to approach bubble-driven flow patterns found in champagne glasses. The influence of the glass geometry was investigated [26]. From a numerical point of view, the two most common approaches to model bubble columns are the Euler-Euler (called also two-fluid approach) and the Euler-Lagrange (called also discrete phase) ones [1, 2]. In the Euler-Euler approach, the continuous liquid phase and the dispersed gas phase are modeled as two interpenetrating continuous phases. In the Euler-Lagrange approach, the volume-averaged Navier-Stokes equations are used to describe the motion of the liquid phase [2]. In the latter situation, each bubble is tracked on the basis of a balance of forces acting upon bubbles and on a motion equation [26]. Even if the dynamics of individual bubbles are now well understood, it seems that there is a lack of data in the study of bubble-driven flow patterns in beverages supersaturated with dissolved gas. Moreover, temperature is strongly suspected as being a key parameter in champagne

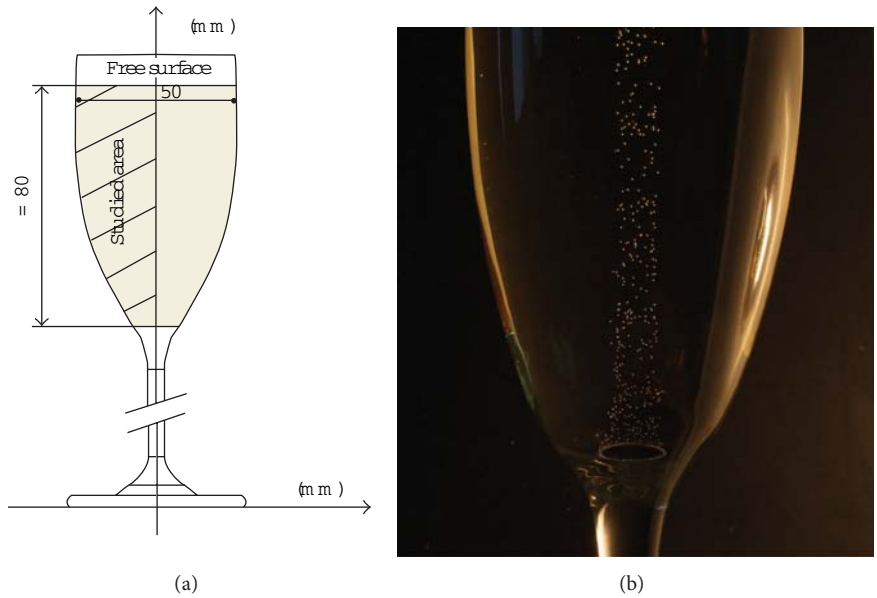

(a) (b)

Figure 2: Champagne flute model used in our study (a); inspired from a real flute etched by the glassmaker on its bottom to promote bubble formation (b); the small ring etched on its bottom has been done with adjoining laser beam impacts.

tasting. The temperature indeed modifies both the liquid viscosity and the vapor pressure of volatile aromatic compounds.

In this paper, the influence of champagne temperature on ascending bubble-driven flow patterns found in a very typical champagne flute was investigated, through numerical modeling. Both bubble dynamics and bubble-driven flow patterns in the champagne bulk were followed with time, during the first 300 seconds after champagne was poured into the flute, and for three champagne temperatures (namely, 4, 12, and 18°C).

2. Materials and Methods

2.1. Geometry and Mesh Generation. A traditional flute has been considered as a reference glass case. The glass geometry used in this study has been created from the real dimensions measured of the glass used for the experiments (see Figure 2(a)).

To ensure a continuous and perfectly controlled process of effervescence, glassmakers usually consider circulary etched glasses (Figure 2(b)). In such a way, as previously mentioned, the flow structure exhibits a quasi-steady two dimensional behavior [22] (Figure 1).

In this situation, a 2D examination in the axis symmetry plane can be considered as sufficient. For this purpose, only half of the studied area was drawn. The study area has a total height of 80 mm which corresponds to the fill level and its diameter is 50 mm at the liquid surface level (Figure 2(a)).

The ANSYS Workbench Design Modeler software has been used to draw the geometry from the real size (scale 1 : 1) of the numerical study glass used as reference.

The mesh of the domain has been carried out using the ANSYS Workbench meshing software. It consists in a two-dimensional mesh efficient in the case of simulations of axisymmetrical flow features. The body has been meshed with quadrilateral elements (0.2 × 0.2 mm). Along the central part of the flow, the mesh is structured but to follow the wall, the mesh is unstructured (Figure 3).

2.2. Equations and Numerical Scheme. Because champagne is a wine in which gaseous as well as liquid phase is simultaneously present, the flows in a glass of champagne have been simulated numerically with a multiphase model. The flow is supposed laminar [19, 27] and transient, so the liquid-phase hydrodynamics are described with the continuity and momentum conservation equations for laminar flows.

2.2.1. Continuity Equation. The general form of the continuity equation can be written as follows:

$$\frac{\partial \rho}{\partial t} + \nabla \cdot (\rho \vec{v}) = S_m. \tag{1}$$

The source S_m is the mass added to the continuous phase from the dispersed second phase.

For 2D axisymmetric geometries, the continuity equation is given by

$$\frac{\partial \rho}{\partial t} + \frac{\partial}{\partial x}(\rho v_x) + \frac{\partial}{\partial r}(\rho v_r) + \frac{\rho v_r}{r} = S_m, \tag{2}$$

where x is the axial coordinate, r is the radial coordinate, v_x is the axial velocity, and v_r is the radial velocity.

2.2.2. Navier-Stokes Equations. Conservation of momentum is described by

$$\frac{\partial}{\partial t}(\rho \vec{v}) + \nabla \cdot (\rho \vec{v}\vec{v}) = -\nabla p + \rho \vec{g} + \vec{F}, \tag{3}$$

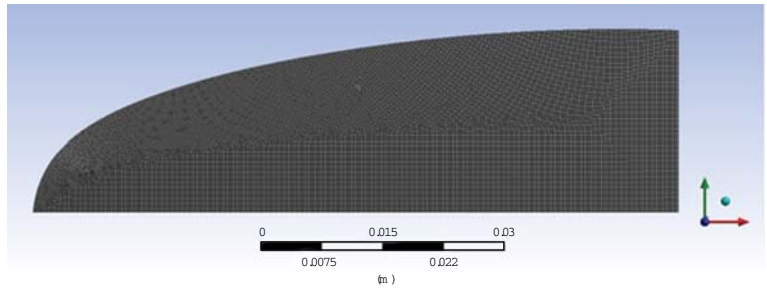

Figure 3: Mesh of the half fluid domain.

where ρ is the static pressure and $\rho\vec{g}$ and $\vec{F}$ are the gravitational body force and external body forces (forces that arise from interaction between the liquid phase and the dispersed one).

For 2D axisymmetric geometries, the axial and radial momentum conservation equations are given by

$$\begin{aligned}\frac{\partial}{\partial t}(\rho v_x) + \frac{1}{r}\frac{\partial}{\partial x}(r\rho v_x v_x) + \frac{1}{r}\frac{\partial}{\partial r}(r\rho v_r v_x) \\ = -\frac{\partial p}{\partial x} + \frac{1}{r}\frac{\partial}{\partial x}\left[r\mu\left(2\frac{\partial v_x}{\partial x} - \frac{2}{3}(\nabla\cdot\vec{v})\right)\right] \\ + \frac{1}{r}\frac{\partial}{\partial r}\left[r\mu\left(\frac{\partial v_x}{\partial r} + \frac{\partial v_r}{\partial x}\right)\right] + F_x,\end{aligned} \tag{4}$$

$$\begin{aligned}\frac{\partial}{\partial t}(\rho v_r) + \frac{1}{r}\frac{\partial}{\partial x}(r\rho v_x v_r) + \frac{1}{r}\frac{\partial}{\partial r}(r\rho v_r v_r) \\ = -\frac{\partial p}{\partial r} + \frac{1}{r}\frac{\partial}{\partial r}\left[r\mu\left(2\frac{\partial v_r}{\partial r} - \frac{2}{3}(\nabla\cdot\vec{v})\right)\right] \\ + \frac{1}{r}\frac{\partial}{\partial x}\left[r\mu\left(\frac{\partial v_r}{\partial x} + \frac{\partial v_x}{\partial r}\right)\right] - 2\mu\frac{v_r}{r^2} + \frac{2}{3}\frac{\mu}{r}(\nabla\cdot\vec{v}) + F_r,\end{aligned} \tag{5}$$

where

$$\nabla\cdot\vec{v} = \frac{\partial v_x}{\partial x} + \frac{\partial v_r}{\partial r} + \frac{v_r}{r}. \tag{6}$$

In this work, we have used the Lagrangian-Eulerian approach which analyzes the liquid phase (primary phase) by the Eulerian method and the bubble phase (secondary phase) by Lagrangian assumption allowing the monitoring of bubbles life cycle.

The Euler-Lagrange approach is the basis of the lagrangian discrete phase model. The dispersed phase is solved by tracking the bubbles through the calculated flow domain while the liquid phase is treated continuously by solving the continuity and Navier-Stokes equations. Exchanges of momentum and mass are realized between the dispersed phase and the fluid one.

According to the Lagrangian multiphase model, the volume fraction of the discrete phase (secondary phase) is quite small.

The bubbles trajectories are computed individually at each time step during the liquid phase calculation. This model is perfectly adapted for modeling the flows in a glass of champagne [26]. In order to reproduce as closely as possible the principle of nucleation, subroutines have been used for the gaseous phase. These subroutines have been written based on physical laws that are taken from previous experimental results [19, 27].

2.2.3. Ascending Bubbles Dynamics. The trajectory of a bubble is predicted by integrating the force balance in a Lagrangian reference frame.

During its rise in the liquid, a bubble is subjected to the action of several forces [19, 27]. The driving force of bubble ascent is buoyancy:

$$F_B = \frac{4}{3}\pi R^3 \rho g. \tag{7}$$

The drag force F_D exerted by the fluid around the bubble is expressed as follows:

$$F_D = \frac{1}{2}C_D\rho u^2 \pi R^2, \tag{8}$$

where C_D is the drag coefficient.

The movement of the surrounding fluid leads to an additional force F_{MA} called "added mass" related to the variation in the amount of movement of liquid displaced:

$$F_{\mathrm{MA}} = \frac{\rho d}{dt}(Vu). \tag{9}$$

The volume V of liquid entrained in the wake of the bubble is roughly equal to the half of the volume of the bubble. Thus

$$F_{\mathrm{MA}} = \frac{2}{3}\rho\pi\frac{d}{dt}\left(R^3 u\right). \tag{10}$$

The equation of motion can be written as follows:

$$\frac{2}{3}\rho\pi R^3\left(\frac{dU}{dt} + \frac{3U}{R}\frac{dR}{dt}\right) = \frac{4}{3}\pi R^3\rho g - \frac{1}{2}C_D\rho U^2\pi R^2. \tag{11}$$

The force of added mass has been compared to the buoyancy along the path of the bubble to the surface. The force of added mass does not exceed 2-3% of the buoyancy, so it can be neglected in the remainder of the study. The equation of motion is finally reduced to a simple equality between the drag force and buoyancy.

During ascent, surface-active materials progressively accumulate at the rear part of the rising bubble, thus increasing the immobile area of the bubble surface.

A rising bubble rigidified by surfactants runs into more resistance than a bubble presenting a more flexible interface free from surface-active materials. The champagne bubbles showed therefore a behavior intermediate between that of a rigid and that of a fluid sphere. To take into account the surfactants accumulation, the two following experimental drag coefficient laws, available in the range of intermediate Reynolds numbers (10^{-1} to 10^{2}) covered by champagne bubbles, have been used. Magnaudet et al. [28] have proposed a semiempirical relationship between the drag coefficient and the Reynolds number:

$$C_D = \frac{16}{\mathrm{Re}}\left(1 + 0.15\sqrt{\mathrm{Re}}\right) \quad (\mathrm{Re} < 50). \tag{12}$$

This experimental determination of the drag coefficient for fluid spheres is available for Reynolds number less than 50.

Since the Reynolds number exceeds the limit of 50 for sufficiently long path, another empirical law has been used available for Re > 50, determined by Maxworthy et al. [29]

$$C_D = 11.1\mathrm{Re}^{-0.74} \quad (1 < \mathrm{Re} < 800). \tag{13}$$

Because bubbles do not exceed a critical diameter of 2 mm, they remain spherical during their ascent. Moreover, the assumption that the bubbles do not coalesce or breakup has been considered.

The Reynolds number is defined by:

$$\mathrm{Re} = \frac{2\rho R u}{\eta}. \tag{14}$$

The density and the viscosity of the champagne wine for the liquid phase and the density and the viscosity of the carbon dioxide for the gaseous phase have been stored in the materials database.

The numerical simulations have been carried out with the ANSYS FLUENT software using finite volume approach. The convergence criteria were based on the residuals resulting from the integration of the conservation equations over finite control volumes. During the iterative calculation process, these residuals were constantly monitored and carefully scrutinized. For all simulations performed in this study, converged solutions were usually achieved with residuals as low as 10^{-5} (or less) for all the governing equations. Calculations have been performed for the three wine's temperatures (4, 12, and 20°C) with the same time steps and the same mesh.

2.3. Boundary Conditions. Models based on classical nucleation theory do not give a satisfactory approach of nucleation in the effervescent wines [30]. The idea has been to create routines to simulate the principle of nucleation and then compare the results with those obtained with experimental data [19, 27]. In order to simulate the bubbles growth, the bubbles velocity, the mass transfer between bubbles, the mass flow rate, and the drag law, we have written user-defined functions (UDF) in C language which defines source terms for

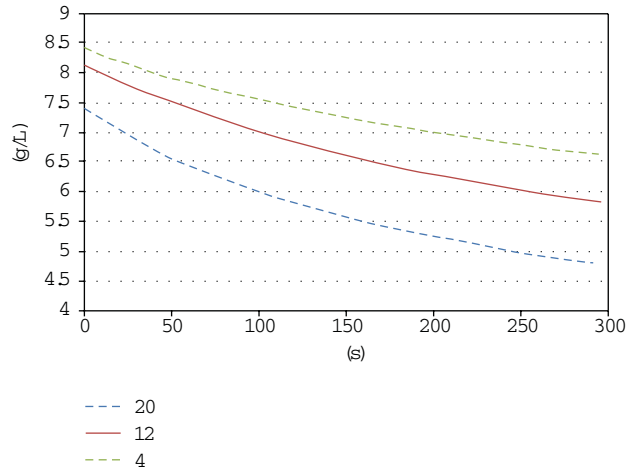

Figure 4: Evolution of the rate of dissolved carbon dioxide according to time in a champagne flute for the three service temperatures. The values have been experimentally measured with the same glass and the same filling level, throughout the 30 minutes following the pouring process of the glass.

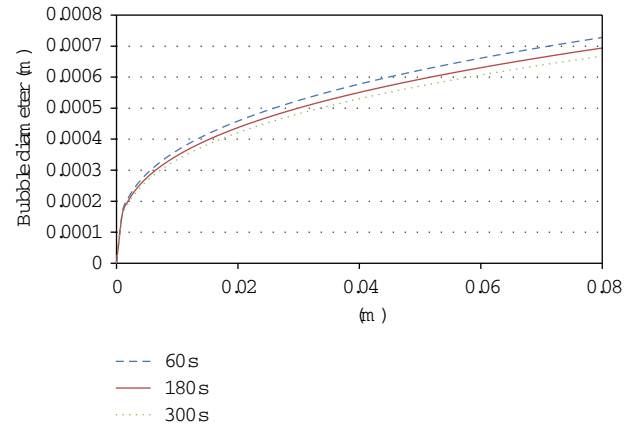

Figure 5: Evolution of the diameter according to the height h for a given champagne temperature of 4°C.

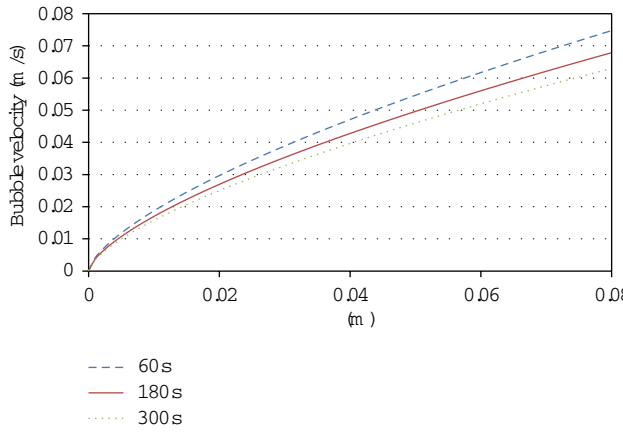

Figure 6: Evolution of the bubble velocity according to the height h for a given champagne temperature of 4°C.

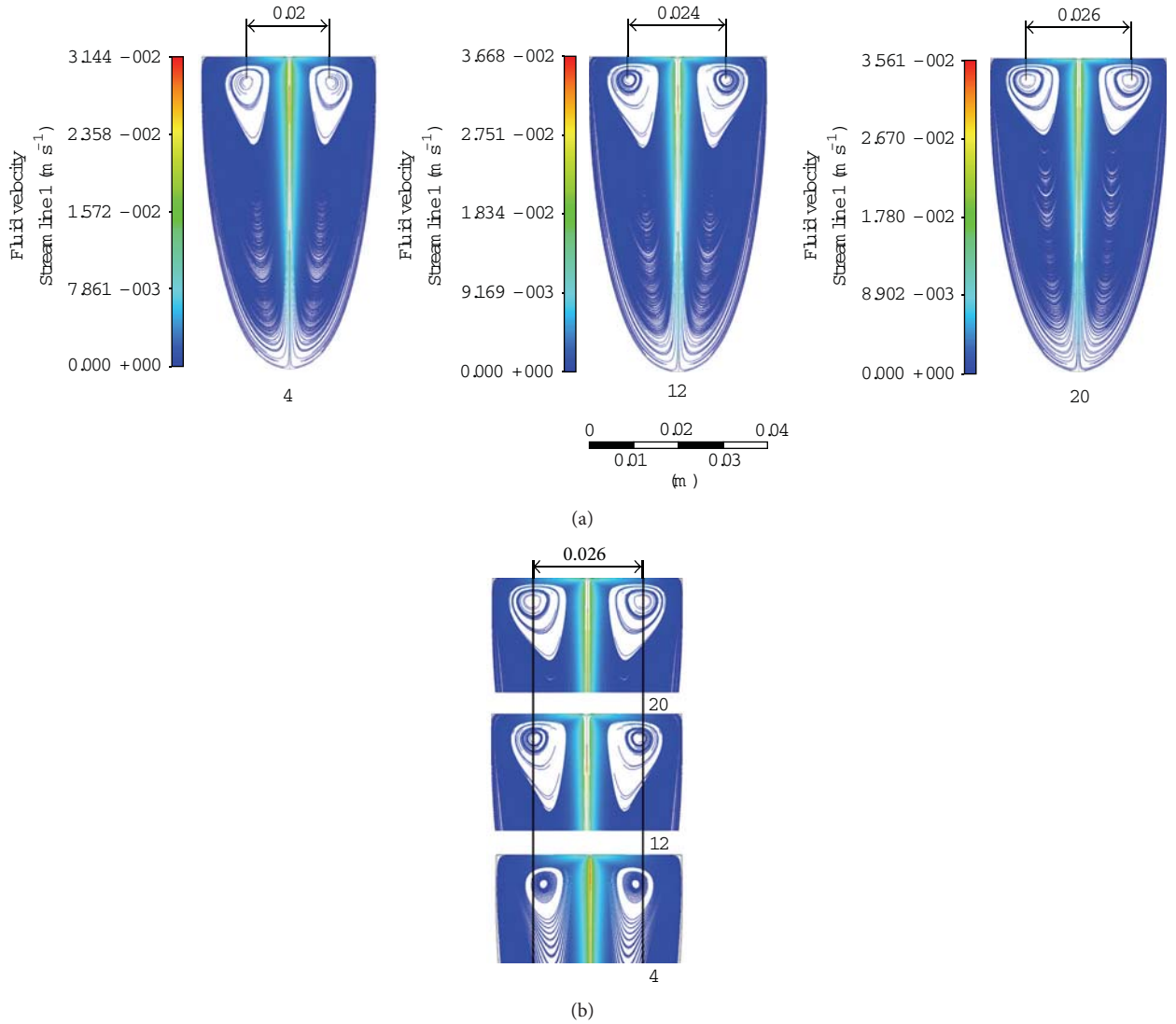

FIGURE 7: Evolution of the location of the vortex cores at 60 s following the pouring process and for three service temperatures (a), detail on the upper part of the glass (b).

the flow regime. The variation of bubbling frequency, which is a function of the CO_2-dissolved concentration, is made possible by changing the time step during the calculation.

The radius R of a bubble increases with time at a constant growth rate $k = dR/dt$, as bubbles rise toward the liquid surface, as experimentally determined by Liger-Belair [19].

Thus, $R(t) = R_0 + kt$, where R_0 is the bubble radius as it detaches from the nucleation site.

The semiempirical growth rate (k, expressed in μm/s) of bubbles rising in champagne was linked with some physicochemical properties of liquids as follows [19]:

$$k = \frac{dR}{dt} \approx 0.63 \frac{\Re\theta}{P_0} D_0^{2/3} \left(\frac{2\alpha\rho g}{9\eta} \right)^{1/3} (C_L - k_H P_0). \quad (15)$$

The bubbles diameter depends on several parameters, including both the distance traveled by the bubble, denoted by h, and the dissolved CO_2 concentration, denoted by C_L which continuously decreases with time (as a result of bubbling). Recently, the rate at which the dissolved CO_2 concentration decreases as time proceeds after pouring champagne into a flute etched on its bottom was experimentally determined for three distinct champagne temperatures (namely, 4, 12, and 20°C) [31]. As illustrated in Figure 4, the rate at which the dissolved CO_2 concentrations escape from champagne is strongly temperature dependent. For more details about the determination of Figure 4, see the article by Liger-Belair et al. [31] and references therein.

The law governing the change in radius R of a bubble is as follows [19]:

$$R \approx 2,7 \times 10^{-3} \times \theta^{5/9} \times \left(\frac{1}{\rho g} \right)^{2/9} \times \left(\frac{C_L - K_H P_0}{P_0} \right)^{1/3} \times h^{1/3}, \quad (16)$$

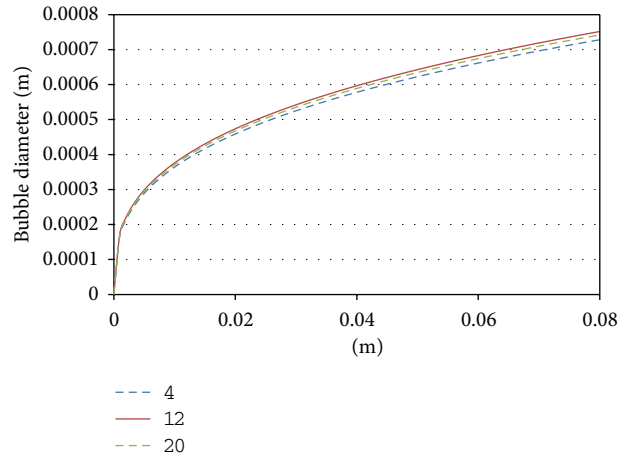

Figure 8: Bubbles' diameters in the bubble column, 60 s after the pouring process, and for the three champagne temperatures.

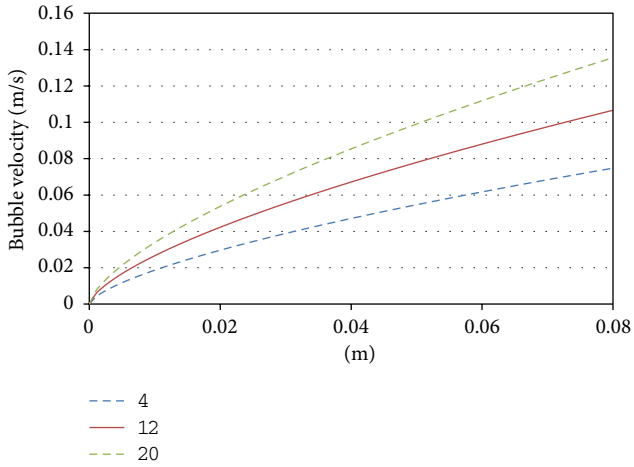

Figure 9: Bubbles' ascending velocities, 60 s after the pouring process, and for the three champagne temperatures.

where α is a numerical coefficient that depends on the fluid in question, estimated to be 0.7 in the case of sparkling wines [19].

The bubbles velocity u(m/s) varies according to the following expression [19, 32]:

$$u \approx \frac{2\alpha\rho g}{9\eta} R^2. \tag{17}$$

This factor accounts the rigidity of the bubble and thus the braking effect due to the presence of surfactant molecules on the surface of bubbles. It will be smaller if the bubble is made rigid by a thick shield of surfactant molecules.

The mass flow rate Q_m (kg/s) is defined by

$$Q_m = \frac{N}{t} \times \rho_p \times V_b. \tag{18}$$

The CO_2-dissolved concentration C_L decreases continuously over time once the wine is poured into the glass (Figure 4).

Table 1: Physicochemical parameters of champagne wine for the three service temperatures.

t (°C)	θ (°K)	k_H (Kg/m^3/Atm)	η (Kg/m/s)	D (m^2/s)
4	277.15	2.59	0.0027	0.751
12	285.15	1.93	0.0020	1.034
20	293.15	1.44	0.0016	1.385

This parameter also varies with the temperature. In this study, we have used the champagne physicochemical parameters for the three wines temperatures (Table 1).

The fluid viscosity varies in a significant way with the temperature; it tends to decrease when the temperature increases. The dependence of the viscosity of the champagne with the temperature follows an Arrhenius-like equation [7]:

$$\eta(\theta) = 1,08 \times 10^{-7} \exp\left(\frac{2806}{\theta}\right). \tag{19}$$

The temperature appears in (16), directly in the term $\theta^{5/9}$, but it is also included in Henry's coefficient k_H as well as in the viscosity η, which both depend on the temperature. Henry's constant depends strongly on some gas and on some liquid considered, as well as on the temperature. The dependence of Henry's constant on the temperature follows a law described by the equation of Van't Hoff:

$$K_H = K_{298\ \mathrm{K}} \exp\left[-\frac{\Delta H_{\mathrm{diss}}}{\Re}\left(\frac{1}{\theta} - \frac{1}{298}\right)\right]. \tag{20}$$

The effects on the bubble growth and on the upward bubbles dynamics are intrinsically connected to the variations of the physico-chemical parameters varying from a temperature to the other one (Table 1). Once (16) solved, we show that the influence of the temperature on the bubbles size is weak. Thanks to the influence of the viscosity and Henry's constant (Table 1), it is worth noting that increasing the temperature of a champagne of about 10°C (from 278° to 288°K) leads to increase of the bubbles size from 5 to 6% (which is totally undetectable in the naked eye). On the contrary, the temperature will have a significant influence on the viscosity of the liquid phase, varying in important way (42% between 4° and 20°). The velocity of the liquid phase, and therefore the mixing mechanisms of the wine, are conditioned by the unsteady evolution of the gaseous phase. Let us call back besides that the evolution of the rate of dissolved carbon dioxide differs for the three champagne temperatures (Figure 4).

3. Results and Discussion

We are going to present the numerical results (diameter and velocities of bubbles and velocity isocontours for the liquid phase) for three champagne temperatures (4°, 12°, and 20°). We will study the influence of these parameters on the liquid phase for 3 moments (60, 180, and 300 s) after the pouring process.

3.1. Ascending Bubbles' Dynamics. During its ascent towards the surface, the bubble grows by accumulating progressively

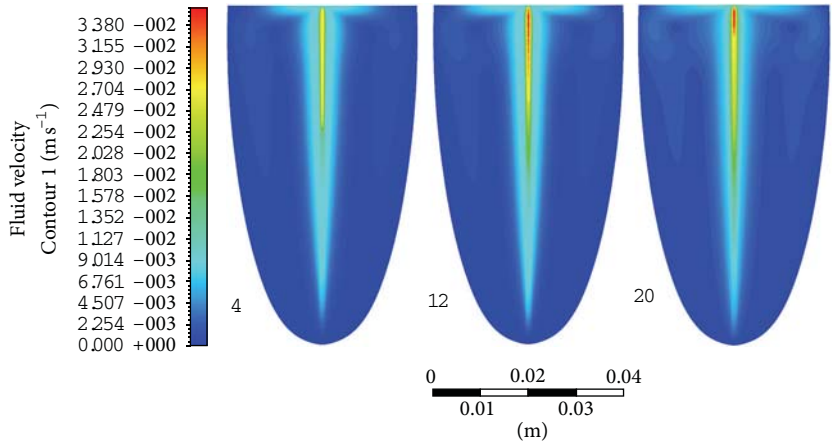

Figure 10: Flow patterns velocity magnitude, 60 s after the pouring process, and for the three champagne temperatures.

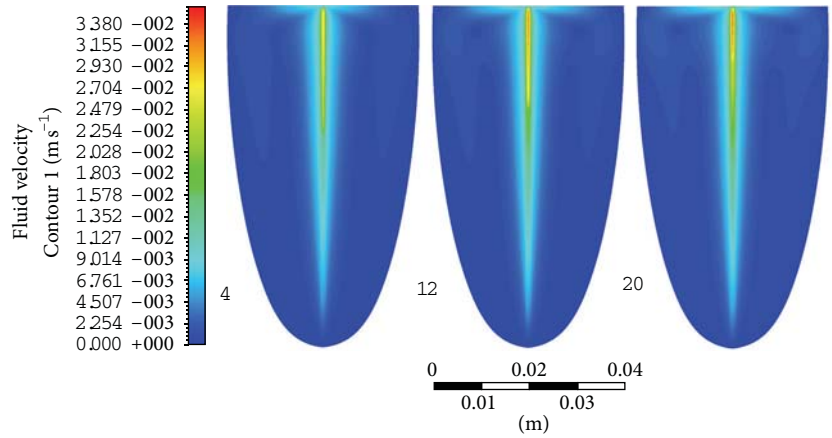

Figure 11: Flow patterns velocity magnitude, 180 s after the pouring process, and for the three champagne temperatures.

the CO_2 dissolved in the wine. The Figure 5 shows the unsteady evolution of the bubbles diameter in the case of a 4° service temperature. One may notice clearly a progressive decrease of the bubbles' size according to time. This is due to the progressive decrease with time of dissolved carbon dioxide in the liquid phase (as shown in Figure 4).

Moreover, because bubbles increase in size while rising toward the champagne surface, bubbles accelerate, as illustrated in Figure 6. Besides, it is worth noting in Figure 6 that the bubbles' velocity decreases with time, due to the progressive decrease of carbon dioxide dissolved in the liquid phase. Once again, the temperature will influence the upward dynamics of bubbles via the temperature dependence of the viscosity of the liquid phase.

3.2. Temperature Dependence of Ascending Bubble-Driven Flow Patterns Dynamics. A strong hypothesis in the tasting of the champagne wine is that there is a relation between the convection movements in the wine and the gaseous and aromatic exchanges which are very important in the gustative perception. During this study, we are going to show the impact of the temperature on the dynamics of mixing mechanisms of the wine.

Figure 7 represents the streamlines of the liquid phase for three champagne temperatures, 60 s after the pouring process. One may observe that the vortex core goes away from the axis of the flute when the temperature and the velocity increase. We can already note a dependence of bubble-driven flow patterns velocities and overall dynamics on the champagne temperature.

Both the progressive increases of ascending bubbles' diameters, and bubbles' velocities are presented in Figures 8 and 9, for the three various champagne temperatures, 60 s after pouring champagne into the flute.

By observing Figure 8, it is worth noting that bubbles' diameters are very close to each other, whatever the champagne temperature. More important differences are nevertheless observed concerning the bubbles' velocities, as shown in Figure 9. This is due to the temperature dependence of the liquid phase viscosity (see Table 1) which contributes to the bubbles' velocity, as shown in (17). Generally speaking, the higher the temperature is, the higher the bubble velocity is. Because the liquid phase is driven by ascending bubbles (through viscous effects), the dynamics of the flow patterns found in the flute are therefore expected to be strongly temperature dependent. As expected, the higher the champagne

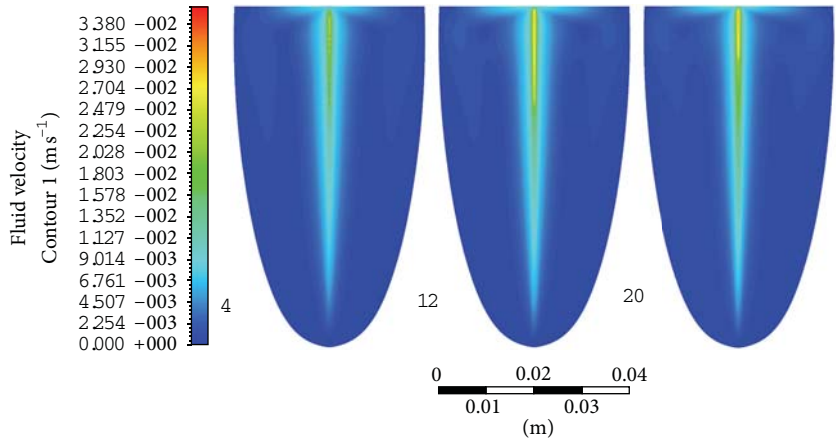

Figure 12: Flow patterns velocity magnitude, 300 s after the pouring process, and for the three champagne temperatures.

temperature is, the higher the velocity of bubble-driven flow patterns found in the liquid phase is, as illustrated in Figure 10 (60 s after pouring). The same trend has been observed 180 (Figure 11) and 300 s (Figure 12) after pouring for the three champagne temperatures, but with overall velocities progressively lowering as time proceeds (mainly because both ascending bubbles' diameters and velocities decrease with time due to the progressive loss of dissolved carbon dioxide found in the liquid phase).

4. Conclusion

In this paper, a numerical modeling of bubble-driven flow patterns found in a glass of champagne has been carried out for three champagne temperatures (4, 12, and 20°C) using the finite-volume method by CFD (computational fluid dynamics). The results, for both the gaseous phase (ascending bubbles) and the liquid phase (bubble-driven flow patterns), were systematically compared at several moments following the pouring process. Because ascending bubbles velocities strongly depend on the champagne temperature, the velocities of ascending bubble-driven flow patterns were found to logically vary with the champagne temperature. The champagne viscosity, which strongly depends on its temperature, plays a crucial role in the temperature dependence of ascending bubble-driven flow patterns. As expected, the higher the champagne temperature, the higher the velocities of the liquid phase. In a near future, these numerical results are expected to be confirmed by PIV experiments. Moreover, since a correlation is strongly suspected between ascending bubble-driven flow patterns and the release of aromatic volatile compounds from champagne, further investigations are to be conducted together with sensory analysis experiments.

Nomenclature

C_D: Drag coefficient (dimensionless)
C_l: Lift coefficient (dimensionless)
C_L: CO_2-dissolved concentration in the liquid (g/l)
D_0: Diffusion coefficient of CO_2 molecules (m^2/s)
F_D: Drag force
g: Acceleration due to gravity ($m \cdot s^{-2}$)
h: Liquid height (m)
k: Theoretical growth rate of bubbles (μm/s)
k_H: Henry's constant (kg/m^3/atm)
L: Characteristic dimension of a mesh element (mm)
N: Bubbling frequency (Hz)
P_0: Atmospheric pressure (atm)
Q_m: Mass flow rate (kg/s)
R: Bubble radius (m)
Re: Reynolds number (dimensionless)
u: Bubble velocity (m/s)
v: Liquid velocity (m/s)
V_b: Bubble volume (m^3)
$\mathfrak{R}$: Ideal gas constant (8.31 J/mol/K)
ρ: Liquid density (kg/m^3)
ρ_p: Density of CO_2 (kg/m^3)
η: Dynamic viscosity (kg/m/s)
α: Numerical coefficient (dimensionless)
θ: Liquid temperature (°C)
λ: Molecular mean free path (m)
$\emptyset$: Bubble diameter (m).

References

[1] A. Akhtar, V. Pareek, and M. Tadé, "CFD simulations for continuous flow of bubbles through gas-liquid columns: application of VOF method," *Chemical Product and Process Modeling*, vol. 2, no. 1, article 9, 2007.

[2] V. V. Buwa, D. S. Deo, and V. V. Ranade, "Eulerian-Lagrangian simulations of unsteady gas-liquid flows in bubble columns," *International Journal of Multiphase Flow*, vol. 32, no. 7, pp. 864–885, 2006.

[3] E. Delnoij, J. A. M. Kuipers, and W. P. M. Van Swaaij, "A three-dimensional CFD model for gas-liquid bubble columns," *Chemical Engineering Science*, vol. 54, no. 13-14, pp. 2217–2226, 1999.

[4] D. Zhang, N. G. Deen, and J. A. M. Kuipers, "Numerical simulation of the dynamic flow behavior in a bubble column: a study of closures for turbulence and interface forces," *Chemical Engineering Science*, vol. 61, no. 23, pp. 7593–7608, 2006.

[5] F. Özkan, M. Wörner, A. Wenka, and H. S. Soyhan, "Critical evaluation of CFD codes for interfacial simulation of bubble-train flow in a narrow channel," *International Journal for Numerical Methods in Fluids*, vol. 55, no. 6, pp. 537–564, 2007.

[6] G. Liger-Belair, C. Cilindre, R. D. Gougeon et al., "Unraveling different chemical fingerprints between a champagne wine and its aerosols," *Proceedings of the National Academy of Sciences of the United States of America*, vol. 106, no. 39, pp. 16545–16549, 2009.

[7] G. Liger-Belair, "The physics behind the fizz in champagne and sparkling wines," *European Physical Journal Special Topics*, vol. 201, pp. 1–88, 2012.

[8] G. Liger-Belair, "The science of bubbly," *Scientific American*, vol. 288, no. 1, pp. 80–85, 2003.

[9] G. Liger-Belair, "Nucléation, ascension et éclatement d'une bulle de champagne," *Annals of Physics*, vol. 31, pp. 1–133, 2006.

[10] G. Polidori, P. Jeandet, and G. Liger-Belair, "Bubbles and flow patterns in champagne," *American Scientist*, vol. 97, no. 4, pp. 294–301, 2009.

[11] T. Hummel, J. F. Delwiche, C. Schmidt, and K. B. Hüttenbrink, "Effects of the form of glasses on the perception of wine flavors: a study in untrained subjects," *Appetite*, vol. 41, no. 2, pp. 197–202, 2003.

[12] M. Vilanova, P. Vidal, and S. Cortés, "Effect of the glass shape on flavor perception of "toasted wine" from ribeiro (NW Spain)," *Journal of Sensory Studies*, vol. 23, no. 1, pp. 114–124, 2008.

[13] C. G. J. Bisperink and A. Prins, "Bubble growth in carbonated liquids," *Colloids and Surfaces A*, vol. 85, no. 2-3, pp. 237–253, 1994.

[14] Y. Zhang and Z. Xu, "Fizzics of bubble growth in beer and champagne," *Elements*, vol. 4, pp. 47–49, 2008.

[15] N. Shafer and R. Zare, "Through a beer glass darkly," *Physics Today*, vol. 44, pp. 48–52, 1991.

[16] J. Chandrashekar, D. Yarmolinsky, L. Von Buchholtz et al., "The taste of carbonation," *Science*, vol. 326, no. 5951, pp. 443–445, 2009.

[17] A. Dunkel and T. Hofmann, "Carbonic anhydrase IV mediates the fizz of carbonated beverages," *Angewandte Chemie*, vol. 49, no. 17, pp. 2975–2977, 2010.

[18] A. Livermore and T. Hummel, "The influence of training on chemosensory event-related potentials and interactions between the olfactory and trigeminal systems," *Chemical Senses*, vol. 29, no. 1, pp. 41–51, 2004.

[19] G. Liger-Belair, "La physique des bulles de champagne," *Annals of Physics*, vol. 27, pp. 1–106, 2002.

[20] G. Liger-Belair, J. B. Religieux, S. Fohanno, M. A. Vialatte, P. Jeandet, and G. Polidori, "Visualization of mixing flow phenomena in champagne glasses under various glass-shape and engravement conditions," *Journal of Agricultural and Food Chemistry*, vol. 55, no. 3, pp. 882–888, 2007.

[21] G. Liger-Belair, F. Beaumont, P. Jeandet, and G. Polidori, "Flow patterns of bubble nucleation sites (called fliers) freely floating in champagne glasses," *Langmuir*, vol. 23, no. 22, pp. 10976–10983, 2007.

[22] G. Polidori, F. Beaumont, P. Jeandet, and G. Liger-Belair, "Artificial bubble nucleation in engraved champagne glasses," *Journal of Visualization*, vol. 11, no. 4, p. 279, 2008.

[23] G. Liger-Belair, G. Polidori, and P. Jeandet, "Recent advances in the science of champagne bubbles," *Chemical Society Reviews*, vol. 37, no. 11, pp. 2490–2511, 2008.

[24] G. Polidori, F. Beaumont, P. Jeandet, and G. Liger-Belair, "Ring vortex scenario in engraved champagne glasses," *Journal of Visualization*, vol. 12, no. 3, pp. 275–282, 2009.

[25] G. Polidori, F. Beaumont, P. Jeandet, and G. Liger-Belair, "Visualization of swirling flows in champagne glasses," *Journal of Visualization*, vol. 11, no. 3, p. 184, 2008.

[26] F. Beaumont, C. Popa, G. Liger Belair, and G. Polidori, "Numerical modeling of bubble-driven flow patterns in champagne glasses," *International Journal of Numerical Methods For Heat and Fluid Flow*, 2013.

[27] G. Liger-Belair and P. Jeandet, "More on the surface state of expanding champagne bubbles rising at intermediate Reynolds and high peclet," *Langmuir*, vol. 19, no. 3, pp. 801–808, 2003.

[28] J. Magnaudet, M. Rivero, and J. Fabre, "Accelerated flows past a rigid sphere or a spherical bubble—part 1. Steady straining flow," *Journal of Fluid Mechanics*, vol. 284, pp. 97–135, 1995.

[29] T. Maxworthy, C. Gnann, M. Kürten, and F. Durst, "Experiments on the rise of air bubbles in clean viscous liquids," *Journal of Fluid Mech*, vol. 321, pp. 421–441, 1996.

[30] E. Herrmann, H. Lihavainen, A. P. Hyvärinen et al., "Nucleation simulations using the fluid dynamics software FLUENT with the fine particle model FPM," *Journal of Physical Chemistry A*, vol. 110, no. 45, pp. 12448–12455, 2006.

[31] G. Liger Belair, G. Polidori, and V. Zéninari, "Unraveling the evolving nature of gaseous and dissolved carbon dioxide in Champagne wines: a state-of-the-art review, from the bottle to the tasting glass," *Analytica Chimica Acta*, vol. 732, pp. 1–15, 2012.

[32] G. Liger-Belair, R. Marchal, B. Robillard et al., "On the velocity of expanding spherical gas bubbles rising in line in supersaturated hydroalcoholic solutions: application to bubble trains in carbonated beverages," *Langmuir*, vol. 16, no. 4, pp. 1889–1895, 2000.

Hindawi Publishing Corporation
Advances in Mechanical Engineering
Volume 2013, Article ID 628490, 12 pages
http://dx.doi.org/10.1155/2013/628490

Research Article

DNS Study of the Turbulent Taylor-Vortex Flow on a Ribbed Inner Cylinder

Takahiro Tsukahara, Manabu Ishikawa, and Yasuo Kawaguchi

Department of Mechanical Engineering, Tokyo University of Science, 2641 Yamazaki, Noda-shi, Chiba 278-8510, Japan

Correspondence should be addressed to Takahiro Tsukahara; tsuka@rs.tus.ac.jp

Received 4 February 2013; Accepted 21 April 2013

Academic Editor: Bo Yu

Turbulent Taylor-vortex flows over regularly spaced square ribs mounted on a rotating inner cylinder surface were investigated using direct numerical simulations (DNSs) for a Reynolds number of 3200 (based on the inner-wall velocity and the gap width between two cylinders) in an apparatus with an inner-to-outer radius ratio of 0.617, while varying the streamwise interval of the ribs. We examined the flow and pressure fields around each rib, focusing on the recirculation zone, the frictional drag coefficient, and the pressure (form) drag. Our results for the Taylor-Couette flows were compared to DNS for plane Poiseuille flows over ribbed surfaces performed by Leonardi et al. (2003). We determined the qualitative consistency between them with respect to the roughness effect, which depends significantly on the rib interval, but the rate of increase in the flow resistance was remarkably dampened by roughness in the present flows. Taylor vortices remaining over roughened cylinder surfaces were found to induce quick pressure recovery behind each rib, leading to less pressure drag and an enhanced backflow in the recirculation zone.

1. Introduction

Turbulent flows over rough surfaces are often encountered in practice. For example, atmospheric and ocean flows occur over rough surfaces and, in an engineering context, most industrial pipes and ducts are not smooth, especially at high Reynolds numbers. Roughness geometry is generally known to cause a large flow resistance. In some industrial applications, roughness elements are applied to enhance heat transfer, even at the expense of drag augmentation. Similarly, in the living world, sharkskin has roughness in the form of riblets that contribute to drag reduction. That is, roughness geometries can seriously influence (favorably or unfavorably) performances of practical applications. From this perspective, the prediction of roughness effects on various different flows is important.

A number of studies addressing this issue have been performed over a long period and have attracted great interest in many industrial applications, for example, [1–5]. A flow accompanied by a separation and a reattachment would significantly affect frictional and pressure drags and would complicate heat transfer and fluid mixing. Therefore, the majority of fundamental investigations in the literature have been performed for a rather canonical flow, that is, Poiseuille flow (hereafter, PF) in a plane but ribbed channel. For instance, Krogstadt and Antonia [6] experimentally demonstrated that the surface geometry significantly affected the turbulent characteristics: Wang et al. [7] investigated the physical process of separated flow in a square channel roughened with periodically transverse ribs on one wall. Many numerical studies [8–12] have been carried out on PF in ribbed channels by means of direct numerical simulation (DNS) or large-eddy simulation (LES). We particularly wished to undertake a comparative study of the present DNS results and those of Leonardi et al. [10], who investigated turbulent PF through transverse square bars attached to one wall. They reported that the ratio of the streamwise interval of ribs (λ) to the rib height (h) was an important parameter for determining the relationship between the flow resistance and the surface roughness. We compile here a database of DNS including a few experiments, as listed in Table 1. However, there have been few studies on the roughness effect for turbulent flows in curved channels and, to the authors' knowledge, there has never been any parametric DNS study

Table 1: Compiled data.

Authors (case)	Flow	Method	Re_δ	h/δ	Geometry	λ/h	L_{re}/h
Agelinchaab and Tachie (2008, Exp.) [4]	OCF	Exp.	17000	0.108	Square rib	∞	7.5
					Semicircular rib	∞	4.7
					Rectangular rib	∞	4.1
Wang et al. [7]	PF	Exp.	11000†	0.300	Square rib	13	3.6
Miyake et al. [8]	PF	DNS	2640	0.033	Rectangular rib	12–24	—
				0.133	Square rib	3–6	—
Cui et al. [9]	PF	LES	10000†	0.200	Square rib	2–5	—
						10	4.5
Leonardi et al. [10]	PF	DNS	4200	0.200	Square rib	8	4.8
						19	5.8
Ikeda and Durbin [12]	PF	DNS	6520†	0.118	Square rib	10	4.5
Ahn et al. [11]	PF	LES	15000†	0.200	Square rib	10	4.5
					Semicircular rib	10	4.5
Le et al. [3]	PF	DNS	15300†	0.333	Backward-facing step	—	6.3
Yang et al. [14]	TCF	DNS	10000	0.033	Backward-facing step	—	4.9
Matsumoto et al. [22]	TCF	Exp.	54000	0.200	Triangular rib	31–122	—
Present							
(R2b)	TCF	DNS	3200	0.100	Rectangular rib	50.6	4.9
(R2)					Square rib	50.6	5.0
(R4)						25.3	4.3
(R8)						12.7	3.8
(R12)						8.4	—
(R16)						6.3	—

OCF, open channel flow; PF, plane Poiseuille flow; TCF, Taylor-Couette flow. The Reynolds number Re_δ is based on the inlet free-stream velocity for each smooth-wall case and δ, which means either the boundary-layer thickness (for OCF), the channel half width (for PF), or the whole gap between cylinders (for TCF). The numbers with † are based on the bulk mean velocity and δ. The ratios among the roughness height h, the roughness interval λ, and the reattachment length L_{re} are also shown.

on a turbulent Taylor-Couette flow (TCF) with regular roughness elements (other than DNS for stepped cylinder [13, 14]).

As is well known, TCF occurs when fluid is contained between two concentric independently rotating cylinders and often provokes Taylor vortices due to Coriolis instability when the inner cylinder rotates at relatively high speed [15, 16]. The Taylor vortex has a size comparable to the cylinder gap and induces significant momentum transfer in the radial direction. Numerous studies on the statistics and structures of turbulent Taylor-vortex flow (between smooth cylinders) are available in the literature dated as early as Coles [17], Barcilon et al. [18], and as recently as Dong [19], van Hout, and Katz [20]. Hence, it is of interest to determine any modulation of the turbulent Taylor-vortex flow by rough surfaces and its influence on the roughness effects. Recently, Matsumoto et al. [21, 22] executed measurements of the flow resistance in TCF with inner cylinders roughened by either regular or irregular elements. They demonstrated a significant increase of the flow resistance that was dependent on the height and interval of roughness elements.

In this study of TCF with roughened inner cylinders, the skin-friction drag and the pressure (form) drag were determined for a range of λ/h. We prepared five different inner cylinders that had square ribs of the same shape but a different number of these ribs. The roughness effects on the flow resistance were investigated, also taking account of influences of the Taylor vortex.

2. Flow System and Numerical Procedure

2.1. Problem Definition and Test Conditions. The flows we consider here are fully developed turbulent Taylor-Couette flows over a roughened inner-cylinder surface. In the Taylor-Couette flow system, the fluid is enclosed between two coaxially rotating cylinders with radii R_1 and R_2 for the inner and the outer cylinders, respectively. The gap width between the cylinders is denoted as d. We limit our present study to the case where the outer cylinder is at rest, while only the inner cylinder is rotating at a constant angular velocity ω. Several transverse ribs acting as roughness blocks are installed on the inner-cylinder surface at regular intervals in the circumferential direction. The configuration with respect to one of the present test cases is schematically illustrated in Figure 1,

Table 2: Computational condition.

Case	Number of ribs	Geometry of rib	λ/h	w/h	$L_\theta^* \times L_r^* \times L_z^*$	$N_\theta \times N_r \times N_z$
Smooth	0	—	0	0	$\pi/2 \times 1 \times 4.56$	$256 \times 128 \times 256$
R2	2	$h \times h$	50.6	49.6	$\pi \times 1 \times 4.56$	$256 \times 128 \times 256$
R2b	2	$6h \times h$	50.6	44.6	$\pi \times 1 \times 4.56$	$256 \times 128 \times 256$
R4	4	$h \times h$	25.3	24.3	$\pi/2 \times 1 \times 4.56$	$256 \times 128 \times 256$
R8	8	$h \times h$	12.7	11.7	$\pi/2 \times 1 \times 4.56$	$256 \times 128 \times 256$
R12	12	$h \times h$	8.4	7.4	$\pi \times 1 \times 4.56$	$256 \times 128 \times 256$
R16	16	$h \times h$	6.3	5.3	$\pi \times 1 \times 4.56$	$256 \times 128 \times 256$

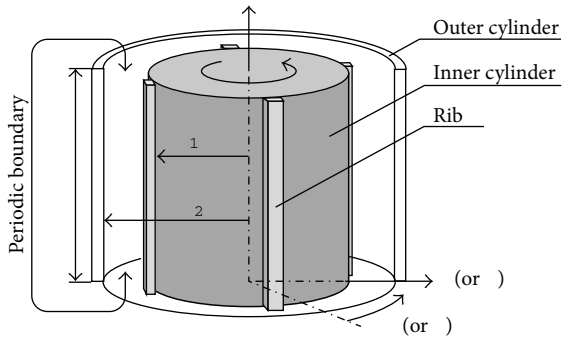

Figure 1: Configuration of Taylor-Couette flow and coordinate systems.

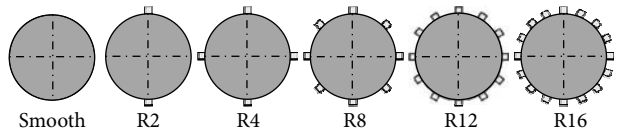

Figure 2: Rib patterns.

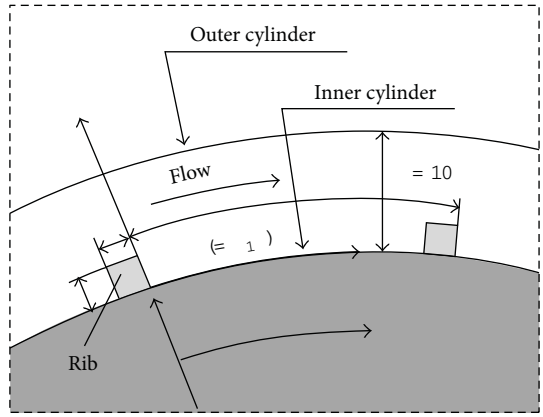

Figure 3: Geometry of a rib on an inner cylinder.

showing the coordinate system and a case where four ribs are located at $\theta = 0^\circ, 90^\circ, 180^\circ$, and 270°. The cross-section of the rib is in the shape of a square, being $h \times h$ with $h = 0.1d$, when mapped to the Cartesian coordinates. In this study, the simulations were carried out in a cylindrical coordinate system: that is, the circumferential (or streamwise), radial (wall-normal), and axial (spanwise) directions are described by θ, r, and z, respectively, and the velocity components in each direction are represented by u, v, and w.

The radius ratio between the cylinders is represented by

$$\eta = \frac{R_1}{R_2} = 0.617, \tag{1}$$

and the aspect ratio is of

$$\Gamma = \frac{L_z}{d} = 4.58. \tag{2}$$

The previous ratios were chosen to compare with another DNS [23] for smooth cylinders under the same conditions. Here, L_z denotes the length of the computational domain in the z direction. The present value of Γ is expected to accommodate at least two Taylor-vortex pairs or four individual vortices, on the basis of an experimental result [24] showing that the spanwise wavelength of the Taylor vortices in the present condition would be $2.29d$. The computational domain size and the grid numbers are summarized in Table 2. Since the ribs were mounted axisymmetrically with respect to the axis of rotation, only one half or a quarter of the entire annular domain is considered. The periodic boundary conditions are imposed in the θ and z directions on the assumption that the flow field should theoretically be either periodic or homogeneous in those directions if a given computational domain is large enough compared to inherent turbulent structures. Nonslip and nonpenetration boundary conditions were applied to the walls including the ribs.

We examined five different numbers of ribs installed on the inner cylinder. Each inner cylinder had either 2, 4, 8, 12, or 16 convex roughness elements, which were in the same shape of a square configuration and arranged at uniform intervals in each case: see Figures 2 and 3. We named each of those test cylinders as an "Rn," where n means the number of ribs. For example, the test cylinder labeled as R4 has four ribs on the inner cylinder. Strictly, it should be noted that the width of upper surface of the rib is about 6% longer than that of the bottom, since the circumferential grid size is altered depending on the radial location because of the cylindrical coordinate.

2.2. Numerical Method. The fluid is assumed to be incompressible and Newtonian. The governing equations for the fluid motion are the equation of continuity

$$\nabla \cdot \mathbf{u} = 0 \tag{3}$$

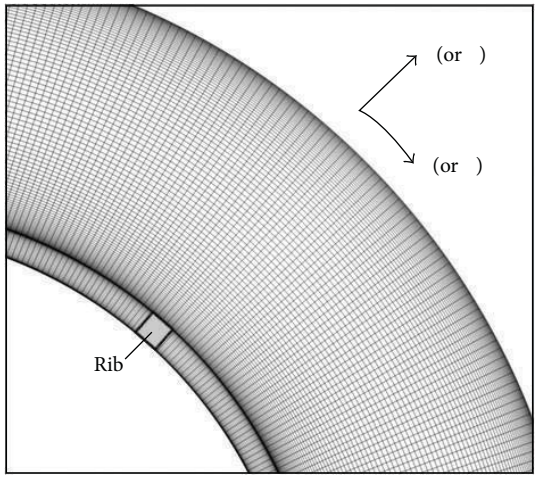

Figure 4: Magnified view of computational grids with emphasis on a rib, viewed from the spanwise direction.

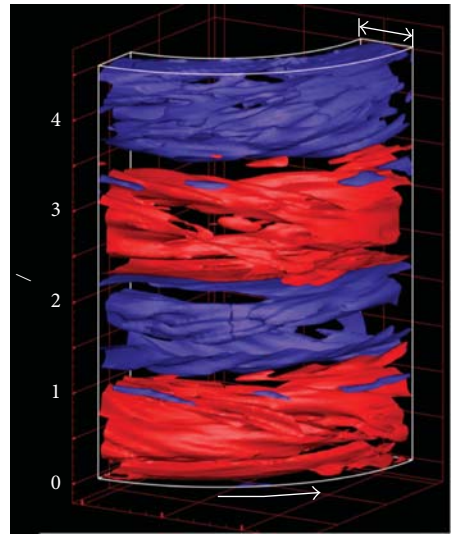

Figure 5: Visualization of Taylor vortices by isosurface of vorticity: red, $\omega_\theta = 0.5$; blue, $\omega_\theta = -0.5$.

and the Navier-Stokes equation

$$\frac{\partial \mathbf{u}}{\partial t} + (\mathbf{u} \cdot \nabla)\,\mathbf{u} = -\frac{1}{\rho}\nabla p + \nu \nabla^2 \mathbf{u} + 2\mathbf{u} \times \Omega + \mathbf{F}, \quad (4)$$

where $\mathbf{u} = (u, v, w)$ represents the velocity (in (θ, r, z) direction), p the pressure, ν the kinematic viscosity of test fluid, $\Omega = (0, 0, \omega)$ the angular velocity of a rotating frame of reference, and $\mathbf{F}$ the body force per unit volume for the immersed boundary method (mentioned later). The static pressure $\widetilde{p}$ and the centrifugal acceleration are combined to give

$$p = \widetilde{p} - \frac{\rho}{2}|\Omega \times \mathbf{r}|^2, \quad (5)$$

and $\mathbf{r}$ is a position vector from the axis of rotation. No turbulence modeling was included: all scales of turbulent fluctuations are resolved using fine grids. In the calculations, the previous governing equations were normalized by the gap width d, and the circumferential speed of the inner-cylinder surface, $U_w = R_1\omega$. Unless specified otherwise, all the flow variables presented henceforth in this paper are normalized by (d) and U_w as the length and velocity scales, respectively. The velocity u in the streamwise direction is used as a relative velocity to the inner-cylinder wall, so that the flow fields are discussed in a reference frame rotating with the inner cylinder. The boundary conditions of the velocity are as follows:

$$\begin{aligned} u = v = w = 0 \quad &\text{at } r = R_1 \text{ and rib surface,} \\ u = R_2\omega, \quad v = w = 0 \quad &\text{at } r = R_2. \end{aligned} \quad (6)$$

For the spatial discretization of governing equations, the finite difference method was adopted on a staggered grid. The central difference scheme with 4th-order accuracy was employed in the θ and z directions, while one of 2nd-order accuracy was applied in the r direction. Equations (3) and (4) were decoupled by the fractional step method. Time advancement was carried out by the 2nd-order Adams-Bashforth method, but the 2nd-order Crank-Nicolson method was used for the viscous term in the r direction. The Poisson equation for pressure correction was solved in the Fourier space using fast Fourier transforms, and a tridiagonal solver was employed for the radial direction. In order to mimic solid bodies of roughness elements installed on the inner cylinder, the direct-forcing immersed boundary technique [25, 26] was applied on the surface and inside of the roughness elements. This approach allows the solution of flows over complex geometries without the necessity of body-fitted grids. Figure 4 shows a magnified view of grids around the cylinder and a rib. The uniform grids were used in the θ and z directions, while the density of the computational mesh was not uniform with more resolution near the edge of rib and wall boundaries, as shown in Figure 4.

The simulation was conducted at a Reynolds number fixed at

$$\mathrm{Re} = \frac{U_w d}{\nu} = 3200, \quad (7)$$

where U_w is the inner-wall velocity, corresponding to $R_1\omega$. This Reynolds number and the radius ratio $\eta = 0.617$, characterizing the flow state of a Taylor-Couette flow, are equivalent to those in DNS performed by Bilson and Bremhorst [23] for the additional advantage of code verification. These conditions were reasonable, because turbulent flows accompanied by Taylor vortices with/without roughness of the inner cylinder are of interest in this work. The onset of turbulent Taylor vortices is a function of the Reynolds number, the radius ratio, the aspect ratio, and even the initial condition. For instance, according to a flow map reported by Andereck et al. [16], the onset occurs at $\mathrm{Re} \approx 1370$ (for $\eta = 0.883$ with a stationary outer cylinder). We expected that the present Reynolds number would be large enough for flows to be turbulent. The first (or preliminary) test case in the present study was run

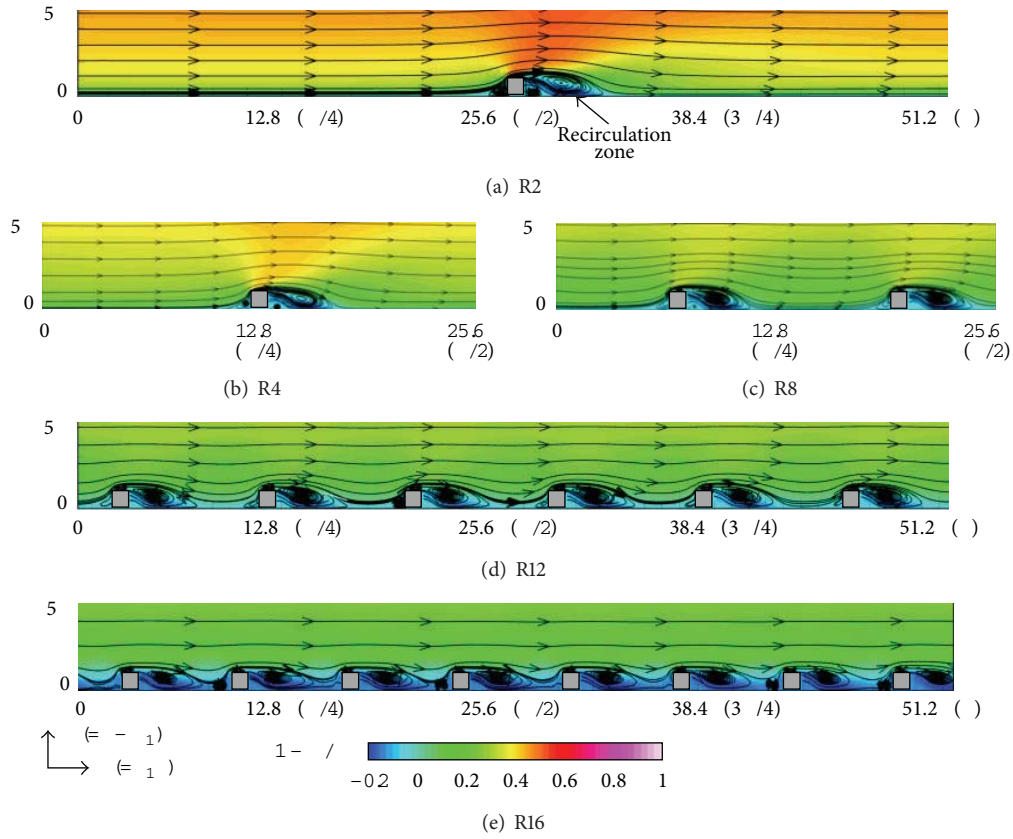

FIGURE 6: Mean streamlines and contour of mean streamwise velocity in the x-y plane.

in smooth-surface cylinders. The primary results considered here were the existence of Taylor vortices and the vortex wavelength, which were identified from visual inspection of the velocity field. Generally, the vortex wavelength was expected to be approximately equal to $2d$ or slightly larger. As shown in Figure 5, we have actually confirmed the presence of four Taylor vortices, that is, a turbulent Taylor-vortex flow, in our simulations under the previous conditions. Although not demonstrated here, various statistical quantities that were obtained for the smooth surface were in excellent agreement with the DNS database of Bilson and Bremhorst [23], showing that the present numerical code was verified successfully.

3. Result and Discussions

3.1. Flow Field around Ribs. Figure 6 shows the streamlines averaged in time and in the homogeneous spanwise (z) direction for the present rib-roughened TCF obtained after the flow reached a statistically steady state. In the figures, the full length of each entire computational domain in the streamwise direction is presented, but in the radial direction only the lower half of the domain is visualized. We now introduce an alternative coordinate $y\ (= r - R_1) \in [0, d]$ as the wall-normal distance from the inner cylinder surface. The contour represents the magnitude of the local mean velocity U in the streamwise direction: hereafter, capital-letter symbols such as U and P denote respective averaged values. In addition, $x\ (= R_1\theta)$ will be used as the streamwise coordinate, instead of θ. In this figure, we can confirm several features characterizing flows over a bluff body such as the separations from the leading and trailing top edges of the body, the recirculation zone behind the body, and the secondary vortex in the upstream corner of the body. The separated flow, which emanates from the leading top edge of a rib, is deflected away from the relevant rib and reattaches to the inner-cylinder surface. The reattachment length L_{re}, defined as a streamwise distance from the downstream face of the rib to the reattachment point, is found to increase with increasing rib interval λ: in the cases of R8, R4, and R2, $L_{re} = 3.8h$, $4.3h$, and $5.0h$, respectively. Since U of the approaching flow to a sparsely located rib increases compared to that for densely-located ribs, the ascending motion of flow separated from the leading edge would also be enhanced. This motion gives rise to a thickening of the recirculation zone behind the rib. As for very short intervals of ribs (R12 and R16), the reattachment does not occur on the cylinder surface but on the vertical facing wall of the next rib, resulting in the formation of a cavity flow between the two ribs. In such cases, owing to the recirculation zone, the streamwise mean velocity is negative above the entire length of the cavity wall and there is no reattachment point. In consequence, as seen in Figure 6, the contour of U exhibits fewer significant streamwise variations in the flows over successive dense cavities (for R12 and R16).

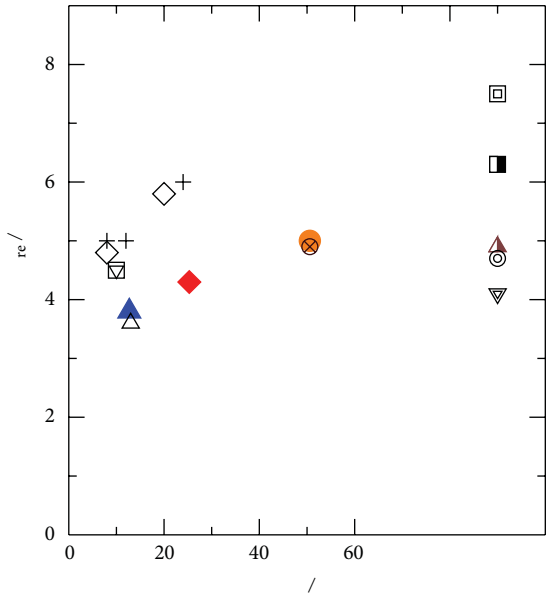

TCF
Present
R2 R2b R4 R8
Backward-facing step
Yang et al. (2003, DNS) [9]
PF
Backward-facing step
Le et al. (1997, DNS) [8]
Square rib
Leonardi et al. (2003, DNS) [5]
Cui et al. (2003, LES) [4]
Ahn et al. (2005, LES) [7]
Wang et al. (2007, Exp.) [2]
OCF
Agelinchaab and Tachie (2008, Exp.) [1]
Square rib
Semicircular rib
Rectangualr rib
TBL
Liu et al. (1966, Exp.) [11]
Square rib

Figure 7: Mean reattachment length for various flow geometries. For abbreviation, see Table 1: TBL, turbulent boundary layer.

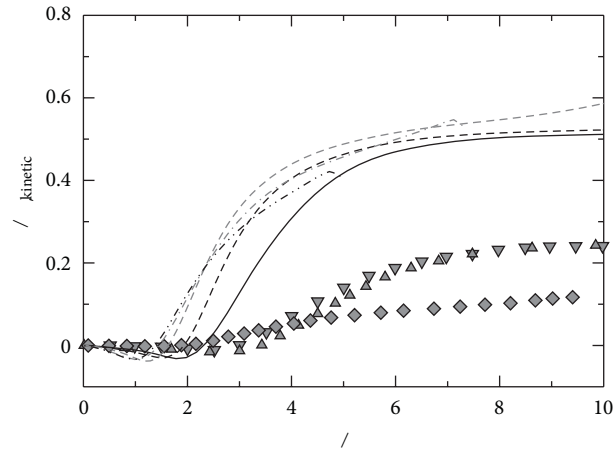

PF with square ribs
Leonardi et al. (2003) [5]
Present
R2
R4
R8
PF with backward-facing step
Jovic et al. (1994) [12]
Le et al. (1997) [8]
R12
R16

Figure 8: Distribution of mean pressure along the bottom surface of the cavity region behind a rib. The pressure is normalized by kinetic pressure $P_{c,\text{kinetic}} = \rho U_c^2/2$ at the channel center of $y = 0.5d$.

The mean reattachment length L_{re} in each case is determined by averaging in time and z with respect to all ribs on the cylinder, as given in Figure 7 and also in Table 1. Also shown are results obtained by simulations and experiments for different flow geometries, that is, backward-facing steps and plane channels roughened by various cross-sectional shapes of ribs. A comparison of those results indicates that L_{re} for the present Taylor-Couette flow is relatively short. This tendency is in good agreement with the result of Yang et al. [14], who examined TCF with backward-facing steps using DNS with a body-fitted grid system. They remarked that the shortening of L_{re} for TCF should be attributed to the curvature effect. In order to elucidate this causation further, we here discuss the pressure distribution and its relationship to the reattachment length. Mean-pressure distributions on the inner-cylinder surface with emphasis on the recirculation zone are shown in Figure 8. Here, the pressure is a mean value that is averaged in time and the z direction and is assumed to be zero at $(x, y) = (0, 0)$. Several results for PF [2, 3, 10] are also plotted for comparison. In all cases shown in the figure, the pressure quickly recovers from a low (or negative) value just behind the rib, especially, in a downstream region of $x/h = 1.5$–6. It can be clearly seen that the pressure recovery is significantly augmented in the present cases of TCF. This implies that the shortening of reattachment length for TCF is caused by the strong adverse pressure gradient behind each rib. Figure 9 shows a typical snapshot of pressure distribution on the inner-cylinder surface. The local pressure has a minimum value near the center of the recirculation zone and a maximum value in front of the leading vertical wall of rib. Large pressure differences are observed at spanwise positions where in-flow motions are induced by counterrotating Taylor vortices. It is interesting to note that the pressure recovery in the region downstream of each rib is also significant because of an enhanced momentum transfer by the in-flow motion. Although the out-flow motion might induce a lowering of the near-wall pressure, this out-flow contribution clearly seems insignificant relative to the in-flow. In the smooth-cylinder case (not shown in figure), the roll cell of Taylor vortices has provided high and low pressure regions alternating in the spanwise direction with an amplitude of ±0.1. From examining these findings, we here draw conclusions that the Taylor vortex in TCF has encouraged the pressure recovery behind each rib, the reduction of pressure by the out-flow motion has been degraded by the presence of ribs, and these phenomena

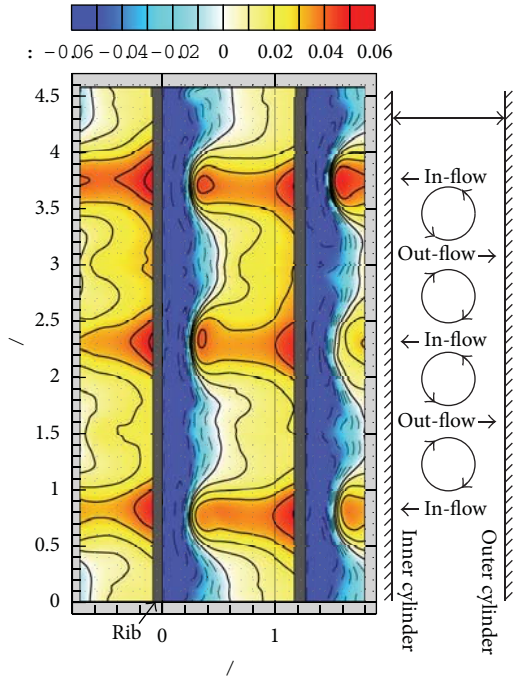

Figure 9: Contour map of instantaneous pressure in a θ-z (or x-z) plane at $y = 0.0015d$ from the inner-cylinder surface for R8 ($\lambda/h = 12.7$). Isolines representing negative values are shown with broken lines. The main flow direction is from left to right. The schematic diagram illustrates a mean secondary flow, that is, pairs of Taylor vortices, occurring between the cylinders.

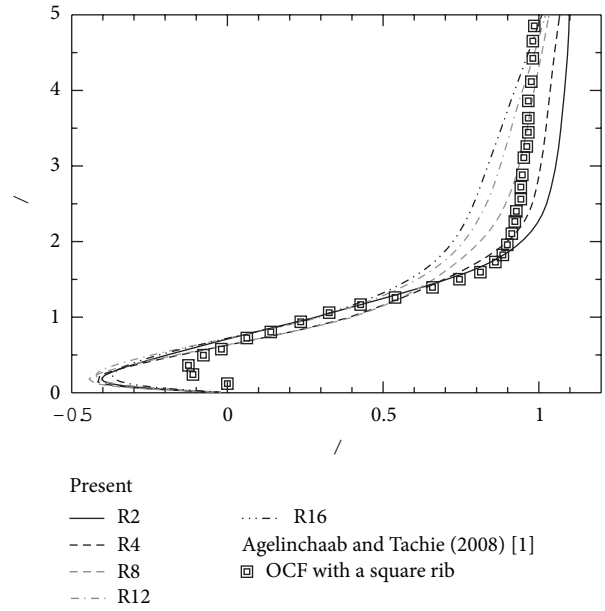

Figure 10: Mean streamwise velocity at the midway point in the streamwise extent of each recirculation zone.

have led to a strong adverse pressure gradient (downstream of each rib) and the shortening of the reattachment length.

Figure 10 shows the mean streamwise velocity in the recirculation zone, that is, at $x = L_{re}/2$ of each case. For R12 and R16 (without reattachment on the bottom surface), the length of the clearance gap between neighboring ribs is given as L_{re}. The velocity is normalized by the channel-centerline velocity U_c averaged also in the streamwise direction: thereby, the value of U/U_c at $y = 5h$ may deviate from the unity. In the core region far from the wall, U/U_c is reasonably increased by decreasing the number of ribs. On the other hand, this dependency on the number of ribs (or the rib interval λ) becomes negligible in $y/h < 1$, where the velocity profiles are found to be scaled well with the present normalization. The magnitude of maximum backflow velocity is around 40% of the reference velocity for the present TCF, whereas that for OCF reveals a smaller magnitude of 10% [4] even under the comparable condition in terms of h/δ. This large difference in the backflow velocity must be caused by the (previous-mentioned) strong adverse pressure gradient occurring in TCF, although the Reynolds-number dependency might also be responsible for that. In the following sections, we will discuss variations of pressure and frictional drags, taking account of the quick-pressure-recovery effect.

3.2. Drag Factors. Prior to the quantifying details of modulations observed in the turbulent characteristics, we estimate the magnitudes of drag factors. Over a segment with the streamwise extent of λ, the contributions of the skin-friction drag (C_f) and the pressure (form) drag (C_p) to the total drag coefficient (C_d) are defined by the following equations:

$$C_d = C_f + C_p, \tag{8}$$

$$C_f = \lambda^{-1} \int_0^{\lambda} \left(\mathrm{Re}^{-1} \left. \frac{\mathrm{d}U}{\mathrm{d}y} \right|_{y=0} \mathbf{n} \cdot \mathbf{r} \right) \mathrm{d}\theta, \tag{9}$$

$$C_p = \lambda^{-1} \int_0^{h} (P\mathbf{n} \cdot \theta)\, \mathrm{d}\theta. \tag{10}$$

Here, $\mathbf{n}$ represents the normal vector of wall and rib surfaces. As for the present square-shape roughness, C_f is calculated by averaging the velocity gradient on the inner-cylinder surface as well as the top surface of the rib; C_p is simply derived as the difference between pressures integrated along each vertical wall.

Figure 11 shows the dependence of C_d on the rib interval normalized by the rib height. The vertical axis represents the coefficient ratio of $C_d/C_{d,\mathrm{smooth}}$, where $C_{d,\mathrm{smooth}}$ is the value obtained for the smooth-surface counterpart, being equivalent to the frictional drag because there is no form drag. In this figure, a DNS result on PF [10] and an experimental result on TCF (for $\eta = 0.939$) [22] are plotted for comparison. Leonardi et al. [10] reported that, in the plane channel flow, the maximum drag was obtained at $\lambda/h = 7$, downstream of which the drag decreased monotonically with increasing λ. In contrast, for $\lambda/h < 7$, the drag was increased linearly as a function of λ/h. In this linear regime, the flows were observed to make cavity flows between the ribs without reattaching to the bottom wall surface, as in the present case of R12. According to our result on TCF, the λ-dependency of the drag coefficient shows quite a similar trend, but the peak

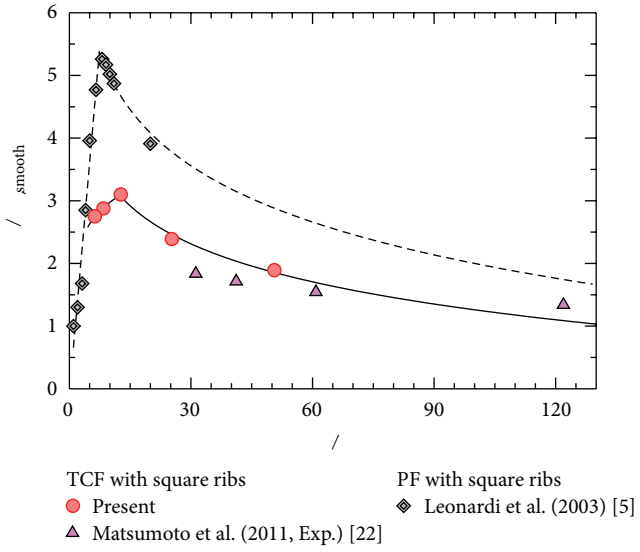

FIGURE 11: Drag coefficients normalized by the smooth values as a function of rib interval.

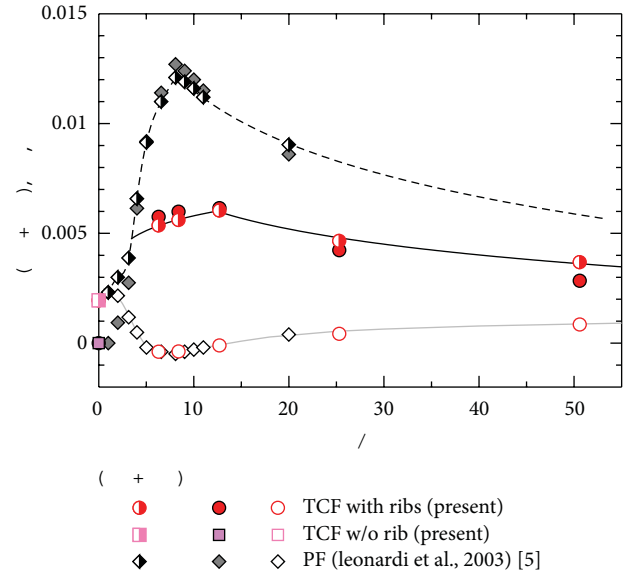

FIGURE 12: Drag coefficients of total $C_f + C_p$ (half-filled symbols), pressure C_p (filled symbols), and friction C_f (open symbols), as a function of rib interval.

location shifts to $\lambda/h = 13$ and the magnitude of $C_d/C_{d,\text{smooth}}$ decreases by about a third. In addition, a good agreement with Matsumoto et al. [22] can be confirmed. Note that, although their measurements were carried out on TCF with rib-roughened inner cylinders, some important parameters were inconsistent with the present conditions: for example, Re = 54000, $\eta = 0.96$, and $h/d = 0.2$ in [22].

In order to gain some insight into the mechanism of the drag variation with λ, let us decompose it into C_f and C_p. Figure 12 shows that there are two distinct regimes for both components: C_f and C_p exhibit either minimum or maximum value with a single peak, at which each trend alters to an upward/downward monotonic tendency. For $0 < \lambda/h < 6$, C_f seems to decrease as λ/h increases, while beyond $\lambda/h = 7$, C_f increases slowly as λ/h increases, showing a remarkable consistency with the results on PF [10]. (Strictly speaking, the rib interval that minimizes C_f for TCF is not clearly determined by the present results.) On the other hand, λ/h that maximizes C_p is obviously changed between PF and TCF, and the magnitude of C_p is less than 60% of that for PF at the same λ/h. These variations in C_p should also be attributed to the enhanced pressure recovery behind rib in TCF. Since $C_p \gg C_f$, the variations in C_d are practically the same as those observed in C_p.

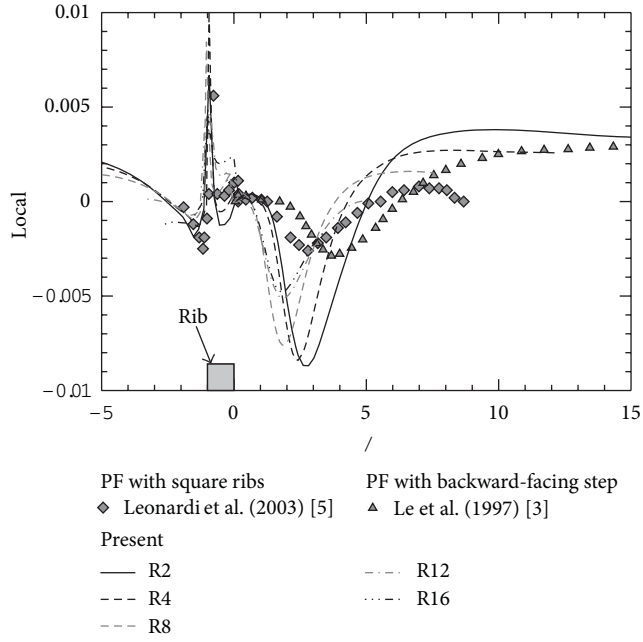

FIGURE 13: Local skin frictional coefficient for different values.

3.3. Local Skin-Friction Drag. Figure 13 shows streamwise distributions of the local skin-friction drag, which is defined as (9) but not averaged in θ. The channel-flow DNS data [3, 10] are also presented. In an upstream region of $-3 < x/h < -1$, a negative C_f is intensified near the rib, because of the presence of a secondary vortex in the upstream corner of the rib. Irrespective of the flow configuration, the local C_f agree reasonably well with each other in this region. The local C_f has a peak at the leading top edge of the rib ($x/h = -1$), at which there exists a separation point. This peak value is increased with increasing λ/h, because the approaching flow velocity at the rib height becomes large for longer λ/h. In the region immediately downstream of the rib, the local C_f becomes largely negative value, because of the backflow induced by the recirculation zone. This negative peak for each present case is pronounced compared to those for the plane channel flows. As previously described (cf. Figures 9 and 10), the backward flow for TCF is enhanced by the strong adverse pressure gradient. Consequently, the local C_f changes more drastically behind the rib in TCF. After the reattachment point (at which $C_f = 0$), the local C_f attains a constant value

more rapidly than in the rib-roughened PF. Comparisons between the result by Leonardi et al. ($\lambda/h = 11$) [10] and of R8 and between Le et al. ($\lambda/h = 30$) [3] and R2 demonstrate large differences around the reattachment point.

In terms of local C_f, there exist noticeable discrepancies between TCF and PF in the recirculation zone and around the reattachment, as remarked previously. This implies that the skin-friction drag as well as the pressure drag should be affected by the flow geometry characterized by the curvature and Coriolis instability. Hence, there still remains a possibility that the good accordance in C_f between TCF and PF, observed in Figure 12, might be either doubtful or accidental.

3.4. Force Balance in the Cavity Region. In this section, we focus on the force balance with respect to the cavity region bounded by consecutive roughness elements: see Figure 14, in which the cavity region can be defined as $\{x, y \mid x_a \le x \le x_b, 0 \le y \le h\}$. This perspective, with reference to Leonardi et al. [10], is useful for analyzing the relationship among the drag factors and the Reynolds shear stress. To derive an equation regarding the force balance, (4) for the mean streamwise velocity U should be integrated throughout the cavity region. By assuming the constant flow rate and the periodicity in the x direction, we may obtain

$$\int_0^h \left(P|_x - P|_x\right) \mathrm{d}y = \int_x^x \mu \left.\frac{\mathrm{d}U}{\mathrm{d}y}\right|_{y=h} \mathrm{d}x - \int_x^x \mu \left.\frac{\mathrm{d}U}{\mathrm{d}y}\right|_{y=0} \mathrm{d}x + \int_x^x \left(-\rho\overline{u'v'}\right)_{y=h} \mathrm{d}x. \tag{11}$$

The term on the left-hand side of this equation corresponds to the difference of pressures exerted on vertical faces of the rib; the first and second terms on the right-hand side represent the viscous shear stress at the rib height and at the bottom surface, respectively, and the last term is the Reynolds shear stress integrated at the rib height. Here, an overbar and a prime denote an averaged and a fluctuating component, respectively. Note again that both U and P are averaged quantities. After dividing by λ and nondimensionalization by U_w and d, (11) is rewritten as

$$C_p = \lambda^{-1} \int_x^x \mathrm{Re}^{-1} \left.\frac{\mathrm{d}U^*}{\mathrm{d}y^*}\right|_{y=h} \mathrm{d}x - \lambda^{-1} \int_x^x \mathrm{Re}^{-1} \left.\frac{\mathrm{d}U^*}{\mathrm{d}y^*}\right|_{y=0} \mathrm{d}x + \lambda^{-1} \int_x^x \left(-\overline{u'^* v'^*}\right)_{y=h} \mathrm{d}x. \tag{12}$$

Accordingly, the pressure drag can be related to balance with three stresses.

Pressure profiles along the upstream- and downstream-side vertical walls of the rib are shown in Figure 15. The pressure is calibrated as zero at the bottom-downstream corner of the rib, the same as with Figure 9. While the pressure remains constant on the downstream-side rib surface, it decreases for

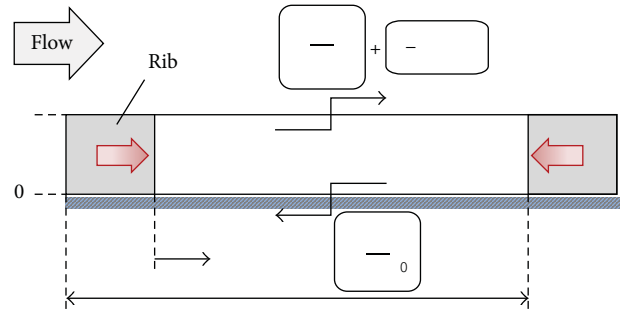

Figure 14: Conceptual diagram of force balance with respect to the cavity region.

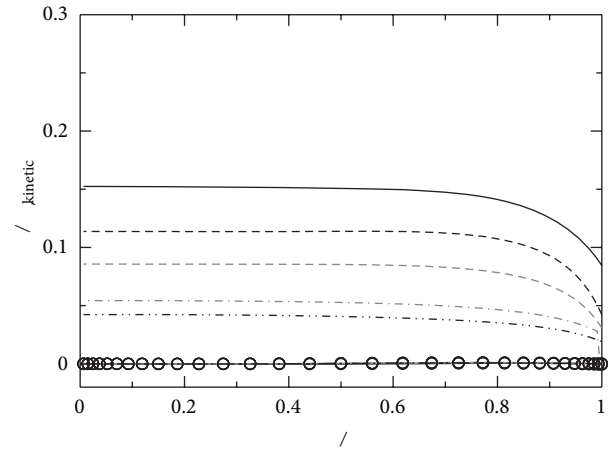

Figure 15: Distribution of mean pressure on the rib surface as a function of y. The pressure is normalized by kinetic pressure $P_{c,\mathrm{kinetic}}$ at the channel center of $y = 0.5d$.

$y/h > 0.7$ on the upstream side. The pressure in the upstream side increases with increasing λ/h, since the velocity of the approaching flow to the rib increases. Figure 16(a) shows the streamwise distribution of $\mathrm{Re}^{-1}(\mathrm{d}U/\mathrm{d}y)_{y=h}$. The velocity gradient increases dramatically near the leading edge of the rib, since the velocity is accelerated by flow contraction. At a sufficiently large distance from the trailing edge of the rib ($x/h > 10$), $\mathrm{Re}^{-1}(\mathrm{d}U/\mathrm{d}y)_{y=h}$ approaches a constant approximate to the value for a smooth surface, so that its relevant integral term in (12) decreases when x/h increases. As for $\mathrm{Re}^{-1}(\mathrm{d}U/\mathrm{d}y)_{y=0}$, Figure 16(b) shows behaviors that are similar to those of local C_f presented in Figure 13. The Reynolds shear stress of $-\overline{u'v'}$, which pertains to turbulent motions as well as in-flow and out-flow motions into/from the cavity region, is shown in Figure 16(c). It is seen that $(-\overline{u'v'})_{y=h}$ is maximum at the same position as the negative

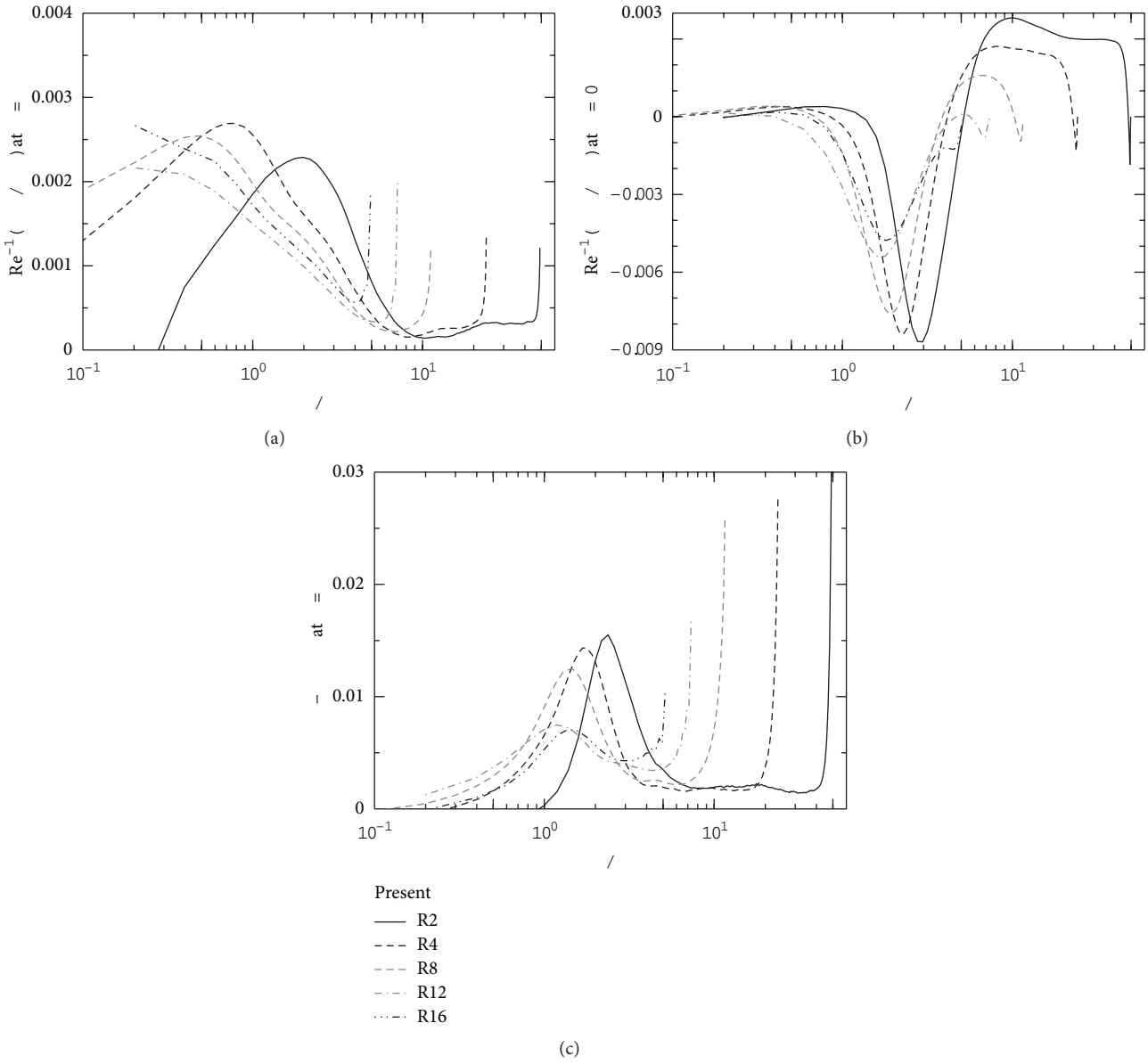

Figure 16: Distributions of shear stress: (a) viscous shear stress at the rib height, (b) viscous shear stress on the bottom surface of the cavity region, and (c) Reynolds shear stress at the rib height.

peak of $\mathrm{Re}^{-1}(\mathrm{d}U/\mathrm{d}y)_{y=0}$ in the recirculation zone. The maximum value and its streamwise distance from the rib are found to increase according to the increase of λ/h. It can be conjectured that the separated shear layer, which makes the turbulent intensity larger, is elongated downstream due to the extended rib interval. In the cases (R12 and R16) in which no reattachment occurs on the bottom surface, the maximum of $(-\overline{u'v'})_{y=h}$ is clearly dampened compared to that of the other cases. If the separated flow reattached to the vertical wall of the next rib, the separated shear layer would be more stable and the turbulent intensity would be decreased.

To evaluate the accuracy of the present analysis, we compared two values for the pressure-drag coefficient C_p, which were separately obtained from either (10) directly or (12) on the basis of the force balance in the cavity region. We have confirmed that the previous approach using (12) is sufficiently applicable to our study and there is residual error of less than 7%.

Based on these results, we discuss the effect of the rib interval on each drag factor (see Figure 17). The first term on the right-hand side of (12) is practically independent of the rib interval, so that the magnitude of its contribution is almost the same, irrespective of λ/h, but almost negligible relative to that of the Reynolds-shear-stress term. The second term contributes to an increase in C_p when the rib interval is shorter than $15h$. On the other hand, in the case of $\lambda/h > 15$, this term gives rise to a decrease in C_p. The trend of the third term (the Reynolds-shear-stress term) changes clearly, depending on λ/h, in particular, at $\lambda/h = 13$. However, its contribution to C_p is maintained at high values

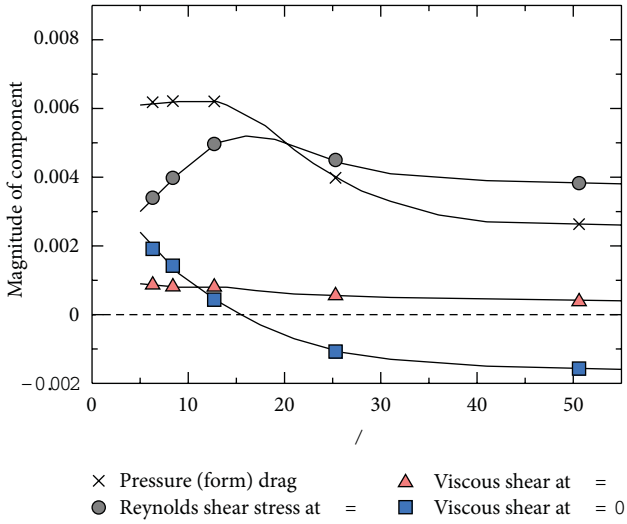

FIGURE 17: Dependence of each drag component on rib distance.

throughout a wide range of λ/h. From these results, it may be concluded that the pressure drag is balanced mainly with the Reynolds shear stress, but its dependency on the rib interval is attributed to the rib-interval dependency of the frictional drag on the bottom surface (at $y = 0$).

4. Conclusion

We studied turbulent Taylor-vortex flows between two concentric cylinders, the inner one of which was roughened with transverse ribs with a regular interval λ. The inner cylinder with a radius of R_1 was rotated at a constant angular velocity of ω, while the outer cylinder with a radius R_2 was stationary. By parametric research by means of direct numerical simulation, we investigated the effect of the rib interval on the flow field around the rib and the flow resistance. We tested five different test cases, varying the number of ribs on the inner cylinder, while the cross-section shape of each rib and the parameters of the Reynolds number and the radius ratio were fixed: $\mathrm{Re} = (R_1\omega(R_2 - R_1)/\nu) = 3200$ and $\eta = R_1/R_2 = 0.617$. The present results for the Taylor-Couette flows were compared with those for various flow geometries, such as Poiseuille flows through rib-roughened plane channels, to elucidate the effects of flow curvature and Coriolis instability characterized by the Taylor vortex on the statistical quantities.

The most important conclusion drawn from this research is that the increment in the pressure (form) drag due to roughness is dampened as a result of the strong adverse pressure gradient behind each rib, which is enhanced by the in-flow motion of the Taylor vortices. In a Taylor-Couette flow under the present conditions, turbulent Taylor vortices that elongates in the circumferential direction would occur for a smooth cylinder: we actually observed their presence in the flow field and moreover they also existed in the cases of rib-roughened inner cylinders. The Taylor vortices induced significant momentum transfer into the near-wall region and encouraged pressure recovery in the downstream region of ribs. The adverse pressure gradient became strong relative to that in the plane channel flow, yielding a shortening of the reattachment length and an intensification of the recirculation. These phenomena were more pronounced as the rib interval was extended. The distributions of the local frictional drag C_f and the mean streamwise velocity U, in conjunction with the mean streamlines indicate that, for $\lambda/h \geq 13$, the ribs are isolated, since the size of the recirculation zone no longer depends on λ/h. The maximum C_p occurred at $\lambda/h = 13$ when the reattachment on the bottom wall took place immediately upstream of the subsequent rib. For $\lambda/h < 13$, the separated flow reattached directly to the downstream rib, giving rise to a recirculation zone like a cavity flow between two ribs. Similar to the case of plane channel flow, the total drag in the present flows was contributed almost entirely by the pressure drag. However, this contribution, that is, the pressure-drag coefficient C_p, was decreased by about a third compared to that in the channel flow. The value of C_p depended on λ/h, so it can be concluded that λ/h was a key parameter even for the Taylor-Couette flow. The insight into the component of the pressure drag was obtained by equalization of various stresses in the cavity region. The pressure drag was mainly affected by the Reynolds shear stress at the rib height, while the viscous shear stress by the mean flow at the same height was negligible.

Finally, the present simulations were conducted using one basic procedure (with h fixed and λ varied stepwisely), one radius ratio $\eta = 0.617$, and one axial length $\Gamma = 4.58$, for the rotating inner cylinder and the stationary outer one. Changing the parameters or the procedure will, to a greater or lesser extent, affect the magnitudes of the drag factors and their dependencies on roughness characteristics, possibly producing other flow states that may show qualitative differences in the influence of organized turbulent structures on drag enhancement/reduction.

Nomenclature

C_d:	Total drag coefficient
$C_{d,\mathrm{smooth}}$:	Total drag coefficient for smooth cylinders
C_f:	Skin-friction drag coefficient
C_p:	Pressure drag coefficient
d:	Channel gap width between cylinders
$\mathbf{F}$:	Body force for immersed boundary method
h:	Height of rib
L_i:	Length of computational domain in i direction
L_{re}:	Reattachment length
N_i:	Number of grid points in i direction
p:	Pressure
P:	Mean pressure
$P_{c,\mathrm{kinetic}}$:	Kinetic pressure at channel center
r:	Radial coordinate
R_1:	Radius of inner cylinder
R_2:	Radius of outer cylinder
Re:	Reynolds number
t:	Time
u:	Velocity vector, (u, v, w) in (x, y, z) or (θ, r, z)

U: Mean streamwise velocity
U_c: Mean velocity at channel center
U_w: Inner-wall surface velocity
x: Streamwise coordinate
y: Wall-normal coordinate
z: Spanwise coordinate
Γ: Aspect ratio of flow cross-section
δ: Characteristic length of outer layer
η: Radius ratio
θ: Azimuthal coordinate
λ: Interval of ribs
μ: Viscosity
υ: Kinematic viscosity
ρ: Density
ω: Angular velocity of inner cylinder
ω_θ: Streamwise vorticity
Ω: Angular velocity vector.

Acknowledgment

The present simulations were performed with the use of NEC SX-9 at Cyberscience Center in Tohoku University.

References

[1] C. K. Liu, S. J. Klein, and J. P. Johnston, "An experimental study of turbulent boundary layer on rough walls," Report MD-15, Department of Mechanical Engineering, Stanford University, 1966.

[2] S. Jovic and D. M. Driver, "Backward-facing step measurement at low Reynolds number, $Re_h = 5000$," NASA Technical Memorandum 108807, 1994.

[3] H. Le, P. Moin, and J. Kim, "Direct numerical simulation of turbulent flow over a backward-facing step," *Journal of Fluid Mechanics*, vol. 330, pp. 349–374, 1997.

[4] M. Agelinchaab and M. F. Tachie, "PIV study of separated and reattached open channel flow over surface mounted blocks," *Journal of Fluids Engineering*, vol. 130, no. 6, Article ID 061206, pp. 1–9, 2008.

[5] P. Burattini, S. Leonardi, P. Orlandi, and R. A. Antonia, "Comparison between experiments and direct numerical simulations in a channel flow with roughness on one wall," *Journal of Fluid Mechanics*, vol. 600, pp. 403–426, 2008.

[6] P.-Å. Krogstadt and R. A. Antonia, "Surface roughness effects in turbulent boundary layers," *Experiments in Fluids*, vol. 27, no. 5, pp. 450–460, 1999.

[7] L. Wang, J. Hejcik, and B. Sunden, "PIV measurement of separated flow in a square channel with streamwise periodic ribs on one wall," *Journal of Fluids Engineering*, vol. 129, no. 7, pp. 834–841, 2007.

[8] Y. Miyake, K. Tsujimoto, and N. Nagai, "Numerical simulation of channel flow with a rib-roughened wall," *Journal of Turbulence*, vol. 3, no. 35, pp. 1–17, 2002.

[9] J. Cui, V. C. Patel, and C. L. Lin, "Large-eddy simulation of turbulent flow in a channel with rib roughness," *International Journal of Heat and Fluid Flow*, vol. 24, no. 3, pp. 372–388, 2003.

[10] S. Leonardi, P. Orlandi, R. J. Smalley, L. Djenidi, and R. A. Antonia, "Direct numerical simulations of turbulent channel flow with transverse square bars on one wall," *Journal of Fluid Mechanics*, no. 491, pp. 229–238, 2003.

[11] J. Ahn, H. Choi, and J. S. Lee, "Large eddy simulation of flow and heat transfer in a channel roughened by square or semicircle ribs," *Journal of Turbomachinery*, vol. 127, no. 2, pp. 263–269, 2005.

[12] T. Ikeda and P. A. Durbin, "Direct simulations of a rough-wall channel flow," *Journal of Fluid Mechanics*, vol. 571, pp. 235–263, 2007.

[13] K.-S. Yang, J.-Y. Hwang, K. Bremhorst, and S. Nesic, "Turbulent flow around a rotating stepped cylinder," *Physics of Fluids*, vol. 14, no. 4, pp. 1544–1547, 2002.

[14] K.-S. Yang, J.-Y. Hwang, K. Bremhorst, and S. Nesic, "Numerical investigation of turbulent flow around a rotating stepped cylinder for corrosion study," *Canadian Journal of Chemical Engineering*, vol. 81, no. 1, pp. 26–36, 2003.

[15] G. P. Smith and A. A. Townsend, "Turbulent Couette flow between concentric cylinders at large Taylor numbers," *Journal of Fluid Mechanics*, vol. 123, pp. 187–217, 1982.

[16] C. D. Andereck, S. S. Liu, and H. L. Swinney, "Flow regimes in a circular Couette system with independently rotating cylinders," *Journal of Fluid Mechanics*, vol. 164, pp. 155–183, 1986.

[17] D. Coles, "Transition in circular Couette flow," *Journal of Fluid Mechanics*, vol. 21, pp. 385–425, 1965.

[18] A. Barcilon, J. Brindley, M. Lessen, and F. R. Mobbs, "Marginal instability in Taylor-Couette flows at a very high Taylor number," *Journal of Fluid Mechanics*, vol. 94, no. 3, pp. 453–463, 1979.

[19] S. Dong, "Direct numerical simulation of turbulent Taylor-Couette flow," *Journal of Fluid Mechanics*, vol. 587, pp. 373–393, 2007.

[20] R. van Hout and J. Katz, "Measurements of mean flow and turbulence characteristics in high-Reynolds number counter-rotating Taylor-Couette flow," *Physics of Fluids*, vol. 23, no. 10, Article ID 105102, pp. 1–11, 2011.

[21] A. Matsumoto, T. Ito, M. Motozawa et al., "Experimental analysis of non-uniform surface roughness affecting to flow resistance," in *Proceedings of 3rd Joint US-European Fluids Engineering Summer Meeting (FEDSM/ICNMM '10)-*, pp. 1–9, Montreal, Canada, 2010.

[22] A. Matsumoto, T. Ito, M. Motozawa et al., "Investigation of turbulent statistics using LDV and its relation to the flow friction of series of ribs in the turbulent Couette flow," in *Proceedings of the 9th International Symposium on Particle Image Velocimetry*, pp. 1–6, Kobe, Japan, 2011.

[23] M. Bilson and K. Bremhorst, "Direct numerical simulation of turbulent Taylor-Couette flow," *Journal of Fluid Mechanics*, vol. 579, pp. 227–270, 2007.

[24] K. Kataoka, H. Doi, and T. Komai, "Heat/mass transfer in taylor vortex flow with constant axial flow rates," *International Journal of Heat and Mass Transfer*, vol. 20, no. 1, pp. 57–63, 1977.

[25] E. A. Fadlun, R. Verzicco, P. Orlandi, and J. Mohd-Yusof, "Combined immersed-boundary finitedifference methods for three-dimensional complex flow simulations," *Journal of Computational Physics*, vol. 161, no. 1, pp. 35–60, 2000.

[26] J. Kim, D. Kim, and H. Choi, "An immersed boundary finite-volume method for simulations of flow in complex geometries," *Journal of Computational Physics*, vol. 171, no. 1, pp. 132–150, 2001.

Hindawi Publishing Corporation
Advances in Mechanical Engineering
Volume 2013, Article ID 194610, 8 pages
http://dx.doi.org/10.1155/2013/194610

Research Article

Mathematical Modeling of the High Temperature Treatment of Birch in a Prototype Furnace

Duygu Kocaefe, Yasar Kocaefe, Ramdane Younsi, Noura Oumarou, and S. Thierry Lekounougou

Department of Applied Sciences, University of Quebec at Chicoutimi, 555 Boulevard de l'Université, Chicoutimi, QC, Canada G7H 2B1

Correspondence should be addressed to Duygu Kocaefe; duygu_kocaefe@uqac.ca

Received 30 December 2012; Accepted 7 April 2013

Academic Editor: Moran Wang

In recent years, various wood modification technologies have been commercialized as alternatives to the traditional chemical treatments for wood preservation. The high temperature heat treatment of wood is one of these commercially viable and environmentally friendly alternative wood modification technologies. During this treatment, wood is heated to temperatures above 200°C by contacting it with hot gas. The chemical structure of wood changes leading to increased dimensional stability and resistance to microorganisms. Wood darkens making it aesthetically more attractive. However, it loses some of its elasticity. Therefore, the high temperature heat treatment has to be optimized for each species and each technology. The mathematical modeling is an important tool for optimization. It can also be used as a powerful tool for furnace modification and design. A reliable and predictive model was developed to simulate numerically the heat treatment process. Heat treatment experiments were carried out in the prototype furnace of the University of Quebec at Chicoutimi. The model was validated by comparing the predictions with the experimental data. In this paper, the results of the model applied to birch heat treatment are presented. The model predictions are in good agreement with the data.

1. Introduction

Wood preservation is mostly carried out by chemical treatment using oil-borne preservatives such as creosote and pentachlorophenol or waterborne preservatives such as chromated copper arsenate, alkaline copper quat, and copper azole [1]. Wood heat treatment developed in Europe is one of the alternatives to chemical wood treatment. There are different technologies such as Finnish Thermowood, Dutch Plato Wood, French Perdure and Retification, and German Oil Heat Treatment [2].

In these processes, wood is heated to temperatures above 200°C. The heating medium and furnace design are different for different technologies. This process changes the structure of wood. Its hardness increases, and it becomes dimensionally more stable and more resistant to biological attacks compared to untreated wood [3–5]. Its color also becomes darker and more attractive. However, this treatment might cause a decrease in wood elasticity [6–8]. In addition, North American species possess different characteristics compared to European species and, consequently, require different treatment conditions. Therefore, the optimization of heat treatment parameters is necessary for a quality product.

Numerous mathematical models for wood drying have been developed. Heat and mass transfer equations proposed by Luikov for capillary systems taking into account the effects of temperature gradient on moisture migration have been widely applied to drying [9–11]. Models taking diffusion as the moisture transfer mechanism as well as those accounting for multiphase moisture (water vapor, bound water, and free water) transfer [11–14] have been reported in the literature.

In recent years, wood heat treatment models have also been developed by applying the principles of drying to this treatment. Luikov model [15, 16] and multiphase models [17] have been applied to a piece of wood subjected to thermotransformation.

Models which couple the phenomena taking place both in wood and gas (heating medium) have also been developed for wood heat treatment. Osma et al. [18] developed a furnace model using Luikov's approach. Younsi et al. [19] developed

a model using diffusion as the unique mechanism of mass transfer within the wood and applied this to small wood pieces surrounded by gas. Furnace models are complicated and require long computation times if all the phenomena are represented in detail; therefore, well-tested approximations are necessary. Kocaefe et al. [20] compared the wood models and concluded that representing the diffusion in wood by Fick's law is a good compromise between the accuracy of the results and the long computation times required by the highly detailed models which take into account the different phases present (free water, bound water, vapor, and air). In this study, a 3D unsteady-state model was used to simulate the high temperature heat treatment process for birch.

2. Mathematical Model

During heat treatment, simultaneous heat and mass transfer takes place both in gas (heating medium) and wood. Wood surface is heated by the hot surrounding gas; consequently, the gas cools down as it flows along the wood. Within the wood, the heat is transferred by conduction. The moisture is transferred from the interior of wood to the surface. It vaporizes from the surface and mixes with the surrounding gas increasing its humidity.

The heat and mass transfer equations for both gas and wood as well as the Navier-Stokes equations in the gas are solved simultaneously in this 3D unsteady-state model in order to calculate the temperature and humidity distributions in both gas and wood and the velocity distribution in the gas. The κ-ε model was used to represent the turbulence in gas. It was assumed that the mechanism of moisture transfer in wood is diffusion, no phase change takes place within the wood, and the phase change occurs on the wood surface by vaporization.

The commercial software ANSYS-CFX10 was used for the solution of the governing equations in the gas (gas submodel). A subprogram was developed using the finite-difference method in order to solve the heat and mass transfer equations in the wood (wood submodel), and the Gauss-Seidel iterative method is used for the solution of the matrix. This subprogram was incorporated into the ANSYS-CFX10 gas model. The interface between the two parts is located at the wood surface where the continuity of temperature, moisture concentration, as well as heat and mass transfer is ensured. A schematic representation of the mathematical model is given in Figure 1. The governing equations for the two parts of the system (gas and wood submodels) are given later.

A total of 23,248 nodes and 124,540 tetrahedral elements on gas side and 64,000 cells on wood side are used. The computation time required for simulating one heat treatment schedule is 8 h on Dell Pentium 4 2GHZ CPU and 500 MO of RAM.

2.1. Gas. We have the following equations.

Continuity Equation. Consider

$$\nabla \cdot \mathbb{V} = 0. \tag{1}$$

Momentum Transfer Equation. Consider

$$\frac{\partial}{\partial t}\left(\rho_f \mathbb{V}\right) + (\mathbb{V} \cdot \nabla)\left(\rho_f \mathbb{V}\right) = -\nabla P + \nabla \cdot \left[\left(\mu_{\text{eff}} \nabla \mathbb{V}\right)\right]. \tag{2}$$

Heat Transfer Equation. Consider

$$\frac{\partial}{\partial t}\left(\rho_f c_{pf} T\right) + (\mathbb{V} \cdot \nabla)\left(\rho_f c_{pf} T\right) = \nabla \cdot \left[\left(k_{\text{eff}} \nabla T\right)\right]. \tag{3}$$

Mass Transfer Equation (*Moisture Concentration*). Consider

$$\frac{\partial C}{\partial t} + (\mathbb{V} \cdot \nabla) C = \nabla \cdot \left[\left(D_{\text{eff}} \nabla C\right)\right]. \tag{4}$$

Turbulence Model Equations. The effective diffusivity is defined as

$$\mu_{\text{eff}} = \mu_f + \mu_t. \tag{5}$$

In the κ-ε model, the turbulent viscosity is calculated from

$$\mu_t = C_\mu \rho_f \frac{k^2}{\varepsilon}. \tag{6}$$

The transport equation for the turbulence kinetic energy (κ) is

$$\begin{aligned} \frac{\partial \rho_f \kappa}{\partial t} + \nabla \cdot \left(\rho_f \mathbb{V} \kappa\right) - \nabla \cdot \left[\left(\mu_f + \frac{\mu_t}{\sigma_\kappa}\right) \nabla \kappa\right] \\ = P_k - G - \rho_f \varepsilon, \end{aligned} \tag{7}$$

and the turbulence dissipation (ε) is given as:

$$\begin{aligned} \frac{\partial \rho_f \varepsilon}{\partial t} + \nabla \cdot \left(\rho_f \mathbb{V} \varepsilon\right) - \nabla \cdot \left[\left(\mu_f + \frac{\mu_t}{\sigma_\varepsilon}\right) \nabla \varepsilon\right] \\ = \frac{\varepsilon}{\kappa}\left(C_1 P_\kappa - C_2 \rho_f \varepsilon\right). \end{aligned} \tag{8}$$

P_κ and G are the production of turbulent kinetic energy due to shear and body forces, respectively. The values of the model constants used are $\sigma_\kappa = 1.0, \sigma_\varepsilon = 1.4, C_1 = 1.44, C_2 = 1.92$, and $C_\mu = 0.09$. In the regions near the wall where the flow is not fully turbulent, the wall functions are used [21].

Boundary Conditions for the Flow Field. No slip condition is considered on the walls. For the inlets and outlets, consider the following:

$$\begin{aligned} &\text{inlets } u = u_{\text{in}}, \quad v = 0, \quad w = 0, \\ &\quad T = T_g, \quad C = C_g, \quad \kappa = \kappa_{\text{in}}, \quad \varepsilon = \varepsilon_{\text{in}}, \\ &\text{outlets } P = 0, \quad \frac{\partial T}{\partial X} = 0, \quad \frac{\partial C}{\partial X} = 0, \\ &\quad \frac{\partial \kappa}{\partial X} = 0, \quad \frac{\partial \varepsilon}{\partial X} = 0. \end{aligned} \tag{9}$$

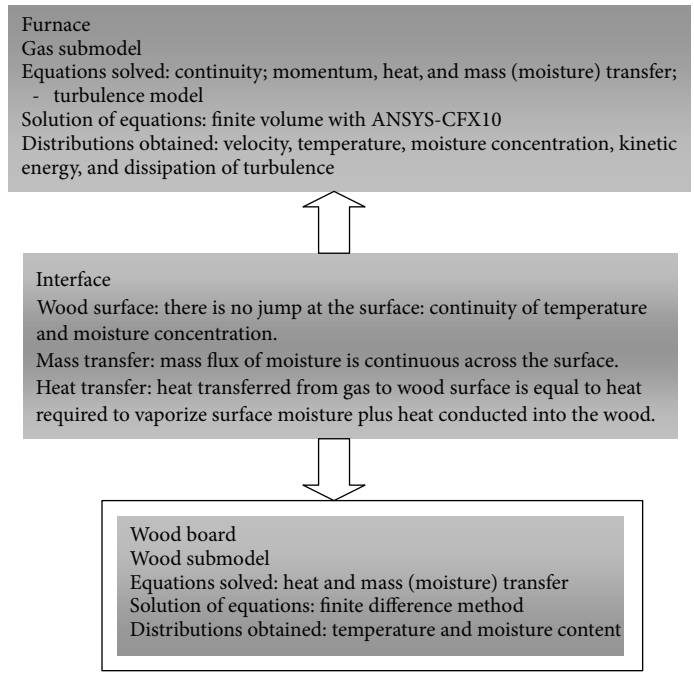

Figure 1: Schematic representation of the mathematical model.

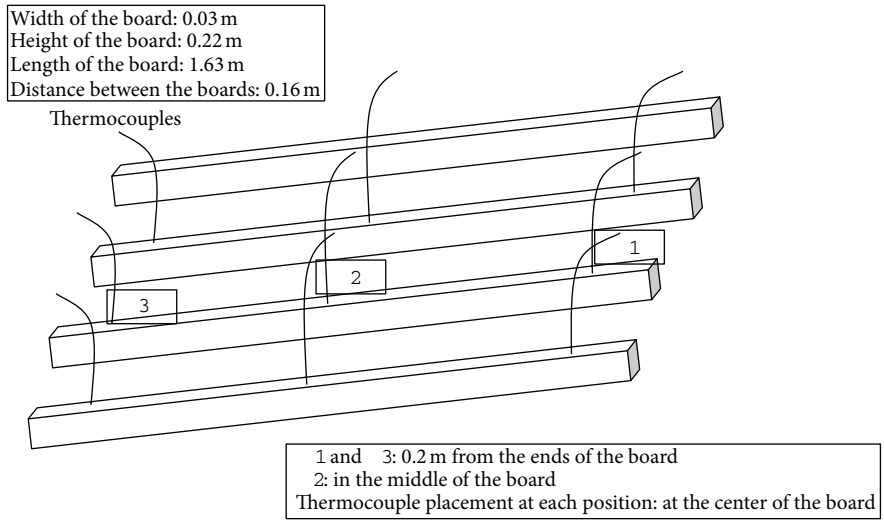

Figure 2: Placement of boards and thermocouples in the furnace.

2.2. Wood. We have the following equations.

Heat Transfer Equation. Consider

$$\rho_m \frac{\partial h_m}{\partial t} = \nabla \cdot \left[\left(k_w \nabla T \right) \right]. \tag{10}$$

Mass Transfer Equation (*Moisture Content*). Consider

$$\frac{\partial M}{\partial t} = \nabla \cdot \left[\left(D_w \nabla M \right) \right]. \tag{11}$$

Initial Conditions. Consider

$$T\left(X, Y, Z, 0\right) = T_0 M\left(X, Y, Z, 0\right) = M_0. \tag{12}$$

2.3. Interface between Wood and Gas at the Wood Surface. These are also the heat and mass transfer boundary conditions on the wood surface for the gas and wood submodels. The temperature and the moisture concentration are continuous across the interface (on the wood surface).

Temperature continuity at the wood-gas interface is as follows:

$$T_f = T_s. \tag{13}$$

Concentration continuity at the wood-gas interface is as follows:

$$C_f = C(T, M)_s. \tag{14}$$

Table 1: Heat treatment conditions.

Case	Maximum temperature (°C)	Heating rate* (°C/h)	Holding time (h)	Presence of humidity in gas
1	195	R	1	Yes
2	205	R	1	Yes
3	205	R	3	Yes
4	205	R	1	Non
5	205	L	1	Yes
6	215	R	1	Yes

*R: regular heating rate; L: low heating rate (values are not given due to confidentiality).

Heat transfer boundary condition at the wood-gas interface states that the heat transferred from the gas to the wood surface is equal to the sum of the heat used for the moisture vaporization and the heat conducted into the wood as follows:

$$k_{\text{eff}}\frac{\partial T}{\partial n} = \nabla H_{lv} D_{\text{eff}}\frac{\partial C_f}{\partial n} + k_f\frac{\partial T}{\partial n}. \tag{15}$$

Mass transfer boundary condition imposes the continuity of mass flux at the wood-gas interface. The moisture that diffuses from the interior of the wood to the wood surface should equal to the amount that vaporizes and is removed by the gas as follows:

$$\rho_w D_w\frac{\partial M}{\partial n} = D_{\text{eff}}\frac{\partial C_f}{\partial n}. \tag{16}$$

2.4. Thermophysical Properties of Birch. The density (ρ_w) and specific gravity (G_m) of dry birch wood were taken as 480 kg/m^3 and 0.48, respectively. Density (ρ_w), specific heat (c_p), and thermal conductivities (k_{qx}, k_{qy}, k_{qz}) of birch containing moisture are determined as a function of temperature and moisture content using relations reported in the literature [11, 22] as follows:

$$\begin{aligned}\rho_m &= 1000 * G_m\left(1 + \frac{M}{100}\right),\\ c_p &= \frac{\left(c_{p0} + 0.01 c_{p\text{H}_2\text{O}} M\right)}{(1 + 0.01M)} + A_c,\end{aligned} \tag{17}$$

where $c_{p\text{H}_2\text{O}}$ is the heat capacity of water taken as 4.185 J·kg^{-1}·K^{-1}, c_{p0} is the heat capacity of dry wood, and A_c is a parameter which is a function of moisture content and temperature given as

$$\begin{aligned}c_{p0} &= 0.1031 + 0.003867T,\\ A_c &= M\left(-0.06191 + 2.36\times 10^{-4}T - 1.33\times 10^{-4}M\right).\end{aligned} \tag{18}$$

Thermal conductivity as a function of spatial direction and heat of vaporization as a function of T are given by Stanish et al. [23] as

$$\begin{aligned}k_{wx} = k_{wy} &= G_m\left(0.1941 + 0.004064M\right)\\ &\quad + 0.01864\left(k_{wx} = k_{wy} = 2k_{wz}\right),\\ \Delta H_{lv} &= 2.792\times 10^6 - 160T - 3.43T^2.\end{aligned} \tag{19}$$

The diffusivity coefficients of wood and gas are calculated using the relation given by Siau [12] as

$$D_w = \frac{\sqrt{\gamma} D_{\text{bt}} D_v}{(1-\gamma)\left(\sqrt{\gamma} D_{\text{bt}} + (1-\sqrt{\gamma})\, D_v\right)}, \tag{20}$$

where γ is the wood porosity and D_{bt} and D_v are the diffusivities of bound water and vapor, respectively.

D_{bt} and D_v are given as [12]

$$\begin{aligned}D_v &= \frac{1.29\times 10^{-13}\,(1.0 + 1.54M)\, p_{\text{sat}} T^{1.5}}{(T + 245.18)}\frac{\partial \varphi}{\partial M},\\ D_{\text{bt}} &= \exp\left(-9.9 + 9.8M - \frac{4.3}{T}\right),\end{aligned} \tag{21}$$

where ϕ is the gas relative humidity, and p_{sat} is the vapor pressure at saturation which is calculated as follows [12]:

$$\begin{aligned}p_{\text{sat}} = 3390 \exp\big(&-1.74 + 0.00759T_C\\ &-0.000424T_C^2 + 2.44\times 10^{-6}T_C^3\big),\end{aligned} \tag{22}$$

where T_C is the critical temperature.

The effective diffusivity of gas is given by Siau [12] as

$$D_{\text{eff}} = \frac{9.2\times 10^{-9} T^{2.5}}{(T + 245.18)}. \tag{23}$$

3. Experimental

The experiments were carried out in the prototype furnace of the University. Predried birch boards were obtained from Scierie Thomas-Louis Tremblay in Ste-Monique, Quebec. Initial wood moisture content was 8%–13% (M_0). Birch boards were heated under neutral gas atmosphere from room temperature (T_0) to the maximum treatment temperature at a given heating rate. Then, they are kept at that temperature for a predetermined period of time (holding time).

Four birch boards were treated per test. During the tests, the gas and wood temperatures at different positions were followed and recorded. Three thermocouples (two thermocouples, each 20 cm from the ends, and one thermocouple in the middle) were installed in each board, and the thermocouple at each position was placed at the center of the wood board. The dimensions of birch boards as well as the placement of thermocouples are shown in Figure 2.

During the tests, the parameters studied are the maximum treatment temperature, heating rate, holding time, and the gas humidity. Table 1 gives the test conditions.

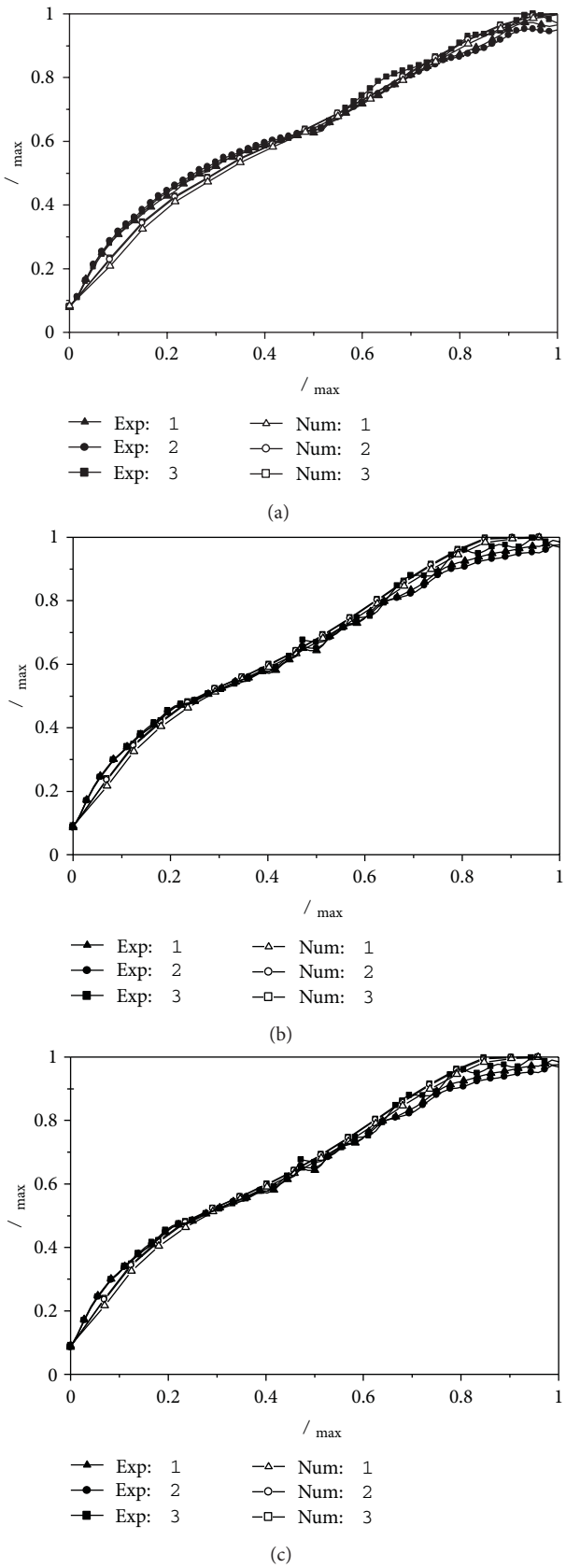

Figure 3: Comparison of model predictions with experimental measurements for thermocouples 1, 2, and 3 at different maximum treatment temperatures for (a) Case 1, (b) Case 2, and (c) Case 6 (see Table 1).

4. Results and Discussion

Figures 3 and 4 compare the temperatures measured by three thermocouples (see Figure 2) with the model predictions under different conditions. Thermocouple readings of all the boards are similar since the treatment conditions were uniform. As it can be seen from this comparison, model predictions are in good agreement with the experimental results for all the cases considered. The average difference between the model results and the experimental data is in the order of 2%-3% depending on the case. The maximum difference is about 3%–5% again depending on the case and is observed in the regions where the wood is heated rapidly ($t/t_{\max} \cong 0.05$ to 0.15). The differences can be attributed to the discrepancy between the calculated and the actual thermophysical properties of birch.

The model parameters used for wood constitute the biggest challenge for the model validation. Wood thermophysical properties are usually functions of both temperature and moisture content; however, they are not readily available at high temperatures. The model takes into account this dependence. Results indicate that the correlations used represent these properties reasonably well.

The temperature distribution within a wood board at different times is shown in Figure 5(a). In this figure, X is the direction along the width, Y is the direction along the thickness, and Z is the direction along the length of the wood board. X_L, Y_L, and Z_L are the width, thickness, and length of the wood boards, respectively. As it can be seen from this figure, the temperature profile at any given time is highly uniform within the wood. There is a small temperature gradient close to the surface between the surface and the interior of wood on both sides. This gradient decreases even further with time. The temperature of the gas is higher than that of the surface of the wood since the wood is heated with a hot gas. Consequently, the surface temperature is slightly higher than that of the interior. The temperature difference between gas and wood surface makes the heat transfer from gas to wood possible. If this difference is greater, the wood will not be heated faster because of its low thermal conductivity. Surface will become a lot hotter than the interior. This can cause the surface to dry up and develop mechanical stresses. Therefore, the adjustment of gas-wood surface temperature difference is very important for wood heat treatment.

Figure 5(b) presents the normalized moisture content profiles in wood at different times. Moisture profiles are flat within wood similar to the temperature profiles; however, the moisture gradient close to the surface is steeper compared to that of the temperature gradient. Moisture gradients (gas/wood surface and wood surface/interior of wood) are equally important for the wood heat treatment. As the moisture is transferred from the wood surface to gas, a gradient forms between the interior of wood and the surface. The difference between the gas humidity and wood surface moisture content should be high enough for the moisture removal, but it should not be so large as to cause excessive dryness near the surface. This would result in a large gradient between the surface and interior of wood which consequently would lead to rapid moisture transfer from the interior to

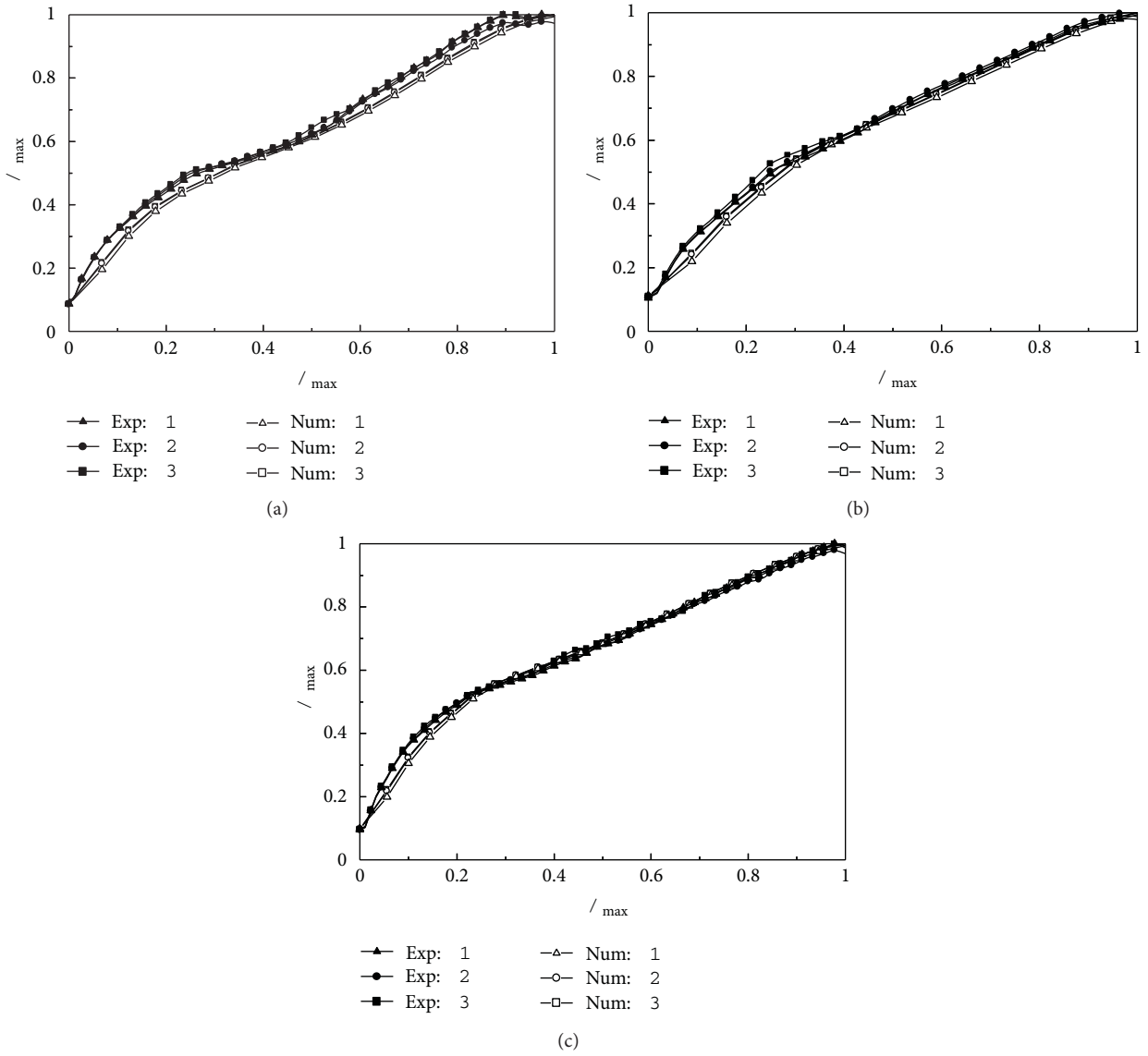

FIGURE 4: Comparison of model predictions with experimental measurements for thermocouples 1, 2, and 3 under different conditions for (a) Case 3, (b) Case 4, and (c) Case 5 (see Table 1).

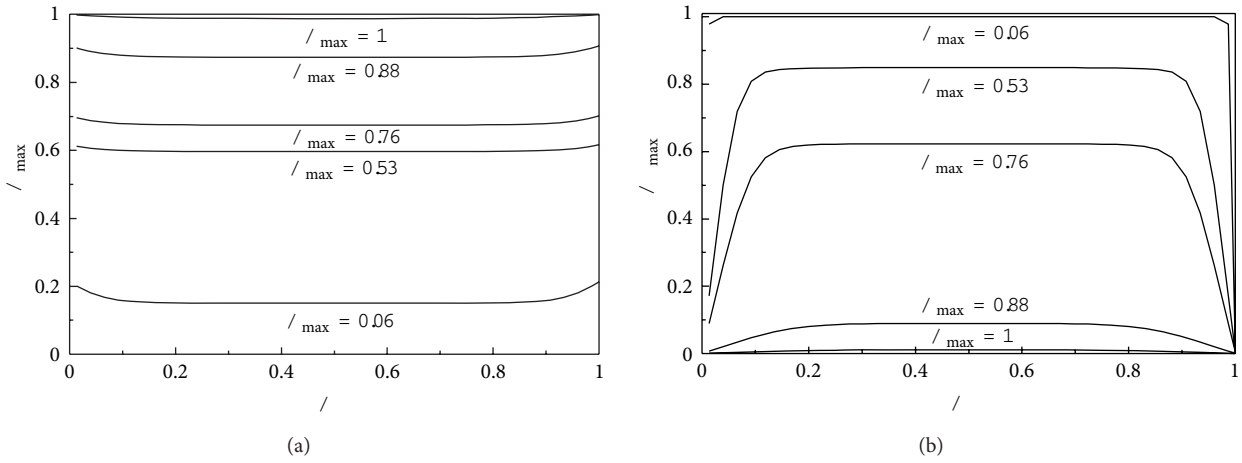

FIGURE 5: (a) Variation of normalized temperature and (b) moisture content with normalized time at the central plane ($Y/Y_L = 0.5$, $Z/Z_L = 0.5$) for Case 2 (see Table 1).

the surface and crack formation due to stress. This gradient decreases with time, and after a certain period of time, it is almost flat since the wood surface and gas reach equilibrium.

5. Conclusions

The mathematical model developed predicts the experimental results reasonably well. The difference between the model predictions and the measurements can be attributed to wood properties used. Model predictions are found to be in good agreement with the temperatures measured during the heat treatment of birch.

The model also predicts humidity, temperature, and velocity profiles in the gas as well as temperature and humidity profiles in the wood. Since it has been successfully validated, it can be used to predict the results of other desired treatments; this, in turn, can reduce the number of experimental trials required for future recipe developments. Model also indicates clearly the uniformity of flow and temperature within the furnace, which is highly important to obtain a good quality product.

Nomenclature

A_c: Constant in c_p calculation
C: Concentration, $kg \cdot m^{-3}$
c_p: Heat capacity, $J \cdot kg^{-1} \cdot K^{-1}$
C_μ, C_1, C_2: Constants of κ-ε turbulence model
D: Diffusion coefficient, $m^2 \cdot s^{-1}$
P_k: Shear production of turbulent kinetic energy, $m^2 \cdot s^{-3}$
h: Enthalpy, $J \cdot kg^{-1}$
k: Thermal conductivity, $W \cdot m^{-1} \cdot K^{-1}$
M: Moisture content, kg H_2O·(kg solid)$^{-1}$

P: Partial pressure of water vapor in wood, Pa
t: time, s
T: Temperature, K
V: Velocity, $m \cdot s^{-1}$
X, Y, Z: Spatial coordinates, m
X_L, Y_L, Z_L: Dimension of wood boards, m
u, v, w: Velocity components in X, Y, and Z directions, $m \cdot s^{-1}$.

Greek Symbols

ρ: Density, $kg \cdot m^{-3}$
μ: Dynamic viscosity, $kg \cdot m^{-1} \cdot s^{-1}$
ΔH_{lv}: Latent heat of vaporization, $J \cdot kg^{-1}$
ε: Viscous dissipation in turbulent flows, $m^2 s^3$
κ: Turbulent kinetic energy, $m^2 s^2$
$\sigma_{k,\varepsilon}$: Turbulent Prandtl numbers of κ, ε
φ: Relative humidity, %
γ: Wood porosity.

Subscripts

0: Initial
bt: Bound water
C: Critical
eff: Effective
f: Fluid
H_2O: Water
in: Inlet
l: Liquid
m: Mixture (wood + moisture)
max: Maximum
s: Surface
sat: Saturation
t: Turbulent
v: Vapor
w: Wood
x, y, z: Spatial direction.

Acknowledgments

The financial support from Le Fonds Québécois de la Recherche sur la Nature et les Technologies (FQRNT), University of Quebec at Chicoutimi (UQAC), Foundation of UQAC (FUQAC), Développement Économique Canada (DEC), Ministère du Développement Économique, de l'Innovation et de l'Exportation (MDEIE), and Conférence Régionale des Élus du Saguenay-Lac-St-Jean (CRÉ) and the contributions of Alberta Research Council, Cégep de Saint-Félicien, Forintek, PCI Ind., Ohlin Thermotech, Kisis Technology, and Industries ISA are greatly appreciated. The project is carried out at the University of Quebec at Chicoutimi.

References

[1] S. Yildiz, "Retention and penetration evaluation of some softwood species treated with copper azole," *Building and Environment*, vol. 42, no. 6, pp. 2305–2310, 2007.

[2] A. O. Rapp, "Review on heat treatments of wood," in *Proceedings of Special Seminar Held in Antibes*, Antibes, France, 2001.

[3] D. Dirol, R. Guyonnet et al., "The Improvement of Wood Durability by Retification Process," Document IRG/WP 98-40015, International Research Group on Wood Protection, Stockholm, Sweden, 1993.

[4] B. Pavlo and P. Niemz, "Effect of temperature on color and strength of spruce wood," *Holzforschung*, vol. 57, pp. 539–546, 2003.

[5] D. Kocaefe, J. L. Shi, D. Q. Yang, and M. Bouazara, "Mechanical properties, dimensional stability, and mold resistance of heat-treated jack pine and aspen," *Forest Products Journal*, vol. 58, no. 6, pp. 88–93, 2008.

[6] A. J. Stamm, "Thermal degradation of wood and cellulose," *Industrial and Engineering Chemistry*, vol. 48, no. 3, pp. 413–417, 1956.

[7] P. Viitaniemi, "Thermowood—modified wood for improved performance. Wood: the ecological material," in *Proceedings of the 4th Eurowood Symposium*, pp. 67–70, Tratek, Swedish Institute for Wood Technology Research, Stockholm, Sweeden, 1997.

[8] S. Poncsák, D. Kocaefe, M. Bouazara, and A. Pichette, "Effect of high temperature treatment on the mechanical properties of birch (*Betula papyrifera*)," *Wood Science and Technology*, vol. 40, no. 8, pp. 647–663, 2006.

[9] A. V. Luikov, "Systems of differential equations of heat and mass transfer in capillary-porous bodies," *International Journal of Heat and Mass Transfer*, vol. 18, no. 1, pp. 1–14, 1975.

[10] A. V. Luikov, *Heat and Mass Transfer*, Mir, Moscow, Russia, 1980.

[11] S. Whitaker, "Simultaneous heat, mass, and momentum transfer in porous media: a theory of drying," *Advances in Heat Transfer*, vol. 13, pp. 119–203, 1977.

[12] J. F. Siau, *Transport Processes in Wood*, Springer, New York, NY, USA, 1984.

[13] J. Bear and Y. Bachmat, *Introduction to Modelling of Transport Phenomena in Porous Media*, Kluwer Academic Publishers, Dordrecht, The Netherlads, 1990.

[14] S. M. Hassanizadeh and W. G. Gray, "General conservation equations for multi-phase systems 1. Averaging Procedure," *Advances in Water Resources*, vol. 2, pp. 131–144, 1979.

[15] R. Younsi, D. Kocaefe, S. Poncsak, and Y. Kocaefe, "Thermal modelling of the high temperature treatment of wood based on Luikov's approach," *International Journal of Energy Research*, vol. 30, no. 9, pp. 699–711, 2006.

[16] R. Younsi, D. Kocaefe, S. Poncsak, and Y. Kocaefe, "A diffusion-based model for transient high temperature treatment of wood," *Journal of Building Physics*, vol. 30, no. 2, pp. 113–135, 2006.

[17] R. Younsi, D. Kocaefe, S. Poncsak, and Y. Kocaefe, "Transient multiphase model for the high-temperature thermal treatment of wood," *AIChE Journal*, vol. 52, no. 7, pp. 2340–2349, 2006.

[18] A. A. Osma, D. Kocaefe, and Y. S. Kocaefe, "Mathematical modelling of an industrial furnace for high-temperature heat treatment of wood," *Canadian Journal of Chemical Engineering*, vol. 86, no. 4, pp. 693–699, 2008.

[19] R. Younsi, D. Kocaefe, S. Poncsak, and Y. Kocaefe, "Computational modelling of heat and mass transfer during the high-temperature heat treatment of wood," *Applied Thermal Engineering*, vol. 27, no. 8-9, pp. 1424–1431, 2007.

[20] D. Kocaefe, R. Younsi, S. Poncsak, and Y. Kocaefe, "Comparison of different models for the high-temperature heat-treatment of wood," *International Journal of Thermal Sciences*, vol. 46, no. 7, pp. 707–716, 2007.

[21] P. Majumdar and P. Deb, "Computational analysis of turbulent fluid flow and heat transfer over an array of heated modules using turbulence models," *Numerical Heat Transfer A*, vol. 43, pp. 669–692, 2003.

[22] W. Simpson and A. Tenwold, "Physical properties and moisture relations of wood," in *Wood Handbook*, pp. 1–23, USDA Forest Service, Forest Product Laboratory, Madison, Wis, U.S, 1999.

[23] M. A. Stanish, G. S. Schajer, and F. Kayihan, "Mathematical model of drying for hygroscopic porous media," *AIChE Journal*, vol. 32, no. 8, pp. 1301–1311, 1986.

Hindawi Publishing Corporation
Advances in Mechanical Engineering
Volume 2013, Article ID 426767, 5 pages
http://dx.doi.org/10.1155/2013/426767

Research Article

Numerical Study of Thermal Behavior in Alternating Current Light-Emitting Diodes

Farn-Shiun Hwu[1] and Hung-Lin Hsieh[2]

[1] *Department of Mechanical Engineering, Taoyuan Innovation Institute of Technology, Jhongli City 32091, Taiwan*
[2] *Department of Mechanical Engineering, National Taiwan University of Science and Technology, Taipei City 106, Taiwan*

Correspondence should be addressed to Farn-Shiun Hwu; hfs@tiit.edu.tw

Received 20 February 2013; Revised 14 April 2013; Accepted 19 April 2013

Academic Editor: Toshio Tagawa

The thermal characteristics of an alternating current light-emitting diode (AC LED) chip based on a three-dimensional unsteady numerical simulation are discussed. In this model, the difficulties due to the tiny scale and extra-low aspect ratio of the AC LED microchip geometry are resolved. A time lag between the maximum forward voltage and the highest mean junction temperature is observed. The influence of different input power frequencies on the thermal fields is also investigated for AC LEDs with 600 μm × 600 μm area. A numerical simulation of the junction temperature distributions shows that the AC LED has a better performance under a higher frequency than under a lower frequency.

1. Introduction

Light-emitting diodes (LEDs) have many advantages compared to the conventional light sources, such as their narrow spectrum, long lifetime, and good mechanical stability [1]. High-brightness LEDs have demonstrated excellent ability for functioning in back and general lighting applications [2]. LEDs are usually considered DC devices, powered by a few volts of direct current. The fabrication process and frequency response of alternating current (AC) polymeric LEDs (e.g., polyaniline, 3-hexylthiophene) have already been discussed in the literature [3, 4]. The structure of the polymer and the frequency of the input AC have an influence on the experimental results, including the luminance and response time of the LEDs. Tamura et al. [5] assembled 697 InGaN-based white LEDs with a series of connections on a glass epoxy substrate to form a 10 candela LED AC 100V-powered array. They then measured the temperature and the basic illumination characteristics of the array. Ao et al. [6] successfully designed a blue 40-chip AC LED array powered by alternating current, which led to the development of chip-level semiconductor AC LEDs. A single device had a chip size of 150 μm × 120 μm while the LED array had a total size of 1.1 mm × 1 mm, and an output power of 40 mW under AC 72 volts. A novel chip design for an AC LED was proposed by Yen et al. [7], which increased the lighting area in each bias direction to improve the device efficiency through the use of a Wheatstone bridge circuit design.

There have been some previous studies focusing on the structure, fabrication, and thermal issues of the DC LED. However, the input power of an AC LED is an alternating current, so the thermal effect is not the same as that for a DC LED. Hwu et al. proposed a method for measuring the mean junction temperature of an AC LED [8]. In the present study, we apply a three-dimensional unsteady numerical model to simulate the thermal behavior of an AC LED chip. The temperature oscillation under AC operation can thus be obtained through numerical simulation.

2. Numerical Model

The AC LED sample consists of a 12 volt AC microchip array, as shown in Figure 1(a); a schematic representation of a cross-section of a microchip in the lateral direction is shown in Figure 1(b). The chip size is 600 μm × 600 μm × 106 μm. The AC LED chip consists of an ITO layer (0.5 μm), p-GaN layer (0.2 μm), MQW (0.8 μm), n-GaN layer (4.5 μm), and sapphire substrate (100 μm). The directions of current flow in

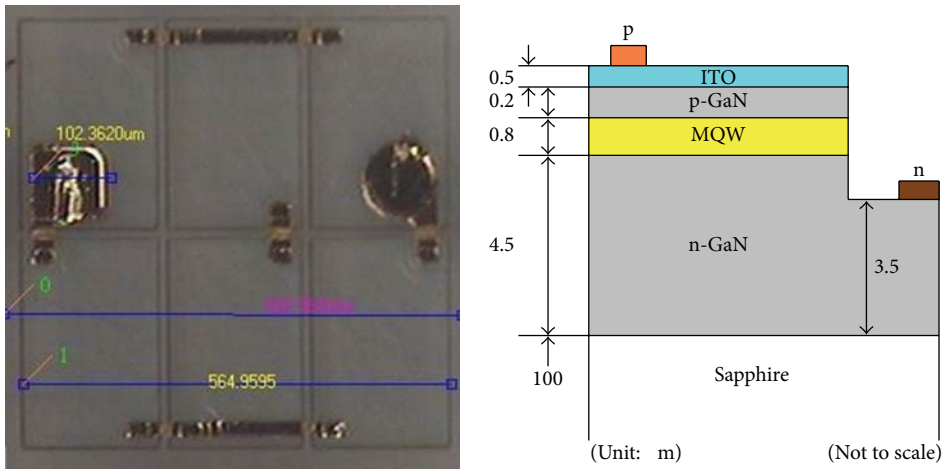

(a) (b)

Figure 1: (a) Photograph of the AC LED chip, and (b) the schematic representation of a cross-section in the lateral direction of a microchip.

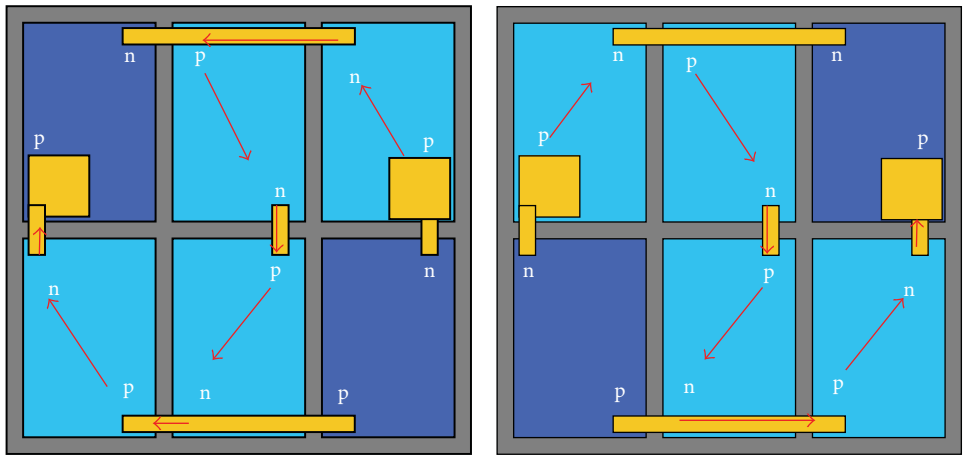

(a) Positive half period (b) Negative half period

Figure 2: Directions of current flow in the chip array.

the array for the positive half period and negative half period under alternating conditions are shown in Figures 2(a) and 2(b), respectively. A self-developed code coupling the thermal and electrical equations is added to the finite element method (FEM) software COMSOL Multiphysics which is used to obtain the temperature in the AC LED chip. The simulation was performed in a three-dimensional, unsteady condition. The meshes of the AC LED are shown in Figure 3. There is a total of 58567 tetrahedral elements. The relative tolerance for the numerical value of the temperature is selected to be 1×10^{-4}.

Following our previous work [9], the current through the active layer is assumed to be in the direction perpendicular to the layer. The specific p- and n- contact resistances also follow previous work. The unsteady governing equation of conduction heat transfer with the heat source is

$$\rho C_p \frac{\partial T}{\partial t} - \nabla \cdot (k \nabla T) = Q, \tag{1}$$

where ρ is the density; C_p is the specific heat; T is the temperature; t is the time; and k is the thermal conductivity. The heat generation term Q in the active layer is as follows [9]:

$$Q = \frac{J_e \times \left[V_j - (\hbar\omega/e) \times \eta_{\text{int}} \times \eta_{\text{ext}} \times \exp\left(-(T - 300)/1600\right)\right]}{l_e}, \tag{2}$$

where J_e is the elemental current density; V_j is the voltage drop between the active layer; $\hbar$ is the reduced Planck constant; ω is the angular frequency; η_{int} is the internal quantum efficiency at room temperature; η_{ext} is the light extraction efficiency at room temperature; and l_e is the elemental thickness of the mesh. The term $\hbar\omega$ is the energy of the photon, thus $(\hbar\omega/e)$ is the electrical potential converted from the energy of photon. The values of the external quantum efficiency ($\eta_{\text{int}} \times \eta_{\text{ext}}$), as obtained in the literature [9], are

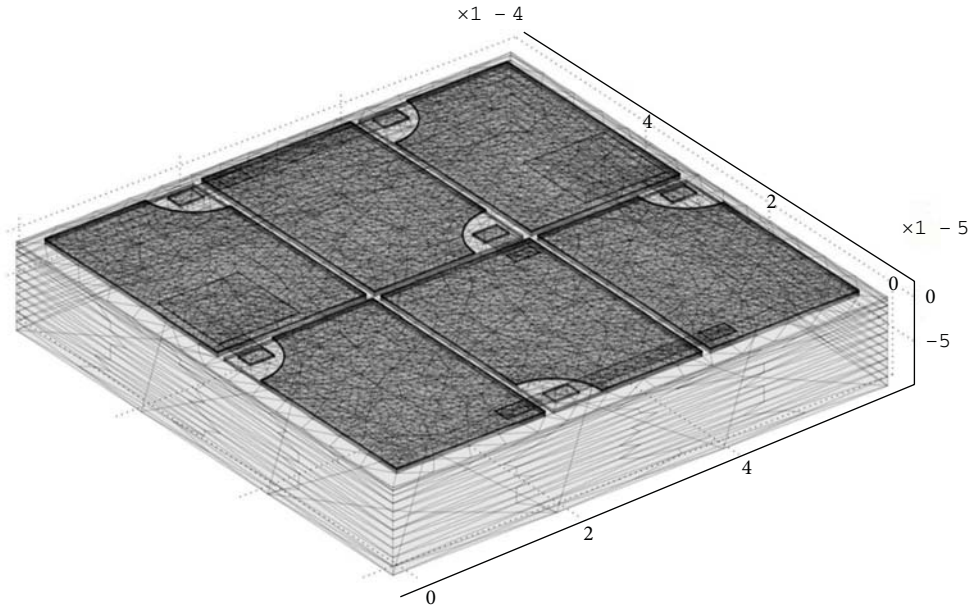

Figure 3: Tetrahedral element structure of the AC LED chip.

between 13% and 43%. Thus, in the present study, $\eta_{\text{int}} \times \eta_{\text{ext}} = 25\%$ is selected.

The heat generation term per unit volume Q due to Joule heating in the other layers of the LED chip is

$$Q = J_e \cdot \nabla V. \tag{3}$$

The physical properties of the materials are summarized in Table 1 [10, 11].

The boundary conditions of the top and lateral surfaces of the AC LED chip are shown by

$$\hat{n} \cdot (k\nabla T) = h\left(T_{\text{inf}} - T\right), \tag{4}$$

where $\hat{n}$ is the unit normal vector of the interface; T_{inf} is the air temperature; and h is the convective heat transfer coefficient. Here, we select $h = 5\ \text{W/m}^2\cdot\text{K}$ and $T_{\text{inf}} = 300\ \text{K}$ since the LED is under the natural convection environment.

The boundary condition at the bottom surface of the AC LED chip is assumed to be

$$\hat{n} \cdot (k\nabla T) = h_e\left(T_{\text{inf}} - T\right), \tag{5}$$

where h_e is the equivalent heat transfer coefficient. A copper slug with a board is usually used to dissipate the heat generated from the AC LED chip. The size is set to be about 7.2 cm^2 in the present study. Under natural convection conditions, the Biot number for the slug is very small, therefore, the temperature variation along the main heat flow direction inside the slug is insignificant. For this case, h_e is about 160,000 $\text{W/m}^2\cdot\text{K}$.

3. Results and Discussion

Figures 4(a)–4(i) show the temperature distributions in the AC LED chip under 12 volts of AC current and a frequency of 60 Hz in one alternating period ($t = 0.0116$ sec–0.0283 sec). These figures indicate the highest and lowest temperatures observed for the whole AC LED chip at different time steps. Under alternating conditions, the two central microchips are both turned on during the positive half period or negative half period, so the temperature of these two microchips varies in the frequency of 120 Hz. The highest temperatures for the negative half period and positive half period are 339.5 K and 338.5 K, respectively. The temperature difference of 1 K between these two half periods may be due to the fact that the mesa structure and the electrode are not totally symmetrical in the middle line of the chip array. The current crowding effect and the heat transfer path at the negative half period and positive half period are both different. The mean junction temperature for the whole AC LED chip for each time step is obtained from the numerical simulation result, as shown in Figure 5. An LED is turned on when the forward voltage is higher than the threshold voltage, thus the voltage is always positive. When an AC LED is driven under the AC condition, the current during the positive half period will flow through a different chip array. Therefore, the forward voltage in Figure 5 is always positive. There is a 0.002 sec time lag between the maximum forward voltage and the highest mean junction temperature as observed in Figure 5. The main reason for this may be that the LEDs have the characteristics of diodes. The chip will be turned on when the threshold voltage is reached after a time difference of about 1/480 sec. The shape of the

Table 1: Physical properties used in the simulation.

Material	ρ (kg/m^3)	C_p (J/kg·K)	k (W/m·K)
Sapphire	3965	730	35
GaN	6150	490	130
ITO	7150	228	10

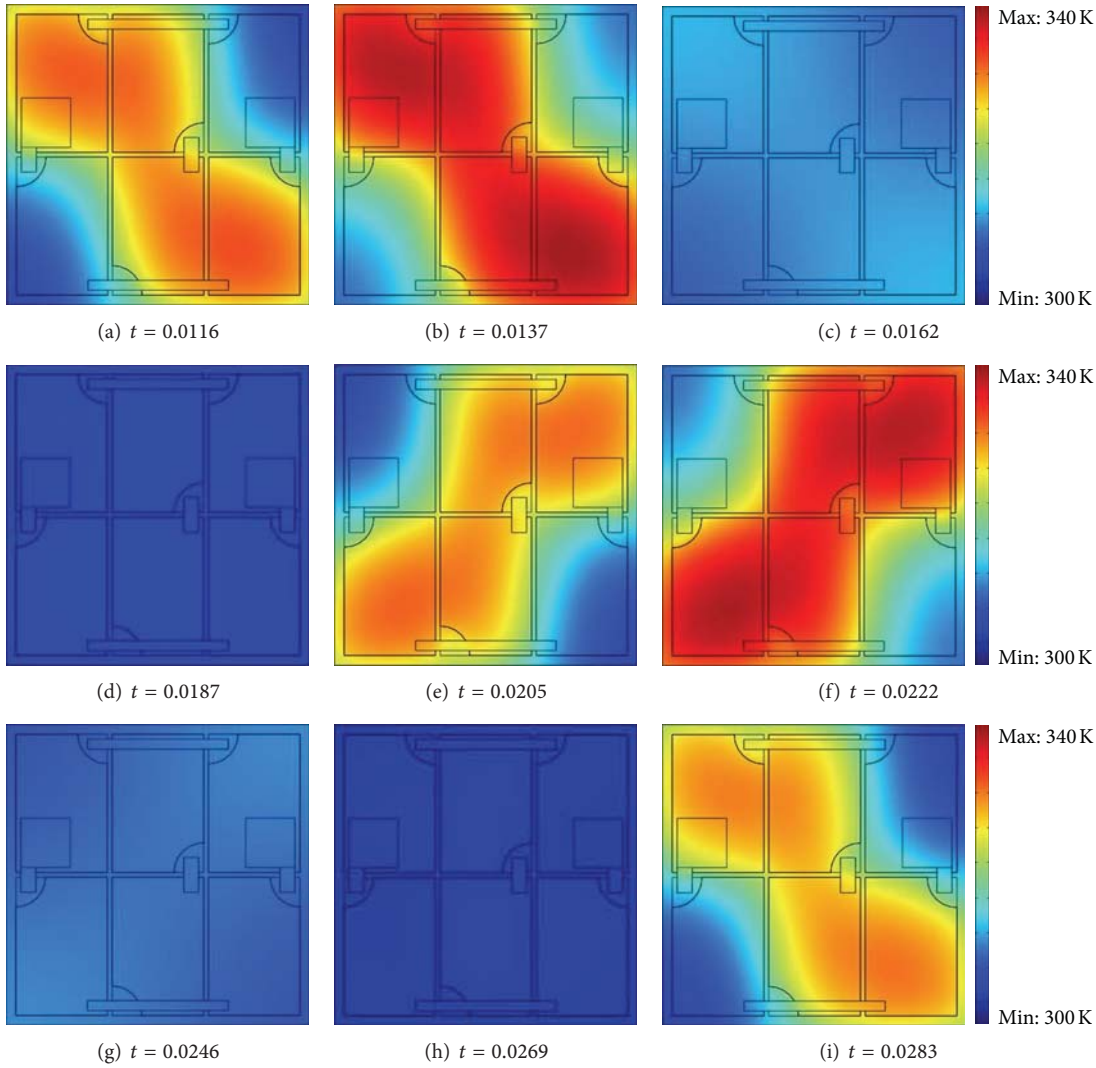

Figure 4: Temperature distributions of the AC LED chip under an AC 12 volts and a frequency of 60 Hz in one alternating period (unit of t: sec).

mean junction temperature curve is not the same as the shape of a sine wave possibly because the thermal diffusion time (0.0012 sec) of this LED chip is far greater than the time scale of the electron diffusion.

Figure 6 shows the mean junction temperature of an AC LED chip driven under different alternating frequencies. When the frequency is higher, the difference between the highest temperature and the lowest temperature is smaller. The temperature difference between the highest and lowest temperature is about 24 K when the frequency is 60 Hz. However, when the frequency is 240 Hz, the temperature difference is only 10 K. Additionally, the curve of the mean junction temperature is more symmetrical under higher frequency than the case with a lower frequency. This is due to the on-off interval of the AC LED for the higher frequency case being shorter than the lower frequency cases. The time is not sufficient for the junction temperature to reach a higher

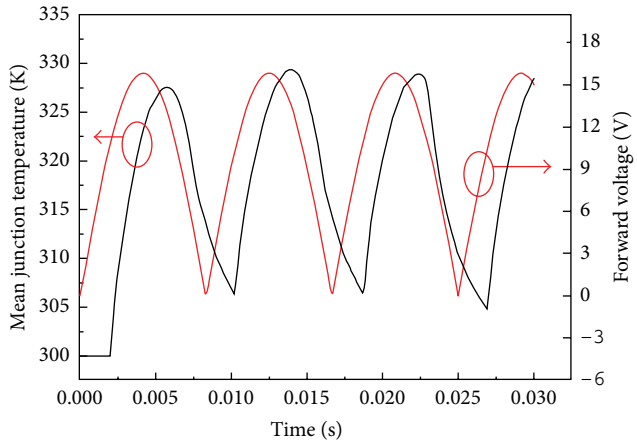

Figure 5: Mean junction temperature of the AC LED chip under AC 12 volts and a frequency of 60 Hz.

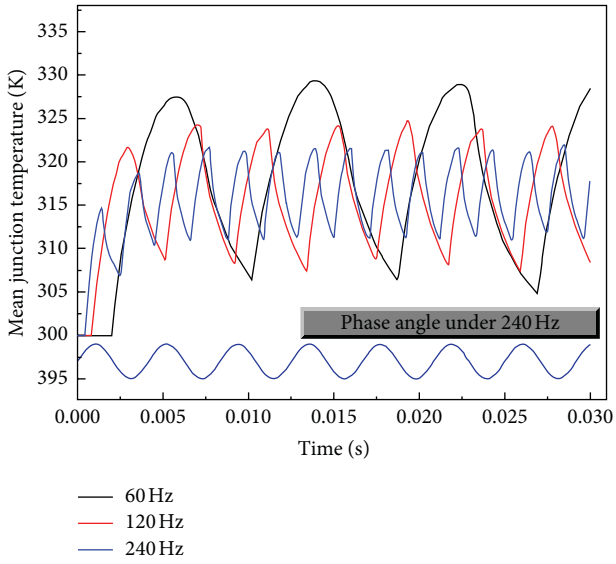

Figure 6: Mean junction temperature of the AC LED chip under different alternating frequencies.

value. Equally, the junction temperature cannot reach a lower value before the chip is turned on again. Therefore, the rates of junction temperature increase and decrease are more stable in the case of higher frequencies than lower frequencies. The AC LED chip is more suitable for driving under higher frequency to avoid the fatigue of the cyclic thermal stress.

4. Conclusions

The present study proposes a three-dimensional unsteady numerical model for AC LED chips. The thermal characteristics of AC LEDs are analyzed through a numerical simulation. The highest temperature of the AC LED chip is about 339 K under AC 12 volt operation with a frequency of 60 Hz. Otherwise, the mean junction temperature can be calculated by the numerical model. The highest mean junction temperature is about 330 K. The numerical simulations results show a time lag of 0.002 sec between the maximum forward voltage and the highest mean junction temperature. The unsteady numerical model can be used to find the thermal characteristics and to design AC LED chip patterns. The influence of the driving frequency on the AC LED is also discussed. A higher driving frequency will lead to a lower mean junction temperature difference for AC LEDs.

Acknowledgment

The authors gratefully acknowledge the support of the National Science Council of Taiwan, Taiwan for this work, through Grant no. NSC 101-2221-E-253-006.

References

[1] F. S. Hwu, T. H. Sung, C. H. Chen, J. Tseng, H. Qiu, and J. Chen, "A numerical model for studying multi-microchip and single chip LEDs with an interdigitated mesa geometry," *IEEE Photonics Journal*, vol. 5, no. 2, p. 6600515, 2013.

[2] Y. C. Hsu, Y. K. Lin, M. H. Chen et al., "Failure mechanisms associated with lens shape of high-power LED modules in aging test," *IEEE Transactions on Electron Devices*, vol. 55, no. 2, pp. 689–694, 2008.

[3] R. Österbacka, A. J. Pal, K.-M. Källman, and H. Stubb, "Frequency response of molecularly thin alternating current light-emitting diodes," *Journalof Applied Physics*, vol. 83, no. 3, pp. 1748–1752, 1998.

[4] R. Österbacka, A. J. Pal, and H. Stubb, "High frequency alternating current light-emitting diodes using Langmuir-Blodgett films," *Thin Solid Films*, vol. 327–329, pp. 668–670, 1998.

[5] T. Tamura, T. Setomoto, and T. Taguchi, "Illumination characteristics of lighting array using 10 candela-class white LEDs under AC 100 V operation," *Journal of Luminescence*, vol. 87–89, pp. 1180–1182, 2000.

[6] J. P. Ao, H. Sato, T. Mizobuchi et al., "Monolithic blue LED series arrays for high-voltage AC operation," *Physica Status Solidi A*, vol. 194, no. 2, pp. 376–379, 2002.

[7] H. H. Yen, W. Y. Yeh, and H. C. Kuo, "GaN alternating current light-emitting device," *Physica Status Solidi A*, vol. 204, no. 6, pp. 2077–2081, 2007.

[8] F. S. Hwu, C. H. Yang, and J. C. Chen, "Method for measuring the mean junction temperature of alternating current light-emitting diodes," *Measurement Science and Technology*, vol. 22, no. 4, Article ID 045701, 6 pages, 2011.

[9] F. S. Hwu, J. C. Chen, S. H. Tu, G. J. Sheu, H. I. Chen, and J. K. Sheu, "A numerical study of thermal and electrical effects in a vertical LED chip," *Journal of the Electrochemical Society*, vol. 157, no. 1, pp. H31–H37, 2010.

[10] M. V. Bogdanov, K. A. Bulashevich, I. Y. Evstratov, A. I. Zhmakin, and S. Y. Karpov, "Coupled modeling of current spreading, thermal effects and light extraction in III-nitride light-emitting diodes," *Semiconductor Science and Technology*, vol. 23, no. 12, Article ID 125023, 10 pages, 2008.

[11] G. E. Myers, *Analytical Methods in Conduction Heat Transfer*, AMCHT Publications, Madison, Wis, USA, 2nd edition, 1998.

Hindawi Publishing Corporation
Advances in Mechanical Engineering
Volume 2013, Article ID 868240, 9 pages
http://dx.doi.org/10.1155/2013/868240

Research Article

Numerical Analysis of Flow around a Moving Object by an Immersed Boundary Method with the Level Set Method

Atsuki Iijima, Tomomitsu Sato, and Toshio Tagawa

Department of Aerospace Engineering, Tokyo Metropolitan University, 6-6 Asahigaoka, Hino, Tokyo 191-0065, Japan

Correspondence should be addressed to Toshio Tagawa; tagawa-toshio@sd.tmu.ac.jp

Received 23 January 2013; Accepted 7 March 2013

Academic Editor: Bo Yu

We developed a new immersed boundary method which has various advantages, such as accuracy, flexibility, and rapidness combining with the level set method. We numerically demonstrated some typical examples, such as flows around a sphere, an ellipsoid, a flapping ellipsoid, and a windmill. We calculated coefficients of drag in those problems and visualized vortical structures and Powell sound sources for the various Reynolds number and then compared our results with some previous researches.

1. Introduction

In recent years, the development of computer performance has enabled us to conduct numerical simulation of highly complex flow phenomena around a moving object whose shape is quite complicated. So far, various types of calculation grids have been proposed. However, the more grids are complicated, the more calculation time and a required memory increase.

Therefore, we paid our attention to the immersed boundary method (later on we abbreviate it as *IB* method), which immerses a complicated-shaped boundary at an orthogonal grid system and the level set method which captures any object shape correctly. Although the *IB* method is a technique proposed by Peskin [1] in 1972, in order to be able to perform highly precise calculation, having a lot of grids with an orthogonal grid system is required. In virtue of improvement in computer performance in recent years, it receives an attracting attention again. On the other hand, the level set method is the technique of capturing any object shape correctly, and now it is used not only in computational fluid dynamics (CFD) but also in the field of image processing. Moreover, it has the advantage that the moving boundary can be tracked with high accuracy.

In this research, we developed the new computational technique which can be applied to the CFD for a moving boundary or a complicated object shape and can carry out numerical computations rapidly by combining the *IB* method for analyzing complicated form by an orthogonal grid system and the level set method for capturing object shape correctly. We calculated the flow around an object by using the level set *IB* method and verified the adaptability of the code by changing the Reynolds number. In this research, after computations of the flow around a sphere or an ellipsoid which is stationary or rotates in the uniform flow, then computations of the flow around a moving object in the uniform flow which imitates flapping wings and a windmill are conducted. In addition, in this research, we paid attention to the aeroacoustics, and the aerodynamic sound source was visualized together with the vortical structure and the coefficient of drag.

2. Dimensionless Equations

The dimensionless equations used in this research are as follows. In addition, since the *IB* method is used, the velocity of an object-inside point and of a boundary adjacent point is corrected by external force term $\vec{F}_{IB}$.

(i) Equation of continuity:

$$\vec{\nabla} \cdot \vec{U} = 0. \tag{1}$$

(ii) Navier-Stokes equation:

$$\frac{D\vec{U}}{D\tau} = -\vec{\nabla}P + \frac{1}{\mathrm{Re}}\nabla^2\vec{U} + \vec{F}_{IB}. \tag{2}$$

A boundary adjacent point ($\vec{U} = \vec{U}_{IB}$):

$$\vec{F}_{IB} = \left(\vec{U} \cdot \vec{\nabla}\right)\vec{U} + \vec{\nabla}P - \frac{1}{\mathrm{Re}}\nabla^2\vec{U} + \frac{\vec{U}_{IB} - \vec{U}^n}{\Delta\tau}. \quad (3)$$

An object-outside point:

$$\vec{F}_{IB} = \vec{0}. \quad (4)$$

An object-inside point ($\vec{U} = \vec{U}_B$):

$$\vec{F}_{IB} = \left(\vec{U} \cdot \vec{\nabla}\right)\vec{U} + \vec{\nabla}P - \frac{1}{\mathrm{Re}}\nabla^2\vec{U} + \frac{\vec{U}_B - \vec{U}^n}{\Delta\tau}. \quad (5)$$

Velocity $\vec{U}_{IB}$ is a velocity given by the level set method, and $\vec{U}_B$ is an object-inside velocity. Besides, the Reynolds number of uniform flow is set to Re, and Reynolds number resulting from rotation and flapping is denoted to Re_r.

3. Immersed Boundary Method and Level Set Method

Although various kinds of approximated methods are proposed for the *IB* method, in this study, we approximate it by using the distance function called a level set function (ϕ), which was first introduced in the IB method by the study of Okita et al. [2]; also the study which used level set *IB* method to a moving boundary is introduced by Sato [3]. As shown in Figure 1, a level set function has the characteristic that the normal distance from a boundary to a grid point is acquired. By calculating the velocity gradients 1 and 2 of two kinds of normal directions ((6) and (7)), the velocity U_{IB} near the boundary is calculated. The existence of a boundary of object is captured correctly from the information of normal distance $\phi_{I-1,K} > 0$, $\phi_{I+1,K} < 0$ as shown in Figure 2, and bordering curvature is judged from that of $\phi_{I,K+1} > \phi_{I,K-1}$. This technique is the level set method, and since a velocity gradient is made as for order to a normal direction by this method, it leads to improvement in arithmetic precision. In this connection, this technique referred to what was invented by Okita et al., and in this study, the technique was extended so that the influence of a normal velocity gradient might be reflected more greatly, and we tried to raise analysis accuracy. Moreover, even when object velocity changes with places like a moving boundary, there is an advantage that the velocity can be acquired easily by using a level set function.

(i) Normal velocity gradient 1 (2 dimension):

$$\left.\frac{\partial U}{\partial n}\right|_{I,K} = \mathrm{sgn}\left(\left.\frac{\partial U}{\partial X}\right|_{I,K} n_X + \left.\frac{\partial U}{\partial Z}\right|_{I,K} n_Z\right) \cdot \sqrt{\left(\left.\frac{\partial U}{\partial X}\right|_{I,K} n_X\right)^2 + \left(\left.\frac{\partial U}{\partial Z}\right|_{I,K} n_Z\right)^2}$$

$$\left(n_X = \frac{\phi_X}{\sqrt{\phi_X^2 + \phi_Z^2}},\ n_Z = \frac{\phi_Z}{\sqrt{\phi_X^2 + \phi_Z^2}},\ \phi_X = \frac{\partial\phi}{\partial X},\ \phi_Z = \frac{\partial\phi}{\partial Z}\right). \quad (6)$$

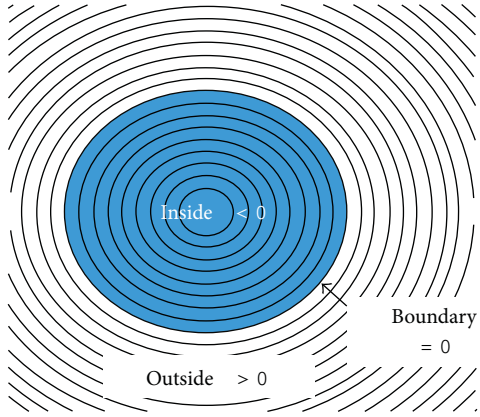

Figure 1: Level set function.

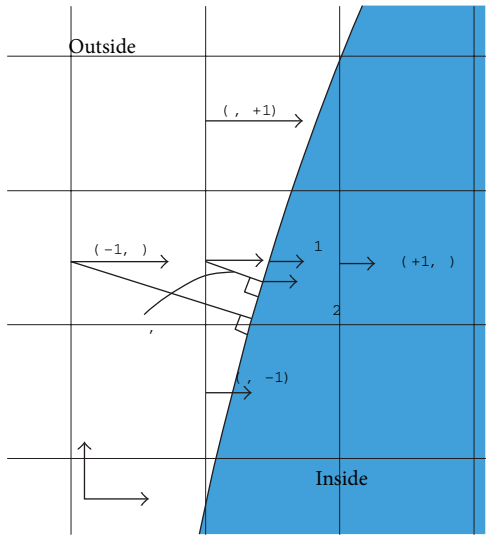

Figure 2: Boundary adjacent velocities. (U_{IB}: boundary adjacent velocity, U_B: object inside velocity, ϕ: level set function.) The situation of the horizontal velocity U near the boundary is shown.

(ii) Normal velocity gradient 2 (2 dimension):

$$\left.\frac{\partial U}{\partial n}\right|_{I,K} = \frac{U_{IB} - U_{B2}}{\phi_{I,K}} \Longleftrightarrow U_{IB} = U_{B2} + \left.\frac{\partial U}{\partial n}\right|_{I,K}\phi_{I,K}. \quad (7)$$

By substituting (6) to (7), the velocity U_{IB} of a boundary adjacent point is calculated. And we calculate V or W with the same procedure. Besides, in this case, angular velocity is uniform, so the velocity can be found if the distance and angle from the center are known. The velocity inside a moving object is as follows:

$$U(I, J, K) = 0, \quad (8)$$

$$V(I,J,K) = \pm\sqrt{(Y(J)-\text{Center}Y)^2 + (ZP(K)-\text{Center}Z)^2}\cdot\Omega \cdot\left[\sin\left\{\arctan\left(\frac{ZP(K)-\text{Center}Z}{Y(J)-\text{Center}Y}\right)\right\}\right], \quad (9)$$

$$W(I,J,K) = \pm\sqrt{(YP(J)-\text{Center}Y)^2 + (Z(K)-\text{Center}Z)^2}\cdot\Omega \cdot\left[\cos\left\{\arctan\left(\frac{Z(K)-\text{Center}Z}{YP(J)-\text{Center}Y}\right)\right\}\right] \left(ZP(K) = \frac{Z(K)+Z(K-1)}{2},\ YP(J) = \frac{Y(J)+Y(J-1)}{2}\right). \quad (10)$$

4. Computational Methods

In this research, each analysis assumes the incompressible Newtonian fluid, and the inequality interval staggered grids are used. The difference schemes we use are the third order upwind difference scheme (UTOPIA) for the advection terms of the equation of motion, the Euler explicit method for the time derivative term, and the second order central differences for other terms. And, the SOR method is used for the solution of the Poisson's equation of pressure, and the fractional step method is applied to the algorithm of calculation.

5. Visualization of Sound Source

In this research, a vortical structure by $\lambda 2$ method, a coefficient of drag, streamlines, and sound source distribution are visualized in each result. Sound source distribution is explained in detail below.

As one of the causes of noise, the aerodynamic noise (aerodynamic sound) which occurs by turbulence of air is often mentioned. Therefore, although it becomes indispensable in acoustical technology to reduce aerodynamic sound, it is difficult to specify a generating part of sound in an experiment for fluid itself. Therefore, we paid attention to the sound source of aerodynamic sound which can investigate the generating part and generation mechanism of sound. The basic equation of aerodynamic sound calculation is the following Lighthill's equation [4]:

$$\left(\frac{\partial^2}{\partial t^2} - c^2\nabla^2\right)\rho = \frac{\partial^2 T_{ij}}{\partial x_i \partial x_j}. \quad (11)$$

T_{ij} expresses the following Lighthill turbulent stress tensor

$$T_{ij} \equiv \rho v_i v_j + p_{ij} - c^2\rho\delta_{ij}. \quad (12)$$

The left-hand side of (11) expresses propagation of sound, and the right-hand side expresses a sound source. Since this is a nonhomogeneous wave equation, it is difficult to make analysis by DNS calculation, and in this research, the sound source was visualized from the following equation of Powell-Howe [5] which can be used under a flow of low Mach number:

$$\left(\frac{\partial^2}{\partial t^2} - c^2\nabla^2\right)\rho = -\rho_0\,\text{div}\,(\vec{\omega}\times\vec{u}). \quad (13)$$

Since ρ_0 is standard density and it is fixed, a sound source is given by $\text{div}(\vec{\omega}\times\vec{u})$ (Powell sound source term) of the right-hand side of (13). After calculating a flow field by a separation solution, a sound source is calculated.

Table 1: Boundary conditions.

	Velocity condition	Pressure condition
Inflow boundary	$U = 1, V = 0, W = 0$	$\dfrac{\partial P}{\partial X} = 0$
Outflow boundary	U, V, W Sommerfeld radiation condition $\dfrac{\partial \vec{U}}{\partial \tau} + U_C\dfrac{\partial \vec{U}}{\partial X} = \vec{0}\ \ (U_C = 1)$	$P = 0$
Lateral boundary	$\dfrac{\partial U}{\partial Z} = 0,\ \dfrac{\partial V}{\partial Z} = 0,\ \dfrac{\partial W}{\partial Z} = 0$	$\dfrac{\partial P}{\partial Z} = 0$

6. Computation around a Rotating Sphere and Ellipsoid

6.1. Computational Conditions. An analysis model is shown in Figure 3. The initial condition assumes external uniform flow ($U = 1, V = 0, W = 0$, and $P = 0$) for the whole domain, and the boundary condition is set up as shown in Table 1. The inflow boundary is given by velocity regularity, the outflow boundary is given by the Sommerfeld radiation condition [6], the velocity at the lateral walls is considered as continuation, and the circumference of an object is set as no-slip condition. Characteristic length D is the diameter of a sphere or the short diameter of an ellipsoid. The long diameter of the ellipsoid is extended only to x-axis orientation as $1.5D$, and rotation is given with respect to the x-axis. In both analysis of the sphere and the ellipsoid, the number of grids is $(X, Y, Z) = (167, 138, 138)$, the calculation area is $8D \times 6D \times 6D$, and the center position of an object is $(3D, 3D, 3D)$. Besides, the computed results are compared with the experimental values which were performed in other researchers by changing Reynolds number in order to show the validity of the present technique. External uniform flow is given in the range of $\text{Re} = 50-5000$, and rotation is given in $\text{Re}_r = 500$ or 1000. Reynolds number resulting from rotation is set to $\text{Re}_r = \omega_0 D^2/\nu$, and a velocity of objects is given by nondimension angular velocity $\Omega = \text{Re}_r/\text{Re}$.

6.2. Results and Discussion. Computational results are shown in Figures 4–7. First, Figure 4 shows coefficient of drags (Cd) value and quantitatively compares it with an experimental value or other calculated values. Concerning Cd value of the nonrotating sphere, the present result almost agrees with an experimental value or other calculated values, and it can be recognized that this analysis is reliable. On the other hand,

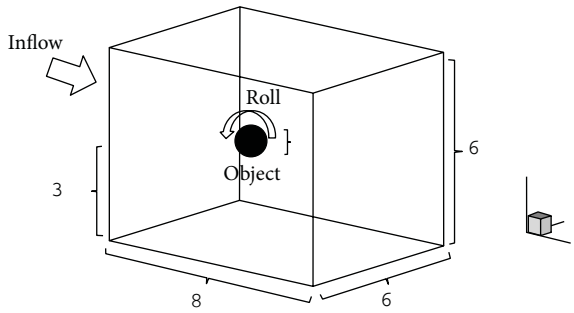

Figure 3: Schematic model of the rotating sphere.

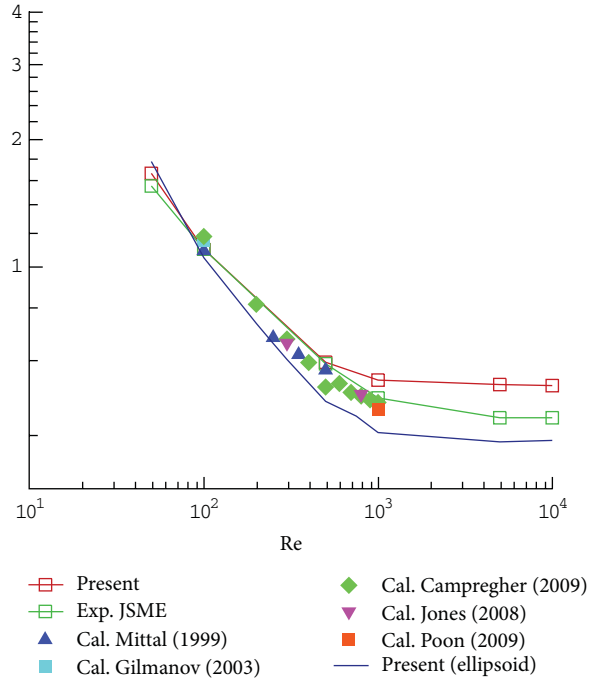

Figure 4: Comparison of drag coefficients (Re-Cd) [7–12].

some discrepancy can be seen at the high Reynolds number beyond Re = 5000. It would be considered to be the great influence of the number of grids or the size of a calculation area. Comparing Cd values of a sphere and an ellipsoid, the Cd of an ellipsoid is lower than that of a sphere, because the separation in the wake is rather suppressed due to the elongation of the object along the flow direction. Also, Figure 5 shows the relation between Cd value and the rotational rate (Re_r). When rotation is given, the Cd value increased in both the sphere and the ellipsoid.

Visualizations of flows are shown in Figures 6 and 7. In Figure 6, the $\lambda 2$ method which was proposed by Jeong and Hussain [13] is used for the visualization of vortical structure. The $\lambda 2$ method can extract the domain where the local pressure is minimum, which eliminated incorrect recognition of the vortex caused by unsteady condition and viscous force, and can capture a core of vortex exactly. The color indicates pressure and the figure has the streamline in addition. For the flow around the nonrotating sphere, hairpin-like vortical

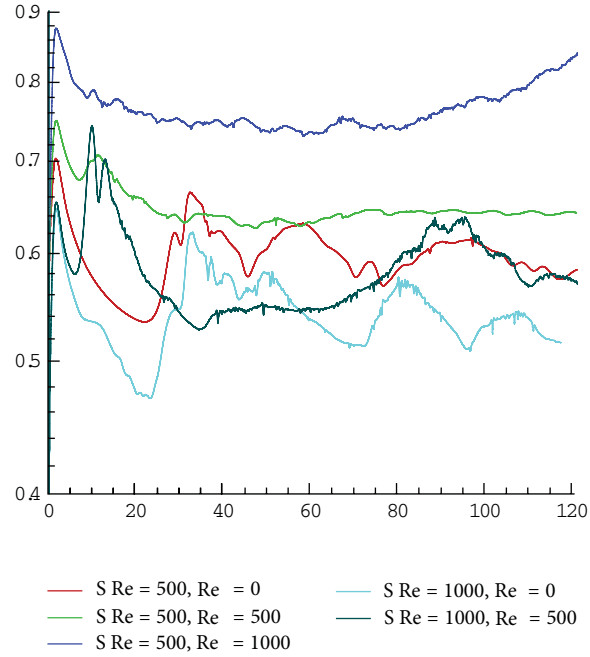

Figure 5: Drag coefficients for rotating spheres (τ–Cd).

structure is observed. There is a close resemblance between the present result and the experiment which was carried out by Sakamoto and Haniu [14]. For the flow in the condition where the sphere is rotating, it is observed that the vortex itself which is transported to the region behind the object is rotated. The hairpin-like vortex changed to a spiral complicated one. In $\mathrm{Re}_r = 1000$, the rotation effect is predominant, and it turns out that the hairpin-like vortex moves in a spiral way.

Figure 7 visualizes the Powell sound source in slices of $Y = 3D$ and $Z = 3D$. The sound source is generated near the object, and many sound sources also occurred from the wake at the high Reynolds number. Besides, it is turned out that there is less generation of a sound source around the ellipsoid compared with the sphere under the same Reynolds number. Also at Re = 500, if there is a rotation of an object, it is recognized from Figure 7 that the sound source of a quantity equivalent to or more than that of Re = 1000, $\mathrm{Re}_r = 0$ (nonrotation) is generated. At Re = 500, $\mathrm{Re}_r = 1000$, by the great influence of rotation, generation of the sound source in a wake is remarkable, and it is carried to a distant position. Furthermore, it is observed that generation of the sound source in the wake is also promoted in Re = 1000 and $\mathrm{Re}_r = 500$ condition in which external uniform flow is predominant.

7. Computation around Flapping Ellipsoid

7.1. Analysis Conditions. The level set *IB* method allows us to conduct moving boundary computations with sufficient accuracy of tracking borders without excessive calculation load. In this section, as an example of analysis of the moving boundary by the *IB* method, flow analysis around the oscillating ellipsoid which imitates flapping wings is conducted. Here, some typical values are given based on flying insects.

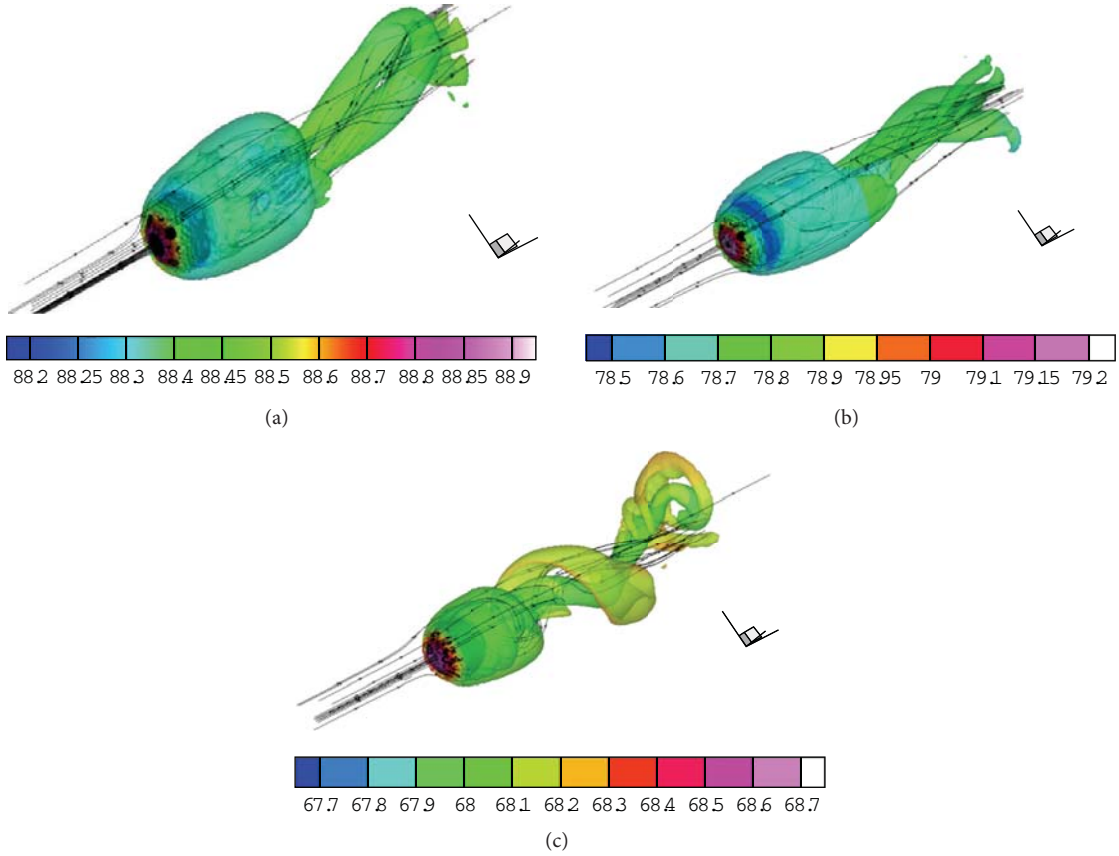

FIGURE 6: Vortical structure around rotating spheres ($\tau = 125$). (a) Re = 500, $\mathrm{Re}_r = 0$, (b) Re = 500, $\mathrm{Re}_r = 500$, and (c) Re = 500, $\mathrm{Re}_r = 1000$.

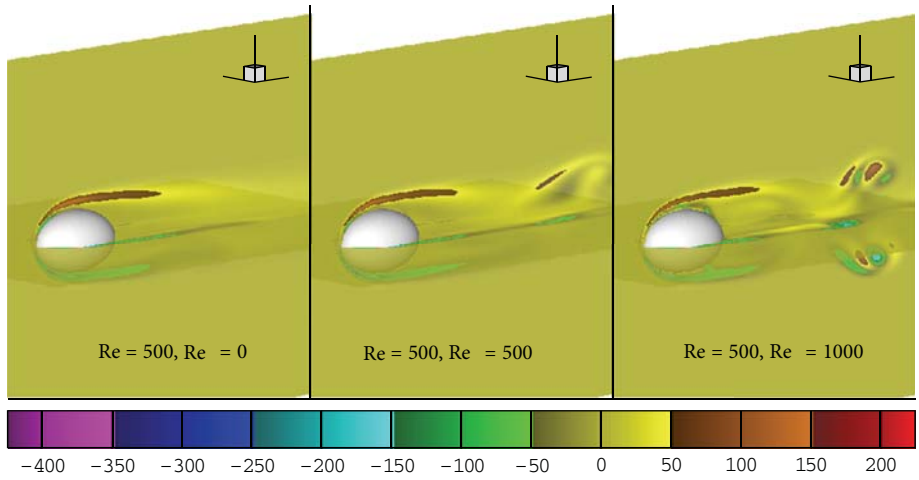

FIGURE 7: Comparison of sound source distribution around rotating ellipsoids ($\tau = 125$).

An analysis model is shown in Figure 8. A computational area is taken as shown in Figure 8. A flat ellipsoid is installed in the center, and it performs a periodic up-and-down motion. In this ellipsoid, the long radius of the $Y-Z$ section is D, and the short diameter is $0.2D$, and another diameter of the $X-Z$ section is also $0.2D$. It is assumed that an external uniform flow along x-axis direction in the whole domain is given, and nondimensional angular velocity is given between 45 degrees of flapping angle. The ellipsoid is shuttling between 22.5 and −22.5 degrees, and the ellipsoid is not twisted in the direction of x-axis. The Reynolds number of an external uniform flow is set to Re = 167, and that of a flapping of wings is set to $\mathrm{Re}_r = 350$. This analysis assumes plane symmetry with respect to the center plane ($Y = 0$), and thus it makes

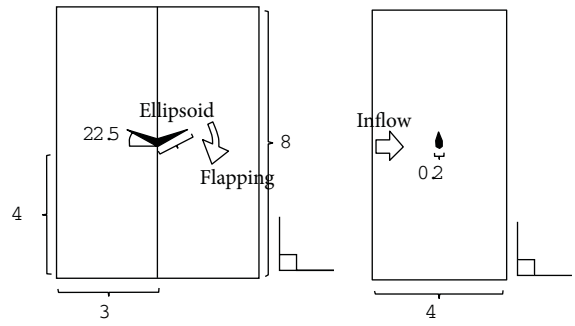

Figure 8: Schematic model of the flapping ellipsoids.

$V = 0$ at the plane; the Neumann type boundary condition is used for other velocity components and the pressure at a side wall and the upper and lower walls. The number of grids is $(X, Y, Z) = (96, 80, 132)$, a calculation area is $4D \times 3D \times 8D$, and the center position of the object is $(2D, 0, 4D)$. Moreover, relating to the movement of the object, position information is obtained from the velocity of the object, and the position of the object is overwritten for every time step.

7.2. Results and Discussion. First, from Figure 9, it exhibits that the lift force is changing periodically caused by the flapping of the object. It turns out that the flow is calculated along the object boundary with sufficient accuracy even when a boundary changes for every time. Figure 10 shows the vortical structure by the $\lambda 2$ method, and Figure 11 shows the distribution of sound source on the slice with respect to $X = 2D$ and $Y = 0$. Also, from Figures 10 and 11, it turns out that vortical structure and a sound source change periodically, and they have changed to the complicated flow in a wake. It can be observed that the vortical structure and the sound source which were generated by the flapping wings are convected by the external uniform flow. And it is especially observed that the sound source is generated in the back of the object and also near the wingtip where the angular velocity takes its maximum. Moreover, it turns out that the sound source is generated at a nearly constant period around the whole object and in the wake which is separated from the object.

8. Computation around a Rotating Ellipsoid

8.1. Computational Conditions. Finally, flow computation around the object which imitates the windmill of two-wings is conducted. The initial condition and the boundary condition are set up like the computation around a rotating sphere and an ellipsoid. Figure 12 shows an analysis model. A computational area is shown in Figure 12. An ellipsoid is installed in the center, and it rotates with a constant angular velocity. The ellipsoid has the long radius of D and the short diameter of $0.2D$ in the $Y - Z$ slice, and the short diameter of $0.067D$ in the $X - Z$ slice. It is assumed that a uniform flow in the whole domain is given, and the rotation starts with nondimension angular velocity $\Omega = \mathrm{Re}_r / \mathrm{Re}$ from the position whose angle with the $X - Y$ slice is 90 degrees. The number of grids is $(X, Y, Z) = (170, 140, 140)$, a calculation area is $4D \times 4D \times 4D$, and the center position of the object is $(D, 2D, 2D)$. The regular Reynolds number of external uniform flow is $\mathrm{Re} = 500$, and the Reynolds number which results from rotation is $\mathrm{Re}_r = 500$.

Moreover, as having shown in the analysis of the moving boundary which imitates flapping wings in the preceding section, relating to the movement of the object, position information is obtained from the velocity of the object, and the position of the object is overwritten for every time step.

8.2. Results and Discussion. Figure 13 shows a vortical structure by the IB method for the flow imitating the windmill, and Figure 14 shows the distribution of the Powell sound source at the slices of (a) $X = D$ and $Y = 2D$, (b) $Z = 2D$, (c) $Y = 2D$, and (d) $X = 1.3D$, respectively. From Figure 13, the vortex which occurred by rotation is convected backward by the external uniform flow without breaking off, and it can be observed that the flow has changed to the complicated flow in the wake. This shows that the level set *IB* method can trace and calculate the flow around the moving boundary with sufficient accuracy. Especially it is recognized from Figure 14 that the sound source has occurred near the object, the wake, and the wingtip. Besides, in each slice of figures, the sound source in the wake behaves like the Karman's vortices and occurs far away compared with the case of the flapping wings.

9. Conclusion

In this study, we computed several typical flows around stationary, rotating, or moving objects by using the level set *IB* method. It combines the advantages of level set method and *IB* method in order to be able to capture the shape of object accurately. Also we visualized the vortical structure and obtained the generating mechanism of the sound source.

By this research, the boundary of a moving object is able to be traced with sufficient accuracy. Moreover, the coefficients of drag and lift were obtained for various types of object that is stationary, rotating, or moving in the wide range of the Reynolds number. The code also can visualize the vortical structure and sound source distribution for various conditions, so it can be considered that these are highly useful and innovative.

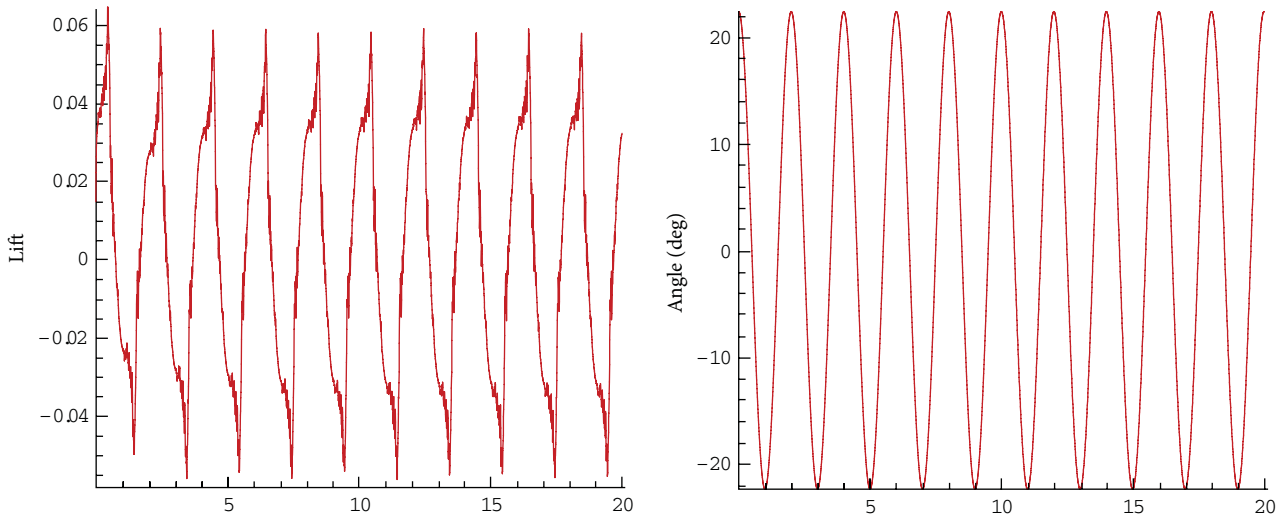

(a) (b)

FIGURE 9: The graph of τ-lift (left) and τ-angle (right).

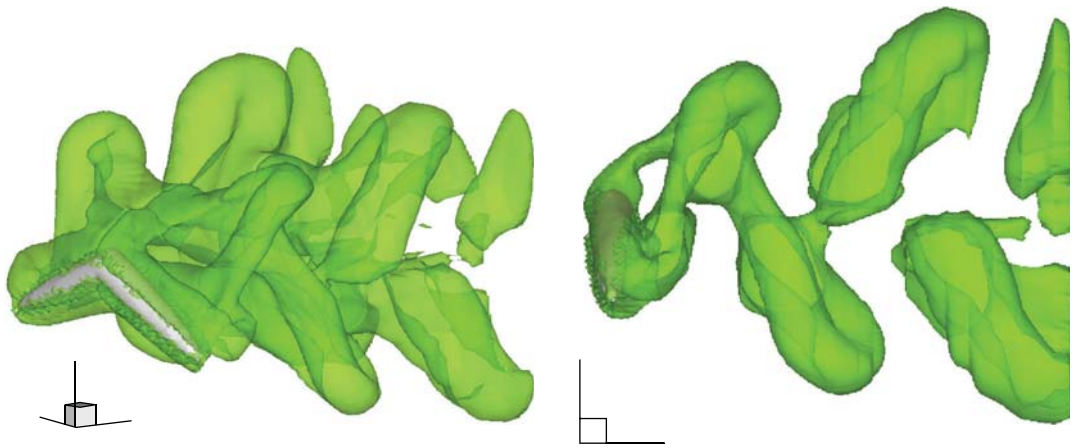

(a) (b)

FIGURE 10: Vortical structure around flapping ellipsoids ($\tau = 17$) (a) $3D$ angle, (b) $X - Z$ slice.

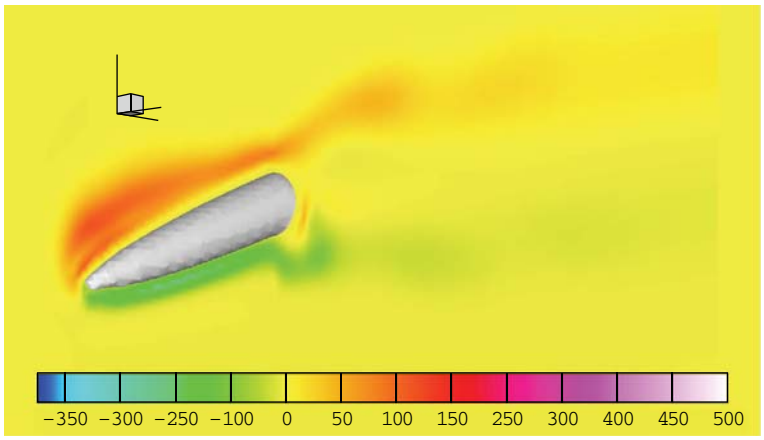

FIGURE 11: Sound source distribution around a flapping ellipsoid ($\tau = 17$).

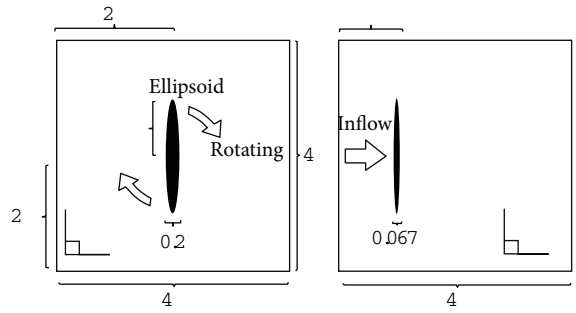

Figure 12: Schematic model of the rotating ellipsoid.

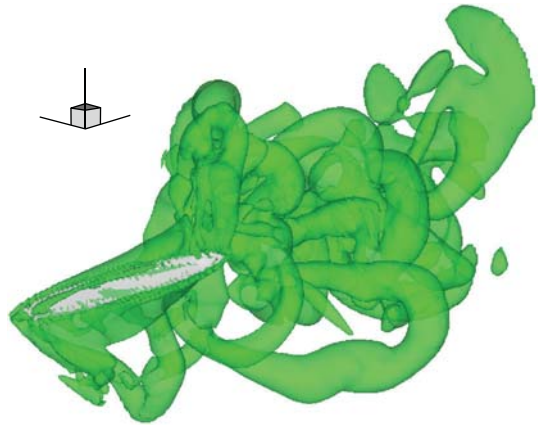

Figure 13: Vortical structure of a rotating ellipsoid ($\tau = 20$).

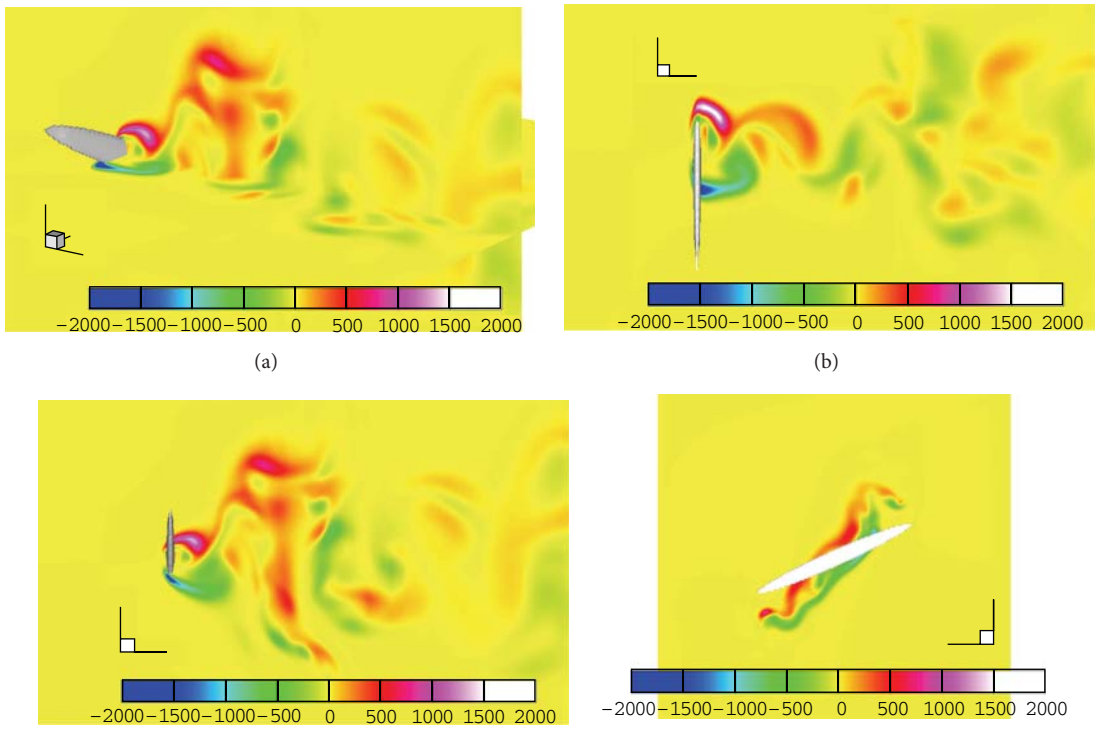

Figure 14: Sound source distribution around rotating ellipsoids ($\tau = 20$). (a) $3D$ angle, (b) $X - Y$ slice, (c) $X - Z$ slice, and (d) $Y - Z$ slice.

Nomenclature

c: Acoustic velocity [m/s]
Cd: Coefficient of drag [—]
D: Characteristic length [—]
$\vec{F}_{IB}$: External force term of IB method [—]
n: Normal vector [—]
n^*: The number of steps of time [—]
n_X: X ingredient of normal vector [—]
n_Z: Z ingredient of normal vector [—]
P: Dimensionless pressure [—]
$p_{i,j}$: Term of shear stress and pressure [—]
Re: Reynolds number [—]
Re_r: Reynolds number due to rotation or flapping [—]
t: Time [s]
T_{ij}: Turbulent flow stress tensor [—]
$\vec{u}$: Velocity vector [m/s]
U: Dimensionless velocity in x-axis [—]
$\vec{U}$: Dimensionless velocity vector [—]
$\vec{U}_B$: Dimensionless velocity vector inside an object [—]
$\vec{U}_{IB}$: Boundary adjacent dimensionless velocity vector [—]
V: Dimensionless velocity in y-axis [—]
v_i: Velocity in the direction of i [m/s]
W: Dimensionless velocity in y-axis [—]
X: Dimensionless coordinates of x-axis [—]
x_i: Coordinates of the direction of x-axis [m]
Y: Dimensionless coordinates of y-axis [—]
Z: Dimensionless coordinates of z-axis [—]
τ: Dimensionless time [—]
ϕ: Level set function[—]
$\phi_{i,k}$: Dimensionless normal distance at the (i, k) point [—]
ϕ_X: X ingredient of dimensionless normal distance [—]
ϕ_Z: X ingredient of dimensionless normal distance [—]
ρ: Density [kg/m^3]
ρ_0: Standard density [kg/m^3]
δ_{ij}: Kronecker delta [—]
$\vec{\omega}$: Vorticity vector [1/s]
ω_0: Angular velocity [rad/s]
Ω: Dimensionless angular velocity [—].

References

[1] C. S. Peskin, "Flow patterns around heart valves: a numerical method," *Journal of Computational Physics*, vol. 10, no. 2, pp. 252–271, 1972.

[2] K. Okita, T. Tawara, and K. Ono, "Development of CFD techniques based on VCAD data," in *RIKEN Symposium*, March 2008.

[3] T. Sato, *Numerical analysis of incompressible flows by an Immersed Boundary Method with the Level Set Method [M.S. thesis]*, Tokyo Metropolitan University, 2010.

[4] M. J. Lighthill, "On sound generated aerodynamically. Part I: General theory," *Proceedings of the Royal Society A*, vol. 221, no. 1107, pp. 564–587, 1952.

[5] A. Powell, "Theory of vortex sound," *Journal of the Acoustical Society of America*, vol. 36, pp. 177–195, 1964.

[6] T. Yoshida, T. Watanabe, and I. Nakamura, "Numerical study of outflow boundary conditions for time-dependent incompressible flows," *Transactions of the Japan Society of Mechanical Engineers B*, vol. 61, no. 588, pp. 2887–2895, 1995.

[7] *JSME Mechanical Engineers' Handbook α4: Fluids Engineering*.

[8] R. Mittal, "A fourier-chebyshev spectral collocation method for simulating flow past spheres and spheroids," *International Journal for Numerical Methods in Fluids*, vol. 30, no. 7, pp. 921–937, 1999.

[9] A. Gilmanov, F. Sotiropoulos, and E. Balaras, "A general reconstruction algorithm for simulating flows with complex 3D immersed boundaries on Cartersian grids," *Journal of Computational Physics*, vol. 191, no. 2, pp. 660–669, 2003.

[10] R. Campregher, J. Militzer, S. S. Mansur, and A. Da Silveira Neto, "Computations of the flow past a still sphere at moderate reynolds numbers using an immersed boundary method," *Journal of the Brazilian Society of Mechanical Sciences and Engineering*, vol. 31, no. 4, pp. 344–352, 2009.

[11] D. A. Jones and D. B. Clarke, "Simulation of flow past a sphere using the fluent code," DSTO Document, 2008.

[12] E. Poon, G. Iaccarino, O. Andrew, and M. Giacobello, "Numerical studies of high Reynolds number flow past a stationary and rotating sphere," in *Proceedings of the 7th International Conference on CFD in the Minerals and Process Industries*, Melbourne, Australia, 2009.

[13] J. Jeong and F. Hussain, "On the identification of a vortex," *Journal of Fluid Mechanics*, vol. 285, pp. 69–94, 1995.

[14] H. Sakamoto and H. Haniu, "A study on vortex shedding from spheres in a uniform flow," *Journal of Fluids Engineering*, vol. 112, no. 4, pp. 386–392, 1990.

Hindawi Publishing Corporation
Advances in Mechanical Engineering
Volume 2013, Article ID 493212, 8 pages
http://dx.doi.org/10.1155/2013/493212

Research Article

Large Eddy Simulation of Inertial Particle Preferential Dispersion in a Turbulent Flow over a Backward-Facing Step

Bing Wang, Huiqiang Zhang, and Xilin Wang

School of Aerospace, Tsinghua University, Beijing 100084, China

Correspondence should be addressed to Bing Wang; wbing@mail.tsinghua.edu.cn

Received 11 January 2013; Accepted 9 April 2013

Academic Editor: Shuyu Sun

Large eddy simulation of inertial particle dispersion in a turbulent flow over a backward-facing step was performed. The numerical results of both instantaneous particle dispersion and two-phase velocity statistics were in good agreement with the experimental measurements. The analysis of preferential dispersion of inertial particles was then presented by a wavelets analysis method for decomposing the two-phase turbulence signal obtained by numerical simulations, showing that the inertial particle concentration is separation from the Gaussian random distribution with very strong intermittencies. The statistical PDF of vorticity seen by particles shows that the inertial particles tend to accumulate in low vorticity regions where $\nabla \mathbf{u} : \nabla \mathbf{u}$ is larger than zero. The concentration distribution of particle preferential dispersion preserves the historical effects. The research conclusions are useful for further understanding the two-phase turbulence physics and establishing accurate engineering prediction models of particle dispersion.

1. Introduction

Recently, inertial particles have been found to be asymmetrically dispersed in a multiscale coherent turbulence field. This kind of particle uneven dispersion cannot be revealed by the statistical Fickian diffusion law, because the diffusion models fail to take into account the particles dispersion dominated by the multiscale turbulence structures and the effects of damping or distortion on turbulent eddies by particles clusters.

Some researches, by means of numerical simulation and experimental measurements, have been carried out on particles asymmetric dispersion in free shear flows which are dominated by large-scale vortexes, for instance, Kobayashi et al. [1], Lazaro and Lasheras [2, 3], Tang et al. [4], Longmire and Eaton [5], Luo et al. [6, 7], and Vuorinen et al. [8]. They found that small inertial particles were flung away from the vortex cores and collected in rings surrounding the vortices in many cases. By using Direct Numerical Simulation (DNS) for homogeneous isotropic turbulence, Squires and Eaton [9] and Lian-Ping Wang and Maxey [10] also found that high and low particle concentrations appear in convergence zones and eddies, respectively, and at the same time local particle concentration is up to 30 times of the mean concentration, when the particle Stokes number is about one based on the Kolmogorov time scale. However, understanding of inertial particle dispersion in turbulent flows is not well presented.

Fessler et al. [11] conceptually proposed the particle preferential concentration (Figure 1(a)) through the experimental investigation of a turbulent channel flow. They observed that particles are dispersed in turbulence neither uniformly nor randomly, preferring some characteristic regions, resulting in particles "clouds." When the particle Stokes number is approximately one, the particles have the maximum departure from a random distribution. Since then, the particle preferential dispersion has become one of the highlights in studies of two-phase turbulent flows [12–14]. Winkler et al. [15] demonstrated that particles accumulated in regions of low vorticity by applying one-way coupled large eddy simulation in a fully developed turbulent square duct flow. Wang and his coworkers [16–20] studied the particle preferential dispersion in the turbulent flows over a backward-facing step and particle-laden turbulent channel flows. They also performed numerical and experimental investigations on particle preferential dispersion in turbulent

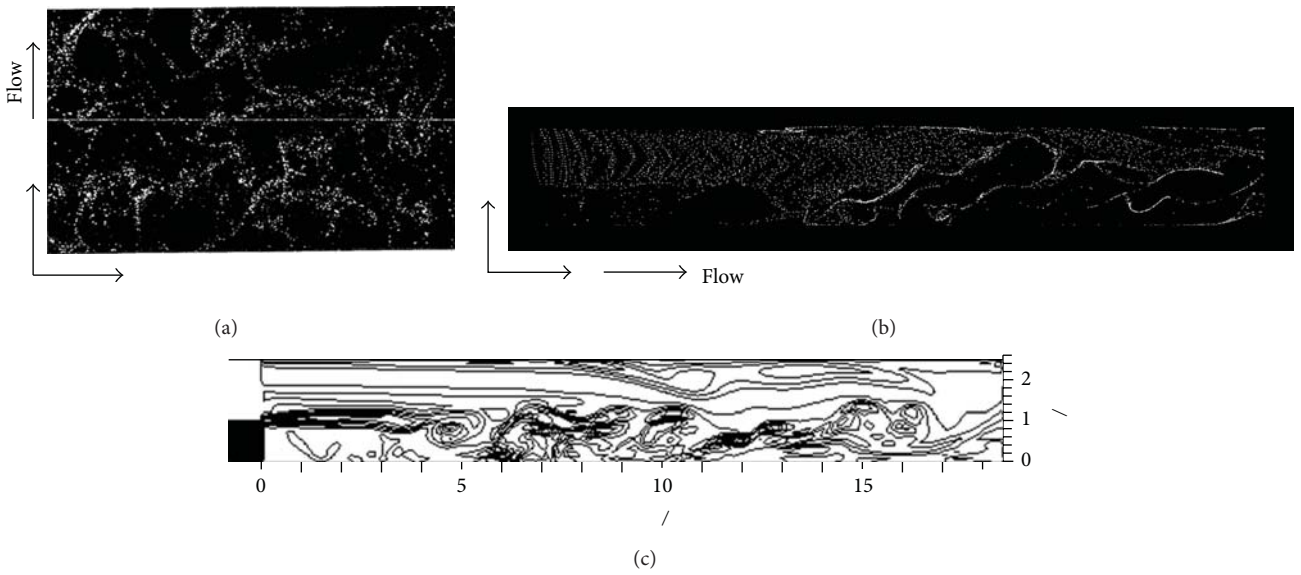

Figure 1: Particle preferential dispersion in turbulent flow fields. (a) Experimental snapshot picture by Fessler et al. in a turbulent channel flow (in [11, Figure 5]) for 28 μm lycopodium particles with Stokes number 1.7. (b) Scatter of 20 μm glass particles with Stokes number 1.11. (c) Vorticity isocontours.

jets [21–23]. Although investigations on the particle dispersion, especially the inertiaparticle preferential dispersion, have become increasingly popular, the characteristics and mechanisms of preferential dispersion are still not very clear, especially in turbulent flows over a backward-step laden with initial particles, which is an important prototype flow widely occurring in industrial and environmental engineering.

In this paper, a large eddy simulation is first performed to numerically compute two-phase turbulent flows over a backward-facing step, and then the analysis is done based on the numerical results. The temporal and spatial evolutions of preferential distribution of particle dispersion are studied by using the wavelets analysis and PDF statistical methods.

2. Mathematical Descriptions and Numerical Results

2.1. Numerical Methods. Large eddy simulation is adopted to simulate the gas-phase turbulence. The flow field variables are separated into a large-scale component and a subgrid-scale (SGS) component by filtering. The SGS stress term is modeled by the Smagorinsky model. The governing equations are written as

$$\frac{\partial \overline{u}_i}{\partial x_i} = 0,$$
$$\frac{\partial \overline{u}_i}{\partial t} + \frac{\partial \overline{u}_i \overline{u}_j}{\partial x_j} = -\frac{1}{\rho}\frac{\partial p}{\partial x_i} + \frac{\partial}{\partial x_j}\left[\frac{\mu^*}{\rho}\left(\frac{\partial \overline{u}_i}{\partial x_j} + \frac{\partial \overline{u}_j}{\partial x_i}\right)\right], \quad (1)$$

where the efficient viscosity $\mu^* = \mu/\mathrm{Re} + \mu_T$; the Reynolds number is given by $\mathrm{Re} = \rho U_0 H/\mu$, where μ is the molecular kinematic viscosity. H is the channel height; U_0 is the channel inlet mean velocity.

The eddy viscosity μ_T is defined as

$$\mu_T = \rho C_{\mathrm{SGS}} \Delta^2 \left|\overline{\mathbf{S}}\right| = \rho C_{\mathrm{SGS}} \Delta^2 \sqrt{2\overline{S}_{ij}\overline{S}_{ij}}, \quad (2)$$

where C_{SGS} is an empirical constant, taken as 0.13 in this paper, and the strain rate tensor is taken as

$$\overline{S}_{ij} = \frac{1}{2}\left(\frac{\partial \overline{u}_i}{\partial x_j} + \frac{\partial \overline{u}_j}{\partial x_i}\right). \quad (3)$$

Equation (1) is solved numerically using the fractional step method as described by Wu et al. [24]. A nonsolenoidal velocity field $\mathbf{V}^{n+1/2}$ is projected onto a solenoidal field by a scalar quantity Φ, which is related to the pressure term P. The continuity equation is satisfied through a Poisson equation for the pressure correction. The viscous term is discretized using second-order central difference. In order to reduce the aliasing errors and instability [25], a second order hybrid scheme is adopted for the advective term. The momentum equations are integrated explicitly using a third-order Runge-Kutta algorithm and the Poisson equation for pressure is solved using series expansions in the streamwise and spanwise directions with tridiagonal matrix inversion.

A Lagrangian approach is used to track each particle released in the flow field. The drag force is taken as the dominant force on each particle in this paper. The nondimensional dynamic equations for a particle along its trajectory are

$$\frac{d\mathbf{X}_p}{dt} = \mathbf{V}_p,$$
$$\frac{d\mathbf{V}_p}{dt} = \frac{\mathbf{F}}{(1/6)\,\pi d_p^3\,\rho_p}, \quad (4)$$

where $\mathbf{V}_p$ is the instantaneous particle velocity and $\mathbf{F}$ is the drag force on the particle such that

$$\mathbf{F} = C_d \cdot \frac{1}{4}\pi d_p^2 \cdot \frac{1}{2}\left|\mathbf{V}_f - \mathbf{V}_p\right|\left(\mathbf{V}_f - \mathbf{V}_p\right). \quad (5)$$

$\mathbf{V}_f$ is the instantaneous grid-scale (or, the resolved scale) fluid velocity. C_d is the drag coefficient given by

$$C_d = \begin{cases} \dfrac{24}{\mathrm{Re}_p}\left(1 + \dfrac{\mathrm{Re}_p^{2/3}}{6}\right), & 1 < \mathrm{Re}_p < 1000, \\ \dfrac{24}{\mathrm{Re}_p}, & \mathrm{Re}_p \le 1. \end{cases} \quad (6)$$

Re_p is the particle Reynolds number defined as

$$\mathrm{Re}_p = \frac{\rho\left|\mathbf{V}_f - \mathbf{V}_p\right| d_p}{\mu}. \quad (7)$$

The effects of subgrid-scale (SGS) turbulence on particle motion are neglected in this study. For the high-inertia particles, the dispersion of particles by turbulence mainly happens at the grid scale, that is, resolved scale, contrary to the expectation that the dispersion mainly happens at scales around or smaller than the subgrid-scale. Large-scale turbulence structures that disperse particles are the primary modes of particle dispersion. Particle inertia plays an important role in filtering turbulence fluctuation, which prevents couplings of SGS components from causing significant effects on turbulence intensities in the high-frequency sphere. Negligibly small differences were found between the statistical velocity results considering the SGS coupling and those considering only the grid-scale coupling mean velocity, which can be referred in to [19].

The particle Stokes number, used to characterize particle motion, is defined as

$$\mathrm{St} = \frac{\tau_p}{\tau_f}, \quad (8)$$

where $\tau_p = \rho_p d_p^2/(18\mu)$ is the particle relaxation or aerodynamic response time scale and $\tau_f = H/U_0$ is the fluid time scale.

Impactions between particles and the wall are considered to be fully elastic. Therefore, only the wall-normal component of particle velocity is reverse in the direction after colliding with the wall

$$\begin{aligned} {V_{p1}}^c &= {V_{p1}}^0, \\ {V_{p2}}^c &= -{V_{p2}}^0, \\ {V_{p3}}^c &= {V_{p3}}^0. \end{aligned} \quad (9)$$

The superscript "c" means the velocity after collision, while "0" means the velocity before collision.

The intercollisions of particle-particle are neglected in this study. The effects of interparticle collisions on evolutions of preferential dispersion are not discussed in the present paper.

The detailed numerical procedure of two-phase governing equations can be referred to in [16, 19].

2.2. Numerical Results. In this paper, the flow Reynolds number is taken as 13,800 for the simulated two-phase turbulent flows over a backward-facing step. Particles, made of glass ($\rho_p = 2500\ \mathrm{kg/m^3}$), in diameters of 2, and 20 micrometers are chosen in the simulations.

The large eddy simulation was verified and validated by comparing the two-phase velocity statistics, detailed analysis is referred to in [16].

The numerical results of particle dispersion are compared with the previous experimental results, shown in Figure 1. 20 μm glass particles, with the particle Stokes number around 1, show preferential distribution in turbulent flow fields. The instantaneous gas-phase vorticity iso-contour at an instant time is shown in Figure 1(c). It is shown that the large eddy vortexes evolve spatially with the separation behind the step and the reattachment on the lower wall.

The particle preferential dispersion can usually occur in a limited range of particle Stokes number, which depends on the turbulence and particle properties. Therefore, the snapshot picture in Figure 1 cannot be implemented in all different particles, but represents the general characteristics of preferential dispersion for particles that can occur. In particular, for the present study in the Figure 1, the particle Stokes number is around 1 both for the experimental observation and numerical simulation. That is to say, once the particles disperse preferentially in turbulence, the snapshot like Figure 1 can represent the basic contours.

3. Analysis of Particle Preferential Dispersion

The temporal signals of turbulence sampled at some typical positions in the flow field, shown in Figure 2(a), are obtained and analyzed, for example, at a position ($x/H = 12$, $y/H = 1$, $z/H = 2$) in the main developing region. The multiscale analysis of turbulence is based on wavelets methods proposed by Farge and coworkers [26, 27].

The wavelet coefficients in wavelet analysis represent the energy in the corresponding scales. Therefore, they can show the energy cascades of turbulence in different scales and also the intermittency of turbulence energy. As shown in Figure 2(b), the signal is decomposed in different scales by means of wavelets analysis. The low frequency large scales are split into high-frequency abundant small scale structures, known as the classical "vortex cascade." Energy is transferred from large-scale eddies to small scale eddies.

Particles scatters together with the isolines of gas-phase vorticity are shown in Figure 3(a), where dots represent particles. By counting the particle number in each cell, particle number density is obtained. The particle number of 20 μm glass particles at a fixed cell as a function of time is shown in Figure 3(b). It is found that particle number density temporal signal is not steady, containing very strong fluctuations.

The wavelets transform is used to analyze the particle number density signal, for example, the glass particles. The

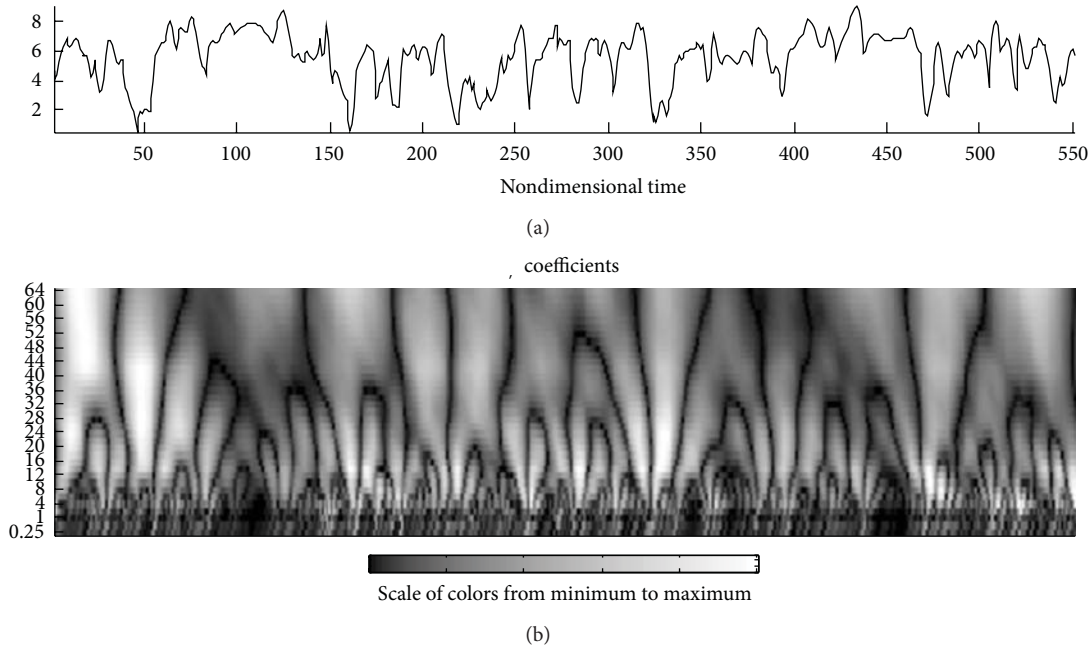

Figure 2: Wavelets analysis of the turbulence temporal signal at a specified position: (a) the temporal turbulence signal, (b) the grey contour of wavelets coefficients in different scales.

skewness factor and flatness factor, which can examine the intermittency contained in the signal, according to the wavelets coefficients $W(a,t)$ at time t and scale a, are defined as

$$\begin{aligned} \mathrm{FF} &= \frac{\left\langle |W(a,t)|^4 \right\rangle_t}{\left\langle |W(a,t)|^2 \right\rangle_t^2}, \\ \mathrm{SF} &= \frac{\left\langle |W(a,t)|^3 \right\rangle_t}{\left\langle |W(a,t)|^2 \right\rangle_t^{3/2}}. \end{aligned} \tag{10}$$

The values of FF and SF are 3 and 0, respectively, for a signal obeying Gauss random distribution. As shown in Figures 3(c) and 3(d), the particle concentration signal is separation from the Gaussian random distribution, containing very strong intermittencies, correlated with turbulence structures, which indicates that the particles preserve the preferential dispersion in turbulence.

The preferential distribution is dominated by both turbulent coherent structures and particle inertia. The particle preferential concentration characteristics are theoretically analyzed as follows.

Let $\mathbf{V}_p(\mathbf{x},t)$ represent the Eulerian particle velocity field, simply rewritten as $\mathbf{V}_p$. If particle response time is small enough, the Eulerian particle velocity can be expanded as [28]

$$\mathbf{V}_p = \mathbf{u} - \mathbf{a}\tau_{\mathrm{rp}} + \left(\frac{D\mathbf{a}}{Dt} + \mathbf{a}\nabla\cdot\mathbf{u}\right)\tau_{\mathrm{rp}}^2 + O\left(\tau_{\mathrm{rp}}^3\right), \tag{11}$$

where D/Dt is total derivative following the fluid element, and a is the modified acceleration, $\mathbf{a} = D\mathbf{u}/Dt$.

Taking the approximate expression of above equation with accuracy $O({\tau_{\mathrm{rp}}}^2)$ and taking divergence of both sides of simplified equation,

$$\begin{aligned} \nabla\cdot\mathbf{V}_p &= \nabla\cdot\mathbf{u} - \tau_{\mathrm{rp}}\left[\frac{\partial(\nabla\cdot\mathbf{u})}{\partial t} + \nabla\cdot\mathbf{u}\cdot\nabla\mathbf{u}\right] \\ &= -\tau_{\mathrm{rp}}(\nabla\mathbf{u}:\nabla\mathbf{u}) = -\tau_{\mathrm{rp}}\frac{\partial u_j}{\partial x_i}\frac{\partial u_i}{\partial x_j}. \end{aligned} \tag{12}$$

Equation (12) indicates that the Eulerian particle velocity field is not divergence-free. If the Eulerian formulation for the particle velocity field is considered, the particle phase is continually taken as a "pseudo" fluid phase.

The particle-phase continuity equation is written as,

$$\frac{\partial\rho_p}{\partial t} + \nabla\cdot\left(\rho_p\mathbf{V}_p\right) = 0, \tag{13}$$

where ρ_p is particle-phase density and $\mathbf{V}_p$ is particle-phase velocity. Particle-phase density ρ_p is defined according to $\rho_p = n_p m_p$, where n_p is particle number density and m_p is particle mass. We can obtain

$$\frac{\partial n_p}{\partial t} + \nabla\cdot\left(n_p\mathbf{V}_p\right) = 0. \tag{14}$$

From (14), the particle number density can be obtained as

$$\frac{\partial n_p}{\partial t} = -n_p\nabla\cdot\mathbf{V}_p - \mathbf{V}_p\nabla\cdot n_p = -n_p\nabla\cdot\mathbf{V}_p. \tag{15}$$

Substitute (12) for (15) and settle to obtain

$$\frac{dn_p}{n_p} = -\nabla\cdot\mathbf{V}_p dt = -\tau_{\mathrm{rp}}\frac{\partial u_j}{\partial x_i}\frac{\partial u_i}{\partial x_j}dt. \tag{16}$$

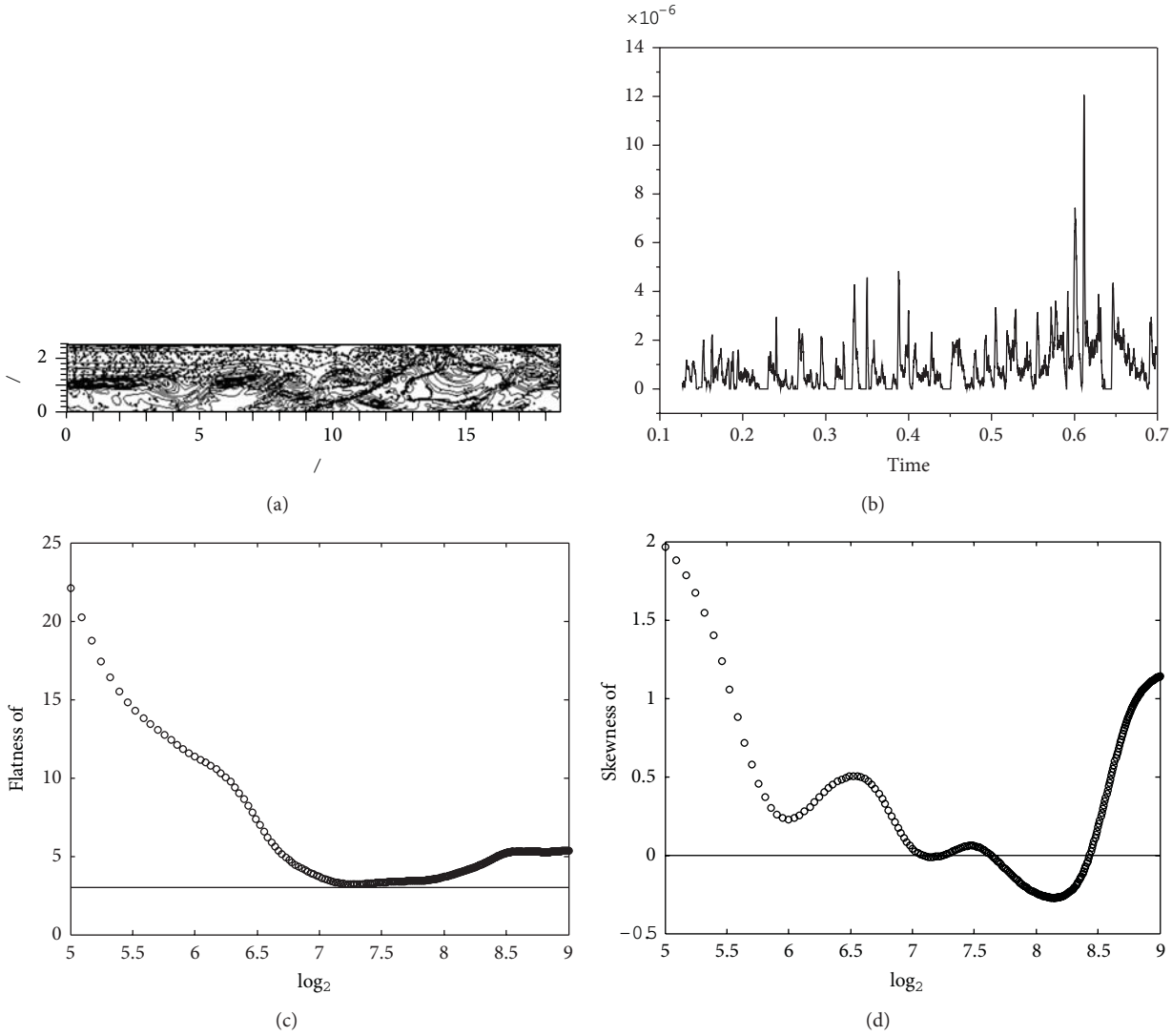

Figure 3: Particle concentration analysis: (a) particle scatters, (b) a temporal signal of particle number density at a fixed cell, (c) flatness factor obtained by means of wavelets transform, (d) skewness factor obtained by means of wavelets transform.

To estimate the particle number density, that is, the particle volume concentration, at location $\mathbf{x}$ and time t, one has to trace back to the previous time t_0 and to the location $\mathbf{x}_0$, such that the trajectory starts at $-t_0$ and location $\mathbf{x}_0$ ends up at t at location $\mathbf{x}$. The particle number density at present time is given by

$$n_p(\mathbf{x}, t) = n_0 \tau_{\mathrm{rp}} \exp\left(\int_{-t_0}^{0} \frac{\partial u_j}{\partial x_i} \frac{\partial u_i}{\partial x_j} dt' \right). \tag{17}$$

From the above analysis, it is summarized as follows.

(1) Particles are advected by an effective velocity field $\mathbf{V}_p$, which is proved as not divergence-free, that is, $\nabla \cdot \mathbf{V}_p \neq 0$ even if the surrounding fluid is incompressible, that is, $\nabla \cdot \mathbf{u} = 0$.

(2) The inertial particle concentration distribution has the historical effects; that is, the present particle concentration is obtained considering the previous particle concentration distribution.

The vorticity PDF distribution is compared in a specified window field in the region $x/H = [7, 12]$ and $y/H = (0, 2.5)$ in the central plane in the spanwise direction, in order to reveal where particles preferentially accumulate in the turbulent flow fields. The PDFs of both continuous-phase fluid vorticity at each computation grid point and vorticity seen by particles at each particle position, interpolated from the value of nearby points by a 6th order Lagrange interpolation method, are statistically obtained.

Figure 4 shows the results of PDF statistics at two different instantaneous dimensionless times $t = 135$ and $t = 142$, for two different particles in diameter of 2 μm whose particle Stokes number is 0.11 and 20 μm whose particle Stokes number is 1.1.

The PDF of vorticity seen by particles shows a concentrated value in the low vorticity region, compared with that

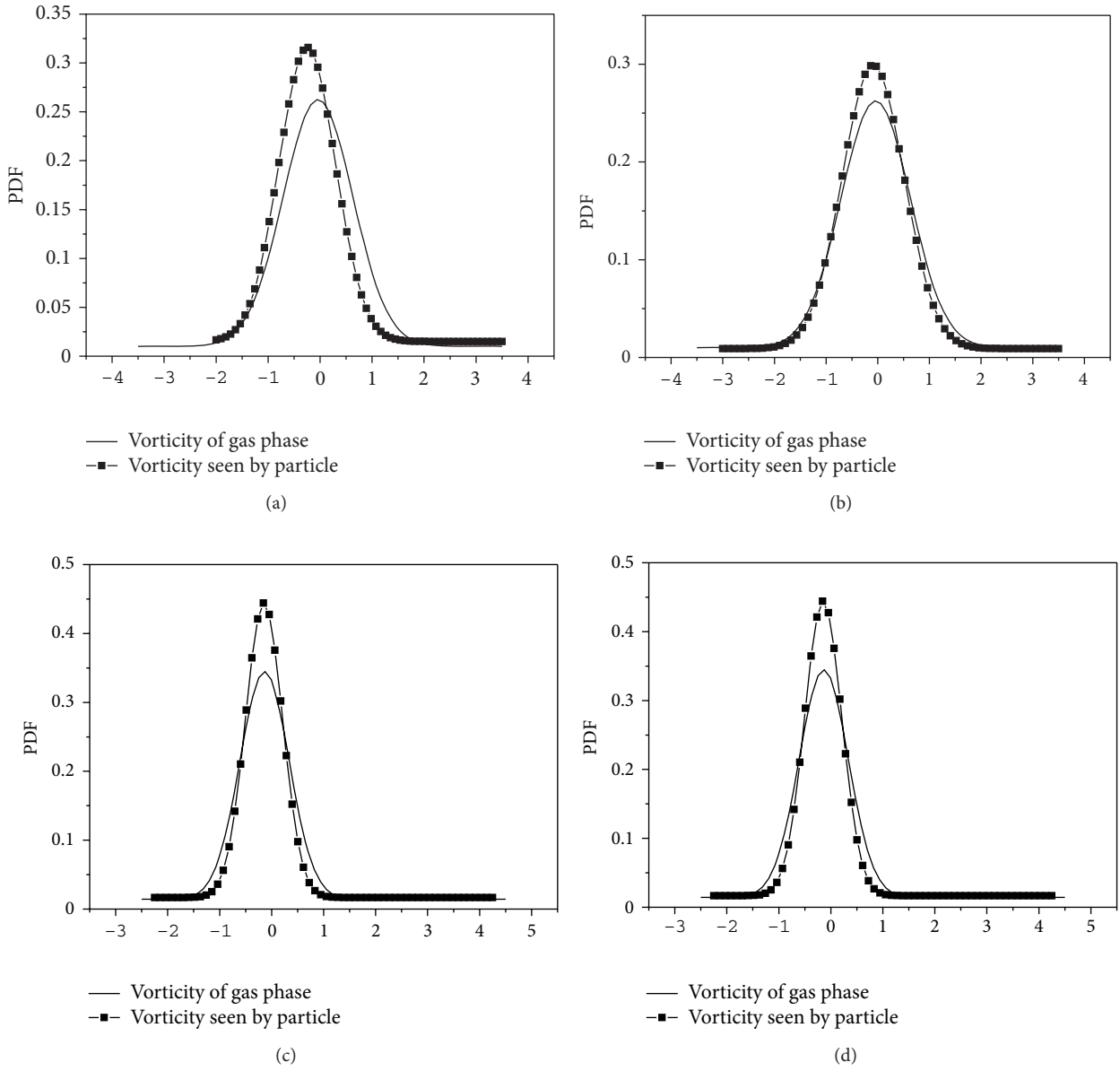

Figure 4: Comparison of PDF of vorticity of fluid phase and vorticity seen by particles in a specified window field: (a) and (b) $t = 135$, (c) and (d) $t = 142$, (a) and (c) laden with 2 μm glass particles, (b) and (d) laden with 20 μm glass particles.

of fluid phase. Particles accumulate around the circumference of a vortex and the braid between two vortices. For different particles in diameters, with different inertia, the dispersion distinguishes from each other in these special regions, due to different response to turbulence.

There are differences of PDF distribution between fluid vorticity and fluid vorticity seen by particles. In general, the PDF of fluid vorticity seen by particles is more concentrated and has a higher value. The difference is induced by the inertial particle's crossing trajectory effects. Inertial particles are supposed to follow the fluid inertia-free particles initially, but they will subsequently separate from the initial fluid particles due to the inertia and lag response. Once these particles are flung to the edges of large vortices, they will see lower vorticity.

The analyses of particle concentration in other time instants are also performed and the same conclusions are drawn. The particle preferential distribution in turbulence is dependent on the particle inertia and turbulent transport.

4. Conclusions and Remarks

The inertial particle dispersion in turbulent flows over a backward-facing step is simulated by means of large eddy simulation with Lagrangian particle trajectory method. The particle instantaneous preferential dispersion is obtained numerically and agrees with the experimental flow visualization.

The particle concentration increases in regions with low vorticity, corresponding to the edge of vortex, and it

decreases in regions with high vorticity, corresponding to the center of vortex. The inertial particle dispersion will become asymmetric and preferential at the next instants, even if the initial particle distribution is uniformed at an arbitrary instant t_0. The particle preferential concentration preserves the historical effects.

The particles preferential dispersion depends on not only the characteristics of gas-phase flow, the multiscale structures, but also the properties of particles themselves, the inertia. τ_{rp} is a key parameter in analyzing the particle preferential dispersion. For the smaller particles, the preferential concentration is retrained for small τ_{rp}. For the larger particles, they do not respond fluid fields quickly due to their large inertia, and their instantaneous distribution does not show a preferential concentration. For the medium particles, their instantaneous distribution shows obvious preferential concentration due to proper τ_{rp}.

Furthermore, the smaller particles accumulate around the circumference of a core of a vortex, which leaves some small "blank" regions in which few or none solid particles are found. The median particles accumulate around the circumference of a vortex and along the braid between two vortices, which leaves some large "blank" regions in the flow fields.

The present conclusions are valuable for establishing more accurate particle dispersion models applied in particle-laden turbulent flows in practice. The analyses are performed in an individual high flow Reynolds number in the present study. Even if the particle preferential dispersion is found commonly to exist in high Reynolds number turbulent flows, the effects of flow Reynolds number on particle dispersion are to be investigated further.

Acknowledgments

The first author gratefully acknowledges the financial support partially by NSFC under Grants. nos. 50706021 and 11132005 and partially by the Ph.D. Programs Foundation of Ministry of Education of China under Grant. no. 20070003018.

References

[1] H. Kobayashi, S. M. Masutani, S. Azuhata et al., "Dispersed phase transport in a plane mixing layer, transport phenomena in turbulent flows," in *Transport Phenomena in Turbulent Flows-Theory, Experiment, and Simulations*, M. Hirata and N. Kasagi, Eds., pp. 433–452, Routledge, New York, NY, USA, 1988.

[2] B. J. Lazaro and J. C. Lasheras, "Particle dispersion in the developing free shear layer—part 1: unforced flow," *Journal of Fluid Mechanics*, vol. 235, pp. 143–178, 1992.

[3] B. J. Lazaro and J. C. Lasheras, "Particle dispersion in the developing free shear layer—part 2: forced flow," *Journal of Fluid Mechanics*, vol. 235, pp. 179–221, 1992.

[4] L. Tang, F. Wen, Y. Yang, C. T. Crowe, J. N. Chung, and T. R. Troutt, "Self-organizing particle dispersion mechanism in a plane wake," *Physics of Fluids A*, vol. 4, no. 10, pp. 2244–2251, 1992.

[5] E. K. Longmire and J. K. Eaton, "Structure of a particle-laden round jet," *Journal of Fluid Mechanics*, vol. 236, pp. 217–257, 1992.

[6] K. Luo, J. Fan, and K. Cen, "Pressure-correlated dispersion of inertial particles in free shear flows," *Physical Review E*, vol. 75, no. 4, Article ID 046309, 2007.

[7] K. Luo, M. Klein, J. R. Fan, and K. F. Cen, "Effects on particle dispersion by turbulent transition in a jet," *Physics Letters A*, vol. 357, no. 4-5, pp. 345–350, 2006.

[8] V. Vuorinen, H. Hillamo, O. Kaario, M. Larmi, and L. Fuchs, "Large eddy simulation of droplet stokes number effects on turbulent spray shape," *Atomization and Sprays*, vol. 20, no. 2, pp. 93–114, 2010.

[9] K. D. Squires and J. K. Eaton, "Particle response and turbulence modification in isotropic turbulence," *Physics of Fluids A*, vol. 2, no. 7, pp. 1191–1203, 1990.

[10] Lian-Ping Wang and M. R. Maxey, "Settling velocity and concentration distribution of heavy particles in homogeneous isotropic turbulence," *Journal of Fluid Mechanics*, vol. 256, pp. 27–68, 1993.

[11] J. R. Fessler, J. D. Kulick, and J. K. Eaton, "Preferential concentration of heavy particles in a turbulent channel flow," *Physics of Fluids*, vol. 6, no. 11, pp. 3742–3749, 1994.

[12] Q. Wang and K. D. Squires, "Large eddy simulation of particle deposition in a vertical turbulent channel flow," *International Journal of Multiphase Flow*, vol. 22, no. 4, pp. 667–682, 1996.

[13] W. S. J. Uijttewaal and R. V. A. Oliemans, "Particle dispersion and deposition in direct numerical and large eddy simulations of vertical pipe flows," *Physics of Fluids*, vol. 8, no. 10, pp. 2590–2604, 1996.

[14] H. Zhang and G. Ahmadi, "Aerosol particle transport and deposition in vertical and horizontal turbulent duct flows," *Journal of Fluid Mechanics*, vol. 406, pp. 55–80, 2000.

[15] C. M. Winkler, S. L. Rani, and S. P. Vanka, "Preferential concentration of particles in a fully developed turbulent square duct flow," *International Journal of Multiphase Flow*, vol. 30, no. 1, pp. 27–50, 2004.

[16] H. Zhang, B. Wang, C. Chan, and X. Wang, "Large Eddy Simulation of a dilute particle-laden turbulent flow over a backward-facing step," *Science in China E*, vol. 51, no. 11, pp. 1957–1970, 2008.

[17] B. Wang, H. Q. Zhang, and X. L. Wang, "Large eddy simulation of particle response to turbulence along its trajectory in a backward-facing step turbulent flow," *International Journal of Heat and Mass Transfer*, vol. 49, no. 1-2, pp. 415–420, 2006.

[18] B. Wang, "Inter-phase interaction in a turbulent, vertical channel flow laden with heavy particles—part II: two-phase velocity statistical properties," *International Journal of Heat and Mass Transfer*, vol. 53, no. 11-12, pp. 2522–2529, 2010.

[19] B. Wang, "Inter-phase interaction in a turbulent, vertical channel flow laden with heavy particles—part I: numerical methods and particle dispersion properties," *International Journal of Heat and Mass Transfer*, vol. 53, no. 11-12, pp. 2506–2521, 2010.

[20] H. Q. Zhang, M. Liu, B. Wang et al., "Dense gas-particle flow in vertical channel by multi-lattice trajectory model," *Science China*, vol. 55, pp. 542–567, 2012.

[21] W. Bing, Z. Huiqiang, and W. Xilin, "Large-eddy simulation of near-field dynamics in a particle-laden round turbulent jet," *Chinese Journal of Aeronautics*, vol. 23, no. 2, pp. 162–169, 2010.

[22] B. Wang, H. Zhang, Y. Liu, X. Yan, and X. Wang, "Particle modulations to turbulence in two-phase round jets," *Acta Mechanica Sinica*, vol. 25, no. 5, pp. 611–617, 2009.

[23] H. Q. Zhang, Y. Rong, B. Wang et al., "Large eddy simulation of a 3-D spatially developing turbulent round jet," *Science China*, vol. 54, pp. 2916–2934, 2011.

[24] X. Wu, K. D. Squires, and Q. Wang, "Extension of the fractional step method to general curvilinear coordinate systems," *Numerical Heat Transfer B*, vol. 27, no. 2, pp. 175–194, 1995.

[25] A. G. Kravchenko and P. Moin, "On the effect of numerical errors in large Eddy simulations of turbulent flows," *Journal of Computational Physics*, vol. 131, no. 2, pp. 310–322, 1997.

[26] M. Farge, "Wavelet transforms and their applications to turbulence," *Annual Review of Fluid Mechanics*, vol. 24, no. 1, pp. 395–457, 1992.

[27] K. Schneider, M. Farge, A. Azzalini, and J. Ziuber, "Coherent vortex extraction and simulation of 2D isotropic turbulence," *Journal of Turbulence*, vol. 7, pp. 1–24, 2006.

[28] J. Ferry and S. Balachandar, "A fast Eulerian method for disperse two-phase flow," *International Journal of Multiphase Flow*, vol. 27, no. 7, pp. 1199–1226, 2001.

Hindawi Publishing Corporation
Advances in Mechanical Engineering
Volume 2013, Article ID 950765, 8 pages
http://dx.doi.org/10.1155/2013/950765

Research Article

Numerical Simulation of Mixed Convection in a Rotating Cylindrical Cavity: Influence of Prandtl Number

Gustavo Urquiza, Laura Castro, Juan García, Miguel Basurto, and Enoc Bogarin

Universidad Autónoma del Estado de Morelos, Centro de Investigación en Ingeniería y Ciencias Aplicadas, Avenida Universidad 1001, Colonia Chamilpa, 62209 Cuernavaca, MOR, Mexico

Correspondence should be addressed to Laura Castro; lauracg@uaem.mx

Received 25 January 2013; Accepted 23 March 2013

Academic Editor: Bo Yu

A numerical study of the flow and heat transfer on a rotating cylindrical cavity solving the mass, momentum, and energy equations is presented in this work. The study describes the influence of the Prandtl number on flow in critical state on a cavity which contains a cooling fluid. Problem studied includes Prandtl numbers $0.001 < \mathrm{Pr} > 15$, aspect ratios $0.25 < A > 1$, and Reynolds numbers $0.001 < \mathrm{Re} > 600$. Differential equations have been discretised using the finite differences method. The results show a tendency followed by heat transfer as the Reynolds number increases from 300 to 600; in addition, emphasis on the critical values of the Rayleigh number for small Prandtl numbers shows that thermal instability in mixed convection depends on the Prandtl number.

1. Introduction

Flows in mixed convection heat transfer frequently happen in engineering systems and natural phenomena. An important issue is the understanding of this phenomenon on cavities, which have applications in the growth of crystals, glass production, flows in nuclear reactors, and atmospheric prediction among others. For the development of new technologies in gas turbines design, which operate at high temperatures, studies of the cooling systems, generators, and rotors are necessary. Optimal design of these cooling systems will be able to improve heat transfer in the region of the rotor. Due to the centrifugal acceleration and temperature difference in the walls on cavity, a flow induced by the action of the centrifugal and body forces will occur, becoming an unstable and oscillating characteristic for the critical regime.

The study of Laje et al. [1] shows the effect of the Prandtl number and the Rayleigh number on the convection of Bénard and concludes that the critical Rayleigh number Ra_c is increased substantially as the Prandtl number decreases to small values. Verhoeven [2] and Soberman [3] investigated the values of the Ra_c for $\mathrm{Pr} = 0.025$ (liquid metals like mercury and sodium), and Bertin and Hiroyuki [4], on the other hand, studied the influence of the Prandtl number, in the rank of 0,001–1000 on the critical Rayleigh number. Chao et al. [5] developed a study of the influence of the Prandtl number on the convection of Bénard, reaching the same conclusion of the study of Laje et al. [1].

A numerical study presented/displayed by Gelfgat et al. [6] shows the transition of stable convective flow oscillating for small Prandtl numbers (Pr = 0,0 to 0,015) in rectangular cavities laterally warmed up in the $0.1 < A > 1$ interval. They showed that the oscillating instabilities were a product of a supercritical bifurcation caused by small infinitesimal disturbances, which means that the heat transfer has a strong effect of the instability of small values of Prandtl numbers. Also, they showed that the critical frequencies of oscillation as well as the number of critical Grashof are responsible for the change for the aspect ratio.

In other studies, Zhang and Nguyen and Durand et al. [7, 8] have investigated the forced convection heat transfer between two short concentric cylinders. The inner-rotating cylinder drives the forced flow, while the end plates and the outer cylinder are stationary. The annulus is filled with a heat-generating fluid where the internal heat source may be due to viscous dissipation or to exothermic reactions. The normal modes (with an inlet flow along the end plates) were studied in terms of the Reynolds and Prandtl numbers for a radius

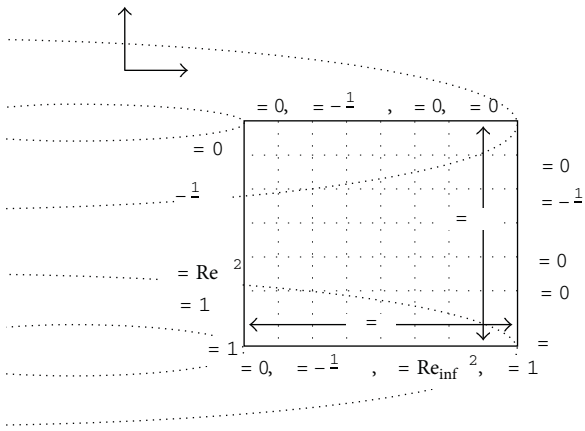

Figure 1: Geometry of the system.

ratio $R = 2$ and an aspect ratio $H = 3.8$. Was found that as flows develops on 2-cell, 4-cell and 2-cell regimes; as Re increases from zero. These results are consistent with the general description given in the papers of Benjamin [9, 10] on the bifurcation phenomena in viscous flows between short cylinders.

Existing studies have thus confirmed the importance and complex interrelation between the centrifugal force due to rotation and the viscous force at the end plate. As a consequence, the flows have been developed in a very different way compared to the case of pure Taylor vortices, and the concepts of primary flow, secondary flow, normal and anomalous modes have been theoretically developed and experimentally realized in an attempt to construct a unified picture of the complex bifurcation phenomena in finite-dimensional systems.

In spite of the works previously developed, very few of them have focused on the behavior of the flow in cylindrical cavities in rotation. In order to obtain a better understanding of the flow and heat transfer, the behavior of the flow within cylindrical cavities in rotation with emphasis on the effect of the Prandtl number appears in the instability of flow in mixed convection.

2. Description of the Problem

The physical problem studied is schematically shown in Figure 1. The system consists of two vertical concentric cylinders of radii R_i and R_0 and a finite length H. The cylinders are closed by two end plates. The outer cylinder and the end plates are fixed, while the inner cylinder rotates with a constant angular velocity Ω.

The annulus is filled with an incompressible Newtonian fluid with density ρ, viscosity ν, diffusivity α, and thermal expansion coefficient β. All thermophysical properties of the fluid may be considered constant, except the variation of density in the buoyancy force according to the Boussinesq approximation. The two cylinders (rotating walls) are maintained at a same uniform temperature and the end plates (static walls) are perfectly insulated.

For axisymmetric flows, the system may be described by a stream function Ψ, vorticity ω, swirl velocity $U = ru_\theta$, and a temperature field T.

By using the scales R_i^2/ν for time, R_i for length, ν/R_i for velocity, and SR_i^2/k for temperature, the nondimensional governing equations may be written as follows:

$$\frac{\partial \omega'}{\partial t'} + u'\frac{\partial \omega'}{\partial r'} - \frac{u'\omega'}{r'} + w'\frac{\partial \omega'}{\partial z'} = \frac{2\Gamma'}{r'^3}\frac{\partial \Gamma'}{\partial z'} + \left(\frac{\partial^2 \omega'}{\partial r'^2} + \frac{1}{r'}\frac{\partial \omega'}{\partial r'} + \frac{\partial^2 \omega'}{\partial z'^2}\right) - \frac{u'\omega'}{r'^2} - Gr\frac{\partial T'}{\partial r'},$$

$$\frac{\partial^2 \psi'}{\partial z'^2} + \frac{\partial^2 \psi'}{\partial r'^2} - \frac{1}{r'}\frac{\partial \psi'}{\partial r'} = -r'\omega',$$

$$\frac{\partial \Gamma'}{\partial t'} + u'\frac{\partial \Gamma'}{\partial r'} + w'\frac{\partial \Gamma'}{\partial z'} = \frac{\partial^2 \Gamma'}{\partial r'^2} - \frac{2}{r'}\frac{\partial \Gamma'}{\partial r'} + \frac{\partial^2 \Gamma'}{\partial z'^2} + \frac{1}{r'}\frac{\partial \Gamma'}{\partial r'},$$

$$\left(\frac{\partial T'}{\partial t'} + u'\frac{\partial T'}{\partial r'} + w'\frac{\partial T'}{\partial z'}\right) - \frac{1}{\mathrm{Pr}}\left(\frac{\partial^2 T'}{\partial r'^2} + \frac{1}{r'}\frac{\partial T'}{\partial r'} + \frac{\partial^2 T'}{\partial z'^2}\right) = 0, \tag{1}$$

where $\mathrm{Pr} = \nu/\alpha$ and $\mathrm{Gr} = g\beta R_i^3 \Delta T/\nu^2$ are the Prandtl and Grashof numbers, respectively.

The boundary conditions for the problems under consideration are

$$\begin{aligned} r = 1 &: \psi = 0, \quad \Gamma = \mathrm{Re}_i r^2, \\ &\omega = -\frac{1}{r}\psi_{rr}, \quad T = 1, \\ r = R &: \psi = 0, \quad \Gamma = 0, \\ &\omega = -\frac{1}{r}\psi_{rr}, \quad T = 0, \\ z = 0 &: \psi = 0, \quad \Gamma = \mathrm{Re}_{\mathrm{inf}} r^2, \\ &\omega = -\frac{1}{r}\psi_{zz}, \quad T = 1, \\ z = H &: \psi = 0, \quad \Gamma = 0, \\ &\omega = -\frac{1}{r}\psi_{zz}, \quad T = 0, \end{aligned} \tag{2}$$

where $\mathrm{Re} = R_i^2\Omega/\nu$ is the Reynolds number.

The previous systems of equations were solved by a finite difference method based on a control-volume formulation [7, 8]. The discretised equations for the flow field were derived using central differences for spatial derivatives and forward difference for the time derivative. The control volume formulation in conjunction with the power-law interpolation scheme was used for high Prandtl, Reynolds, and/or Rayleigh numbers.

The numerical approach used in this study has been validated by comparison with the results obtained by Ball

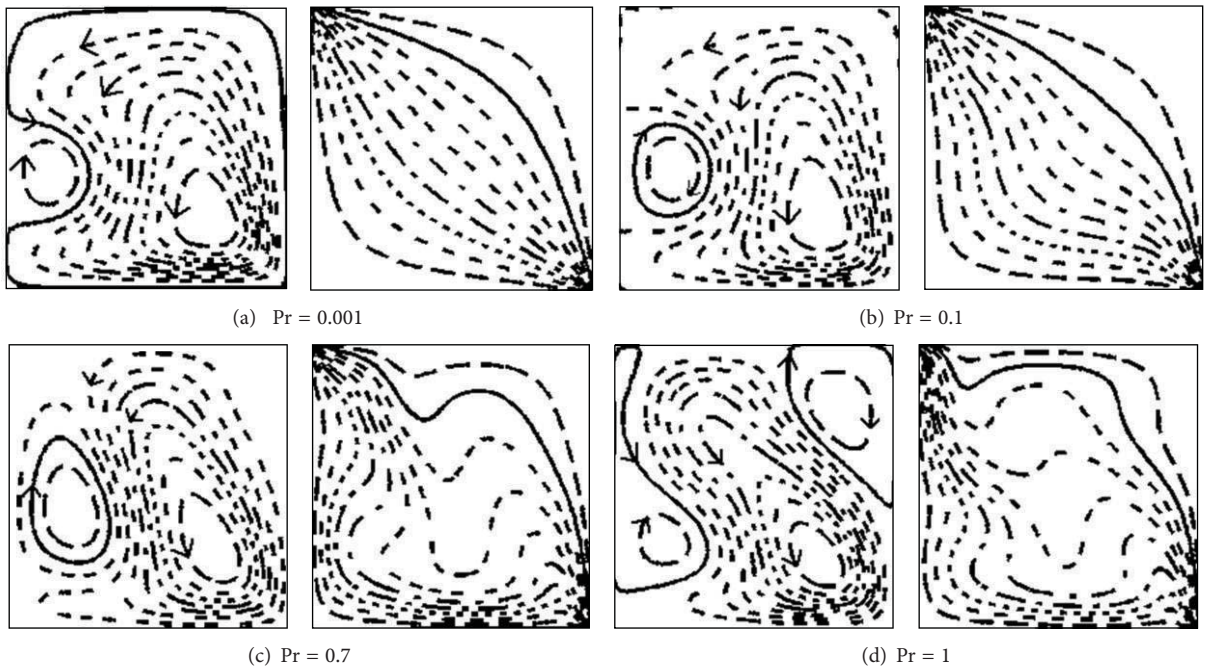

(a) Pr = 0.001 (b) Pr = 0.1

(c) Pr = 0.7 (d) Pr = 1

Figure 2: Streamlines and isotherms for $A = 1$, Re = 300, and Ra_c = (a) 40, (b) 4×10^3, (c) 4×10^4, and (d) 7×10^4 and 51×51 mesh.

and Farouk [11] and Fasel and Booz [12]. The agreement was satisfactory within the graphical precision.

A 41×49 mesh was selected, because with it the maximum stream function value of the 2-cell mode at Re = 200 only changed by 0.2% [8].

This condition was applied to all quantities at all mesh points as a convergence criterion for the following steady solution:

$$\frac{\left|\psi^{k+1} - \psi^{k}\right|}{\max \psi^{k}} = 10^{-6}. \quad (3)$$

3. Results and Discussion

The effect of the Prandtl number on the instability of flow has attracted a great scientific interest after experimental investigations showed that the oscillations caused by the thermaldynamic instability produce a change in the structure of the flow of numerous processes in growth of crystals in liquid phase (Hurle et al., 1974 [13]). Nevertheless, for very small Prandtl numbers, the dependency of the transition from the stable state to oscillating on the change in the aspect ratio widely has not been studied until 1997 by Gelfgat et al. [6].

3.1. Effects of the Prandtl Number on the Heat Transfer. This problem was studied for a range of the Prandtl number $0.001 < \mathrm{Pr} > 1$, with aspect ratios $A = 1$, finding the critical Rayleigh numbers for the interval of the Reynolds number to be $100 < \mathrm{Re} > 600$, making emphasis on the critical values of the Rayleigh number for small Prandtl numbers, and demonstrating that thermal instability in mixed convection depends on the Prandtl number. If in the system heating did not exist (Gr = 0), flow only becomes unstable due to dynamic effects by increasing the Reynolds number. For this, the dynamic instability is strongly stabilized by an increase in the potential of temperatures and the flow returns to destabilize itself when the body forces are increased to their critical value, showing 2 types of instabilities of thermal origin.

At first, as shown in Figures 2(a), 2(b), 3(a), and 3(b), for small values of Prandtl number ($\mathrm{Pr} < 0.1$), there is a weak influence of body forces on the centrifugal forces, streamlines are predominant in opposite to clockwise, and heat transfer has a conductive nature. Second, Figures 2(c), 2(d), 3(c), and 3(d) for high Prandtl numbers ($\mathrm{Pr} \gg 0.1$) the flow becomes unstable by the increase of the body effects that distort the velocity profiles; for this, the flow becomes unstable by the increase of the body effects that distort the velocity profiles; in this case, the fluid is not a good heat conductor, the disturbance of temperatures is located more in a region, and the strong action of the body forces initiates the instability.

For small values of the Prandtl number, thermal effects do not have influence on the flow instability; the temperature difference is small, so that the centrifugal forces come to be the main influence on flow. This is shown in Figure 4; the critical Rayleigh number is seen to be strongly increased in agreement with the viscous fluid.

3.2. Effects of the Prandtl Number on the Reynolds Number. While the Reynolds number is smaller, the body forces will affect the centrifugal forces from small Prandtl numbers. This is shown by means of the comparison of Figure 6(a) with Figure 7(a) and the streamlines of Figure 2(a) with Figure 3(a). In Figure 2(a), for Re = 300, it is possible to observe that the cell formed in the hot wall of the internal

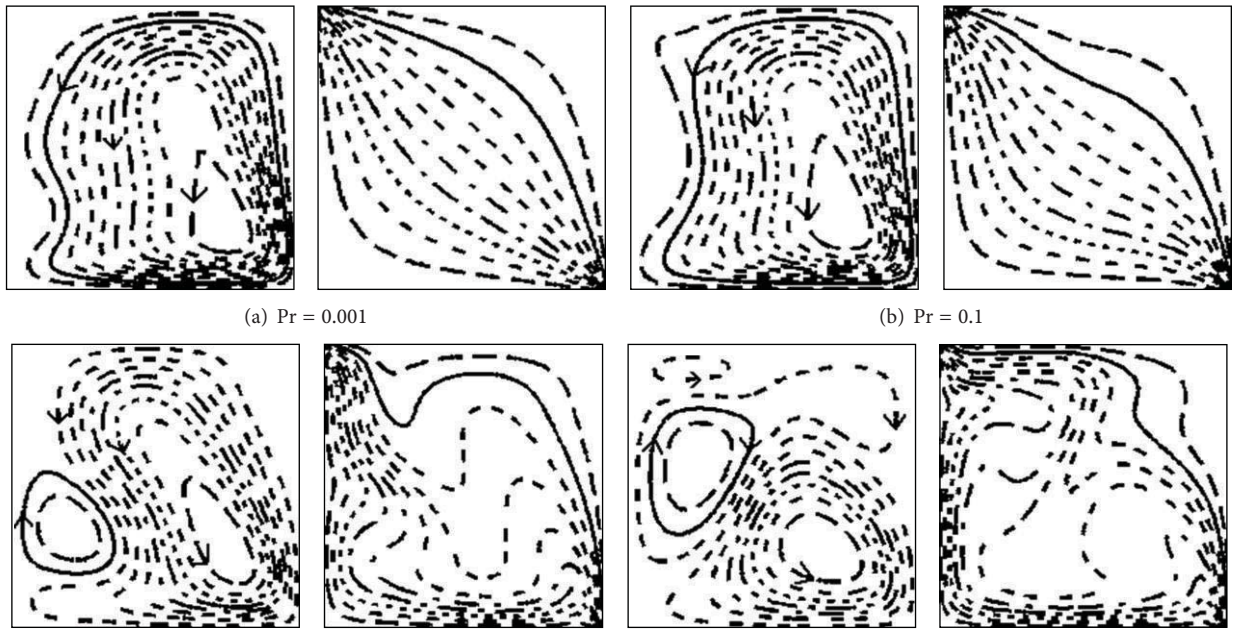

(a) Pr = 0.001 (b) Pr = 0.1

(c) Pr = 0.7 (d) Pr = 1

Figure 3: Streamlines and isotherms for $A = 1$, Re = 400, and Ra_c = (a) 50, (b) 5×10^3, (c) 6×10^4, and (d) 1.2×10^5 and 51×51 mesh.

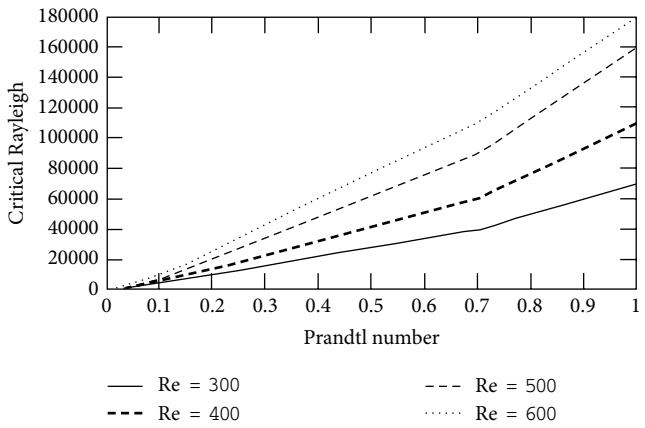

Figure 4: Critical Rayleigh versus Prandtl number for $A = 1$, $300 \leq$ Re ≤ 600 and 51×51 mesh.

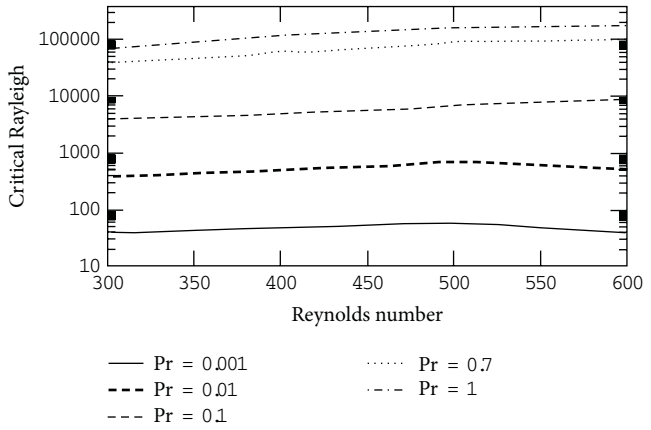

Figure 5: Critical Rayleigh versus Reynolds number for $A = 1$, $0.001 \leq$ Pr ≤ 1.0 and 51×51 mesh.

cylinder shows a growth as the Prandtl number grows; this cell is the one that determines the magnitude of the body forces and has a clockwise direction of rotation.

The previous examples explain why the critical Rayleigh number decreases from fluid with high Prandtl numbers to low Prandtl numbers, for moderate Reynolds numbers 300 < Re > 600. In order to exemplify the previous observation, Figure 5 shows clearly this tendency. For an increase in the Reynolds number, the critical Rayleigh and Nusselt numbers are increased and the body forces are cushioned by the centrifugal forces. On the other hand, an increase in the Prandtl number causes a strong increase in the heat transfer in the hot walls, the isotherms are highly distorted, and the convective terms come to be predominant. Figures 6, 7, 8, and 9 visualize the mentioned behaviors.

For detailed analysis, a study of the effect of the Prandtl number 0.001 < Pr > 15 on the number of Nusselt in the walls of the cavity for numbers of Re = 0–600 and aspect ratios $A = 1$, 0.5, and 0.25 was carried out, where the number of Grashof was taken like 1000. This analysis did not reach a regime of critical flow, showing that the tendency of heat transfer for a flow below the critical Grashof number, for different ratios, is similar to the ones produced in a regime of flow for critical Grashof numbers and superior to these.

Figures 10, 11, and 12 show the effect of Prandtl and Reynolds numbers on the Nusselt on the inferior surface of the cavity, which is warmed up, as well as the surface

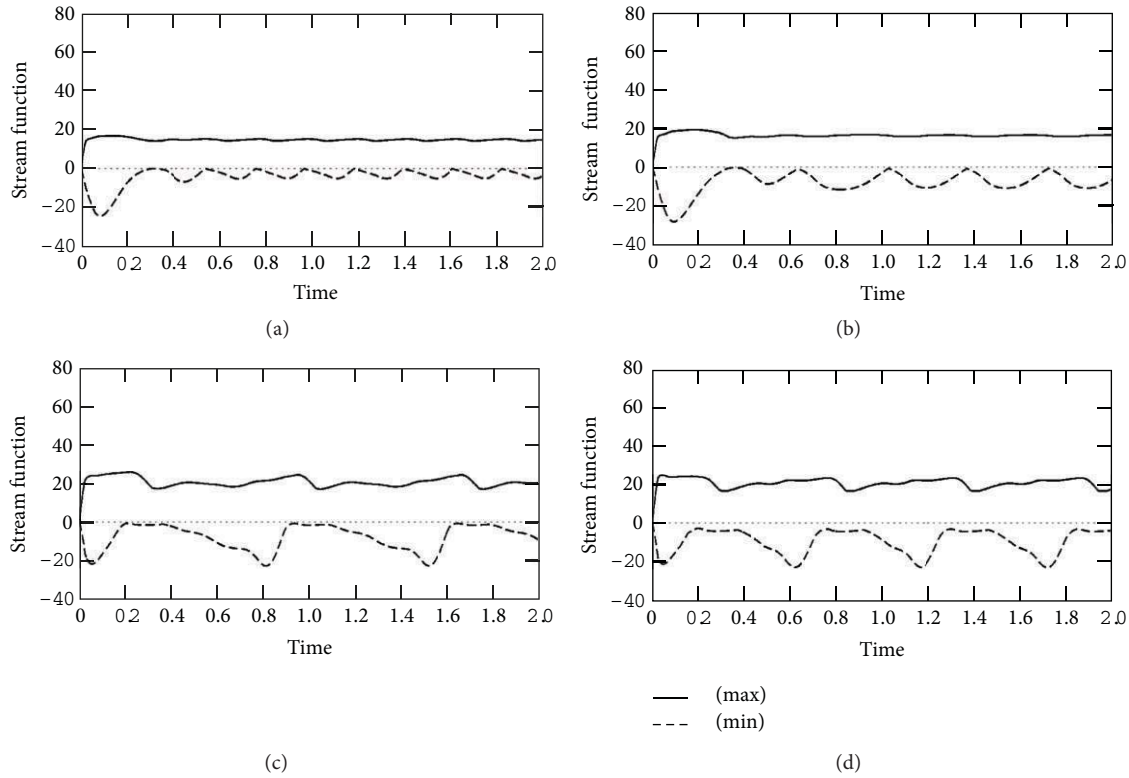

FIGURE 6: Streamline versus time for $A = 1$, Re = 300, (a) Pr = 0.001, (b) Pr = 0.1, (c) Pr = 0.7, (d) Pr = 1, and $Ra_c = 40, 4 \times 10^3, 4 \times 10^4$, and 7×10^4 and 51×51 mesh.

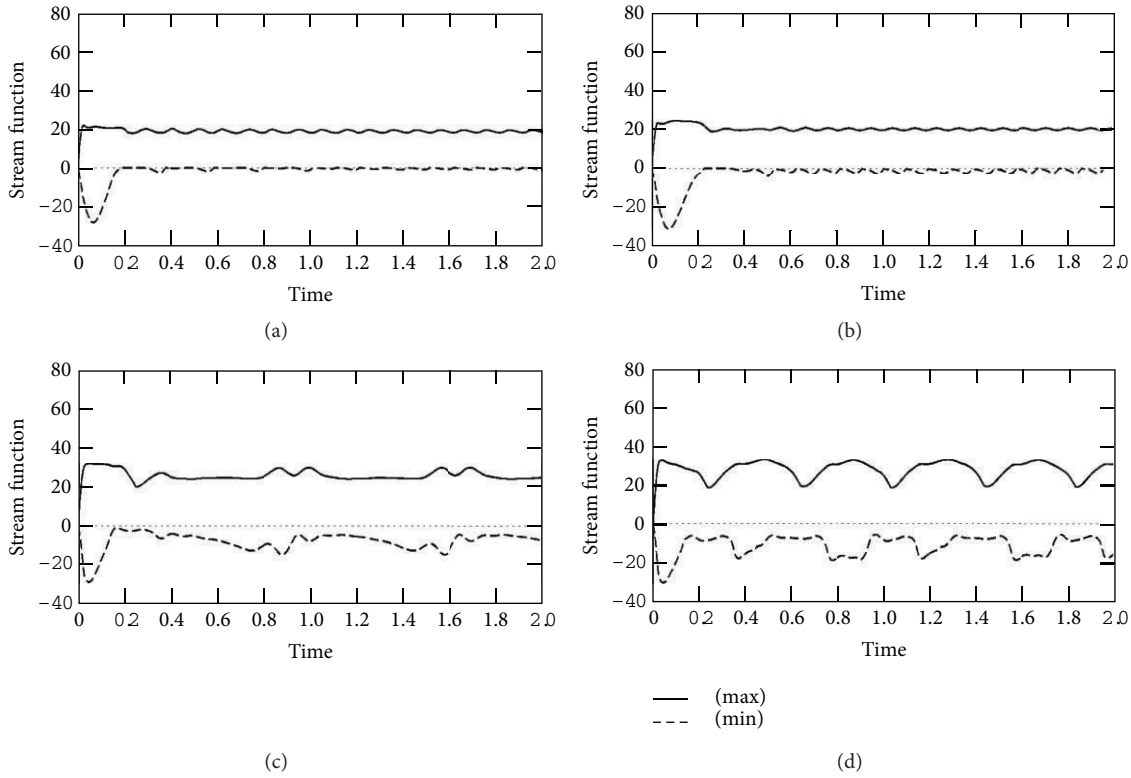

FIGURE 7: Streamline versus time for $A = 1$, Re = 400, (a) Pr = 0.001, (b) Pr = 0.1, (c) Pr = 0.7, (d) Pr = 1, and $Ra_c = 50, 5 \times 10^3, 6 \times 10^4$, and 1.2×10^5 and 51×51 mesh.

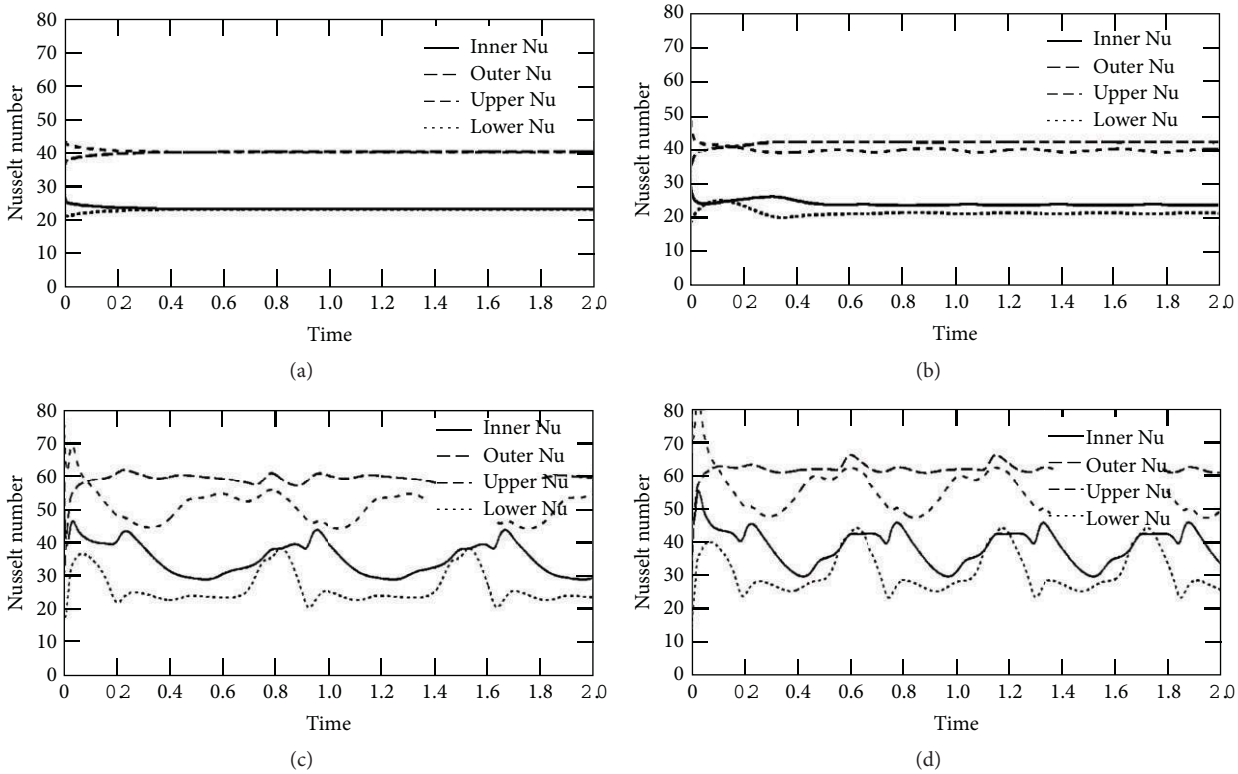

FIGURE 8: Nusselt number versus time for $A = 1$, Re = 300, (a) Pr = 0.001, (b) Pr = 0.1, (c) Pr = 0.7, (d) Pr = 1, and $Ra_c = 40, 4 \times 10^3, 4 \times 10^4$, and 7×10^4 on a 51×51 mesh.

of the internal cylinder. The continuous lines represent the natural convection within the cavity (Re = 0) and show an ascending heat transfer from Pr > 1. This should happen only because body forces have action over the flow, and there is a cell with clockwise turn. To increase Reynolds number, a strong action of the centrifugal forces on those of body will increase the percentage of transfer of heat in the walls.

This effect begins in the interval of 0.1 < Pr > 0.5; the flow undergoes drastic changes in the dynamic patterns, where it stops values of the inferior Prandtl number to 0.1 is dominated by the forces of body and values superior to 0.5 that by the centrifugal forces. Making comparisons between Figures 10, 11, and 12, makes it possible to observe the change in the flow patterns that happens between 0.1 < Pr < 0.3 and has a smaller effect for smaller aspect ratios. On the other hand, the heat transfer in the inferior wall is increased in agreement with the aspect ratio decreases.

From the results of Figures 10, 11, and 12, some correlations to determine the number of Nusselt of the inferior wall can be deduced. For all the cases, the number of Grashof is 1000, that is why the flow is in laminar regime.

The correlation for natural convection (Re = 0) is expressed in (4), all the values for this variables are mentioned in Tables 1, 2, and 3:

$$\mathrm{Nu} = C\mathrm{Pr}^m. \tag{4}$$

TABLE 1: Values for constant C and m.

$A = 1$	$C = 46.2$	for $0.001 \le \mathrm{Pr} \le 15$
	$m = 0.007$	for $0.001 \le \mathrm{Pr} \le 1$
	$m = 0.105$	for $1 < \mathrm{Pr} \le 15$

The correlation for mixed convection is expressed in (5); all the values for this variable are in Tables 4, 5, and 6:

$$\mathrm{Nu} = C\mathrm{Pr}^m. \tag{5}$$

The values of constant m used in the correlation for mixed convection (5) are shown in Table 2.

4. Conclusions

Present work demonstrates that for values of Pr $\ll$ 0.01, the convective terms of heat transfer are negligible. This means that body forces are constant and only hydrodynamic effects cause instability. In spite of the weak influence of the forces of body on the flow for small Prandtl numbers, the study demonstrated that the thermal instability in mixed convection depends strongly on the Prandtl number.

The dynamic instability is strongly stabilized by an increase in the potential of temperatures, and the flow returns to destabilize itself when the body forces are increased to their critical values. Two instabilities of thermal origin first

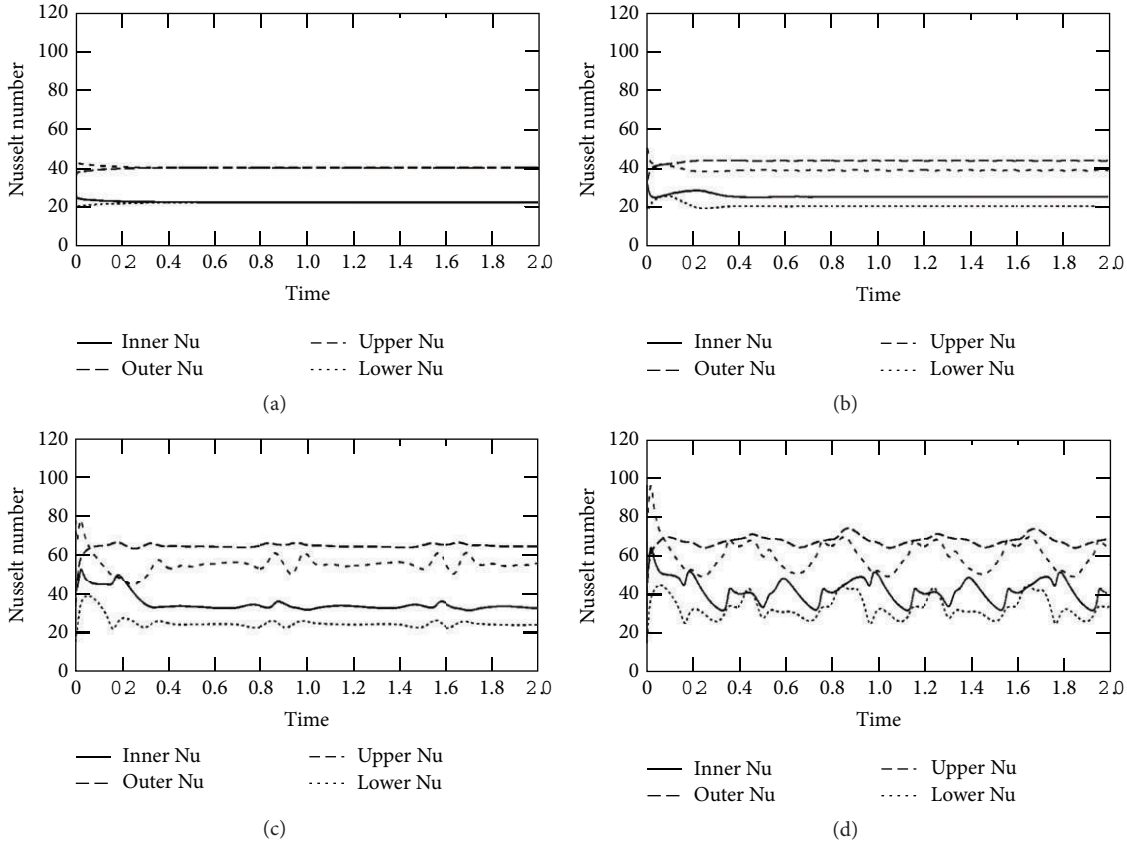

Figure 9: Nusselt number versus time for $A = 1$, Re = 400, (a) Pr = 0.001, (b) Pr = 0.1, (c) Pr = 0.7, (d) Pr = 1, and $Ra_c = 50, 5 \times 10^3, 6 \times 10^4$, and 1.2×10^5 and mesh = 51×51.

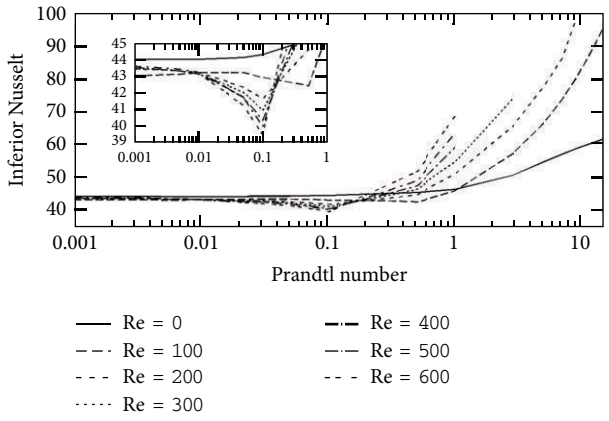

Figure 10: Nusselt number versus Prandtl number for $A = 1$, $300 \leq \text{Re} \leq 600$, and $\text{Gr} = 1 \times 10^3$ and 71×71.

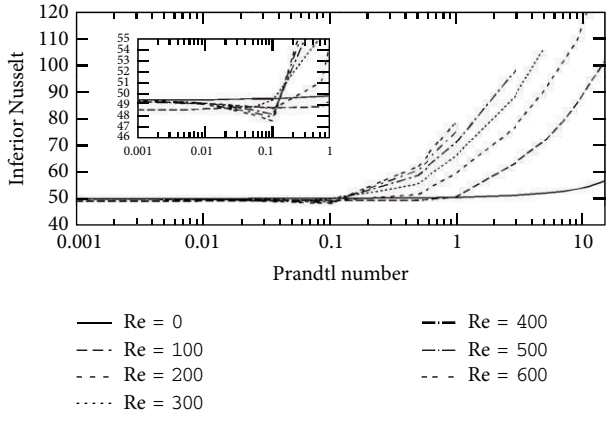

Figure 11: Nusselt number versus Prandtl number for $A = 0.5$, $300 \leq \text{Re} \leq 600$, and $\text{Gr} = 1 \times 10^3$ and 81×41.

Table 2: Values for constant C and m.

$A = 0.5$	$C = 46.2$	for $0.001 \leq \text{Pr} \leq 15$
	$m = 0.0014$	for $0.001 \leq \text{Pr} \leq 1$
	$m = 0.04$	for $1 < \text{Pr} \leq 15$

Table 3: Values for constant C and m.

$A = 0.25$	$C = 46.2$	for $0.001 \leq \text{Pr} \leq 15$
	$m = 0.001$	for $0.001 \leq \text{Pr} \leq 1$
	$m = 0.014$	for $1 < \text{Pr} \leq 15$

happened for very small values of the Prandtl number, where the heat transfer has a conductive character. Second, for high Prandtl numbers, it is shown that the body effects that distort the velocity profiles cause heat transfer to have a convective character.

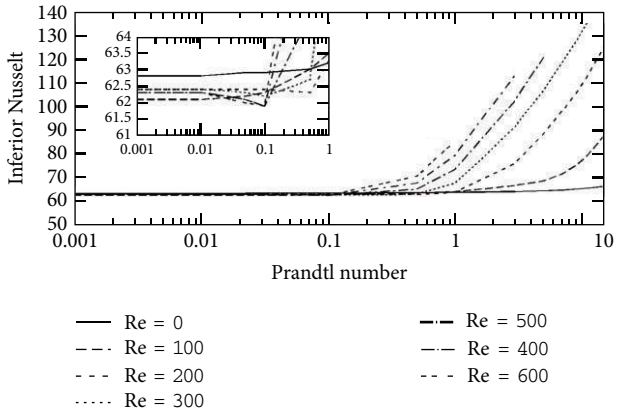

Figure 12: Nusselt number versus Prandtl number for $A = 0.25$, $300 \leq \mathrm{Re} \leq 600$, and $\mathrm{Gr} = 1 \times 10^3$ and 81×21.

Table 4: Values for constant C and m.

$A = 1$	$C = 39.22$	for $0.001 \leq \mathrm{Pr} \leq 0.1$
	$C = 62.64$	for $0.1 < \mathrm{Pr} \leq 15$

Table 5: Values for constant C and m.

$A = 0.5$	$C = 47.92$	for $0.001 \leq \mathrm{Pr} \leq 0.1$
	$C = 74.91$	for $0.1 < \mathrm{Pr} \leq 15$

Table 6: Values for constant C and m.

$A = 0.25$	$C = 61.89$	for $0.001 \leq \mathrm{Pr} \leq 0.1$
	$C =$ On Table 2	for $0.1 < \mathrm{Pr} \leq 15$

For small Reynolds numbers the body forces affect with greater magnitude the centrifugal forces from very small Prandtl numbers. Then, the critical Rayleigh number, for moderate Reynolds numbers ($300 < \mathrm{Re} < 600$), diminishes from convective fluids with high Prandtl numbers to conductive fluids with very low Prandtl numbers.

The tendency of the heat transfer from a flow below the number of critical Grashof to different aspect ratios is very similar to the one produced in a regime of flow for numbers of Grashof that are critical and superior to these. On the other hand, the heat transfer in the inferior wall increases as the Prandtl number increases and aspect ratio decreases.

References

[1] J. L. Laje, A. Bejan, and J. Georgiadis, "On the effect of the Prandtl number on the onset of Bénard convection," *Journal of Heat and Fluid Flow*, vol. 12, no. 2, pp. 184–188, 1991.

[2] J. D. Verhoeven, "Experimental study of thermal convection in a vertical cylinder of mercury heated from below," *Physics of Fluids*, vol. 12, no. 9, pp. 1733–1740, 1969.

[3] R. K. Soberman, "Onset of convection in liquids subjected to transient heating from below," *Physics of Fluids*, vol. 2, no. 2, pp. 131–138, 1959.

[4] H. Bertin and O. Hiroyuki, "Numerical study of two-dimensional natural convection in a horizontal fluid layer heated from below, by finite-element method: influence of Prandtl number," *International Journal of Heat and Mass Transfer*, vol. 29, no. 3, pp. 439–449, 1986.

[5] P. Chao, S. W. Churchill, and H. Ozoe, "The dependence of the critical Rayleigh number on the Prandtl number," in *Convection Transport and Instability Phenomena*, J. Zierep and H. Oertel, Eds., pp. 55–70, G. Braun Karlsruhe, FRG, 1982.

[6] A. Y. Gelfgat, P. Z. Bar-Yoseph, and A. L. Yarin, "On oscillatory instability of convective flows at low Prandtl number," *Journal of Fluids Engineering*, vol. 119, no. 4, pp. 823–830, 1997.

[7] X. L. Zhang and T. H. Nguyen, "Forced convection by Taylor-Couette flow between two concentric rotating cylinders with internal heat generation," in *Proceedings of the Fundamentals of Forced Convection Heat Transfer*, vol. 210, ASME, 1992.

[8] S. G. Durand, B. G. Urquiza, and H. T. Nguyen, "Thermoconvective fluid flow between concentric rotating cylinders of finite lenght," in *Proceedings of the 2nd International Thermal Energy Congress (ITEC '95)*, pp. 480–486, Agadir, Morocco, June 1995.

[9] T. B. Benjamin, "Bifurcation phenomena in steady flows of a viscous fluid. Part I: theory," *Proceedings of the Royal Society A*, no. 359, pp. 1–26, 1978.

[10] T. B. Benjamin, "Bifurcation phenomena in steady flows of a viscous fluid. Part II. experiments," *Proceedings of the Royal Society A*, no. 359, pp. 27–43, 1978.

[11] K. S. Ball and B. Farouk, "Bifurcation phenomena in Taylor-Couette flow with buoyancy effects," *Journal of Fluid Mechanics*, vol. 197, pp. 479–501, 1988.

[12] H. Fasel and O. Booz, "Numerical investigation of supercritical Taylor-Vortex flow for a wide gap," *Journal of Fluid Mechanics*, vol. 138, pp. 21–52, 1984.

[13] D. T. J. Hurle, E. Jakeman, and C. P. Johnson, "Convective temperature oscillations in molten gallium," *Journal of Fluid Mechanics*, vol. 64, no. 3, pp. 565–576, 1974.

Hindawi Publishing Corporation
Advances in Mechanical Engineering
Volume 2013, Article ID 929236, 8 pages
http://dx.doi.org/10.1155/2013/929236

Research Article

An Analytical Approximation for Continuous Flow Microwave Heating of Liquids

G. Cuccurullo,[1] L. Giordano,[1] and G. Viccione[2]

[1] *Department of Industrial Engineering, University of Salerno, Via Ponte don Melillo, 84084 Fisciano, Italy*
[2] *Department of Civil Engineering, University of Salerno, Via Ponte don Melillo, 84084 Fisciano, Italy*

Correspondence should be addressed to G. Viccione; gviccion@unisa.it

Received 21 February 2013; Revised 4 April 2013; Accepted 6 April 2013

Academic Editor: Moran Wang

Both a numerical and an analytical models were developed to simulate temperature profiles in continuous laminar pipe flow during microwave heating. Fully developed velocity and thermally developing conditions were assumed. The numerical solution was obtained by first solving Maxwell equations and then by coupling them with the energy balance for the flowing fluid. On the other hand, the same problem was solved analytically under the simplifying assumption foreseeing uniform heat generation inside the pipe. With the aim of reducing computational efforts, numerical and analytical results were compared in order to investigate conditions for which the two models allowed to recover the same temperature patterns. Thus, it has been shown that suitable conditions can be found for which the simplified analytical model can lead to an easy way to predict the heat transfer through the pipe.

1. Introduction

Nowadays, it is widely accepted that using microwaves (MWs) as a source of energy turns out into a viable alternative for high-temperature/short-time processing featuring several industrial food treatments. In fact, volumetric heating due to microwaves leads to higher heat transfer rates and hence to shorter processing times than conventional processes. These features are appealing since reduced thermal transients as well as the absence of high-temperature surfaces in contact with the foods could ensure both a lower stress for the food under processing [1] and improved food quality; in particular, a better conservation of vitamins during pasteurization processes than traditional heating is usually observed [2, 3]. Additional benefits can be related to continuous flow MW heating systems since they enable in realizing increased productivity, easier clean up and automation with respect to standard batch ones [4]; space saving and simplified piping when compared with traditional heat plants are expected too. Therefore, increasing demand for industrial applications is actually taking place. In this framework, it is worth noting that

(1) since available energy densities are typically smaller than the ones achievable by conventional techniques, laminar flow conditions are often realized in order to realize acceptable temperature increases [5, 6];

(2) wishing to enhance heat transfer rates, laminar flow is not disadvantageous since heat transfer is no more driven by wall conditions; therefore, reduced heat transfer coefficients could even be helpful, the walls being warmer than the external air.

On the other hand, the complexity due to the electromagnetic (EM) field prediction and, in turn, to the related heat generation term is a major obstacle in designing industrial applications for microwave food heating. In fact, thermal response is to be correlated to relative load and system configurations and to thermal and dielectric properties of the material as a function of chemical composition, temperature, and frequency [7–12]. Moreover, difficulties are experienced in measuring and/or controlling temperature in the cavity because traditional probes fail and highly uneven temperature patterns are usually realized [13, 14]. In addition, adequate experimentation may be impractical, as a large number of tests are usually required to obtain representative results [15, 16]. Further difficulties in recovering theoretical solutions have to be accounted for when considering continuous pipe flow: solving simultaneously high-frequency

electromagnetism, heat transfer, and fluid-flow problems requires high-computation time, programming, and numerical analysis skills [17]. In addition, numerical discretization in time and space leads to variations in numerical phase velocities which in turn can bring cumulative errors ("grid dispersion" phenomenon). Therefore, special care has to be paid in mesh generation. Since common criteria (e.g., the Nyquist-Shannon sampling theorem) may fail [18, 19], in Section 3 a more restrictive criterion, still based on simplified assumptions, is proposed.

Almost recently, the numerical approach, in view of several simplifying assumptions, allowed a satisfying description of the coupled thermal-EM problems and an accurate identification of the effects which the operating parameters have on the process at hand [9, 12, 17, 18, 20–23]. In addition, numerical techniques represent an effective way for solving more complex problems (e.g., [24]) in which temperature-dependent dielectric permittivity as well as non-Newtonian liquids carrying food subjected to MW heating may be taken into account. In the above framework, alternative procedures based on approximate methods can be found; the latter are essentially based on attempting a suitable simplified modelling for the generation term in the energy equation. The latter procedure is acceptable by considering that in the field of food engineering it is often desired to control the thermal effect of microwave heating, while detailed knowledge of EM field behaviour is unnecessary. Of course, approximate theoretical approaches can be helpful in pointing out the overall thermal behaviour and the main parameters controlling the problem at hand and their influence on the thermal response [5] before realizing an experimental validation. Meanwhile, costs and the outlined problems related to experimental procedures are avoided.

As a consequence of the foregoing discussion, aiming to a faster and easier model for continuous microwave heating of liquids, the possibility of recovering the fluid thermal behaviour by an analytical solution is investigated in the present paper; uniform heat generation inside the pipe is assumed, retaining the proper average value. This presumption is suggested by supposing that

(1) temperature patterns for the flowing fluid are determined by the volume-averaged heat generation, rather than by its local values, as much as the fluid speed increases;

(2) the illuminated cavity volume is sufficiently large with respect to the applicator pipe to behave as a reverberating chamber, thus reducing uneven EM-field patterns.

Conditions, if any, are then searched for which the above assumptions become effective, thus leading to convergence between the simplified analytical problem and the reference-numerical solution for the temperature field.

To address the problem, a three-dimensional numerical model was first developed to predict the distribution of the EM field in water continuously flowing in a circular duct subjected to microwave heating. The Maxwell's equations were solved using the finite element method (FEM) in the frequency domain to describe the electromagnetic field configuration in the MW cavity.

As a first approach to the problem, water is described as an isotropic and homogeneous dielectric; its properties are assumed to be independent of temperature. Therefore, the momentum and the energy equations turn out to be one way coupled with Maxwell's equations and are then solved both numerically and analytically; the developing temperature field for an incompressible laminar duct flow subjected to heat generation is considered. The latter is sought as the effective one arising from the solution of the electromagnetic problem at hand, whereas its average value over the water volume is assumed with reference to the analytical solution.

2. Basic Equations

2.1. MW System Description. A general-purpose pilot plant producing microwaves by a magnetron rated at 2 kW and emitting at a frequency of 2.45 GHz is available to the heat transfer laboratory, at the University of Salerno, Figure 1; it will be used for future development of the present work, aiming to validate the results herein presented. Thus, the following models are referred to such an experimental setup. The insulated metallic cubic chamber houses one PTFE applicator pipe; the pipe is embedded in a box made by a closed-cell polymer foam. The matrix foam was proven to be transparent to microwaves at 2.45 GHz. As stated in the introduction, the cavity is designed such that its volume is much greater than the applicator pipe, aiming to approximate a reverberant chamber behaviour.

2.2. Electromagnetic Problem. Three-dimensional numerical modelling of continuous flow microwave heating was carried out by employing the commercial code COMSOL v4.3 [25]. The latter can provide coupling of three physical phenomena, electromagnetism, fluid, and energy flow. First, the Maxwell's equations are solved by means of the finite element method (FEM) [26] using unstructured tetrahedral grid cells; then, the electric field distribution $\underline{E}$ in the microwave cavity, both for air and for the applicator pipe carrying the fluid under process, is determined by imposing

$$\nabla \times \left(\frac{1}{\mu_r} \nabla \times \underline{E} \right) - k_0^2 \left(\varepsilon_r - \frac{i\sigma}{\omega \varepsilon_0} \right) \underline{E} = \underline{0}, \tag{1}$$

where $\underline{E}$ is the electric field intensity, ε_r is the relative permittivity, ω is the angular wave frequency, μ_r is the relative permeability of the material, k_0 is the wavenumber in vacuum, and σ is the electric conductivity. Air and the PTFE applicator tube were both supposed to be completely transparent to microwaves. Assuming negligible resistive material losses, boundary conditions for the radio frequency module included perfect electric conductors walls, that is, $\underline{n} \times \underline{E} = 0$, for the waveguide and the cavity, being $\underline{n}$ the local normal vector. At the port, an amount of 2 kW EM power, 2450 MHz frequency, was supplied through a rectangular TE10 mode waveguide (WR 340).

Continuity boundary condition was set by default for all the interfaces between the confining domains, that is, the

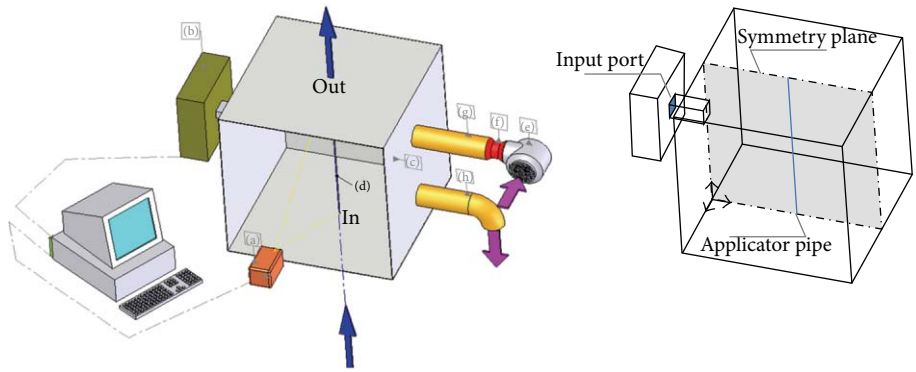

(a) IR camera with computer for aided thermography and on/off control
(b) Magnetron and standard rectangular WR-340 waveguide
(c) Cubic cavity
(d) Applicator pipe
(e) Centrifugal fan
(f) Electric heater
(g) Air inlet channel
(h) Air outlet channel

Figure 1: Sketch of the available setup.

pipe, the cavity, and the waveguide. Formally, such condition may be expressed as

$$\underline{n} \times \left(\underline{E}_i - \underline{E}_j\right) = \underline{0}, \tag{2}$$

i and j being the domains sharing the interface at hand. Scattering boundary conditions were applied at the inlet and the outlet of the pipe to make the pipe's ends transparent to incoming waves, avoiding that undesired reflected waves travel inward [15].

Total volumetric power generation due to microwaves is calculated by

$$U_{\text{gen}} = 2\pi\varepsilon_0\varepsilon'' f\left|\underline{E}\right|^2, \tag{3}$$

where ε_0 is the free-space permittivity and ε'' is the relative dielectric loss of the material.

Only one-half of the problem was modelled due to the symmetric geometry and load conditions around the XY plane crossing vertically the oven, the waveguide, and the pipe, see Figure 1, right side. The condition of perfect magnetic conductor was applied for the surfaces lying on the symmetry plane:

$$\underline{n} \times \underline{H} = \underline{0}, \tag{4}$$

$\underline{H}$ being the magnetic field, which has to be therefore parallel to the local normal vector $\underline{n}$ on the XY plane.

2.3. Heat Transfer Problem. The power-generation term realizes the coupling of the EM field with the energy balance equation where it represents the "heat source" term. Convective terms in the energy equation require specifying velocity components, which are evaluated considering fully developed velocity profiles. Thus, for Newtonian-incompressible fluid in laminar motion, the Navier-Stokes equations yield the well-known axial Poiseille velocity profile $U(R)$ with no radial component ($V = 0$), being the radius $R \in (0, D_i/2)$ and D_i the internal pipe diameter.

In view of the above assumptions and considering constant properties, the energy balance reduces to

$$\rho c_p U \frac{\partial T}{\partial X} = k\nabla^2 T + U_{\text{gen}}, \tag{5}$$

where T is the temperature, ρ is the fluid density, c_p is the specific heat, k is the thermal conductivity, X is the axial coordinate, and U_{gen} is the specific heat generation.

The PTFE tube carrying the fluid exposed to microwave irradiation is considered thermally meaningless. The inlet temperature is set to 10°C, while the remaining boundaries are assumed as adiabatic. Fixed average velocities (namely, U_{av} = 0.02, 0.04, 0.08, 0.16 m/s) were chosen.

After processing the numerical model, the average spatial value for heat generation was obtained; then, it was used as a source term for feeding the analytical solution. Consider that, in practice, such parameter can be measured by calorimetric methods, avoiding numerical calculations, therefore enabling the application of the analytical model with ease.

3. Numerical Model

A numerical model was developed in COMSOL 4.3 [25] to predict temperature patterns in the fluid continuously heated in a multimode microwave illuminated chamber. The radio frequency package, developed for the analysis of propagating electromagnetic waves, was one way coupled with the heat transfer module to solve the energy balance equation in the thermally developing region. The fluid dynamics problem was considered laminar and fully developed, and thus, velocity profiles were assumed to be known and parabolic.

3.1. Geometry Building. The assumed configuration for the system at hand is sketched in Figure 1, left side. The pipe carrying the fluid to be heated was 6 mm internal diameter and 0.90 m long. The three-dimensional setup was generated in SolidWorks, providing symmetrical geometry and load conditions about the XY symmetry plane. Such a choice

was performed having in mind to suitably reduce both computational burdens and mesh size while preserving the main aim of the paper that is to compare the simplified analytical solution with the numerical one. In particular, a cubic cavity chamber (side length, $L = 0.9$ m) and a standard WR340 waveguide were assumed.

3.2. Mesh Generation. The available computational domain, reduced by one half as previously specified, was discretized using unstructured tetrahedral grid elements. Special care was devoted in choosing their size, as numerical dispersion may result in the presence of a numerical phase velocity error in the solution. Grid dispersion may appear in numerical methods such as finite-element or finite-difference methods. The phenomenon should not be underestimated because such propagating errors are cumulative, yielding unacceptable solution once propagating waves travel over considerable distances. Common sampling criteria, such as Nyquist's, may fail under certain circumstances.

For the sake of clarity, the simple case of the homogeneous lossless 1D Maxwell wave equation travelling in time t over the x-axis direction is considered

$$\frac{\partial^2 E}{\partial t^2} = c^2 \frac{\partial^2 E}{\partial X^2}, \tag{6}$$

$c = 1/\sqrt{\varepsilon\mu}$ being the wave speed in the medium, $\varepsilon = \varepsilon_r \varepsilon_0$ the absolute electrical permittivity, and $\mu = \mu_r \mu_0$ the absolute magnetic permeability. Free space permittivity and permeability are known to be $\varepsilon_0 = 8.854\ 10^{-12}$ F/m and $\mu_0 = 4\pi 10^{-7}$ H/m, respectively. This equation is known to be dispersionless. In fact, the general solution expressed in phasor form

$$E(X,t) = e^{j(\omega t - kX)}, \quad j = \sqrt{-1} \tag{7}$$

admits as continuous dispersion relationship the following equation

$$k = \pm \frac{\omega}{c}, \tag{8}$$

the wavenumber k being the function of the angular frequency ω. The latter arises by introducing the second temporal and spatial derivatives of (7) in (6), which gives for the wave phase velocity

$$v_p \stackrel{\text{def}}{=} \frac{\omega}{k} = \pm c, \tag{9}$$

a quantity independent from the linear f or angular frequency ω. Such nondependence cannot be stated when considering a numerical discretization of (6). Let us consider its finite difference approximation of second-order accuracy in space and time (whose local coordinates are referred to the electric field subscripts and superscripts, resp.):

$$\begin{aligned} &\frac{E_p^{m+1} - 2E_p^m + E_p^{m-1}}{(\Delta t)^2} + O\left[(\Delta t)^2\right] \\ &\quad = c^2 \left\{ \frac{E_{p+1}^m - 2E_p^m + E_{p-1}^m}{(\Delta X)^2} + O\left[(\Delta X)^2\right] \right\}. \end{aligned} \tag{10}$$

Neglecting higher-order terms yields the explicit relation:

$$E_p^{m+1} \cong \left(\frac{c\Delta t}{\Delta X}\right)^2 \left(E_{p+1}^m - 2E_p^m + E_{p-1}^m\right) + 2E_p^m - E_p^{m-1}. \tag{11}$$

In analogy to (7), the general numerical solution in phasor form is introduced:

$$E_p^m \cong \left(\frac{c\Delta t}{\Delta X}\right)^2 e^{j(\omega m \Delta t - \bar{k} p \Delta X)}, \tag{12}$$

where $\bar{k} = \bar{k}_{\text{re}} + j\bar{k}_{\text{im}}$ is the complex wavenumber satisfying (12). The Courant number, $\text{CO} = c\Delta t/\Delta X$, appearing in (12) must be lower than unity in order to guarantee a stable numerical solution. Such a stability limit is automatically checked by Comsol software each time step; hence, no more details concerning this aspect are here discussed. Numerical dispersion arises from the discrepancy between k and $\bar{k}$ wavenumbers. Again, introducing the second temporal and spatial derivatives of (12) in (11) yields the following identity for the complex wavenumber:

$$\bar{k} = \frac{1}{\Delta X} \arccos\left\{1 + \left(\frac{\Delta X}{c\Delta t}\right)^2 \left[\cos(\omega \Delta t) - 1\right]\right\}. \tag{13}$$

It can be noted that in this case the numerical wave phase velocity

$$\bar{v}_p = \frac{\omega}{\bar{k}} \tag{14}$$

turns out to be function of the angular frequency ω. Grid resolution directly affects (14). Considering the typical case corresponding to a wavelength $\lambda \stackrel{\text{def}}{=} c/f = \Delta X/20$ and $c\Delta t = \Delta X/2$ (i.e., a grid sampling density $N_\lambda = \lambda/\Delta X = 20$ and $\text{CO} = 0.5$) yields the real equation:

$$\bar{v}_p = 0.9968c, \tag{15}$$

that is, $\varepsilon = 0.31\%$ less than the wave speed c. Note that the error $\varepsilon = \bar{v}_p/c$ is lower than 1% for $N_\lambda > 10$ (horizontal line in Figure 2). Since it was considered a grid mesh resolution, spacing in the range $0.0107 \div 0.03$ m and $0.002 \div 0.003$ m for the vacuum and water, respectively, such a limit was strictly satisfied for the moving fluid (i.e., $\lambda_{\text{water}}/\Delta X_{\text{water}} > 30$, λ_{water} being 0.09 m). The same limit is satisfied for the vacuum only where needed.

Extending to the general case, keeping N_λ and CO as variables, one can rewrite (13) as

$$\begin{aligned} \bar{k} &= \frac{1}{\Delta X} \arccos\left\{1 + \left(\frac{1}{\text{CO}}\right)^2 \left[\cos\left(\frac{2\pi \text{CO}}{N_\lambda}\right) - 1\right]\right\} \\ &= \frac{1}{\Delta X} \arccos(\xi), \end{aligned} \tag{16}$$

in which $\xi = -1$ marks the limit between real and complex values for $\bar{k}$. Grid sampling resolution assumes correspondently the transitional value

$$N_{\lambda,\text{tr}} = \frac{2\pi \text{CO}}{\arccos\left(1 - 2\text{CO}^2\right)}. \tag{17}$$

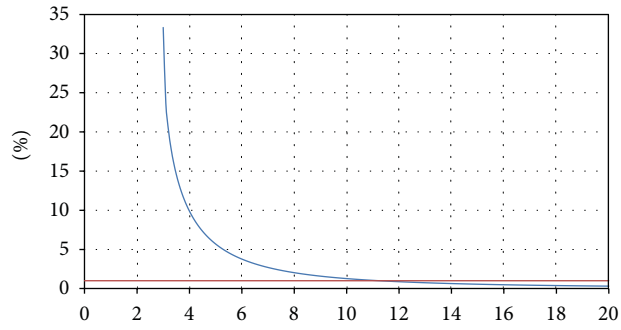

FIGURE 2: Error $\varepsilon = (1 - \overline{v}_p/c) \cdot 100$ of $\overline{v}_p$ expressed as function of the grid sampling density N_λ, for Courant number CO = 0.5 ($N_{\lambda,\mathrm{tr}} = 3$). Maximum absolute error can be estimated by setting c to the corresponding value for the fluid.

Limiting the analysis to the real values of (16), that is, $N_\lambda > N_{\lambda,\mathrm{tr}}$, the relative error for $\overline{v}_p$ is shown in Figure 2, where $N_{\lambda,\mathrm{tr}} = 3$ for the choice CO = 0.5.

As can be noted from the above discussion, assuming the maximum grid element size $\Delta X_{\max}$ on the basis of the Nyquist criterion [19] (i.e., $N_\lambda = 2$) may turn in nonnegligible errors for the numerical wave phase velocity. Some studies (see, for instance, [18]) suggest that an acceptable criterion for the FEM solution of Maxwell's equations is to use six grids per wavelength; this is more stringent than Nyquist criterion, yet not always satisfying as reported in the above discussion.

4. The Analytical Model

The thermal model provides laminar-axisymmetric thermally developing flow of a Newtonian fluid with constant properties and negligible axial conduction. In such hypotheses, the dimensionless energy balance equation and the boundary conditions in the thermal entrance region turn out to be

$$\begin{aligned} u \cdot \frac{\partial \theta}{\partial x} &= \frac{1}{r} \cdot \frac{\partial}{\partial r}\left(r \cdot \frac{\partial \theta}{\partial r}\right) + u_{\mathrm{gen}}, \\ \left.\frac{\partial \theta}{\partial r}\right|_{r=1} &= 0, \\ \left.\frac{\partial \theta}{\partial r}\right|_{r=0} &= 0 \\ \theta(0, r) &= 1, \end{aligned} \tag{18}$$

where $\theta = (T - T_s)/(T_i - T_s)$ is the dimensionless temperature, T_s and T_i being the temperature of the environment surrounding the tube and the inlet flow temperature, respectively; $x = (4 \cdot X)/(\mathrm{Pe} \cdot D_i)$ is the dimensionless axial coordinate; the Peclet number is defined as $\mathrm{Pe} = (U_{\mathrm{av}} \cdot D_i)/\alpha$, U_{av} being the mean fluid velocity and α the thermal diffusivity; $r = (2 \cdot R)/D_i$ is the dimensionless radial coordinate; $u_{\mathrm{gen}} = (U_{\mathrm{gen}} \cdot D_i^2)/(4 \cdot k \cdot (T_i - T_s))$ is the dimensionless heat generation, k being the thermal conductivity; $u = 2 \cdot (1 - r^2)$ is the dimensionless radial velocity profile, u being U/U_{av}. The generation term has been obtained by evaluating the spatial average of the "electromagnetic power loss density" (W/m^3) resulting from the EM problem.

The problem being linear, the thermal solution has been written as the sum of two partial solutions:

$$\theta(x, r) = \theta_G(x, r) + u_{\mathrm{gen}} \cdot \theta_V(x, r). \tag{19}$$

The $\theta_G(x, t)$ problem represents the solution of the extended Graetz problem featured by a nonhomogeneous equation at the inlet and adiabatic boundary condition at wall. On the other hand, the $\theta_V(x, t)$ problem takes into account the microwave heat dissipation and includes a non homogeneous differential equation. Thus, the two partial solutions have to satisfy the two distinct problems expressed in terms of $\theta_G(x, t)$ and $\theta_V(x, t)$, respectively. Details can be found in [5]. The θ_G problem is solved in closed form by the separation of variables method; thus, the structure of the solution is sought as follows:

$$\begin{aligned} \theta_G(x, r) &= \sum_{m=1}^{M} c_m F_m(r)\, e^{-(\lambda^2/2) \cdot x}, \\ F_m(r) &= e^{-(r^2 \cdot \lambda/2)} \cdot \Lambda\left[\frac{1}{4}(-2 + \lambda_m), r^2 \cdot \lambda_m\right], \end{aligned} \tag{20}$$

where F_m are the eigenfunctions, Λ being the orthonormal Laguerre polynomials and λ_m the related eigenvalues arising from the characteristic equation $F_m'(1) = 0$. Imposing the initial condition and considering the orthogonality of the eigenfunctions, the constants c_m were obtained.

The "θ_v" problem, featured by single nonhomogeneous equation, was solved assuming the solution as the sum of two partial solutions:

$$\theta_v(x, r) = \theta_1(r) + \theta_2(x, r). \tag{21}$$

The "θ_1" problem holds the nonhomogeneus differential equation and represents the "x-stationary" solution. On the other hand, the "θ_2" problem turns out to be linear and homogenous with the exception of the "x-boundary" condition "$\theta_2(0, r) = -\theta_1(r)$"; then, it can be solved by the separation of variables method, recovering the same eigenfunctions and eigenvalues of the Graetz problem and retaining the same structure of (20):

$$\theta_2(x, r) = \sum_{m=1}^{M} b_m F_m(r)\, e^{-(\lambda^2/2) \cdot x}. \tag{22}$$

5. Results

5.1. Electromagnetic Power Generation and Cross-Section Spatial Power Density Profiles. The port input power was set to 2000 W. Due to the high impedance mismatch, as the available cavity was designed for higher loads, the amount of microwave energy absorbed by the water was 255.7 W, that is, 12.8% of the total input power. The corresponding density ranged from 2.6 10^3 W/m^3 to 5.83 10^7 W/m^3; its distribution

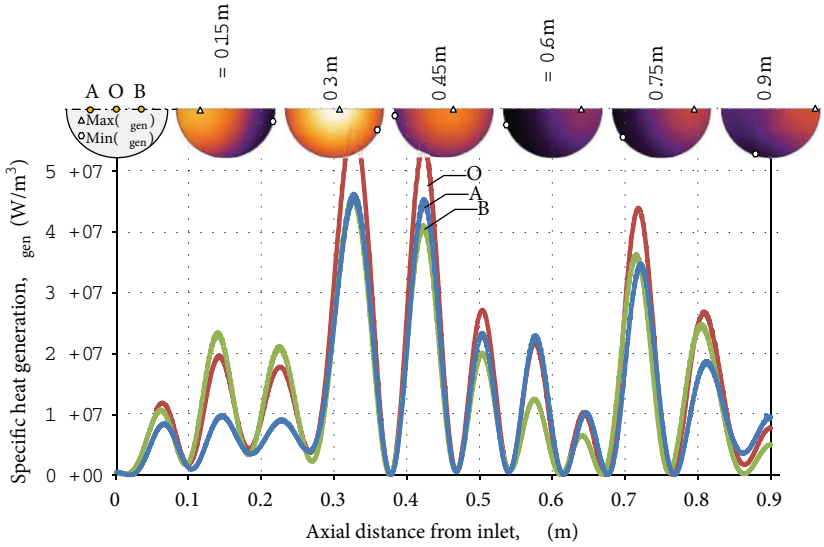

FIGURE 3: Contour plots and longitudinal distributions of specific heat generation U_{gen} along three longitudinal axes corresponding to the points O (tube centre), A and B.

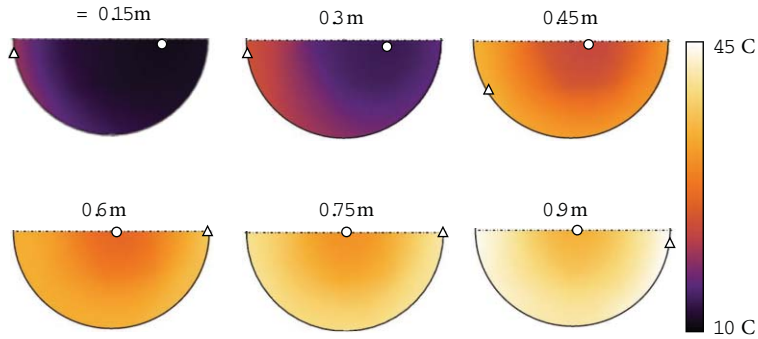

FIGURE 4: Cross-sections, equally spaced along the x-axis, of temperature spatial distribution.

along three selected longitudinal paths (namely, $R = 0$, $\pm D_i/2$) is represented in Figure 3. In the upper side of the figure, six maps related to sections equally spaced along the pipe length are reproduced. The maps evidence the collocations of the maximum (triangular dot) and minimum (circular dot) values. The fluctuating density profiles exhibit an average period of about 90 mm for water and are featured by high radial and axial gradients. As evidenced in Figure 3, while moving downstream, maximum and minimum intensities occur at different locations off centre; the minimum always falls on the edges, while the maximum partially scans the cross-tube section along the symmetry axis aiming to the periphery.

5.2. Comparison between Analytical and Numerical Temperature Data. Temperature field resulting from the numerical analysis is sketched in Figure 4 for the previously selected six equally spaced cross-sections and for a fixed average velocity, that is, 0.08 m/s. It is evident that the cumulative effect of the heat distribution turns out into monotonic temperature increase along the pipe axis, irrespective of the driving specific heat generation distribution. Moreover,

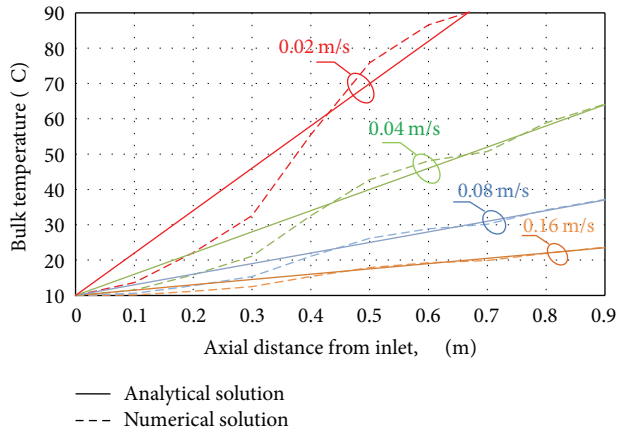

FIGURE 5: Bulk temperature profiles.

the temperature patterns tend to recover an axisymmetric distribution while moving downstream, as witnessed by the contour distribution as well as by the cold spot collocations (still evidenced as circular dots in Figure 4), moving closer

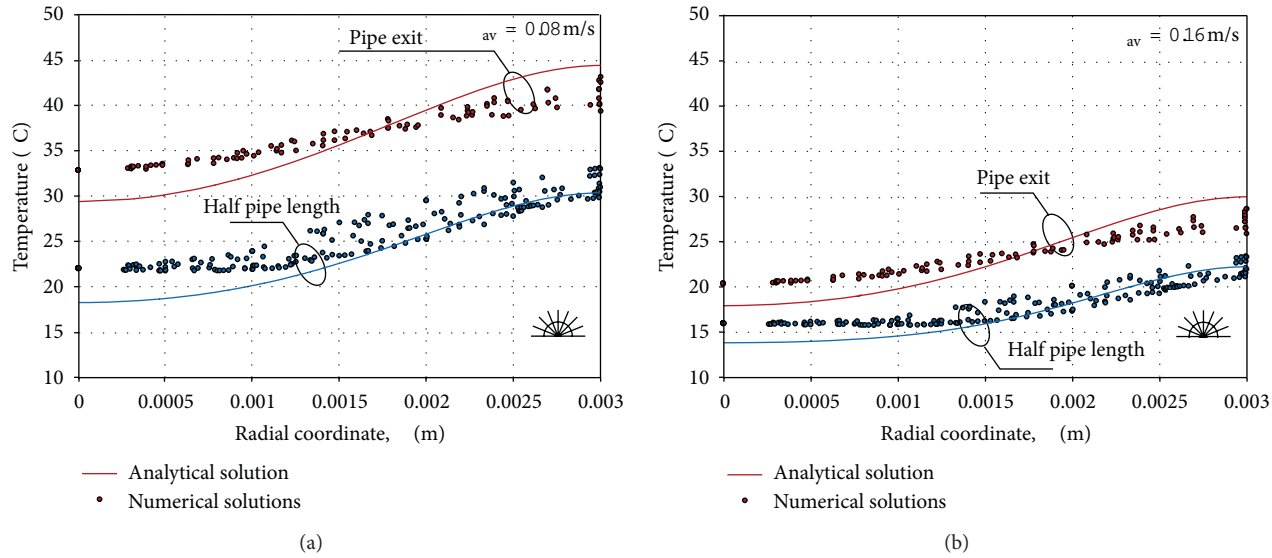

Figure 6: Temperature radial profiles.

and closer to the pipe axis. Thus, it is shown that the main hypothesis ruling the analytical model is almost recovered. A similar behaviour is widely acknowledged in the literature [9, 15, 17, 20, 27] that is, (1) temperature distribution appears noticeable even at the tube entrance, but it becomes more defined as the fluid travels longitudinally; (2) higher or lower central heating is observed depending on the ratio between the convective energy transport and MW heat generation. As a further observation, it can be noted that the difference between the extreme temperature values is about 10°C ± 0.5°C almost independently of the section at hand. It seems to be a quite surprising result if one considers that similar differences were realized by employing similar flow rates, pipe geometries, and powers in single mode designed microwave cavities [9, 15]. These latter aimed to reduce uneven heating by applying an electric field with a more suitable distribution providing maximum at the centre of the tube where velocity is high and minimum at the edges where velocity is low.

To clutch quantitative results and compare the analytical and numerical solutions, the bulk temperature seems to be an appropriate parameter; thus, bulk temperature profiles along the stream are reported in Figure 5. For a fixed average velocity, a fairly good agreement is attained as much as the fluid approaches the pipe exit; regions can be singled out where numerical solutions recover the corresponding linear behaviour of the analytical solution within the limit of ±1°C. The extension of such regions turns out to increase with increasing speeds (0.53, 0.48, 0.13, and 0.04 m measured from the pipe exit for 0.16, 0.08, 0.04, and 0.02 m/s, resp.). This behaviour can be attributed to the flatter energy distribution felt by the running fluid, which is not able to follow along EM energy spatial fluctuations as much as its speed increases. In other words, as the average velocity increases, the frequency of the heat generation fluctuations felt by moving particles increases; thus, their thermal response is not able to follow along.

Radial temperature profiles both for the analytical and numerical solutions are reported in Figure 6 for U_{av} = 0.16 m/s and 0.08 m/s and for two selected sections, that is, $X = L/2$ and $X = L$. The analytical solution being axisymmetric, a single profile is plotted versus nine numerical ones taken at the directions evidenced in the lower left corner in Figure 6, that is shifted $\pi/8$ rad over the half tube; a cloud of points is formed in correspondence of each analytical profile. Once again, it appears that the dispersion of the numerical points is more contained and the symmetry is closely recovered for increasing speeds. For the two selected sections and for both velocities, analytical curves underestimate the numerical points around the pipe axis. Vice versa, analytical predictions tend to overestimate the corresponding cloud points close to the wall. In any case, temperature differences are contained within a maximum of 5.2°C (attained at the pipe exit on the wall for the lower velocity); thus, the analytical and numerical predictions of temperature profiles seem to be in acceptable agreement with practical applications in the field of food engineering.

6. Concluding Remarks and Further Activities

The process of continuous flow microwave heating was simulated using both a multiphysics software package and a simplified analytical model encompassing uniform heat dissipation inside the entrance region of the heated pipe.

Care was taken in realizing an appropriate mesh discretization by assuring a relative error for phase velocity lower than 1%. Therefore, a new and simplified criterion is proposed which is more restrictive with respect to the traditional one by Nyquist.

In spite of the uneven heat generation inside the applicator pipe, it has been shown that under suitable conditions analytical predictions for temperature patterns adequately

recover the corresponding numerical results, thus leading to an easy way to predict temperature patterns through the pipe.

Further developments of the present work are intended to study the influence of the pipe position on the amount of absorbed energy and the effect of temperature-dependent fluid properties. Moreover, several pipes in parallel will be introduced in the model, in order to study a configuration that could more closely meet the needs of industrial applications. Finally, numerical and analytical predictions will be compared to the corresponding experimental ones, after performing tests on the available MW system.

References

[1] J. Zhu, A. V. Kuznetsov, and K. P. Sandeep, "Numerical simulation of forced convection in a duct subjected to microwave heating," *Heat and Mass Transfer*, vol. 43, no. 3, pp. 255–264, 2007.

[2] I. Sierra, C. Vidal-Valverde, and A. Olano, "The effects of continuous flow microwave treatment and conventional heating on the nutritional value of milk as shown by influence on vitamin B1 retention," *European Food Research and Technology*, vol. 209, no. 5, pp. 352–354, 1999.

[3] S. Tajchakavit, H. S. Ramaswamy, and P. Fustier, "Enhanced destruction of spoilage microorganisms in apple juice during continuous flow microwave heating," *Food Research International*, vol. 31, no. 10, pp. 713–722, 1998.

[4] J. Ahmed and S. Hosahalli Ramaswamy, "Microwave pasteurization and sterilization of foods," in *Handbook of Food Preservation*, M. Shafiur Rahman, Ed., chapter 28, pp. 691–711, 2nd edition, 2007.

[5] G. Cuccurullo and V. Spingi, "An approximate solution for the entrance region in laminar pipe flow with temperature dependent heat generation," in *Proceedings of the 29th UIT Heat Transfer Conference*, Torino, Italy, June 2011.

[6] G. Cuccurullo, L. Giordano, V. Spingi, F. D'Agostino, M. Migliozzi, "A numerical-analytical solution for continuous flow microwave heating of liquids in laminar motion," in *Proceedings of the 30th UIT Heat Transfer Conference*, Bologna, Italy, June 2012.

[7] R. Vadivambal and D. S. Jayas, "Non-uniform temperature distribution during microwave heating of food materials-a review," *Food and Bioprocess Technology*, vol. 3, no. 2, pp. 161–171, 2010.

[8] P. Coronel, J. Simunovic, and K. P. Sandeep, "Temperature profiles within milk after heating in a continuous-flow tubular microwave system operating at 915 MHz," *Journal of Food Science*, vol. 68, no. 6, pp. 1976–1981, 2003.

[9] D. Salvi, J. Ortego, C. Arauz, C. M. Sabliov, and D. Boldor, "Experimental study of the effect of dielectric and physical properties on temperature distribution in fluids during continuous flow microwave heating," *Journal of Food Engineering*, vol. 93, no. 2, pp. 149–157, 2009.

[10] N. M. Gerbo, D. Boldor, and C. M. Sabliov, "Design of a measurement system for temperature distribution in continuous-flow microwave heating of pumpable fluids using infrared imaging and fiber optic technology," *Journal of Microwave Power and Electromagnetic Energy*, vol. 42, no. 1, pp. 55–65, 2008.

[11] C. M. Sabliov, D. A. Salvi, and D. Boldor, "High frequency electromagnetism, heat transfer and fluid flow coupling in ANSYS multiphysics," *Journal of Microwave Power and Electromagnetic Energy*, vol. 41, no. 4, pp. 5–17, 2007.

[12] A. Datta, H. Prosetya, and W. Hu, "Mathematical modeling of batch heating of liquids in a microwave cavity," *Journal of Microwave Power and Electromagnetic Energy*, vol. 27, no. 1, pp. 38–48, 1992.

[13] G. Cuccurullo, L. Cinquanta, and G. Sorrentino, "A procedure to achieve fine control in MW processing of foods," *Infrared Physics and Technology*, vol. 49, no. 3, pp. 292–296, 2007.

[14] G. Cuccurullo, L. Giordano, D. Albanese, L. Cinquanta, and M. Di Matteo, "Infrared thermography assisted control for apples microwave drying," *Journal of Food Engineering*, vol. 112, pp. 319–325, 2012.

[15] P. D. Muley and D. Boldor, "Multiphysics numerical modeling of the continuous flow microwave-assisted transesterification process," *Journal of Microwave Power and Electromagnetic Energy*, vol. 46, no. 3, pp. 139–162, 2012.

[16] K. Knoerzer, M. Regier, and H. Schubert, "Microwave heating: a new approach of simulation and validation," *Chemical Engineering and Technology*, vol. 29, no. 7, pp. 796–801, 2006.

[17] D. Salvi, D. Boldor, G. M. Aita, and C. M. Sabliov, "COMSOL Multiphysics model for continuous flow microwave heating of liquids," *Journal of Food Engineering*, vol. 104, no. 3, pp. 422–429, 2011.

[18] Q. Zhang, T. H. Jackson, and A. Ungan, "Numerical modeling of microwave induced natural convection," *International Journal of Heat and Mass Transfer*, vol. 43, pp. 2141–2154, 2000.

[19] C. Mirabito, A. Narayanan, D. Perez, and B. Stone, *FEMLAB Model of a Coupled Electromagnetic-Thermal Boundary Value Problem. Research Experience*, Worcester Polytechnic Institute, Worcester, Mass, USA, 2005.

[20] J. Zhu, A. V. Kuznetsov, and K. P. Sandeep, "Mathematical modeling of continuous flow microwave heating of liquids (effects of dielectric properties and design parameters)," *International Journal of Thermal Sciences*, vol. 46, no. 4, pp. 328–341, 2007.

[21] P. Ratanadecho, K. Aoki, and M. Akahori, "A numerical and experimental investigation of the modeling of microwave heating for liquid layers using a rectangular wave guide (effects of natural convection and dielectric properties)," *Applied Mathematical Modelling*, vol. 26, no. 3, pp. 449–472, 2002.

[22] A. Le Bail, T. Koutchma, and H. S. Ramaswamy, "Modeling of temperature profiles under continuous tube-flow microwave and steam heating conditions," *Journal of Food Process Engineering*, vol. 23, pp. 1–24, 2000.

[23] D. A. Salvi, D. Boldor, C. M. Sabliov, and K. A. Rusch, "Numerical and experimental analysis of continuous microwave heating of ballast water as preventive treatment for introduction of invasive species," *Journal of Marine Environmental Engineering*, vol. 9, no. 1, pp. 45–64, 2008.

[24] J. Zhu, A. V. Kuznetsov, and K. P. Sandeep, "Investigation of a particulate flow containing spherical particles subjected to microwave heating," *Heat and Mass Transfer*, vol. 44, no. 4, pp. 481–493, 2008.

[25] COMSOL Multiphysics Version 4.3a User Guide, October 2012.

[26] O. C. Zienkiewicz, R. L. Taylor, and J. Z. Zhu, *The Finite Element Method: Its Basis and Fundamentals*, Butterworth-Heinemann, 6th edition, 2005.

[27] D. Salvi, D. Boldor, J. Ortego, G. M. Aita, and C. M. Sabliov, "Numerical modeling of continuous flow microwave heating: a critical comparison of COMSOL and ANSYS," *Journal of Microwave Power and Electromagnetic Energy*, vol. 44, no. 4, pp. 187–197, 2010.

Hindawi Publishing Corporation
Advances in Mechanical Engineering
Volume 2013, Article ID 257283, 11 pages
http://dx.doi.org/10.1155/2013/257283

Research Article

Pressure Change in Tee Branch Pipe in Oscillatory Flow

Daisuke Sakamoto,[1] Chongho Youn,[2] and Toshiharu Kagawa[2]

[1] *Department of Mechano-Micro Engineering, Tokyo Institute of Technology, R2-45, 4259, Nagatuda, Midoriku, Yokohamasi, Kanagawaken 2268503, Japan*
[2] *Precision and Intelligence Laboratory, Tokyo Institute of Technology, R2-45, 4259, Nagatuda, Midoriku, Yokohamasi, Kanagawaken 2268503, Japan*

Correspondence should be addressed to Daisuke Sakamoto; sakamoto.d.aa@m.titech.ac.jp

Received 25 January 2013; Accepted 14 March 2013

Academic Editor: Bo Yu

The purpose of this paper is to contribute to the understanding of unsteady flow of branch pipes in pneumatic systems. Branch pipes are used in pneumatic pipe systems in various industrial fields. To predict the unsteady pressure changes in the pneumatic piping systems, it is necessary that the dynamic characteristics of branch pipes are at hand, in addition to the dynamic characteristic of single pipe. However, while so many studies are accumulated for a single pipe dynamics, few studies have reported the pressure changes in branch pipes due to oscillatory flow. This paper reports an experimental study on the dynamic characteristics of the pressure change in a pneumatic branch pipe under given oscillatory flow. The paper also proposes a simulation method to predict the pressure changes in a pneumatic branch pipe under oscillatory flow. The validity of simulation is verified for oscillatory flows up to 5 Hz, comparing with the experimental results.

1. Introduction

The purpose of this paper is a prediction of unsteady pressure change at the T-joint of a branch pipe, which is induced by oscillatory compressible fluid flow. Unsteady flow of gas in piping is treated not so often as liquid in piping. In liquid pipe works, the water hammer is a remarkable unsteady phenomenon, which can generate a dangerously high pressure [1]. In gas pipe systems, however, no comparable high pressure is generated; hence, the unsteady phenomena in gas and pneumatic piping had drawn relatively little attention of engineers.

In recent years, the use of pneumatic power systems widely spread in industries [2]. The pneumatic power systems include actuators such as cylinders, air motors, and air springs. In the control of the pneumatic power systems, transient pressure has influence on the motion of the pneumatic actuators. Consequently, relationships between piping configuration and the transient pressure changes are beginning to draw the attention of engineers.

Usual pneumatic systems are supplied with compressed air from a compressor; this means that branch pipes are inevitably accompanied by pneumatic systems. Similar to the water piping, unsteady flow in uniform straight pipe is rather easily understood. The situation drastically changes when the pipe works include branch pipes. Actually, pipe flow with a branch pipe is complex even when the flow is steady.

The correlation of the branch pipe pressure loss to the energy saving should be added. In recent years in the industry, requirement for low-pressure-loss piping systems for energy saving is growing. An accurate prediction of the pressure loss in systems is required at the design stage. Because branch pipes are frequently used in piping systems, the understanding of the pressure losses in them is therefore important.

The pressure loss in a branch pipe under steady flow condition has been studied in many years [1–7]. Some modern studies [8–11] showed precise structure of pressure change in branch pipe or T-joint. Many of these studies, however, considered flow of liquid. The pressure losses for compressible fluid are often assumed to be approximated by those of liquids [12]. Recent studies for gas flow partly validated the traditional view and showed necessary corrections [13–15].

The pressure loss in a branch pipe under unsteady condition is influenced by reflection of pressure and velocity waves from the pipe ends. The wave motion causes the complexity of the pressure loss at the joint, since the phases of pressure and velocity waves do not generally coincide. In the traditional study of fluid transients, the steady pressure loss coefficients at pipe junctions are used also for unsteady flows [1]. It is necessary to examine the validity of the traditional assumption because few studies have been carried out to report the pressure change in a branch pipe under unsteady flow.

This study investigates the pressure change in a tee branch pipe under oscillatory compressible flows. A simulation model and a corresponding computer program are built for prediction of oscillatory pressures and flows in the branch pipe. The model is based on the one-dimensional compressible flow assumption. The produced simulation model can predict the flow and pressure changes in all parts of the piping system. Experiments are performed using the flow meter that can measure instantaneous gas flow rate [16]. Comparison between the experiments and the simulation is carried out for oscillatory flows; discrepancies between the experimental results and simulation are within acceptable level for the estimate of the pressure losses in pneumatic power systems.

2. Static Characteristics

2.1. Experimental Setups. Figure 1 shows the branch pipe used in the experiments. A T-joint is used to form the branch pipe. The two flow patterns considered in this study are shown in Figures 1(a) and 1(b), which will be referred to hereafter as pattern A and pattern B, respectively. In pattern A, the flow is divided into the straight direction and the perpendicular direction. In pattern B, the flow is divided symmetrically into two perpendicular directions.

Figure 2 shows the drafting of the T-joint made of acrylic resin. Steel pipes are connected to the joint. The inner diameter of the drilling hole of the joint is 16 mm. The pressure measurement taps are made at positions 25 mm away from the intersection of the pipe axes. The connected pipes are STPG370 (JIS G3454) carbon steel pipe (15 A of Scheme 40). The inner diameter of the pipes is 16.1 mm; internal surfaces are generally smooth. The working fluid for the experiment is compressed air.

Figures 3 and 4 show the rigs for static measurement of pattern A and pattern B, respectively. In the static characteristic measurement, the pressure measured at 25 mm upstream from the intersection of pipe axes is taken as the reference pressure. The pressures in each downstream pipe are measured at points 100 mm away from the axes intersection. The differential pressure between the reference point and the pipe downstream points is measured and used for estimation of pressure losses due to the branch. The pipe length in upstream, namely, from T-joint to the upstream pressure regulator, is about 1 m. The pipe lengths in the downstream of the T-joint, namely, from the T-joint to the flow meter inlet, are about 1 m.

The pressure sensors for P_1, P_2, and P_3 are a metal diaphragm type ("AP-13" from the KEYENCE Corp., Japan). The differential pressure sensors for ΔP_1 and ΔP_2 are also metal diaphragm type ("KL17" from the Nagano Keiki Inc., Japan). Mass flow meters are installed; however, their indication is volumetric flow rate at the ISO standard state (ISO 6358, temperature 293.15 K with pressure 100 kPa). The mass flow meters installed in the test rigs are laminar type flow meters, of which structure and characteristics are precisely described in [16].

2.2. Experimental Results. Figure 5 illustrates definitions of variables and related nomenclatures. Throughout the experiments, the upstream flow rate Q_1 is kept constant. The flow rates Q_2 and Q_3 are adjusted using throttle valves placed in the downstream of the flow meters in Figures 3 and 4.

The loss coefficient is calculated using the following energy equations and measured flow rates and pressures. The flow directions from point 1 to point 2 and point 3 in patterns A and B are illustrated in Figures 5(a) and 5(b).

The energy conservation from point 1 to point 2 is expressed by

$$P_1 + \frac{\rho u_1^2}{2} = P_2 + \frac{\rho u_2^2}{2} + \left(\lambda_1 \frac{L_1}{d_1} + \xi_{12}\right) \frac{\rho u_1^2}{2} + \lambda_2 \frac{L_2}{d_2} \frac{\rho u_2^2}{2}. \tag{1}$$

The energy conservation from point 1 to point 3 is expressed by

$$P_1 + \frac{\rho u_1^2}{2} = P_3 + \frac{\rho u_3^2}{2} + \left(\lambda_1 \frac{L_1}{d_1} + \xi_{13}\right) \frac{\rho u_1^2}{2} + \lambda_3 \frac{L_3}{d_3} \frac{\rho u_3^2}{2}. \tag{2}$$

The flow velocities shawn in these equations are calculated using the following formula:

$$u_i = \frac{\left(\rho_a Q_i / \rho_i\right)}{A}. \tag{3}$$

The absolute pressure at the joint is about 600 kPa; however, the magnitude of the differential pressure is level of 100 Pa. While density of air is proportional to its absolute pressure, the change of the density at any point near the joint can be neglected. Hence, we can assume

$$\rho_1 = \rho_2 = \rho_3 = \rho. \tag{4}$$

The loss coefficients of a T-joint change with the flow ratios Q_2/Q_1 and Q_3/Q_1. Figure 6 shows the static characteristic test results for pattern A, and Figure 7 shows those for pattern B. The solid lines in these figures are fit curves for the loss coefficients obtained from the experimental points in each graph. The fit curves are obtained using the least squares technique and expressed by the following polynomials of the ratio of flow rates:

$$\xi_{1j} = \sum_{n=0}^{6} A_n q^n, \quad q = \frac{Q_2}{Q_1}. \tag{5}$$

For pattern A, the curves in Figure 8 are fourth-order polynomials; for pattern B, the curves in Figure 9 are sixth-order polynomials. In these equations, subscripts $1j = 12$ or

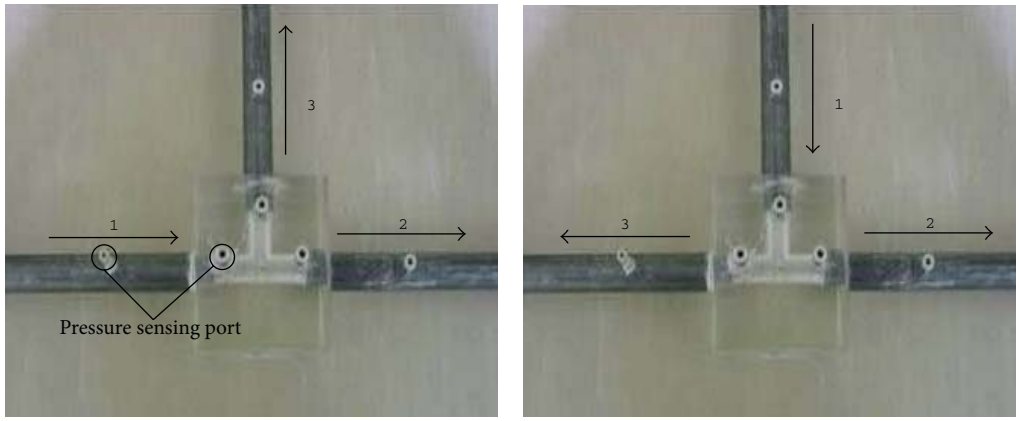

(a) Pattern A (b) Pattern B

Figure 1: The tee branch pipe.

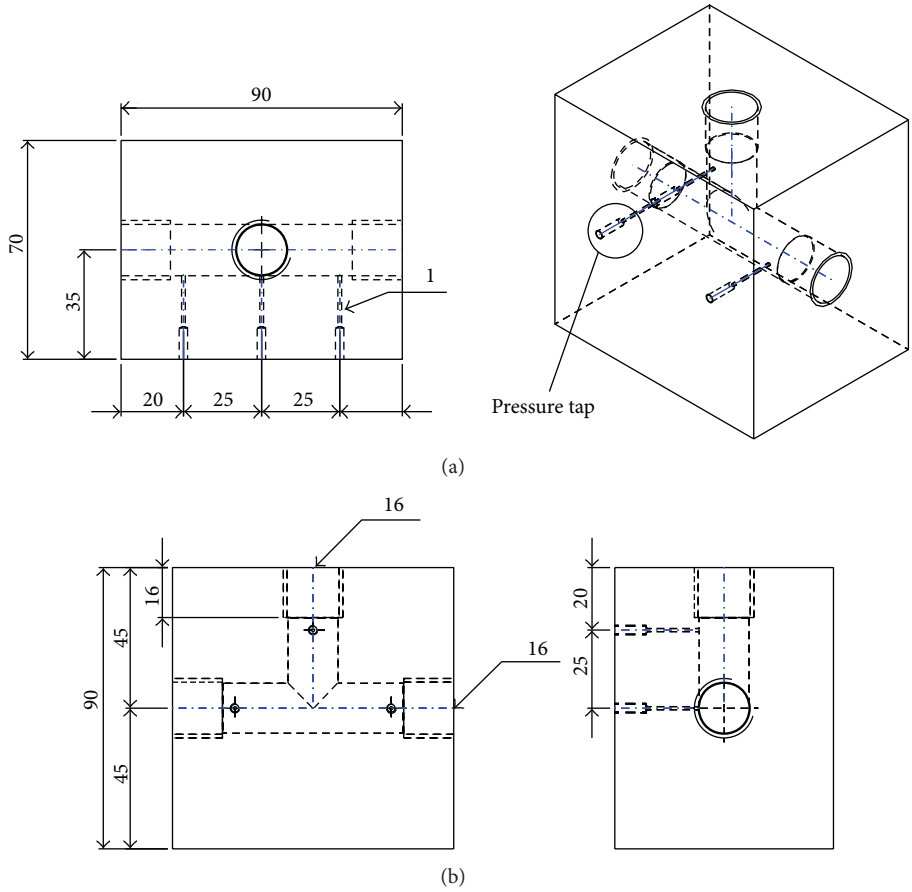

(a)

(b)

Figure 2: Draftings of T-joint (unit: mm).

13 and the values of the coefficients of polynomials are shown in Table 1. The level of fit error is less than 0.3% for pattern A and 2.2% for pattern B.

The static characteristic test results for pattern A shown in Figure 6 indicate that the loss coefficient ξ_{13} in the right-angled direction is large compared with that in the straight direction. This result shows that the loss in the flow in the right-angled direction is larger than that in the flow in the straight direction. The loss coefficients shown in Figure 6 have almost the same form as the curves reported in the literature, for example, [7].

Intuitively, the loss coefficients ξ_{12} and ξ_{13} for pattern B will be symmetric with respect to $q = 0.5$. However, the measured two curves for pattern B shown in Figure 7 are not symmetric with each other. Moreover, the curves for pattern B are not so smooth as curves for pattern A.

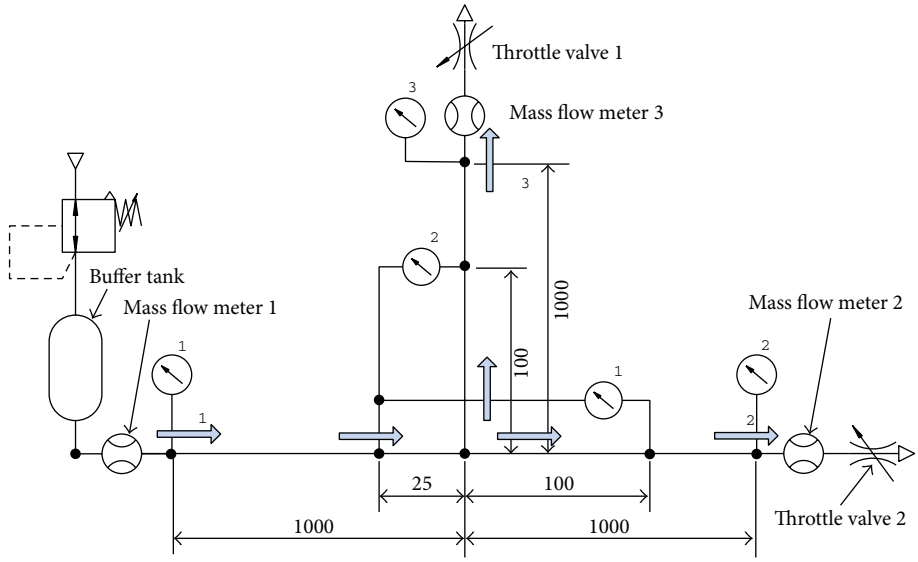

Figure 3: Experimental rig for static characteristic measurements in flow pattern A.

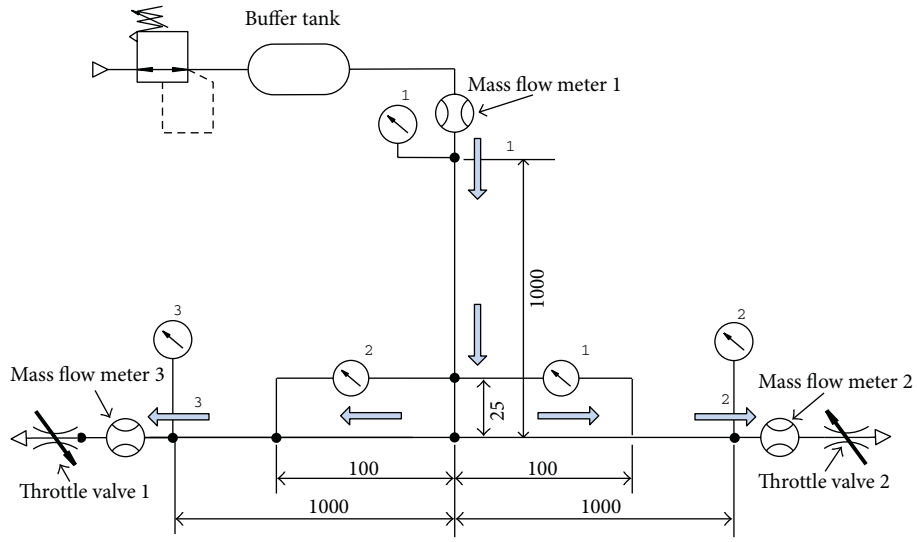

Figure 4: Experimental rig for static characteristic measurements in flow pattern B.

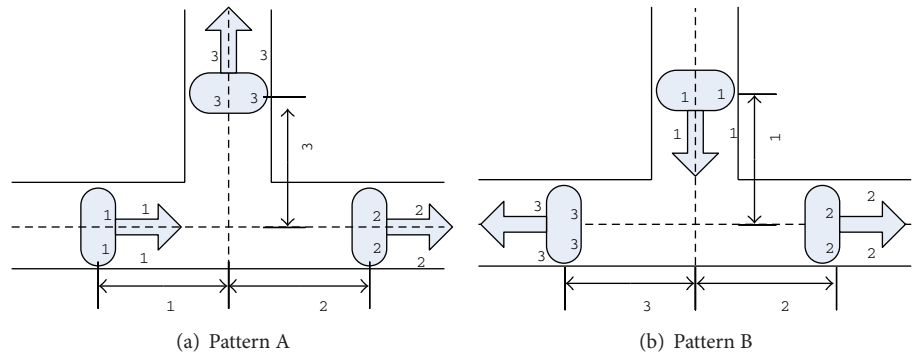

(a) Pattern A (b) Pattern B

Figure 5: Notation used for the flow parameters in both flow patterns.

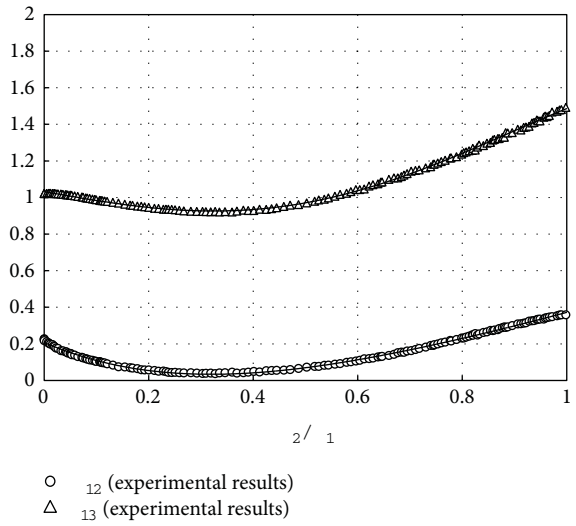

Figure 6: Loss coefficients for the tee branch pipe in flow pattern A.

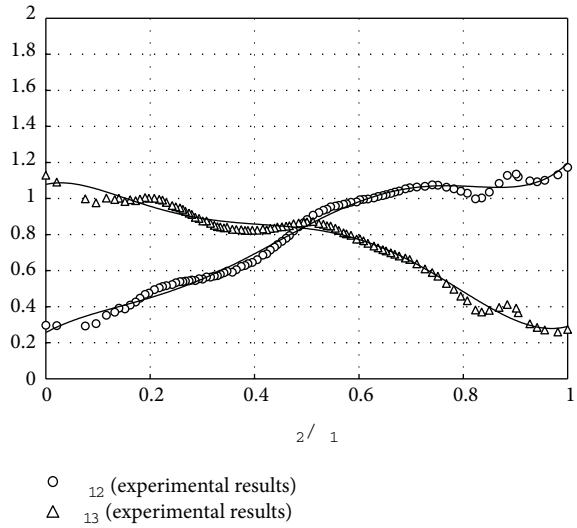

Figure 7: Loss coefficients for the tee branch pipe in flow pattern B.

The cause of the complexity of the curves and deviation from symmetricity is supposed to be a result of complex, and sometimes irregular, eddy formation near the joint. Eddies near a T-joint of pattern B were reported by Ito et al. [8], in which they visualized the flow of water.

3. Basic Equations and Difference Equations for Simulation

In this section, an original simulation program is developed for effective and convenient study of branch pipes. One-dimensional model of fluid flow in pipes is assumed. The basic equations of one-dimensional unsteady flow in a uniform straight pipe are as follows.

Equation of motion:

$$\frac{\partial u}{\partial t} + u\frac{\partial u}{\partial x} = -\frac{1}{\rho}\frac{\partial P}{\partial x} - \frac{\lambda}{2d}u^2. \tag{6}$$

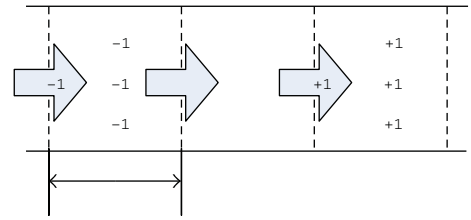

Figure 8: Discretized blocks of pipe model.

Equation of continuity:

$$\frac{\partial \rho}{\partial t} + \frac{\partial (\rho u)}{\partial x} = 0. \tag{7}$$

Equation of energy conservation:

$$\frac{\partial}{\partial t}\left[\rho A\left(e + \frac{u^2}{2}\right)\right] + \frac{\partial}{\partial x}\left[\rho u A\left(e + \frac{u^2}{2} + \frac{P}{\rho}\right)\right] - \pi d h(\theta - \theta_a) = 0. \tag{8}$$

Equation of state:

$$P = \rho R\theta. \tag{9}$$

Boundary conditions for the above system of equations are determined by the pipe end conditions and the mass and energy conservation at the T-joint. The boundary conditions are summarized as follows.

At the upstream end of the supply pipe:

$$P = P_1 = \text{const.} \qquad T = T_1 = \text{const.} \tag{10}$$

At the downstream end of the branched pipe:

$$f_2(P_2, Q_2) = 0, \qquad f_3(P_3, Q_3) = 0. \tag{11}$$

The functional relationships f_1 and f_2 are determined by throttles mounted at the pipe ends. At the T-joint, the mass conservation law is expressed by the following volumetric flow rates relation since the mass flow rate is converted to the volume flow rate using the industrial standard condition (P = 100 kPa (abs) , with θ = 293.15 K):

$$Q_1 = Q_2 + Q_3. \tag{12}$$

For the simulation, a straight pipe is divided into short blocks of length Δx. Time variation of the variables will be calculated with time step of Δt. The condition for convergence for hyperbolic partial differential equations [17] and reliability of calculation must be considered throughout parameter settings. A straight pipe is discretized as shown in Figure 8. The subscript of the variables in Figure 8 indicates block number.

For the simulation of unsteady flow, numbering for time step is also necessary. The second subscript is added to each variable after the block number. The first subscript in the variables in the following difference equations is the block number shown in Figure 8. The second subscript indicates the time-step number; for example, $u_{i,j}$ means velocity at the entrance of ith block at jth time step. The upwind difference scheme is used for calculating the convection terms.

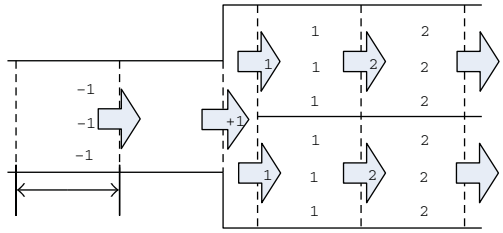

Figure 9: Model of the T-joint for simulation.

3.1. Difference Equations for Velocity. According to (6) and Figure 8, the flow velocity in ith block at jth time step can be expressed by

$$u_{i,j+1} = u_{i,j} - \frac{\Delta t}{\Delta x} u_{\text{conv}} - \frac{1}{\overline{\rho}} \frac{\Delta t}{\Delta x} \left(P_{i,j} - P_{i-1,j}\right) - \frac{\lambda \Delta t}{2D} \left|u_{i,j}\right| u_{i,j},$$

$$u_{\text{conv}} = \frac{u_{i,j} + \left|u_{i,j}\right|}{2} \left(u_{i,j} - u_{i-1,j}\right) - \frac{u_{i,j} - \left|u_{i,j}\right|}{2} \left(u_{i+1,j} - u_{i,j}\right),$$

$$\overline{\rho} = \frac{\left(\rho_{i-1,j} + \rho_{i,j}\right)}{2}. \tag{13}$$

The boundary conditions for the equation of motion are as follows.

Figure 9 shows the relationships at the joint. The algebraic expression with respect to the velocity is

$$u_{n+1,j} = u_{a1,j} + u_{b1,j}, \tag{14}$$

and the density is

$$\rho_{n+1,j} = \frac{\rho_{a1,j} + \rho_{b1,j}}{2}. \tag{15}$$

The flow velocity in the a_1 block (inlet of the first branched pipe) is expressed by

$$u_{a1,j+1} = u_{a1,j} - \frac{\Delta t}{\Delta x} u_{\text{conv}} - \frac{1}{\overline{\rho}} \frac{\Delta t}{\Delta x} \left(P_{a1,j} - P_{a0,j}\right) - \frac{\lambda \Delta t}{2D} \left|u_{a1,j}\right| u_{a1,j} - \frac{\xi_a \Delta t}{2\Delta x} \frac{\rho_{m,j}}{\rho_{a1,j}} \left|u_{a0,j}\right| u_{a0,j},$$

$$u_{\text{conv}} = \frac{u_{a0,j} + u_{a1,j}}{2} \left(u_{a1,j} - u_{a0,j}\right) = \frac{1}{2} \left(u_{a1,j}^2 - u_{a0,j}^2\right),$$

$$u_{a0,j} = u_{n,j}. \tag{16}$$

The flow velocity in the b_1 block (inlet of the second branched pipe) is obtained replacing a with b in the above three equations.

3.2. Difference Equations for Density. The density shown in the above equations must be given to satisfy the mass conservation law, (7). According to the ith block in Figure 8 and applying the upwind difference scheme for the convection term, the difference equation of density in the ith block becomes

$$\rho_{i,j+1} = \rho_{i,j} - \frac{\Delta t}{\Delta x} \rho_{i,j} \left(u_{i+1,j} - u_{i,j}\right) - \frac{\Delta t}{\Delta x} \rho_{\text{conv}},$$

$$\rho_{\text{conv}} = \frac{\overline{u}_{i,j} + \left|\overline{u}_{i,j}\right|}{2} \left(\rho_{i,j} - \rho_{i-1,j}\right) + \frac{\overline{u}_{i,j} - \left|\overline{u}_{i,j}\right|}{2} \left(\rho_{i+1,j} - \rho_{i,j}\right). \tag{17}$$

The velocity with over bar in the above is

$$\overline{u}_{i,j} = \frac{u_{i,j} + u_{i+1,j}}{2}. \tag{18}$$

The boundary condition at the joint with respect to the density is

$$\rho_{\text{conv}} = \frac{\overline{u}_{a1,j} + \left|\overline{u}_{a1,j}\right|}{2} \left(\rho_{a1,j} - \rho_{a0,j}\right) + \frac{\overline{u}_{a1,j} - \left|\overline{u}_{a1,j}\right|}{2} \left(\rho_{a2,j} - \rho_{a1,j}\right),$$

$$\rho_{a0,j} = \rho_{n,j}. \tag{19}$$

The boundary condition at the inlet end of the main pipe is illustrated in Figure 10; numerical values of variables are given as input at the first block. The boundary condition at the exit ends is illustrated in Figure 11. In this case, functional relationship between the pressure P_m and velocity difference $(u_m - u_{m+1})$ will be given as a functional relation.

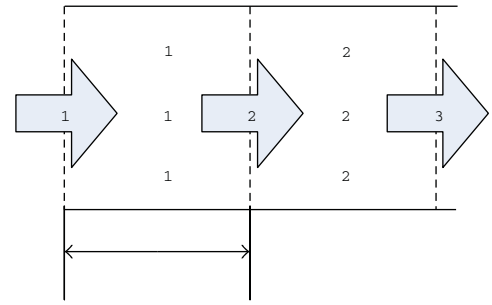

Figure 10: Boundary condition of pipe inlet end.

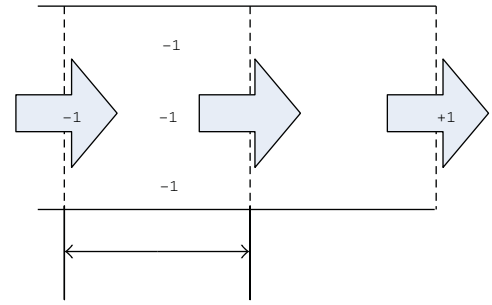

Figure 11: Boundary condition of pipe exit end.

3.3. Difference Equations for Temperature. According to (8) and Figure 8, we can derive the following difference equation for temperature change in intermediate blocks of pipe model:

$$\theta_{i,j+1} = \theta_{i,j} - \Delta t \frac{4h\left(\theta_{i,j} - \theta_a\right)}{\rho_{i,j} C_V D} - \frac{\Delta t}{\Delta x}\theta_{\text{conv}} - \frac{\Delta t}{\Delta x}\frac{R\theta_{i,j}}{C_V}\left(u_{i+1,j} - u_{i,j}\right) + \frac{\lambda \Delta t}{2C_V D}\left|\overline{u}_{i,j}\right|\overline{u}_{i,j}^2,$$

$$\theta_{\text{conv}} = \frac{\overline{u}_{i,j} + \left|\overline{u}_{i,j}\right|}{2}\left(\theta_{i,j} - \theta_{i-1,j}\right) + \frac{\overline{u}_{i,j} - \left|\overline{u}_{i,j}\right|}{2}\left(\theta_{i+1,j} - \theta_{i,j}\right),$$

$$\overline{u}_{i,j} = \frac{u_{i,j} + u_{i+1,j}}{2}. \tag{20}$$

The boundary condition for the temperature at the T-joint is

$$\theta_{\text{conv}} = \frac{\overline{u}_{a1,j} + \left|\overline{u}_{a1,j}\right|}{2}\left(\theta_{a1,j} - \theta_{a0,j}\right) + \frac{\overline{u}_{a1,j} - \left|\overline{u}_{a1,j}\right|}{2}\left(\theta_{a2,j} - \theta_{a1,j}\right), \tag{21}$$

$$\theta_{a0,j} = \theta_{n,j}.$$

3.4. Difference Equation for Pressure. Pressure at any block is estimated using the equation of state, (9),

$$P_{i,j} = \rho_{i,j} R \theta_{i,j}. \tag{22}$$

All these discretized equations are solved simultaneously at each time step. In these equations, ξ_a, ξ_b, λ, and h are given as input variable to the simulation program. The loss coefficient obtained in Section 3 is used as $\xi_a = \xi_{12}$ and $\xi_b = \xi_{13}$.

4. Experiment of Dynamic Characteristics

4.1. Experimental Setups for Dynamic Characteristic Measurements. The experimental rigs for the static characteristic measurement, which are explained in Section 2, are arranged for measurement of dynamic characteristics. Figures 12 and 13 show the rigs for the dynamic characteristic measurement for the flow patterns A and B, respectively. For pattern A, the throttle valve 2 in the downstream of the straight pipe is replaced with a servo valve. Similarly, for pattern B, the throttle valve 2 in the downstream of the branched pipe is replaced with a servo valve. In both of them, the flow rate through the servo valve is the reference input.

The flow meters used in this study are selected to meet the requirement of fast response. The working principle of the flow meters is explained in [16]; a correct measurement of oscillatory flow of up to 10 Hz is established with the flow meters. The reference pressure for the dynamic test is set to 600 kPa (abs) at the reference point stated in Section 2.

4.2. Experimental and Simulation Results. An unsteady flow was generated by giving a periodic wave signal to the servo valve. The electric signal is adjusted to generate a sinusoidal wave of flow rate. The frequencies of the sine wave signal are 1 Hz and 5 Hz. The level of flow rate Q_1 is 600 L/min (ANR); amplitude is 200 L/min (ANR). The flow through the servo valve is 100 ~ 500 L/min (ANR); the flow through the throttle valve 1 is about 300 L/min (ANR). The temperature of the air at the T-joint is 297 + −2 K, which is nearly equal to the ISO standard condition.

Time variations of the pressures, flow rate, and pressure differences are recorded. The differential pressures between the reference point for the T-joint and the pressure tap points, which are placed 100 mm downstream from the intersection of the pipe axes, are measured and compared with the simulation results. The experimental and simulation results are shown in Figures 14 and 15.

Figures 14(a) and 14(b) show differential pressure variation in pattern A for frequencies 1 and 5 Hz, respectively. When input wave frequency is 1 Hz, the simulation and experimental results coincide well; discrepancy between the simulation and experiment rather increases at frequency 5 Hz. Figures 15(a) and 15(b) show differential pressure variation in pattern B for frequencies 1 and 5 Hz, respectively. Similar to pattern A, the simulation agrees well with the experiment at 1 Hz, and the discrepancy between the simulation and the experiment increases by 5 Hz oscillation.

A significant feature of the difference between the simulation and the experiment is the existence of higher harmonics in experimentally obtained pressure curves.

5. Discussions

The static characteristics experiment in this study was carried out to obtain the loss coefficient necessary for simulation of pressure change in oscillatory flow. Its results were not simple as expected from the literature. Therefore, we explained the result of the static loss coefficient rather precisely.

The pipe Reynolds number in the static experiment lies between 18,000 and 53,000. In this range, the change of loss coefficient with the Reynolds number is very small. While the Mach number varies along the pipes, it is smaller than 0.1 throughout the experiment. Hence, the influence of the Mach number is also negligible, and the flow can be assumed to be incompressible. In this state, each loss coefficient at the T-joint becomes single function of the ratio of the flow rates. The obtained experimental results for the static characteristics are compared with the data in the literature, for example, [7]. The data of pattern A agree with [7]. However, no equivalent data for pattern B was found. In this experiment, diameter of the main and the branched pipes is the same; data in the literature shows diameter ratio of smaller than 1. Under this circumstance, the obtained data for pattern B was rather curious; the two loss coefficients for geometrically equivalent branches did not show expected symmetry with respect to flow ratio $q = 0.5$. Naturally, the conclusion will become different if smaller Reynolds number is selected; however, it will be a subject of another study.

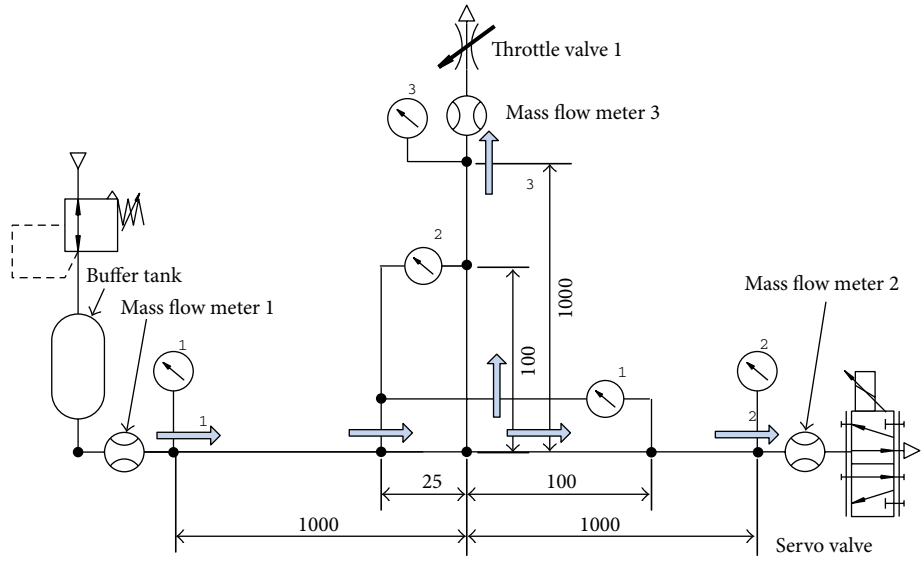

Figure 12: Experimental rig for dynamic characteristic measurements in flow pattern A.

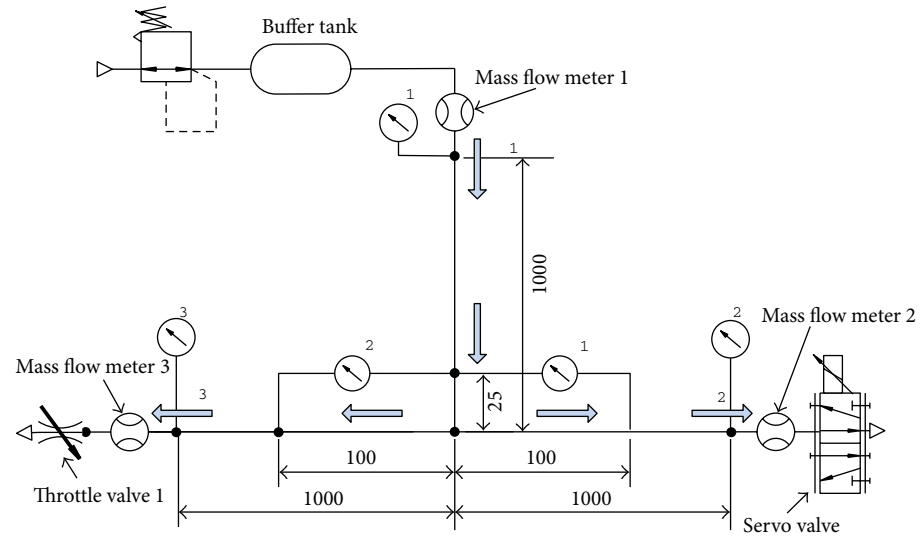

Figure 13: Experimental rig for dynamic characteristic measurements in flow pattern B.

The dynamic characteristics are not simply dependent on the flow ratio. It is influenced by additional parameters that do not appear in the steady state. For example, pressure wave reflections from pipe ends take a part of the pressure at the T-joint in dynamics while they give no influence for static characteristics. Therefore, the influence of compressibility is not negligible in dynamic characteristics.

The simulation in Section 4 was carried out using the statically measured values of the loss coefficient. As shown in Section 4, the discrepancy of the differential pressures between simulation and the corresponding experiment for 5 Hz is greater than that of 1 Hz. This indicates frequency dependence of the loss coefficient.

The wave forms of the differential pressure for pattern A with 1 Hz are very similar to a sine wave; however, those for pattern B show rather large distortion from sine waves. This reflects the nonuniformity of loss coefficient curves in Figure 9.

There is commercial simulation software from many companies. Such software is designed to meet nonspecified customers, which is often inconvenient for a special scientific purpose. Therefore, this study built a simulation program specialized for branch pipe. The validity of the simulation model built in Section 4 is examined giving input flow of different frequencies. Results of simulation are compared with experimental results. The difference between the experiments and the simulation is by no means zero. The cause of difference can exist in the modeling error and the noise in the experimental data.

There are two major causes of modeling error: discretizing errors with respect to time and space and the one-dimensional assumption. The discretizing error became

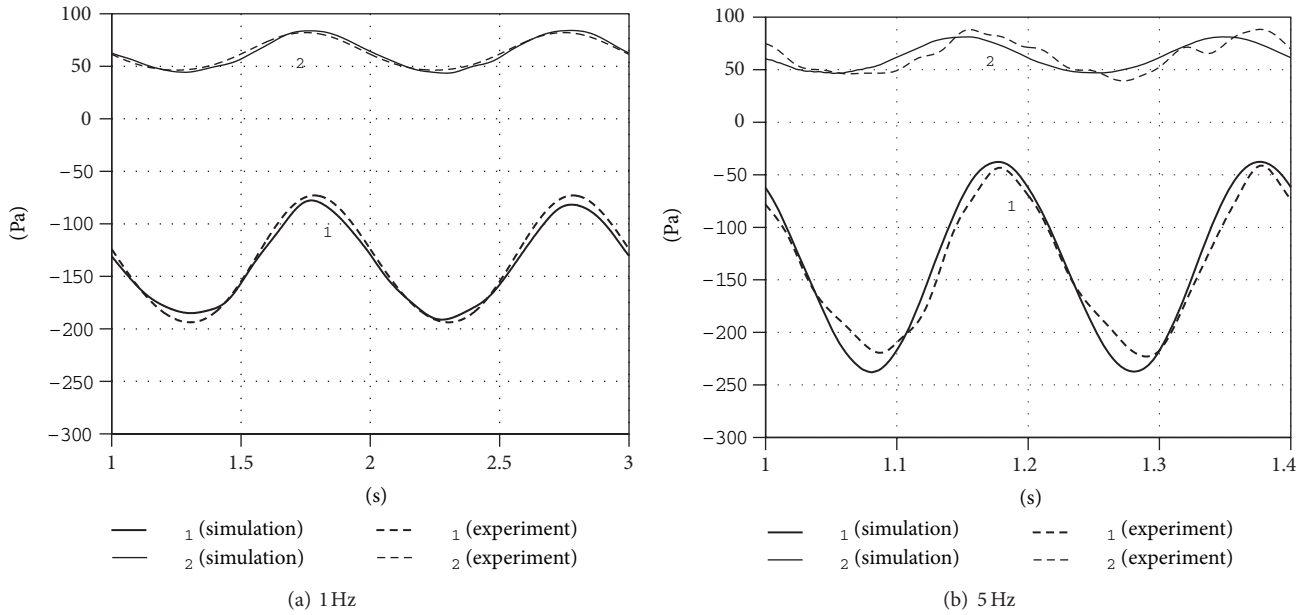

(a) 1 Hz (b) 5 Hz

Figure 14: Comparison of simulation and experimental results (pattern A: 1 Hz and 5 Hz).

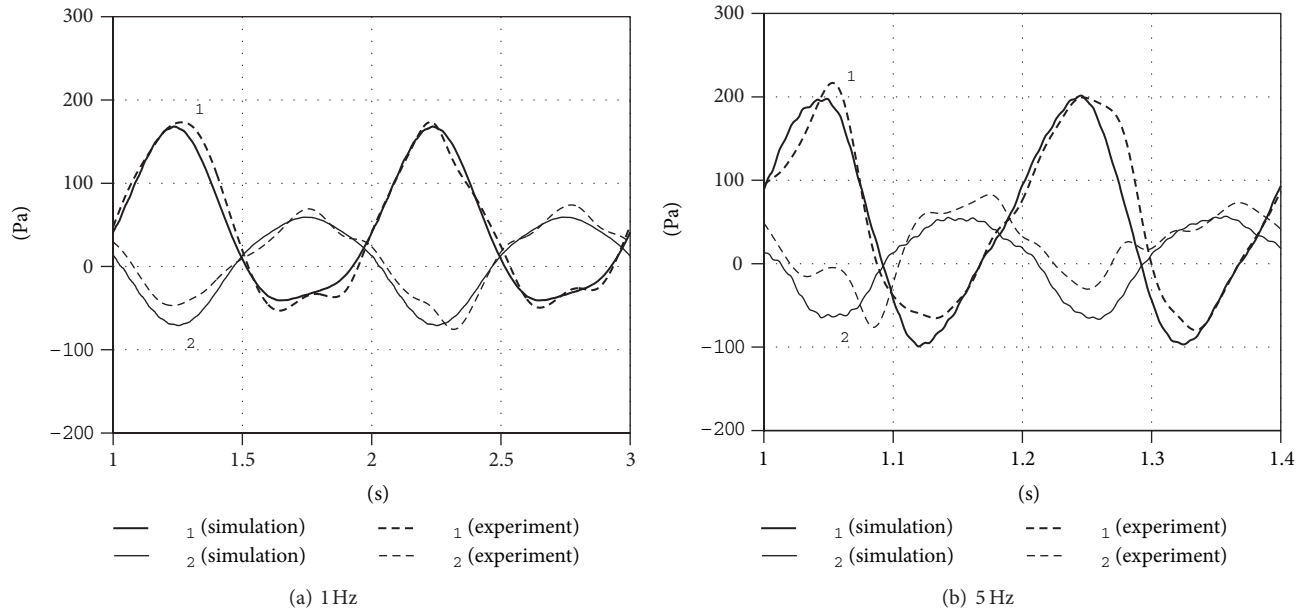

(a) 1 Hz (b) 5 Hz

Figure 15: Comparison of simulation results with experimental results (pattern B: 1 Hz and 5 Hz).

Table 1: Coefficients of polynomial fit for loss coefficients ζ_{1j}.

Pattern	j	A_0	A_1	A_2	A_3	A_4	A_5	A_6
A	2	0.3593	−0.6529	−0.2008	0.5926	0.1068	0	0
	3	1.0379	−0.5263	0.2735	1.7097	−0.9126	0	0
B	2	0.2567	1.5448	−6.088	19.431	16.816	−5.186	8.054
	3	0.2910	−0.8093	14.470	−32.43	20.117	8.600	−9.161

acceptable level by repeated trials of different step sizes. While the one-dimensional assumption is widely used [18–20], and its validity is proved to a certain degree, however, its definitive validation for each practical case requires experimental evidence. Therefore, comparison of simulation and experimental results is carried out in this study.

In the dynamics experiment, the sensor and amplifier output involves noises from various sources; therefore, filters are used to reject the noises. Although the use of a filter is effective for removing the noises, it also attenuates higher harmonics in a real signal. A suitable cut-off frequency is influenced by the noise that depends on experimental rigs and circumstances; therefore, careful trial-and-error process for selection of the cut-off frequency is important. After some trial of cut-off frequencies, we found that cut-off frequencies about five times as high as input frequency is near-best choice in this series of experiment. Therefore, the filter cut-off frequency is five times as high as the input sine wave frequency in the dynamics experiment.

Figures 14 and 15 shows two cycles of the signals; the good periodicity of the experimental results indicates that noises are effectively removed. Non-linearity in a system causes sometimes generation of sub-harmonics. The two figures suggest that a small component of 1/2 harmonic might exist in the experimental result although it is not appear in the simulation. Therefore, the observed sub-harmonic in the experimental result is not caused by the theoretical non-linearity, which is expressed by square of velocity in equations; it must be low frequency noise.

6. Conclusions

The pressure loss coefficients at a T-joint are measured for two patterns of flow. While the data from pattern A gave supposed values, data from pattern B did not have supposed symmetric feature.

Simulation and experimental measurement are carried out for the pressure change in a branch pipe induced by oscillatory flow at a terminal of a branch. Simulation program is made based on the one-dimensional flow model. Experiments and simulation are compared for oscillatory flow of 1 and 5 Hz; they concide well in the two patterns of branch pipe flow.

Nomenclature

A: Pipe cross-sectional area (m^2)
D: Pipe diameter (m)
e: Internal energy per unit mass (J/kg)
h: Heat transfer coefficient ($W/(m^2 \cdot K)$)
P: Pressure (Pa)
Q: Volumetric flow (m^3/s)
R: Gas constant ($J/(kg \cdot K)$)
t: Time (s)
u: Flow velocity (m/s)
x: Coordinate along pipe axis (m)
θ: Temperature (K)
θ_a: Atmospheric temperature (K)
λ: Darchy-Weisbach's pipe friction coefficient (-)
ρ: Density of air (kg/m^3)
ρ_a: Density of air at the ISO standard condition (kg/m^3)
ξ: Loss coefficient (-).

Acknowledgment

This research is partly funded by the Tokyo Gas Co., Ltd.

References

[1] V. L. Streeter and B. Wylie, *Hydraulic Transients*, McGraw-Hill, New York, NY, USA, 1967.

[2] F. Yeaple, *Fluid Power Design Handbook*, Marcel Dekker, New York, NY, USA, 3rd edition, 1995.

[3] J. M. Saleh, "Flow minor losses," in *Fluid Flow Handbook*, J. M. Saleh, Ed., chapter 10, pp. 32–34, McGraw-Hill, New York, NY, USA, 2002.

[4] R. L. Daugherty, J. B. Franzini, and E. J. Finnemore, *Fluid Mechanics with Engineering Applications*, McGraw-Hill, 5th edition, 1954.

[5] V. L. Streeter, *Fluid Mechanics. International Student Edition*, McGraw-Hill, New York, NY, USA, 4th edition, 1966.

[6] W. Beitz and K. H. Küttner, *Dubbel Tachenbuch für den Maschinenbau, 6 Hydro Und Aerodynamik, B51*, Springer, Berlin, Germany, 1990.

[7] Japan Society Mechanical Engineering, *JSME Data Book: Hydraulic Losses in Pipes and Ducts*, Japan Society Mechanical Engineering, Tokyo, Japan, 1980.

[8] H. Ito, M. Sato, and K. Oka, "Complete characteristics of energy losses due to division and combination of flow at a screwed tee," *Journal of the Japan Society of Mechanical Engineers*, vol. 44, no. 387, pp. 3902–3907, 1978 (Japanese).

[9] W. H. Hager, "An approximate treatment of flow in branches and bends," *Proceedings of the Institution of Mechanical Engineers C*, vol. 198, no. 4, pp. 63–69, 1984.

[10] R. Ikeda, F. Goto, and Y. Shoji, "Pulsatile flow in a 90 branched tube (1st report, experimental study on the flow ratio and branching losses for turbulent flow)," *Journal of the Japan Society of Mechanical Engineers*, vol. 52, no. 481, pp. 3166–3170, 1986.

[11] A. I. P. Miranda, P. J. Oliveira, and F. T. Pinho, "Steady and unsteady laminar flows of Newtonian and generalized Newtonian fluids in a planar T-junction," *International Journal for Numerical Methods in Fluids*, vol. 57, no. 3, pp. 295–328, 2008.

[12] A. H. Shapiro, *The Dynamics and Thermodynamics of Compressible Fluid Flow, Chapter 6*, vol. 1, John Wiley & Sons, 1953.

[13] J. Pérez-García and E. Sanmiguel-Rojas, "New experimental correlations to characterize compressible flow losses at 90-degree T-junctions," *Journal of Experimental Thermal and Fluid Science*, vol. 33, no. 2, pp. 261–266, 2009.

[14] J. Pérez-García, E. Sanmiguel-Rojas, and A. Viedma, "New coefficient to characterize energy losses in compressible flow at T-junctions," *Applied Mathematical Modelling*, vol. 34, no. 12, pp. 4289–4305, 2010.

[15] J. Pérez-García, E. Sanmiguel-Rojas, J. Hernández-Grau, and A. Viedma, "Numerical and experimental investigations on internal compressible flow at T-type junctions," *Journal of Experimental Thermal and Fluid Science*, vol. 31, no. 1, pp. 61–74, 2006.

[16] T. Funaki, K. Kawashima, and T. Kagawa, "Characteristic analysis of laminar flow meter for gases with high speed response," *Transactions of the Society of Instrument and Control Engineers*, vol. 40, no. 10, pp. 1008–1013, 2004.

[17] J. H. Mathews and K. D. Fink, *Numerical Methods Using MATLAB*, Prentice Hall, 3rd edition, 1992.

[18] E. Bideaux and S. Scavarda, "Pneumatic pipe modeling: theory and experimental approach (Part II)," in *Fluid Power Systems and Technology*, pp. 77–81, American Society of Mechanical Engineers, New York, NY, USA, 2000.

[19] K. J. Melcher, *User Guide for Compressible Flow Toolbox Version 2.1 for Use with MATLAB, Version 7, NASA/TM-2006-214086*, 2006.

[20] P. Puddu, "Dimensionless flow equations for dynamic simulation of turbomachine components and fluid systems," *Proceedings of the Institution of Mechanical Engineers A*, vol. 224, no. 3, pp. 419–431, 2010.

Hindawi Publishing Corporation
Advances in Mechanical Engineering
Volume 2013, Article ID 986984, 9 pages
http://dx.doi.org/10.1155/2013/986984

Research Article

Modeling and Numerical Simulation of the Grinding Temperature Field with Nanoparticle Jet of MQL

C. H. Li, J. Y. Li, S. Wang, and Q. Zhang

School of Mechanical Engineering, Qingdao Technological University, Qingdao 266033, China

Correspondence should be addressed to C. H. Li; sy_lichanghe@163.com

Received 23 January 2013; Accepted 20 March 2013

Academic Editor: Yi Wang

In this research, the heat transfer model of surface grinding temperature field with nanoparticle jet flow of MQL as well as the proportionality coefficient model of energy input workpiece was established, respectively. The numerical simulation of surface grinding temperature field of three workpiece materials was conducted. The results present that, in the workpiece, the surface temperature was significantly higher than the subsurface temperature, presenting relatively large temperature gradient along the direction of workpiece thickness. The impact of the grinding depth on grinding temperature was significant. With the increase of the cut depth, peak values of the grinding temperature rocketed. Distribution rules of the temperature field of 2Cr13 in four cooling and lubrication approaches were the same. Based on the excellent heat transfer property of nanofluids, the output heat through the grinding medium acquired an increasingly high proportion, leading to the drop of the temperature in the grinding zone. For the same cooling and lubrication conditions, grinding temperature presented insignificant changes along the direction of grinding width. Yet, under different cooling conditions, the temperature variation was significant. MQL grinding conditions with additive nanoparticles demonstrated great impact on the weakening of temperature effect on the grinding zone.

1. Introduction

Minimum quantity lubrication (MQL) refers to the minimum quantity of lubricants that enters the high-temperature grinding zone after being mixed in high-pressure gas and atomized with high pressure draft (4.0–6.5 bar). The traditional flood cooling feed liquid of grinding fluid is 60 L/h for a unit of the width of grinding wheel, while the consumption of MQL grinding fluid is 30–100 mL/h for a unit of the width of the grinding wheel [1–8]. High pressure draft serves as cooling and chip removal. Lubricants attached to the finished surface of the workpiece, forming a layer of protective film and serving as the lubrication. This technology integrates the advantages of flood cooling grinding and dry grinding, presenting similar lubrication effects compared with traditional flood cooling grinding. Lubricants adopt vegetable oil as alkyl ester of base oil, which shows features like as excellent biodegradability, lubricating properties, high viscosity index, low volatility, recycling, short production cycle and insignificant environmental diffusion, and so forth. The consumption of lubricants is only parts per thousand or a few hundredths of a percentage point compared with the traditional grinding approaches, which greatly improved the working environment. Thus, high pressure draft is an efficient low-carbon processing technology. However, studies show that cooling effect of high pressure draft is too limited to meet the needs of strengthened high-temperature heat transfer of the grinding zone [8–12]. The processing quality of the workpiece and the grinding wheel life is worse than the traditional flood cooling grinding, indicating that MQL technique requires further improvements.

In order to improve the defects in cooling effect of MQL grinding, the Sanchez [12] team from Spain applied the low-temperature CO_2 to the MQL grinding, that is, to inject low-temperature CO_2 (238 K) and MQL medium with two nozzles in the grinding zone with the form of jet flow. Given the advantage of low-temperature heat transfer property of CO_2, the temperature of the grinding zone can be further reduced. Studies have shown that the consumption of CO_2 is remarkable (40 L/min), and two sets of feeding systems are needed. The costs are high and the rapid volatile property of CO_2 constrains its strengthened heat transfer in the grinding

Table 1: The coefficient of thermal conductivity of matters.

Matters	Copper	Aluminum	Copper oxide	Aluminum oxide	Zinc oxide	Carbon nanotube	Diamond	Silicon	Water	Engine oil	Ethylene glycol
Thermal conductivity /W(m·K)$^{-1}$	401	237	19.6	40	100	3000	2300	148	0.613	0.145	0.253

zone (low-temperature CO_2 MQL grinding ratio $G = 4.5$; flood cooling lubrication grinding ratio $G = 4.22$). Hence, the cooling effect of cryogenic gas on improving MQL subjects to certain restrictions.

According to strengthened heat transfer theory, the heat transfer ability of the solid greatly exceeds the liquid and gas. At room temperature, the coefficient of thermal conductivity of solid materials is greater than the fluid material by several orders of magnitude. In Table 1, we compared the coefficient of thermal conductivity of solid with liquid materials. It can be inferred that the coefficient of thermal conductivity of liquid with suspended metal, nonmetallic or polymeric solid particles exceeded the pure liquid significantly. If solid particles are added in MQL medium, it is expected to greatly increase the coefficient of thermal conductivity of fluid medium so as to improve the convective heat transfer and offset the defects of insufficient cooling effects of MQL. In addition, nanoparticles (referring to ultrafine tiny solid particles with at least one dimension in the three-dimensional space that is, in the nanoscale range (1–100 nm)) also present tribological features such as special antifriction and high carrying capacity in aspects of lubrication and tribology. In this research, we added nanoscale solid particles in MQL fluid medium to produce nanofluids. Specifically, we injected nanoscale solid particles after the mixing and atomization of nanoparticle, lubricants (oil or oil-water mixture) and high-pressure gas in the grinding zone with the form of jet flow. Nanoparticle jet flow of MQL grinding provides an innovative grinding technology as well as the special equipment that integrates all advantages of MQL technology and presents better cooling effect as well as tribological features. This technology intends to effectively address the issue of grinding burn and to improve the workpiece surface completeness. It embodies important significance in the realization of efficient, environmentally friendly, resource-saving and low-carbon green production with low consumption.

The removed volume of unit materials during the grinding in the interface of the grinding wheel/workpiece generates a mass of energies. The introduction of MQL with insufficient cooling effect in the grinding is more challenging than other cutting methods. So far, only a few research groups conducted an exploratory study on MQL grinding technology. Xiu et al. explored the application prospect of MQL in the grinding from the aspect of environmental protection and ecology. The research demonstrated that, compared with the traditional flood cooling grinding, costs of MQL grinding fluid were reduced by 65%, and the investment of device was reduced by 22%. In addition, with the naturally degraded synthetic esters as lubricants, harms of the grinding fluid on the environment and human were minimized [13–15]; Aurich et al. [16] studied the surface completeness of workpiece, specific energy, and abrasion contrast of the grinding wheel under different conditions including dry grinding, flood cooling wet grinding, and MQL. The results showed that, compared with the other two flood cooling methodology conditions, MQL provided effective lubrication, yet insufficient cooling effect. The completeness of the processed workpiece surface was deteriorated; Malkin and Guo [17] researched on the impact of grinding parameters on the workpiece surface quality in the flat grinder experiment. Compared with the flood cooling wet grinding, the workpiece surface quality as improved under the conditions of the optimization of grinding consumption and feed liquid parameters, with improved quality and reduced tangential grinding force and specific grinding energy; Huang and Liu [18] applied the precision surface grinder experiment to study the grinding power, grinding force, grinding temperature and surface roughness contrast of MQL grinding and flood cooling dry grinding. The results show that, with a suitable material removal rate, the grinding force and the grinding power of MQL were prior to that of flood cooling methodology. Yet, the roughness of the workpiece surface and residual stress was inferior to that of flood cooling methodology. Xu et al. [19] conducted the minimum cutting-in (5 μm) grinding contrast experiment on the precise DC grinder with the water droplets processing liquid attached by minimum quantity oil film, emulsion solution, soluble concentrates, minimum quantity spray and minimum quantity oil mist processing liquid. Furthermore, they measured the grinding force, surface roughness, the temperature of the grinding zone, and grinding ratio. Results showed that the cooling effect of the water droplets processing liquid attached by minimum quantity oil film as inferior to traditional processing liquid such as emulsion solution and soluble concentrates, yet presenting sound lubricating property [20–23]. It also presented excellent advantages in regard of processing precision and the grinding wheel life. Yet, this method is applied for the grinding under the low grinding heat condition due to the limited heat transfer of minimum quantity water drops.

On account of the damages on environment and workers' health from the extensive use of grinding fluid in flood cooling methodology as well as the severely insufficient cooling effects of MQL grinding, nanoscale solid particles were injected in the grinding zone with the form of jet flow after the mixing and atomization of nanoparticle, lubricants (oil or oil-water mixture), and high-pressure gas because of the prior heat transfer of solid particles than liquid and gas. In this way, the defects of MQL cooling effect can be offset, which greatly improved the production environment, saving energy, and cost reduction and achieved low-carbon manufacturing. Furthermore, lubricants were injected in the grinding zone more effectively via breaking the airbond,

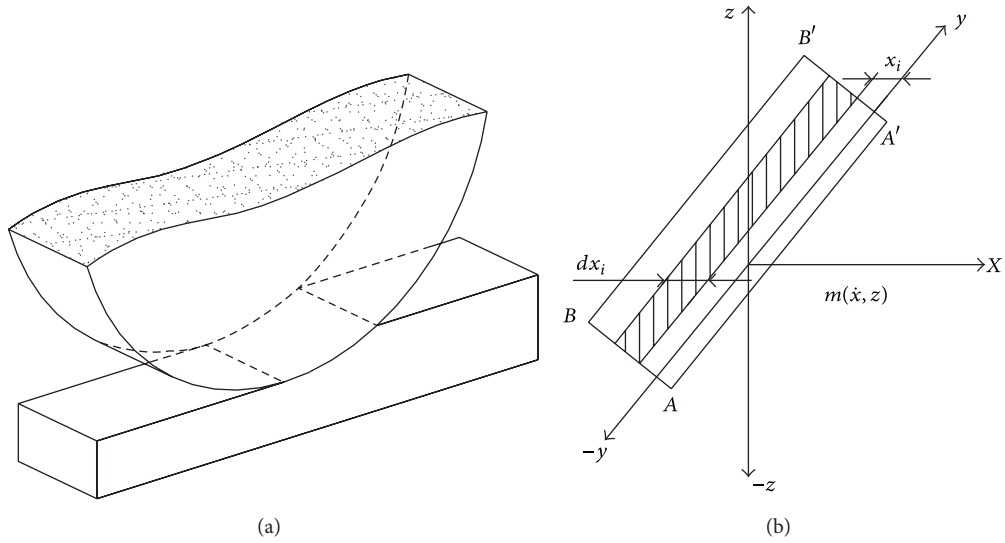

Figure 1: Planar heat source conduction.

improving effective flow rate of the grinding wheel/workpiece interface grinding medium. Compared with the wet grinding, the fluid dynamic pressure and introduction force generated by the grinding medium in the wedge-shaped contact area were reduced, as well as the deflection deformation of the principal axis of the grinding wheel [24–27]. It also improved the precision of the workpiece processing. Furthermore, with the special lubricating property and tribological properties of nanoscale solid particles for jet flow, a nanoparticle shearing oil layer can be found on the interface of the grinding wheel/workpiece, which can enhance the improvement of lubricating property of MQL grinding and present practical meanings. In this research, the modeling and numerical simulation was conducted on nanoparticle jet flow of MQL grinding temperature field.

2. The Mathematical Model of Temperature Field

With the planar shallow-cut grinding as the study objective, Figure 1 shows heat source conduction of the grinding zone. Assume the grinding contact arc zone AA′B′B as the band-shape heat source, Y direction was regarded as infinitely long, and the intensity of heat source is q_m [J/m^2·K·s]; the contact arc length is l_s, and the heat source AA′B′B is the set of countless linear heat sources d_{xi}. One linear heat source d_{xi} was taken with the intensity of $q_m d_{xi}$, which moved along the X direction with the velocity of V.

The temperature rise equation of the point $m(x, 0, z)$ from linear heat source $q_m dx' d_t$ with the width of dx':

$$d\theta_m = \frac{q_m}{\pi\lambda} \exp\left[\frac{(x - x_i)\, v}{2\alpha}\right] k_0\left[\frac{v}{2\alpha}\sqrt{(x - x_i)^2 + z_m^2}\right] dx_i. \tag{1}$$

The temperature variation equation of the point m from the entire heat source belt is

$$\theta_{(x,z)} = \frac{q_m}{2\pi\lambda}\int_{-l}^{l} dx_i \int_0^{\infty} \frac{dt}{t} \exp\left\{-\frac{\left[x - x' + vt\right]^2 + z^2}{4\alpha t}\right\}$$
$$= \frac{q_m}{2\pi\lambda}\int_{-l}^{l} e^{(x-x)v/2\alpha} K_0\left[\frac{v}{2\alpha}\sqrt{(x_i - x)^2 + z^2}\right] dx_i, \tag{2}$$

$$u = \frac{\left(x - x'\right)v}{2\alpha}; \qquad X = \frac{vx}{2\alpha}; \qquad Z = \frac{vz}{2\alpha}; \qquad L = \frac{vl}{2\alpha}. \tag{3}$$

To substitute (3) in (2), we get the following equation:

$$\theta_{(x,z)} = \frac{2q_m\alpha}{\pi\lambda v}\int_{X-L}^{X+L} e^{-u} K_0\sqrt{Z^2 + u^2}\, du, \tag{4}$$

where q_m is the surface heating source intensity of semi-infinite body, λ is the thermal conductivity of workpiece material W/(m·K), α is thermal diffusivity (cm^2/s) $\alpha = \lambda/\rho c_p$, c_p is specific heat capacity (J/(kg·K)$^{-1}$, ρ is density (g/cm^3), V is the movement velocity of heat source, and $K_0(u)$ is zero-order-modified Bessel function of the second kind.

2.1. Energy Proportionality Coefficient. Assume the theoretical contact area and actual contact area of grinding wheel and the workpiece as S and S_e respectively; q_w was used to express the internal input energy in unit time to obtain

$$q_w = \frac{1}{2}(\theta_m b)\left[2\left(\lambda\rho c_p\right)_w v\frac{S_e}{S} l_c\right]^{1/2}. \tag{5}$$

Input energy of the grinding wheel in unit time is

$$q_s = \frac{1}{2}(\theta_m b)\left[2\left(\lambda\rho c_p\right)_s v_s\frac{S_e}{S} l_c\right]^{1/2}. \tag{6}$$

Table 2: Performance parameters of 2Cr13 material.

Temperature (°C)	25	100	200	300	400	500
Modulus of elasticity (GPa)	228	214	208	200	189	180
Coefficient of thermal conductivity (W/m·K)	23.8					
Specific heat (J/Kg·K)	460					
Coefficient of thermal expansion (10^{-5}/K)	10.3					
Density (Kg/m^3)	7750					
Poisson's ratio	0.29					
Yield strength (MPa)	440					

Table 3: Performance parameters of 45 steel.

Temperature (°C)	25	100	200	300	400	500	600	700
Thermal conductivity (W/m·K)	41.7	43.4	43.2	41.4	39.1	36.7	34.1	32.0
Specific heat (J/Kg·K)	480	498	524	560	615	700	854	1064
Coefficient of thermal expansion (10^{-5}/K)	—	1.159	1.232	1.309	1.371	1.418	1.467	1.498
Density (Kg/m^3)	7850							
Modulus of elasticity (GPa)	209							
Poisson's ratio	0.296							
Yield strength (MPa)	355							

Table 4: Performance parameters of ZrO_2.

Density (Kg/m^3)	Coefficient of thermal conductivity (W/m·K)	Specific heat (J/Kg·K)	Coefficient of thermal expansion (10^{-5}/K)	Modulus of elasticity (GPa)	Poisson's ratio	Breaking tenacity (Mpa)
5500	3.5	660	9.6	209	0.3	8.1

Output energy via nanofluids in unit time is

$$q_f = \frac{1}{2}(\theta_m b)\left[2\left(\lambda\rho c_p\right)_f v_s l_c\right]^{1/2}. \quad (7)$$

The proportionality coefficient R_w of input energy is

$$R_w = \frac{q_w}{q_s + q_f}, \quad = 1 \times \left(1 + \sqrt{\left(\lambda\rho c_p\right)_s / \left(\lambda\rho c_p\right)_w \times \left(S_e/S\right) v_s/v} + \sqrt{\left(\lambda\rho c_p\right)_f / \left(\lambda\rho c_p\right)_w \times v_s/v}\right)^{-1}, \quad (8)$$

where v_s, the speed of grinding wheel; b, grinding width; $(\lambda\rho c_p)_w$, performance parameters of workpiece; $(\lambda\rho c_p)_s$, performance parameters of grinding wheel; $(\lambda\rho c_p)_f$, performance parameters of nanofluids.

Surface heating source intensity of the workpiece is

$$q_m = \frac{R_w F_t v_s}{l_s b}. \quad (9)$$

3. Numerical Simulation of Temperature Field

3.1. Simulation Conditions. The planar grinding process was regarded as the movement of planar heat source on the workpiece surface, and temperature field rules of 2Cr13, 45 Steel, and ZrO_2 at 25°C were studied. Material properties and grinding parameters are shown in Tables 2, 3, 4, 5, and 6 [28–31].

Table 5: Technological parameters of grinding.

Speed of grinding wheel (v_s)	Work speed (v_w)	Grinding depth (a_p)	grinding width (b)
40 m/s	3 m/min	5 μm	16 mm

Table 6: Performance parameters of cooling and lubrication approaches.

Cooling and lubrication approaches	Performance parameter
Flood cooling Methodology	Water-based grinding fluid, delivery value: 100 L/min
MQL	Pure oil base (35 mL/H)
Nanoparticle jet flow of MQL	Carbon nanotube particles with the diameter of 10–20 nm; oil base (vegetable oil); volume fraction: 1%; delivery value: 15 mL/min
Dry grinding	None

3.2. Finite Element Grid Division. In the finite element analogue simulation, grid division has a decisive effect on the precision of the calculation analysis. The less width of the grid

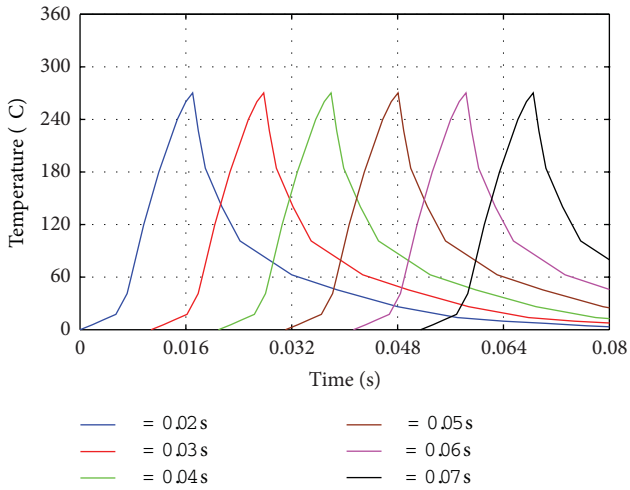

Figure 2: Graph of temperature distribution at different points along the grinding direction.

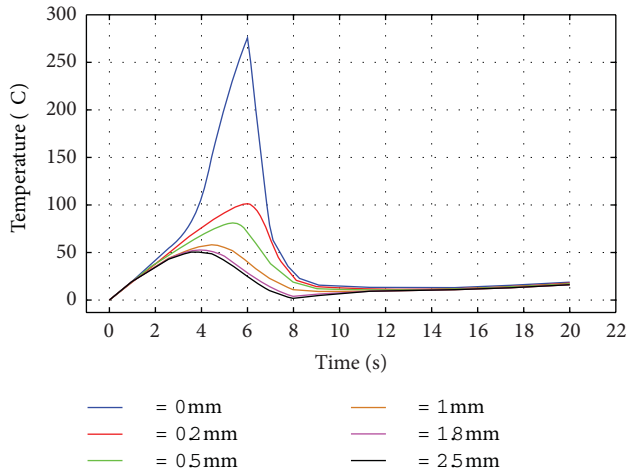

Figure 3: Temperature distribution diagram of nodes along the direction of grinding depth.

division, the higher the corresponding computational accuracy, and the more computation time is needed. Hence, to improve the computational accuracy and efficiency, in this model, the DC3D8 mode of 8-node implicit linear heat conduction unit was adopted for the grid division of workpiece.

3.3. Thermal Loading. The mobile heat source model was discretized, that is, in the time of one analysis step, uniform and constant heat source was loaded to a certain area. In the next analysis step, the heat source was moved to another area. Meanwhile, the previous analysis results were used as the initiative conditions in the simulation so as to achieve the continuous moving loading of the heat source.

4. Result Analysis

4.1. Temperature Distribution along the Grinding Direction. In the planar grinding, with the constant feeding of the grinding wheel, the workpiece surface is influenced by the heat source effects, and its heat flux density and temperature field changed with the time. Rules of temperature variation at different positions are shown in Figure 2.

As shown in Figure 2, along the feeding direction of the grinding wheel, 6 nodes on the finished surface were taken with equidistance successively to acquire the temperature-time diagram. It can be seen from the figure that the temperature variation tendency of the six nodes was much the same, progressing forward in the form of waves respectively. When the heat source moves to the grinding arc zone of nodes, the node temperature was rapidly increased and reached the peak value when the heat source was about to leave the grinding arc zone. When the position of heat source was removed from the grinding arc zone, energies of each node rapidly diffused with the temperature gradually getting stabilized. Furthermore, the nodes closer to the heat source will have higher equilibrium temperature at the steady state.

4.2. Temperature Distribution along the Workpiece Thickness Direction. Figure 3 shows the surface temperature field variation rules along the workpiece thickness direction of 45 Steel under the condition of nanoparticle jet flow of the MQL. It can be seen from the Figure 3 that in the grinding, the heat source had an extremely short effect time on the workpiece surface. In addition, due to the relatively small thermal conductivity of the workpiece material, the input heat on the workpiece surface from the heat source cannot be timely diffused, thus forming the local high temperature as shown in the Figure 3. Moreover, the workpiece surface temperature was much higher than the subsurface temperature of the workpiece, presenting a relatively large temperature gradient along the direction of workpiece thickness. The temperature variation of the workpiece along the direction of thickness is mainly related with the material properties of heat source and the workpiece. The coefficient of thermal conductivity of the workpiece imposes significant impacts on longitudinal temperature variation.

As shown in Figure 3, four points with 0 mm, 0.2 mm, 0.5 mm, 1.0 mm, 1.8 mm, and 2.5 mm from the workpiece-finished surface along the workpiece thickness were taken, generating the time varying temperature diagram. It can be seen from the figure that the node with $Z = 0$ mm located on the surface of the grinding zone, and its maximum temperature, that is, the maximum temperature in the grinding zone, was about 280°C; with the node of $Z = 0.5$ mm, the maximum temperature of the node dropped to about 80°C. In addition, with the node of $Z = 1.8$ mm and $Z = 2.5$ mm, the temperature curve of the two nodes almost overlapped, and the maximum temperature at the steady state was about 50°C. It can be observed from the temperature curve of each node that in the planar grinding, from the temperature variation below the grinding surface, the node farther from the grinding surface will be less affected by the mobile heat source. When $Z < -1.5$ mm, the temperature variation tendency of nodes along the direction of grinding depth.

Table 7: Grinding technological parameters of 2Cr13.

Grinding depth a_p	Contact Arc length l_c	Heat distribution coefficient R_w	Grinding tangential force F_t	Heat flux density q_t
1 μm	0.45 mm	83%	28.4 N	8.57 W/mm^2
5 μm	1 mm	90%	51.3 N	15.4 W/mm^2
10 μm	1.41 mm	92%	51.3 N	20.8 W/mm^2

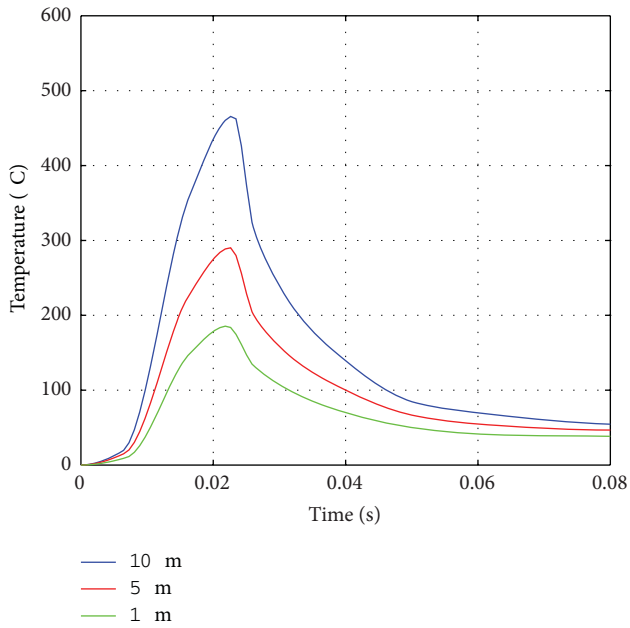

Figure 4: 2Cr13 Temperature variation diagram.

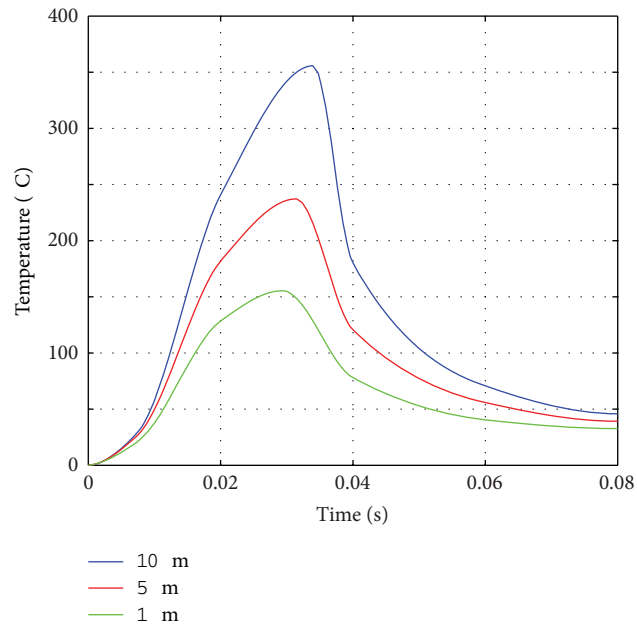

Figure 5: Time-varying diagram of ceramics temperature.

4.3. Simulation Results of Grinding Temperature Field with Different Cut Depths. In order to research on the time-varying of temperature fields of the three kinds of materials, the analog simulation of these materials under working conditions of different grinding depths was conducted.

4.3.1. Analysis of Simulation Parameters. In the planar grinding, parameters were interrelated and mutually influenced. With the changes of grinding depths, other simulation technological parameters (such as grinding zone contact arc length, heat distribution coefficient, heat flux density of mobile heat source etc.) were changed. Analog simulation of temperature fields with different grinding depths was conducted. Firstly, parameters were calculated. Corresponding grinding technological parameters of three grinding depths were shown in Table 7.

Similarly, corresponding heat flux densities of 45 Steel with the grinding depth of 1 μm, 5 μm and 10 μm were respectively 17.8 W/mm^2, 21.6 W/mm^2, and 23.0 W/mm^2. Meanwhile, the corresponding heat flux densities of the ceramic material at three different grinding depths were 10.3 W/mm^2, 12.5 W/mm^2, and 14.5 W/mm^2.

4.3.2. Simulation Results. Figures 4-5 showed the time-varying temperature diagram of the stainless steel 2Cr13 and zirconia ceramics in nanometer size with the grinding depth of 1 μm, 5 μm, and 10 μm. It can be observed from the figure that, in the planar grinding, different grinding depths should be adopted for different workpiece materials, without changing the shape of time-dependent grinding temperature curve. The only change was the grinding temperature peak value. In other words, the larger the grinding depth is, the higher the grinding temperature is. With the gradual decrease of the cut depth, the temperature variation curve tended to be flat. With the consideration that the removal mechanism of ceramic material is brittle rupture, the grinding wheel squeezed with ceramic materials during the grinding so that ceramic materials produced a large sum of cracks, which kept on extending and eventually led to the brittle removal of abrasive dusts. Under the same grinding condition, brittle rupture removal materials only consumed relatively low specific energies. Hence, the temperature in the grinding zone was relatively lower. The two materials generated temperatures with remarkable gradients in the grinding zone. When the mobile heat source left the grinding zone, the temperature gradually decreased and tended to be stable. However, with different physical property parameters of the materials (such as thermal conductivity, specific heat and coefficient of thermal expansion etc.), the general tendency of temperature curves was similar but the temperature generated from the grinding zone was different.

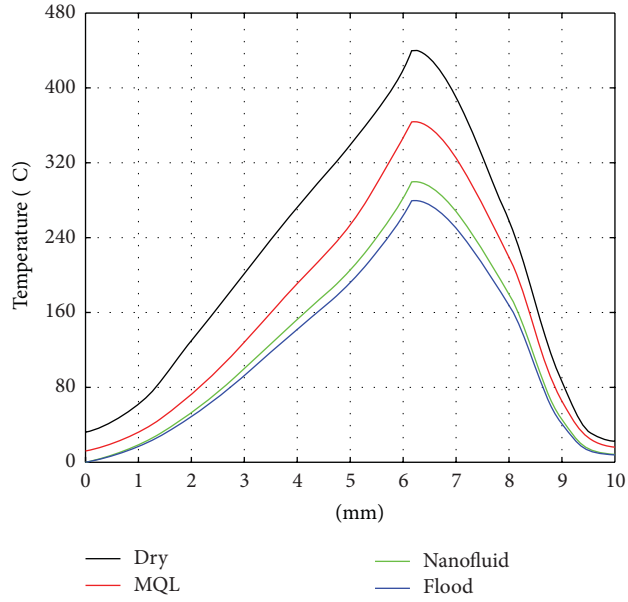

Figure 6: Temperature distribution along the grinding direction.

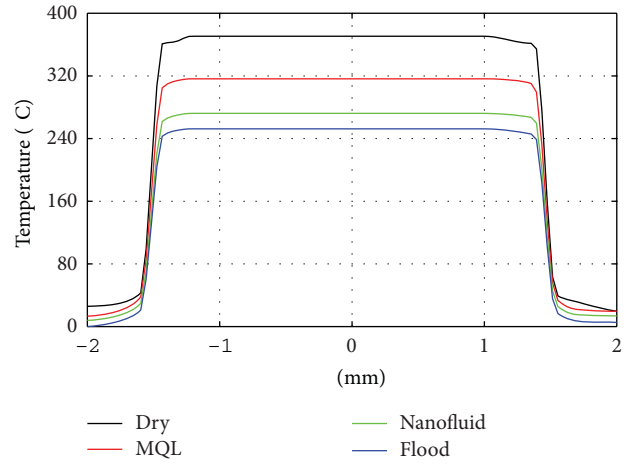

Figure 7: Regularities of temperature distribution along the direction of grinding width.

4.4. Simulation Analysis under Different Cooling and Lubrication Conditions. Figure 6 shows the simulation results of temperature field of 2Cr13 in four cooling and lubrication approaches. As shown in Figure 6, regularities of temperature field distribution are the same. Yet, due to different thermal ratios through grinding mediums, the temperatures of the grinding zone are different. However, based on excellent heat transfer property of nanofluids, the temperature of the grinding zone was greatly reduced. As shown in Figure 7, the location with the maximum temperature difference was in the grinding zone, indicating that only the injection of lubricants in the grinding zone and the maximum grinding temperature can be reduced to the most extent so as to prevent grinding burns and other issues during the grinding. Under the four cooling and lubrication conditions, the variations of grinding

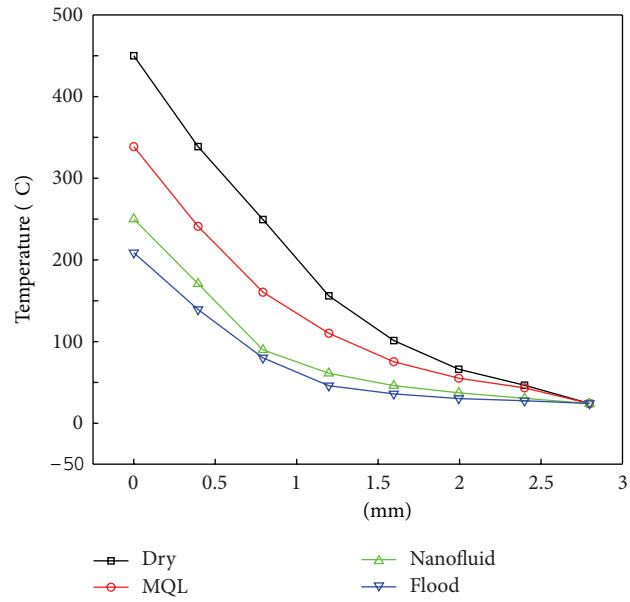

Figure 8: Variation rules of grinding temperature along the direction of depth.

temperature along the grinding width were insignificant but temperature variations were significant. The addition of nanoparticle MQL in grinding remarkably weakened the temperature effect of the grinding zone.

Figure 8 shows the regularities of distribution of grinding temperature along the direction of workpiece thickness under four grinding conditions. Large temperature gradient can be observed from Figure 8. Besides, the temperature gradient of dry grinding obviously exceeded that of MQL. In addition, at the deep layer with $Z = 2.8$ mm, the internal grinding temperature was close to the initial temperature.

5. Conclusions

The heat transfer model of surface grinding temperature field with nanoparticle jet flow of MQL as well as the proportionality coefficient model of energy input workpiece was established, respectively. The numerical simulation of surface grinding temperature field of three workpiece materials was conducted, namely, 45 Steel, 2Cr13 and zirconia ceramics in nanometer size. In the grinding, the surface temperature of workpiece was the highest, with a large temperature gradient along the direction of workpiece thickness. Furthermore, the grinding depth greatly affected the grinding temperature. With the increase of the cut depth, the peak value of grinding temperature was rapidly elevated.

Distribution rules of the temperature field of 2Cr13 are the same in four cooling and lubrication approaches, namely, dry grinding, flood cooling methodology, MQL, and nanoparticle jet flow of MQL. Due to different thermal ratios from grinding medium, the temperature of the grinding zone was differed. Meanwhile, with the outstanding heat transfer property of nanofluids, the temperature in the grinding zone was greatly reduced. Under four cooling and lubrication

conditions, little change of grinding temperature along the direction of grinding width was observed, however, with significant temperature variation. MQL with nanoparticle imposed the most significant impact on reducing the temperature effect of the grinding zone. During the grinding, only with the effective injection of grinding fluid in the grinding zone, the temperature of the grinding zone can be reduced to the most degree so as to prevent the grinding burn and improve the workpiece surface completeness.

Acknowledgment

This research was financially supported by the National Natural Science Foundation of China (50875138 and 51175276), the Shandong Provincial Natural Science Foundation of China (Z2008F11 and ZR2009FZ007), and the Specialized Construct Fund for Taishan Scholars.

References

[1] J. Kopac and P. Krajnik, "High-performance grinding—a review," *Journal of Materials Processing Technology*, vol. 175, no. 1–3, pp. 278–284, 2006.

[2] B. Varghese, S. Pathare, R. Gao, C. Guo, and S. Malkin, "Development of a sensor-integrated "intelligent" grinding wheel for in-process monitoring," *CIRP Annals—Manufacturing Technology*, vol. 49, no. 1, pp. 231–234, 2000.

[3] E. Brinksmeier, Y. Mutlugünes, F. Klocke, J. C. Aurich, P. Shore, and H. Ohmori, "Ultra-precision grinding," *CIRP Annals—Manufacturing Technology*, vol. 59, no. 2, pp. 652–671, 2010.

[4] K. Wegener, H. W. Hoffmeister, B. Karpuschewski et al., "Conditioning and monitoring of grinding wheels," *CIRP Annals—Manufacturing Technology*, vol. 60, no. 2, pp. 757–778, 2011.

[5] J. F. G. Oliveira, E. J. Silva, C. Guo, and F. Hashimoto, "Industrial challenges in grinding," *CIRP Annals—Manufacturing Technology*, vol. 58, no. 2, pp. 663–680, 2009.

[6] J. H. Liu, Z. J. Pei, and G. R. Fisher, "Grinding wheels for manufacturing of silicon wafers: a literature review," *International Journal of Machine Tools and Manufacture*, vol. 47, no. 1, pp. 1–13, 2007.

[7] C. H. Li, G. Q. Cai, and S. C. Xiu, "Auto-correlation study on the surface profile finished by abrasive jet with grinding wheel as restraint," *International Journal of Computer Applications in Technology*, vol. 29, no. 2–4, pp. 262–266, 2007.

[8] C. H. Li, Y. L. Hou, C. Du, and Y. C. Ding, "An analysis of the electric spindle's dynamic characteristics of high speed grinder," *Journal of Advanced Manufacturing Systems*, vol. 10, no. 1, pp. 159–166, 2011.

[9] T. Jin and G. Q. Cai, "Analytical thermal models of oblique moving heat source for deep grinding and cutting," *Journal of Manufacturing Science and Engineering*, vol. 123, no. 2, pp. 185–190, 2001.

[10] S. Malkin and C. Guo, "Thermal analysis of grinding," *CIRP Annals—Manufacturing Technology*, vol. 56, no. 2, pp. 760–782, 2007.

[11] E. Brinksmeier, J. C. Aurich, E. Govekar et al., "Advances in modeling and simulation of grinding processes," *CIRP Annals—Manufacturing Technology*, vol. 55, no. 2, pp. 667–696, 2006.

[12] F. Klocke, E. Brinksmeier, and K. Weinert, "Capability profile of hard cutting and grinding processes," *CIRP Annals—Manufacturing Technology*, vol. 54, no. 2, pp. 557–580, 2005.

[13] S. C. Xiu, C. X. Chao, and S. Y. Pei, "Experimental research on surface integrity with less or non fluid grinding process," *Key Engineering Materials*, vol. 487, no. 8, pp. 89–93, 2011.

[14] C. Li, Y. Hou, Y. Ding, and G. Cai, "Feasibility investigations on compound process: a novel fabrication method for finishing with grinding wheel as restraint," *International Journal of Computational Materials Science and Surface Engineering*, vol. 4, no. 1, pp. 55–68, 2011.

[15] C. H. Li, S. Wang, Q. Zhang, and Y. C. Ding, "Influence of unbalanced response of ultra-high speed grinder spindle on dynamic performance," *International Journal of Materials and Product Technology*, vol. 45, no. 1–4, pp. 119–131, 2012.

[16] J. C. Aurich, O. Braun, and G. Warnecke, "Development of a superabrasive grinding wheel with defined grain structure using kinematic simulation," *CIRP Annals—Manufacturing Technology*, vol. 52, no. 1, pp. 275–280, 2003.

[17] S. Malkin and C. Guo, *Grinding Technology: The Way Things Can Work: Theory and Application of Machining with Abrasives*, Industrial Press Inc., 2008.

[18] H. Huang and Y. C. Liu, "Experimental investigations of machining characteristics and removal mechanisms of advanced ceramics in high speed deep grinding," *International Journal of Machine Tools and Manufacture*, vol. 43, no. 8, pp. 811–823, 2003.

[19] X. P. Xu, Y. Q. Yu, and H. J. Xu, "Effect of grinding temperatures on the surface integrity of a nickel-based superalloy," *Journal of Materials Processing Technology*, vol. 129, no. 1–3, pp. 359–363, 2002.

[20] J. Webster and M. Tricard, "Innovations in abrasive products for precision grinding," *CIRP Annals—Manufacturing Technology*, vol. 53, no. 2, pp. 597–617, 2004.

[21] C. J. Evans, E. Paul, D. Dornfeld et al., "Material removal mechanisms in lapping and polishing," *CIRP Annals—Manufacturing Technology*, vol. 52, no. 2, pp. 611–634, 2003.

[22] T. W. Hwang, C. J. Evans, and S. Malkin, "An investigation of high speed grinding with electroplated diamond wheels," *CIRP Annals—Manufacturing Technology*, vol. 49, no. 1, pp. 245–248, 2000.

[23] C. H. Li, Z. R. Liu, G. Y. Liu, and Y. C. Ding, "Experimental investigations of mechanical characteristics and tribological mechanisms of nanometric zirconia dental ceramics," *The Open Materials Science Journal*, vol. 5, pp. 178–183, 2011.

[24] C. H. Li, Z. R. Liu, Y. L. Hou, and Y. C. Ding, "Critical conditions for brittle-ductile removal transition in nano-ZrO_2 dental ceramic grinding," *International Journal of Machining and Machinability of Materials*, vol. 11, no. 4, pp. 342–352, 2012.

[25] L. D. Zhu and W. S. Wang, "Modeling and experiment of dynamic performance of the linear rolling guide in Turn-milling Centre," *Advanced Science Letter*, vol. 4, no. 6, pp. 1913–1917, 2011.

[26] G. Byrne, D. Dornfeld, and B. Denkena, "Advancing cutting technology," *CIRP Annals—Manufacturing Technology*, vol. 52, no. 2, pp. 483–507, 2003.

[27] Y. Hou, C. Li, Z. Han, J. Li, and H. Zhao, "Examination of the material removal mechanisms during the abrasive jet finishing of 45 steel," *Advanced Science Letters*, vol. 4, no. 4-5, pp. 1478–1484, 2011.

[28] Y. L. Hou, C. H. Li, and Q. Zhang, "Investigation of structural parameters of high speed grinder spindle system on dynamic performance," *International Journal of Materials and Product Technology*, vol. 44, no. 1-2, pp. 92–114, 2012.

[29] C. H. Li, Z. R. Liu, Y. L. Hou, and Y. C. Ding, "Analytical and experimental investigations into material removal mechanism of abrasive jet precision finishing with grinding wheel as restraint," *International Journal of Machining and Machinability of Materials*, vol. 12, no. 3, pp. 266–279, 2012.

[30] Y. L. Hou, C. H. Li, and Y. Zhou, "Applications of high-efficiency abrasive process with CBN Grinding wheel," *Engineering*, vol. 2, no. 3, pp. 184–189, 2010.

[31] R. J. Gu, M. Shillor, G. C. Barber, and T. Jen, "Thermal analysis of the grinding process," *Mathematical and Computer Modelling*, vol. 39, no. 9-10, pp. 991–1003, 2004.

Hindawi Publishing Corporation
Advances in Mechanical Engineering
Volume 2013, Article ID 708785, 7 pages
http://dx.doi.org/10.1155/2013/708785

Research Article

Numerical Simulation on the Food Package Temperature in Refrigerated Display Cabinet Influenced by Indoor Environment

Chang Zhijuan, Wu Xuehong, Lu Yanli, Ma Qiuyang, and Zhang Wenhui

Zhengzhou University of Light Industry, Zhengzhou 450002, China

Correspondence should be addressed to Wu Xuehong; wuxh1212@yahoo.com.cn

Received 29 December 2012; Accepted 17 February 2013

Academic Editor: Bo Yu

In order to study the relation between the food package temperature and ambient environment, the food package temperature is investigated by numerical simulation under the different conditions, such as evaporator outlet velocities, ambient temperatures, and relative humidity. In the present computation, the influence of mass transfer and radiation is considered. The computational results show that the front and top food package temperature rises to 0.1 ~ 1.2°C due to the effect of light. At the investigated range of this paper, the food package temperature decreases when the air curtain velocity increases, but the food package temperature also increases with increase of ambient temperature and humidity. At the same time, the food package temperature decreases 0.2 ~ 1.1°C when air curtain outlet velocity increased by 0.15 m/s. The food package temperature rises about 0.6°C when ambient temperature increases by 2°C. The food package temperature rises about 0.9°C when ambient humidity increases by 20%. Therefore, the study can provide the reference for the design of refrigerated display cabinet.

1. Introduction

At the end of the food cold chain, refrigerated display cabinets play a very important role in ensuring quality and freshness of perishable food, which also can beautify the supermarket environment and allow customers free access to food inside the cabinets. According to investigation, more than 70% of total cooling capacity is produced by air curtain. However, many factors can affect the performance of air curtain, such as the width of discharge air grill, discharge air temperature, velocity, and external environmental conditions. In present, many researchers have focused mainly on the performances of the air curtain including using the CFD and experimental method.

Howell [1] found that energy saving could reach 20%–30% for most display cabinets when the relative humidity was lowered from 50% to 35%. Stribling et al. [2] showed that the CFD method was an efficient tool to investigate the performance of refrigerated display cabinet. The correlations of the total heat transfer across the air curtain were developed based on the finite difference method by Ge and Tassou [3]. Cortella pointed out that CFD was an important tool to study air flow and food temperature of inner refrigerated display cabinet [4]. Navaz et al. [5] studied the flow field characteristics and performance of the air curtain of refrigerated display cabinet combined using CFD method and digital particle image velocimetry. Foster et al. [6] showed that the CFD results could be applied to design refrigerated display cabinet and improve its performance. Navaz et al. [7] investigated influencing parameters of air entrainment in an open refrigerated display cabinet by CFD and experimental method. Chen and Yuan [8] investigated several important influencing factors of refrigerated display cabinet, such as ambient temperature and relative humidity, ambient air velocity, air supply flow, air flow from perforated back panels and night cover. D'agaro et al. [9] applied 2D and 3D models to investigate the air flow and temperature distribution in vertical refrigerated display cabinet. Gray et al. [10] observed that a 70-30 distribution of flow between the air curtain and rear duct could yield a good performance. Yu et al. [11] proposed modified two-fluid turbulence model to simulate the fluid flow and heat transfer characteristics of air curtains in an open vertical display cabinet. Yu et al. [12] developed the correlation model of TEF (the entrainment factor)

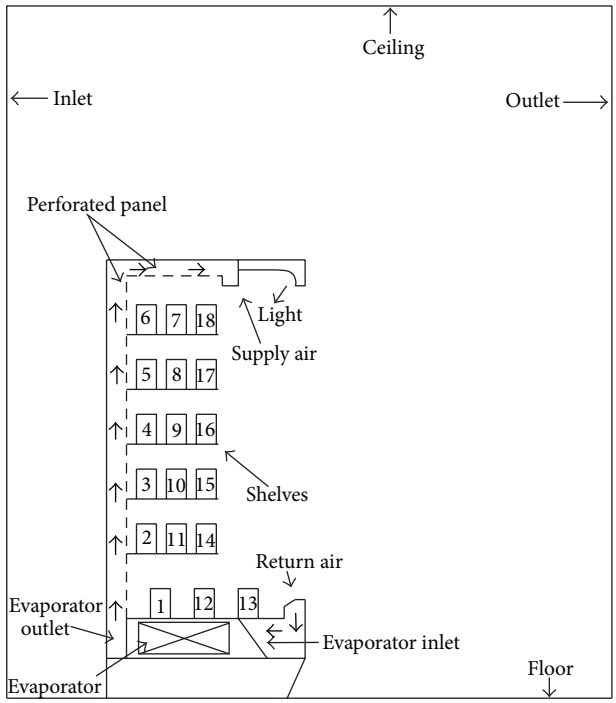

Figure 1: Two-dimensional diagram of refrigerated display cabinet.

for air curtain based on the CFD simulation. Amin et al. [13] developed a new approach using tracer gas to study the steady-state infiltration rate of display cabinet. Chen [14] studied thermal insulation of air curtains by simulation under different structural parameters. Moureh et al. [15] found that could be the performance of refrigerated display cabinet improved by the use of mist flow whereby fine water droplets were injected into the air curtain. Cao et al. [16] used the new algorithms and model to optimize air curtains. Ge et al. [17] applied the integration of CFD and cooling coil models to investigate flow field and temperature distribution of refrigerated display cabinet taking into account the effect of ambient temperature and humidity. Gaspar et al. [18] presented the variation of heat transfer rate and TEF obtained different ambient air conditions, varying air temperature, relative humidity, velocity, and its direction relatively to the display cabinet frontal opening. Hammond et al. [19] developed a model based on the Richardson number for a recirculating curtain sealing an open fronted display cabinet without back panel flow. Amin et al. [20, 21] investigated the effects of factors on the infiltration rate of open refrigerated vertical display cabinet. Laguerre et al. [22] developed mathematical model of food temperature in refrigerated display cabinets.

From the previous literature reviews, we can see that previous researches mainly focus on the performance of air curtain. Few literatures take into account the effect of external environment conditions. So this paper is to investigate the effects of some important factors on food temperature in refrigerated display cabinet, such as the light, ambient temperature and relative humidity, and supply air velocity by fan blade.

2. Physical Model

The 2D CFD model of refrigerated display cabinet (shown in Figure 1) is established in this paper. The main structure data of the refrigerated display cabinet is described in detail as follows.

(1) The computational domain's geometry dimensions are 3600 mm in width and 3600 mm in height. The dimensions of refrigerated display cabinet are 995 mm × 2200 mm (width × height).

(2) The distance from back panel to the left boundary is 500 mm.

(3) The cabinet shelf is divided into six product shelves; The length of the shelf is 460 mm. the distance between two shelves is 275 mm while the gap between the fifth and bottom shelves is 325 mm.

(4) Three rows of food packages are placed in each shelf. According to GB/T21001.2-2007, the size of food package is 100 mm × 50 mm ((width × height), so the height of food packages is 150 mm, food package pitch is 50 mm in each shelf, and the food package pitch is 120 mm in bottom shelf. The food package number is 1 to 18.

(5) The power of light is 30 W.

3. Mathematical Model and Computational Method

3.1. Mathematical Model and Computational Method. Air flow is assumed to be a two-dimensional steady, incompressible turbulent flow problem and neglects viscous dissipation. The influence of ambient air relative humidity is considered by making use of a species transport model. The fluid is considered as a mixture of dry bulb air and water vapour. Its mathematical model is as follows:

$$\operatorname{div}(\rho V\varphi) = \operatorname{div}\left(\Gamma_{\varphi}\operatorname{grad}\varphi\right) + S_{\varphi}, \tag{1}$$

where φ is common variable; Γ is generalized diffusion coefficient; S is generalized source term corresponding to φ; the turbulent Schmidt (Sct) number's value is 0.7. Different equations are referred in [23]. Table 1 gives the parameters of different partial differential equations. Classically recommended values are applied as the constants for the K-ε model in Table 1, which can be obtained in Table 2.

The heat gain of refrigerated display cabinet by thermal radiation is one of the most important cooling load components between food package and walls. The radiation equation is as follows:

$$\frac{dI}{ds} + (a + \sigma_s) I = a\frac{\sigma T^4}{\pi} + \frac{\sigma_s}{4\pi}\int_0^{4\pi} I d\Omega, \tag{2}$$

where I is directional radiation intensity; s is optical path length; a is absorption rate; σ_s is scattering rate; T is local temperature; σ is Stefan-Boltzmann constant; Ω is solid angle.

In the present computation, a surface-to-surface radiation model (based on surfaces view factors calculation) is

Table 1: Variables, diffusion coefficients, and source terms of each governing equations.

Equation	φ	Γ	s_φ
Mass equation	1	0	0
Momentum equation in X-direction	u	$\eta + \eta_t$	$-\frac{\partial p}{\partial x} + \frac{\partial}{\partial x}(\eta_{\text{eff}}\frac{\partial u}{\partial x}) + \frac{\partial}{\partial y}(\eta_{\text{eff}}\frac{\partial \nabla}{\partial x})$
Momentum equation in Y-direction	∇	$\eta + \eta_t$	$-\frac{\partial p}{\partial y} + \frac{\partial}{\partial x}(\eta_{\text{eff}}\frac{\partial u}{\partial y}) + \frac{\partial}{\partial y}(\eta_{\text{eff}}\frac{\partial \nabla}{\partial y})$
K-equation	K	$\eta + \frac{\eta_t}{\sigma_k}$	$\rho G_K - \rho\varepsilon$
ε-equation	ε	$\eta + \frac{\eta_t}{\sigma_\varepsilon}$	$\frac{\varepsilon}{K}(C_1\rho G_K - C_2\rho\varepsilon)$
Energy	T	$\frac{\eta}{\text{Pr}} + \frac{\eta_t}{\sigma_T}$	0
Species transport equation	C	$D + \frac{\eta_t}{\text{Sc}_t}$	0

$G_K = (\eta_t/\rho)\{2[(\partial u/\partial x)^2 + (\partial \nabla/\partial y)^2] + ((\partial u/\partial y) + (\partial \nabla/\partial x))^2 + (\partial w/\partial x)^2 + (\partial w/\partial y)^2\}$;
$\eta_{\text{eff}} = \eta + \eta_t$; $\eta_t = (\rho C_\mu K^2/\varepsilon)$.

Table 2: The coefficients in K-ε model.

C_μ	C_1	C_2	σ_K	σ_ε	σ_T
0.09	1.4	1.92	1.0	1.3	0.9–0.8

used to take into account the heat gain component. The discrete ordinates model is employed as the radiation model in the present computation. The SIMPLE algorithm is used as the solution method for the coupling of pressure-velocity. The second upwind scheme is applied to the convection term.

3.2. Boundary Conditions. In the present computation, the left and right walls of computational domain are defined as pressure inlet and pressure outlet, respectively. The ceiling and floor are defined as adiabatic walls, and boundary conditions of the evaporator inlet and outlet are defined as velocity inlet and pressure outlet, respectively. In addition, the boundary condition of the face permeability is correlated as constant. The perforated panel is defined as a porous jump condition of which the parameters can be adjusted according to the panel perforated rate. Others are all defined as wall. Because light generates continuous heat, it is defined as a wall with heat source. Food packages are set as solid; the physical property of food packages is defined in accordance with GB/T21001.2-2007. Under different relative humidity and temperature, mass fraction of water vapour on each boundary is shown in Tables 3 and 4, respectively.

4. Grid Independence

A careful check for the grid independence of the numerical solutions has been made to ensure the computational accuracy. The grid independence is performed by using the progressively finer grid until the most food package difference less than 0.5°C. For this purpose, three grid systems, 45059, 56667, and 62677, are tested (Figure 2). The temperature difference of three grids is less than 0.5°C. Therefore, in order to obtain the accurate results and save computer resource, the grid of 56667 is used for all the calculations. All of the grid cases are used as structured/unstructured grids. In order to resolve the temperature and the velocity gradient near the refrigerated display cabinet, a fine mesh is placed, as shown in Figure 3.

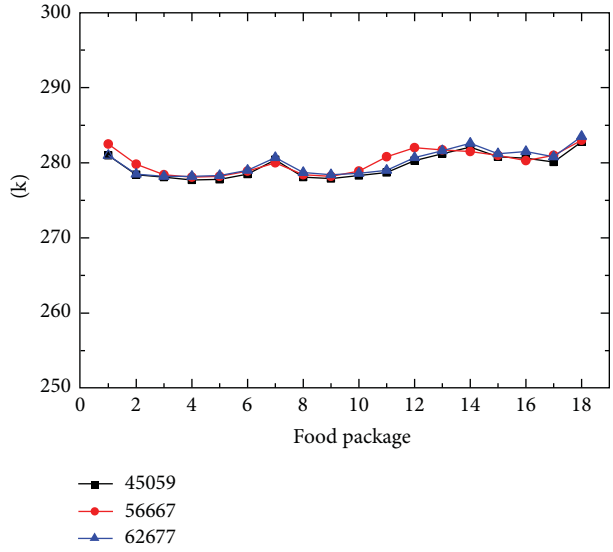

Figure 2: Grid independency test.

Table 3: The mass fraction of vapor under different relative humidity at temperature 25°C.

humidity	30%	50%	70%
Inlet (%)	0.59	0.99	1.39
Evaporator outlet (%)	0.35	0.50	0.61
Evaporator inlet (%)	0.31	0.36	0.40

Table 4: The mass fraction of vapor under different temperature at relative humidity 50%.

Temperature	23°C	25°C	27°C
Inlet (%)	0.73	0.99	1.128
Evaporator outlet (%)	0.50	0.50	0.50
Evaporator inlet (%)	0.36	0.36	0.36

5. Numerical Results and Discussions

The velocity field and temperature field are shown in Figures 4 and 5 at the given light, ambient temperature 25°C, relative humidity 50%, and inlet velocity 1.5 m/s, respectively.

It can be seen from Figure 4 that air curtain is formed between discharge air grill and return air grill. Because of entrainment, and width of air curtain increases gradually. Backflow can be formed between the food package and

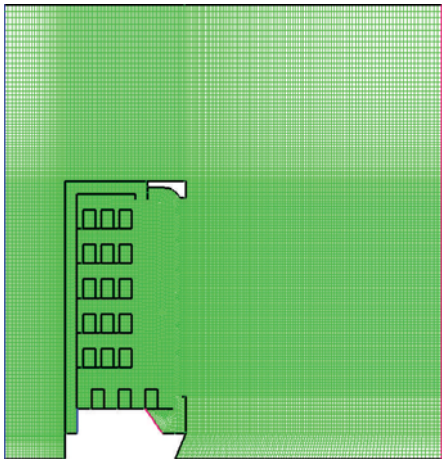

Figure 3: Grid systems.

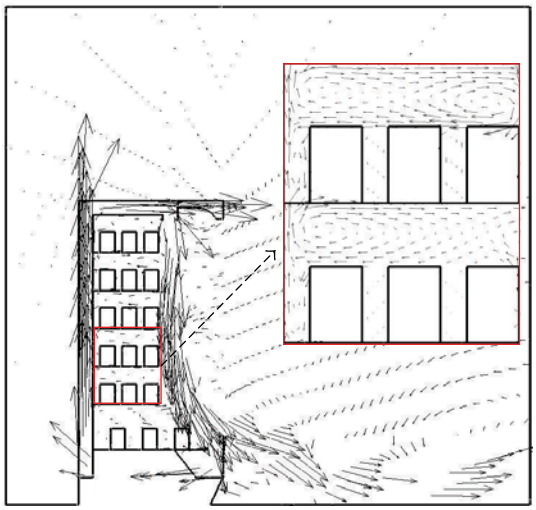

Figure 4: Velocity field.

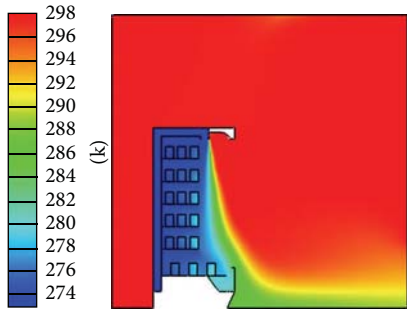

Figure 5: Temperature field.

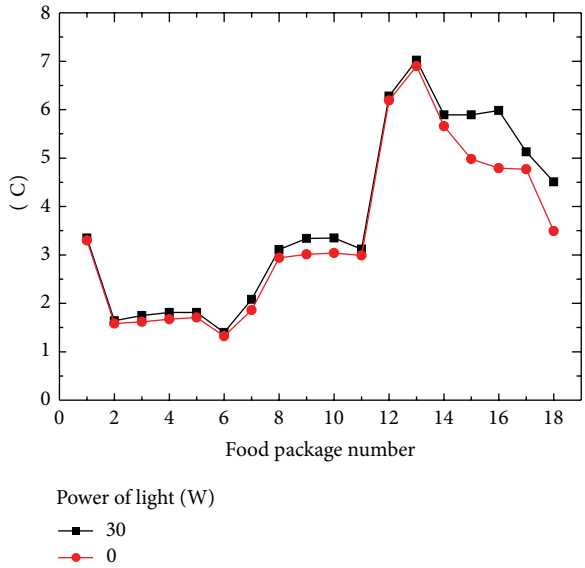

Figure 6: Food package temperature without light or with light.

shelf because the seepage of cold air from perforated back panel is influenced by food package and air curtain. The air entrainment from ambient space occurs in the upper regions of the air curtain and spills in the lower, which therefore increases the infiltration load of refrigerated display cabinet. From Figure 5, we can see that the air curtain is very efficient to form the heat transfer barrier between the internal display cabinet and the external environment. The food package temperature in the vicinity of air curtain has relatively higher temperature than those nearer the back panel because of the air entrainment and thermal radiation. So the good performance and stabilization of air curtain are the goals of any new refrigerated display cabinet.

5.1. The Effect of Light. Food temperature is influenced by generating heat of light. By comparing the food temperature with and without light, it can be seen from Figure 6 that the rear and top food packages temperature is affected obviously by light. Under the 30 W, the temperature of food packages 6, 7, 14, 15, 17, 18 with light presents about 0.1–1.0°C higher than those without light; food temperature of 16 is higher than 1.2°C. Therefore, the effect of light must be considered in the computation.

5.2. The Effect of Air Velocity. Figure 7 shows food temperature with the change of air velocities of evaporator outlet. From the figures, it can be seen that the food temperature dwindles with the rising of air velocity. When air velocity increases, it will enhance heat transfer of food package and can decrease the seepage of heat by air curtain from the external environment. In the meantime, it brings some problems, such as the blade power increase and more cold air spill on return air grill. Therefore, to determine the optimum air velocity, food package temperature and power consumption must be taken into account.

5.3. Effect of Ambient Temperature and Relative Humidity. The indoor environment greatly influences the performance of air curtains when refrigerated display cabinet is operating. The present investigations are to evaluate the effects of ambient temperature and relative humidity. Figure 8 shows the food temperature distribution under different ambient

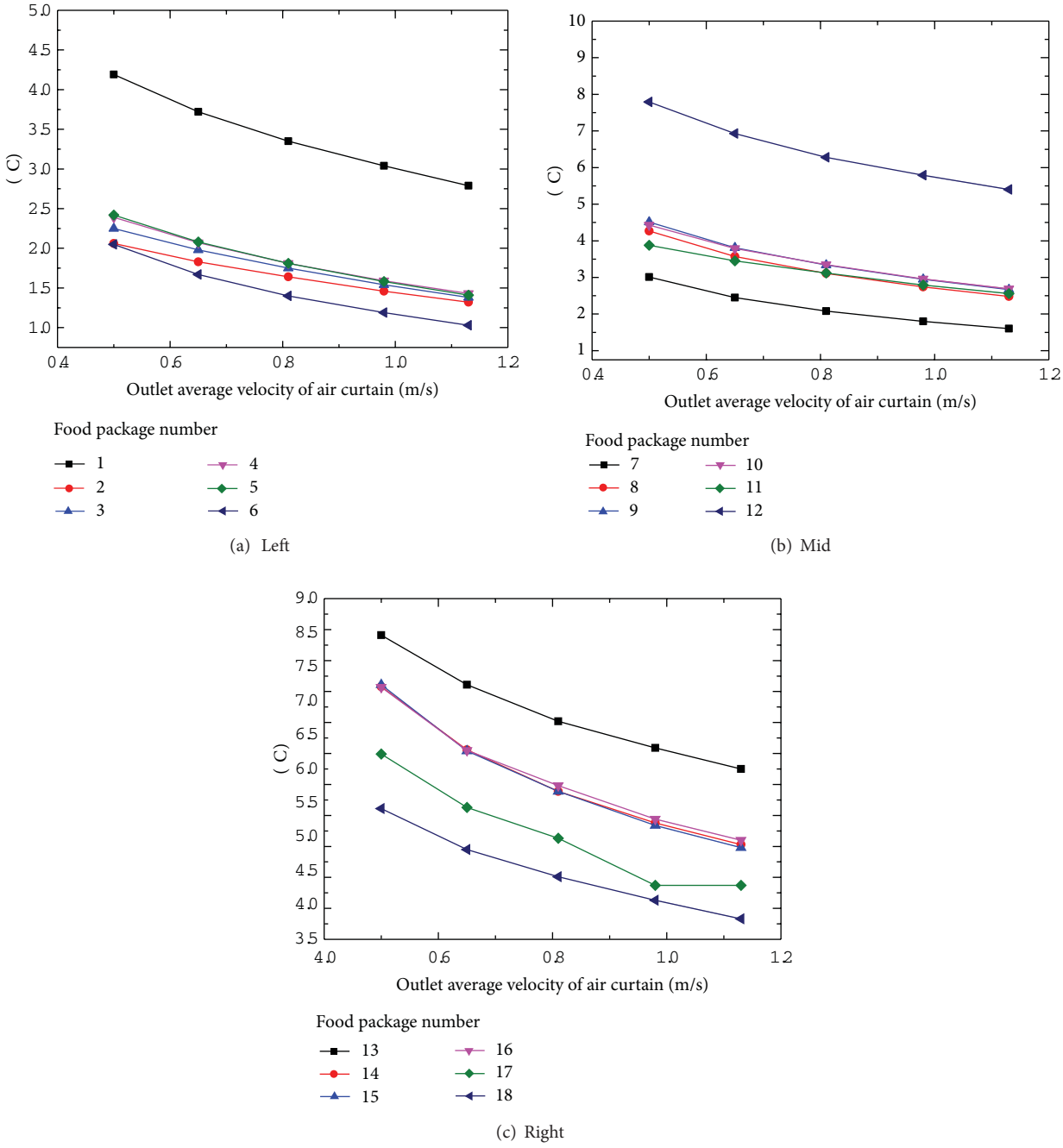

Figure 7: Food temperature under different outlet velocity of air curtain.

temperature at relative humidity 50% and different ambient relative humidity at ambient temperature 25°C. Results show that the food temperature increases with increasing ambient temperature and ambient relative humidity. When the indoor temperature is increased by 2°C, the food temperature increases by about 0.3°C; in the meantime, indoor relative humidity is increased by 20% and the temperature of the food temperature increases by about 0.9°C. The air entering the evaporator includes part of indoor air entrainment by the air curtain. Therefore, when the indoor relative humidity is constant, the temperature of the evaporator outlet cold air rises with increasing the temperature of indoor air, and convective heat transfer between food and cold air of cabinet decreases with increasing the temperature of indoor air, so the food temperature and thermal radiation also rise. As for increasing relative humidity at a certain temperature, food temperature also rises (see Figure 9).

6. Conclusions

In this paper, the food temperature which is affected by light, air velocity of air curtain outlet, and indoor temperature

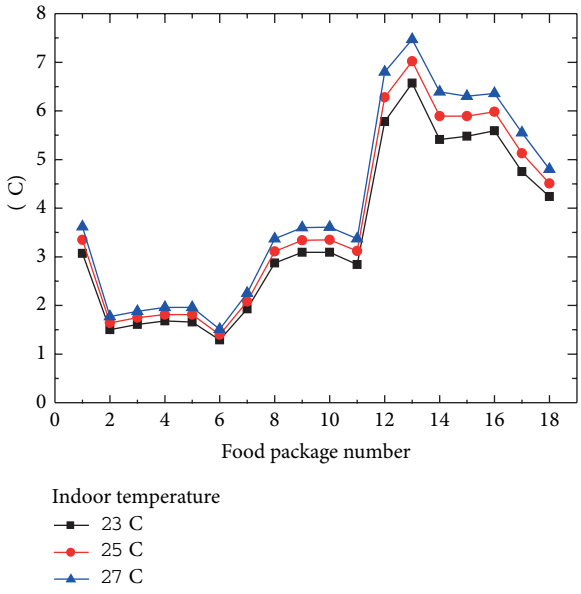

(a) Food temperature versus indoor temperature

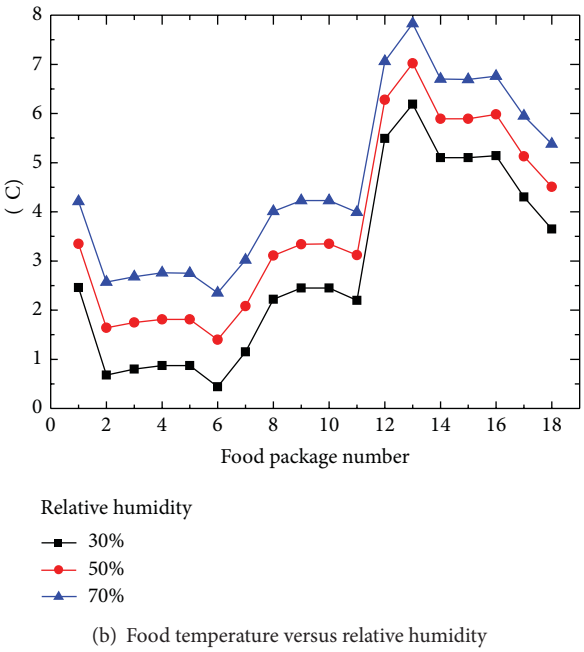

(b) Food temperature versus relative humidity

FIGURE 8: Comparisons of food temperature under different ambient temperature and relative humidity.

and relative humidity in the refrigerated display cabinet is investigated by numerical simulation. The main conclusions are as follows.

(1) The light has a great impact on food temperature in the refrigerated display cabinet. The right-side food temperature of the refrigerated display cabinet with light is 0.1–1.2°C higher than that without light.

(2) The food temperature decreases with increasing the air velocity of air curtain outlet.

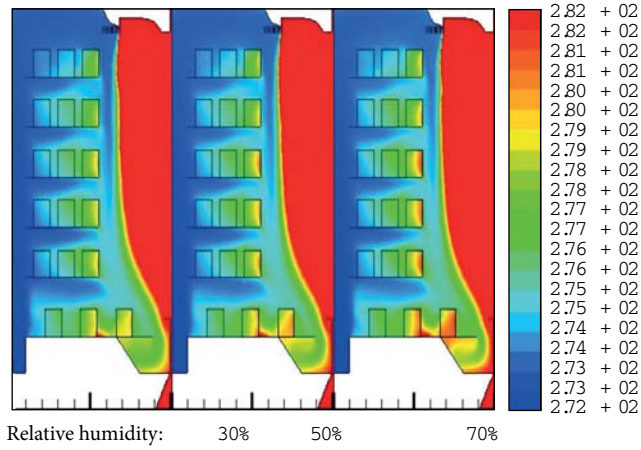

FIGURE 9: Food temperature contours under different ambient relative humidity.

(3) Results show that the food temperature increases with increasing ambient temperature and relative humidity. When the indoor temperature is increased by 2°C, the food temperature increases by about 0.3°C; in the meantime, indoor relative humidity is increased by 20%, and the food temperature rises by about 0.9°C.

Acknowledgments

This work is supported by the National Natural Science Foundation of China (21076200, 21006099) and Foundation of Henan Educational Committee (2011A470013).

References

[1] R. H. Howell, "Calculation of humidity effects on energy requirements of refrigerated display cases," in *Proceedings of the Winter Meeting of ASHRAE Transactions*, pp. 679–693, January 1993.

[2] D. Stribling, S. A. Tassou, and D. Marriott, "A two-dimensional CFD model of a refrigerated display case," *Transactions-American Society of Heating Refrigerating and Air Conditioning Engineers*, vol. 103, pp. 88–94, 1997.

[3] Y. T. Ge and S. A. Tassou, "Simulation of the performance of single jet air curtains for vertical refrigerated display cabinets," *Applied Thermal Engineering*, vol. 21, no. 2, pp. 201–219, 2001.

[4] G. Cortella, "CFD-aided retail cabinets design," *Computers and Electronics in Agriculture*, vol. 34, no. 1–3, pp. 43–66, 2002.

[5] H. K. Navaz, R. Faramarzi, M. Gharib, D. Dabiri, and D. Modarress, "The application of advanced methods in analyzing the performance of the air curtain in a refrigerated display case," *Journal of Fluids Engineering*, vol. 124, no. 3, pp. 756–764, 2002.

[6] A. M. Foster, M. Madge, and J. A. Evans, "The use of CFD to improve the performance of a chilled multi-deck retail display cabinet," *International Journal of Refrigeration*, vol. 28, no. 5, pp. 698–705, 2005.

[7] H. K. Navaz, B. S. Henderson, R. Faramarzi, A. Pourmovahed, and F. Taugwalder, "Jet entrainment rate in air curtain of open

refrigerated display cases," *International Journal of Refrigeration*, vol. 28, no. 2, pp. 267–275, 2005.

[8] Y. G. Chen and X. L. Yuan, "Experimental study of the performance of single-band air curtains for a multi-deck refrigerated display cabinet," *Journal of Food Engineering*, vol. 69, no. 3, pp. 261–267, 2005.

[9] P. D'agaro, G Cortella, and G. Croce, "Two-and three-dimensional CFD applied to vertical display cabinets simulation," *International Journal of Refrigeration*, vol. 29, no. 2, pp. 178–190, 2006.

[10] I. Gray, P. Luscombe, L. McLean, C. S. P. Sarathy, P. Sheahen, and K. Srinivasan, "Improvement of air distribution in refrigerated vertical open front remote supermarket display cases," *International Journal of Refrigeration*, vol. 31, no. 5, pp. 902–910, 2008.

[11] K. Z. Yu, G. L. Ding, and T. J. Chen, "Modified two-fluid model for air curtains in open vertical display cabinets," *International Journal of Refrigeration*, vol. 31, no. 3, pp. 472–482, 2008.

[12] K. Z. Yu, G. L. Ding, and T. J. Chen, "A correlation model of thermal entrainment factor for air curtain in a vertical open display cabinet," *Applied Thermal Engineering*, vol. 29, no. 14-15, pp. 2904–2913, 2009.

[13] M. Amin, D. Dabiri, and H. K. Navaz, "Tracer gas technique: a new approach for steady state infiltration rate measurement of open refrigerated display cases," *Journal of Food Engineering*, vol. 92, no. 2, pp. 172–181, 2009.

[14] Y. G. Chen, "Parametric evaluation of refrigerated air curtains for thermal insulation," *International Journal of Thermal Sciences*, vol. 48, no. 10, pp. 1988–1996, 2009.

[15] J. Moureh, G. Letang, B. Palvadeau, and H. Boisson, "Numerical and experimental investigations on the use of mist flow process in refrigerated display cabinets," *International Journal of Refrigeration*, vol. 32, no. 2, pp. 203–219, 2009.

[16] Z. K. Cao, B. Gu, H. Han et al., "Application of an effective strategy for optimizing the design of air curtains for open vertical refrigerated display cases," *International Journal of Thermal Sciences*, vol. 49, no. 6, pp. 976–983, 2010.

[17] Y. T. Ge, S. A. Tassou, and A. Hadawey, "Simulation of multi-deck medium temperature display cabinets with the integration of CFD and cooling coil models," *Applied Energy*, vol. 87, no. 10, pp. 3178–3188, 2010.

[18] P. D. Gaspar, L. C. Gonçalves, and R. A. Pitarma, "Experimental analysis of the thermal entrainment factor of air curtains in vertical open display cabinets for different ambient air conditions," *Applied Thermal Engineering*, vol. 31, no. 5, pp. 961–969, 2011.

[19] E. Hammond, J. Quarini, and A. Foster, "Development of a stability model for a vertical single band recirculated air curtain sealing a refrigerated cavity," *International Journal of Refrigeration*, vol. 34, no. 6, pp. 1455–1461, 2011.

[20] M. Amin, D. Dabiri, and H. K. Navaz, "Comprehensive study on the effects of fluid dynamics of air curtain and geometry, on infiltration rate of open refrigerated cavities," *Applied Thermal Engineering*, vol. 31, no. 14-15, pp. 3055–3065, 2011.

[21] Amin, M. Dabiri, and D. Navaz H. K, "Effects of secondary variables on infiltration rate of open refrigerated vertical display cases with single-band air curtain," *Applied Thermal Engineering*, vol. 35, no. 1, pp. 120–126, 2012.

[22] O. Laguerre, M. H. Hoang, and D. Flick, "Heat transfer modelling in a refrigerated display cabinet: the influence of operating conditions," *Journal of Food Engineering*, vol. 108, no. 2, pp. 353–364, 2012.

[23] W. Q. Tao, *Numerical Heat Transfer*, Xi'an Jiaotong University Press, Xi'an, China, 2nd edition, 2001.

Hindawi Publishing Corporation
Advances in Mechanical Engineering
Volume 2013, Article ID 951298, 10 pages
http://dx.doi.org/10.1155/2013/951298

Research Article

Numerical Simulation of Gas-Liquid-Solid Three-Phase Flow in Deep Wells

Jianyu Xie,[1] Bo Yu,[1] Xinyu Zhang,[1] Qianqian Shao,[1] and Xianzhi Song[2]

[1] *National Engineering Laboratory for Pipeline Safety, Beijing Key Laboratory of Urban Oil and Gas Distribution Technology, China University of Petroleum, Beijing 102249, China*
[2] *MOE Key Laboratory of Petroleum Engineering, China University of Petroleum, Beijing 102249, China*

Correspondence should be addressed to Bo Yu; yubobox@vip.163.com

Received 7 January 2013; Accepted 20 March 2013

Academic Editor: Yi Wang

A gas-liquid-solid flow model which considers the effect of the cuttings on the pressure drop is established for the annulus flow in the deep wells in this paper, based on which a numerical code is developed to calculate the thermal and flow quantities such as temperature and pressure distributions. The model is validated by field data, and its performance is compared with several commercial software. The effects of some important parameters, such as well depth, gas kick, cuttings, and drilling fluid properties, on the temperature and pressure distributions are studied.

1. Introduction

With the worldwide increasing energy consumption and the development of petroleum industry, deep well and ultradeep well will become an important approach to explore oil and gas in the future. When the wellbore pressure is below the formation pressure during the drilling process, minor incidents such as gas cut and gas kick may emerge to form air pocket, which may in the worst case lead to disastrous blowout to generate formidable pressure and shock waves to cause heavy casualties and extensive property damages, especially in deep well drilling process. Besides, the property parameters and rheological parameters of the multiphase fluid in the wellbore are the sensitive functions of the temperate. Therefore, In order to predict the pressure distribution and optimize the design and operation of the production of the oil well systems, the accurate calculation of the temperature distribution of the wellbore should be guaranteed. Therefore, accurate prediction of the pressure and temperature changes under the gas kick condition to guide the deep drilling operation has practical significance.

For pressure prediction, early researchers used the empirical correlations [1–3], which are still widely used in commercial software. For example, the Beggs-Brill correlation is used in MUDLITE, based on which the bottomhole pressure, liquid holdup, and so forth can be evaluated. However, the empirical correlations sometimes result in great deviations for limited valid ranges [4]. Recently, numerical models have been developed to predict the multiphase flow behaviors in the wellbore, for example, Hasan and Kabir's two-phase flow model [5], Ping et al.'s modified model [6] based on Hasan and Kabir's work, Bijleveld et al.'s unbalanced drilling model [7], and Perez-Tellez et al.'s unified unbalanced drilling model [8]. Comparison studies show that the solutions of those models are generally much more accurate than the empirical correlations [9].

As to temperature prediction, both analytical and numerical methods are used. With regard to analytical solutions, representative works can be referred to those of Ramey [10], Holmes and Swift [11], Kabir et al. [12], and Hasan et al. [13]. Since numerical solutions obtained with less simplified models are generally more accurate than the analytical solutions, numerical simulation methods are widely adopted nowadays. Raymond [14] neglected effects of energy source in the drilling system and presented the first numerical model that coupled unsteady-state heat transfer in the formation and the steady heat transfer in the wellbore. On this basis, Keller et al. [15] made a hypothesis that no axial heat transfer existed

in the drilling fluid and developed a mathematical model for temperature distribution of circulating fluid in the wellbore. Later, Marshall and Bentsen [16] analyzed solution stability and velocity of the finite difference method on the basis of Keller et al.'s work.

The available studies have been carried out primarily for shallow wells with a depth around 3 kilometers, while very few studies have been reported for the flow and thermal characteristics of deep wells though they should have deserved much more attention. Based on this point, in this study we aim to develop a model, taking important parameters into account, to describe the fluid flow and thermal properties in the deep drilling and then apply the established model to simulate the temperature and pressure drop distribution under the influences of different factors.

2. Hydraulic Model

2.1. Flow Patterns Transition Criteria. The pressure distribution in the wellbore is greatly affected by flow patterns, which is generally determined by flow patterns transition criteria in the calculations. Flow patterns transition criteria were primarily proposed for circular pipe flow such as those proposed by Taitel et al. [17]. The flow patterns transition criteria for annulus flows firstly presented by Caetano [18] and Kelessidis and Dukler [19] in 1986 and improved later by many researchers as presented below.

2.1.1. Bubble-to-Slug Transition. Caetano [18] indicated that the bubble-to-slug transition occurs when the velocity of dispersed bubbles is greater than that of Taylor bubbles, with the mean gas volumetric fraction being around 0.2. The flow pattern transition formula is given by the critical superficial velocity of liquid phase as follows:

$$u_{\mathrm{SL}} = 4.0u_{\mathrm{SG}} - 1.224\left[\frac{(\rho_L - \rho_G)}{\rho_L^2}\right]^{0.25}. \tag{1}$$

2.1.2. Slug-to-Churn Transition. In 1999, Tengesdal et al. [20] first built a slug-to-churn transition model based on the drift-flux model, and it was improved by Kaya et al. [21] in 2001, in which the gas volumetric fraction of the fluid was evaluated by

$$\alpha = \frac{u_{\mathrm{SG}}}{\left[1.2u_M + 0.35\left(\left(\rho_L - \rho_G\right) g d_h/\rho_L\right)\right]^{0.5}}. \tag{2}$$

Kaya et al. [21] declared that slug-to-churn transition occurs at a critical void fraction of 0.78; later Yu et al. [22] argued that the critical value should be 0.64 based on their experimental data. In this paper, the value of 0.64 is adopted.

2.1.3. Bubble/Slug-to-Dispersed Bubble Transition. When the velocity of liquid phase is relatively large, bubbles are scattered in it, and then the bubble/slug to dispersed bubble transition appears. Based on Caetano's model [18], the expression describing the transition curve can be given as below:

$$2\left[\frac{0.4\sigma}{(\rho_L - \rho_G)\, g}\right]^{0.5}\left(\frac{\rho_L}{\sigma}\right)^{0.6}\left(\frac{2f}{d_h}\right)^{0.4}(u_M)^{1.2} = 0.725 + 4.15\left(\frac{u_{\mathrm{SG}}}{u_M}\right)^{0.5}. \tag{3}$$

2.1.4. Churn-to-Annular Transition. With flux and superficial velocity of the gas phase being large enough, churn flow transforms to annular flow. In fully developed annular flow, the liquid phase moves upward along the pipe wall smoothly and continuously in the form of liquid film, with continuous air stream entrained in the pipe center. Taitel et al. [17] announced that annular flow occurs only when gas superficial velocity is high enough to lift the entrained liquid droplets and carry them along. On this basis, an equilibrium relationship exists between the gravity of a liquid droplet and the resistance imposed on it by the gas stream, according to which the expression of churn to annular transition can be deduced as

$$\frac{u_{\mathrm{SG}}\rho_G^{0.5}}{\left[(\rho_L - \rho_G)\, g\sigma\right]^{0.25}} = 3.1. \tag{4}$$

2.2. Pressure Drop Model in the Drill String. The drilling mud is assumed to be injected into the drill string as a single-phase fluid without any solid particles or gas, and thus, the total pressure drop in the drill string is composed of gravity component and friction component, which is given by

$$\left(\frac{dp}{dz}\right)_T = \rho_L g - \frac{2f\rho_L u_L^2}{d_1} \tag{5}$$

with f evaluated by Colebrook formula:

$$\frac{1}{\sqrt{f}} = 4\lg\left(\mathrm{Re}_L\sqrt{f}\right) - 0.395. \tag{6}$$

2.3. Pressure Drop Model in the Annulus. The total pressure drop in the annulus is composed of the contributions of gravity, friction drag, convective acceleration loss, and interaction between cuttings and fluid:

$$\left(\frac{dp}{dz}\right)_T = \left(\frac{dp}{dz}\right)_{\mathrm{Hy}} + \left(\frac{dp}{dz}\right)_{\mathrm{Fric}} + \left(\frac{dp}{dz}\right)_{\mathrm{Acc}} + \left(\frac{dp}{dz}\right)_C. \tag{7}$$

For annular flow, two total pressure drop formulae can be deduced as follows:

$$\left(\frac{dp}{dz}\right)_T + \rho_G g + \frac{S_o\tau_o + S_i\tau_i}{A_G} + \left(\frac{dp}{dz}\right)_C = 0,$$
$$\left(\frac{dp}{dz}\right)_T + \left[\alpha\rho_G + (1-\alpha)\,\rho_L\right] g + \frac{2f}{d_h}\rho_L\overline{u}^2 + \left(\frac{dp}{dz}\right)_C = 0. \tag{8}$$

The total pressure drop can be obtained by solving (8), and the details can be referred to [19]. For other flow patterns, the first three terms on the right hand side of (7) are calculated by the formulae listed in Table 1.

2.3.1. Pressure Drop Caused by Cuttings. For simplification, the following assumptions are made in this paper when modeling the pressure drop caused by cuttings:

(a) the cuttings elements are uniformly distributed in the liquid phase and have no effects on the flow pattern;

(b) the properties of the cuttings elements are assumed the same;

(c) the interaction among the discrete elements is neglected.

And then the pressure drop caused by cuttings can be calculated by

$$\left(\frac{dp}{dz}\right)_C = 0.5NC_d\pi r_C^2\left(u_L - u_C\right)^2\rho_L, \tag{9}$$

where, C_d is given by [26]:

$$C_d = \frac{30}{\mathrm{Re}_L} + \frac{67.289}{e^{5.03\Phi}}, \tag{10}$$

and N can be calculated by

$$N = \frac{3u_L C_e}{4\pi r_C^3} \tag{11}$$

with C_e being

$$C_e = \left[1 + \frac{u_L}{\mathrm{ROP}}\left(1 - \frac{d_{\mathrm{bh}}^2}{d_{\mathrm{et}}^2}\right)\right]^{-1}. \tag{12}$$

And the term $(u_L - u_C)$ is the velocity difference between the liquid phase and the cuttings entrained in the liquid stream, which can be figured out through Newton's second law and velocity interpolation.

3. Thermal Model

In this study, the flow and heat transfer are assumed to be steady at a certain drilling step due to the very low rate of penetration. Several assumptions have been made to establish a steady-state thermal model to describe the heat transfer process:

(a) the fluid flow and heat transfer are assumed to be symmetric as shown in Figure 1;

(b) since heat convection is dominant both in the drilling string and in the annulus during the drilling process, heat conduction between the drilling muds is neglected;

(c) the heat convection is simplified as a one-dimensional problem.

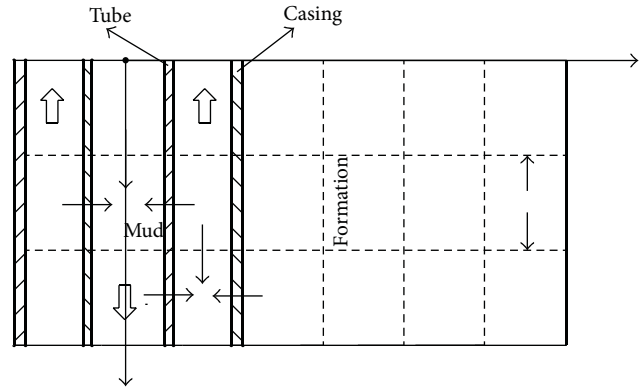

Figure 1: Physical model.

Based on the above assumptions, the heat transfer governing equations for the drilling muds in the drill string and annulus and that for the formation can be written as (13), (14), and (15), respectively, as follows:

$$q_m\frac{\partial\left(C_{p1}T_1\right)}{\partial z} - \frac{\pi\left(T_2 - T_1\right)}{\left(1/d_1h_1\right) + \left(1/d_2h_2\right) + \ln\left(d_2/d_1\right)/2\lambda_t} - \frac{\Delta p_{\mathrm{Fric}}}{\Delta z}\cdot q_v = 0, \tag{13}$$

$$q_m\frac{\partial\left(C_{p2}T_2\right)}{\partial z} + \frac{\pi\left(T_2 - T_1\right)}{\left(1/d_1h_1\right) + \left(1/d_2h_2\right) + \ln\left(d_2/d_1\right)/2\lambda_t} - \pi h_3 d_3\left(T_w - T_2\right) - \frac{\Delta p_{\mathrm{Fric}}\cdot q_v}{\Delta z} = 0, \tag{14}$$

$$\frac{\partial}{\partial z}\left(\lambda_f\frac{\partial T}{\partial z}\right) + \frac{1}{r}\frac{\partial}{\partial r}\left(r\lambda_f\frac{\partial T}{\partial r}\right) = 0. \tag{15}$$

The convective heat transfer coefficient correlations [27] used in the present study are listed in Table 2.

For the dispersed bubble and slug/churn cases, the h_M/h_L is the same in both the laminar state and the turbulent state.

4. Model Solving and Validation

The models are implemented in a FORTRAN computer program. The well is divided into 150 segments. Calculation starts from the surface, based on the pressure and temperature at the wellhead, proceeds down the drilling string to the bottomhole, then up through the wellbore, and then terminates in the ground surface. And at each increment, the pressure and temperature are solved alternately. The model and numerical code are validated by the field data of Muspac53 well in the Mexican field [32] with the main test conditions given in Table 3. Figure 2 shows the comparisons of the field data with the predicted wellbore pressures by the present model and the other four models, that is, LSU model by Perez-Tellez, MUDLITE V-2, MUDLITE V-3, and Neotec WELLFLO 7 in [9]. The absolute errors and relative errors

Table 1: Expressions of pressure drop components of various flow patterns.

Flow patterns	$(dp/dz)_{Hy}$	$(dp/dz)_{Fric}$	$(dp/dz)_{Acc}$	Notation
Dispersed bubble	$\rho_M g$	$\frac{4f}{(d_2-d_1)}\rho_M\frac{(u_{SG}+u_{SL})^2}{2}$	0	
Bubble	$\rho_M g$	$\frac{4f}{(d_2-d_1)}\rho_M\frac{(u_{SG}+u_{SL})^2}{2}$	0	$H_L^{n+2}-H_L^{n+1}+\frac{(u_{SL}+u_{SG})H_L-u_{SL}}{1.53[(\rho_L-\rho_G)g\sigma/\rho_L^2]^{0.25}}=0$ [18] $n=$ 0.5 [23]
Slug	$\rho_M g$	$\frac{2f}{d_h}\rho_M u_M^2\frac{l_{LS}}{l_{SU}}$	$\frac{(1-\alpha_{LS})}{l_{SU}}\rho_L(u_{LLS}-u_{LF})(u_{TB}-u_{LLS})$	$\alpha_{LS}=\frac{u_{SG}}{0.425+6.25u_M}$ [24]
Churn	$\rho_M g$	$\frac{2f}{d_h}\rho_M u_M^2\frac{l_{LS}}{l_{SU}}$	$\frac{(1-\alpha_{LS})}{l_{SU}}\rho_L(u_{LLS}-u_{LF})(u_{TB}-u_{LLS})$	$\alpha_{LS}=\frac{u_{SG}}{1.126u_M+1.41[(\rho_G-\rho_L)g\sigma/\rho_L^2]^{0.25}}$ [25]

Table 2: Convective heat transfer coefficient correlations under different flow patterns.

Flow patterns	Convective heat transfer coefficient correlations
Dispersed bubble [28]	$\frac{h_M}{h_L}=\left(1+\frac{u_{SG}}{u_{SL}}\right)^{1/3}$ Laminar flow: $Nu_L=1.86\left(Re_{SL}Pr_L\frac{d}{l}\right)^{1/3}\left(\frac{\mu_{FT}}{\mu_{WT}}\right)^{0.14}$ Turbulent flow: $Nu_L=0.027(Re_{SL})^{0.8}(Pr_L)^{0.33}\left(\frac{\mu_{FT}}{\mu_{WT}}\right)^{0.14}$
Bubble [29]	Laminar flow: $\frac{h_M}{h_L}=(1-\alpha)^{-1/3}$ $Nu_L=1.615\left(Re_{SL}Pr_L\frac{d}{l}\right)^{-1/3}\left(\frac{\mu_{FT}}{\mu_{WT}}\right)^{0.14}$ Turbulent flow: $\frac{h_M}{h_L}=(1-\alpha)^{-0.83}$ $Nu_L=0.0155(Re_{SL})^{0.83}(Pr_L)^{0.5}\left(\frac{\mu_{FT}}{\mu_{WT}}\right)^{0.33}$
Slug/Churn [30]	$\frac{h_M}{h_L}=(1-\alpha)^{-0.9}$ Laminar flow: $Nu_L=1.86\left(Re_{SL}Pr_L\frac{d}{l}\right)^{1/3}\left(\frac{\mu_{FT}}{\mu_{WT}}\right)^{0.14}$ Turbulent flow: $Nu_L=0.027(Re_{SL})^{0.8}(Pr_L)^{0.33}\left(\frac{\mu_{FT}}{\mu_{WT}}\right)^{0.14}$
Annular [31]	$Nu_M=0.56\left(\frac{u_{SG}}{u_{SL}}\right)^{0.3}\left(\frac{\mu_G}{\mu_L}\right)^{0.2}(Re_{SL})^{0.6}(Pr_L)^{1/3}\times\left(\frac{\mu_{FT}}{\mu_{WT}}\right)^{0.14}$

between the five models and the field data are, respectively, listed in Table 4. It is seen clearly that the predicted pressure

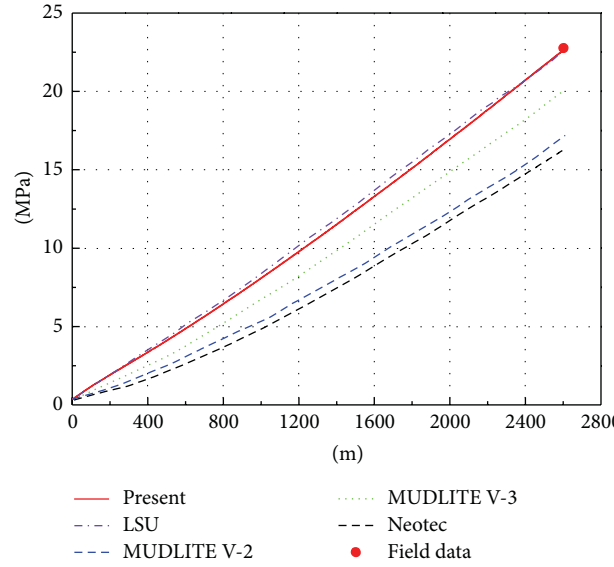

Figure 2: Wellbore pressures by different pressure models.

by the present model agrees well with the field data and agrees better than the other three empirical-correlations-based models for this case.

5. Results and Discussions

In this section, the influences of the well depth, the gas kick, the cuttings, and the physical properties of the drilling mud on the temperature and pressure distributions are studied by employing the validated model and code. The relationship between pressure and temperature of the gas phase per mole is given by

$$pv = ZRT. \tag{16}$$

Table 3: Data of pseudosteady state conditions in Muspac53.

Geometrical parameters of the annulus											
z	d_3	d_2	z_W	T_s	$d(T_f)$	p_b	q_{vdm}	ρ_{dm}	μ_{dm}	ρ_{N_2}	q_{vN_2}
0–2572	0.1525	0.0889	2614	28	0.0283	0.6895	0.0883	940	0.01	0.97	0.336
2572–2614	0.1525	0.1207									

Table 4: Comparison of the accuracies of different models.

	Neotec	MUDLITE V-2	MUDLITE V-3	LSU	Present
δ_a (MPa)	5.75	5.00	2.02	0.40	0.39
δ_r (%)	25.9	22.5	9.1	1.8	1.76

Table 5: Equipment parameters and formation parameters.

z_W	d_1	d_2	d_3	λ_t	d_{bh}	ROP	T_s	$d(T_f)$	λ_f
6000	0.108	0.127	0.245	50.0	0.312	9	20	0.022	2.25

The density and viscosity of the drilling mud used in the calculations are modeled as the functions of temperature and pressure and given as follows:

$$\rho = \rho_{\text{LSC}} e^{a(T-299.82)+(b+cT)p},$$
$$\mu = \mu_{\text{LSC}} e^{[A(1.8T-534.67)+Bp]}, \quad (17)$$

where a, b, c, A, and B are fitting constants and the unit of temperature T is K here.

The other main common used parameters for calculations are given in Tables 5 and 6.

Without special illustrations, the parameters given in Tables 5 and 6 are employed in the subsequent calculations. In Section 5.1, besides the well depth of 6000 m, the wells of 2500 m, 4000 m, and 5000 m are studied to analyze the effect of the well depth on the flow characteristics with the gas kicks at the bottomhole kept at 2.5×10^{-3} m^3/s. In Section 5.2, four gas kicks of 0.1 m^3/s, 0.5 m^3/s, 1 m^3/s, and 2 m^3/s under standard condition are used. For the case of a gas kick of 0.5 m^3/s, we studied the effect of cuttings on the pressure drop. In Section 5.3, drilling mud densities and viscosities are studied separately. Four densities at standard condition (900, 1000, 1100, and 1200 kg/m^3) are employed, and four standard viscosities (0.03, 0.04, 0.05, and 0.06 Pa·s) are used.

5.1. Influence of the Well Depth on Deep Drilling. Figure 3 describes the relation between the temperatures of the drilling mud in the annulus with the depths in the four wells. It can be seen that at the same depth, the temperature of the drilling mud increases evidently with the increase of the well depth. The temperature in the deep well of 6000 m is highest, and it is 45°C higher than the bottomhole temperature in the 2500 m well. Such large temperature difference is because of the large amount of heat absorbed from the deeper formation when drilling mud goes upward.

When gas kicks at the bottomhole are the same, the holdups in the annulus differ obviously for the four wells as shown in Figure 4, with lower holdup existing in deeper

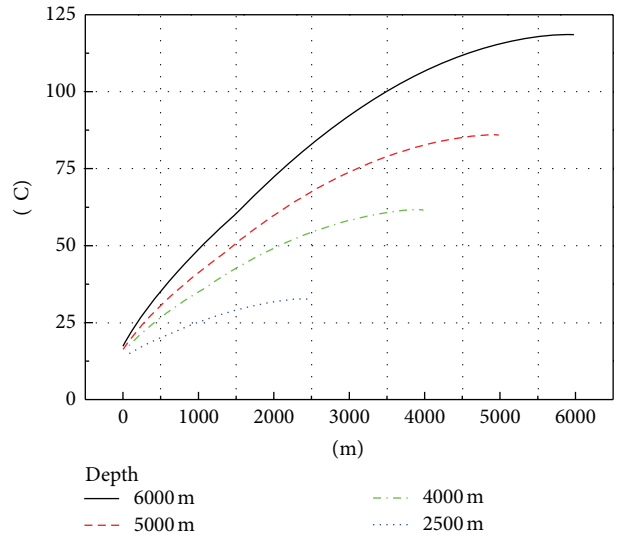

Figure 3: Temperature versus depth in different wells.

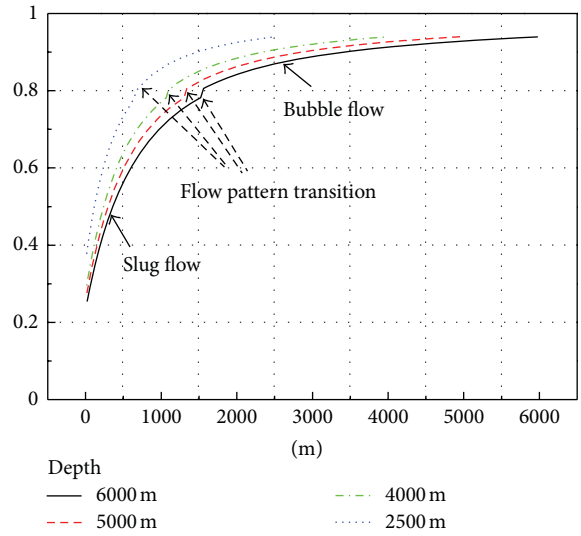

Figure 4: Liquid holdup versus depth in different wells.

well. It is also seen that though for all the wells, there are two identical flow patterns, slug flow and bubble flow, but the transition location is different. The deeper the well is, the lower the transition occurs. For the well of 6000 m, transition occurs 1500 m from the surface, while for the well of 2500 m, it is 1000 m. In addition, at the same depth the liquid holdup of the deeper well is smaller, because when the mud goes

Table 6: Parameters of the gas phase, the liquid phase, and the cuttings.

ρ_{GSC}	μ_{GSC}	q_{mL}	p_b	T_0	C_{pL}	σ	λ_L	ρ_{LSC}	μ_{LSC}	ρ_C	Φ	d_C
0.74	1.8×10^{-5}	29.7	1.0	10	1676	0.04	1.73	1000	0.04	2400	0.8	0.008

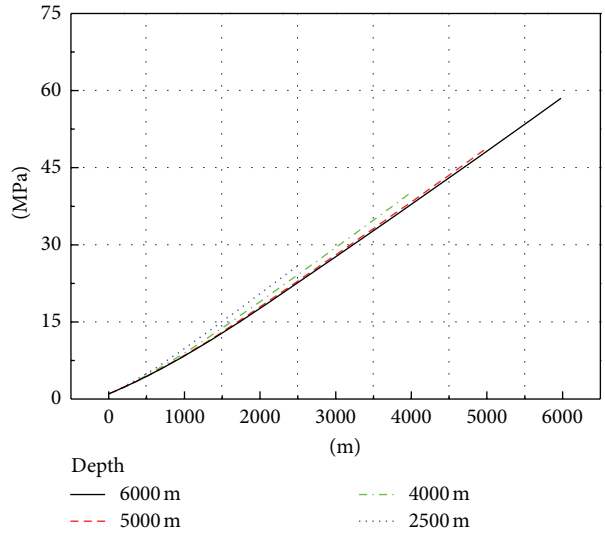

Figure 5: Pressure versus depth in different wells.

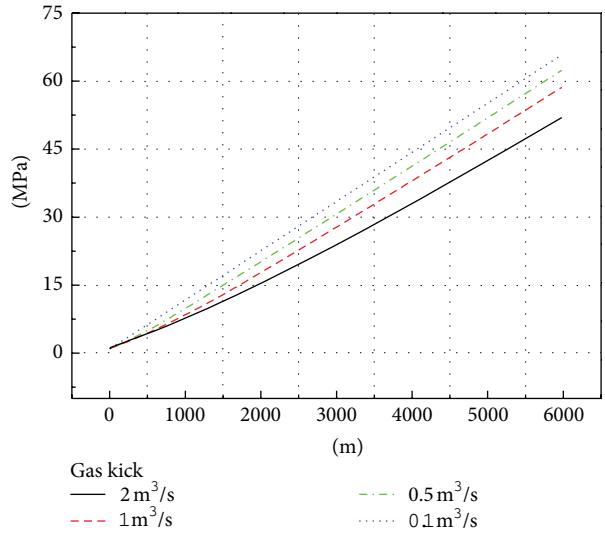

Figure 7: Pressure versus depth under different gas kicks.

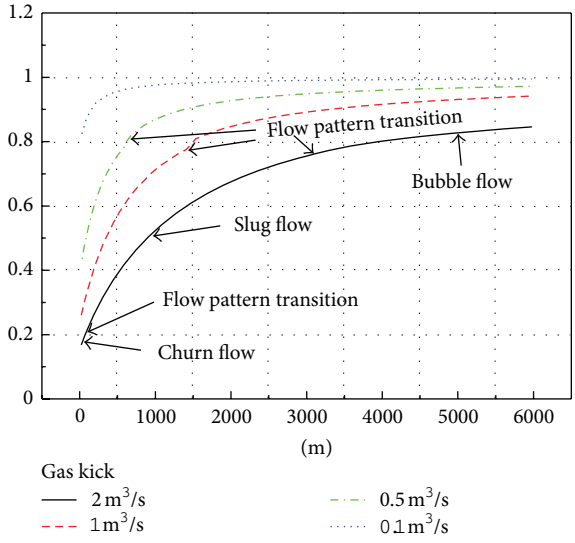

Figure 6: Liquid holdup versus depth under different gas kicks.

upward, the pressure becomes smaller and the gas volume becomes larger.

Figure 5 compares the pressure distributions in the annulus of the four wells. It is seen that at the same depth, the pressure difference is small compared with the pressure itself. The maximum pressure difference among them is only 3.2 MPa at the depth of 2,500 m, which indirectly shows that pressure due to the gravity force plays the most important role. The pressure difference is mainly due to different holdups and flow patterns, and so forth.

5.2. Influence of the Gas Kick and Cuttings on Deep Drilling. The effects of gas kick on liquid holdup and pressure distributions in the annulus are shown in Figures 6 and 7, respectively. It is seen clearly in Figure 6 that with the increase of gas kick, more flow pattern exists along the wellbore. From the smallest gas kick volume 0.1 m^3/s to the largest 2.0 m^3/s, the number of flow patterns varies from 1 to 3. When the gas kick is 0.1 m^3/s, only bubble flow occurs. When the gas kicks are 0.5 m^3/s and 1.0 m^3/s, bubble flow and slug flow coexist. When the gas kick is 2.0 m^3/s, three flow patterns coexist with churn flow existing near the ground surface. With the increase of the gas kick volume, the transition of bubble flow to slug flow occurs at a deeper depth. Figure 7 shows that gas kick greatly affects the magnitude of pressure, the larger the gas kick volume, the smaller the pressure. The smaller pressure at the bottomhole at the larger gas kick volume is due to the smaller density of the drilling fluid leading to a smaller gravity force. It should be noted that the decreasing bottomhole pressure at large gas kick volume may further induce the increase of the gas kick due to the large pressure difference between the formation and the bottomhole of the well and may eventually destroy the normal operations and result in dangerous blowout.

In most previous models, the effect of cuttings on pressure is ignored completely or treated as a correction factor; in the present study its effect is clarified by solving (9). Figure 8 presents the pressure distributions in the annulus with and without cuttings with the gas kick being 0.5 m^3/s under the standard condition. It is seen that cuttings do have effects on the pressure, but the influence is not so large; for this case, the maximum increment of pressure is about 0.7 MPa at the bottomhole.

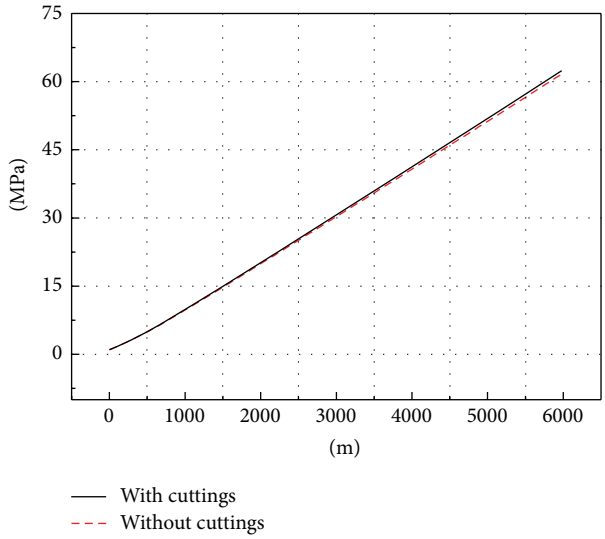

Figure 8: Pressure versus depth with and without cuttings.

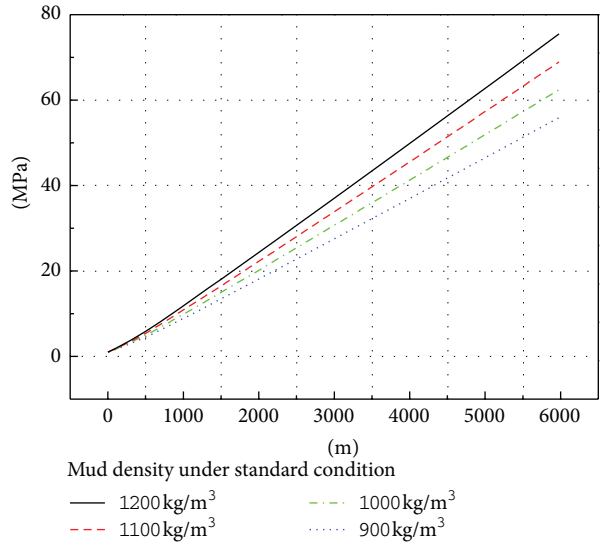

Figure 9: Pressure versus depth under different mud densities.

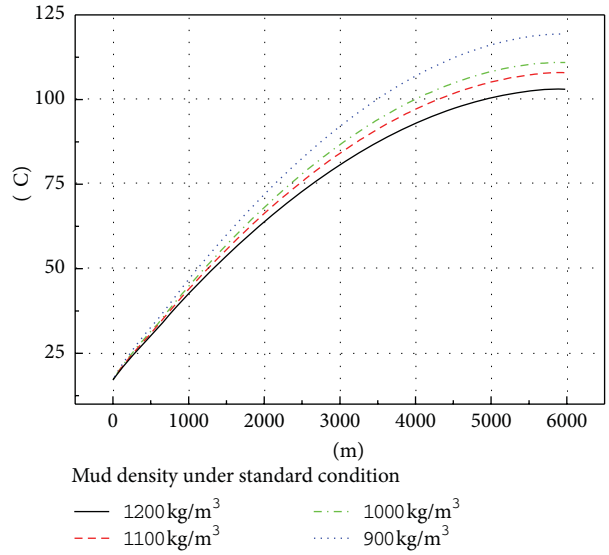

Figure 10: Temperature versus depth under different mud densities.

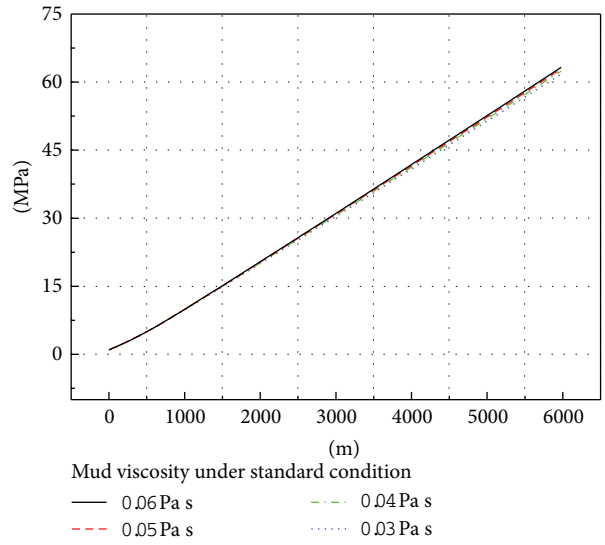

Figure 11: Pressure versus well depth under different mud viscosities.

5.3. Influences of Mud Properties on Deep Drilling. Since the physical properties of drilling mud may affect the drilling process greatly, in this section two most important parameters are studied, that is, density and viscosity. The gas kick of 0.5 m^3/s under the standard condition is employed in the calculation.

Figure 9 reveals that the density of the drilling mud can greatly affect the bottomhole pressure, whose value is only 55.9 MPa at density of 900 kg/m^3 (standard condition) but increases to 75.5 MPa at the density of 1200 kg/m^3. It is seen that the increase ratio of the pressure (35%) is almost linearly proportional to the increase ratio of the mud density (33.3%). This is due to that the gravity contribution to pressure is almost proportional to density. It is seen in Figure 10 that with the increase of the drilling mud density, the temperature decreases. The major reason is due to the increase of the heat capacity per mass.

Figures 11 and 12, respectively, present the pressure and temperature distributions in the annulus under different drilling mud viscosities. It is seen that the effect of mud viscosity on pressure is much smaller than that of mud density, showing again that frictional drag pressure loss is a small component in the deep well. However, the temperature is also apparently affected by the viscosity. When density at the standard condition increases from 0.03 Pa·s to 0.06 Pa·s, the bottomhole temperature drops from 117°C to 108°C. The increase of viscosity decreases the turbulent heat transfer, leads to less heat absorption from the formation, and results in a lower temperature.

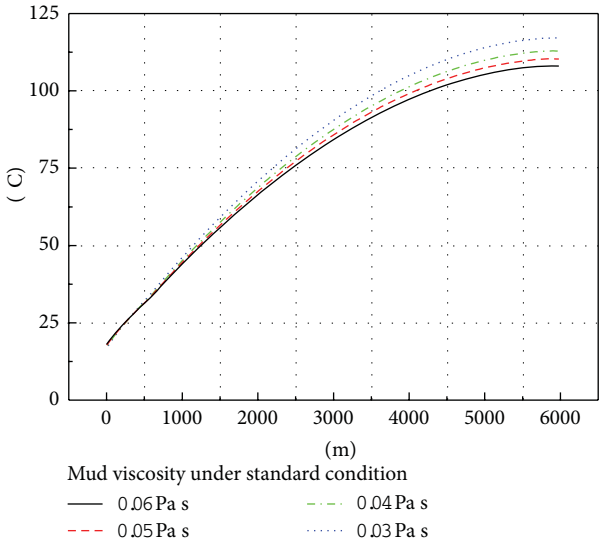

Figure 12: Temperature versus well depth under different mud viscosities.

6. Conclusions

In this study, a gas-liquid-solid model is proposed to study the heat and fluid flow characteristics in annulus of deep wells. The model has been validated by field data. Based on the validated model, the effect of cuttings, gas kick, well depth, and drilling mud physical properties are clarified. It is found that the effect of the cuttings on the total pressure drop is small; temperature and pressure are greatly affected by well depth, drilling mud density, and gas kick; though drilling mud viscosity weakly affects the total pressure, it may obviously affect the temperature distributions in the annulus. The quantitative data obtained in this study can give a reference to the deep well drilling practice.

Nomenclatures

A : Flow area (m^2)
C_d: Factor of drag force, dimensionless
C_e: Volume concentration of the cuttings, dimensionless
C_p: Specific heat capacity of the fluid (J/(kg·°C))
C_{pk}: Specific heat capacity of the fluid in the drill string ($k = 1$) and in the annulus ($k = 2$) (J/(kg·°C))
d: Diameter (m)
d_k: Inner ($k = 1$) and outer ($k = 2$) diameters of the tube, inner ($k = 3$) diameter of the casing ($k = 3$) (m)
$d(T)$: Temperature gradient (°C/m)
f: Fanning friction factor, dimensionless
g: Acceleration due to gravity (m/s^2)
h: Convective heat transfer coefficient ($W/(m^2 \cdot °C)$)
h_k: Convective heat transfer coefficient of the inner wall of the tube ($k = 1$), that of the outer wall of the tube ($k = 2$), and that of the surface of the casing ($k = 3$) ($W/(m^2 \cdot °C)$)
H_L: Liquid holdup, dimensionless
l: Length (m)
N: Number of cuttings elements, dimensionless
Nu: Nusselt number, dimensionless
p: Pressure (Pa without otherwise specified)
p_b: Wellhead back pressure (MPa)
Pr: Prandtl number, dimensionless
q: Flow rate (kg/s or m^3/s)
r: Radius (m)
R: Perfect gas constant, which is equals 8.314 J/(mol·°C)
Re: Reynolds number, dimensionless
ROP: Rate of penetration (m/h)
S: Wetted perimeters (m)
T: Temperature (°C without otherwise specified)
T_k: Temperature of the drilling mud in the drill string ($k = 1$) and in the annulus ($k = 2$) (°C)
u: Velocity (m/s)
$\overline{u}$: Mean velocity (m/s)
v: Volume (m^3)
z: Depth (m)
Z: Compressibility factor.

Greek Symbols

α: Gas volumetric fraction, dimensionless
δ: Error follows the units of the physical quantities, or dimensionless as relative errors
λ: Thermal conductivity (W/(m·°C))
μ: Dynamic viscosity (Pa·s)
π: An irrational number equals 3.14 with two decimal places, dimensionless
ρ: Density (kg/m^3)
ρ_M: Density of the mixture, $\rho_M = \rho_L H_L + \rho_G(1 - H_L)$ (kg/m^3)
σ: Interfacial tension (N/m)
τ: Shear stress (N/m^2)
Φ: Form factor of the cuttings, dimensionless.

Subscripts

0: Initial
a: Absolute
Acc: Convective acceleration
bh: Borehole
C: Cuttings
dm: Drilling mud
et: External wall of the coiled tubing
f: Formation

Fric: Friction drag
FT: Fluid temperature
G: Gas phase
GSC: Gas under standard condition
h: Hydraulic
Hy: Gravity
i: Inner
L: Liquid phase
LF: Liquid film
LLS: Liquid phase in liquid slug
LS: Liquid slug
LSC: Liquid under standard condition
m: Mass
M: Mixture of the liquid and gas phase
N_2: Nitrogen
o: Outer
r: Relative
s: Earth's surface
SG: Superficial gas
SL: Superficial liquid
SU: Slug unit
t: Tube
T: Total
TB: Taylor bubble
v: Volume
w: Wall
W: Well
WT: Well temperature.

Prefix

$\triangle$: Increment.

Acknowledgments

The study is supported by the National Key Projects of Fundamental R/D of China (973 Project: 2010CB226704) and the Science Foundation of China University of Petroleum, Beijing (no. 2462011LLYJ33, no. 2462011LLYJ55, no. 2462012KYJJ0403, and no. 2462012KYJJ0404).

References

[1] G. Fancher and K. Brown, "Prediction of pressure gradients for multiphase flow in tubing," *Old SPE Journal*, vol. 3, pp. 59–69, 1963.

[2] A. Hagedorn and K. Brown, "Experimental study of pressure gradients occurring during continuous two-phase flow in small-diameter vertical conduits," *Journal of Petroleum Technology*, vol. 17, pp. 475–484, 1965.

[3] H. D. Beggs and J. R. Brill, "A study of two-phase flow in inclined pipes," *Journal of Petroleum Technology*, vol. 25, pp. 607–617, 1973.

[4] L. E. Gomez, O. Shoham, Z. Schmidt, R. N. Chokshi, A. Brown, and T. Northug, "Unified mechanistic model for steady-state two-phase flow in wellbores and pipelines," in *Proceedings of the SPE Annual Technical Conference and Exhibition*, Houston, Tex, USA, October 1999.

[5] A. R. Hasan and C. S. Kabir, "A study of multiphase flow behavior in vertical wells," *SPE Production Engineering*, vol. 3, no. 2, pp. 263–272, 1988.

[6] L. Q. Ping, Z. M. Wang, and J. G. Wei, "Pressure drop model for gas-liquid two-phase flow and its application in underbalanced drilling," in *Proceedings of the Conference of Global Chinese Scholars on Hydrodynamics*, vol. 18, pp. 405–411, July 2006.

[7] A. F. Bijleveld, M. Koper, and J. Saponja, "Development and application of an underbalanced drilling simulator," in *Proceedings of the IADC/SPE Drilling Conference*, pp. 113–121, Dallas, Tex, USA, March 1998.

[8] C. Perez-Tellez, J. R. Smith, and J. K. Edwards, "A new comprehensive, mechanistic model for underbalanced drilling improves wellbore pressure predictions," in *Proceedings of the SPE International Petroleum Conference and Exhibition in Mexico*, vol. 18, pp. 199–208, Villahermosa, Mexico, 2003.

[9] C. Perez-Tellez, *Improved bottomhole pressure control for underbalanced drilling operations [Ph.D. thesis]*, Universidad Nacional Autonoma de Mexico, 2003.

[10] J. R. Ramey, "Wellbore heat transmission," *Journal of Petroleum Technology*, vol. 14, pp. 427–435, 1962.

[11] C. Holmes and S. Swift, "Calculation of circulating mud temperatures," *Journal of Petroleum Technology*, vol. 22, pp. 670–674, 1970.

[12] C. S. Kabir, A. R. Hasan, G. E. Kouba, and M. M. Ameen, "Determining circulating fluid temperature in drilling, workover, and well-control operations," *SPE Drilling and Completion*, vol. 11, no. 2, pp. 74–78, 1996.

[13] A. R. Hasan, C. S. Kabir, and M. M. Ameen, "A fluid circulating temperature model for workover operations," *SPE Journal*, vol. 1, pp. 133–144, 1996.

[14] L. Raymond, "Temperature distribution in a circulating drilling fluid," *Journal of Petroleum Technology*, vol. 21, pp. 333–341, 1969.

[15] H. H. Keller, E. J. Couch, and P. M. Berry, "Temperature distribution in circulating mud columns," *SPE Journal*, vol. 13, no. 1, pp. 23–30, 1973.

[16] D. W. Marshall and R. G. Bentsen, "A computer model to determine the temperature distributions in a wellbore," *Journal of Canadian Petroleum Technology*, vol. 21, no. 1, pp. 63–75, 1982.

[17] Y. Taitel, D. Bornea, and A. E. Dukler, "Modelling flow pattern transitions for steady upward gas-liquid flow in vertical tubes," *AIChE Journal*, vol. 26, no. 3, pp. 345–354, 1980.

[18] E. F. Caetano, *Upward vertical two-phase flow through an annulus [Ph.D. thesis]*, University of Tulsa-USA, Tulsa, Okal, USA, 1986.

[19] V. C. Kelessidis and A. E. Dukler, "Modeling flow pattern transitions for upward gas-liquid flow in vertical concentric and eccentric annuli," *International Journal of Multiphase Flow*, vol. 15, no. 2, pp. 173–191, 1989.

[20] J. Ø. Tengesdal, A. S. Kaya, and C. Sarica, "Flow-pattern transition and hydrodynamic modeling of churn flow," *SPE Journal*, vol. 4, no. 4, pp. 342–348, 1999.

[21] A. S. Kaya, C. Sarica, and J. P. Brill, "Mechanistic modeling of two-phase flow in deviated wells," *SPE Production and Facilities*, vol. 16, no. 3, pp. 156–165, 2001.

[22] T. T. Yu, H. Q. Zhang, M. X. Li, and C. Sarica, "A mechanistic model for gas/liquid flow in upward vertical annuli," *SPE Production and Operations*, vol. 25, no. 3, pp. 285–295, 2010.

[23] R. C. Fernandes, R. C. Fernandes, R. Semiat, and A. E. Dukler, "Hydrodynamic model for gas—liquid slug flow in vertical tubes," *AIChE Journal*, vol. 29, no. 6, pp. 981–989, 1983.

[24] Z. Schmidt, *Experimental study of two-phase slug flow in a pipeline-riser pipe system [Ph.D. thesis]*, University of Tulsa, Tulsa, Okal, USA, 1977.

[25] R. N. Chokshi, Z. Schmidt, and D. R. Doty, "Experimental study and the development of a mechanistic model for two-phase flow through vertical tubing," in *Proceedings of the SPE 66th Annual Western Regional Meeting*, pp. 255–267, Anchorage, Alaska, USA, May 1996.

[26] E. M. Ozbayoglu, S. Z. Miska, T. Reed, and N. Takach, "Cuttings transport with foam in horizontal & highly-inclined wellbores," in *Proceedings of the SPE/IADC Drilling Conference*, Amsterdam, The Netherlands, February 2003.

[27] D. Kim, A. J. Ghajar, R. L. Dougherty, and V. K. Ryali, "Comparison of 20 two-phase heat transfer correlations with seven sets of experimental data, including flow pattern and tube inclination effects," *Heat Transfer Engineering*, vol. 20, no. 1, pp. 15–40, 1999.

[28] R. F. Knott, R. N. Anderson, A. Acrivos, and E. E. Petersen, "An experimental study of heat transfer to nitrogen-oil mixtures," *Industrial & Engineering Chemistry*, vol. 51, pp. 1369–1372, 1959.

[29] M. A. Aggour, *Hydrodynamics and heat transfer in two-phase two-component flow [Ph.D. thesis]*, University of Manitoba, Winnipeg, Canada, 1978.

[30] K. S. Rezkallah and G. E. Sims, "An examination of correlations of mean heat transfer coefcients in two-phase and two-component flow in vertical tubes," *AIChE Symposium Series*, vol. 83, pp. 109–114, 1987.

[31] S. R. Ravipudi and T. M. Godbold, "The effect of mass transfer on heat transfer rates for two-phase flow in a vertical pipe," in *Proceedings of the 6th International Heat Transfer Conference*, vol. 1, pp. 505–510, Toronto, Canada, 1978.

[32] C. A. Lopes, *Feasibility study on the reduction of hydrostatic pressure in a deep water riser using a gas-lift method [Ph.D. thesis]*, Louisiana State University, Baton Rouge, La, USA, 1997.

Hindawi Publishing Corporation
Advances in Mechanical Engineering
Volume 2013, Article ID 592940, 10 pages
http://dx.doi.org/10.1155/2013/592940

Research Article

Comparisons of LES and RANS Computations with PIV Experiments on a Cylindrical Cavity Flow

Wen-Tao Su,[1,2] Xiao-Bin Li,[1,3] Feng-Chen Li,[1] Xian-Zhu Wei,[2] Zhi-Ying Zheng,[1] and Xin Zhang[4]

[1] *School of Energy Science and Engineering, Harbin Institute of Technology, Harbin 150001, China*
[2] *State Key Laboratory of Hydro-Power Equipment, Harbin 150040, China*
[3] *School of Mechatronics Engineering, Harbin Institute of Technology, Harbin 150001, China*
[4] *TSI Incorporated, Minneapolis, MN 55126, USA*

Correspondence should be addressed to Feng-Chen Li; lifch@hit.edu.cn

Received 13 January 2013; Revised 6 March 2013; Accepted 20 March 2013

Academic Editor: Tomoaki Kunugi

A comparison study on the numerical computations by large eddy simulation (LES) and Reynolds-averaged Navier-Stokes (RANS) methods with experiment on a cylindrical cavity flow was conducted in this paper. Numerical simulations and particle image velocimetry (PIV) measurement were performed for two Reynolds numbers of the flow at a constant aspect ratio of $H/R = 2.4$ (R is the radius of the cylindrical cavity, and H is liquid level). The three components of velocity were extracted from 100 sequential PIV measured velocity frames with averaging, in order to illustrate the axial jet flow evolution and circulation distribution in the radial direction. The results show that LES can reproduce well the fine structure inside the swirling motions in both the meridional and the horizontal planes, as well as the distributions of velocity components and the circulation, in good agreement with experimental results, while the RANS method only provided a rough trend of inside vortex structure. Based on the analysis of velocity profiles at various locations, it indicates that LES is more suitable for predicting the complex flow characteristics inside complicated three-dimensional geometries.

1. Introduction

Turbulence is a universal flow phenomenon in the nature world and engineering application systems. Research on turbulence has long been a hot topic, which directly influences the prediction of environment and engineering application. There are currently three main approaches for numerically simulating turbulent flows, that is, Reynolds-averaged Navier-Stokes (RANS), large eddy simulation (LES), and direct numerical simulation (DNS). For RANS method, its governing equation (Reynolds time- and space-averaged equation) "flattens" the local flow parameters, and so it only predicts the overall characteristics of turbulent flows. Since it computes the flow parameters by dividing them into the mean part (average), which represents the main flow, and the fluctuating part, which is calculated by turbulence models, it greatly reduces the computation burden. However, the results are strongly influenced by the turbulence models adopted. For DNS method, it directly solves the Navier-Stokes (N-S) equation without introducing any turbulence models. Thus, DNS needs very fine computational meshes and large computer resources in order to resolve the smallest turbulence scale (Kolmogorov scale). So, currently it cannot handle complex flow at a relatively large flow Reynolds number (Re) and is still far from the needs for real engineering applications.

Recently, LES was used widely in the engineering applications, due to a balance of great development of computer capacity and computational cost. The basic idea of LES is to decompose the flow variables into large-scale parameters and small-scale parameters by using a "cutoff" filter function. Thus, it explicitly simulates the large eddies but parameterizes

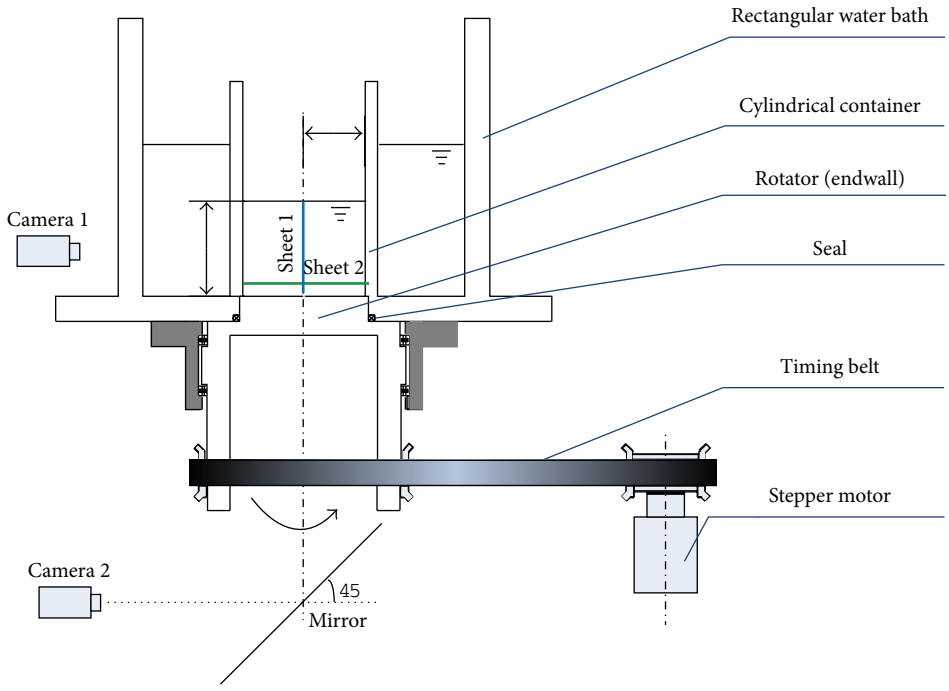

Figure 1: Schematic of experimental setup.

the small eddies using a subgrid scale (SGS) model, by which it can provide accurate results at different length-scales above the cutoff threshold in a complex fluid flow.

LES was initially proposed for global weather forecasting by meteorologist Smagorinsky [1]. After this pioneering work, LES method has been greatly developed so far in respect to the SGS model development, improvement of numerical simulation efficiency for LES, robustness of LES for turbulent flow with complex flow passage geometry, and application area extension (e.g., [2–10] among a large amount of others). Many studies show that the LES method can simulate complex flow phenomena such as vortex shedding, buoyancy influence, curved streamlines, and rotation flow, where the RANS method cannot capture the delicate flow structure in such flow conditions.

Among the complex flow phenomena, swirling flow is a fine example to test the numerical computation with different turbulent models. Swirling flows in a cylindrical cavity have attracted much attention in the past decades due to such kind of flows having close associations with frequently encountered natural phenomena like tornadoes, complex engineering applications such as centrifugal machinery and cylindrical cyclone separator, and classical studies on fluid mechanics such as flow bifurcation, symmetry breaking, and vortex break-down phenomena. The vortex structures in the rotated cavity flow show abundant flow patterns, which crucially depend on Re, the height to radius aspect ratio, H/R, and also the fluid properties. Lopez et al. [11, 12] have conducted numerical simulations and experiments on both deep and shallow cylinder flows, showing that the rotating waves were the main pattern of vorticity distribution. Li et al. [13] investigated the flow patterns in a cylindrical cavity flow of viscoelastic fluid by using a two-dimensional (2D) particle image velocimetry (PIV) system, indicating that the viscoelasticity of fluids influenced both meridional and planar flow characteristics and then the flow transition to symmetry breaking.

It is conjectured that flow characteristics in swirling flow should be well captured by the LES methods. Due to the rapid development in computer performance and numerical simulation techniques, computational fluid dynamics (CFD) developed greatly in the past decades. The commercial CFD software greatly facilitates the research on the turbulent flows in complicated flow geometries. We have carried out a comparative study on the performances of LES and RANS methods in predicting complicated three-dimensional flow characteristics in a hydraulic power machinery model [14], showing that LES is much superior to RANS for this complex flow, and only the LES results were well coinciding with the experiments. This paper aims at making further comparative study on LES and RANS computations focusing on the characteristics of the cylindrical cavity flow, especially on the vorticity distribution and velocity profiles. A carefully regulated 2D PIV experiment is performed to obtain database of velocity distribution and vortex structures for comparisons.

2. Experimental Procedures

The experimental setup is shown in Figure 1. The cylindrical cavity (inner diameter of 50 ± 0.12 mm) and its end-wall (driven by a precise stepper motor via the timing belt) are made of transparent acrylic resin. The cylindrical cavity flow is driven by the rotation of the end-wall, and the liquid flow in the cavity has a free surface in contact with the

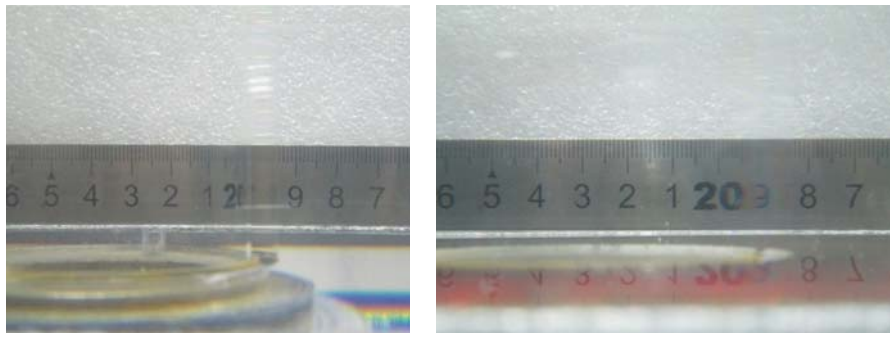

(a) (b)

Figure 2: Images of light passing through the water bath (a) and the refractive-index-matched NaI solution bath (b).

air. The hollow cylinder is bathed in a transparent acrylic resin rectangular container with the same working fluid. For detailed information of this experimental apparatus, one refers to [13].

For a swirling flow in a cylindrical container, the curved wall may bring about serious quantitative deviation to the PIV-measured velocity field in the meridional plane due to optical refraction if the difference of refractive index between the working fluid and the transparent wall material is obviously large. Therefore, tuning of working fluid refractive index has been performed in order to match with the transparent acrylic resin wall. The sodium iodide (NaI) is used as a refractive index tuning material. Eventually, an NaI solution of 61 wt% concentration is finalized so as to assure the refractive index of 1.49 in both the working fluid and the bath fluid, which are similar with that of acrylic resin. It is known that this solution is chemically stable, and its refractive index is thermally stable [15]. For the measurement of refractive index, a refractive-index meter is used at the temperature of 295 K. By using this refractive-index-matched NaI solution, image distortions have been essentially eliminated, as seen from Figure 2 showing the comparison between images of light passing through the water bath and that passing through the prepared NaI solution bath.

A standard 2D two-component PIV system (TSI Inc., Shoreview, MN, USA) is utilized to measure the velocity fields in two planes, that is, the meridional plane and lateral plan as indicated in Figure 1 as sheet 1 and sheet 2, respectively, in the cylindrical cavity swirling flow. For the illumination system of PIV, the double-pulsed YAG200-NWL (New Wave) laser generator has a power output of 200 mJ/pulse, maximum repetition rate of 15 Hz, and the emission wavelength of 532 nm. The thickness of light sheet is 0.5 mm. Sets of digital images are captured by 12-bit CCD cameras (TSI Powerview Plus with 2048 × 2048 pixel resolution). A TSI synchronizer box controls the strobing and timing of the camera and laser. The dual frame acquisition rate is 8 Hz, and so the sampling frequency of velocity frames is 4 Hz. For the resolution of measurement, all the picture frames in the x-z plane (the Cartesian coordinates is shown in Figure 3) cover the full height of liquid, that is, an area of $x \times z = 50 \times 60\ \text{mm}^2$ with the spacing between adjacent vectors $\Delta x = \Delta z = 0.82$ mm. And in the x-y plane, the images cover a planar disc area of $\pi \times 25^2\ \text{mm}^2$, with the spacing between adjacent vectors $\Delta x = \Delta y = 0.60$ mm and $\Delta x = \Delta y = 0.96$ mm at $z = 6.0$ mm and 30.0 mm planes, respectively. The interrogation area is set as 32 × 32 pixels (with 50% overlap in each direction) for velocity vector analyses.

Teflon tracer particles with an average diameter of 10 μm are used to seed the flow. Although the density of tracer particle is somewhat smaller than that of working fluid, for the measurement within 30 minutes, the tracer particles follow the working fluid very well. Carefully adjusting the position (both horizontal and perpendicular) of laser sheets and the focal distance, the tracer particles can be uniformly illuminated and so clear images can be sampled. To meet the demand of this measurement, a Nikkon 50 mm/F1.8 camera lens is used with camera to capture the flow field in the meridional plane (sheet 1 and camera 1 as indicated in Figure 1), and a Sigma Micro 105 mm/F2.8 lens is for the horizontal plane measurement (sheet 2 and camera 2). The illuminated image in the horizontal plane (sheet 2) is taken from the end-wall bottom through a mirror set at 45° angle.

The measured cylindrical cavity flow has a constant aspect ratio of $H/R = 2.4$. PIV images are acquired for 100 dual frames (200 PIV photographs) for each run of measurements. For the image post processing, flow vectors are obtained by TSI INSIGHT 3G software (Version 3.3), then the bad vectors are filtered by using a homemade FORTRAN program based on the "three-sigma" principle.

3. Numerical Simulation Procedures

To study the fine structures of the swirling flow with free surface, numerical simulations are conducted based on RANS method and LES method, respectively. The solvers in commercial CFD code FLUENT (version 6.3) are utilized to solve the governing equations defined for the problem.

The computational model adopted in the numerical simulation is shown in Figure 3. The height of liquid level is 0.06 m under stationary state, which is the same as experiment. In order to capture the gas-liquid interface, an air domain with 0.02 m height is added over the water domain. The computational domains are meshed with structured grids.

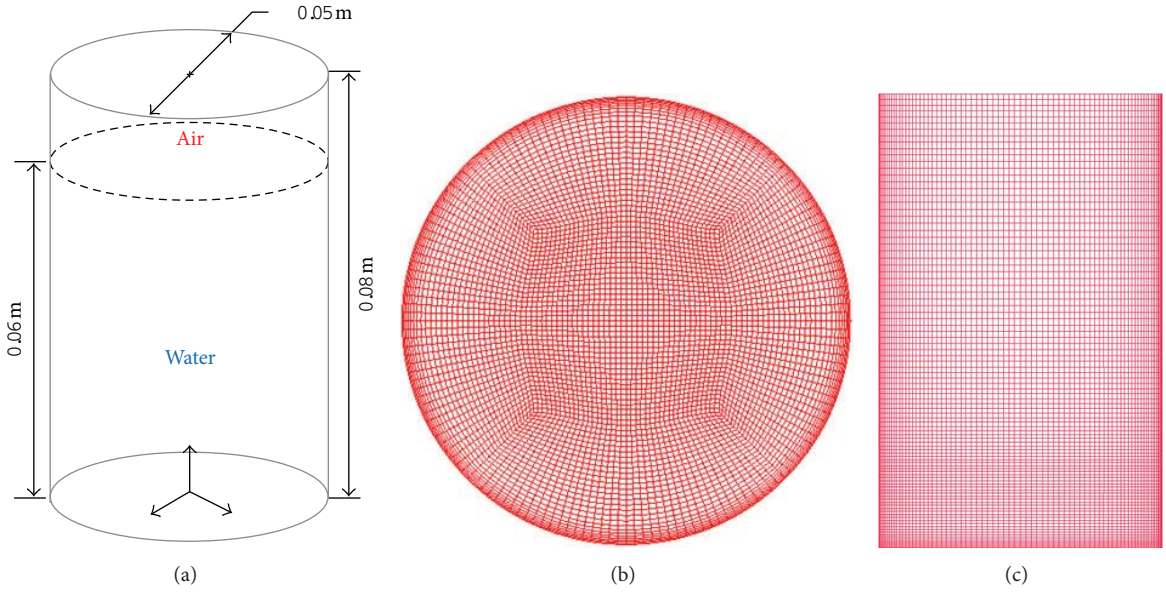

FIGURE 3: Schematic diagram and mesh of the computational domain. (a) Schematic of computational domain; (b) mesh in the horizontal plane; (c) mesh in the meridional plane.

Near the cylinder wall and the bottom end-wall around which the high shear stresses exist, the grids are well refined. For the refinement, the viscous layer grid $y^+ (= yu_\tau/\upsilon)$ is set less than 8, where u_τ is the wall friction velocity and υ is the kinematic viscosity.

The generated mesh system contains over 1.4 million cells in the whole domain and is displayed in Figure 3(b) and Figure 3(c). Though the liquid phase is water in numerical simulations, the results are still comparable with experiments since Res of the simulated cylindrical cavity flow are set to be the same as that of corresponding experimental cases.

Numerical simulations are performed for an incompressible fluid flow. The LES and RANS methods are introduced briefly as follows.

LES method is realized in a way of reducing the number of freedom degrees in the simulated turbulent flow. This is done by calculating only the low-frequency modes (corresponding to turbulent structures larger than the cutoff threshold) but modeling the high frequency (smaller than the cutoff threshold) ones. The scale separation is performed by filtering in space the N-S equations. Small eddies can be modeled by the additional term in the LES governing equations resulting from the filtered N-S equations. The additional term is referred to as the SGS model which is derived from the interaction of unresolved scales and resolved scales. Under the assumption of constant fluid property, the governing equations of LES are as follows:

$$\frac{\partial \overline{u}_i}{\partial x_i} = 0, \tag{1}$$

$$\frac{\partial \overline{u}_i}{\partial t} + \frac{\partial \overline{u}_j\,\overline{u}_i}{\partial x_j} = -\frac{1}{\rho}\frac{\partial \overline{p}}{\partial x_i} + \upsilon\frac{\partial^2 \overline{u}_i}{\partial x_j\,\partial x_j} - \frac{\partial \tau_{ij}}{\partial x_j}, \tag{2}$$

where τ_{ij} represents the subfilter tensor comprising the terms that are not expressed directly from resolved scales, $\tau_{ij} = \overline{u_j}\,\overline{u_i} - \overline{u}_j\,\overline{u}_i$. In order to obtain the correct subfilter tensor, Smagorinsky-Lilly model is used in this study [16].

The most widely used approach in industrial applications for the modeling of turbulent flow is RANS. From the viewpoint of engineering applications, the focus is the change of time-averaged flow field induced by the turbulence. Therefore, solving the time-averaged N-S equations is taken into consideration. This approach assumes that nonconvective transport in a turbulent flow is governed by random three-dimensional turbulence possessing a broadband spectrum with no distinct frequencies. The model represents a very wide range of scales with the smallest scales being influenced by the fluid viscosity. In this study, the standard k-ε model and high-accuracy RNG k-ε model in RANS are adopted. The RNG k-ε model improves the accuracy of the prediction on the turbulent vortices and near-wall flow, compared with the standard one.

To consider the air-water interface at the free surface of swirling flow, the volume of fluid (VOF) model for two-phase flow is adopted to conduct numerical simulation. In VOF model, there is no interpenetration for parameters in two or more fluids (or phases). A new variable for each additional phase is added into the model, that is, the volume fraction α of the phase in the computational cell. And the sum of the volume fraction of all phases in each cell reaches unity. The fields for all variables and properties are shared by the phases and represent volume-averaged values, as long as the volume fraction of each phase at each location is known. Based on the volume fraction of the qth fluid in the cell α_q, the tracking of the interface between the phases is completed by solving the continuity equation for volume fraction of one or more

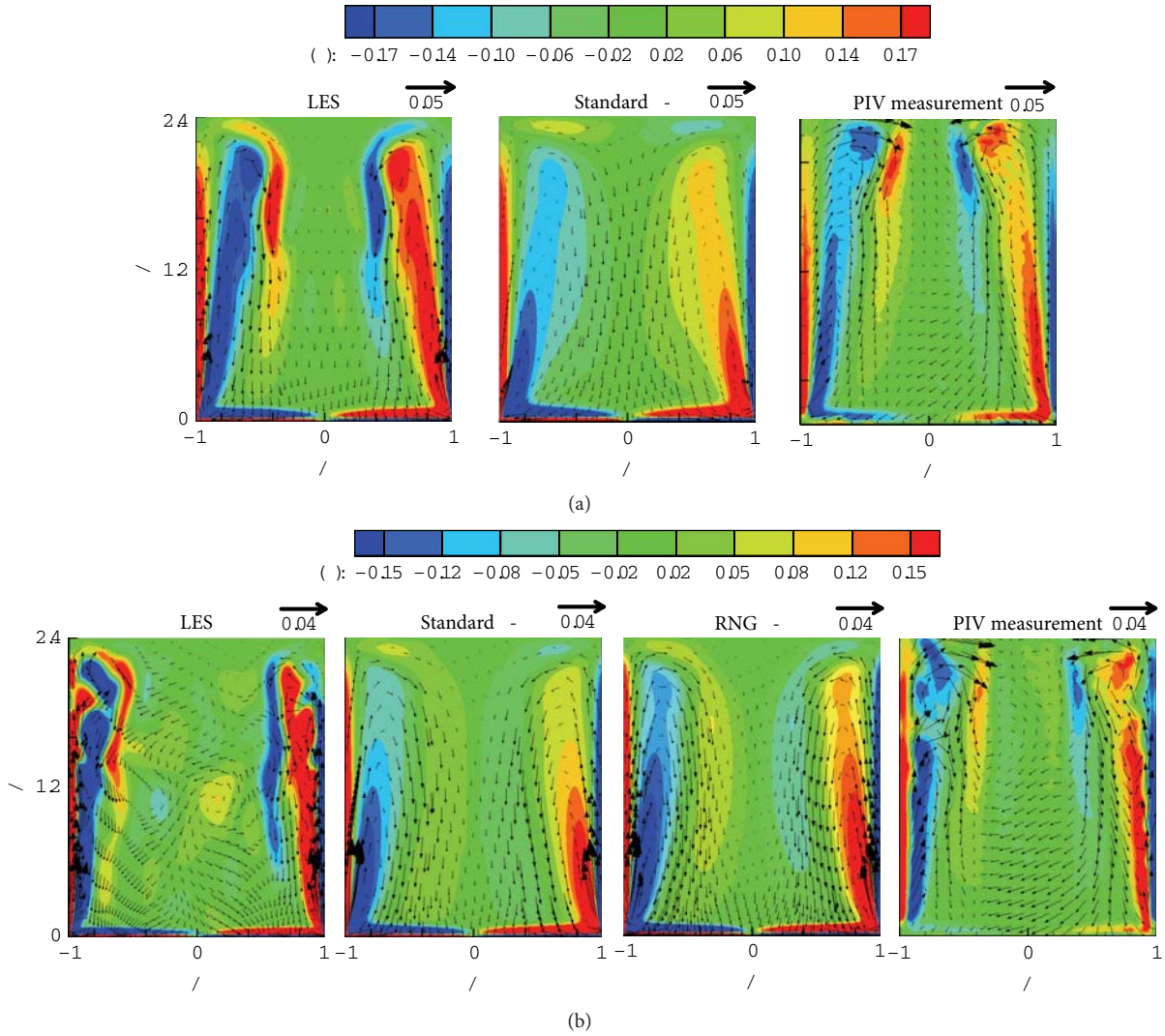

Figure 4: Flow structures in the meridional plane for the cylindrical cavity flow at different Res obtained by numerical simulations and PIV measurement. (a) Re = 2616; (b) Re = 6541.

phases. For the qth phase, the equation is defined as [16]

$$\frac{1}{\rho_q}\left[\frac{\partial}{\partial t}\left(\alpha_q\rho_q\right)+\nabla\cdot\left(\alpha_q\rho_q\vec{u}\right)\right]=\frac{S_a}{\rho_q}+\frac{1}{\rho_q}\sum_{p=1}^{n}\left(\dot{m}_{pq}-\dot{m}_{qp}\right), \tag{3}$$

where $\dot{m}_{qp}$ is mass transfer from qth phase to pth phase, and $\dot{m}_{pq}$ is mass transfer from pth phase to qth phase. $\vec{u}$ in (3) is hereby the same velocity vector in N-S (2).

The bottom end-wall of the geometry is set as the slip wall (the absolute velocity near the wall is nonzero) with constant rotational velocity which ensures the same Re as the one in the corresponding experimental case. The sidewall surface of the cylinder is set as nonslip wall condition, and the top plane of liquid is defined as pressure outlet with a standard atmospheric pressure. Fluid media in the simulation are air and water. In VOF model, air is set as the primary phase, while water is set as the secondary phase.

The SIMPLE scheme is used for the computation of velocity-pressure coupling. PRESTO! and the first-order upwind scheme are, respectively, adopted to discretize the pressure equation and the volume fraction equation. For the momentum equation discretization in LES, bounded central differencing scheme is utilized. For standard and RNG k-ε models, second-order upwind scheme is used to discretize the momentum equation, turbulent kinetic energy (k) equation, and turbulent dissipation rate (ε) equation. For the time marching, it is set as the implicit second-order method.

4. Results and Discussions

For convenience, a cylindrical coordinates (r, θ, z) (correspondingly, the velocity field is (u, v, w)) is defined instead of the Cartesian coordinates (x, y, z), with the origin locating at the center of the bottom end-wall. Therefore, horizontal and meridional planes refer to (r-θ) plane and (r-z) plane,

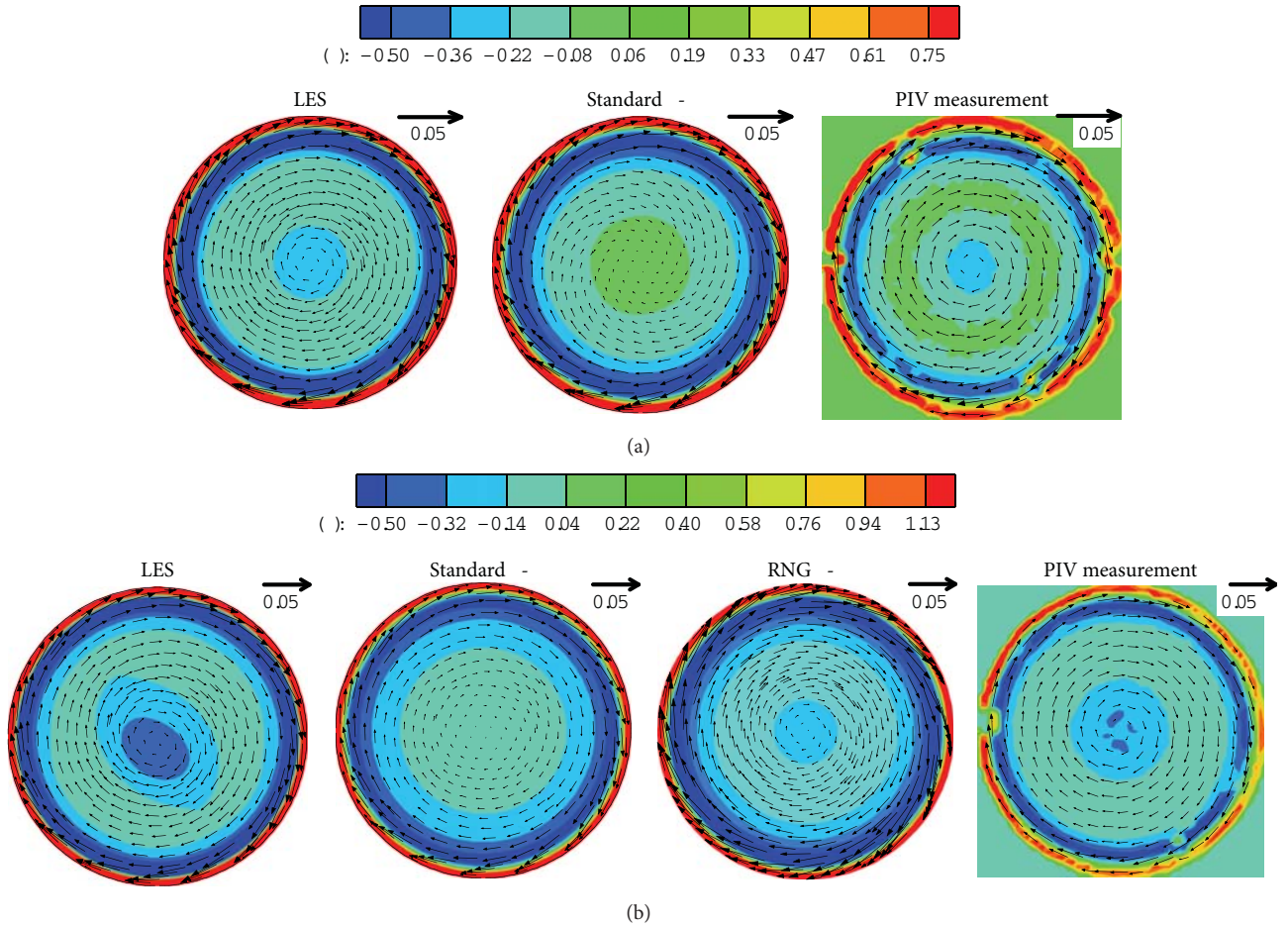

FIGURE 5: Velocity field and vorticity distribution in the parallel plane at $z/R = 0.24$ for the cylindrical cavity flow at different Res obtained by numerical simulations and PIV measurement. (a) Re = 2616; (b) Re = 6541.

respectively. The Reynolds number of the investigated cylindrical cavity flow is defined as $\mathrm{Re} = \Omega R^2/\upsilon$, where Ω is angular velocity. Two flow cases are tested at $\mathrm{Re} = 2616$ and 6541, respectively. The Froude number is defined as $\mathrm{Fr} = \Omega^2 R^2/(\mathrm{Hg})$, where g is the gravitational accelerator, and it reads 0.0186 and 0.1165 for the two investigated cases, respectively. For a free-surface rotating flow at Fr number less than 1, the surface perturbation in an open container is trivial [17]. In this case, therefore, the deformation of air-water interface is considered to be negligible, and the surface tension does not influence the flow structures.

The flow structures in the meridional plane and two parallel planes are captured in both experiments and numerical simulations. Distributions of the radial and axial velocity components, u and w, and the circulation $\Gamma(r) = vr/(\Omega R^2)$, respectively, along the radius are also obtained from the meridional and horizontal planes. Comparisons of these results obtained from LES and RANS with that of the experiment are presented as follows.

4.1. Flow Structures in the Meridional Plane. The 2D velocity fields in the meridional plane (r-z) obtained from PIV measurement and numerical simulations of the cylindrical cavity flow are shown in Figure 4. The vectors are normalized velocities ($u/(\Omega R)$, $w/(\Omega R)$), and colored contours represent the normalized circumferential vorticity $\omega(\theta)$ calculated by u and w distributions in the (r-z) plane. Note that all the PIV measurement results are treated by a 100-frames-averaging, due to the steady flow structures at the given flow conditions. As Re gets higher, the flow should be more irregular, so the RNG k-ε model is introduced to make a comparison within the RANS category and to check how it performs comparing with others.

Figure 4 depicts the velocity field and vorticity obtained by LES and RANS (RNG k-ε model is used additionally for Re = 6541) and PIV measurement for the same configuration and setup. The swirling flow driven by the bottom end-wall displays an axisymmetric pattern, which radially flows outwards in the Ekman layer near the bottom and is restricted into the vertically axial direction near the cylinder sidewall, forming a jet-like shear layer flow. Finally, in the axis of the cylinder, the fluid overturns near the interface then diverts down into the bulk. This "swirling nature," in both the azimuthal and vertical directions, is much similar to the tealeaf motion with the spoon stirring in a cup. Compared

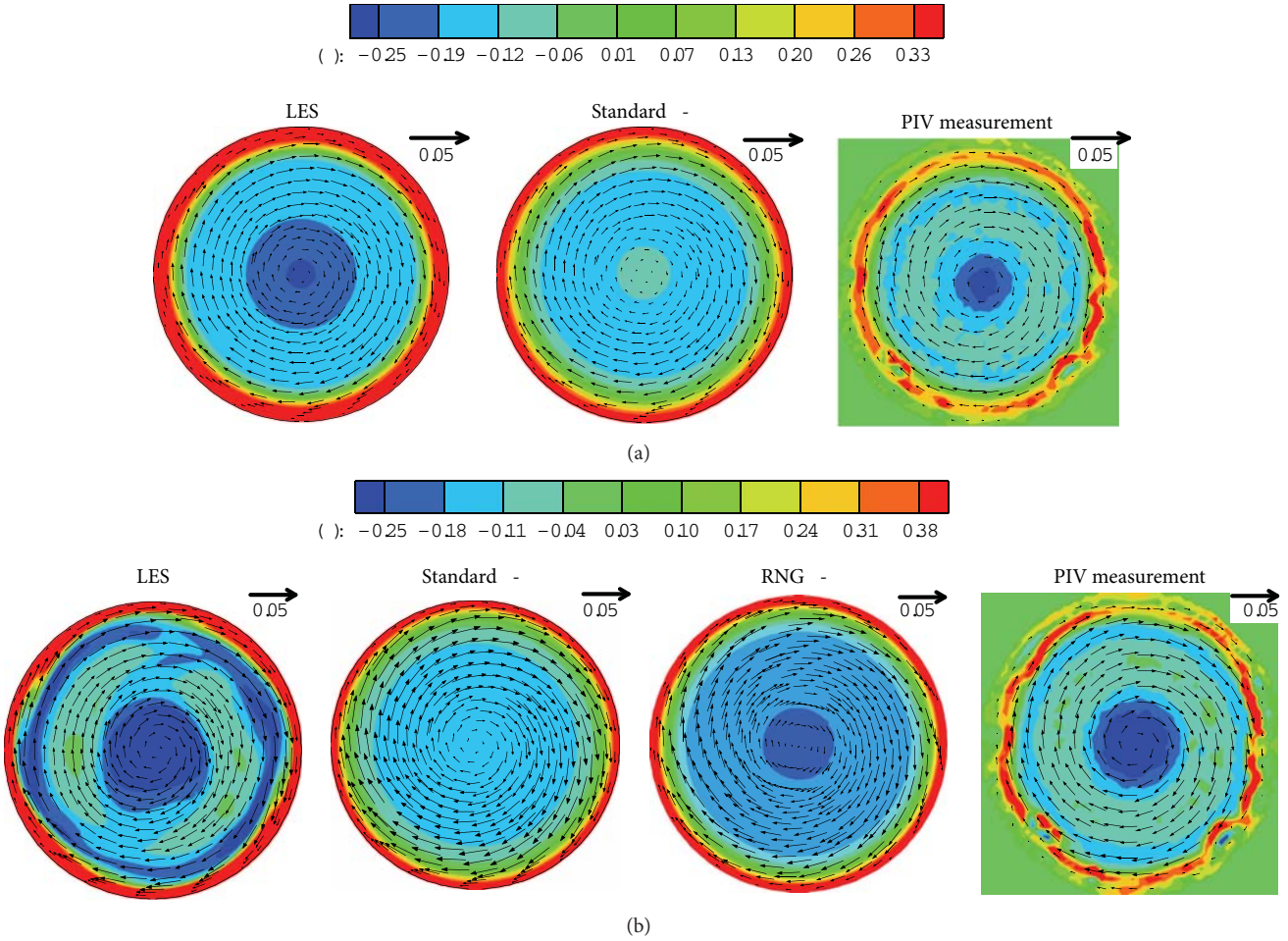

FIGURE 6: Velocity field and vorticity distribution in the parallel plane at $z/R = 1.2$ for the cylindrical cavity flow at different Res obtained by numerical simulations and PIV measurement. (a) Re = 2616; (b) Re = 6541.

with the RANS method (for both k-ε models), the vector profile and vorticity distribution by LES method in the (r-z) plane are much sharper and more reasonable as a symmetric swirling flow and agree with the PIV measurement better. Note that the result by RNG k-ε model proves to be better than that by standard k-ε model on the vorticity structures, and velocity distribution in the shear layer is also better. That should be due to the good treatment of RNG k-ε model near the wall. However, the two RANS models both do not predict well the flow near the free surface and in the bulk where the fluid changes direction. And in comparison, LES shows much better results which resemble the experimental measurement. It implies that the high-accuracy k-ε model still cannot reproduce as fine detailed information as LES does. Therefore, in the following, we just show the results of RANS by using standard k-ε model, along with the LES and PIV for Re = 2616.

At least, the result by RANS with a k-ε model shows an overall prediction of the axisymmetric structures in the (r-z) plane; however, it encompasses a much larger zone of overturning flow in the bulk as compared with LES and PIV measurement results. Such difference probably stems from the numerical simulation approach of RANS, which has the "smearing effect" for the turbulence modeling [18].

The LES method reproduces better the PIV measurement result. Nevertheless, more discrepancies appear when Re gets high. When the flow gets more chaotic, the fluid motions under the small scales will be more robust to transport the injected energy. Therefore, the flow information at the high frequency needs refined girds and numerical method to predict, which is just limited by SGS models in the LES. The bulk flow by LES is more irregular than experimental result, which should be due to the limitation of SGS model adopted in this study. Anyway, for both numerical methods (LES and RANS), the vertical Ekman layers near the sidewall of cylinder coincide well with that of experimental result, indicating the local mesh for simulation is good enough. And more detailed differences come from the essence of the numeric treatment and turbulence models.

4.2. Flow Structures in the Horizontal Plane. For the flow pattern in the parallel plane (r-θ), the motions show an axisymmetric pattern as well. Figures 5 and 6 display the simulated and measured velocity field together with the

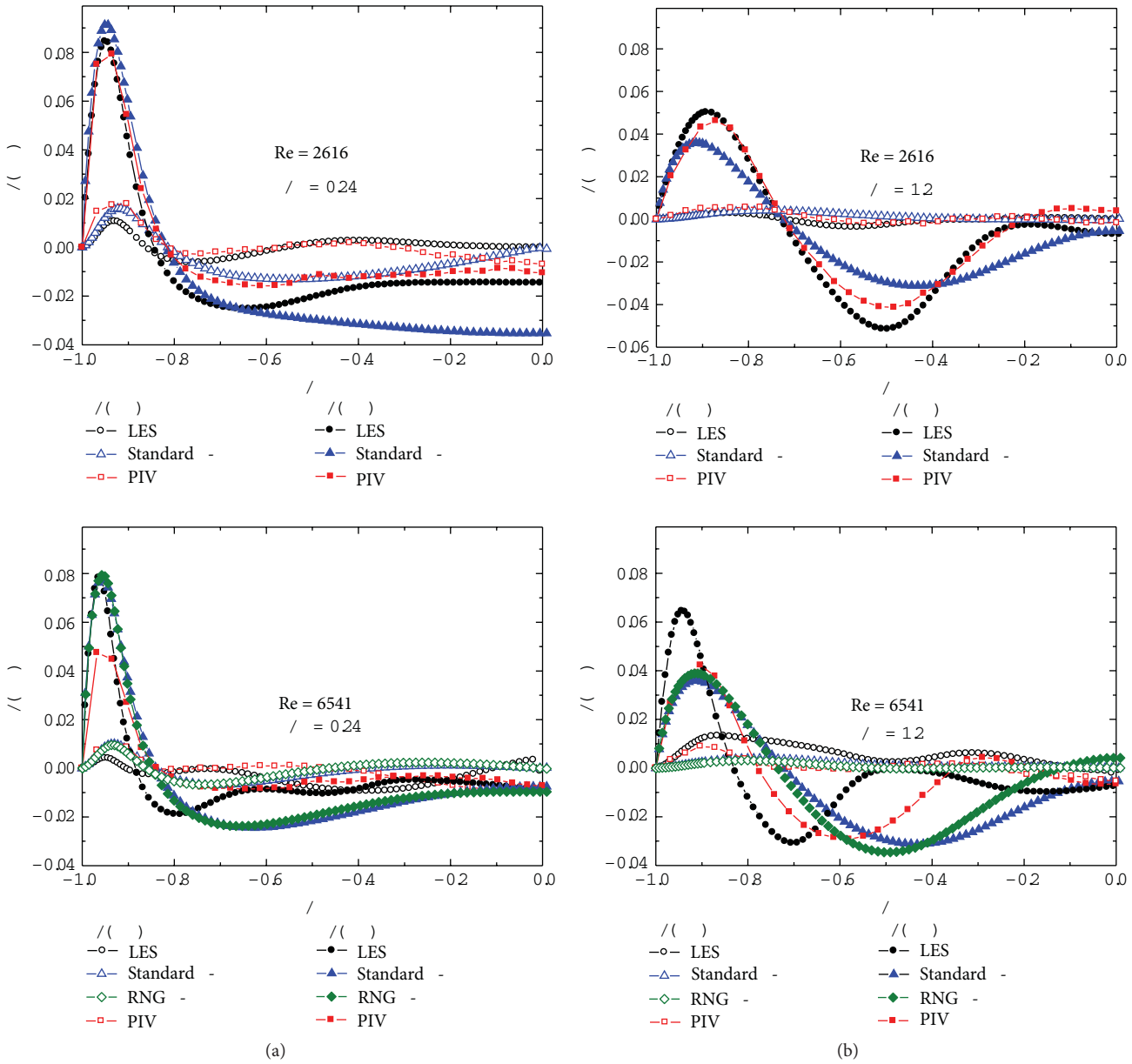

Figure 7: Radial and axial velocity distribution in the parallel planes for the swirling flow at different Res.

normalized axial vorticity $\omega(z)$ at depths of $z/R = 0.24$ and 1.2 for two different Res, respectively. As depicted in the experimental setup, the lower horizontal plane is physically $z = 6$ mm, near to the bottom end-wall, the flow is strongly influenced by the end-wall rotating motion. So the velocity in this (r-θ) plane should be composed of a large azimuthal component and a small radial component. The larger the rotation speed is, the more chaotic the flow in the bulk becomes. At the upper horizontal plane $z = 30$ mm, the flow in the bulk shows axisymmetric pattern, which is consistent with that in the (r-z) plane. Again, the result by LES method is shaper than that by RANS method, and for the vectors both agree well with experimental result, but for the vorticity distribution, compared with RANS method LES result shows more similar pattern as that of experiment at the two measured Res. However, the PIV images at the parallel planes are truly rough in the rim, which should be due to the possible contamination of particle tracers closed to the wall during the long-time measurement.

To compare the k-ε models within RANS method, the RNG k-ε model performs clearer prediction near the bottom wall (Figure 5), whereas LES method outperforms their both near the cylinder wall (Figure 6). This indicates that LES is more suitable for simulating the swirling flow, with high shearing effect existing near the wall.

4.3. Radial Distributions of Velocity Components and Circulation. To further compare the simulated results with experiments, the radial distributions of two velocity components, u and w, and the circulation $\Gamma(r)$ at two liquid levels ($z/R = 0.24$

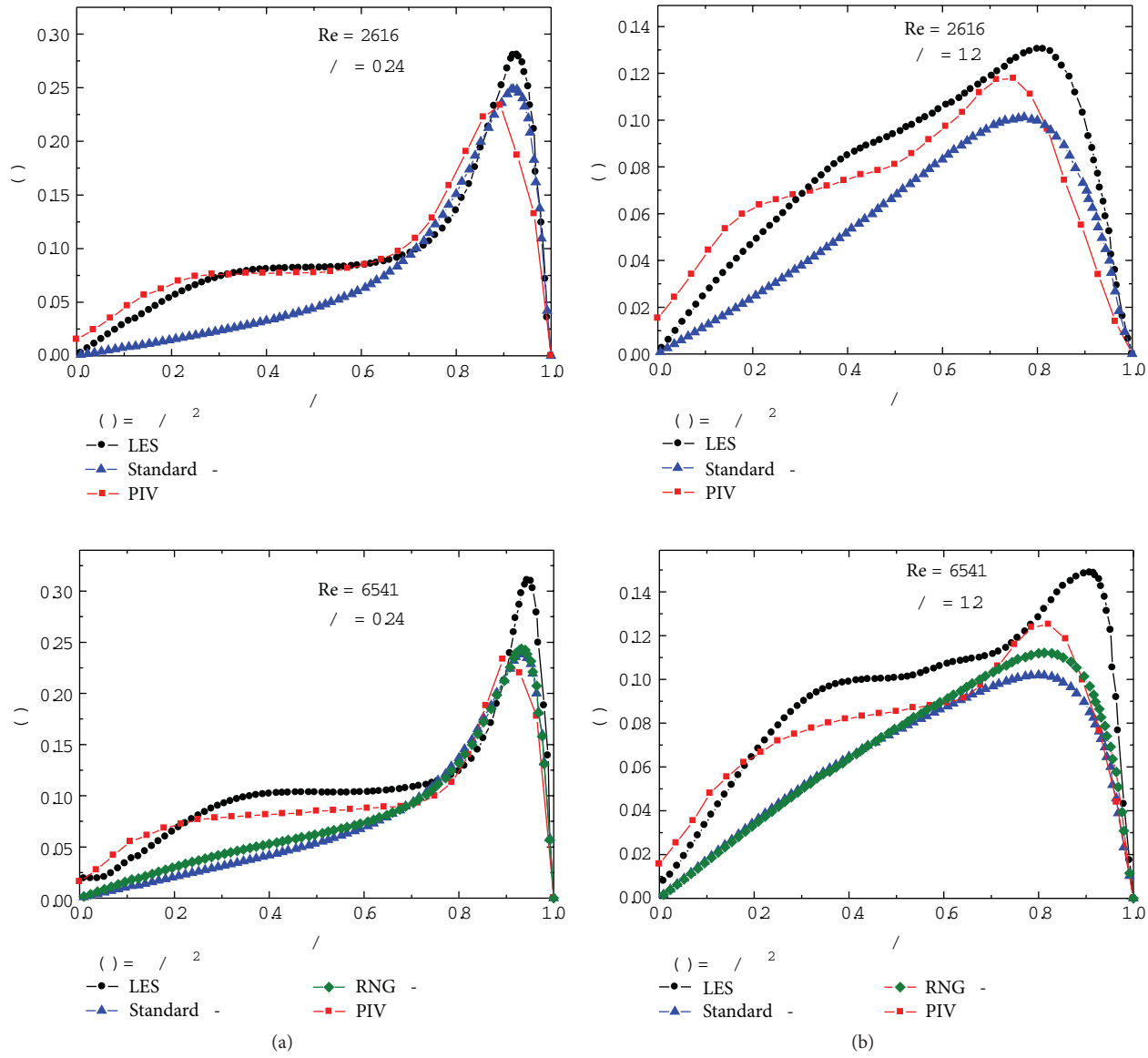

Figure 8: Azimuthal velocity distribution in the parallel planes at $z/R = 0.24$ and 1.2 for the swirling flow at different Res, respectively.

and 1.2), and two Res (Re = 2616 and 6541) are calculated and shown in Figures 7 and 8, respectively. The distributions of u and w are extracted from velocity vectors in the $(r\text{-}z)$ plane as plotted in Figure 4. The distribution of $\Gamma(r)$ is calculated using the velocity field in the two (r, θ) planes as plotted in Figures 5 and 6. Note that the RNG k-ε model is used for high Re to make better illustration, and it shows much similar result with that by standard k-ε model.

For the radial distribution of w, the peaky structure moves towards the bulk when the observed plane varies from low to high (from $z/R = 0.24$ to 1.2, as seen from the comparison between Figures 7(a) and 7(b)). The width of peak gets narrow as Re rises (as seen from the comparison between the upper and lower ones in Figure 7), which means the jet flow near the sidewall of cylinder becomes stronger, and the shear layer correspondingly becomes thinner. More importantly, it is seen from Figure 7 that, for all the runs, the overall variation trend of w along the radial direction obtained by LES matches with the PIV measurements much better than that by RANS, although there are still some quantitative differences between LES and PIV measurement results.

For the radial distribution of u, the magnitude is apparently smaller than that of w. Again, the matching between LES method and PIV result is fairly good. As for the result by RANS method, the evolution of both u and w flattens in the radial direction, especially in the core region of the cylinder. It indicates that the LES method for such a swirling flow can capture the detailed characteristics of the vortex motions but RANS can only capture overall ones.

For a cylindrical cavity flow, the circulation $\Gamma(r)$ is an important parameter to illustrate the influence of swirling motion on the structure of the vortex flow by showing its

radial distributions in different horizontal cross-sections [13]. As shown in Figure 8, the circulation continuously increases from the core (about zero magnitude) to a maximum near the sidewall and then decreases to zero on the sidewall of the cylinder. With the increase of z, the maximum $\Gamma(r)$ decreases in its amplitude, and its location moves away from the sidewall. It can be seen from Figure 8 that the overall variation trend of $\Gamma(r)$ in the radial direction can be captured by LES method quite well, as compared with PIV measurements. Particularly in the bulk flow, the matches between LES and PIV measurement are good enough that the plateau zones are successfully predicted. The RANS method fails to capture this feature in the bulk flow though it also depicts good circulation distribution near the wall.

From the comparisons of flow structures in the cylindrical cavity flow obtained by LES, RANS and PIV measurement, it is confirmed that LES can reproduce the overall information of swirling flow, and probably most of engineering flows. As speculated, RANS method loses precision in the prediction of detailed information of vortex structures, but can only provide the gross patterns of swirling flow.

5. Conclusions

Comprehensive comparisons between LES, RANS simulations, and PIV measurement for a swirling flow in a cylinder with bottom end-wall rotating have been carried out in this paper, through presenting the important parameters including velocity, vorticity distributions in both the meridional and parallel planes, and the radial distributions of different velocity components and circulation, at two Reynolds numbers, respectively.

The comparison with PIV measurement shows that LES method can capture more detailed information in such a swirling motion, with good matches in flow structures, overall characteristics of the radial distributions of the investigated velocity components and the circulation distribution. However, RANS method fails to regenerate the fine structures in the bulk. Together with our previous study, it is again verified that LES has great potential in serving as a powerful tool for the prediction of engineering flows inside complicated geometries.

Acknowledgments

This work is supported by National Natural Science Foundation of China (51276046, 51076036), Specialized Research Fund for the Doctoral Program of Higher Education of China (20112302110020), National Key Technology R&D Program (2011BAF03B01), and Heilongjiang Scientific Funds for Distinguished Young Scientist (JC201115).

References

[1] J. Smagorinsky, "General circulation experiments with the primitive equation," *Monthly Weather Review*, vol. 91, no. 3, pp. 99–164, 1963.

[2] J. W. Deardorff, "Convective velocity and temperature scales for the unstable planetary boundary layer and Rayleigh convection," *Journal of Atmospheric Sciences*, vol. 27, pp. 1211–1213, 1970.

[3] U. Schumann, "Subgrid scale model for finite difference simulations of turbulent flows in plane channels and annuli," *Journal of Computational Physics*, vol. 18, no. 4, pp. 376–404, 1975.

[4] N. N. Mansour, P. Moin, W. C. Reynolds, and J. H. Ferziger, "Improved methods for large-eddy simulations of turbulence," in *Symposium on Turbulent Shear Flows*, pp. 14.21–14.29, Pennsylvania State University, 1977.

[5] U. Schumann, "Subgrid length-scales for large-eddy simulation of stratified turbulence," *Theoretical and Computational Fluid Dynamics*, vol. 2, no. 5-6, pp. 279–290, 1991.

[6] M. Germano, U. Piomelli, P. Moin, and W. H. Cabot, "A dynamic subgrid-scale eddy viscosity model," *Physics of Fluids A*, vol. 3, no. 7, pp. 1760–1765, 1991.

[7] N. Y. Liu, X. Y. Lu, and L. X. Zhang, "A dynamic SGS model for large eddy simulation of stratified shear-flow," *Scientia Sinica Mathematica*, no. 2, pp. 145–153, 2000.

[8] X. L. Tang, Z. D. Qian, and Y. L. Wu, "Second-order dynamic sub-grid-scale stress model with double coefficients," *Advances in Water Science*, vol. 15, no. 1, pp. 50–55, 2004.

[9] X. X. Li, R. E. Britter, T. Y. Koh et al., "Large-eddy simulation of flow and pollutant transport in urban street canyons with ground heating," *Boundary-Layer Meteorology*, vol. 137, no. 2, pp. 187–204, 2010.

[10] X. X. Li, R. E. Britter, L. K. Norford, T. Y. Koh, and D. Entekhabi, "Flow and pollutant transport in urban street canyons of different aspect ratios with ground heating: large-eddy simulation," *Boundary-Layer Meteorology*, vol. 142, no. 2, pp. 289–304, 2012.

[11] A. H. Hirsa, J. M. Lopez, and R. Miraghaie, "Symmetry breaking to a rotating wave in a lid-driven cylinder with a free surface: experimental observation," *Physics of Fluids*, vol. 14, no. 6, pp. L29–L32, 2002.

[12] J. M. Lopez, F. Marques, A. H. Hirsa, and R. Miraghaie, "Symmetry breaking in free-surface cylinder flows," *Journal of Fluid Mechanics*, vol. 502, pp. 99–126, 2004.

[13] F. C. Li, M. Oishi, Y. Kawaguchi, N. Oshima, and M. Oshima, "Experimental study on symmetry breaking in a swirling free-surface cylinder flow influenced by viscoelasticity," *Experimental Thermal and Fluid Science*, vol. 31, no. 3, pp. 237–248, 2007.

[14] W. T. Su, F. C. Li, X. B. Li, X. Z. Wei, and Y. Zhao, "Assessment of LES performance in simulating complex 3D flows in turbomachines," *Engineering Applications of Computational Fluid Mechanics*, vol. 6, no. 3, pp. 355–364, 2012.

[15] K. Yuki, "Visualization of complex flow structures by matched refractive-index PIV method," in *Aeronautics and Astronautics*, M. Mulder, Ed., 2011.

[16] *Fluent User Manual*, Version 6.3.2., 2006.

[17] B. Freeze, S. Smolentsev, N. Morley, and M. Abdou, "Characterization of the effect of Froude number on surface waves and heat transfer in inclined turbulent open channel water flows," *International Journal of Heat and Mass Transfer*, vol. 46, no. 20, pp. 3765–3775, 2003.

[18] N. C. Nguyen, P. O. Persson, and J. Peraire, "RANS solutions using high order discontinuous Galerkin methods," in *Proceedings of the 45th AIAA Aerospace Sciences Meeting and Exhibit*, pp. 11080–11095, Reno, Nev, USA, January 2007.

Hindawi Publishing Corporation
Advances in Mechanical Engineering
Volume 2013, Article ID 905379, 11 pages
http://dx.doi.org/10.1155/2013/905379

Research Article

Aerodynamic Performance Prediction of Straight-Bladed Vertical Axis Wind Turbine Based on CFD

L. X. Zhang, Y. B. Liang, X. H. Liu, Q. F. Jiao, and J. Guo

College of Mechanical and Electrical Engineering, Harbin Engineering University, Harbin 150001, China

Correspondence should be addressed to Y. B. Liang; lyingbin@163.com

Received 15 October 2012; Revised 9 March 2013; Accepted 10 March 2013

Academic Editor: Toshio Tagawa

Numerical simulation had become an attractive method to carry out researches on structure design and aerodynamic performance prediction of straight-bladed vertical axis wind turbine, while the prediction accuracy was the major concern of CFD. Based on the present two-dimensional CFD model, a series of systematic investigations were conducted to analyze the effects of computational domain, grid number, near-wall grid, and time step on prediction accuracy. And then efforts were devoted into prediction and analysis of the overall flow field, dynamic performance of blades, and its aerodynamic forces. The calculated results agree well with experimental data, and it demonstrates that RNG k-ε turbulent model is great to predict the tendency of aerodynamic forces but with a high estimate value of turbulence viscosity coefficient. Furthermore, the calculated tangential force is more dependent on near-wall grid and prediction accuracy is poor within the region with serious dynamic stall. In addition, blades experience mild and deep stalls at low tip speed ratio, and thus the leading edge separation vortex and its movement on the airfoil surface have a significant impact on the aerodynamic performance.

1. Introduction

As one of the most promising renewable energy resources, wind energy plays an important role in response to shortage of fossil fuels and climate change [1]. With widely use of small-scale wind turbine, the straight-bladed vertical axis wind turbine (S-VAWT) is attractive for its simple blade design, making it relatively easy to be fabricated and cost saving. There are some distinct advantages over to the commercial horizontal axis wind turbine [2–5], where no yaw mechanism is required and it responds well to changes of wind direction for its omni-directional virtue. Whereas, the unsteady flow around blades, Darrieus motion [6], and dynamic changes of angle of attack have a significant impact on aerodynamic loads on blades. Therefore aerodynamic prediction models of VAWT are still immature [7, 8], although concept of VAWT has been proposed by Darrieus [9] as early as 1931. Accurate prediction and effective and efficient optimization tools are urgently needed to realize the goal for an S-VAWT with better performance.

It is commonly believed that streamtube models and vortex models make great contributions to overall aerodynamic performance optimization and local interaction mechanism of blade. Aerodynamic models still cannot meet the demands for various purposes, although the streamtube and vortex models have been improved for many times, including multiple streamtube model [10], double multiple streamtube model [11], FEVDTM [12], and VPM2D method [13]; more details can be found in the literature [14–16]. But with the rapid development of computational fluid dynamics (CFD), which has not only accelerated the design process but also has brought down the overall cost of design, the CFD become an attractive solution for aerodynamic performance prediction.

CFD method had been widely used for overall performance prediction. A CFD prediction model based on BE-M theory was presented by Raciti Castelli et al. [17] for evaluating the aerodynamic forces of S-VAWT. Calculation results obtained from large eddy simulation of Iida et al. [18] indicated that the results at high tip speed ratios (TSR) show good agreement with that of momentum theory, but it was not accurate for low TSR cases. Howell et al. provided three-dimensional CFD model based on RNG k-ε turbulence model [19], and the effects of turbine solidity, roughness, and tip vortices were considered. Numerical investigations on flow curvature effects were conducted by Coiro et al. [20],

and he argued the difference between DMS model and VAT-VOR3D code. Hwang et al. proposed a cycloidal water turbine with individual blade pitch control [21], along with optimized cycloidal motion for better performance obtained from CFD simulations.

In addition, CFD simulation is an effective solution for analysis of local flow field around blades, particularly for dynamic stall and wake flow. Two-dimensional computational investigations on dynamic stall with different blade pitching patterns were carried out by Wang et al. [22], and he stated that obtained results agreed well with the experimental data except for high angle of attack. Amet et al. provided a detailed numerical analysis of the physical phenomena that occurs during dynamic stall where compressible RANS k-ω model and multiblock structured mesh structure were used [23]. Furthermore, studies of dynamic stall show that SST k-ω turbulence model was better than k-ω model as reported by Ekaterinaris and Platzer [24] and Qian et al. [25]; Qian et al. said that SST k-ω turbulence model was an effective model for dynamic stall simulation with high accuracy and the predicted aerodynamic coefficients agreed well with the experimental data.

Due to that CFD method is an attractive solution for performance optimization, thus reliability and accuracy of CFD have become the key factors. The work presented here addressed the issues that the influences of process of numerical simulation on accuracy and efforts were devoted into the effects of mesh structure and time step, expecting for a better performance prediction. Both 2D and 3D CFD simulations of S-VAWT were conducted to assist a better understanding of dynamic stall. In addition, comparison analysis between experimental data from literature [13] and calculated results was done to verify the reliability and accuracy of CFD.

2. Flow Field of Blade

The present work here aims at obtaining the relationship between prediction accuracy and preset parameters of CFD. In order to have an overall understanding of interference terms, it is better to get knowledge of local velocity field around blade.

2.1. Macro Flow Field. Figure 1 is the local velocity field of blade in first quadrant and its transient aerodynamic forces exerting on blade. It indicates that the local relative velocity W_θ is dependent on local wind speed V_θ and tangential velocity U. In addition, Reynolds number and angle of attack α_θ are in dynamic change and are functions of azimuth angle θ. more details can be found in literature [26].

The aerodynamic forces acting on blade, lift F_l and drag F_d, can be decomposed into tangential force F_τ along the rotor and radial force F_n, as shown in Figure 1.

$$\begin{Bmatrix} F_{\tau\theta} \\ F_{n\theta} \end{Bmatrix} = \begin{Bmatrix} \int_{-h}^{h} C_q \cdot C_\tau \cdot C dz \\ \int_{-h}^{h} C_q \cdot C_n \cdot C dz \end{Bmatrix}, \quad (1)$$

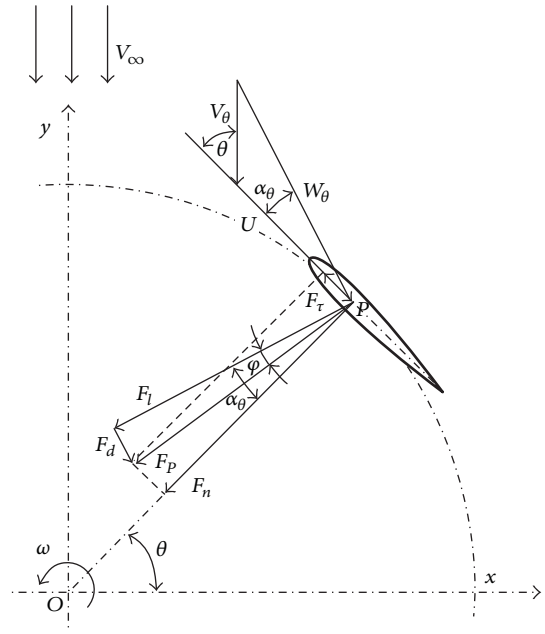

Figure 1: Local velocity field and transient aerodynamic loads of blade.

where C_q is dynamic pressure coefficient and is equal to $C_q = 1/2 \cdot \rho W_\theta^2 \cdot C_\tau$ and C_n are tangential force coefficient and radial force coefficient, respectively, and can be derived by

$$\begin{bmatrix} C_\tau \\ C_n \end{bmatrix} = \begin{bmatrix} \sin\alpha_\theta & -\cos\alpha_\theta \\ \cos\alpha_\theta & \sin\alpha_\theta \end{bmatrix} \begin{bmatrix} C_l \\ C_d \end{bmatrix}. \quad (2)$$

Thus the torque coefficient C_m of S-VAWT is

$$C_m = \sigma \cdot \sum_{i=1}^{m} \frac{C_\tau}{m} \left(\frac{W_\theta}{V_\theta} \right)^2, \quad (3)$$

where σ and m are solidity and the number of streamtubes, respectively. Equation (3) suggests that operational capacity of S-VAWT is closely related to velocity field and configuration parameters σ of wind turbine, and the tangential force states the torque coefficient to some extent.

2.2. Microflow Field. Based on boundary layer theory and mixing length theory, the flow field around blade can be divided into three regions: external potential flow, boundary layer, and wake flow, as shown in Figure 2. The external potential flow is assumed to be ideal fluid, ignoring the effect of viscosity, and it can be solved by potential flow theory. While the boundary layer is sensitive to viscosity and needs more concerns, for that it is the region where vortexes take place, grow up, and shed, which leads to dynamic stall. The wake flow is extremely complex and it affects performance of itself and that of next blades. In this work, attentions were paid to boundary layer, taking local Reynolds number and thickness of boundary layer into account.

Due to the dependence of characteristics of boundary layer on Reynolds number [27], the thickness of boundary

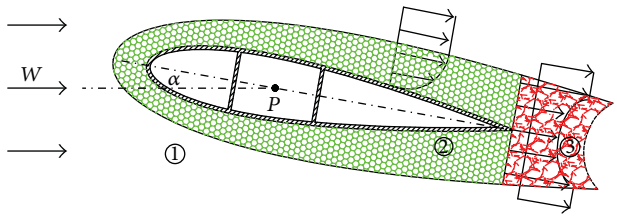

(1) External potential flow
(2) Boundary layer
(3) Wake flow

Figure 2: Microflow field around blade.

layer will be affected by the local relative velocity W_θ. Schlichting and Gersten [27] stated that Reynolds number had a significant impact on thickness of boundary layer which was the cradle of vortexes and turbulence, and thus solving turbulence was more dependent on grids than laminar flow. Also, tangential velocity fluctuation can be reduced by viscous damping of near-wall region and normal velocity fluctuation is arrested by the wall. Thus the predicated accuracy is dependent on the mesh structure of boundary layer.

For the sensitivity of turbulent flow on thickness of boundary layer, the near-wall around blade is divided into three regions: viscous sublayer, blending region, and fully turbulent region, see the literature [28]. In viscous sublayer, dimensionless average velocity u^+ is equal to dimensionless distance y^+, while the dimensionless average velocity of fully turbulent region can be derived by (4). In blending region, turbulent stresses and viscous stresses have the same order of magnitude, and the blending region cannot be ignored with the decrease of Reynolds number:

$$u^+ = \frac{1}{\kappa} \ln y^+ + B, \tag{4}$$

where κ and B are Karman parameter and parameter relating to surface roughness, respectively; for the cases of smooth wall, $\kappa = 0.4$, $B = 5.5$ and u^+ and y^+ can be expressed as

$$u^+ = \frac{u}{u_\tau}, \qquad y^+ = \frac{y \cdot u_\tau}{\rceil}, \tag{5}$$

where the wall friction speed $u_\tau = (\tau_w/\rho)^{1/2}$, $\rceil$ and τ_w, respectively, are wall shear stress and kinematic viscosity.

The dimensionless distance y^+ is related to flow velocity, viscosity, and shear stress. The wind turbine operates at low speed and the Reynolds number is quite small; in general, the distance from the center of the first layer grid to the wall can be estimated by (6)

$$\frac{y}{y^+} = 8.6 \cdot L \cdot \mathrm{Re}_L^{-13/14}, \tag{6}$$

where is L characteristic length.

3. CFD Model

3.1. Theoretical Background. Discretization is one of the critical steps for CFD method, where continuous space will

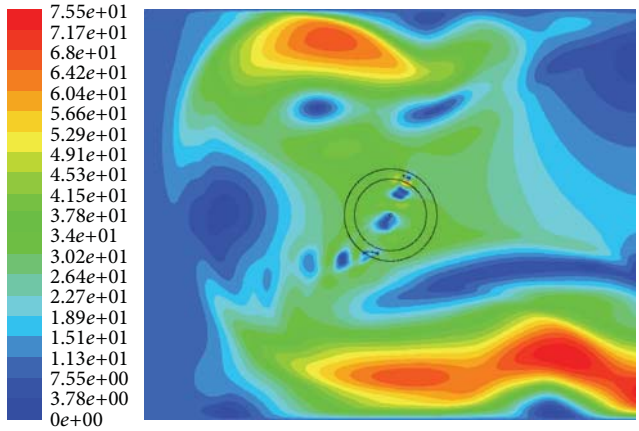

Figure 3: Effects of computational domain.

be discretized into finite control volumes, realizing the transformation form differential equations to algebraic equations. However, the discretization error, closing error, and rounding error during transformation, as well as the numerical dissipation, have great impacts on accuracy, reliability, and convergence. Performance prediction of S-VAWT also depends on mesh structure and its solution algorithm, and only the grids structure and solution algorithm are matched, and a higher accuracy and efficiency will be achieved.

The CFD model depends on mass, momentum, and energy conservation equations, and thus the distribution of physical quantities and their changes over time at any position of the complex flow field can be obtained by using CFD method. Flow around wind turbine is assumed to be incompressible, and the energy dissipation is ignored during numerical simulation, and thus the general control equation is

$$\frac{\partial(\rho\phi)}{\partial t} + \mathrm{div}(\rho u\phi) = \mathrm{div}(\Gamma \mathrm{grad}\phi) + S, \tag{7}$$

where ϕ is universal variable, standing for u, $\rceil$, w, T, and so on, and Γ is generalized diffusion coefficient.

For the CFD method, it must be discretized before solving the control equations, where the variables are interpolated into control decent, as shown in (8),

$$V_{\mathrm{cell}} \frac{\partial(\rho\phi)}{\partial t} + \sum_f^{N_{\mathrm{faces}}} \rho V_f \phi_f A_f = \sum_f^{N_{\mathrm{faces}}} \Gamma_\phi \nabla\phi_f A_f + S_\phi V_{\mathrm{cell}}. \tag{8}$$

Terms in (8) are successively transient term, convection term, diffusion term, and original term. For time saving and high accuracy, first-order upwind scheme is used in the first place (usually after approximately three to five operation cycles) with a better convergence, and then second-order upwind scheme is employed for higher accuracy.

3.2. Effect of Computational Domain. Computational domain must be determined before meshing, which is significant for accuracy. At a given grid density, there are fewer grids and it is time saving when computational domain is much smaller.

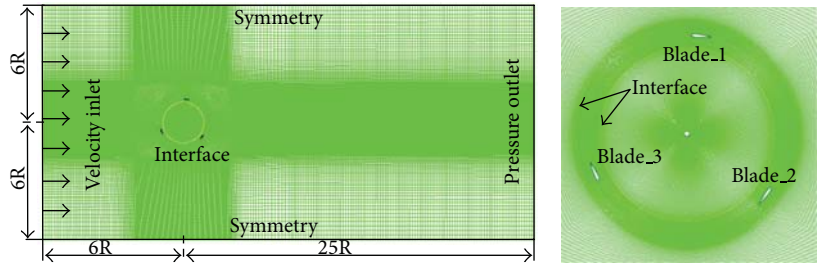

(a) (b)

Figure 4: Mesh structure of the 2D computational domain of S-VAWT.

But, it will have great impact on accuracy if the domain is too small. It is due to that flow velocity that passed through the S-VAWT does not yet fully be back to inflow speed, thus pressure of wake flow is much smaller than outlet pressure, leading to adverse pressure gradient and recirculation at outlet, see Figure 3. Furthermore, recirculation zone extends with the increase of adverse pressure gradient, leading to meaningless calculated results.

However, the computation time will be increased with a large computational domain. Taking the accuracy and computing time into account, the distance between rotor axis and inlet (or the two sides) is usually more than five times than radius of S-VAWT, and the distance from outlet to the rotor axis is more than ten times of the radius. In this paper, a computational domain of rectangular shape had been chosen, as shown in Figure 4. The three-bladed wind turbine, using a NACA0015 blade profile with a chord length of 0.4 m, was 4 m in diameter. The computational domain was 62 m in length, 24 m in width, and the distance between rotor axis and inlet was 12 m. The front of domain was defined with velocity inlet, the outlet of domain was pressure outflow, and the two symmetry boundary conditions were defined as nonslip walls.

In order to control the mesh structure for analyzing its influences on prediction accuracy, thus structured meshes and the sliding mesh technology were employed. For turbulence, Reynolds-averaged method had been widely used, where instantaneous N-S equation was replaced by time-averaged one. In addition, the Reynolds number in boundary layer is much smaller and viscous plays a leading role, and thus wall function method or low Reynolds number modeling method will be employed to solve the turbulent flow. Due to that the wall function can reduce the computing time and storage space, and the accuracy can be guaranteed by introducing empirical equations, therefore RNG k-ε model and wall function were employed in this paper for high accuracy at low Reynolds number.

3.3. Effect of Grid Number. Due to that the density of grids has a significant impact on accuracy, grid number will be considered in this present paper. Effects of grid number on accuracy of CFD simulations were shown in Figures 5 and 6. Figure 5 is the effects of grid independence on the accuracy. It indicates that torque coefficient gradually becomes stable when the grid number is more than 100 thousand, meanwhile the accuracy is acceptable. In addition,

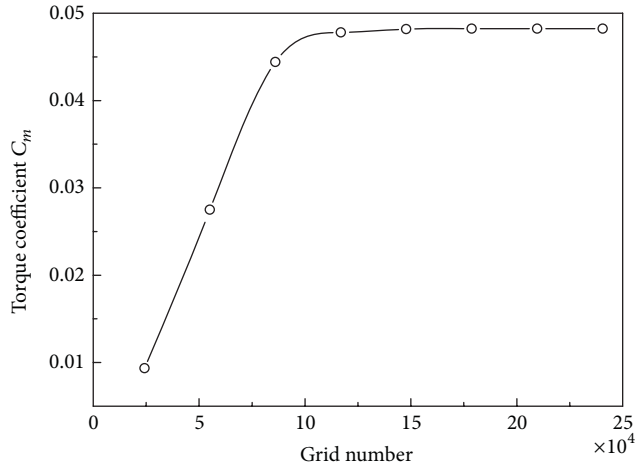

Figure 5: Effects of grid independence on accuracy.

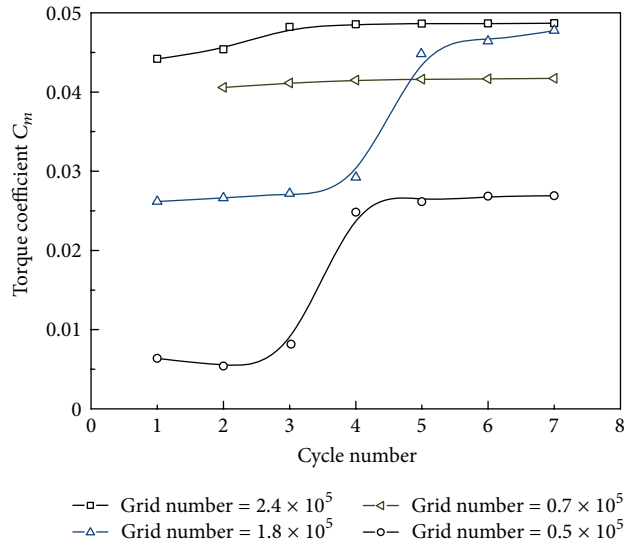

Figure 6: Effects of grid number on accuracy.

the calculated accuracy will not improve significantly with more grids, but with too much computational time. It also shows that obtained results make no sense for too small grid number, and the computational results are incredible when the grid number is less than 100 thousands. (Note:

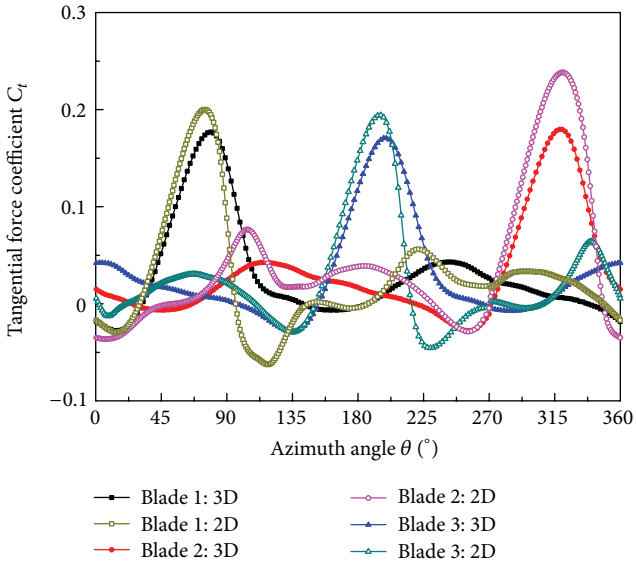

FIGURE 7: Comparison analysis of tangential force coefficient of 3D and 2D for S-VAWT.

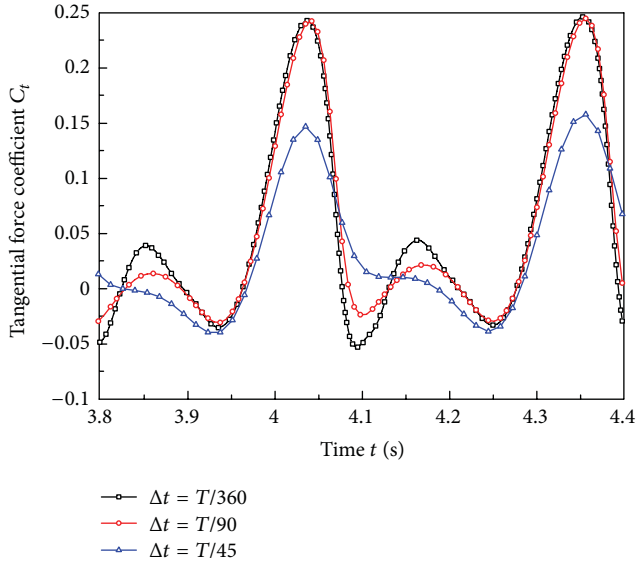

FIGURE 8: Curves of instantaneous tangential force coefficient of S-VAWT at various time steps.

the increase of grid number is for the whole computational domain, the condition of local grid refinement and low density of other domain are nonexistent).

Figure 6 shows the relationship between grid number and accuracy. In this thesis, it is regarded as convergent when the error between inlet and outlet flow is less than 0.1% of the total flow, or the errors of the flow field variables in the adjacent cycle are less than 1%. As shown in Figure 6, the torque coefficient becomes stable when it operates more than five cycles, meanwhile the residual for convergence is less than 0.0001, and thus it is concluded that it is convergent and calculations are terminated. The sudden increase of torque coefficient for cases with grid numbers 50 thousands and 70 thousands is caused by conversion of discrete formats. The solutions were initially obtained using first-order discrete format until periodic solutions were achieved, and then second-order discrete format were used to have a higher accuracy. Figure 6 also demonstrates that the more grids are utilized when the grid independence has not been achieved, the higher prediction accuracy can be obtained, while much too less grids will lead to wrong conclusion which is consistent with Figure 5.

3.4. Effects of Near-Wall Grid Size. Dimensionless distance y^+ is related to flow velocity, viscosity, and shear stress, and near-wall grid affects the calculated accuracy of turbulence for low wind speed and Reynolds number. Comparison analysis of instantaneous tangential force coefficient of 3D and 2D for S-VAWT was shown in Figure 7.

From $C_\tau \sim \theta$ curves, the instantaneous tangential force coefficient presented to be periodic change and the number of peak values was equal to blade number. It also indicates that the torque coefficient obtained by 3D simulation is smaller than that of 2D and lags behind, which is due to the effects of cross-flow of wingtip and spanwise flow.

Figure 7 suggests that maximum of instantaneous tangential force occurs at the azimuth angle nearby 75 degrees of upstream, and upstream plays an important role in driving the wind turbine than downstream. It is found that the peak value of blade 2 is obviously higher than that of blade 1 and blade 3. However, the tangential force at upstream should be the same even though it was affected by the curvature effect. With large-scale investigations being done, it was found that the primary cause was the y^+ value of near-wall grid of blade 2, and the big difference was eliminated by adjusting the near-wall grid of blade-2. It is clearly seen that the y^+ value of near-wall grid has a significant impact on accuracy of CFD method.

3.5. Effect of Time Step. For the unsteady flow around S-VAWT, setting of time step has a significant impact on the calculation accuracy. With a big time step, it will lead to serious false diffusion and stability of CFD becomes poor. Meanwhile the truncation error increases with the time step which cannot well demonstrate the change of flow field over time, failing to obtain expected results. Sometimes the calculation accuracy of a large time step can be improved by increasing the iterative steps in a single time step, but it is not always effective.

Plenty of researches showed that time step was dependant on the thickness of the first layer of near-wall grids. The smaller the thickness of the first near-wall grid, the smaller the time step to achieving convergence, and it was time-consuming. It was proved that the thickness of near-wall grid played an important role in accuracy and stability, and the time step could be determined based on the near-wall grid parameters. Usually, the time step Δt can be calculated by $\Delta t \le 60/(N \cdot C \cdot \omega)$.

The effect of time step on accuracy was shown in Figure 8. It is clearly seen that the accuracy of the case of time step $\Delta t = T/360$ is the best, followed by case of $\Delta t = T/90$, and case

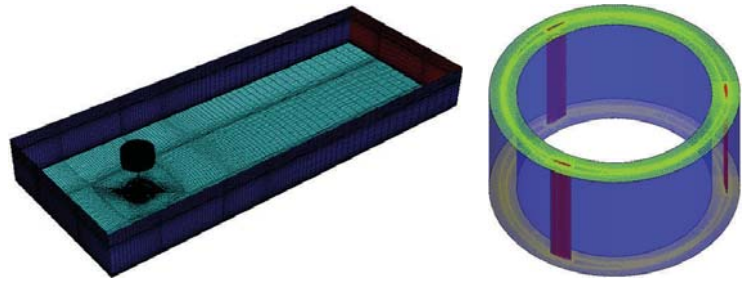

(a) (b)

Figure 9: Computational domain for the 3D simulation and details of the mesh structure of the rotor blades.

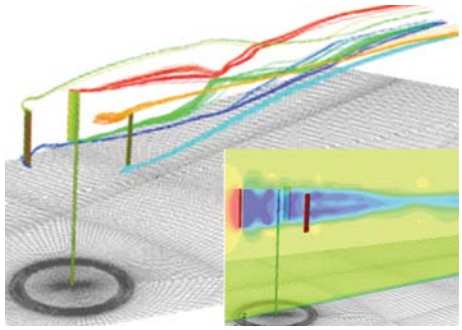

Figure 10: Diagrams of streamline and slice of 3D flow field.

of $\Delta t = T/45$ is the worst, indicating that the calculation accuracy can be guaranteed by a smaller time step.

4. Performance Prediction of S-VAWT

4.1. 3D Flow Field of S-VAWT. In order to have a better understanding of the tip flow, 3D investigations had been conducted but also for comparison analysis of the difference between 3D and 2D. Based on the computational domain of 2D simulation shown in Figure 4, mesh structure of 3D flow field and detailed mesh structure of rotor blades were shown in Figure 9. The distance from top of the rotor to the ground was 7 m, and length of blade was 2 m. with the purpose to build a realistic flow field for better prediction accuracy, a "sky" (not shown in Figure 9) with 13 m in depth was stacked on the top of the wind turbine, and at the end the total grid of the 3D model was approximately 1.3 million.

Figure 10 was the three-dimensional flow field of S-VAWT. As shown in Figure 10, it is clearly seen that the velocity from upstream to downstream decreases gradually, leading to a relative low-velocity zone behind the rotor. It is also found that streamlines of leaf blade move down to middle of the blade and streamlines of bottom blade move up to middle of blade. It is due to that pressure is high at pressure surface and low at suction surface, leading to a big accelerating pressure gradient between the two surfaces, and then cross-flows occur both at leaf blade and bottom blade. Also, the pressure of middle of blade is relatively lower than that of the ends of blade, thus fluids at the ends of blade move

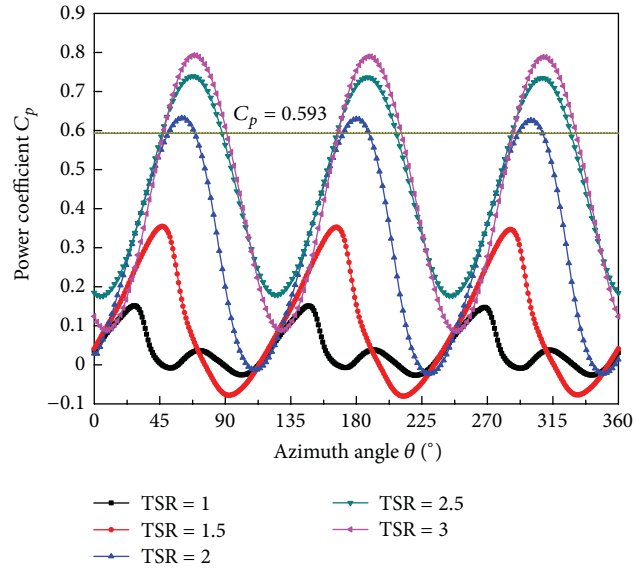

Figure 11: Average power coefficient of three-bladed S-VAWT at various TSRs.

to the middle of blade. The two strands of fluid mix at wake region and fully develop, producing a free inflow at father wake region.

Due to cross-flow at the ends of blade, the calculation results of 3D were slightly smaller than that of 2D, seen in Figure 7. The difference between 2D and 3D computational results was acceptable by comparison analysis with that of the literature [19], and it basically met the demands for aerodynamic performance prediction of S-VAWT. In order to reduce the computational time, 2D simulations were employed for the following work.

4.2. Aerodynamic Forces of S-VAWT. Two-dimensional investigations had been carried out to obtain the operational capability of the turbine at various TSRs, as shown in Figure 11. Figure 11 suggests that averaged power coefficient at various TSRs is periodic and lags behind each other by 120 degrees. Curves of $Cp \sim \theta$ suggest that fluctuation of flow becomes smaller with the increase of TSR, and the averaged power coefficient becomes more stable. This is due to that Reynolds number increases with the TSR, but the angle of

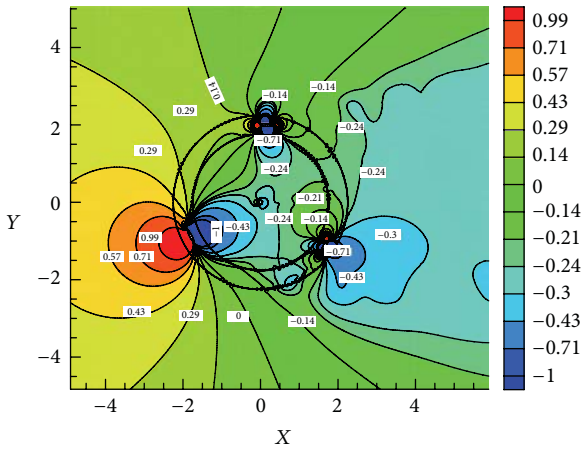

Figure 12: Pressure distribution of S-VAWT (TSR = 3).

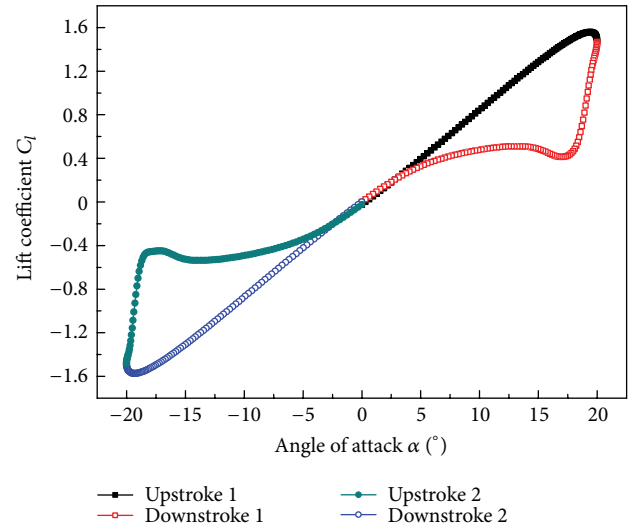

Figure 13: Lift coefficient hysteresis loops of blade under sinusoidal motion.

attack becomes smaller, and therefore the region where deep stall might happen becomes smaller, and thus the power generation becomes more stable.

As can be seen from Figure 11, it is obviously seen the averaged power coefficient of cases of TSR ≧ 1.5 beyond the Bates limitation 0.593, which is unlikely to occur according to Bates law. Nevertheless, Jonkman [29] stated that the static pressure on the boundary of the streamtube portion enclosing the rotor disc should be equal to unperturbed ambient static pressure. However, this hypothesis is not verified for the present work but can be explained by the pressure distribution of wind turbine, see Figure 12.

Form the pressure distribution of S-VAWT, it is found that the pressure of windward side is positive, but there is a sudden drop of pressure coefficient at suction surface, especially for the region with high-power generation. For example, when the blade comes to azimuth angle 109 degrees, the pressure coefficient of pressure surface is 0.99, while it is −1 at suction surface. Due to the big differential pressure, the thrust exerted to the blade increases sharply, thus the averaged power coefficient exceeds the Bates limit at some region.

As shown in Figure 11, there is a large fluctuation for the power coefficient at TSR = 1, and there is a smaller peak value following the big peak value. The main reasons are the sinusoidal pattern of angle of attack, and more serious dynamic stalls and secondary vortexes; these make great contribution to the formation of aerodynamic forces.

4.3. Dynamic Performance of Blade. The variation of angle of attack with azimuth angle at different TSRs is sinusoidal function [22, 30], and thus we assume that the blades are under sinusoidal oscillatory motion when S-VAWT is under operation. Due to the investigations on effects of reduced frequency, amplitude and original value of sinusoidal function had been extensively conducted [23, 25]; we did an example with NACA0015 blade profile at the sinusoidal pattern of $\alpha = 20^{\circ}\sin(\omega t)$ in this paper. The blade executes an oscillatory motion at a fixed pivot (1/4 chord length) with an oscillating period of 2 s; the time step is 0.005 s, and the inflow velocity is 10 m/s. The dynamic performance of blade is shown in Figure 13.

As seen from Figure 13, it is found that there is a hysteresis loop that the blade cannot immediately return to the flow field before dynamic stall. It shows that the difference between upstroke and downstroke is small at small stage of angle of attack, while the difference cannot be ignored for high angle of attack. Meanwhile, the results suggest that lift coefficient of upstroke at high angle of attack is better than that of downstroke, whereas slightly lower at small angle of attack.

As can be seen in Figure 11, the power coefficient of TSR = 2.5 was relatively good than other cases. In addition, for a better understanding of the flow field of S-VAWT and the effects of angle of attack on aerodynamic performance, changes of flow field and aerodynamic forces of TSR 2.5 during a revolution were shown in Figures 14 and 15.

Figure 14 demonstrates that it is attached flow at azimuth angle $\theta = 0^{\circ}$ and viscosity plays an important role at that region. Effective angle of attack increase with azimuth angle and flow begins to separate at trailing edge, and then the separation point moves to leading edge along with the azimuth angle. Meanwhile, a clockwise circulation occurs at trailing edge at suction surface and the blade is in mild stall. When passes though azimuth angle of 30 degrees, vortex occurs at leading edge with the increase of azimuth angle, and the lift coefficient is proportional to the angle of attack during this process, see Figure 15. The vortex keeps growing in size, meanwhile the interaction with the growing circulation at trailing edge gets stronger with a further increase of azimuth angle, leading to serous energy dissipation, and thus the lift coefficient grows nonlinear.

When it comes to azimuth angle 70 degrees, the vortex rises up and begins to leave the surface of blade, and the blade is in deep stall, leading to a sudden drop in lift coefficient, see Figure 15, and coming into the peak value. With the increase of azimuth angle, the angle of attack begins to decrease, and secondary vortex is formed at trailing edge, which makes

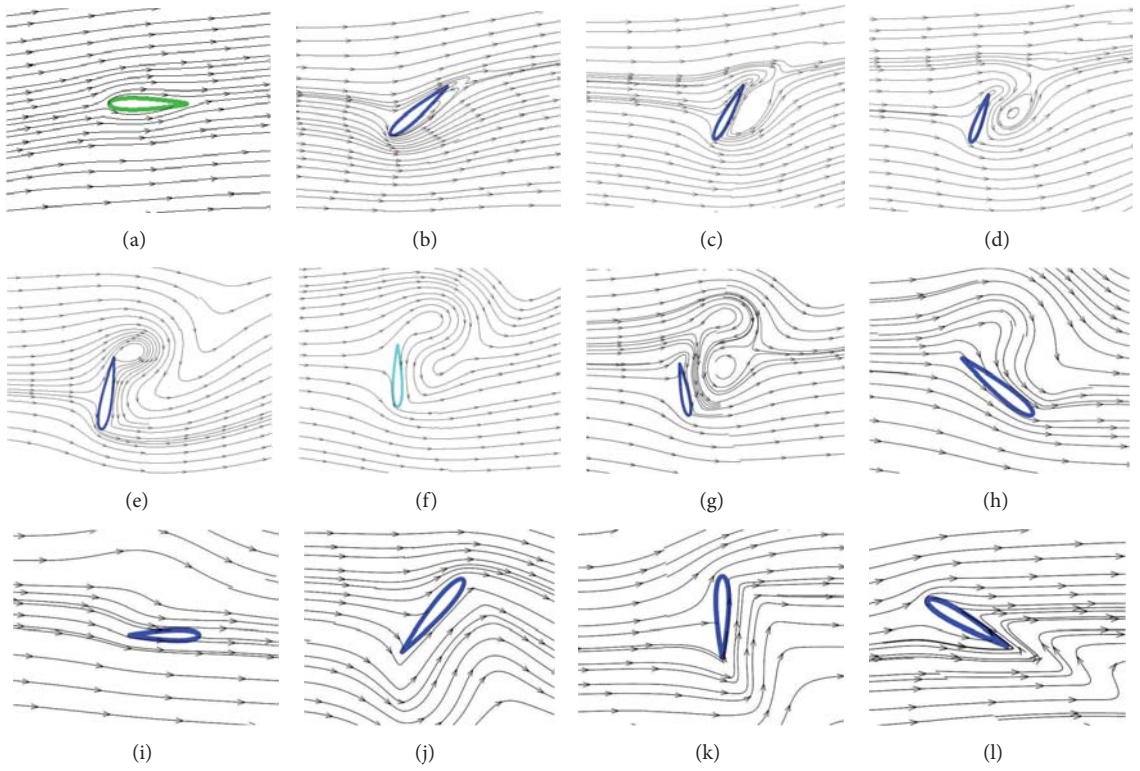

FIGURE 14: Flow field around blade in one revolution.

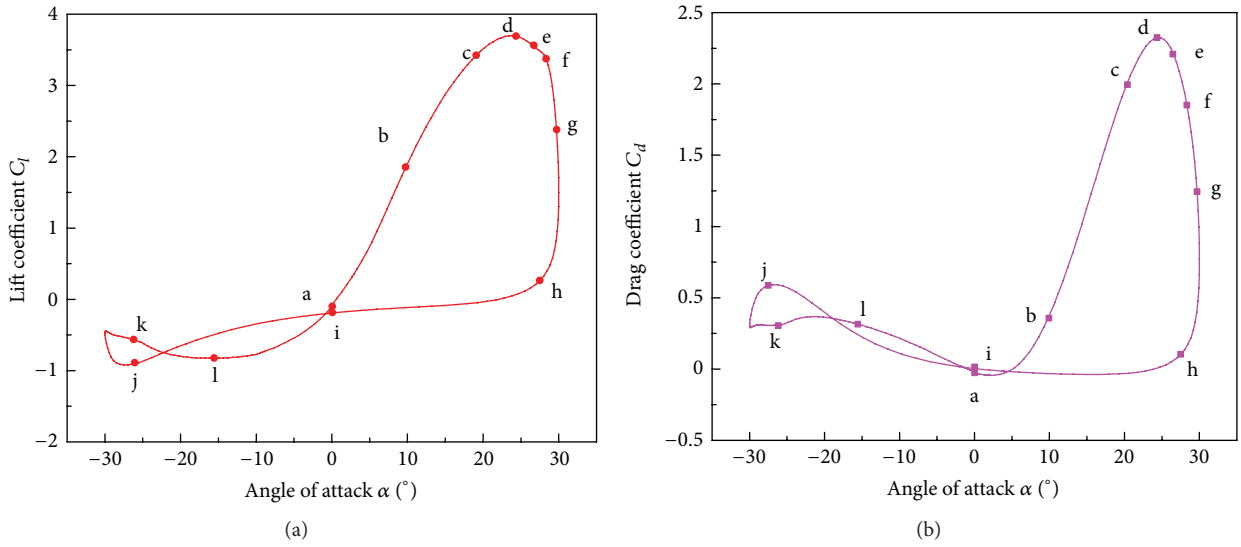

FIGURE 15: Curves of dynamic changes of lift and drag coefficients of one blade in one revolution.

significant contributions to the increase of aerodynamic forces during downstroke motion. The induced vortex grows in size but the angle of attack begins to decrease, and therefore the vortex sheds from the suction surface of blade and it becomes to be attached flow when it is at azimuth angle of 180 degrees. At downstream, the flow penetrated from the pressure side of blade into the suction side and the angle of attack began to increase, and therefore a reversed flow occurs at trailing edge, which has a significant impact on the aerodynamic forces.

From Figure 14, it can be concluded that the blade has experienced five stages: attached flow, mild stall, deep stall, stage of secondary vortex, and reattached flow. The separation at trailing edge marks the blade enter into mild stall, and the shedding of leading vortex states that the blade is in deep stall and the highest lift coefficient is obtained.

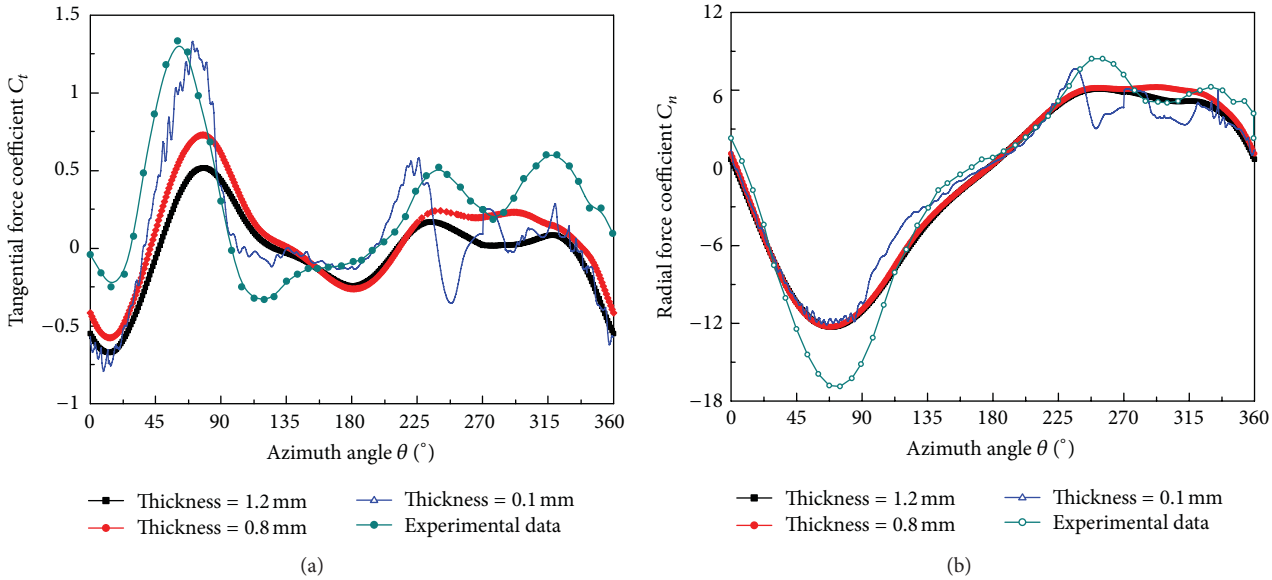

FIGURE 16: Comparison analysis of tangential and radial force coefficient between CFD and experimental date.

5. Experimental Verification

The present work here aimed at finding the effects of near-wall grid on prediction accuracy, and then more efforts were devoted to the influences of thickness of first layer near-wall grids on mechanical properties. Investigations by CFD were performed and compared with the experimental data reported by Wang et al. [13]. Based on plenty of attempts, it comes to be convergent at time step of 0.5 s, as shown in Figure 16.

Figure 16 indicates that the thickness of the first-layer near-wall grids has a great impact on accuracy. It is clearly seen that calculation results obtained from RNG k-ε turbulence model agree well with the experimental data, especially for the radial force coefficient. Furthermore, the thickness of grids has less impact on the accuracy of radial force than that of tangential force. And the vibration frequency of radial force is significantly less than that of tangential force. It is because that the drag makes great contribution to radial force and the drag is quite small compared with the lift, thus the radial force changes smoothly.

From the curves in Figure 16(a), it is also found that curves of 0.8 mm and 1.2 mm are far away from the experimental data. While the result of 0.1 mm is much better, particularly the results at upstream show well agreement with experimental data but are much smaller than experimental data at downstream. It is probably caused by the shedding vortexes form upstream as well as the lower flow velocity, leading to serious dynamic stall and blade flutter. In addition, prediction values of vortexes by using RNG k-ε model are a bit larger than the real values due to the high estimate value of turbulence viscosity coefficient, and therefore the tangential force at downstream is much smaller than that of upstream and its fluctuation is severe.

In addition, comparison analysis between calculation results and experimental data of literature [19] has been carried out, and the calculated results are shown in Figure 17. Figure 17 states that the results at higher TSR are in good agreement with experimental data, while there is big difference at low TSR, about 3.8%. It is probably due to that the region where dynamic stall takes place expends at lower TSR, thus dynamic stall is severe and effects of vortexes enhanced. Furthermore, prediction results of the employed turbulence models are larger than those of real values and lead to a poor accuracy.

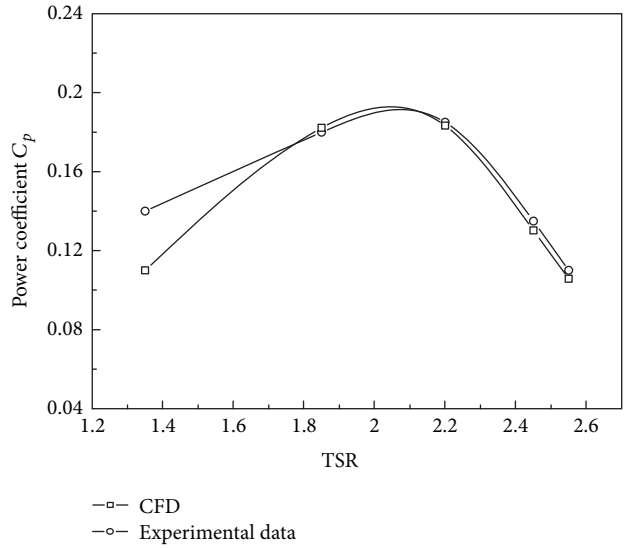

FIGURE 17: Comparison analysis of power coefficient between CFD and experimental data.

6. Conclusion

The present paper aimed at getting a better aerodynamic performance prediction of S-VAWT, and efforts were devoted

to the effects of computational domain, grid independent, near-wall grid, and time step on calculated accuracy. For the present two-dimensional CFD model, the calculated accuracy from RNG k-ε model is accepted when the total grid number is more than 100,000. In addition, the prediction values of aerodynamic loads agree well with the experimental data, and the near-wall grids have a significant impact on prediction of tangential force than radial force. The calculation results are smaller than those of experimental data especially at downstream; it is because that the employed turbulent model has a larger prediction values than the real values. Thus, a turbulent model should be carefully selected for a higher accuracy.

From the flow field analysis, it is concluded that the blade experiences a complex process during one revolution, including attached flow, mild stall, deep stall, and reattached flow. The highest lift coefficient is obtained with the shedding of leading vortex, and the secondary vortexes also make significant contributions to the aerodynamic performance.

Acknowledgments

The authors would like to acknowledge the financial support of the Fundamental Research Funds for the Central Universities (HEUCF110707) and the Heilongjiang Province Natural Science Foundation, China (E201216) for this work.

References

[1] S. C. Pryor and R. J. Barthelmie, "Climate change impacts on wind energy: a review," *Renewable and Sustainable Energy Reviews*, vol. 14, no. 1, pp. 430–437, 2010.

[2] N. C. K. Pawsey, *Development and evaluation of passive variable-pitch vertical axis wind turbines [Ph.D. thesis]*, University of New South Wales, 2002.

[3] B. K. Kirke, *Evaluation of self-starting vertical axis wind turbines for stand-alone applications [Ph.D. thesis]*, Griffith University, 1998.

[4] R. G. Dominy, P. Lunt, A. Bickerdyke, and J. Dominy, "Self-starting capability of a Darrieus turbine," *Journal of Power and Energy*, vol. 221, no. 1, pp. 111–120, 2007.

[5] S. Eriksson, H. Bernhoff, and M. Leijon, "Evaluation of different turbine concepts for wind power," *Renewable and Sustainable Energy Reviews*, vol. 12, no. 5, pp. 1419–1434, 2008.

[6] M. Brahimi, A. Allet, and I. Paraschivoiu, "Aerodynamic analysis models for vertical-axis wind turbines," *International Journal of Rotating Machinery*, vol. 2, no. 1, pp. 15–21, 1995.

[7] I. M. Asher, M. Drela, and J. Peraire, "A low order model for vertical axis wind turbines," in *Proceedings of the 28th AIAA Applied Aerodynamics Conference*, Chicago, Ill, USA, July 2010.

[8] P. Deglaire, S. Engblom, O. Ågren, and H. Bernhoff, "Analytical solutions for a single blade in vertical axis turbine motion in two-dimensions," *European Journal of Mechanics B*, vol. 28, no. 4, pp. 506–520, 2009.

[9] G. J. M. Darrieus, "Turbines having its rotating shaft transverse to the flow of the current," USA patent no. 1835018, 1931.

[10] J. H. Strickland, *The Darrieus Turbine: A Performance Prediction Model Using Multiple Streamtubes*, Sandia Laboratories, Albuquerque, NM, USA, 1975.

[11] I. Paraschivoiu, "Double-multiple streamtube model for Darrieus in turbines," in *Proceedings of the 2nd DOE/NASA Wind Turbines Dynamics Workshop*, pp. 19–25, Cleveland, Ohio, USA, 1981, NASA CP-2186.

[12] F. L. Ponta and P. M. Jacovkis, "A vortex model for Darrieus turbine using finite element techniques," *Renewable Energy*, vol. 24, no. 1, pp. 1–18, 2001.

[13] L. B. Wang, L. Zhang, and N. D. Zeng, "A potential flow 2-D vortex panel model: applications to vertical axis straight blade tidal turbine," *Energy Conversion and Management*, vol. 48, no. 2, pp. 454–461, 2007.

[14] P. Deglaire, *Analytical aerodynamic simulation tools for vertical axis wind turbines [Ph.D. thesis]*, Umeå University, 2010.

[15] M. Islam, D. S. K. Ting, and A. Fartaj, "Aerodynamic models for Darrieus-type straight-bladed vertical axis wind turbines," *Renewable and Sustainable Energy Reviews*, vol. 12, no. 4, pp. 1087–1109, 2008.

[16] F. Scheurich, *Modelling the aerodynamics of vertical-axis wind turbines [Ph.D. thesis]*, University of Glasgow, 2011.

[17] M. Raciti Castelli, A. Englaro, and E. Benini, "The Darrieus wind turbine: proposal for a new performance prediction model based on CFD," *Energy*, vol. 36, no. 8, pp. 4919–4934, 2011.

[18] A. Iida, K. Kato, and A. Mizuno, "Numerical simulation of unsteady flow and aerodynamic performance of vertical axis wind turbines with les," in *Proceedings of the 16th Australasian Fluid Mechanics Conference (AFMC '07)*, Gold Coast, Australia, 2007.

[19] R. Howell, N. Qin, J. Edwards, and N. Durrani, "Wind tunnel and numerical study of a small vertical axis wind turbine," *Renewable Energy*, vol. 35, no. 2, pp. 412–422, 2010.

[20] D. Coiro, F. Nicolosi, A. De Marco, S. Melone, and F. Montella, "Flow curvature effects on dynamic behaviour of a novel vertical axis tidal current turbine: numerical and experimental analysis," in *Proceedings of the 24th International Conference on Offshore Mechanics and Arctic Engineering*, pp. 601–609, Halkidiki, Greece, June 2005.

[21] I. S. Hwang, Y. H. Lee, and S. J. Kim, "Optimization of cycloidal water turbine and the performance improvement by individual blade control," *Applied Energy*, vol. 86, no. 9, pp. 1532–1540, 2009.

[22] S. Wang, D. B. Ingham, L. Ma, M. Pourkashanian, and Z. Tao, "Numerical investigations on dynamic stall of low Reynolds number flow around oscillating airfoils," *Computers and Fluids*, vol. 39, no. 9, pp. 1529–1541, 2010.

[23] E. Amet, T. Maître, C. Pellone, and J. L. Achard, "2D numerical simulations of blade-vortex interaction in a darrieus turbine," *Journal of Fluids Engineering*, vol. 131, no. 11, Article ID 111103, 15 pages, 2009.

[24] J. A. Ekaterinaris and M. F. Platzer, "Computational prediction of airfoil dynamic stall," *Progress in Aerospace Sciences*, vol. 33, no. 11-12, pp. 759–846, 1998.

[25] W. Q. Qian, S. Fu, and J. S. Cai, "Numerical study of airfoil dynamic stall," *Acta Aerodynamica Sinica*, vol. 19, no. 4, pp. 427–433, 2001.

[26] Y. Staelens, F. Saeed, and I. Paraschivoiu, "A straight-bladed variable-pitch VAWT concept for improved power generation," in *Proceedings of the 41st Aerospace Sciences Meeting and Exhibit*, pp. 146–154, Reno, Nev, USA, January 2003.

[27] H. Schlichting and K. Gersten, *Boundary-Layer Theory*, Springer, New York, NY, USA, 2000.

[28] W. J. Qin, C. G. Hu, L. P. Guo, and Z. X. Zuo, "Effect of near-wall grid size on turbulent flow solutions," *Transactions of Beijing Institute of Technology*, vol. 26, no. 5, pp. 388–392, 2006.

[29] J. M. Jonkman, *Modeling of the UAE Wind Turbine for Refinement of FAST_AD*, Colorado State University, 2001.

[30] M. Islam, D. S. K. Ting, and A. Fartaj, "Desirable airfoil features for smaller-capacity straight-bladed VAWT," *Wind Engineering*, vol. 31, no. 3, pp. 165–196, 2007.

Hindawi Publishing Corporation
Advances in Mechanical Engineering
Volume 2013, Article ID 743201, 10 pages
http://dx.doi.org/10.1155/2013/743201

Research Article

Numerical Simulation of the Transient Process of Power Failure in a Mixed Pump

Xudan Ma, Jintao Liu, and Leqin Wang

Institute of Process Equipment, Zhejiang University, 38 Zheda Road, Hangzhou 310027, China

Correspondence should be addressed to Leqin Wang; hj_wlq2@zju.edu.cn

Received 29 December 2012; Accepted 16 March 2013

Academic Editor: Tomoaki Kunugi

A hydraulic-force coupling method was used to simulate the transient process of power failure condition. Computational fluid dynamics (CFD) was used to study the three-dimensional (3D), unsteady, incompressible viscous flows in a mixed flow pump in power failure accident. The dynamic mesh (DM) method with nonconformal grid boundaries was applied to simulate the variation of rotational speed of the field around the impeller. User-defined function (UDF) was used to obtain the rotational speed by solving the momentum conservation equation. External characteristics, such as rotational speed, head, flow rate, and hydraulic torque, were obtained during the transient process. Numerical speed and flow rate were compared with results calculated by semiempirical equation and they were in good agreement. The differences between transient and quasisteady results were also studied. Transient head and quasisteady head did not differ too much. The reason that caused this deviation was theoretically analyzed. The difference was explained to be caused by the inertia effect of the fluid contained in the pump and the pipeline. Internal flow field was also shown. Relative velocity vectors showed that the stall form and existence time in transient simulation were different from those in the quasisteady simulation. It is suspected to be one reason for head deviation.

1. Introduction

Transient process of pumps existed in various occasions. Power failure was one of the most common accidents in pump operation. The study on idle rotation of a coolant pump in a power failure accident was of great importance. For example, in a nuclear power plant, coolant pump was one of the main equipment in reactor coolant system and was the only rotating equipment. It was considered to be the heart of the nuclear power plant. The reliability and security in special processes were particularly emphasized. Power failure of a coolant pump was a serious accident. During the blackout of a nuclear power plant, the coolant pump started with an idle rotating process. The refrigerant quantity through the reactor core decreased abruptly and brought threat to the safety of reactor core components. In order to ensure the security of the reactor core, the coolant pump required a longer idle rotating period.

Lots of researches on transient characteristic during stopping process had been done by numerical, theoretical, and experimental methods. Tsukamoto et al. [1] used both the experimental and the theoretical methods to study the characteristic of a radial pump during stopping period. Their study showed that when the deceleration rate of the pressure and flow rate exceeded a certain limit, the flow deviated greatly from the result of steady state. Kittredge and Princeton [2] studied the transient process during power failure condition by an analytical method. They discussed the methods of integrating equations for an assumed rigid fluid column and elastic fluid column. Zhang [3] built up a set of equations of coolant pump and pipe system by moment conservation law. He used these equations to study the head and flow rate change law during idle rotation. In their study, the speed variation was prescribed and the transient characteristic of the pump was obtained by the steady-state head curve. Thanapandi and Prasad [4] carried out a theoretical and experimental study on the transient characteristics of a centrifugal pump during both starting and stopping periods. In his study, the dynamic characteristic of the test pump had been analyzed by a numerical model using

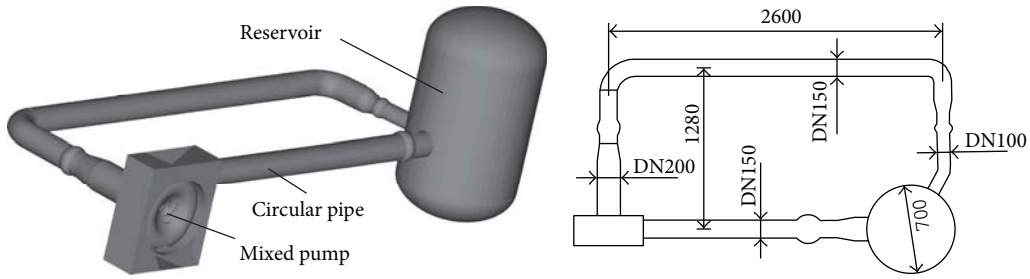

Figure 1: Pumping circulation system.

the method of characteristics. Their research showed that the transient head characteristics closely followed the steady-state system head curve. This was a rough result because only the centrifugal action was considered in their pump model. And also in their research, the instantaneous speed was provided as known. Liu et al. [5] studied the transient characteristic of coolant pump idle rotation by experiment. Liu et al. [6] studied the internal and external characteristics in a radial pump during stopping period by computational fluid dynamics (CFD) method, and they revealed the flow field under both transient and quasisteady conditions. Their research also showed that the transient characteristic was different from the quasisteady result.

In the studies of power failure accidents, there were following limitations that could be improved. Firstly, the rotational speed was assumed to be changing in a hypothetical law. In fact, the rotational speed was unknown in power failure accidents. Once the physical model was set, the speed variation was predetermined. The hypothetical law was not identical with the practical situation. Because the rotational speed played an important role in pump head, it was essential to obtain a more practical rotational speed variation law. Secondly, the quasisteady curve was often used to analyze the performance of a transient process especially in theoretical studies. This was obviously convenient but with great deviations in severe transient processes. The transient and quasisteady results would be discussed in this paper.

Nowadays, with the development of CFD technology, numerical simulation was greatly developed and widely used in the design and optimization of hydraulic machineries. CFD technology had been successfully used in the transient calculation of pumps during starting and stopping periods [6–9]. With this method, not only the external characteristic but also the internal flow field could be obtained clearly. In this paper, a numerical method was proposed to simulate the evolution of the transient flow of power failure process in a mixed pump. The major objective of this study was to develop a hydraulic-force coupling method to get the realistic external and internal characteristics of a mixed pump in power failure condition by CFD method.

2. Numerical Model

The computational model used in this paper is a circulation pipeline system. It consists of a mixed pump, a reservoir, and a circular pipe. Since it is difficult to identify the specific boundary conditions of the pump in the stopping period, a circular pipe system is used in the study. It is convenient for the self-set of boundary conditions. Water from the reservoir is pumped by the mixed pump and flowed into the reservoir through the outlet pipe. 3D model is shown in Figure 1. Pipe dimensions are indicated in Figure 1(b). The reservoir is 815 mm high, 700 mm in diameter. The volume ratio of the reservoir and the pump is about 6.

3D model of the mixed pump impeller is shown in Figure 2 and the parameters are listed in Table 1. The 3-D model is exactly the same scale with the experimental testing bench. Some steady characteristics of this pump have been tested by previous studies.

The model is meshed in Gambit. The grid independence and temporal test have been done in former studies [8] and here is a brief introduction. The mesh information is listed in Table 2. The impeller, inlet pipe, and volute are meshed separately. Nonconformal boundary conditions are set between the impeller and inlet pipe, the impeller and the volute. In order to decrease the deviation caused by the nonconformal boundaries, the same size and structure mesh type are applied on the interfaces. The nonconformal boundary conditions are described in Figure 3.

3. Computational Method

3.1. Mathematical Model. The revolution of rotor followed the momentum conservation law. The total input torque of the pump would overcome the hydraulic torque to sustain the medium flow in the pump, the rotor friction torque, and inertia moment of rotor. The relationship between these parameters could be described by the following equation:

$$T = T_h + T_f + I\frac{d\omega}{dt}, \tag{1}$$

where T is the total input torque, T_h is the hydraulic torque of the pump, T_f is the rotor friction torque, I is the rotary inertia of the pump system, and ω is the rotor angular speed.

When the pump loses power supply which leads to (2), the input torque disappears and the pump starts with inertial motion:

$$T = 0. \tag{2}$$

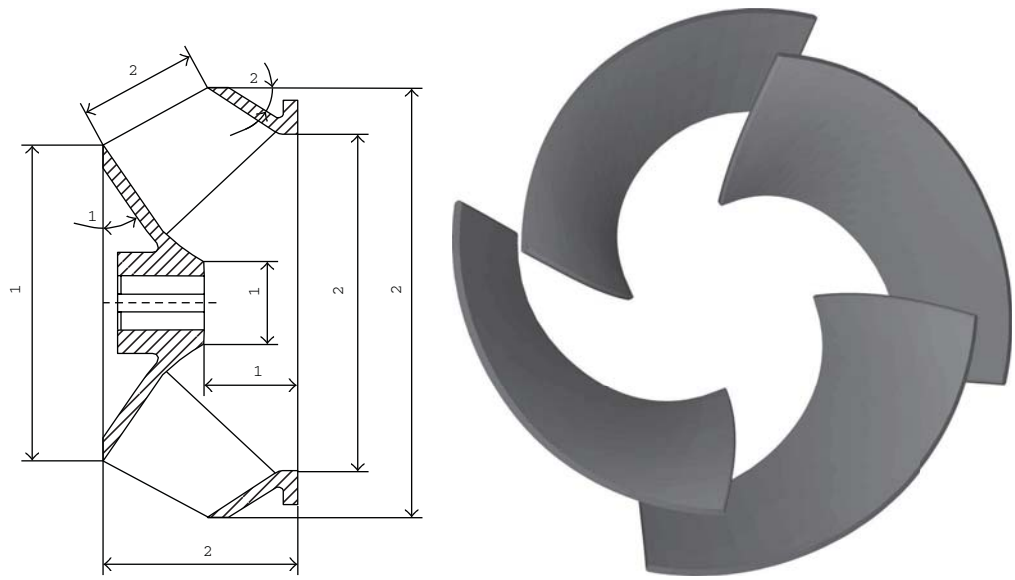

(a) (b)

Figure 2: Geometry of the impeller and the 3-D blade model.

Table 1: Specifications of the pump model.

Geometric specifications			Hydraulic specifications		
Outlet width (mm)	b_2	66	Nominal speed (r/min)	N_0	1450
Inlet diameter (mm)	D_{i1}	45	Nominal flow rate (m^3/h)	Q_0	360
Inlet diameter (mm)	D_{i2}	187	Nominal total head (m)	H_0	8
Outlet diameter (mm)	D_{o1}	175			
Outlet diameter (mm)	D_{o2}	238			
Inlet length (mm)	L_1	52			
Outlet length (mm)	L_2	108			
Front shroud angle (deg)	ε_1	34			
Back shroud angle (deg)	ε_2	32			

Table 2: Mesh information.

Mesh type	Tetrahedron		Hexahedron	Total
Regions	Volute	Impeller	Reservoir and pipe	
Mesh numbers	444245	470427	909335	1824007
Node numbers	87226	92735	468796	648758

So (1) becomes.

$$T_h + T_f + I\frac{d\omega}{dt} = 0. \tag{3}$$

Equation (3) is the torque equation which determines the rotational speed variation law during power failure accident. In (3), T_h could be obtained by flow field computation of the transient process. Compared with friction torque T_f, hydraulic friction T_h constitutes a high proportion in a pump. Assuming T_f is linear with T_h:

$$T_f = \alpha T_h, \tag{4}$$

α is an empirical factor and usually set as 0.01–0.03. In this case hydraulic friction is not considered and it is set as 0. Equation (3) can be converted into a difference schema:

$$\omega(t + \Delta t) = \omega(t) + \Delta t\frac{T_h}{I}. \tag{5}$$

T_h can be obtained by Fluent simulation. Time step Δt and inertia of the pump system are known. The initial value of total torque can be obtained by unsteady simulation with $n = n_0$ in Fluent 6.3. Once the initial condition is given, according to (5), transient characteristic of power failure can be calculated. As time goes on, the rotational speed decreases very slowly which makes the simulation lasts very long. So the transient process is considered to be completed when the final rotational speed is smaller than $0.02n_0$. The whole procedure can be described as in Figure 4.

3.2. CFD Method. The simulation of transient process is taken by commercial software Fluent 6.3. Fluent is a solver based on finite volume method and contains various models.

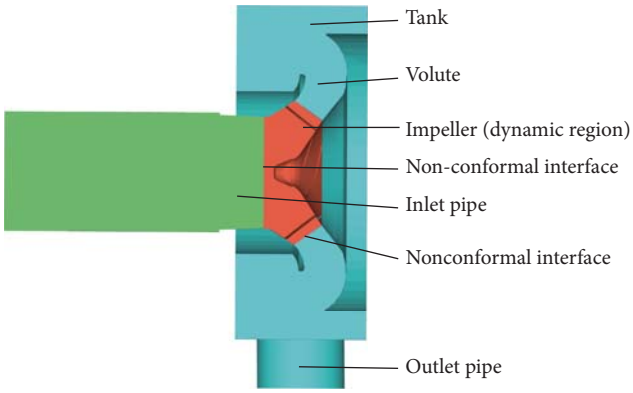

Figure 3: Details of dynamic mesh method.

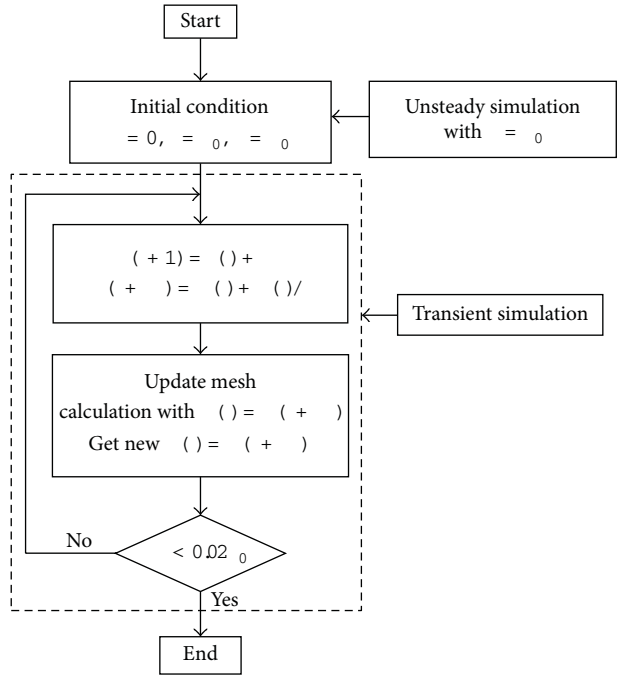

Figure 4: Calculating procedure.

In this case of simulation, three different models [10] are used to calculate the motion of the impeller in quasisteady condition, unsteady condition, and transient condition.

In quasisteady condition, the pump works in a specific rotational speed and the flow rate is constant. Because of the simplicity of the quasisteady calculation, in previous studies, quasisteady results are usually used to replace the transient results. Since the flow field in a pump is not steady, an unsteady calculation is an improved and more realistic calculation. It can capture the unsteady characteristic in the pump operation such as rotating stall. And also, the rotational speed and flow rate are constant in unsteady calculation. In transient simulation, operating condition such as the rotational speed or the flow rate is changing from time to time. So in each time step, the condition is different.

In the quasisteady simulation, multiple reference frame (MRF) is adopted. MRF model is the simplest approach for multiple zones. When using MRF model, the grid remains fixed for the computation. The flow in moving cell zone is solved using the moving reference frame equations which contain Coriolis acceleration and centrifugal acceleration. The flow around the moving part can be modeled as a steady-state problem with respect to the moving frame.

Before the transient simulation, an unsteady case with $n = n_0$ is presimulated to get the initial condition of the power failure process. In unsteady simulation, moving mesh method is used to simulate the motion of the impeller. When a time-accurate solution for the rotor-stator interaction (rather than a time-averaged solution) is desired, the sliding mesh model is the most accurate method for simulating flows in multiple moving reference frames. The interface zones of adjacent cell zones are associated with one another to form a "mesh interface." The two cell zones will move relative to each other along the mesh interface.

In the transient process simulation, dynamic mesh (DM) technology is used to simulate the motion of the impeller. DM method has been successfully used in transient simulation of a 2-dimensional centrifugal pump during starting period [11]. Then Li et al. [7] pushed on a further application of DM method in a 3-D centrifugal pump to simulate the transient characteristic during starting period. Liu et al. [6] used DM method to simulate the stopping transient process. And Wu et al. [9] used it to simulate transient process during the rapid opening period of the discharge valve in the pump system. In their studies, the motion of the impeller was prescribed. In this paper, the impeller motion is determined by solving the momentum equation (5). According to [7], k-ε turbulence model is adopted and the SIMPLE algorithm is used. Unsteady time step size is set as 0.0001 s. At each time step, the maximum iteration is set as 300.

4. Results

4.1. External Characteristics in Power Failure Condition. In the unsteady simulation, the case is considered to be in a "steady-going" state when the torque fluctuates regularly and in small amplitude. When the rotational speed is low enough, the transient process is considered to be completed.

The variation of hydraulic torque is shown in Figure 5. In Figure 5, the solid line is the change of hydraulic torque with time. Assuming that the sum of hydraulic torque and the friction torque are proportional to the rotational speed squared [12] which can be described by

$$T_h = \left(\frac{n(t)}{n_0}\right)^2 T_0. \tag{6}$$

In Figure 5, the theoretical torque calculated by Fluent is shown with dash lines. From the figure it can be found that they are in good agreement.

With (6), (3) can be written as

$$c\omega(t)^2 + I\frac{d\omega}{dt} = 0, \tag{7}$$

Table 3: Comparison between CFD and theoretical results.

	Time (s)					
	0	0.1	0.2	0.3	0.4	0.5
CFD result (r/min)	1500	1141.2	923.7	774.9	648.5	578.1
Model 1 (r/min)	1500	1143.2	923.5	774.6	667.1	585.8
Model 2 (r/min)	1500	1107.6	877.9	727.1	620.5	541.2

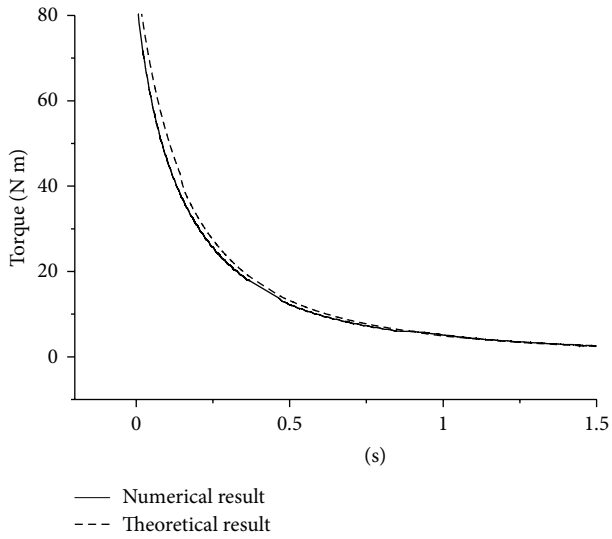

Figure 5: Hydraulic torque variation in transient process.

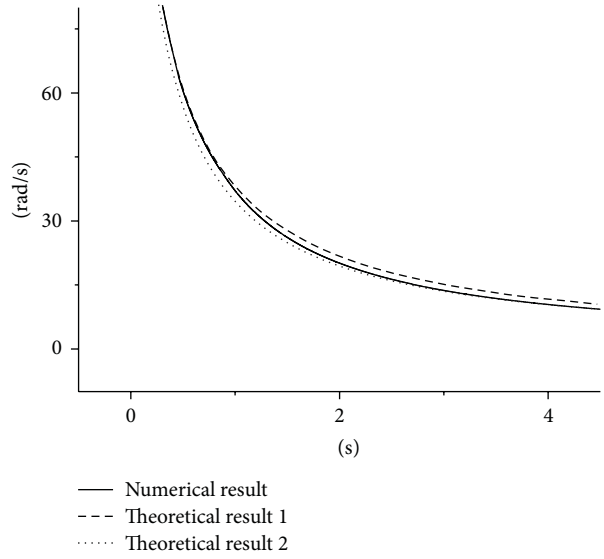

Figure 6: Angular speed variation with time.

where c is constant. So the transient speed can be described by the following equation

$$\omega(t) = \frac{\omega_0}{1 + t/t_{pn}}. \tag{8}$$

ω_0 is the initial angular speed, and t_{pn} is the time when the instantaneous rotational speed is half of the initial speed.

Integrating (6) and substituting the initial condition, (9) can be obtained:

$$\omega(t) = \frac{\omega_0}{1 + (T_h/I\omega_0)\, t}. \tag{9}$$

There are two mathematical models, (8) and (9), to simplify the transient process. In this case, the initial rotational speed is 1500 r/min. According to the simulation result, half-speed time t_{pn} is 0.32038 s. This theoretical result is taken as theory model 1. And in physical model calculated by (8), t_{pn} is 0.28224 s. It is taken as theory model 2. These three results are all shown in Figure 6. In Table 3, there are some specifically given values of speed in different times calculated both by theoretical and CFD methods. The deviation between CFD and theoretical model 1 is small while the deviation between CFD and theoretical model 2 is much larger. But in all, CFD result and the theoretical result coincide well. This result indicates that (7) describes rotational speed variation better. The difficulty is how to get a correct half-speed time t_{pn}. The theoretical model of (9) is convenient but the result is rough.

Flow rate is another specifically emphasized parameter. According to the pump similarity law, the flow rate is linear to the rotational speed and the head is proportional to the square of rotational speed. It is concluded that the flow rate changes in the same form as speed variation law. So assuming the flow rate variation can be described by (10):

$$Q(t) = \frac{Q_0}{1 + t/t_{pq}}, \tag{10}$$

where Q_0 is the initial flow rate. Similar to the equation of rotational speed variation, t_{pq} is the time when the instantaneous flow rate is half of the initial flow rate. In this case, t_{pq} is 0.54224 s, which is almost twice of the half-speed time. It indicates that the flow rate does not decrease as fast as the rotational speed. It can be explained by the large inertia effect of the fluid on the pump and the pipe. The simulation result and theoretical result are shown in Figure 7. At the beginning, the theoretical and the numerical results fit well. But as time goes on (when $t = 1\,\text{s} - 6\,\text{s}$), numerical results decrease much faster than the theoretical one. After $t = 6\,\text{s}$, the deviation becomes small again.

Figure 8 is the change of axial and radial forces with time. The axial force F_z changes in the same form as head. Because the sealing clearance is not modeled in this case, the axial force here stands for the hydraulic force applied to the impeller shroud and hub. The radial force, which is the composition of F_x and F_y, decreases with rotational

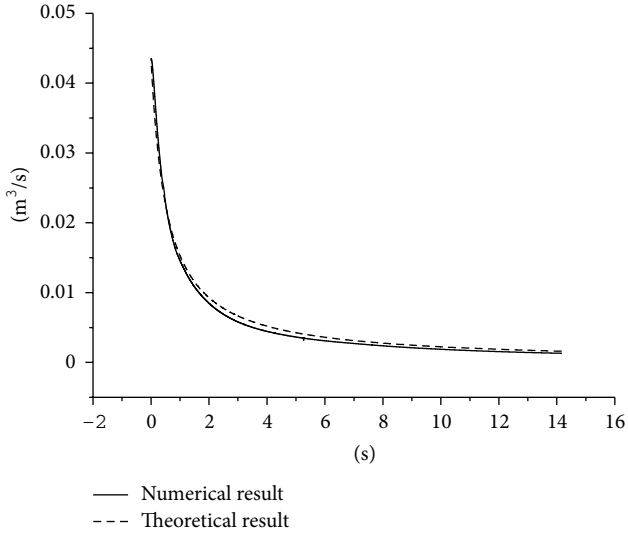

Figure 7: Flow rate variation with time.

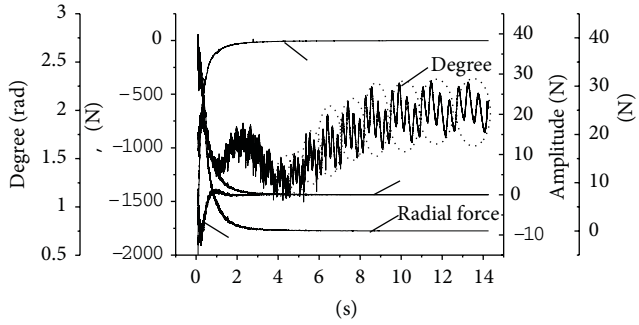

Figure 8: Forces variation with time.

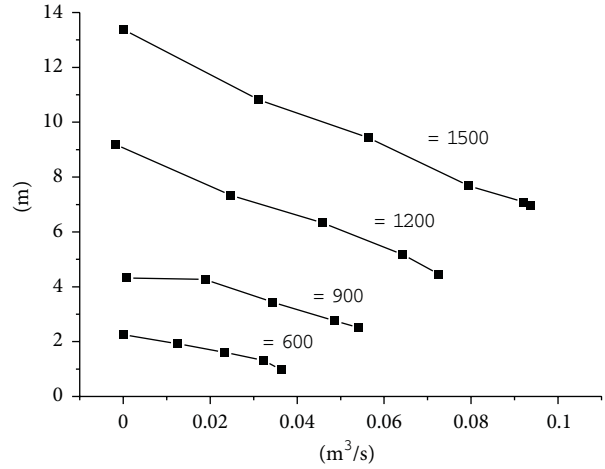

Figure 9: Steady characteristic.

speed. The degree of the force fluctuates with time firstly irregularly and then fluctuates around a specific value. Since the calculation time is too short and data is not sufficient, frequency is not analyzed. But it can be deduced that the variation of the radial and axial force may result in vibration, even damage the pump.

4.2. Comparison between Quasisteady and Transient Result. Since the quasisteady head is usually used to substitute for the transient head, in this paper a comparison is also done between the quasisteady and transient results. Experiment had been done to get the head curve of the mixed pump [13]. According to the similarity law, the steady head is a function of rotational speed and flow rate. Figure 9 is the head curve in different rotational speed. Quasisteady head can be obtained by

$$H_s(t) = -41.96Q^2 - 57.44Q\frac{n(t)}{1500} + 12.68\left(\frac{n(t)}{1500}\right)^2. \quad (11)$$

Figure 10 is the comparison between quasisteady head and transient head variation with flow rate and time, respectively. In Figure 10, it is clearly showed that the quasisteady head is larger than the transient head especially in large capacity ($Q = 0.2$–$0.4\,\mathrm{m}^3/\mathrm{s}$). So at the beginning of power failure accidents (about $t < 0.3\,\mathrm{s}$), quasisteady head and transient head differ greatly. As time goes on, the deviation is getting smaller. The different results between transient and quasisteady results could be explained by Dazin's research [14]. Dazin built a mathematical model to calculate the transient head of a radial pump and applied it to the starting process. According to his research, the transient head can be calculated by the following equation:

$$H_t(t) = H_s(t) + K_\omega\frac{\partial\omega}{\partial t} - K_Q\frac{\partial Q}{\partial t}. \quad (12)$$

In (12), K_ω and K_Q are constant parameters determined by the pump dimensions. The equation shows that compared with the steady head, transient head has extra components of speed acceleration term and inertia term which is related to the flow rate acceleration. The speed acceleration and fluid inertia contented in the impeller and volute will affect the transient total head. In power failure process, speed deceleration will decrease the transient total head, while the flow rate deceleration will increase the transient total head. Obviously, these two factors are not considered in quasisteady results. This is the reason for the deviation between the quasisteady and transient heads. The speed acceleration and flow rate acceleration with time are shown in Figure 11. From Figure 11, it can be found that in the transient process, the speed decreases abruptly and makes very large speed deceleration, while flow rate does not change so fast. This could also be explained by the similarity law. So the decrease by speed deceleration is larger than the increment by flow rate deceleration. This might explain why transient total head is smaller than the quasisteady head. In addition, because the transient head is related to the flow rate and the inertia effect of the fluid, it can be concluded that as the size of the quasisteady pump increases, the transient head and the quasisteady head curve would deviate much larger. And also because of the inertia effect, with a longer pipeline, the transient behavior of the pump would be affected and cause other problems like water hammer vibration.

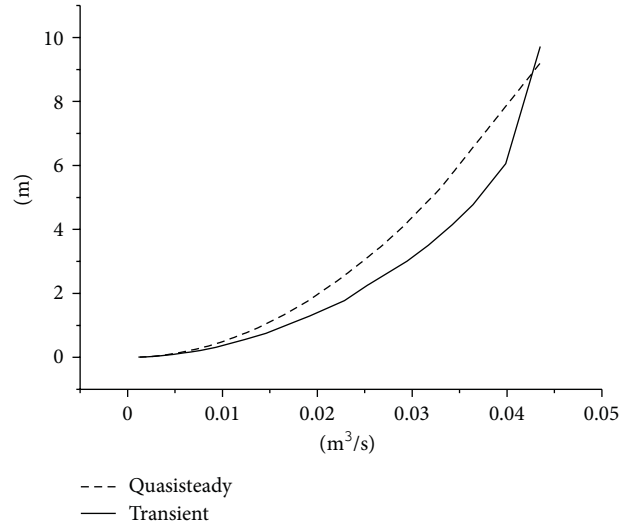

Figure 10: Comparison between quasisteady, and transient head.

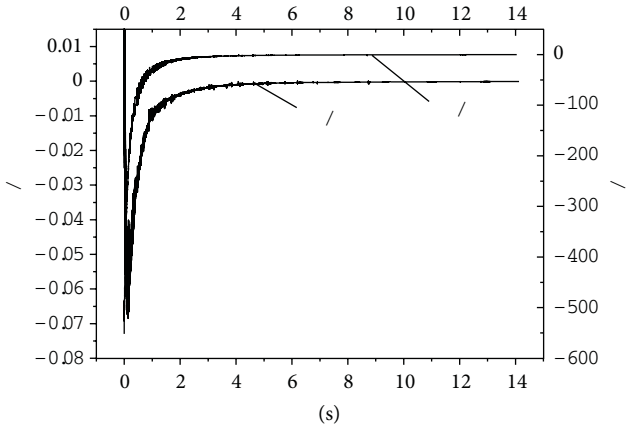

Figure 11: Derivatives of external characteristic.

Pressure coefficient is nondimensional and stands for the pump characteristic. It is defined as follows:

$$P_{\text{coeff}} = \frac{2P}{[\rho u_2^2]}, \tag{13}$$

where P is the total pressure rise and u_2 is the peripheral speed of the impeller at the blade outlet. Figure 12 is the transient and quasisteady pressure coefficient change. Although transient head and quasisteady head do not deviate too much, the pressure coefficient variation is totally different. The quasisteady pressure coefficient decreases with time as the flow rate decreases, but quite the other way the transient pressure coefficient increases. As the speed is not reflected in the pressure coefficient, the difference between the transient and quasisteady coefficients is deduced to be caused by the speed deceleration and the inertia effect of the fluid. Comparing the speed deceleration curve with pressure coefficient curve, it can be found that their absolute value changes in the same trend.

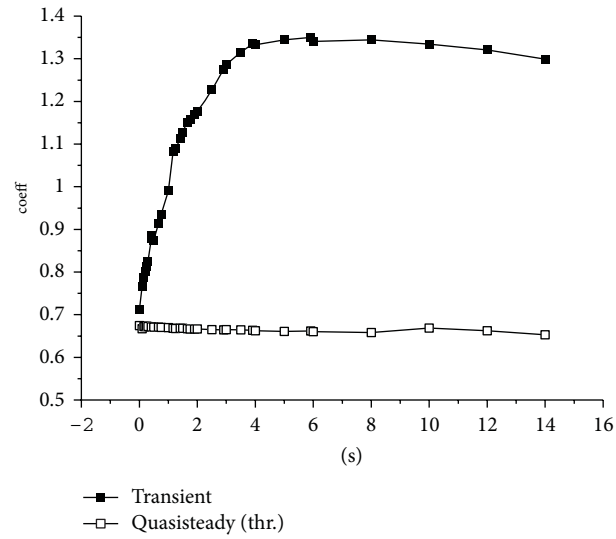

Figure 12: Comparison between quasisteady and transient coefficients.

4.3. Comparison of Flow Field. The quasisteady conditions listed in Table 3 are also simulated by CFD method with MRF model to get the internal flow field. Figure 13 is the comparison of the relative velocity vector in the impeller at different times. The reference frame is rotating at the same rotational speed with the blade. Although the quasisteady head and the transient head do not differ too much, distinctive differences are shown in the flow field. In the transient calculation, there is a stall at the beginning of the power failure condition. As time goes on, the stall declines and disappears fast (when $t = 0.2$ s). But the relative speed is still small at the outlet suction side. After $t = 0.3$ s, the flow is uniform and there is no stall. In quasisteady flow field, the stall exists in each of the impeller channels by the suction side all the time. On the other hand, the stall form in the transient simulation is also different from that appeared in the quasisteady simulation. It indicates that the reverse pressure gradients appeared in the suction side that are different. In transient case (Figure 13(a1)), the stall appeases like flow separation. Maybe the fluid is going in a most-energy-saving way. In quasisteady simulation (Figure 13(a2)), the stall is shown as backflow. Besides, at the same rotational speed, flow rate in transient case is larger than that in quasisteady case. This is caused by inertia effect. Difference of the internal flow field is suspected to be one of the reasons for the deviation of transient head and quasisteady head.

5. Conclusion

In this paper, the transient characteristic during power failure accident in a mixed pump is studied by CFD method and theoretical methods. The rotational speed, transient head, and flow rate change law are obtained and researched in this study. The quasisteady characteristic in the same speed condition is also studied and compared with the transient result. There are the following conclusions.

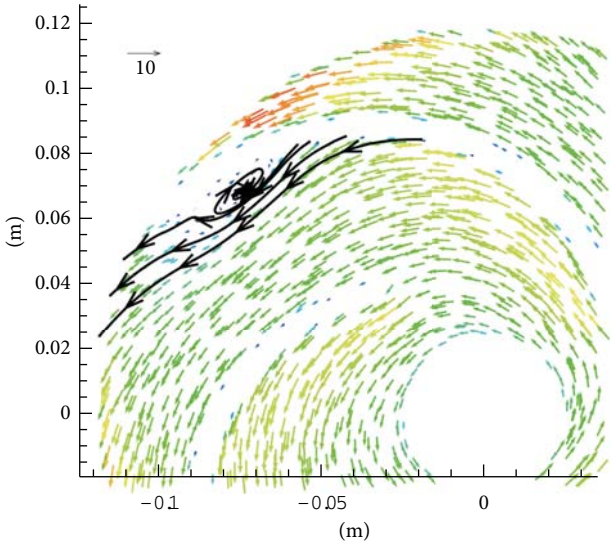

(a1) Transient = 0.1 s

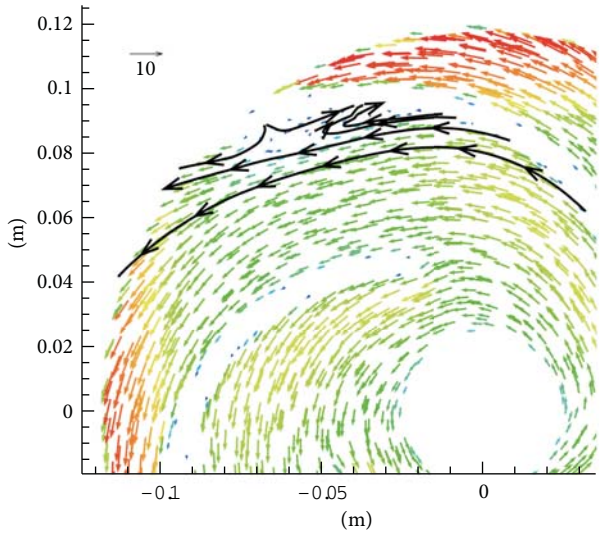

(a2) Quasisteady = 0.1 s

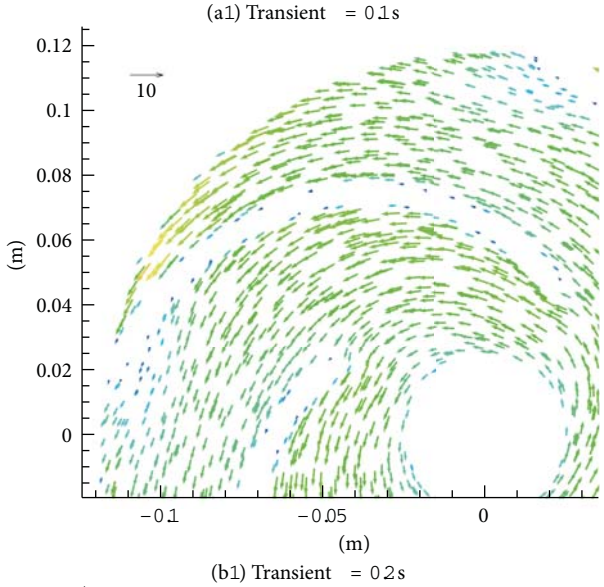

(b1) Transient = 0.2 s

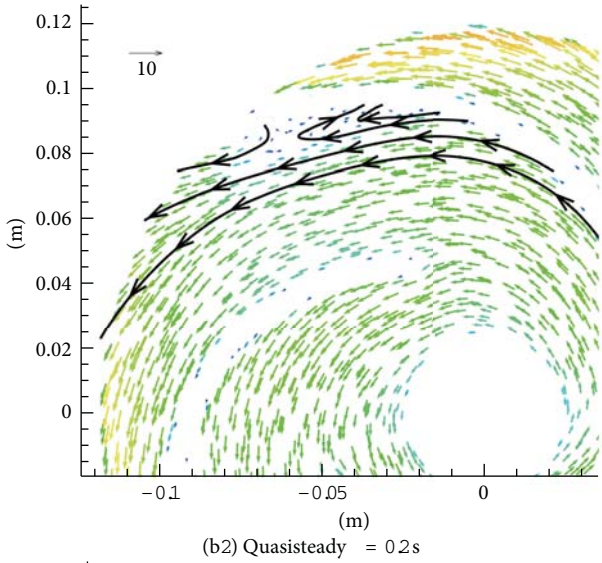

(b2) Quasisteady = 0.2 s

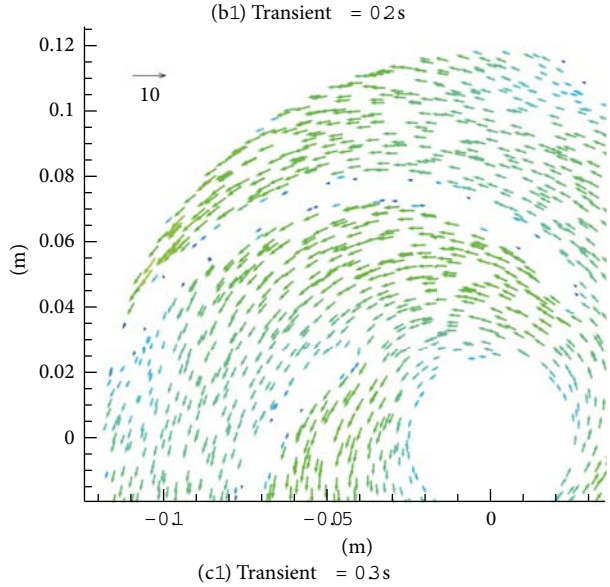

(c1) Transient = 0.3 s

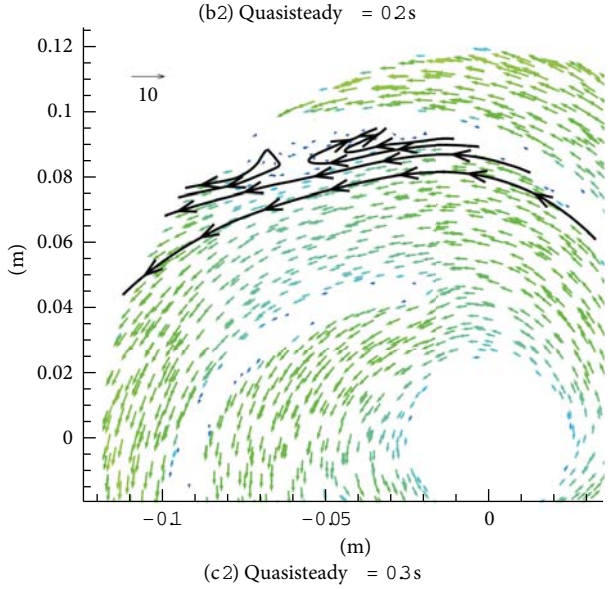

(c2) Quasisteady = 0.3 s

Figure 13: Continued.

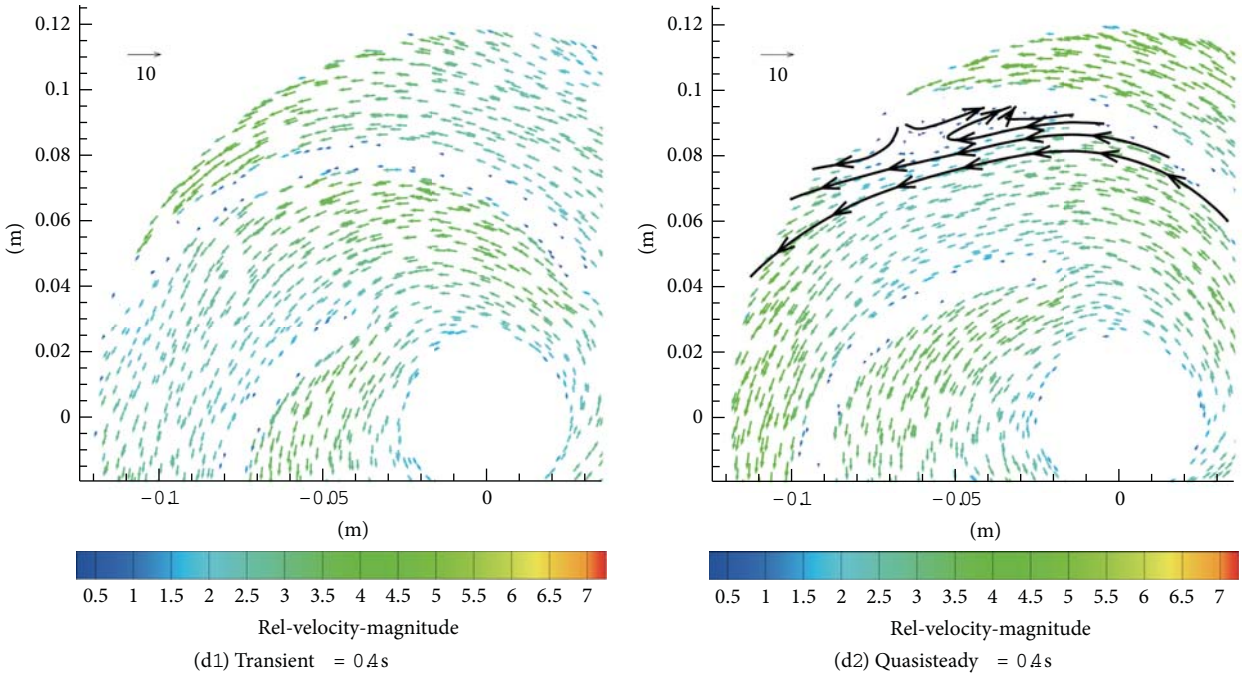

Figure 13: Flow field comparison.

(1) Hydraulic-force coupling method is available for the power failure stopping process. External and internal characteristics of the pump are obtained.

(2) In power failure accidents, the rotational speed decreases much faster than the flow rate. Half-capacity time is almost twice the half-speed time.

(3) In pump stopping process, quasisteady head is larger than transient head. The deviation is especially distinct at the beginning of the process ($t < 0.3$ s). It is caused by the inertia effect of the fluid contained in the pump. Differences are also shown in the internal flow field.

Nomenclature

b_2: Outlet width (mm)
C: Constant
D_{i1}: Inlet diameter one (mm)
D_{i2}: Inlet diameter two (mm)
D_{o1}: Outlet diameter one (mm)
D_{o2}: Outlet diameter two (mm)
F_x: Force in x direction (N)
F_y: Force in y direction (N)
F_z: Axial force (N)
H_0: Nominal total head (m)
H_s: Quasisteady head (m)
I: Rotary inertia of the pump system (kg·m^2)
K_ω: Parameter
K_q: Parameter
L_1: Inlet length (mm)
L_2: Outlet length (mm)
N_0: Nominal speed (r/min)
n: Rotational speed (r/min)
n_0: Initial rotational speed (r/min)
P_{coeff}: Pressure coefficient
P: Total pressure rise (Pa)
Q_0: Nominal flow rate (m^3/h)
T: Total input torque (N·m)
T_0: Initial hydraulic torque (N·m)
T_h: Hydraulic torque of the pump (N·m)
T_f: Rotor friction torque (N·m)
Δt: Time step size (s)
t_{pn}: Half-speed time (s)
t_{pq}: Half-capacity time (s)
u_2: Peripheral speed of the impeller at the blade outlet (m/s).

Greek Letters

α: Empirical factor
ε_1: Front shroud angle (degree)
ε_2: Back shroud angle (degree)
ρ: Fluid density (kg/m^3)
ω: Rotor angular speed (rad/s)
ω_0: Initial angular speed (rad/s).

Acknowledgment

This study was carried out as a part of the National Natural Science Foundation of China (the Project no are 51276213 and 51176168). The support is gratefully acknowledged.

References

[1] H. Tsukamoto, S. Matsunaga, H. Yoneda, and S. Hata, "Transient characteristics of a centrifugal pump during stopping period," *Journal of Fluids Engineering*, vol. 108, no. 4, pp. 392–399, 1986.

[2] C. P. Kittredge and N. J. Princeton, "Hydraulic transients in centrifugal pump system," *Transactions of ASME*, vol. 78, pp. 1307–1321, 1956.

[3] S. R. Zhang, "Transient behavior calculation for reactor coolant circulation pump," *Nuclear Power Engineering*, vol. 14, no. 2, pp. 183–190, 1993.

[4] P. Thanapandi and R. Prasad, "Centrifugal pump transient characteristics and analysis using the method of characteristics," *International Journal of Mechanical Sciences*, vol. 37, no. 1, pp. 77–89, 1995.

[5] X. J. Liu, J. S. Liu, D. Z. Wang, Z. Yang, and J. G. Zhang, "Test study on safety features of station blackout accident for nuclear main pump," *Atomic Energy Science and Technology*, vol. 43, no. 5, pp. 448–451, 2009.

[6] J. T. Liu, Z. F. Li, and L. Q. Wang, "Numerical simulation of the transient flow in a radial flow pump during stopping period," *Journal of Fluids Engineering*, vol. 133, no. 11, Article ID 111101, 7 pages, 2011.

[7] Z. F. Li, D. Z. Wu, L. Q. Wang, and B. Huang, "Numerical simulation of the transient flow in a centrifugal pump during starting period," *Journal of Fluids Engineering*, vol. 132, no. 8, Article ID 081102, 2010.

[8] Z. F. Li, D. Z. Wu, and L. Q. Wang, "Experimental and numerical study of transient flow in a centrifugal pump during startup," *Journal of Mechanical Science and Technology*, vol. 25, no. 3, pp. 749–757, 2011.

[9] D. Z. Wu, P. Wu, Z. F. Li, and L. Q. Wang, "The transient flow in a centrifugal pump during the discharge valve rapid opening process," *Nuclear Engineering and Design*, vol. 240, no. 12, pp. 4061–4068, 2010.

[10] FLUENT Inc., Lebanon, NH, USA, 2005.

[11] L. Q. Wang, Z. F. Li, W. P. Dai, and D. Z. Wu, "2-D numerical simulation on transient flow in centrifugal pump during starting period," *Journal of Engineering Thermophysics*, vol. 29, no. 8, pp. 1319–1322, 2008.

[12] Y. J. Yang, J. L. Zhang, S. J. Qiu, and G. H. Su, "A calculation model of flow characteristic of coolant pump for nuclear reactor system," *Chinese Journal of Nuclear Science and Engineering*, vol. 15, no. 3, pp. 220–225, 1995.

[13] Z. F. Li, *Numerical simulation and experimental study on the transient flow in centrifugal pump during starting period [Ph.D. dissertation]*, Zhejiang University, Hang Zhou, China, 2009.

[14] A. Dazin, G. Caignaert, and G. Bois, "Transient behavior of turbomachineries: applications to radial flow pump startups," *Journal of Fluids Engineering*, vol. 129, no. 11, pp. 1436–1444, 2007.

Hindawi Publishing Corporation
Advances in Mechanical Engineering
Volume 2013, Article ID 310432, 9 pages
http://dx.doi.org/10.1155/2013/310432

Research Article

Evaluation of Artificial Caudal Fin for Fish Robot with Two Joints by Using Three-Dimensional Fluid-Structure Simulation

Yogo Takada, Noboru Fukuzaki, Toshinori Ochiai, Tomoki Tajiri, and Tomoyuki Wakisaka

Osaka City University, 3-3-138 Sugimoto, Sumiyoshi-ku, Osaka-shi, Osaka 558-8585, Japan

Correspondence should be addressed to Yogo Takada; takada@mech.eng.osaka-cu.ac.jp

Received 18 January 2013; Accepted 1 March 2013

Academic Editor: Bo Yu

A fish robot with image sensors is useful to research for underwater creatures such as fish. However, the propulsion velocity of a fish robot is very slow compared with live fish. It is necessary to swim at a speed several times faster than the speed of the current robots for various usages. Therefore, we are searching for the method of making the robot swim fast. The simulation before making the robot is important. We have made the computational simulation program of three-dimensional fluid-structure analysis. The flow around the caudal fin can be examined by analyzing the fin as an elastic body. We compared the results of numerical analysis with the results of PIV measurement. Both were agreed well. Because the performance of a fish robot with two joints is better than that of a fish robot with one joint, we searched for an excellent fin for the fish robot with two joints by using CFD. We confirmed that the swimming performance of a fish robot becomes very good when the caudal fin is rigid except for the root of the fin which is comparatively flexible.

1. Introduction

A fin driving a fish robot which imitates a live fish never gives the caution to other underwater creatures. Therefore, the fish robot becomes useful for the investigation of the ecosystem in water, the usage of the environmental surveillance, and so on. Moreover, because the fish robot does not have the screw propeller which becomes tangled in water plants and fibrous floats, propulsive mechanism of caudal fin is suitable.

Many researchers have been studying propulsion mechanism about various caudal fins of the underwater creatures such as fishes in respect to the fluid phenomenon around the propulsive caudal fin for a long time [1–3]. However, the speed of fish robots manufactured by imaging live fish which swim with its caudal fin is very slow in comparison with the speed of an actual live fish. Live fishes can swim in the distance three times the fish size in length for one second. Besides, the propulsion efficiency of fish robot is much lower than live fishes. Though fish's swim mechanism is becoming clear step by step, those study results have not been tied into manufacturing of good-performance robots.

When practical use is tried for the ecosystem investigation, the same cruising speed as the fish is demanded. Therefore, it is necessary for the fish robot to swim at more high speed than the current state. Because the condition of an appropriate fin in each fish robot is different, repeated experiment is necessary in order to find the best fin in various fins made with a different condition whenever the fish robot is made for trial purposes. The best fin for the designed fish robot is hoped to be clarified before the fish robot is produced.

For a long time, we have conducted numerical flow analysis regarding fishes and fish robots [4–6]. The purpose of this study is to enable three-dimensional fluid-structure analysis to search for the good fin to use for a fish robot with two joints. For that purpose, three-dimensional elastic deformation analysis of the fin by finite element method (FEM) was combined with an existing three-dimensional fluid numerical analysis code (GTT code: generalized tank and tube code) [4]. Weak coupling method which solves alternately plural phenomena shown by separate governing equations has been employed. The propulsive performances of the fish robot that swam with carangiform locomotion of

Table 1: Induced variable ϕ, effective diffusion coefficient Γ_ϕ, and source term S_ϕ in each conservation equation.

Equation	ϕ	Γ_ϕ	S_ϕ
Mass	1	0	0
Momentum	u	μ	$-\frac{\partial p}{\partial x}+\frac{1}{3}\frac{\partial}{\partial x}(\mu_{\text{eff}}\,\text{div}\,\vec{\nabla})$
	V	μ	$-\frac{\partial p}{\partial y}+\frac{1}{3}\frac{\partial}{\partial y}(\mu_{\text{eff}}\,\text{di}\mathrm{V}\,\vec{\nabla})$
	w	μ	$-\frac{\partial p}{\partial z}+\frac{1}{3}\frac{\partial}{\partial z}(\mu_{\text{eff}}\,\text{di}\mathrm{V}\,\vec{\nabla})$

various fins were compared by using improved fluid-structure analysis code.

2. Three-Dimensional Fluid-Structure Simulation

2.1. Method of Flow Analysis. The equation of mass conservation and the equations of momentum conservation of flow are shown by the general conservation equation as follows:

$$\frac{\partial(\rho\phi)}{\partial t}+\text{div}\left(\rho\vec{\nabla}\phi-\Gamma_\phi\,\text{grad}\,\phi\right)=S_\phi, \tag{1}$$

where ϕ is the induced variable, Γ_ϕ is the diffusion coefficient, and S_ϕ is the source term, respectively. Because the analytical object in this study is to flow around a moving object such as a fish or a robot, the fluid has been analyzed as a moving boundary problem where the computational grid moves. Equation (1) becomes (2) by considering the movement of the computational grid:

$$\frac{\partial(\rho\phi)}{\partial t}+\text{div}\left(\rho\left(\vec{\nabla}-\vec{\nabla}_s\right)\phi-\Gamma_\phi\,\text{grad}\,\phi\right)=S_\phi, \tag{2}$$

where $\vec{\nabla}_s$ is the moving velocity of each computational grid. Table 1 shows the induced variable ϕ, the effective diffusion coefficient Γ_ϕ, and the source term S_ϕ in (2). In Table 1, μ_{eff} is the effectiveness coefficient of viscosity. Because the Reynolds number of fluid in this study is very small, the analytical object can be considered to be laminar flow. The fluid around a fish robot is general water. Therefore, the incompressible fluid without the temperature change was added to the calculation condition.

In this research, we used the generalized tank and tube method (GTT method)which adopted the technique of conversion into generalized curvilinear coordinates based on the Tank and Tube method that Gosman et al. [7] and Spalding and Pun [8] developed.

In this method, first of all, the physical space shown by Cartesian coordinate system (x, y, z, t) is divided into small hexahedral volume elements of arbitrary shape. Then, each control volume is converted into a cubic control volume in the calculation space by general curvilinear coordinate transformation. The allocation of independent variables such as pressure p, density ρ, and components of the velocity vector u, V, and w is based on the regular grid (nonstaggered grid) method, and therefore, all variables are allocated at the center of each control volume. The pressure correction equation is calculated based on SIMPLER method [9], where pressure is calculated by satisfying the equation of continuity.

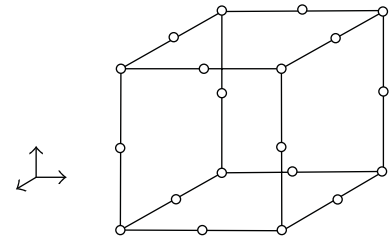

Figure 1: 20-node hexahedral elements of some serendipity families.

2.2. Method of Elastic Deformation Analysis. In this research, the caudal fin of a fish robot is assumed to be a linear elastic body. The deformation of linear elastic body is modeled by equilibrium equation in consideration of inertia force. Newmark-β method [10] is used for time discretization, and FEM is used for space discretization:

$$\nabla\cdot\{\sigma\}+\{f\}=\rho\left\{\frac{\partial^2 u_B}{\partial t^2}\right\}, \tag{3}$$

where ∇ is the nabla differential operator, $\{\sigma\}$ is the stress tensor, $\{f\}$ is the body force vector, and ρ is the density.

To calculate by the FEM, the entire material to be analyzed is divided into 20-node hexahedral elements of some serendipity families. Figure 1 shows the example of one divided element. When the displacement vector in an arbitrary point in each element is defined by $\{u_B\}^T=\{u_B, \mathrm{V}_B, w_B\}$, $\{u_B\}^T$ is obtained as (4) by using displacement in each node:

$$\{u_B\}^T=\left\{\sum_{i=1}^{20}N_i u_{Bi}^*\ \sum_{i=1}^{20}N_i \mathrm{V}_{Bi}^*\ \sum_{i=1}^{20}N_i w_{Bi}^*\right\}, \tag{4}$$

where N_i is a form function of 20-node hexahedral element of serendipity family, u_{Bi}^* is adisplacement along x-axis on node i, V_{Bi}^* is adisplacement along y-axis on node i, and w_{Bi}^* is adisplacement along z-axis on node i. Therefore, the displacement in each element is expressed as follows by the matrix form:

$$\{u_B\}=[N]\{u_B^*\}, \tag{5}$$

where $[N]$ is expressed by the following matrix and $\{u_{Bi}^*\}^T=\{u_{B1}^*, \mathrm{V}_{B1}^*, w_{B1}^*, u_{B2}^*, \mathrm{V}_{B2}^*, w_{B2}^*, \ldots, u_{B20}^*, \mathrm{V}_{B20}^*, w_{B20}^*\}$:

$$[N]=\begin{bmatrix} N_1 & 0 & 0 & N_2 & 0 & 0 & \cdots & N_{20} & 0 & 0 \\ 0 & N_1 & 0 & 0 & N_2 & 0 & \cdots & 0 & N_{20} & 0 \\ 0 & 0 & N_1 & 0 & 0 & N_2 & \cdots & 0 & 0 & N_{20} \end{bmatrix}. \tag{6}$$

When the virtual displacement $\{\delta u_B\}$ is set as the weighting function and the fundamental equation (3) is integrated

for a single element, the following (7) is obtained. In addition, when Green's theorem is applied to (7), (8) is obtained:

$$\iiint_V \{\delta u_B\}^T \{\nabla \cdot \{\sigma\}\}\, dV + \iiint_V \{\delta u_B\}^T \{f\}\, dV = \iiint_V \{\delta u_B\}^T \rho \left\{\frac{\partial^2 u_B}{\partial t^2}\right\} dV, \tag{7}$$

$$\iint_S \{\delta u_B\}^T \{\sigma\}\, \vec{n}\, dS - \iiint_V \{\delta\epsilon\}^T \{\sigma\}\, dV + \iiint_V \{\delta u_B\}^T \{f\}\, dV = \iiint_V \{\delta u_B\}^T \rho \left\{\frac{\partial^2 u_B}{\partial t^2}\right\} dV, \tag{8}$$

where ϵ is the strain and $\{\delta\epsilon\}$ is the virtual strain for the displacement $\{\delta u_B\}$.

By space discretization, (9)–(12) can be derived from the first term, second term, and third term in the left side of (8) and the right term of the same equation, respectively:

$$\iint_S \{\delta u_B\}^T \{\sigma\}\, \vec{n}\, dS = \{\delta u_B^*\}^T \{p^*\}, \quad \{p^*\} = \iint_S [N]^T \{p\}\, dS, \tag{9}$$

$$\iiint_V \{\delta\epsilon\}^T \{\sigma\}\, dV = \{\delta u_B^*\}^T [k] \{u_B^*\}, \quad [k] = \iiint_V [B]^T [D] [B]\, dV, \tag{10}$$

$$\iiint_V \{\delta u_B\}^T \{f\}\, dV = \{\delta u_B^*\}^T \{f^*\}, \quad \{f^*\} = \iiint_V [N]^T \{f\}\, dV, \tag{11}$$

$$\iiint_V \{\delta u_B\}^T \left\{\frac{\partial^2 u_B}{\partial t^2}\right\} dV = \{\delta u_B^*\}^T [m] \left\{\frac{\partial^2 u_B^*}{\partial t^2}\right\}, \quad [m] = \iiint_V [N]^T \rho [N]\, dV, \tag{12}$$

where $[B]$ is a displacement-strain conversion matrix and $[D]$ is an elasticity coefficient matrix.

The dynamic equation in an element is shown as follows, as a result of arranging after substituting (9)–(12) for (8):

$$[m] \left\{\frac{\partial^2 u_B^*}{\partial t^2}\right\} + [k] \{u_B^*\} = \{f^*\} + \{p^*\}. \tag{13}$$

If (13) is overlapped over all elements, the dynamic equation of all elements becomes as follows:

$$[M] \left\{\frac{\partial^2 u_B^*}{\partial t^2}\right\} + [K] \{u_B^*\} = \{F\}, \tag{14}$$

where $[M]$ is all elements mass matrix, $[K]$ is all elements stiffness matrix, and $\{F\}$ is the external force vector.

2.3. Coupling of CFD and Deformation Calculation. The fluid analysis method and elasticity deformation method were described in the foregoing section. In this section, the coupling method of the fluid analysis and elastic deformation are described. There are a strong coupling method and a weak coupling method as a means to couple the fluid analysis and elastic deformation analysis.

The weak coupling method separately solves governing equations of the fluid and structure. Then, the weak coupling method conducts the calculation to satisfy dynamic equilibrium and a geometrically continuous condition on the fluid boundary surface and the structural boundary surface. It is inferior in respect of the accuracy of calculation and stability compared with the strong coupling method. However, different discretization techniques can be adopted to solve the governing equations of the fluid and structure.

In this study, three-dimensional CFD code (GTT code) of a finite volume method is adopted for the fluid analysis. We decided to use the weak coupling method because it is easy to combine elastic deformation analysis with the existing GTT code. Pressure on the fluid-structure boundary surface obtained by the fluid analysis is sent to the role part of the elastic deformation analysis as a dynamic boundary of beam. Moreover, displacement on the boundary surface obtained by the elastic deformation analysis is sent to the role part of the fluid analysis as a geometrical boundary. Dynamic equilibrium and a geometrical continuous condition on the fluid-structure boundary surface were satisfied by this method. We explain each step as follows.

Step 1. The time is increased by an interval Δt.

Step 2. The computational grid for the fluid analysis is created based on the displacement of the fluid-structure boundary surface determined in the former time step. The Poisson equation with the Dirichlet condition is solved not to make the complex computational grid, and then the grid is smoothed. If the computational grid was not smoothed in this step, the grid lines would have crossed each other and CFD calculation would have stopped with errors.

Step 3. The fluid is analyzed by the GTT code by using the computational grid made with Step 2. The repetition calculation continues until a converged solution is obtained in consideration of the nonlinearity of the fluid.

Step 4. The converged solution of pressure obtained with Step 3 is given as a dynamic boundary condition of the structure, and the deformation analysis is conducted by the FEM.

The nonstationary fluid-structure analysis is conducted by repeating Steps 1 to 4.

3. Experimental Fish Robot

It is necessary to compare the results of fluid-structure simulation and the results of the experiment to examine the validity of the program for the fluid-structure calculation used in this study. The fish robot for the experiment of

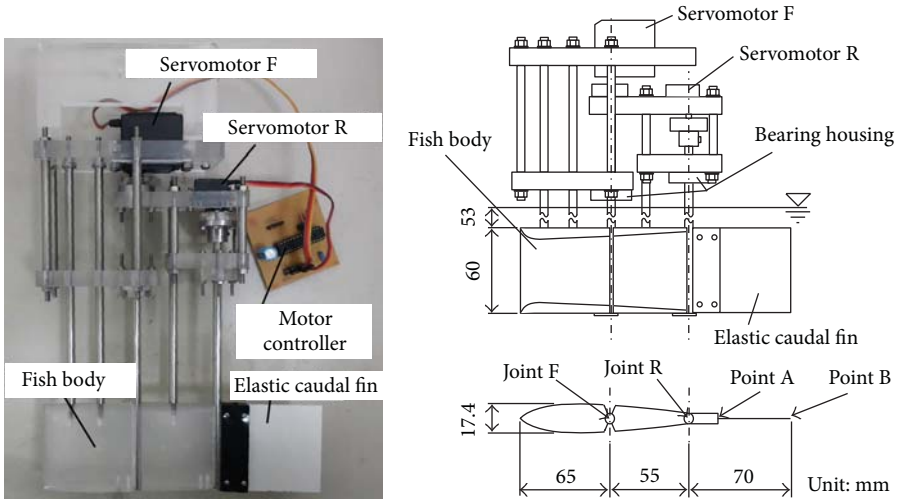

(a) Externals photograph of the fish robot for experiment

(b) Structure of the fish robot for experiment

Figure 2: Externals photograph and structure of the fish robot.

the verification was manufactured. Then, the amount of deformation of caudal fin tip was examined after a flexible caudal fin was attached to the robot. Moreover, the flow behind the fish robot was measured by the PIV measurement.

Figure 2(a) shows the externals photograph of the fish robot produced for experimental use for the verification, and Figure 2(b) shows the structural drawing.

The manufactured fish robot was used to verify the result of the numerical analysis. Therefore, the driving system, the electric circuit, and so forth were put out on the surface of the water. Servomotors which can control the angle easily were used for driving the fish robot. The servomotor at the front joint is RB995b made. MiniStudio Inc; the rated voltage is 4.8 V, and the rated torque is 0.833 Nm. Then, the servo motor at the rear joint is DS385 made by Japan Remote Control Co.; the rated voltage is 4.8 V, and the rated torque is 0.196 Nm.

The total length of the fish robot is 190 mm, and the length of the body part is 120 mm. There are two rotation axles, and the rear of the body and the caudal fin are shaken from side to side through the shaft installed on the servomotors. The shafts restrain to move with housings so that the shafts do not move vertically and horizontally. All parts are rigid bodies from the head to the position (point A) which is at 20 mm behind joint R. The shape of the body part is NACA0012 which is one of the typical symmetrical airfoil. This shape is often used for the fluid analysis as fish's shape [11]. In addition, the part from the point A to the position of caudal fin edge (point B) is elastically deformable as a fin. In the experiment, a polystyrene board of 0.3 mm in thickness was used as a flexible caudal fin. The Young modulus of the polystyrene board was 2.74 GPa. the PIC18F2520 made by Microchip Technology Inc. was used for the control of the servo motor. Moreover, DC 5 V was supplied from the stabilized power supply PW18-1.3AT made by Kenwood Co., and it was connected to the control circuit and servo motors.

We examined the amount of the deformation of the caudal fin when the fish robot was moving. The fish robot was fixed to a circulating water channel, and the flow velocity in the circulating water channel was set to 0.2 m/s. The flow of water in the vicinity of the fin was taken of pictures at 200 frames per second from the lower side with the high-speed camera k-II which was made Katokoken Co. The amount of the fin's deformation was obtained from the pictures.

Particle image velocimetry (PIV) measurement was used to measure the flow velocity distribution of water around the caudal fin of the fish robot. with respect to the size of area for PIV measurement, the length in traveling direction is 150 mm, and the length in lateral direction is 184 mm. The area around the robot was illuminated with a laser sheet located at the side of the measurement chamber. A PIV laser G1000 (1 W), the above-mentioned CCD camera, and the software FlowExpert made by Katokoken were used to measure the flow velocity distribution.

4. Flow Analysis around the Fish Robot by Three-Dimensional Fluid-Structure Simulation

In this section, the validity of fluid-structure simulation used in this study is examined by comparing the calculation results and the experimental results. Figure 3 shows the computational grid used in calculation. The computational grid was divided into $62 \times 50 \times 159$, and the grid spacing in the vicinity of the caudal fin and its downstream region is narrower.

Table 2 shows the calculation condition of the fluid and the elastic body used in this calculation. As the upstream boundary condition in computation, the inlet velocity of water flow at the upstream end was uniformly set at 0.2 m/s. The density, Young's modulus, and the geometrical moment

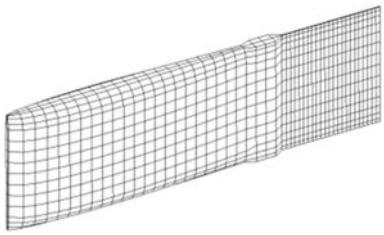

(a) Outline of the fish robot

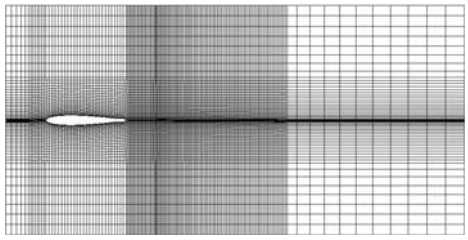

800 mm × 400 mm × 250 mm

(b) z-x Plane (j = 26)

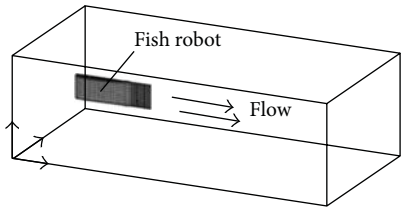

(c) Axes of coordinate

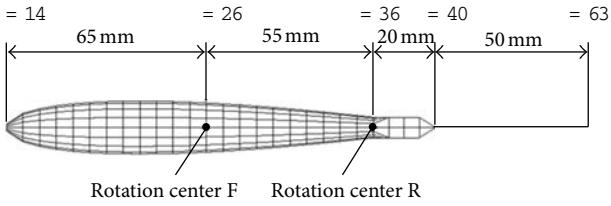

(d) Computational grid for deformation analysis

Figure 3: Computational grid around the fish robot.

of inertia which have an affair with the flexibility of the fin are the same values as the polystyrene board of 0.3 mm in thickness which had been used to experiment in the foregoing section. Then, the computational grid used for the deformation analysis by the FEM is shown in Figure 3(d). The same computational grid as the fluid analysis is used in the deformation analysis. The range where k is from 36 to 63 (i: from 31 to 33, j: from 19 to 33) shown in Figure 3(d) is calculated by the deformation analysis. In this study, 20-node serendipity element of the fin deformation described in section 2 was applied. The number of elements is 756, and the number of nodes is 4491. Three degrees of freedom of the displacement of each x, y and z direction, given at each node. Because the part of 20 mm in length where k is from 36 to 40 is rigid body, the Young modulus of this part is set to 2.74×10^6 GPa so as to avoid the elastic deformation. The center of rotation concerning the rear part of the robot body is the position where k is 26, and that concerning the caudal fin is the position where k is 36.

Table 2: Calculation condition.

Fluid condition	Temperature	293 K
	Water pressure	1.01325×10^5 Pa
	Water density	998.2 kg/m^3
	Water viscosity	1.002×10^{-3} Pa · s
	Inlet velocity	0.2 m/s
Solid condition	Density of elastic tail fin	1039 kg/m^3
	Cross-section area	1.77×10^{-5} m^2
	Young's modulus	2.74 GPa
	Geometrical moment of inertia	1.327×10^{-13} m^4

5. Evaluation of the Propulsive Performance

We have examined various fins to discover good-performance caudal fin by using this fluid-structure simulation code. In this study, the five different caudal fins shown in Figure 4 were investigated in the simulation. The overall shape and area of each fin are the same. However they have different flexibilities. In Case 1, the entire fin is rigid and has a very high Young's modulus. In Case 2, the entire fin is elastic sheet whose flexibility is the same as polystyrene, and the Young modulus is 2.74 GPa. In Case 3 and Case 4, the fins have a very soft part that bends easily. In Case 5, the fin has an elastic part and a rigid part. This fin is rigid except for the root of the fin which is flexible.

First of all, the distribution of the vorticity calculated based on the speed obtained by CFD and PIV measurement in case of each caudal fin was compared. This result is shown in Figure 5. It can be confirmed that the numerical result and the experimental result agreed well in any case. In Case 1, Case 2, and Case 5, vorticity is strong, and the vortices widely extend in Case 5. On the other hand, in Case 3 and Case 4 that have a soft part on each fin, vorticity is small, and the extension of the vortices is suppressed to small. Concerning the size of vortices, the big difference is not seen among Case 1, Case 2, and Case 5. The extension of vortices of Case 2 and Case 5 is a little narrower than Case 1 if they are seen in detail. In Case 3 and Case 4, the vorticity is smaller than the other cases, and the diffusion angle of the vortices is also narrower. The softness of the fin affects the diffusion angle. At t = 0.0 s in Figure 5, each joint in the robot is controlled to become a defined angle by all cases. However, the position of the rear end of caudal fin is different in each case. The vortices extend widely if the rear end of the fin moves widely. Then, if the diffusion angle of Case 4 is compared with that of Case 3, the angle of Case 4 is narrower, and the vortices are smaller. The soft part in the fin of Case 4 is near the root of the fin. Therefore, the softness of the fin in the root will greatly influence the flexibility of the entire fin. In this study, reverse Karman vortex street was not generated in the numerical results and experimental results. It is guessed that this robot did not generate the reverse Karman vortex street because the shape of the fin is a rectangle.

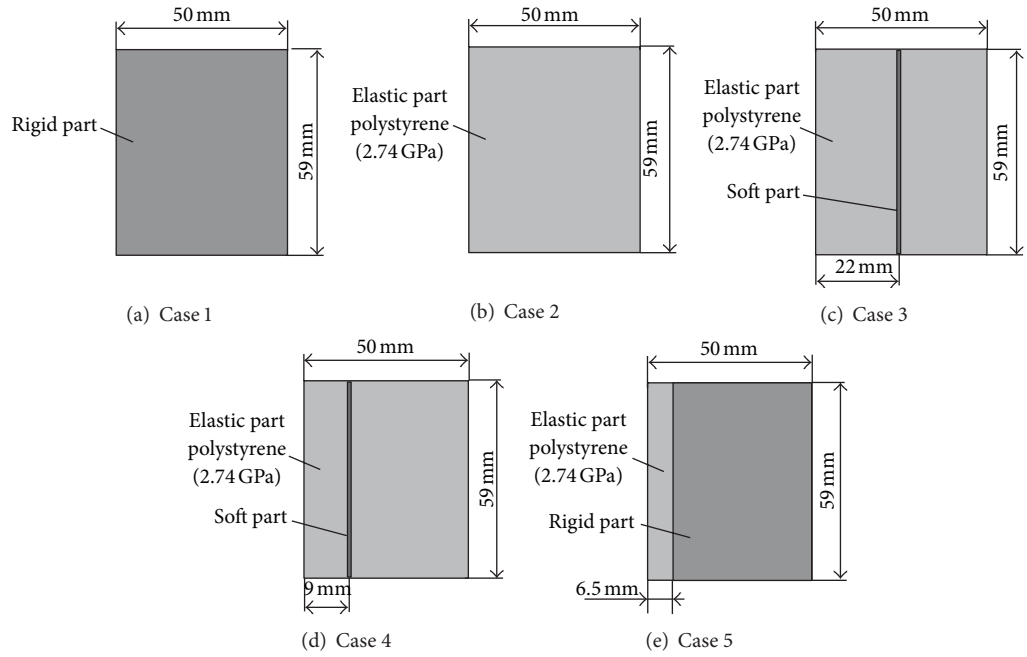

Figure 4: Various fins of the fish robot in the simulation study.

Figure 6(a) shows the value of each static thrust obtained by the experiment that used a measurement device with a load cell. Then, Figure 6(b) shows the value of mean net propulsive force obtained by the simulation. Figure 6(c) shows the value of each side force. The propulsive force is qualitatively corresponding well, though a quantitative agreement cannot be confirmed because the physical quantity is different. The propulsive performance of Case 5 was the best in Figure 6, and the robot with the fin of Case 5 swam speediest in a water tank actually.

In Case 1, Case 2, and Case 5, because the water pressure on the fin surface is large, their net propulsive force and side force are strong. In contrast, in Case 3 and Case 4, the net propulsive force and the side force are weak because the water pressure on the fin surface is small.

Moreover, the fin of Case 5 was examined by using CFD analysis in detail. The relationship between the flexibility in the elastic part and the propulsive performance of the robot was investigated. The net propulsive force and the side force were calculated by CFD with respect to each Young's modulus and each length X mm in Figure 7. Each net propulsive force and each side force are shown in Figure 8. The Young modulus of the elastic part is different from Case A to Case J. The material of Case A is polystyrene. In Case A, each propulsive force does not depend on length X mm. All propulsive forces of Case A were almost the same value. The impellent becomes the maximum when X is 6.5 mm (corresponding to the above-mentioned Case 5). On the other hand, when the length of X becomes long, side force becomes small.

Young's modulus of the elastic part in each case is indicated in Table 3. According to Figure 8, if the Young modulus of fin is low, both the propulsive force and the side force are weak except for the case of $X = 2.2$ mm.

Table 3: Flexibility of the elastic part in Figure 7.

Case	Young's modulus
A	2.74 GPa
B	1.37 GPa
C	0.913 GPa
D	0.685 GPa
E	0.548 GPa
F	0.457 GPa
G	0.391 GPa
H	0.343 GPa
I	0.304 GPa
J	0.274 GPa

In Case C (the Young modulus is 0.913 GPa) and $X = 2.2$ mm, the propulsive force is strongest. The propulsive performance improves theoretically, if the fin is made of a material which is three times softer than polystyrene.

The side force is weak if the fin is soft. However, when the material is soft like Case J, the side force does not depend on the length of X. The rigid part in the fin edge may be twirled right and left because of the softness at the root of the fin. If the ratio of Young's modulus and length X is the same, fin's overall flexibility and the propulsive performance becomes similar except for the case that the material is too soft. For instance, Case A (2.74 GPa), $X = 6.5$ mm, and Case C (0.913 GPa), $X = 2.2$ mm, have almost the same flexibility. Besides, each case's propulsive force and side force are almost the same. In a word, the suitable fin can be prepared by the adjustment of the length X even if there is no material that has appropriate flexibility as a fin for the fish robot.

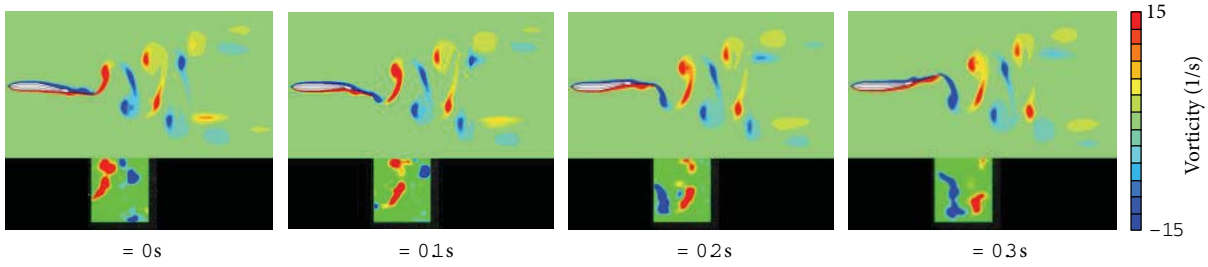

(a) Case 1

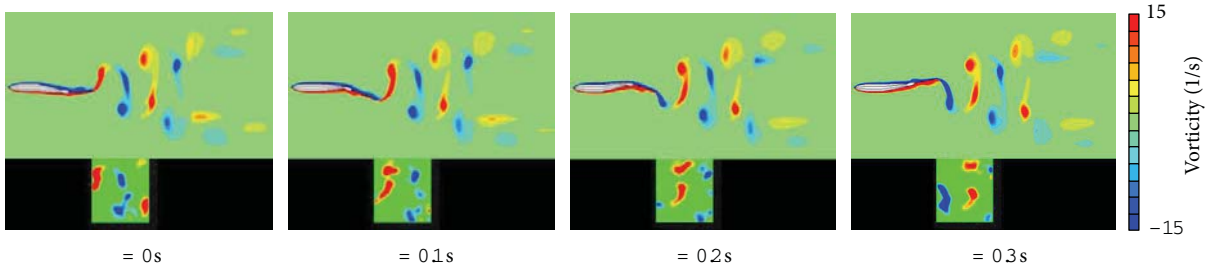

(b) Case 2

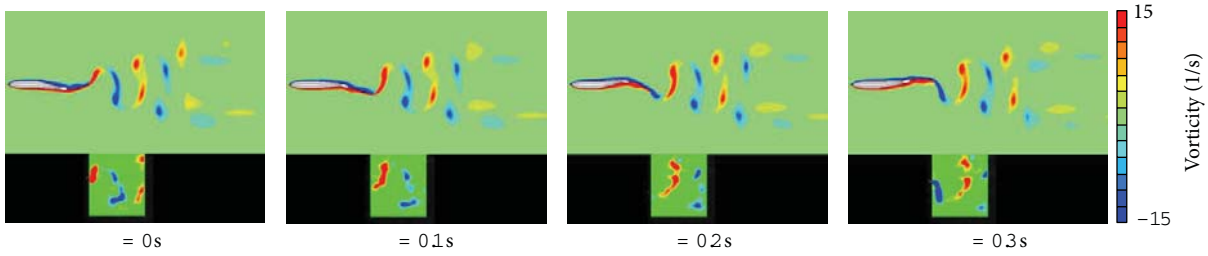

(c) Case 3

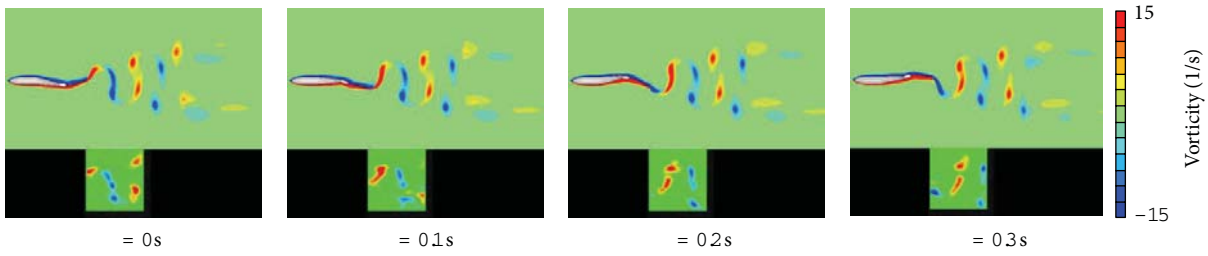

(d) Case 4

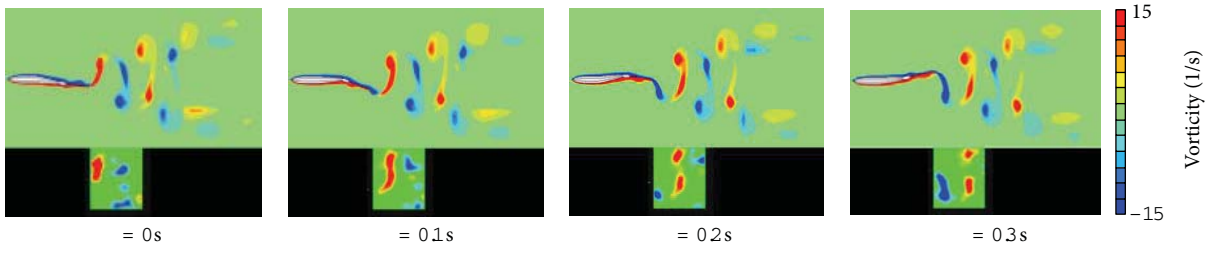

(e) Case 5

Figure 5: Comparative results of CFD and PIV measurement (upper side: CFD, downside: PIV in each result).

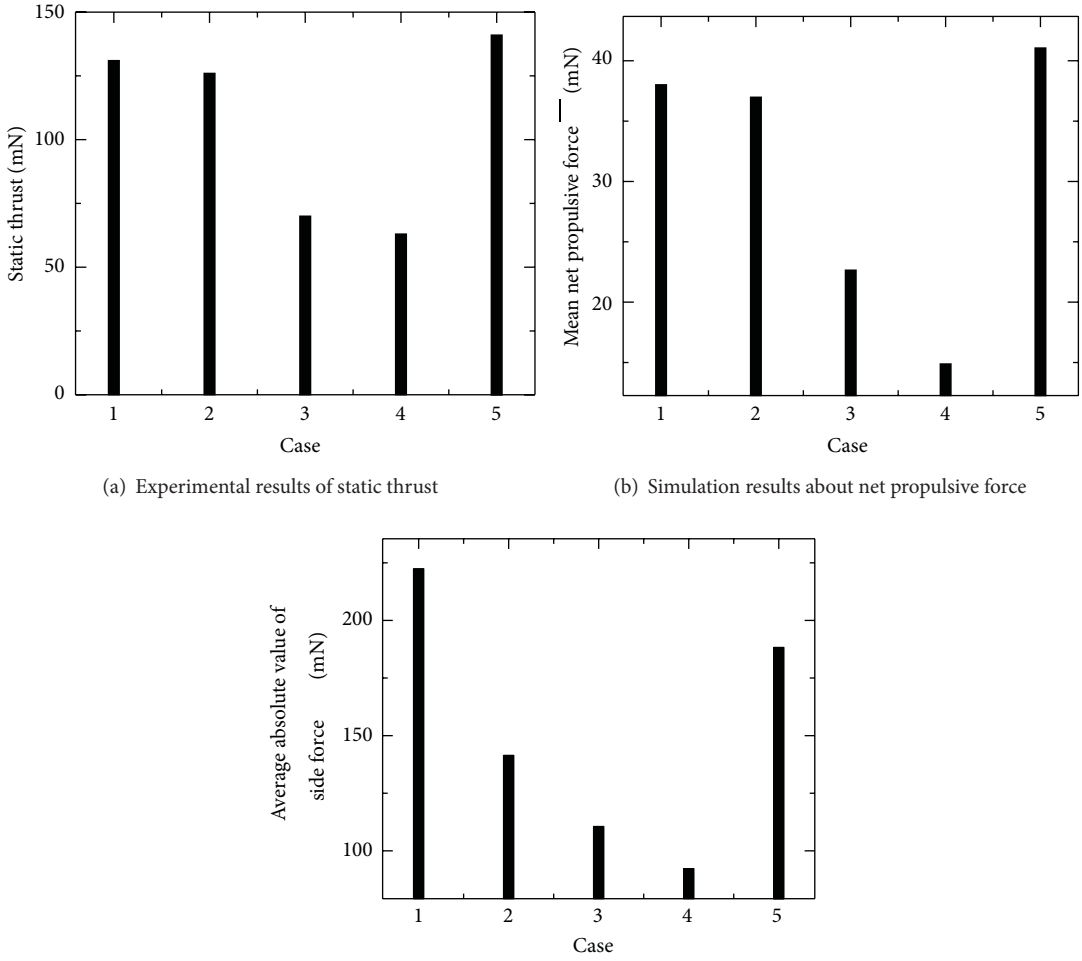

(a) Experimental results of static thrust

(b) Simulation results about net propulsive force

(c) Simulation results about side force

Figure 6: Each force obtained by experiment and simulation.

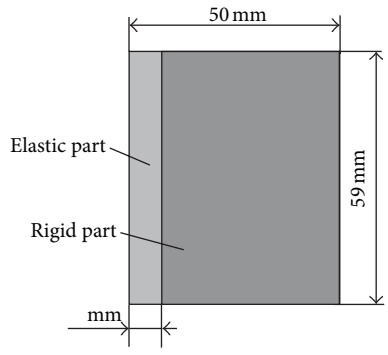

Figure 7: Caudal fin with various length on root of fin.

6. Conclusions

In this study, three-dimensional fluid-structure analysis was conducted to examine the influence that the flexibility of the fin has on the propulsive performance on the simulation.

An improved three-dimensional flow numerical analysis code (GTT code) was used to simulate the fin deformation of a swimming fish robot. Three-dimensional elastic deformation analysis of the fin using FEM has been combined with the GTT code allowing the fluid-structure analysis to be carried out. To verify the simulation result, an experimental fish robot using a flexible fin was made for trial purposes. This robot has two degrees of freedom. The simulation result and experimental result for both the fin deformation and flow pattern behind the fin were compared. It has been confirmed that both are corresponding.

By using the three-dimensional fluid-structure interaction analysis, we confirmed good caudal fin for fish robot with two active joints is a rigid fin with a flexible material on the root. If robot manufacturer do not have most suitable material concerning the flexibility, good fin can be obtained by adjustment of the root length.

Conflict of Interests

There is no conflict of interests.

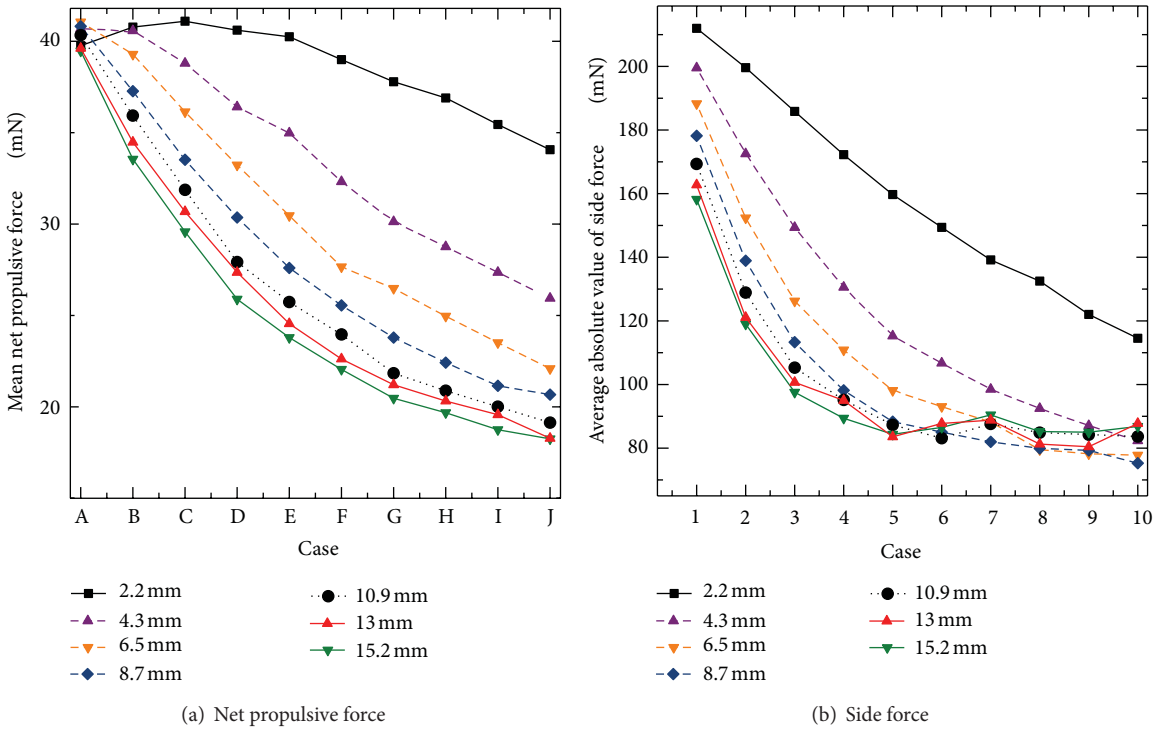

(a) Net propulsive force

(b) Side force

Figure 8: Simulation result in case of various flexible root of fin.

Acknowledgment

The authors would like to express their gratitude to the Japan Society for the Promotion of Science which subsidized them (Grant-in-Aid for Scientific Research (C), no. 24560301).

References

[1] J. Gray, "Studies in animal locomotion. VI. The propulsive power of the dolphin," *The Journal of Experimental Biology*, no. 13, pp. 192–199, 1935.

[2] M. J. Lighthill, "Note on the swimming of slender fish," *Journal of Fluid Mechanics*, vol. 9, no. 2, pp. 305–317, 1960.

[3] M. Nagai, I. Teruya, K. Uechi, and T. Miyazato, "Study on an oscillating wing propulsion mechanism," *Transactions of the Japan Society of Mechanical Engineers, Part B*, vol. 62, no. 593, pp. 200–206, 1996.

[4] Y. Takada, Y. Nakanishi, R. Araki, and T. Wakisaka, "Investigation of propulsive force and water flow around a small fish robot by PIV measurement and three-dimensional numerical analysis," *Transactions of the Japan Society of Mechanical Engineers, Part C*, vol. 76, no. 763, pp. 665–672, 2010.

[5] Y. Takada, R. Araki, T. Ochiai, T. Tajiri, and T. Wakisaka, "Effects of tail fin flexibility on propulsive performance in small fish robots (investigation by fluid-structure interaction analysis considering elastic deformation of tail fin)," *Transactions of the Japan Society of Mechanical Engineers, Part C*, vol. 77, no. 778, pp. 2351–2362, 2011.

[6] Y. Takada, T. Ochiai, N. Fukuzaki, T. Tajiri, T. Omichi, and T. Wakisaka, "Analysis for flow around a fish robot by three-dimensional fluid-structure simulation and evaluation of the propulsive performance," in *Proceedings of the 5th International Symposium on Aero Aqua Bio-Mechanisms (ISABMEC '12)*, p. S41, 2012.

[7] A. D. Gosman, W. M. Pun, A. K. Runchal, D. B. Spalding, and M. Wolfshstein, *Heat and Mass Transfer in Recirculating Flow*, Academic Press, London, UK, 1969.

[8] D. B. Spalding and W. M. Pun, "A general computer program for twodimensional elliptic flows," Report HTS/76/2, Department of Mechanical Engineering, Imperical College, London, UK, 1976.

[9] S. V. Patanker, *Numerical Heat Transfer and Fluid Flow*, McGraw-Hill, New York, NY, USA, 1980.

[10] N. M. Newmark, "A method of computation for structural dynamics," *Journal of the Engineering Mechanics Division*, vol. 8, no. 3, pp. 67–94, 1959.

[11] K. Ishimatsu, K. Kage, and T. Okubayashi, "Numerical simulation for propulsion by elastic oscillating foil," *JSME Annual Meeting*, vol. 2000, no. 4, pp. 247–248, 2000.

Hindawi Publishing Corporation
Advances in Mechanical Engineering
Volume 2013, Article ID 857941, 13 pages
http://dx.doi.org/10.1155/2013/857941

Research Article

Performance Analysis and Application of Three Different Computational Methods for Solar Heating System with Seasonal Water Tank Heat Storage

Dongliang Sun,[1] Jinliang Xu,[2] and Peng Ding[3]

[1] *State Key Laboratory of Alternate Electrical Power System with Renewable Energy Sources, North China Electric Power University, Beijing 102206, China*
[2] *Beijing Key Laboratory of Energy Safety and Clean Utilization, North China Electric Power University, Beijing 102206, China*
[3] *College of Storage & Transportation and Architectural Engineering, China University of Petroleum (Huadong), Qingdao, Shandong 266555, China*

Correspondence should be addressed to Jinliang Xu; xjl@ncepu.edu.cn

Received 26 January 2013; Accepted 10 March 2013

Academic Editor: Bo Yu

We analyze and compare three different computational methods for a solar heating system with seasonal water tank heat storage (SHS-SWTHS). These methods are accurate numerical method, temperature stratification method, and uniform temperature method. The accurate numerical method can accurately predict the performance of the system, but it takes about 4 to 5 weeks, which is too long and hard for the performance analysis of this system. The temperature stratification method obtains relatively accurate computation results and takes a relatively short computation time, which is about 2 to 3 hours. Therefore, this method is most suitable for the performance analysis of this system. The deviation of the computational results of the uniform temperature method is great, and the time consumed is similar to that of the temperature stratification method. Therefore, this method is not recommended herein. Based on the above analyses, the temperature stratification method is applied to analyze the influence of the embedded depth of water tank, the thickness of thermal insulation material, and the collection area on the performance of this system. The results will provide a design basis for the related demonstration projects.

1. Introduction

The solar heating systems include the central solar heating plants with diurnal storage (CSHPDS) and the central solar heating plants with seasonal storage (CSHPSS). CSHPSS can transfer the solar energy from summer to winter. Its heat storage capacity is far beyond that of CSHPDS. Therefore, CSHPSS has become one of the most popular and potential systems for large-scale application of solar energy.

CSHPSS mainly consists of three parts, which are seasonal heat storage system, collection system, and heating system. According to different heat storage mediums, the seasonal heat storage systems are divided into two types, which are the sensible heat storage systems [1] and the latent heat storage systems [2]. The sensible heat storage systems include the embedded pipe heat storage system [3], the aquifer heat storage system [4], the gravel-water heat storage system [5], and the water tank heat storage system [6, 7]. For the embedded pipe heat storage system, the heat is stored in the surrounding soil by means of the embedded pipes underground. For the aquifer heat storage system, the heat is stored in the underground water by means of the cold and hot wells. However, due to the geological limitations, the applications of these two systems are restricted. The gravel-water heat storage system exchanges heat by the pipes installed in different layers inside the store. However, it is not widely applied due to its low heat capacity and great volume. The water tank heat storage system has relatively great heat capacity and good heat storage/releasing performance and is relatively less affected by geological structures. Therefore, it is most widely applied in the world. For example, among the ten largest solar energy heating demonstration projects

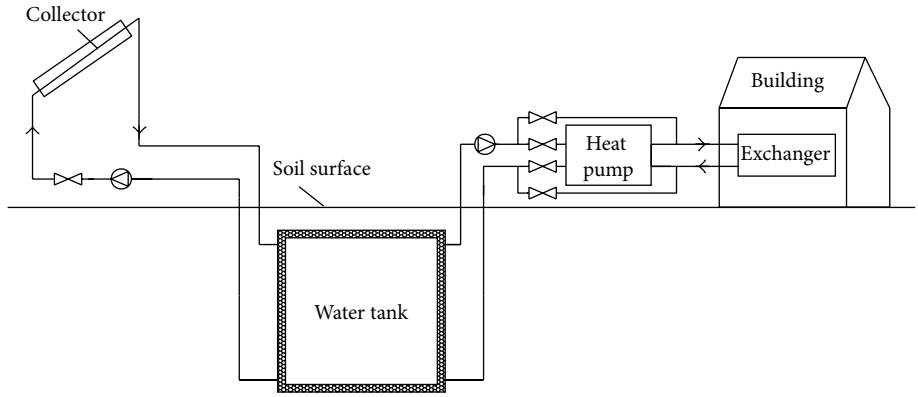

Figure 1: Solar heating system with seasonal water tank heat storage (SHS-SWTHS).

in Europe, eight projects have adopted the water tank heat storage systems [1].

Presently, the calculation studies on the water tank heat storage system are mostly based on simplified models. Yumrutas and Unsal [8, 9] have made computational researches on the hemispherical water tank in earth. Flows and thermal stratifications in the water tank are omitted and the temperature is assumed to be uniform in the water tank. Then, an analytical solution is obtained for the transient temperature field outside the hemispherical water tank by the application of the Complex Finite Fourier Transform (CFFT) and the Finite Bessel Transform (FBT) techniques. Ucar and Inalli [10] have made computational researches on the trapezoid water tank embedded in earth. Same as the hemispherical water tank, the temperature is assumed to be uniform. Then, a finite element method is applied to compute the temperature field in the surrounding soil. Chung et al. [11] have applied TRNSYS software to research the columnar water tank on the ground surface, with the same assumption that the temperature in the tank is uniform. Empirical formulas are used to compute the thermal loss of the water tank. Nordell and Hellstrom [12] have established a soil heat storage model (DST) by TRNSYS and MINSUN with the same uniform temperature assumption, and empirical formulas are also used to compute and analyze the system. Presently, most of the computational researches are based on the uniform temperature assumption. However, the assumption is greatly different from the actual conditions; that is, there exist obvious thermal stratifications in the water tank. To work out an optimal solution, this paper compares the three different computational methods (accurate numerical method, temperature stratification method, and uniform temperature method) for the solar heating system with seasonal water tank heat storage (SHS-SWTHS).

2. Basic Structure of SHS-SWTHS

This paper makes researches on the SHS-SWTHS for a 9,000 m^2 building located at Beijing, China. The system consists of three parts, which are collection system, heat storage system, and heating system, as shown in Figure 1.

The solar collector is flat type and installed horizontally. The collection efficiency η_c is influenced by the inlet temperature T_{ci}, the ambient air temperature T_a, and the solar radiation intensity I_t. According to the efficiency curve provided by the manufacturer, its efficiency [2] is expressed as follows:

$$\eta_c = 0.744 - \frac{4.45\left(T_{ci} - T_a\right)}{I_t}. \tag{1}$$

The collected energy is

$$Q_c = A_c I_t \eta_c, \tag{2}$$

where A_c refers to the collection area. The unit area flow rate of the solar collector is set as $0.01\,\mathrm{kg\cdot m^{-2}\cdot s^{-1}}$. Therefore, the flow rate of the collection system when opened is $0.01A_c$, that is, $\dot{M}_c = 0.01A_c$.

The water tank is a cube with the side length of $L = 15\,\mathrm{m}$ and the volume of $V_t = 3375\,\mathrm{m^3}$. It is embedded underground.

The thermal load of the building during the heating period is

$$Q_h = (UA)_h\left(T_i - T_a\right), \tag{3}$$

where $(UA)_h$ refers to the thermal load of the building under unit temperature difference and equals to $16665\,\mathrm{W\cdot K^{-1}}$. T_i refers to the indoor design temperature and equals to 18°C. To meet the requirement of thermal load, the fluid temperature in the heat exchangers should match the following condition:

$$T_{he} = T_i + \frac{Q_h}{(UA)_{he}}, \tag{4}$$

where $(UA)_{he}$ refers to the heat transfer rate of the heat exchangers under unit temperature difference and equals to $13887.5\,\mathrm{W\cdot K^{-1}}$. The flow rate of the heating system when opened is $9\,\mathrm{kg\cdot s^{-1}}$, that is, $\dot{M}_h = 9\,\mathrm{kg\cdot s^{-1}}$. When $T_{hi} \geq T_{he}$, the hot water is used for heating directly. When $288\,\mathrm{K} < T_{hi} < T_{he}$, the heat pump is opened and its COP [8] is defined as

$$\mathrm{COP} = \frac{T_{hi} - 173}{70}\ln\left(\frac{T_{he}}{T_{he} - T_{hi}}\right) + \frac{308 - T_{he}}{40}. \tag{5}$$

When $T_{hi} \leq 288\,\mathrm{K}$, the heating system is closed.

3. Introduction of Three Different Computational Methods

Introductions will be made, respectively, on the accurate numerical method, the temperature stratification method, and the uniform temperature method as follows.

3.1. Accurate Numerical Method. In the accurate numerical method, the governing equations are given based on the fluid flow and heat transfer in the water tank and the coupled heat transfer between the water tank and the surrounding soil, and the collection system and the heating system are given as boundary conditions. Due to the symmetry of the structure, this paper applies one-quarter of the water tank and the surrounding soil as computational domain, as shown in Figure 2. The distance from the water tank bottom to the boundary $A'B'C'D'$ is 10 m, and the distances from the water tank sides to the boundaries $AA'B'B$ and $BB'C'C$ are, respectively, 15 m.

The governing equations are given based on the assumptions which are laminar, incompressible, and constant properties.

Continuity equation:

$$\nabla \cdot \vec{u} = 0. \tag{6}$$

Momentum equation:

$$\frac{\partial(\vec{u})}{\partial t} + \vec{u} \cdot \nabla \vec{u} = -\frac{1}{\rho}\nabla p + \nabla \cdot (\nu \nabla \vec{u}) - \alpha (T - T_c)\vec{g}. \tag{7}$$

Energy equation:

$$\frac{\partial(T)}{\partial t} + \vec{u} \cdot \nabla T = \nabla \cdot (a \nabla T). \tag{8}$$

Here, the Boussinesq assumption [13] is adopted to deal with the buoyancy force term in the momentum equation.

Solar radiation intensity, outdoor temperature, and outdoor wind speed are obtained from the meteorological data of Beijing. The heating period of Beijing is from November 15 to March 15. This paper selects the time 00:00 on March 16 as the starting time of the computation. The initial temperature in the surrounding soil is calculated according to the following formula [14]:

$$T(h) = 12.9e^{-0.3h}\cos(0.3h - 4.13) + 287. \tag{9}$$

The initial temperature and the initial velocity in the water tank are set as 288 K and 0 m/s, respectively.

The velocity boundary condition at the water inlet of the collection system is

$$v_{ci} = \frac{\dot{M}_c}{(\rho A_{ci})}. \tag{10}$$

The temperature boundary condition is

$$\frac{\partial T_{ci}}{\partial \vec{n}} = 0. \tag{11}$$

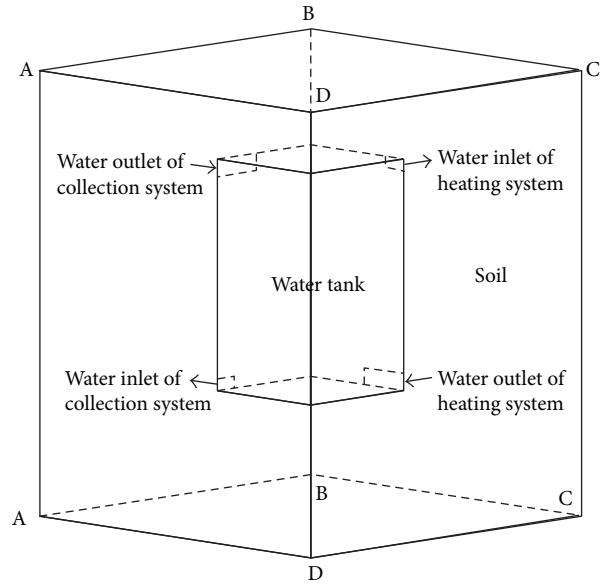

Figure 2: Computational domain of the SHS-SWTHS used for the accurate numerical method.

The velocity boundary condition at the water outlet of the collection system is

$$v_{co} = \frac{\dot{M}_c}{(\rho A_{co})}. \tag{12}$$

The temperature boundary condition is

$$T_{co} = T_{ci} + \frac{Q_c}{(C_p \dot{M}_c)}. \tag{13}$$

The velocity boundary condition at the water inlet of the heating system is

$$v_{hi} = \frac{\dot{M}_h}{(\rho A_{hi})}. \tag{14}$$

The temperature boundary condition is

$$\frac{\partial T_{hi}}{\partial \vec{n}} = 0. \tag{15}$$

The velocity boundary condition at the water outlet of the heating system is

$$v_{ho} = \frac{\dot{M}_h}{(\rho A_{ho})}. \tag{16}$$

The temperature boundary condition is:

$$T_{ho} = \begin{cases} T_{hi} - \dfrac{Q_h}{C_p \dot{M}_h} & T_{hi} \geq T_{he} \\ T_{hi} - \dfrac{Q_h (\mathrm{COP} - 1)/\mathrm{COP}}{C_p \dot{M}_h} & T_{hi} < T_{he}. \end{cases} \tag{17}$$

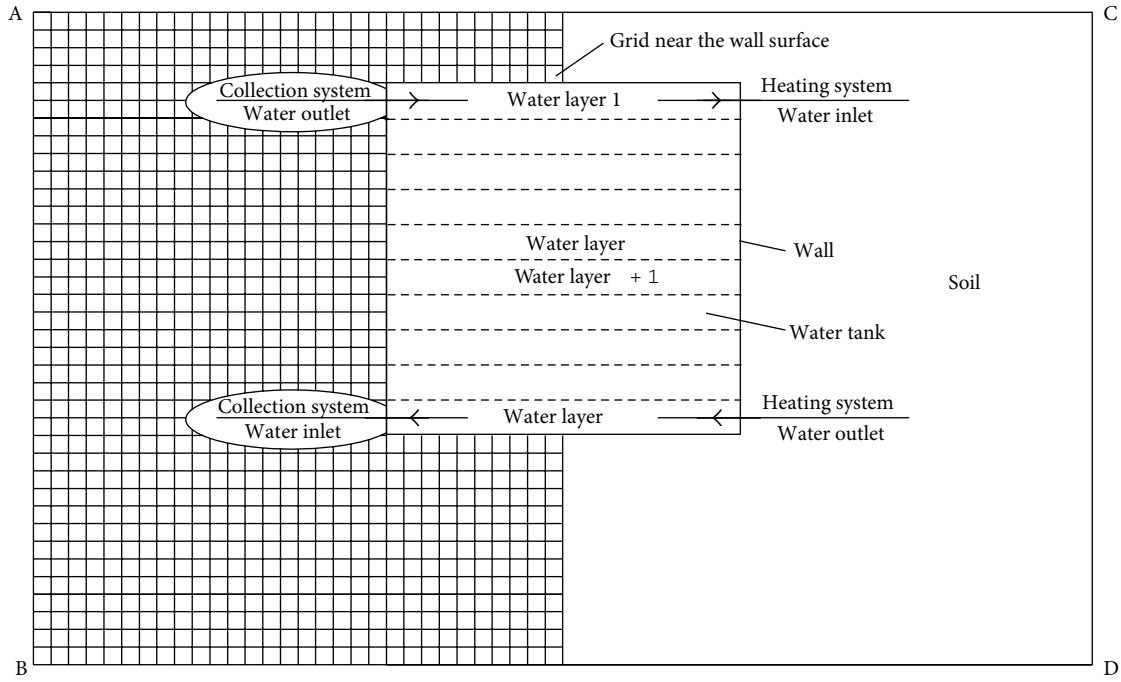

Figure 3: Computational domain of the SHS-SWTHS used for the temperature stratification method.

The temperature boundary condition at the soil surface ABCD [10] is

$$-\lambda \frac{\partial T_s}{\partial \vec{n}} = h_s \left(T_s - T_a\right) = \left(5.7 + 3.8 v_s\right) \times \left(T_s - T_a\right). \quad (18)$$

The temperature at the soil bottom $A'B'C'D'$ is 288 K. The temperature boundary conditions at $AA'D'D$, $DD'C'C$, $AA'B'B$, and $BB'C'C$ are symmetrical boundary conditions.

This paper uses the implicit and unsteady solver with double precision for the solution of the system of governing equations [15]. The momentum and energy equations are discretized using the second-order upwind scheme, pressure equation by body force weighted scheme. The discretized equations are solved using the PISO algorithm. The time step is set as 900 s.

3.2. Temperature Stratification Method. The temperature stratification method is established based on the multinode model. The water tank is stratified uniformly into N layers. The water temperature in the same layer is uniform, while the temperatures in different layers are different. Then the computations are made based on this assumption. Figure 3 shows the computational domain of the SHS-SWTHS. For convenience, only central sectional view is given herein. The computational process consists of two steps. Step 1: calculate the temperatures in different layers of the water tank; Step 2: calculate the temperature distribution in the surrounding soil. The computational process is detailed as follows.

Step 1. Calculate the temperatures in different layers of the water tank.

The flow rate of the collection system is

$$\dot{m}_c = \begin{cases} \dot{M}_c & \text{When opened} \\ 0 & \text{When closed.} \end{cases} \quad (19)$$

The flow rate of the heating system is

$$\dot{m}_h = \begin{cases} \dot{M}_h & \text{When opened} \\ 0 & \text{When closed.} \end{cases} \quad (20)$$

The total flow rate of the collection and heating systems is given as $\dot{m} = \dot{m}_c - \dot{m}_h$.

The energy conservation expression in layer 1 of the water tank is given as follows:

$$\begin{aligned} & m_1 C_{p,w} \frac{T_1^{n+1} - T_1^n}{\delta t} \\ & = \dot{m}_c C_{p,w} T_{co}^n - \dot{m}_h C_{p,w} T_1^n \\ & \quad - \left\{ \dot{m} C_{p,w} T_1^n \ (\text{when } \dot{m} > 0) ; \dot{m} C_{p,w} T_2^n \ (\text{when } \dot{m} < 0) \right\} \\ & \quad + \lambda_w A_w \frac{T_2^n - T_1^n}{d_l} + \sum_{j \in W_1} \lambda_s A_{g,j} \frac{T_{g,j}^n - T_1^n}{d_{g,j}}. \end{aligned} \quad (21)$$

The term of the left side of (21) represents the heat change in layer 1 during the time interval δt. The first term of the right side represents the heat inflow from the collection system to layer 1. The second term of the right side represents the heat outflow from layer 1 to the heating system. The third term of the right side represents the heat outflow from layer 1 to

layer 2 if $\dot{m} > 0$, or refers to the heat inflow from layer 2 to layer 1 if $\dot{m} < 0$. The fourth term of the right side represents the heat conducted from the layer 2 to the layer 1. The last term of the right side represents the heat conducted from the surrounding soil to layer 1, where W_1 refers to the wall surface contacting with layer 1.

The energy conservation expression in the intermediate layer I $(1 < I < N)$ of the water tank is described as follows:

$$\begin{aligned} m_I C_{p,w} \frac{T_I^{n+1} - T_I^n}{\delta t} &= \left\{ \dot{m} C_{p,w} \left(T_{I-1}^n - T_I^n\right) \text{ (when } \dot{m} > 0); \right. \\ &\quad \left. \dot{m} C_{p,w} \left(T_{I+1}^n - T_I^n\right) \text{ (when } \dot{m} < 0) \right\} \\ &\quad + \lambda_w A_w \frac{T_{I-1}^n - T_I^n}{d_l} + \lambda_w A_w \frac{T_{I+1}^n - T_I^n}{d_l} \\ &\quad + \sum_{j \in W_I} \lambda_s A_{g,j} \frac{T_{g,j}^n - T_I^n}{d_{g,j}}. \end{aligned} \tag{22}$$

The energy conservation expression in the last layer N of the water tank is described as follows:

$$\begin{aligned} m_N C_{p,w} \frac{T_N^{n+1} - T_N^n}{\delta t} &= -\dot{m}_c C_{p,w} T_N^n + \dot{m}_h C_{p,w} T_{ho}^n \\ &\quad + \left\{ \dot{m} C_{p,w} T_{N-1}^n \text{ (when } \dot{m} > 0); \dot{m} C_{p,w} T_N^n \text{ (when } \dot{m} < 0) \right\} \\ &\quad + \lambda_w A_w \frac{T_{N-1}^n - T_N^n}{d_l} + \sum_{j \in W_N} \lambda_s A_{g,j} \frac{T_{g,j}^n - T_N^n}{d_{g,j}}. \end{aligned} \tag{23}$$

The initial temperature in the water tank is set as 288 K.

Step 2. Calculate the temperature distribution in the surrounding soil.

The temperature distribution in the surrounding soil can be obtained by solving the following energy equation:

$$\frac{\left(T^{n+1} - T^n\right)}{\delta t} = \nabla \cdot \left(a \nabla T^{n+1}\right). \tag{24}$$

The initial temperature in the surrounding soil is computed according to (9). The temperature boundary condition at the soil surface AC is described as (18). The temperature at the wall surface of the water tank is T_I, which may be calculated according to Step 1. The temperature at the soil bottom BD is 288 K. The temperature boundary conditions at AB and CD are symmetric boundary conditions.

3.3. Uniform Temperature Method. The uniform temperature method is a special case of the temperature stratification method. When the layer number $N = 1$, the temperature stratification method can be seen as the uniform temperature method.

Table 1: Thermal properties of two typical soils.

Soil type	Density ($\text{kg} \cdot \text{m}^{-3}$)	Specific heat ($\text{J} \cdot \text{m}^{-3} \cdot \text{K}^{-1}$)	Thermal conductivity ($\text{W} \cdot \text{m}^{-1} \cdot \text{K}^{-1}$)
Granite	2640	2.14×10^6	3
Sand	1500	1.20×10^6	0.3

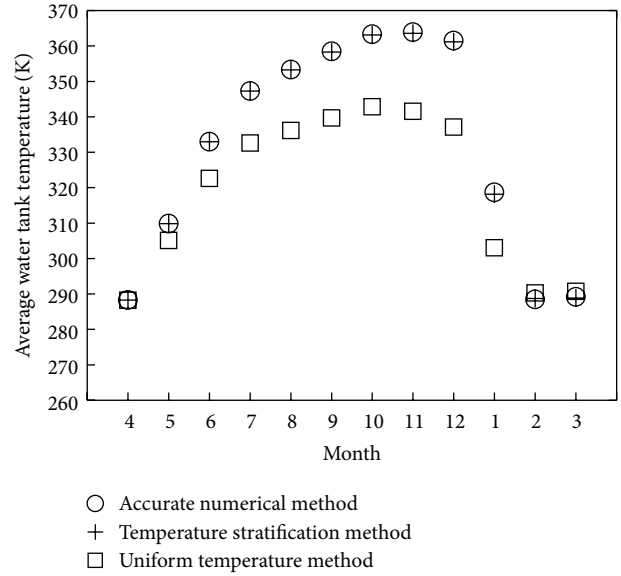

Figure 4: Monthly average water tank temperature computed by three different methods.

4. Comparison and Analysis of Three Different Computational Methods

This paper compares and analyzes the accurate numerical method, the temperature stratification method ($N = 10$), and the uniform temperature method. Here, the soil type is sand and its thermal properties are detailed in Table 1. The collection area is 1200 m^2; the embedded depth of water tank is 2 m; and the thickness of thermal insulation material is zero.

The accurate numerical method can accurately predict the performance of the SHS-SWTHS, but it takes about 4 to 5 weeks, which is too long and hard for the performance analysis of this system.

As shown in Figure 4, the average water tank temperature computed by the temperature stratification method is basically consistent with that of the accurate numerical method. As shown in Table 2, the error of the yearly heat loss of the water tank is 5.1% compared with the accurate numerical method. The error of the yearly collection efficiency is 0.3%. The error of the yearly solar fraction is 0.3%. Here, the solar fraction equals to the ratio of the heat provided by the system over the thermal load of the building. The computation results agree very well with the accurate numerical method. Therefore, the accuracy of the computation results by the thermal stratification method is high. Meanwhile, the computation time is short, which is about 2 to 3 hours. Therefore,

Table 2: Yearly computation results calculated by three different methods.

Method	Yearly heat loss of water tank (10^{11} J)	Yearly collection efficiency (%)	Yearly solar fraction (%)
Accurate numerical method	2.15	34.3	69.8
Temperature stratification method	2.26	34.2	69.6
Uniform temperature method	7.89	41.5	64.6

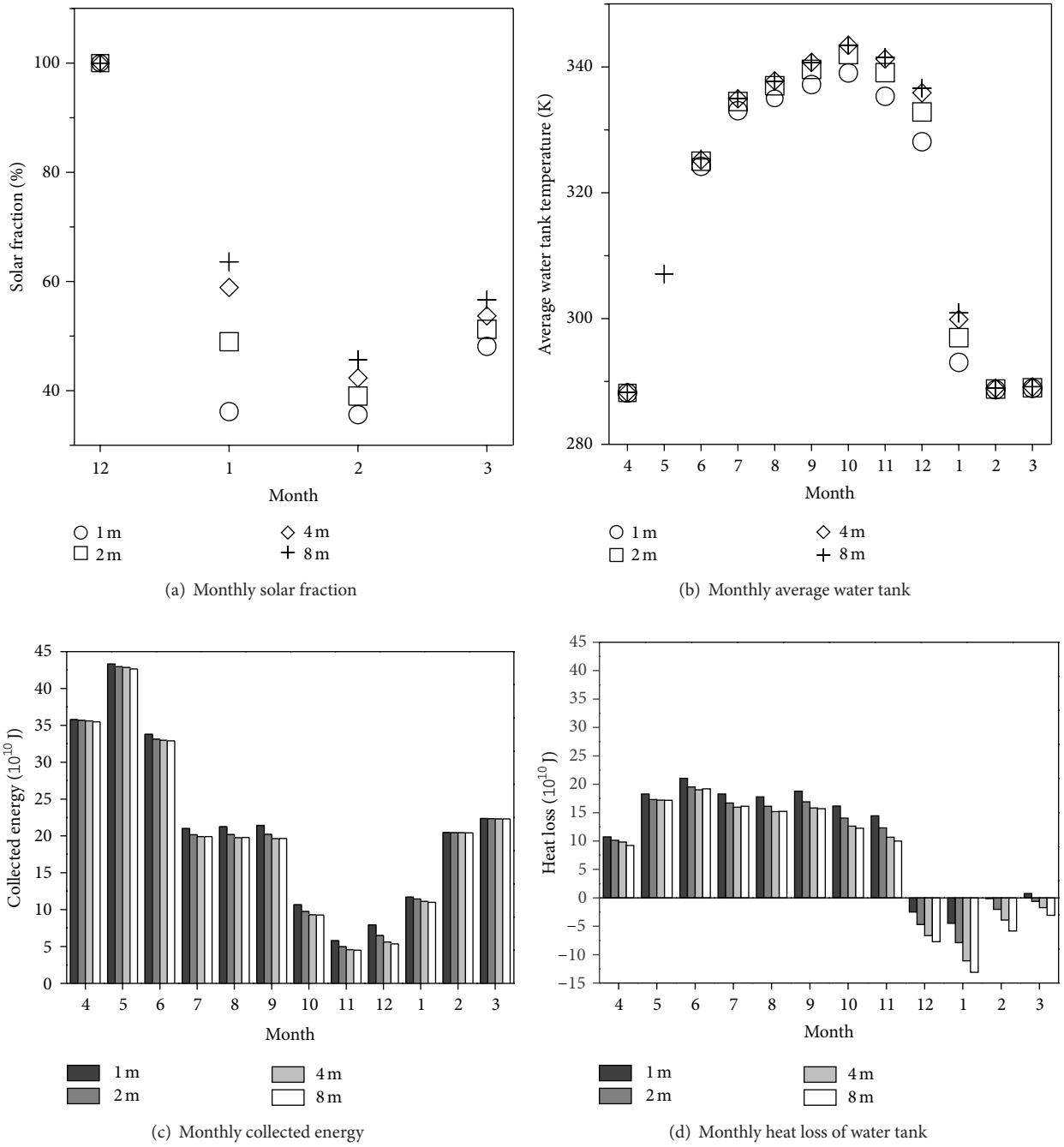

(a) Monthly solar fraction

(b) Monthly average water tank

(c) Monthly collected energy

(d) Monthly heat loss of water tank

Figure 5: Influences of different embedded depths of water tank on the system performance in granite soil.

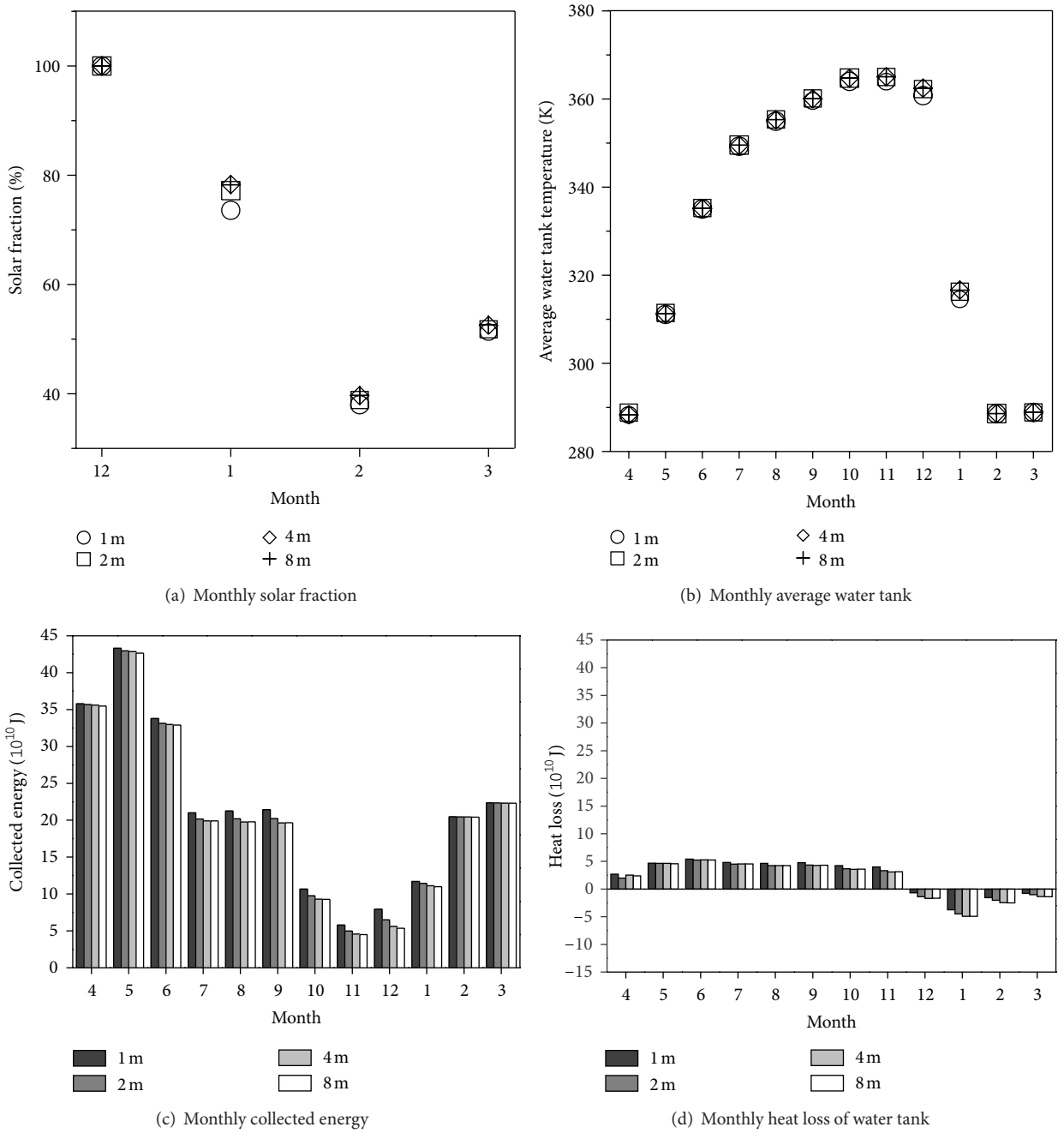

(a) Monthly solar fraction

(b) Monthly average water tank

(c) Monthly collected energy

(d) Monthly heat loss of water tank

Figure 6: Influences of different embedded depths of water tank on the system performance in sand soil.

this method is optimal for the performance analysis of this system.

The average water tank temperature computed by the uniform temperature method is lower than that by the accurate numerical method. The difference is great with the maximum value as high as 24.38 K, as shown in Figure 4. The error of the yearly heat loss is as high as 267.0% compared with the accurate numerical method. The error of the yearly collection efficiency is 21.0%. The error of the yearly solar fraction is 7.4%, as shown in Table 2. Therefore, the deviations of the computation results by the uniform temperature method are great. Meanwhile, the computation time is similar to that of the temperature stratification method. Therefore, it is not recommended in this paper.

5. Performance Analysis on SHS-SWTHS

Based on the above analysis, the temperature stratification method is applied to analyze the influence of the embedded depth of water tank, the thickness of thermal insulation material, and the collection area on the performance of the SHS-SWTHS.

5.1. Influence of the Embedded Depth of Water Tank. The influence mechanism of the embedded depth of water tank is researched based on two typical soils: granite and sand. The corresponding thermal properties of these two soils are shown in Table 1. In this system, the collection area is 1200 m^2 and the thickness of thermal insulation material is zero.

5.1.1. Granite Soil. Figure 5 shows the influences of different embedded depths on the monthly solar fraction, the monthly average water tank temperature, the monthly collected energy, and the monthly heat loss of water tank in granite soil. Here, the months shown in Figure 5 are different from the actual months. For example, April shown in this figure refers to the period from March 16th to April 15th. Thus, the period from April to November may be defined as nonheating period, and the period from December to next March may be defined as heating period. For convenience, the heat conducted from the water tank to the soil is named the heat loss of water tank, while the heat conducted from the soil to the water tank is named the reverse heat conduction of water tank hereinafter. When the temperature of the water tank is lower than that of the surrounding soil, the heat loss of water tank is negative; in other words, the reverse heat conduction of water tank is positive.

In the first month of heating period, that is, December, the monthly solar fraction as a constant of 100% is not influenced by the embedded depth of water tank, as shown in Figure 5(a). The reason is that, in the first month of heating period, the heat provided by the system comes from the heat stored in the water tank, the heat collected at the current month, and the reverse heat conduction of water tank. For the four different embedded depths of water tank, the heat of the abovementioned three parts is greater than the thermal load of the building at the current month. Therefore, the thermal load may be guaranteed.

In the second month of heating period, that is, January, the monthly solar fraction is lower than 100%, as shown in Figure 5(a). The reason is that after the heating for the first month of heating period, the temperature in the water tank is dramatically decreased. The stored heat as well as the collected heat and the reverse heat conduction cannot meet the thermal load of the building at the current month. According to Figure 5(a), with the increment of the embedded depth of water tank, the solar fraction is increased gradually. The reason is that the average water tank temperature and the reverse heat conduction increase with the increment of the embedding depth, as shown in Figures 5(b) and 5(d).

In the third and fourth months of heating period, that is, February and March, the monthly average water tank temperatures are both equal to the lowest temperature 288 K set by the system, as shown in Figure 5(b). The stored heat is zero, and the heat provided by the system only comes from the collected heat and the reverse heat conduction. Though the collected heats at different embedded depths are the same (as shown in Figure 5(c)), the reverse heat conduction increases with the increment of the embedded depth. Therefore, the solar fractions of February and March are increased with the increment of the embedded depth, as shown in Figure 5(a).

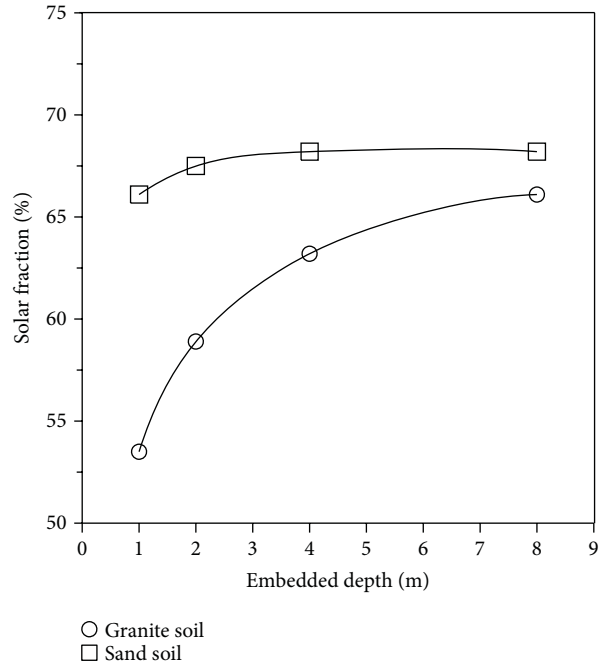

Figure 7: Yearly solar fractions at different embedded depths of water tank.

Generally, due to high thermal conductivity and heat capacity of granite soil, the heat loss of water tank is great and is influenced greatly by the embedded depth, as shown in Figure 5(d). With the increment of the embedded depth, the heat loss of water tank in nonheating period is decreased and the reverse heat conduction in heating period is increased. With the joint effect of these two factors, the solar fraction is increased gradually with the increment of embedded depth.

5.1.2. Sand Soil. Figure 6 shows the influences of different embedded depths of water tank on the monthly solar fraction, the monthly average water tank temperature, the monthly collected energy, and the monthly heat loss of water tank in sand soil. Due to low thermal conductivity and heat capacity of sand soil, the heat loss of water tank is little and nearly is not influenced by the embedded depth, as shown in Figure 6(d). As a result, the influence of the embedded depth on the solar fraction is quite little, which almost remains unchanged.

5.1.3. Influence of Embedded Depth on Yearly Solar Fraction. Figure 7 shows the yearly solar fractions at different embedded depths of water tank based on two typical soils: granite and sand. Due to different thermal conductivities and specific heats, the influences of the embedded depths on the system performance are also different. In granite soil, the yearly solar fraction is increased with the increment of the embedded depth; however, the increasing amplitudes are lowered gradually. When the embedded depth is increased from 1 m to 8 m, the yearly solar fraction is increased by 23.6%. In sand soil, the influence of the embedded depth on

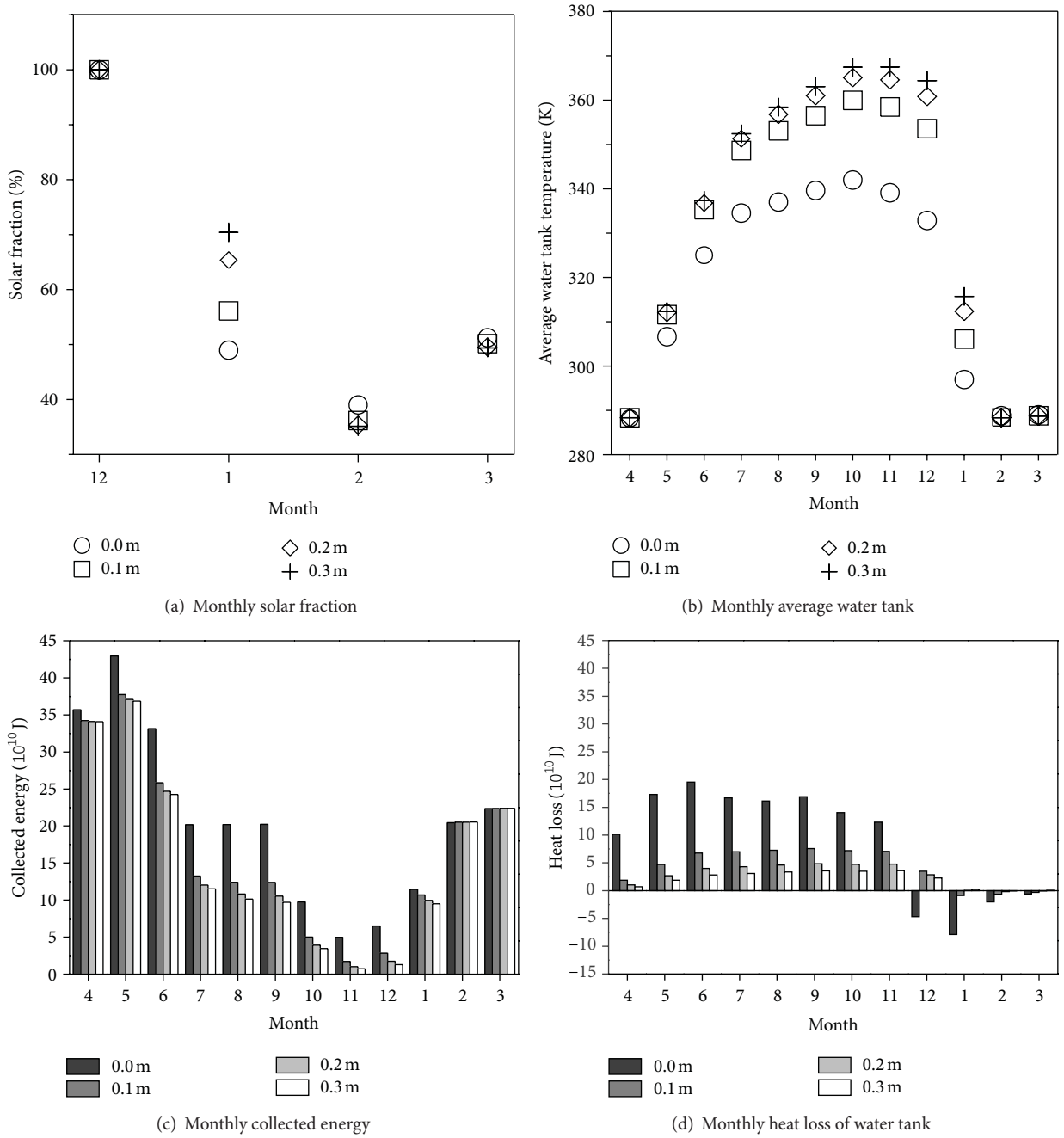

(a) Monthly solar fraction

(b) Monthly average water tank

(c) Monthly collected energy

(d) Monthly heat loss of water tank

Figure 8: Influences of different thicknesses of thermal insulation material on the system performance in granite soil.

the yearly solar fraction is quite little. When the embedded depth is increased from 1 m to 8 m, the yearly solar fraction is only increased by 3.2%. In addition, according to Figure 7, with the increment of the embedded depth, the yearly solar fractions in different soils tend to be consistent.

5.2. Influence of the Thickness of Thermal Insulation Material. The influence mechanism of the thickness of thermal insulation material is researched based on two typical soils: granite and sand. Glass wool is applied as the thermal insulation material. Its density is $135\,\mathrm{kg}\cdot\mathrm{m}^{-3}$, its specific heat is $1.8 \times 10^5\,\mathrm{J}\cdot\mathrm{m}^{-3}\cdot\mathrm{K}^{-1}$, and its thermal conductivity is $0.045\,\mathrm{W}\cdot\mathrm{m}^{-1}\cdot\mathrm{K}^{-1}$. In this system, the collection area is $1200\,\mathrm{m}^2$ and the embedded depth of water tank is 2 m.

5.2.1. Granite Soil. Figure 8 shows the influences of different thicknesses of thermal insulation material on the monthly solar fraction, the monthly average water tank temperature, the monthly collected energy, and the monthly heat loss of water tank in granite soil. Due to high thermal conductivity and heat capacity of the granite soil, the heat loss of water tank is great, which leads to great influence of the thickness

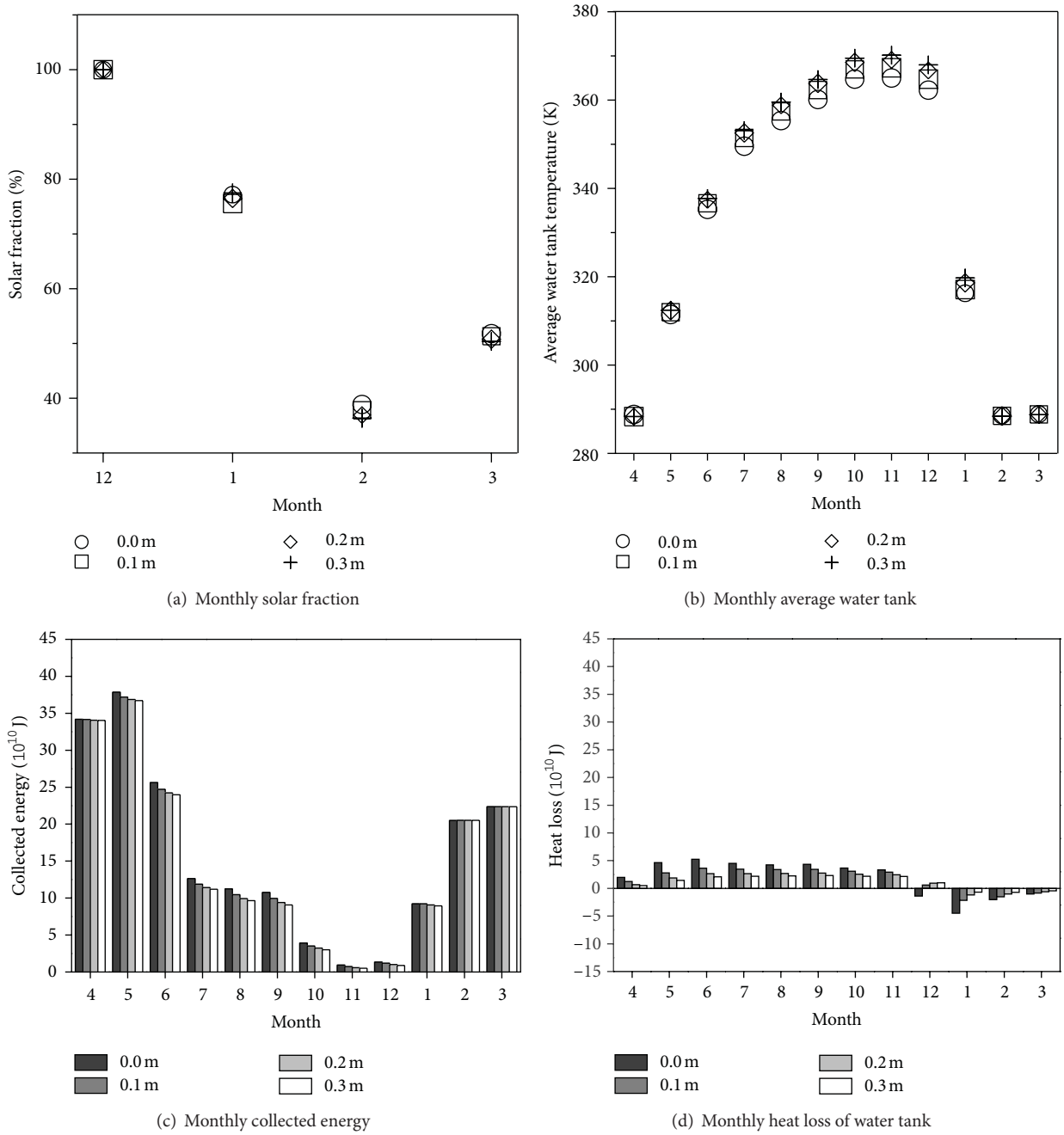

(a) Monthly solar fraction

(b) Monthly average water tank

(c) Monthly collected energy

(d) Monthly heat loss of water tank

Figure 9: Influences of different thicknesses of thermal insulation material on the system performance in sand soil.

of thermal insulation material on the system performance. During the nonheating period, with the increment of the thickness of thermal insulation material, the heat loss of water tank is lowered gradually, leading to gradual increment of the water tank temperature. This factor is favorable to improve the solar fraction. During the heating period, with the increment of the thickness of thermal insulation material, the reverse heat conduction is lowered gradually; in other words, the heat conducted from the soil to the water tank is lowered gradually. This factor is of no good to improve the solar fraction. Compared with the heat loss during the nonheating period, the reverse heat conduction during the heating period is relatively lower. Therefore, the first factor is dominant. Generally, for granite soil, with the increment of the thickness of thermal insulation material, the solar fraction is increased gradually, as shown in Figures 8(a) and 10.

5.2.2. Sand Soil. Figure 9 shows the influences of different thicknesses of thermal insulation material on the monthly solar fraction, the monthly average water tank temperature, the monthly collected energy, and the monthly heat loss

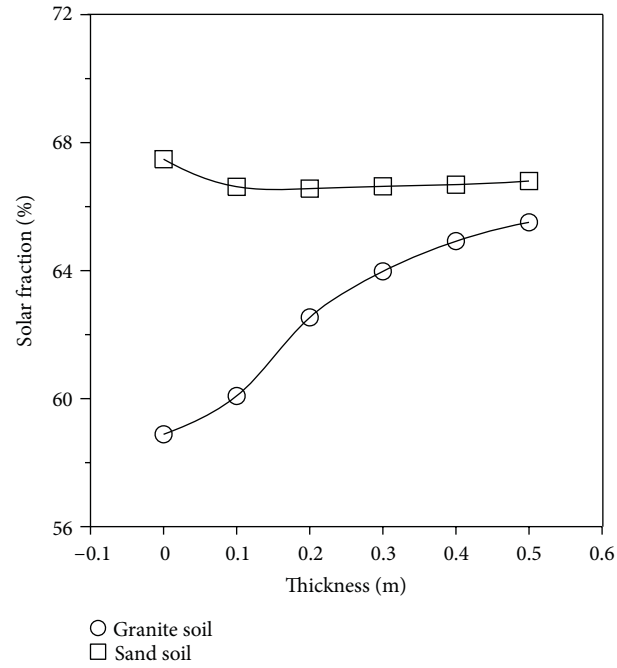

Figure 10: Yearly solar fractions at different thicknesses of thermal insulation material.

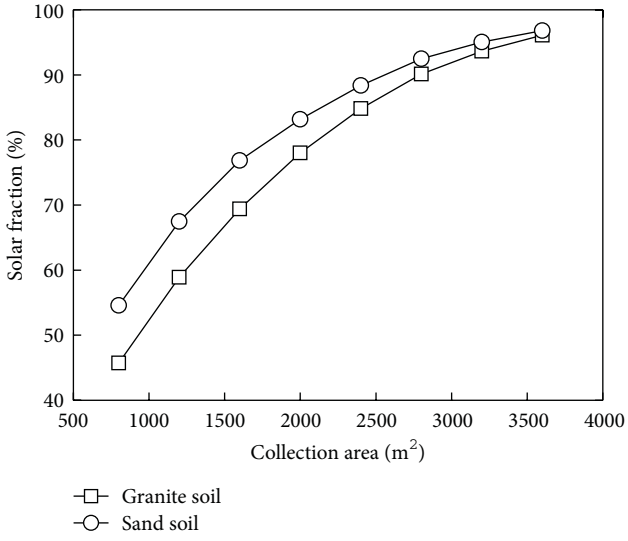

Figure 11: Influences of the collection area on the system performance.

of water tank in sand soil. Due to low thermal conductivity and heat capacity of sand soil, the heat loss of water tank is little. Meanwhile, due to the existence of the reverse heat conduction during the heating period, the increment of the thickness of thermal insulation material slightly decreases the solar fraction conversely, as shown in Figures 9(a) and 10.

5.2.3. Influence of Thickness of Thermal Insulation Material on Yearly Solar Fraction. Figure 10 shows the yearly solar fractions at different thicknesses of thermal insulation material based on two typical soils: granite and sand. Due to different thermal conductivities and specific heats, the influences of the thicknesses of thermal insulation material on system performance are also different. In granite soil, the yearly solar fraction is increased with the increment of the thickness of thermal insulation material. When the thickness is increased from 0 m to 0.5 m, the yearly solar fraction is increased by 11.2%. Therefore, for the granite soil, the thermal insulation material with certain thickness should be laid to reduce the heat loss and increase the heat storage of the system. In sand soil, the influence of the thickness of thermal insulation material on the yearly solar fraction is quite little. Due to the existence of the reverse heat conduction during the heating period, the increment of the thickness slightly decreases the solar fraction conversely. When the thickness is increased from 0 m to 0.1 m, the yearly solar fraction is lowered by 1.2%, and further increment of the thickness bears hardly any influence on the system performance.

5.3. Influence of the Collection Area. The influences of the collection area on the system performance are also researched based on two typical soils: granite and sand. In this system, the embedded depth of water tank is 2 m and no thermal insulation material is applied. As an important influence factor, the collection area bears relatively great influence on the system performance. Figure 11 shows the influences of the collection area on the yearly solar fraction in two different soil conditions. The solar fraction of sand soil is greater than that of granite soil. With the increment of collection area, their solar fractions are increased gradually. However, the degree of growth is reduced gradually. When the collection area reaches 3200 m^2, the solar fractions of both soil types are basically the same. At this point, the soil type has no influence on the system performance.

6. Conclusion

In this paper we analyze and compare three different computational methods for the SHS-SWTHS, including the accurate numerical method, the temperature stratification method, and the uniform temperature method. The following conclusions can be obtained.

(1) The accurate numerical method can accurately predict the performance of the system, but it takes about 4 to 5 weeks, which is too long and hard for the performance analysis of this system.

(2) The temperature stratification method provides relatively accurate computation results and takes relatively short computation time, which is about 2 to 3 hours. Therefore, this method is most suitable for the performance analysis of this system.

(3) The deviation of the computational results of the uniform temperature method is great, and the time consumed is similar to that of the temperature

stratification method. Therefore, this method is not recommended herein.

Based on the above analysis and comparison, this paper applies the temperature stratification method to research the influences of the embedded depth of water tank, the thickness of thermal insulation material, and the collection area on the performance of the SHS-SWTHS and reaches the conclusions as follows.

(1) For granite soil, due to high thermal conductivity and heat capacity, the heat loss of water tank is great and is influenced greatly by the embedded depth. With the increment of the embedded depth, the heat loss of water tank in nonheating period is reduced and the reverse heat conduction in heating period is increased. With the joint effect of these two factors, the solar fraction is increased gradually with the increment of the embedded depth. When the embedded depth is increased from 1 m to 8 m, the yearly solar fraction is increased by 23.6%. For sand soil, due to low thermal conductivity and heat capacity, the heat loss of water tank is little and nearly is not influenced by the embedded depth. When the embedded depth is increased from 1 m to 8 m, the yearly solar fraction is only increased by 3.2%.

(2) For granite soil, with the increment of the thickness of thermal insulation material, on one hand, the heat loss of water tank during the nonheating period is lowered gradually, and on the other hand, the reverse heat conduction of water tank during the heating period is also reduced gradually. The influences of these two factors on the system performance are opposite. Compared with the heat loss in the nonheating period, the reverse heat conduction in the heating period is relatively less, leading to the increase of the yearly solar fraction with the increment of the thickness. When the thickness is increased from 0 m to 0.5 m, the yearly solar fraction is increased by 11.2%. For sand soil, due to the existence of the reverse heat conduction during the heating period, the increment of the thickness slightly lowers the solar fraction conversely. When the thickness is increased from 0 m to 0.1 m, the yearly solar fraction is lowered by 1.2%, and further increment of the thickness bears hardly any influence on the system performance.

(3) With the increment of the collection area, the solar fractions of granite soil and sand soil are increased. However, the degree of growth is reduced gradually. When the collection area reaches 3200 m^2, the solar fractions of both soil types are basically the same. At this point, the soil type has no influence on the system performance.

The above-mentioned researches provide a design basis for the related demonstration projects.

Nomenclature

a: Thermal diffusion coefficient, $m^2 \cdot s^{-1}$
A_c: Collection area, m^2
A_{ci}: Inlet area of the collection system, m^2
$A_{g,j}$: Cross section area of the grid j, m^2
A_{co}: Outlet area of the collection system, m^2
A_{hi}: Inlet area of the heating system, m^2
A_{ho}: Outlet area of the heating system, m^2
A_w: Cross section area of the water tank, m^2
COP: Coefficient of performance of the heat pump
C_p: Specific heat, $J \cdot kg^{-1} \cdot K^{-1}$
$d_{g,j}$: Distance from the center of grid j to the wall surface of water tank, m
d_l: Layer thickness, m
$\vec{g}$: Gravity acceleration, $m \cdot s^{-2}$
h: Soil depth, m
h_s: Heat transfer coefficient at the soil surface, $W \cdot K^{-1}$
I_t: Solar radiation intensity, $W \cdot m^{-2}$
m: Mass, kg
$\dot{m}$: Total flow rate of the collection and heating systems, $kg \cdot s^{-1}$
$\dot{m}_c$: Flow rate of the collection system, $kg \cdot s^{-1}$
$\dot{M}_c$: Flow rate of the collection system when opened, $kg \cdot s^{-1}$
$\dot{m}_h$: Flow rate of the heating system, $kg \cdot s^{-1}$
$\dot{M}_h$: Flow rate of the heating system when opened, $kg \cdot s^{-1}$
p: Pressure, Pa
Q_c: Collected energy, J
Q_h: Thermal load, J
t: Time, s
T: Temperature, K
T_a: Ambient air temperature, K
T_c: Reference temperature, K
T_{ci}: Inlet temperature of the collection system, K
$T_{g,j}$: Temperature at the grid j, K
T_{co}: Outlet temperature of the collection system, K
T_{he}: Fluid temperature in the heat exchanger, K
T_{hi}: Inlet temperature of the heating system, K
T_{ho}: Outlet temperature of the heating system, K
T_i: Indoor design temperature, K
T_s: Soil surface temperature, K
$\vec{u}$: Velocity, $m \cdot s^{-1}$
v_{ci}: Inlet velocity of the collection system, $m \cdot s^{-1}$
v_{co}: Outlet velocity of the collection system, $m \cdot s^{-1}$
v_{hi}: Inlet velocity of the heating system, $m \cdot s^{-1}$
v_{ho}: Outlet velocity of the heating system, $m \cdot s^{-1}$
v_s: Wind speed, $m \cdot s^{-1}$
α: Expansion coefficient, K^{-1}
δt: Time interval, s
η_c: Collection efficiency
λ: Conductivity coefficient, $W \cdot m^{-1} \cdot K^{-1}$
ρ: Density, $kg \cdot m^{-3}$
ν: Kinematic viscosity, $m^2 \cdot s^{-1}$.

Subscript

1: Layer 1
2: Layer 2
I: Layer I
N: Layer N
j: Number of the grid near the wall surface on the soil side
s: Soil
w: Water.

Superscript

n: Current time layer
$n + 1$: Next time layer.

Conflict of Interests

Dongliang Sun, Jinliang Xu, and Peng Ding declare that the paper does not have any conflict of interests including any financial, personal, or other relationships with other people or organizations.

Acknowledgments

This work was supported by the Young Scientists Fund of the National Natural Science Foundation of China (51106049), the Beijing Natural Science Foundation (3112022), the Hebei Natural Science Foundation (E2011502057), the National Basic Research Program of China (2011CB710703), the Fundamental Research Funds for the Central Universities (12MS44), and the 111 Project (B12034).

References

[1] T. Schmidt, D. Mangold, and H. Muller-Steinhagen, "Central solar heating plants with seasonal storage in Germany," *Solar Energy*, vol. 76, no. 1–3, pp. 165–174, 2004.

[2] Q. Qi, S. Deng, and Y. Q. Jiang, "A simulation study on a solar heat pump heating system with seasonal latent heat storage," *Solar Energy*, vol. 82, no. 8, pp. 669–675, 2008.

[3] D. Pahud, "Central solar heating plants with seasonal duct storage and short-term water storage: design guidelines obtained by dynamic system simulations," *Solar Energy*, vol. 69, no. 6, pp. 495–509, 2000.

[4] H. O. Paksoy, O. Andersson, S. Abaci, H. Evliya, and B. Turgut, "Heating and cooling of a hospital using solar energy coupled with seasonal thermal energy storage in an aquifer," *Renewable Energy*, vol. 19, no. 1-2, pp. 117–122, 2000.

[5] M. Pfeil and H. Koch, "High performance-low cost seasonal gravel/water storage pit," *Solar Energy*, vol. 69, no. 6, pp. 461–467, 2000.

[6] S. Raab, D. Mangold, W. Heidemann, and H. Muller-Steinhagen, *Solar Assisted District Heating System with Seasonal Hot Water Heat Store in Friedrichshafen*, Euro-Sun, Freiburg, Germany, 2004.

[7] S. Raab, D. Mangold, and H. Muller-Steinhagen, "Validation of a computer model for solar assisted district heating systems with seasonal hot water heat store," *Solar Energy*, vol. 79, no. 5, pp. 531–543, 2005.

[8] R. Yumrutas and M. Unsal, "A computational model of a heat pump system with a hemispherical surface tank as the ground heat source," *Energy*, vol. 25, no. 4, pp. 371–388, 2000.

[9] R. Yumrutas and M. Unsal, "Analysis of solar aided heat pump systems with seasonal thermal energy storage in surface tanks," *Energy*, vol. 25, no. 12, pp. 1231–1243, 2000.

[10] A. Ucar and M. Inalli, "A finite element model of solar heating system with underground storage," *International Journal of Thermal Sciences*, vol. 47, no. 12, pp. 1639–1646, 2008.

[11] M. Chung, J. U. Park, and H. K. Yoon, "Simulation of a Central Solar Heating system with Seasonal Storage in Korea," *Solar Energy*, vol. 64, no. 4–6, pp. 163–178, 1998.

[12] B. O. Nordell and G. Hellstrom, "High temperature solar heated seasonal storage system for low temperature heating of buildings," *Solar energy*, vol. 69, no. 6, pp. 511–523, 2000.

[13] D. D. Gray and A. Giorgini, "The validity of the boussinesq approximation for liquids and gases," *International Journal of Heat and Mass Transfer*, vol. 19, no. 5, pp. 545–551, 1976.

[14] J. J. Wang, Y. D. Xu, and J. N. Mao, "Influence of soil temperature field on heat transfer performance of vertical U-tube ground heat exchangers," *Chinese Journal of HV&AC*, vol. 39, pp. 89–93, 2009.

[15] W. Q. Tao, *Numerical Heat Transfer*, Xi'an Jiaotong University Press, Xi'an, China, 2nd edition, 2001.

Hindawi Publishing Corporation
Advances in Mechanical Engineering
Volume 2013, Article ID 204974, 12 pages
http://dx.doi.org/10.1155/2013/204974

Research Article

Vortex-Induced Vibrations of a Square Cylinder with Damped Free-End Conditions

S. Manzoor,[1] J. Khawar,[2] and N. A. Sheikh[3]

[1] *Department of Mechanical Engineering, University of Engineering and Technology, Taxila, Pakistan*
[2] *Beijing University of Aeronautics and Astronautics (BUAA), Beijing, China*
[3] *Department of Mechanical Engineering, Muhammad Ali Jinnah University, Islamabad, Pakistan*

Correspondence should be addressed to N. A. Sheikh; ndahmed@gmail.com

Received 28 November 2012; Accepted 28 February 2013

Academic Editor: Yi Wang

The authors report the results of vortex-induced vibrations of a square cylinder in a wind tunnel. This constitutes a high mass ratio environment. The square cylinder is mounted in the wind tunnel in such a fashion that it only performs rigid body oscillations perpendicular to the flow direction with damped free-end conditions. This physical situation allows a direct evaluation for analytical models relying on simplified 2D assumptions. The results are also compared with two-dimensional fluid-structure (CFD-CSD) numerical simulations. The comparison shows that despite having one-dimensional motion, the analytical model does not predict the VIV region with correctness. Results show that the numerical simulations and experimental results differ from the analytical model for the prediction of reduced velocity corresponding to peak amplitude. Also the analytical reduced velocity envelope is underpredicted compared to both numerical simulations and experimental data despite the structure being lightly damped. The findings are significant as the experimental results for freely oscillating high mass ratio body show differences from the low mass ratio especially in the transition between VIV and galloping regions. However the numerical simulations show comparatively close agreement.

1. Introduction

Vortex shedding excitation of a cylinder is probably one of the most studied problems in flow-induced vibrations. This mechanism, referred to as vortex-induced vibration (VIV), occurs when the vortices, developed in the wake, can couple with the dynamics of the cylinder. It can be seen roughly as a resonance mechanism appearing when the frequency of the vortex shedding, controlled by the fluid flow, is close to the natural frequency of the cylinder. However, the physics of the interaction between the flow and the cylinder transverse motion is not simply linear. Mathematical modelling for predicting the amplitude of the cylinder motion has become a widely studied problem in engineering. Wilkinson [1], Otsuki et al. [2], and Nakamura and Mizota [3] presented some experimental data on the forced oscillations of square section cylinders. Sarpkaya [4] presented a selective review of the then existing know-how about vortex-induced oscillations. Bearman and Obasaju [5] studied the pressure fluctuations on both fixed and forced oscillating square cylinders. They determined that the amplification of the fluctuating lift coefficient for a square cylinder at lock-in was much less than that of a circular cylinder subjected to similar conditions. Ongoren and Rockwell [6] have studied the effects of cylinder inclination with respect to the mean free stream, using a forced circular cylinder in a water channel. Ongoren and Rockwell [7] repeated some experiments with square and triangular cross-section cylinders. Their experimental setup involved vertically arranged cylinders subjected to low mass ratio environment. Williamson and Roshko [8] provided the mechanism of vortex formation and the underlying physics for mode shifts. Parkinson [9] resumed the phenomenology and the theoretical modelling tools available to understand the vortex-induced oscillations and the galloping instability in case of flow past bluff bodies. Brika and Laneville [10] studied a hollow slender cylinder in a wind tunnel and showed that the cylinder's steady response was hysteretic. Each branch in the hysteresis loop is associated to either the

2S or the 2P mode of vortex shedding. Abrupt change in the amplitude curve is attributed to the sudden mode shift. Govardhan and Williamson [11] presented the transverse vortex-induced oscillations of an elastically mounted rigid cylinder in a fluid flow. The authors point out that in a classical high mass ratio system the initial and lower amplitude branches can be distinctly identified due to a discontinuous mode transition. In case of lower mass ratio systems a further upper amplitude branch is clearly identifiable attributed to a second instance of mode transition. Hémon and Santi [12] submitted experimental and numerical results on the aeroelastic behavior of slender rectangular and square cylinders subjected to a cross flow. Morse and Williamson [13] discovered the $2P_{overlap}$ mode using high-resolution data from a forced oscillating cylinder at a fixed Reynolds number. Manzoor et al. [14] presented their experimental results based on the free oscillations of a square cylinder in a high mass ratio environment. Vortex shedding mode switch at the resonant velocity was identified. Hysteresis in the reduced amplitude curve was observed for one of the experimental cases. The same author has presented a possible theoretical explanation of the experimental results in Manzoor et al. [14]. The reduced-order van der Pol model proposed by Facchinetti et al. [15] was used. Distinct limitations of the van der Pol model in predicting the VIV behavior have been identified. Sen and Mittal [16] recently submitted their numerical investigation of the two dimensional behavior of a square cylinder oscillating freely in a low mass ratio environment. The authors have neglected the effect of structural damping in their study while varying the Reynolds number in the lower range.

As catalogued above, almost all of the work being reported is largely focused on forced oscillations of circular cylinders in setups with lower mass ratios generally. Experimental data on noncircular bluff bodies is obtained either with lower mass ratio configurations or with forced oscillations mechanisms. Mostly, the experimental setups demonstrate bending modes of vibration rather than rigid body motion. In this study we use an experimental setup which allows only the rigid body modes of oscillations with damped-free ends, thereby providing ground for direct testing of analytical and numerical models relying on planar kinematics. This work contributes also in the sense that we use experimental results for a more realistic configuration in comparison with the numerical simulations and analytical predictions for a practical real-life problem, civil engineering projects for example. For comparison with experimental data, analytical as well as numerical models are used to simulate the free vibration of lightly damped square section with free ends. To best of our knowledge this work is the first attempt to simulate and understand the physics of square section oscillation with free-end conditions.

The organization of this paper is as follows. First we introduce the experimental setup and the details of measurement system with details of system parameters. This is followed with experimental results along with comparison of analytical model predictions for the setup. In the next section the details of the numerical simulation model and the parameters for the coupled fluid structure interaction simulations are detailed. A detailed discussion on the comparison of numerical simulations and experimental results is also included. At the end we conclude the findings of this research paper.

2. Experimental Methods

2.1. Wind Tunnel and Flexibly Mounted Cylinder. The square cylinder has a cross-section, $D = 0.02$ m, and a span, $b = 0.15$ m. The cylinder is put in place in the test section using four linear springs mounted outside the test section. Specific chord wiring is used to restrain the cylinder such that it oscillates only transverse to the air flow executing rigid body motion. The use of linear spring mountings allows a damped free-end condition for the cylinder rather than conventional fixed and/or cantilever-type boundary conditions. Special attention is paid to keep the structural damping as low as possible. The experiment is conducted in a vertical axis Eiffel Wind Tunnel which has a closed circular test section of a diameter of 0.20 m. A centrifugal fan, downstream of the test section, is used to produce the wind stream. This free stream flow velocity can be safely assumed to be uniform over the cylinder span given the comparison between the cylinder span and the test section diameter. Mean velocity in the test section is varied from 2 m/sec to ~7 m/sec. Turbulence level of the upstream airflow is measured and found less than 1% over the velocity range during the course of this study, Amandolèse and Hémon [19].

For this experimental setup no endplates are attached to the test structure. Due to the high aspect ratio of the cylinder used in this experiment ($b/D = 7.5$), flow around the longitudinal ends can have a significant effect on the vortex dynamics, the correlation of the induced fluid forces on the body, and thus the vibrations. However the proximity of both the ends of the cylinder with the test section wall reduces the effect of the end conditions. As reported by Morse et al. [20], for a circular cylinder the vortex-induced vibrations for attached and unattached endplates are nearly the same.

2.2. Measurement System. At low flow velocity accurate measurement is always challenging. In the present case, a nozzle is mounted downstream of the test section. Using Bernoulli's theorem we calculate the airflow velocity in the test section and compare it with the flow velocity in the nozzle section. Pressure readings in the test section and the nozzle section are obtained by using pairs of static pressure taps in each section. A thermocouple is also employed for temperature correction. This technique allows us to measure low flow velocities with accuracy better than 1%, Manzoor et al. [14].

Measurements of the transversely displacement of the cylinder are obtained by a laser displacement sensor. The measurement resolution is 40 μm and the accuracy is 1% of the full scale range. Signals from the laser displacement sensors are transmitted to an acquisition system named PAK provided by Mueller-BBM. It consists of an 8-channel acquisition card of 24 bit with a signal processing software. Sampling resolution is 1024 Hz and the typical duration of data accumulation is 60 s. However this duration can be

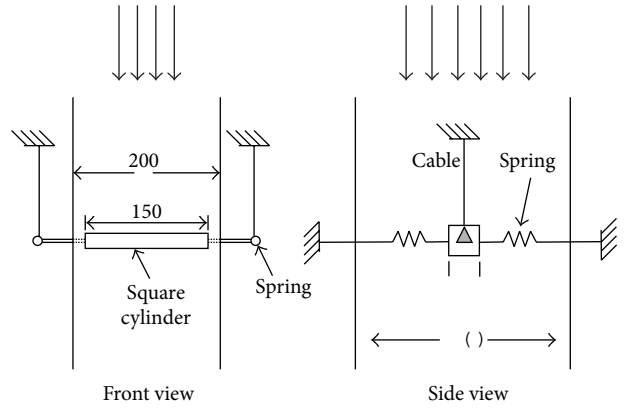

Figure 1: Sketch showing the principles of the experimental setup [14].

increased to 300 s to enable the frequency measurements of the limit cycle oscillation (LCO) of the cylinder. Increasing the time duration also enabled us to obtain a better frequency resolution of the measurements. The physical degree of freedom "z" is obtained through the recombination of the measured signals using the system kinematics, Manzoor et al. [14].

2.3. Structural Parameters of the Experiments. The structure is a rigid square cylinder with the length of the side "D". The external attachments of the cylinder makes it constrained to oscillate in a direction normal to the mean flow direction as depicted in Figure 2.

Flow is assumed to be uniform all along the cylinder length. The cross flow displacement "z" of the cylinder can be described by the standard damped linear oscillator:

$$m\ddot{z} + r\dot{z} + kz = S. \tag{1}$$

The undamped natural frequency of the system is defined as

$$f_o = \frac{1}{2\pi}\sqrt{\frac{k}{m}}. \tag{2}$$

Here structural parameters are obtained under zero cross wind velocity. The natural frequency f_z and the system damping r_s are obtained using spectral analysis; Manzoor et al. [14]. A static weight calibration technique is used to calculate the stiffness k. Mass m is then calculated using:

$$m = \frac{k}{\left(2\pi f_o\right)^2}. \tag{3}$$

The reduced velocity, U_r, is given as $U_r = U/f_o D$ and the RMS amplitude, Z^*, is given as $Z^* = z/D$. Structural supports are assumed to behave linearly throughout the amplitude envelope. Important physical parameters of the experiment are resumed in Table 1. Pertinent nondimensional parameters are also reported in Table 2. From the two tables, it is clear that the system has a high mass ratio $m^* \approx 905$ associated with a very low damping ratio $\eta \approx 0.0828\%$. Very low damping leads to a relatively small Scruton number, Sc $\approx$ 1.5 which is the key parameter in the observation of vortex shedding vibrations.

Table 1: Physical parameters of the experiments.

Diameter of the cylinder	D	20	Mm
Length of the cylinder	L	150	Mm
Stiffness of the setup	K	597.6 ± 35	N/m
Mass of the cylinder	M	0.0654 ± 0.004	Kg
Critical damping	c_c	12.5 ± 0.75	N·s/m
Structural damping	c	0.0104 ± 0.0008	N·s/m
Natural frequency	f_o	15.21875 ± 0.01563	Hz
Wind tunnel velocity	U	1.5–6.0	m/s
Air density	ρ	1.205	kg/m^3
Kinematic viscosity	ν	$15e^{-6}$	m^2/s

Table 2: Nondimensional parameters.

Reynolds number	Re	$U\ D/\nu$	2000–8000
Mass ratio	m^*	$m/\rho\ D^2\ L$	905
Damping ratio	η	c/c_c	0.000828 ± 0.000014
Scruton number	Sc	$2\eta m^*$	1.498
Strouhal number	St	$f_w\ D/U$	0.127
Skop-Griffin parameter	S_G	$4\pi^2\ \mathrm{St}^2\ \mathrm{Sc}$	0.954
Reduced velocity	U_r	$U/f_0\ D$	5–20

Unsteady wake measurements have also been performed in order to measure the Strouhal number of the cylinder at rest. Measurements were obtained using a single-component hot wire anemometer installed downstream of the square cylinder at a distance equal to one length of the cylinder side. For the system under consideration, the Strouhal number was found to be 0.127 over the velocity range of the vortex shedding oscillation regime. This is in accordance with Norberg's data for low Reynolds number, Norberg [21].

2.4. Experimental Results. Experimental results presented in Figure 3 show limit cycle oscillations (LCO) of a square cylinder measured for reduced velocity ranging from $U_r \approx 6 \approx 16$. Different symbols in the figure signify different experimental runs conducted at different times to ensure repeatability of the experimental procedure. Apart from the obvious dispersion of experimental points at higher reduced velocities we can safely assume that the resonant frequencies lie approximately in the same reduced velocity range for each experimental run. The result can be explained by the type-II frequency coalescence mechanism, Shehryar [17]. As obvious from the figure, no significant oscillations take place at lower reduced mean free stream velocities, $U_r < 6$, when the two natural frequencies of the system are far apart. The fluid structure interaction mechanism is dominated by the

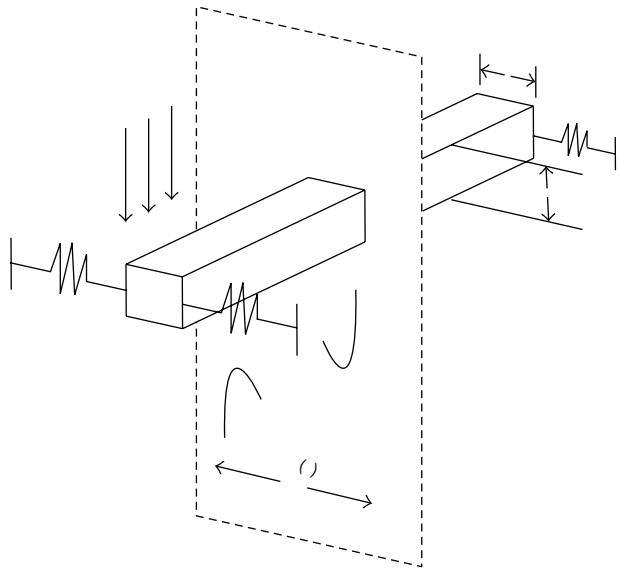

Figure 2: Schematic for square cylinder coupled wake oscillator for 2D vortex-induced vibrations in a vertical wind tunnel [17].

inertial effects due to the incoming flow. As the U_r increases, the vortex shedding frequency downstream of the cylinder gets increasingly synchronized with the cylinder oscillating frequency ($6 \leq U_r \leq 13$). This results in an increasing energy transfer from the wake to the oscillating cylinder. Facchinetti et al. [15] have stated that for a positive energy transfer of this sort, $0 < (-\varphi/\pi) < 1$, where ϕ is the phase angle between the vortex shedding frequency and the cylinder oscillating frequency. Increased energy transfer shows as higher cylinder oscillating amplitude. The cylinder exhibits maximum oscillation amplitude for a critical flow velocity where the two frequencies of the system match exactly. Generally, this point of maximum amplitude for a circular cylinder with higher mass ratio is achieved for a reduced upstream velocity close to (1/St), $U_r \approx 8$. For the square cylinder, however, it occurs at $U_r \approx 10$ which is slightly more than (1/St) in our case. As the mean free stream velocity is increased further, ($U_r > 10$), a sudden phase shift results in an abrupt change in the wake mode pattern, Khalak and Williamson [22] and Brika and Laneville [10]. This point can be identified on the amplitude curves where there is a sudden change in amplitude. Shehryar [17] observed that for such type-II fluid structure interaction systems, the phase between the structure and wake oscillators showed an overall jump of π passing through the lock-in range.

As the mean free stream velocity increases, a negative energy transfer takes place accredited to the sudden phase shift. Consequently, the cylinder oscillations amplitude decreases, Figure 3, until a second critical value of the reduced mean free stream velocity is reached ($U_r \approx 14$). Experimental data presented in Figure 3 depicts amplitude values for a velocity just below this second critical value. Beyond this second critical value of U_r, the two system frequencies bifurcate, Shehryar [17]. If the mean free stream velocity is increased further, ($U_r > 14$), the secondary galloping instability sets in; interestingly it starts immediately after the VIV region.

3. Comparison with the Analytical Model

For a one-dimensional case the equation of motion of a rigid cylinder oscillating in the transverse z-direction (normal to the flow) reads as (4), where "m" is the mass of the cylinder, "r" is a viscous damping coefficient, "k" is the stiffness of the setup, and "S" is the aerodynamic force resulting from the fluid structure interaction in this case, mainly due to vortex shedding.

The mass "m" takes into account the cylinder mass and the fluid added mass m_f which models the inviscid inertial effects. Following Blevins [18] we can define

$$m = m_s + m_f;$$
$$m_f = C_{M_a} \rho D^2 \frac{\pi}{4}; \tag{4}$$
$$\mu = \frac{m}{\rho D^2}$$

$$r = r_s + r_f; \qquad r_f = \gamma \Omega \rho D^2; \tag{5}$$

where "γ" is a stall parameter as Skop and Balasubramanian [23] and "Ω" is a reference angular frequency. Assuming that the mean free stream velocity "U" is zero, "Ω" is the angular frequency of the structure oscillation and "γ" is a function of the amplitude of oscillations related to the mean structural drag coefficient C_D, Blevins [18]. Blevins [18] defines "γ" for a circular cylinder as:

$$\gamma = \frac{1}{4\pi \mathrm{St}} C_D. \tag{6}$$

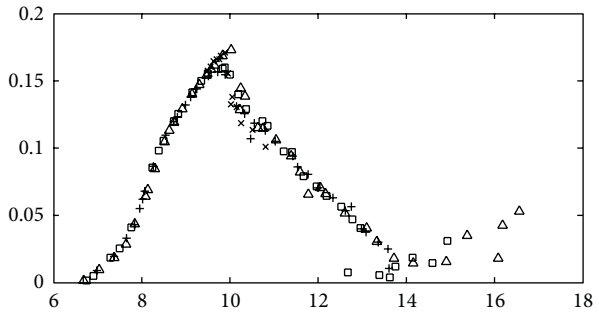

Figure 3: Reduced RMS amplitude of the limit cycle oscillations versus reduced velocity [17].

In our case, however, "Ω" is the vortex shedding angular frequency, $\Omega = \Omega_f = 2\pi \mathrm{St}(U/D)$. "St" is the Strouhal number. Following Skop and Balasubramanian [23], "γ" will be assumed to remain constant for the sake of simplicity. Govardhan and Williamson [11] used two distinct formulations of the equation of motion for the "total force" and the "vortex force". Following the same approach the fluid effects, namely, the added mass and added damping, have been included directly in the structural oscillator in (4) through (1) and (2). The vorticity effects are modelled by the forcing term at the right hand side in (4). Structural angular frequency Ω_s is typically defined as $\Omega_s = \sqrt{k/m}$ and the reduced structural damping $\xi = r_s/2m\Omega_s$. Equation (1) may be re written as

$$\ddot{z} + \left(2\xi\Omega_s + \frac{\gamma}{\mu}\Omega_f\right)\dot{z} + \Omega_s^2 z = \frac{S}{m}. \tag{7}$$

Facchinetti et al. [15] and de Langre [24] have used the standard van der Pol equation to model the fluctuating nature of the vortex street downstream of the oscillating square cylinder:

$$\ddot{q} + \left(\varepsilon\Omega_f\left(q^2 - 1\right)\right)\dot{q} + \Omega_f^2 q = F. \tag{8}$$

The fluid variable "q" is defined as the reduced vortex lift coefficient. Mathematically, $q = 2(C_L/C_{L_o})$. C_{L_o} is the reference lift coefficient measured on a fixed cylinder subjected to vortex shedding. "F" shall be "Az" for displacement coupling, "$A\dot{z}$" for velocity coupling, and "$A\ddot{z}$" for acceleration coupling. Facchinetti et al. [15] have presented a detailed study of the dynamics of such a coupled system. They estimated the near wake van der Pol parameter "ε" and the coupling force scaling "A" from the available experimental data. The oscillation amplitude at lock-in, "z_M", is obtained from

$$z_M = \frac{C_{L_o}/2}{S_G + 4\pi^2\mathrm{St}^2\gamma}\sqrt{1 + \frac{A}{\varepsilon}\frac{C_{L_o}/4}{S_G + 4\pi^2\mathrm{St}^2\gamma}}. \tag{9}$$

3.1. Den Hartog's Instability Criteria. It should be kept in mind here that the model proposed by Facchinetti et al. [15] as discussed above is valid for circular cylinders. The present study however is based on the vortex-induced vibrations of a square section cylinder. It is imperative to remark here that this basic difference in geometry has to be taken into account to be able to compare theoretical findings and experimental results later. Blevins [18] suggested a simplified system to be considered, Figure 4.

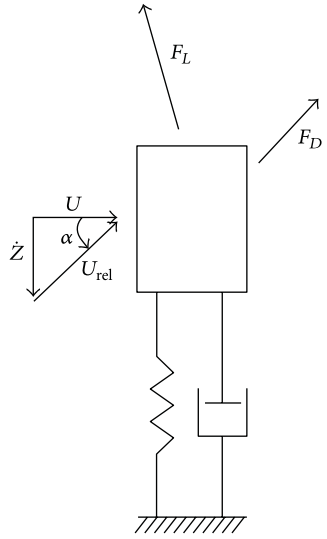

Figure 4: Single degree of freedom galloping model. reproduced as blevins [18].

The angle of attack "α" can be calculated as $\alpha = \tan^{-1}(\dot{z}/U)$ such that if $\alpha = 0$, $z = 0$ implying that the cylinder is at its equilibrium position. Also, if "α" is very small, $\alpha \approx \dot{z}/U$ and $U_{\mathrm{rel}} \approx U$. Now from Figure 4, the resultant vector is assumed to be positive downwards:

$$F_z = -F_L\cos\alpha - F_D\sin\alpha = \frac{1}{2}\rho U^2 DLC_z, \tag{10}$$

where C_z is the vertical force coefficient:

$$C_z = -\frac{U_{\mathrm{rel}}^2}{U^2}\left[C_L\cos\alpha + C_D\sin\alpha\right]. \tag{11}$$

Now because "α" is very small, advancing the last equation

$$C_z(\alpha) = -C_L - \left(-\frac{\partial C_L}{\partial\alpha} + C_D\right)\alpha. \tag{12}$$

In the last equation if $\partial C_z/\partial\alpha < 0$ or equivalently $(\partial C_L/\partial\alpha) + C_D > 0$, total damping of the system remains positive. The system remains stable. This is known as the *Den Hartog's Stability Criteria.* Equation (12) at $\alpha \approx 0$ gives $C_z = C_L$. Trivial algebraic manipulation of (10) and (12) yields

$$F_z = -\frac{1}{2}\rho U^2 DLC_L + \frac{1}{2}\rho UDL\frac{\partial C_z}{\partial\alpha}\dot{z}. \tag{13}$$

Comparing (1) and (13), retaining only lower-order terms of α, we arrive at

$$\gamma = \frac{1}{8\pi\mathrm{St}}\frac{\partial C_z}{\partial\alpha}, \tag{14}$$

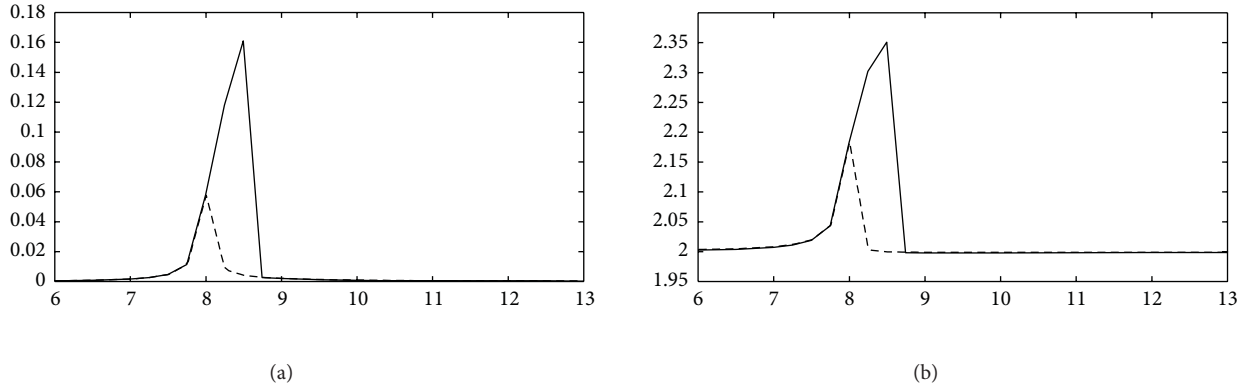

Figure 5: Hysteresis standard wake oscillator model solved numerically using velocity coupling as in Facchinetti et al. [15]. Solid line: Increasing Velocity, dashed line: decreasing velocity. Z^* is the amplitude normalized with respect to the dimension "D" of the square cylinder, Figure 1, and q is the reduced vortex lift coefficient.

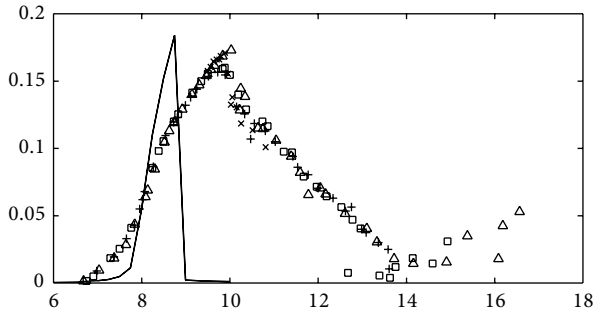

Figure 6: Reduced RMS amplitude of the limit cycle ocillations starting from rest configuration. solid line: velocity coupling simulations of the wake ocillator model as presented in Facchinetti et al. [15].

where $(\partial C_z/\partial\alpha)$ is 3 for a square cylinder in smooth flow and 3.5 for a square cylinder in turbulent flow, Blevins [18].

Investigations by Facchinetti et al. [15] revealed that using acceleration coupling in the forcing term of the wake oscillator best matches with the then available experimental results. The coupling terms were formulated to essentially allow only the linear functions of the wake variable "q" and displacement "z" and their temporal derivatives. In order to set the values of parameters "A" and "ε", the total lift coefficient was assumed to be the same as the vortex lift coefficient. Although Facchinetti et al. [15] recommend acceleration coupling as the most suitable, it is important to keep in mind that the theoretical model was devised for systems with lower mass ratios. Since this experimental work involves a higher mass ratio system we refer to the lock-in domain calculations as a function of mass ratio by the same authors. Given the seemingly asymptotic relationship between the upper and lower bounds of the lock-in region in the velocity coupling model at lower mass ratios, we can conclude that it is the velocity coupling model which is best suitable for our high mass ratio experimental setup. This study therefore focuses on the velocity coupling model.

Following the same approach as Facchinetti et al. [15] and the references there in, we solved the model numerically as presented in (7) and (8) using the Fox and Goodwin iteration scheme. Details of the iteration scheme are described in Shehryar [17]. System parameters are described in Tables 1 and 2, Figure 5.

We shall now compare our experimental results as presented with the theoretical wake oscillator model. As can be observed from Figure 6, the wake oscillator model predicts the location of maximum limit cycle amplitude closer to the expected value of (1/St) for this case. However, the extent of frequency lock-in domain does not match the experimental result. We can safely state that only the lock-in amplitude model in (9) provides acceptable results given that the added aerodynamic damping effect due to bluff body cross section (14) has been taken into account. de Langre [24] states that the extent of the lock-in domain is in fact controlled by the product AM where "A" is the coupling force scaling in the wake oscillator model. Following Facchinetti et al. [15], we determine $A = 2.7$ for our case. "M" is a mass parameter such that

$$M = \frac{C_{L_o}}{2}\frac{1}{2\pi^2 \mathrm{St}^2 \mu}. \tag{15}$$

4. Comparison with Numerical Simulations

For the current case we also carried out coupled fluid-structure interaction of the square cylinder to resolve the physics of the flow and its effect on the rigid body oscillations. The flow physics shall enable us to visualize the dynamics of wake structure and its influence on the structure through coupled simulation. For simplicity, the coupled model is reduced to 2D interaction only because of the nature of the vibration (one dimensional oscillation) and low turbulence. This section details the coupled computational fluid dynamics (CFD) - computational structural dynamics (CSD) model and the simulation results.

4.1. Coupled CFD-CSD Model. The coupled CFD-CSD simulations are carried out using Fluent through its user defined function (UDF) feature. An in-house developed UDF developed using C-Language was linked with Fluent through Dynamic Link Library (DLL). The coupled CFD-CSD system is modelled using loosely coupled partition procedure Matthies and Steindorf [25]. The time step size chosen for unsteady CFD-CSD simulation is $2e-4$ sec based on the vortex shedding frequency of the structure measured experimentally.

4.2. Computational Fluid Dynamics Model. For computational fluid dynamics simulations the chosen domain is two dimensional containing 60000 cells and 60600 nodes as shown in Figure 7. For the square cylinder a solid boundary nonslip wall condition was prescribed while pressure-far-field boundary condition was used on the outer domain boundaries. The distance between the solid wall boundary and the outer boundary of the domain was set at more than 10 times the size of the square cylinder as shown in the Figure 7. The grid size is selected after carrying out a grid independence study.

The two-dimensional flow was modelled using viscous two-dimensional Navier strokes equations along with shear stress transport (SST) *kw* turbulence model, Menter [26]. This particular turbulence model was used because of its good performance for the flows with adverse-pressure gradients, Dina et al. [27]. The initial turbulence intensity was set to be equal to one percent because the Reynolds number based on the size of the square cylinder is in low Reynolds number regime (2000~6000). The numerical simulations are performed for various flow velocities ranging from 1.5 m/sec to 6 m/sec. Value for the air density was kept constant at 1.205 kg/m^3 with static air pressure of 101325 Pa to match the experimental test conditions.

4.3. Computational Structural Dynamics Model. The computational structural dynamics (CSD) model used for the square cylinder has a single degree of freedom in plunge direction "z". The mass "m" of cylinder is 0.0654 kg with the stiffness "k" of the cylinder is modeled using a lineal spring attached to the center of the cylinder with stiffness of 597.6 N·m. The value of structural damping "ξ" coefficient was taken to be around 0.0104 to match the parameters of experiments.

For the single degree of freedom a mass spring-damper system is modeled (see (1)) and solved numerically using fourth-step Rung Kutta (RK4) method with the lift force "S" as the input to the system. The lift force, generated due to airflow, was calculated by numerically integrating pressure, calculated through CFD, around the cylinder.

The time-resolved coupled CFD-CSD simulation show that initially a separation bubble is formed downstream the cylinder as shown in the velocity magnitude plot of Figure 8. This velocity magnitude contour plot is shown for free-stream flow of 5.5 m/sec at time 0.14 sec. As shown, initially the contour plot is symmetric about the cylinder, but after a certain time the separation bubble starts to become asymmetric as shown in Figure 9. The asymmetry is induced by the fluid itself without the requirement of an external plug or trigger. The asymmetry leads to the formation of an alternating vortex which is continuously shed in the wake of square cylinder as shown in Figures 10 and 11. The resultant is the formation of a continuous vortex street behind the square section as seen in Figure 12. This asymmetric vortex shedding introduces asymmetric pressure distribution around the cylinder which introduces fluctuating lift force. This lift forces causes the square cylinder to vibrate. As the incoming velocity is varied the amplitude of the lift force increases; this results in the higher amplitudes of vibrations. However this does not continue for all incoming velocities. At a certain critical velocity, the amplitude maximizes to its highest value and after than the peak amplitude decreases.

A comparison of the peak amplitudes of oscillations predicted by the coupled CFD-CSD simulations and experimental data is shown in Figure 13. For illustration, comparison of results predicted by the analytical model is already shown in Figure 6. It is evident that the analytical model is by far the least demonstrative of the trend seen in the experiments. On the other hand the coupled CFD-CSD simulations show good comparison with the peak amplitude prediction as well as the width of the VIV region.

5. Discussion

Different authors have published their work in attempts to enhance the wake oscillator model since it was proposed by Currie and Hartlen [28]. Such models are based on the reduced vortex lift coefficient manipulated in the form of a standard van der Pol equation to model the effects of the vortex shedding on the solid object. The solid object in turn is modeled in the form of a standard damped spring mass system. Forcing terms in both the equations impose the necessary coupling. An important aspect associated with using this type of theoretical models is the fact that the ratio between the coupling force scaling "A" and the near wake van der Pol parameter "ε" has to be fixed independently for each case of a bluff body executing vortex-induced vibrations. This ratio governs the maximum limit cycle amplitude at lock-in. The extent of the lock-in domain is controlled by the product of the coupling force scaling "A" and the mass parameter "M", de Langre [24]. While our experimental results validate the model's ability to predict the maximum lock-in amplitude, the comparison reflects an important drawback regarding the extent of the lock-in range. Especially the model fails to predict the complete VIV envelope in the post peak amplitude region as observed in Figure 3. It can also be noticed that the van der Pol model predicts a sudden decrease in the amplitude of vibration after the point of peak vibration amplitude. This suggests that the force scaling parameter "A" in this region may not remain constant for the entire envelope and requires further tuning. As described earlier, the change in the amplitude curve can be linked with the mode shift in the vortex shedding pattern, Govardhan and Williamson [11]. However the van der Pol model does not account for the change in the lift force scaling in the region.

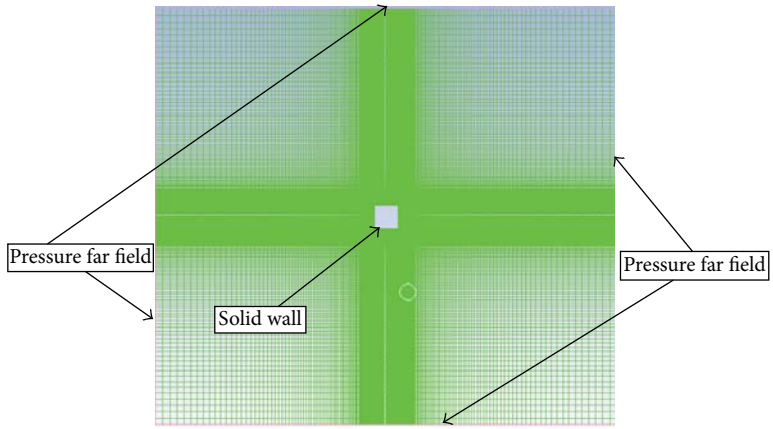

Figure 7: Illustrating the mesh around the square cylinder.

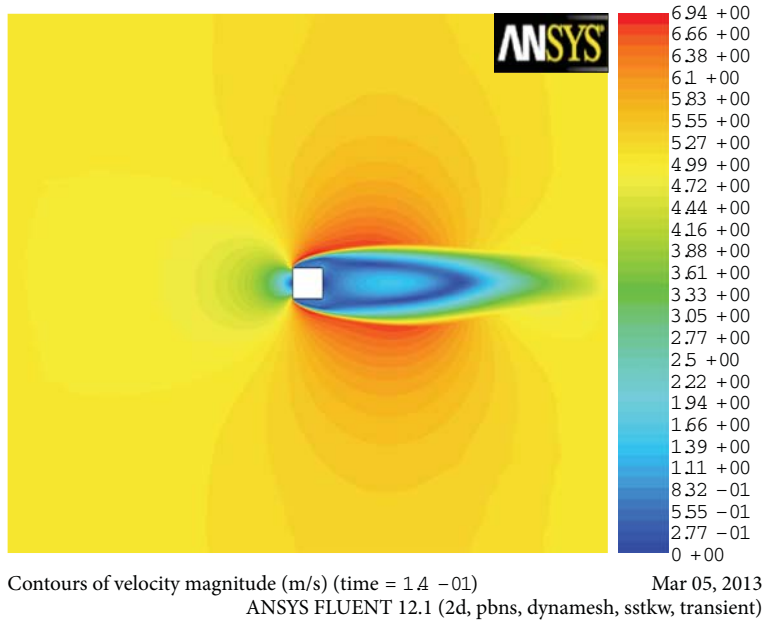

Figure 8: Velocity magnitude contour plot for free-stream velocity of 5.5 m/sec at time 0.14 sec.

Also, a closer inspection of our experimental results in Figure 3 shall reveal that the maximum lock-in amplitude lies at a slightly higher value of the reduced velocity than the expected (1/St). The wake oscillator model proposes that this maximum amplitude should lie indeed at reduced velocity closer to (1/St). This discrepancy in the location of the maximum lock-in amplitude and the extent of the lock-in domain may be connected. A detailed investigation of the blockage effects in this case may yield new experimental evidence. At the same time extending the model to consider higher-order terms in the forcing functions could improve the accuracy of theoretical curves. Another important tool which could be used is a visualization study. The ability to simply see the vortex shedding patterns in real time could shed some more light on any existing phenomena near resonance. One easier approach is to simulate the coupled fluid-structure interaction. Here, we solved 2D Navier-Stokes with the simplest of the structural model which only accounts for the structural damping. Despite the nonlinearity, the model has been able to predict the maximum lock-in amplitude as well as the VIV envelope reasonably. The structural model can be upgraded to include other forms of damping and forcing terms to improve the comparison. Significantly the only difference is the coupled numeric simulation of the flow field that links the wake dynamics with the oscillations. The wake physics is highly complex especially with the introduction of turbulence. The wake oscillator model (Section 4) cannot account for such nonlinearity.

As we know that the value of the van der pol parameter is tuned to obtain the range of reduced velocity, we suspect that the parameter is highly nonlinear and cannot be fixed for the complete reduced velocity envelope. Rather we think that the parameter should evolve into a form at different reduced velocities and mass ratios so that it accounts for the

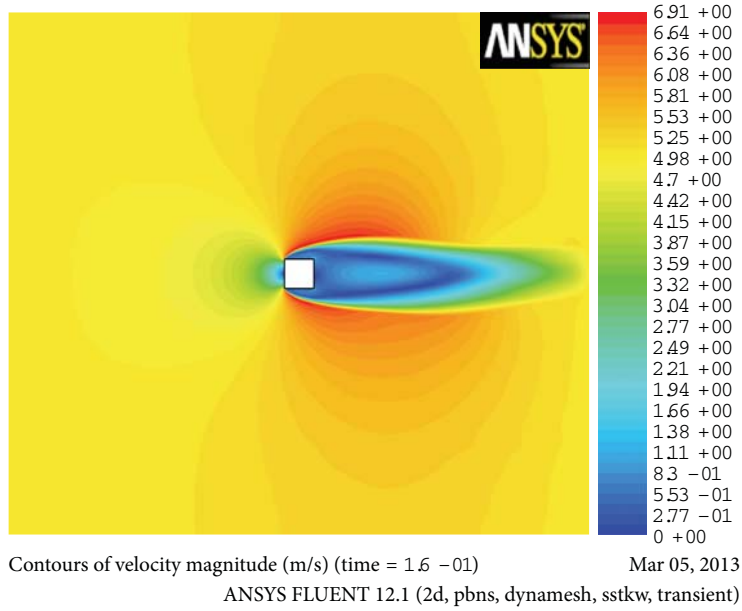

Figure 9: Velocity magnitude contour plot for free-stream velocity of 5.5 m/sec at time 0.16 sec.

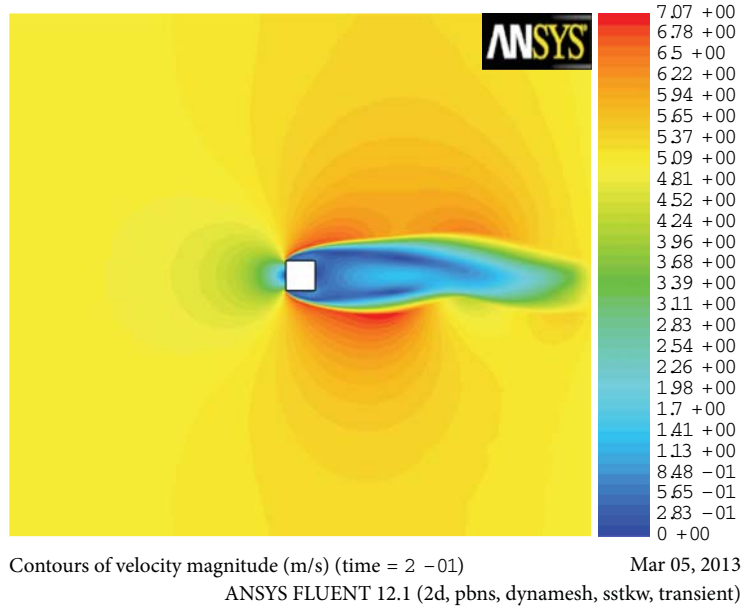

Figure 10: Velocity magnitude contour plot for free-stream velocity of 5.5 m/sec at time 0.2 sec.

wake dynamics especially when transition from laminar to turbulent occurs. It is recommended that further theoretical investigation is conducted so as to find a better approximation of the van der Pol parameter especially for the free vortex-induced oscillations of noncircular cross sections. In this regard we suggest that reduced-order modelling technique can be used.

6. Conclusion

The research paper summarizes the vortex-induced vibrations of a square cylinder subject to cross flow. The cylinder is held with the damped free-end conditions. The experimental findings show lock-in peak amplitude away from region of reduced velocity predicted by the analytical models. On the other hand numerical simulations show peak amplitude and VIV envelope corresponding well with the experimental data. However, the predictions of the analytical model show lesser spread of VIV region with the peak lock-in amplitude in accordance with the experimental findings. The comparison of analytical and numerical results suggests that the wake model used for analytical lift force predictions needs revision. Especially the van der Pol parameter needs correction to incorporate the effects of turbulence experienced in the wake.

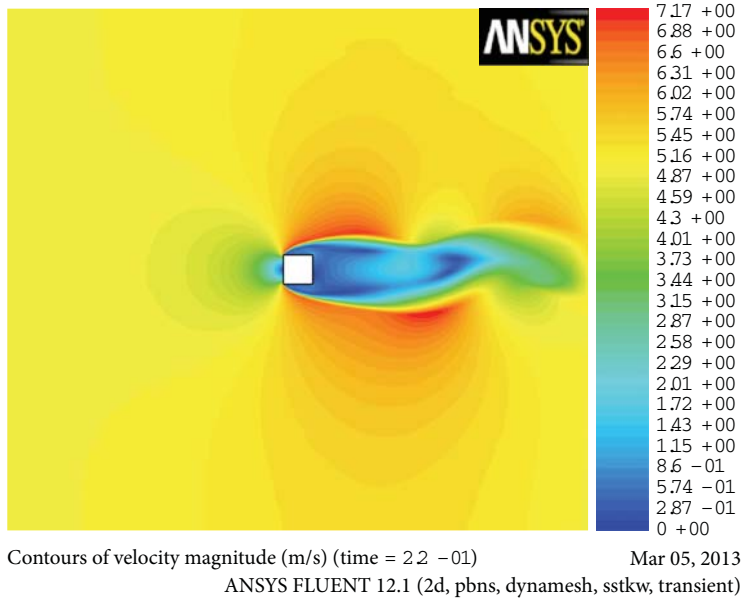

Figure 11: Velocity magnitude contour plot for free-stream velocity of 5.5 m/sec at time 0.22 sec.

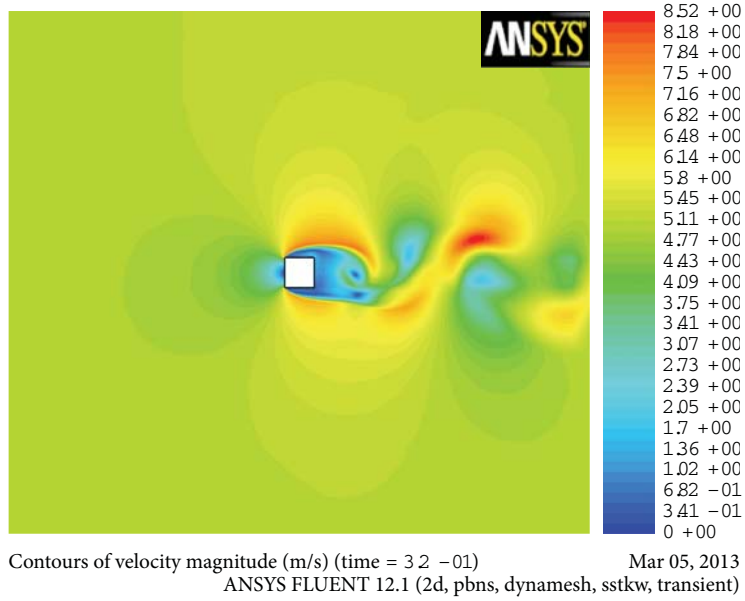

Figure 12: Velocity magnitude contour plot for free-stream velocity of 5.5 m/sec at time 0.32 sec.

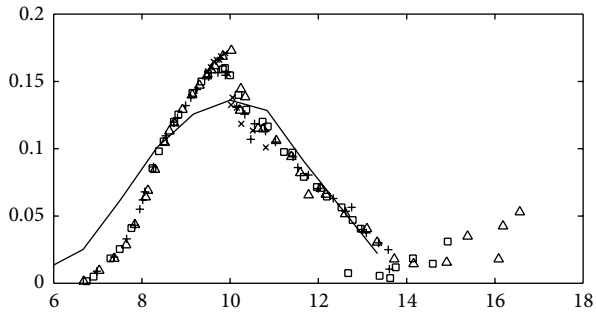

Figure 13: Comparison of coupled CFD-CSD simulations (solid line) with experimental data (symbols).

At the moment the van der pol parameter is tuned to adjust the spread of the region, but it needs better understanding using first principles. We expect that in the near future further numerical simulations and experimental results along with reduced-order modelling may help in improving the formulation of the van der Pol parameter.

Nomenclature

c: Structural damping
f_o: Undampednatural frequency (Hz)
f: Frequency of the LCO (Hz)
f_w: Vortex shedding frequency ($f_w = f_o \mathrm{St} U_r$)
St: Strouhal number
F: Lift force (N)
f^*: Reduced frequency of the LCO ($f^* = f/f_o$)
L, D: Span and chord of the square cylinder (m)
k: Stiffness (N·m/rad) and (N/m)
m: Mass (kg)
$\overline{U}$: Mean wind velocity (m/s)
U_r: Reduced velocity ($U_r = \overline{U}/Df_o$)
$\widehat{Z}$: Amplitude of the LCO
Z^*: Reduced RMS amplitude of LCO ($Z^* = \widehat{Z}/D$)
η: Damping ratio $\eta = c/2\sqrt{km}$.

Acknowledgments

The experimental part of this work was done at the Laboratoire d'Hydrodynamique (LadHyX) under the supervision of Dr. Pascal Hèmon and in collaboration with Dr. Xavier Amandolèse. Portions of the work have already been published in ASME 3rd FEDSM and in Shehryar [17]. This is an attempt to further the ongoing discussion in the light of computational fluid and structure dynamics. The authors acknowledge the contribution by the team at LadHyX in designing the experiment and comprehending the experimental data.

References

[1] R. H. Wilkinson, *On the vortex induced loading on long bluff cylinders [Ph.D. thesis]*, Faculty of Engineering, University of Bristol, Bristol, UK, 1974.

[2] Y. Otsuki, K. Washizu, H. Tomizawa, and A. Ohya, "A note on the aeroelastic instability of a prismatic bar with square section," *Journal of Sound and Vibration*, vol. 34, no. 2, pp. 233–248, 1974.

[3] Y. Nakamura and T. Mizota, "Unsteady lifts and wakes of oscillating rectangular prisms," *Journal of Engineering Mechanics*, vol. 101, no. 6, pp. 855–871, 1975.

[4] T. Sarpkaya, "Vortex induced oscillations, a selective review," *Journal of Applied Mechanics*, vol. 46, pp. 241–258, 1979.

[5] P. W. Bearman and E. D. Obasaju, "An experimental study of pressure fluctuations on fixed and oscillating square-section cylinders," *Journal of Fluid Mechanics*, vol. 119, pp. 297–321, 1982.

[6] A. Ongoren and D. Rockwell, "Flow structure from an oscillating cylinder. Part 1: mechanisms of phase shift and recovery in the near wake.," *Journal of Fluid Mechanics*, vol. 191, pp. 197–223, 1966.

[7] A. Ongoren and D. Rockwell, "Flow structure from an oscillating cylinder. Part 2: mode competition in the near wake.," *Journal of Fluid Mechanics*, vol. 191, pp. 225–245, 1988.

[8] C. H. K. Williamson and A. Roshko, "Vortex formation in the wake of an oscillating cylinder," *Journal of Fluids and Structures*, vol. 2, no. 4, pp. 355–381, 1988.

[9] G. Parkinson, "Phenomena and modelling of flow-induced vibrations of bluff bodies," *Progress in Aerospace Sciences*, vol. 26, no. 2, pp. 169–224, 1989.

[10] D. Brika and A. Laneville, "Vortex-induced vibrations of a long flexible circular cylinder," *Journal of Fluid Mechanics*, vol. 250, pp. 481–508, 1993.

[11] R. Govardhan and C. H. K. Williamson, "Modes of vortex formation and frequency response of a freely vibrating cylinder," *Journal of Fluid Mechanics*, vol. 420, pp. 85–130, 2000.

[12] P. Hémon and F. Santi, "On the aeroelastic behaviour of rectangular cylinders in cross-flow," *Journal of Fluids and Structures*, vol. 16, no. 7, pp. 855–889, 2002.

[13] T. L. Morse and C. H. K. Williamson, "Fluid forcing, wake modes, and transitions for a cylinder undergoing controlled oscillations," *Journal of Fluids and Structures*, vol. 25, no. 4, pp. 697–712, 2009.

[14] S. Manzoor, P. Hémon, and X. Amandolèsse, "Vortex induced vibrations of a square cylinder in a wind tunnel," in *Proceedings of the 3rd ASME 2010 Fluids Engineering Summer Meeting (FEDSM '10)*, Montreal, Canada, 2010.

[15] M. L. Facchinetti, E. de Langre, and F. Biolley, "Coupling of structure and wake oscillators in vortex-induced vibrations," *Journal of Fluids and Structures*, vol. 19, no. 2, pp. 123–140, 2004.

[16] S. Sen and S. Mittal, "Free vibration of a square cylinder at low Reynolds numbers," *Journal of Fluids and Structures*, vol. 27, no. 5-6, pp. 875–884, 2011.

[17] M. Shehryar, *Transient instability mechanisms by frequency coalescence in fluid structure systems [Ph.D. thesis]*, Hydrodynamics Lab (LadHyX), Ecole Polytechnique, Palaiseau, France, 2010.

[18] R. D. Blevins, *Flow Induced Vibrations*, Van Nostrand Reinhold, New York, NY, USA, 1990.

[19] X. Amandolèse and P. Hémon, "Vortex-induced vibration of a square cylinder in wind tunnel," *Comptes Rendus Mécanique*, vol. 338, no. 1, pp. 12–17, 2010.

[20] T. L. Morse, R. N. Govardhan, and C. H. K. Williamson, "The effect of end conditions on the vortex-induced vibration of cylinders," *Journal of Fluids and Structures*, vol. 24, no. 8, pp. 1227–1239, 2008.

[21] C. Norberg, "Flow around rectangular cylinders: pressure forces and wake frequencies," *Journal of Wind Engineering and Industrial Aerodynamics*, vol. 49, no. 1-3, pp. 187–196, 1993.

[22] A. Khalak and C. H. K. Williamson, "Motions, forces and mode transitions in vortex-Induced vibrations at low mass-damping," *Journal of Fluids and Structures*, vol. 13, no. 7-8, pp. 813–851, 1999.

[23] R. A. Skop and S. Balasubramanian, "A new twist on an old model for vortex-excited vibrations," *Journal of Fluids and Structures*, vol. 11, no. 4, pp. 395–412, 1997.

[24] E. de Langre, "Frequency lock-in is caused by coupled-mode flutter," *Journal of Fluids and Structures*, vol. 22, no. 6-7, pp. 783–791, 2006.

[25] H. G. Matthies and J. Steindorf, "Partitioned strong coupling algorithms for fluid-structure interaction," *Computers and Structures*, vol. 81, no. 8-11, pp. 805–812, 2003.

[26] F. R. Menter, "Two-equation eddy-viscosity turbulence models for engineering applications," *AIAA journal*, vol. 32, no. 8, pp. 1598–1605, 1994.

[27] J. E. Dina, P. G. Huang, and T. H. Coakley, *Turbulence Modeling Validation, Testing and Development*, NASA Technical Memorandum, 110446, 1997.

[28] I. G. Currie and R. T. Hartlen, "Lift oscillator model of vortex induced vibration," *Journal of Engineering Mechanics*, vol. 96, no. 5, pp. 577–591, 1970.

Hindawi Publishing Corporation
Advances in Mechanical Engineering
Volume 2013, Article ID 658591, 8 pages
http://dx.doi.org/10.1155/2013/658591

Research Article

Study on the Fluidic Component of the Complete Fluidic Sprinkler

Hong Li,[1] Chao Wang,[1] Chao Chen,[1] and Zhenhua Shen[2]

[1] *Research Center of Fluid Machinery Engineering and Technology, Jiangsu University, Zhenjiang, Jiangsu 212013, China*
[2] *Grundfos R&D China, Suzhou, Jiangsu 215021, China*

Correspondence should be addressed to Chao Wang; wangc1985@126.com

Received 3 September 2012; Revised 22 February 2013; Accepted 3 March 2013

Academic Editor: Shuyu Sun

The PXH fluidic sprinkler controlled by the outlet clearance is a new type sprinkler which is driven and controlled by the Coanda effect. This paper analyzes the offset jet with control stream in the simplified model. Based on the special design of the fluidic component of the fluidic sprinkler, a control stream coefficient was proposed and the air entrance hole distance was considered as one of the key factors that, influence the offset flow field. Based on the numerical simulations and the experiments, the influences made by different air entrance hole distances, offset ratios, and working pressures on the water-air two-phase flow field of the simplified fluidic component have been studied. The offset distance, the pressure distribution on the offset wall, the yaw angle of the main jet flow and their variations with the pressure, and the structural parameters were obtained. The air velocity variation in the air entrance hole was regarded as the judgment for a complete attachment. Visualization experiments and pressure distribution experiments were carried out and the experimental results show a good agreement with simulation results.

1. Introduction

Coanda effect is frequently used in numerous industries, such as aviation, building construction, energy, and power, and so forth. With the diversified application, the study of the Coanda effect has also been expanded [1–6]. Most of the researches about the Coanda effect were derived from the research achievements made by Bourque and Newman [7]. Pin [8] summarized the classic research methods, built the mathematical model of the dualistic incompressible offset jet with injecting control stream or pumping control stream, and proposed some equations about the stream centre line and the correlative parameters of the offset jet with control stream. Wang [9] simplified these equations and calculated the impingement angle and the dimensionless offset distance of the offset jet under different control stream volumes. However, all of these researches only investigated the one-phase flow, and ignored the influence of the different locations of the control stream on the offset field.

Previous research work about the fluidic component of the fluidic sprinklers mainly focused on the external characteristics of the sprinkler, for example, the spraying performance by the orthogonal tests, and so on. The design methods of the fluidic sprinklers were based on these experiments. Yuan et al. [10] simulated the flow in a fluidic sprinkler controlled by outlet for the first time, but the research ignored the influence of the structural parameters or the reattachment length. Li et al. [11] also had done some research on the inner flow of the fluidic component, on which this research is built.

To study the flow of the fluidic component, this paper proposed the control stream location (also named air entrance hole distance in this paper) coefficient based on the existing computational formula. Both the experimental and numerical simulation methods are used to study the influence of the air entrance hole distance on the offset flow field in the simplified component of the fluidic sprinkler.

2. Theoretic Analyses

All the mathematical models of the offset jet flow are built on certain hypotheses. Figure 1 shows the model of offset jet with control stream Q_c.

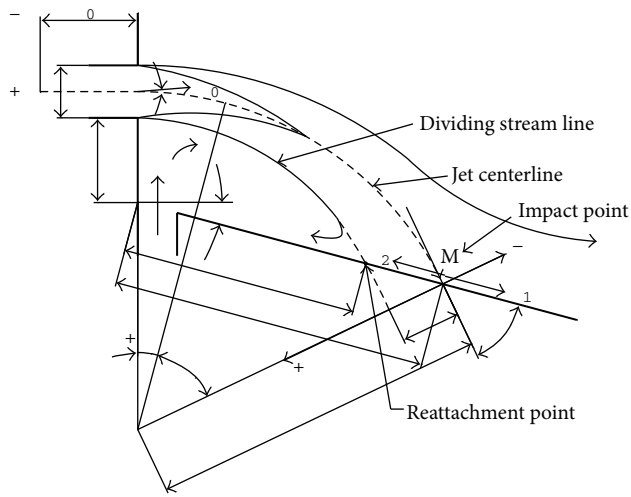

Figure 1: Model of offset jet with control stream.

As shows in Figure 1, under the influence by the control stream and the pressure difference between the two sides of the fluidic component, the main jet flow sprays forward with the direction changing and finally impacts the sidewall at point M. Then, the main jet flow attaches to the wall and flows downstream. Based on the previous research, the approximate value of the yaw angle of the main jet flow, β, can be expressed as follows:

$$\beta = \arctan \frac{J_c}{J_0}, \tag{1}$$

where J_0 is the momentum of the main jet flow at the outlet of the jet nozzle, and J_c is the momentum obtained when the control stream from the control nozzle arrives at the outlet of the jet nozzle. J_0 can be expressed as follows:

$$J_0 = \rho b u_0^2, \tag{2}$$

where ρ is the density of the main jet flow, u_0 is the velocity of the outlet flow, and b is the width of the nozzle. If the pressure at the control stream nozzle is p_c, the discharge of the control stream nozzle is Q_c, the nozzle width is b_c, the wall pressure in the low-pressure area is p_b, and the density of the control stream is ρ_c, according to the momentum theory, J_c can be expressed as follows:

$$J_c = (p_c - p_b) \cdot b_c + \rho_c \cdot \frac{Q_c}{b_c}. \tag{3}$$

The main jet flow in the component is water flow and the control flow is air flow, which makes the flow in the component even more complex. From the research on the fluidic component of the fluidic sprinkler, we can find out that if the outlet velocity of the main jet flow is big enough, the entrainment of the main jet flow will affect the velocity of the air in the air entrance hole. The closer to the outlet of the main jet flow, the more intensive is the air entrainment, which will make the air velocity bigger in the air entrance hole. Meanwhile, the pressure difference between the two sides of the main jet flow is changing while the main jet flow develops from a straight spray jet to an offset jet. So, we should consider the influence caused by the location of the control stream nozzle, when investigating the flow inside the fluidic sprinkler. In this case, the air entrance hole in the wall of the fluidic component works as the control stream nozzle. This paper introduces a control stream coefficient, A_r, which is influenced by the air entrance hole distance h, the offset ratio D/b, and the jet dispersion coefficient σ, as shown in Figure 2. Then, the yaw angle of the main jet flow β can be expressed as

$$\beta = A_r \arctan \frac{(p_c - p_1) b_c + \rho_c \cdot \left(Q_c^2 / b_c\right)}{\rho u_0^2 b}. \tag{4}$$

The attachment angle of the offset jet flow θ is the angle at the intersection between the main jet flow centre line and the offset wall. According to the geometrical relationship and the analytic method, we can get the attachment angle of the offset jet, as follows:

$$\begin{aligned} R \cdot (\beta + \theta) &= \frac{\sigma \cdot b \cos\beta \cdot (1 + Q_c)^2}{3} \\ &\quad \cdot \left(\frac{1}{4\cos^2((\theta + \pi)/3)} - 1 \right), \\ \left(\frac{D}{b} + \frac{1}{2} \right) \cdot \frac{\cos\alpha \cdot (\alpha + \beta + \theta)}{\cos(\alpha + \beta) - \cos\theta} &= \frac{\sigma \cdot b \cos\beta \cdot (1 + Q_c)^2}{3} \\ &\quad \cdot \left(\frac{1}{4\cos^2((\theta + \pi)/3)} - 1 \right). \end{aligned} \tag{5}$$

As shown in (5), θ is correlative with the geometrical parameters. It can be regarded as influenced by the offset ratio D/b, the yaw angle of main jet flow β, and the wall inclination angle α.

The side wall of the fluidic component of the fluidic sprinkler is perpendicular to the nozzle outlet, so the wall inclination angle α is zero, as shown in Figure 2. The attachment angle of the offset jet flow θ is only correlative with β and D/b. As analyzed above, the air entrance hole distance h influences the yaw angle of the main jet flow β, and the attachment angle of the offset jet θ. Based on the theoretical analyses, this paper has combined numerical simulations and experiments to study the offset field influenced by the difference distances of the air entrance hole.

3. Numerical Simulations of the Flow Field

3.1. Structural Models. To study the relationship between the air entrance hole distance and the yaw angle of the main jet flow, the attachment angle of the offset jet and the wall-attachment point distance and the simplified three-dimensional models with different sizes are made to process unsteady numerical calculation. The simplified model and the 3D model are shown in Figure 3. The channel of the simplified

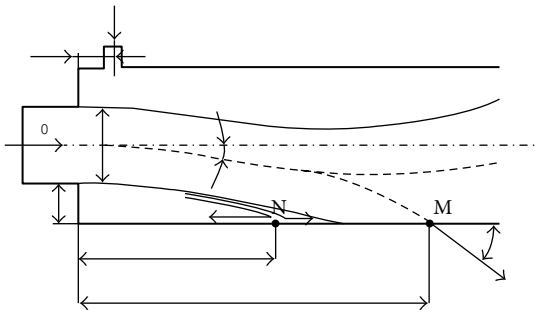

Figure 2: The structure of the simplified fluidic component.

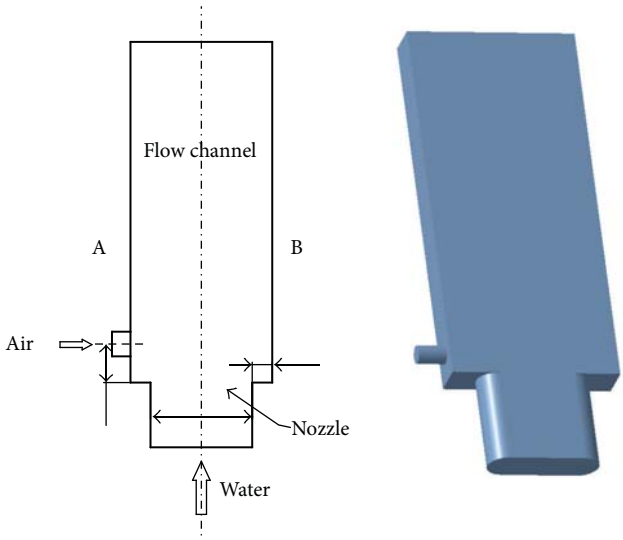

Figure 3: The simplified model of the fluidic component.

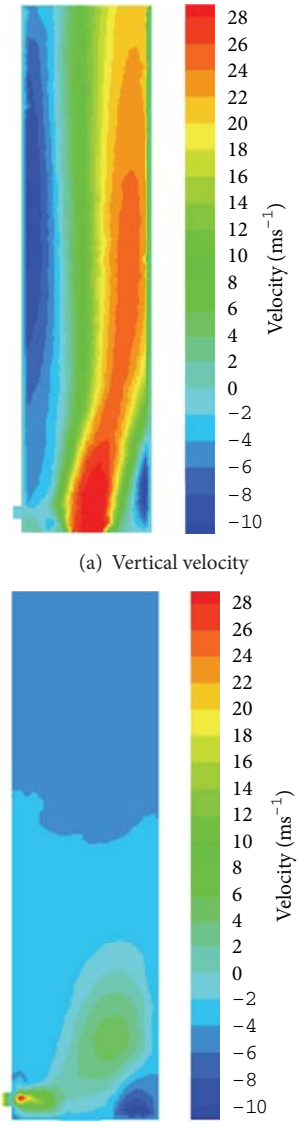

(a) Vertical velocity

(b) Horizontal velocity

Figure 4: Velocity distribution.

fluidic component is made longer to make the offset jet fully developed. The sidewall with air entrance hole is marked as side A, and the opposite sidewall is marked as side B.

3.2. Boundary Conditions. The authors choose the fundamental equations of 3D incompressible flow as the solving equations. The turbulence model is standard $k - \varepsilon$ turbulence model. The fluid media are water and air and choose mixture model as two-phase flow model.

3.3. Simulation Results

3.3.1. Velocity Distribution. The normal and enlarged views of the vertical and horizontal velocity distributions of the flow field on the central cut plane are shown in Figures 4 and 5.

The region where the attachment point locates can be observed from the enlarged counters of the vertical velocity, as shown in Figure 5(a). The back flow in horizontal direction near the sidewall B is caused by the entrainment of the main jet flow, as shown in Figure 5(b). The entrainment effect brings air into the main jet flow from the air entrance hole. The horizontal velocity changes intensively near the air entrance hole, while the velocity changes a little in the downstream of the centerline of the main jet flow. That is the basic difference between the previous offset model and this model. The previous offset jet model usually ignored the horizontal velocity, taking the vertical velocity as the velocity of the jet. Actually, the air velocity in the air entrance hole and the pressure difference of the two sides of the main jet flow lead the flow to get attached to the wall, which means that the horizontal velocity component should be considered as one of the influencing factors.

3.3.2. Pressure Distribution. The enlarged view of the pressure distribution of the stable offset jet flow is shown in Figure 6. We can see that the pressure of the offset jet flow field varies highly.

A low-pressure vortex is formed in the region near the sidewall B. The static pressure is lower at the center and

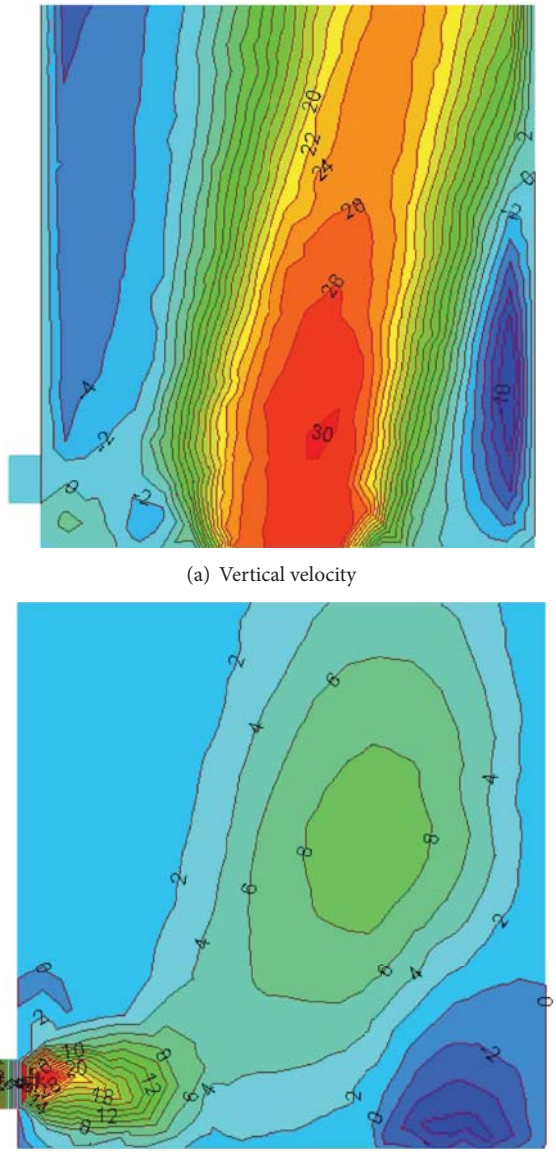

(a) Vertical velocity

(b) Horizontal velocity

Figure 5: Enlarged counters of velocity distribution.

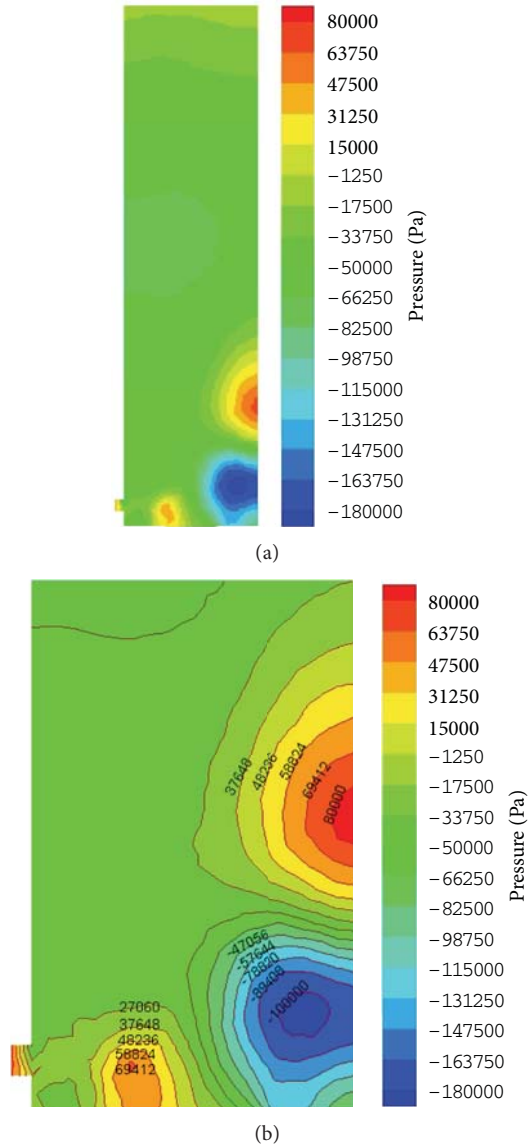

Figure 6: The pressure distribution of the stable offset jet

higher on the edge. The maximum pressure appears on the sidewall at the downstream of the vortex, with the pressure decreasing along the internal direction. The high-pressure vortex region has been formed between the air entrance hole and the nozzle on the sidewall B. It is the pressure difference between the high-pressure vortex region and the atmosphere that enables the function of the air complement. Likewise, the main jet flow is impelled to attach the low-pressure side by the differential pressure between the two sides.

3.3.3. Judgment of the Fully Attachment Time. From the numerical simulation, we can find that when the offset jet flow is developing, the volume between the sidewall A and the boundary of the main jet flow is enlarged, and the pressure difference between the volume and the atmosphere increases as well. The air velocity in the air entrance hole is also changing. The velocity of the air and the pressure difference between the volume and the atmosphere tends to constant after the main jet attached to the wall. As is shown in Figure 7, the velocity of the air gradually attains to a constant for the time 0.2 s. Based on the analysis above, this paper notes that the fully attachment time is the period from the beginning of the attachment to the end when the velocity of the air complement approaches to a constant.

3.3.4. Effect of the Structural Parameters on the Offset Field. The numerical simulation results of the offset field affected by air entrance holes distance are shown in Figure 8.

(1)*Influence on the Fully Attachment Time.* As shown in Figure 8(a), under the same working pressure, the fully attachment time changes with the air entrance hole distances. The fully attachment time decreases when the air entrance

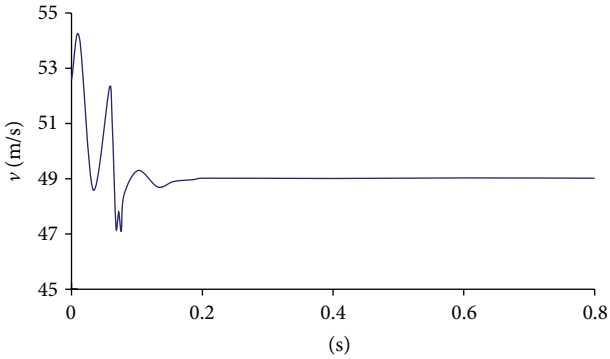

Figure 7: Air complement velocity changes with time.

hole distance increases, but it is not influenced by the offset ratios.

(2) *Influence on the Distance of Attachment Point*. The relation between the location of the attachment point and the air entrance hole is more dependent on the offset ratio. In Figure 8(b), the attachment point distance X_r is the shortest when h is 3 mm and offset ratio D/b is 0.2. Also, the shortest attachment point distance X_r appears when D/b is 0.4, h is 5 mm, D/b is 0.7, and h is 10 mm. Because the volume of the fluidic element of the sprinkler is small, in order to get the offset jet in the limited flow channel, we should know the rules of the locations of the attachment point and the impact point firstly. So the optimum position of the air complement of the fluidic element should be changed according to the offset ratios.

(3) *Influence on the Pressure Distribution*. Because the dynamic pressure is produced by the jet velocity, the impact on the wall during the attachment will change the dynamic pressure, so the point with the largest dynamic pressure on the offset side wall can be taken as the impact point. In Figures 8(c) and 8(d), it is shown that the distances from the impact point to the nozzle decrease X_m at the beginning and then increase with the air entrance hole distances increasing, and the tendency is the same as different ratios' change. But on the offset side, the maximum dynamic pressure varies with the distances of the air entrance hole, and the tendency varies with the different ratios.

3.3.5. Influence of Working Pressure on the Fluidic Element. Table 1 shows the parameters of the offset field under different inlet pressures when D/b is 0.2, and h is 5 mm. According to the data in the table, the air velocity in the complement holes, v_a, increases with the working pressure; the fully attachment time, t_0, decreases with it, which indicates that the air volume is in direct proportion to the entrainment of the flow. The location of the attachment point has no relationship with the working pressure. Both the yaw angle of jet and the impact angle of the offset jet increase with the pressure, but change little when the pressure is higher than 0.5 MPa. The maximum pressure on the wall and the minimum negative pressure in the flow field are increased with the working pressure.

Table 1: Parameters of the offset field.

P (kPa)	v_a (m/s)	t_0 (s)	X_r (mm)	β (°)	θ (°)	P_{min} (Pa)	P_{max} (Pa)
200	28.57	0.214	16.97	4.6	16.6	−67121	87209
300	30.11	0.182	16.97	6.6	18.2	−79380	89153
400	38.42	0.143	16.97	7	21.9	−88040	102889
500	44.67	0.131	16.97	7.8	23.1	−96980	111869
600	52.34	0.106	16.97	7.8	23.2	−112310	119514

4. Experimental Study

In order to confirm the results of the numerical simulation, a test rig is built to study the relationship between the offset field of the fluidic component and the offset ratio and the air entrance hole distance and the working pressure. The yaw angle and the impact angle of the offset jet flow are obtained from the flow field photographs of the fluidic element which has been taken in the visualization experiment. Meanwhile, the pressures on the wall under stable-attachment state are measured to investigate the influence of working pressure and structural parameters on the pressure distribution on the sidewall.

4.1. Test Procedure. The prototype is shown in Figure 9(a). The main observation part of the prototype is made up of organic glass. Two air entrance holes with the distance of 5 mm and 10 mm are set on Side A. The air entrance holes are plugged with special plug when they are not in use. Figure 9(b) shows the flow fields of straight jet and offset jet, respectively.

The phenomenon of stable attachment flow with different air entrance hole distances and different working pressures is recorded with a digital camera. The photographs are processed to make the boundary of the jet sharpened, and the streamline patterns are drawn upon. The yaw angle and the impact angle of the offset jet flow in the offset are measured from the photos to make comparison with the development of the jets.

The fluidic component prototype in the pressure test is the same as the one in the photographic test. The distribution of the pressure test points is shown in Figure 10. The air entrance holes on Side A are marked as pressure points 1a and 1b, which are 5 mm and 10 mm away from the outlet nozzle. Five pressure points are labeled as 2, 3, 4, 5, and 6 at Side A, which are 5 mm, 12 mm, 20 mm, 30 mm, and 50 mm away from the outlet of nozzle, as shown in Figure 10. The pressure gauge is typed YB-150A, with the accuracy 0.4 M, the span 0–0.1 MPa and −0.1–0 MPa, and the minimal scale 0.5 kPa. The main jet flow is impelled to be attached to Side B by opening and closing air entrance holes 1a and 1b manually (the pressure at 1a is measured when it is used as air entrance hole, so is 1b). The pressure distribution on the wall is detected by the pressure points. The results of the test are shown in Table 2.

From Table 2, it is clear that the yaw angle varies greatly with different air entrance hole distances. For the two prototypes with different offset ratios in this test, the stable yaw angle and the impact angle reach the highest values when h is 5 mm.

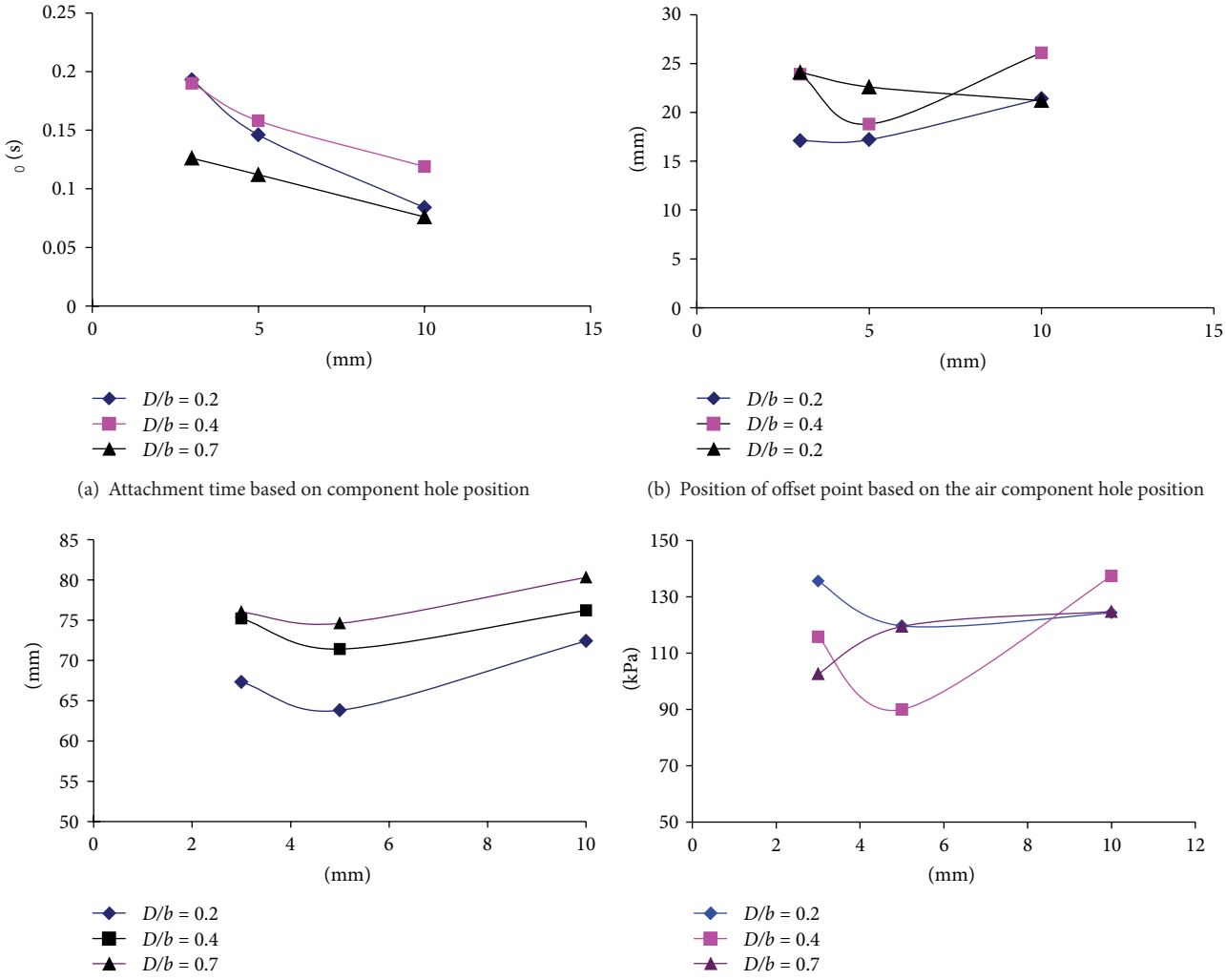

(a) Attachment time based on component hole position

(b) Position of offset point based on the air component hole position

(c) Position of maximum dynamic pressure point based on different air component hole position

(d) Dynamic pressure distribution based on air component hole position

Figure 8: The numerical simulation results.

Table 2: Results of the visualization test.

Pressure (kPa)	300		400		500		600	
D/b	0.2							
h (mm)	5	10	5	10	5	10	5	10
β (°)	4.1	3.1	4.9	4	5.3	4.1	5.8	5.6
θ (°)	16.6	15.2	17.3	15.9	17.4	16.	17.6	16.6
D/b	0.4							
h (mm)	5	10	5	10	5	10	5	10
β (°)	5	3.7	5.2	4.4	5.7	4.9	5.6	5.2
θ (°)	16.9	16.1	18.3	18.5	20.9	20.6	21.3	21

From the comparison shown in Figure 11, the tendency of the test results is consistent with the numerical simulation, and the values from the test are lower than that from the simulation. It is caused by the difference between the idealized conditions in the numerical simulation and the actual operation conditions. Also, the inevitable errors in the manufacture of the prototype will lead to the air leakage at the pressure test points, which makes the vacuum in the low-pressure region decrease and also the yaw angle and the impact angle.

The pressures on Side B with different offset ratios and different positions of the air entrance hole are presented in Figure 12. On Side B, the pressure increases at first and then decreases from Point 2 to Point 6, and the tendencies are identical with the results obtained from the simulation. A transition from a positive pressure to a negative pressure occurs on side B, which indicates that the attachment point is supposed to be located in this area. For these two prototypes in the test, when the hole 1a is open, the conversion place is located between pressure Point 2 and Point 3 (12 mm to 20 mm); when the hole 1b is open, the conversion place is located between pressure Point 3 and Point 4 (20 mm to 30 mm). These factors confirm the results from the numerical simulation of the location of the attachment point. At the

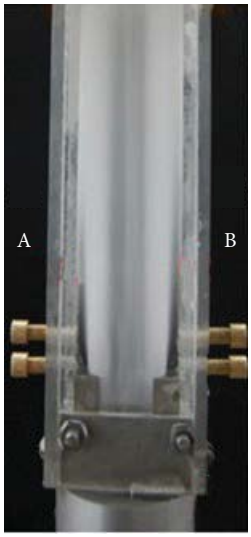

(a)

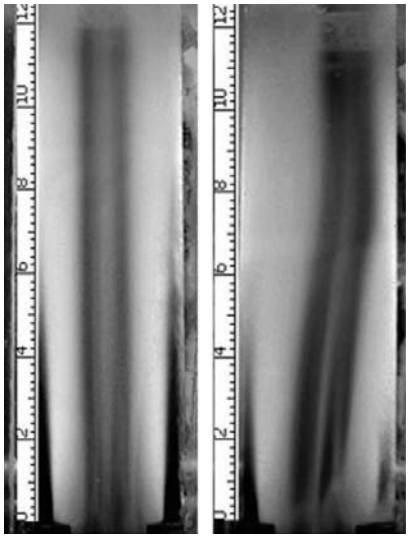

(b)

Figure 9: The prototype and the picture of the flow field.

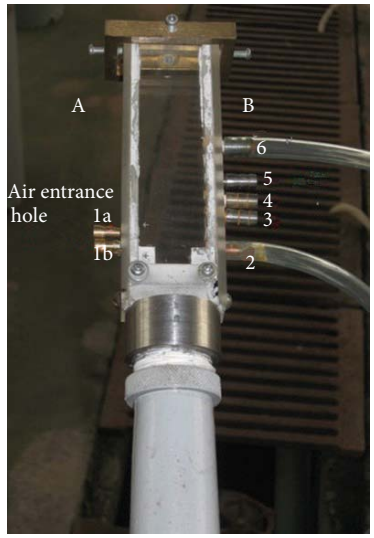

(a)

(b)

Figure 10: The test rig and the distribution of the pressure test points.

same air entrance hole, the pressure conversion place on Side B has not changed with the pressure.

5. Conclusions

The main influencing factors on the offset flow field are analyzed theoretically at first, and then the flow in the fluidic component is investigated with numerical simulations and experimental tests. The conclusions are as follows.

(1) The fully attachment time decreases with the increasing of the air entrance hole distance and the working pressure.

(2) The location of the attachment point is influenced by the air entrance hole distance and the offset ratio. It has nothing to do with the working pressure. Therefore, the air entrance hole distances should be different as the offset ratio changes.

(3) The location with maximum dynamic pressure goes forward at first and then backward when the air entrance hole distance is enlarged, and the tendency is not influenced by the offset ratio. The yaw angle and the attachment angle of the offset jet flow increase with the pressure increasing and vary little when the pressure is more than 0.5 MPa.

(4) To optimize the structure of the fluidic component, we can change the air entrance hole distance to get the best offset ratio and to reduce the maximum dynamic pressure point distance and the attachment distance, in order to cut down the length of the fluidic component with the offset jet flow fully developed.

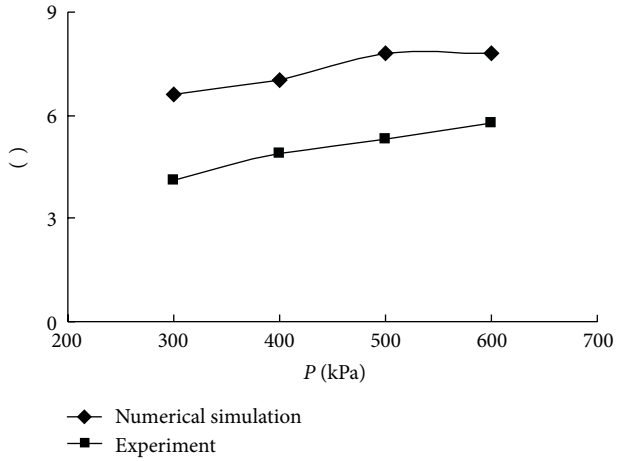

Figure 11: The comparison of the simulation and the experimental result.

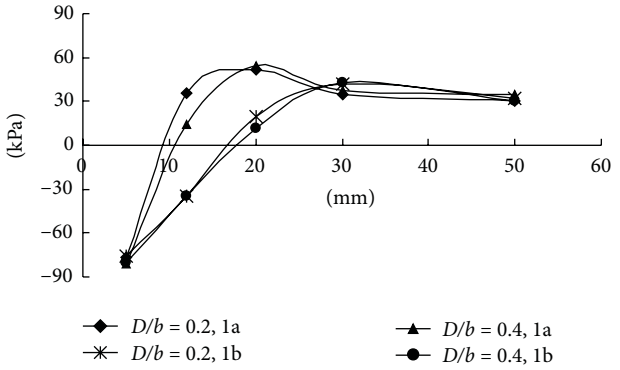

Figure 12: The influence of D/b and h on the pressure distribution.

Nomenclature

b : Nozzle width
b_c: Control stream nozzle width
X_r: Reattachment length on the lateral wall
D: The distance from the wall to the lower nozzle edge
u: Jet velocity
u_0: Exit velocity
v_a: Air velocity in the air entrance hole
t_0: Fully attachment time
J: Jet momentum
y_r: Plumb distance between the intersection point on the lateral wall and the extended dividing streamline
y: Vertical distance to the jet centerline
x: Distance to nozzle exit along the centerline
s_0 : Distance between jet virtual origin and the nozzle exit
h: Distance between nozzle outlet and the centerline of the air entrance hole
R: Radius of curvature
p: Pressure
p_∞: Atmospheric pressure
p_c: Control stream pressure
Q_c: Control stream flux
Re: Reynolds number
ρ : Density of water
α: Oblique angle
β: Jet yaw angle caused by control flow
θ: Angle between jet centerline and sidewall on attachment point.

Acknowledgments

Part of this research was supported by the National High-tech R&D Program of China (863 Program, no. 2011AA100506), National Agricultural Science and Technology Achievements Application Foundation of China (no. 2011GB2C100015), and part by Agricultural Foundation of Jiangsu (no. BE2010393).

References

[1] M. Rosemarie, "Characteristics of a dual-slotted circulation control wing of low aspect ratio intended for naval hydrodynamic applications," *Science and Technology Highlights*, vol. 4, pp. 111–123, 2000.

[2] W. S. Eliphas, F. Rogerio, E. B. L. Roberto et al., "Microfluidic oscillator for gas flow control and measurement," *Flow Measurement and Instrumentation*, vol. 16, no. 1, pp. 7–12.

[3] Y. Bai and X. Ming, "Numerical simulation of wall-attached jet device," *Journal of Nanjing University of Aeronautics and Astronautics*, vol. 40, no. 1, pp. 32–36, 2008.

[4] H. L. Xu, H. Y. Chen, and H. Q. Bi, "Numerical simulation of superfine powder classification based on Coanda effect," *Journal of SWUST*, vol. 20, no. 1, pp. 42–46, 2005.

[5] D. D. Guo, X. B. Li, B. Xie et al., "Coanda-effect applications and spreading of higher precise air-fluiding classification about rare earth polishing powder," *Chinese Rare Earths*, vol. 12, no. 22, pp. 54–59, 2001.

[6] X. H. Ji and W. Liu, "Numerical simulation of floe field of static gas wave refrigerator," *Fluid Machinery*, vol. 33, no. 2, pp. 62–65, 2005.

[7] C. Bourque and B. G. Newman, "Reattachment of two-dimensional incompressible jet to adjacent flat plate," *The Aeronautical Quarterly*, no. 11, pp. 201–232, 1960.

[8] J. Pin, *The Theory and Application of the Jet*, China Astronautic, Beijing, China, 1995.

[9] C. Y. Wang, *Research on Key Technologies in Fluidic Flow Meter*, Zhejiang University, Zhejiang, China, 2008.

[10] S. Yuan, X. Zhu, H. Li, and Z. Ren, "Numerical simulation of inner flow for complete fluidic sprinkler using computational fluid dynamics," *Transactions of the Chinese Society of Agricultural Machinery*, vol. 36, no. 10, pp. 46–49, 2005.

[11] H. Li, S. Q. Yuan, Q. J. Xiang, and C. Wang, "Theoretical and experimental study on water offset flow in fluidic component of fluidic sprinklers," *Journal of Irrigation and Drainage Engineering*, vol. 137, no. 4, pp. 234–243, 2011.

Hindawi Publishing Corporation
Advances in Mechanical Engineering
Volume 2013, Article ID 573542, 7 pages
http://dx.doi.org/10.1155/2013/573542

Research Article

Optimal Model of Operation Parameters of Gathering Pipeline Network with Triple-Line Process

Yongtu Liang,[1] Cen Lu,[2] Kuijie Ren,[2] Qiao Xiao,[1] and Guoxi He[1]

[1] *China University of Petroleum, Beijing 102200, China*
[2] *Petroleum Engineering Technology Research Institute of East China Branch, SINOPEC, Nanjing, Jiangsu 210031, China*

Correspondence should be addressed to Qiao Xiao; xiaoqiaobob@163.com

Received 14 January 2013; Accepted 5 March 2013

Academic Editor: Bo Yu

This is a mathematic model for the optimal operation of the gathering pipeline network and its solution provides this gathering pipeline network having a triple-line heat-tracing process, a method for reducing the operational costs and increasing economic benefit. The model consists of an objective function, minimum total operation cost, and 3 constraints including water temperature constraint at pipe nodes, inlet oil temperature constraints, and outlet water temperature constraint. By using a sequential quadratic programming algorithm, the model can be solved and a set of optimal mass rate and the desired temperature of tracing water are attained. The method is here specifically applied to the optimal operation analysis of a gathering pipeline network in North China Oilfield. The result shows its operation cost can be reduced by 2076RMB/d, which demonstrates that this method contributes to the production cost reduction of old oilfields in their high water-cut stage.

1. Introduction

Triple-line process has been widely used in early oilfield development in China. With oilfields now entering the high water-cut stage, it has become more and more clear that the triple-line process has the disadvantages of high energy consumption and low efficiency. In the last twenty years, research has been mostly based on the optimal design of pipeline network [1–4] and the simulation of pipeline network [5–7], but seldom on optimal operation problems of triple-line process. On the condition that the triple-line process is not changed, research was carried out on optimizing the operation parameters of oilfield gathering and transportation system which had positive effects on cost reduction and economic benefit increases for those areas unsuited to the low-temperature gathering and transportation process.

2. Thermodynamic Calculation of Tracing Oil Pipelines

The cross-section of the tracing oil pipelines is divided into 5 parts [8] (Figure 1). S^1 is the heat transfer surface between an oil pipeline and the soil, S^2 is the heating surface between the pipes' interspace and the soil, S^3 is the heat transfer surface between a water pipeline and the soil, S^4 is the heat transfer surface between an oil pipeline and the pipes' interspace, and S^5 is the heat transfer surface between a water pipeline and the pipes' interspace. By solving the pipe element thermodynamic differential equation [9], Oil/water temperature at the end of the oil/water pipeline can be obtained as shown in Figure 1, where $S^1 \cdots S^5$ are the areas of 5 heat transfer surfaces of unit pipe length, m^2 Consider.

$$T^Z = D^1 e^{r^1 L} + D^2 e^{r^2 L} + t^f, \tag{1}$$

where T^z is the liquid temperature at the end of the oil pipe, °C. t^f is the average soil temperature at the depth of pipes, °C

$$t^z = \frac{A^o r^1 - B^1}{B^2} D^1 e^{r^1 L} + \frac{A^o r^2 - B^1}{B^2} D^2 e^{r^2 L} + t^f, \tag{2}$$

where t^z is the water temperature at the end of a tracing pipe, °C.

r^1, r^2, D^1,and D^2 are given by

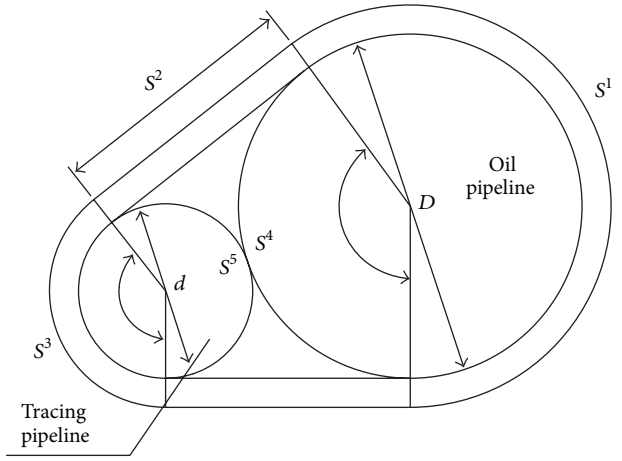

Figure 1: Cross-section diagram for tracing oil pipelines.

$$r^{1,2} = \frac{-p \pm \sqrt{p^2 - 4q}}{2},$$

$$D^1 = \frac{1}{A^o\left(r^1 - r^2\right)} \times \left[\left(B^1 - A^o r^2\right)T^q + B^2 t^q + \left(B^3 + A^o r^2\right)t^f\right], \tag{3}$$

where T^q is the liquid temperature at the beginning of an oil pipe, $^\circ C$. t^q is the water temperature at the beginning of a tracing pipe, $^\circ$C,

$$D^2 = \frac{1}{A^o\left(r^1 - r^2\right)}\left[\left(A^o r^1 - B^1\right)T^q - B^2 t^q - \left(B^3 + A^o r^1\right)t^f\right], \tag{4}$$

$$p = \frac{C^1}{A^w} - \frac{B^1}{A^o}, \tag{5}$$

$$q = \frac{C^2 B^2 - C^1 B^1}{A^w A^o}, \tag{6}$$

$$A^o = Gc^o, \tag{7}$$

where c^o is the specific heat of an oil pipe liquid, J/($^\circ$C $\cdot$ kg) Consider

$$A^w = g^w c^w, \tag{8}$$

where c^w is the specific heat of water, J/($^\circ$C $\cdot$ kg). g^w is the mass rate of water, kg/s Consider

$$B^1 = \frac{\left(K^4 S^4\right)^2}{K^2 S^2 + K^4 S^4 + K^5 S^5} - K^1 S^1 - K^4 S^4, \tag{9}$$

where $K^1 \cdots K^5$ are the overall heat transfer coefficients of 5 heat transfer surfaces, W/(m^2 $\cdot^\circ$C),

$$B^2 = \frac{K^4 S^4 \cdot K^5 S^5}{K^2 S^2 + K^4 S^4 + K^5 S^5},$$

$$B^3 = K^1 S^1 + \frac{K^4 S^4 \cdot K^2 S^2}{K^2 S^2 + K^4 S^4 + K^5 S^5},$$

$$C^1 = \frac{-\left(K^5 S^5\right)^2}{K^2 S^2 + K^4 S^4 + K^5 S^5} + K^3 S^3 + K^5 S^5, \tag{10}$$

$$C^2 = -\frac{K^4 S^4 \cdot K^5 S^5}{K^2 S^2 + K^4 S^4 + K^5 S^5},$$

$$C^3 = -\left(K^3 S^3 + \frac{K^2 S^2 \cdot K^5 S^5}{K^2 S^2 + K^4 S^4 + K^5 S^5}\right).$$

3. Thermodynamic Calculation of Pipeline Network

3.1. Pipe Network Numbering Method. The oil wells, the metering stations, the transfer station, and the pipelines connecting them are ranked and numbered with the following rules. The transfer station is level 0 node, with no subscript; the metering station is level 1 node, with subscript i as its number; the oil well is level 2 node, with subscript ij as its number. A transfer station is the highest level, a metering station comes second, and an oil well is the lowest. The number of pipelines connecting two nodes follows the lower one. n is the total number of metering stations, and m_i is the total number of oil wells connected with the metering station i. As shown in Figure 2, the transfer station has 2 metering stations, one of them has 3 wells and the other has 2.

3.2. Node Parameters Calculation of Heat Tracing Pipelines. (1) Mass rate and specific heat of an oil pipe liquid at nodes:

$$G_{ij} = Q_{ij} \cdot w_{ij} \cdot \rho^w + Q_{ij} \cdot \left(1 - w_{ij}\right) \cdot \rho^o,$$

$$G_i = \sum_{j=1}^{m_i} G_{ij}, \tag{11}$$

where G_i/G_{ij} is the mass rate of an oil pipe's liquid i/ij, kg/s. ρ^w is the water density, kg/m^3. ρ^o is the crude density, kg/m^3. Q_{ij} is the volumetric flow rate of an oil pipe liquid ij, m^3/s. w_{ij} is the volumetric water cut of a well ij,

$$c_{ij}^o = \frac{Q_{ij} \cdot w_{ij} \cdot \rho^w \cdot c^w + Q_{ij} \cdot \left(1 - w_{ij}\right) \cdot \rho^o \cdot c^o}{Q_{ij} \cdot w_{ij} \cdot \rho^w + Q_{ij} \cdot \left(1 - w_{ij}\right) \cdot \rho^o},$$

$$c_i^o = \frac{\sum_{j=1}^{m_i} c_{ij}^o G_{ij}}{G_i}, \tag{12}$$

where c_i^o/c_{ij}^o is the specific heat of an oil pipe's liquid i/ij, J/($^\circ$C $\cdot$ kg).

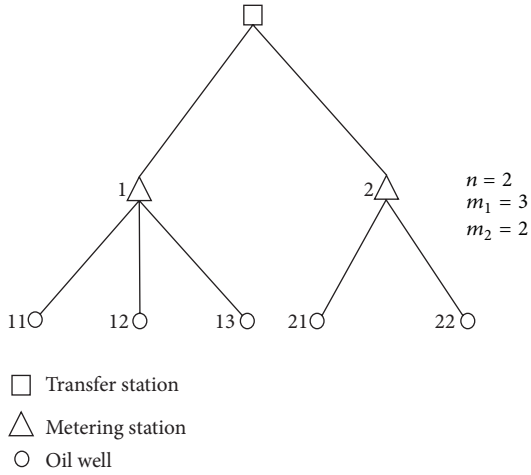

Figure 2: Pipe network numbering method.

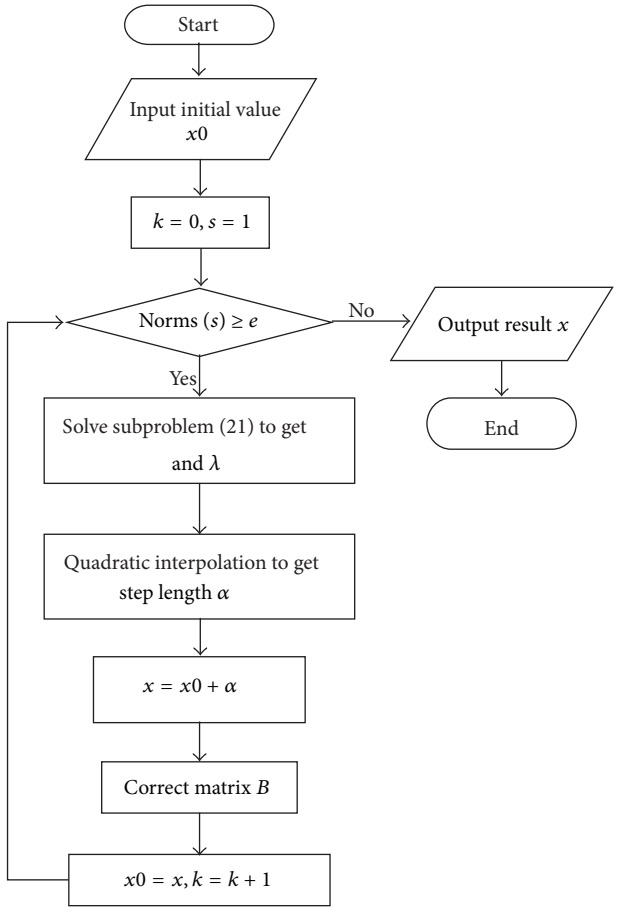

Figure 3: Main framework of the algorithm.

(2) Temperature of an oil pipe liquid at nodes:

$$T_i^q = \frac{\sum_{j=1}^{m_i} c_{ij}^o G_{ij} T_{ij}^z}{c_i^o G_i} \tag{13}$$

T_i^q is the resulting oil pipes' liquid temperature when mixed at their node i, ˚C. T_{ij}^z is the liquid temperature at the end of an oil pipe ij, ˚C.

(3) Temperature of a water pipe liquid at nodes

$$t_i^q = \frac{\sum_{j=1}^{m_i} g_{ij}^w t_{ij}^z}{g_i^w}, \tag{14}$$

where t_{ij}^z is the water temperature at the end of a tracing pipe ij, ˚C. t_i^q is the resulting tracing pipes' water temperature when mixed at their node i, ˚C. g_i^w/g_{ij}^w is the mass rate of water distributed to a node i/ij, kg/s.

3.3. Node Parameters Calculation of Water Pipeline Network. Mass Rate of Water at the Nodes. The mass rate of water at a node is calculated serially from the lower level to the higher one:

$$g_i^w = \sum_{j=1}^{m_i} g_{ij}^w, \qquad g^w = \sum_{i=1}^{n} g_i^w. \tag{15}$$

Water Temperature at Nodes. Water temperature at a node is calculated by using the Sukhov Formula serially from the lower level to the higher one:

$$\begin{aligned} t_{ij}^Q &= \left(t_{ij} - t^f\right) e^{(K_{ij}\pi d_{ij}/g_{ij}^w c^w)L_{ij}} + t^f, \\ t_i^Q &= \left(t_i - t^f\right) e^{(K_i\pi d_i/g_i^w c^w)L_i} + t^f, \end{aligned} \tag{16}$$

where t_i^Q/t_{ij}^Q is the water temperature at the beginning of a water pipe i/ij, ˚C. t_i/t_{ij} is the water temperature at the end of a water pipe i/ij, ˚C. K_i/K_{ij} is the overall heat transfer coefficient of a water pipe i/ij, W/(m^2 ·˚C). d_i/d_{ij} is the diameter of the water pipe i/ij, m. L_i/L_{ij} is the length of the water pipe i/ij, m.

4. Optimal Mathematic Model

4.1. Objective Function. With a water mass rate $\{g_{ij}\}$ and a water temperature $\{t_{ij}\}$ as decision variables and the minimum total operation cost, including heating cost and power cost, as the target, assuming that ΔH is a known quantity, the objective function is given by

$$\min F\left(\left\{g_{ij}\right\}, \left\{t_{ij}\right\}\right) = \frac{p^r c^w g^w \left(t - t^y\right)}{q^r \eta} + \frac{p^d g^w g \Delta H}{\eta'}, \tag{17}$$

where p^r is the fuel price, RMB/kg. p^d is the price of electricity RMB/J. t^y is the water temperature before heated, ˚C. g is the acceleration of gravity, N/kg. ΔH is the water head of the pump, m. q^r is the lower heating value, J/kg. η is the efficiency of heating furnace. η' is the pump's efficiency.

4.2. Constraints Condition. Water Temperature Constraint at the Nodes. One node has multiple outlets. The water temperatures of these outlets are the same:

$$\Delta t_i = 0, \qquad \Delta t_{ij} = 0, \tag{18}$$

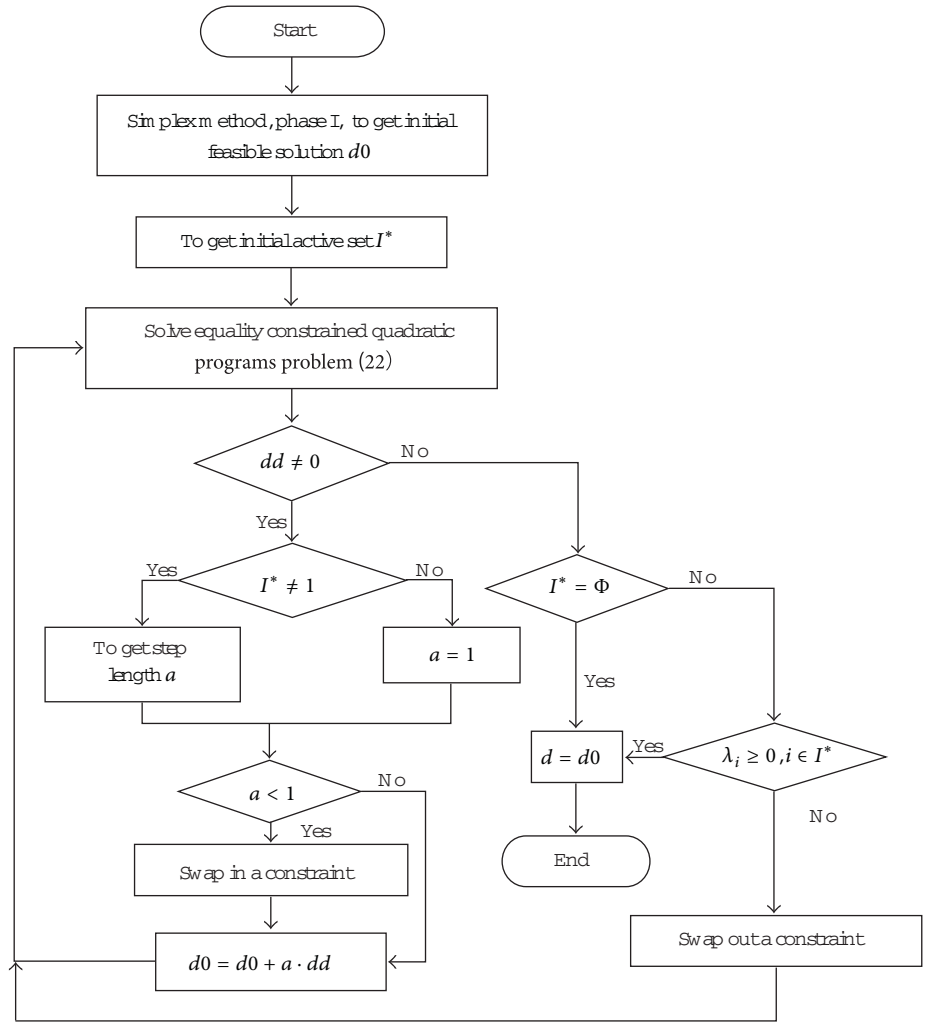

Figure 4: Program chart of active set algorithm.

where Δt_i is the commencing temperature difference between a water pipe i and a water pipe $(i+1)$,°C. Δt_{ij} the commencing temperature difference between a water pipe ij and a water pipe $i(j+1)$,°C.

Inlet Oil Temperature Constraint. To ensure the safe operation of the pipeline, the minimum inlet temperature [10] is specified to be higher than the freezing point of crude oil:

$$T_i^Z \geq T^n + \Delta t, \tag{19}$$

where T_i^z is the transfer station's inlet temperature of an oil pipe i, °C. T^n is the freezing point of crude oil, °C. Δt is the temperature allowance, °C.

Outlet Water Temperature Constraint. The outlet water temperature of the transfer station is usually (90 ~ 100)°C [11, 12]:

$$t \leq 100, \tag{20}$$

where t is the outlet water temperature of a transfer station, °C.

5. Model Solutions

There are n metering stations, $\sum_{i=1}^{n} m_i$ oil wells in this model, and correspondingly, $2\times\sum_{i=1}^{n} m_i$ decision variables, $\sum_{i=1}^{n} m_i - 1$ equality constraints and $(n + 1)$ inequality constraints are generated. The model is a highly nonlinear problem, of which the most common method used to solve is the sequential quadratic programming algorithm. The sequential quadratic programming algorithm is a fast and effective method, of which the convergence rate is proved to be superliner under certain conditions [13, 14].

5.1. Sequential Quadratic Programming Algorithm. The main idea of the algorithm is to build a simple series of approximate optimization problems, namely, quadratic programming problems, using the information from the original nonlinear program. By solving these new problems, current iteration can be updated and gradually approximate the solution of the original nonlinear programming problem [15].

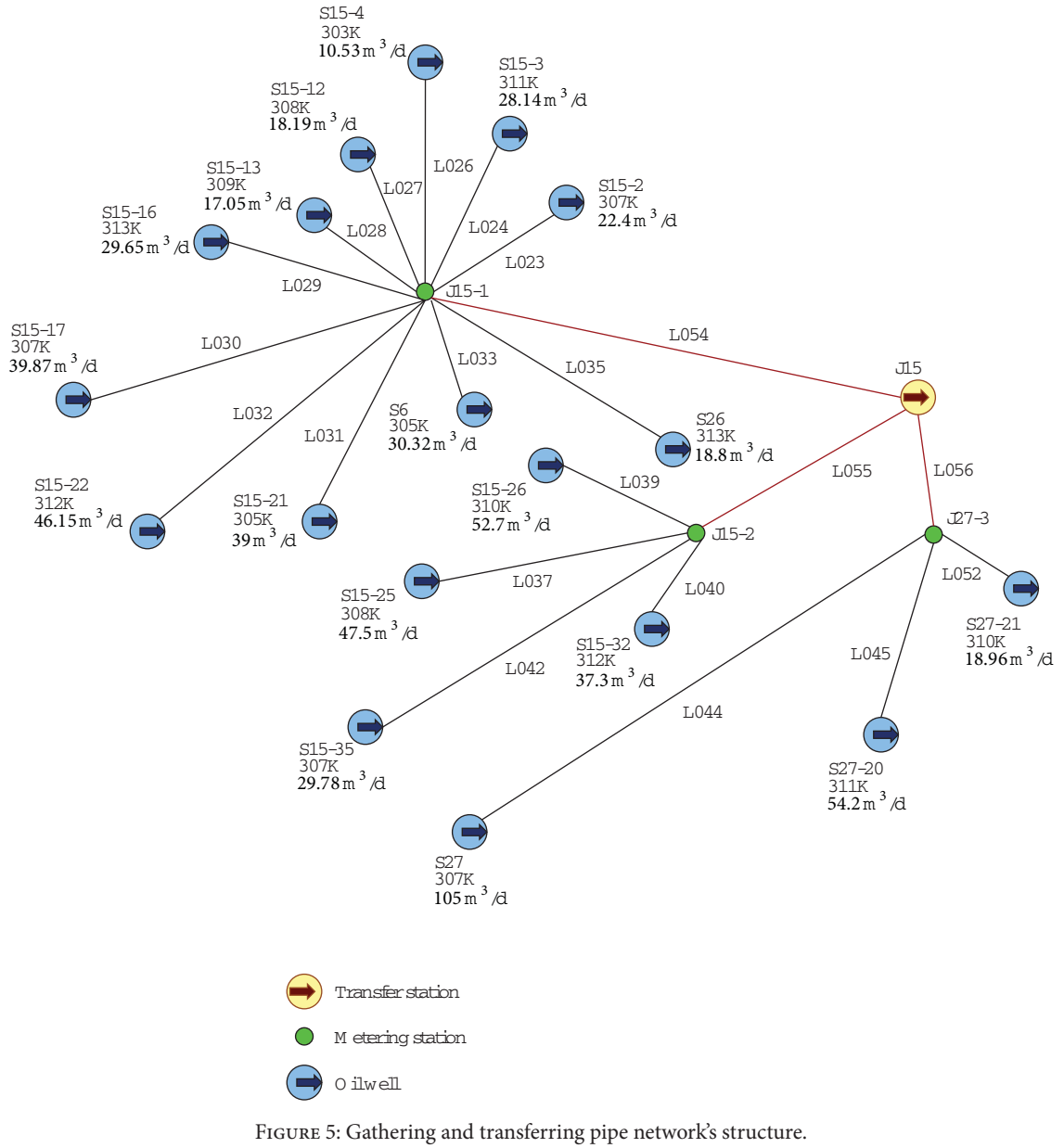

Figure 5: Gathering and transferring pipe network's structure.

At the kth step, the approximate programming problem is as follow:

$$\begin{aligned} \min \quad & q(d) = d^T \nabla f(x) + \frac{1}{2} d^T B d \\ \text{s.t.} \quad & d^T \nabla c_i(x) + c_i(x) = 0, \quad i \in E, \\ & d^T \nabla c_j(x) + c_j(x) \geq 0, \quad j \in I, \end{aligned} \tag{21}$$

where d is the difference between former and later iterations, named iteration direction; $q(d)$ is the objective function of new programming; $f(x)/c_i(x)$ is the objective function/constraints of original programming; $\nabla f(x)/\nabla c_i(x)$ is the gradient of $f(x)/c_i(x)$; B is Hessian matrix of $f(x)$; E/I is the set of subscripts of equality/inequality constraints.

As shown in Figure 3, the algorithm mainly includes 3 steps: (a) solve the subproblem with active-set method to get d and Lagrange multiplier λ; (b) employ quadratic interpolation and linear search to get step length α; (c) update Hessian matrix B with BFGS (Broyden-Fletcher-Goldfarb-Shanno) method, where k is the number of iterations, s is the difference between former and later iterations, and e is the control error.

5.2. Active-Set Method. Subproblem (21) is a standard quadratic programming problem. The active-set method is the key to solving such problems. By swapping in/out the inequality constraints according to some rules, A convex

Table 1: Optimal operational parameters.

Well	Water mass rate (t/d)		Water temperature (°C)	
	Before	After	Before	After
s15-2	115.5	77.0	75	79
s15-3	94.7	79.0	75	79
s15-4	44.2	34.0	70	73
s15-12	55.4	39.5	74	78
s15-13	50.2	45.7	75	79
s15-16	74.4	56.0	75	79
s15-17	111.3	79.5	75	79
s15-21	224.7	149.8	75	79
s15-22	166.3	151.3	76	80
s6	120.2	87.1	76	81
s26	76.6	46.3	73	77
s15-25	129.9	77.8	75	79
s15-26	194.5	104.5	75	79
s15-32	83.7	67.0	75	79
s15-35	127.0	86.4	74	77
s27	241.9	216	72	76
s27-20	186.7	121.2	74	78
s27-21	62.8	48.0	74	77

Table 2: Comparison between costs before and after optimization.

Item	Before	After
Outlet water temperature of transfer station (°C)	77	82
Total mass rate of water (t/d)	2160.0	1566.1
Amount of fuel (t/d)	7.3	6.9
Heating cost (RMB/d)	33580	31655
Electricity consumption (kWh/d)	784.0	568.4
Power cost (RMB/d)	548.8	397.9
Total cost (RMB/d)	34129	32053

quadratic programming (22) only with equality constraints is obtained:

$$\begin{aligned} \min \quad & q(dd) = dd^T g^k + \frac{1}{2} dd^T B dd \\ \text{s.t.} \quad & dd^T \nabla c_i(x)^k = 0, \quad i \in E, \\ & dd^T \nabla c_j(x)^k = 0, \quad j \in I^*, \end{aligned} \tag{22}$$

where

$$g^k = Bd + \nabla f(x). \tag{23}$$

Problem (22) converts the solution of d into the solution of the direction of d, named dd.

Figure 4 gives the steps of the solution of d.

6. Example Analyses

As shown in Figure 5, the transfer station of North China Oilfield has 3 metering stations and 18 oil wells. The well effluent of each well has a mass rate of 10.5~53.6 t/d, a water cut of higher than 80%, and a temperature of 30~40°C.

The model has 36 decision variables, 17 equality constraints, and 4 inequality constraints. It takes 114 iterations, about 4.24 seconds to get the optimal results, as shown in Table 1.

Table 2 sets out the comparison between costs before and after optimization. It shows that the optimized heating cost and power cost decrease by 1925 RMB/d and 151 RMB/d, respectively, which means the total cost can be reduced by 2076 RMB/d in sum.

7. Conclusions

(1) A mathematic model of the gathering pipeline network optimal operation and its solution are given in this paper, which can provide optimal operation parameters for triple-line process.

(2) Using a gathering pipeline network of North China Oilfield as an example, a mathematic model has been established. After comparing the optimal results with the actual operation data, it concludes that by using the new model, there is a considerable cost saving in accordance with the optimized parameters over that which exists at present.

Nomenclature

Set and Indices

N: Set of meter stations $(1 \cdots n)$
M_i: Set of wells connected to a meter station $i(1 \cdots m_i)$
i, j: Indices corresponding to a meter station and a well, $i \in N$ and $j \in M_i$.

Parameters

c^o: The specific heat of an oil pipe liquid, J/(°C · kg)
c^w: The specific heat of water, J/(°C · kg)
$S^1 \cdots S^5$: Areas of 5 heat transfer surfaces of unit pipe length, m^2
$K^1 \cdots K^5$: The overall heat transfer coefficients of 5 heat transfer surfaces, W/(m^2 · °C)
t^f: The average soil temperature at the depth of pipes, °C
ρ^w: The water density, kg/m^3
ρ^o: The crude density, kg/m^3

Q_{ij}: The volumetric flow rate of an oil pipe liquid *ij*, m^3/s
w_{ij}: The volumetric water cut of a well *ij*
K_i/K_{ij}: The overall heat transfer coefficient of a water pipe *i/ij*, $W/(m^2 \cdot {}^\circ C)$
d_i/d_{ij}: The diameter of the water pipe *i/ij*, m
L_i/L_{ij}: The length of the water pipe *i/ij*, m
p^r: The fuel price, RMB/kg
t^y: The water temperature before being heated, ˚C
q^r: The lower heating value, J/kg
η: The efficiency of heating furnace
p^d: The price of electricity RMB/J
g: The acceleration of gravity, N/kg
ΔH: The water head of the pump, m
η': The pump's efficiency
T^n: The freezing point of crude oil, ˚C
Δt: The temperature allowance, ˚C.

Variables

G: The mass rate of an oil pipe liquid, kg/s
T^z: The liquid temperature at the end of the oil pipe, ˚C
g^w: The mass rate of water, kg/s
t^z: The water temperature at the end of a tracing pipe, ˚C
T^q: The liquid temperature at the beginning of an oil pipe, ˚C
t^q: The water temperature at the beginning of a tracing pipe, ˚C
G_i/G_{ij}: The mass rate of an oil pipe's liquid *i/ij*, kg/s
c_i^o/c_{ij}^o: The specific heat of an oil pipe's liquid *i/ij*, $J/(^\circ C \cdot kg)$
T_{ij}^z: The liquid temperature at the end of an oil pipe *ij*, ˚C
T_i^q: The resulting oil pipes' liquid temperature when mixed at their node *i*, ˚C
T_i^z: The transfer station's inlet temperature of an oil pipe *i*, ˚C
t_{ij}^z: The water temperature at the end of a tracing pipe *ij*, ˚C
t_i^q: The resulting tracing pipes' water temperature when mixed at their node *i*, ˚C
t_i^z: The transfer station's inlet temperature of a tracing pipe *i*, ˚C
g_i^w/g_{ij}^w: The mass rate of water distributed to a node *i/ij*, kg/s
t_i^Q/t_{ij}^Q: the water temperature at the beginning of a water pipe *i/ij*, ˚C
t_i/t_{ij}: The water temperature at the end of awater pipe *i/ij*, ˚C
t: The outlet water temperature of a transfer station, ˚C
Δt_i: The commencing temperature difference between a water pipe i and a water pipe $(i+1)$,˚C
Δt_{ij}: The commencing temperature difference between a water pipe ij and a water pipe $i(j+1)$,˚C.

References

[1] R. J. Barnes, A. Kokossis, and Z. Shang, "An integrated mathematical programming approach for the design and optimisation of offshore fields," *Computers and Chemical Engineering*, vol. 31, no. 5-6, pp. 612–629, 2007.

[2] D. A. Antonenko, V. A. Pavlov, V. N. Surtaew, and K. K. Sevastyanova, "Selecting an optimal field development strategy for the vankor oilfield using an integrated-asset-modeling approach," in *Proceedings of the SPE Europec/EAGE Conference and Exhibition*, Rome, Italy, June 2008.

[3] Y. Liu and G. Chen, "Optimal parameters design of oilfield surface pipeline systems using fuzzy models," *Information Sciences*, vol. 120, no. 1, pp. 13–21, 1999.

[4] S. A. Van Den Heever and I. E. Grossmann, "An iterative aggregation/disaggregation approach for the solution of a mixed-integer nonlinear oilfield infrastructure planning model," *Industrial and Engineering Chemistry Research*, vol. 39, no. 6, pp. 1955–1971, 2000.

[5] J. M. Duan, W. Wang, Y. Zhang et al., "Calculation on inner wall temperature in oil-gas pipe flow," *Journal of Central South University of Technology*, vol. 19, pp. 1932–1937, 2012.

[6] P. Floquet, X. Joulia, A. Vacher, M. Gainville, and M. Pons, "Numerical and computational strategy for pressure-driven steady-state simulation of oilfield production," *Computers and Chemical Engineering*, vol. 33, no. 3, pp. 660–669, 2009.

[7] C. J. Alvarez, M. H. Al-awwami, and S. Aranco, "Wet crude transport through a complex hilly terrain pipeline network," in *Proceedings of the SPE Annual Technical Conference and Exhibition*, Houston, Tex, USA, October 1999.

[8] W. X. Wang, *Operation optimization and project setting for heavy oil three pipe tracing gathering and transferring system [M.S. thesis]*, Daqing Petroleum Institute, Daqing, China, 2006.

[9] Department of Mathematics at Tongji university, *Advanced Mathematics[M]*, Higher Education Press, Beijing, China, 2007.

[10] X. L. Gao and M. Kuang, "The determination on the minimum allowable inlet temperature of waxy crude oil pipeline," *Oil & Gas Storage and Transportation*, vol. 21, no. 11, pp. 17–21, 2002.

[11] The Writing Committee of Technical Manual of Oilfield Oil-gas Gathering and Transportation Design, *Technical Manual of Oilfield Oil-Gas Gathering and Transportation Design*, Petroleum Industry Press, Beijing, China, 1994.

[12] GB 50350-2005, *Code for Design of Oil-Gas Gathering and Transportation System*, GB, Beijing, China, 2005.

[13] G. P. He, Z. Y. Gao, and Y. G. Zheng, "An effective sequential quadratic programming algorithm for nonlinear optimization problems," *Numerical Mathematics a Journal of Chinese Universities (English Series)*, no. 1, pp. 34–51, 2002.

[14] Q. Ni, "A new inexact sequential quadratic programming algorithm," *Numerical Mathematics a Journal of Chinese Universities (English Series)*, no. 1, pp. 1–12, 2002.

[15] G. P. He, Z. Y. Gao, and Y. L. Lai, "New sequential quadratic programming algorithm with consistent subproblems," *Science in China Series A*, vol. 40, no. 2, pp. 137–150, 1997.

Hindawi Publishing Corporation
Advances in Mechanical Engineering
Volume 2013, Article ID 527182, 10 pages
http://dx.doi.org/10.1155/2013/527182

Research Article

Numerical Study on the Mixed Convection Heat Transfer between a Sphere Particle and High Pressure Water in Pseudocritical Zone

Liping Wei, Youjun Lu, and Jinjia Wei

State Key Laboratory of Multiphase Flow in Power Engineering, Xi'an Jiaotong University, Xi'an 710049, China

Correspondence should be addressed to Youjun Lu; yjlu@mail.xjtu.edu.cn

Received 10 January 2013; Accepted 28 February 2013

Academic Editor: Bo Yu

Mixed convection heat transfer between supercritical water and particles is a major basic problem in supercritical water fluidized bed reactor, but little work focused on this new area in the past. In this paper, a numerical model fully accounting for thermophysical property variation has been established to investigate heat transfer between supercritical water and a single spherical particle under gravity. Flow field, temperature field and Nusselt number are analyzed based on the simulation results. Results show that buoyancy force has a remarkable effect on flow and heat transfer process. When the direction of gravity and flow are opposite, the gravity enhances the heat transfer before the separation point and inhibits the heat transfer after the separation point. When gravity is incorporated in calculation, a higher temperature gradient and a thinner boundary layer in the vicinity of the particle surface are observed before separation point, and the situations are just the reverse after separation point. Variation of specific heat and conductivity plays a main role in determination of heat transfer coefficient.

1. Introduction

Supercritical water fluidized bed reactor (SCWFBR) is a new promising reactor for gasifying wet biomass to product hydrogen [1]. It is a promising technology because it could avoid plugging effectively and produce hydrogen efficiently [2]. However, determination of heat transfer rate from solid particles to supercritical water (SCW) is a hard work due to complicated gas-solid phase flow and huge property variation of SCW in the reactor. Dong et al. (2012) [3] numerically studied the heat transfer process between bed and wall in SCWFBR. They found that the transfer process in SCWFBR was very different from that in traditional gas-solid fluidized bed. First, the heat transfer in SCWFBR was dominated by the heat transfer of supercritical water. The shape of curves of heat transfer coefficient with bed temperature is similar to the case of supercritical water flow through duct. Second, particle concentration enhanced the heat transfer process, but particle concentration did not greatly affect the heat transfer rate as that in gas-solid fluidized bed. Those differences make the studying the heat transfer processes in SCWFBR become interesting and significant. The reactor always works at a low superficial velocity. So, the mixed convection heat transfer from particles to SCW is obvious, and a simple case for this problem is SCW flowing over a single sphere particle. Little work studied this area in the past.

Mixed convective heat transfer from a sphere in infinite fluid has been studied by many researchers for different interests because it represents a problem related to numerous engineering applications. An exact analytical solution of this problem is hard to achieve due to the nonlinearity in the governing equations [4]. The earliest analytical studies on the combined effect of free and forced convection in assisting mixed convective flow were conducted by Acrivos (1966) (boundary-layer approximation) and Hieber and Gebhart (1969) (matched asymptotic expansion) [5, 6]. Experimental data about mixed convection heat transfer around a sphere in variable fluid were obtained by several researchers by different equipments. Yuge (1960) experimentally studied

the mixed convection heat transfer around an isothermal sphere in air flow with a wide range of Reynolds numbers ($3.5 \leq Re \leq 1.44 \times 10^5$) and Grashof numbers ($1 \leq Gr \leq 10^5$) [7]. Tang and Johnson (1990) obtained various flow patterns of opposing flow by mixed convection experiments with a Grashof number of 9.0×10^5 and Reynolds numbers up to 1100 [8]. Recently, Ziskind et al. (2001) and Mograbi et al. (2002) studied the cross-flow, assisting and opposing flows at low Grashof number and Reynolds number in an electrodynamics chamber (EDC) [9, 10]. Koizumi (2004) studied the time and spatial heat transfer performance around an isothermal sphere in a uniform, downwardly directed air flow by conducting an experiments with Grashof number of $Gr = 3.3 \times 10^5$ and Reynolds numbers up to 1800 [11]. Later, they (2010) revealed transition process from a steady axisymmetric separated flow to a chaotic flow of an isothermally heated sphere placed in a uniform, downwardly directed flow by experimentation and transient 3D numerical simulation [12].

Due to limitation of experimental and analytical solution, it is necessary to study this problem through numerical simulation. Chen and Mucoglu (1977) numerically investigated the laminar mixed convection around a sphere with constant surface temperature. They found that both the local friction factor and the local Nusselt number increase with increasing buoyancy force for aiding flow and decrease with increasing buoyancy force for opposing flow [13]. In their later work, they presented a similar study for a sphere with a uniform heat flux [14]. Recently, Antar and El-Shaarawi (2002) numerically studied the problem of mixed convection around a liquid sphere in an air stream for aiding and opposing flows [15]. They found that increasing Reynolds number or decreasing the interior-to-exterior viscosity ratio delays the flow separation. The similar conclusions were obtained by later researches. Nazar and Amin (2002) numerically studied the mixed convection flow of an incompressible viscous fluid around a solid sphere with constant surface temperature for both aiding and opposing flow [4]. They found that the aiding flow delays separation of the boundary-layer but the opposing flow brings the separation point closer to the lower stagnation point of the sphere. Later, they extended this problem to micropolar fluid [16]. Kotouč et al. (2008) numerically investigated the issue of loss of axisymmetry in the assisting flow [17]. They found that the acceleration of the flow due to buoyancy considerably stabilized the flow and pushed the onset of instabilities. Bhattacharyya and Singh (2008) studied the aiding flow from an isolated spherical particle with moderate range of Reynolds number ($1 \leq Re \leq 200$) and Grashof number ($0 \leq Gr \leq 10^4$) [18]. They revealed that the decrease in drag coefficient with increase of Reynolds number is due to the increase of the wake size, and the heat transfer is dominated by the convection effect at higher Reynolds number.

Most of the earlier work on natural or mixed convection was based on the Boussinesq approximation, which treated variable density as a linear relationship with temperature. However, variation of flow thermophysical property becomes very critical in some cases such as heat transfer of supercritical fluid in critical zone. This paper studied the mixed convection around a sphere particle in SCW of pseudocritical zone with moderate range of Reynolds number ($5 \leq Re \leq 200$), which represents supercritical water fluidized bed works at relatively low superficial velocity. The influence of buoyancy force on heat transfer has been investigated. Flow field and heat transfer is analyzed for different values of the Richardson number ($Ri = Gr/Re^2$). Effect of thermophysical property on the flow and heat transfer is studied.

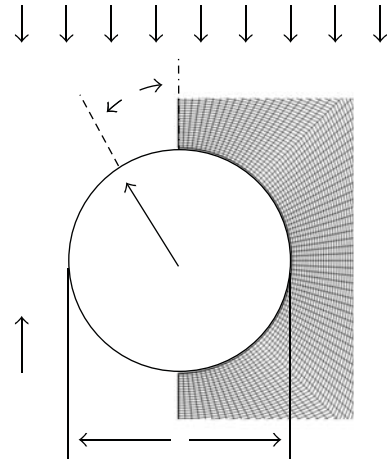

Figure 1: Schematics of a spherical particle in SCW under gravity.

2. Problem Statement and Solution

2.1. Physical Problem. Strictly speaking, the heating of a particle in SCW flow is a transient process. However, as the focus of this study is to understand the effect of flow property variation, the transient particle temperature variations are not considered. Johnson and Patel (1999) numerically and experimentally investigated the flow of incompressible viscous fluid passing a sphere over flow regimes including steady and unsteady laminar flow at Reynolds numbers up to 300 [19]. They found that steady axisymmetric flow maintains at Reynolds numbers up to 200. Although there are no studies verifying weather the results are suitable for supercritical condition, the time average values of drag coefficient and Nusselt number are close to the data obtained in steady assumption with Reynolds number over 200 [13]. Furthermore, based on the results obtained by Antar and El-Shaarawi (2002), Nazar et al. (2002), and Kotouč et al. (2008), buoyancy force keeps the flow steady and symmetry for aiding flow [4, 15, 17]. This work considers that steady, axisymmetric convection heat transport from particle to SCW flow occurs for particles with constant surface temperature at moderate Reynolds numbers. Figure 1 shows the schematics of the SCW flow over a sphere and relative boundary conditions.

2.2. Mathematical Formulation and Solution. Governing continuum conservation equations for steady flow with

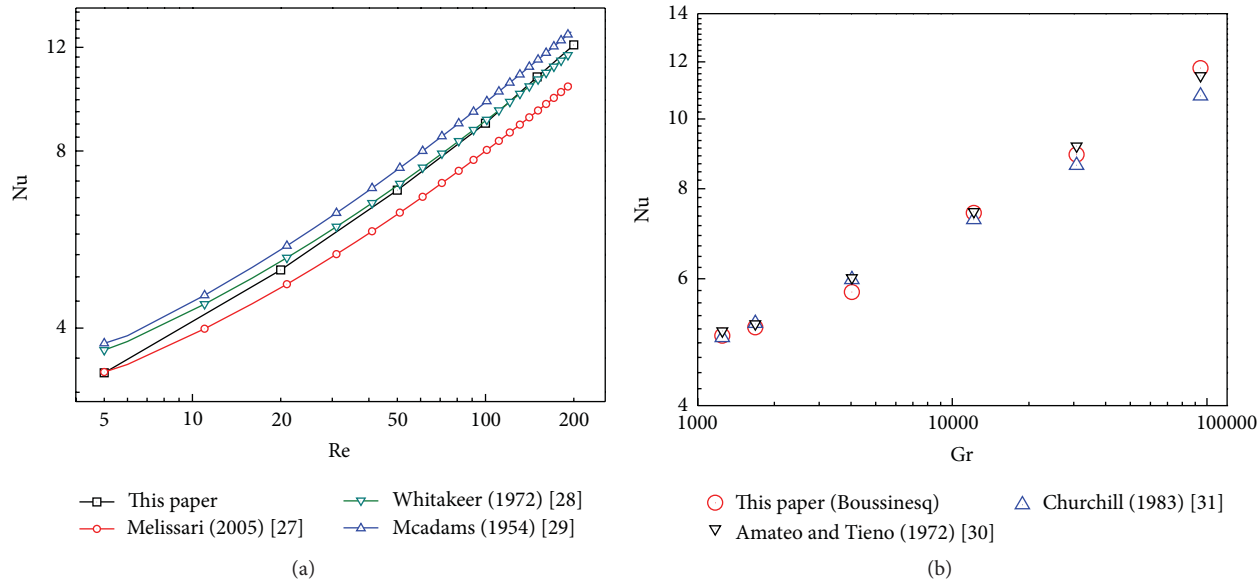

FIGURE 2: Comparison of average Nusselt number obtained by simulation with correlation: (a) forced convection heat transfer; (b) free convection heat transfer.

variable property over a particle with gravity and negligible viscous dissipation can be given as follows.

Mass conservation is written as

$$\nabla \cdot \rho \vec{u} = 0. \tag{1}$$

The momentum equation is written as

$$(\vec{u} \cdot \nabla)\, \rho \vec{u} = -\nabla p + \nabla \left(\mu \nabla \cdot \vec{u}\right) + g. \tag{2}$$

The energy equation is written as

$$(\vec{u} \cdot \nabla)\, \rho h = \nabla \cdot (k \nabla T)\,. \tag{3}$$

The Grashof number is defined as

$$\mathrm{Gr} = \frac{g\beta\rho^2 d^3 \Delta T}{\mu^2}. \tag{4}$$

The thermal expansion coefficient of the fluid is defined as

$$\beta = -\frac{1}{\rho_\infty}\left(\frac{\partial \rho}{\partial T}\right). \tag{5}$$

The Nusselt number is defined as

$$\mathrm{Nu} = \frac{d}{2k_\infty \left(T_w - T_\infty\right)} \int_0^\pi k_\theta \left(\frac{dT}{dr}\right)_\theta d\theta. \tag{6}$$

These equations are solved using a finite volume method. The boundary conditions include specified uniform far field temperature and velocity (free stream), no-slip condition and specified temperature at the particle surface, axisymmetry condition along the centerline, moving wall at the upper boundary (the velocity of wall is the same with free stream), and fully developed exit conditions. The properties of supercritical water are calculated by IAPWS-IF97 equations [20]. The convective terms are discretized using second-order upwind scheme. The SIMPLEC algorithm is applied for the pressure-velocity coupling. Typical values of under-relaxation factors were set from 0.1 to 0.5. A convergence criterion of 10^{-6} for each scaled residual component was specified for the relative error between two successive iterations.

2.3. Grid. Figure 1 shows the schematic of the nonuniform grid structure used in this work. It needs a lager domain zone for small Grashof number and low Reynolds number case because of strong viscous reaction and thick boundary layer. The domain size can be determined by the values of R_∞/r. Based on the similar domain grid independence studies conducted by Feng and Michaelides (2000), Dhole et al. (2006), Kumar and Kishore (2009), Dudek et al. (1988), Geoola and Cornish (1981), and Prhashanna and Chhabra (2010) about forced and free convective heat transfer from a sphere, domain grid zone has been determined separately by two flow regimes with different Reynolds number [21–26]. One is steady flow without wake formation for Re < 20 and the other is 2-D steady flow with wake formation in the range of 20 ≤ Re ≤ 200. In this work, the value of R_∞/r is 150 for Re < 20 and 100 for 20 ≤ Re ≤ 200.

2.4. Validation. There are no any experimental data, simulation results, or theoretical solutions for mixing convective heat transfer from a sphere in supercritical pressure. In order to validate the simulations in this work, Nusselt numbers for constant property fluid passing over a sphere have been compared with the correlations calculated results in the literature. The thermophysical properties of SCW in this paper are calculated by IAPWS-IF97 equations at

far field temperature and pressure [20]. The simulations are conducted in consideration of gravity or not referred to Richardson number equaling zero or not. Figure 2(a) shows average Nusselt number predicted by this work for forced convection flow being very close to those correlations proposed by Melissari and Argyropoulos (2005), Whitaker (1972), and McAdams (1954) [27–29]. Predictions by heat transfer correlations and present numerical studies are accurate with deviation generally within ±10%. In order to validate the model under gravity, average Nusselt numbers are obtained by simulation with Boussinesq approximation $(\rho - \rho_\infty) = -\rho_\infty \beta(T - T_\infty)$. Boussinesq model assumes that the fluid density is constant in all terms of the momentum equation except the body force term. All properties are evaluated at the fluid film temperature, T_m, defined as $(T_w + T_\infty)/2$. Figure 2(b) shows the comparison of average Nusselt number obtained by simulation with correlations presented by different researchers [30, 31]. It is clear that the trend of the simulation results is consistent with those correlations. The predicted values of Nusselt number by simulation have an agreement with that calculated by Amateo and Tieno's and Churchill's correlations within deviation generally within ±5%. Those comparisons validate the computational model used in this work for constant property fluid. The next section will carefully analyse the effect of variable properties.

3. Results and Discussion

3.1. Flow Field. Effect of gravity on the mixed convection flow field for SCW flowing over a sphere is analyzed in this work. The properties of flow are calculated at the far field temperature in this section. The dimensionless parameters (Nusselt number, Grashof number, Reynolds number, and so on) are all calculated at the temperature in far field.

Figure 3 shows effect of gravity on the flow stream around a sphere in SCW flow in the pseudocritical zone. The general shape of the flow field does not change significantly at rear hemisphere even if the gravity is considered. However, the zone of flow streamlines near the leading hemisphere becomes wide when gravity is incorporated in computed model at Reynolds number of 5. The recirculation zone after sphere becomes smaller under gravity. The rear vortex will vanish if buoyancy force is strong enough. The collapse of rear vortex due to density stratification was also observed by Torres et al. (2000) and Bhattacharyya and Singh (2008) for an assisting convective flow [18, 32]. The buoyancy force is determined by the density difference which results from the nonuniform temperature field. When the direction of gravity is against the flow direction, the buoyancy force assists the convective flow. More fluid is driven by buoyancy force to the leading hemisphere and more fluid is put forward by buoyancy force after rear hemisphere. Another interesting phenomenon is that the divergence in flow stream between Figures 3(a) and 3(b) becomes unconspicuous with an increase in Reynolds number. This is attributed to the fact that the convective effect becomes strong relative to buoyancy force with an increase in Reynolds number.

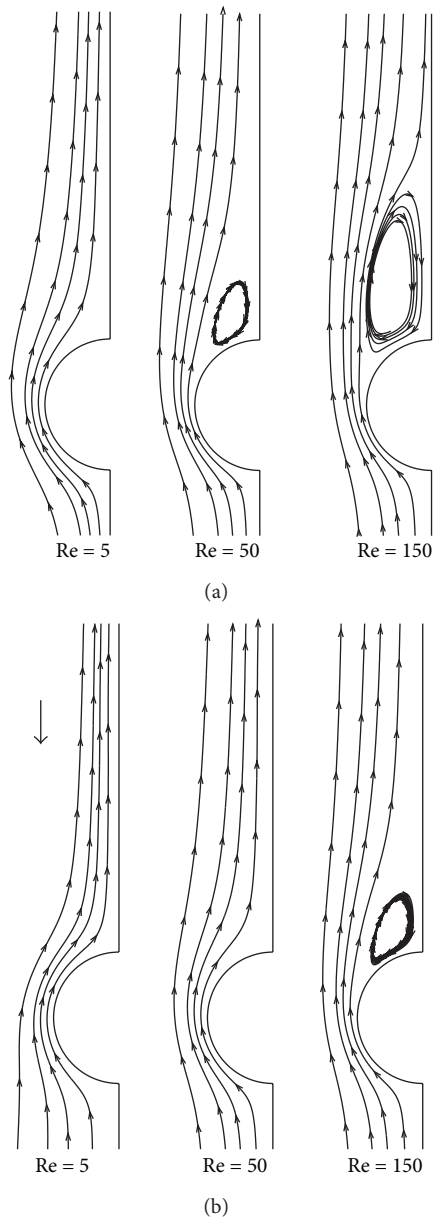

Figure 3: Streamlines around spherical particle, $P = 23$ MPa, $T_w = 657$ K, and $T_\infty = 647$ K: (a) without gravity; (b) under gravity.

Figure 4 shows the effect of gravity on surface vorticity magnitude in pseudocritical zone. The surface vorticity increases over the leading hemisphere and then reduces over the rear after it reaches a peak value in both calculations. Obviously, the magnitude of surface vorticity under gravity is much higher than that without gravity. At the same time, the position of surface vorticity maximum value moves toward the back of sphere which is in the same direction of the buoyancy force. When gravity is considered, a thinner boundary layer was formed. With the effect of buoyancy force, fluid around the sphere surface is accelerated. A higher flow velocity near the sphere surface indicates a stronger convective effect, which results in a higher momentum diffusivity and a thinner boundary layer thickness.

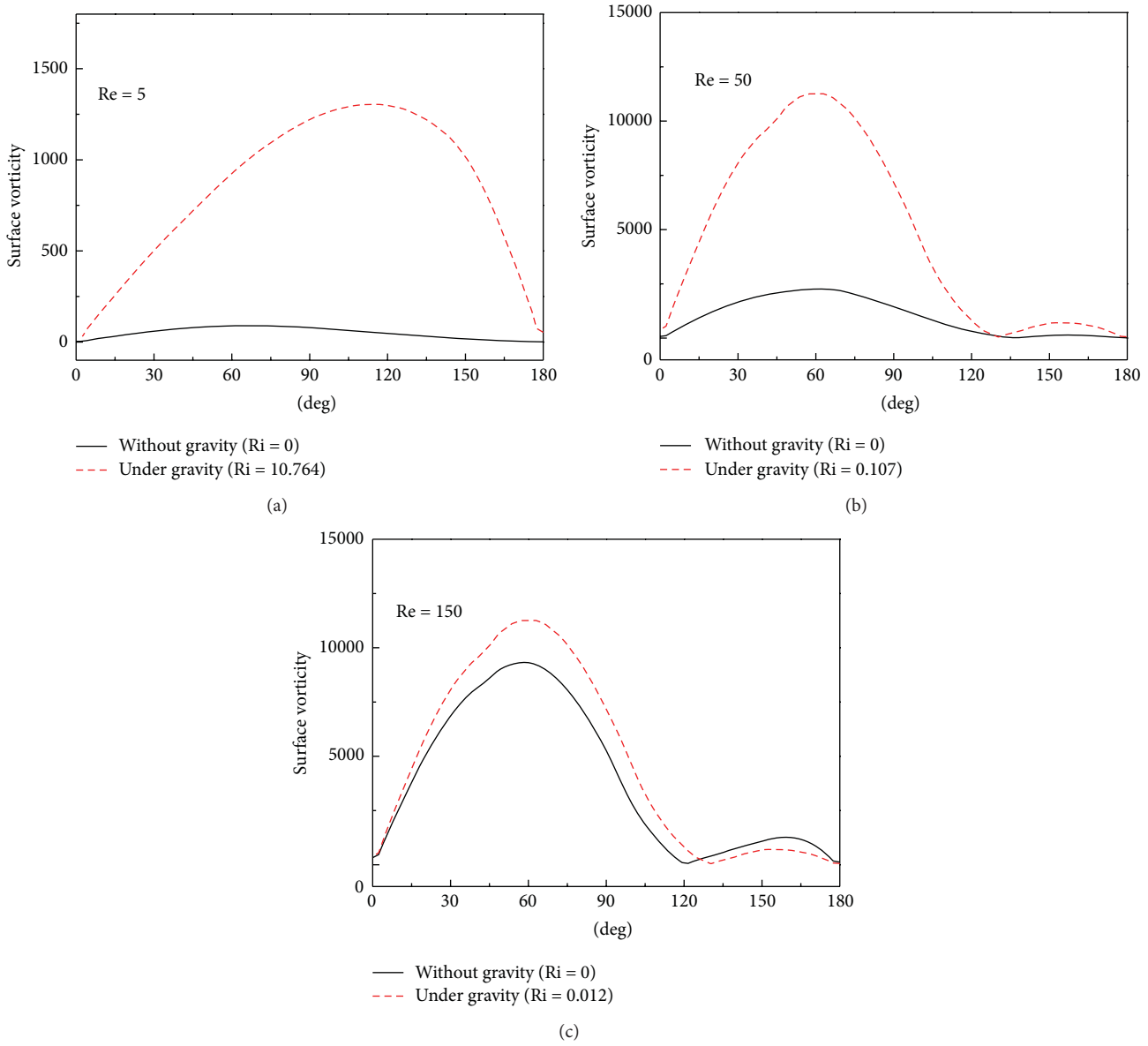

FIGURE 4: Surface vorticity at different Reynolds number, $P = 23$ MPa, $T_w = 657$ K, and $T_\infty = 647$ K: (a) Re = 5; (b) Re = 50; (c) Re = 150.

Figure 4 further shows a decrease in divergence with a decrease in Richardson number. This is attributed to forced convection which becomes more important in determination of the mixed convection with an increase in Reynolds number. Another noticed phenomenon is that the value of surface vorticity magnitude in recirculation zone under gravity is smaller than that without gravity, as shown in Figure 4(c). It means that the boundary layer thickness in recirculation zone becomes thicker on the effect of buoyancy force. The flow velocity near the sphere surface in recirculation zone is decelerated by buoyancy force because the directions of flow and buoyancy are opposite. A small recirculation zone under gravity is just result from the low fluid inertia force caused by a low fluid velocity.

Figure 5 shows surface pressure variation around the sphere at three conditions: constant property flow, SCW flow, and SCW flow under gravity. The dimensionless pressure was obtained by the free stream momentum $\rho_\infty U_\infty^2/2$. The trends of pressure variation along sphere for constant property flow and SCW flow are similar to the literature [33]. The highest value of surface pressure is formed at the stagnation point. The dimensionless pressure at the front stagnation point was closer to 1 at Reynolds number of 50 and 150, but nearly 2.5 at Reynolds number of 5. The pressure first decreases and then increases with an increase in streamwise angle. Wen and Jog (2005) [34] obtained similar results when they studied continuum plasma flow over spherical particles. They also found that dimensionless pressure at front stagnation

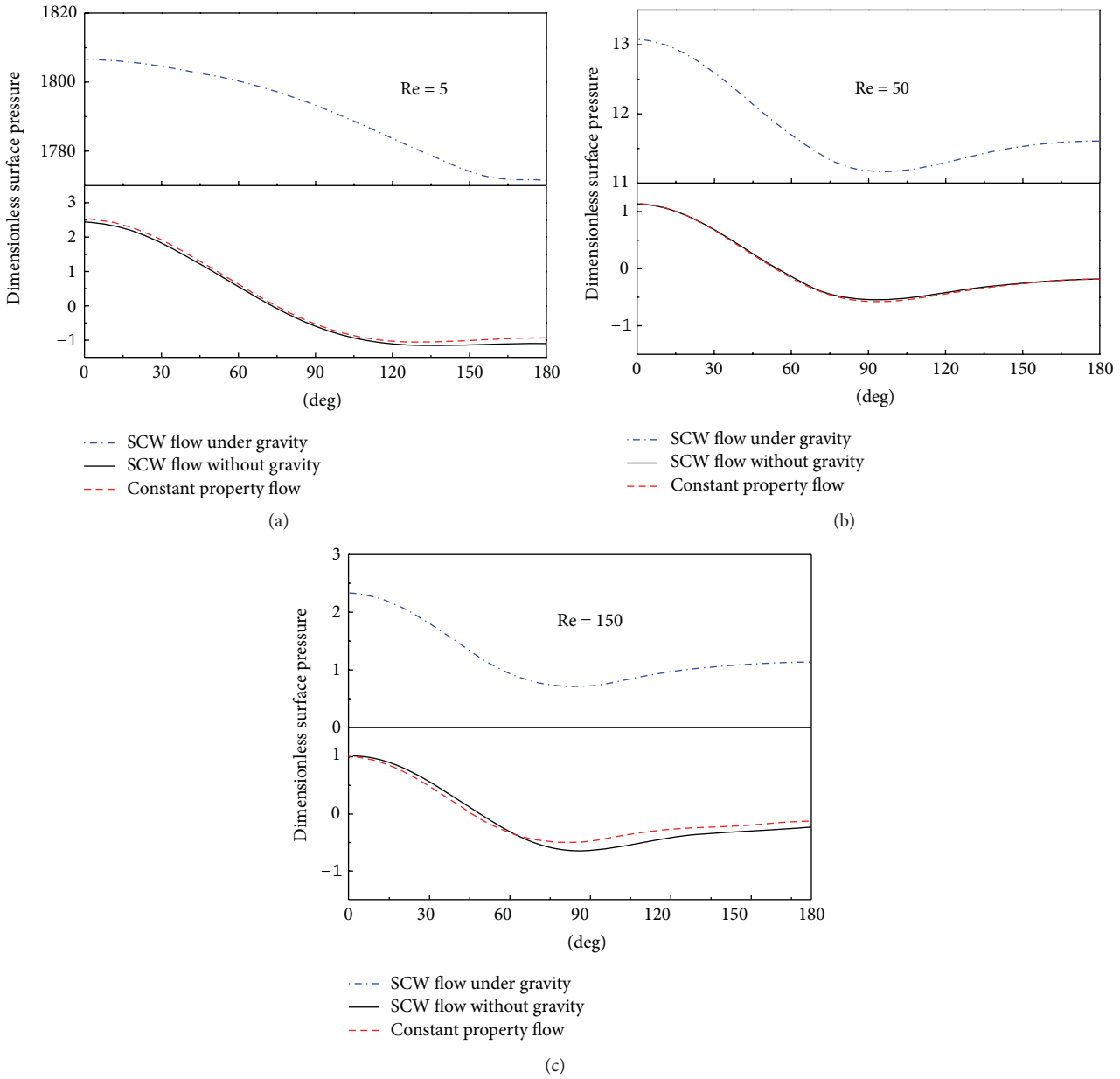

FIGURE 5: Dimension pressure distribution at surface of sphere, $P = 23$ MPa, $T_w = 657$ K, and $T_\infty = 647$ K: (a) Re = 5; (b) Re = 50; (c) Re = 150.

point was closer to 1 at Reynolds number of 50, but greater than 1 at Reynolds number of 20. It is attributed to the effect of strong viscous forces at low Reynolds number. There was no big difference of dimensionless pressure between constant property flow and SCW flow with gravity. So, the variable properties have little influence on the pressure distribution. Besides, the small adverse pressure at low Reynolds number may inhibit the flow separation. Both the gradient and value of dimensionless pressure are elevated when gravity is considered. This results in a small recirculation zone and flow separation delay at the same Reynolds number.

3.2. Temperature Field and Local Nusselt Number. Figure 6 shows the effect of gravity on temperature contours in pseudocritical zone. The shapes of temperature contours for two cases are similar. However, when gravity is incorporated in the computations, the temperature gradients become higher before the separation point and lower in the recirculation zone. High temperature gradient results in high heat flux transfer from sphere particle to fluid. Figure 7 shows that the local Nusselt number obtained before the separation point under gravity is higher than that without gravity. However, the local Nusselt number predicted after the separation point becomes lower under gravity. The increase or decrease in

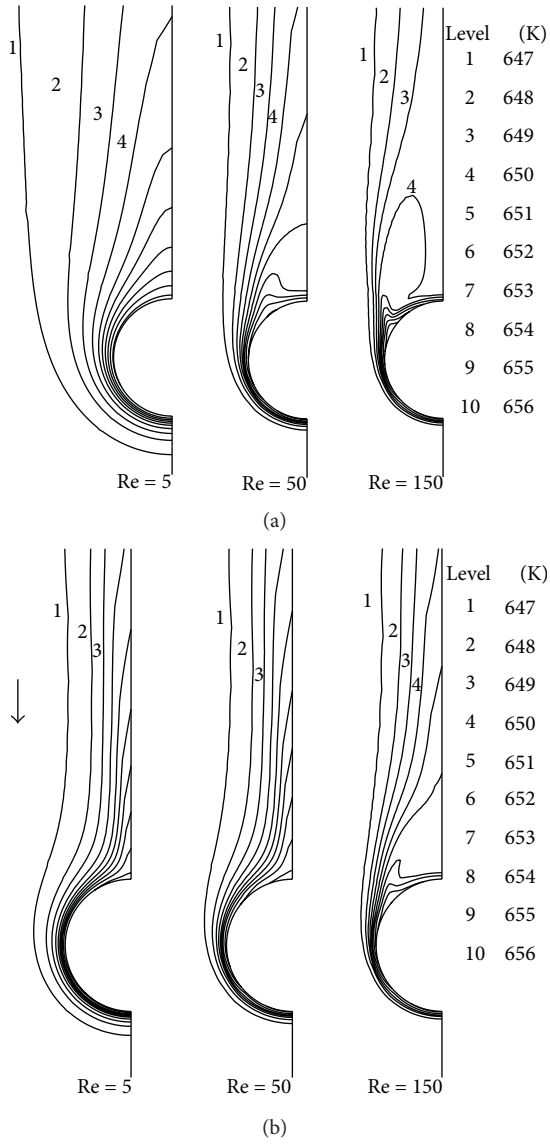

FIGURE 6: Temperature contour around sphere particle, $P = 23$ MPa, $T_w = 657$ K, and $T_\infty = 647$ K: (a) without gravity; (b) under gravity.

the temperature gradient is due to the thinner or thicker thermal boundary layer, which is caused by a higher or lower fluid velocity driven by boundary force. There is a peak of thermal conductivity and specific heat in pseudocritical temperature point. High thermal conductivity results in high heat rate transferring from sphere particle to fluid. At the same time, fluid with higher specific heat is able to store more energy, which makes diffusion of energy confined to a smaller radial distance and results in a higher temperature gradient.

3.3. Nusselt Number. Based on the previous analyses, effect of gravity on flow and temperature field is obvious for SCW flow. Figure 8 further compares the average Nusselt number between forced convection and mixed convection in the ranges of $5 \leq \mathrm{Re} \leq 200$. At low Reynolds number, the gravity assists the convective heat transfer. However, the gravity inhibits the convective heat transfer with the increasing Reynolds number. Based on the analysis in Section 3.2, gravity plays an opposite role in two sides of separation point. Figure 8 further shows this point.

At the same time, effect of properties on the heat transfer for SCW cannot be ignored in pseudocritical zone. In order to study the roles that thermophysical property plays, the simulations are conducted in this work by varying one or two properties with temperature while the rest of properties are maintained constant as values in the far field. Figure 8 shows the effect of each property on the Nusselt number. Effect of variable fluid density on the flow and temperature contours under gravity includes two parts: the free convection part and the forced convection part. The free convection part comes from the effect of buoyancy force which formed by density stratification. The forced convection part is shown clearly in the literature. For the effect of other properties except density, the main factor which enhances the mix convection heat transfer from particle to flow is the variation of specific heat and thermal conductivity. Effect of variation of viscosity on the average Nusselt number is relatively weak.

The results indicate that effect of variation of specific heat and thermal conductivity on the Nusselt number should be considered when developing a correlation. At a fixed Grashof number, the relationship between Reynolds number and Nusselt number for variable property flow is nearly linear in logarithmic coordinates.

4. Conclusions

The mixed convection heat transfer from sphere particle in SCW was studied by numerical method. A computational model considering the thermal property variation of SCW was developed successfully to describe the flow and heat transfer phenomena. Good agreement on Nusselt number was found between the simulation and correlation for constant property flow. Results show that buoyancy force has remarkable effect on flow and heat transfer process at low Reynolds number. The fluid velocity in mixed convection is influenced by the directions of buoyancy force and flow. When the directions of gravity and flow are opposite, the gravity enhances the heat transfer before the separation point, and inhibits the heat transfer after the separation point. Higher temperature gradient and thinner boundary layer thickness in the vicinity of the particle surface are observed before separation point and the situation is just the reverse after separation point. Effect of variable density on the mixed convection flow includes two parts: the forced convective part and free convective part. Variation of specific heat and conductivity plays a main role in determination of heat transfer coefficient, but variation of viscosity is an ignored factor that influences heat transfer.

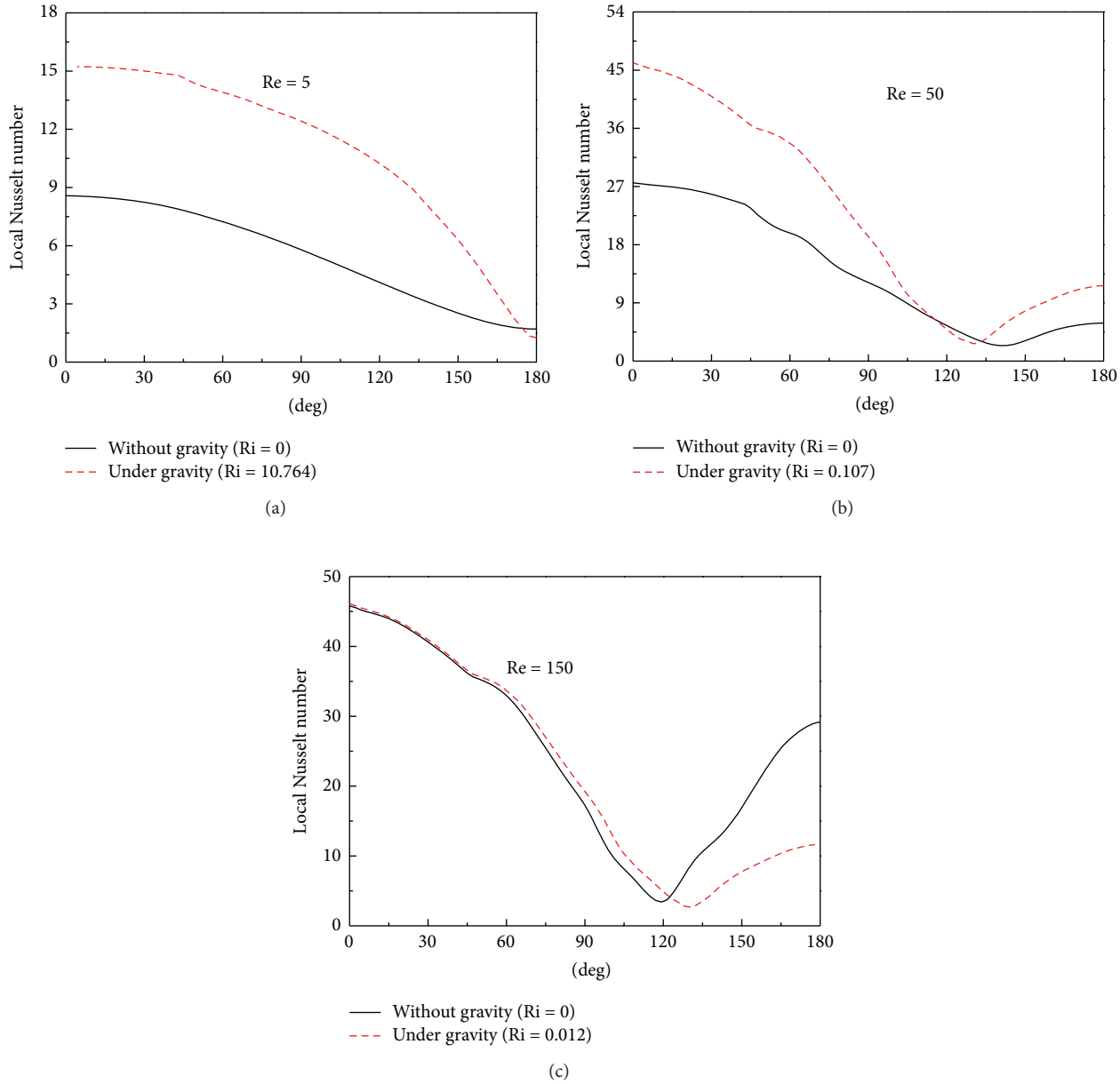

FIGURE 7: Local Nusselt number around spherical particle. P = 23 MPa, T_w = 657 K, and T_∞ = 647 K: (a) Re = 5; (b) Re = 50; (c) Re = 150.

Nomenclature

C_p: Special heat (J/(kg·K))
d: Diameter of sphere particle (mm)
g: Acceleration of gravity
Gr: Grashof number
h: Enthalpy (J/kg)
k: Conductive coefficient (W/(m·K))
Nu: Nusselt number
r: Radius of sphere particle (mm)
R_∞: Diameter of computed zone (mm)
P: Pressure (MPa)
Pe: Peclet number
Pr: Prandtl number
Ra: Rayleigh number
Re: Reynolds number
Ri: Richardson number
SCW: Supercritical water
SCWFBR: Supercritical water fluidized bed reactor
T: Temperature (K)
u: Velocity (m/s)

Greek Letters

β: Thermal expansion coefficient
μ: Viscosity (Pa·s)
ρ: Density (kg/m^3)
θ: Streamwise angle (degree)

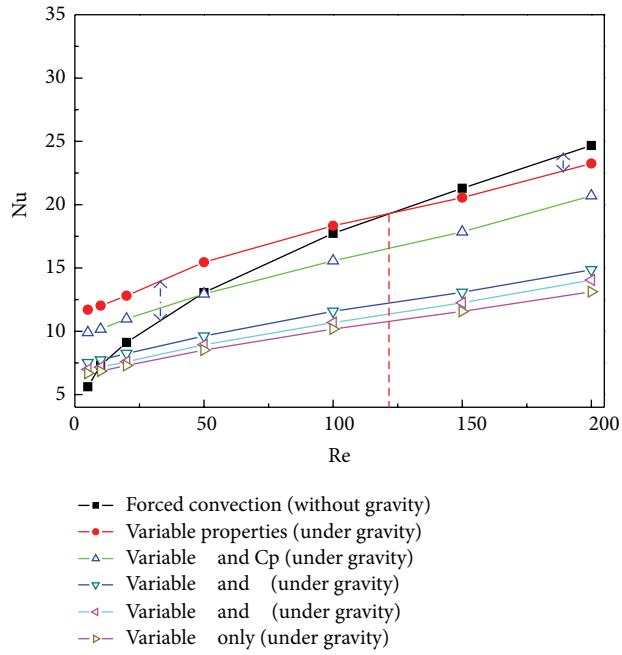

Figure 8: Effect of property variation on average Nusselt number under gravity.

Subscripts

∞: Far field
m: Film temperature
w: Wall surface.

Acknowledgments

This work is currently supported by the National Natural Science Foundation of China through Contract no. 50906069 and Program for New Century Excellent Talents in University (NCET-10-0678).

References

[1] Y. J. Lu, H. Jin, L. J. Guo, X. M. Zhang, C. Q. Cao, and X. Guo, "Hydrogen production by biomass gasification in supercritical water with a fluidized bed reactor," *International Journal of Hydrogen Energy*, vol. 33, no. 21, pp. 6066–6075, 2008.

[2] Y. Lu, L. Zhao, Q. Han et al., "Minimum fluidization velocities for supercritical water fluidized bed within the range of 633–693K and 23–27MPa," *International Journal of Multiphase Flow*, vol. 49, pp. 78–82, 2013.

[3] X. Dong, Y. Lu, and L. Wei, "Numerical study the heat transfer between bed and wall in supercritical water fluidized bed reactor," in *Proceedings of the Annual Meeting of the Multiphase Flow*, Xi'an, China, 2012.

[4] R. Nazar, N. Amin, and I. Pop, "On the mixed convection boundary-layer flow about a solid sphere with constant surface temperature," *Arabian Journal for Science and Engineering*, vol. 27, no. 2, pp. 117–135, 2002.

[5] A. Acrivos, "On the combined effect of forced and free convection heat transfer in laminar boundary layer flows," *Chemical Engineering Science*, vol. 21, no. 4, pp. 343–352, 1966.

[6] C. Hieber and B. Gebhart, "Mixed convection from a sphere at small Reynolds and Grashof numbers," *Journal of Fluid Mechanics*, vol. 38, no. 1, pp. 137–159, 1969.

[7] T. Yuge, "Experiments on heat transfer from spheres including combined natural and forced convection," *Journal of Heat Transfer*, vol. 82, pp. 214–220, 1960.

[8] L. Tang and A. T. Johnson, "Flow visualization of mixed convection about a sphere," *International Communications in Heat and Mass Transfer*, vol. 17, no. 1, pp. 67–77, 1990.

[9] G. Ziskind, B. Zhao, D. Katoshevski, and E. Bar-Ziv, "Experimental study of the forces associated with mixed convection from a heated sphere at small Reynolds and Grashof numbers. Part I: cross-flow," *International Journal of Heat and Mass Transfer*, vol. 44, no. 23, pp. 4381–4389, 2001.

[10] E. Mograbi, G. Ziskind, D. Katoshevski, and E. Bar-Ziv, "Experimental study of the forces associated with mixed convection from a heated sphere at small Reynolds and Grashof numbers. Part II: assisting and opposing flows," *International Journal of Heat and Mass Transfer*, vol. 45, no. 12, pp. 2423–2430, 2002.

[11] H. Koizumi, "Time and spatial heat transfer performance around an isothermally heated sphere placed in a uniform, downwardly directed flow (in relation to the enhancement of latent heat storage rate in a spherical capsule)," *Applied Thermal Engineering*, vol. 24, no. 17-18, pp. 2583–2600, 2004.

[12] H. Koizumi, Y. Umemura, S. Hando, and K. Suzuki, "Heat transfer performance and the transition to chaos of mixed convection around an isothermally heated sphere placed in a uniform, downwardly directed flow," *International Journal of Heat and Mass Transfer*, vol. 53, no. 13-14, pp. 2602–2614, 2010.

[13] T. S. Chen and A. Mucoglu, "Analysis of mixed forced and free convection about a sphere," *International Journal of Heat and Mass Transfer*, vol. 20, no. 8, pp. 867–875, 1977.

[14] A. Mucoglu and T. S. Chen, "Mixed convection about a sphere with uniform surface heat flux," *Journal of Heat Transfer*, vol. 100, no. 3, pp. 542–544, 1978.

[15] M. A. Antar and M. A. I. El-Shaarawi, "Mixed convection around a liquid sphere in an air stream," *Heat and Mass Transfer*, vol. 38, no. 4-5, pp. 419–424, 2002.

[16] R. Nazar, N. Amin, and I. Pop, "Mixed convection boundary layer flow about an isothermal sphere in a micropolar fluid," *International Journal of Thermal Sciences*, vol. 42, no. 3, pp. 283–293, 2003.

[17] M. Kotouč, G. Bouchet, and J. Dušek, "Loss of axisymmetry in the mixed convection, assisting flow past a heated sphere," *International Journal of Heat and Mass Transfer*, vol. 51, no. 11-12, pp. 2686–2700, 2008.

[18] S. Bhattacharyya and A. Singh, "Mixed convection from an isolated spherical particle," *International Journal of Heat and Mass Transfer*, vol. 51, no. 5-6, pp. 1034–1048, 2008.

[19] T. A. Johnson and V. C. Patel, "Flow past a sphere up to a Reynolds number of 300," *Journal of Fluid Mechanics*, vol. 378, pp. 19–70, 1999.

[20] W. Wagner and H. J. Kretzschmar, *International Steam Tables: Properties of Water and Steam Based on the Industrial Formulation IAPWS-IF97: Tables, Algorithms, Diagrams, and CD-ROM Electronic Steam Tables: All of the Equations of IAPWS-IF97 Including a Complete Set of supplementary backward Equations for fast calculations of heat Cycles, Boilers, and Steam Turbines*, Springer, 2008.

[21] Z. G. Feng and E. E. Michaelides, "A numerical study on the transient heat transfer from a sphere at high Reynolds and Peclet

numbers," *International Journal of Heat and Mass Transfer*, vol. 43, no. 2, pp. 219–229, 2000.

[22] S. D. Dhole, R. P. Chhabra, and V. Eswaran, "A numerical study on the forced convection heat transfer from an isothermal and isoflux sphere in the steady symmetric flow regime," *International Journal of Heat and Mass Transfer*, vol. 49, no. 5-6, pp. 984–994, 2006.

[23] N. Kumar and N. Kishore, "2-D newtonian flow past ellipsoidal particles at moderate reynolds numbers," in *Proceedings of the 7th International Conference on CFD in the Minerals and Process Industries*, Melbourne, Australia, 2009.

[24] D. R. Dudek, T. H. Fletcher, J. P. Longwell, and A. F. Sarofim, "Natural convection induced drag forces on spheres at low Grashof numbers: comparison of theory with experiment," *International Journal of Heat and Mass Transfer*, vol. 31, no. 4, pp. 863–873, 1988.

[25] F. Geoola and A. R. H. Cornish, "Numerical solution of steady-state free convective heat transfer from a solid sphere," *International Journal of Heat and Mass Transfer*, vol. 24, no. 8, pp. 1369–1379, 1981.

[26] A. Prhashanna and R. P. Chhabra, "Free convection in power-law fluids from a heated sphere," *Chemical Engineering Science*, vol. 65, no. 23, pp. 6190–6205, 2010.

[27] B. Melissari and S. A. Argyropoulos, "Development of a heat transfer dimensionless correlation for spheres immersed in a wide range of Prandtl number fluids," *International Journal of Heat and Mass Transfer*, vol. 48, no. 21-22, pp. 4333–4341, 2005.

[28] S. Whitaker, "Forced convection heat transfer correlations for flow in pipes, past flat plates, single cylinders, single spheres, and for flow in packed beds and tube bundles," *AIChE Journal*, vol. 18, no. 2, pp. 361–371, 1972.

[29] W. H. McAdams, *Heat Transmission*, McGraw-Hill, 1954.

[30] A. Bejan and A. D. Kraus, *Heat Transfer Handbook*, Wiley-Interscience, 2003.

[31] S. W. Churchill, "Comprehensive, theoretically based, correlating equations for free convection from isothermal spheres," *Chemical Engineering Communications*, vol. 24, no. 4–6, pp. 339–352, 1983.

[32] C. R. Torres, H. Hanazaki, J. Ochoa, J. Castillo, and M. Van Woert, "Flow past a sphere moving vertically in a stratified diffusive fluid," *Journal of Fluid Mechanics*, vol. 417, pp. 211–236, 2000.

[33] R. Clift, J. R. . Grace, and M. E. . Weber, *Bubbles, Drops, and Particles*, Dover, 2005.

[34] Y. Wen and M. A. Jog, "Variable property, steady, axi-symmetric, laminar, continuum plasma flow over spheroidal particles," *International Journal of Heat and Fluid Flow*, vol. 26, no. 5, pp. 780–791, 2005.

Hindawi Publishing Corporation
Advances in Mechanical Engineering
Volume 2013, Article ID 402094, 10 pages
http://dx.doi.org/10.1155/2013/402094

Research Article

Effect of Step-Change Radiation Flux on Dynamic Characteristics in Tower Solar Cavity Receiver

Zhengwei Chen,[1,2] Yueshe Wang,[1] Yun Hao,[1] and Qizhi Wang[1]

[1] *State Key Laboratory of Multiphase Flow in Power Engineering, Xi'an Jiaotong University, Xi'an 710049, China*
[2] *Beijing Institute of Space Long March Vehicle, Beijing 100076, China*

Correspondence should be addressed to Yueshe Wang; wangys@mail.xjtu.edu.cn

Received 11 January 2013; Accepted 18 February 2013

Academic Editor: Bo Yu

The heat flux on the inner surface of the tower solar thermal power plant system will show the characteristics of noncontinuous step change, especially in nonnormal and transient weather conditions, which may result in a continuous dynamic variation of the characteristic parameters. Therefore, the research of dynamic characteristics plays a very important role in the operation and the control safely in solar cavity receiver system. In this paper, based on the noncontinuous step change of radiation flux, a nonlinear dynamic model is constructed to obtain the effects of the non-continuous step change radiation flux and step change feed water flow on the receiver performance by sequential modular approach. The subject investigated in our study is a 1 MW solar power station constructed in Yanqing county, Beijing, China. This study has obtained the dynamic responses of the characteristic parameters in the cavity receiver such as drum pressure, drum water level, main steam flow, and main steam enthalpy under step change radiation flux. And the influence of step-change feed water flow to the dynamic characteristics has also been analyzed. The results could provide general guidance for security operation and control in solar cavity receiver system.

1. Introduction

The solar cavity receiver is an important light energy to thermal energy convector in the tower solar thermal power plant system. Extensive research on the solar tower power plant principle has been conducted in America, Germany, Spain, France, Italy, the former Soviet Union, and Japan ever since it was put forward in the early 1970s. As a key listed project of the 11th Five-Year Plan of China National Hi-Tech R&D (863 Plan), the first 1 MW solar power tower system located in Beijing has been sponsored and is under construction now. In addition, the solar cavity receiver is an important light energy to thermal energy convector in the tower solar thermal power plant system, which is apt to be operated under the condition of high-density, ever-changing heat radiation flux frequently [1]. The heat flux may result in a continuous variation of the characteristic parameters, which will seriously affect the stability and safe operation of the solar cavity receiver. And with the improvement of cycling parameters, these problems will be more prominent.

A volume of research has been performed on high-temperature and high-pressure tower solar cavity receiver at home and abroad, and it mainly involved the structural design of cavity receiver, the thermal performance simulation, the system efficiency evaluation, and optimization design of the heliostat field [2, 3]. However, little attention has been focused on the instability of the steam-water system caused by noncontinuous heat flux in the cavity. Up to now, the inherent mechanism of dynamic characteristics and the control strategies of solar cavity receiver have not been clearly mastered.

In this study, in order to obtain the effects of the noncontinuous step change radiation flux on the receiver performance, a nonlinear dynamic model under step change radiation flux is constructed based on the distributed parameters, two-phase flow in the steam-water system, and the noncontinuous step change of radiation flux. This study aims to present the dynamic responses of the parameters in the cavity receiver such as drum pressure, drum water level, main steam flow, and main steam enthalpy under noncontinuous step

change radiation flux. Meanwhile, the feed water flow is also one of the influencing factors on the receiver performance, so the influence law of step-change feed water flow to the dynamic characteristics in the receiver was also analyzed. The results of this study could provide general guidance for the design of cavity receivers and identification of the operational strategy of the solar thermal power tower plant.

2. The Steam-Water System

The subject investigated in our study is a 1 MW solar power station constructed in Yanqing county, Beijing, China. The solar cavity receiver has a hexagonal prism shape. The profile of the cavity receiver is shown in Figure 1. Solar radiation enters through the front face and is absorbed by the interior walls of the cavity. As shown in Figure 1, the boiling zone has three panels of vertical pipes welded together to form a membrane wall, and two panels are at the sides of the cavity and one is at the center. The other two faces are coated with insulation, which can decrease the absorbing energy. Evaporation surfaces are arranged in both sides and the center of the cavity, and superheat surfaces are arranged in the sides of the cavity. In order to achieve steam-water separation and stabilize the steam-water system, drum and circulating pump were designed in the system. The circulating flowchart of the steam-water system is shown in Figure 2. Spray desuperheater is arranged between the superheaters in order to obtain acceptable superheated steam. The superheated steam temperature designed can reach 410°C.

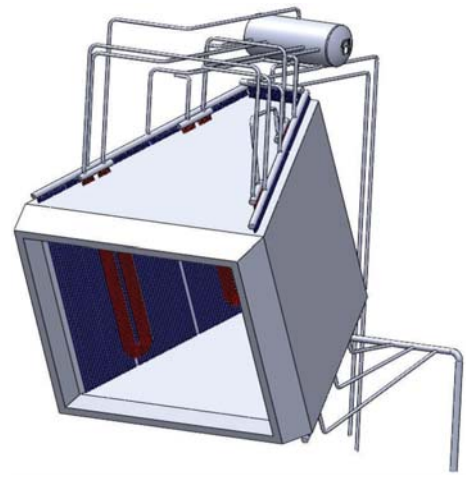

Figure 1: Profile of cavity receiver.

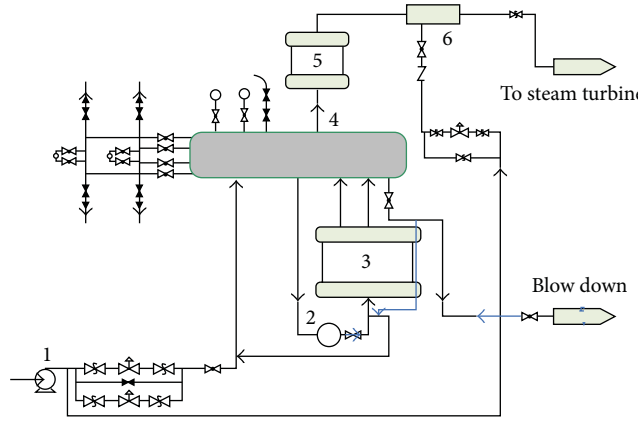

(1) Feed water pump
(2) Circulating pump
(3) Evaporation surfaces
(4) Boiler barrel
(5) Superheat surfaces
(6) Desuperheater

Figure 2: Steam and water system of cavity receiver.

3. Mathematical Model

In this paper, in order to accurately obtain variable law of the dynamic characteristic, lumped parameter method and sequential modular approach are adopted to build a nonlinear dynamic mathematical model of the steam-water system in the solar cavity receiver. According to sequential modular approach, the steam-water system of the cavity receiver can be simplified into several typical parts based on modularization modeling method. This method can not only improve the model's accuracy but also reduce the complexity in model establishment and numerical solution. The steam-water system is composed of evaporation zone and superheat zone. And evaporation zone is simplified into several typical parts including downcomer, water-wall metal, water wall, steam-water catheter, and drum which are coupled by pressure variation and state parameters. In particular, the water-wall surface is divided into supercooled-water section and two-phase section, and the convective heat transfer coefficient is determined by the flow pattern in each section. And mathematics description of drum pressure and drum water level is analyzed and derived considering various influencing factors. A nonlinear dynamic mathematical model for the cavity receiver based on the laws of mass conservation, energy conservation, and momentum conservation, which give a comprehensive consideration of flash or condensation in the two-phase flow, is proposed. Furthermore, superheat zone is simplified into two typical parts including superheat tube and the superheat tube metal. The schematic diagram of dynamic parameters in steam-water system is shown in Figure 3.

3.1. Evaporation Zone Model. According to the specific structure and working process of the cavity receiver, the dynamic mathematical model for these typical modules, including downcomer, water-wall, steam-water catheter, and drum, is built based on the distributed parameters, two-phase flow in steam-water system.

3.1.1. Downcomer Module. Mass conservation equation is as follows:

$$D_x = D_{xj}. \tag{1}$$

Energy conservation equation is as follows:

$$\frac{d\left(V_{xj}\rho' H_{xj} + M_{jxj}C_j T_j\right)}{d\tau} = D_x H_x - D_{xj} H_{xj}, \tag{2}$$

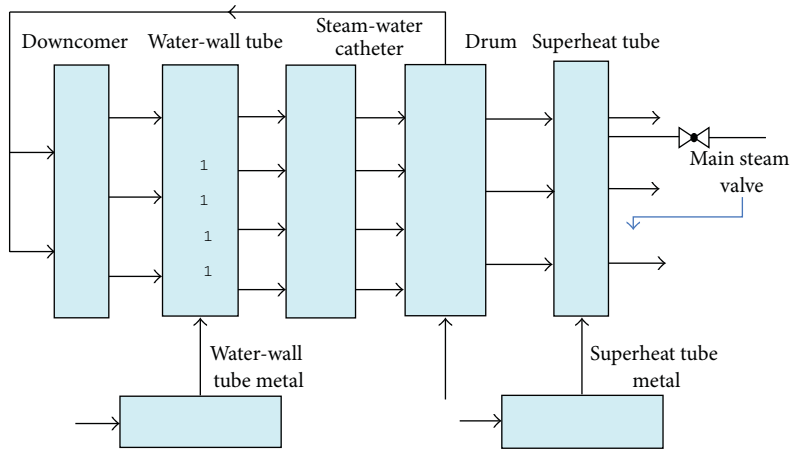

Figure 3: Schematic diagram of dynamic parameters.

where D_x and D_{xj} are the inlet and outlet mass flow of the downcomer, V_{xj} is the volume of the downcomer, ρ' is the density of saturated water, M_{jxj} is the mass of the downcomer metal, C_j is the specific heat capacity of metal pipe, T_j is the temperature of downcomer metal, and H_x and H_{xj} are the inlet and outlet enthalpy in the downcomer.

3.1.2. Water-Wall Module. The change of radiation flux will result in a variation of the temperature of the metal wall, which may cause thermal inertia of the heat absorption [4], so metal wall should be considered as an independent link.

Energy conservation equations of the water-wall metal are as follows:

$$M_{jlb}C_j\frac{dT_{bw}}{d\tau} = Q - Q_{zf} - Q_{fs} - Q_{dl},$$
$$Q_{zf} = hA\left(T_{bw} - T\right), \tag{3}$$

where M_{jlb} is the mass of the water-wall tube metal, T_{bw} is the temperature of tube metal, Q is the solar radiation flux, Q_{zf} is the heat absorption of working fluid in the water wall, Q_{fs} is the loss of radiant heat, Q_{dl} is the loss of convective heat, and h is the convective heat transfer coefficient of the evaporation surface.

Dynamic equations of the water wall, including mass conservation equation, energy conservation equation, mass conservation equation for steam, and mass conservation equation for water, based on convective heat transfer between tube metal and working fluid, which give a comprehensive consideration of flash and condensation caused by pressure change in the two-phase flow, are built as follows:

$$\frac{d\left(V'\rho' + V''\rho''\right)}{d\tau} = D_{xj} - D_{lb},$$
$$\frac{d\left(V'\rho'H' + V''\rho''H''\right)}{d\tau} = D_{xj}H_{xj} - D_{lb}H_{lb} + Q_{zf},$$
$$\frac{d\left(V''\rho''\right)}{d\tau} = D_{zf} + D_{sz} - D_{lb}x,$$
$$\frac{d\left(V'\rho'\right)}{d\tau} = D_{xj} - D_{lb}\left(1 - x\right) - D_{zf} - D_{sz}, \tag{4}$$

where V' is the volume of water in the water wall, V'' is the volume of steam in the water wall, H' and H'' are enthalpy of saturated water and steam, D_{lb} is the outlet mass flow of water-wall tube, x is the mass rate of vapor content in the outlet of water wall tube; and D_{sz} is the mass of flash or condensation in water-wall, within this model we thus derive the following:

$$D_{sz} = -\left(\left(\left(\rho'\frac{\partial H'}{\partial P} + \frac{r\rho''}{\rho' - \rho''}\frac{\partial \rho'}{\partial P}\right)V' + \left(\rho''\frac{\partial H''}{\partial P} + \frac{r\rho'}{\rho' - \rho''}\frac{\partial \rho''}{\partial P}\right)V''\right)\times\left(H'' - H'\right)^{-1}\right) \times \frac{\partial P}{\partial \tau}, \tag{5}$$

where r is the latent heat of vaporization.

In our model, water-wall surface is divided into supercooled-water section and two-phase section, and the length of two-phase section y_{rs} can be calculated as $y_{rs} = D_{xj}(H' - H_{xj})/Q_{zf}$. The convective heat transfer coefficient between tube wall and working fluid is determined by the physical parameters and the flow pattern of the working fluid in each section. The convective heat transfer coefficient of the evaporation surfaces can be calculated as single-phase fluid forced flow and nucleate heat transfer coefficient in two-phase fluid forced flow in this model.

The Dittus-Boelte formula [5] given below is used to calculate the heat transfer coefficient h in single-phase fluid forced flow directly:

$$h = 0.023\frac{\lambda}{d}\mathrm{Re}^{0.8}\mathrm{Pr}^{0.4}, \tag{6}$$

where λ is the heat conduction coefficient of the saturated water, Re is the Reynolds number, Pr is prenatal number, and d is the equivalent diameter of the heating surface.

Nucleate heat transfer coefficient in two-phase fluid forced flow can be computed by the Chen formula [5] as follows:

$$\begin{gathered}
h = h_{NB} + h_c,\\
h_{NB} = 0.00122\left[\frac{0.79\lambda'{C_p'}^{0.45}\rho'^{0.49}}{\sigma^{0.5}\mu'^{0.29}\gamma^{0.24}\rho''^{0.49}}\right]\Delta t_{\mathrm{sat}}^{0.24}\Delta p_{\mathrm{sat}}^{0.75}s,\\
s = \left[1 + 2.53 \times 10^{-6}(\mathrm{Re})^{1.17}\right]^{-1},\\
(\mathrm{Re})_{\mathrm{TP}} = \left[\frac{D_{lb}(1-x)\,d}{\mu'}\right]F^{1.25},\\
X = \left(\frac{1-x}{x}\right)^{0.9}\left(\frac{\rho''}{\rho'}\right)^{0.05}\left(\frac{\mu'}{\mu''}\right)^{0.1},\\
\frac{1}{X} \le 0.1, \qquad F = 1.0,\\
\frac{1}{X} > 0.1, \qquad F = 2.35\left(\frac{1}{X} + 0.213\right)^{0.736}\\
h_c = 0.023\frac{\lambda'}{d}\left[\frac{D_{lb}(1-x)\,d}{\mu'}\right]^{0.8}\left[\frac{\mu'C_p'}{\lambda'}\right]^{0.4}F,
\end{gathered} \tag{7}$$

where h_{NB} and h_c are heat transfer coefficient in bubble state boiling and convective heat transfer, σ is interfacial force coefficient, γ is the latent heat of vaporization, μ is viscosity of working fluid, Δt_{sat} is overheat rate of the pipe wall, Δp_{sat} is the saturated pressure difference corresponding to Δt_{sat}, s is the inhibition coefficient of bubble state boiling, x is the mass rate of vapor content, F is the coefficient relevant to the Martinelli number, $(\mathrm{Re})_{\mathrm{TP}}$ is the two-phase Reynolds number, and X is the Martinelli number.

3.1.3. Steam-Water Catheter Module. Dynamic equations of the steam-water catheter module, including mass conservation equation, energy conservation equation, mass conservation equation for steam, and mass conservation equation for water, which give a comprehensive consideration of flash and condensation caused by pressure change in the two-phase flow, are built as follows:

$$\begin{gathered}
\frac{d\left(V_{qs}'\rho' + V_{qs}''\rho''\right)}{d\tau} = D_{lb} - D_{qs},\\
\frac{d\left(V_{qs}'\rho'H' + V_{qs}''\rho''H'' + M_{jqs}C_jT_{bh}\right)}{d\tau} = D_{lb}H_{lb} - D_{qs}H_{qs},\\
\frac{d\left(V_{qs}''\rho''\right)}{d\tau} = D_{lb}x + D_{szqs} - D_{qs}x_{qs},\\
\frac{d\left(V_{qs}'\rho'\right)}{d\tau} = D_{lb}(1-x) - D_{qs}\left(1 - x_{qs}\right) - D_{szqs},
\end{gathered} \tag{8}$$

where V_{qs}' is the water volume in the steam-water catheter, V_{qs}'' is the steam volume in the steam-water catheter, D_{qs} is the outlet mass flow of steam-water catheter tube, x_{qs} is the mass rate of vapor content of the outlet of steam-water catheter tube, and D_{szqs} is the mass of flash or condensation of two-phase flow in steam-water catheter; within this model we thus derive the following:

$$\begin{aligned}
D_{szqs} = -\Bigg(&\left(\rho'\frac{\partial H'}{\partial P} + \frac{r\rho''}{\rho' - \rho''}\frac{\partial \rho'}{\partial P}\right)V_{qs}'\\
&+ \left(\rho''\frac{\partial H''}{\partial P} + \frac{r\rho'}{\rho' - \rho''}\frac{\partial \rho''}{\partial P}\right)V_{qs}''\\
&+ M_{jqs}C_j\frac{\partial T_{bh}}{\partial P}\Bigg)\frac{(\partial P/\partial \tau)}{(H'' - H')}.
\end{aligned} \tag{9}$$

3.1.4. Drum Module. Dynamic equations of the drum module, including mass conservation equation, energy conservation equation, mass conservation equation for steam, and mass conservation equation for water, which give a comprehensive consideration of flash and condensation caused by pressure change in the drum, are built as follows:

$$\begin{aligned}
&\frac{d\left(V_{qb}'\rho'H' + V_{qb}''\rho''H'' + M_{jqb}C_jT_{bh}\right)}{d\tau}\\
&\quad = D_{gs}H_{gs} + D_{qs}H_{qs} - D_{qb}H'' - D_xH_x - D_{pw}H',\\
&\frac{d\left(V_{qb}'\rho' + V_{qb}''\rho''\right)}{d\tau} = D_{gs} + D_{qs} - D_{qb} - D_x - D_{pw},\\
&\frac{d\left(V_{qb}''\rho''\right)}{d\tau} = D_{qs}x_{qs} - D_{qb} + D_{szqb},\\
&\frac{d\left(V_{qb}'\rho'\right)}{d\tau} = D_{gs} + D_{qs}\left(1 - x_{qs}\right) - D_x - D_{pw} - D_{szqb},
\end{aligned} \tag{10}$$

where M_{jqb} is the mass of drum metal, V_{qb}' and V_{qb}'' are the volume of water and steam in the drum, D_{qb} is mass flow of main steam, D_{pw} is pollutant quantity of the drum; and D_{szqs}

is the mass of flash or condensation in the drum, within this model we thus derive the following:

$$D_{szqb} = -\left(\left(\rho' \frac{\partial H'}{\partial P} + \frac{r\rho''}{\rho' - \rho''} \frac{\partial \rho'}{\partial P}\right) V'_{qb} + \left(\rho'' \frac{\partial H''}{\partial P} + \frac{r\rho'}{\rho' - \rho''} \frac{\partial \rho''}{\partial P}\right) V''_{qb} + M_{jqb} C_j \frac{\partial T_{bh}}{\partial P}\right) \frac{(\partial P/\partial \tau)}{(H'' - H')}. \quad (11)$$

The dynamic variable law of the state parameters in each module can be obtained by solving these nonlinear equations and partial differential equations above. The drum pressure is seen as a lumped parameter, so the influencing factors in all modules should be considered in the derivation of pressure dynamic respond equation [6]. The dynamic respond equation of drum pressure is as follows:

$$\frac{dP}{d\tau} = \left[Q_{zf} + \left(\frac{r\rho''}{\rho' - \rho''} - H_{qh}\right) D_{gs} - \frac{r\rho'}{\rho' - \rho''} D_{qb} - \frac{r\rho''}{\rho' - \rho''} D_{lp}\right] \times \left(\left[\left(\rho' \frac{\partial H'}{\partial P} + \frac{r\rho''}{\rho' - \rho''} \frac{\partial \rho'}{\partial P}\right) VV' + \left(\rho'' \frac{\partial H''}{\partial P} + \frac{r\rho'}{\rho' - \rho''} \frac{\partial \rho''}{\partial P}\right) VV'' + \left(\rho' \frac{dH_{xj}}{dP} + H_{xj} \frac{d\rho'}{dP}\right) V_{xj} + \left(M_{jxj} + M_{jqs} + M_{jqb}\right) C_j \frac{\partial T_{bh}}{\partial P}\right]\right)^{-1}. \quad (12)$$

The drum water level is determined by the water cubage in the drum and steam cubage in water, that is, $(\partial h/\partial \tau) S_{qb} = (\partial V'_{qb}/\partial \tau) + (\partial V''_{sx}/\partial \tau)$. According to the specific structure of the drum, we can obtain the dynamic respond equation of drum water level given in the following:

$$\frac{dh}{d\tau} = \frac{\left(D_{gs} - D_{qb} - D_{lp}\right)}{S_{qb}\left(\rho' - \rho''\right)} - \frac{\left(V'_{qb}\left(\partial \rho'/\partial P\right) + V''_{qb}\left(\partial \rho''/\partial P\right)\right)}{S_{qb}\left(\rho' - \rho''\right)} \frac{dP}{d\tau} - \frac{\partial M_{xh}/\partial \tau}{S_{qb}\left(\rho' - \rho''\right)} + \frac{1}{S_{qb}} \frac{\partial V'_{sx}}{\partial \tau}, \quad (13)$$

where H_{qh} is the enthalpy difference, VV' is total water volume in the evaporation zone, which can be calculated as $VV' = V_{xj} + V' + V'_{qs} + V'_{qb}$, VV'' is total steam volume in the evaporation zone, which can be calculated as $VV'' = V'' + V''_{qs} + V''_{qb}$, M_{xh} is total mass of working fluid in the downcomer module, water-wall module, and steam-water catheter module, V''_{sx} is steam cubage in water in the drum, and S_{qb} is the cross-section area of the drum water level, which is determined by the structure of the drum.

3.2. Superheated Zone Model. The modeling method of superheater metal wall is similar to that of the water-wall metal module above. As for the superheating surface, a chain structure dynamic mathematical model [7], which gives a comprehensive consideration of model precision, is established, and the superheating surface is divided into 15 segments.

Energy conservation equation is as follows:

$$\frac{d\left(V_{gr}\rho_{gr}e\right)}{d\tau} = D_{qb}H_{qb} + Q_{gr} - D_{gr}H_{gr}. \quad (14)$$

Mass conservation equation is as follows:

$$V_{gr} \frac{d\rho_{gr}}{dP_{gr}} \frac{dP_{gr}}{d\tau} = D_{qb} - D_{gr}. \quad (15)$$

We can obtain the dynamic respond equations of superheater outlet pressure and superheater outlet steam temperature as shown in (16) and (17):

$$\frac{dP_{gr}}{d\tau} = \left(Q_{gr} + \left(D_{qb}H_{qb} - D_{gr}H_{gr}\right) - \left(H_{gr} + \rho_{gr}c_p \frac{\partial T_{gr}}{\partial \rho}\right)\left(D_{qb} - D_{gr}\right)\right) \times \left(V_{gr}\left(\rho_{gr}c_p \frac{\partial T_{gr}}{\partial P_{gr}} - 1\right)\right)^{-1}, \quad (16)$$

$$\frac{dT_{gr}}{d\tau} = \left(Q_{gr} + \left(D_{qb}H_{qb} - D_{gr}H_{gr}\right) - \left(\rho_{gr}c_p \frac{\partial P_{gr}}{\partial \rho} - H_{gr}\right)\left(D_{qb} - D_{gr}\right)\right) \times \left(V_{gr}\left(\rho_{gr}c_p - \frac{\partial P_{gr}}{\partial T_{gr}}\right)\right)^{-1}, \quad (17)$$

where e is the internal energy of superheated steam, ρ_{gr} is the density of superheated steam, P_{gr} is superheater outlet pressure, Q_{gr} is the exchanged heat between steam and metal pipe, V_{gr} is volume of the superheated tube, H_{gr} is superheater outlet temperature, D_{gr} is the mass flow of superheated steam, and c_p is the specific heat capacity of superheated steam.

4. Simulation Results

In order to master the influence law of noncontinuous radiation flux on the receiver performance in nonnormal weather conditions, a numerical study on the basis of the

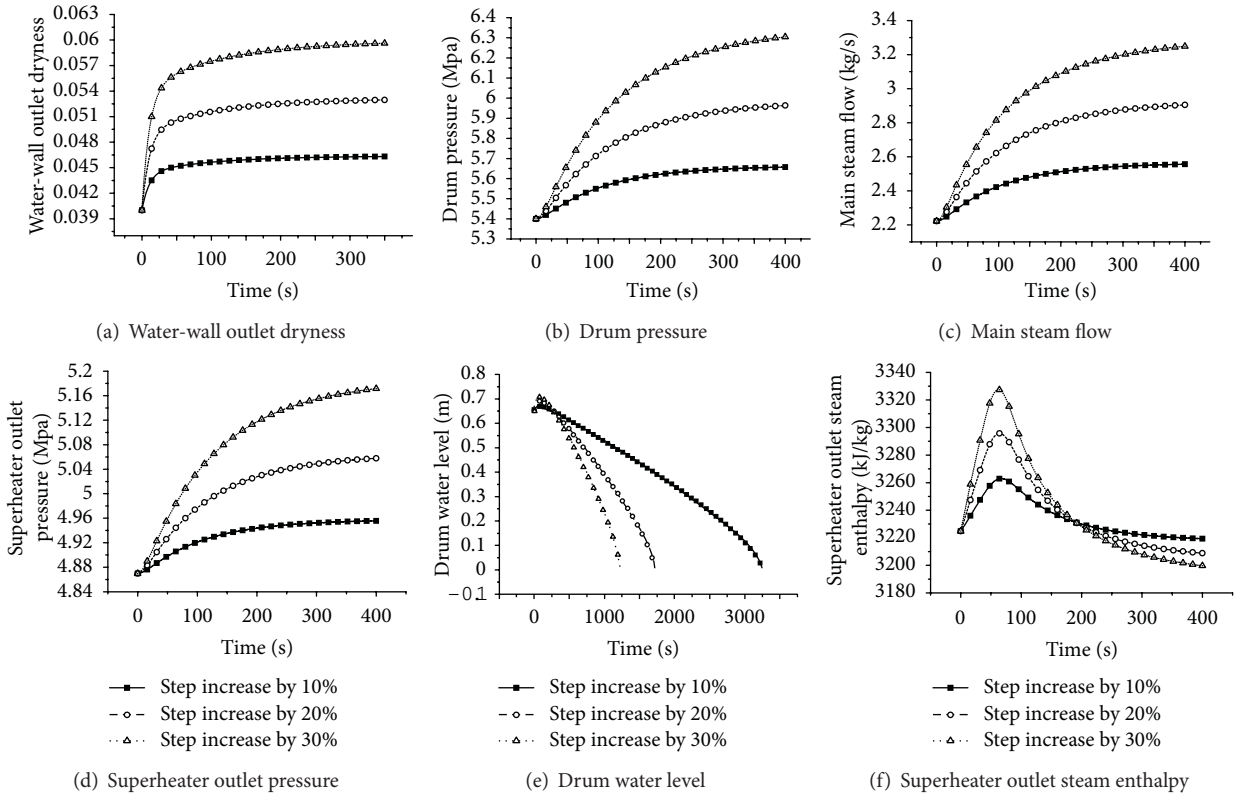

(a) Water-wall outlet dryness (b) Drum pressure (c) Main steam flow

(d) Superheater outlet pressure (e) Drum water level (f) Superheater outlet steam enthalpy

Figure 4: The dynamic responses of characteristic parameters with step increase of radiation flux.

nonlinear dynamic mathematical model, which can be solved by the Runge-Kutta method, is carried out focusing on the cavity receiver of 1 MW solar power station constructed in Yanqing county, Beijing. The dynamic responses of the characteristic parameters of the cavity receiver under step change radiation flux and step change feed water flow have been obtained in this paper.

4.1. Step Increase of Radiation Flux. The step change of radiation flux in nonnormal and transient weather conditions may result in a continuous variation of the characteristic parameters in the solar cavity receiver. So it will seriously affect the stability and safe operation of the solar cavity receiver. The designed value of radiation flux in the receiver is 100.5 kw/m^2. The dynamic responses of characteristic parameters in the cavity receiver, such as water-wall outlet dryness, drum pressure, main steam flow, superheater outlet pressure, drum water level, and superheater outlet enthalpy, are shown in Figures 4(a)–4(f) when there is a step increase by 10%, 20%, and 30% of solar radiation flux.

When there is a step increase of solar radiation flux, the water-wall outlet dryness first increases rapidly and then reaches the steady state about 350 s later than the step increase of radiation flux, and the rate of increase is from fast to slow, as shown in Figure 4(a). This is because the water-wall outlet dryness depends on both radiation flux and the flash or condensation caused by pressure variation in two-phase flow. As shown in Figures 4(b)–4(d), the drum pressure increases regardless of the increased radiation flux, and the superheater outlet pressure increases more slowly than that of drum pressure, so there is a very rapid increase of the main steam flow due to the increase of pressure drop in superheater. The main steam flow D_{qb} has a negative feedback on the drum pressure [8, 9], and the increase of D_{qb} can slow down the increase rate of pressure and make it become stable. Due to the pressure increase and condensation caused by increasing pressure, the main steam flow D_{qb} tends to be stable about 400 s later than the step change.

The dynamic response of drum water level is shown in Figure 4(e). It shows the phenomenon of false water level in the case of a sudden increase in radiation flux. Based on dynamic analysis and the simulation of water level model, this paper indicates that the changing mass storage in evaporation area and the steam cubage in water are two important factors of false water level. On the one hand, the steam cubage in water and pressure will increase along with the heat absorption in evaporation area. On the other hand, the length of single-phase section in water wall and the working fluid density will decrease, which can result in a decrease of mass storage in evaporation area. There emerges a relatively serious phenomenon indicating a false water level as shown in Figure 4(e), and the water in the drum will dry up, respectively, at 3250 s, 1716 s, and 1223 s when there is a step increase by 10%, 20%, and 30% of solar radiation flux. So necessary measures should be taken in order to make the water level stable.

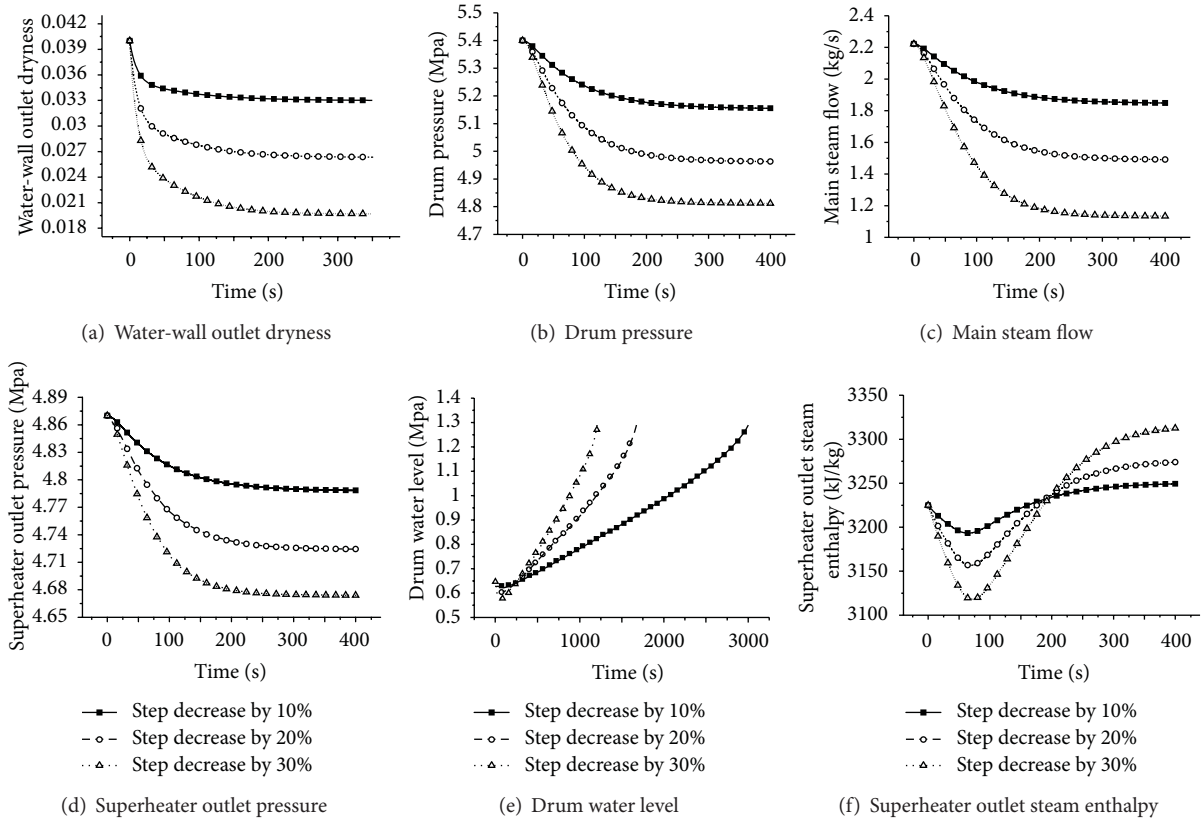

(a) Water-wall outlet dryness (b) Drum pressure (c) Main steam flow

(d) Superheater outlet pressure (e) Drum water level (f) Superheater outlet steam enthalpy

Figure 5: The dynamic responses of characteristic parameters with step decrease radiation flux.

The dynamic response of superheater outlet enthalpy is shown in Figure 4(f). The superheater outlet enthalpy first increases rapidly and then decreases and stabilizes gradually to a certain value. It follows from (17) that the main cause of superheater outlet enthalpy change is not only the function of received solar energy in the superheater but also the superheater steam flow. The rate of steam generation is slower than the change of solar radiation flux. Thus, the above-mentioned result will appear, and the superheater outlet steam enthalpy tends to be stable about 400 s later than the step change.

4.2. Step Decrease of Radiation Flux. The occlusion of cloud layer in nonnormal and transient weather conditions may result in a step decrease of radiation flux in the receiver. The dynamic responses of characteristic parameters in the cavity receiver, such as water-wall outlet dryness, drum pressure, main steam flow, superheater outlet pressure, drum water level, and superheater outlet enthalpy, are shown in Figures 5(a)–5(f) when there is a step decrease by 10%, 20%, and 30% of solar radiation flux.

As shown in Figures 5(a)–5(d), the water-wall outlet dryness first decreases rapidly and then reaches the steady state. The drum pressure, the superheater outlet pressure, and the main steam flow decrease because of the increased radiation flux, and the rate of decrease is from fast to slow. Due to the pressure decrease and flash caused by decreasing pressure, the main steam flow D_{qb} tends to be stable about 400 s later than the step change.

The dynamic response of drum water level is shown in Figure 5(e). There emerges a relatively serious phenomenon of indicating a false water level at the beginning, and then the water will fulfill the drum at 3002 s, 1674 s, and 1209 s when there is a step decrease by 10%, 20%, and 30% of solar radiation flux.

The dynamic response of superheater outlet steam enthalpy is shown in Figure 5(f). The superheater outlet steam enthalpy first decreases rapidly to a certain value and then increases to a stable value. As is analyzed above, the superheater steam outlet enthalpy depends on both the main steam flow D_{qb} and the heat absorption of steam in the superheater. In the end, the superheater outlet steam enthalpy tends to be stable about 400 s later than the step change.

4.3. Step Increase of Feed Water Flow. As shown in the model, the feed water flow is also one of the influencing factors of the receiver performance [10]. The designed value of feed water flow in the receiver is 8 t/h. The dynamic responses of characteristic parameters in the cavity receiver are shown in Figures 6(a)–6(f) when there is a step increase to 9 t/h, 10 t/h, and 11 t/h of feed water flow.

As shown in Figure 6(a), there is a sudden increase of the water-wall outlet dryness that is because the step change of feed water flow can result in a rapid change of pressure in

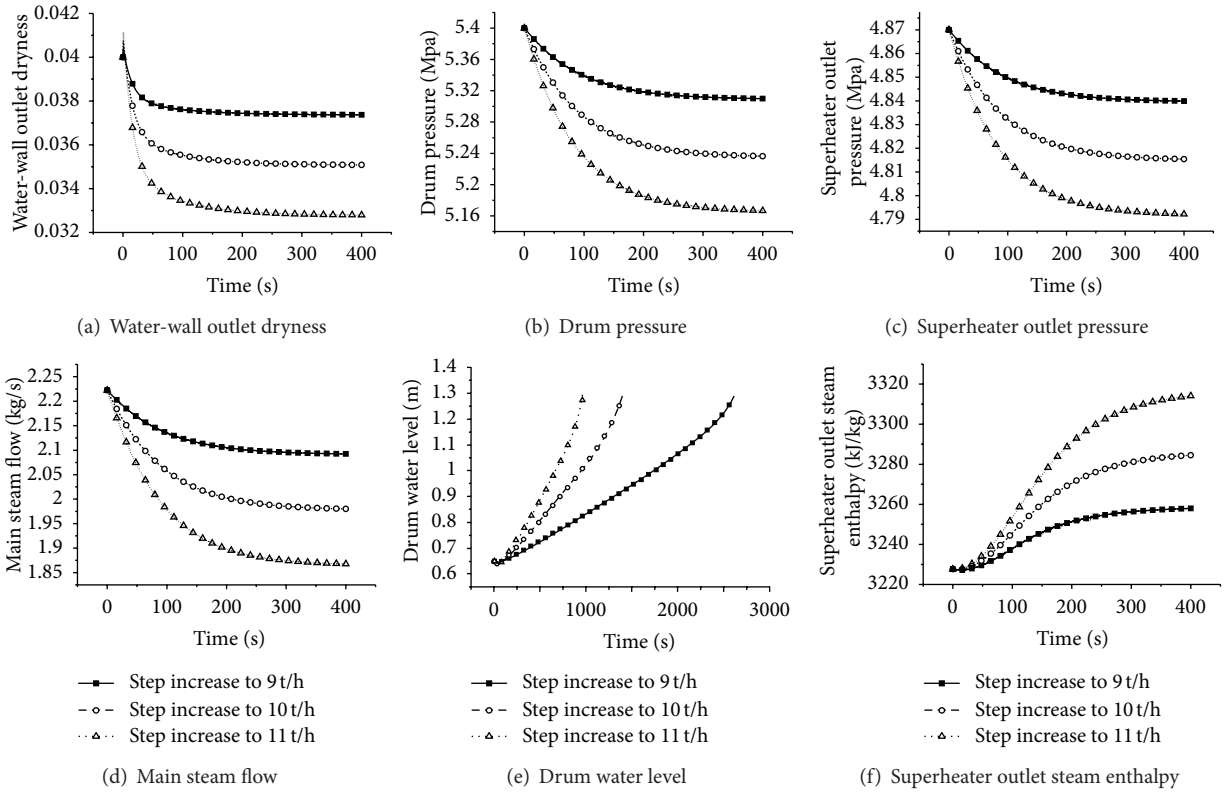

Figure 6: The dynamic responses of characteristic parameters with step increase of feed water flow.

the beginning, and the flash or condensation will appear. And then due to the fact that the inlet enthalpy in the downcomer H_x decreases regardless of the increased feed water flow, the water-wall outlet dryness decreases gradually and reaches the steady state. It follows from (12) that the drum pressure will decrease during the dynamic process, and the superheater outlet pressure decreases more slowly than that of drum pressure, and the main steam flow D_{qb} is independent of the pressure drop in superheater. Therefore, the main steam flow D_{qb} increases and tends to be stable about 400 s later than the step change. Figure 6(e) shows the dynamic response of drum water level. It shows the phenomenon of false water level in the case of a sudden increase in feed water flow. For one thing, the steam cubage in water will decrease due to the supercooling degree of feed water. For another, the length of single-phase section in water wall and the working fluid density will increase, which can result in a decrease of mass storage M_{xh} in evaporation area. Thus, the above-mentioned result will appear, but the phenomenon of false water level is less serious than that of step change of radiation flux.

The water in the drum will fulfill the drum at 2615 s, 1390 s, and 967 s when there is a step increase to 9 t/h, 10 t/h, and 11 t/h of feed water flow.

Figure 6(f) shows the dynamic response of superheater outlet steam enthalpy in the receiver. In the dynamic process, the solar energy received in the superheater is essentially constant. Therefore, the main cause of superheater outlet steam enthalpy change is the superheater steam flow D_{qb} as shown in Figure 6(d). The superheater outlet steam enthalpy increases gradually and stabilizes to a certain value about 400 s later.

4.4. Step Decrease of Feed Water Flow. The dynamic responses of characteristic parameters in the cavity receiver are shown in Figures 7(a)–7(f) when there is a step decrease to 7 t/h, 6 t/h, and 5 t/h of feed water flow.

As shown in Figures 7(a)–7(f), there is a sudden decrease of the water-wall outlet dryness in the beginning, and then the water-wall outlet dryness increases gradually and reaches the steady state. The drum pressure and the superheater outlet pressure will increase during the dynamic process, and the main steam flow D_{qb} is independent of the pressure drop in superheater. In the end, the main steam flow D_{qb} increases and tends to be stable about 400 s later than the step change.

Figure 7(e) shows the dynamic response of drum water level. It shows the phenomenon of false water level. And the water in the drum will dry up at 2835 s, 1441 s, and 992 s when there is a step decrease to 7 t/h, 6 t/h, and 5 t/h of feed water flow.

The dynamic response of superheater outlet steam enthalpy is shown in Figure 7(f). The superheater outlet steam enthalpy decreases and stabilizes gradually to a certain value owing to the increase of D_{qb} shown in Figure 7(d).

5. Conclusions

Based on noncontinuous step change of radiation flux, a nonlinear dynamic model, which gives a comprehensive

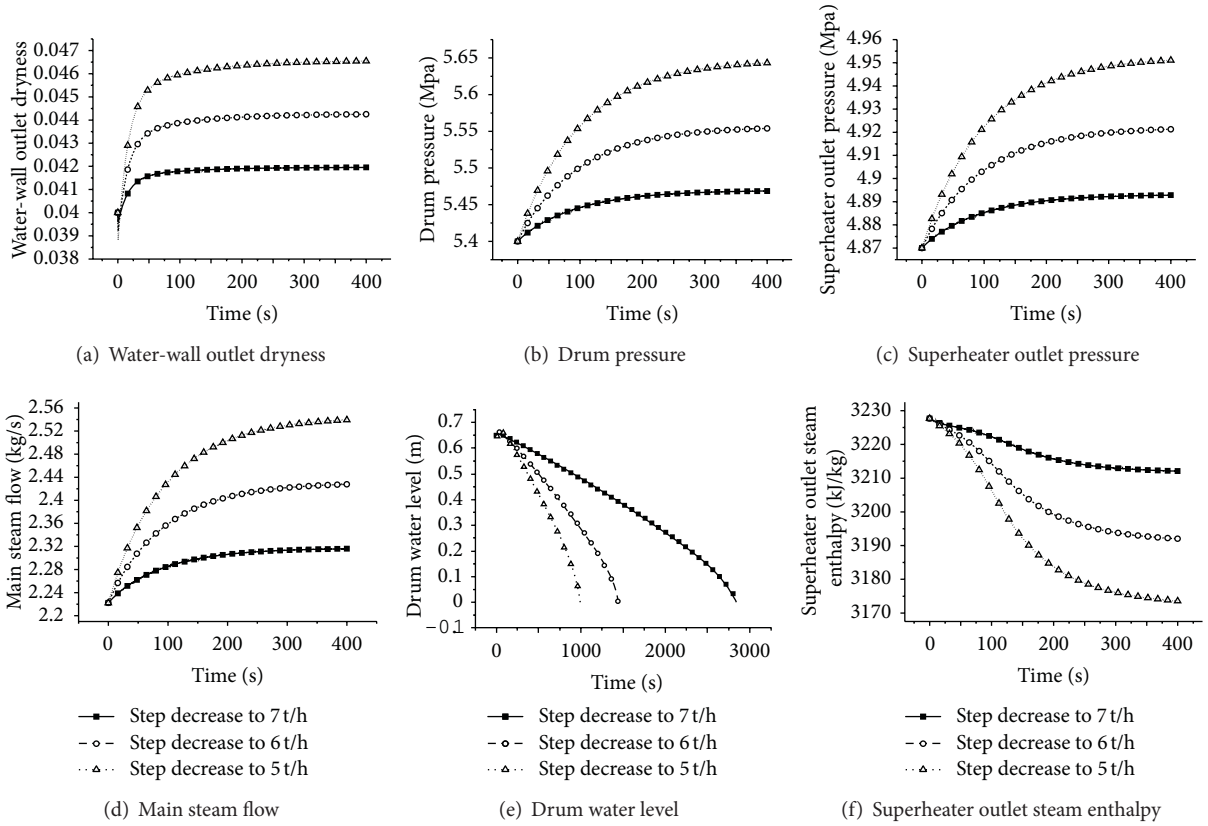

Figure 7: The dynamic responses of characteristic parameters with step decrease feed water flow.

consideration of flash and condensation in two-phase flow, has been constructed to obtain the effects of the noncontinuous step change radiation flux and step change feed water flow on the receiver performance by sequential modular approach. The study of the thermal dynamic characteristics of the cavity receiver of 1 MW solar power station constructed in Beijing was conducted with a step change radiation flux and feed water flow in this paper. The variation trends of water-wall outlet dryness, drum pressure, main steam flow, superheater outlet pressure, drum water level, and superheater outlet steam enthalpy, were obtained and discussed. We can find that the water-wall outlet dryness, drum pressure, main steam flow, superheater outlet pressure, and superheater outlet steam enthalpy have self-balance ability, and they can tend to be stable in the end. However, the drum water level is easily going to destabilize, thus, necessary measures must be taken to make water-steam system stable. The results obtained could provide general guidance for solar thermal power tower system designing and operation.

Acknowledgments

This work has been financed by the National Natural Science foundation of China (no. 51276144) and China National Science and Technology Plan (no. 2010CB227102).

References

[1] Y. Zhiqiang and W. Zhifeng, "The development strategy research series of Chinese renewable energies," *Solar Energy*, vol. 86, pp. 7–11, 2008.

[2] Y. Wang, X. Dong, J. Wei, and H. Jin, "Numerical simulation of the heat flux distribution in a solar cavity receiver," *Frontiers of Energy and Power Engineering in China*, vol. 4, no. 4, pp. 571–576, 2010.

[3] Z. Yao, Z. Wang, Z. Lu, and X. Wei, "Modeling and simulation of the pioneer 1 MW solar thermal central receiver system in China," *Renewable Energy*, vol. 34, no. 11, pp. 2437–2446, 2009.

[4] D. R. Tucakovic, V. D. Stevanovic, T. Zivanovic, A. Jovovic, and V. B. Ivanović, "Thermal-hydraulic analysis of a steam boiler with rifled evaporating tubes," *Applied Thermal Engineering*, vol. 27, no. 2-3, pp. 509–519, 2007.

[5] Z. Lin, *Liquid-Vapor Phase-Change Phenomena*, Xi'an Jiaotong University Press, Xi'an, China, 2nd edition, 2001.

[6] K. J. Åström and R. D. Bell, "Drum-boiler dynamics," *Automatica*, vol. 36, no. 3, pp. 363–378, 2000.

[7] H. Kim and S. Choi, "A model on water level dynamics in natural circulation drum-type boilers," *International Communications in Heat and Mass Transfer*, vol. 32, no. 6, pp. 786–796, 2005.

[8] E. J. Adam and J. L. Marchetti, "Dynamic simulation of large boilers with natural recirculation," *Computers and Chemical Engineering*, vol. 23, no. 8, pp. 1031–1040, 1999.

[9] T. M. I. Mahlia, M. Z. Abdulmuin, T. M. I. Alamsyah, and D. Mukhlishien, "Dynamic modeling and simulation of a palm wastes boiler," *Renewable Energy*, vol. 28, no. 8, pp. 1235–1256, 2003.

[10] Y. Lei, *Modeling and Simulation of In-Boiler Process of Naturally Circulation Boiler*, North China Electric Power University, Beijing, China, 2009.

Hindawi Publishing Corporation
Advances in Mechanical Engineering
Volume 2013, Article ID 561875, 10 pages
http://dx.doi.org/10.1155/2013/561875

Research Article

Comparison Study on Linear Interpolation and Cubic B-Spline Interpolation Proper Orthogonal Decomposition Methods

Xiaolong Wang, Yi Wang, Zhizhu Cao, Weizhong Zou, Liping Wang, Guojun Yu, Bo Yu, and Jinjun Zhang

National Engineering Laboratory for Pipeline Safety, Beijing Key Laboratory of Urban Oil and Gas Distribution Technology, China University of Petroleum, Beijing 102249, China

Correspondence should be addressed to Yi Wang; wy1031@yahoo.com.cn

Received 18 January 2013; Accepted 23 February 2013

Academic Editor: Shuyu Sun

In general, proper orthogonal decomposition (POD) method is used to deal with single-parameter problems in engineering practice, and the linear interpolation is employed to establish the reduced model. Recently, this method is extended to solve the double-parameter problems with the amplitudes being achieved by cubic B-spline interpolation. In this paper, the accuracy of reduced models, which are established with linear interpolation and cubic B-spline interpolation, respectively, is verified via two typical examples. Both results of the two methods are satisfying, and the results of cubic B-spline interpolation are more accurate than those of linear interpolation. The results are meaningful for guiding the application of the POD interpolation to complex multiparameter problems.

1. Introduction

When the complex heat and fluid flow problems are simulated by computers, usually large groups of equations need to be solved at high computational cost. To reduce the computational burdens while maintaining acceptable resolutions for engineering application, the POD method, which was proposed and developed in 1940s, has been used recently in computational fluid dynamics [1–5]. The advantage of the POD method is that we solve the problems by a reduced model; that is, the physical field can be accurately and rapidly reconstructed [6, 7] by a linear combination of orthogonal basis functions (eigenfunctions) and their amplitudes in a low-dimensional way.

The reduced model by POD can be classified into two groups. One is to project the governing equations onto a low-dimensional space spanned by eigenfunctions with the Galerkin method to obtain the equations for amplitudes, while the other is to calculate amplitudes by interpolation. Both methods have their own advantages and disadvantages. The former is suitable for either steady or unsteady problems and is able to convert the partial differential equations of the complex physical process into the ordinary differential ones. However, the deduction of the reduced model is complex, and the method is not applicable to the processes, which cannot be described in the form of partial differential equations. The latter is suitable for the steady problems and accurate even for strong nonlinear situation, which is usually used to deal with single-parameter problems in engineering practice [8] by using linear interpolation to establish the reduced model. Recently, this method is extended to the double-parameter problems by cubic B-spline interpolation [1]. To the authors' best knowledge, the POD interpolation method has not been applied in triple-parameter problems. In this paper, the applicability of the reduced model by POD interpolation is tested for multi-parameter problems, and then the accuracy of the reduced models achieved by linear interpolation and cubic B-spline interpolation is examined via two typical examples, that is, Czochralski crystal growth problem [9] and lid-driven cavity flow problem.

2. A Brief Introduction to POD and SVD

POD is a powerful and elegant method for model reduction aimed at obtaining low-dimensional approximate descriptions of a high-dimensional space [10]. The low-dimensional

space is spanned by orthogonal eigenfunctions. The reduced order description of physical process can be reconstructed by linear superposition of eigenfunctions and corresponding amplitudes:

$$\vartheta(x,t) = \sum_{i=1}^{\infty} a_i(t)\,\varphi_i(x); \quad a_i(t) = \left(\vartheta(x,t), \varphi_i(x)\right). \tag{1}$$

The most striking features of the POD are its optimality of minimizing the average squared distance between the original data and its reduced linear representation with only a few leading eigenfunctions capturing nearly all energy of dynamic physical process [11]. The feature can be described in the following mathematical ways:

$$\text{maximize} \left\langle \left| \left(\vartheta^k, \varphi\right) \right|^2 \right\rangle, \quad \text{with } \|\varphi\|^2 = 1, \tag{2}$$

where the inner product in Ω is presented by $(f,g) = \int_\Omega f(x)\, g(x) d\Omega$; $\langle\cdot\rangle$ is the averaging operation; $\|\cdot\|$ stands for the norm; $|\,|$: denotes the modulus.

Introduce a Lagrange multiplier λ to obtain the eigenfunctions:

$$J[\varphi] = \left\langle \left|(\vartheta, \varphi)\right|^2 \right\rangle - \lambda\left(\|\varphi\|^2 - 1\right). \tag{3}$$

This condition can be reduced to the following integral eigenvalue problem [12]:

$$\int_\Omega \left\langle \vartheta^k(x)\, \vartheta^k\left(x'\right) \right\rangle \varphi\left(x'\right) dx' = \lambda\varphi(x), \tag{4}$$

where $\langle \vartheta^k(x) \vartheta^k(x') \rangle$ represents the averaged autocorrelation function.

The energy ε is defined as the sum of the eigenvalues; that is, $\varepsilon = \sum_j \lambda_j$. Thus, the energy percentage of the ith eigenfunctions is given by $\lambda_i / \sum_j \lambda_j$.

The POD eigenfunctions and corresponding amplitudes can be obtained by applying the singular-value decomposition (SVD) method to the sample space. Klema and Laub indicated that the SVD was established for real-square matrices in the 1870s by Beltrami and Jordan, for complex square matrices in 1902 by Autonne, and for general rectangular matrices in 1939 by Eckart and Young [13]. SVD is much more general than the eigenvalue decomposition and intimately relates to the matrix rank and reduced-rank least-squares approximation; thus, SVD can be viewed as the extension of the eigenvalue decomposition for the case of nonsquare matrices [11].

The implementation of POD by using the SVD is described as follows.

Suppose that $x_1, x_2, \ldots, x_n$ are n sample vectors given out by sampling properly, where $x_i \in R^m$ $(i = 1, 2, \ldots, n)$. Assume that the number of samples is large enough, which means $n > m$. Denote $X = (x_1, x_2, \ldots, x_n)$; thus, $X \in R^{m\times n}$ and $XX^T \in R^{m\times m}$ is the auto-correlation matrix. The eigenvalues of XX^T in decreasing order are given out as follows: $\lambda_1 \geq \lambda_2 \geq \cdots \geq \lambda_r > \lambda_{r+1} = \cdots = \lambda_m = 0$. $\sigma_i = \sqrt{\lambda_i}$ $(i = 1, 2, \ldots, m)$ are defined as the singular values of X^T. Then the eigenvectors of XX^T are $\upsilon_1, \upsilon_2, \ldots, \upsilon_m$ with their corresponding eigenvalues $\lambda_1, \lambda_2, \ldots, \lambda_m$. Defining $V = [V_1, V_2]$ with $V_1 = (\upsilon_1, \upsilon_2, \ldots, \upsilon_r)$, $V_2 = (\upsilon_{r+1}, \upsilon_{r+2}, \ldots, \upsilon_m)$, and r is the rank of matrix XX^T. Denote $U = [U_1, U_2]$ with $U_1 = X^T V_1 \Sigma_r^{-1}$ and $\Sigma_r^{-1} = \text{diag}(\sigma_1^{-1}, \sigma_2^{-1}, \ldots, \sigma_r^{-1})$. Due to the basis extension theorem of vector space, there exist $n - r$ orthonormal vectors $u_{r+1}, u_{r+2}, \ldots, u_n$ orthogonal to U_1 in R^n. Let $U_2 = (u_{r+1}, u_{r+2}, \ldots, u_m)$; then U is an $n \times n$ orthonormal matrix. For SVD method, $u_1, u_2, \ldots, u_m$ and $\upsilon_1, \upsilon_2, \ldots, \upsilon_m$ are defined as left and right singular vectors of X^T corresponding to eigenvalues $\sigma_1, \sigma_2, \ldots, \sigma_m$, respectively [11].

Thus, the samples can be presented in the following form:

$$X^T = U \begin{pmatrix} \Sigma_r & 0 \\ 0 & 0 \end{pmatrix} V^T. \tag{5}$$

From (5), it follows that

$$\left[x_1, x_2, \ldots, x_n\right] = V \begin{pmatrix} \Sigma_r & 0 \\ 0 & 0 \end{pmatrix} U^T. \tag{6}$$

Define the matrix $\left(\begin{smallmatrix} \Sigma_r & 0 \\ 0 & 0 \end{smallmatrix}\right) U^T$ as $d_1, d_2, \ldots, d_n$.

From (6), it follows that

$$x_i = V d_i, \quad (i = 1, 2, \ldots, n). \tag{7}$$

Thus, the sampled vectors of POD have been obtained.

3. POD Interpolation

The reduced model by the POD interpolation can be achieved by the three steps: first, we should get sufficient data to construct a sample matrix. Then, eigenfunctions and the corresponding amplitudes can be calculated by SVD. Finally, the amplitudes out of sampling parameters are obtained by interpolation. Since the interpolation affects the accuracy of the reduced model and few studies have been made to clarify the effects of different interpolations, we make the accuracy comparison between linear interpolation and cubic B-spline interpolation in this paper.

POD interpolation method is usually used to deal with one-parameter problems in engineering practice [8] by using linear interpolation to establish the reduced model. Recently, this method is extended to the double-parameter problems by the cubic B-spline interpolation in [1].

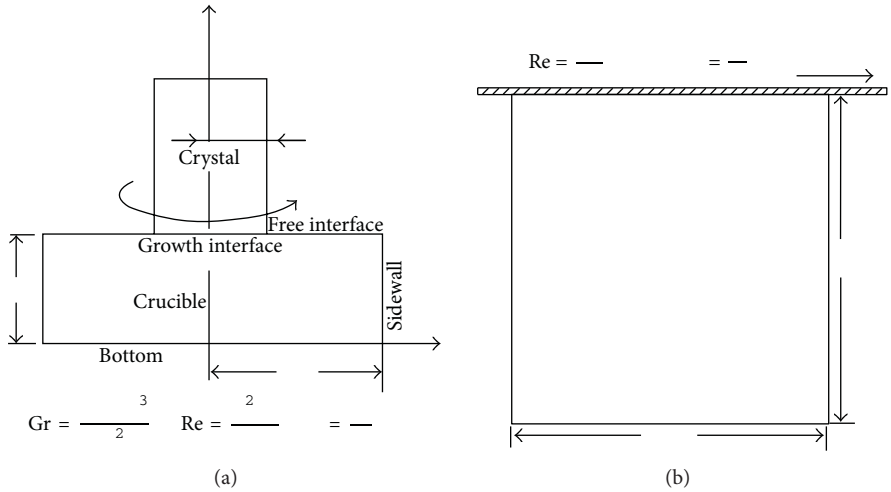

Figure 1: Czochralski crystal growth problem.

For a linear interpolation problem with N parameters $(x_1, \ldots, x_N)$, the nonsample amplitudes can be calculated by

$$\begin{aligned} & a\left(x^1, \ldots, x^N\right) \\ & = a\left(x_{a1}^1, \ldots, x_{aN}^N\right) \\ & \quad + \sum_{i=0}^{N-1} \sum_{j_{N-i}=1}^{N} \frac{x^{j_{N-i}} - x_{bj_{N-i}}^{j_{N-i}}}{x_{bj_{N-i}}^{j_{N-i}} - x_{aj_{N-i}}^{j_{N-i}}} \cdots \\ & \quad \times \sum_{j_k=N-i+1-k}^{N} \frac{x^{j_k} - x_{bj_k}^{j_k}}{x_{bj_k}^{j_k} - x_{aj_k}^{j_k}} \cdots \sum_{j_1=N-i}^{N} \frac{x^{j_i} - x_{bj_1}^{j_i}}{x_{bj_1}^{j_i} - x_{aj_1}^{j_i}} \\ & \quad \times \left\{(-1)^{N-i} \left[a\left(x_{a1}^1, \ldots, x_{aj_k}^{j_k}, \ldots, x_{aN}^N\right)\right.\right. \\ & \qquad \left.\left. - a\left(x_{a1}^1, \ldots, x_{bj_k}^{j_k}, \ldots, x_{aN}^N\right)\right]\right\}, \end{aligned} \tag{8}$$

where the superscript i of parameter xi is used to differentiate various parameters, while the subscripts a and b stand for the upside and downside values of interpolation.

The cubic B-spline interpolation is widely used in numerical approximation, the calculation of ordinary differential equations, and computation in science and technology, because it can give out a smooth interpolation curve. For brevity, the expression of a cubic B-spline interpolation is hence omitted. The detailed information about it can be found in the help documentation MATH. PDF in function library IMSL of FORTRAN language.

4. Computational Cases

Accuracy comparisons are carried out for POD reduced models established by linear interpolation and cubic B-spline interpolation, respectively, for two steady flow problems, that is, Czochralski crystal growth problem and lid-driven cavity flow problem sketched in Figure 1. For the first problem, the temperature fields are reconstructed while the stream-functions are reconstructed for the second problem. The lid-driven cavity flow problem is a very famous one in the field of computational fluid dynamics and the governing equations and boundaries can be easily found in the literature. Here we only present the governing equations and boundary conditions for the Czochralski crystal growth problem as follows:

Table 1: Generalized diffusion coefficient and generalized source term.

Equations	Φ	Γ	S
Continuity	1	0	0
Momentum	U	1	$-\frac{\partial P}{\partial R} - \frac{U}{R^2} + \frac{V^2}{R}$
	V	1	$-\frac{V}{R^2} - \frac{UV}{R}$
	W	1	$-\frac{\partial P}{\partial Z} + \mathrm{Gr}T$
Energy	T	1/Pr	0

$$\begin{aligned} & \frac{1}{R}\frac{\partial}{\partial R}(RU\Phi) + \frac{\partial}{\partial Z}(W\Phi) \\ & \quad = \frac{1}{R}\frac{\partial}{\partial R}\left(R\Gamma\frac{\partial \Phi}{\partial R}\right) + \frac{\partial}{\partial Z}\left(\Gamma\frac{\partial \Phi}{\partial Z}\right) + S. \end{aligned} \tag{9}$$

The general variables, generalized diffusion coefficient, and generalized source term are summarized in Table 1. In Table 1, the definitions of the dimensionless variables are

$$\begin{aligned} \mathrm{Gr} &= \frac{g\beta\Delta t \mathrm{Re}_c^3}{]^2}, \qquad \mathrm{Re}_r = \frac{R_r^2\Omega_r}{]}, \\ \alpha &= \frac{H}{R_c}, \qquad \beta = \frac{R_r}{R_c}, \\ \mathrm{Pr} &= \frac{]}{\kappa}, \qquad \mathrm{Re}_c = \frac{R_c^2\Omega_c}{]}, \end{aligned} \tag{10}$$

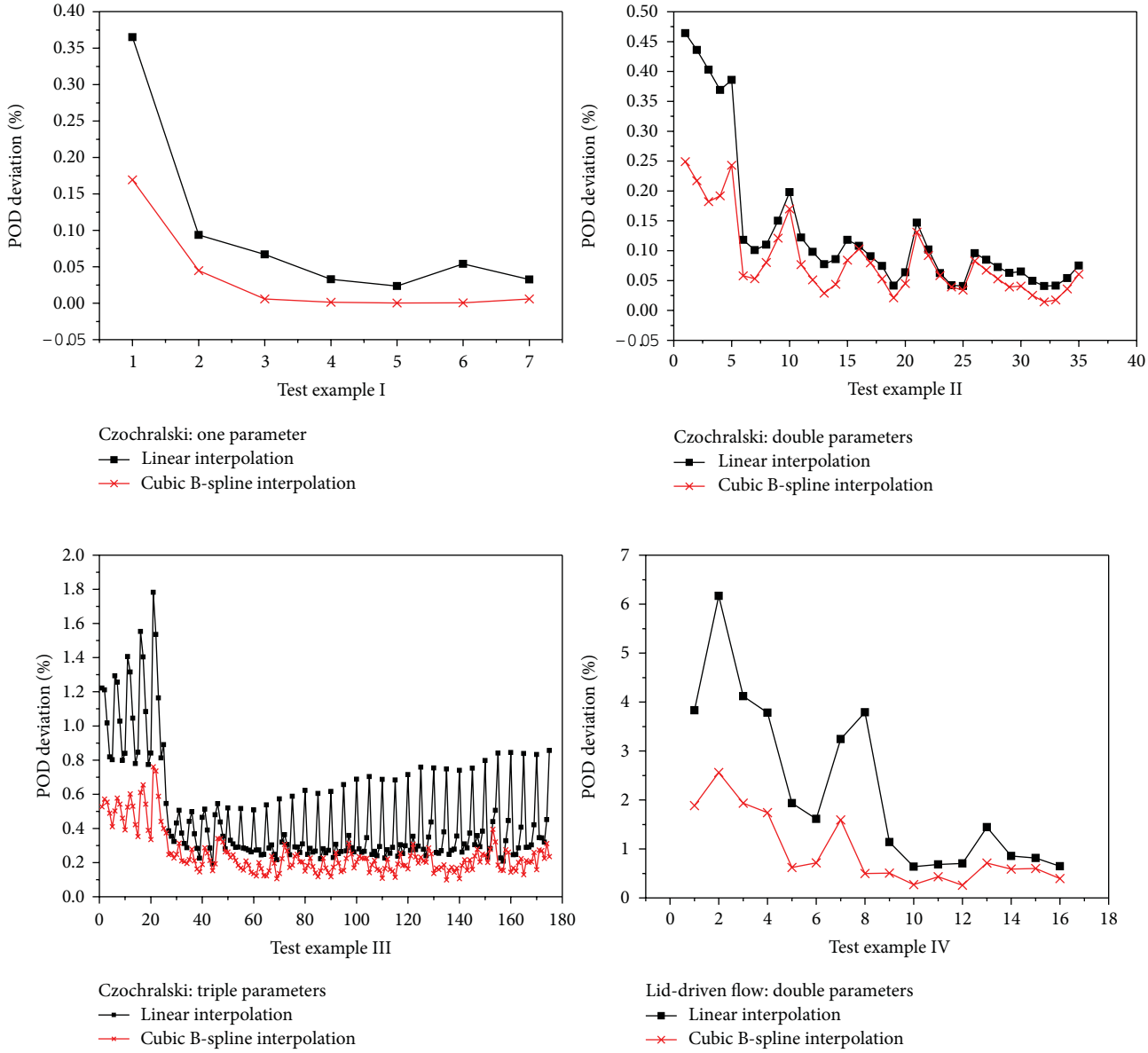

Figure 2: The error of POD interpolation with 8 eigenfunctions.

where Re_r and Re_c are the Reynolds numbers based on the angular velocity of crystal and crucible, respectively. In this paper, Gr, α, and Re_r are changeable while $\beta = 0.4$, $Pr = 0.05$, and $Re_c = 0$ are fixed in the calculation. The boundary conditions are given in Table 2.

A finite volume method is used for the discretization of the governing equations. 80×80 uniform grids are employed for both problems. The convective terms and diffusion terms are discretized by QUICK scheme and a central difference scheme, respectively. A staggered grid system is used to avoid unphysical zigzag pressure field. The SIMPLE algorithm is adopted to couple the velocity field and pressure. The discretized algebraic equations are solved by TDMA method. The details on the above numerical techniques are referred to in [14].

5. Results and Discussion

The reduced models by means of POD interpolations of single, double, and triple parameters for the Czochralski crystal growth problem as well as double parameters for the lid-driven flow problem are established. To establish the reduced models, first of all, sufficient data are required to construct a sample matrix to obtain the eigenfunctions of a temperature field for the Czochralski crystal growth problem and a flow field for the lid-driven flow problem at different conditions. The matrices can be obtained through finite volume method (FVM), stated in Section 4. The samplings of these two problems are as follows. As for the Czochralski crystal growth problem with one parameter, Gr is selected as a variable, and its 8 values varying in the range of 10^5 to 10^6 are listed in

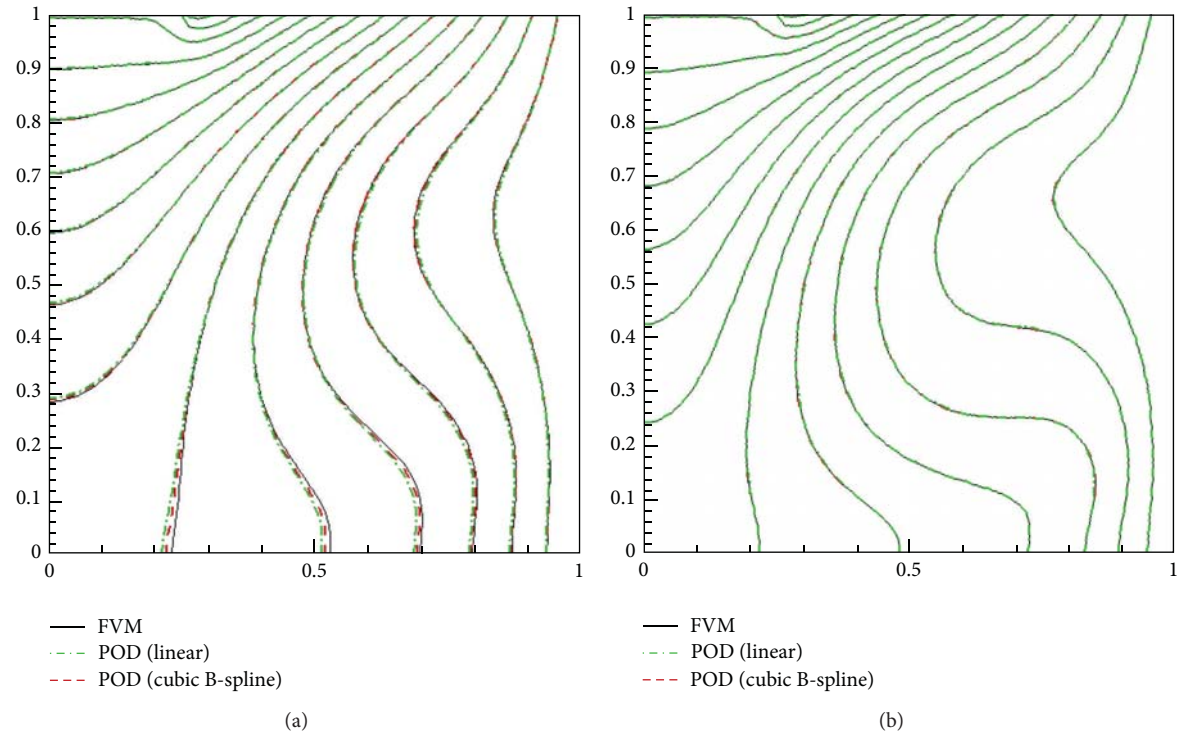

Figure 3: The comparison of temperature field in Czochralski crystal growth problem with one parameter: (a) the example with maximum error ($Gr = 1.5 \times 10^5$), (b) the example with minimum error ($Gr = 5.5 \times 10^5$).

Table 2: Boundary conditions of Czochralski crystal growth problem.

Parameters	Velocity			Temperature
Place	U	V	W	T
Growth interface	$U = 0$	$V = R\Omega_r$	$W = 0$	$T = 0$
Bottom of crucible	$U = 0$	$V = R\Omega_c$	$W = 0$	$\dfrac{\partial T}{\partial Z} = 0$
Sidewall of crucible	$U = 0$	$V = R_c\Omega_c$	$W = 0$	$T = 1$
Free interface	$\dfrac{\partial U}{\partial Z} = 0$	$\dfrac{\partial V}{\partial Z} = 0$	$W = 0$	$T = \dfrac{R - R_r}{R_c - R_r}$
Along symmetrical axis	$U = 0$	$V = 0$	$\dfrac{\partial W}{\partial R} = 0$	$\dfrac{\partial T}{\partial R} = 0$

Note: for the free interface boundary condition in the above table, we assume that temperature changes linearly.

column A of Table 3; and for double parameters case, Gr and Re are selected as the two variables, and their values are listed in columns A and B of Table 3, respectively. 48 calculation cases are obtained by the combination of the two parameter values. As for triple parameters case, another variable α (the ratio of liquid height to radius of crucible) is added, besides Gr and Re, whose value is in column C of Table 3. The combination of triple parameters increases to 288 calculation cases. As for the lid-driven flow problem, the two parameters are Re and γ (the ratio of height to width), whose values are, respectively, listed in columns D and E of Table 3 and the number of combinations is 25.

Then the SVD method [15, 16] is applied to obtain the eigenfunctions and corresponding amplitudes. The nonsampling amplitudes can be calculated by linear interpolation and cubic B-spline interpolation, respectively. The test examples are selected in Table 4. For the Czochralski crystal growth problem and lid-driven flow problem, the numbers of test examples by combination are 7, 35, 175, and 16, respectively. Around 280 s and 130 s are taken by FVM to get solutions using a personal computer that contained an I7-860 CPU and 4 GB DDR3 memory for a Czochralski crystal growth case and a lid-driven flow case, respectively, and comparatively only around 0.03 s is taken by POD interpolation to get

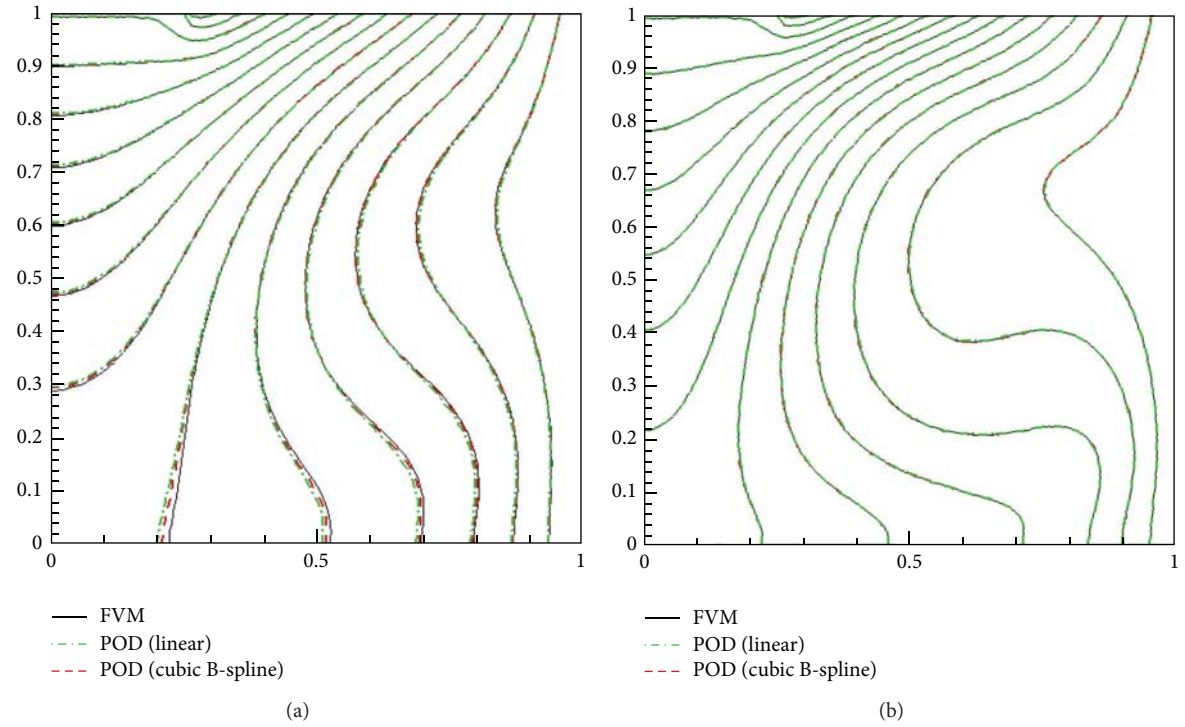

Figure 4: The comparison of temperature field in Czochralski crystal growth problem with double parameters: (a) the example with maximum error ($Gr = 1.5 \times 10^5$, $Re_r = 550$), (b) the example with minimum error ($Gr = 9.0 \times 10^5$, $Re_r = 650$).

Table 3: Selected samples.

	Czochralski crystal growth problem			Lid-driven flow
	One parameter	Double parameters	Triple parameters	double parameters
Gr	A	A	A	—
Re	—	—	—	D
Re_r	0.0	B	B	—
α	1.0	1.0	C	E
The number of samples	8	48	288	25

Note: $A = (0.1, 0.2, 0.3, 0.4, 0.5, 0.6, 0.8, 1.0) \times 10^6$; $B = (0.5, 0.6, 0.7, 0.8, 0.9, 1.0) \times 10^3$; $C = (0.5, 0.6, 0.7, 0.8, 0.9, 1.0)$; $D = (1.0, 2.0, 3.0, 4.0, 5.0) \times 10^3$; $E = (0.5, 0.75, 1.0, 1.5, 2.0)$.

Table 4: Selected test samples.

	Czochralski crystal growth problem			Lid-driven flow
	One parameter	Double parameters	Triple parameters	double parameters
Gr	A	A	A	—
Re	—	—	—	D
Re_r	0.0	B	B	—
α	1.0	1.0	C	E
The number of test samples	7	35	175	16

Note: $A = (0.15, 0.25, 0.35, 0.45, 0.55, 0.7, 0.9) \times 10^6$; $B = (0.55, 0.65, 0.75, 0.85, 0.95) \times 10^3$, $C = (0.55, 0.65, 0.75, 0.85, 0.95)$, $D = (1.5, 2.5, 3.5, 4.5) \times 10^3$, $E = (0.625, 0.875, 1.25, 1.75)$.

a solution. Apparently, the POD method much outweighs the FVM method in terms of computational cost.

In order to quantitatively validate the accuracy of reduced model given by POD interpolation, we define the relative average error as E in the following expression:

$$E = \frac{\sum_{i=1}^{n} \left(\left| f - f_M \right| / \left| f \right| \right)}{n} \times 100\%, \tag{11}$$

Table 5: The temperature error of Czochralski crystal growth problem with one parameter in various numbers of eigenfunctions.

Eigenfunctions	First 1	First 2	First 3	First 4	First 5	First 6	First 7	First 8
$(E_l)_m$	5.344	0.673	0.414	0.369	0.365	0.365	0.365	0.365
$(E_B)_m$	5.344	0.719	0.281	0.181	0.169	0.169	0.169	0.169
$(E_l)_a$	2.673	0.405	0.156	0.099	0.095	0.096	0.096	0.096
$(E_B)_a$	2.675	0.404	0.126	0.045	0.033	0.032	0.032	0.032

Note: $(E_l)_m$ and $(E_B)_m$ stand for the maximum relative error of linear interpolation and cubic B-spline interpolation, respectively. $(E_l)_a$ and $(E_B)_a$ stand for the average error of linear interpolation and cubic B-spline interpolation, respectively. The subscript l is represented for linear interpolation, while B is represented for cubic B-spline interpolation.

Table 6: The temperature error of Czochralski crystal growth problem with double parameters in various numbers of eigenfunctions.

Eigenfunctions	First 1	First 2	First 3	First 4	First 5	First 6	First 7	First 8
$(E_l)_m$	5.544	0.887	0.625	0.466	0.464	0.464	0.464	0.464
$(E_B)_m$	5.545	0.924	0.484	0.250	0.249	0.249	0.249	0.249
$(E_l)_a$	2.755	0.461	0.199	0.134	0.133	0.133	0.133	0.133
$(E_B)_a$	2.757	0.459	0.170	0.085	0.084	0.084	0.084	0.084

Note: $(E_l)_m$ and $(E_B)_m$ stand for the maximum relative error of linear interpolation and cubic B-spline interpolation, respectively. $(E_l)_a$ and $(E_B)_a$ stand for the average error of linear interpolation and cubic B-spline interpolation, respectively. The subscript l is represented for linear interpolation, while B is represented for cubic B-spline interpolation.

Table 7: The temperature error of Czochralski crystal growth problem with triple parameters in various numbers of eigenfunctions.

Eigenfunctions	First 1	First 2	First 3	First 4	First 5	First 6	First 7	First 8
$(E_l)_m$	24.775	7.457	3.927	1.833	1.822	1.777	1.781	1.782
$(E_B)_m$	24.602	7.464	3.595	1.196	0.938	0.748	0.756	0.761
$(E_l)_a$	10.231	3.199	1.192	0.754	0.640	0.504	0.486	0.481
$(E_B)_a$	10.228	3.208	1.125	0.610	0.474	0.290	0.260	0.249

Note: $(E_l)_m$ and $(E_B)_m$ stand for the maximum relative error of linear interpolation and cubic B-spline interpolation, respectively. $(E_l)_a$ and $(E_B)_a$ stand for the average error of linear interpolation and cubic B-spline interpolation, respectively. The subscript l is represented for linear interpolation, while B is represented for cubic B-spline interpolation.

Table 8: The temperature error of lid-driven flow problem with double parameters in various numbers of eigenfunctions.

Eigenfunctions	First 1	First 2	First 3	First 4	First 5	First 6	First 7	First 8
$(E_l)_m$	46.270	16.978	11.793	5.809	6.501	6.367	6.314	6.167
$(E_B)_m$	46.308	20.921	11.678	5.572	2.781	2.764	2.744	2.558
$(E_l)_a$	21.416	6.746	4.753	2.905	2.356	2.210	2.203	2.213
$(E_B)_a$	21.418	7.295	4.239	2.208	1.187	1.069	1.008	0.957

Note: $(E_l)_m$ and $(E_B)_m$ stand for the maximum relative error of linear interpolation and cubic B-spline interpolation, respectively. $(E_l)_a$ and $(E_B)_a$ stand for the average error of linear interpolation and cubic B-spline interpolation, respectively. The subscript l is represented for linear interpolation, while B is represented for cubic B-spline interpolation.

where f is the FVM result, while f_M is the one achieved by POD interpolation. n is the grid numbers. The maximum relative error and average error are shown in Tables 5, 6, 7, and 8 under various conditions and various numbers of eigenfunctions. In these tables, $(E_l)_m$ and $(E_B)_m$ stand for the maximum relative error of linear interpolation and cubic B-spline interpolation, respectively, while $(E_l)_a$ and $(E_B)_a$ represent the average error by using linear interpolation and cubic B-spline interpolation, respectively.

From Tables 5–8, we can see that when the number of eigenfunctions applied in the reduced model is small (first 1 or 2 groups of eigenfunctions), the errors for both of the POD interpolations are great with the maximum error being 46%. When more eigenfunctions are used, the results are predicted more accurately for the reduced model. On the other hand, if the number of eigenfunctions exceeds 5, the computational accuracy is improved a little. For example, when we choose eight eigenfunctions to describe Czochralski crystal growth problem, the maximum error $(E_l)_m/(E_B)_m$ is 0.365%/0.169%, 0.464%/0.249%, and 1.782%/0.761% for different parameter numbers, that is, single variable, double variables, and triple variables, respectively, while the maximum error $(E_l)_m/(E_B)_m$ for the lid-driven flow problem is 6.167%/2.558%.

When the number of eigenfunctions is less than 3, the numerical accuracy of the two interpolation methods is almost the same. When more eigenfunctions are employed, higher accuracy is achieved by cubic B-spline interpolation. Figure 2 illustrates that the deviation of cubic B-spline

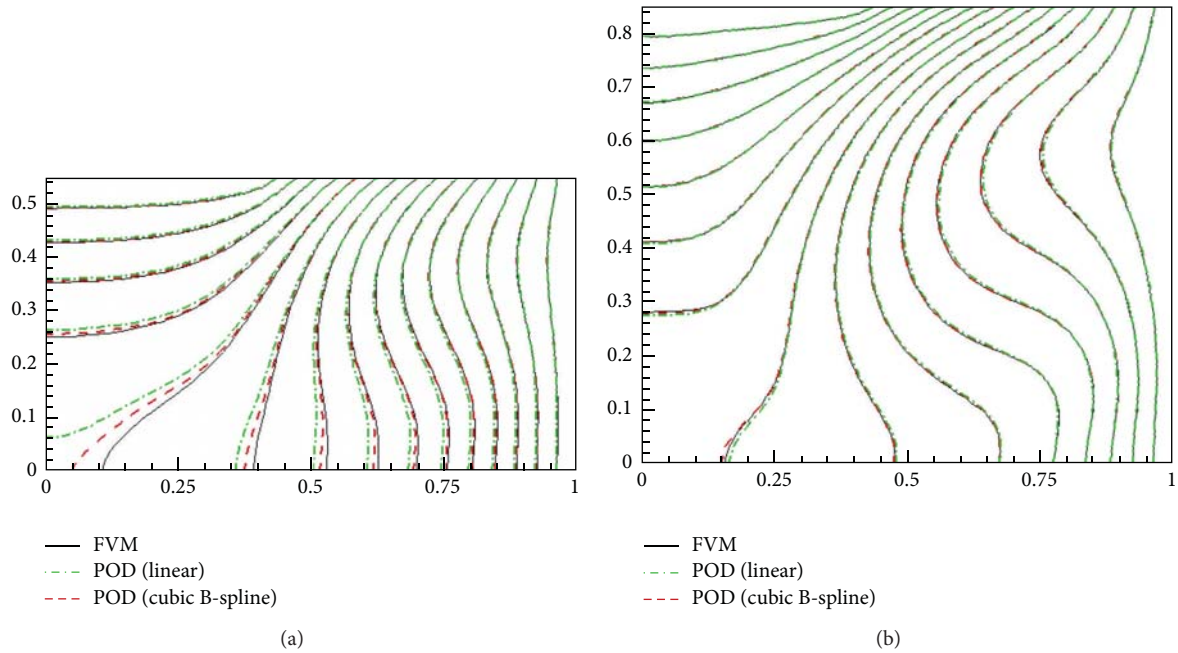

FIGURE 5: The comparison of temperature field in Czochralski crystal growth problem with triple parameters: (a) the example with maximum error ($Gr = 1.5 \times 10^5$, $Re_r = 950$, $\alpha = 0.55$), (b) the example with minimum error ($Gr = 3.5 \times 10^5$, $Re_r = 850$, $\alpha = 0.85$).

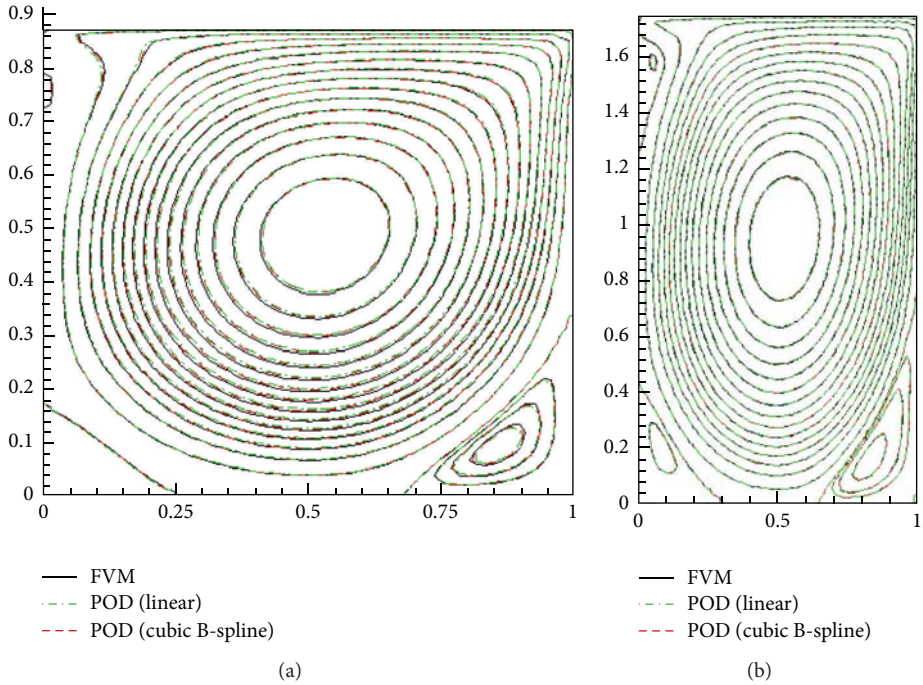

FIGURE 6: The comparison of stream functions in lid-driven flow problem with double parameters: (a) the example with maximum error ($Re = 1500$, $\gamma = 0.875$), (b) the example with minimum error ($Re = 3500$, $\gamma = 1.75$).

interpolation is less than its counterpart, that is, linear interpolation, among all the test examples when the first 8 eigenfunctions are applied. The maximum and minimum errors of the POD interpolation are shown in Figures 3, 4, 5, and 6. In these figures, the solid line stands for the results of FVM method, while the dash line and dotted line are representative of the results of cubic B-spline interpolation and linear interpolation, respectively. Obviously, the results of POD interpolation agree well with those of FVM. In a word, POD interpolation method can simulate the physical process

precisely for multivariable; in addition, the cubic B-spline POD interpolation presents higher accuracy.

6. Conclusion

The POD linear interpolation and cubic B-spline interpolation are employed to work out the nonsample amplitudes, and their accuracy for multivariable problems is verified via two typical heat and fluid flow problems. Through a large number of examples, we can conclude that POD interpolation method outweighs the FVM method in terms of computational cost, and the cubic B-spline POD interpolation has higher accuracy than the linear one.

Nomenclature

$a_i(t)$: The amplitude of POD corresponding to the ith eigenfunction
$(E_l)_m$: The maximum relative error of linear interpolation
$(E_B)_m$: The maximum relative error of cubic B-spline interpolation
$(E_l)_a$: The average error of linear interpolation
$(E_B)_a$: The average error of cubic B-spline interpolation
Gr: The Grashof number
H: The height of crucible
$P_{i,j,k}$: The point achieved by interpolation
P_{i_1,j_1,k_1}, P_{i_2,j_2,k_2}: Interval circumscribed interpolation points
Pr: The Prandtl number
R_r: The radius of crystal in Czochralski crystal growth problem
R_c: The radius of crucible in Czochralski crystal growth problem
Re: The Reynolds numbers in lid-driven flow problem
Re_r: The Reynolds number due to the rotation of crystal in Czochralski crystal growth problem
Re_c: The Reynolds number due to the rotation of crucible in Czochralski crystal growth problem
r, θ, z: The spatial cylindrical coordinates in Czochralski crystal growth problem
U, V, W: Thevelocity components in the cylindrical coordinate
$u_1, u_2, \ldots, u_m$: Left singular vectors of sample matrix
$v_1, v_2, \ldots, v_m$: Right singular vectors of sample matrix
X: The sample matrix
α: The ratio of height to radius in Czochralski crystal growth problem
β: The radius ratio of crystal to crucible in Czochralski crystal growth problem
γ: The ratio of height to width in lid-driven flow problem
ε: The total energy of the POD eigenfunctions
$\varphi_i(x)$: The ith eigenfunction of POD
λ_i: The eigenvalue of the ith eigenfunction
$\vartheta(x,t)$: The physical field
σ_i: The ith singular value of samples
Ω_r: The angular velocity of crystal in Czochralski crystal growth problem
Ω_c: The angular velocity of crucible in Czochralski crystal growth problem.

Acknowledgments

The study is supported by the National Science Foundation of China (nos. 51206186, 51134006, 51176204) and Science Foundation of China University of Petroleum-Beijing (nos. 2462011LLYJ33, 2462011LLYJ55, 2462012KYJJ0403, 2462012-KYJJ0404).

References

[1] P. Ding, *Reduced order model based algorithm for inverse convection heat transfer problem [Ph.D. thesis]*, Xi'an Jiaotong University, Xi'an, China, 2009.

[2] W. Zhang, C. Chen, and D. J. Sun, "Numerical simulation of flow around two side-by-side circular cylinders at low Reynolds numbers by a POD-Galerkin spectral method," *Chinese Journal of Hydrodynamics A*, vol. 24, no. 1, pp. 82–88, 2009.

[3] J. L. Lumley, *Atmospheric Turbulence and Radio Wave Propagation*, Nauka, Moscow, Russia, 1967.

[4] J. L. Lumley, *Transition and Turbulence*, Academic Press, New York, NY, USA, 1981.

[5] N. Aubry, P. Holmes, and J. L. Lumley, "The dynamics of coherent structures in the wall region of turbulent boundary layer," *Journal of Fluid Mechanics*, vol. 192, pp. 115–173, 1988.

[6] K. Karhunen, *Über Linere Methoden in der Wahrscheinlichkeitsrechnung*, vol. 37 of *Annales Academiæ Scientiarum Fennicæ Series. A1 Mathematica and Physica*, 1946.

[7] D. Kosambi, "Statistics in function space," *The Journal of the Indian Mathematical Society*, vol. 7, pp. 76–88, 1943.

[8] Y. G. Wang, Z. N. Li, B. Gong, and Q. S. Li, "Reconstruction & prediction of wind pressure on heliostat," *Acta Aerodynamica Sinica*, vol. 27, no. 5, pp. 586–591, 2009.

[9] O. Hiroyuki, *Magnetic Convection*, Imperial College Press, London, UK, 2005.

[10] G. Kerschen, J. C. Golinval, A. F. Vakakis, and L. A. Bergman, "The method of proper orthogonal decomposition for dynamical characterization and order reduction of mechanical systems: an overview," *Nonlinear Dynamics*, vol. 41, no. 1–3, pp. 147–169, 2005.

[11] Y. C. Liang, H. P. Lee, S. P. Lim, W. Z. Lin, K. H. Lee, and C. G. Wu, "Proper orthogonal decomposition and its applications-part I: theory," *Journal of Sound and Vibration*, vol. 252, no. 3, pp. 527–544, 2002.

[12] P. Holmes, J. L. Lumley, and G. Berkooz, *Turbulence, Coherent Structures, Dynamical Systems and Symmetry*, Cambridge University Press, New York, NY, USA, 1996.

[13] V. C. Klema and A. J. Laub, "The singular value decomposition: its computation and some applications," *IEEE Transactions on Automatic Control*, vol. AC-25, no. 2, pp. 164–176, 1980.

[14] W. Q. Tao, *Recent Advances of Numerical Heat Transfer*, Science Press, Beijing, China, 2005.

[15] L. R. Ma, "Application of SVD in numerical calculation of engineering," *Journal of Ningxia University*, vol. 19, pp. 125–127, 1998.

[16] T. D. Lu, "An algorithm for least-square collocation by singular value decomposition," *Science of Surveying and Mapping*, vol. 33, no. 3, pp. 47–51, 2008.

Hindawi Publishing Corporation
Advances in Mechanical Engineering
Volume 2013, Article ID 514325, 10 pages
http://dx.doi.org/10.1155/2013/514325

Research Article

Wavelet Analysis on Turbulent Structure in Drag-Reducing Channel Flow Based on Direct Numerical Simulation

Xuan Wu, Bo Yu, and Yi Wang

Beijing Key Laboratory of Urban Oil and Gas Distribution Technology, China University of Petroleum, Beijing 102249, China

Correspondence should be addressed to Bo Yu; yubobox@vip.163.com

Received 24 December 2012; Accepted 31 January 2013

Academic Editor: Shuyu Sun

Direct numerical simulation has been performed to study a polymer drag-reducing channel flow by using a discrete-element model. And then, wavelet analyses are employed to investigate the multiresolution characteristics of velocity components based on DNS data. Wavelet decomposition is applied to decompose velocity fluctuation time series into ten different frequency components including approximate component and detailed components, which show more regular intermittency and burst events in drag-reducing flow. The energy contribution, intermittent factor, and intermittent energy are calculated to investigate characteristics of different frequency components. The results indicate that energy contributions of different frequency components are redistributed by polymer additives. The energy contribution of streamwise approximate component in drag-reducing flow is up to 82%, much more than 25% in the Newtonian flow. Feature of turbulent multiscale structures is shown intuitively by continuous wavelet transform, verifying that turbulent structures become much more regular in drag-reducing flow.

1. Introduction

It is well known that the addition of a small amount of polymer solution into liquid such as water at high Reynolds number can suppress turbulence and significantly reduce turbulent friction drag. This phenomenon, the so-called Toms effect [1], is useful for saving energy in turbulent flow systems and has recently been implemented in several industrial systems for energy conservation and environmental protection [2–4]. The mechanism of drag reduction induced by polymer has been studied for several years, but there is still an absence of a widely accepted theory.

In the latest 20 years, along with the development of computer, more and more researchers studied the mechanism of polymer drag reduction by DNS. Sureshkumar et al. [5] performed DNS for a fully developed turbulence channel flow with FENE-P model and proposed a set of criteria for the onset of drag reduction. Dimitropoulos et al. [6] predicted drag reduction for a variety of rheological parameters in the FENE-P and the Giesekus models, and verified the hypothesis that one of the prerequisites for the phenomenon of drag reduction is sufficiently enhanced extensional viscosity, corresponding to the level of intensity and duration of extensional rates typically encountered during the turbulent flow. Angelis et al. [7] further confirmed the ability of the FENE-P model to reproduce most of the essential effects of polymers in dilute solutions on the wall turbulence. Min et al. [8, 9] studied the role of elastic energy in turbulence drag-reduction caused by polymer additives using an elastic Oldroyd-B model and obtained the maximum drag-reduction rate, showing good agreement with Virk's asymptote at the same Reynolds number. Ptasinski et al. [10] performed an analysis of the turbulent kinetic energy budgets and found that the ability of polymers to stretch is an essential ingredient for high drag reduction. Yu and Kawaguchi [11] studied the effect of Weissenberg number on the turbulent flow structure using a Giesekus model. Housiadas et al. [12] examined the efforts of changes in the flow viscoelasticity and the friction Reynolds number on several higher order statistics and on coherent structures of turbulence. Kajishima and Miyake

[13] established a discrete-element model (spring-dumbbell model) to simulate the extension of polymer chain in drag-reducing flow. Then, this model was employed by Wang et al. [14] to investigate the mechanism of drag reduction by polymer. The decrease of the Reynolds shear stress found in the experiments was first reproduced in the simulation when the spring coefficient is relatively small.

However, most of the investigations mentioned above paid more attention to turbulent statistics relating to mean features of drag-reducing flow rather than different scale structures. Wang et al. [15, 16] attempted this topic especially for drag-reducing flow and its heat transfer by proper orthogonal decomposition. To make a further study on mechanism of drag reduction, multiresolution analysis method should be applied to investigate the energy distribution and turbulent structures of different time scales in drag-reducing flow. Fortunately, wavelet analysis theory provides an effective tool for detecting multiscale flow structures in turbulence. This theory is more and more widely used to analyze a series of turbulent phenomena such as atmosphere, ocean, river, and cloud [17–20].

The first idea to use the wavelet analysis for studying turbulence was proposed by Farge [21] and some tools such as local intermittency and energy of wavelet decompositions, wavelet power spectrum, were developed to examine the structure of atmospheric turbulence. Camussi and Guj [22] conducted the wavelet decompositions with orthogonal-based wavelets to permit the identification of time signal series of coherent structures in artificial turbulence. Gilliam et al. [23] further verified that wavelet analysis can be employed to detect coherent structures in long-time series and introduce two statistical techniques, an intermittency rate estimator and an event-counting technique based on wavelet analysis to extract coherent structures from experimental data of wind. Smith and Jonas [20] proved that wavelet analysis is a useful tool for analyzing the turbulent data in cirrus clouds and found that wavelet spectra not only can be used to identify processes which produce energy at larger scales but also have the additional advantage to capture smaller-scale localized processes containing high-energy events along with their position in the time series, which may be lost in Fourier spectra obtained from long-time signals. Farge et al. [24] introduced a wavelet-based coherent vortex extraction technique for two-dimensional flows using scalar-valued orthogonal wavelet decompositions and decompose, turbulent flows into two orthogonal parts: a coherent, inhomogeneous, non-Gaussian component and an incoherent, homogeneous, Gaussian component, which have different correlations, different probability distributions, and different scaling laws. And then, this technique was extended to three dimensional conditions [25]. Based on wavelet, a new method called coherent vortex simulation was designed to model three-dimensional turbulent flows [26–29]. Wavelet can also extract the characteristics of turbulence or eddy structures from experimental or computational data [30–35]. Zhen and Hassan [36] applied wavelet analysis to the streamwise fluctuating velocity fields in the microbubbles drag-reducing flow for multiscale study and overcome many shortcomings of the Fourier analysis. In addition, wavelet analysis has been applied successfully in mechanics and chemical engineering for they provide both time and frequency information that helps in the industrial design of vessels and pipes [37, 38].

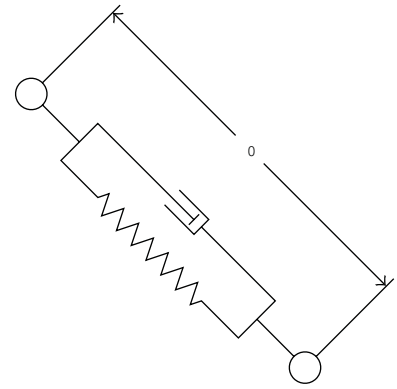

Figure 1: The discrete-element model.

In the present study, the instantaneous information of polymer drag-reducing flow is provided by direct numerical simulation with the discrete-element model. Based on these DNS data, multiresolution structures of drag-reducing flow are analyzed by wavelet transformation and wavelet decomposition in time domain. Characteristics of different frequency components of time traces, such as wavelet energy spectra, intermittent factor, and intermittent energy, are examined by wavelet multiresolution decomposition to identify the polymer effect on turbulent energy distribution. Multiscale flow structures of Newtonian flow and drag-reducing flow are shown by continuous wavelet transform, respectively.

2. Physical Model and Numerical Method

In this study, the discrete-element model established by Kajishima and Miyake [13] is employed to simulate the polymer drag-reducing flow. The polymer chain is treated as a discrete-element and the polymer macromolecule is modeled as two beads linked by a spring and a damper as shown in Figure 1. The parameters in this model such as the spring coefficient k, damping coefficient η, and length l_0 represents elasticity, viscosity, and the natural length of the polymer chain, respectively. There are some assumptions introduced in the model: (1) the mass of the polymer is concentrated on the beads p and q, (2) linear transformation but not broken of spring, (3) the density of the discrete-elements equal to the solvent, (4) elastic collision between the beads and the wall, (5) ignore the interaction among the discrete-elements, (6) ignore the Brownian motions. Based on the assumptions mentioned above, the drag-reducing flow by polymer can be described as a sort of "two-phase" flow, a kind of liquid containing a large amount of discrete elements.

DNS is performed for turbulent channel flow as shown in Figure 2. The dimensionless governing equations [14] for fully developed turbulent drag-reducing channel flow based on the discrete-elements model can be written as follows.

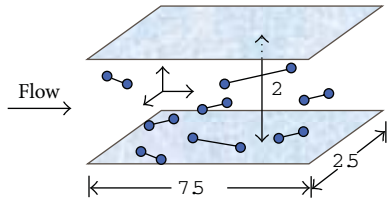

Figure 2: Drag-reducing channel flow by polymer.

Discrete-elements motion equation:

$$\frac{d\mathbb{V}_{pi}^{+}}{dt^{*}} = \frac{f_{pi}^{*} - k^{*}\xi^{*}\left(\left(x_{pi}^{*} - x_{qi}^{*}\right)/l^{*}\right) - \eta^{*}\left(\mathbb{V}_{pi}^{*} - \mathbb{V}_{qi}^{*}\right)}{V^{*}}, \quad f_{pi}^{*} = -C^{*}\left(\mathbb{V}_{pi}^{+} - u_{pi}^{+}\right). \tag{1}$$

For the solvent:

continuity equation:

$$\frac{\partial u_{i}^{*}}{\partial x_{i}^{*}} = 0, \tag{2}$$

momentum equation:

$$\frac{\partial u_{i}^{*}}{\partial t^{*}} + \frac{\partial}{\partial x_{j}^{*}}\left(u_{i}^{*}u_{j}^{*}\right) = \delta_{i1}^{*} - \frac{\partial p^{*}}{\partial x_{i}^{*}} + \frac{1}{\mathrm{Re}_{\tau}}\frac{\partial^{2}u_{i}^{*}}{\partial x_{j}^{*}\partial x_{j}^{*}} + F_{i}^{*}, \tag{3}$$

additional force equation:

$$F_{i}^{*} = -\frac{1}{V_{c}^{*}}\sum_{x_{p}^{*}\in V_{c}^{*}} f_{pi}^{*}, \tag{4}$$

where $k^{*} = k/\rho u_{\tau}^{2}h$, $\eta^{*} = \eta/\rho u_{\tau}h^{2}$, $C^{*} = 6\pi r^{*}/\mathrm{Re}_{\tau}$, $\mathrm{Re}_{\tau} = \rho u_{\tau}h/\mu$, $u_{i}^{*} = u_{i}/u_{\tau}$, $x_{i}^{*} = x_{i}/h$, $r^{*} = r/h$, $t^{*} = t/(h/u_{\tau})$, $p^{*} = p/\rho_{f}u_{\tau}^{2} + x^{*}$, $V^{*} = 4\pi r^{*3}/3$, and $V_{c}^{*} = V_{c}/h^{3}$.

The initial state of discrete-elements is assumed to be uniformly distributed in the solvent. The number of the elements is 10^{5}. The dimensionless parameters r^{*}, ${l_{0}}^{*}$, k^{*}, and η^{*} are 0.01, 0.13, 0.001, and 0.0013, respectively. Calculations are made for a friction Reynolds number $\mathrm{Re}_{\tau} = 150$, which is based on the wall friction velocity u_{τ} and half the channel height h. The dimensionless computational domain $7.5 \times 2 \times 2.5$ in the streamwise, wall-normal, and spanwise directions, respectively, is chosen, as shown in Figure 2. A grid system of $64 \times 64 \times 64$ $(x \times y \times z)$ meshes is adopted. The dimensionless time step 10^{-4} is used. The periodic boundary conditions are imposed in both the streamwise and the spanwise directions, while nonslip boundary conditions are adopted for the walls.

The Euler-Lagrange two-way method [39, 40], by which the motion of each element is tracked independently, is applied to obtain the distribution of discrete elements in drag-reducing flow. In this method, trajectories of elements' motion are obtained by solving the Newton equations of motion in Lagrange frame of reference. The computational algorithm is a fractional step method using the Adams-Bashforth scheme for time advancement [41] with the dimensionless time step 3×10^{-4} to solve velocities of solvent and beads. An implicit projection method is used for coupling velocity and pressure. Crank-Nicolson scheme is used for calculating the instantaneous locations of the beads. In discrete elements motion equation, the fluid velocity at the location of the beads is obtained by bilinear interpolation.

3. Wavelet Analysis

Wavelet transform is local transform revealing information in both the frequency and time domain. Continuous wavelet transform (CWT) of a given time series $s(t)$ is defined as a convolution operation between the time series $s(t)$ and a wavelet function $\psi_{a,b}(t)$ as follows:

$$\mathrm{CWT}_{s}(a,b) = \left\langle s, \psi_{a,b}\right\rangle = \int_{R} s(t)\cdot\psi_{a,b}(t)\,dt, \quad \psi_{a,b}(t) = \frac{1}{\sqrt{a}}\psi\left(\frac{t-b}{a}\right), \tag{5}$$

where $\psi_{a,b}(t)$ is wavelet function at translation b and scale a of the basic wavelet function $\psi(t)$, also known as the mother wavelet.

Discrete wavelet transform is defined as following:

$$\mathrm{DWT}_{a,b} = a^{-1/2}\cdot\Delta t\cdot\sum_{R} s(t)\,\psi\left(\frac{t-b}{a}\right) = {a_{0}}^{-m/2}\cdot\Delta t\cdot\sum_{R} s(t)\,\psi\left({a_{0}}^{-m}t - nb_{0}\right), \tag{6}$$

where $a = a_{0}^{m}$, $b = nb_{0}a_{0}^{m}$, $\Delta t = a^{m}b_{0}$. a_{0}, and b_{0} are the scale and time translation of wavelet function in first-level wavelet transform.

The original signal $s(t)$ can be decomposed into $n+1$ parts by n-level wavelet decomposition, including an approximate component A_{n} and n detailed components D_{i} shown as follows:

$$s(t) = A_{n} + \sum_{i=1}^{n} D_{i}. \tag{7}$$

The energy $E_{a,b}$ in the sense of time translation b and for scale a can be approximated by square of wavelet transform coefficients:

$$E_{a,b} = \left|\mathrm{DWT}_{a,b}\right|^{2}. \tag{8}$$

Therefore, the total energy of scale a can be calculated as follows:

$$E_{a} = \sum_{b}\left|\mathrm{DWT}_{a,b}\right|^{2}, \quad a = A_{j}, D_{j}, D_{j-1}, \ldots, D_{2}, D_{1}. \tag{9}$$

Energy contribution of different frequency (or scale) component is defined as the ratio between the energy of each level and total energy as follows:

$$\mathrm{EC}_{a} = \frac{E_{a}}{\sum E_{a}}, \quad a = A_{j}, D_{j}, D_{j-1}, \ldots, D_{2}, D_{1}. \tag{10}$$

Intermittency factor of components from wavelet decompositions is defined as a ratio between the number of higher energy events over energy threshold ($I_{a,b} = 1$) and total signals (N_a), which is written as follows:

$$\mathrm{IF}_a = \frac{\sum_{b=1}^{N_a} I_{a,b}}{N_a}, \qquad I_{a,b} = \begin{cases} 1, & \mathrm{DWT}_{a,b} > \mathrm{th}\,(a), \\ 0, & \text{others.} \end{cases} \tag{11}$$

The energy threshold is defined as twice the average energy of that scale [21, 42]:

$$\mathrm{th}\,(a) = 2\overline{E_{a,b}}. \tag{12}$$

Intermittent energy is defined as energy percentage of higher energy events in wavelet decompositions over their total energy as follows:

$$\mathrm{IE}_a = \frac{\sum E_{a,b(I_{a,b}=1)}}{E_a}. \tag{13}$$

For wavelet analysis, 6000 snapshots of velocity are selected and the interval dimensionless time is 3×10^{-2}.

4. Results and Discussions

Time and space averages of turbulent statistics in fully developed condition should be selected to obtain the mean flow field. It is written as follows:

$$\overline{F\,(y^*)} = \frac{1}{N_x \cdot N_z \cdot N_t} \sum_{i=1}^{N} F\,(x^*, y^*, z^*, t_i^*)\,. \tag{14}$$

The fluctuating field can be calculated from the instantaneous field and the mean field as follows:

$$F'\,(x^*, y^*, z^*, t^*) = F\,(x^*, y^*, z^*, t^*) - \overline{F\,(y^*)}. \tag{15}$$

Intensity of turbulent fluctuation is defined as the root mean square of the fluctuations [16]:

$$F_{\mathrm{rms}}\,(y^+) = \sqrt{\frac{\left[\sum_{m=1}^{N_t} \sum_{k=1}^{N_z} \sum_{i=1}^{N_x} F'(x_i^+, y^+, z_k^+, t_m^*)^2\right]}{(N_x \cdot N_z \cdot N_t)}}, \tag{16}$$

where y^+ is the wall unit ($y^+ = (1 + y^*) \cdot \mathrm{Re}_\tau$) and $F_{\mathrm{rms}}(y^+)$ represents instantaneous physical field such as fluctuating velocity and vorticity. Drag reduction rate is defined as the reduction of the friction factor with respect to the Newtonian fluid at an equal mean Reynolds number [43]:

$$\mathrm{DR\%} = \frac{C_{f\mathrm{Dean}} - C_f}{C_{f\mathrm{Dean}}} \times 100\%, \tag{17}$$

where DR% is the drag-reduction rate, C_f is the friction factor from DNS data and $C_{f\mathrm{Dean}}$ is the friction factor of Newtonian fluid flow evaluated by Dean's correlation at the same mean Reynolds number of drag reducing flow. The main results such as frictional factor and drag reduction rate are listed in Table 1.

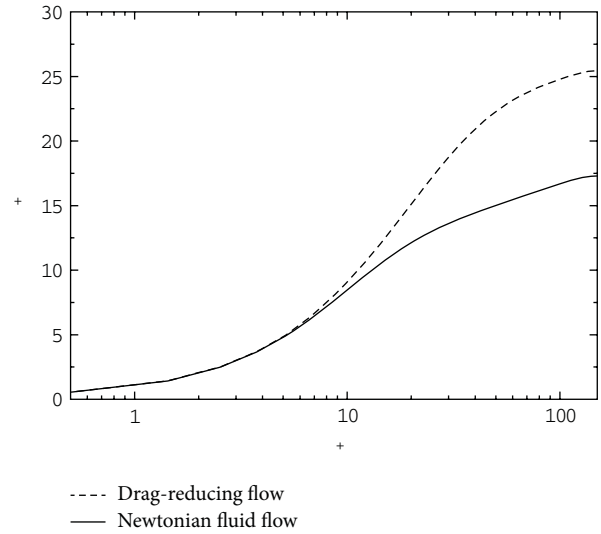

Figure 3: Mean velocity profile.

Table 1: Main results of direct numerical simulation.

	$U_m{}^+$	Re_m	C_f	$C_{f\mathrm{Dean}}$	DR%
Drag-reducing	21.2	6373	4.432×10^{-3}	8.170×10^{-3}	45.8%
Newtonian	14.8	4443	9.119×10^{-3}	8.941×10^{-3}	—

The mean velocity profile is shown in Figure 3. It can be seen that the mean velocity is in good agreement with linear distribution $U^+ = y^+$ in the viscous sublayer. In the buffer layer, mean velocity of drag-reducing flow increases significantly compared to those of Newtonian fluid flow.

Figure 4 shows the velocity fluctuation intensities in the streamwise, wall-normal, and spanwise directions, respectively. The streamwise velocity fluctuation intensity of drag-reducing flow becomes larger than Newtonian fluid flow and its peak value position shifts to the bulk flow region. The other two components of velocity fluctuation intensities are depressed by drag-reducing additives, especially in the buffer layer. All the results mentioned above support that the buffer layer is the most effective region for drag-reducing additives to induce drag reduction.

Turbulent statistics show the mean characteristics of flow. However, they cannot provide details of turbulent structure. In fact, turbulence is a very complicated phenomenon, which contains many multiscale structures in both time and space domain. Turbulent fluctuation consists of many different frequency components, of which large-scale structures represent low-frequency component of fluctuation in time series, while small-scale structures represent high-frequency component. Further investigation of the variation of different scale structures induced by polymer, multi-scale wavelet decomposition is employed to decompose the time series of velocity signals at a typical point into approximate

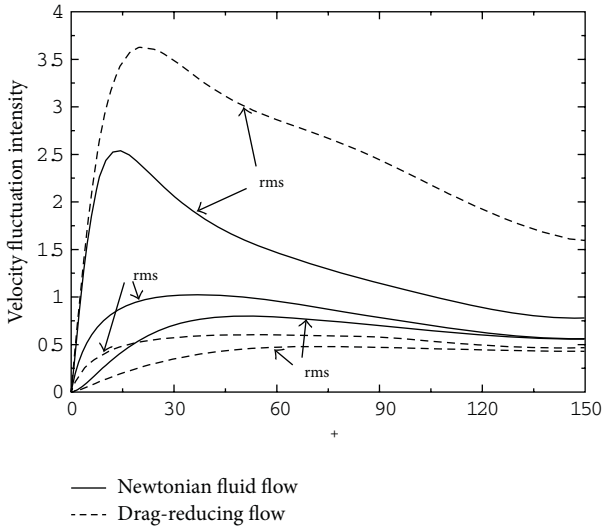

Figure 4: Velocity fluctuation intensities.

component (A) and detailed components (D). In this paper, a typical point in the buffer layer ($y^+ = 15$) is chosen for wavelet analysis because polymer plays a very important role in the buffer layer where peak values of important turbulent statistics and the maximum elongation of polymer molecules occur [16]. Then, the original velocity fluctuation signal $u(t)$ can be decomposed into ten parts by nine-level wavelet decompositions (7) with 3rd order Daubechies wavelet.

Figure 5 shows the nine-level wavelet decompositions of velocity fluctuation. In these pictures, the first lines are time series of instantaneous velocity, and the others are different frequency components obtained from wavelet decompositions. From the 2nd line (A_9) to the 11th line (D_1), the frequencies of the components get higher and higher. It is obvious that the lowest frequency component (the 2nd line) can approximate the main features of the instantaneous velocity, which is in correspondence with the whole variation tendency of the local mean velocity along with time. And the higher frequency components can describe the details of turbulence, which reflect the occurrence of turbulent events. Comparing streamwise velocity components of Newtonian flow (Figure 5(a)) with drag-reducing flow (Figure 5(b)), it can be seen that the approximate component of the drag reducing flow has larger amplitude than that of Newtonian fluid flow (the amplitude is $-4 \sim 2$ for Newtonian fluid flow as A_9 of Figure 5(a) and $-5 \sim 5$ for the drag reducing flow as A_9 of Figure 5(b)). For Newtonian fluid flow, the detailed components show continuous stronger fluctuation along with time. The detailed components of the drag reducing flow show regular intermittent pulse as comparative weak fluctuation between every two strong fluctuations. All components of fluctuations of drag reducing flow show regular intermittence, indicating more regular burst events as compared with those of Newtonian fluid flow. Further explanations about these phenomena will be made later.

In order to further explain the polymer effect on velocity fluctuation, the energy contribution of different frequency components is calculated. Figure 6 shows the wavelet energy spectra of different levels from velocity decomposition. It is obvious that energy distribution of different frequency components has been changed in three directions by polymer additives. In partiular for the components in streamwise direction (Figure 6), there are remarkable differences in energy contribution between Newtonian fluid flow and drag-reducing flow. The energy contribution of approximate component (A_9) in drag-reducing flow is up to 82%, which is much higher than that of Newtonian flow 25%. For detailed components ($D_9 \sim D_1$), the energy contributions of $D_9 \sim D_4$ of drag-reducing flow are much less than those of Newtonian flow. These results show that energy of streamwise velocity is concentrated to the lowest frequency component and decrease in detailed components of drag-reducing flow, indicating that the energy redistribution induced by polymer makes the lowest frequency component have more significant effect on drag-reducing flow than on Newtonian flow. These conclusions are also in accordance with Figure 5 that the amplitude of streamwise approximate component becomes larger but almost all the amplitudes of streamwise detailed components get smaller in drag-reducing flow. On the other hand, the decrease of energy contributions of detailed components, which have a close relationship with turbulent dissipation, implies that there is a less energy loss in turbulent dissipation of drag-reducing flow, which may be another reason for drag reduction. It can be also found that polymer has a very weak effect on $D_3 \sim D_1$ because these higher frequency components have smaller intensity so that they conclude tiny energy.

Intermittent factor and intermittent energy of different velocity components are shown in Figures 7 and 8, respectively. It can be seen that most energy is contained in high-energy events, a minority of all turbulent events. In drag-reducing flow, the intermittent factor of approximate component of streamwise velocity is about 20% but the intermittent energy is close to 65%. The intermittent factor and intermittent energy of approximate component (A_9) of drag-reducing flow are higher than those of Newtonian fluid flow, indicating that the number of high energy events of approximate component increases, intermittency strengthens, and more turbulent kinetic energy concentrates on high energy events in drag-reducing flow. High-energy burst events play a leading role in the formation of turbulent coherent structure. That is, stronger intermittency leads to larger-scale structures and more regular flow. Therefore, energy concentration on high-energy events signifies that turbulences are controlled and become more regular in drag-reducing flow. Moreover, intermittent factors of detailed components in drag-reducing flow are smaller, but intermittent energy is larger than those in Newtonian fluid flow, implying that the number of high energy events of detailed components decrease but turbulent kinetic energy of small scale structures remain concentrating on high energy events in drag-reducing flow. These support that turbulent events become more regular in drag-reducing flow. The conclusions from these two figures are also agree well with Figure 5 that number of larger amplitude of detailed

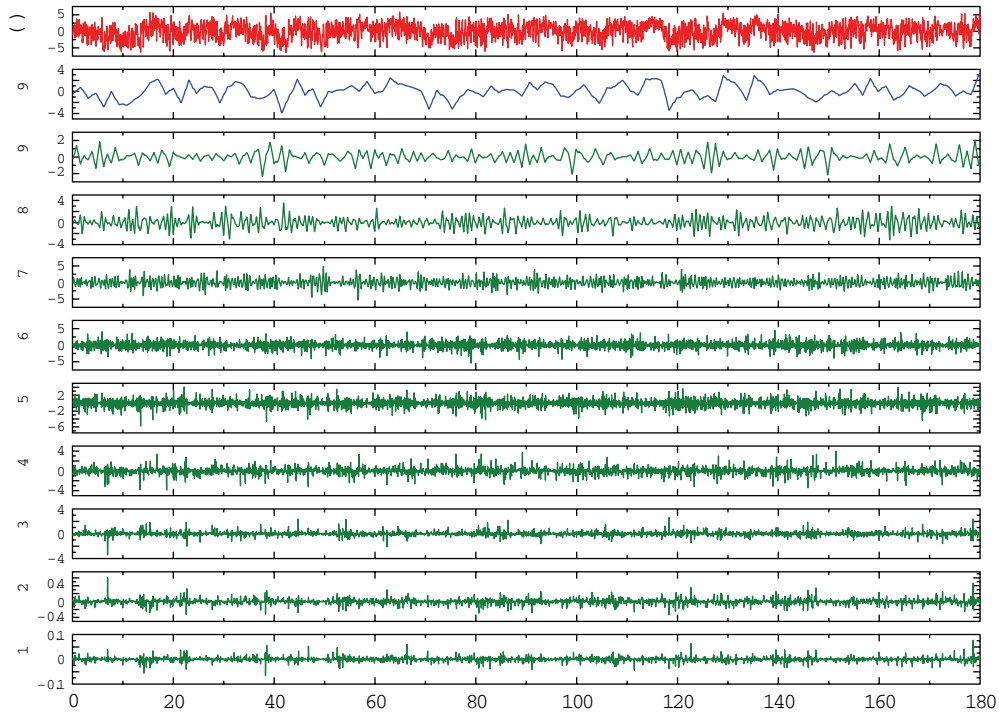

(a) Streamwise velocity of Newtonian fluid flow

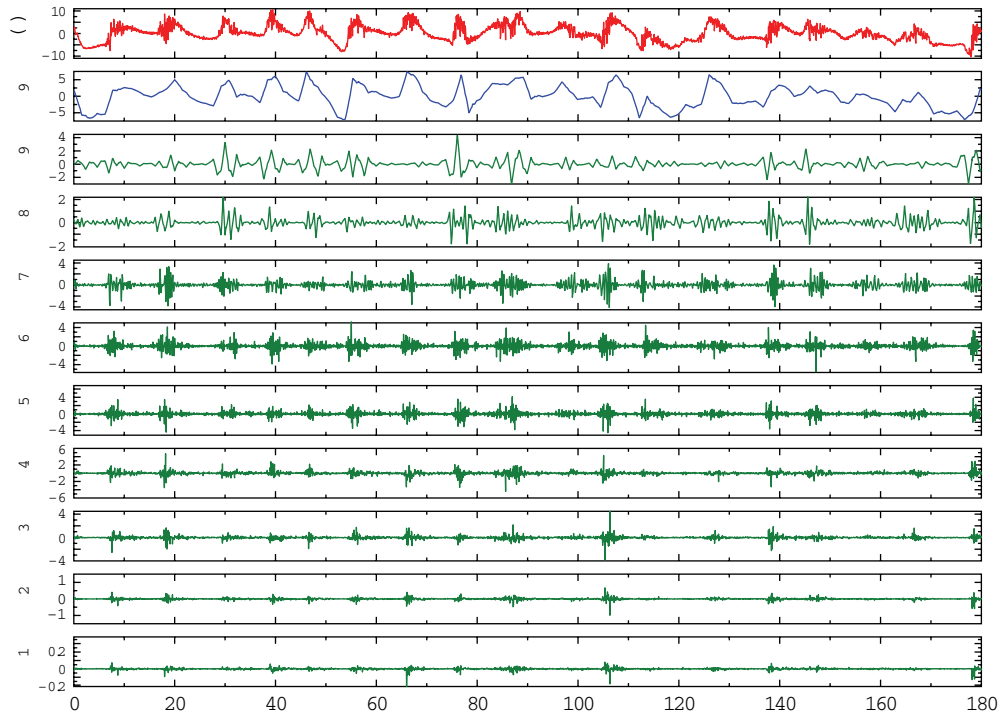

(b) Streamwise velocity of drag-reducing flow

Figure 5: Wavelet decompositions of the fluctuating velocity time series at the center point of the x-z plane at $y^+ = 15$.

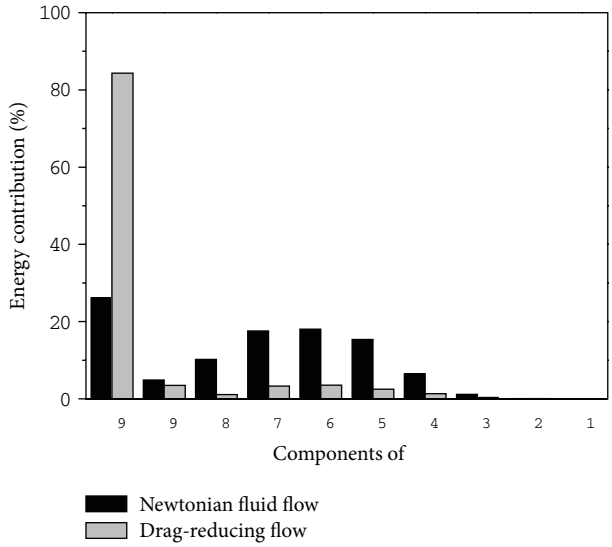

FIGURE 6: Energy contributions of different frequent components.

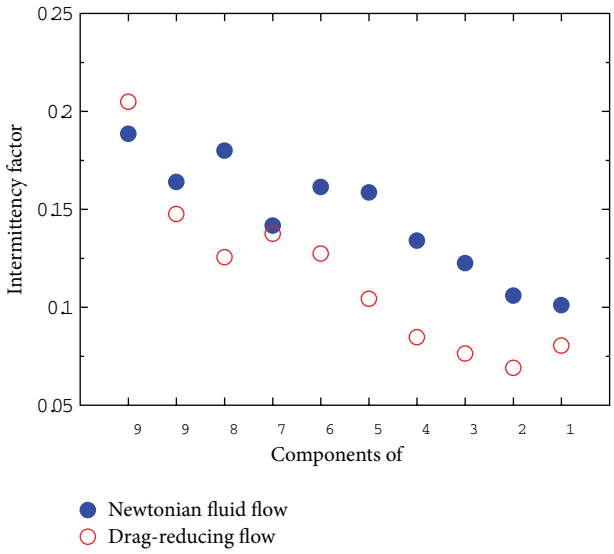

FIGURE 7: Intermittent factors of different frequent components.

components decrease and turbulent burst events appear more regular in drag-reducing flow.

Continuous wavelet transform with Morlet wavelet is used to investigate the influence of drag-reducing additives on turbulent multiscales structure. The continuous wavelet transform coefficients of instantaneous velocity time traces are shown in Figure 9. The lighter color indicates the larger wavelet transform coefficients, which means an intense turbulent event of time scale a occurs at time position b. On the contrary, the darker color indicates the smaller wavelet transform coefficients. In addition, the wider the coefficient streak along time axis (horizontal axis) is, the larger the scale of the structure is. From Figure 9, it can be found that when

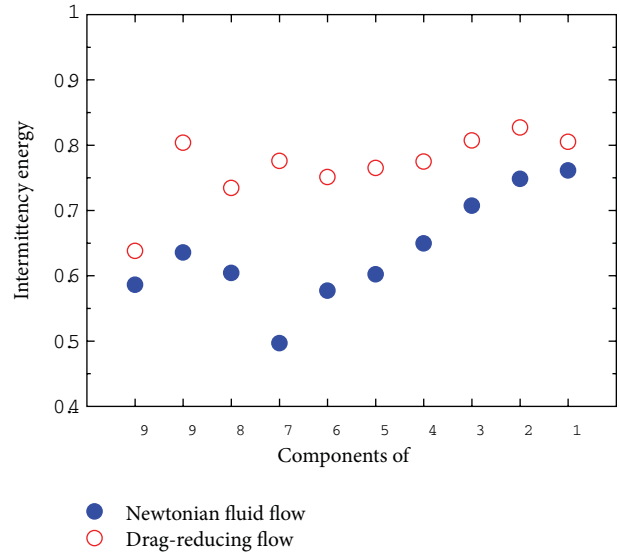

FIGURE 8: Intermittent energy of different frequent components.

the time scale (vertical axis) decreases, the coefficient streaks become slimmer and their number increases exponentially. When time scale a decreases to less than about 25, coefficient streaks break down and several points with light or dark color appear. These phenomena intuitively show that turbulence is composed of many different scale structures. Obviously, coefficient streaks of Newtonian flow have more furcations. Nevertheless, drag-reducing flow has more regular and wider coefficient streaks, which are corresponding to larger-scale structures. On the other hand, small lighter points, corresponding to small-scale (higher frequency) structures, are distributed disorderly in Newtonian flow, indicating that small scale intense turbulent events occur irregularly. However, in drag-reducing flow, these lighter points concentrate to be a series of light cluster located along the time translation axis. It can also be seen obviously that medium-scale structures (time scale factor a between 25 and 80) in drag-reducing flow are less but more regular than those in Newtonian flow, indicating that energy loss in turbulent energy cascade, that is, energy transfer from large-scale structures to dissipative scale structures, can be cut down in drag-reducing flow. All the phenomena show that the streaks and lighter points are more regular in drag-reducing flow than those in Newtonian flow, supporting that multiscale structures of drag-reducing flow are arranged more regularly than those of Newtonian flow, which agree well with conclusions above. It can be certified again that drag-reducing additives have a strong effect on turbulence control by making multi-scale structures orderly.

5. Conclusions

Direct numerical simulation based on discrete element model has been used to study polymer drag-reducing flow.

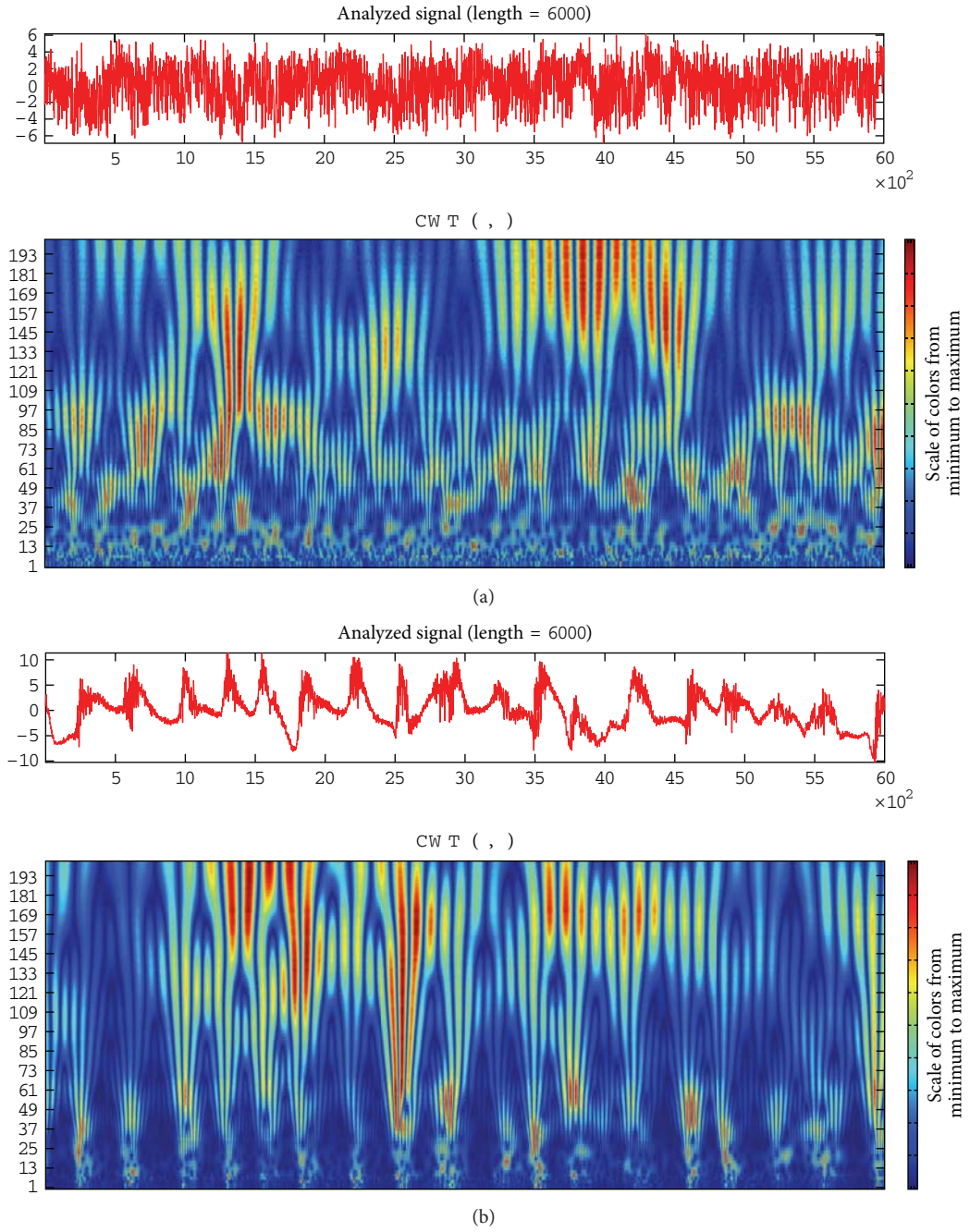

Figure 9: Continuous wavelet transform of velocity time series at the center point of the x-z plane at $y^+ = 15$.

According to the DNS results and wavelet analyses, characteristics of multiresolution structures in drag-reducing flow have been investigated and some conclusions can be drawn as follow.

(1) The velocity fluctuation intensity is increased at streamwise direction but depressed at the other two directions in whole in drag-reducing flow. For streamwise direction, energy contribution of approximate component is extremely large in drag-reducing flow, but almost all detailed components are dramatically suppressed.

(2) Detailed components have more regular intermittent events in drag-reducing flow than Newtonian fluid flow. High-energy events of detailed components become fewer, but contain more turbulent kinetic energy in drag-reducing flow. Multiscale structures can be arranged more regularly by drag-reducing additives.

Nomenclature

C_f: Friction factor
h: Half height of the channel, (m)
k: Spring coefficient of discrete element, (N/m)
l_0: Lengthofspring, (m)
p: Pressure, (Pa)
r: Radius of bead of discrete element, (m)
Re_m: Reynolds number based on channel height and mean velocity $= 2\rho u_m h/\mu$
Re_τ: Reynolds number based on half channel height and friction velocity $= \rho u_\tau h/\mu$
t: Time, (s)
u: Velocity, (m/s)
u_m: Mean velocity, (m/s)
u_τ: Friction velocity $= \sqrt{\tau_w/\rho}$, (m/s)
V: Radius of bead of discrete element, (m^3)
x_1, x: Streamwise direction, (m)
x_2, y: Wall-normal direction, (m)
x_3, z: Spanwise direction, (m).

Greek Symbols

η: Damping coefficient of discrete element, ($N \cdot s/m$)
ξ: Elongation of discrete element, (m)
δ: Kronecker symbol
ρ: Density, (kg/m^3)
μ: Dynamic viscosity, ($Pa \cdot s$)
τ_w: Statistically averaged wall shear stress, (Pa).

Superscripts and Subscripts

$()^+$: Normalized by u_τ, ρ, μ and h
$()^*$: Nondimensional coordinate (x, y and z) and coefficients
$()_{\mathrm{rms}}$: Root-mean-square fluctuations
$()_{p,q}$: Beads of discrete element.

Acknowledgments

The study is supported by the National Science Foundation of China (no. 51176204 and no. 51206186), the Science Foundation of China University of Petroleum, Beijing (no. 2462011LLYJ33, no. 2462011LLYJ55, no. 2462012KYJJ0403, no. 2462012KYJJ0404), and National Key Projects of Fundamental R/D of China (973 Project: 2011CB610306).

References

[1] B. A. Toms, "Some observations on the flow of linear polymer solutions through straight tubes at large Reynolds numbers," in *Proceedings of the of the 1st International Congress on Rheology*, vol. 2, p. 135, Amsterdam, The Netherlands, 1949.

[2] J. F. Motier, L. C. Chou, and N. S. Kommareddi, "Commercial drag reduction: past, present, and future," in *Proceedings of the ASME Fluids Engineering Division Summer Meeting*, pp. 229–234, San Diego, Calif, USA, 1996.

[3] J. Golda, "Hydraulic transport of coal in pipes with drag reducing additives," *Chemical Engineering Communications*, vol. 43, no. 1–3, pp. 53–67, 1986.

[4] G. Wu, J. Xu, and J. Miles, "Polymer drag reduction in large diameter coal log pipeline," in *Proceedings of the International Technical Conference on Coal Utilization Fuel Systems*, vol. 23, pp. 889–900, 1998.

[5] R. Sureshkumar, A. N. Beris, and R. A. Handler, "Direct numerical simulation of the turbulent channel flow of a polymer solution," *Physics of Fluids*, vol. 9, no. 3, pp. 743–755, 1997.

[6] C. D. Dimitropoulos, R. Sureshkumar, and A. N. Beris, "Direct numerical simulation of viscoelastic turbulent channel flow exhibiting drag reduction: effect of the variation of rheological parameters," *Journal of Non-Newtonian Fluid Mechanics*, vol. 79, no. 2-3, pp. 433–468, 1998.

[7] E. De Angelis, C. M. Casciola, and R. Piva, "DNS of wall turbulence: dilute polymers and self-sustaining mechanisms," *Computers and Fluids*, vol. 31, no. 4–7, pp. 495–507, 2002.

[8] T. Min, J. Y. Yoo, H. Choi, and D. D. Joseph, "A role of elastic energy in turbulent drag reduction by polymer additives," in *Proceedings of the 2nd International Symposium on Turbulence Shear Flow Phenomena*, vol. 3, pp. 35–50, KTH, Stockholm, Sweden, 2001.

[9] T. Min, H. Choi, and J. Y. Yoo, "Maximum drag reduction in a turbulent channel flow by polymer additives," *Journal of Fluid Mechanics*, no. 492, pp. 91–109, 2003.

[10] P. K. Ptasinski, B. J. Boersma, F. T. M. Nieuwstadt, M. A. Hulsen, H. A. A. van den Brule, and J. C. R. Hunt, "Turbulent channel flow near maximum drag reduction: simulations, experiments and mechanisms," *Journal of Fluid Mechanics*, vol. 490, pp. 251–291, 2003.

[11] B. Yu and Y. Kawaguchi, "Effect of Weissenberg number on the flow structure: DNS study of drag-reducing flow with surfactant additives," *International Journal of Heat and Fluid Flow*, vol. 24, no. 4, pp. 491–499, 2003.

[12] K. D. Housiadas, A. N. Beris, and R. A. Handler, "Viscoelastic effects on higher order statistics and on conherent structures in turbulent flow," *Physics of Fluids*, vol. 17, Article ID 035106, 2005.

[13] T. Kajishima and Y. Miyake, "Drag reduction by polymer additives in turbulent channel flow simulated by discrete-element models," *Transactions of the Japan Society of Mechanical Engineers B*, vol. 64, no. 627, pp. 3636–3643, 1998 (Japanese).

[14] Y. Wang, B. Yu, J. J. Wei, F. C. Li, and Y. Kawaguchi, "Direct numerical simulation on drag-reducing flow by polymer additives using a spring-dumbbell model," *Progress in Computational Fluid Dynamics*, vol. 9, no. 3–5, pp. 217–224, 2009.

[15] Y. Wang, B. Yu, X. Wu, J. Wei, F. Li, and Y. Kawaguchi, "POD study on the mechanism of turbulent drag reduction and heat transfer reduction based on direct numerical simulation," *Progress in Computational Fluid Dynamics*, vol. 11, no. 3-4, pp. 149–159, 2011.

[16] Y. Wang, B. Yu, X. Wu, and P. Wang, "POD and wavelet analyses on the flow structures of a polymer drag-reducing flow based on DNS data," *International Journal of Heat and Mass Transfer*, vol. 55, no. 17-18, pp. 4849–4861, 2012.

[17] A. Heidarinasab, B. Dabir, and M. Sahimi, "Multiresolution wavelet-based simulation of transport and photochemical reactions in the atmosphere," *Atmospheric Environment*, vol. 38, no. 37, pp. 6381–6397, 2004.

[18] S. R. Massel, "Wavelet analysis for processing of ocean surface wave records," *Ocean Engineering*, vol. 28, no. 8, pp. 957–987, 2001.

[19] T. Rajaee, "Wavelet and ANN combination model for prediction of daily suspended sediment load in rivers," *Science of the Total Environment*, vol. 409, no. 15, pp. 2917–2928, 2011.

[20] S. A. Smith and P. R. Jonas, "Wavelet analysis of turbulence in cirrus clouds," *Annales Geophysicae*, vol. 15, no. 11, pp. 1447–1456, 1997.

[21] M. Farge, "Wavelet transforms and their applications to turbulence," *Annual Review of Fluid Mechanics*, vol. 24, no. 1, pp. 395–457, 1992.

[22] R. Camussi and G. Guj, "Orthonormal wavelet decomposition of turbulent flows: intermittency and coherent structures," *Journal of Fluid Mechanics*, vol. 348, pp. 177–199, 1997.

[23] X. Gilliam, J. Dunyak, A. Doggett, and D. Smith, "Coherent structure detection using wavelet analysis in long time-series," *Journal of Wind Engineering and Industrial Aerodynamics*, vol. 88, no. 2-3, pp. 183–195, 2000.

[24] M. Farge, K. Schneider, and N. Kevlahan, "Non-Gaussianity and coherent vortex simulation for two-dimensional Nurbulence using an adaptive orthogonal wavelet basis," *Physics of Fluids*, vol. 11, no. 8, pp. 2187–2201, 1999.

[25] M. Farge, G. Pellegrino, and K. Schneider, "Coherent vortex extraction in 3D turbulent flows using orthogonal wavelets," *Physical Review Letters*, vol. 87, no. 5, Article ID 054501, 2001.

[26] M. Farge and K. Schneider, "Coherent Vortex Simulation (CVS), a semi-deterministic turbulence model using wavelets," *Flow, Turbulence and Combustion*, vol. 66, no. 4, pp. 393–426, 2001.

[27] M. Farge, K. Schneider, G. Pellegrino, A. A. Wray, and R. S. Rogallo, "Coherent vortex extraction in three-dimensional homogeneous turbulence: comparison between CVS-wavelet and POD-Fourier decompositions," *Physics of Fluids*, vol. 15, no. 10, pp. 2886–2898, 2003.

[28] K. Schneider, M. Farge, G. Pellegrino, and M. M. Rogers, "Coherent vortex simulation of three-dimensional turbulent mixing layers using orthogonal wavelets," *Journal of Fluid Mechanics*, vol. 534, pp. 39–66, 2005.

[29] K. Schneider, M. Farge, A. Azzalini, and J. Ziuber, "Coherent vortex extraction and simulation of 2D isotropic turbulence," *Journal of Turbulence*, vol. 7, pp. 44–67, 2006.

[30] H. Li, "Identification of coherent structure in turbulent shear flow with wavelet correlation analysis," *Journal of Fluids Engineering*, vol. 120, pp. 778–785, 1998.

[31] R. Camussi, "Coherent structure identification from wavelet analysis of particle image velocimetry data," *Experiments in Fluids*, vol. 32, no. 1, pp. 76–86, 2002.

[32] C. Schram, P. Rambaud, and M. L. Riethmuller, "Wavelet based eddy structure eduction from a backward facing step flow investigated using particle image velocimetry," *Experiments in Fluids*, vol. 36, no. 2, pp. 233–245, 2004.

[33] D. E. Goldstein and O. V. Vasilyev, "Stochastic coherent adaptive large eddy simulation method," *Physics of Fluids*, vol. 16, no. 7, pp. 2497–2513, 2004.

[34] O. Roussel, K. Schneider, and M. Farge, "Coherent vortex extraction in 3D homogeneous turbulence: comparison between orthogonal and biorthogonal wavelet decompositions," *Journal of Turbulence*, vol. 6, pp. 11–25, 2005.

[35] N. Okamoto, K. Yoshimatsu, K. Schneider, M. Farge, and Y. Kaneda, "Coherent vortices in high resolution direct numerical simulation of homogeneous isotropic turbulence: a wavelet viewpoint," *Physics of Fluids*, vol. 19, no. 11, Article ID 115109, 2007.

[36] L. Zhen and Y. A. Hassan, "Wavelet autocorrelation identification of the turbulent flow multi-scales for drag reduction process in microbubbly flows," *Chemical Engineering Science*, vol. 61, no. 21, pp. 7107–7114, 2006.

[37] C. Galletti, E. Brunazzi, M. Yianneskis, and A. Paglianti, "Spectral and wavelet analysis of the flow pattern transition with impeller clearance variations in a stirred vessel," *Chemical Engineering Science*, vol. 58, no. 17, pp. 3859–3875, 2003.

[38] M. Prek, "Wavelet analysis of sound signal in fluid-filled viscoelastic pipes," *Journal of Fluids and Structures*, vol. 19, no. 1, pp. 63–72, 2004.

[39] S. Laín, D. Bröder, M. Sommerfeld, and M. F. Göz, "Modelling hydrodynamics and turbulence in a bubble column using the Euler-Lagrange procedure," *International Journal of Multiphase Flow*, vol. 28, no. 8, pp. 1381–1407, 2002.

[40] M. Pang, J. J. Wei, and B. Yu, "Numerical study of bubbly upflows in a vertical channel using the Euler-Lagrange two-way model," *Chemical Engineering Science*, vol. 65, pp. 6215–6228, 2010.

[41] J. Banaszek, Y. Jaluria, T. A. Kowalewski, and M. Rebow, "Semi-implicit FEM analysis of natural convection in freezing water," *Numerical Heat Transfer, Part A*, vol. 36, no. 5, pp. 449–472, 1999.

[42] M. R. Hajj, "Intermittency of energy-containing scales in atmospheric surface layer," *Journal of Engineering Mechanics*, vol. 125, no. 7, pp. 797–803, 1999.

[43] R. B. Dean, "Reynolds number dependence of skin friction and other bulk flow variables in two-dimensional rectangular duct flow," *Journal of Fluids Engineering*, vol. 100, no. 2, pp. 215–223, 1978.

Hindawi Publishing Corporation
Advances in Mechanical Engineering
Volume 2013, Article ID 948980, 10 pages
http://dx.doi.org/10.1155/2013/948980

Research Article

Analyses on Heating Energy Saving of Two Hot Waxy-Crude Oil Pipelines Laid Parallel in One Ditch

Changzheng Sun[1] and Bo Yu[2]

[1] *South-East Asia Crude Oil Pipeline Company Ltd., Beijing 102200, China*
[2] *National Engineering Laboratory for Pipeline Safety, Beijing Key Laboratory of Urban Oil and Gas Distribution Technology, China University of Petroleum, Beijing 102249, China*

Correspondence should be addressed to Bo Yu; yubobox@vip.163.com

Received 5 January 2013; Accepted 4 February 2013

Academic Editor: Yi Wang

Laying two pipelines in one ditch is a new technology recently employed by the petroleum companies of China and has great advantages of minimizing environmental disruption as well as bringing tremendous economic and social benefits. In this study, by means of numerical simulations analyses are carried out to evaluate heating energy saving for the operation of two hot crude oil pipelines laid parallel in one ditch. Comparisons are made based on three various operating scenarios, among which the best operation is proposed. The effects of some important parameters such as the gap between the two pipelines (also called pipeline interval) and pipe length are investigated. It is found that two hot crude oil pipelines laid parallel in one ditch can dramatically save heating energy when compared with two pipelines laid, respectively, in two separate ditches.

1. Introduction

Before 2005 a common practice of oil pipeline construction was laying pipelines, respectively, in separate ditches (one ditch for one pipeline). In 2005, one ditch for two parallel pipelines (two parallel pipelines laid in one ditch) was considered and started to be adopted due to its obvious advantage of capital investment saving for pipeline construction. Therefore and since then, several hundred kilometers of crude oil pipeline and product pipeline in parallel in Western China were laid in one ditch since 2005. It was the first application of the technology of two pipelines in one ditch in the long-distance oil pipeline construction in China. The thermal effects between the crude oil pipeline and the products pipeline buried parallel in one ditch have been analyzed in [1–3]. Now with continuous development of new oil fields and huge demands on the crude oil, extension on pipeline network and increase in its throughput are in dire need, and laying two pipelines in one ditch would be an effective solution to this problem.

For crude oils with high pour point or high viscosity, heating transport is usually used to reduce the viscosity and keep pipeline operation temperature above the pour point along the pipeline for economical and safe pipelining operation [4–6]. The main shortcoming of heating transport is high energy/fuel consumption. However laying and operating two hot crude oil pipelines parallel in one ditch, due to the mutual thermal impact, may help reduce the loss of heat and thus save considerable amount of heating energy. This is of course only a qualitative estimation, and it is apparently not enough for the design and operation requirement. To precisely determine the energy saving amount by operating two pipelines in one ditch, detailed analyses should be carried out, which is the major aim and task of this paper. The results of this study will not only directly provide technical support for the pipeline construction in better way, but also give some guidelines for the operation optimization of the technology of laying two hot crude oil pipelines in one ditch.

2. Mathematical Modeling and Numerical Solution

Figure 1 shows the cross-section of the two pipelines buried in one ditch. The thermal status of the two buried hot crude oil

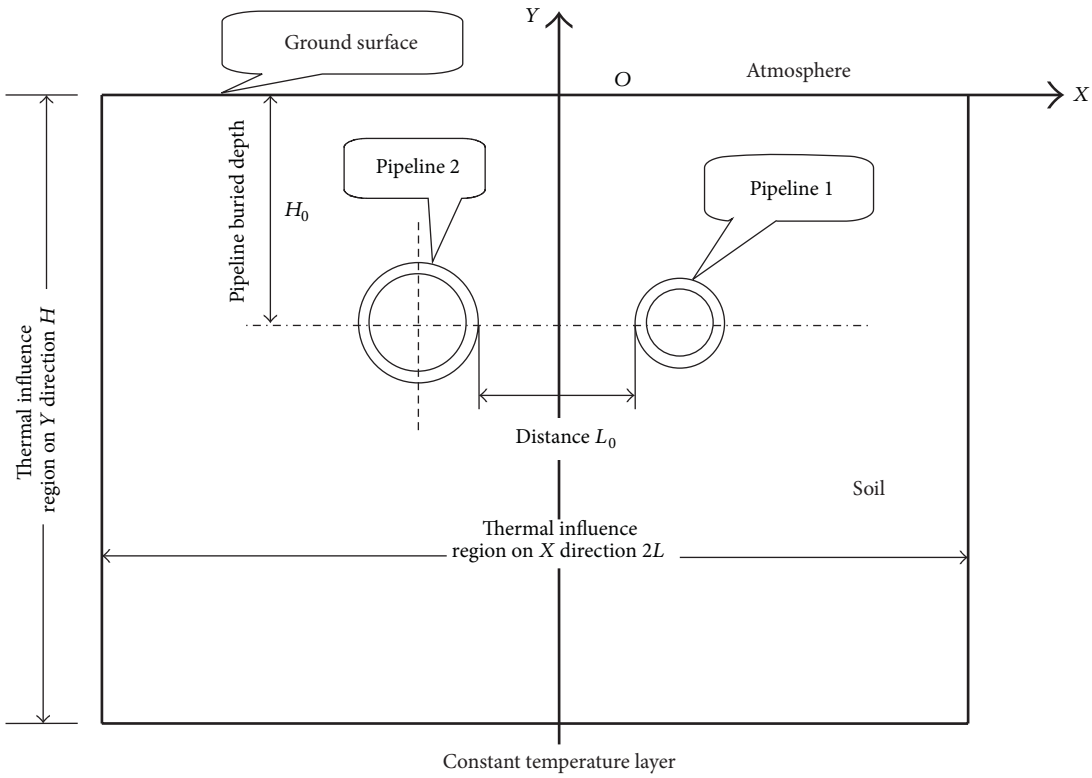

Figure 1: Two hot crude oil pipelines laid in one ditch.

pipelines consists of the convective heat transfer of the oil in the pipelines and the heat conduction outside the pipelines, and the latter is affected by a lot of parameters such as the air temperature, the thickness of wax deposit, the properties of soil, and the anticorrosion coating. To simplify the analyses, the following assumptions are made in the study.

(1) The oil temperature on a fixed pipeline cross-section is assumed to be the same; in other words, the oil temperature is only the function of time and axial position.

(2) The soil outside the pipeline is assumed as an isotropic medium, even though it is anisotropic in reality.

(3) The thickness of the wax deposit is assumed to be constant along the pipeline.

(4) The heat conduction of the pipeline is assumed to be two-dimensional neglecting the axial temperature drop. Since the radial temperature gradient is much greater than the axial temperature gradient, the three-dimensional heat conduction of the wax deposit, the pipe wall, and the anticorrosion coating can be simplified by using two spatial dimensions.

(5) The thermal-influenced region of the pipeline is assumed to be within 10 meters from the axial line of the pipe. This means that beyond 10 meters from the pipeline the soil temperature is almost not affected by the pipeline. This has been demonstrated by both experimental data and numerical analysis [7]. By this simplification, a finite soil domain is generated in numerical simulation as shown in Figure 1.

Based on the previous assumptions and simplifications, a mathematical model describing the thermal status of the buried hot oil pipeline is established as follows [8].

(1) Oil flow equations:

mass conservation equation:

$$\frac{\partial}{\partial \tau}(\rho A) + \frac{\partial}{\partial z}(\rho V A) = 0, \tag{1}$$

momentum conservation equation:

$$\frac{\partial V}{\partial \tau} + V\frac{\partial V}{\partial z} = -g\sin\alpha - \frac{1}{\rho}\frac{\partial p}{\partial z} - \frac{f}{D}\frac{V^2}{2}, \tag{2}$$

energy conservation equation:

$$\frac{\partial}{\partial \tau}\left[(\rho A)\left(u + \frac{V^2}{2} + gs\right)\right] + \frac{\partial}{\partial z}\left[(\rho V A)\left(h + \frac{V^2}{2} + gs\right)\right] = -\pi D q. \tag{3}$$

The heat transfer equation of the oil flow can be obtained from the three equations listed previously [8]:

$$C_p\frac{dT}{d\tau} - \frac{T + 273.15}{\rho}\beta\frac{dp}{d\tau} - \frac{fV^3}{2D} = -\frac{4q}{\rho D}. \tag{4}$$

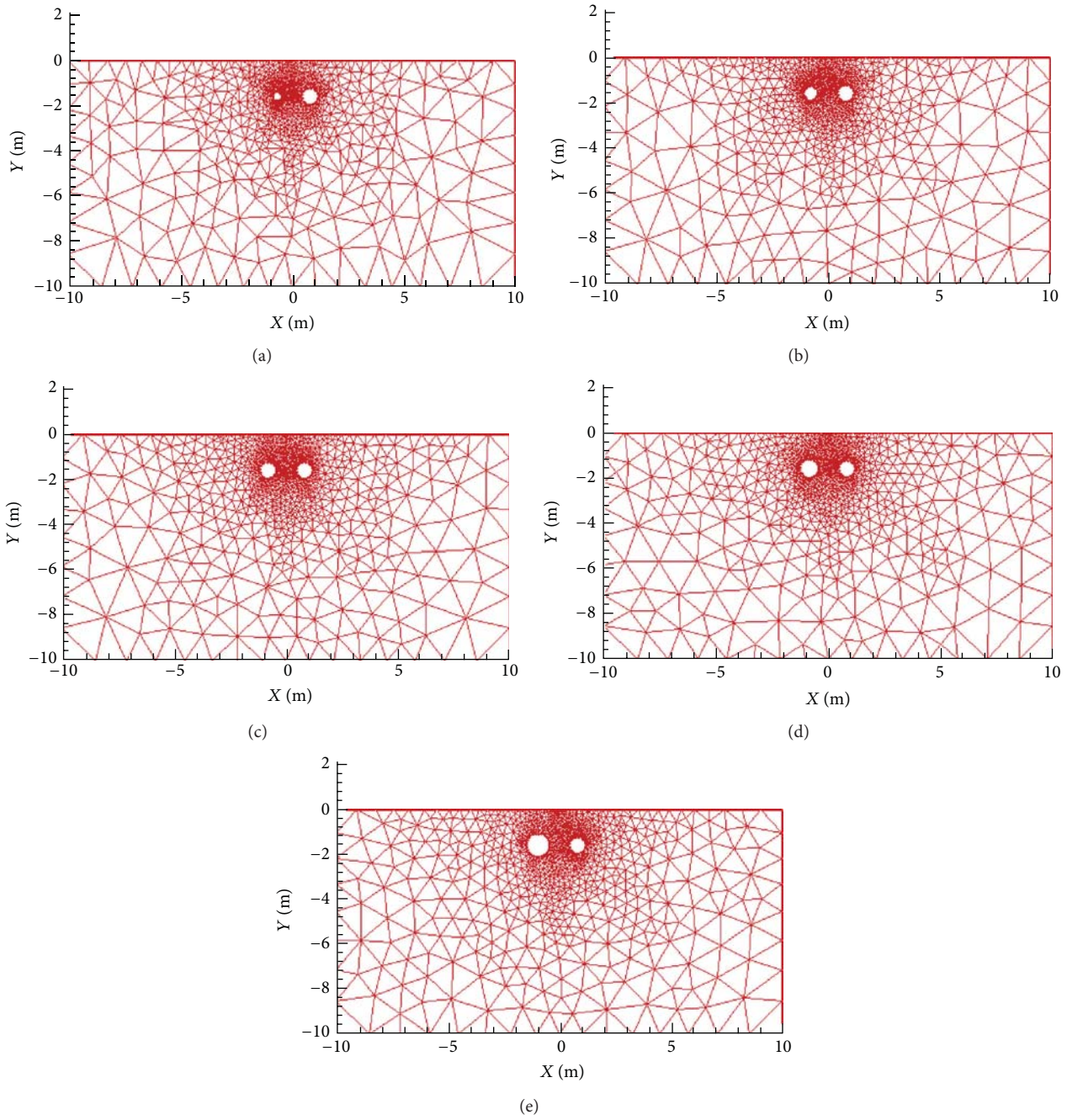

Figure 2: The unstructured grids of the soil.

(2) Heat transfer equations of the wax deposit, the pipe wall, and the anticorrosion coating:

$$\rho_k C_{Pk} \frac{\partial T_k}{\partial \tau} = \frac{1}{r}\frac{\partial}{\partial r}\left(\lambda_k r \frac{\partial T_k}{\partial r}\right) + \frac{1}{r^2}\frac{\partial}{\partial \theta}\left(\lambda_k \frac{\partial T_k}{\partial \theta}\right), \quad (5)$$

where $k = 1, 2, 3$ stands for the wax deposit, the pipe wall, and the anticorrosion coating, respectively.

(3) Heat conduction equation of the soil

$$\rho_s C_s \frac{\partial T_s}{\partial \tau} = \frac{\partial}{\partial x}\left(\lambda_s \frac{\partial T_s}{\partial x}\right) + \frac{\partial}{\partial y}\left(\lambda_s \frac{\partial T_s}{\partial y}\right). \quad (6)$$

(4) Matching conditions.

The crude oil, the wax deposit, the pipe wall, and the ananticorrosion coating and the surrounding soil are highly coupled in the heat transfer process, one component greatly interacting with and affecting the others. Their coupling interactions can be described by the following equations:

$$-\lambda_1 \left.\frac{\partial T_1}{\partial r}\right|_{r=R_0} = \alpha_0 (T - T_0),$$

$$\lambda_k \left.\frac{\partial T_k}{\partial r}\right|_{r=R_k} = \lambda_{k+1} \left.\frac{\partial T_{k+1}}{\partial r}\right|_{r=R_k} \quad k = 1, 2,$$

$$T_k|_{r=R_k} = T_{k+1}|_{r=R_k} \quad k = 1, 2$$

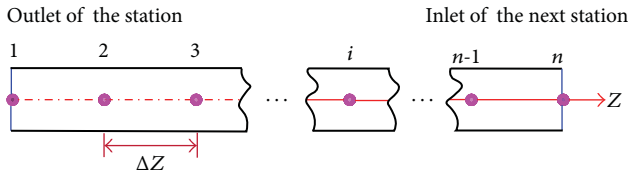

Figure 3: Grids of the pipeline.

$$\lambda_3 \frac{\partial T_3}{\partial r}\bigg|_{r=R_3} = \lambda_s \frac{\partial T_s}{\partial r}\bigg|_{r=R_3}$$
$$T_3|_{r=R_3} = T_s|_{r=R_3}. \tag{7}$$

(5) Boundary conditions:

$$\frac{\partial T_s}{\partial y} = \frac{\alpha_a}{\lambda_s}(T_a - T_s), \quad at\ y = 0$$
$$\frac{\partial T_s}{\partial x} = 0, \quad at\ |x| = 0 \tag{8}$$
$$T_s = T_n, \quad at\ |y| = H.$$

The Delaunay triangulation method [9, 10] is used to generate the grids of the soil domain automatically with denser meshes near the pipelines. For simplicity, the wax deposit is not taken into account. A structural grid generation in polar coordinates is applied to the steel pipe wall and anticorrosion coating. The unstructured grids at the cross-section around the pipelines are shown as in Figure 2. Figure 3 shows the uniform grids along the pipeline. A second-order finite volume method is used to discretize the heat conductive equations of soil, pipe wall, and anticorrosion coating. The governing equations in soil domains and the pipeline are discretized in different ways and coupled along their interfaces in an iterative procedure. An implicit method is used for time discretization. The discretized equations are solved by a Gauss-Seidel method.

For simplicity, in the simulation, it is assumed that the double-pipeline system has N heating stations with the same station spacings and both pipelines transport the same crude oil. The inlet temperature of each heating station is T_{in} while the outlet temperature of each station after heating is T_{out}. Note that according to the China's Operating Rules for Pipelines Delivering Waxy Oil with Heating, T_{in} should be not lower than the pour point of the crude T_P. Then for the double-pipeline system, the heating energy can be calculated as

$$Q_D = \left[C_P m_1 \sum_{i=1}^{N} \left(T1_{\text{out}_{iD}} - T1_{\text{in}_{iD}} \right) + C_P m_2 \sum_{i=1}^{N} \left(T2_{\text{out}_{iD}} - T2_{\text{in}_{iD}} \right) \right] \Delta t. \tag{9}$$

Table 1: The outer and inner diameters of pipes.

	Case 1	Case 2	Case 3	Case 4	Case 5
D_{outl} (mm)			720.0		
D_{in1} (mm)			704.0		
D_{out2} (mm)	406.4	610.0	720.0	813.0	1016.0
D_{in2} (mm)	392.2	594.2	704.0	792.4	981.0

For the two independent single-pipeline system the consumed heating energy is

$$Q_S = \left[C_P m_1 \sum_{i=1}^{N} \left(T1_{\text{out}_{iS}} - T1_{\text{in}_{iS}} \right) + C_P m_2 \sum_{i=1}^{N} \left(T2_{\text{out}_{iS}} - T2_{\text{in}_{iS}} \right) \right] \Delta t. \tag{10}$$

Then the heating energy saving rate of the double-pipeline system can be obtained as follows:

$$\text{HR} = \frac{Q_S - Q_D}{Q_S} \times 100\%, \tag{11}$$

where Q is the energy or heat quantity absorption of the crude oil, J; m is the mass flow rate in the pipeline, kg/s; and C_P is heat capacity of the crude oil, J/ (kg·°C). The heat capacity of the crude oil in the calculations is set as 2100 J/ (kg·°C). Δt is the operating time, and s. HR is energy saving rate. The subscripts s and D stand for single-pipeline system and double-pipeline system, respectively, and subscripts 1 and 2 represent pipeline 1 and pipeline 2 (namely P-1 and P-2), respectively, as shown in Figure 1. For both single-pipeline system and double-pipeline system, T_{in} at the first heating station is assumed to be equal to the pour point.

3. Computations and Economy Analysis

For single-pipeline system, it is assumed that $T_{\text{out1}} = T_1$ and $T_{\text{out2}} = T_2$ for both pipeline 1 and pipeline 2, and all inlet temperatures at stations are equal to the pour point, that is, $T_{\text{in1}} = T_{\text{in2}} = T_P$. It can be expected that in the double-pipeline system, if the outlet temperatures of the two pipelines are set the same as those of the corresponding single-pipeline system, due to the mutual heating impact, the inlet temperatures of both two pipelines in the double-pipeline system would be most likely higher than that of single-pipeline system; hence, compared with single-pipeline system, the outlet temperatures in double-pipeline system could be lowered down less or more with the inlet temperatures still maintained above the pour point to meet the operating rules.

Since the outlet temperature is a key factor determining heating energy consumption, optimization could be made on this parameter to reduce the energy consumption. In this study, three operating scenarios are presented to analyze the economy of different operating conditions in the double-pipeline system as follows. (a) The outlet temperature of P-1 is set the same as that of the single-pipeline system whereas the

Table 2: Outlet and inlet temperatures when the station spacing is 120 km.

		Double-pipeline system				
		Case 1	Case 2	Case 3	Case 4	Case 5
Scheme 1	T_{out1} (°C)			44.77		
	T_{in1} (°C)	33.34	32.75	32.49	32.72	32.78
	T_{out2} (°C)	65.11	42.66	39.00	37.25	35.29
	T_{in2} (°C)			30.00		
Scheme 2	T_{out1} (°C)	36.92	38.77	39.00	39.23	39.34
	T_{in1} (°C)			30.00		
	T_{out2} (°C)	81.95	50.78	44.77	41.89	38.07
	T_{in2} (°C)	34.19	33.31	32.49	32.46	31.60
Scheme 3	T_{out1} (°C)	38.77	39.92	40.03	39.92	39.92
	T_{in1} (°C)			30.00		
	T_{out2} (°C)	67.74	43.80	40.03	37.99	35.80
	T_{in2} (°C)			30.00		
		Single-pipeline system				
	T_{out1} (°C)			44.77		
	T_{in1} (°C)			30.0		
	T_{out2} (°C)	81.95	50.78	44.77	41.89	38.07
	T_{in2} (°C)			30.0		

Table 3: Effect of pipeline interval on heat energy saving rate (%).

	Case 1	Case 2	Case 3	Case 4	Case 5
0.6 m	37.87	36.72	36.72	37.48	35.94
0.9 m	33.69	33.20	32.00	32.81	30.40
1.2 m	29.21	28.52	27.34	30.46	30.40
1.5 m	23.09	24.41	25.00	25.40	24.96
1.8 m	20.04	23.05	22.66	22.66	20.22

outlet temperature of P-2 is tentatively and gradually reduced until the inlet temperatures of the P-1 and P-2 drop down no more than pour point. (b) The outlet temperature of P-2 is set the same as that of the single-pipeline system whereas the outlet temperature of P-1 is tentatively and gradually reduced until the inlet temperatures of the P-1 and P-2 drop down no more than pour point. (c) Both outlet temperatures of P-1 and P-2 in the double-pipeline are put in gradual decrease until their inlet temperatures drop down to just above the pour point.

Calculations are first made for five typical cases as shown in Table 1, and some other important computation parameters are listed in the following. The heating station spacings are all 120 km: The gap between two pipelines is 0.9 m and constant. The mean flow velocity in the pipes is 1.5 m/s. The pour point of the waxy crude oil is 30°C. The thermal conductivity of the soil is 1.4 W/(m·°C) and the soil temperature at the buried depth is 1.6°C. The thickness of anticorrosion coating is 4 mm.

Table 2 shows the outlet and inlet temperatures for the three operating scenarios presented previously of different double-pipeline systems with the temperatures of single-pipeline system included. It can be seen that for the single-pipeline system, to maintain the inlet temperature not lower than pour point, the highest required outlet temperature is 81.95°C and the lowest is 38.07°C; the smaller the pipe, the higher the outlet temperature required. This is because at the same mean velocity, the smaller the pipeline, the lower flow rate. As known, lower flow rate contains lower heat capacity which will lead to a quicker temperature drop; hence smaller pipeline needs higher outlet temperature to maintain the same inlet temperature than larger pipeline does. Table 2 indicates that under scenarios 1 and 2, by only adjusting one pipeline's outlet temperature, the pipeline being adjusted reaches the lowest allowable inlet temperature, that is, pour point, and the other pipeline still holds a higher inlet temperature. In scenario 3, the two pipelines' outlet temperatures are adjusted simultaneously to make both pipelines hold lowest temperatures inlet. To achieve this, both outlet temperatures have to be reduced greatly.

Figure 4 shows the energy saving rates of double-pipeline systems under different operating scenarios or scenarios and with different numbers of heating stations. Figure 4 also shows that scenario 3 can save 33.7%, 33.2%, 32.0%, 32.8%, and 30.4% heating energy for cases 1–5, respectively, regardless of the number of heating stations. In comparison, for the other two scenarios, energy saving rate increases with the increase of the number of heating station and when the heating stations are more than 10, the energy saving rate reaches maximum value and is then kept constant. Figure 4 further indicates that scenario 3 can save much more energy than the other two scenarios. This indicates that when the inlet temperatures of double-pipeline system are maintained closer to the pout point, the lower outlet temperatures are required when compared with single-pipeline system, hence the less the heating energy consumption is required resulted in saving of heating fuel. Scenario 3 consumes the least energy

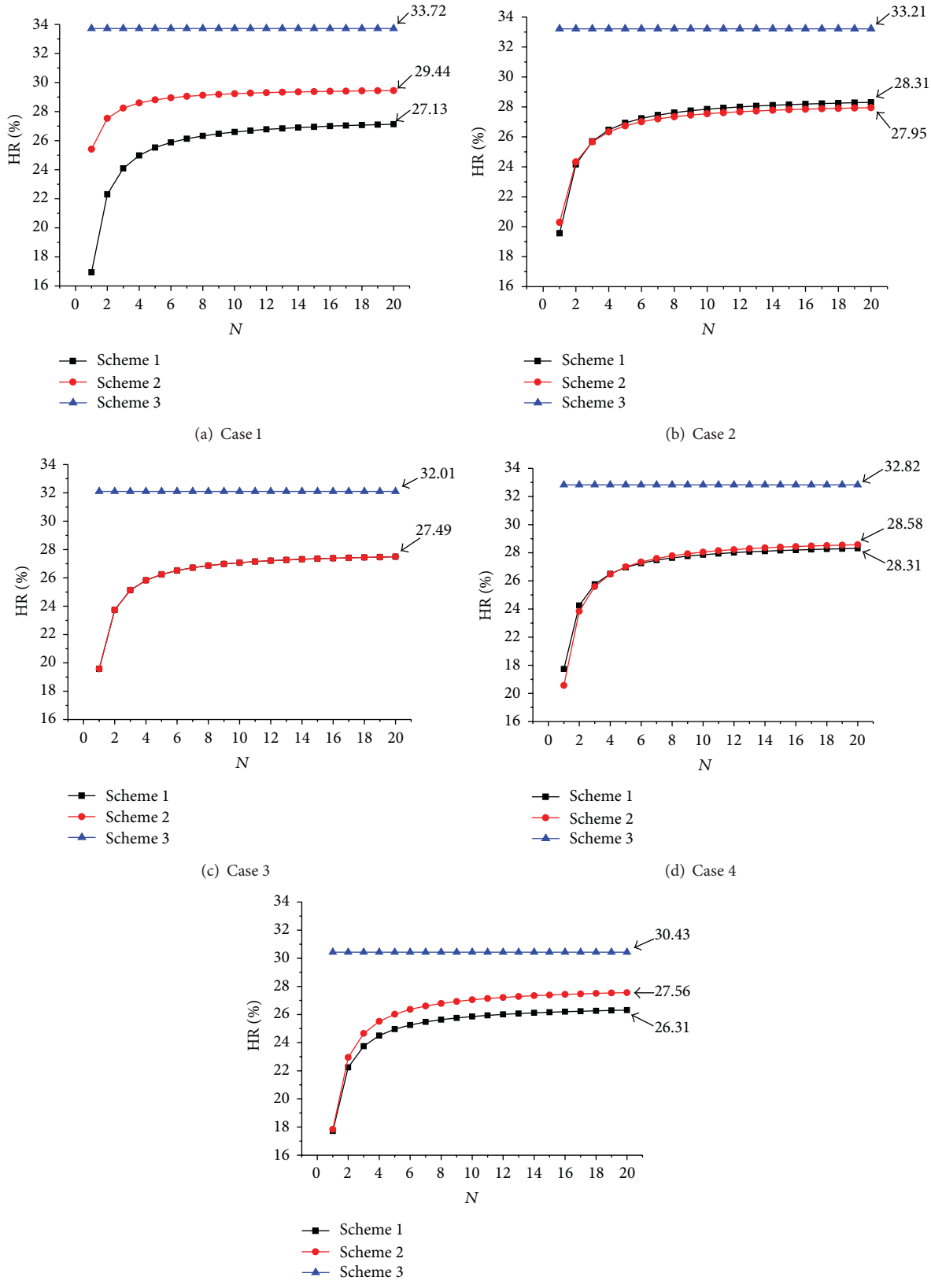

Figure 4: The energy saving rate for different cases when the station spacing is 120 km.

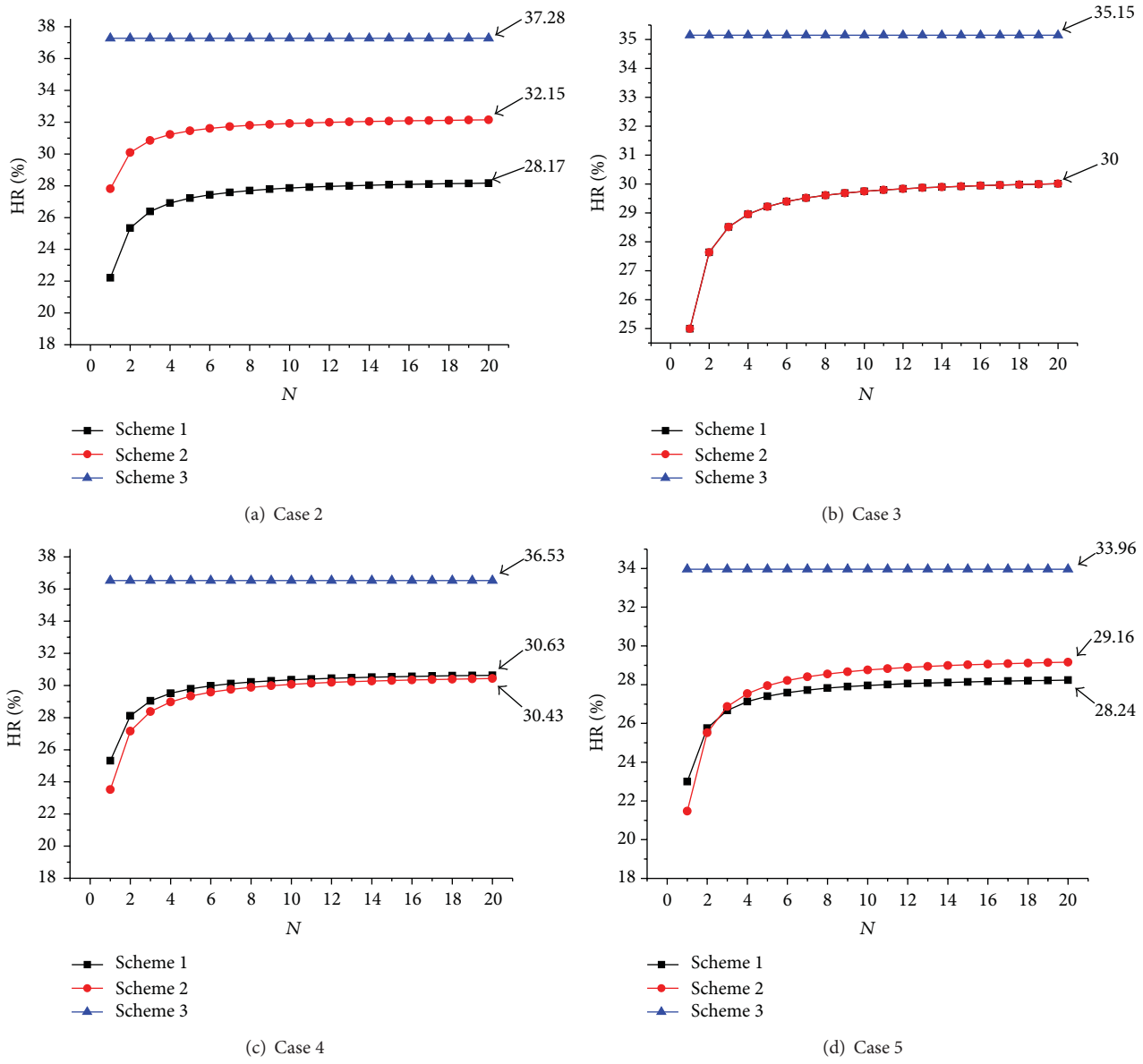

Figure 5: The energy saving rate for different cases when the station spacing is 240 km.

because generally speaking lower outlet temperatures will reduce the temperature difference between the crude oil and soil temperature, and thus reduce heat loss compared with the other scenairos. Therefore, operating scenario 3 is the best and recommended.

One question may be raised: why the heating energy saving rate is independent of the number of heating station under scenario 3. This is because for operation scenario 3 station all inlet temperatures are the same and so are all outlet temperatures. From (9) to (11) that the energy saving ratio for scenario 3 can be determined as follow:

$$\mathrm{HR} = \frac{m_1\left(T1_{\mathrm{out}_S} - T1_{\mathrm{out}_D}\right) + m_2\left(T2_{\mathrm{out}_S} - T2_{\mathrm{out}_D}\right)}{m_1\left(T1_{\mathrm{out}_S} - T1_{\mathrm{in}_S}\right) + m_2\left(T2_{\mathrm{out}_S} - T2_{\mathrm{in}_D}\right)} \times 100\%. \tag{12}$$

Equation (12) demonstrates that energy saving rate is independent of heating station as it does not involve the term representing the number of heat stations. As (12) is independent of the number of heating stations, the subscript i is omitted.

For the other scenarios, from (9) to (11), the energy saving rates can be determined in a similar way:

$$\begin{aligned}\mathrm{HR} = \Bigg(&\frac{1}{N-1}\left[m_1\left(T1_{\mathrm{out}_S} - T1_{\mathrm{out}_D}\right) + m_2\left(T2_{\mathrm{out}_S} - T2_{\mathrm{out}_D}\right)\right] \\ &+ \left[m_1\left(T1_{\mathrm{out}_S} - T1_{\mathrm{in}_S} - T1_{\mathrm{out}_D} + T1_{\mathrm{in}_D}\right)\right. \\ &\left. + m_2\left(T2_{\mathrm{out}_S} - T2_{\mathrm{in}_S} - T2_{\mathrm{out}_D} + T2_{\mathrm{in}_D}\right)\right]\Bigg)\end{aligned}$$

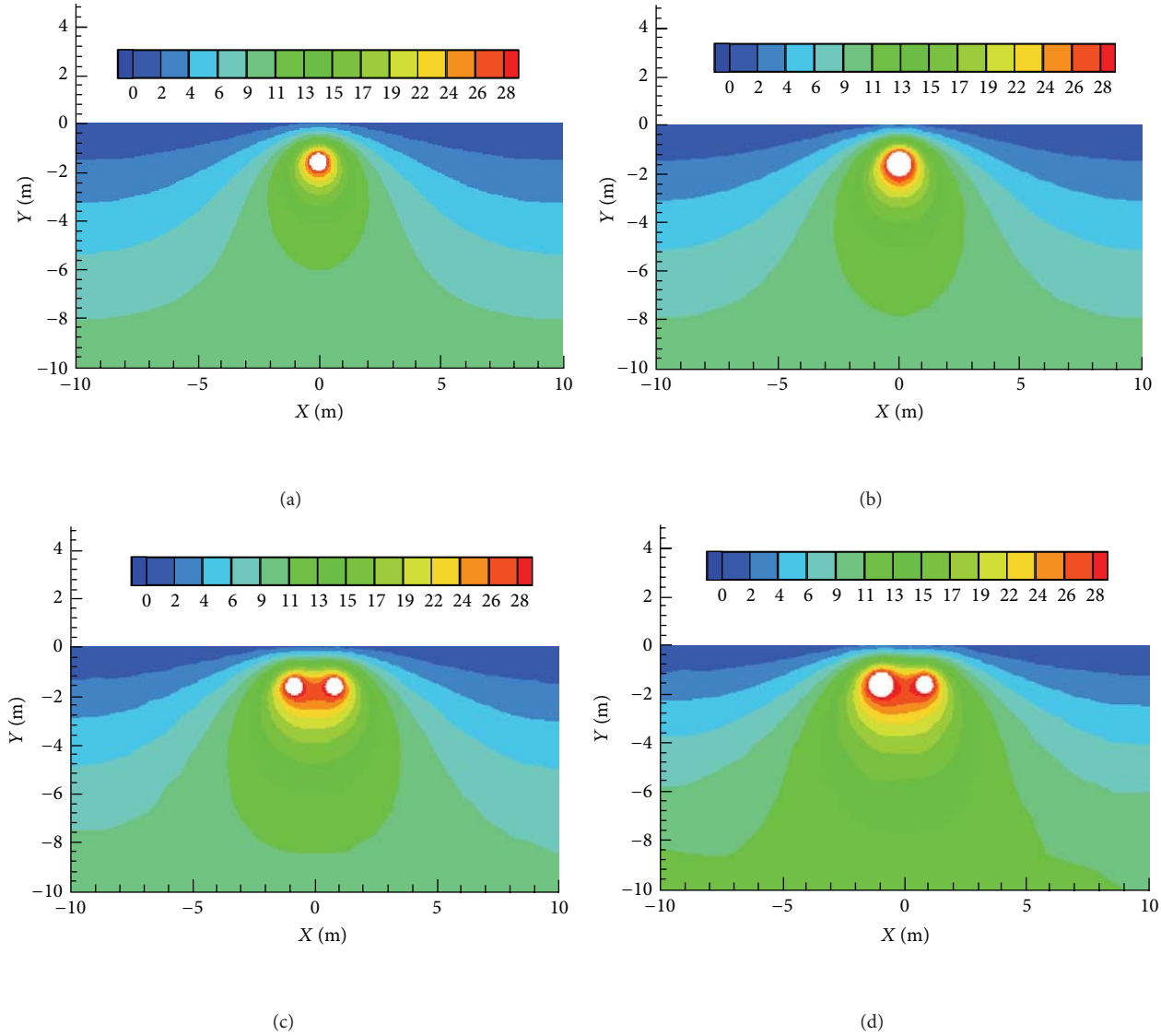

FIGURE 6: Comparison of the inlet temperature contours.

$$\times\left(\frac{1}{N-1}\left[m_1\left(T1_{\text{out}_S}-T1_{\text{in}_{iS}}\right)+m_2\left(T2_{\text{out}_S}-T2_{\text{in}_{iS}}\right)\right]+\left[m_1\left(T1_{\text{out}_S}-T1_{\text{in}_S}\right)+m_2\left(T2_{\text{out}_S}-T2_{\text{in}_S}\right)\right]\right)^{-1}. \tag{13}$$

In the previous equation, note that from heating station 2 to N, the inlet and outlet temperatures are identical, and the subscript i is omitted. Equation (13) shows that for the other scenarios the energy saving rate is related to station number N. It can be seen clearly that its effect becomes weaker with the increase of N and the energy saving rate gradually approaches to the maximum value:

$$\text{HR} \longrightarrow \left(\left[m_1\left(T1_{\text{out}_S}-T1_{\text{in}_S}-T1_{\text{out}_D}+T1_{\text{in}_D}\right)+m_2\left(T2_{\text{out}_S}-T2_{\text{in}_S}-T2_{\text{out}_D}+T2_{\text{in}_D}\right)\right]\right)\times\left(\left[m_1\left(T1_{\text{out}_S}-T1_{\text{in}_S}\right)+m_2\left(T2_{\text{out}_S}-T2_{\text{in}_S}\right)\right]\right)^{-1}. \tag{14}$$

In one word, (13) explains why for scenarios 1 and 2 heating energy saving rate increases with the increase of the number of heating stations and approaches to the maximum value.

With the improvement and development of the construction technology in pipeline industry, there is a tendency to save the construction cost by extending the station spacing and thus reducing the number of heating stations. When the spacing is extended to 240 km, much higher outlet temperatures are required to maintain the inlet temperature above a certain point, say pour point as required, and the temperature difference between different scenarios becomes greater. The energy saving rate in the double-pipeline systems

for greater station spacing is shown in Figure 5. For case 1 the energy saving rate is not shown. This is because for such a case the outlet temperature of the smaller pipeline has to be higher than 100°C which is impractical in reality. It can be seen that the energy saving rate is greater than that of smaller station spacing; the advantages of the new technology laying two pipelines in a ditch are more significant.

Apparently pipeline gap or interval imposes the most important effect on energy saving. Table 3 shows the heating energy saving rates for scenario 3 at different pipeline intervals with other calculation parameters fixed. As indicated, the energy saving rate is about 20% with the pipeline interval at 1.8 m and can be as high as about 37% with the pipeline interval reduced to 0.6 m. For all the cases, the smaller the pipeline interval, the greater the energy saving rate. From the view of heat transfer, the smaller the interval between the two crude oil pipelines, the lower the outlet temperatures will be needed which resulted in less heating cost; therefore reducing the interval would be considered a priority in pipeline construction. However, it should be noted that besides the matter of heat transfer, in actual pipeline construction still many other factors have to be taken into consideration to determine pipeline intervals. The determination of the optimal interval should involve thermal condition of operation and conveniences for construction and reparation and all factors have to be well considered and balanced.

Figure 6 shows the temperature field (contours) at the inlet cross-section for scenario 3. As showed, generally the soil temperatures for a double-pipeline system are higher than those of a single-pipeline system, which benefits pipelining waxy-crude oil with high pour point. This is because the region with lowest temperature near the inlet of heating station is usually the most dangerous region during normal operation and especially after the pipeline shutdown. For the double-pipeline system, the higher soil temperature near the entrance of the next heating station can reduce the heat loss of crude oil and consequently enhance the operation safety.

4. Conclusions

In this paper heating energy saving evaluations in the operation of two hot crude oil pipelines laid in one ditch as compared with the single-pipeline system are performed. In the calculations a Delaunay triangulation method is used to generate the grids of the soil domain automatically with denser meshes near the pipelines. A structural grid generation in polar coordinates is applied to the steel pipe wall and anticorrosion coating. A finite volume method combined with a finite difference scheme is used to discretize the governing equations. The discretized equations are solved by a Gauss-Seidel method. The thermal impact between two hot crude oil pipelines laid in one ditch under three operating scenarios is numerically analyzed. It is shown that the operating scenario in which both the inlet temperatures reach the allowed lowest temperatures (pour point) can save the greatest deal of energy. With the increase of the pipeline interval, the thermal impact between double-pipelines becomes less, which results in the decrease of the energy saving. When the spacing between two heating stations extends, the energy saving increases. The energy saving rate is about 20% with the pipeline interval at 1.8 m and can be as high as about 37% with the pipeline interval reduced to 0.6 m. In addition to the advantage of energy saving, laying two hot pipelines in one ditch can also enhance the operation safety according to the result of the study.

Nomenclature

A: Cross-section area of the pipeline (m^2)
C_k: Heat capacity of the kth layer, including wax deposit, pipe wall, and anticorrosion coating (J/(kg · °C))
C_p: Heat capacity under constant pressure of the crude oil (J/(kg · °C))
C_s: Heat capacity of the soil (J/(kg · °C))
D: Inner diameter of the wax deposit layer (m)
f: Darcy friction coefficient
g: Acceleration of gravity (m/s^2)
h: Specific enthalpy of the crude oil (J/kg)
H: Height of the computational domain of the soil (m)
H_0: Buried depth of the pipeline (m)
L: Half width of the computational domain of the soil (m)
p: Average pressure on the pipeline cross-section (Pa)
q: Heat loss of the crude oil on unit area of the pipe wall during $\Delta\tau$ time (W/m^2)
r: Radial direction (m)
R_0: Reduced inner radius with the wax deposit layer (m)
R_k: Outer radius of the kth layer, including wax deposit, pipe wall, and anticorrosion coating (m)
s: Elevation difference (m)
T: Temperature of the crude oil (°C)
T_0: Inner wall temperature of the wax deposit (°C)
T_α: Air temperature (°C)
T_k: temperature of the kth layer, including wax deposit, pipe wall and anticorrosion coating (°C)
T_n: Temperature of the constant temperature layer (°C)
T_s: Soil temperature (°C)
u: Specific energy of the crude oil (J/kg)
V: Average flow velocity of the crude oil (m/s)
x: Horizontal direction (m)
y: Vertical direction (m)
z: Axial direction of the pipeline (m)
α: Angle between the axis of the pipeline and the horizontal line
α_0: Heat transfer coefficient of the pipe flow ($W/(m^2 \cdot °C)$)

α_a: Heat transfer coefficient at the ground surface (W/(m^2 ·°C))
β: Expansion coefficient of the crude oil (°C^{-1})
θ: Circumferential direction
λ_k: Thermal conductivity of the kth layer, including wax deposit, pipe wall and anticorrosion coating (W/(m ·°C))
λ_s: Thermal conductivity of the soil (W/(m ·°C))
ρ: Density of the crude oil (kg/m^3)
ρ_k: Density of the kth layer, including wax deposit, pipe wall, and anticorrosion coating (kg/m^3)
ρ_s: Soil density (kg/m^3)
τ: Time (s).

Acknowledgment

The study is supported by the National Science Foundation of China (no. 51176204 and no. 51206186), and the Science Foundation of China University of Petroleum, Beijing (no. 2462011LLYJ33, no. 2462011LLYJ55, no. 2462012KYJJ0403, and no. 2462012KYJJ0404).

References

[1] B. Yu, X. Ling, J. Zhang, and Y. Wang, "Study on laying technology of products pipeline along with hot crude pipeline in one ditch," *Acta Petrolei Sinica*, vol. 28, no. 5, pp. 149–152, 2007 (Chinese).

[2] B. Yu, Y. Wang, J. J. Zhang, X. Liu, Z. W. Zhang, and K. Wang, "Thermal impact of the products pipeline on the crude oil pipeline laid in one ditch—the effect of pipeline interval," *International Journal of Heat and Mass Transfer*, vol. 51, no. 3-4, pp. 597–609, 2008.

[3] B. Yu, Y. Wang, X. Liu, J. J. Zhang, Z. W. Zhang, and K. Wang, "Model studies thermal effects of liquid pipeline colocation," *Oil and Gas Journal*, vol. 105, no. 18, pp. 54–58, 2007.

[4] J. J. Zhang, "Technologies for pipelining high-pour-point and viscous crudes and their development," *Engineering Science*, vol. 4, no. 6, pp. 71–76, 2002.

[5] T. H. Luo, *Rheology and Transportation Process of Crude Oil*, Petroleum Industry Press, Beijing, China, (Chinese), 1st edition, 1995.

[6] J. L. Ding, "China's oil and gas pipeline technology and its development current," *Oil Gas Storage and Transportation*, vol. 22, no. 22, pp. 22–25, 2003 (Chinese).

[7] X. G. Cui and J. J. Zhang, "Determination of the thermal influence zone of buried hot oil pipeline on steady operation," *Journal of the University of Petroleum, China*, vol. 28, no. 2, pp. 75–78, 2004 (Chinese).

[8] X. G. Cui, *Analysis of transient hydraulic-thermal interaction duringcool and hot oil batch pipelining and its applications [Ph.D. thesis]*, China University of Petroleum-Beijing, Beijing, China, (Chinese), 2005.

[9] B. Yu, M. J. Lin, and W. Q. Tao, "Automatic generation of unstructured grids with Delaunay triangulation and its application," *Heat and Mass Transfer*, vol. 35, no. 5, pp. 361–370, 1999.

[10] W. Q. Tao, *Recent Advances of Numerical Heat Transfer*, Science Press, Beijing, China, (Chinese), 1st edition, 2005.

Hindawi Publishing Corporation
Advances in Mechanical Engineering
Volume 2013, Article ID 950681, 7 pages
http://dx.doi.org/10.1155/2013/950681

Research Article

Effective Resistance of Gas Flow in Microchannels

Xiao-Dong Shan and Moran Wang

Department of Engineering Mechanics and CNMM, Tsinghua University, Beijing 100084, China

Correspondence should be addressed to Moran Wang; moralwang@gmail.com

Received 6 December 2012; Accepted 4 February 2013

Academic Editor: Tomoaki Kunugi

The resistance of gas flow in microchannels is higher because of the relatively more importance of interfacial effects at microscale. We studied the effective resistance of gas from the wall interactions, the ends effect, and the rarefication effect quantitatively using the three-dimensional (3D) direct simulation Monte Carlo (DSMC) method. The effective resistance is enhanced by the wall interactions, increasing exponentially as the concerned walls distance decreases. For short microchannels, the ends effects from both inlet and outlet also raise the effective resistance of gas flow in microchannels following a reciprocal exponential relationship with the aspect ratio of length to height. The gas rarefication strengthens the effective resistance enhancement by either the wall interaction effects or the ends effects. This work turns a complicated micromechanical problem into simple available formulae for designs and optimization of microengineering.

1. Introduction

It is now very important to fully understand the gas flow and heat transfer mechanism in microchannels because of various applications in microelectronic cooling systems, bipolar plates of fuel cells, compact heat exchangers and reactors for material processes, and advanced propulsion systems [1, 2]. The gas flow characteristics in microchannels does not agree well any more with the classical continuum theories because of slippage, compressibility, thermal creep, and so on [2–9]. The resistance in microgas flow has been one of the most arrestive concerns among scientists and engineers. Quite a few experiments have been performed on the friction constant ($f \cdot \mathrm{Re}$) in microchannel gas flow; however the results are inconsistent, with some [10] higher than while some others [11, 12] lower than the predictions based on the classical continuum theories. The studies with both experiments and numerical simulations showed that the inconsistencies might come from the relatively larger roughness degree [13], the nonnegligible effects from the entrance and exit regions [14, 15], the larger effects of compressibility [16] and the rarefaction [17] in microchannels, or even the instrument errors [16]. Despite of much progress in this topic, the quantitative description of effective resistance of gas flow in microchannel and the fundamental understanding of microscale gas flow are still not sufficient to the authors' best knowledge.

There are three major interfacial effects: the wall interaction effect, the end effect (including inlet and outlet effects), and the rarefied gas effect, dominating the effective resistance of gas flow in microchannels different from the bulk flow or the continuum flows. In this work, we introduce an effective resistant force to describe the overall resistance of gas flow which is induced not only by the viscosity of gas but also by all the interfacial effects in microchannels. Our object is to find the quantitative formulations for the effective resistance with the related key factors of interfacial effects in microchannels by numerical simulations.

2. Numerical Methods

2.1. Direct Simulation Monte Carlo Method. The direct simulation Monte Carlo (DSMC) method is a probabilistic simulation method based on molecular motion and statistical principle to simulate rarefied gas flows [18] or microgas flows [19]. The position, velocity, and other information are stored and modified in every time step by tracking the motions, collisions, and interactions with boundaries of all particles. The key ideas of DSMC method are the

uncoupling of molecular motion and collisions during the time step Δt, and the simulation of molecular collisions by disregarding molecular position coordinates in the spatial cell in the condition that the time step Δt is much smaller than the mean collision time, and the spatial steps Δx, Δy, and Δz are much smaller than the molecular mean free path, respectively [20]. In this work, the variable hard sphere (VHS) model and the diffusive wall boundary condition are used for the collision processes. We consider gas flows in straight microchannels driven by a pressure drop, and the pressure boundaries at the inlet and outlet are implemented using the method proposed by Wang and Li [21], which actually assumes uniform pressures at inlet and outlet. The code has been tested and validated by various previous studies [20–23]. The 200×40 uniform rectangular cells with 4×4 subcells in each cell were applied to ensure the subcell size is smaller than the local mean free path in the simulations [20]. Over 1×10^5 molecules were simulated, and the sample sizes were over 3×10^5. Convergence was also verified by monitoring mass balance maximum errors which were less than 0.3%.

2.2. Mathematical Model. For microgas flows, the Knudsen number defined as the ratio of gas mean free path to the characteristic length of channel (Kn $= \lambda/H$ *with* λ *representing the gas mean free path and* H *the channel height*) may be so high that the flows fall into the slip or even the transition flow regime. After simulations using the molecule-based DSMC method, we are aiming to summarize the effective resistance f based on the continuum momentum equation to bridge up the multiscale problem as follows:

$$\rho\left(\frac{\partial \mathrm{U}}{\partial t} + \mathrm{U}\cdot\nabla \mathrm{U}\right) + \nabla P + \mathrm{f} = 0, \tag{1}$$

where ρ is the gas density, U the velocity vector (u, V, w), P the pressure, and f the effective resistance per unit volume ($\mathrm{N/m^3}$) including the viscous force and all the resistant forces from the interfacial effects. For gas flows in a straight microchannel, the two velocity components across the channel, V and w, are negligible since they are one to two order of magnitude lower than u, the velocity component along the channel. For a steady state, integrating both sides of (1) through the channel leads to

$$A\left(P_1 - P_2\right) - F = Q_m\left(u_2 - u_1\right), \tag{2}$$

where A denotes the area of cross-section, F the overall effective resistance force, and Q_m the mass flow rate. The subscripts 1 and 2 represent the inlet and the outlet, respectively. The effective resistance per unit volume is therefore calculated by

$$f = \frac{F}{AL} = \frac{\overline{P_1} - \overline{P_2} + \overline{\rho_1 u_1^2} - \overline{\rho_2 u_2^2}}{L} = \Delta p - \frac{\left(q_2 u_2 - q_1 u_1\right)}{L}, \tag{3}$$

where the bars denote the average values across the section 1 or 2, Δp the overall pressure gradient, q the mass flux per unit area, and L the length of the microchannel.

As mentioned above, we consider three major interfacial effects: the wall interaction effect, the end effect (including inlet and outlet effects), and the rarefied gas effect, which influence the effective resistance of gas flows in microchannels. For a straight channel with a rectangular cross-section, the wall interaction effect varies with the width-height ratio ($s = W/H$), which will be illustrated in details in the next session. The relative importance of the end effects from both inlet and outlet depends on the dimensionless channel length ($l = L/H$). With the rarefied gas effect considered as well, the effective resistance per unit volume of gas flow in microchannels (f) can be formulated as a function as (4), and the task of this work is to find the exact formulation of this function:

$$f = \mathrm{fun}\left(s, l, \mathrm{Kn}\right). \tag{4}$$

3. Results and Discussion

Consider nitrogen gas flows through a three-dimensional (3D) straight microchannel with a rectangular cross-section driven by a pressure difference between inlet and outlet as shown in Figure 1. The channel is L in length, W in width, and H in height of the microchannel, respectively. The parameters of properties of the nitrogen gas are from the book of Bird [18]. We use the state of gas at the inlet as a reference to determine the cell size and the time step of our simulations. The cell size is taken as a half of the molecular mean free path and the time step as a half of the mean collision time of the reference gas [21].

3.1. Wall Interaction Effects. The wall interaction effects refer to the effects on the effective resistance when the distance of two concerned walls varies. This effect differs from the rarefication effect which is determined by the Knudsen number. For example, for a gas flow in a 3D channel as shown in Figure 1, the rarefication effect is characterized by the channel height H (assuming $H \leqslant W$), while the wall interaction effect relates to the channel W for a given H, if the two side walls are movable and concerned. When the wall interaction effect is studied, the width-height ratio s is treated as an independent variable, increased from a small value to a large one. In the simulation, we keep the height as a constant and vary the width of the microchannel. If the width is large enough, the 3D flow approaches a 2D flow.

In this work, the height of the microchannel (H) is 0.2 μm, and the length is 5 μm. The inlet and outlet pressures are 15 kPa and 10 kPa, respectively. The independent variable s is 1, 2, 4, 8, 10, and 15 for case 1 to 6, respectively. The gas temperature at the inlet and the wall temperature are both at 300 K. After simulations, we calculate the properties of gas flow in microchannel, including the local density and velocity components [18, 21]. The effective resistance can therefore be calculated based on (3). In our simulations, the inlet and outlet pressures difference is kept constant, and therefore we introduce a new variable, f_i which means the inertial force

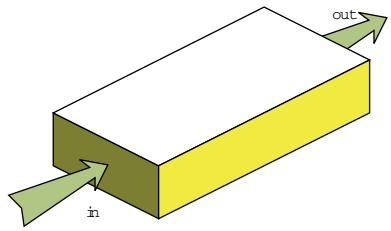

Figure 1: Sketch of the simulated 3D geometry of microchannel, where W, H, and L denote the width, height, and length of the channel, respectively. P_{in} and P_{out} are the local pressures at inlet and outlet.

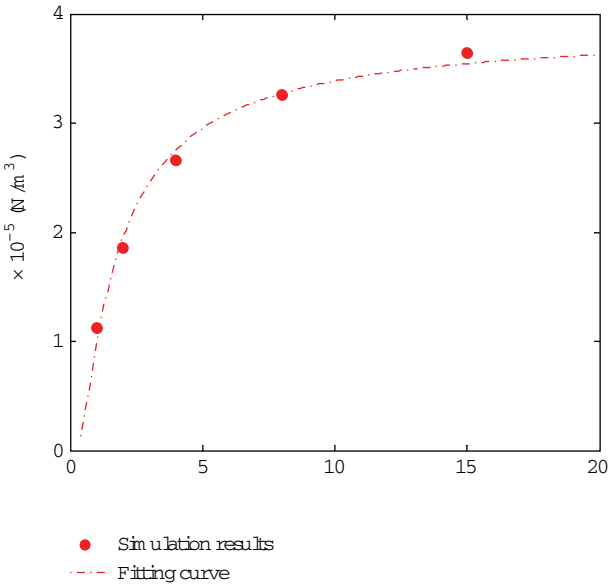

Figure 2: Inertial force f_i versus the width-height ratio s, where $f_i = \Delta p - f$. The symbols are results from our DSMC simulations, and the dash line is the fitting curve at a function of $f_i = c_1 e^{-c_2/s}$, where $c_1 = 3.8881 \times 10^5$, $c_2 = 1.3738$.

of the gas flow. The direction of f_i is opposite to the pressure difference, and its value is calculated by

$$f_i = \Delta p - f = \frac{(q_2 u_2 - q_1 u_1)}{L}. \quad (5)$$

The symbols in Figure 2 are results from our simulations of the inertial force f_i versus the width-height ratio s, while the solid line is a fitting relation following a reciprocal exponential law of $f_i = c_1 e^{-c_2/s}$. Noting the constant pressure difference in our simulations, we can obtain a formulation between the effective resistance with the width-height ratio s as

$$f = \Delta p - f_i = c_3 - c_1 e^{-c_2/s}, \quad (6)$$

where c_1, c_2, and c_3 are constants. The constants may vary case by case, but the formulation form holds, which will be discussed later in this work.

In a microchannel gas flow, when the width-height ratio s is at a small value, the wall interactions have a significant effect on enhancement of the effective resistance. The effective resistance increases at an exponential law as the walls distance decreases. If the width-height ratio $s \gg 1$, the 3D gas flow behavior approaches a 2D one. In our current simulations of this work above, the effective resistance enhancement of 3D gas flows is less than 3% or negligible, compared with the corresponding 2D gas flows when the width-height ratio is $s \geq 10$.

3.2. End Effects. The end effects from inlet and outlet of a channel have been reported earlier [14, 15] to be a nonnegligible factor in microflows; however no quantitative studies have been presented to show how the end effects influence the effective resistance in microchannel gas flows up to now. In order to characterize the end effects exactly, we propose a "truncation channel" scheme inspired by an experimental technology [13]. The scheme is illustrated in Figure 3. First, we need a long microchannel as a reference. Let the gas flow through the long channel driven by a pressure difference, and we can get the pressure distribution along the channel by DSMC simulations. And then we cut the long channel to shorter ones gradually from one end. For examples, if we are focusing on the outlet effect, we cut the channel from the outlet as shown in Figure 3(a); otherwise we cut the channel from the inlet end to consider the inlet effects. After the channel is cut, we have a new end and assign the pressure at the same position of the long reference channel as the new boundary condition to this end. By comparing the resistances of the shorter channel with the reference one, we can figure out the end effects on the effective resistance enhancement changing with the channel length. It is clear that such effects are negligible, when the channel is long enough, and more and more significant as the channel becomes shorter and shorter.

The reference microchannel is 5 μm in length (L) and 0.2 μm in both width (W) and height (H). The gas is driven flowing by a pressure difference of 15 kPa to 10 kPa. The effective resistance is calculated by (3). Based on the "truncation channel" scheme, the resistance enhancement by the end effects is characterized by the ratio of resistances between the truncated channel and the reference channel at the corresponding length.

Moreover,

$$\frac{f_x}{f_{x,r}} = \frac{\Delta p/x + (q_1 u_1 - q_2 u_2)/x}{\Delta p_{x,r}/x + (q_{1'} u_{1'} - q_{2'} u_{2'})/x}, \quad (7)$$

where x denotes the length of the truncated channel, f_x is the effective resistance per unit volume of truncated channel, while $f_{x,r}$ is the local effective resistance per unit volume of reference channel from the inlet down to x position for considering the outlet effect or from the outlet up to x position for the inlet effect. The subscripts 1 and 2 denote the real inlet and outlet of the truncated channel, while the subscripts $1'$ and $2'$ are the corresponding positions on the reference channel. For instance, when the outlet effect is studied, the subscript $2'$ does not mean the real

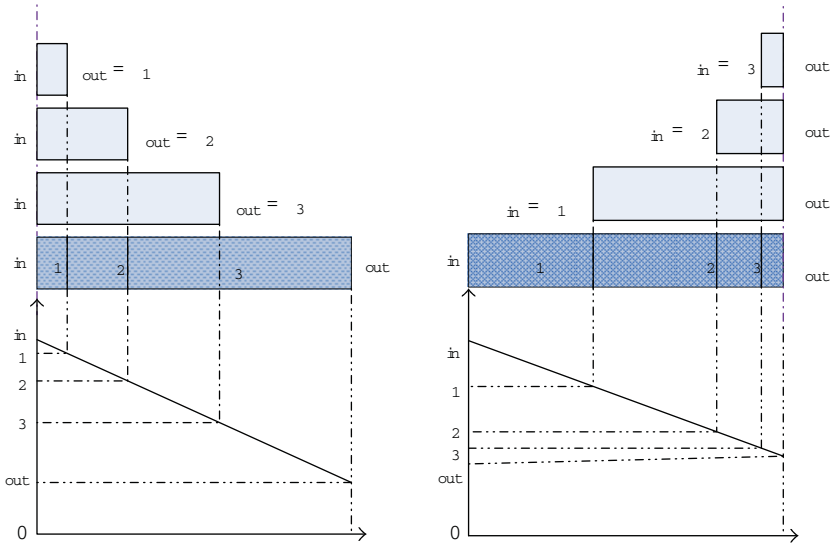

(a) Scheme for the outlet effect (b) Scheme for the inlet effect

FIGURE 3: Illustration of the "truncation channel" schemes to study the end effects. P_{in} and P_{out} are the inlet and outlet pressures of the reference long channel. P_1, P_2, and P_3 are the local pressures on the reference channel where we may truncate the channel to form a new end. We assign P_1, P_2, or P_3 as the pressure boundary condition (P'_{in} or P'_{out}) to the new end of the truncated channel.

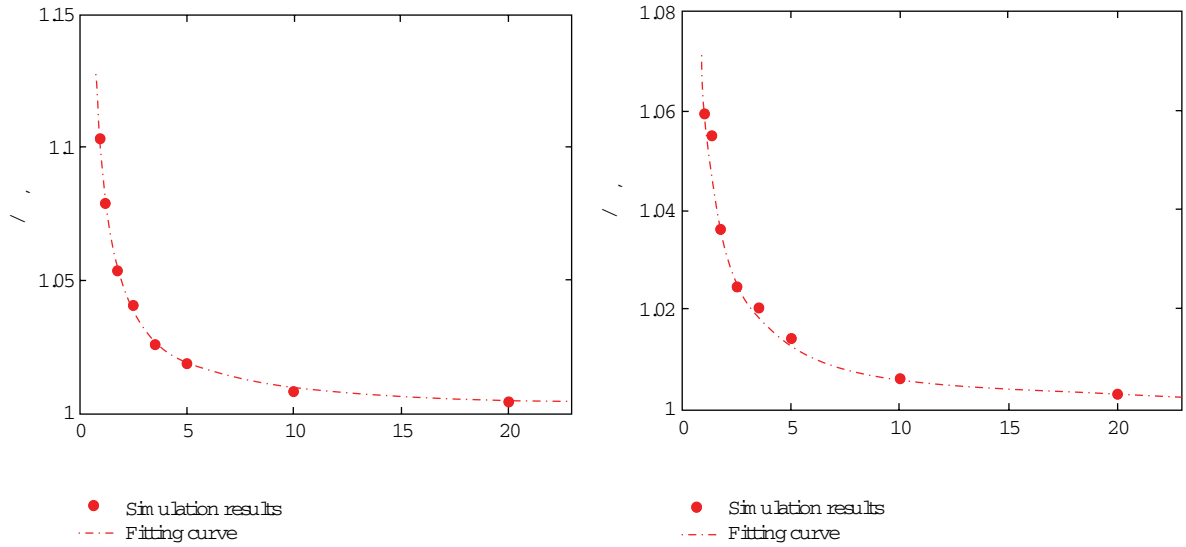

(a) Outlet effect (b) Inlet effect

FIGURE 4: The effective resistance enhancement by the end effects changing with the dimensionless length of microchannels, where f_x denotes the effective resistance of the truncated channel at length x and $f_{x,r}$ the effective resistance of the reference channel at the corresponding region. The symbols are results from our DSMC simulations, and the dash lines are the fitting curves at a function of $f_x/f_{x,r} = e^{c/l}$ with $l = x/W$. For the outlet effect, $c = 0.0954$, while, for the inlet effect, $c = 0.0618$.

outlet position of the reference channel, but the position x away from the inlet along the channel. $\Delta p_{x,r}$ denotes overall pressure gradient for the concerned region on the reference channel.

Figure 4 shows the effective resistance enhancement from the ends effects varying with the dimensionless truncated channel length $l = x/W$. The symbols are the simulation results, and the solid lines are fitting curves. The results indicate that the effective resistance enhancement rate ($f_x/f_{x,r}$) varies with the channel length (l) at a reciprocal exponential law as

$$\frac{f_x}{f_{x,r}} = e^{c/l}. \tag{8}$$

Since the properties of gas flow, such as velocity and temperature, drastically change near the ends region (inlet and outlet) [15, 22, 24, 25], the resistance at the ends is much

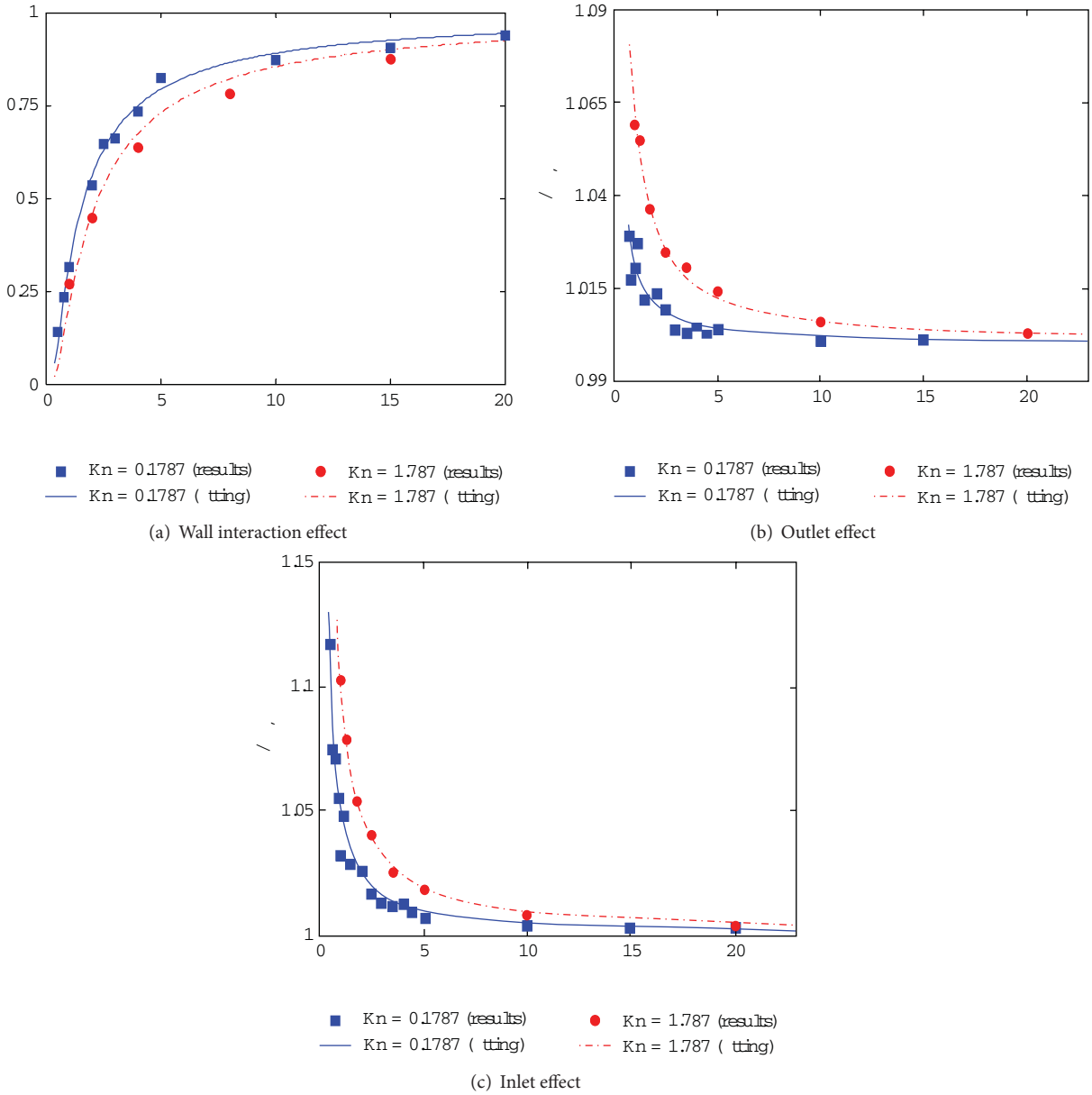

FIGURE 5: Comparison of effective resistances between $\mathrm{Kn}_{\mathrm{in}} = 1.787$ and $\mathrm{Kn}_{\mathrm{in}} = 0.1787$. Symbols denote the simulation results, and the curves are fitting ones. The symbols are results from our DSMC simulations, and the dash lines are the fitting curves at a function of $f_i^* = e^{-c_w/s}$ for (a) and $f_x/f_{x,r} = e^{c_j/l}$ for (b) and (c). For $\mathrm{Kn} = 0.1787$, $c_w = 1.16$ the for wall interaction effect, $c_{\mathrm{out}} = 0.0206$ for the outlet effect, and $c_{\mathrm{in}} = 0.0489$ for the inlet effect, while, for $\mathrm{Kn} = 1.787$, $c_w = 1.5789$ for the wall interaction effect, $c_{\mathrm{out}} = 0.0617$ for the outlet effect, and $c_{\mathrm{in}} = 0.0956$ for the inlet effect.

larger than other parts of channel. When the microchannel is long enough, the end effects are negligible. However if the channel length is comparable with the channel width ($l \sim 1$), the ends may have a significant effect by enhancing the effective resistance. The results also indicate that the end effects are limited to a finite region. In our simulations above, when the dimensionless length l reaches 2~4 or above, the effective resistance enhancement is less than 3%.

3.3. Rarefied Gas Effects. The rarefied gas effects on the effective resistance enhancement are studied by changing the Kn number of the gas flows in microchannels. In this study, we are concerning how the wall interaction effects or the end effects vary with a different Kn number. To do this, we just simply set the inlet and outlet pressures at 150 kPa and 100 kPa, respectively, in the same microchannel to reduce the Kn number ten times smaller.

When the gas gets ten times denser, the wall interaction effects are dramatically enhanced because the gas molecules colloid much more with the walls. The inertial force calculated by (3) may differ in orders of magnitude for these two Kn numbers. In order to make a comparison in the same figure,

we introduce a dimensionless inertial force normalized by the corresponding 2D gas flow under the same boundary conditions as follows:

$$f_i^* = \frac{f_{i,3D}}{f_{i,2D}}. \quad (9)$$

Figure 5(a) indicates that the inertial force and therefore the effective resistance force vary with the width-height ratio at a very similar exponential law even though the Kn number changes ten times, and the gas flow status transfers from the transition region (Kn = 1.787) to the slip region (Kn = 0.1787). A larger Kn number leads to a wider region of the wall interaction effects. When we consider the ends effects for different Kn numbers, as shown in Figures 5(b) and 5(c), the gas rarefication strengthens the effective resistance enhancement by the ends effects of gas flow in microchannels.

4. Conclusions

As well known that the resistance of gas flow in microchannels is higher than that in bulk or continuum flows because of the relatively more importance of interfacial effects at microscale, in this work, we first quantified the effective resistance enhanced by the wall interactions, the ends effect, and the rarefied gas effect using a 3D direct simulation Monte Carlo (DSMC) method. For a narrow microchannel (small H), the effective resistance increases at an exponential law as the distance between side walls (W) decreases. For a short microchannel, the averaged resistance density is higher than that of a long channel because of the dramatic variation of gas flow structures at the inlet and outlet regions. We proposed a "truncated channel" scheme to study the ends effects and found that both inlet and outlet effects raise the effective resistance of gas flow in microchannels following a reciprocal exponential relationship with the aspect ratio of length to height. After comparing two cases with different Kn numbers, we found that the gas rarefaction strengthens the effective resistance enhancement by either the wall interaction effects or the ends effects of gas flow in microchannels. This paper provides simple formulae available for designs and optimization of microengineering from complicated micromechanics.

Acknowledgments

This work is financially supported by the NSFC Grant (no. 51176089), the Tsinghua Initiative Scientific Research Program, and the startup funding for the Recruitment Program of Global Young Experts of China (no. 320503002).

References

[1] H. A. Stone, A. D. Stroock, and A. Ajdari, "Engineering flows in small devices: microfluidics toward a lab-on-a-chip," *Annual Review of Fluid Mechanics*, vol. 36, pp. 381–411, 2004.

[2] Z. Y. Guo and Z. X. Li, "Size effect on microscale single-phase flow and heat transfer," *International Journal of Heat and Mass Transfer*, vol. 46, no. 1, pp. 149–159, 2003.

[3] G. L. Morini, M. Lorenzini, and S. Salvigni, "Friction characteristics of compressible gas flows in microtubes," *Experimental Thermal and Fluid Science*, vol. 30, no. 8, pp. 733–744, 2006.

[4] H. W. Liu, M. Wang, J. Wang et al., "Monte Carlo simulations of gas flow and heat transfer in vacuum packaged MEMS devices," *Applied Thermal Engineering*, vol. 27, no. 2-3, pp. 323–329, 2007.

[5] C. Cai, Q. Sun, and I. D. Boyd, "Gas flows in microchannels and microtubes," *Journal of Fluid Mechanics*, vol. 589, pp. 305–314, 2007.

[6] M. Wang, X. D. Lan, and Z. X. Li, "Analyses of gas flows in micro- and nanochannels," *International Journal of Heat and Mass Transfer*, vol. 51, no. 13-14, pp. 3630–3641, 2008.

[7] C. Cai, "Heat transfer in vacuum packaged microelectromechanical system devices," *Physics of Fluids*, vol. 20, no. 1, Article ID 017103, 2008.

[8] X. D. Shan and M. Wang, "Understanding of thermal conductance of thin gas layers," *Advances in Mechanical Engineering*, vol. 2013, Article ID 692842, 7 pages, 2013.

[9] M. Wang and Z. Li, "Similarity of ideal gas flow at different scales," *Science in China E*, vol. 46, no. 6, pp. 661–670, 2003.

[10] S. Lin, C. C. K. Kwok, R. Y. Li, Z. H. Chen, and Z. Y. Chen, "Local frictional pressure drop during vaporization of R-12 through capillary tubes," *International Journal of Multiphase Flow*, vol. 17, no. 1, pp. 95–102, 1991.

[11] T. Araki, M. S. Kim, H. Iwai, and K. Suzuki, "An experimental investigation of gaseous flow characteristics in microchannels," *Microscale Thermophysical Engineering*, vol. 6, no. 2, pp. 117–130, 2002.

[12] E. B. Arkilic, M. A. Schmidt, and K. S. Breuer, "Gaseous slip flow in long microchannels," *Journal of Microelectromechanical Systems*, vol. 6, no. 2, pp. 167–178, 1997.

[13] Z. X. Li, D. X. Du, and Z. Y. Guo, "Experimental study on flow characteristics of liquid in circular microtubes," *Microscale Thermophysical Engineering*, vol. 7, no. 3, pp. 253–265, 2003.

[14] M. E. Steinke and S. G. Kandlikar, "Single-phase liquid friction factors in microchannels," *International Journal of Thermal Sciences*, vol. 45, no. 11, pp. 1073–1083, 2006.

[15] C. Li, L. Jia, and T. Zhang, "The entrance effect on gases flow characteristics in micro-tube," *Journal of Thermal Science*, vol. 18, no. 4, pp. 353–357, 2009.

[16] M. J. Kohl, S. I. Abdel-Khalik, S. M. Jeter, and D. L. Sadowski, "An experimental investigation of microchannel flow with internal pressure measurements," *International Journal of Heat and Mass Transfer*, vol. 48, no. 8, pp. 1518–1533, 2005.

[17] D. Valougeorgis, "The friction factor of a rarefied gas flow in a circular tube," *Physics of Fluids*, vol. 19, no. 9, Article ID 091702, pp. 1–4, 2007.

[18] G. A. Bird, *Molecular Gas Dynamics and the Direct Simulation of Gas Flows*, Clarendon Press, Oxford, UK, 1994.

[19] G. E. Karniadakis and A. Beskok, *Micro Flows: Fundamentals and Simulation*, Springer, New York, NY, USA, 2002.

[20] M. Wang and Z. Li, "Gas mixing in microchannels using the direct simulation Monte Carlo method," *International Journal of Heat and Mass Transfer*, vol. 49, no. 9-10, pp. 1696–1702, 2006.

[21] M. Wang and Z. Li, "Simulations for gas flows in microgeometries using the direct simulation Monte Carlo method," *International Journal of Heat and Fluid Flow*, vol. 25, no. 6, pp. 975–985, 2004.

[22] M. Wang and Z. Li, "Micro- and nanoscale non-ideal gas Poiseuille flows in a consistent Boltzmann algorithm model,"

Journal of Micromechanics and Microengineering, vol. 14, no. 7, pp. 1057–1063, 2004.

[23] M. R. Wang and Z. X. Li, "Numerical simulations on performance of MEMS-based nozzles at moderate or low temperatures," *Microfluidics and Nanofluidics*, vol. 1, no. 1, pp. 62–70, 2004.

[24] W. W. Liou and Y. Fang, "Heat transfer in microchannel devices using DSMC," *Journal of Microelectromechanical Systems*, vol. 10, no. 2, pp. 274–279, 2001.

[25] M. Wang and Z. Li, "Nonideal gas flow and heat transfer in micro- and nanochannels using the direct simulation Monte Carlo method," *Physical Review E*, vol. 68, no. 4, Article ID 046704, pp. 467041–467046, 2003.

Hindawi Publishing Corporation
Advances in Mechanical Engineering
Volume 2013, Article ID 379839, 7 pages
http://dx.doi.org/10.1155/2013/379839

Research Article

Turbulence Modulation by Small Bubbles in the Vertical Upward Channel Flow

Mingjun Pang,[1,2] Jinjia Wei,[1] and Bo Yu[3]

[1] *State Key Laboratory of Multiphase Flow in Power Engineering, Xi'an Jiaotong University, Xi'an 710049, China*
[2] *School of Mechanical Engineering, Changzhou University, Changzhou 213016, China*
[3] *Beijing Key Laboratory of Urban Oil and Gas Distribution Technology, China University of Petroleum, Beijing 102249, China*

Correspondence should be addressed to Jinjia Wei; jjwei@mail.xjtu.edu.cn

Received 3 November 2012; Revised 31 December 2012; Accepted 7 January 2013

Academic Editor: Tomoaki Kunugi

The liquid turbulence modulation by small bubbles was investigated detailedly in a vertical upward channel flow with a finite number of small bubbles with the developed Eulerian-Lagrangian method. Small bubbles are treated as pointwise spheres subject to gravity, drag, added mass, pressure gradient, lift, and wall lift forces. The momentum transfer between phases was realized through interphase forces. The present investigation shows that the liquid turbulence is intensified near the wall and is slightly weakened in the channel central region due to the bubble addition. The turbulence modulation mechanisms by bubbles were also analyzed in the paper.

1. Introduction

Bubbly flows exist extensively in industrial processes such as two-phase heat exchangers, bubble column reactors, smelting of metals, aeration and stirring of reactors, air-conditioning engineering, wastewater treatment, fermentation reactions, mineral floatation, cavitating flows, and transportation lines, [1–3]. The above applications have stimulated many researches on bubbly flows and have demanded a deep understanding of bubbly hydrodynamics. Therefore, the bubbly flow has received much attention in the academic world over the past 30 years. Of numerous study contents on the bubbly flow, it is very important to accurately and quantitatively understand the turbulence modulation by bubbles, because it controls directly heat transfer and mixing efficiency of bubbly flows and the drag reduction rate by bubbles.

Currently, some researchers had performed definite studies on the turbulence modulation by bubbles and had obtained some important conclusions. Serizawa and Kataoka summarized three kinds of turbulence suppression mechanisms [4]. Kato et al. deduced that the bubble influencing the liquid turbulence is just like the influence of the solid particle on the gas turbulence: large bubbles enhance the liquid-phase turbulence, whereas small bubbles reduce the liquid turbulence [5]. This view is also accepted by Kim et al. [6], and they pointed out that when there is no change in volume of the dispersed phase, the turbulence production and dissipation can be understood by similar mechanisms. So et al. [7] and Molin et al. [8] considered that the lift force direction and magnitude are sensitive to the bubble size, so it is possible that the reason for the suppressed velocity fluctuations is the modification of the global flow structure caused by the bubble accumulation near the wall. Kawamura and Kodama [9] pointed out that the bubble can influence velocity fluctuations in two ways: one is the so-called "pseudo-turbulence" and the other is the liquid-phase turbulence modulated by bubbles. Mazzitelli et al. considered that microbubbles accumulating in down-flow regions locally transfer momentum upwards, and, therefore, the microbubble addition reduces the vertical velocity fluctuation intensity and the turbulent kinetic energy [10]. Ferrante and Elghobashi argued that microbubbles in a spatially developing turbulent boundary layer push the developing streamwise vortices away from the wall, leading to less dissipation in the boundary layer [11]. Van den

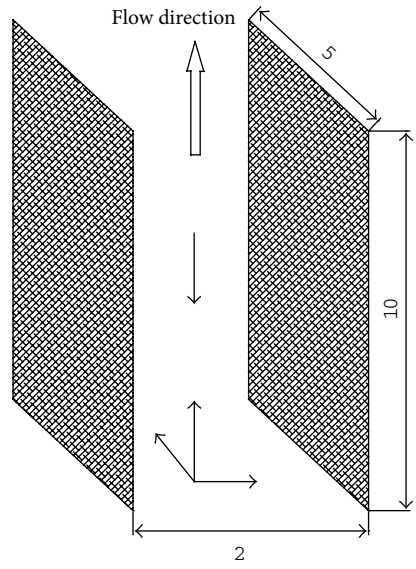

Figure 1: The simulation domain and coordinate system.

Berg et al. pointed out that the microbubbles modulation on the turbulence is a boundary layer effect [12]. Lu and Tryggvason believed that bubble deformation has a great influence on the liquid turbulence [13]. Yeo et al. considered that the turbulence modulation only slightly depends on the dispersion characteristics but is closely related to the stresslet component of flow disturbances [14].

From the above review, one can see that many investigations on the turbulence modulation by bubbles have been performed, but the turbulence modulation mechanism is still not clear. That is just our study motivation. In order to understand the turbulence modulation mechanism by bubbles, an Eulerian-Lagrangian method was developed and applied to simulate a bubbly flow laden with finite number bubbles. The liquid-phase velocity field was solved with direct numerical simulations, and the bubble trajectories were tracked by Newtonian motion equations. The interphase momentum coupling was realized through considering the interphase force as a momentum source term of the liquid phase. For the present investigation, hydrodynamic direct interactions between bubbles were negligible due to the low global void fraction ($\alpha_0 < 10^{-3}$) according to Elghobashi [15], and Bunner and Tryggvason [2] also verified that the spherical bubbles never touch in the dilute bubbly flow. The bubble deformation and breakup were also neglected due to the too small diameter (Weber number, We $\ll$1) [16].

2. Computational Condition and Method

A vertical channel flow laden with small bubbles (see Figure 1) is simulated, and gravity is s directed along the negative x direction. The size of the computational domain is $x \times y \times z = 10\,h \times 2\,h \times 5\,h$, where h is the channel half width. Note that the x, y, and z axes denote the streamwise, wall-normal, and spanwise directions, respectively. The flow field and the bubble motion are periodic both in the stream-wise and in the spanwise directions, while no-slip conditions are imposed on the channel wall for liquid, and the wall elastic collision reflection condition is used in the wall-normal direction for bubbles. The flow is driven by an imposed pressure gradient, with bubbles seeded at a void fraction low enough to ensure the dilute system condition and negligible bubble-bubble interactions. For the bubbly simulation, when a statistically steady state of the liquid turbulence is reached, the bubbles are injected into the flow. The liquid phase is considered to be incompressible, isothermal, and with constant properties, and its thermophysical property data are used as that of water at room temperature, $\rho_f = 1000\,\mathrm{kg/m^3}$. The bubbles are regarded as spherical in shape, and their density is $\rho_b = 1.3\,\mathrm{kg/m^3}$. The bubble diameter is $d_b = 0.011h$, and the global void fraction is $\alpha_0 = 1.34 \times 10^{-4}$.

2.1. Equations for the Liquid Phase. For the present investigation, the governing equations for the liquid phase are continuity equation and a modified Navier-Stokes equation in which the feedback force on the liquid is included as an effective body force. Governing equations of the liquid phase in the dimensionless form are presented as follows. The normalized process of the related parameters can be referred to the literature [17]:

$$\frac{\partial u_{f_i}^+}{\partial x_i^*} = 0, \tag{1}$$

$$\frac{\partial u_{f_i}^+}{\partial t^*} + u_{f_j}^+ \frac{\partial u_{f_i}^+}{\partial x_j^*} = -\frac{\partial p^{+*}}{\partial x_i^*} + \delta_{1i} + \frac{1}{\mathrm{Re}_\tau}\nabla^2 u_{f_i}^+ - \overline{f_i^*}, \tag{2}$$

where u_i is the ith component of the liquid velocity vector, p is the fluctuating kinematic pressure, δ_{1i} is the mean pressure gradient that drives the liquid flow, and $\mathrm{Re}_\tau = u_\tau h/v_f$ is the shear Reynolds number based on the shear velocity ($u_\tau = (\delta_{1i}h/\rho_f)^{1/2}$). Note that bubbles cause pressure drop changes so the shear velocity is not defined using the shear stress at the wall (τ_w) as usually done in the single-phase system. The last term on the right-hand side of (2), $\overline{f_i^*}$, represents the interphase momentum coupling, given by the force per unit mass exerted by the bubbles on the liquid, and is modeled using the famous particle-source-in-cell method proposed by Crowe et al. [18].

Equations (1) and (2) were solved directly using a finite difference scheme. A second-order central difference scheme was applied to discrete the spatial term. For the time integration, the Adams-Bashforth scheme is used for all the terms except that the implicit method is used for the pressure term. The velocity-pressure coupling is made with the MAC method. A staggered grid system is used to prevent a checkboard pressure field, which leads to the fact that velocity components are located at cell faces and other variables are located at cell centers. The uniform meshes are used in the x and z directions, whereas the nonuniform meshes are adopted in the y direction. The grid system of 64^3 meshes is adopted. The grid spacings in the streamwise and spanwise directions are $\Delta x^+ = 2.34$ and $\Delta z^+ = 11.7$, respectively. Δy^+ varies from 0.45 next to the wall to about 9

near the center of the flow. The incompressibility condition results in a nonseparable elliptic equation for the pressure term, for which a multiple grid solver is developed. The basic numerical method is described in detail in [19].

2.2. Equations for the Bubble Phase. The single bubble motion is computed by solving Newton motion equation in the Lagrangian frame. It can be given as follows:

$$\begin{aligned}\frac{\rho_b}{\rho_f}\frac{du_{b_i}^+}{dt^*} &= \frac{Du_{f_i}^+}{Dt^*} + \frac{3}{4}\frac{C_D}{d_b^*}\left|u_{f_i}^+ - u_{b_i}^+\right|\left(u_{f_i}^+ - u_{b_i}^+\right) \\ &\quad + C_v\left(\frac{Du_{f_i}^+}{Dt} - \frac{du_{b_i}^+}{dt^*}\right) \\ &\quad + C_{\mathrm{LF}}\varepsilon_{ijk}\varepsilon_{klm}\left(u_{f_i}^+ - u_{b_i}^+\right)\frac{\partial u_{f_i}^+}{\partial x_m^*} \\ &\quad + \delta_{2i}\left|u_{f_i}^+ - u_{b_i}^+\right|^2 \max\left(0, \frac{-0.0064}{d_b^*} + \frac{0.016}{y_b^*}\right) \\ &\quad + \left(1 - \frac{\rho_{b_i}}{\rho_f}\right)\frac{1}{\mathrm{Fr}^2},\end{aligned} \tag{3}$$

where u_i is the ith component of the velocity vector, ρ is the density, y_b is the distance between the bubble and the wall, ε is sign of permutation, t is the time variable, and x is the coordinate variable. Fr is the Froude number, $\mathrm{Fr} = u_\tau/(gh)^{1/2}$. Subscripts b and f denote the bubble and liquid phase, respectively. In (3), the right-hand terms are the pressure gradient force, the drag force, the added mass force, the shear lift force, the wall lift force, and the buoyant force, respectively. The wall lift force is calculated according to Krepper et al. [20]. For the spherical bubble, the added mass force coefficient is $C_v = 0.5$. The drag coefficient is calculated by the empirical correlation developed by Laín et al. [21], and the lift coefficient is computed with the expression developed by Legendre and Magnaudet [22]. The drag coefficient is expressed as follows:

$$C_D = \begin{cases} \dfrac{16}{\mathrm{Re}_b} & \mathrm{Re}_b \le 1.5 \\ \dfrac{14.9}{\mathrm{Re}_b^{0.78}} & 1.5 \le \mathrm{Re}_b < 80 \\ \dfrac{48}{\mathrm{Re}_b}\left(1 - \dfrac{2.21}{\sqrt{\mathrm{Re}_b}}\right) + 1.86 \times 10^{-15}\mathrm{Re}_b^{4.756} & 80 \le \mathrm{Re}_b < 1500 \\ 2.61 & \mathrm{Re}_b \ge 1500. \end{cases} \tag{4}$$

The lift coefficient, C_{LF}, is written as

$$C_{\mathrm{LF}} = \kappa\sqrt{\left\{C_L^{\text{low Re}}(\mathrm{Re}_b, \mathrm{Sr}_b)\right\}^2 + \left\{C_L^{\text{high Re}}(\mathrm{Re}_b)\right\}^2}, \tag{5}$$

where

$$\begin{aligned} C_L^{\text{low Re}}(\mathrm{Re}_b, \mathrm{Sr}_b) &= \frac{6}{\pi^2}(\mathrm{Re}_b \cdot \mathrm{Sr}_b)^{-0.5} \\ &\quad \times \left[\frac{2.255}{\left(1 + 0.2\zeta^{-2}\right)^{1.5}}\right], \\ C_L^{\text{high Re}}(\mathrm{Re}_b) &= \frac{1}{2}\left(\frac{1 + 16/\mathrm{Re}_b}{1 + 29/\mathrm{Re}_b}\right), \\ \kappa &= 2 - \exp\left(2.92 d_b^{*2.21}\right) \end{aligned} \tag{6}$$

where Sr_b and Re_b are the nondimensional shear rate and the bubble Reynolds number defined as $\mathrm{Sr}_b = |\omega_b| d_b/2|u_f - u_b|$ and $\mathrm{Re}_b = |u_f - u_b| d_b/\nu_f$, respectively. Here, d_b is the bubble diameter, ω_b is the velocity gradient around the bubble, and $\zeta = \sqrt{\mathrm{Sr}_b/\mathrm{Re}_b}$. The time derivative $Du/Dt = \partial u/\partial t + u \cdot \nabla u$ is the total acceleration of the liquid at the bubble location, whereas $du/dt = \partial u/\partial t + u \cdot \nabla u$ is calculated along bubble trajectories.

To analyze the effect that bubbles exert collectively on the liquid turbulence, the flow should be laden with $O(10^4)$ bubbles at least [8]. Because there is a limit to the present computational capability, it is not feasible to track such many bubbles using fully resolved simulations. An alternative Eulerian-Lagrangian approach was developed so as to track large swarms of bubbles at reduced computational costs by the following method: (i) regarding bubbles as points, (ii) neglecting interactions among bubbles, and (iii) using effective force models for the interphase force.

The trajectory of each bubble is computed simultaneously in time with the liquid-phase equations. The motion equation of each bubble, for the time advancement, is solved using the second-order Crank-Nicholson scheme. To calculate interphase forces related to the relative velocity between the bubble and local liquid, a three-dimensional 8-node combined with a two-dimensional 4-node Lagrangian interpolation polynomials are used to compute velocities of liquid at the same positions of bubbles (near the wall, the interpolation scheme switches to one-sided).

3. Results and Discussion

3.1. Bubble Distribution. It was reported that the lateral distribution of bubbles plays an important role in understanding the liquid turbulence modulation by bubbles, and thus the bubble distribution was investigated firstly. Figure 2 shows the lateral distribution of bubbles along the wall-normal direction. Figure 2(a) displays the instantaneous distribution of bubbles when the bubble motions reach a statistically steady state. It can be seen from Figure 2(a) that a large swarm of bubbles accumulate near the walls, whereas a minority of bubbles scatter evenly in a wide central region of the channel. Figure 2(b) shows the statistical distribution of bubbles for statistically steady states. It shows that the present distribution pattern of bubbles is somewhat similar to the wall-peaked profile; that is, a sharp peak with relatively high void fraction appears near the wall and a plateau with very low

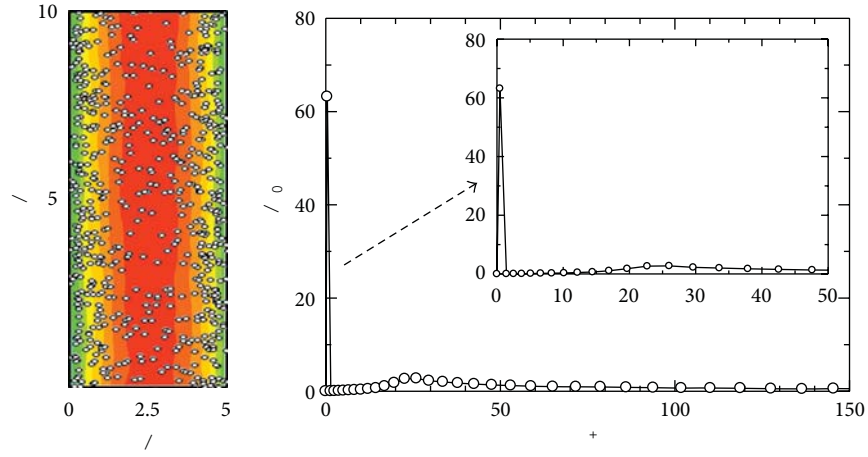

(a) Instantaneous distribution

(b) Statistical distribution

Figure 2: The lateral distribution of bubbles in the channel.

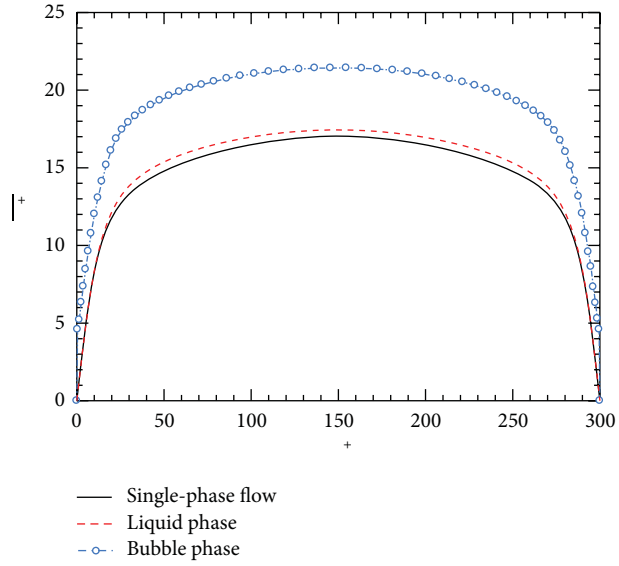

Figure 3: Average velocity profiles.

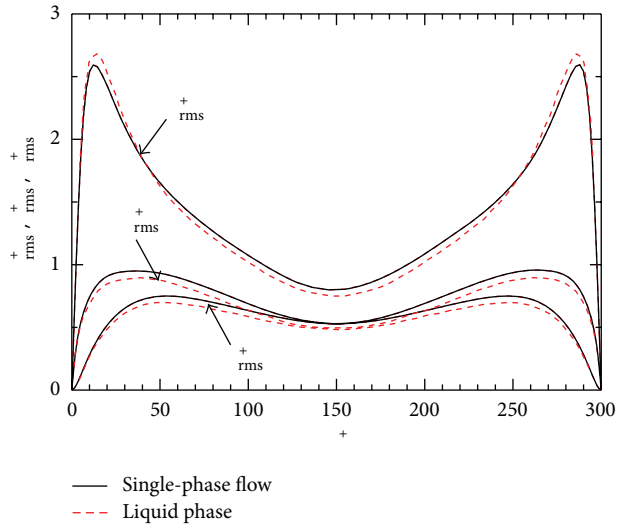

Figure 4: Turbulence intensity profiles.

void fraction around the wide central region of the channel. Many investigations show that a great peak appearance near the wall is related to the shear lift force [23]. Bubbles move firstly toward the wall from the central under the aid of the turbulence and then slowly approach to the wall under the assistance of the lift force. Note that bubbles only stay at the balance region between the lift force and the drag force, and they cannot come into contact with the wall due to the limit of the wall lift force too.

3.2. Turbulence Modulation by Bubbles. In order to understand the liquid turbulence modulation by bubbles, the bubbles influence on the turbulence statistics of the liquid phase was analyzed in detail. Figure 3 shows average velocity profiles of the liquid and bubble phases. One can see from

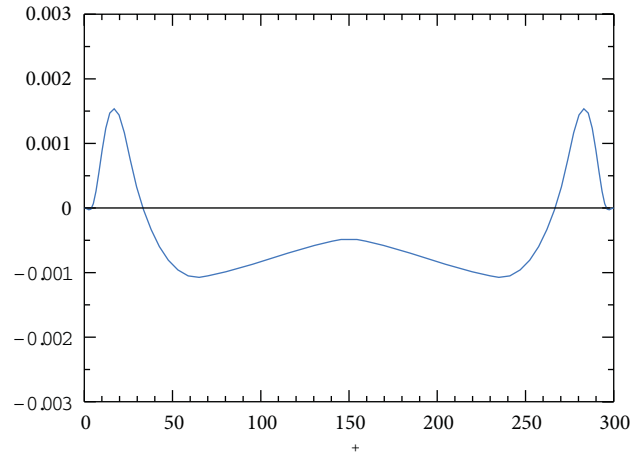

Figure 5: Turbulence modulation profile.

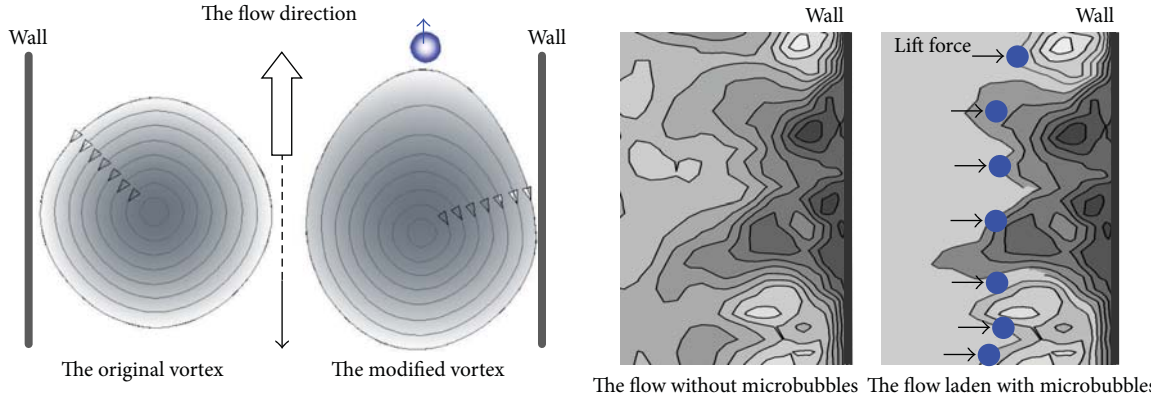

(a) Bubbles pulling a turbulence vortex

(b) Bubbles preventing the spanwise vortex

FIGURE 6: Models of bubbles influencing liquid turbulence vortex.

Figure 3 that the bubble moves faster than the liquid due to the buoyancy pulling, and the liquid without bubbles flows slightly slower than the liquid laden with bubbles. Our previous studies showed that the increase of the liquid-phase velocity has a direct relation to the bubble drag in the gravitational field; namely, due to the buoyancy force, the bubbles move faster that the liquid, and then the bubbles drag the liquid acceleration, which leads to the increase of the liquid-phase velocity, and it seems to have nothing to do with the liquid turbulence suppressions by bubbles for the dilute bubbly flow [24]. It was also checked that the reduction in weight of the mixture influences the liquid velocity, and it was discovered that the liquid velocity increasing rate is far higher than the reduction rate in weight of the mixture. And thus, it can be concluded that the liquid velocity increase seems to have little to do with the reduction in weight of the mixture due to the bubble addition. It needs to be further investigated whether the liquid turbulence suppressions can cause the increase of the liquid velocity for the dense bubbly flow. However, it is a pity that the presently developed method cannot deal with the dense bubbly flow laden with a huge mount of bubbles due to the huge computation cost.

Figure 4 shows turbulence intensity profiles of the liquid with and without bubbles. It shows that the bubble injection, to a different degree, reduces the liquid-phase turbulence intensity components in the lateral direction compared with ones of the single-phase flow in the whole channel, whereas it shows different influences on the streamwise component of the turbulence intensity; that is, the streamwise component of the turbulence intensity is increased near the wall, and it is reduced in the channel central region. To examine the general influence of bubbles on the liquid turbulence, the turbulence modulation was defined as follows in [25]:

$$\Delta\sigma = \left(\frac{\overline{u'_{f_i}u'_{f_i}}}{U_0^2}\right)_{\text{liquid phase}} - \left(\frac{\overline{u'_{f_i}u'_{f_i}}}{U_0^2}\right)_{\text{single phase liquid}}, \quad (7)$$

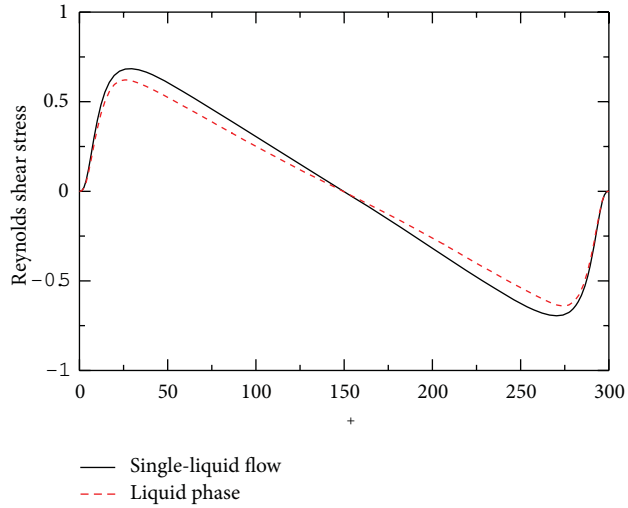

FIGURE 7: Reynolds shear stress profile.

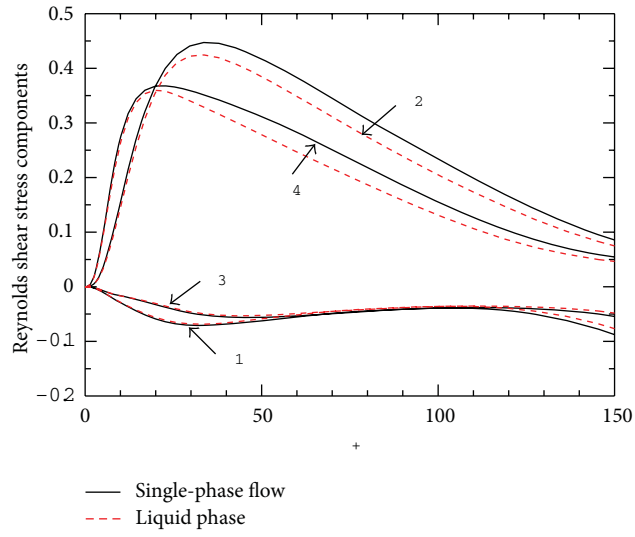

FIGURE 8: Quadrant analysis of Reynolds shear stress.

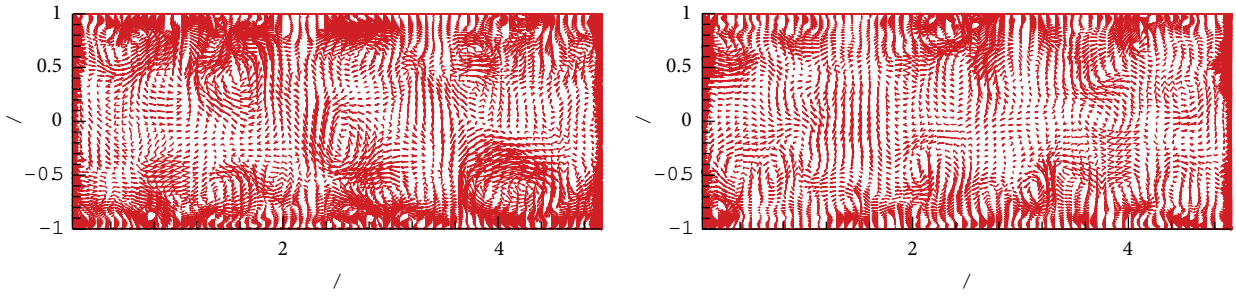

(a) Single-phase flow (b) Liquid phase

Figure 9: Instantaneous velocity distribution.

where U_0 is the mean velocity of the pure liquid at the channel centre, $\overline{u'_{f_i}u'_{f_i}}$ is the liquid velocity variance, $\overline{u'_{f_i}u'_{f_i}} = \overline{u'u'} + \overline{v'v'} + \overline{w'w'}$. Figure 5 shows the turbulence modulation profile. It can be seen from Figure 5 that the liquid turbulence is enhanced in the region near the wall, and it is suppressed in the channel central region. The enhancement of the liquid turbulence near the wall probably relates to the fact that a large number of bubbles swarm near the wall, which causes their wakes to come into being interactions. Especially in the streamwise direction, the wake interactions of bubbles are relatively intenser than those in the lateral direction due to a high velocity. That corresponds to the fact that the streamwise component of the turbulence intensities is strengthened near the wall due to the bubble injection.

In the channel central region, the liquid turbulence suppression may be explained by the following two mechanisms. One is that the bubbles move faster than the liquid due to the buoyancy effect; that is, the bubbles flow faster than the turbulence vortexes, which leads to the fact that the bubbles can quickly pass through a variety of the liquid turbulence vortexes, and thus they can cause a variety of vortexes to attenuate and even to vanish, as shown in Figure 6(a). The other is that a violent accumulation of bubbles near the wall can prevent the spanwise vortex from developing and propagating, which further leads to the decrease of the streamwise vortex since the streamwise vortex evolves from the spanwise vortex, as shown in Figure 6(b).

The liquid turbulent intensity and vortex changes are bound to change Reynolds shear stress. Figure 7 displays the influence of the bubbles on the Reynolds shear stress. It can be seen that the bubble addition reduces the liquid-phase Reynolds shear stress compared with the single liquid-phase one. Due to its complexity of the Reynolds shear stress, it is relatively difficult to ascertain its changing reasons. To understand the detailed contribution to the total turbulence production from different events in a turbulent flow, and to provide information on the influence of the bubbles on each contribution, the quadrant analysis of the fluctuating velocity field is carried out. Figure 8 exhibits the fractional contribution of the Reynolds shear stress from different quadrant motions. One can see that the bubble addition has greater influence on the second (Q_2) and fourth quadrant (Q_4) motions than on the first (Q_1) and third quadrant (Q_3) ones. That means that the bubbles significantly suppress the ejection and sweep motions occurring near the wall, which results in a reduction of the liquid-phase Reynolds shear stress.

Figure 9 shows the instantaneous secondary velocity vectors distribution of the liquid at a z-y plane. It shows that the busting events of the liquid turbulence are weakened by the bubble injection near the wall, and the circulation spatial size is larger for the flow laden with bubbles than one for the single-phase flow. That corresponds to the fact that the liquid fluctuation components are reduced due to the bubble injection, as shown in Figure 4.

4. Conclusions

The turbulence modulation by small bubbles was studied with the developed quasidirect numerical simulation method, and several important conclusions can be summarized as follows.

(1) Bubbles move violently toward the wall under the aid of the shear lift force and the turbulence, which leads to the present distribution pattern similar to the typical wall-peaked profile.

(2) The bubble injection leads to the liquid velocity increase by the bubble pulling, slightly intensifies the liquid turbulence due to mutual influence of bubble wakes near the wall, and somewhat weakens the liquid turbulence in the channel central region. In the channel central region, the liquid turbulence suppression may be related to the vortex decay by a single bubble and the spanwise vortex prevention by a bubble swarm.

(3) The bubble addition reduces the liquid-phase Reynolds stress due to the turbulence ejection and sweep motions suppressed by the bubbles.

Acknowledgments

The authors gratefully acknowledge the financial support from the NSFC Fund (nos. 51225601 and 51076124) and the Specialized Research Fund for the Doctoral Program of Higher Education of China (no. 20090201110002).

References

[1] J. Magnaudet and I. Eames, "The motion of high-reynolds-number bubbles in inhomogeneous flows," *Annual Review of Fluid Mechanics*, vol. 32, pp. 659–708, 2000.

[2] B. Bunner and G. Tryggvason, "Effect of bubble deformation on the properties of bubbly flows," *Journal of Fluid Mechanics*, no. 495, pp. 77–118, 2003.

[3] S. Guet and G. Ooms, "Fluid mechanical aspects of the gas-lift technique," *Annual Review of Fluid Mechanics*, vol. 38, pp. 225–249, 2006.

[4] A. Serizawa and I. Kataoka, "Turbulence suppression in bubbly two-phase flow," *Nuclear Engineering and Design*, vol. 122, no. 1–3, pp. 1–16, 1990.

[5] H. Kato, T. Iwashina, M. Miyanaga, and H. Yamaguchi, "Effect of microbubbles on the structure of turbulence in a turbulent boundary layer," *Journal of Marine Science and Technology*, vol. 4, no. 4, pp. 155–162, 2000.

[6] S. Y. Kim, K. B. Lee, and C. G. Lee, "Theoretical approach on the turbulence intensity of the carrier fluid in dilute two-phase flows," *International Communications in Heat and Mass Transfer*, vol. 32, no. 3-4, pp. 435–444, 2005.

[7] S. So, H. Morikita, S. Takagi, and Y. Matsumoto, "Laser doppler velocimetry measurement of turbulent bubbly channel flow," *Experiments in Fluids*, vol. 33, no. 1, pp. 135–142, 2002.

[8] D. Molin, C. Marchioli, and A. soldati, "Turbulence modulation and microbubble dynamics in vertical channel flow," *International Journal of Multiphase Flow*, vol. 42, no. 6, pp. 80–95, 2012.

[9] T. Kawamura and Y. Kodama, "Numerical simulation method to resolve interactions between bubbles and turbulence," *International Journal of Heat and Fluid Flow*, vol. 23, no. 5, pp. 627–638, 2002.

[10] I. M. Mazzitelli, D. Lohse, and F. Toschi, "The effect of microbubbles on developed turbulence," *Physics of Fluids*, vol. 15, no. 1, pp. L5–L8, 2003.

[11] A. Ferrante and S. Elghobashi, "On the physical mechanisms of drag reduction in a spatially developing turbulent boundary layer laden with microbubbles," *Journal of Fluid Mechanics*, no. 503, pp. 345–355, 2004.

[12] T. H. van den Berg, D. P. M. van Gils, D. P. Lathrop, and D. Lohse, "Bubbly turbulent drag reduction is a boundary layer effect," *Physical Review Letters*, vol. 98, no. 8, Article ID 084501, 2007.

[13] J. C. Lu and G. Tryggvason, "Effect of bubble deformability in turbulent bubbly upflow in a vertical channel," *Physics of Fluids*, vol. 20, no. 4, Article ID 040701, 2008.

[14] K. Yeo, S. Dong, E. Climent, and M. R. Maxey, "Modulation of homogeneous turbulence seeded with finite size bubbles or particles," *International Journal of Multiphase Flow*, vol. 36, no. 3, pp. 221–233, 2010.

[15] S. Elghobashi, "On predicting particle-laden turbulent flows," *Applied Scientific Research*, vol. 52, no. 4, pp. 309–329, 1994.

[16] R. Detsch, "Small air bubbles in reagent grade water and seawater: I. Rise velocities of 20 to 1000 μm diameter bubbles," *Journal of Geophysical Research*, vol. 96, no. 5, pp. 8901–8906, 1991.

[17] M. J. Pang, J. J. Wei, and B. Yu, "Numerical study of bubbly upflows in a vertical channel using the Euler-Lagrange two-way model," *Chemical Engineering Science*, vol. 65, no. 23, pp. 6215–6228, 2010.

[18] C. T. Crowe, D. E. Stock, and M. P. Sharma, "The Particle-Source-In Cell (PSI-CELL) model for gas-droplet flows," *Journal of Fluids Engineering*, vol. 99, no. 2, pp. 325–332, 1977.

[19] B. Yu and Y. Kawaguchi, "Direct numerical simulation of viscoelastic drag-reducing flow: a faithful finite difference method," *Journal of Non-Newtonian Fluid Mechanics*, vol. 116, no. 2-3, pp. 431–466, 2004.

[20] E. Krepper, D. Lucas, and H. M. Prasser, "On the modelling of bubbly flow in vertical pipes," *Nuclear Engineering and Design*, vol. 235, no. 5, pp. 597–611, 2005.

[21] S. Laín, D. Bröder, and M. Sommerfeld, "Modeling hydrodynamics and turbulence in a bubble column using the Euler-Lagrange procedure," *International Journal of Multiphase Flow*, vol. 28, no. 6, pp. 1381–1407, 2002.

[22] D. Legendre and J. Magnaudet, "The lift force on a spherical bubble in a viscous linear shear flow," *Journal of Fluid Mechanics*, vol. 368, pp. 81–126, 1998.

[23] S. P. Antal, J. R. T. Lahey, and J. E. Flaherty, "Analysis of phase distribution in fully developed laminar bubbly two-phase flow," *International Journal of Multiphase Flow*, vol. 17, no. 5, pp. 635–652, 1991.

[24] M. J. Pang, J. J. Wei, and B. Yu, "Study on dependence of hydrodynamic characteristics on gravity in a vertical upward channel bubbly flow," *Advances in Space Research*, vol. 48, no. 8, pp. 1391–1401, 2011.

[25] K. Hadinoto and J. S. Curtis, "Numerical simulation of the Reynolds number effect on gas-phase turbulence modulation," *International Journal of Multiphase Flow*, vol. 35, no. 2, pp. 129–141, 2009.

Hindawi Publishing Corporation
Advances in Mechanical Engineering
Volume 2013, Article ID 921524, 8 pages
http://dx.doi.org/10.1155/2013/921524

Research Article

The Polymer Effect on Nonlinear Processes in Decaying Homogeneous Isotropic Turbulence

Wei-Hua Cai,[1,2,3] Feng-Chen Li,[1] Hong-Na Zhang,[1] Yue Wang,[1,3] and Lu Wang[1]

[1] *School of Energy Science and Engineering, Harbin Institute of Technology, Harbin 150001, China*
[2] *School of Civil Engineering, Harbin Institute of Technology, Harbin 150090, China*
[3] *School of Municipal and Environmental Engineering, Harbin Institute of Technology, Harbin 150090, China*

Correspondence should be addressed to Wei-Hua Cai; caiwh@hit.edu.cn

Received 9 October 2012; Revised 16 January 2013; Accepted 16 January 2013

Academic Editor: Tomoaki Kunugi

In order to study the polymer effect on the behavior of nonlinearities in decaying homogeneous isotropic turbulence (DHIT), direct numerical simulations were carried out for DHIT with and without polymers. We investigate the nonlinear processes, such as enstrophy production, strain production, polymer effect, the curvature of vortex line, and many others. The analysis results show that the nonlinear processes like enstrophy production (and many others) are strongly depressed in regions dominated by enstrophy as compared to those dominated by strain either in the Newtonian fluid case or in polymer solution case. Polymers only decrease the values of these parameters in the strongest enstrophy and strain regions. In addition, polymer additive has a negative effect on enstrophy and strain production, that is, depression of nonlinearity in DHIT with polymers.

1. Introduction

Kraichnan and Panda [1] suggested comparing the key nonlinear terms in real turbulent flows with their Gaussian counterparts, which are involved in the description of nonlinear dynamics in physical space, and firstly introduced the notion of *depression of nonlinearity*. In decaying homogeneous isotropic turbulence (DHIT), they found that $J \equiv \langle|\mathbf{u}\times\boldsymbol{\omega}|^2\rangle/N_4$ (where $\mathbf{u}$ and $\boldsymbol{\omega}$ are velocity and vorticity vectors, resp.; $\boldsymbol{\omega} = \nabla\times\mathbf{u}$) drops to 87% of the value for a Gaussianly distributed velocity field with the same instantaneous velocity spectrum and $H \equiv \langle|\mathbf{u}\cdot\boldsymbol{\omega}|^2\rangle/N_4$ rises to 120% of the Gaussian value. Here $N_4 = \langle|\mathbf{u}|^2\rangle\langle|\boldsymbol{\omega}|^2\rangle$ is a normalization factor. And also they observed a depression of normalized mean-square total nonlinear term $Q = \langle|\mathbf{u}\times\boldsymbol{\omega} - \nabla(p + (1/2)u^2)|^2\rangle/N_4$ (where p and u are pressure and velocity magnitude, resp.) to 57% of the Gaussian value [1]. Some other investigations on the depression of nonlinearity from the nonlinear term $\langle|\mathbf{u}\times\boldsymbol{\omega} - \nabla(p + (1/2)u^2)|^2\rangle$ [2] and the Lamb vector $\boldsymbol{\omega}\times\mathbf{u}$ [3, 4] have been carried out. It is thus known that a study on the depression of nonlinearity is of profound importance for fluid dynamics in general and for the dynamics of turbulence in particular. Besides, the numerical results of Kraichnan and Panda [1] showed that the alignment of velocity and vorticity in physical space is not the sole source of the depression of nonlinearity. Shtilman and Polifke [5] argued that another source of the depression of nonlinearity seems to be a tendency of the Lamb vector $\boldsymbol{\omega}\times\mathbf{u}$ in Fourier space to align with the wave vector $\mathbf{k}$. These aforementioned investigations mainly focused on the relationship between velocity and vorticity.

However, as compared with velocity, the field of velocity gradient is much more sensitive to the non-Gaussian nature of turbulence or more generally to its structure and hence reflects more of its physics [6]. It is also a Galilean invariance containing significant fluid mechanics information independent of the reference of a moving observer. Moreover, its dynamical behavior governs the mechanism of vortex stretching which in turn contributes to the energy cascade process in turbulent flows (as pointed in [6] "*The turbulent kinetic cascade in Fourier space must be replaced with the generation of velocity gradients* (i.e., *both vorticity and strain*) *in physical space*."). Therefore, its evolution is of primary importance in the understanding of the kinematics and

dynamics of turbulence. The velocity gradient includes two parts: vorticity and strain. Therefore, it is very important to investigate the nonlinearity process from vorticity and strain transport equations. Tsinober [7] defined all four regions in real turbulent flow: (i) regions of concentrated vorticity; (ii) regions of "structureless" background; (iii) regions of strong vorticity/strain (self) interaction and strong enstrophy generation; (iv) regions with negative enstrophy production. The results of turbulent grid experiment [8] and DHIT [7] demonstrated that all four regions are strongly non-Gaussian, dynamically significant, and possess structures, and it is also argued that due to the strong nonlocality of turbulence in physical space all the four regions are in continuous interaction and are strongly correlated. Tsinober [7] also highly stressed the role of regions of strong vorticity/strain (self) interaction and argued that important regions of concentrated vorticity are not as important as is commonly believed. Then he [9, 10] investigated the behavior of key nonlinearities related to velocity gradients in flow regions dominated by enstrophy and strain, such as the magnitude of the vortex stretching vector $W = |\omega_j S_{ij}|$ (where $S_{ij} = (\partial u_i/\partial x_j + \partial u_j/\partial x_i)/2$ is the rate-of-strain tensor), the enstrophy generation $\omega_i\omega_j S_{ij}$, and the curvature of vortex lines. It is shown that the nonlinear processes like enstrophy production (and many others) are strongly depressed in regions dominated by enstrophy as compared to those dominated by strain.

In the present paper, the purpose is to investigate the polymer effect on the behavior of nonlinearity in DHIT and study which region (as Tsinober defined in [7]) is influenced by polymers. We use the dataset from direct numerical simulation in the periodic cubic domain of size $\mathrm{R} = 2\pi$ computed with a pseudo-spectral code for Navier-Stokes equations and finite difference code for FENE-P (finitely extensible nonlinear elastic Peterlin) constitutive model with resolution 96^3 using the Adams-Bashforth scheme [11]. The Taylor-scale Reynolds number Re_λ and the Weissenberg number Wi are defined as $\mathrm{Re}_\lambda = \sqrt{20}\xi_m^{[N]}/\sqrt{3\upsilon^{[s]}\varepsilon_m^{[N]}}$ and $\mathrm{Wi} = \tau_p\sqrt{\varepsilon_m^{[N]}/\upsilon^{[s]}}$. Here $\xi_m^{[N]}$ and $\varepsilon_m^{[N]}$ are the turbulent kinetic energy and energy-dissipation rate for the Newtonian fluid flow at $t = t_m$, where t_m corresponds to the moment at which $\varepsilon^{[N]}$ reaches to its maximum amplitude; $\upsilon^{[s]}$ is the solvent kinetic viscosity; τ_p is the polymer relaxation time. In this paper, $\beta = \upsilon^{[s]}/(\upsilon^{[s]} + \upsilon^{[p]})$ is a dimensionless measure of dilute polymer solution concentration, the smaller β is, the denser polymer solution is; here $\upsilon^{[p]}$ is the polymer viscosity. The results presented in this paper are at a time right after the total enstrophy has reached its maximum and at which time $\mathrm{Re}_\lambda = 26$ and for polymer solution flow, $\mathrm{Wi} = 0.62$, $\beta = 0.6$. For more information, the reader can be referred to [11].

2. Enstrophy and Strain Transport Equations

In one of our previous studies [12], we have paid our attention to velocity gradient, especially for vorticity and strain field. These two quantities must be considered in parallel, as they are weakly correlated in isotropic turbulence and they are tied by a strongly nonlocal relation. So we firstly give the fundamental evolution equations for the enstrophy $\omega^2/2$ and the total strain $S_{ij}S_{ij}/2$.

The enstrophy transport equation of DHIT with polymers is as follows:

$$\frac{\partial\Omega}{\partial t} + u_j\frac{\partial\Omega}{\partial x_j} = \omega_i\omega_j S_{ij} + \upsilon^{[s]}\omega_i\frac{\partial^2\omega_i}{\partial x_j\partial x_j} + \omega_i\frac{\partial^2 T_{mj}^{[p]}}{\partial x_m\partial x_n}\varsigma_{nji}, \quad (1)$$

where ς_{nji} is the permutation symbol; $\Omega = \omega_i\omega_i/2$ the enstrophy, here $\omega_i = (\partial u_k/\partial x_j)\varsigma_{ijk}$; $S_{\mathrm{ens}} = \omega_i\omega_j S_{ij}$ the enstrophy production due to the interaction between vorticity and strain; $V_{\mathrm{ens}} = \upsilon^{[s]}\omega_i(\partial^2\omega_i/\partial x_j\partial x_j)$ the enstrophy viscous dissipation; $W_i^{[p]} = \omega_i(\partial^2 T_{mj}^{[p]}/\partial x_m\partial x_n)\varepsilon_{nji}$ the polymer effect vector; $P_{\mathrm{ens}} = \omega_i W_i^{[p]}$ the polymer effect due to the interaction between vorticity and polymer conformation and does not appear in the Newtonian fluid case.

The strain transport equation of DHIT with polymers is as follows:

$$2\frac{\partial S}{\partial t} + 2u_j\frac{\partial S}{\partial x_j} = 2\left(-S_{ik}S_{kj}S_{ij} - \frac{1}{4}\omega_i\omega_j S_{ij} - S_{ij}\frac{\partial p}{\partial x_i\partial x_j} + \upsilon^{[s]}S_{ij}\frac{\partial^2 S_{ij}}{\partial x_j\partial x_j} + \frac{\partial^2 T_{ik}^{[p]}}{\partial x_k\partial x_j}S_{ij}\right), \quad (2)$$

where $S = S_{ij}S_{ij}/2$ is the total strain; $S_{\mathrm{str}} = -S_{ik}S_{kj}S_{ij}$ the strain production from strain self-amplification; $W_{\mathrm{str}} = \omega_i\omega_j S_{ij}/4$ the enstrophy production effect on the total strain; $R_{\mathrm{str}} = S_{ij}(\partial^2 p/\partial x_i\partial x_j)$ the interaction of strain with pressure Hessian; $V_{\mathrm{str}} = \upsilon^{[s]}S_{ij}\nabla^2 S_{ij}$ the strain viscous dissipation; $B_{ij}^{[p]} = \partial^2 T_{ik}^{[p]}/\partial x_k\partial x_j$ the polymer effect tensor influencing on the generation of strain; $P_{\mathrm{str}} = B_{ij}^{[p]}S_{ij}$ the polymer effect due to the interaction between strain and polymer elastic stress (or polymer conformation) and does not appear in the Newtonian fluid case.

It is found that $\omega_i\omega_j S_{ij}$ term appears in (1) and (2). When $\omega_i\omega_j S_{ij}$ is positive, the production of total strain is decreased and the production of total enstrophy is increased; when $\omega_i\omega_j S_{ij}$ is negative, the results are contrary. However, $\langle\omega_i\omega_j S_{ij}\rangle$ is always positive [11]. So enstrophy production results from the interaction of vorticity with the strain field, whereas the production of total strain mainly comes from self-amplification of the strain field. The relationship among velocity, velocity gradient tensor, rate-of-strain tensor, vorticity, enstrophy production, and strain production is schematically shown in Figure 1 [6]. And also there exists the relationship as follows: $\langle S_{ij}S_{jk}S_{ki}\rangle = (-3/4)\langle\omega_i\omega_j S_{ij}\rangle$ and $\langle S_{ij}(\partial p/\partial x_i\ \partial x_j)\rangle = 0$ due to homogeneity and incompressibility; $-S_{ij}S_{jk}S_{ki} = -(\alpha_1^3 + \alpha_2^3 + \alpha_3^3) = -3\alpha_1\alpha_2\alpha_3$, where α_i $(i = 1, 2, 3)$ are the corresponding eigenvalues reordered of rate-of-strain tensor **S**. Moreover, the eigenvalues of velocity gradient tensor, $\lambda_1 > 0$, and λ_2 is positively skewed [10]. Due to the nonlocal relation between the rate-of-strain tensor and vorticity, it is useful to investigate the above quantities in

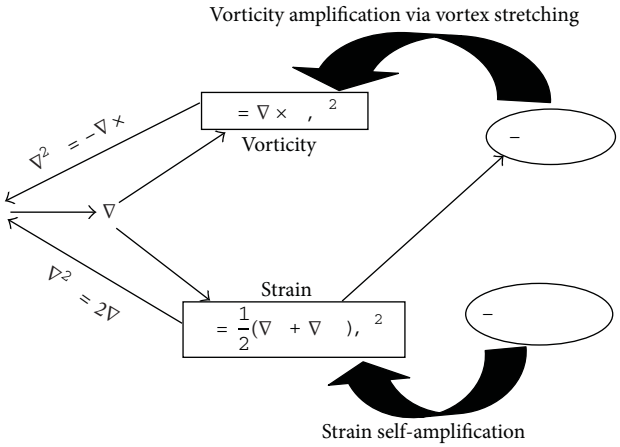

Figure 1: Schematic view of the velocity-gradient self-amplification process in isotropic turbulence.

parallel, such as the third moments $\omega_i\omega_j S_{ij}$, $S_{ij}S_{jk}S_{ki}$, which are of key importance for turbulence dynamics. However, for DHIT with polymers, we must highly investigate the polymer effect on the important terms in these transport equations, such as $\omega_i(\partial^2 T^{[p]}_{mj}/\partial x_m \partial x_n)\varepsilon_{nji}$ and $(\partial^2 T^{[p]}_{ik}/\partial x_k \partial x_j)S_{ij}$.

3. Results and Discussion

We take dissipation rate, enstrophy production, strain production, and vortex stretching herein as the measurement of nonlinearity in DHIT. Conditional averages of all quantities here are conditioned on $\omega/\langle\omega\rangle$ and $s/\langle s\rangle$, here $\omega = |\boldsymbol{\omega}|$ and $s = (S_{ij}S_{ij})^{1/2}$. Firstly, we define the regions of the strongest interaction of vorticity and strain where $3 \le \omega/\langle\omega\rangle \le 4$ and $3 \le s/\langle s\rangle \le 4$. We give the conditional average of dissipation rate, as shown in Figure 2(a). It is clearly suggested that the addition of polymers into DHIT can only change dissipation rate in the regions of *the strongest enstrophy and strain*. And also, dissipation rate appears smaller in the regions dominated by enstrophy than that in the regions dominated by strain (as pointed out by ellipse identifier in Figure 2(a)). Besides, the result of conditional average of polymer elastic energy is shown in Figure 2(b). It is also found that $e^{[p]}$ is much smaller in the enstrophy dominated regions than that in regions dominated by strain (ellipse identifier in Figure 2(b)).

One of the aspects of the problem in question concerns the enstrophy production $S_{\text{ens}} = \omega_i\omega_j S_{ij}$, enstrophy viscous dissipation $V_{\text{ens}} = \upsilon^{[s]}\omega_i(\partial^2\omega_i/\partial x_j \partial x_j)$, and the polymer effect on enstrophy $P_{\text{ens}} = \omega_i W_i^{[p]}$ and vortex stretching W^2. These parameters are very important for investigating the nonlinear processes and the polymer effect in DHIT, and the conditional averages of which are shown in Figure 3. It can be seen that the addition of polymers only depresses the values of these parameters in the strongest regions of enstrophy and strain. And also, it is shown that the values of these parameters are smaller in regions dominated by enstrophy than those in regions dominated by strain (as

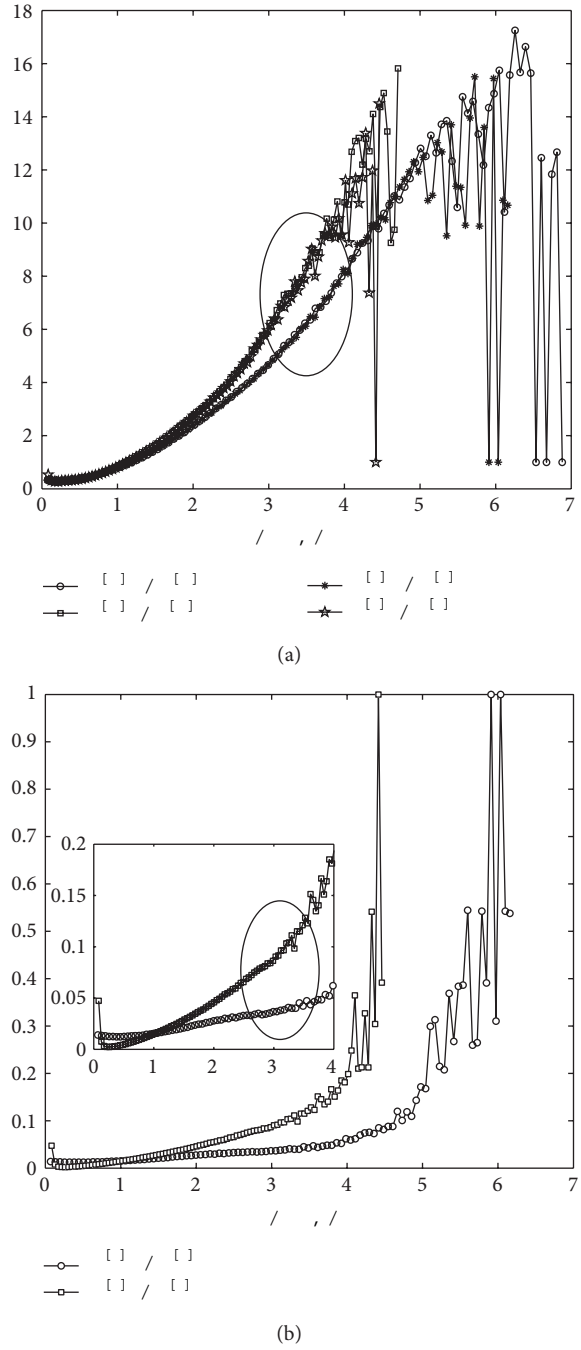

(a)

(b)

Figure 2: Conditional averages of (a) dissipation rate and (b) polymer elastic energy in slots of $\omega/\langle\omega\rangle$ and $s/\langle s\rangle$.

pointed out by ellipse identifiers in Figure 3). This adequately suggests that the depression of the nonlinearity is strengthened due to the existence of polymers. In addition, the main contribution to vortex stretching and enstrophy production comes from the regions dominated by strain. So it is out of question to say that the regions dominated by strain (the regions of the strongest interaction of vorticity and strain) are more important than the enstrophy dominated regions. And the polymer additive has the same influence on strong

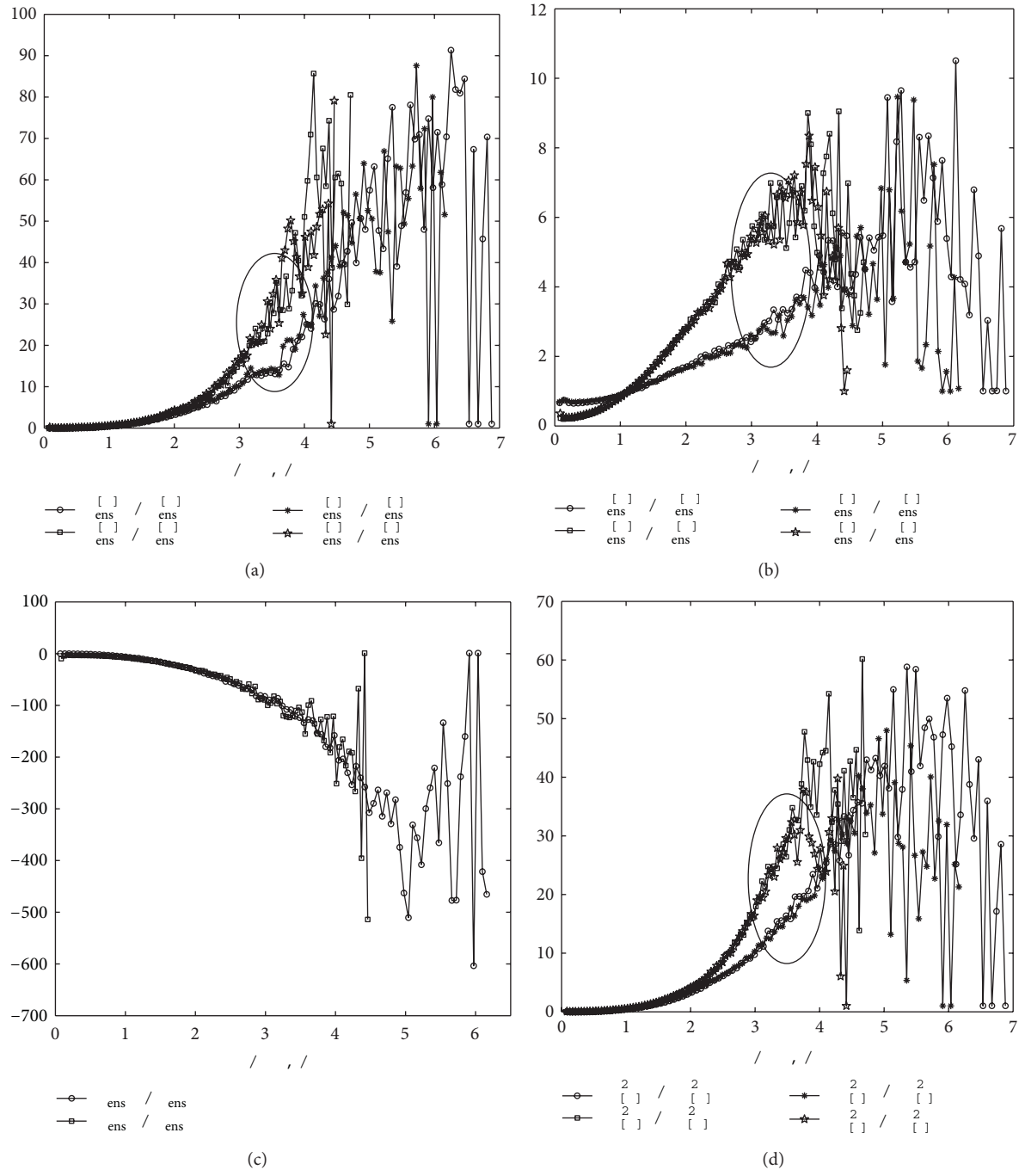

Figure 3: Conditional averages of (a) enstrophy production; (b) enstrophy viscous dissipation; (c) the polymer effect; (d) vortex stretching in slots of $\omega/\langle\omega\rangle$ and $s/\langle s\rangle$.

vorticity/strain (self) interaction and has a negative effect on enstrophy production, suggesting that the decrease on enstrophy production is the depression of nonlinearity in DHIT with polymers. That is to say, the negative effect of polymers on enstrophy production (causing the decrease of vortex stretching) in DHIT is similar to a negative torque on vortices as investigated in the polymeric channel flow [13, 14].

It is equally important to investigate the nonlinear behavior of strain production ($S_{\text{str}} = -S_{ik}S_{kj}S_{ij}$ and $2(S_{\text{str}} - W_{\text{str}}) = 2(-S_{ik}S_{kj}S_{ij} - \omega_i\omega_jS_{ij}/4)$), strain viscous dissipation ($V_{\text{str}} = \upsilon^{[s]}S_{ij}\nabla^2S_{ij}$), and the polymer effect on strain ($P_{\text{str}} = B_{ij}^{[p]}S_{ij}$), and the conditional averages of which are shown in Figure 4. It follows that the mean rate of strain production $\langle 2(-S_{ik}S_{kj}S_{ij} - \omega_i\omega_jS_{ij}/4 - S_{ij}\partial p/\partial x_i\partial x_j)\rangle = \langle\omega_i\omega_jS_{ij}\rangle$ is equal to that of enstrophy, hence (and also due to $\langle\omega^2\rangle = 2\langle S_{ij}S_{ij}\rangle$) a coefficient 2 is used in (2) on both sides. From Figure 4, it can be seen that the addition of polymers also

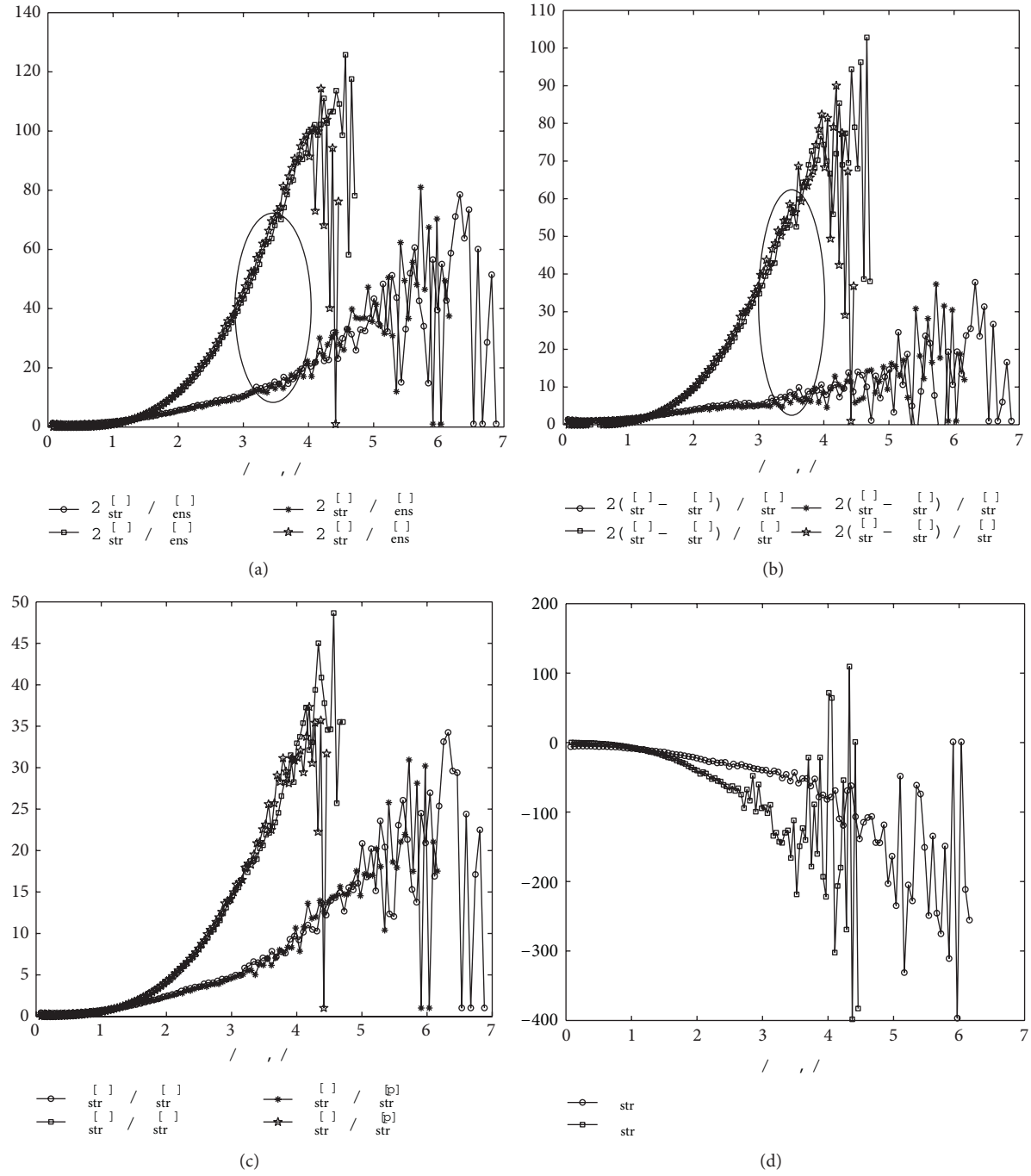

Figure 4: Conditional averages of (a) strain production; (b) strain production and enstrophy production effect on the total strain; (c) strain viscous dissipation; (d) the polymer effect in slots of $\omega/\langle\omega\rangle$ and $s/\langle s\rangle$.

only depresses the values of these parameters in the strongest regions of enstrophy and strain, which is the same tendency as the results of conditional averages of those parameters in enstrophy transport equation. And also, these parameters are smaller in the enstrophy dominated regions than those in regions dominated by strain (ellipse identifier in Figure 4). And the polymer additive has the same influence in strong vorticity/strain (self) interaction and almost has a negative effect on strain production, suggesting the decrease on the strain production, that is, the polymer effect depressing the nonlinear processes in DHIT.

Another manifestation of the depression of nonlinearity is the decrease of curvature of vortex lines in the enstrophy dominated regions. As is known, it is easy to obtain three-dimensional vorticity $\boldsymbol{\omega}$, its magnitude $\omega = |\boldsymbol{\omega}|$, its direction vector $\widehat{\boldsymbol{\omega}} = \boldsymbol{\omega}/\omega$, and the curvature of vortex line $R = |\widehat{\boldsymbol{\omega}} \cdot \nabla \widehat{\boldsymbol{\omega}}|$.

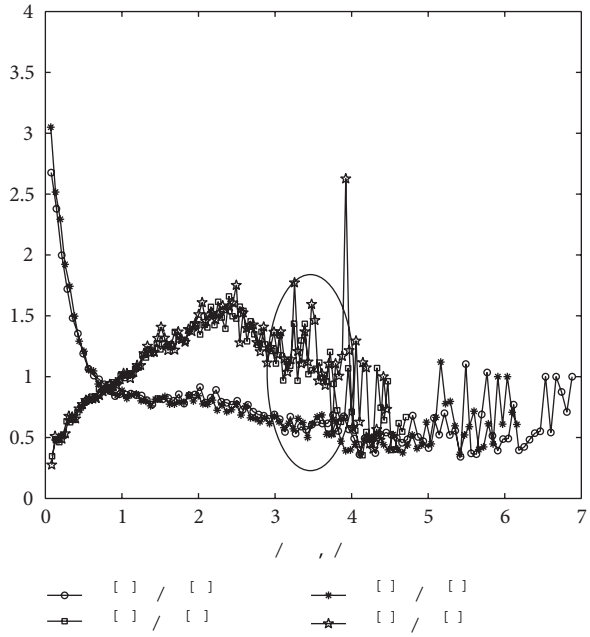

Figure 5: Conditional average of curvature in slots of $\omega/\langle\omega\rangle$ and $s/\langle s\rangle$.

So we get the conditional average of curvature R in slots of $\omega/\langle\omega\rangle$ and $S/\langle S\rangle$, as shown in Figure 5. It is seen that the curvature is decreasing with $\omega/\langle\omega\rangle$, and it is firstly increasing and then decreasing with $S/\langle S\rangle$. And also, the curvature of vortex line in the enstrophy dominated regions is smaller than that in the strain dominated regions (ellipse identifier in Figure 5). This suggests that vortex structures are distorted tempestuously in the strong vorticity/strain regions.

Also we consider that the conditional averages of enstrophy, strain, and dissipation rate conditioned on $e^{[p]}/\langle e^{[p]}\rangle$, as shown in Figure 6. It is clearly shown that these parameters firstly are increasing and then decreasing with $e^{[p]}/\langle e^{[p]}\rangle$, but mainly existing in the elastic regions where $e^{[p]} \approx 10\langle e^{[p]}\rangle$. In addition, strain is much larger than enstrophy in the polymer elastic energy regions, suggesting much well correlation between strain and polymer elastic energy.

In order to expatiate the distribution of enstrophy production, enstrophy viscous dissipation, and the polymer effect in the polymer elastic energy region, the conditional averages of these parameters are carried out, as shown in Figure 7. It is clearly shown that the enstrophy production and enstrophy viscous dissipation are firstly increasing with $e^{[p]}/\langle e^{[p]}\rangle$ and then decreasing with $e^{[p]}/\langle e^{[p]}\rangle$. But for the polymer additive, it always has a negative effect on enstrophy production in regions where $e^{[p]} \leq 10\langle e^{[p]}\rangle$ and sometimes a positive effect on enstrophy production in regions where $e^{[p]} > 10\langle e^{[p]}\rangle$. So it is sufficient to say that the strongest contribution of the polymer effect exists in regions where $e^{[p]} \approx 10\langle e^{[p]}\rangle$.

Also, we show the conditional averages of strain production, strain viscous dissipation, and the polymer effect in the polymer elastic energy regions, as shown in Figure 8.

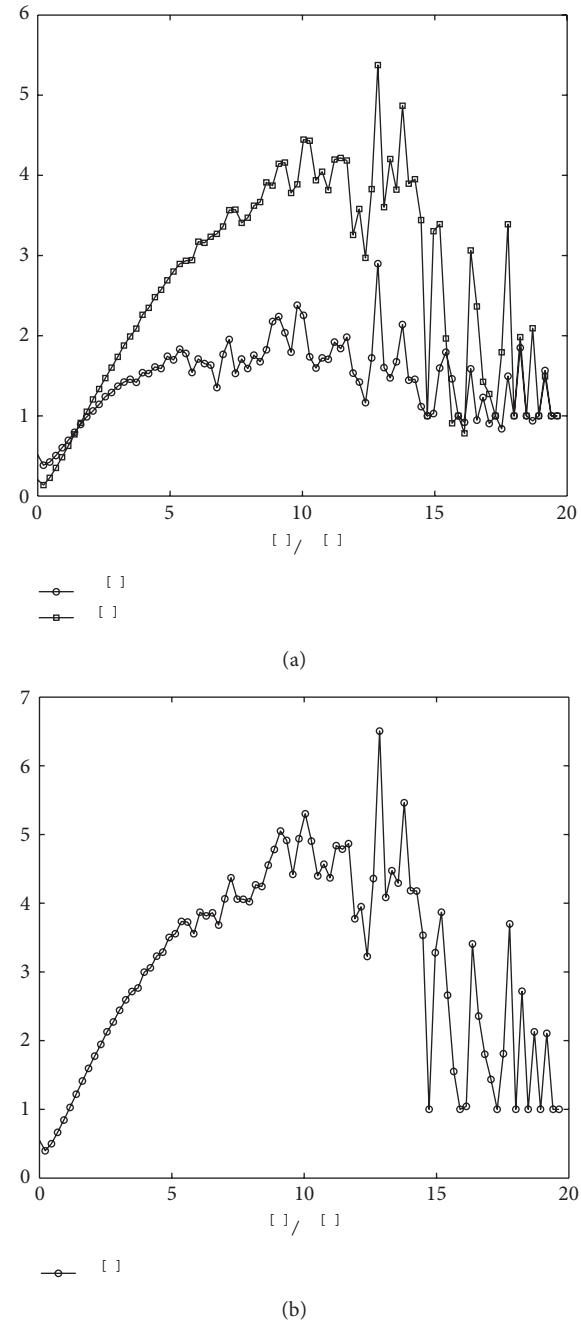

Figure 6: Conditional averages of (a) enstrophy and strain; (b) dissipation rate in slot of $e^{[p]}/\langle e^{[p]}\rangle$.

Compared with the results in Figure 7(a), it can be seen that the values of $2(S_{\text{str}} - W_{\text{str}})$ and V_{str} are much larger than the values of S_{ens} and V_{ens}. This indicates again the well correlation between strain and polymer elastic energy, which is consistent with the conclusion of polymers mainly stretching in strain dominated regions in our previous study [11]. The polymer additive always has a negative effect on strain, suggesting the inhibition of strain production by polymer additives. The value of conditional averages of P_{str}

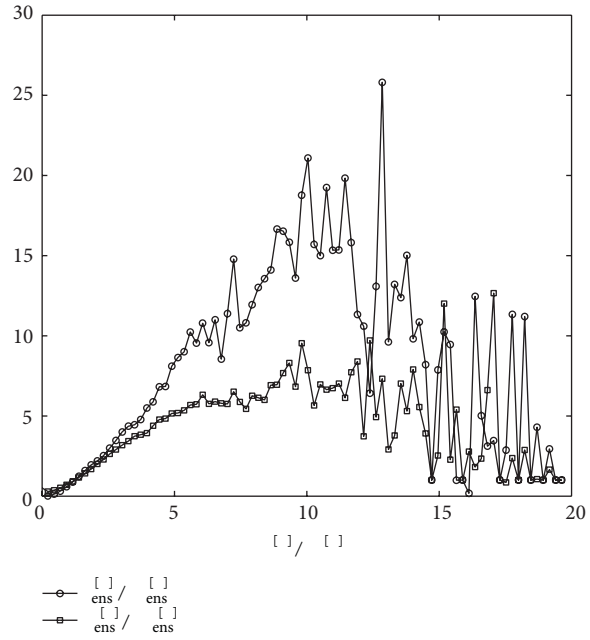

(a)

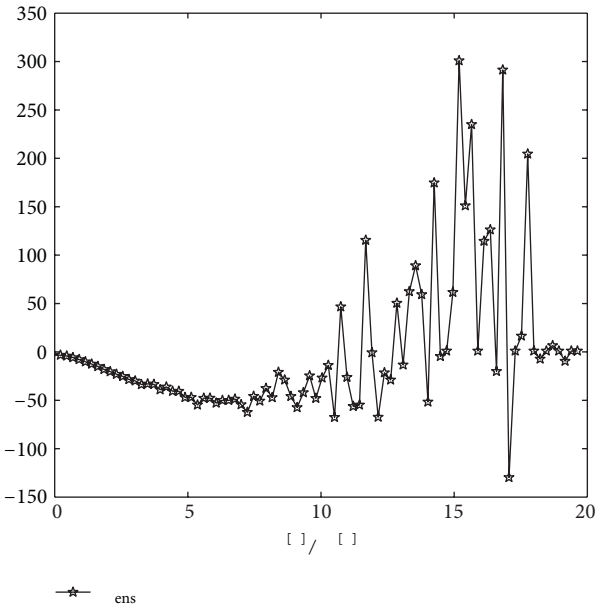

(b)

Figure 7: Conditional averages of (a) enstrophy production and enstrophy viscous dissipation; (b) the polymer effect in slot of $e^{[p]}/\langle e^{[p]}\rangle$.

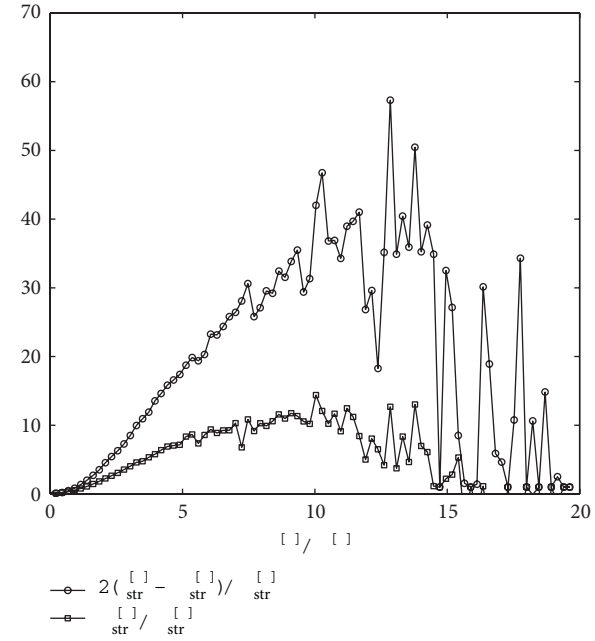

(a)

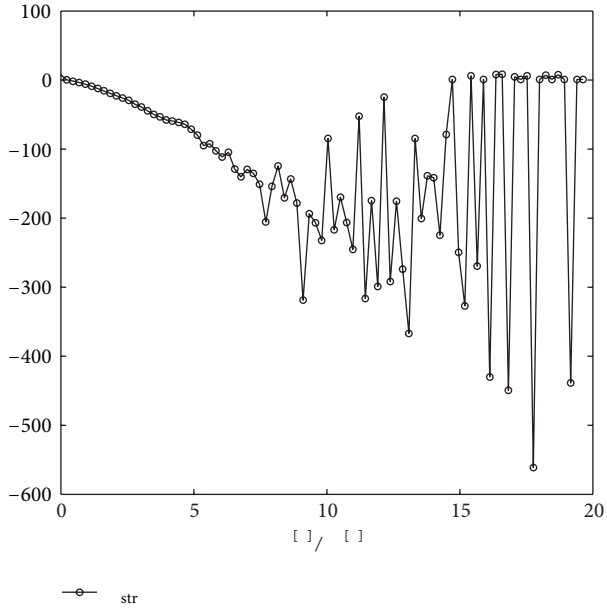

(b)

Figure 8: Conditional averages of (a) strain production and enstrophy production effect on the total strain and strain viscous dissipation; (b) the polymer effect in slot of $e^{[p]}/\langle e^{[p]}\rangle$.

is much larger than that of P_{ens}, indicating that the polymer effect on strain field is stronger than that on enstrophy field. Overall, polymers have an important and negative effect on enstrophy and strain fields. From this viewpoint, the nonlinear processes in DHIT of polymer solution are depressed due to the existence of polymer additives.

4. Conclusions

DNS of DHIT with and without polymers have been carried out based on Navier-Stokes equation coupled with FENE-P constitutive model. We investigated the polymer effect on the nonlinear processes based on the important parameters in the enstrophy/strain transport equations and the curvature of vortex line. Some important conclusions have been drawn as follows.

(1) The existence of polymers in DHIT only decreases the values of the important parameters in the strongest regions of enstrophy and strain. And also, polymers have a negative effect on enstrophy production and strain production, suggesting the depression of nonlinearity in DHIT with polymers.

(2) The curvature of vortex line in the enstrophy dominated regions is smaller than that in the strain dominated regions. This suggests that vortex structures are distorted tempestuously in the strong vorticity/strain regions.

(3) The strongest contribution of the polymer effect exists in regions where $e^{[p]} \approx 10\langle e^{[p]}\rangle$. And also, strain is much larger than enstrophy in the polymer elastic energy regions, suggesting much well correlation between strain and polymer elastic energy.

Acknowledgments

The authors thank Professor B. Yu of China University of Petroleum (Beijing) and Dr. Y. Yamamoto of Kyoto University, for their discussion on DNS. This study was supported by National Natural Science Foundation of China (Grant no. 51206033), the Fundamental Research Funds for the Central Universities (Grant no. HIT.NSRIF.2012070), the China Postdoctoral Science Foundation (Grant no. 2011M500652), and the Heilongjiang Postdoctoral Science Foundation (Grant no. 2011LBH-Z11139). The authors are also very grateful for the enthusiastic help of all members of Complex Flow and Heat Transfer Laboratory of Harbin Institute of Technology.

References

[1] R. H. Kraichnan and R. Panda, "Depression of nonlinearity in decaying isotropic turbulence," *Physics of Fluids*, vol. 31, no. 9, pp. 2395–2397, 1988.

[2] H. Chen, J. R. Herring, R. M. Kerr, and R. H. Kraichnan, "Non-Gaussian statistics in isotropic turbulence," *Physics of Fluids A*, vol. 1, no. 11, pp. 1844–1854, 1989.

[3] A. Tsinober, "On one property of Lamb vector in isotropic turbulent flow," *Physics of Fluids A*, vol. 2, no. 4, pp. 484–486, 1990.

[4] L. Shtilman, "On the solenoidality of the Lamb vector," *Physics of Fluids A*, vol. 4, no. 1, pp. 197–199, 1992.

[5] L. Shtilman and W. Polifke, "On the mechanism of the reduction of nonlinearity in the incompressible Navier-Stokes equation," *Physics of Fluids A*, vol. 1, no. 5, pp. 778–780, 1989.

[6] P. Sagaut and C. Cambon, *Homogeneous Turbulence Dynamics*, Cambridge University Press, New York, NY, USA, 2008.

[7] A. Tsinober, "Is concentrated vorticity that important?" *European Journal of Mechanics B*, vol. 17, no. 4, pp. 421–449, 1998.

[8] A. Tsinober, E. Kit, and T. Dracos, "Experimental investigation of the field of velocity gradients in turbulent flows," *Journal of Fluid Mechanics*, vol. 242, pp. 169–192, 1992.

[9] A. Tsinober, M. Ortenberg, and L. Shtilman, "On depression of nonlinearity in turbulence," *Physics of Fluids*, vol. 11, no. 8, pp. 2291–2297, 1999.

[10] A. Tsinober, "Vortex stretching versus production of strain/dissipation," in *Turbulence Structure and Vortex Dynamics*, J. C. R. Hunt and J. C. Vassillicos, Eds., Cambridge University Press, New York, NY, USA, 2000.

[11] W. H. Cai, F. C. Li, and H. N. Zhang, "DNS study of decaying homogeneous isotropic turbulence with polymer additives," *Journal of Fluid Mechanics*, vol. 665, pp. 334–356, 2010.

[12] W. H. Cai, F. C. Li, and H. N. Zhang, "Direct numerical simulation study of the interaction between polymer effect and velocity gradient tensor in decaying homogeneous isotropic turbulence," *Chinese Physics B*, vol. 20, no. 12, Article ID 124702, 2011.

[13] K. Kim, C. F. Li, R. Sureshkumar, S. Balachandar, and R. J. Adrian, "Effects of polymer stresses on eddy structures in drag-reduced turbulent channel flow," *Journal of Fluid Mechanics*, vol. 584, pp. 281–299, 2007.

[14] K. Kim, R. J. Adrian, S. Balachandar, and R. Sureshkumar, "Dynamics of hairpin vortices and polymer-induced turbulent drag reduction," *Physical Review Letters*, vol. 100, no. 13, Article ID 134504, 4 pages, 2008.

)JOEBXJ1VCMJTIJOH$PSQPSBUJPO
"EWBO DFTJO.FDIBOJDBM&OHJOFFSJOH
7PMVNF "SUJDMFT*%
IUUQ EY EPJ PSH

3FTF BSDI " S U J D M F

6 OEF ST U B OE J O H PG 5 I F S N B M$ P O E V D U

9J B P E P O H 4I B O B O E . P S B O 8 B O H

%FQBSUNFOUPG&OHJOFF SJOH.FDIBOJDTBOE$/.. 5TJOHIVB6OJWFSTJ

$PSSFTQPOE FODFTIP VM ECF BEESF TTFE UP.PSBO8BOH NPSBMXBOH

3FDF JWF E /PWFNCFS 3FWJTFE %FDFNCFS "DDFQUFE

"DBEFNJD&EJUPS 4IVZV4VO

$PQZSJH IU" 9 4I BO BOE.8B OH J TJTB OPQF OB DD FTTBSUJDMF
-JDF OTF XI JDIQFS NJ UTVOSF TU SJDUFEV T F E JTUSJCVUJPO BOESFQSPEV
DJUFE

8FTU VEJFEIFBU DPOEVDUJPOTJ OBUIJOHBTMBZFS BUNJD SP BOEOBOPTDBME
UIF,OVETFOO VNCFSJTIJHIXIJMFU IFHBTNBZC FOPU SFBMM ZSBSF FE XE
GPS TJNVM BUJ POT FU IFS NBMDPOEV DUJWJUZPGU IJOH BTMBZ FSJTSF EVDFE
FYBN JO FEBGFXQPTTJ CMFDBVTFTJODMVE JOHUIFSB SF FEH BTF FDUBOEU IFU
UIF UFNQF SB UVSFKVN QPOXBMMTVSG BDFTBO EUIFQSPQFSU JFTDI BOHJOHTJ
UPUIF UIFSNBMDPOE VDUJWJUZS FEVDUJPOPGUIJOHBTMBZFST

*OUSPEVDUJPO MB SHFT DBMF F M JUBF TEBFNPVOSTFS<BUFE
OBUVSBMD POWFDUJPOJ TOFHM JHJCMFB
8J U IUI FSBQ JE E FWFMPQNFOUTPG NBJSM SPPJ NV MBBUOJPPUF DXIQJE MNPFHBJFTUI
G PSGBCS J D BUJPO BO E NBO V GBDU VNJESPEF BJ NBTD BXHFEN FEOPUQMMDBZTJ B
B NPS FBO ENP SFJ NQPS UBOU SPM F4JFOSGBVE SEUJTDKVS TETFFWEFUMIFQ NFFDOUPTH B T
P G .& . 4 / &. 4 ' PSB OFYBN QDMPEPVGBUNEOD XIPPNTEUD FEJSOFFUE DBMQ S F
1JS BOJ T>F OJTUPTSNF< D I BOJ TN JT U DPMOE BJTDV SVNFBUOEEUHFEGTSFFN PMFDVMB S S F
QSFT T VSF CZ TF O TJ OHUI F UI FSN BXMBTJFOWEBMJDEJUQUWSJBUZTPUGUHJPQDSQPQBMSJNE
U IFNJD S PC FBN NJD SPQ MBU FT FBSOFRX PTSMEUGNPSEJFNMQESP WTMJNQF OPXTPTU
BDDV SBD ZPGTVDIEFW J DFT VOE F S STFUHBJNE JEOFHWPFSMPIQFEBBUODBPOBMEZUJDDBJMBQ
DIBSBDUFS JTUJ DTBUNJD SP BOEO BTUFBEZ BTMUFBTUCIFFDBF NFO TEWDFUSJZQUJNQTE
UBOU *OSFDFOUZFBST UI FT UPSBH FEJTBDVBT DEUUZHPFGFIDBUSQEQE BSTULJEBMSMJZWUFIS
DPOU JOVFTJO DSFB TJ OH G PSJOT UpBOOUDIFFUI FBUSDFPDEVS EJJPOOHJEOFUSBTOJTUJZU
I BTBQQ S P BDIFE UXP JD5ICMJFUBE TUOP BUT JFHNOCJZ %4.B$T UNVMBUJPOT / FWFSUI
EFDS FB TFP GUI F ZJO H IFJH IUP G UJOEJTMU E,FSVEPTBFQQSSF PHYJJNFBDBEMZM
OoN <# F DBV TF PGU IFIJ HI IF B UBDDVYSBUF OET WFUSZBQHSFPIEFVBDUFEEV YE U%IFFOI
C ZI JHIG SJD UJ PO CFU XF F OUIF ZDJFOOHEVDM JUE FOSJBOOBEHB DQCFSUXFB EUOXGBGF
EJTL U IF BOPNBMP VTI F BU DPOE V D U%SP SOFP GEU HBTHQBSTPCIMFNOTMTBZOH$4O$
CF U XFFOS FTUS JDU TB DUVB MJNQ SP W F GNHFBCTTUQTFDPJGFTTU TPVSSGBHDFFDBFQNEQFDSJBUUZVPS
IB SEE JTL "EEJ UJP OBM MZIF BUN BDOF HDF NFOOUPTDIBFOBEUQDFOGCVDSJNBOO DXFI
PQ UJNJ [BUJPOTGPSFMFDUSPOJ DJO UUFHFSJEFSNBMDJPSEVVDUJUWDJUZEQFDEMFNEGB
B TXFMMDMFBSVOEFSTUBO EJOH TP GDIBOTJUTUSFBOUXTJQUPISUINFYDUIFBGE>T4NPR
HBTMBZFSTB UNJDSPoBOEOBOPTDBEXMFWF<SUIFJ SSF TVMU TX F SFGPSU
FSFGPSFIFB UUSBOTGFSBUNJ D SJPI FNJDOSBPOBPOTEDOBMQFPTIDBMTCHFBFTO
PGH SFBUJOU FSFT UT JOU I EQ BcT UTUIFROXZOJEBISBTUU< I FN F DI BOJTNP GHBT
>)FBUUS BO T GFS JOU IJ OH BT MB ZNFJSDTSEPJ BCF SCTEGSPPTNDUBMI BFNJBHUI UCE


L
T1

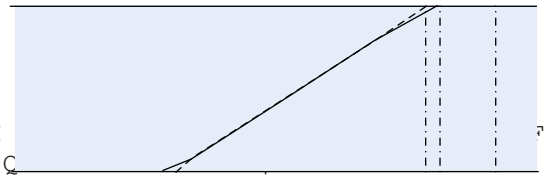
T1
T2

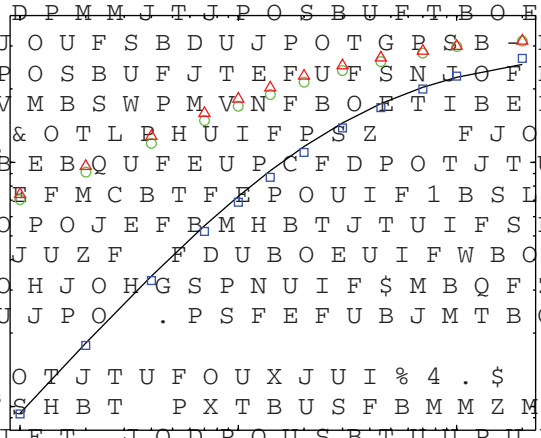
Thermal conductivity (W/mK)
10^-2
10^-1
10^0
10^1
10^2
10^3
Characteristic length (nm)
Simulation
Theory
k
k

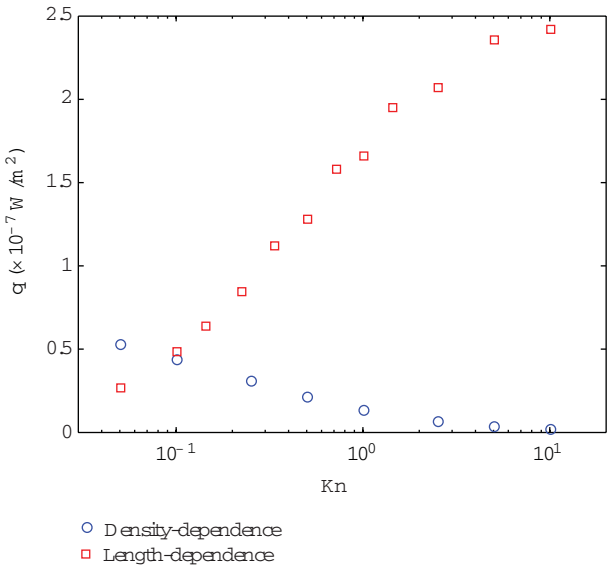
2.5
2
1.5
1
0.5
0
10^{-1}
10^{0}
10^{1}
Kn
q ($\times 10^{-7}$ W /m^2)
Density-dependence
Length-dependence

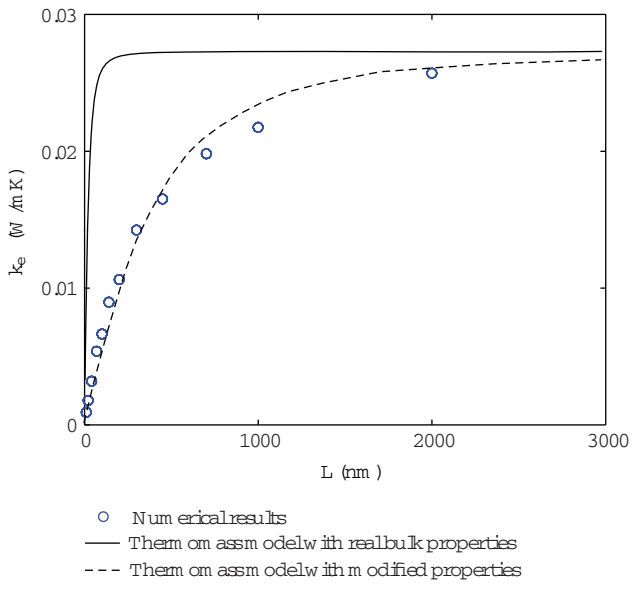

B

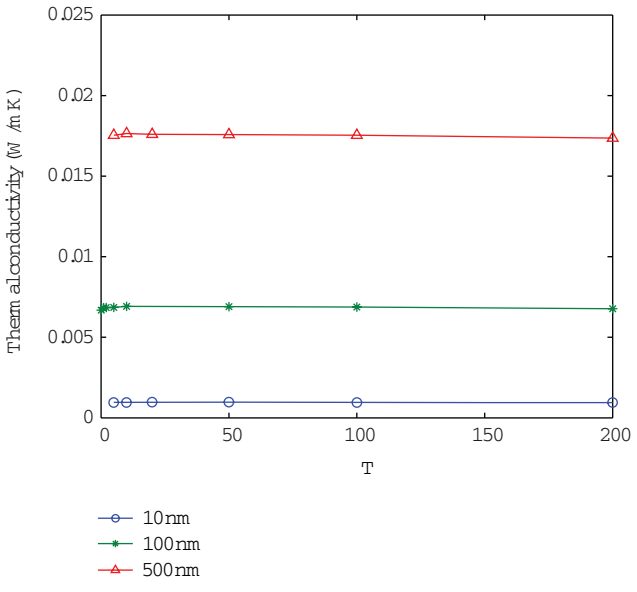

C

' 6 4 B $ 2 P N Q B S J T P O T X J U I U I F U I F S N P N B T T N P E F M B & F D U J W F U I F S N B M D P O E V
O V N F S J D B M E B U B C Z (& . $ B O E U I F M J O F T B F J F T C B M D F V E P U B D E E X B J O U E F ! S N , B N O E T T N
! , F S F B M Q S P Q F S U J F T V T F E J O U I E H U I N ! S N P & N B N T ! T ! N P + E F I M H B F S H F O + > ?
F N P E J F E Q S P Q F S U Z V T F E $ O U C I F E F B D T U J W F E U M F J S N E F M D P O E V D U J W J U Z B T B G V O D U J E
E J F S F O U D I B S B D U F S J T U J D M F O H U I T

U I F S F T V M U T P G (& . $ T Z N C P M T D D E P N E Q V B S J F E C X J C U I L J Q H S B F M E B Z D F U S J U P I O F T E J
G S P N U I F U I F S N P N B T T N P E F M V T J V C T H T U P N F R C S T F Q M S Q B S U F P Q F S U F J P E M T Z P E S J F
N P E J F E Q S P Q F S U J F T M J O F T & W U F D F U U I J P V M B I Z C F P S U B D E U U I F B C U V N B F C S V J M D L B G M S
T J N V M B U J P O T B O E U I F U I F S N P N B T T Q Q B S D F E Z U D I U F D M P D T E E U F X D P M J B O M M X J U F I D E
U I F E F D S F B T F E U I J D L O F T T P G H B T M U B I Z F F H S B T Q U S H Q F Z S E J F W T J U B E F F W G J B U P F N G F S B P D N I U
P U I F S T J H O J D B O U M Z) P X F W F S J G X ' F N E P E S T U T F U E F Q I U F I T Q E F T D L J J O E D U J F D B U U I
D B Q B D J U Z C Z B N V M U J Q M J F S P G U D I P E D E U V D I U F J P W S J F U U I Z J P D G B $ M B N T P C E X E F M J S T E F S F F T
X J U I U I F O V N F S J D B M E B U B X F M M B E T U F D I F J E W F T E I J F N E C M U I J J O E F F N I F C E V P W N X F C M E P S G F Q U Z
U P O P X O P U I F P S Z P S F Y Q F S J N F O U B N P E M E B D V B M B B S T N E B M O B G S S F F Q E F U E I U ' E B U I U E H E F M
T Q F D J D I F B U D B Q B D J U Z P G H B T B U T N N E P M E M D T V M B B S M W F F E M F D J S U F Z B B O T E T T Q U F E J D I P F G
J U T W B M V F B U O P S N B M T D B M F F S F G G P E S B J H U J W F O T U U F J N M Q M F E S E D U V B S M F M E O C E H E U F P
D P N Q B S F U I F U I F S N P N B T T N P E F M X E J U F I S U N I J F O O F V E N Z F U S I J F D N E P M E E B V U M B G S N S F B O
U I J O H B T M B Z F S Z F U F Y B N J O F U I F W B S J B U J P O P G N F B O G
" O P U I F S J N Q P S U B O U J O G F S F O D G F S P F G F U Q I E F U U I U F O S B D P O G F T E T N Q P B E D F J M T D B M
J T U I B U U I F F F D U J W F U I F S N B M D E J O T U E V O D F U W S V J B W E M M G E U C Z J B O N M P W E Z H F Q S B S U
T I P V M E E F D S F B T F X J U I J O D S F B T J O H X U E I N F Q U E I S F B S B O V P S U E H F S Q B B E S J U E U O M U F E V S E U U I E
U I F F O I B O D F E U I F S N B M J O F S U J B F D M P F T E U S U I F I S P F M G E F J S P F O X Q F E D T I T J F C D J L M F J E U Z
T V D I F F D U T C Z P V S B U P N J T U J D T J X E V M M T B J U O D J S P F O B T T F ' T P S U I S F F H J W F O
U I J D L O F T T F T P G U I J O H B T M B Z F S T X ' E U E I V S B O E H P N Q E B U S E F T U X N P Q P M E S D B V M V S S E U S
E J F S F O D F X I J M F L F F Q U I F B W F S B H E E U F F S N F Q U F U S B J U D V L G S F E T T B G H B O T M T B Z B F O S U
B U ! , ' J H V S E O E J C D B U F T U I B U U I F F O F N D U I J E N F P M F D V M F N P W F T M J L F
U I F S N B M D P O E V D U J W J U Z P G H B T M B Z U E I S F X J B T M E T M J N O P T V U F O D O F E J F U Q T E N O E W F N O F U O P U G T
U I F U F N Q F S B U V S F H S B E J F O U X I J M B Z I F S U F I W J D B O U F F T T J B T H D M B P J T O F G U S P U P I N F U I E F P S
U I F S N P N B T T N P E ' J H M V T S V E H S F F T G U E S J E N E B M F D V M F T D P M M J E F X J U I U I F X B M M G S E
N F D I B O J T N P G T D B M F F F D U P G U I F S U N S B W M F D M E B T E C V B D M U M J V S T E U U P Z O C P X G B I Z B I U U O E H N B P T
M B Z F S E P F T O P U S F M B U F U P U I F U I F S N B N M E J O O G S S F E Q J B E U I E P G S H U B T J F O U I F E S J O M M B E T F
N P E F M I B T U P C F T J H O J D B O U M Z E F X W E M U P I Q F F S E E G V V D S F U E U E J S D G P O S F T V T D P G B I E
D B T F Q B U I P G H B T C F U X F F O X B M M T J T D M P T F U
T Q B D F X I F O U I F U I J D L O F T T P G H B T M B Z
& F D U T P G $ P M O U I O P F V H E I 4 U Q I E F U D F F S F N S E M G E T F F S N T D P O T J T U F O U X J U I U I E
U J B T F F N T O P U I J O H U P E P X J U I U X I F J T D D I B N E Z T F V H E E T U U P G I J B U I F S N D B I M B O H

" E W B O D F T J O . F D I B O J D B M & O H J O F F S J O H

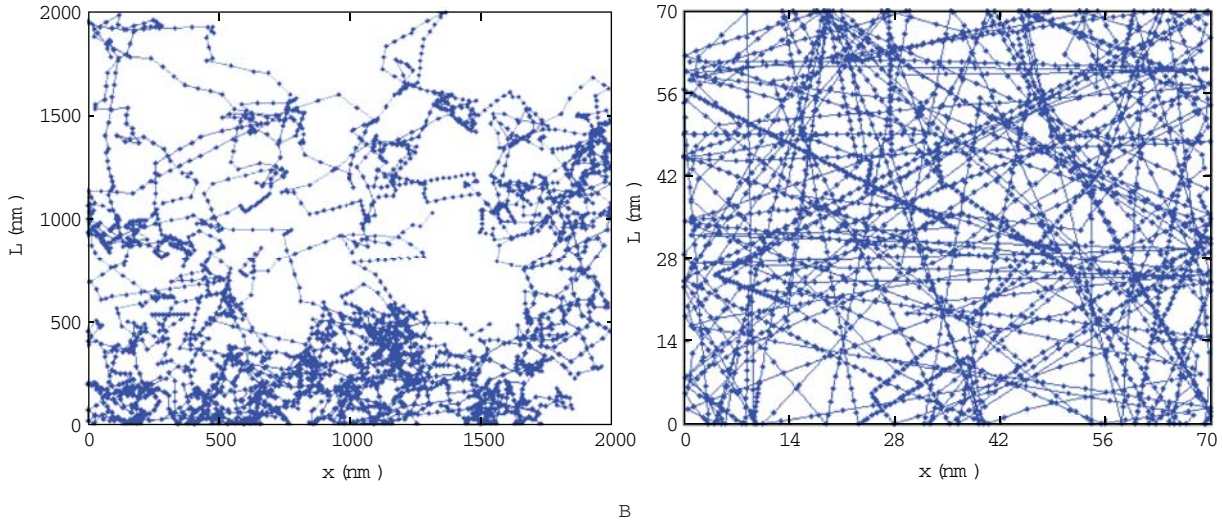

B

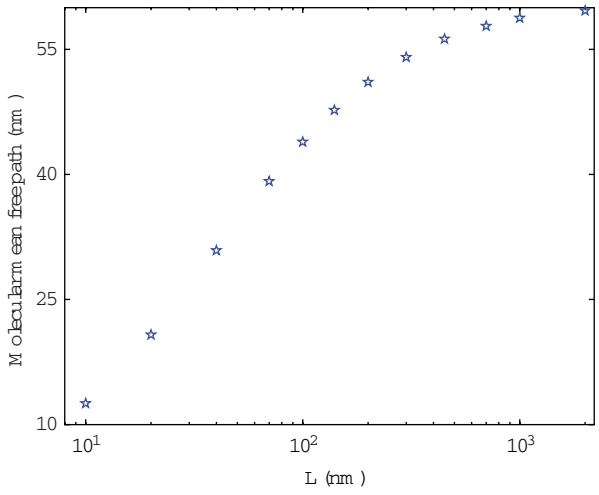

C

' 6 4 B 4J2[F F F D U P G H B T N P M F D V M B S N F B O G S F F Q B U I J O U I F U I J O M B Z F S B .P M F D V M B
F M F Q B O F M J T G P S O N B O E U I F S J H I U Q B O F M J T G P S O N M B Z F S F T Q F D V M B
J O E J D B U J P O P G U S B K F D U P S J F T C V U U I F Q F S J P E J D C P V O E B S Z D P O E J U J P O J T J N Q M F N F O
U I J D L O F T T P G H B T M B Z F S F X B M M ! U F , N B Q O F E S B ,U V S F T B S F H J W F O B U

Q B U I N B Z C F P O F P G U I F L F Z S F B T J K O D S T F G B T P J S O U H T I J H T O D J B M B K O F U M Z F X D J U U P I G U I F B
F F D U J W F U I F S N B M D P O E V D U J W J U Z U P I G F U H B J T D M L B O Z F F T S T P G U I F H B T M B Z F S &
* O D P O W F O U J P O B M L J O F U J D U I F P U S I J D E I G B F O T E J U T M F B S S N H P E S Z O I B B O N J J T D U T J O M N M
U I F T Q F D J D I F B U D B Q Q M B Z E E J Q U E Z O E F O N U V P D G I U J F H N I Q F S U S I B B O U I F W B M V F B U M B S H F
U V S F / P P O F I B T S F Q P S U F E B T D B M T F P B K Q Q S P D U I J F E Q F S N B M W I B M V F
D B Q B D J U Z P G H B T J O B U I J O M B Z F S Z F U * O P B T F E P P O U J D U E F F N S B Z O < W P M O P P G J
$! % œ $ X & U œ S I F Q S F T F O U J O H U I F J O U F S O B M E O F S H Z X F N P M F D V M F T J T P O M Z B G V O D U $ J P 3 5 P G U F
D P V M E D B M $ O Z M B U F 8 I F O U I F H B T N P M F D V M F T D B O P O M
T Q B D F C F U X F F O U X P D M P T F X B M M T U
N P M F D V M F T J T B M T P B G V O D U J P O P G U I
E J T U B O D F B J T H T V S P X O F C N O F B O W F M P D J U
N P M F D V M F T B S F D B M D V M B U F E C Z B W F S B H J
J O U I F E P N B J O F S F T V M U J O E J D B U F
O F T T P G H B T M B Z F S M F B E T U P B M P X F
N P M F D V M F T
U I J D L O F T T P G U I F H B T M B Z F S % J F S F O U G S P N E F T D S J Q U J P O P G
U I F D P O W F O U J P O B M L J O F U J D U I F P S Z U " I T F S F Q T F V D M U U D I F F B E D U E W Q F B U D I J F U S Z N J F
E S B N B U J D B M M Z D I B O H F E C Z U I F D P O D B M D V F M E T Q F E C B T C F P U X F E $ L O Z X O M M T D U

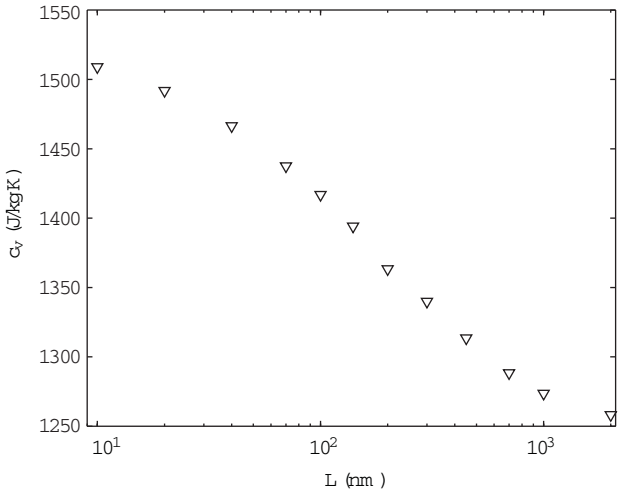

B

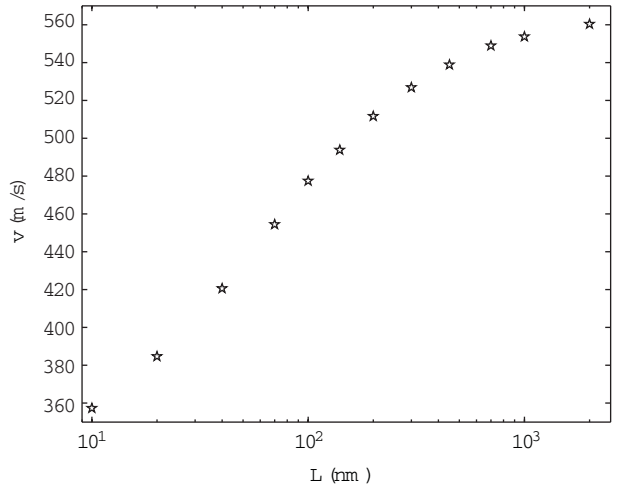

C

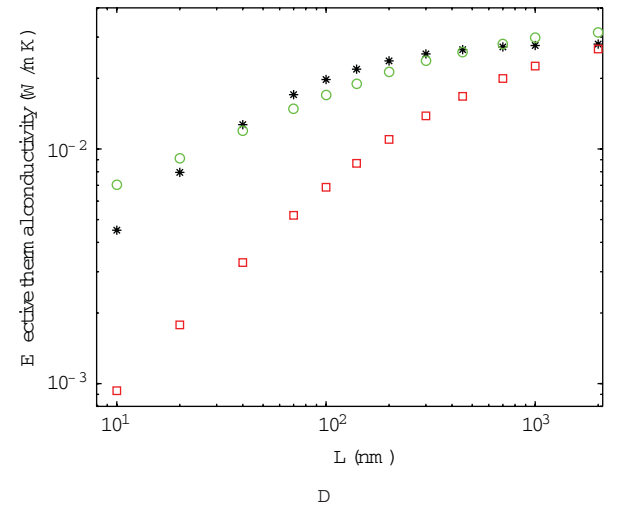

D

S F Q S F T F O U J O H U I F F F D U J W F E J N F O
E J N F O T J P O B M (& . $ N P E F M ! J X I H J J M O F U I
U I F T U V E J F E D B T F T B S F B D U V B M G M P Z S P O F
Q F S J P E J D C P V O E B S J F T P O M F B O E S J
B E P Q U ! F D M F D U J D ' B H M V S Z J P S U I F P S F U J
Q S F E J D U J P O U I F T U B S T J T N F U I P E
O P U T P S J H P S P V T C V U T V S Q S J T J O H M
Q S F E J D U J P O T X J U I U I F B E B Q U T U H B T
D P O O F E T Q B D F B H S F R V J U C V M E M S M X B J M U
D P O E V D U J W X J U F Z S F U I F T V S G B D F U F N Q R
F Y D M V E F E

$ P O D M V T J P O T

F N F D I B O J T N P G U I F S N B M D P O E V D U
B U N J D S P O B O P T D B M F I B T C F F O O V N F S
H F O F S B M J [F E & O T L P H . P O U F $ B S M
F F D U J W F U I F S N B M D P O E V D U J W J U Z E F D S R
S F E V D F E U I J D L O F T T P G H B T M B Z F S 8 I
X B M M T J T B T T N B M M B T N J D S P B O E O B O R
B O E U I F U F N Q F S B U V S F K V N Q P O T V S G B D
T J N V M B U J P O T J O E J D B U F E U I B U U I F F F D
T U J M M E F D M J O F E T J H O J D B O U M Z X J U I U I R
J G U I F U F N Q F S B U V S F K V N Q X B T F Y D M V E
U I F U F N Q F S B U V S F K V N Q X B T O P U U I F P O
F F D U B C V M L F S N B M D P O E V D U J W J U Z P G H R
B M T P D I B O H F E 8 F U I F O F Y B N J O F E U I F
U J B C B T F E P O U I F U I F S N P N B T T N P E F M
T U J M M O F F E F E G V S U I F S E F W F M P Q N F O U G
' J O B M M Z X I F O D P O T J E F S J O H U I F F F D
P O U I F H B T F F D U J W F Q S P Q F S U J F T X I
Q B U I P G H B T T I P X F E U I F T B N F W B S J B U J
U I F S N B M D P O E V D U J W J U Z F T Q F D J D I
N P M F D V M B S W F M P D J U Z X I J D I X F S F H F O F
P G T J [F J O D M B T T J D B M L J O F U J D U I F P S
B M T P W B S J F E X J U I U I F D I B S B D U F S J T U
N J D S P B O E O B O P T D B M F T Q B D F F S F T
H B T F F D U J W F Q S P Q F S U J F T X I J D I X F S
U I F D P O O F E T Q B D F C F U X F O X B M M T B M
D P O E V D U J W J U Z S F E V D U J P O P G U I J O H B

" D L O P X M F E H N F O U T

J T X P S L J T O B O D J B M M Z T V Q Q P S U F E C Z
*OJUJ BU JW F 4DJ FOUJ D 3F TF BSD I 1 S R
B O E U I F T U B S U V Q G V O E J
1 S P H S B N P G (M P C B M : P V O H & Y Q F S U T P G

3 F G F S F O D F T

< $) . B T U S B O H F M P B O E 3 4 . V M M F S i .
B C T P M V U F Q S F T T V S F T F O T P S X J U I P O D I J
' 6 4 B & 2 F D U J W F Q S P Q F S U J F T P G H B T M B Z F T S D
T Q B D F B) F B U D B Q B D J U Z W F S T V T U I F U I J D L O F T T P G H B T U I J O M B Z F S
C H B T N P M F D V M B S N F B O W F M P D J U Z W F S T V T U I F U I J D L O F T T P G H B T U I J O
M B Z F S D F F D U J W F U I F S N B M D P O E V D U J W J U Z D B M D V M B U E E C Z U I F L J O F U J F
U I F P S Z T U B S T D P N Q B S F E X J U I U I F N P E F M J O H S F T V M U T V T J O H E J F S F O U
U F N Q F S B U V S F E J T R V F B S S F O D U S B T O B D U J P W F M O .

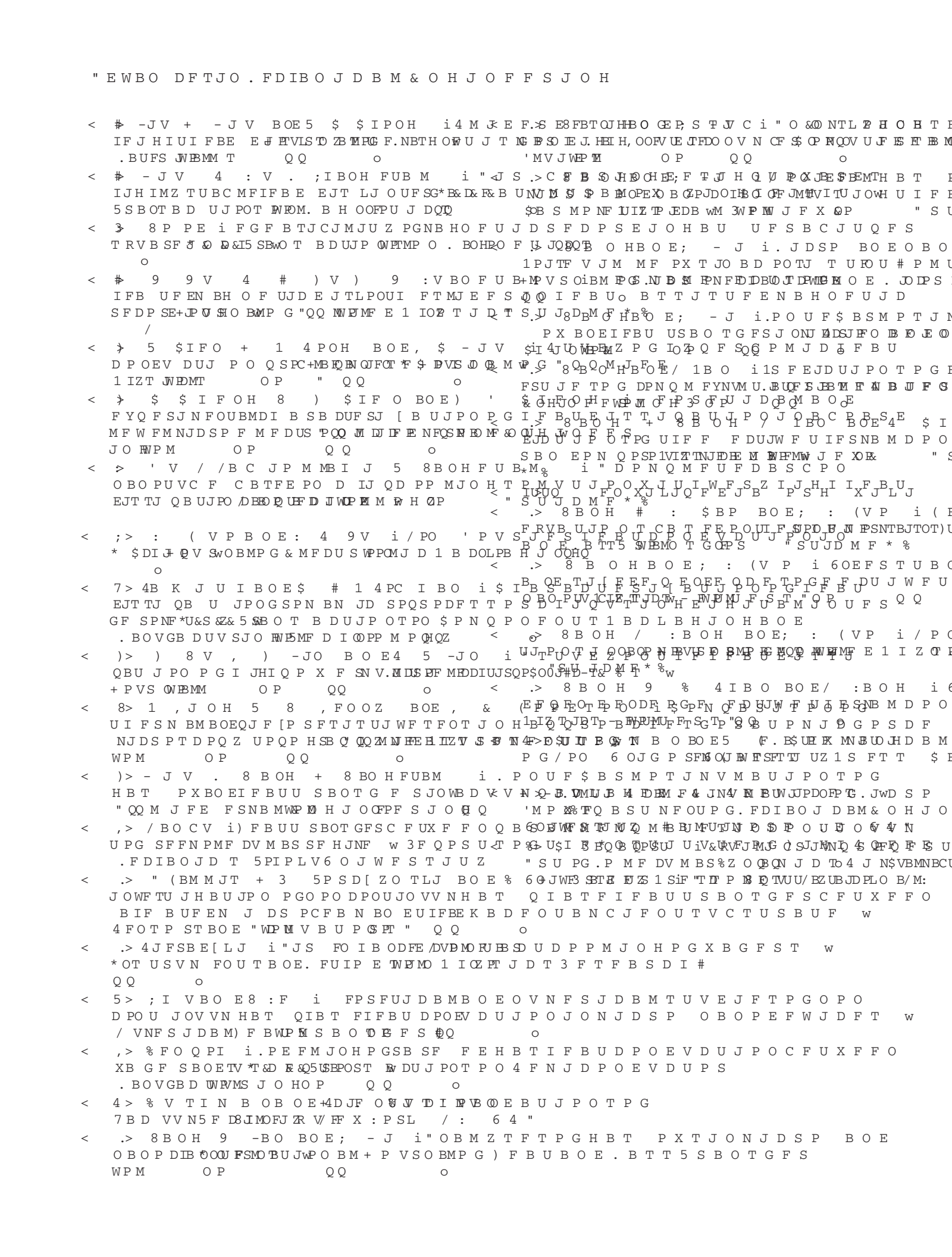

)JOEBXJ1VCMJTIJOH$PSQPSBUJPO
"EWBODFTJO.FDIBOJDBM&OHJOFFSJOH
7PMVNF "SUJDMF%
IUUQ EYEPJ PSH

3FTF BSDI " S U J D M F

" .PEJ[E.FPEF M G PS$ PNQ V UB U J P O P G '
-B SHF 4U S F BNMJO F $ V S W B U V S F

+VO -JB%F:J;OI PO H8 B-JHD8 W% ,FJUI8 BMUFST

4DIP PMPG.FDIBOJDBM&OHJO FFSJOH 4IBOHIBJ+JBP5POH6OJWFSTJUZ
4UBUF,FZ-BCPSBUPSZPG)ZESPTDJFO DFBOE&OHJOFFSJOH %FQBSUNFOUPG
#FJKJOH $IJOB
%FQBSUNFOUPG.FDIB OJDBM&OH JOFFSJOH .JTTJTTJQQJ4UBUF6OJWFSTJ

$PSSFTQPOE FODFT IPVME C FBEESFTTFEU P%F ;IPOH8BOH E[XBOH!

3FDFJWFE 0DUPCFS 3FWJTFE %FDFNCFS "DDFQUFE

"DBEFNJD&EJUPS #P:V

$PQZSJHIU" +VO -JBO:JOFU BM JTJTBOPQFOB DDFTTBSUJDMFEJTU
XIJDIQFSNJUTVOSFTUSJDUFEVTF EJTUSJCVUJPO BOESFQSPEVDUJPOJOBO

JTQBQFSQSFTF OUTBOJNQSPWFE NFUI P EGPSJODMVTJPOPG TZTUFNSPUBU
FRVBUJPOFEEZ WJT DPTJ U ZU VSCVMFODFNP EF MT "OFXGPS NV MBU JP OG P S D B
JNQMF NFOUFJOUPU¤NPEFSMEXEJUIUBJUX2D MBZ FSOFBS XB MMUSFBUNFOUJOBDP
TPMWFS JTQSPQPTFE *ODPOU SBTUUPQSF DJPVTNPEFM UIFNPEJ FESPUBUJPO
DPF DJFOUJTIFSFJOF YQSFTT FEFYBDUMZBOEVOJWFSTBMMZ VT JUQSPWJE

*OUSPEVDUJPO

UIFQIZTJDT FODPVOUF SFEJOQBSUJ
NPSFDPNQMFY 'PSFYBNQMF JONBC
FVTF PGDPNQVUBUJPO BM VJEFZ$'% GPSSQSFE
EJD UJPOPGDPNQMFY PXTIBTC SPVHFHBCDVUVCTUBOUBMM
JNQSPWFNFOUTJOBOBMZTJTGPSUIE EFTJHOPGJOEVTUSJBMQSE
VDUT 'PSIJHI3FZOPMETOVNCFS FEEZ-WJTDPTUUZNPEFMT
PGUIF$'%NPEFMJTUIFUVSCVM OBOFPSUUPNFSFBDDVSBUFMZSFT
FYJTUJOHUFDIOPMPHJFT EJSFDUQOVNFSJDBMTJNVMBUJPO %/4
BOEMBSHFFEZTJNVMBUJPO -&4 UIBUNPSFBDDVSBUFMZQSFUJDUUIF
DPNQMFUFNPEFMJOH BQQSPBDIFTVTFEUPQSFEUDUUVSCVMFQU
PXT)PXFWFS UIFTFNFUIPETSFRVJSFTJHOJDBOUDPNQV
UBUJPOBMSFTPVSDFT JODMVEJOHCPUINFNPSZBOEQSPDFTTJOH
QPXFS BOEDVSSFOUFTUTUVMBUFUTUCLZ4UQJBUMBSU<
XJMMCFTFWFSBMZFBST JGOPUEFDBEPNQOQOFQUTODBMFWBOUBHEUPNUIF
WJBCMFBMUFSOBUJWFTGPSBO BMZTJTPGMBSHFDVSWBUVSFBOE
FMETGPSJOEV TUSJBMEFTJHOQVSQPTT3FZOPMETBWFSBHEE
/BWJFS 4UPLFTNFUIPET 3"/4 BSFUSFGPSFNPZ
VTFEJOQSBDUJDFBTB DPNQSPNJTFCFOXFDPNQVUBUSJBMBQMJ
FDJFODZBOESBTPBCMFBDDVSBUFMZ3NDPVOUBOEDBMJOH
NFUIPET UXP FRVBUJONFEEZ WJTDPTJUUZNPEFMT UIFUUBOEBSE
¤NPEFM BSFUIFNPTUQPQ VMBSBOEIBWFCFMPTIIFP#PVTTJOFTR
UPQSPWJEFUIFDBQBCJMJUZGPSFOH JOFUVSGVMFOUFWSFMQTDPNEQPOUOJUPTOU
)PXFWFS UIFTFNPEFMTTV FSBSUVSEVDJOHBDDDIZBBDDIZBBDUF

"EWBO DFTJO.FDIBOJDBM

UIS PVH ITDBM BSUS BO TQ P S..U W B S JUBSCFMFFETJTNVFOTIJBPDB MF FD UTBOETUS P
FF FDUP GS PUBUJ POBOEDVS WB U V MSMF UP DFO VNSFCSVDMBFMO TDJFNEVZMOBBUNJPDT I
J T E V FUP 3FZ O PMETT US F T T BOJT P UBSWBRJQEZCMXFEYUQDFSJJNFOOUBUMEEJBSUBBBUWMBZ M
JODMV EFEJONPTUTDB MBSF EEZ WJ TPXBPOTEUVUSZCNVMFOEDFMRTV B%OVFJUPJUETF
MB DL PGBOZEJSF DUTFOTJ UJ WJUZPGUIFTFUPTUSFBNMJOFDVSWBUVS
B OESFGFS FODFG SBNFS PUBUJPO N P T U Q P O V M B S F E E Z W J T D P T J U Z
N PEFMTM J¤IN PEFIMFBNDEE F MN B ZMF B E U P M B S H F
FSSP S TJOUI F QS FE J DUJPO PG DP N Q MFBYJTBXTPJQUZVBSUODOTBHNSQ TSVDTTBTCM
UIPTF FODPVOU FSFEJOUVS CP N B D I FYQS FTTFEJOUFSNTPGUV S CBMEFUOIUFL
4FWFSBMSF TF BS DI F STIBWF BUU F NFQZUOPMEETTPUJSOFDTPTSUQFOSTBSBQTI Z T
JDB MMZSFBMJ TU JDSPUBUJPO BO EDVS WBUVSFTFOTJUJWJUZJOUPTDBM
FEEZ WJ TDP TJUZN PE FM T * O J U J B M M Z U I F T F#¥F S F C B T F E P O B E
I P DN PEJ DB UJPO TUPUIF N P E F M G P S N V M B U J!P O T§ B O E J O N B O Z
DB TF T EJEO PUT BUJTGZNB UIFNBUJDBMJOWBSJBODFQSJODJQMFT B
OFDF TT BSZDPOEJUJPO GPSH FOFSBMXIQ¥S QPTF,NSPPEOFMDJLPSENFMUBI P EFTB
.PSFSFD FOUMZ N FUIPETI BW FC F DFOOE EJWOFSMFMQFWF B XOUJJODGPSNBUJFPNQPUO U
UPJODPSQPSBUFUIF BEWBOUB HFTP GBCOPEUNIVFTEEFZF WBJMVTBPFEBTUBZGWODEEFMT
T JNQMJ DJUZ D PNQV U BUJP OBMF JDJ EIOPTZN VBMEJ3JPZ O PSMMEJTOFBSSFFETETZ
NPEFMT QIZTJDBMMZ DPSSFD USF TRQORTDPTUSHPZDUMOSTMSBUTNJSSFFBUMEZSFMUBF
UJPO 'PSFYBNQMF >4JNQBSMPBWESEUBEBEG4PJMMSXRTBM
NPEFMUIS PVHIU IFNPEJ DBUJPOPGQSPEVDUJPOUFSNT
XIJMF1F UUFSTT PQOS3PFQJPGTHEUBBOMPOMJOFBSFEEZ,—c—
WJTDPTJUZU VS CV MFODFNPEFM XIJDISFTQPOET'D P S S F D U M Z U P C P U I
TUBCJ MJ [JOHBO EEFTUB C J M J [J O H D V S W B U V S F
)FS FJT UIJFUV SCVMF OUWJ TDPTJU>Z (B
"MUFSOBUJ WFM Z>QS:PPQSPLTF UEBTMJ N<Q MFNPEJ FE
GP SN PGUIFUVSCVM FOUW JUTPDJ PTPS Q B F F D J F O G M JD J UG VODUJPOBMGP
SPUB U J POBO EDVSWB UVSFF FNDRETMBEUIFSFTVMUJOH
XBTWBM JEBUFE CZUZ QJDBM PXDBT FTTVDIBTSPUBUJOHDIBOOFM 4U
3FZOPMETTUSFTTUSBOTQPSUFRVBUJPO
PX 6 CF OE PX BO EJOU FSOBM M Z D P P M F E U V S C J O F B J S G P J M
B OEUSBQT Q P S U U F SNT BOEVOEFSU
DPOKVHBUFIF B UUSBOTGFS FN PE F M T B U J T F T S F B M J I B C J M J U Z B O
FRVJMJCSIVN JUXBTTIPXOUIBU
JOWBSJBODFQ S J ODJQMFTBO EXBTQ S F T F O U F E B T B T J N Q M F I Q M V H J O
GPS VT FXJUIFYJTU JOHUX P FR V BUJPOUVSCVMFODFNPEFMT F
F FDUPGDV SWBU VSFBO ESPUBUJPOJTJOD!M V E F E J O U I FUVSCVMFOU
WJTDPTJUZDPF DJFOUWJ BU IFF FDUJWFSPU BUJPOSBUFNBHOJUVE
UFSN XIJDIXB T BQQSPY JONBBTUFFEEPCOZ : P S L F U B M <
UIFB TT VN QUJPOU IBUUIFMPDBM PXDPOEJUUJPOBMPTTFTQPOE
UPUXP EJNFOTJPOBM TJNQMFTIFBS PXJOBGSBNFSPUBUJOH
XJUIUIF PX 'PSUIFUFT UDBTFTDPOTJEFSFEUIFNPEFMXBT
GPVOEUPNBLFB TJHOJ DBOUJNQSPWFNFOUJOUXP E J§N"P"OTJPOBM
PXQSP CMFNT)PX FWFS JOEVTUSJBM PXTBSFP FOWFSZ
DPNQMFY BOEUI F JE FBMJ [BUJPOFUGFQSNEBSUHOTTUSVDUPJXNOBTPGCUEFNI
GBS GSPNUIFBDUVBMJUZPGUIFMPDBTMXFMMBTTUDEUJVSGJVMFOOTDFUSPBGBUTFU
DBTFTJUJ TFYQFDUFE UIB U UIFTJNNQMEBTTTVNQUJPONBZMPTFJUT
F FDUJWFOFTT * OBOBUUFNQUUPJNQSPWFUIFQFSGPSNBODFPGUIF
NPEFM BOECBTFEPOUIFXPSL PG8BMMJOBO"E!+PIBOTTPO<
BOFYBDUDB MD VMBUJPOP GUIFF FDUJWFSPUBUJPOSBUFNBHOJUVEF
JTBE P QUFEJOUIJTQBQF S XIJDIJTJOUFOEFEUPNBLFUIF
NPEFMNPSFVOJ WFST BM XIJMFSFUBJOJOHUIFBEWBOUBHFPG
QSPWJEJOHBTJNQMF iQMVH JOwTPMVUJPOGPSD_B QUVSJOHSPUBUJP
BOEDVSWBUVSFF FDUTJOUXP FRVBUJPOFEEZWTDPTJUZNPEFMT
FOFXFEEZ WJTDPTJUZ DPF DJFOUFYQSFTTJPXBTJNQMF
NFOUF EJOUPBSNXPPEFMBZDFUSIFTBNFNBOOFSSBT¤ c¶
UIBU>J O*<OUIFQSFTF OU TUVEZ UIFNPEFMXBTUFTUEGPS
UXPSFQSFTF OUBUJWF PXQSPCMFNT 'JSTU,!TJNQMF6 CFOE PX
XBTUFTUFEU PDPNQBSFUIFEJ FSFODFTCFUXFIFCOUÏFDVSSFOU
NPEFM BOEUIFPSJHJOBMNPEFMQSFTFOUECZ:PSLFUBM 'MPX
XBTUIFODBMDV MBiUHFEEHNIRSEFMUHPIBBTTFTTUIF
QFSGPSNB ODFPGUIFNPEFMTGPSBTJNQMFD!BTF¤IBUJODMVEFT

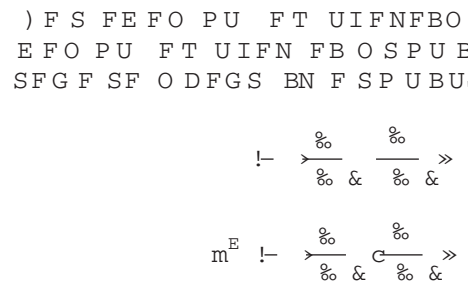

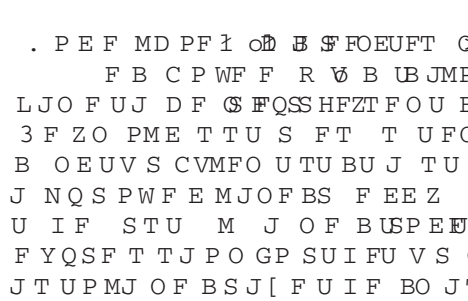

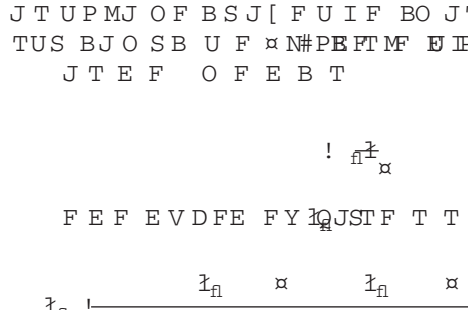

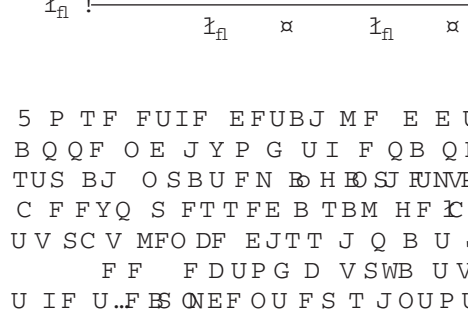

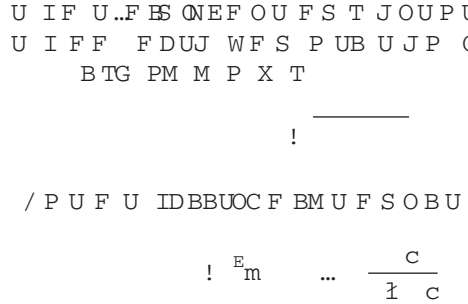

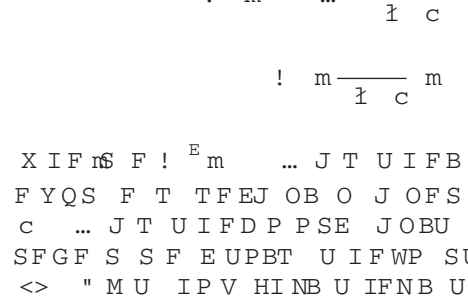

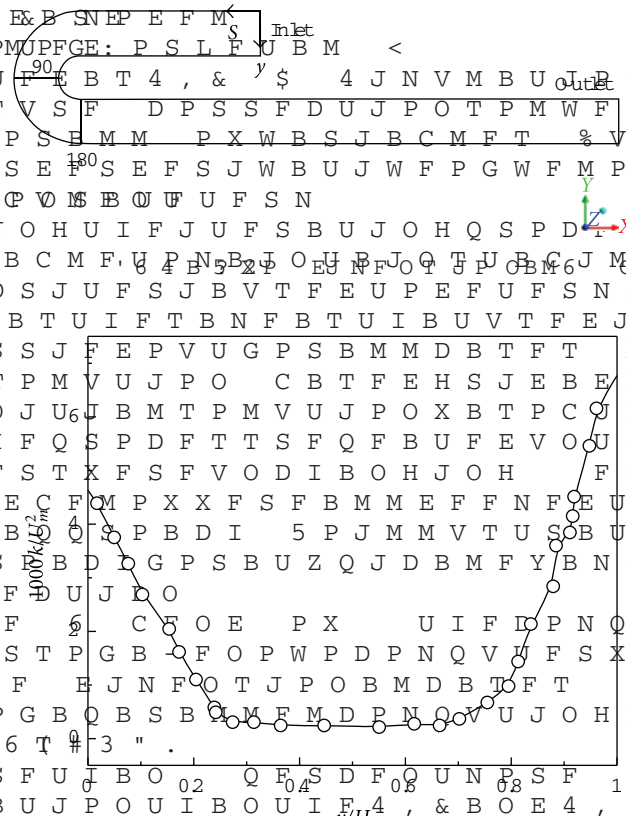
Inlet
Outlet
90
180
y
x
Y
X
$100K_t/U_{in}^2$
y/H
0
0.2
0.4
0.6
0.8
1
4
2
Computations
Experiment et al. (1990)

5FTU$BTFT

" E W B O D F T J O . F D I B O J D B M & O H J O F F S J O H

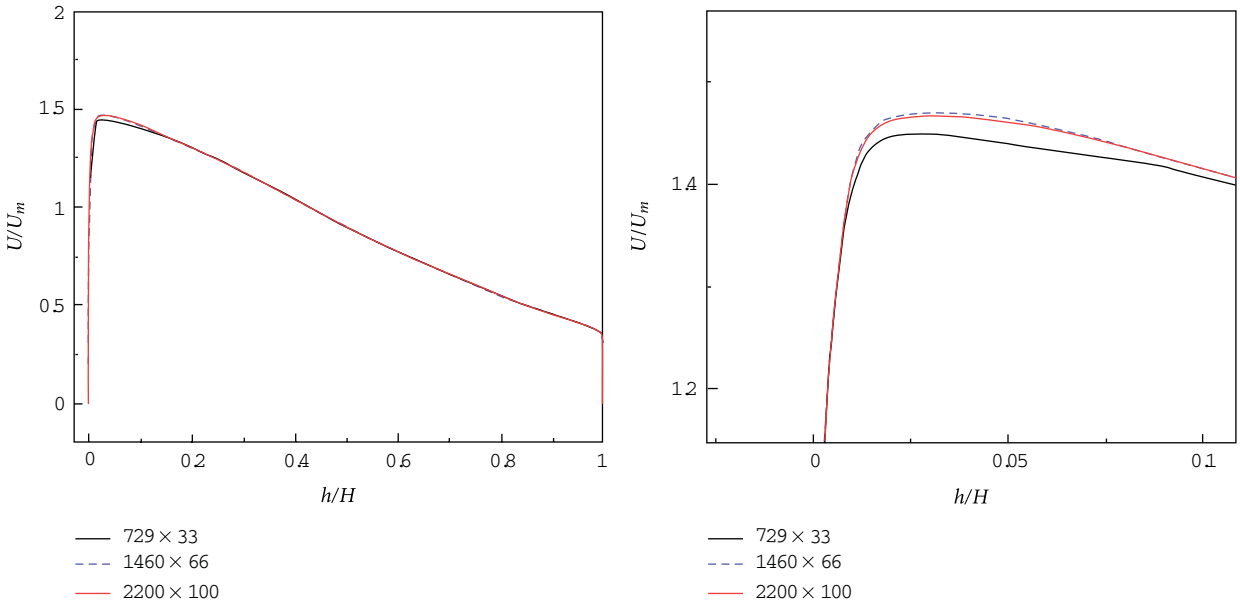

B C

' 6 4 B P S 2P M F TPG OPS N B M J [F E T U S F B N X JT F W F M P D! J J U O Z U B I O F E V S C M O M E O U L

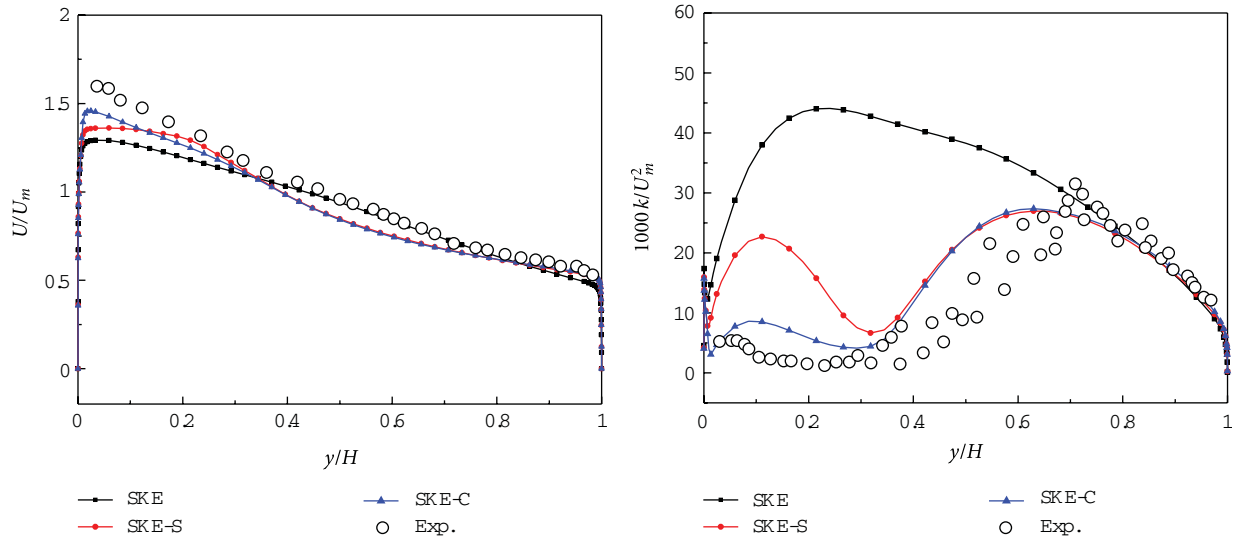

B C

' 6 4 B P S 2P M F TPG OPS N B M J [F E T U S F B N X JT F W F M P D! J J U O Z U B I O F E V S C M O M E O U L

B H S F F N F O U X J U I P O F B O P U I F S F Y D B W F Q S B J H O W U F I M E P S S D F H U T Z R U O F D I B O O F M 0 C
" O F O M B S H F E W J F X P G U I J T [W P M O E D J U Z E R X U O S R J O V U J F S J U H I F E D D F M F S
T J E F J P H G V J S O E J D B U F T U I B U U I F N J E E H E F D F U M Z H S S B J U E P O P O U I F D P O D B W F T J
J T T V D J F O U M Z B D D V S B U F G P S U " M U F I Q E S V H H T T F J O N U V M E B U V J E Z O T X O J E U B I M F M U I
S F N B J O J O H S F T V M U T Q S F T F O U F E J O U W E I M P T D T J E D N B H O P J O N V F S H F S H F O E B U B J W O F F U E P P U C
U I J T H S J E U I F D P O W F Y T J E F U I F S F T V M U P C U B
' J H V T S I F P X T U I F P X E F W F M P Q H N F O B $ U U J T F U I F N P T U B D D V S B U F ' V
T F D U J P O J O U F S N T P G U I F U B S O E H N U S B T U F W F D M P D W D F V Z D V S W B U V S F I B T B T U
C V M F O U L J O F U J Q S F O M F F S T H E B D I O P S U M S C M V M F O F D E F C X U J M F U I F D P O D B W F D V S W

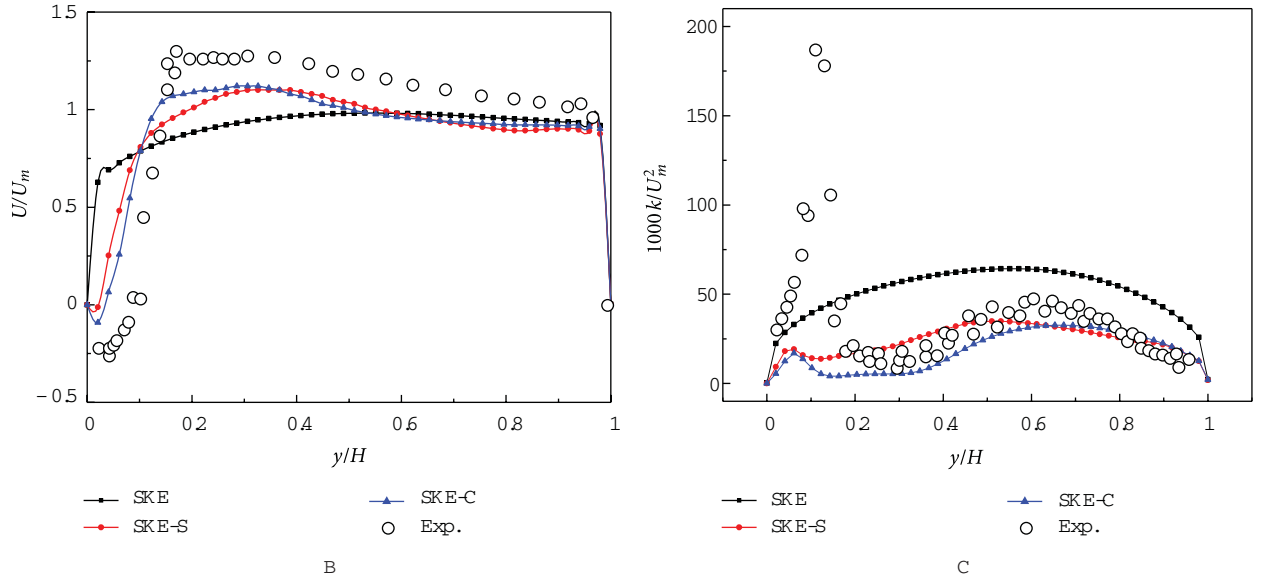
15
1
0.5
0
−0.5
0
0.2
0.4
0.6
0.8
1
U/U_m
y/H
SKE
SKE-S
SKE-C
Exp.
B
200
150
100
50
0
0
0.2
0.4
0.6
0.8
1
$1000\,k/U_m^2$
y/H
SKE
SKE-S
SKE-C
Exp.
C

"EWBO DFTJO.FDIBOJDBM&OHJOFFSJOH

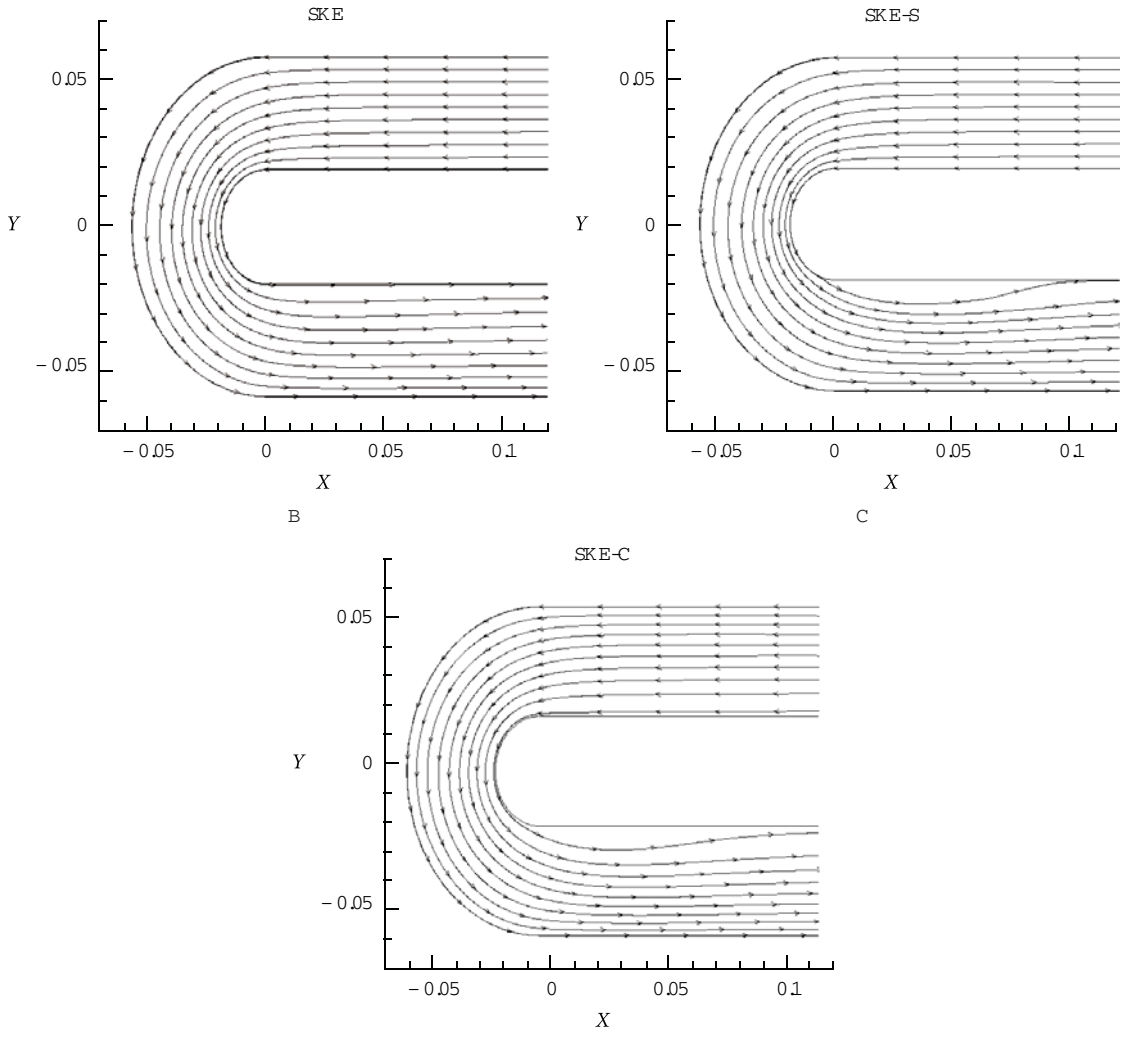

'64B4U2SFBNMJOFTDBMDVMBUFECZUIFUISFFNPEFMTTIPXJOHEJFS0ÙTJ[FE

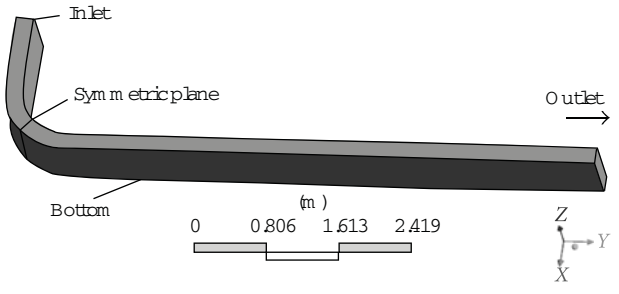

'64B?i2CFOE PXHFPNFUSZ

JOUIFSFHJPO"MMUISFFPGUIFNPE
PWFSQSFEJDUJPOPGUIFQFBLTUSFBNXJ
DPOWFY TVSGBDF/PU BCMZIPXFWE
BCM FUPQSFEJDUUIFCPVOEBSZMBZF
XBMM SFTPMWJOHUIFSFVDFOFBS X E
FYQFSJNFOUBMEBUBJO'UIJFTCFHEWPJO
JTEVFUPUIF TVQQSFTTJPOPGUVSCVM
SFEVDFEWBMVFPGUIFEEZWJTDPTJUZ
TIPX'QHVOS F

'JHVTSIFPXTUIFOPSNBMJ[FEUSBOTWFS
CVUJPOXIJDIJTEF OFEUPCFOFHBUJ
UIFJOOFSTJEFXB MMUPUIFPVTJEFXB
UIBUBWPSUFYQBJSJTGPSNFBU UIJTM
F FDUPGUIFWPSUFYGPSNBUJPOJTUP
JOOFSDPDBWFTVSGBDF"NPOHUIFU
4'&&JONPTIFTPGUVVNEFFDJUWSBUFMZ
XJUIFYQFSJNFOUBMBUB

WFSTTFWFMPDJUZPWFSUIFDIBOOFMIFJH
EJTUSJCVUJPO OPSNBMJ[FECZUIFBWFSBHFWFMPDJUZBDSPTTUIE
DIBO OFM FBDDFMFSBUJPOPG VJEPQUIFQWFYJJEFBOE
UIFEFDFMFSBUJPOPDBWFTVSGBDFOPHUIFU
DBQUVSFCZUIFOFXNPEFM JODMVDJOHXJUIPVUVNEFDJUU
WJTJCMFJOUIFCPVOEBSZMBZFSSFHJPOPOUIFDPDBWFTVSGBDF

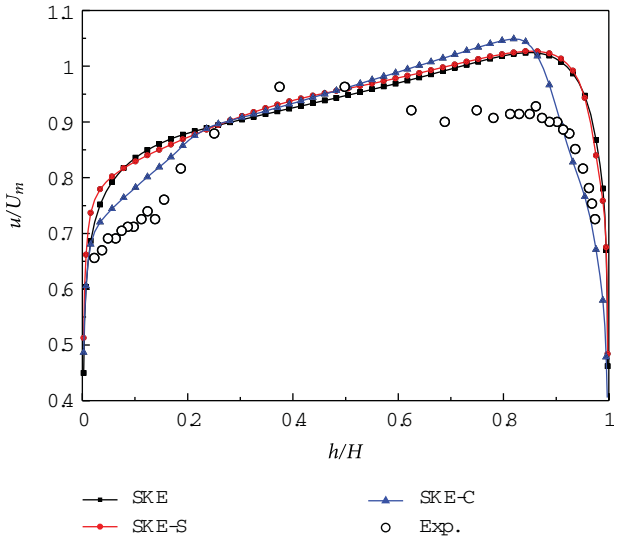

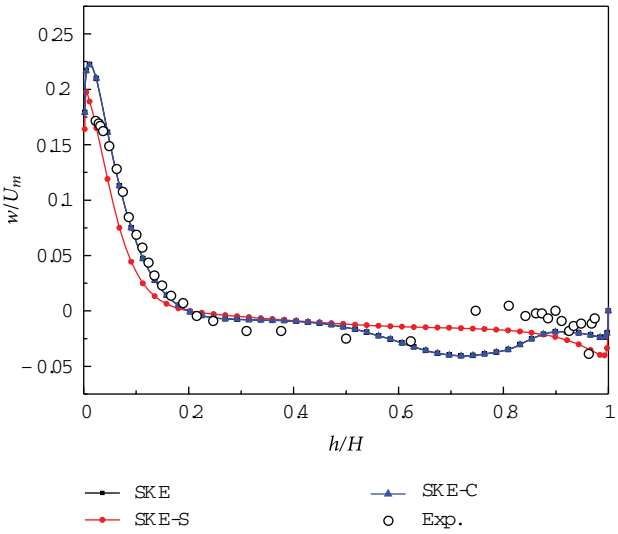

' 6 4 B 4U2S FB NX JT F#WF SNB M J U[EE C Z U I F J O M F U B W F S B H F WF MP D J U Z

' 6 4 B ?42Q BO XJ TF WKF M SNB JMU Z[FE C Z U I F J O M F WF MP D J U Z

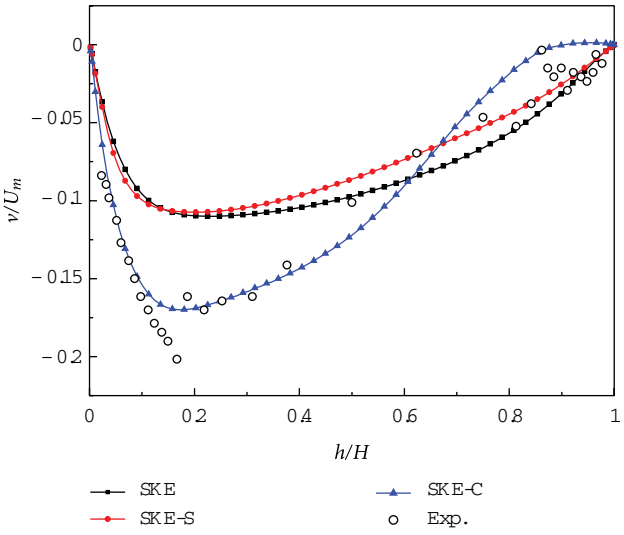

' 6 4 B 52BOT WF ST F$WF SNB M J U[EE C Z U I F J O M F U B W F S B H F WF MP D J U Z

4 V N N B S Z B O E $ P O D M V T J P

J T Q B Q F S Q S F T F O U T B T J N Q M F F E E Z J O D M V E F T F O T J U J W J U Z U P T U S F B N M J O F F D U T J O U P U X P F R V B U J P O U V S C V M E J T C B T F E P O U I F X P S L X IGP QS P ESTLFD U E M E G P S N V M B G P S U I F F E E Z W J T D P T J U Z D P F U J P O B O E D V S W B U V S F F F D U T F O F X N P W F S U I B U P S J H J O B M N P E F M C Z J O D P S Q P S P G M P D B M P X S P U B U J P O X I J D I J T S E P G D P N Q V U F E T F D P O E E F S J W B U J W F T P G 4 U B C J M J U Z J T N B J O U B J O F E J O U I F O F X M F W F M P G V O E F S S F M B Y B U J P O G P S U I F U S F T V M U J O H G P S N V M B U J P O G P S F E E Z W J T D B O E T B U J T F T Q S J O D J Q M F T P G G S B N F J O W B F O F X N P E F M X B T U F T U F E P O U X P D B G P S X I J D I F Y Q F S J N F O U B M E B U B B S F B W B J S F T V M U T X F S F B M T P D P N Q B N S F E E F U M E B U O E U P U I F P S J H J O B M D V S W B U V S F ' P S B S U S X F P D E J N F O T J P O B M 6 C F O E P X U I F O F X B D D V S B U E S F T Q P O T F U P T U S F B N M J O F D V O J D B O U M Z T I P X J O H B O J N Q S P W F E Q S F E M F W F M T O F B S U I F D P O W F Y T J E F P G U I F E J N F O T J P O B M 6 C F O E P X U I F O F X N P E F M J N Q S P W F E B D D V S B D Z W F S T V T U I F Q S F U P N P S F B D D V S B U F M Z S F Q S F T F O U U I F

' J O B M J M H Z V S F P X T U I F O P S N B M J [F E T Q O B B O D V X S J W B F W S F M P E D P J N U J Z O B U F E P X F E J T U S J C V U J P O B U U I J T M P D B U J P O J O U H E T F U D F E B P O M M Z U I F O M F X N S P H E F F M Q X B T T B J C U M J F W W B M V F O F B S U I F D P O W F Y T V S G B D F J T J N B H O J U D V B E U F J P G W U H I P U S B O I T F W T F S I T P W O F M B S Z W P S U F Y N P U J P O " H S F F N F O U O F B S S U P U B F U D J B H W D P S W F Y Q B V J S G U H B U F E J T H E M P P Q E T G P S C P U I P G U I F D V S W B U V S F D P S S F D I B O F O F N M P E F M T I P X F W F S U I F C F I B W J P S P O U I F D P O W T F O P T U X H E M M D B G R T V M S U E G P S B M M P G U I F U F T U D B T F T J O X J U I U I F 4 , & $N P E F M J X O W E M P D B U Z J D H E N P Q X H E B O P Q U W S E W J B M J N Q S P W F N F O U P O F O U J O D P O U S B T U U P U I F F Y Q F S J N F O R U B P M E F B M U H E B C M F U P R V V B S M D J F U P G J U W I F J M T Z E J T B H S F F N F O U J T O P U D M F B S C V U J T B M F N H P D T U T H E G F S S P U B U J O P M Z S E F D M V S W U B R U V E S U F P P U O I V O E F S Q S F E J D U J P O P G Q F B L T U S J F H B V N S X H U T F O W B R U X M P D F J R V U B U J P I O F E D J Z O W J T D P T Q S F T F O U F E I F S F B S F F O D P V S B H J O H C V U

" N F S J D B O 4 P D J F U Z P G . F D I B O J D B M & O H J O F F S T 8 B T I J O H % $
6 4 "

< ,> : B L J O U I P T ; 7 M B I P T U F S H J P T B O E " (P V M B T i . P E F M J O H U I F
P X J O E D U B O H V M B S E V D U V T J O H P O F 3 F Z O P M E T T U S F T T B O E
U X P F E E Z W J T D P * T U F S B U E F M E T + P w V S O B M P G) F B U B O E
' M V J E W M M P X O P Q Q o

Hindawi Publishing Corporation
Advances in Mechanical Engineering
Volume 2012, Article ID 973652, 10 pages
doi:10.1155/2012/973652

Research Article

Numerical Study on the Effect of Wax Deposition on the Restart Process of a Waxy Crude Oil Pipeline

Qing Miao[1,2]

[1] *National Engineering Laboratory for Pipeline Safety/Beijing Key Laboratory of Urban Oil and Gas Distribution Technology, China University of Petroleum, Beijing 102249, China*
[2] *PetroChina Pipeline Research and Development Center, Langfang 065000, China*

Correspondence should be addressed to Qing Miao, miaoqing@petrochina.com.cn

Received 16 October 2012; Accepted 20 November 2012

Academic Editor: Bo Yu

A new model for wax deposition is established based on the loop tests data of 9 typical crude oils in conjunction with the concept of the effective wax precipitation which occurs in the heat boundary layer in the pipeline. The thickness of the wax deposition of a waxy oil pipeline is predicted by the established model, and the results of the model agree well with the field data. Subsequently, the models for the shutdown and restart processes of a waxy crude oil pipeline are established. Then the restart process of a wax crude oil pipeline is investigated numerically, the temperature drop during the shutdown process and the transient inlet pressure are presented, and the effect of the wax deposition on the safety of the restart process is clarified.

1. Introduction

Wax precipitation in crude oil pipelines at or below the wax appearance temperature (WAT) can lead to gelling that inhibits flow by causing significant non-Newtonian behaviour and increasing effective viscosities as the temperature of a waxy crude oil approaches its pour point [1]. When the temperature of the pipeline wall is below WAT, the deposition of a layer of paraffin molecules would form near the pipe wall, constricting the flow. In the practical pipeline transportation engineering, pigging is often conducted periodically for a hot waxy crude oil pipeline to keep its throughput and operation pressure relatively steady. But for some hot crude pipelines, the throughputs of which decline with the reductions of the outputs of the upstream oil fields; pigging operations are not done regularly or even not done at all for a long period. For these pipelines, the existence of the wax deposition in them could help reduce the increment of heat loss resulting from the reduction of the throughput and even make it possible to keep the pipeline operating safely without increasing the heat capacities of heat stations. But the heat preservation of wax deposition does not imply that it will also keep or improve the safety of a long-term unpigged hot crude pipeline during its shutdown and restart. Since the wax deposition decreases the accumulation heat of a hot crude pipeline in the soil around itself during running, which is a disadvantage to the thermal conditions after the shutdown of the pipeline, the influences of thicker wax deposition on the shutdown and restart of a long-term unpigged hot crude pipeline cannot be deduced directly from normal operation and should be investigated quantitatively in detail for assessing the safety of such a pipeline.

Some researchers, such as Del Carmen García and Urbina [2] and Del Carmen García [3], have studied correlations between the properties of crude oils and their flowing properties, including the precipitation and deposition of wax during flow. Models have been developed to predict the onset of wax precipitation and the deposition of wax along pipeline walls. However, accurately modelling deposition in pipelines can be a complex and difficult undertaking, because, while precipitation is mainly a function of thermodynamic variables such as composition, pressure, and temperature, deposition is also dependent on flow hydrodynamics, heat and mass transfer, and solid-solid and surface-solid interactions [4]. Some researches about the wax deposition could be referred to [5–15].

The studies on the calculation of the restart process of oil pipeline are extensive. Some valuable researches can be found in [16–21]. But the impacts of wax deposition on the restart process are rare. In this paper, the impact of the wax deposition formed during the running without pigging on the safety of the restart process of a pipeline is analyzed and some significant conclusions are drawn.

The layout of this paper is as follows. The characteristic of wax deposition is to be investigated first. Then the models for the shutdown and restart processes of a waxy crude oil pipeline will be established. Lastly, the effects of wax deposition on the shutdown and restart processes of a waxy crude oil pipeline will be investigated.

2. Mathematical Model for Predicting the Wax Deposition

When the crude oil is transported in the pipeline, since the ambient temperature at a certain length of the pipeline is usually lower than the crude temperature at the same length, the temperature near the inner pipe wall cools faster than that far from the inner wall and causes a temperature gradient pointing to inner pipe wall. And the temperature at inner pipe wall firstly reduces to WAT, and the wax precipitates near the wall in the first place and then crystallizes and deposits on the wall. The wax deposition near the wall results in the reduction of the liquid wax concentration in this area and causes a solved wax concentration gradient pointing to the inner wall, which impels the liquid wax molecules in the central area of pipe cross-section moving to inner wall and precipitating and depositing there continuously. This temperature gradient induced solved wax concentration is just the impetus of the wax deposition, and thus it is deduced that only the wax precipitation occurred in a region where an oil temperature gradient exists and contributes to the wax deposition, or say, is effective to the wax deposition. From this issue, even if all the oil temperatures along a radius in some pipe cross section have reduced below the WAT so the wax precipitation has occurred anywhere in the cross section; however, only the wax precipitation in the area near the pipe wall in which heat flux points outwards has contribution to the wax deposition on the pipe wall, instead of the whole amount of wax precipitation in the cross section, while the wax precipitations in other areas will flow downstream in wax crystals forms.

According to the above analyses, the concept of effective wax precipitation (EWP) is proposed, which associated with the wax precipitation occurred in the region where an oil temperature gradient exists and contributes to the wax deposition. Since the flow states in most industrial crude pipelines are in turbulent regimes, the temperature gradient only exists in laminar region near the wall. As for the laboratory loop test for wax deposition (which is the focus of our study), because the length of the test tube in a loop is usually about 1.5 meters to 2 meters and the heat boundary layer in the tube would not expand fully according to heat transfer method, the temperature gradient also exists in the heat boundary layer near the wall, shown in Figure 1.

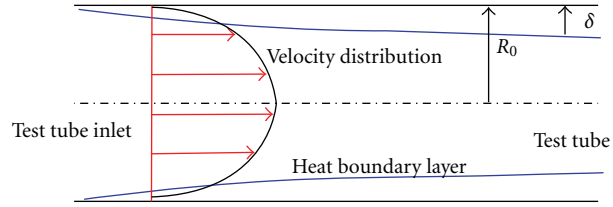

Figure 1: Diagram of heat boundary layer in test tube.

Since the ambient temperature around the test tube changes axially in practical test process, the oil temperature varies along the test tube and the heat boundary layer thickness also changes along the test tube. In order to calculate the EWP in test tube accurately, the length of the test tube would be divided into several segments. Then the thickness of the heat boundary layer of each section could be calculated according to heat transfer method and thus the whole effective mass of crude which flows through the heat boundary layer during a test can be calculated according to the following formulae:

$$
\begin{aligned}
G_{\,i} &= G\left[1 - \left(\frac{\mathrm{R}i - {}_{i}}{\mathrm{R}i}\right)^{2}\right]^{2}, \\
M_{\,i} &= G_{\,i} \cdot t, \\
M &= \sum M_{\,i}, \\
i &= 1, 2, \ldots, n, \quad n = 10,
\end{aligned}
\tag{1}
$$

where ${}_{i}$ indicates the thickness of heat boundary layer of the ith section; $G_{\,i}$ and G represent the mass flow rate for the ith section and the mass flow rate of the whole test tube; $\mathrm{R}i$ indicates the effective inside diameter for the ith section; t represents the test time for wax deposition; M indicates the whole effective mass of crude which flows through the heat boundary layer during a test.

Once M is obtained, the EWP for the tested crude during the test time can be determined from it according to the wax precipitation characteristics of the crude.

For studying the relationship between wax precipitation and its deposition, a variable named effective deposition ratio (EDR) should be defined to connect the EWP with the wax deposition, which is defined as

$$
\phi = \frac{W_d}{W_E}, \tag{2}
$$

where W_d is the whole amount of wax deposition and W_E is for EWP. In the following, effective deposition ratio will be abbreviated as EDR.

In order to detect the hidden relationship between EDR and EWP, a test loop shown in Figure 2 was devised to obtain the necessary data. In the figure, D_{p1} and D_{p2} are two differential pressure gauges used to measure the pressure drop of test tube 1 and 2; cooling circulator 1 and 2 are temperature control equipments used to control the ambient temperatures around test tube 1 and 2; mass flow meter is used to measure the mass flow rate of the loop; oil jar

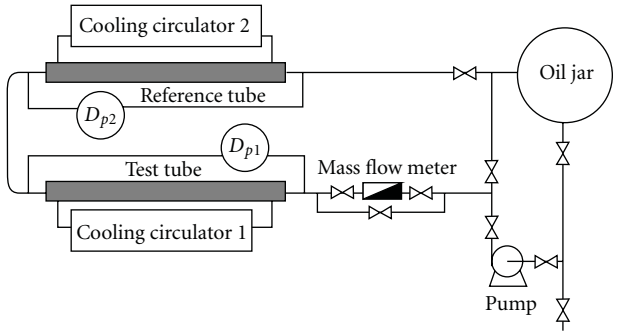

Figure 2: Diagram of wax deposition test loop.

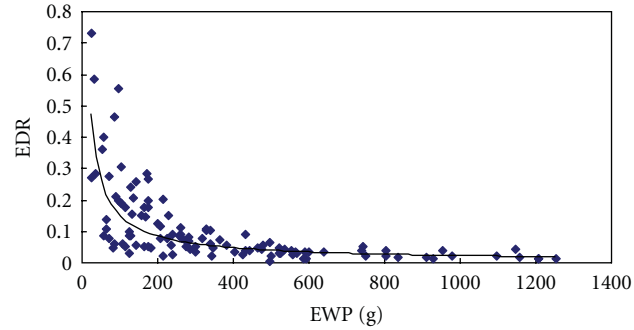

Figure 3: EDR versus EWP curve of nine kinds of representative crude oils.

provides sample source and compensates wax concentration; pump provides power to keep sample circulating.

With the experiment data of nine different crude oils, it is discovered that the relationships between effective deposition ratio (EDR) and effective wax precipitation (EWP) for each kind of representative crudes studied and tested in the test loop obey the same rule; that is, the EDR decreases with the increase of the EWP and, when the EWP is less, the EDR changes rapidly; when the EWP increases to some extent, the EDR begins to change slowly. Further, put all the EDR and EWP data from 9 kinds of crude oils together, the tendency concluded above is clear at a glance (see Figure 3). It is further found that the statistic rule on the relationship of EDR and EWP is obvious and could be expressed in power law mathematically as follows:

$$\phi = k_0 W_E^m, \tag{3}$$

where W_E represents the EWP; k_0 and m are two constants.

Based on the results above, the significance for introducing the concept of EWP is emphasized. Through the definition of EWP, the universal rule on the relationship between EWP and wax deposition available to many crude oils is found quantitatively. The concept of EWP uncovers the internal connection of the wax deposition with the wax precipitation and provides a method to divide the part contributing to wax deposition from the whole wax precipitation in pipeline or in test tube. More important, the rule common to the wax deposition of many kinds of crude oils in the test loop makes it possible that a common wax deposition model could be created for many kinds of crude oils and a large number of loop tests necessary for wax deposition prediction previously could be left out.

In fact, the outline of the common wax deposition model has been given in formula (3) theoretically. But that form might not be used for practice yet for the reason that the EWP is unknown for a new kind of crude never tested in the test loop. From the definition and calculation of EWP, it is explicit that EWP is connected with the thickness of heat boundary layer and the thickness of heat boundary layer strongly depends on the velocity and temperature distributions in the test tube at different test conditions, so the factors such as the viscosity of crude, shear stress at inner pipe wall, radial temperature gradient at pipe wall, oil temperature in central area of test tube, and the velocity of oil flow which have impacts on velocity and temperature distributions would all influence the determination of EWP. In other words, the EWP is a function of all factors mentioned above. From the above discussion, the practical common wax deposition model should have the following form:

$$\phi = k_0 \mu^{k_1} \cdot \tau_w^{k_2} \cdot \left(\frac{dT}{dr}\right)^{k_3} \cdot \left(\frac{dC}{dT}\right)^{k_4} \cdot T^{k_5} \cdot v^{k_6}, \tag{4}$$

where $k_0 \sim k_6$ are constants needed to be determined; μ and τ_w are the viscosity of tested crude at test condition and shear stress at inner pipe wall, respectively; dT/dr and dC/dT are radial temperature gradient at pipe wall and the amount of wax precipitation from tested crude for unit oil temperature reduction, respectively; T and v are oil temperature in the central area of test tube and the average velocity of oil flow, respectively.

On the basis of wax deposition loop test results of 9 kinds of crude oils and applying the method of linear multivariable stepwise regression to check and analyze the formula (4), the final form of the common wax deposition model is determined as follows:

$$\phi = 0.0204 \mu^{1.03} \left(\frac{dT}{dr}\right)^{-0.157} \left(\frac{dC}{dT}\right)^{-0.576} \tau_w{}^{-1.036}. \tag{5}$$

Formula (5) is the common wax deposition model which is available to most kinds of crude oils. From now on, an efficient and sample-saving wax deposition model can be created for any crude in the case of no wax deposition loop tests.

3. Mathematical Models for the Shutdown and Restart Processes of a Waxy Crude Pipeline

During pipeline shutdown, heat transfer in crude oil can be divided into three stages as (1) natural-convection-dominated stage, (2) joint control of natural convection and heat conduction, and (3) pure heat conduction [22]. With the following assumptions the temperature drop process is then simplified as a heat conductive process.

(a) The variation of the specific heat capacity of the crude oil is applied to describe the latent heat of wax crystallization during shutdown.

(b) Stagnation point introduced in the second stage describes the internal pipeline as a liquid region with natural convection and a solid region with thermal conductivity.

(c) Natural convection can be solved as conduction after an equivalent thermal conductivity is applied [23]. By this means, we can convert the calculation of natural convection into a conductive heat transfer. The equivalent thermal conductivity is dependent on the natural convection coefficient, the temperature of oil, and the temperature gradient on the interface. Then the heat transfer equation of the oil is then shown as

$$\rho C_p \frac{\partial T}{\partial r} = \frac{1}{r}\frac{\partial}{\partial r}\left(\lambda r \frac{\partial T}{\partial r}\right) + \frac{1}{r}\frac{\partial}{\partial \theta}\left(\frac{\lambda}{r}\frac{\partial T}{\partial \theta}\right), \qquad \lambda = \frac{-\alpha(T - T_w)}{(\partial T/\partial r)_w} \tag{6}$$

in which, $(\partial T/\partial r)_w$ is a temperature gradient at the interface.

Though the equivalent thermal conductivity is not a real heat conduction coefficient, it guaranteed energy conservation and greatly simplified the calculation. This approximation is verified by field data of crude oil pipelines [23].

Heat transfer equations of wax deposition layer, pipe wall, and corrosion protective coating as well as the heat conduction equation of the soil are the same as those in the normal operation process. Matching conditions are shown in (7) while boundary conditions are the same as those in the normal operation process. Consider

$$\begin{aligned} &\lambda_0 \frac{\partial T_0}{\partial r}\bigg|_{r=R_0} = \lambda_1 \frac{\partial T_1}{\partial r}\bigg|_{r=R_0}, \\ &\lambda_k \frac{\partial T_k}{\partial r}\bigg|_{r=R_k} = \lambda_{k+1} \frac{\partial T_{k+1}}{\partial r}\bigg|_{r=R_k}, \quad k = 1, 2, \\ &T_k|_{r=R_k} = T_{k+1}|_{r=R_k}, \quad k = 1, 2, \\ &\lambda_3 \frac{\partial T_3}{\partial r}\bigg|_{r=R_3} = \lambda_s \frac{\partial T_s}{\partial r}\bigg|_{r=R_3}, \\ &T_3|_{r=R_3} = T_s|_{r=R_3}, \end{aligned} \tag{7}$$

where R_0 to R_3 are shown in Figure 4 and CPC in Figure 4 is the abbreviation for the corrosion protective coating.

During the process of restart, the thermodynamic model is the same with that during normal operation, which can be referred to [24]. In addition, the hydrodynamic model for the restart process is as follows.

Momentum equation:

$$\frac{\partial p}{\partial z} + \rho \frac{\partial v}{\partial t} + g \sin\theta + \frac{4\tau_w}{D_{\text{eff}}} = 0, \tag{8}$$

where v is the average velocity of the oil flow; p is the restart pressure along the line; θ is the inclination angle of the pipeline; ρ is the density of the crude; g is the gravity acceleration; D_{eff} is the effective inside diameter of the pipe; τ_w is the shear stress at inner pipe wall, Pa.

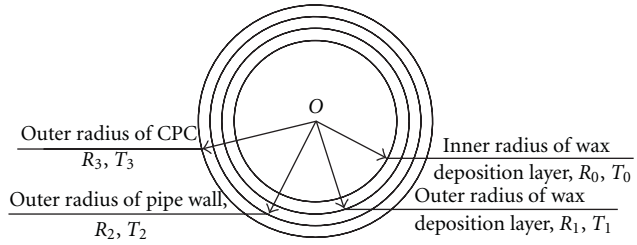

Figure 4: The three-layer system of the crude oil pipeline.

The shear stress at inner pipe wall τ_w depends on the flow pattern and flow behavior of the crude and can be determined according to the following formulae.

(1) When the crude belongs to Newtonian fluid:

Re < 2000:

$$\tau_w = 4.15\rho g \frac{Q}{4{D_{\text{eff}}}^3}, \tag{9}$$

Re ≥ 2000:

$$\tau_w = 0.0246\rho g \frac{Q^{1.75\ \ 0.25}}{4{D_{\text{eff}}}^{3.75}}. \tag{10}$$

(2) When the crude belongs to non-Newtonian fluid:

$\text{Re}_{\text{MR}} < 2000$:

$$\tau_w = K\left(\frac{3n+1}{4n}\right)^n \left(\frac{8v}{D_{\text{eff}}}\right)^n, \tag{11}$$

$\text{Re}_{\text{MR}} \geq 2000$:

$$\tau_w = \frac{1}{8}\lambda v^2 \rho, \tag{12}$$

where Re and Re_{MR} are the Reynolds number and Metzner-Reynolds number, respectively; Q is the volumetric flow rate; and λ are the viscosity of the crude and friction coefficient, respectively; K and n are consistency coefficient and flow behavior index of pseudoplastic fluid, respectively.

(3) When the crude presents a thixotropic behavior,

$$\tau = \tau_{y0} + \lambda\tau_{y1} + (K + \lambda\Delta K)\dot{\gamma}^n, \qquad \frac{d\lambda}{dt} = a_\lambda(1 - \lambda) - b_\lambda \lambda \dot{\gamma}^m. \tag{13}$$

τ_w can be determined by solving the Houska thixotropic model.

Initial and boundary conditions:

$$p(z, 0) = \text{constant}, \qquad p(0, t) = \rho g(A - BQ^{1.75}), \tag{14}$$

where A and B are two constants.

4. Numerical Methods

Here a thermal influence zone [25] is adopted as a computational domain and then the numerical simulation is performed. The pipeline is divided into $n-1$ segments in axial direction, shown in Figure 5. A Delaunay triangulation method is applied in a software package to generating the grids in a Cartesian coordinate system (as shown in Figure 6) specified by the parameters of pipeline burial depth and radius defined by users. The soil domain was divided into nonoverlapped triangles by the method mentioned above. In order to simulate the temperature field more accurately, a mesh that is dense near the pipeline but coarse far away from it is used to improve the computational efficiency while resolving the temperature gradient that is high near the pipeline and low away from it. Grid independence was tested by applying three sets of grids of different sizes, and the numerical simulation results show that the results are independent of mesh size. Due to the temperature drop during the shutdown and restart processes, the temperature is not uniform in the radial direction. The temperatures of oil, wax deposit, and corrosion-inhibiting coating were calculated, respectively, in a polar coordinate system shown in Figure 7. Then the governing equations are discretized by the combination of the finite volume method and the finite difference method, and details can be found in [24, 26, 27].

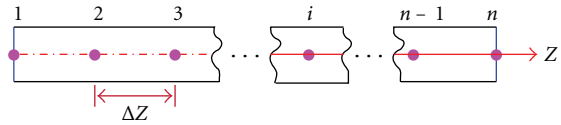

Figure 5: The pipeline infinitesimal segments.

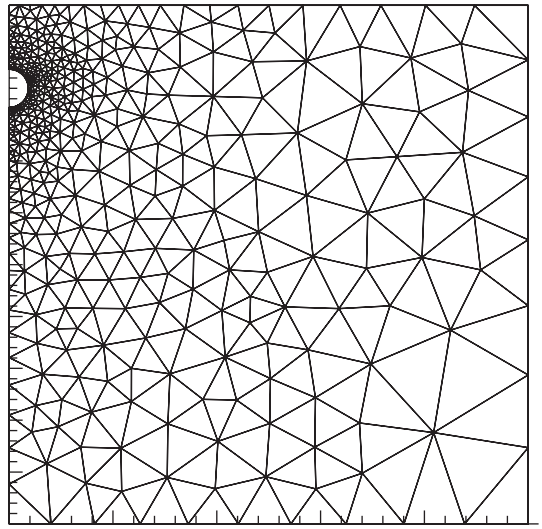

Figure 6: Grids generation of the soil domain.

5. Results and Discussion

5.1. Characteristic of the Wax Deposition of a Waxy Crude Oil Pipeline. A hot crude oil pipeline transporting Daqing crude in the Northeast of China had not been pigged over the past four years due to the reductions on throughputs. The hot crude pipeline is 436.3 km long and its diameter is 720×8 mm. The maximum allowed inlet oil temperature of each pipeline interval is 70°C and the maximum allowed operation pressure (MAOP) is 4.32 MPa. The design annual throughput of the pipeline is $2000 \times 10^4\, t$. During the past four years, the throughputs of this pipeline reduced year after year from $1168 \times 10^4\, t/a$ to $1144 \times 10^4\, t/a$, then to $1016 \times 10^4\, t/a$ and $743 \times 10^4\, t/a$. With the reduction of the throughput and the growth of the wax deposition, the thermal insulation effect of successively increasing wax deposition appeared gradually, which kept the outlet oil temperatures of each pipeline interval almost unchanged without adding more heat capacities to the heat stations. Based on the mathematical wax deposition model created for Daqing crude, numerical simulation for the wax deposition of this long-term unpigged hot crude pipeline is conducted. The results for the first interval of the pipeline are shown in Figure 8.

From Figure 8, it can be found that the wax deposition is not identical along the pipeline. In the middle of the fifth year during no pigging, the maximum wax deposition of the first pipeline interval is about 117 mm and the wax deposition at the outlet of the same interval is near 80 mm. The simulation shows that the position where the maximum wax deposition occurs has moved towards the outlet of the interval at the end of the fourth year and the displacement is about 11 km, which results in the widening of the range of the maximum wax deposition. The phenomenon results from the nonequality of the wax deposition of Daqing crude in this hot pipeline and is the accumulation of the point-by-point movements of the maximum wax deposition during the fourth year. The mechanism lies in when the throughput and the inlet oil temperature of a pipeline interval keep constant, the wax deposition will make the oil temperatures along the line increase slowly. For a hot crude pipeline along which the wax deposition distributes unevenly, the oil temperature at the position of the maximum wax deposition occurring initially would increase and the temperature difference between the oil flow and the inner pipe wall there would reduce. The next downstream position will replace the initial position as a new maximum wax deposition position. Thus the location of maximum wax deposition will move downstream successively, which can bring a span of maximum wax deposition.

In the case of a long-term unpigged hot crude pipeline with reducing throughputs, whether the location of maximum wax deposition will move depends on two effects jointly: one is the reductions of the oil temperatures caused by lower throughput, another is the increments of the oil temperatures due to the wax deposition. Generally, at the beginning of the operation without pigging, the wax deposition is thinner and the heat loss caused by low throughput is stronger than the heat preservation of the wax deposition, which may result in the location of maximum wax deposition moving upstream. With the growth of the wax deposition, the insulation of wax deposition enhances and the heat

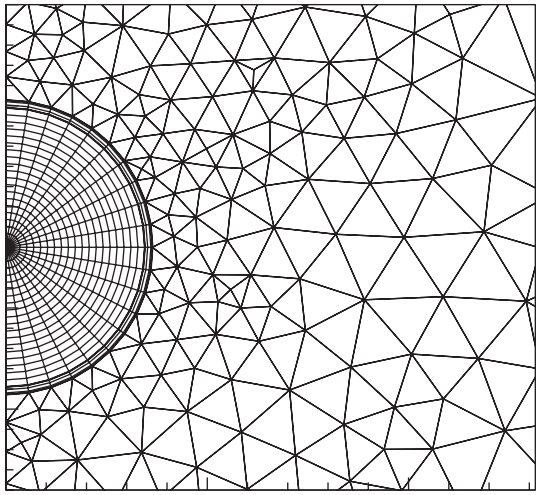

Figure 7: Local expanded view of the structural grids generation during shutdown.

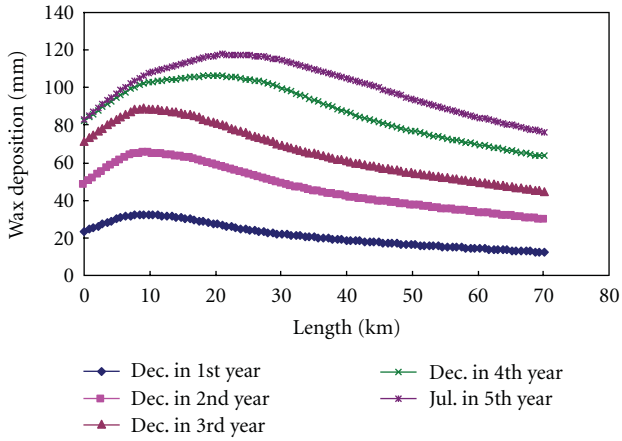

Figure 8: Wax deposition simulation of the first interval of the long-term unpigged pipeline.

loss rate arising from the reduction of throughput decreases due to the reduction of the inner pipe diameter, which will make the location of maximum wax deposition moving downstream. When the maximum wax deposition grows to a certain value (depending on pipeline sizes and operation conditions), the two effects balances and the location of maximum wax deposition will stop moving. Referring to Figure 8, it can be reasoned that the pipeline runs nearby the equilibrium point in the former three years under no pigging and over that point in the fourth year. It needs to be noted that the unpigged hot pipeline transporting Daqing crude began to transport a kind of light crude after no pigging of more than 4 years. Some maintenance and repairs were done for the pipeline to satisfy the new demand, so it was possible to measure the real wax deposition in situ. The following Figures 9 and 10 exhibit the maximum wax deposition and the wax deposition at the outlet of the first pipeline interval in situ, respectively, verifying the accuracy of the simulation.

Figure 9: Maximum wax deposition of the first interval of the long-term unpigged pipeline (about 110 mm).

Figure 10: Wax deposition at the outlet of the first interval of the long-term unpigged pipeline (about 80 mm).

5.2. Temperature Drop Characteristics of the Waxy Crude Oil Pipeline. Based on the above model, numerical simulations for the temperature drops along the pipeline with the shutdown duration of the unpigged hot crude pipeline carrying Daqing crude are completed. The results for the first pipeline interval in December of the 4th year of no pigging are shown in Figure 11.

To investigate the impact of the wax deposition formed through a long-term operation on the temperature drop of the hot crude pipeline, the oil temperatures at the outlet of the first pipeline interval after 20-hour shutdown in December of each year during four years under no pigging are selected from the simulation results. Also the wax depositions at the same position in the same time are selected from the wax deposition simulations. All the data are drawn in the same figure, see Figure 12.

For analyses, the operation data for this pipeline interval corresponding to Figure 12 are listed in Table 1.

From Table 1, the insulation effect of the increasing wax deposition is obvious in spite of the successive reduction of throughputs during no-pigging operation. When the throughputs decreased slowly and the inlet oil temperatures kept constant (in Decembers of the 1st and 2nd years), the increasing wax deposition ensured the same outlet oil temperatures. While the throughputs declined a lot and the inlet oil temperature was enhanced a few (in December of

Table 1: Operation data during no pigging.

Time (no pigging)	Throughput (m^3/h)	Inlet temperature (°C)	Outlet temperature (°C)
December of 1st year	1537	43	35
December of 2nd year	1467	43	35
December of 3rd year	1359	44	35
December of 4th year	975	45	34

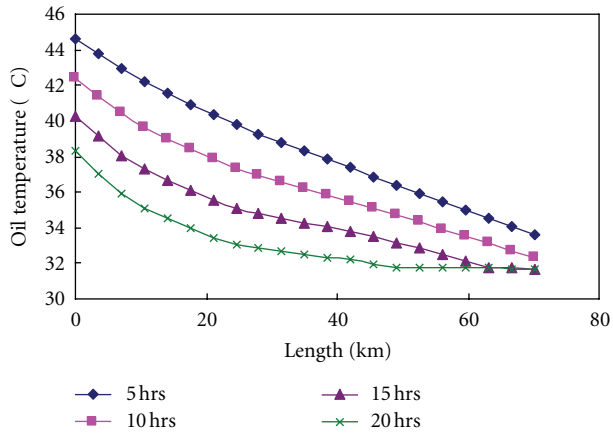

Figure 11: Oil temperatures along the line with the shutdown duration of the first pipeline interval in December of the 4th year of no pigging.

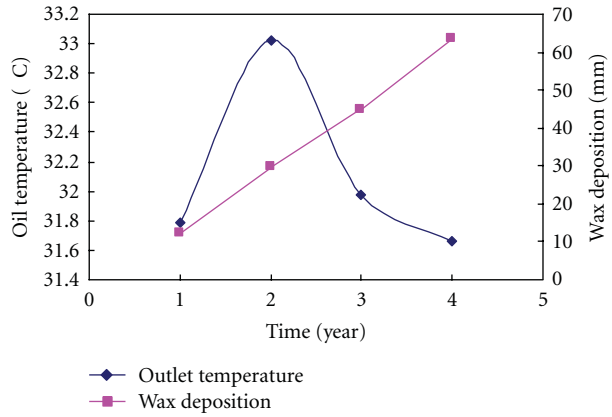

Figure 12: Oil temperatures after 20-hour shutdown and wax depositions at the outlet of the first pipeline interval in December of each year of no pigging.

the 3rd year, especially in December of the 4th year), the wax deposition made the outlet oil temperatures relatively steady.

But from Figure 12, it can be concluded that the wax deposition formed during normal operation will not always be positive to keeping the oil temperature after the shutdown of the pipeline. The existence of a turning point corresponding to the 2nd year proves this issue. It can be explained as follows: on the one hand, the wax deposition slows down the heat transfer between oil and the surrounding soil and thus reduces the oil temperature drop rate during the shutdown. On the other hand, the reduction of the flow rate reduces the

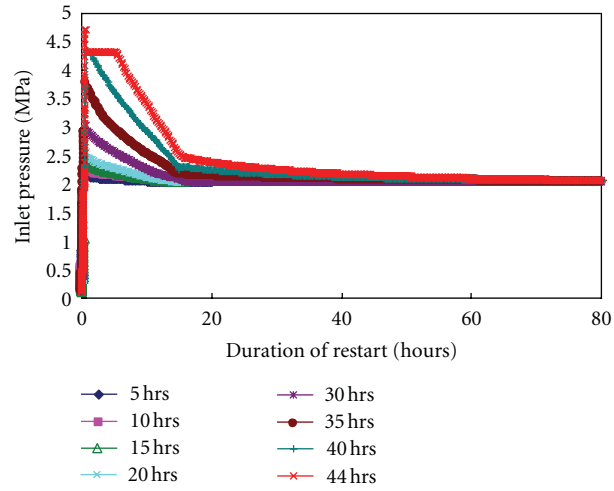

Figure 13: Inlet pressure with the duration of restart after the different shutdown time of the 1st pipeline interval in December of the 1st year of no pigging.

outlet oil temperature during the normal operation, leading to a lower oil temperature with the same shutdown duration. So the final impact of the wax deposition on the temperature drop of a hot crude pipeline after its shutdown depends on the two effects simultaneously: the insulation enhancement of the wax deposition and the flow rate reduction in the pipeline, each of which advances oppositely. Also, there is a balance point between the two effects. For the case in Figure 12, the balance point corresponds to the wax deposition of about 30 mm at the outlet of the first pipeline interval.

5.3. The Effect of Wax Deposition on the Restart Process of the Waxy Crude Oil Pipeline. Combining the hydrodynamic model with the thermodynamic model introduced above, numerical simulation for the restart process of the long-term unpigged hot crude pipeline is carried out. The results aimed at the first pipeline interval are selected for analyses, which show how the inlet pressures vary with the duration of restart for different shutdown durations in different years of no pigging (see Figures 13, 14, 15, 16, and 17).

Inspection of Figure 13 reveals that the safe maximum shutdown duration for the first pipeline interval in December of the first year of no pigging is 40 hours, at which the inlet pressure already reaches the MAOP of the pipeline, namely, 4.32 MPa. When the shutdown durations lie between 40 and 44 hours, the retaining times of maximum inlet pressure on MAOP delay with the shutdown time and are 0.5

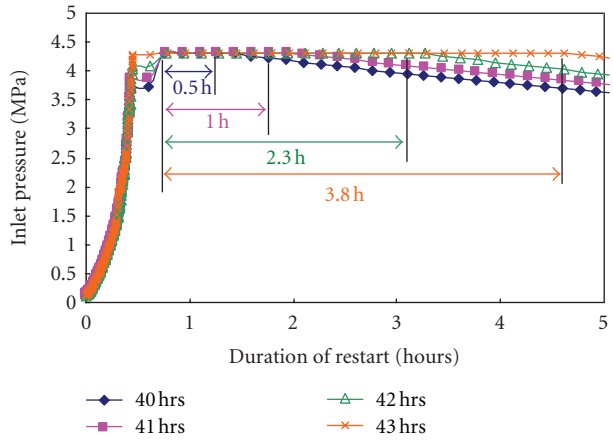

Figure 14: Duration of the maximum inlet pressure at different shutdown times of the 1st pipeline interval in December of the 1st year of no pigging.

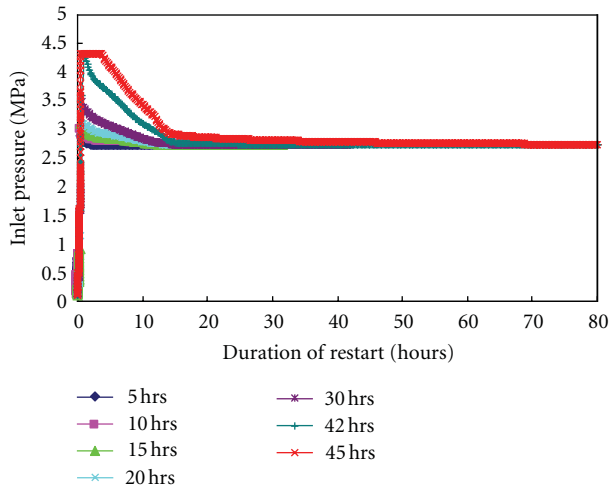

Figure 15: Inlet pressure with the duration of restart after the different shutdown time of the 1st pipeline interval in December of the 2nd year of no pigging.

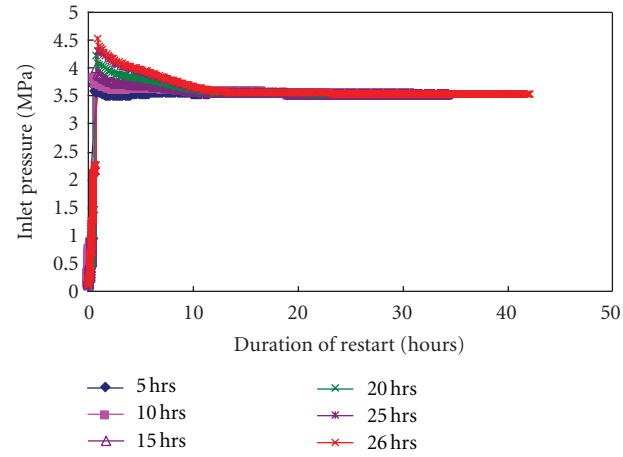

Figure 16: Inlet pressure with the duration of restart after different shutdown time of the 1st pipeline interval in December of the 3rd year of no pigging.

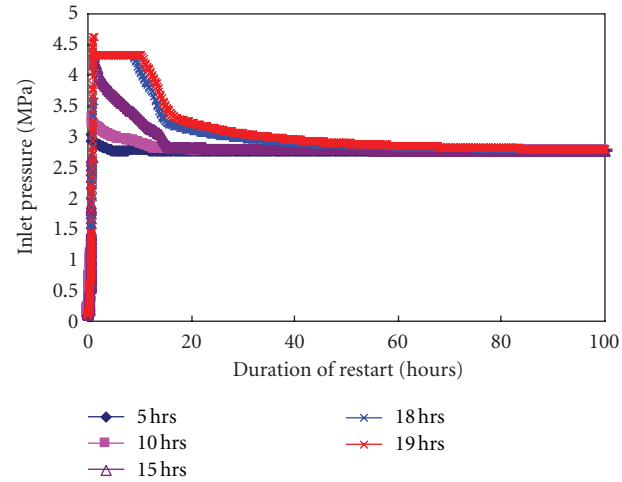

Figure 17: Inlet pressure with the duration of restart after the different shutdown time of the 1st pipeline interval in December of the 4th year of no pigging.

hour, 1 hour, 2.3 hours, and 3.8 hours, respectively, as shown in Figure 14. The longer the duration of the maximum inlet pressure on MAOP is, the larger the risk of restart failure is. So, the safe maximum shutdown duration for the case in Figure 13 should be determined as 40 hours despite the fact that the pipeline interval may be restarted successfully above 40 hours but below 44 hours. Once the pipeline interval discussed was shut down over 44 hours under operation conditions in December of the first no-pigging year, it would not be restarted normally according to the operation regulations for the pipeline and emergency procedures should be activated.

From Figure 15, it is clear that the safe maximum shutdown duration for the first pipeline interval in December of the second year of no pigging is 42 hours. Between 42 and 45 hours of shutdown durations, the pipeline interval might be restarted but the risk of the restart failure is large. Over 45 hours, the pipeline interval could not be restarted normally.

From Figure 16, the safe maximum shutdown duration for the first pipeline interval in December of the third year of no pigging is 25 hours. Over 26 hours, the pipeline interval could not be restarted normally.

From Figure 17, the safe maximum shutdown duration for the first pipeline interval in December of the fourth year of no pigging is 18 hours. The pipeline interval could not be restarted normally when the shutdown delayed over 19 hours.

The restart safeties of the first pipeline interval during no pigging are derived from the above analysis and listed in Table 2.

In Table 2, SMSD is the abbreviation for safe maximum shutdown duration, IPRF for interval of possible restart

Table 2: Comparison of restart safety after shutdown.

Time (no pigging)	SMSD (hours)	IPRF (hours)	CSDURN (hours)
December of 1st year	40	40~44	44
December of 2nd year	42	42~45	45
December of 3rd year	25	25~26	26
December of 4th year	18	18~19	19

failure, and CSDURN for critical shutdown duration unable to restart normally.

From Figure 13 to Figure 17, it could be found that the SMSDs of the first pipeline interval in Decembers during no pigging reduced with the growth of the wax deposition except in the second year. One of the causes is the final impact of wax deposition on the thermodynamics process during shutdown, which is discussed in Section 5.2. Another one arises from the fact that the growth of the wax layer reduces the effective inner diameter of the pipe resulting in the increasing of the restart pressure, even if the reduction of the throughput can counteract partly this tendency. Furthermore, the IPRF almost does not exist since the second year, which implies that there is no buffer between safe restart and the limit state of restart failure after the second year of no pigging, namely, the restart safety margin of the pipeline reduces.

6. Conclusions

In this paper, the characteristic of the wax deposition of a waxy crude oil pipeline is investigated. A new model for wax deposition is established and validated by the field data. Besides, the effects of wax deposition on shutdown and restart process of the crude oil pipeline are studied and the following conclusions are obtained.

The wax deposition in a long-term unpigged hot crude pipeline decreases the heat loss of the pipeline to the surroundings at any time and the heat accumulation in the soil as well. The insulation of the wax deposition is beneficial to the heat preservation of a hot crude pipeline during its normal running, especially under decreasing throughputs. However, the reduction of the flow rate reduces the outlet oil temperature during the normal operation, leading to a lower oil temperature with the same shutdown duration. Finally, the increasing insulation for the pipeline and the reducing flow rate caused by the growth of wax deposition jointly affect the safety of the shutdown and restart of such a special pipeline.

Acknowledgment

The study is financially supported by the National Science Foundation of China (no. 51134006).

References

[1] K. S. Pedersen and H. P. Rønningsen, "Influence of wax inhibitors on wax appearance temperature, pour point, and viscosity of waxy crude oils," *Energy and Fuels*, vol. 17, no. 2, pp. 321–328, 2003.

[2] M. Del Carmen García and A. Urbina, "Effect of crude oil composition and blending on flowing properties," *Petroleum Science and Technology*, vol. 21, no. 5-6, pp. 863–878, 2003.

[3] M. Del Carmen García, "Paraffin Deposition in Oil Production," in *SPE International Symposium on Oilfield Chemistry*, pp. 161–167, SPE, Houston, Tex, USA, February 2001.

[4] A. Hammami, J. Ratulowski, and J. A. P. Coutinho, "Cloud points: can we measure or model them?" *Petroleum Science and Technology*, vol. 21, no. 3-4, pp. 345–358, 2003.

[5] P. Singh, R. Venkatesan, H. S. Fogler, and N. Nagarajan, "Formation and aging of incipient thin film wax-oil gels," *AIChE Journal*, vol. 46, no. 5, pp. 1059–1074, 2000.

[6] R. Venkatesan and H. S. Fogler, "Comments on analogies for correlated heat and mass transfer in turbulent flow," *AIChE Journal*, vol. 50, no. 7, pp. 1623–1626, 2004.

[7] H. S. Lee, *Computational and rheological study of wax deposition and gelation in subsea pipelines [Ph.D. thesis]*, University of Michigan, Ann Arbor, Mich, USA, 2008.

[8] A. Matzain, *Multiphase flow paraffin deposition modeling [Ph.D. dissertation]*, The University of Tulsa, Tulsa, Okla, USA, 1999.

[9] H. K. Mirazizi, *Investigation of single-phase paraffin deposition characteristics under turbulent flow [M.S. thesis]*, The University of Tulsa, Tulsa, Okla, USA, 2011.

[10] M. Lashkarbolooki, A. Seyfaee, F. Esmaeilzadeh, and D. Mowla, "Experimental investigation of wax deposition in Kermanshah crude oil through a monitored flow loop apparatus," *Energy and Fuels*, vol. 24, no. 2, pp. 1234–1241, 2010.

[11] R. Hoffmann and L. Amundsen, "Single-phase wax deposition experiments," *Energy and Fuels*, vol. 24, no. 2, pp. 1069–1080, 2010.

[12] J. F. Tinsley, *The effects of polymers and asphaltenes upon wax gelation and deposition [Ph.D. dissertation]*, Princeton University, Princeton, NJ, USA, 2008.

[13] H. O. Bidmus and A. K. Mehrotra, "Solids deposition during "cold flow" of wax-solvent mixtures in a flow-loop apparatus with heat transfer," *Energy and Fuels*, vol. 23, no. 6, pp. 3184–3194, 2009.

[14] R. Tiwary and A. K. Mehrotra, "Deposition from wax-solvent mixtures under turbulent flow: effects of shear rate and time on deposit properties," *Energy and Fuels*, vol. 23, no. 3, pp. 1299–1310, 2009.

[15] N. V. Bhat and A. K. Mehrotra, "Modeling the effect of shear stress on the composition and growth of the deposit layer from "waxy" mixtures under laminar flow in a pipeline," *Energy and Fuels*, vol. 22, no. 5, pp. 3237–3248, 2008.

[16] J. Sestak, M. E. Charles, M. G. Cawkwell, and M. Houska, "Start-up of gelled crude oil pipelines," *Journal of Pipelines*, vol. 6, no. 1, pp. 15–24, 1987.

[17] M. G. Cawkwell and M. E. Charles, "An improved model for start-up of pipelines containing gelled crude oil," *Journal of Pipelines*, vol. 7, no. 1, pp. 41–52, 1987.

[18] H. Petter Rønningsen, "Rheological behaviour of gelled, waxy North Sea crude oils," *Journal of Petroleum Science and Engineering*, vol. 7, no. 3-4, pp. 177–213, 1992.

[19] C. Chang, Q. D. Nguyen, and H. P. Rønningsen, "Isothermal start-up of pipeline transporting waxy crude oil," *Journal of Non-Newtonian Fluid Mechanics*, vol. 87, no. 2-3, pp. 127–154, 1999.

[20] M. R. Davidson, Q. D. Nguyen, C. Chang, and H. P. Rønningsen, "A model for restart of a pipeline with compressible gelled waxy crude oil," *Journal of Non-Newtonian Fluid Mechanics*, vol. 123, no. 2-3, pp. 269–280, 2004.

[21] G. Vinay, A. Wachs, and I. Frigaard, "Start-up transients and efficient computation of isothermal waxy crude oil flows," *Journal of Non-Newtonian Fluid Mechanics*, vol. 143, no. 2-3, pp. 141–156, 2007.

[22] W. Li and J. J. Zhang, "Studies of temperature drop of buried waxy crude pipelines in shutdown," *Oil & Gas Storage and Transportation*, vol. 23, pp. 4–8, 2004 (Chinese).

[23] X. H. Yang, *Design and Management of Oil Pipelines*, China University of Petroleum Press, Dongying, Shandong, China, 2006.

[24] B. Yu, C. Li, Z. Zhang et al., "Numerical simulation of a buried hot crude oil pipeline under normal operation," *Applied Thermal Engineering*, vol. 30, no. 17-18, pp. 2670–2679, 2010.

[25] X. G. Cui and J. J. Zhang, "Determination of the thermal influence zone of buried hot oil pipeline on steady operation," *Journal of the University of Petroleum*, vol. 28, no. 2, pp. 75–78, 2004.

[26] C. Xu, B. Yu, Z. Zhang, J. Zhang, J. Wei, and S. Sun, "Numerical simulation of a buried hot crude oil pipeline during shutdown," *Petroleum Science*, vol. 7, no. 1, pp. 73–82, 2010.

[27] B. Yu and C. Xu, "Study on restart of crude oils batch pipelined with different outlet temperature," *Oil & Gas Storage and Transportation*, vol. 28, pp. 4–16, 2009.

Hindawi Publishing Corporation
Advances in Mechanical Engineering
Volume 2012, Article ID 863731, 7 pages
doi:10.1155/2012/863731

Research Article

Numerical Model on Frost Height of Round Plate Fin Used for Outdoor Heat Exchanger of Mobile Electric Heat Pumps

Moo-Yeon Lee

Department of Mechanical Engineering, Dong-A University, 37 Nakdong-Daero 550beon-gil saha-gu, Busan 604-714, Republic of Korea

Correspondence should be addressed to Moo-Yeon Lee, mylee@dau.ac.kr

Received 30 October 2012; Accepted 27 November 2012

Academic Editor: Bo Yu

The objective of this study is to provide the numerical model for prediction of the frost growth of the round plate fin for the purpose of using it as a round plate fin-tube heat exchanger (evaporator) under frosting conditions. In this study, numerical model was considering the frost density change with time, and it showed better agreement with experimental data of Sahin (1994) than that of the Kim model (2004) and the Jonse and Parker model (1975). This is because the prediction on the frost height with time was improved by using the frost thermal conductivity reflecting the void fraction and density of ice crystal with frost growth. Therefore, the developed numerical model could be used for frosting performance prediction of the round plate fin-tube heat exchanger.

1. Introduction

Frost formation and growth of the evaporator operated under frosting conditions are very essential phenomena because it acts as a thermal resistance with decreasing the frosting heat transfer performances in many refrigeration systems, air conditioning systems, and heat pump systems [1, 2]. Especially, numerous experimental and numerical studies on frosting and its growth have been reported for a long time. Padhmanabhan et al. [3] studied the semiempirical model to predict the nonuniform frost growth on fin-tube heat exchangers and validated with the experimental data. The considered fin configuration is rectangular type. Hong et al. [4] studied frost growth on louvered folded fins of microchannel heat exchangers. They provided several new data for frost growth on louvered fins and experimentally demonstrated the feasibility of the frost mass and frost height measurements. Xia and Jacobi [5] studied exact solution to steady heat conduction in a two-dimensional slab on a one-dimensional fin for the purpose of application to frosted heat exchangers. They mentioned that the exact solution is useful in gaining physical insights into the problem, and it is simple, accurate, and less costly to use than numerical solutions. Shao et al. [6] showed the comparison of heat pump performance using fin and tube and microchannel heat exchangers under frosting conditions. Lee et al. [7] studied the air-side heat transfer characteristics of spirally-coiled circular fin-tube heat exchanger operating under frosting conditions. They suggested the useful heat transfer correlation to predict the frosting heat transfer coefficient of the fin-tube heat exchanger. In summary, frosting including the frost height and growing is a key factor related to the previously mentioned thermal systems because it is a transient phenomenon and not easy to predict.

In these days, concerns of frosting performances of the round plate fin-tube heat exchanger in zero emission vehicles that do not use fossil fuels have been also increased because it considers as outdoor heat exchanger of the electric-driven heat pump system for cabin both heating and cooling. Lee et al. [8] studied experimentally frost height of round plate fin-tube heat exchangers under cold weather conditions for mobile heat pumps which have relatively large fin pitches. They mentioned that frosting problem is very important in adoption of the heat exchanger used in the electric-driven heat pump system for zero emission vehicles such as electric vehicles, fuel cell electric vehicles, and hybrid electric vehicles and So, the round plate fin-tube heat exchangers with large fin pitches might be used for zero emission. Also, Cho et al. [9] mentioned that the use of heat pumps instead of a PTC (positive temperature coefficient) heater is more

effective for the longer driving ranges of the previously mentioned vehicles. However, there is a limited amount of data available on the frosting and its performance on the round plate fin. Therefore, the various studies for predictions of the frosting performances including frost height and growing are generally necessary for usages of the outdoor heat exchangers (especially, an evaporator) as applications in the zero emission vehicles.

In this respect, this study aims to predict the frosting behavior on round plate fin under cold weather conditions. The predicted result was then compared with the experimental data suggested by Lee et al. [8]. In addition, the predicted data could be effectively used for designing the round plate fin-tube heat exchanger of the electric-driven heat pumps for zero emission vehicles.

2. Numerical Model

Figure 1 shows the schematic diagram of the round plate fin used in this study. The heat transfer rate on the frost was divided into the latent and sensible heat transfer as a function of the temperature and humidity ratio difference between the passing air and frost surface on the cold round plate fin. Based on the numerical modeling results of other researchers Jones and Parker [10], Kim [11], the heat and mass transfer rates were calculated by

$$\begin{aligned} q_t &= h_h(T_a - T_s) + \dot{m}\Delta h \\ h_h(T_a - T_s) + \rho_f \frac{dX_s}{dt}\Delta h + X_s \frac{d\rho_f}{dt}\Delta h &= k_f\left(\frac{dT}{dX_s}\right), \\ \dot{m} = h_m(\omega_a - \omega_s) &= \frac{d}{dt}\left(X_s\rho_f\right) = \rho_f \frac{dX_s}{dt} + X_s\frac{d\rho_f}{dt}. \end{aligned} \tag{1}$$

However, they calculated with an assumption of a constant frost density on the frost with time. This assumption is unrealistic because the process of the frost growth on the cold plate was a very slow but unsteady process. So, it was treated in an unsteady state in this study. The density changes of the frost surface of the newly developed frost layer were considered with time. Namely, whenever a frost was transferred to a new environment, the continued frost growth assumed a new habit characteristic of the new conditions. The frost density of the newly developed frost layer was calculated from

$$\rho_f = \beta \times \rho_c + (1 - \beta) \times \rho_a. \tag{2}$$

In order to reflect the density changes of newly developed frost layer, the sublimation density of ice crystals was expressed like (3) as a function of crystal formation temperature, based on the experimental studies of Fukuta [12] and Miller and Young [13]. The least squares approximation of the experimental data that is used for frost growth model is performed by Sahin [14]. This is because the frost layer is assumed to be consisted of the several frost columns.

Frost columns also consist of ice crystals. The conductivity of frost columns (k_{fc}) only is a function of the frost column density (ρ_c). consider

$$\begin{aligned} \rho_c &= -10429.56 + 41.574T, \quad 255.15\,\text{K} < T < 273.15\,\text{K}, \\ \rho_c &= 180, \quad T < 255.15\,\text{K}. \end{aligned} \tag{3}$$

Volumetric ratio (β) of the frost column considering the void fraction was expressed as functions of plate temperature, air temperature, and humidity ratio of moist air like (4) based on the experimental results of Sahin [15] as follows:

$$\beta = -11.8916 + 0.01371T_P + 0.03269T_a - 112.677\omega_a. \tag{4}$$

Equation (5) calculated the internal energy changes in control volume, as the humid air was changed into the frost crystal and a saturated air of the frost layer inside. As the humid air is infiltrated into the frost, a part of the humid air was used for formations of the new frost layer, and the rest of humid air was used to increase the densification of the previous frost layer. consider

$$\left(\frac{dE}{dt}\right)_{\text{sys}} = \left(\rho_c A_c h_{\text{fc}} + \rho_a A_a h_{a\_s} - (A_c + A_a)\rho_a h_a\right)\frac{dX_s}{dt}. \tag{5}$$

Equation (6) indicated the energy transfer rate by the saturated humid air infiltrated into the previous frost layer as follows:

$$\sum_{\text{out}}(\dot{m} \times\ h) = A_a X_s \frac{d\rho_f}{dt} h_{a\_s}. \tag{6}$$

Equation (7) suggested by Sanders [16] was used to calculate the thermal conductivity of the frost column as follows:

$$k_{\text{fc}} = \left(1.202 \times 10^{-3}\right)\rho_c^{0.963}. \tag{7}$$

The diffusivity of water vapor in air (D) is calculated from (8), and thermal conductivity of the air-side can be approximated to (9) suggested by Tso et al. [17] and Pruppacher and Klett [18] as follows:

$$D = 2.19 \times 10^{-5}\left(\frac{T}{T_0}\right)^{1.81}, \quad \text{for } T_0 = 273.15\,\text{K}, \tag{8}$$

$$k_a = (1.0465 + 0.017T) \times 10^{-5}. \tag{9}$$

Thus, thermal conductivity of the frost layer can be expressed as (10) suggested by Sahin [14]. The first term is the effect of the diffusion and sublimation of water vapor in the frost layer. This term is apparently a function of temperature; therefore, the contribution of this term to the frost thermal conductivity varies with the location in the frost layer. The second and third terms are the thermal conductivity contributions of the frost column and the moist air

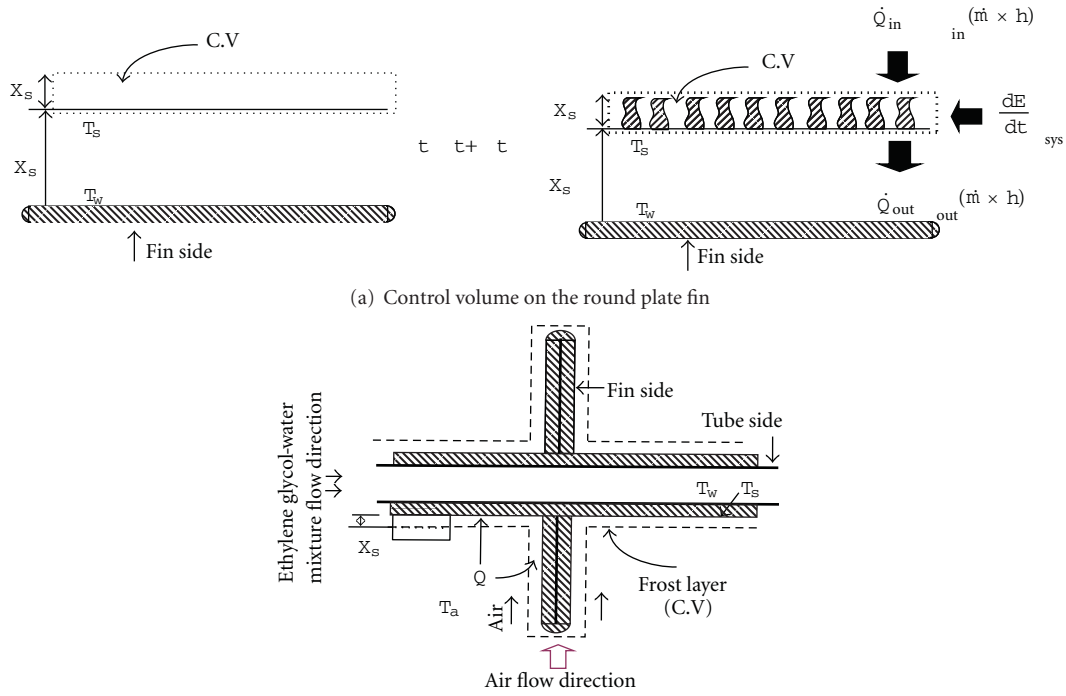

(a) Control volume on the round plate fin

(b) Control volume on fin-tube

Figure 1: Numerical model on frost height prediction at a round plate fin and fin-tube heat exchanger. (a) Control volume on the round plate fin. (b) Control volume on fin-tube.

around the frost columns, respectively, as mentioned in Sahin [14]. Consider

$$k_f = 0.131 \times 10^{-6}(1-\beta) \times \frac{\Delta h P_o P_{\text{atm}}}{T_0^{1.94} R^2 T^{1.06}} \times \exp\left[\frac{\Delta h}{R}\left(\frac{1}{T_o} - \frac{1}{T}\right)\right] + \beta k_{\text{fc}} + (1-\beta)k_a, \tag{10}$$

where P_o is the partial pressure of water vapor at $T_o = 273.15\,\text{K}$.

In order to calculate the heat transfer coefficient of the round plate fin-tube heat exchanger, (11) is used because the flow pattern between the fins could be considered as an internal flow [19]. Thus, (11) for an internal flow is the modified form of the heat transfer coefficient suggested by Holman [20], and the mass transfer rate is calculated by (12) [21] as follows:

$$h_h = 0.023 \frac{k_a}{D_h} \text{Re}^{0.8} \text{Pr}^{0.3}, \tag{11}$$

$$h_m = 0.023 \frac{D}{D_h} \text{Re}^{0.8} \text{Sc}^{0.3} \rho_a, \qquad \dot{m} = h_m(\omega_a - \omega_s). \tag{12}$$

Therefore, the heat transfer rate through frost layer and mass transfer rate inside the frost layer were calculated, then surface temperature and density of new developed frost layer were finally calculated. Figure 2 shows the block diagram of the frost growth model in this study. As Step 1 was converged with Step 2, surface temperature and density of new developed frost layer were calculated.

3. Results and Discussion

The developed numerical model reflects the various environmental parameters and unsteady processes of the frost formation and growth. Especially, the density changes of the newly developed frost layer were considered with time reflecting a new habit characteristic of the new conditions whenever a frost was transferred to a new environment. These points make the present numerical model more realistic than the existing numerical model for prediction of the frost growth.

3.1. Numerical Results. The present numerical model on frosting prediction was compared with Jones and Parker model [10], the experimental data of Sahin [15], and the Kim model [11, 22]. The present model showed a similar prediction to those of other models for the beginning of the frost formation but better agreement with the experimental data during the processing of the frost growth with time than the other models. The Jones and Parker model [10] has been the most commonly used frost growth model until now. However, the Jones and Parker model makes an important assumption to simplify the development of the model. There was assumed to be no spatial variation of frost density even though it varies with time. Accordingly, their model did not

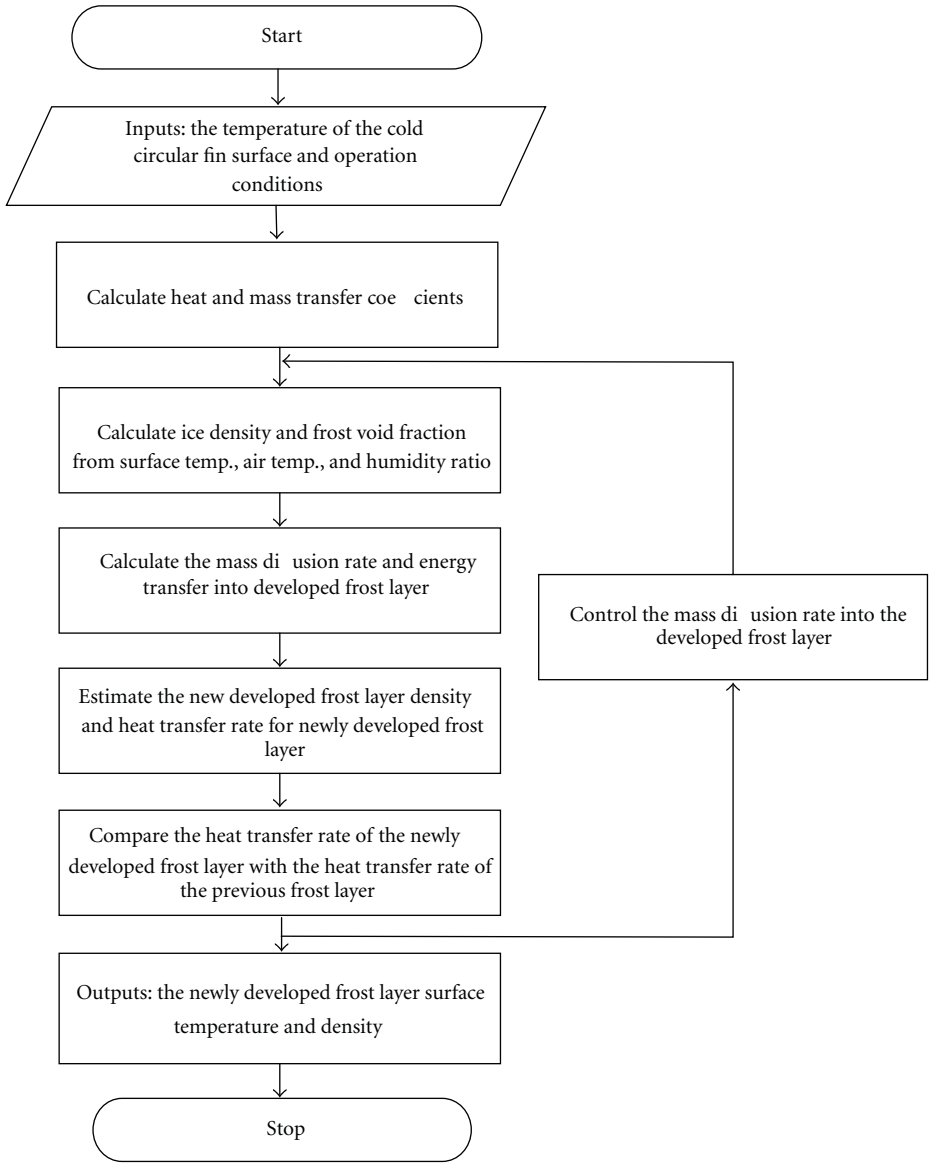

Figure 2: Flow diagram of the numerical model.

consider density changes on the frost surface with frost growth. The Kim model [11, 22] considered the frost thermal conductivity with frost density changes with frost growth. This model made good predictions at the beginning of the frost formation but not so good predictions as the frost growth progressed. The present numerical model considered the frost thermal conductivity according to the humidity ratio, surface temperature, density change, and void fraction of the frost surface with time. This will be shown to make good predictions for the frost growth.

Figure 3 shows the comparisons of the present model with experimental data provided by Sahin [15], the Jones and Parker model [10], and the Kim model [11, 22] under specified conditions with an air temperature of 18.0°C, plate temperature of −28.0°C, air velocity of 2.1 m/s, and humidity ratio of 0.007 kg/kg$_a$. The newly developed model in this study showed better agreement with the experimental data of Sahin [15] than the Kim model [11, 22], which considered the frost thermal conductivity as a function of the frost density, as well as the Jones and Parker model [10], which assumed the frost density to be constant with time.

Generally, fin configuration and space of the outdoor heat exchanger used in heat pump system for zero emission vehicles such as hybrid electric vehicles, electric vehicles, and fuel cell electric vehicles should be simple and large because of the frosting problem and easy defrosting water disposal. So, the round plate fin configuration is a good option to adapt as an outdoor heat exchanger for mobile electric heat pumps as mentioned in Lee et al. [8].

3.2. Validation with Experimental Data of Lee et al. [8]. The predicted data using numerical model were compared with

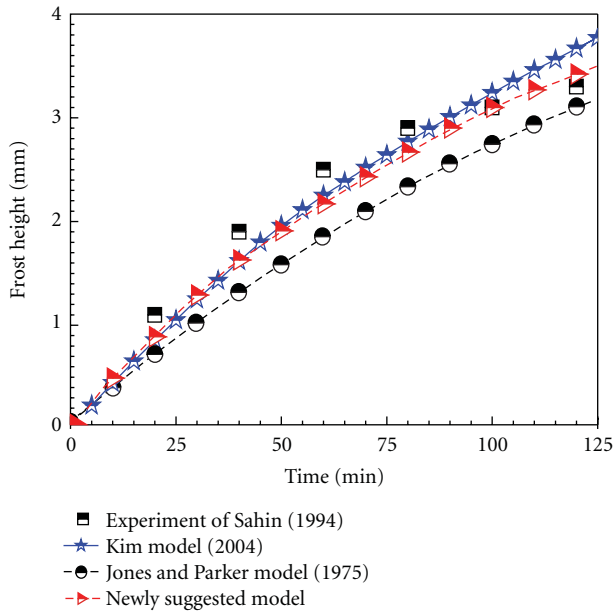

Figure 3: Comparisons between the present model and other data.

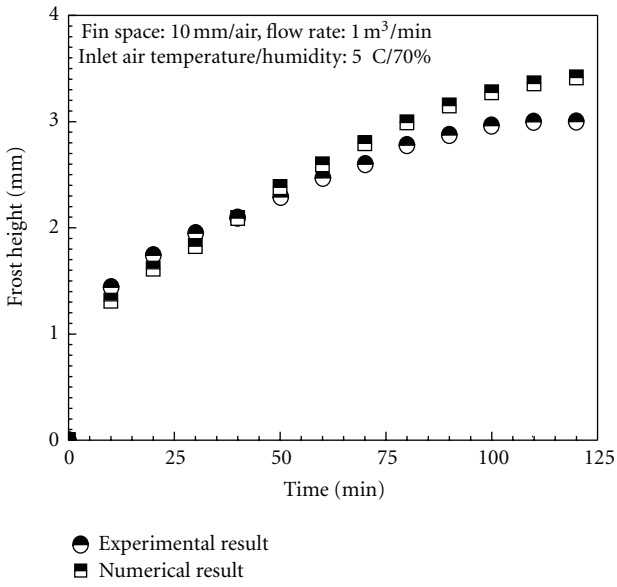

Figure 4: Comparison between the experimental data and numerical data with frost growth.

the experimental results obtained using a round fin-tube heat exchanger suggested by Lee et al. [8]. Figure 4 shows the comparisons between the numerical data and the experimental data for frost height of the round fin-tube heat exchanger with a fin space of 10.0 mm. It is simulated under an ethylene glycol-water mixture inlet temperature of −15.0°C, air flow rate of 1.0 m^3/min, air temperature of 5.0°C, and relative humidity of 70.0%. The considered fin-tube specifications are expressed in Table 1. Table 1 shows the simulation conditions and specifications of the considered heat exchanger.

Table 1: Conditions and specifications of the considered heat exchanger.

Parameter	Value
Fin space (mm)	10.0
Fin diameter (mm)	23.0
Fin thickness (mm)	0.25
Tube diameter (mm)	8.2
Tube thickness (mm)	0.5
Tube length (mm)	650.0
Materials for a fin and a tube	Aluminum
Inlet air temperature (°C)	5.0
Inlet air relative humidity (%)	70
Airflow rate (m^3/min)	1.0
Inlet temperature of an ethylene glycol-water mixture (°C)	−15.0

The numerical result was validated against the experimental result; both results matched on average to within −3.4%. The numerical data is underpredicted on average 5.8% at first 40 minutes and then overpredicted on average −7.9% after 40 minutes. The frost height predicted from numerical model showed good agreement with the experimental data during the first 40 minutes because the air flow rate was almost unchanged with frost growth. Moreover, the boundary layer interruption between the fins theoretically did not occur until the frost height on the fin surface reached 2.0 mm. However, the agreement between the numerical data and the experimental data after the frost height reached 2.0 mm at 40 minutes showed a slight difference because the numerical model did not consider the boundary layer interruption and pressure drop increase between the fins with frost growth. Based on the theoretical results of the boundary layer analysis using the techniques of Lee [23] and Mon and Gross [24], the velocity boundary layer thickness on one side of the fin surface was approximately 3.5 mm at the fin diameter of 23.0 mm with the tube diameter of 8.2 mm. Therefore, boundary layer interruption between fins can occur theoretically for a fin space of 7.0 mm at an air flow rate of 1.0 m^3/min. That is, the boundary layer interruption for a fin space of more than 7.0 mm can be avoided under the given conditions because the boundary layer interruption is largely dependent on the fin space [25].

This is consistent with the results of Kim [22]. The error on frost height between experimental data and numerical data is decreased as boundary layer interruption in the fins is considered with time. Namely, based on his results, errors between numerical data and experimental data were on average 1.4% with boundary layer interruption but were on average 5.5% without boundary layer interruption. In addition, in our next work, the effects of frost height on boundary layer interruption between the fins with frost growth will be studied because the boundary layer thickness and interruption are important factors in the design of heat exchangers.

4. Conclusions

The frost height and growing on the round plate fin, which could be used as the outdoor heat exchanger of an electric-driven heat pump in zero emission vehicles, were numerically predicted and validated with the published experimental data. The fundamental equation used for the calculation of the heat and mass transfer rate was simple enough to minimize the iteration time. This feature is important when numerical model is used for designing heat exchangers for low temperature heat pumps under cold weather conditions. The present model showed better predictions than the Jones and Parker model [10] and the Kim model [11, 22] for the frost height and growing with time. The following points summarize the current study.

(1) The present model developed in this study considered the frost thermal conductivity with the humidity ratio, surface temperature, density change, and void fraction of the frost surface with time.

(2) The frost height for 10.0 mm of fin space showed a similar rate of increase during the 40 minutes because the boundary layer interruption theoretically did not occur for a fin space of during the tests.

(3) The frost height predicted by using the frost growth model showed good agreement with published experiment data suggested by Lee et al. [8]. This is because the prediction of the frost height with time was improved by using an expression for the frost thermal conductivity that reflects the variation of the void fraction and density of ice crystals with the frost growth.

(4) The numerical result was validated against the experimental result; both results matched on average to within −3.4% during the tests.

Nomenclature

A: Surface area (m^2)
A_c: Area of frost column (m^2)
A_a: Area of air (m^2)
D: Thermal diffusivity in air (m^2/s)
D_h: Hydraulic diameter (mm) ($D_h = 4A_cL/A$)
D_o: Tube diameter (m)
G: Mass flux (kg/m^2 s)
h: Heat transfer coefficient (W/m^2 K)
h_m: Mass transfer coefficient (kg/m^2 s)
h_h: Heat transfer coefficient of frost layer (W/m^2 K)
h_{fc}: Enthalpy of the frost crystal (kJ/kg)
h_a: Air enthalpy (kJ/kg)
h_{a_s}: Saturated air enthalpy of the frost layer inside (kJ/kg)
Δh: Latent heat of vapor (kJ/kg)
k_a: Thermal conductivity of the air (W/m K)
k_{fc}: Thermal conductivity of the frost column (W/m K)
k_f: Thermal conductivity of the frost layer (W/m K)
L: Core depth or appropriate characteristic length (mm)
$\dot{m}$: Mass flux (kg/m^2 s)
P_{atm}: Atmospheric pressure (kPa)
P_o: Partial pressure of the water vapor at $T_o = 273.15$ K (kPa)
Pr: Prandtl number
Re: Reynolds number based on the tube diameter (GD_o/μ)
R: Gas constant (J/Kg K)
Sc: Schmidt number ($\mu/\rho D$)
T: Crystal formation temperature (°C)
T_a: Air temperature (°C)
T_p: Plate temperature (°C)
T_s: Surface temperature (°C)
T_w: Wall temperature (°C)
t: Time (min)
μ: Dynamic viscosity coefficient (N s/m^2)
ω_a: Humidity ratio of the moist air (kg/kg_a)
ω_s: Humidity ratio of the air at the frost surface (kg/kg_a)
X_s: Frost layer height (m)
x: Length (m)
β: Volumetric ratio of frost columns considering void fraction
ρ: Density (kg/m^3)
ρ_f: Frost layer density (kg/m^3)
ρ_a: Density of the air (kg/m^3)
ρ_c: Sublimation density of the frost crystal (kg/m^3).

Acknowledgment

This work was supported by the Dong-A University research fund (2012).

References

[1] W. M. Yan, H. Y. Li, Y. J. Wu, J. Y. Lin, and W. R. Chang, "Performance of finned tube heat exchangers operating under frosting conditions," *International Journal of Heat and Mass Transfer*, vol. 46, no. 5, pp. 871–877, 2003.

[2] M. Lee, T. Kang, and Y. Kim, "Air-side heat transfer characteristics of spiral-type circular fin-tube heat exchangers," *International Journal of Refrigeration*, vol. 33, no. 2, pp. 313–320, 2010.

[3] S. K. Padhmanabhan, D. E. Fisher, L. Cremaschi, and E. Moallem, "Modeling non-uniform frost growth on a fin-and-tube heat exchanger," *International Journal of Refrigeration*, vol. 34, no. 8, pp. 2018–2030, 2011.

[4] T. Hong, L. Cremaschi, E. Moaellem, and D. E. Fisher, "Measurements of frost growth on louvered folded fins of microchannel heat exchangers part 1: experimental methodology," *ASHRAE Transactions*, vol. 118, no. 1, pp. 1101–1115, 2012.

[5] Y. Xia and A. M. Jacobi, "An exact solution to steady heat conduction in a two-dimensional slab on a one-dimensional fin: application to frosted heat exchangers," *International Journal*

of Heat and Mass Transfer, vol. 47, no. 14–16, pp. 3317–3326, 2004.

[6] L. L. Shao, L. Yang, and C. L. Zhang, "Comparison of heat pump performance using fin-and-tube and microchannel heat exchangers under frost conditions," *Applied Energy*, vol. 87, no. 4, pp. 1187–1197, 2010.

[7] M. Lee, T. Kang, Y. Joo, and Y. Kim, "Heat transfer characteristics of spirally-coiled circular fin-tube heat exchangers operating under frosting conditions," *International Journal of Refrigeration*, vol. 34, no. 1, pp. 328–336, 2011.

[8] M. Y. Lee, Y. Kim, and D. Y. Lee, "Experimental study on frost height of round plate fin-tube heat exchangers for mobile heat pumps," *Energies*, vol. 5, no. 9, pp. 3479–3491, 2012.

[9] C. W. Cho, H. S. Lee, J. P. Won, and M. Y. Lee, "Measurement and evaluation of heating performance of heat pump systems using wasted heat from electric devices for an electric bus," *Energies*, vol. 5, pp. 658–669, 2012.

[10] B. W. Jones and J. D. Parker, "Frost formation with varying environmental parameters," *Journal of Heat Transfer*, vol. 97, no. 2, pp. 255–259, 1975.

[11] Y. H. Kim, *Study on the frosting and defrosting performance of finned tube heat exchangers [Ph.D. thesis]*, Korea University, 2004.

[12] N. Fukuta, "Experimental studies on the growth of small ice crystals," *Journal of the Atmospheric Sciences*, vol. 26, pp. 521–531, 1969.

[13] T. L. Miller and K. C. Young, "A numerical simulation of ice crystal growth from the vapor phase," *Journal of the Atmospheric Sciences*, vol. 36, pp. 458–469, 1979.

[14] A. Z. Sahin, "Effective thermal conductivity of frost during the crystal growth period," *International Journal of Heat and Mass Transfer*, vol. 43, no. 4, pp. 539–553, 2000.

[15] A. Z. Sahin, "An experimental study on the initiation and growth of frost formation on a horizontal plate," *Experimental Heat Transfer*, vol. 7, no. 2, pp. 101–119, 1994.

[16] C. T. Sanders, *The influence of frost formation and defrosting on the performance of air coolers [Ph.D. thesis]*, Delft Technical University, 1974.

[17] C. P. Tso, Y. C. Cheng, and A. C. K. Lai, "An improved model for predicting performance of finned tube heat exchanger under frosting condition, with frost thickness variation along fin," *Applied Thermal Engineering*, vol. 26, no. 1, pp. 111–120, 2006.

[18] H. R. Pruppacher and J. D. Klett, "Microphysics of clouds and precipitation," *Nature*, vol. 284, no. 5751, p. 88, 1980.

[19] Y. Kim and Y. Kim, "Heat transfer characteristics of flat plate finned-tube heat exchangers with large fin pitch," *International Journal of Refrigeration*, vol. 28, no. 6, pp. 851–858, 2005.

[20] J. P. Holman, *Heat Transfer*, McGraw-Hill, Berkshire, UK, 7th edition, 1992.

[21] F. P. Incropera and D. P. DeWitt, *Fundamentals of Heat and Mass Transfer*, John Wiley & Sons, New York, NY, USA, 4th edition, 1996.

[22] Y. H. Kim, *Study on the frosting and defrosting performance of finned tube heat exchangers [Ph.D. thesis]*, Korea University, 2004.

[23] M. Y. Lee, *Heat and mass transfer characteristics of a spirally-coiled circular fin-tube heat exchanger [Ph.D. thesis]*, Korea University, 2010.

[24] M. S. Mon and U. Gross, "Numerical study of fin-spacing effects in annular-finned tube heat exchangers," *International Journal of Heat and Mass Transfer*, vol. 47, no. 8-9, pp. 1953–1964, 2004.

[25] H. Lee, M. Lee, Y. Kim, and Y. Kim, "Air-side heat transfer characteristics offlat plate finned-tube heat exchangers with large fin pitches under frosting conditions," *International Journal of Heat and Mass Transfer*, vol. 53, no. 13-14, pp. 2655–2661, 2010.

Hindawi Publishing Corporation
Advances in Mechanical Engineering
Volume 2012, Article ID 461708, 10 pages
doi:10.1155/2012/461708

Research Article

Experimental Validation of Volume of Fluid Method for a Sluice Gate Flow

A. A. Oner,[1] M. S. Akoz,[2] M. S. Kirkgoz,[2] and V. Gumus[2]

[1] *Civil Engineering Department, Aksaray University, 68100 Aksaray, Turkey*
[2] *Civil Engineering Department, Cukurova University, 01330 Adana, Turkey*

Correspondence should be addressed to A. A. Oner, alperoner38@gmail.com

Received 10 September 2012; Accepted 30 October 2012

Academic Editor: Bo Yu

Laboratory experiments are conducted for 2D turbulent free surface flow which interacts with a vertical sluice gate. The velocity field, on the centerline of the channel flow upstream of the gate is measured using the particle image velocimetry technique. The numerical simulation of the same flow is carried out by solving the governing equations, Reynolds-averaged continuity and Navier-Stokes equations, using finite element method. In the numerical solution of the governing equations, the standard $k-\varepsilon$ turbulence closure model is used to define the turbulent viscosity. The measured horizontal velocity distribution at the inflow boundary of the solution domain is taken as the boundary condition. The volume of fluid (VOF) method is used to determine the flow profile in the channel. Taking into account of the flow characteristics, the computational domain is divided into five subdomains, each having different mesh densities. Three different meshes with five subdomains are employed for the numerical model. A grid convergence analysis indicates that the discretization error in the predicted velocities on the fine mesh remains within 2%. The computational results are compared with the experimental data, and, the most suitable mesh in predicting the velocity field and the flow profile among the three meshes is selected.

1. Introduction

The laboratory experiments on physical models of flow phenomena which have interactions with various types of hydraulic structures may be expensive and time consuming, and also the results are bound to be somewhat scale-affected. On the other hand, the computational fluid dynamics (CFDs) simulation of flow fields may be capable of providing precise solutions for the efficient designing of hydraulic structures.

According to the results of CFD studies in recent years, the volume of fluid (VOF) method, which provides a simple way of treating the topological changes of the air-water interface in free-surface flows, appears to be a powerful computational tool for the analysis of steady and unsteady free-surface flows interacting with spillways, weirs, and wall type hydraulic structures [1, 2]. The numerical results for turbulent flows so far obtained from the experimental validations on physical models [3–10] and on prototypes [11] show that the VOF-based CFD modeling is capable of investigating the performance of hydraulic structures. However, from the results of VOF-based numerical simulations so far, it seems that further experimental validations are useful before this method is confidently applied to the future studies of different free-surface flows.

In predicting the various characteristics of flow under the gates that are widely used hydraulic structures for controlling and metering the open channel flow, many experimental and theoretical studies have recently been undertaken [12–15]. The present work is concerned with the experimental validation of the VOF-based finite element analysis of the rectangular open channel flow interacting with a vertical sluice gate. Using particle image velocimetry (PIV) technique, laboratory experiments were conducted to determine the velocity field of 2D flow upstream of the gate. The computational results for the velocity field and the free-surface profile obtained from the VOF-based CFD modeling, were compared with the experimental data.

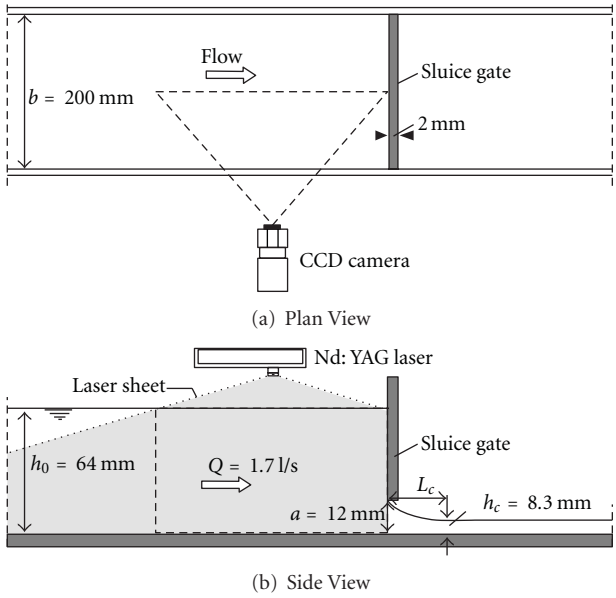

Figure 1: Experimental arrangement for velocity measurement using PIV system.

2. Experiments

The experiments were conducted in a glass-walled (including the bed), hydraulically smooth, horizontal laboratory channel which was 2.4 m long with cross-sectional dimensions of 0.2×0.2 m. A smooth, sharp-edged vertical sluice gate model with 2 mm thickness was mounted in the channel. The experimental conditions of the flow are shown in Figure 1 and given in Table 1, where Q is the discharge, h_0 is upstream subcritical flow depth, a is gate opening from the channel bed, h_c is flow depth at the contraction section of the rapidly varied flow under the gate, L_c is the contraction length, C_c is the contraction coefficient, C_d is the discharge coefficient, Fr_0 is Froude number, and Re_0 is Reynolds number. The discharge was measured using a volumetric tank. In Table 1, $V_0 = Q/(bh_0)$ is average velocity, b is channel width, R_0 is hydraulic radius of upstream flow, g is gravitational acceleration, and ν is kinematic viscosity of water.

For measuring the flow velocities, various experimental techniques such as the laser doppler anemometry [16], particle image velocimetry [17], and acoustic doppler velocimetry [18] have been employed in recent years. In the present study, the flow velocities were measured using the particle image velocimetry (PIV) technique. The experimental arrangement for the measurement of velocity field upstream of the vertical gate is shown in Figure 1. The instantaneous velocities of the flow field at the mid-span of the channel were measured using the Dantec PIV flow measuring system. The flow was illuminated via a 2 mm thick laser sheet from a pair of double-pulsed Nd:YAG laser unit. Within the 2D measuring area of the flow, the velocity vectors were determined by recording the displacements of the seeding particles between the two locations during a specified time intervals of the two pulses which were 2.5 ms. The movement of the particles were recorded by a CCD camera with a resolution of 1024×1024 pixels. From the recorded particle image velocity data, the displacement vectors were obtained. The size of the velocity measuring field viewed by the laser sheet was 222.5×224.3 mm. By postprocessing of the measured instantaneous velocities, the time-averaged velocity vector field was determined.

3. Governing Equations and Numerical Solution

3.1. Governing Equations and Turbulence Modeling. The open channel flow under the vertical sluice gate is 2D, Newtonian, incompressible, turbulent flow whose governing equations are Reynolds-averaged continuity and the Navier-Stokes equations (RANSs) which can be written in the following form in the Cartesian coordinate system:

$$\frac{\partial \overline{u}}{\partial x} + \frac{\partial \overline{v}}{\partial y} = 0, \tag{1}$$

$$\rho\left(\frac{\partial \overline{u}}{\partial t} + \overline{u}\frac{\partial \overline{u}}{\partial x} + \overline{v}\frac{\partial \overline{u}}{\partial y}\right) = \rho g_x - \frac{\partial \overline{p}}{\partial x} + \mu\nabla^2\overline{u} + \frac{\partial}{\partial x}\left(-\rho\overline{u'^2}\right) + \frac{\partial}{\partial y}\left(-\rho\overline{u'v'}\right), \tag{2}$$

$$\rho\left(\frac{\partial \overline{v}}{\partial t} + \overline{u}\frac{\partial \overline{v}}{\partial x} + \overline{v}\frac{\partial \overline{v}}{\partial y}\right) = \rho g_y - \frac{\partial \overline{p}}{\partial y} + \mu\nabla^2\overline{v} + \frac{\partial}{\partial x}\left(-\rho\overline{u'v'}\right) + \frac{\partial}{\partial y}\left(-\rho\overline{v'^2}\right). \tag{3}$$

In (1)–(3), $\overline{u}$ and $\overline{v}$ are the mean velocity components, and u' and v' are turbulent velocity fluctuations in horizontal (x) and vertical (y) directions, respectively, g_x and g_y are the body force components due to gravity, $\overline{p}$ is the mean pressure, μ is dynamic viscosity, ρ is fluid density, $-\rho\overline{u'^2}(= \tau_{xx})$, $-\rho\overline{u'v'}(= \tau_{xy} = \tau_{yx})$, and $-\rho\overline{v'^2}(= \tau_{yy})$ are the mean turbulence stresses. Turbulence stresses in (2) and (3) may be obtained from the constitutive equation which is defined by

$$\tau_{ij} = -\rho\overline{u_i'u_j'} = \mu_t\left(\frac{\partial \overline{u}_i}{\partial x_j} + \frac{\partial \overline{u}_j}{\partial x_i}\right) - \frac{2}{3}\rho k\delta_{ij}, \tag{4}$$

in which μ_t is the turbulent viscosity, $k(= \overline{u_i'u_i'}/2)$ is the turbulent kinetic energy, and δ_{ij} is the Kronecker delta.

In determining μ_t in (4), various turbulence models in computational fluid dynamics have so far been used [19, 20]. In the present computations, the standard $k - \varepsilon$ turbulence model was used [21]. This model expresses the turbulent viscosity in terms of turbulent kinetic energy, k, and its dissipation rate, ε, as

$$\mu_t = \rho C_\mu \frac{k^2}{\varepsilon}. \tag{5}$$

In (5), C_μ is the turbulence constant that has a value of 0.09. In the $k - \varepsilon$ model, the following two transport partial

Table 1: Experimental conditions.

Q (L/s)	h_0 (mm)	a (mm)	h_c (mm)	L_c (mm)	$C_c = h_c/a$	$C_d = Q/[ba(2gh_0)^{1/2}]$	$\mathrm{Fr}_0 = V_0/(gh_0)^{1/2}$	$\mathrm{Re}_0 = 4V_0R_0/\nu$
1.7	64	12	8.3	14	0.69	0.63	0.17	19 930

differential equations were solved for the values of k and ε, respectively:

$$\begin{aligned}
&\rho\overline{u}\frac{\partial k}{\partial x} + \rho\overline{v}\frac{\partial k}{\partial y} + \rho\frac{\partial k}{\partial t} \\
&\quad = \frac{\partial}{\partial x}\left[\left(\mu + \frac{\mu_t}{\sigma_k}\right)\frac{\partial k}{\partial x}\right] + \frac{\partial}{\partial y}\left[\left(\mu + \frac{\mu_t}{\sigma_k}\right)\frac{\partial k}{\partial y}\right] + \mu_t G - \rho\varepsilon, \\
&\rho\overline{u}\frac{\partial \varepsilon}{\partial x} + \rho\overline{v}\frac{\partial \varepsilon}{\partial y} + \rho\frac{\partial \varepsilon}{\partial t} \\
&\quad = \frac{\partial}{\partial x}\left[\left(\mu + \frac{\mu_t}{\sigma_\varepsilon}\right)\frac{\partial \varepsilon}{\partial x}\right] + \frac{\partial}{\partial y}\left[\left(\mu + \frac{\mu_t}{\sigma_\varepsilon}\right)\frac{\partial \varepsilon}{\partial y}\right] \\
&\qquad + C_1\mu_t\frac{\varepsilon}{k}G - C_2\rho\frac{\varepsilon^2}{k},
\end{aligned} \tag{6}$$

where G, which represents the generation of turbulent kinetic energy, is defined by

$$G = 2\left[\left(\frac{\partial \overline{u}}{\partial x}\right)^2 + \left(\frac{\partial \overline{v}}{\partial y}\right)^2\right] + \left(\frac{\partial \overline{u}}{\partial y} + \frac{\partial \overline{v}}{\partial x}\right)^2 \tag{7}$$

and $C_1 = 1.44, C_2 = 1.92, \sigma_k = 1.0$, and $\sigma_\varepsilon = 1.3$.

3.2. Near Wall Treatment. The standard $k-\varepsilon$ model, which is the first and the most widely used two-equation turbulence closure model, has been applied to many types of flow with varying degrees of success. Unfortunately, it is insensitive to adverse pressure gradients and this causes a serious limitation to its general utility. The standard $k-\varepsilon$ model avoids the integration of model equations through to the wall where the viscosity effects have to be taken into account. There are two approaches for modeling the near wall region: wall function and two-layer approach. In the wall function approach, the viscosity-affected region (i.e., viscous sublayer and buffer layer) is not solved and a semiempirical function called wall function is used to bridge the viscosity-affected region between the wall and fully turbulent region. The application of wall functions may significantly reduce both the processing and storage requirements of a numerical model. The application of the wall functions leads (provided that the grid is not too coarse) to reasonably accurate results for attached boundary layers. However, the use of wall functions becomes highly questionable for separated flows [22]. In two-layer approach, the turbulence models are modified to resolve the viscosity-affected region by extremely fine grids with no slip condition and a damping functions to account for viscous effects near the wall.

In the $k-\varepsilon$ modeling of the present computations, a sufficiently fine mesh was used in simulating the near-wall viscosity-affected region with no-slip condition and the damping function presented by van Driest [23]. Based on the experimental data, van Driest [23] proposed that the mixing length, $\ell = \kappa y$, should be multiplied by a damping function:

$$f_\mu = 1 - \exp\left(-\frac{y^+}{A}\right), \tag{8}$$

where $y^+ = \nu * y/\nu$ is the dimensionless distance, and the Kármán's constant $\kappa = 0.4$ and the constant $A = 26$. van Driest modification given by (8) improves the predictive accuracy by asymptotic description of the mixing length in the limit $y \to 0$ [18]. Using (8), the behaviors of the mixing length and the turbulence stress are described as $\ell \sim y^2$ and $\tau'_{xy} \sim y^2$, respectively, as $y \to 0$.

3.3. Numerical Solution. Numerical solution of (1)–(3) for the unknown variables $\overline{u}$, $\overline{v}$, and $\overline{p}$ were carried out using the finite element method (FEM). In the finite element discretization, the conservation forms, that is, the transport equations of the governing equations were used. These equations for a transferable fluid property ϕ defined per unit mass in a unit control volume read

$$\frac{\partial(\rho\phi)}{\partial t} + \mathrm{div}\left(\rho\phi\vec{V}\right) = \mathrm{div}\left(\Gamma_\phi\,\mathrm{grad}\,\phi\right) + S_\phi \tag{9}$$

in which $\vec{V}$ is the velocity vector, Γ_ϕ is the generalized diffusion coefficient, and S_ϕ is the generalized source term. The fluid property ϕ takes values of 1 and $\vec{V}$ for the conservation of mass and momentum, respectively.

The discretization process consists of deriving the element matrices to put together the matrix equation as

$$\left(\left[A_e^{\text{transient}}\right] + \left[A_e^{\text{advection}}\right] + \left[A_e^{\text{diffusion}}\right]\right)\{\phi_e\} = \left\{S_e^{\phi}\right\}. \tag{10}$$

Galerkin's method of weighted residuals is used to form the element integrals. Petrov-Galerkin approach of second-order accurate was used to discretize the advection term in the momentum equations. The time integration of the governing equations was carried out using the backward difference method. The convergence criterion for the computations of the velocity components u and v was assumed 10^{-6}.

3.4. Solution Domain, Boundary, and Initial Conditions. The 2D solution domain for the numerical analyses of the gate flow is shown in Figure 2. The origin of the Cartesian coordinate system, (x, y), was located at the bottom left corner of the solution domain. The air-filled upper boundary was taken some distance above the free-surface of the subcritical upstream flow, and the lower boundary was the solid channel bed. The vertical gate was located at a distance $x = 218$ mm. No-slip boundary condition was invoked by specifying the velocity components to be zero at the fluid-wall interface, that is, at the lower boundary and on the gate

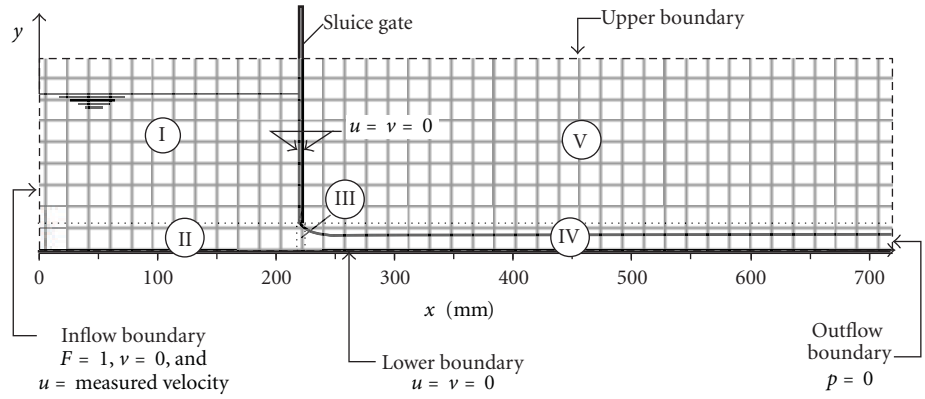

Figure 2: Geometry and boundary conditions of the solution domain for the gate flow.

surfaces, the velocity components in x and y directions were taken as $u = v = 0$. At the inflow boundary, the horizontal velocities, u, were specified as the measured velocity profile, and the vertical velocity, $v = 0$. The outflow boundary of the computational domain was the supercritical free overfall at the end of the channel where $p = 0$.

The time-dependent solution procedure was started with the initial condition that at the inflow boundary $F = 1$, and continued with a time step of 0.01 s which was found suitable to speed up the convergence.

3.5. Volume of Fluid Method for Free-Surface Modeling. In the computation of free-surface flows, a method called volume of fluid (VOF) which is based on a concept of a fractional volume of fluid, whereby the shape and location of the constant-pressure free-surface boundary are determined successfully [4, 6, 11]. On general fixed meshes, this method uses a filling process which determines which cell in the meshing volume is filled and which is emptied [2]. Consider an Eulerian structured fixed mesh and an actual curved free liquid surface of a 2D flow field cutting through it. Then, one can define a volume fraction (F) field in this mesh that can take values between 1 and 0. That is the value of F is 1 when the cell of the meshing volume is filled with liquid and is equal to 0 when it is emptied. A value of F between 0 and 1 means a fractional fill that is the free-surface lies in the cell. When $0 < F < 1$, the fluid properties ρ and μ in the transport equations are calculated as the volume-fraction averaged values of water (ρ_w) and air (ρ_a) as follows:

$$\begin{aligned} \rho &= \rho_w F + \rho_a (1 - F), \\ \mu &= \mu_w F + \mu_a (1 - F). \end{aligned} \tag{11}$$

The time-dependent computational scheme of the VOF method proceeds as follows. At some moment in time on a finite mesh, a unique volume fraction field, F, of the water phase is calculated for a given interface and then the velocity field of the flow is obtained from the governing equations, and at the next time step, the new F field (i.e., the advected volume fraction field) is calculated and the reconstruction and orientation of the new interface is determined. For the new free-surface position the velocity field is obtained from the governing equations. The advection equation of the volume fraction is given by

$$\frac{\partial F}{\partial t} + \vec{\nabla} \cdot \left(\vec{V} F \right) = 0. \tag{12}$$

The evolution of the free-surface in the time-dependent computational scheme is herein accomplished using an algorithm so-called Computational Lagrangian-Eulerian Advection Remap (CLEAR-VOF) which is detailed in Ashgriz et al. [5]. This algorithm utilizes exact geometric tools with no special requirement on the mesh topology, the aspect ratio, or the mesh orientation. CLEAR-VOF algorithm is based on an approach for the computation of the fluxes of fluid originating from a certain element toward each of its neighboring elements during the advection process to find out how much of fluid remains in the element, and how much of it passes into each of the neighboring cells. From an initial interface and corresponding F field, the advected polygonal shape of the free-surface, after a time step, is identified through a Lagrangian local motion using the velocities at its vertices, and the new values for the local F field of the advected liquid domain for the original Eulerian fixed mesh is determined. At the next stage, F field of the cells of the fixed mesh is redistributed and corrected so that the conservation of mass is satisfied. The corrected new F field serves as input to the interface reconstruction of the VOF code and to the flow solver for the next time step. Computation of free-surface profile by the VOF method, and the numerical solution of (1)–(3) for the 2D sluice gate flow were carried out using the software called ANSYS 10.0 which contains a general-purpose CFD package based on the FEM.

3.6. Computational Meshing

3.6.1. Mesh Design. The results of the preliminary computations showed that in order to increase the computational accuracy, the density of mesh should be changed locally as appropriate. Accordingly, taking into account the basic features of the present subcritical and supercritical flow fields upstream and downstream of the gate, the computational domain given in Figure 2 is divided into five local

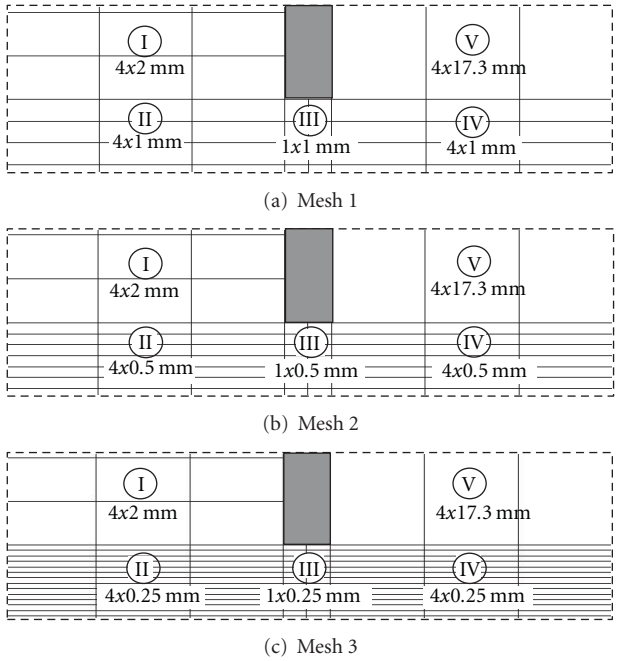

(a) Mesh 1

(b) Mesh 2

(c) Mesh 3

Figure 3: Three computational meshes used in the numerical model.

subdomains in which different mesh concentrations were tested. Uniform rectangular meshes were structured in all the subdomains. In constructing the computational mesh, relatively finer meshes in y-direction were used in the near-wall regions and in the region of rapid variation of free-surface profile in the contraction region of flow just after the gate (i.e., in regions II, III, and IV in Figure 2). In accordance with above considerations, three different meshes given in Figure 3 were constructed for the computations. The sizes of the mesh elements for each subdomain are given on the figure. As may be seen in Figure 3, the differences between the three meshes are implemented in subdomains II, III, and IV only, where the vertical dimensions of the mesh elements are $\Delta y = 1$, 0.5, and 0.25 mm for Mesh 1, Mesh 2, and Mesh 3, respectively. The horizontal dimensions of the mesh elements were kept constant for all three meshes as $\Delta x = 4$ mm for the subdomains I, II, IV, and V, and $\Delta x = 1$ mm for the subdomain III below the gate.

3.6.2. Estimation of Discretization Error. A grid convergence index (GCI) proposed by Roache [24] was determined for the verification of computed velocities using the three mesh system described above. According to this technique, for the quantification of the discretization uncertainty of the numerical results, the fine-grid convergence index is defined as

$$\mathrm{GCI}_{23}^{\mathrm{fine}} = \frac{1.25|E_{23}|}{r_{23}^{P} - 1}, \tag{13}$$

where $E_{23} = (u_{s3} - u_{s2})/u_{s3}$ = approximate relative error between the medium and fine meshes, u_{s2} and u_{s3} = medium and fine mesh solutions for velocities obtained with grid spacing d_2 and d_3, respectively, and P = local order of accuracy. For the three-grid solutions, P is obtained by solving the following equation:

$$P = \frac{1}{\ln r_{23}} \ln \frac{\left(r_{23}^{P} - 1\right) e_{12}}{\left(r_{12}^{P} - 1\right) e_{23}} \tag{14}$$

in which $e_{12} = u_{s1} - u_{s2}$, $e_{23} = u_{s2} - u_{s3}$, and $r_{12} = d_1/d_2$ and $r_{23} = d_2/d_3$ = grid refinement factors between coarse and medium, and medium and fine grid, respectively. For the present three-grid comparisons the grid spacing have the following order, $d_3 < d_2 < d_1$.

In this study, the profiles of the computed horizontal velocities of supercritical flow at $x = 0.24$ m, just downstream of the sluice gate, were used to determine the numerical uncertainties due to discretization (Table 2). In the assessment of GCI values in (13), the average order of accuracy, $P = P_{\mathrm{ave}}$, over the flow section was used. It is seen that the maximum discretization uncertainty in the chosen velocity profile (with 16 number of points) for the fine-grid solutions on Mesh 3 is 0.73% corresponding to ± 0.0070 m/s which remains within 2% and shows an excellent indication for a mesh-independent solution.

Table 2: Discretization error estimate in velocity profile at $x = 0.24$ m.

Quantity	Error estimates in velocity
Number of points	16
P_{min}, P_{max}, P_{ave}	0.43, 6.97, 2.28
Max $\mathrm{GCI}_{23}^{\mathrm{fine}}$	0.73% (± 0.0070 m/s)

4. Experimental and Numerical Results

In the following, the numerical results for the velocity field and free-surface profile from the VOF-based CFD modeling of 2D rectangular open channel flow under a vertical sluice gate are presented. The results of the numerical simulation obtained from the three meshes given in Figure 3 are compared with experimental results, and the sensitivity of the numerical model to the computational meshing is discussed. It is generally accepted that very near the wall from no-slip at the wall to about $y^+ = v * y/\nu \approx 30$, turbulence is damped out and the boundary layer is dominated by viscous shear [19], where $v_* = (\tau_0/\rho)^{1/2}$ is shear velocity and τ_0 is boundary shear stress. In the present computational results of all three meshes, the values of y^+ remain within 30 for $x \leq 205$ mm. That means, up to a location very close to the wall, the flow in the near-wall elements is treated as viscous in character.

4.1. Comparison of Computed and Measured Velocities. From the PIV measurements of flow velocities, the vertical distributions of the horizontal velocity components at different locations upstream of the vertical gate are given in Figure 4. The vertical distribution of horizontal velocities at $x = 0$ is used as the inflow boundary condition for the

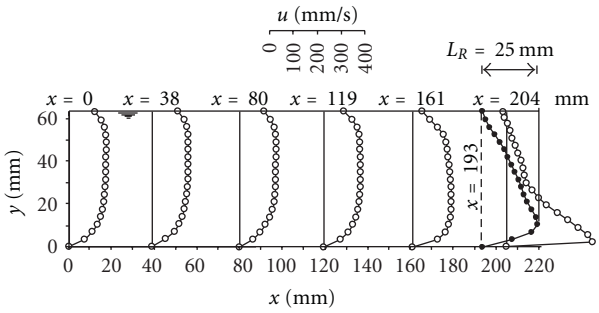

Figure 4: Experimental horizontal velocity profiles at various locations upstream of the gate.

numerical computations. The horizontal velocity profile at $x = 193$ mm corresponds to the Reynolds ridge position on the water surface, where the horizontal velocity is zero. The ridge position which is characterized as the plunging point of the stagnation flow behind the vertical gate has a horizontal distance of $L_R = 25$ mm from the gate for the present experimental conditions.

Vertical distributions of experimental and numerical results of dimensionless horizontal velocities, u/V_0, at locations of $x = 38, 80, 119, 161$, and 204 mm for the three meshes are given in Figure 5. From the comparisons of the velocity distributions, it is seen that the computational results from Mesh 1, Mesh 2, and Mesh 3 are very close to each other and in general they show reasonable agreement with experimental velocity distributions. The disagreement between the results of numerical model and experiment in Figure 5 seems to slightly increase toward the free-surface in part of the solution domain where $x \leq 80$ mm, in that region Mesh 3 is the most successful.

For a quantitative evaluation of the comparison of the experimental (u_m) and predicted (u_p) velocities, the mean square error (MSE) is calculated at section $x = 204$ mm. The MSE is given as

$$\text{MSE} = \frac{1}{N} \sum_{n=1}^{N} \left(u_m - u_p\right)^2. \tag{15}$$

The MSE values are found as 0.00210, 0.00196, and 0.00174 for Mesh 1, Mesh 2 and Mesh 3, respectively. That means the predicted accuracy of the simulation regarding the flow velocity is the best for Mesh 3.

Figure 6 shows the vertical distributions of measured and computed dimensionless vertical flow velocities, v/V_0, at the two sections $x = 193$ mm and 204 mm, close to the gate from the three meshes. The vertical velocity comparisons show generally good agreement between the results of numerical model from the three meshes and experiment. However Figure 6 clearly demonstrates that the computed results produced by Mesh 3 are relatively better over the entire flow depths.

From the examination of the velocity distributions given in Figures 5 and 6, it is difficult to detect a very distinct effect of mesh density on the computed velocities throughout the solution domain. Since the increasing of the mesh concentration does not result so much improvement on the computed velocities, and besides considering the advantage of shorter computing time, Mesh 1, that is the coarsest of the three meshes, can be used to adequately describe the computed velocity field for the flow region upstream of the gate. Actually, a reasonable investigation into the mesh density effect on the flow properties must also include the problem of accurate prediction of flow profile which will be discussed in the following section.

Figure 7 gives the measured and computed velocity vector fields upstream of the gate using Mesh 3. It is seen that experimental and computed velocity fields display a clear zone of swirling motion, called the recirculation region, behind the gate where the water in the surface flows in reverse direction. The ridge position on the water surface can be detected from the velocity vector field.

4.2. Comparison of Computed and Measured Flow Profiles. Figure 8 shows the computed and measured subcritical flow profiles upstream of the gate from the three meshes. It is seen that the computational upstream flow profiles are almost similar for the three different meshes. From the computations using the three meshes, the upstream flow depths were all found as $h_0 = 66$ mm which is slightly higher than the measured depth of 64 mm.

The supercritical downstream flow contains a rapidly varied profile between the gate outlet and the contraction section. Because there is a considerable change of flow depth along the rapidly varied contraction region, regarding the mesh effect, this portion of the flow within the solution domain is considered as the most decisive in comparing the computed and measured flow profiles. Computed flow profiles in the rapidly varied contraction region under the gate and the values of the contraction coefficient, C_c, obtained from the three meshes are given in Figure 9. From the examination of the three computed profiles in Figure 9, it is seen that in contrast to the velocity distributions presented in Figures 5 and 6, the shape of the flow profile and the value of contraction coefficient are very sensitive to the mesh refinement. Figure 9 clearly shows that the refinement of the mesh in vertical direction has improving effect on the flow profile. Regarding the physical appearance of the computed profiles in Figure 9, Mesh 1 produces a contraction profile which is far from the real occurrence. On the other hand, Mesh 3 seems to give the most realistic surface profile with contraction coefficient of $C_c = 0.71$, and contraction length of $L_c = 14.8$ mm, these two quantities are quite in agreement with the experimental values of 0.69 and 14 mm, respectively. From the computed flow profiles in Figure 9, Mesh 3 appears to be the most suitable of the three meshes in predicting the flow profile in the contraction region under the gate.

During the running process of the VOF analysis, the development of the computational free-surface profile within the solution domain, using Mesh 3, is given in Figure 10. According to the VOF analysis, the time dependent filling process of the solution domain is demonstrated through Figures 10(a) to 10(f). As may be seen in Figures 10(e) and 10(f), the flow profiles are almost identical at times $t = 13$ s and 15 s, that means the filling process of the

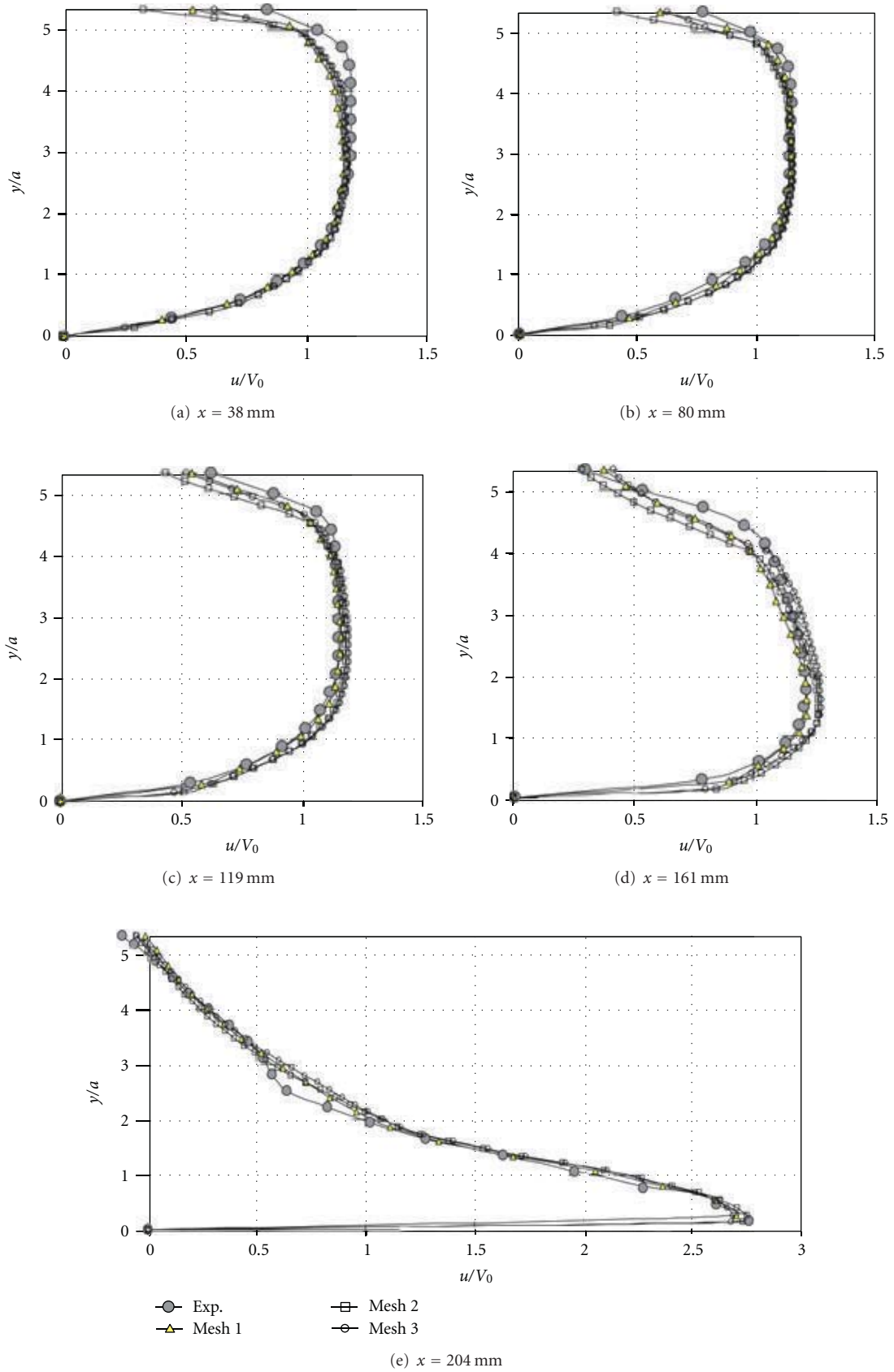

(a) $x = 38$ mm (b) $x = 80$ mm

(c) $x = 119$ mm (d) $x = 161$ mm

(e) $x = 204$ mm

Figure 5: Comparison of experimental and computed horizontal velocity profiles for three meshes.

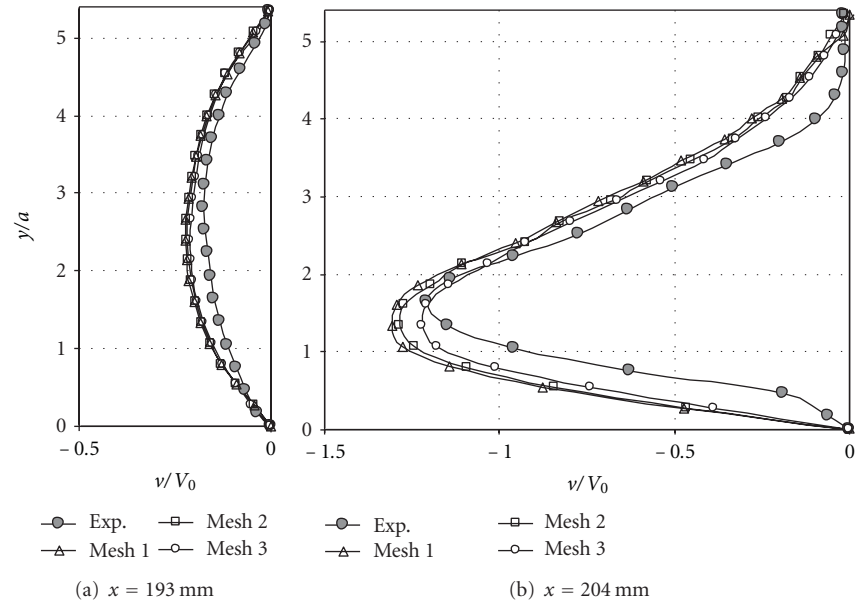

Figure 6: Comparison of experimental and computed vertical velocities for three meshes.

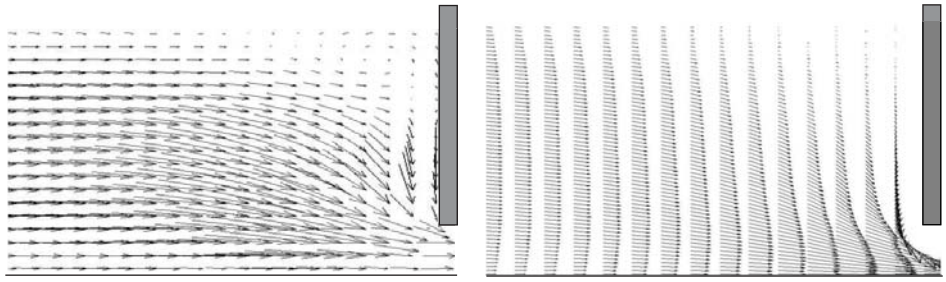

Figure 7: Measured and computed velocity vector fields upstream of the gate using Mesh 3.

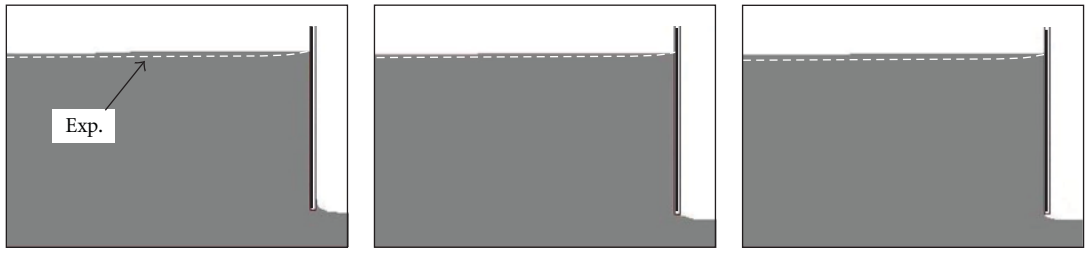

Figure 8: Computed and measured flow profiles just upstream of the gate for three meshes.

solution domain is completed and the computed free-surface development is stabilized at $t = 13$ s. It is seen in Figure 10(e) that the final shape of the computed flow profile displayed within the solution domain is well in agreement with the experimental profile.

From the comparisons of the computed and experimental results discussed above, Mesh 3 among the three computational meshes given in Figure 3(c) may be suggested as the most suitable mesh construction in predicting both the velocity field and the free-surface profile of the present flow case.

The present numerical simulation is based on the 2D analysis of the flow which ignores the side wall effect on the mid-span of the channel. It is widely accepted that this case

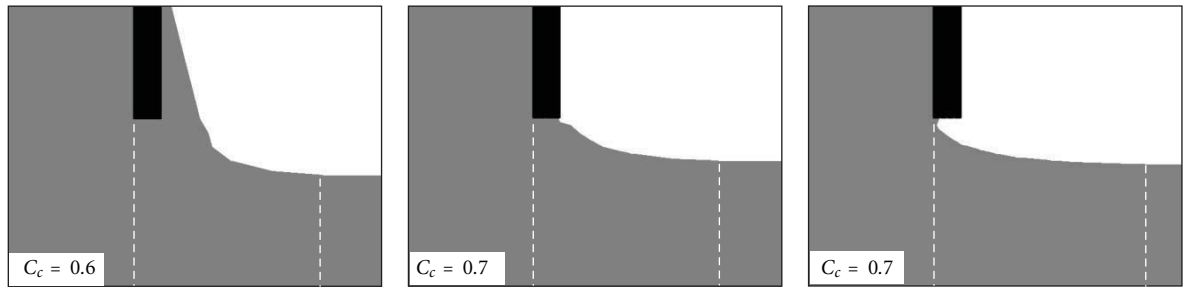

(a) Mesh 1 (b) Mesh 2 (c) Mesh 3

Figure 9: Computed flow profiles in the rapidly varied contraction region under the gate for three meshes.

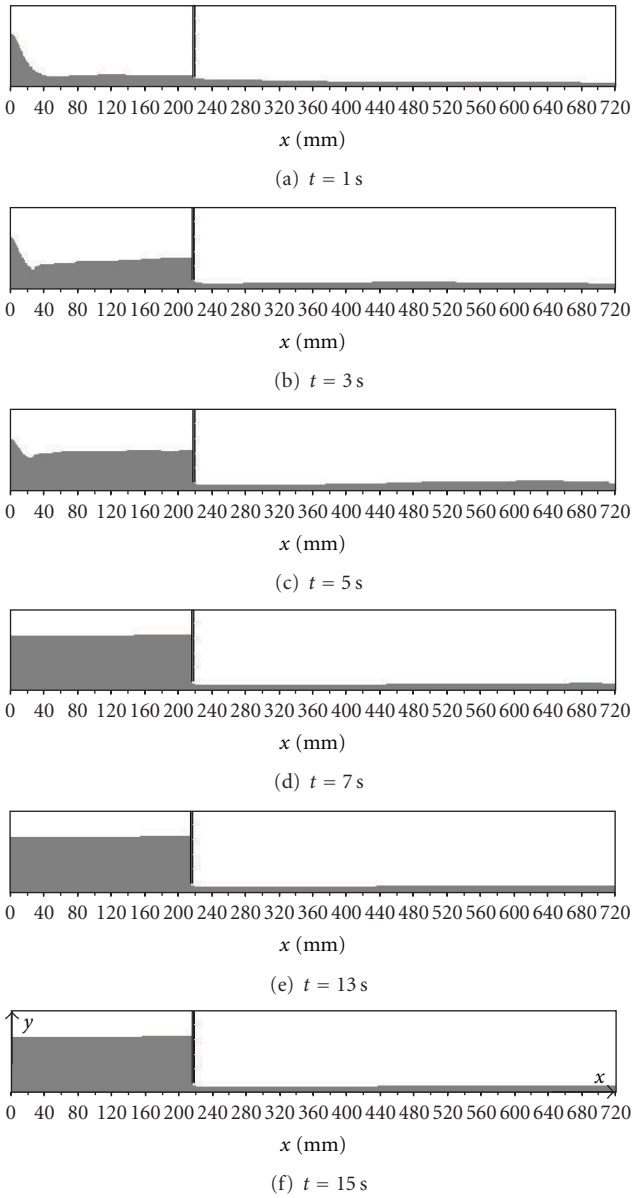

Figure 10: Development of the computed free-surface profile using Mesh 3.

is realized when the aspect ratio of the flow section is greater than 5. This condition is presently well satisfied in the supercritical flow downstream of the gate. In the subcritical upstream region the aspect ratio is 3.125 which is less than 5. However with the existing aspect ratio and considering the level of Reynolds number for the upstream flow, it is expected that the results of the present 2D analysis have acceptable numerical accuracies.

5. Conclusions

Experimental and numerical study of 2D open channel flow under a vertical sluice gate is carried out. Using the standard $k - \varepsilon$ turbulence model, the governing equations of the flow are solved by finite element method. In the numerical simulation, the VOF method is used to determine the flow profile. Experimental and computed velocities and free-surface profiles from three different meshes are presented. A grid convergence analysis is carried out for the verification of computed velocities. Mesh density is relatively increased in the lower part of the flow which comprises the boundary layer of the upstream flow and supercritical downstream flow where rapid variation of the surface profile occurs. In the lower part of the computational domain, different mesh densities in y-direction for each one of the three meshes are used to determine the sensitivity of computed results to the meshing of solution domain. From the comparisons of experimental and numerical results of three structured meshes used in the present computations, it is found that the computed flow profile is much more sensitive to the refinement of the mesh than the computed velocity field. That means in regions where flow profile changes rapidly, the mesh construction must be given special attention to design the mesh refinement in vertical direction. Based on the comparisons of experimental and numerical results of this study, it may be concluded that the VOF-based CFD modeling can successfully be used to analyze the 2D open channel flows which interact with vertical sluice gates, provided that suitable computational mesh is constructed.

References

[1] B. D. Nichols and C. W. Hirt, "Methods for calculating multidimensional, transient free surface flows past bodies," in *Proceedings of the 1st International Conference on Ship Hydrodynamics*, pp. 253–277, Gaithersburg, Md, USA, 1975.

[2] C. W. Hirt and B. D. Nichols, "Volume of fluid (VOF) method for the dynamics of free boundaries," *Journal of Computational Physics*, vol. 39, no. 1, pp. 201–225, 1981.

[3] S. Kvicinsky, F. Longatte, J. L. Kueny, and F. Avellan, "Free surface flows: experimental validation of volume of fluid (VOF) method in the plane wall case," *Proceedings of the 3rd ASME/JSME Joint Fluids Engineering Conference*, pp. 1–8, 1999.

[4] B. M. Savage and M. C. Johnson, "Flow over ogee spillway: physical and numerical model case study," *Journal of Hydraulic Engineering*, vol. 127, no. 8, pp. 640–648, 2001.

[5] N. Ashgriz, T. Barbat, and G. Wang, "A computational Lagrangian-Eulerian advection remap for free surface flows," *International Journal for Numerical Methods in Fluids*, vol. 44, no. 1, pp. 1–32, 2004.

[6] M. A. Sarker and D. G. Rhodes, "Calculation of free-surface profile over a rectangular broad-crested weir," *Flow Measurement and Instrumentation*, vol. 15, no. 4, pp. 215–219, 2004.

[7] M. S. Akoz and M. S. Kirkgoz, "Numerical and experimental analyses of the flow around a horizontal wall-mounted circular cylinder," *Transactions of the Canadian Society for Mechanical Engineering*, vol. 33, no. 2, pp. 189–215, 2009.

[8] M. S. Kirkgoz, M. S. Akoz, and A. A. Oner, "Numerical modeling of flow over a chute spillway," *Journal of Hydraulic Research*, vol. 47, no. 6, pp. 790–797, 2009.

[9] M. S. Akoz, M. S. Kirkgoz, and A. A. Oner, "Experimental and numerical modeling of a sluice gate flow," *Journal of Hydraulic Research*, vol. 47, no. 2, pp. 167–176, 2009.

[10] L. Cassan and G. Belaud, "Experimental and numerical investigation of flow under sluice gates," *Journal of Hydraulic Engineering-ASCE*, vol. 138, no. 4, pp. 367–373, 2012.

[11] D. K. H. Ho, K. Boyes, S. M. Donohoo, and B. Cooper, "Numerical flow analysis for spillways," in *Proceedings of the 43rd Australian National Committee on Large Dams Conference*, pp. 1–11, Hobart, Tasmania, Australia, 2003.

[12] J. S. Montes, "Irrotational flow and real fluid effects under planar sluice gates," *Journal of Hydraulic Engineering*, vol. 123, no. 3, pp. 219–231, 1997.

[13] A. Roth and W. H. Hager, "Underflow of standard sluice gate," *Experiments in Fluids*, vol. 27, no. 4, pp. 339–350, 1999.

[14] Y. Shammaa, D. Z. Zhu, and N. Rajaratnam, "Flow upstream of orifices and sluice gates," *Journal of Hydraulic Engineering*, vol. 131, no. 2, pp. 127–133, 2005.

[15] F. Daneshmand, S. A. S. Javanmard, T. Liaghat, M. M. Moshksar, and J. F. Adamowski, "Numerical solution for two-dimensional flow under sluice gates using the natural element method," *Canadian Journal of Civil Engineering*, vol. 37, no. 12, pp. 1550–1559, 2010.

[16] M. S. Kirkgöz and M. Ardiçlioğlu, "Velocity profiles of developing and developed open channel flow," *Journal of Hydraulic Engineering*, vol. 123, no. 12, pp. 1099–1106, 1997.

[17] J. M. Lennon and D. F. Hill, "Particle image velocity measurements of undular and hydraulic jumps," *Journal of Hydraulic Engineering*, vol. 132, no. 12, pp. 1283–1294, 2006.

[18] S. Dey and A. K. Barbhuiya, "Velocity and turbulence in a scour hole at a vertical-wall abutment," *Flow Measurement and Instrumentation*, vol. 17, no. 1, pp. 13–21, 2006.

[19] F. M. White, *Viscous Fluid Flow*, McGraw-Hill, Singapore, 1991.

[20] D. C. Wilcox, *Turbulence Modeling for CFD*, DCW Industries, Los Angeles, Calif, USA, 2000.

[21] B. E. Launder and D. B. Spalding, "The numerical computation of turbulent flows," *Computer Methods in Applied Mechanics and Engineering*, vol. 3, no. 2, pp. 269–289, 1974.

[22] J. Blazek, *Computational Fluid Dynamics: Principles and Applications*, Elsevier Science, Oxford, UK, 2001.

[23] E. R. van Driest, "On turbulent flow near a wall," *Journal of the Aeronautical Sciences*, vol. 23, no. 11, pp. 1007–1011, 1956.

[24] P. J. Roache, "Verification of codes and calculations," *AIAA Journal*, vol. 36, no. 5, pp. 696–702, 1998.